

South China Sea Rifted Margin

Zhen Sun, Zhimin Jian, Joann M. M Stock, Hans-Christian Larsen, Adam Klaus, Carlos A. Alvarez Zarikian, Anne Briais

▶ **To cite this version:**

Zhen Sun, Zhimin Jian, Joann M. M Stock, Hans-Christian Larsen, Adam Klaus, et al.. South China Sea Rifted Margin. 367/368, 2018, Proceedings of the International Ocean Discovery Program, ⟨10.14379/iodp.proc.367368.2018⟩. ⟨hal-02352167⟩

HAL Id: hal-02352167

https://hal.science/hal-02352167v1

Submitted on 12 Nov 2019

HAL is a multi-disciplinary open access archive for the deposit and dissemination of scientific research documents, whether they are published or not. The documents may come from teaching and research institutions in France or abroad, or from public or private research centers.

L'archive ouverte pluridisciplinaire **HAL**, est destinée au dépôt et à la diffusion de documents scientifiques de niveau recherche, publiés ou non, émanant des établissements d'enseignement et de recherche français ou étrangers, des laboratoires publics ou privés.

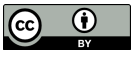

Distributed under a Creative Commons CC BY 4.0 - Attribution - International License

Proceedings of the International Ocean Discovery Program

Volume 367/368

South China Sea Rifted Margin

Expeditions 367 and 368 of the riserless drilling platform
from and to Hong Kong, China
Sites U1499–U1500
7 February–9 April 2017
and
Hong Kong, China, to Shanghai, China
Sites U1501–U1505
9 April–11 June 2017

Volume authorship
Sun, Z., Jian, Z., Stock, J.M., Larsen, H.C., Klaus, A., Alvarez Zarikian, C.A., and the Expedition 367/368 Scientists

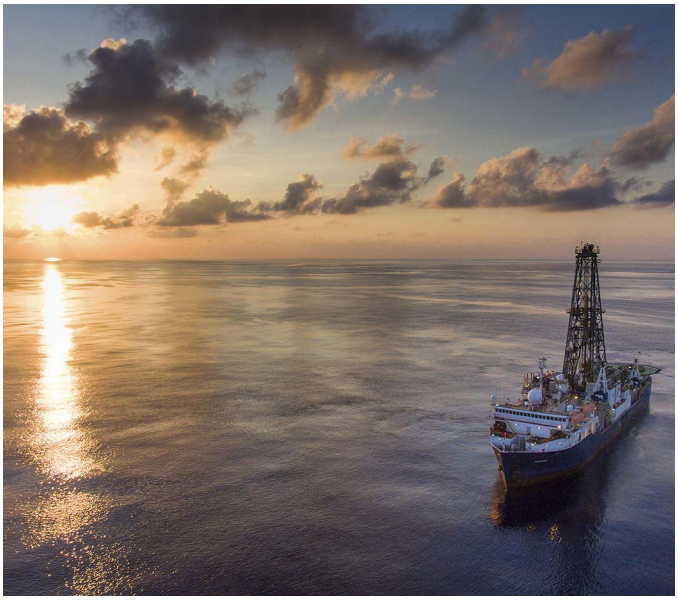

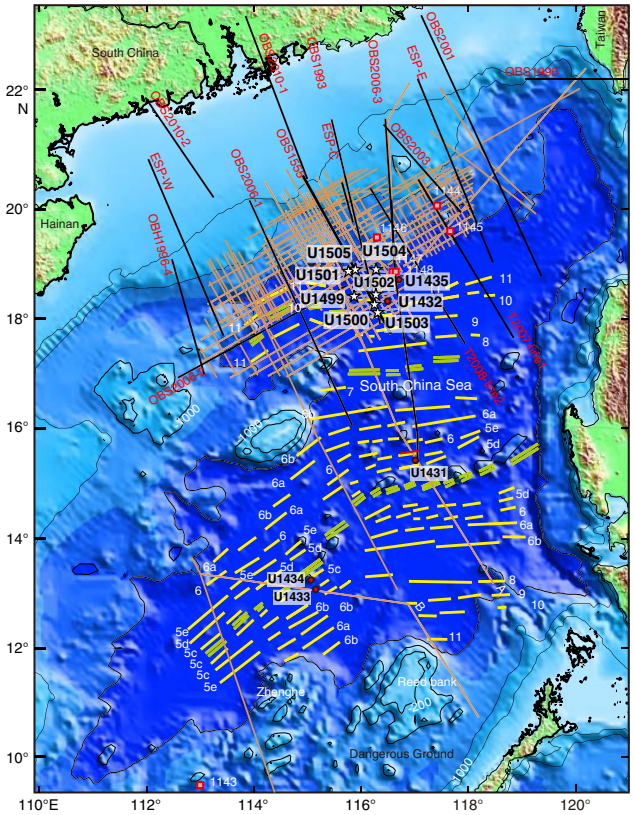

Published by
International Ocean Discovery Program

Publisher's notes

This publication was prepared by the *JOIDES Resolution* Science Operator (JRSO) at Texas A&M University (TAMU) as an account of work performed under the International Ocean Discovery Program (IODP). Funding for IODP is provided by the following international partners:

National Science Foundation (NSF), United States
Ministry of Education, Culture, Sports, Science and Technology (MEXT), Japan
European Consortium for Ocean Research Drilling (ECORD)
Ministry of Science and Technology (MOST), People's Republic of China
Korea Institute of Geoscience and Mineral Resources (KIGAM)
Australia-New Zealand IODP Consortium (ANZIC)
Ministry of Earth Sciences (MoES), India
Coordination for Improvement of Higher Education Personnel (CAPES), Brazil

Any opinions, findings, and conclusions or recommendations expressed in this publication are those of the author(s) and do not necessarily reflect the views of the participating agencies, TAMU, or Texas A&M Research Foundation.

The bulk of the shipboard-collected core data from this expedition is accessible at **http://iodp.tamu.edu/database/index.html**. If you cannot access this site or need additional data, please contact Data Librarian, International Ocean Discovery Program *JOIDES Resolution* Science Operator, Texas A&M University, 1000 Discovery Drive, College Station TX 77845-9547, USA. Tel: (979) 845-8495; Fax: (979) 458-1617; Email: **database@iodp.tamu.edu**.

A complete set of the logging data collected during the expedition is available at **http://mlp.ldeo.columbia.edu/logdb/scientific_ocean_drilling**. If you have problems downloading the data, wish to receive additional logging data, or have questions regarding the data, please contact Database Administrator, Borehole Research Group, Lamont-Doherty Earth Observatory of Columbia University, PO Box 1000, 61 Route 9W, Palisades NY 10964, USA. Tel: (845) 365-8343; Fax: (845) 365-3182; Email: **logdb@ldeo.columbia.edu**.

Supplemental data were provided by the authors and may not conform to IODP publication formats.

JRSO expedition photos are the property of IODP and are public access.

Some core photographs have been tonally enhanced to better illustrate particular features of interest. High-resolution images are available upon request.

Cover photograph shows the R/V *JOIDES Resolution* on site in the South China Sea during Expedition 368. Photo credit: Shuhao Xie and IODP JRSO.

Copyright

Except where otherwise noted, this work is licensed under the Creative Commons Attribution 4.0 International (CC BY 4.0) license (**https://creativecommons.org/licenses/by/4.0/**). Unrestricted use, distribution, and reproduction are permitted, provided the original author and source are credited.

Examples of how to cite this volume or part of this volume are available at **http://publications.iodp.org/proceedings/367_368/367368title.html#bib**.

ISSN
World Wide Web: 2377-3189

Volume DOI
https://doi.org/10.14379/iodp.proc.367368.2018

Publication date
28 September 2018

Contents

Expedition reports

Chapters

Expedition 367/368 summary
H.C. Larsen et al.

Expedition 367/368 methods
Z. Sun et al.

Site U1499
Z. Sun et al.

Site U1500
J.M. Stock et al.

Site U1501
H.C. Larsen et al.

Site U1502
H.C. Larsen et al.

Site U1503
H.C. Larsen et al.

Site U1504
H.C. Larsen et al.

Site U1505
Z. Jian et al.

Core descriptions

Visual core descriptions (VCDs) are presented in PDF files for each site. Smear slides and/or thin sections are presented in PDF and/or CSV files for each site and/or hole (CSV files are available in the CORES directory). The entire set of core images in PDF is available in the IMAGES directory.

Site U1499
Visual core descriptions · Smear slides · **Thin sections**

Site U1500
Visual core descriptions · Smear slides · **Thin sections**

Site U1501
Visual core descriptions · Smear slides · **Thin sections**

Site U1502
Visual core descriptions · Smear slides · **Thin sections**

Site U1503
Visual core descriptions

Site U1504
Visual core descriptions · Smear slides · **Thin sections**

Site U1505
Visual core descriptions · Smear slides

Supplementary material

Supplementary material for the Volume 367/368 expedition reports includes DESClogik workbooks in Microsoft Excel format, an original seismic section figure in PDF and Adobe Illustrator format, downhole measurement data in PDF, and captions in Microsoft Word format. A full list of directories can be found in SUPP_MAT in the volume zip folder or on the **Supplementary material for Volume 367/368 expedition reports** web page.

Expedition research results

Data reports

Titles are available in **HTML**.

Syntheses

Titles are available in **HTML**.

Drilling location maps

A site map showing the drilling locations for this expedition and maps showing the drilling locations of all International Ocean Discovery Program (IODP) expeditions, produced using QGIS (**http://www.qgis.org**), and all Integrated Ocean Drilling Program, Ocean Drilling Program (ODP), and Deep Sea Drilling Project (DSDP) expeditions, produced using Generic Mapping Tools (GMT) of Paul Wessel and Walter H.F. Smith (**http://gmt.soest.hawaii.edu**), are available in PDF.

IODP Expedition 367/368 site map
IODP map (Expeditions 349–357, 359–368, and 370)
Integrated Ocean Drilling Program map (Expeditions 301–348)
ODP map (Legs 100–210)
DSDP map (Legs 1–96)

Dedication



We dedicate this volume to our good friend and colleague Dr. Kirk D. McIntosh who passed away during Expedition 368 at the age of 59. Those who worked closely with Kirk on the years-long preparations for the South China Sea expeditions learned to know him as a person of the finest qualities. His prior work in the region was crucial to the scientific foundation of the project, and the rigor that he applied in processing and interpreting the seismic data greatly helped to shape our final drilling plans. His treatment for leukemia prevented him from sailing with us, but he remained engaged in our discussions even as we sailed. We were devastated by the news of his sudden death. His contributions will not be forgotten. Photo credit: David Stephens, Bureau of Economic Geology, University of Texas at Austin.

Acknowledgments

Complementary Project Proposal (CPP) Expeditions 367 and 368 received generous funding from the Ministry of Science and Technology (MOST; China). We are grateful to the China National Offshore Oil Corporation (CNOOC) for their powerful support with the regional deep crustal seismic data on which the entire project builds and to the Guangzhou Marine Geological Survey (GMGS) for releasing high-resolution bathymetry data from around the drilling sites. The success of the expeditions, from proposal preparation to the supporting work related to the expeditions, greatly benefited from support by the IODP-China office and the major research program "The South China Sea Deep" (2011–2018) funded by the National Natural Science Foundation of China (NSFC). We express our most sincere thanks to Professor Pinxian Wang, who made it possible to develop the proposal into two CPP expeditions. Professor Chunfeng Li is also greatly appreciated for his contributions to proposal preparation and partial data support.

Foreword

The International Ocean Discovery Program (IODP) represents the latest incarnation of almost five decades of scientific ocean drilling excellence and is generally accepted as the most successful international collaboration in the history of the Earth sciences. IODP builds seamlessly on the accomplishments of previous phases: the Deep Sea Drilling Project, Ocean Drilling Program, and Integrated Ocean Drilling Program. The 2013–2023 IODP Science Plan (*Illuminating Earth's Past, Present, and Future*) defines four themes and thirteen challenges for this decade of scientific ocean drilling that are both of fundamental importance in understanding how the Earth works and of significant relevance to society as the Earth changes, at least in part in response to anthropogenic forcing. This phase of IODP represents a renewed level of international collaboration in bringing diverse drilling platforms and strategies to increasing our understanding of climate and ocean change, the deep biosphere and evolution of ecosystems, connections between Earth's deep processes and surface manifestations, and geologically induced hazards on human timeframes.

The *Proceedings of the International Ocean Discovery Program* presents the scientific and engineering results of IODP drilling projects, expedition by expedition. As in the preceding Integrated Ocean Drilling Program, expeditions in the new IODP are conducted by three implementing organizations, each providing a different drilling capability. These are the US Implementing Organization (USIO; through September 2014) and the *JOIDES Resolution* Science Operator (JRSO; as of October 2014), providing the leased commercial vessel *JOIDES Resolution* for riserless drilling operations; JAMSTEC's Center for Deep Earth Exploration (CDEX), providing the drillship *Chikyu* for riser and occasional riserless operations; and the European Consortium for Ocean Research Drilling (ECORD) Science Operator (ESO), providing "mission-specific" platforms (MSPs) for expeditions that extend the IODP operational range where neither drillship is suitable, for example, in polar environments and in shallow waters. Scheduling decisions for each capability are made by three independent Facility Boards, each of which includes scientists, operators, and platform funding partners: the *JOIDES Resolution* Facility Board (JRFB), *Chikyu* IODP Board (CIB), and ECORD Facility Board (EFB). At the beginning of the new IODP, the three Facility Boards agreed to utilize Publication Services at the USIO and now the JRSO for production of all expedition *Proceedings* volumes and reports.

The new IODP differs from prior scientific ocean drilling programs in that it has neither a central management organization nor commingled funding for program-wide activities. Yet this phase of IODP retains a fundamental integrative structural element: a "bottom-up" evaluation of all proposals for drilling expeditions by a single advisory structure composed of scientists representing all international program partners. International scientists may submit drilling proposals to the Science Support Office; all submitted proposals are then evaluated by a Science Evaluation Panel in the context of the Science Plan.

The new IODP also has a second internationally integrative level for high-level discussion and consensus-building: the IODP Forum. The Forum is charged with assessing program-wide progress toward achieving the Science Plan. At present, IODP involves 26 international financial partners, including the United States, Japan, an Australia/New Zealand consortium (ANZIC), Brazil, China, India, South Korea, and the eighteen members of ECORD (Austria, Belgium, Canada, Denmark, Finland, France, Germany, Ireland, Israel, Italy, the Netherlands, Norway, Poland, Portugal, Spain, Sweden, Switzerland, and the United Kingdom). This enhanced membership in the new IODP represents a remarkable level of international collaboration that remains one of the greatest ongoing strengths of scientific ocean drilling.

James A. Austin Jr.
Chair, IODP Forum

International Ocean Discovery Program

JOIDES Resolution Science Operator

Website: **http://iodp.tamu.edu**

IODP JRSO
International Ocean Discovery Program
Texas A&M University
1000 Discovery Drive
College Station TX 77845-9547
USA
Tel: (979) 845-2673; Fax: (979) 845-4857
Email: **information@iodp.tamu.edu**

IODP JRSO Curation and Laboratories
IODP Gulf Coast Repository (GCR)
Texas A&M University
1000 Discovery Drive
College Station TX 77845-9547
USA
Tel: (979) 845-8490; Fax: (979) 845-1303
Email: **rumford@iodp.tamu.edu**

European Consortium for Ocean Research Drilling, Science Operator (ESO)

Website: **http://www.ecord.org**

IODP ESO Coordinator: Science, Logistics, and Operations
British Geological Survey
The Lyell Centre
Research Avenue South
Edinburgh EH14 4AP
United Kingdom
Tel: (44) 131-667-1000; Fax: (44) 131-668-4140
Email: **eso@bgs.ac.uk**

IODP ESO Curation and Laboratories
IODP Bremen Core Repository (BCR)
Center for Marine Environmental Sciences (MARUM)
University of Bremen
Leobener Strasse
28359 Bremen
Germany
Tel: (49) 421-218-65560; Fax: (49) 421-218-98-65560
Email: **bcr@marum.de**

IODP ESO Petrophysics
European Petrophysics Consortium
Department of Geology
University of Leicester
Leicester LE1 7RH
United Kingdom
Tel: (44) 116-252-3611; Fax: (44) 116-252-3918
Email: **sjd27@leicester.ac.uk**

Japan Agency for Marine-Earth Science and Technology (JAMSTEC)

Website: **http://www.jamstec.go.jp/chikyu/e**

IODP Japan Science Operator
Center for Deep Earth Exploration (CDEX)
Japan Agency for Marine-Earth Science and Technology
Yokohama Institute for Earth Sciences
3175-25 Showa-machi
Kanazawa-ku, Yokohama
Kanagawa 236-0001
Japan
Tel: (81) 45-778-5643; Fax: (81) 45-778-5704
Email: **cdex@jamstec.go.jp**

IODP Japan Curation and Laboratories
IODP Kochi Institute for Core Sample Research (KCC)
Japan Agency for Marine-Earth Science and Technology
200 Monobe Otsu
3175-25 Showa-machi
Nankoku City, Kochi 783-8502
Japan
Tel: (81) 88-864-6705; Fax: (81) 88-878-2192
Email: **kcc.contact@jamstec.go.jp**

Expedition 367/368 participants*

Expedition 367 scientists

Zhen Sun
Co-Chief Scientist
CAS Key Laboratory of Ocean and Marginal Sea Geology
South China Sea Institute of Oceanology
China
zhensun@scsio.ac.cn

Joann M. Stock
Co-Chief Scientist
Division of Geological and Planetary Sciences
California Institute of Technology
USA
jstock@gps.caltech.edu

Adam Klaus
Expedition Project Manager/Staff Scientist
International Ocean Discovery Program
Texas A&M University
USA
aklaus@iodp.tamu.edu

Jacopo Boaga
Petrophysics (Physical Properties) Specialist
Dipartimento di Geoscienze
Università degli Studi di Padova
Italy
jacopo.boaga@unipd.it

Anne Briais
Petrophysics (Physical Properties) Specialist
Observatoire Midi-Pyrenes
Centre National de la Recherche Scientifique
France
anne.briais@cnrs.fr

Yifeng Chen
Inorganic Geochemist
Guangzhou Institute of Geochemistry
Chinese Academy of Sciences
China
yfchen@gig.ac.cn

Michael J. Dorais
Inorganic Geochemist
Department of Geological Sciences
Brigham Young University
USA
dorais@byu.edu

Akira Furusawa
Paleontologist (foraminifers)
Department of Geoscience
Shimane University
Japan
zerozaki.1130@gmail.com

Jessica L. Hinojosa
Sedimentologist
Division of Geological and Planetary Sciences
California Institute of Technology
USA

Present affiliation (20 September 2017):
Shell International Exploration and Production
USA
j.hinojosa@shell.com

Tobias W. Höfig
Petrologist
International Ocean Discovery Program
Texas A&M University
USA
hoefig@iodp.tamu.edu

Kan-Hsi Hsiung
Sedimentologist
Japan Agency for Marine-Earth Science and Technology
Japan
hsiung@jamstec.go.jp

Baoqi Huang
Paleontologist (foraminifers)
Department of Geology
Peking University
China
bqhuang@pku.edu.cn

Xiao-Long Huang
Petrologist
Guangzhou Institute of Geochemistry
Chinese Academy of Sciences
China
xlhuang@gig.ac.cn

Benjamin G. Johnson
Sedimentologist
Geology and Geography
West Virginia University
USA
bgjohnson@mix.wvu.edu

Chao Lei
Petrophysics (Physical Properties) Specialist
Department of Marine Science
College of Marine Science and Technology
China University of Geosciences in Wuhan
China
clei@cug.edu.cn

*Affiliations at time of expedition, except where updated by participants.

Li Li
Organic Geochemist
State Key Laboratory of Marine Geology
Tongji University
China
lilitju@tongji.edu.cn

Zhifei Liu
Sedimentologist
State Key Laboratory of Marine Geology
Tongji University
China
lzhifei@tongji.edu.cn

Antonio Luna
Petrologist
Department of Geology
University of South Florida, Tampa
USA
aluna2@mail.usf.edu

Claudia Lupi
Paleontologist (nannofossils)
Department of Earth and Environmental Sciences
Università degli Studi di Pavia
Italy
claudia.lupi@unipv.it

Anders J. McCarthy
Petrologist
Institute of Earth Sciences
University of Lausanne
Switzerland
anders.mccarthy@unil.ch

Michael Nirrengarten
Structural Geologist
Institut de Physique du Globe de Strasbourg
France

Present affiliation (20 September 2017):
Laboratoire Géosciences et Environnement Cergy (GEC)
Maison Internationale de la Recherche
Université de Cergy-Pontoise
France
michael.nirrengarten@u-cergy.fr

Caroline M. Robinson
Sedimentologist
School of Earth Sciences
Ohio State University
USA
robinson.2071@osu.edu

Isabel Sauermilch
Petrophysics (Physical Properties) Specialist
Institute for Marine and Antarctic Studies (IMAS)
University of Tasmania
Australia
isabel.sauermilch@utas.edu.au

Steven M. Skinner
Paleomagnetist
Department of Geology
California State University, Sacramento
USA
steven.skinner@csus.edu

Xiang Su
Paleontologist (nannofossils)
CAS Key Laboratory of Ocean and Marginal Sea Geology
South China Sea Institute of Oceanology, Chinese Academy of Sciences
China
suxiang@scsio.ac.cn

Rong Xiang
Paleontologist (foraminifers)
CAS Key Laboratory of Ocean and Marginal Sea Geology
South China Sea Institute of Oceanology, Chinese Academy of Sciences
China
rxiang@scsio.ac.cn

Rajeev Yadav
Petrophysics (Physical Properties) Specialist
Department of Marine Geophysics
National Centre for Antarctic and Ocean Research (NCAOR)
India
ryadav@ncaor.gov.in

Liang Yi
Paleomagnetist
State Key Laboratory of Marine Geology
Tongji University
China
yi.liang82@gmail.com

Cuimei Zhang
Structural Geologist
CAS Key Laboratory of Ocean and Marginal Sea Geology
South China Sea Institute of Oceanology, Chinese Academy of Sciences
China
cmzhang@scsio.ac.cn

Jinchang Zhang
Petrophysics (Physical Properties) Specialist
CAS Key Laboratory of Ocean and Marginal Sea Geology
South China Sea Institute of Oceanology, Chinese Academy of Sciences
China
jzhang@scsio.ac.cn

Yang Zhang
Paleomagnetist
Department of Earth and Atmospheric Sciences
Purdue University
USA
zhan2214@purdue.edu

Ning Zhao
Sedimentologist
Department of Geology and Geophysics
Woods Hole Oceanographic Institution
USA

Present affiliation (20 September 2017):
Department of Geology and Geophysics
Max Planck Institute for Chemistry
Germany
ningzhao2009@hotmail.com

Lifeng Zhong
Petrologist
School of Marine Sciences
Sun Yat-Sen University
China
zhonglf@scsio.ac.cn

Expedition 367 observer

Chih-Chieh Su
Sedimentologist/Observer
Institute of Oceanography
National Taiwan University
Taiwan
donccsu@ntu.edu.tw

Expedition 367 education and outreach

Alessia Cicconi
Education/Outreach Officer
Liceo Classico "F. Stabili - E. Trebbiani" Ascoli Piceno
School of Science and Technology
Geology Division
University of Camerino
Italy
alessia.cicconi@unicam.it

Jiansong Zhang
Education/Outreach Officer
China
13311669691@163.com

Expedition 368 scientists

Zhimin Jian
Co-Chief Scientist
School of Ocean and Earth Science
Tongji University
China
jian@tongji.edu.cn

Hans Christian Larsen
Co-Chief Scientist
Geological Survey of Denmark and Greenland
Denmark
hclarseniodp@gmail.com

Also at:
Tongji University
China

Carlos A. Alvarez Zarikian
Expedition Project Manager/Staff Scientist
International Ocean Discovery Program
Texas A&M University
USA
zarikian@iodp.tamu.edu

Stephen A. Bowden
Organic Geochemist
School of Geosciences
University of Aberdeen
United Kingdom
s.a.bowden@abdn.ac.uk

Deniz Cukur
Petrophysics (Physical Properties) Specialist
Marine Geology Department
Petroleum & Marine Research Division
Korea Institute of Geoscience and Mineral Resources (KIGAM)
Republic of Korea
dcukur@kigam.re.kr

Kelsie A. Dadd
Sedimentologist
School of Geosciences
University of Sydney
Australia
kelsie.dadd@sydney.edu.au

Weiwei Ding
Structural Geologist
Key Laboratory of Submarine Geoscience
Second Institute of Oceanography (SIO), State Oceanic Administration (SOA)
China
wwding@sio.org.cn

Eric C. Ferré
Paleomagnetist
Department of Geology
Southern Illinois University at Carbondale
USA
eferre@geo.siu.edu

Fabricio Ferreira
Paleontologist (foraminifers)
Institute for Geosciences, Universidade Federal Fluminense (UFF), Brazil
CAPES Foundation
Ministry of Education of Brazil
ferreira_paleo@hotmail.com

Aaron J. Gewecke
Paleontologist (diatoms)
Earth and Atmospheric Sciences
University of Nebraska, Lincoln
USA
aarongewecke@gmail.com

Enqing Huang
Petrophysics (Physical Properties) Specialist
School of Ocean and Earth Science
Tongji University
China
ehuang@tongji.edu.cn

Shijun Jiang
Paleontologist (nannofossils)
College of Life Science and Technology
Jinan University
China
sjiang@jnu.edu.cn

Haiyan Jin
Paleontologist (foraminifers)
State Key Laboratory of Marine Geology
Tongji University
China
jinhy@tongji.edu.cn

Robert M. Kurzawski
Petrologist/Structural Geologist
GEOMAR Helmholtz Center for Ocean Research Kiel
Christian-Albrechts-Universität zu Kiel
Germany
rkurzawski@geomar.de

Baohua Li
Paleontologist (foraminifers)
Department of Micropalaeontology
Nanjing Institute of Geology and Palaeontology
Chinese Academy of Sciences
China
bh-li@nigpas.ac.cn

Yanping Li
Inorganic Geochemist
School of Geographical and Oceanographical Sciences
Nanjing University
China
ypli@nju.edu.cn

Jian Lin
Petrophysics (Physical Properties) Specialist
Department of Geology and Geophysics
Woods Hole Oceanographic Institution
USA
jlin@whoi.edu

Chang Liu
Sedimentologist
Department of Geology and Geophysics
Louisiana State University
USA
cliu14@lsu.edu

Chuanlian Liu
Paleontologist (nannofossils)
School of Ocean and Earth Science
Tongji University
China
liucl@tongji.edu.cn

Geoffroy Mohn
Petrologist/Structural Geologist
Laboratoire Géosciences et Environnement Cergy (GEC)
Maison Internationale de la Recherche
Université de Cergy-Pontoise
France
Geoffroy.Mohn@u-cergy.fr

Lachit Singh Ningthoujam
Petrophysics (Physical Properties) Specialist
Department of Marine Geophysics
National Centre for Antarctic and Ocean Research (NCAOR)
India
lachit@ncaor.gov.in

Nobuaki Osono
Petrophysics (Physical Properties) Specialist
Faculty of Science
Graduate School of Science and Technology for Innovation, Yamaguchi University
Japan
t004dg@gmail.com

David W. Peate
Petrologist
Earth & Environmental Sciences
University of Iowa
USA
david-peate@uiowa.edu

Patricia Persaud
Petrophysics (Physical Properties) Specialist
Department of Geology and Geophysics
Louisiana State University
USA
ppersaud@lsu.edu

Ning Qiu
Petrophysics (Physical Properties) Specialist
Key Laboratory of Marginal Sea Geology
Chinese Academy of Sciences
China
ningqiu@scsio.ac.cn

Sara Satolli
Paleomagnetist
Department of Engineering and Geology
University of Chieti-Pescara
Italy
sara.satolli@unich.it

Julie C. Schindlbeck
Sedimentologist
GEOMAR Helmholtz Center for Ocean Research Kiel
Germany
jschindlbeck@geomar.de

Present affiliation (20 September 2017):
Institute of Earth Sciences
Heidelberg University
Germany

Susanne M. Straub
Sedimentologist/Petrologist
Lamont-Doherty Earth Observatory
Columbia University
USA
smstraub@ldeo.columbia.edu

Liyan Tian
Inorganic Geochemist
Institute of Deep-sea Science and Engineering
Chinese Academy of Sciences
China
lytian@idsse.ac.cn

Froukje M. van der Zwan
Petrologist
Institute of Geosciences
Christian Albrechts University Kiel
Germany
fvdz@gpi.uni-kiel.de

Shiming Wan
Sedimentologist
Institute of Oceanology
Chinese Academy of Sciences
China
wanshiming@ms.qdio.ac.cn

Huaichun Wu
Paleomagnetist
School of Ocean Sciences
China University of Geosciences
China
whcgeo@cugb.edu.cn

Guangfa Zhong
Sedimentologist
School of Ocean and Earth Science
Tongji University
China
gfz@tongji.edu.cn

Expedition 368 observers

Pai-Sen Yu
Paleontologist (foraminifers)
National Applied Research Laboratories (NARLabs)
Taiwan Ocean Research Institute (TORI)
Taiwan
epson_yu@narlabs.org.tw

Gailun Zhang
China
jyjj1234567@126.com

Expedition 368 education and outreach

Amanda M. Wolfe
Education/Outreach Officer
USA
wolfe.amanda.marie@gmail.com

Shuhao Xie
Education/Outreach Officer
China
rafaelxie@qq.com

Operational and technical staff

SIEM Offshore AS officials

Expedition 367

Terry Skinner
Master of the Drilling Vessel

Sam McLelland
Offshore Installation Manager

Expedition 368

Steve Bradley
Master of the Drilling Vessel

Wayne Malone
Offshore Installation Manager

JRSO shipboard personnel and technical representatives

Expedition 367

Robert Aduddell
Engineer

Alexis Armstrong
X-Ray Laboratory

Heather Barnes
Assistant Laboratory Officer

Chad Broyles
Curatorial Specialist

Michael Cannon
Marine Computer Specialist

Etienne Claassen
Marine Instrumentation Specialist

Ty Cobb
Physical Properties Laboratory

William Crawford
Senior Imaging Specialist

Benjamin Daniel
Core Laboratory

Roy Davis
Laboratory Officer

David Fackler
Applications Developer

Seth Frank
Thin Section Laboratory

Edwin Garrett
Paleomagnetism Laboratory

Rachael Gray
Core Laboratory

Jan Jurie Kotze
Marine Instrumentation Specialist

Zenon Mateo
Underway Geophysics Laboratory/Downhole Tools Laboratory

Stephen Midgley
Operations Superintendent

Erik Moortgat
Chemistry Laboratory

Chieh Peng
Assistant Laboratory Officer

Vincent Percuoco
Chemistry Laboratory

Alyssa Stephens
Publications Specialist

Kerry Swain
Logging Engineer

Steven Thomas
Marine Computer Specialist

Rui Wang
Applications Developer

Expedition 368

Susan Boehm
Thin Section Laboratory

Lisa Brandt
Chemistry Laboratory

Lisa Crowder
Assistant Laboratory Officer

Aaron de Loach
Core Laboratory

Keith Dupuis
Underway Geophysics Laboratory

Sheryl Frazier
Physical Properties Laboratory

Timothy Fulton
Senior Imaging Specialist

Clayton Furman
Logging Engineer

Randy Gjesvold
Marine Instrumentation Specialist

Kevin Grigar
Operations Superintendent

Sandra Herrmann
Assistant Laboratory Officer

Michael Hodge
Marine Computer Specialist

Minh Nhut Huynh
Marine Computer Specialist

Nicolette Lawler
X-Ray Laboratory

Brittany Martinez
Curatorial Specialist

Aaron Mechler
Chemistry Laboratory

Mike Meiring
Engineer

William Mills
Laboratory Officer

Algie Morgan
Applications Developer

Beth Novak
Paleomagnetism Laboratory

Garrick Van Rensburg
Marine Instrumentation Specialist

Jean Wulfson
Publications Specialist

Hai (James) Zhao
Applications Developer

IODP Publication Services staff*

Douglas Cummings
Graphics Specialist II

Gudelia ("Gigi") Delgado
Publications Coordinator

Ekanta Desai
Graphics Specialist II

Patrick H. Edwards
Production Editor IV

Jaime A. Gracia
Supervisor of Production and Graphics

Jenni Hesse
Editor III

Rhonda Kappler
Graphics Specialist III

Shana C. Lewis
Editor III

Ginny Lowe
Reports Coordinator

Amy McWilliams
Supervisor of Editing

Julie Myers
Production Editor II

Lorri Peters
Manager of Publication Services

Sandi Sherar Ruddick
Editor II

Kenneth Sherar
Production Editor III

Alyssa Stephens
Graphics Specialist III

Crystal Wolfe
Production Editor III

Jean Wulfson
Graphics Specialist III

Ann Yeager
Distribution Specialist

*At time of publication.

Expedition-related bibliography*

IODP publications

Scientific Prospectus

Sun, Z., Stock, J., Jian, Z., McIntosh, K., Alvarez-Zarikian, C.A., and Klaus, A., 2016. *Expedition 367/368 Scientific Prospectus: South China Sea Rifted Margin.* International Ocean Discovery Program. **https://doi.org/10.14379/iodp.sp.367368.2016**

Sun, Z., Stock, J., Jian, Z., Larsen, H.-C., Alvarez Zarikian, C.A., and Klaus, A., 2016. *Expedition 367/368 Scientific Prospectus Addendum: South China Sea Rifted Margin.* International Ocean Discovery Program. **https://doi.org/10.14379/iodp.sp.367368add.2016**

Preliminary Report

Sun, Z., Stock, J., Klaus, A., and the Expedition 367 Scientists, 2018. *Expedition 367 Preliminary Report: South China Sea Rifted Margin.* International Ocean Discovery Program. **https://doi.org/10.14379/iodp.pr.367.2018**

Jian, Z., Larsen, H.C., Alvarez Zarikian, C.A., and the Expedition 368 Scientists, 2018. *Expedition 368 Preliminary Report: South China Sea Rifted Margin.* International Ocean Discovery Program. **https://doi.org/10.14379/iodp.pr.368.2018**

Proceedings volume

Sun, Z., Jian, Z., Stock, J.M., Larsen, H.C., Klaus, A., Alvarez Zarikian, C.A., and the Expedition 367/368 Scientists, 2018. *South China Sea Rifted Margin*. Proceedings of the International Ocean Discovery Program, 367/368: College Station, TX (International Ocean Discovery Program). **https://doi.org/10.14379/iodp.proc.367368.2018**

Expedition reports

Larsen, H.C., Sun, Z., Stock, J.M., Jian, Z., Alvarez Zarikian, C.A., Klaus, A., Boaga, J., Bowden, S.A., Briais, A., Chen, Y., Cukur, D., Dadd, K.A., Ding, W., Dorais, M.J., Ferré, E.C., Ferreira, F., Furusawa, A., Gewecke, A.J., Hinojosa, J.L., Höfig, T.W., Hsiung, K.-H., Huang, B., Huang, E., Huang, X.-L., Jiang, S., Jin, H., Johnson, B.G., Kurzawski, R.M., Lei, C., Li, B., Li, L., Li, Y., Lin, J., Liu, C., Liu, C., Liu, Z., Luna, A., Lupi, C., McCarthy, A.J., Mohn, G., Ningthoujam, L.S., Nirrengarten, M., Osono, N., Peate, D.W., Persaud, P., Qui, N., Robinson, C.M., Satolli, S., Sauermilch, I., Schindlbeck, J.C., Skinner, S.M., Straub, S.M., Su, X., Tian, L., van der Zwan, F.M., Wan, S., Wu, H., Xiang, R., Yadav, R., Yi, L., Zhang, C., Zhang, J., Zhang, Y., Zhao, N., Zhong, G., and Zhong, L., 2018. Expedition 367/368 summary. *In* Sun, Z., Jian, Z., Stock, J.M., Larsen, H.C., Klaus, A., Alvarez Zarikian, C.A., and the Expedition 367/368 Scientists, *South China Sea Rifted Margin*. Proceedings of the International Ocean Discovery Program, 367/368: College Station, TX (International Ocean Discovery Program). **https://doi.org/10.14379/iodp.proc.367368.101.2018**

Sun, Z., Jian, Z., Stock, J.M., Larsen, H.C., Klaus, A., Alvarez Zarikian, C.A., Boaga, J., Bowden, S.A., Briais, A., Chen, Y., Cukur, D., Dadd, K.A., Ding, W., Dorais, M.J., Ferré, E.C., Ferreira, F., Furusawa, A., Gewecke, A.J., Hinojosa, J.L., Höfig, T.W., Hsiung, K.-H., Huang, B., Huang, E., Huang, X.-L., Jiang, S., Jin, H., Johnson, B.G., Kurzawski, R.M., Lei, C., Li, B., Li, L., Li, Y., Lin, J., Liu, C., Liu, C., Liu, Z., Luna, A., Lupi, C., McCarthy, A.J., Mohn, G., Ningthoujam, L.S., Nirrengarten, M., Osono, N., Peate, D.W., Persaud, P., Qui, N., Robinson, C.M., Satolli, S., Sauermilch, I., Schindlbeck, J.C., Skinner, S.M., Straub, S.M., Su, X., Tian, L., van der Zwan, F.M., Wan, S., Wu, H., Xiang, R., Yadav, R., Yi, L., Zhang, C., Zhang, J., Zhang, Y., Zhao, N., Zhong, G., and Zhong, L., 2018. Expedition 367/368 methods. *In* Sun, Z., Jian, Z., Stock, J.M., Larsen, H.C., Klaus, A., Alvarez Zarikian, C.A., and the Expedition 367/368 Scientists, *South China Sea Rifted Margin*. Proceedings of the International Ocean Discovery Program, 367/368: College Station, TX (International Ocean Discovery Program). **https://doi.org/10.14379/iodp.proc.367368.102.2018**

Sun, Z., Stock, J.M., Klaus, A., Larsen, H.C., Jian, Z., Alvarez Zarikian, C.A., Boaga, J., Bowden, S.A., Briais, A., Chen, Y., Cukur, D., Dadd, K.A., Ding, W., Dorais, M.J., Ferré, E.C., Ferreira, F., Furusawa, A., Gewecke, A.J., Hinojosa, J.L., Höfig, T.W., Hsiung, K.-H., Huang, B., Huang, E., Huang, X.-L., Jiang, S., Jin, H., Johnson, B.G., Kurzawski, R.M., Lei, C., Li, B., Li, L., Li, Y., Lin, J., Liu, C., Liu, C., Liu, Z., Luna, A., Lupi, C., McCarthy, A.J., Mohn, G., Ningthoujam, L.S., Nirrengarten, M., Osono, N., Peate, D.W., Persaud, P., Qui, N., Robinson, C.M., Satolli, S., Sauermilch, I., Schindlbeck, J.C., Skinner, S.M., Straub, S.M., Su, X., Tian, L., van der Zwan, F.M., Wan, S., Wu, H., Xiang, R., Yadav, R., Yi, L., Zhang, C., Zhang, J., Zhang, Y., Zhao, N., Zhong, G., and Zhong, L., 2018. Site U1499. *In* Sun, Z., Jian, Z., Stock, J.M., Larsen, H.C., Klaus, A., Alvarez Zarikian, C.A., and the Expedition 367/368 Scientists, *South China Sea Rifted Margin*. Proceedings of the International Ocean Discovery Program, 367/368: College Station, TX (International Ocean Discovery Program). **https://doi.org/10.14379/iodp.proc.367368.103.2018**

Stock, J.M., Sun, Z., Klaus, A., Larsen, H.C., Jian, Z., Alvarez Zarikian, C.A., Boaga, J., Bowden, S.A., Briais, A., Chen, Y., Cukur, D., Dadd, K.A., Ding, W., Dorais, M.J., Ferré, E.C., Ferreira, F., Furusawa, A., Gewecke, A.J., Hinojosa, J.L., Höfig, T.W., Hsiung, K.-H., Huang, B., Huang, E., Huang, X.-L., Jiang, S., Jin, H., Johnson, B.G., Kurzawski, R.M., Lei, C., Li, B., Li, L., Li, Y., Lin, J., Liu, C., Liu, C., Liu, Z., Luna, A., Lupi, C., McCarthy, A.J., Mohn, G., Ningthoujam, L.S., Nirrengarten, M., Osono, N., Peate, D.W., Persaud, P., Qui, N., Robinson, C.M., Satolli, S., Sauermilch, I., Schindlbeck, J.C., Skinner, S.M., Straub, S.M., Su, X., Tian, L., van der Zwan, F.M., Wan, S., Wu, H., Xiang, R., Yadav, R., Yi, L., Zhang, C., Zhang, J., Zhang, Y., Zhao, N., Zhong, G., and Zhong, L., 2018. Site U1500. *In* Sun, Z., Jian, Z., Stock, J.M., Larsen, H.C., Klaus, A., Alvarez Zarikian, C.A., and the Expedition 367/368 Scientists, *South China Sea Rifted Margin*. Proceedings of the International Ocean Discovery Program, 367/368: College Station, TX (International Ocean Discovery Program). **https://doi.org/10.14379/iodp.proc.367368.104.2018**

Larsen, H.C., Jian, Z., Alvarez Zarikian, C.A., Sun, Z., Stock, J.M., Klaus, A., Boaga, J., Bowden, S.A., Briais, A., Chen, Y., Cukur, D., Dadd, K.A., Ding, W., Dorais, M.J., Ferré, E.C., Ferreira, F., Furusawa, A., Gewecke, A.J., Hinojosa, J.L., Höfig, T.W., Hsiung, K.-H., Huang, B., Huang, E., Huang, X.-L., Jiang, S., Jin, H., Johnson, B.G., Kurzawski, R.M., Lei, C., Li, B., Li, L., Li, Y., Lin, J., Liu, C., Liu, C., Liu, Z., Luna, A., Lupi, C., McCarthy, A.J., Mohn, G., Ningthoujam, L.S., Nirrengarten, M., Osono, N., Peate, D.W., Persaud, P., Qui, N., Robinson, C.M., Satolli, S., Sauermilch, I., Schindlbeck, J.C., Skinner, S.M., Straub, S.M., Su, X., Tian, L., van der Zwan, F.M., Wan, S., Wu, H., Xiang, R., Yadav, R., Yi, L., Zhang, C., Zhang, J., Zhang, Y., Zhao, N., Zhong, G., and Zhong, L., 2018. Site U1501. *In* Sun, Z., Jian, Z., Stock, J.M., Larsen, H.C., Klaus, A., Alvarez Zarikian, C.A., and the Expedition 367/368 Scientists, *South China Sea Rifted Margin*. Proceedings of the International Ocean Discovery Program, 367/368: College Station, TX (International Ocean Discovery Program). **https://doi.org/10.14379/iodp.proc.367368.105.2018**

Larsen, H.C., Jian, Z., Alvarez Zarikian, C.A., Sun, Z., Stock, J.M., Klaus, A., Boaga, J., Bowden, S.A., Briais, A., Chen, Y., Cukur, D., Dadd, K.A., Ding, W., Dorais, M.J., Ferré, E.C., Ferreira, F., Furusawa, A., Gewecke, A.J., Hinojosa, J.L., Höfig, T.W., Hsiung, K.-H., Huang, B., Huang, E., Huang, X.-L., Jiang, S., Jin, H., Johnson, B.G., Kurzawski, R.M., Lei, C., Li, B., Li, L., Li, Y., Lin, J., Liu, C., Liu, C., Liu, Z., Luna, A., Lupi, C., McCarthy, A.J., Mohn, G., Ningthoujam, L.S., Nirrengarten, M., Osono, N., Peate, D.W., Persaud, P., Qui, N., Robinson, C.M., Satolli, S., Sauermilch, I., Schindlbeck, J.C., Skinner, S.M., Straub, S.M., Su, X., Tian, L., van der Zwan, F.M., Wan, S., Wu, H., Xiang, R., Yadav, R., Yi, L., Zhang, C., Zhang, J., Zhang, Y., Zhao, N., Zhong, G., and Zhong, L., 2018. Site U1502. *In* Sun, Z., Jian, Z., Stock, J.M., Larsen, H.C., Klaus, A., Alvarez Zarikian, C.A., and the

*The Expedition-related bibliography is continually updated online (**http://publications.iodp.org/proceedings/367_368/367368title.html#bib**). Please send updates to **PubCrd@iodp.tamu.edu**.

Expedition 367/368 Scientists, *South China Sea Rifted Margin*. Proceedings of the International Ocean Discovery Program, 367/368: College Station, TX (International Ocean Discovery Program). **https://doi.org/10.14379/iodp.proc.367368.106.2018**

Larsen, H.C., Jian, Z., Alvarez Zarikian, C.A., Sun, Z., Stock, J.M., Klaus, A., Boaga, J., Bowden, S.A., Briais, A., Chen, Y., Cukur, D., Dadd, K.A., Ding, W., Dorais, M.J., Ferré, E.C., Ferreira, F., Furusawa, A., Gewecke, A.J., Hinojosa, J.L., Höfig, T.W., Hsiung, K.-H., Huang, B., Huang, E., Huang, X.-L., Jiang, S., Jin, H., Johnson, B.G., Kurzawski, R.M., Lei, C., Li, B., Li, L., Li, Y., Lin, J., Liu, C., Liu, C., Liu, Z., Luna, A., Lupi, C., McCarthy, A.J., Mohn, G., Ningthoujam, L.S., Nirrengarten, M., Osono, N., Peate, D.W., Persaud, P., Qui, N., Robinson, C.M., Satolli, S., Sauermilch, I., Schindlbeck, J.C., Skinner, S.M., Straub, S.M., Su, X., Tian, L., van der Zwan, F.M., Wan, S., Wu, H., Xiang, R., Yadav, R., Yi, L., Zhang, C., Zhang, J., Zhang, Y., Zhao, N., Zhong, G., and Zhong, L., 2018. Site U1503. *In* Sun, Z., Jian, Z., Stock, J.M., Larsen, H.C., Klaus, A., Alvarez Zarikian, C.A., and the Expedition 367/368 Scientists, *South China Sea Rifted Margin*. Proceedings of the International Ocean Discovery Program, 367/368: College Station, TX (International Ocean Discovery Program). **https://doi.org/10.14379/iodp.proc.367368.107.2018**

Larsen, H.C., Jian, Z., Alvarez Zarikian, C.A., Sun, Z., Stock, J.M., Klaus, A., Boaga, J., Bowden, S.A., Briais, A., Chen, Y., Cukur, D., Dadd, K.A., Ding, W., Dorais, M.J., Ferré, E.C., Ferreira, F., Furusawa, A., Gewecke, A.J., Hinojosa, J.L., Höfig, T.W., Hsiung, K.-H., Huang, B., Huang, E., Huang, X.-L., Jiang, S., Jin, H., Johnson, B.G., Kurzawski, R.M., Lei, C., Li, B., Li, L., Li, Y., Lin, J., Liu, C., Liu, C., Liu, Z., Luna, A., Lupi, C., McCarthy, A.J., Mohn, G., Ningthoujam, L.S., Nirrengarten, M., Osono, N., Peate, D.W., Persaud, P., Qui, N., Robinson, C.M., Satolli, S., Sauermilch, I., Schindlbeck, J.C., Skinner, S.M., Straub, S.M., Su, X., Tian, L., van der Zwan, F.M., Wan, S., Wu, H., Xiang, R., Yadav, R., Yi, L., Zhang, C., Zhang, J., Zhang, Y., Zhao, N., Zhong, G., and Zhong, L., 2018. Site U1504. *In* Sun, Z., Jian, Z., Stock, J.M., Larsen, H.C., Klaus, A., Alvarez Zarikian, C.A., and the Expedition 367/368 Scientists, *South China Sea Rifted Margin*. Proceedings of the International Ocean Discovery Program, 367/368: College Station, TX (International Ocean Discovery Program). **https://doi.org/10.14379/iodp.proc.367368.108.2018**

Jian, Z., Larsen, H.C., Alvarez Zarikian, C.A., Sun, Z., Stock, J.M., Klaus, A., Boaga, J., Bowden, S.A., Briais, A., Chen, Y., Cukur, D., Dadd, K.A., Ding, W., Dorais, M.J., Ferré, E.C., Ferreira, F., Furusawa, A., Gewecke, A.J., Hinojosa, J.L., Höfig, T.W., Hsiung, K.-H., Huang, B., Huang, E., Huang, X.-L., Jiang, S., Jin, H., Johnson, B.G., Kurzawski, R.M., Lei, C., Li, B., Li, L., Li, Y., Lin, J., Liu, C., Liu, C., Liu, Z., Luna, A., Lupi, C., McCarthy, A.J., Mohn, G., Ningthoujam, L.S., Nirrengarten, M., Osono, N., Peate, D.W., Persaud, P., Qui, N., Robinson, C.M., Satolli, S., Sauermilch, I., Schindlbeck, J.C., Skinner, S.M., Straub, S.M., Su, X., Tian, L., van der Zwan, F.M., Wan, S., Wu, H., Xiang, R., Yadav, R., Yi, L., Zhang, C., Zhang, J., Zhang, Y., Zhao, N., Zhong, G., and Zhong, L., 2018. Site U1505. *In* Sun, Z., Jian, Z., Stock, J.M., Larsen, H.C., Klaus, A., Alvarez Zarikian, C.A., and the Expedition 367/368 Scientists, *South China Sea Rifted Margin*. Proceedings of the International Ocean Discovery Program, 367/368: College Station, TX (International Ocean Discovery Program). **https://doi.org/10.14379/iodp.proc.367368.109.2018**

Supplementary material

Sun, Z., Jian, Z., Stock, J.M., Larsen, H.C., Klaus, A., Alvarez Zarikian, C.A., and the Expedition 367/368 Scientists, 2018. Supplementary material, **https://doi.org/10.14379/iodp.proc.367368supp.2018**. *Supplement to* Sun, Z., Jian, Z., Stock, J.M., Larsen, H.C., Klaus, A., Alvarez Zarikian, C.A., and the Expedition 367/368 Scientists, *South China Sea Rifted Margin*. Proceedings of the International Ocean Discovery Program, 367/368: College Station, TX (International Ocean Discovery Program). https://doi.org/10.14379/iodp.proc.367368.2018

Sun, Z., Jian, Z., Stock, J.M., Larsen, H.C., Klaus, A., Alvarez Zarikian, C.A., and the Expedition 367/368 Scientists
Proceedings of the International Ocean Discovery Program Volume 367/368
publications.iodp.org

https://doi.org/10.14379/iodp.proc.367368.101.2018

Expedition 367/368 summary[1]

Hans Christian Larsen, Zhen Sun, Joann M. Stock, Zhimin Jian, Carlos A. Alvarez Zarikian, Adam Klaus, Jacopo Boaga, Stephen A. Bowden, Anne Briais, Yifeng Chen, Deniz Cukur, Kelsie A. Dadd, Weiwei Ding, Michael J. Dorais, Eric C. Ferré, Fabricio Ferreira, Akira Furusawa, Aaron J. Gewecke, Jessica L. Hinojosa, Tobias W. Höfig, Kan-Hsi Hsiung, Baoqi Huang, Enqing Huang, Xiao-Long Huang, Shijun Jiang, Haiyan Jin, Benjamin G. Johnson, Robert M. Kurzawski, Chao Lei, Baohua Li, Li Li, Yanping Li, Jian Lin, Chang Liu, Chuanlian Liu, Zhifei Liu, Antonio Luna, Claudia Lupi, Anders J. McCarthy, Geoffroy Mohn, Lachit Singh Ningthoujam, Michael Nirrengarten, Nobuaki Osono, David W. Peate, Patricia Persaud, Ning Qiu, Caroline M. Robinson, Sara Satolli, Isabel Sauermilch, Julie C. Schindlbeck, Steven M. Skinner, Susanne M. Straub, Xiang Su, Liyan Tian, Froukje M. van der Zwan, Shiming Wan, Huaichun Wu, Rong Xiang, Rajeev Yadav, Liang Yi, Cuimei Zhang, Jinchang Zhang, Yang Zhang, Ning Zhao, Guangfa Zhong, and Lifeng Zhong[2]

Keywords: International Ocean Discovery Program, IODP, *JOIDES Resolution*, Expedition 367, Expedition 368, Site U1499, Site U1500, Site U1501, Site U1502, Site U1503, Site U1504, Site U1505, northern South China Sea, rifted margin, continent–ocean transition zone, hyperextension, continental breakup, lithosphere thinning, igneous activity, outer margin high, embryonic ocean, steady-state ocean, basalt, altered basalt, greenschist, gravel, Cenozoic, subsidence, T60 unconformity, red clay, turbidite, marine microfossil

Contents

1 Abstract
2 Introduction
3 Background
6 Expedition objectives
7 Coring and logging strategy
10 Site summaries
34 Preliminary scientific assessment
37 References

Abstract

The primary objectives of International Ocean Discovery Program (IODP) Expedition 367/368 to the northern South China Sea (SCS) margin were to (1) examine its history of continental breakup and (2) compare it with other nonvolcanic or magma-poor rifted margins with the broader goal of testing models for continental breakup. A secondary objective was to further our understanding of the paleoceanographic and environmental development of the SCS and southeast Asia during the Cenozoic. Four primary sites were selected for the overall program: one in the outer margin high (OMH) and three seaward of the OMH on distinct, margin-parallel basement ridges. These three ridges are informally labeled A, B, and C and are located in the continent–ocean transition (COT) zone ranging from the OMH to the interpreted steady-state oceanic crust (Ridge C) of the SCS. The main scientific objectives include the following:

- Determining the nature of the basement in crustal units across the COT of the SCS that are critical to constrain style of rifting,
- Constraining the time interval from initial crustal extension and plate rupture to the initial generation of igneous ocean crust,
- Constraining vertical crustal movements during breakup, and
- Examining the nature of igneous activity from rifting to seafloor spreading.

In addition, the sediment cores from the drill sites targeting primarily tectonic and basement objectives will provide information on the Cenozoic regional environmental development of the Southeast Asia margin.

Site U1499 on Ridge A and Site U1500 on Ridge B were drilled during Expedition 367. Expedition 368 was planned to drill at two primary sites (U1501 and U1503) at the OMH and Ridge C, respectively, but based on drilling results from Expedition 367, Expedition 368 chose to insert an alternate site on Ridge A (Site U1502). In ad-

[1] Larsen, H.C., Sun, Z., Stock, J.M., Jian, Z., Alvarez Zarikian, C.A., Klaus, A., Boaga, J., Bowden, S.A., Briais, A., Chen, Y., Cukur, D., Dadd, K.A., Ding, W., Dorais, M.J., Ferré, E.C., Ferreira, F., Furusawa, A., Gewecke, A.J., Hinojosa, J.L., Höfig, T.W., Hsiung, K.-H., Huang, B., Huang, E., Huang, X.-L., Jiang, S., Jin, H., Johnson, B.G., Kurzawski, R.M., Lei, C., Li, B., Li, L., Li, Y., Lin, J., Liu, C., Liu, C., Liu, Z., Luna, A., Lupi, C., McCarthy, A.J., Mohn, G., Ningthoujam, L.S., Nirrengarten, M., Osono, N., Peate, D.W., Persaud, P., Qui, N., Robinson, C.M., Satolli, S., Sauermilch, I., Schindlbeck, J.C., Skinner, S.M., Straub, S.M., Su, X., Tian, L., van der Zwan, F.M., Wan, S., Wu, H., Xiang, R., Yadav, R., Yi, L., Zhang, C., Zhang, J., Zhang, Y., Zhao, N., Zhong, G., and Zhong, L., 2018. Expedition 367/368 summary. *In* Sun, Z., Jian, Z., Stock, J.M., Larsen, H.C., Klaus, A., Alvarez Zarikian, C.A., and the Expedition 367/368 Scientists. *South China Sea Rifted Margin*. Proceedings of the International Ocean Discovery Program, 367/368: College Station, TX (International Ocean Discovery Program). https://doi.org/10.14379/iodp.proc.367368.101.2018

[2] **Expedition 367/368 Scientists' addresses.**

MS 367368-101: Published 28 September 2018

This work is distributed under the **Creative Commons Attribution 4.0 International** (CC BY 4.0) license.

dition, Expedition 368 added two more sites on the OMH (Sites U1504 and U1505). Expedition 367/368 completed operations at six of the seven sites (U1499–U1502, U1504, and U1505). Site U1503, however, was not completed beyond casing without coring to 990 m because of mechanical problems with the drilling equipment that prevented the expedition, after 25 May 2017, from operating with a drill string longer than 3400 m. New alternate Site U1504, proposed during Expedition 367, met this condition. Original Site U1505 also met the operational constraints of the 3400 m drill string (total) and was an alternate site for the already-drilled Site U1501.

At Site U1499, we cored to 1081.8 m in 22.1 days with 52% recovery and then logged downhole data from 655 to 1020 m. In 31 days at Site U1500, we penetrated to 1529 m, cored a total of 1012.8 m with 37% recovery, and collected log data from 842 to 1133 m. At Site U1501, we cored to 697.1 m in 9.4 days with 78.5% recovery. We also drilled ahead for 433.5 m in Hole U1501D and then logged downhole data from 78.3 to 399.3 m. In 19.3 days at Site U1502, we penetrated 1679.0 m in Holes U1502A (758 m) and U1502B (921 m), set 723.7 m of casing and cored a total of 576.3 m with 53.5% recovery, and collected downhole log data from 785.3 to 875.3 m and seismic data through the 10¾ inch casing. At Site U1503, we penetrated 995.1 m and set 991.5 m of 10¾ inch casing, but no cores were taken because of a mechanical problem with the drawworks. At Site U1504, we took 40 rotary core barrel (RCB) cores over two holes. The cored interval between both holes was 277.3 m with 26.8% recovery. An 88.2 m interval was drilled in Hole U1504B. At Site U1505, we cored 668.0 m with 101.1% recovery. Logging data was collected from 80.1 to 341.2 m. Operations at this site covered 6.1 days. Except for Sites U1503 and U1505, all sites were drilled to acoustic basement. A total of 6.65 days were lost due to mechanical breakdown or waiting on spare supplies for repair of drilling equipment, but drilling options were severely limited from 25 May to the end of the expedition by the defective drawworks limiting deployment of drill string longer than 3400 m.

At Site U1499, coring ~200 m into the interpreted acoustic basement sampled sedimentary rocks, possibly including early Miocene chalks underlain by Oligocene polymict breccias and poorly cemented gravels of unknown age comprising sandstone pebbles and cobbles. Preliminary structural and lithologic analysis suggests that the gravels might be early to late synrift sediment. At Site U1500, the main seismic reflector corresponds to the top of a basalt sequence at ~1379.1 m. We cored 149.90 m into this volcanic package and recovered 114.92 m (77%) of sparsely to moderately plagioclase-phyric basalt comprising numerous lava flows, including pillow lavas with glass, chilled margins, altered veins, hyaloclastites, and minor sediment. Preliminary geochemical analyses indicate that the basalt is tholeiitic.

Sampling of the Pleistocene to lower Miocene sedimentary section at Sites U1499 and U1500 was not continuous for two reasons. First, there was extremely poor recovery in substantial intervals interpreted to be poorly lithified sands, possibly turbidites. Second, we chose to drill down without coring in some sections at Site U1500 to ensure sufficient time to achieve this site's high-priority deep drilling objectives. The upper Miocene basin sequence, which consists of interbedded claystone, siltstone, and sandstone can be correlated between the two sites by seismic stratigraphic mapping and biostratigraphy.

At Site U1501 on the OMH, coring ~45 m into the acoustic basement sampled prerift(?) deposits comprising sandstone to conglomerate of presumed Mesozoic age. These deposits are overlain by siliciclastic synrift sediments of Eocene to Oligocene age followed by primarily carbonaceous postrift sediments of early Miocene to Pleistocene age. Site U1502 on Ridge A was cased to 723.7 m. No coring was attempted shallower than 380 m to save operational time and because of low expectations for core recovery in the upper Plio–Pleistocene sequence. At this site, we recovered 180 m of hydrothermally altered brecciated basalts comprising sheet and pillow lavas below deep-marine sediments of Oligocene to late Miocene age. At Site U1503 on Ridge C, 991.5 m of casing was installed in preparation for the planned deep drilling to ~1800 m. No coring was performed due to mechanical failures, and the site was abandoned without further activity except for installation of a reentry cone. Coring at Site U1504 on the OMH, located ~45 km east of Site U1501, recovered mostly foliated, greenschist facies metamorphic rocks below late Eocene(?) carbonate rocks (partly reef debris) and early Miocene to Pleistocene sediments. At Site U1505, we cored to 480.15 m through Pleistocene to late Oligocene mainly carbonaceous ooze followed at depth by early Oligocene siliciclastic sediments.

Efforts were made at every drill site to correlate the core with the seismic data and seismic stratigraphic unconformities interpreted in the Eocene to Plio–Pleistocene sedimentary sequence prior to drilling. The predrilling interpretation of ages of these unconformities was in general confirmed by drilling results, although some nontrivial corrections can be expected from detailed postexpedition work on integrating seismic stratigraphic interpretations with detailed bio- and lithostratigraphy.

As a result of the limited length of drill string that could be deployed during the later part of Expedition 368, the secondary expedition objectives addressing the environmental history of the SCS and Southeast Asia received more focus than originally planned, allowing Site U1505 (alternate to Site U1501) to be included. Despite this change in focus, Expedition 367/368 provided solid evidence for a process of breakup that included vigorous synrift magmatism as opposed to the often-favored interpretation of the SCS margin as a magma-starved margin or a margin possibly overprinted at a much later stage by plume-related magmatism. In this broader perspective, Expedition 367/368 accomplished a fundamental objective of the two-expedition science program.

Introduction

The South China Sea (SCS) margin (Figure **F1**) is an accessible and seismically well-imaged location where drilling of synrift sediment and underlying basement will provide key constraints on the processes of rifting and eventual rupturing of the continental lithosphere during breakup at a highly extended rifted margin. Expedition 367/368 was based on International Ocean Discovery Program (IODP) drilling Proposals 878-CPP, 878-Add, 878-Add2, and 878-Add3. This project was implemented as a single science program with 114 days of drilling operations spread across two IODP expeditions as outlined in the Expedition 367/368 *Scientific Prospectus* (Sun et al., 2016b). Two expeditions were required to drill four high-priority, deep-penetration sites in a transect across the margin. Of these, three sites targeted acoustic basement in the continent–ocean transition (COT), and one site targeted prerift through synrift to postrift sequences on the landward side of the transect. Although the primary focus of this drilling expedition was to discriminate among possible models for rifting and plate rupture, the drilling, along with results from Ocean Drilling Program (ODP) Leg 184 and IODP Expedition 349, addressed a secondary objective to improve our understanding of the Cenozoic environmental evolution of the southeast Asian area as recorded in the sediments of the SCS basin.

Figure F1. Seismic data coverage and magnetic anomalies in the SCS basin, Expedition 367/368. Black lines = ocean-bottom seismometer (OBS) refraction data. Other seismic lines are mostly multichannel seismic reflection data. Yellow lines = magnetic isochrons (labeled with white text) from Briais et al. (1993). White stars = Expedition 367/368 drill sites. ODP Leg 184 (red squares) and IODP Expedition 349 (red circles) sites are shown with site numbers. For more details, see Figure F4.

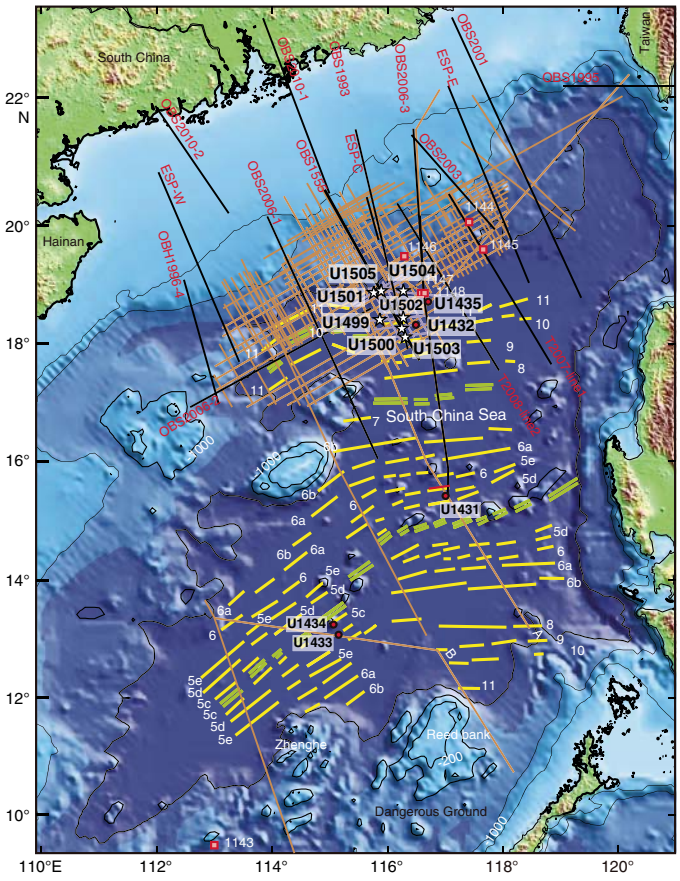
South China
Taiwan
Hainan
South China Sea
Zhenghe
Reed bank
Dangerous Ground
U1505
U1504
U1501
U1502
U1435
U1499
U1432
U1500
U1503
U1431
U1434
U1433
1145
1146
1143
OBS2001
OBS2006-3
OBS2002
OBS2006-1
OBS2010-1
OBS2010-2
OBS1993
OBS1994
OBS1995
OBS1996-4
OBS2006-2
ESP-E
ESP-C
ESP-W
T20
T30
T40
T50
T60
T70
T80
T90
T100
T110
T120
T130
T140
T150
T160
T170
T180
T190
T200
T210
T220
T230
T240
T250
T260
T270
T280
T290
T300
T310
T320
T330
T340
T350
T360
T370
T380
T390
T400
T410
T420
T430
T440
T450
T460
T470
T480
T490
T500
T510
T520
T530
T540
T550
T560
T570
T580
T590
T600
T610
T620
T630
T640
T650
T660
T670
T680
T690
T700
T710
T720
T730
T740
T750
T760
T770
T780
T790
T800
T810
T820
T830
T840
T850
T860
T870
T880
T890
T900
T910
T920
T930
T940
T950
T960
T970
T980
T990
T1000
T1010
T1020
T1030
T1040
T1050
T1060
T1070
T1080
T1090
T1100
T1110
T1120
T1130
T1140
T1150
T1160
T1170
T1180
T1190
T1200
T1210
T1220
T1230
T1240
T1250
T1260
T1270
T1280
T1290
T1300
T1310
T1320
T1330
T1340
T1350
T1360
T1370
T1380
T1390
T1400
T1410
T1420
T1430
T1440
T1450
T1460
T1470
T1480
T1490
T1500
T1510
T1520
T1530
T1540
T1550
T1560
T1570
T1580
T1590
T1600
T1610
T1620
T1630
T1640
T1650
T1660
T1670
T1680
T1690
T1700
T1710
T1720
T1730
T1740
T1750
T1760
T1770
T1780
T1790
T1800
T1810
T1820
T1830
T1840
T1850
T1860
T1870
T1880
T1890
T1900
T1910
T1920
T1930
T1940
T1950
T1960
T1970
T1980
T1990
T2000
T2010
T2020
T2030
T2040
T2050
T2060
T2070
T2080
T2090
T2100
T2110
T2120
T2130
T2140
T2150
T2160
T2170
T2180
T2190
T2200
T2210
T2220
T2230
T2240
T2250
T2260
T2270
T2280
T2290
T2300
T2310
T2320
T2330
T2340
T2350
T2360
T2370
T2380
T2390
T2400
T2410
T2420
T2430
T2440
T2450
T2460
T2470
T2480
T2490
T2500
T2510
T2520
T2530
T2540
T2550
T2560
T2570
T2580
T2590
T2600
T2610
T2620
T2630
T2640
T2650
T2660
T2670
T2680
T2690
T2700
T2710
T2720
T2730
T2740
T2750
T2760
T2770
T2780
T2790
T2800
T2810
T2820
T2830
T2840
T2850
T2860
T2870
T2880
T2890
T2900
T2910
T2920
T2930
T2940
T2950
T2960
T2970
T2980
T2990
T3000
T3010
T3020
T3030
T3040
T3050
T3060
T3070
T3080
T3090
T3100
T3110
T3120
T3130
T3140
T3150
T3160
T3170
T3180
T3190
T3200
T3210
T3220
T3230
T3240
T3250
T3260
T3270
T3280
T3290
T3300
T3310
T3320
T3330
T3340
T3350
T3360
T3370
T3380
T3390
T3400
T3410
T3420
T3430
T3440
T3450
T3460
T3470
T3480
T3490
T3500
T3510
T3520
T3530
T3540
T3550
T3560
T3570
T3580
T3590
T3600
T3610
T3620
T3630
T3640
T3650
T3660
T3670
T3680
T3690
T3700
T3710
T3720
T3730
T3740
T3750
T3760
T3770
T3780
T3790
T3800
T3810
T3820
T3830
T3840
T3850
T3860
T3870
T3880
T3890
T3900
T3910
T3920
T3930
T3940
T3950
T3960
T3970
T3980
T3990
T4000
T4010
T4020
T4030
T4040
T4050
T4060
T4070
T4080
T4090
T4100
T4110
T4120
T4130
T4140
T4150
T4160
T4170
T4180
T4190
T4200
T4210
T4220
T4230
T4240
T4250
T4260
T4270
T4280
T4290
T4300
T4310
T4320
T4330
T4340
T4350
T4360
T4370
T4380
T4390
T4400
T4410
T4420
T4430
T4440
T4450
T4460
T4470
T4480
T4490
T4500
T4510
T4520
T4530
T4540
T4550
T4560
T4570
T4580
T4590
T4600
T4610
T4620
T4630
T4640
T4650
T4660
T4670
T4680
T4690
T4700
T4710
T4720
T4730
T4740
T4750
T4760
T4770
T4780
T4790
T4800
T4810
T4820
T4830
T4840
T4850
T4860
T4870
T4880
T4890
T4900
T4910
T4920
T4930
T4940
T4950
T4960
T4970
T4980
T4990
T5000
T5010
T5020
T5030
T5040
T5050
T5060
T5070
T5080
T5090
T5100
T5110
T5120
T5130
T5140
T5150
T5160
T5170
T5180
T5190
T5200
T5210
T5220
T5230
T5240
T5250
T5260
T5270
T5280
T5290
T5300
T5310
T5320
T5330
T5340
T5350
T5360
T5370
T5380
T5390
T5400
T5410
T5420
T5430
T5440
T5450
T5460
T5470
T5480
T5490
T5500
T5510
T5520
T5530
T5540
T5550
T5560
T5570
T5580
T5590
T5600
T5610
T5620
T5630
T5640
T5650
T5660
T5670
T5680
T5690
T5700
T5710
T5720
T5730
T5740
T5750
T5760
T5770
T5780
T5790
T5800
T5810
T5820
T5830
T5840
T5850
T5860
T5870
T5880
T5890
T5900
T5910
T5920
T5930
T5940
T5950
T5960
T5970
T5980
T5990
T6000
T6010
T6020
T6030
T6040
T6050
T6060
T6070
T6080
T6090
T6100
T6110
T6120
T6130
T6140
T6150
T6160
T6170
T6180
T6190
T6200
T6210
T6220
T6230
T6240
T6250
T6260
T6270
T6280
T6290
T6300
T6310
T6320
T6330
T6340
T6350
T6360
T6370
T6380
T6390
T6400
T6410
T6420
T6430
T6440
T6450
T6460
T6470
T6480
T6490
T6500
T6510
T6520
T6530
T6540
T6550
T6560
T6570
T6580
T6590
T6600
T6610
T6620
T6630
T6640
T6650
T6660
T6670
T6680
T6690
T6700
T6710
T6720
T6730
T6740
T6750
T6760
T6770
T6780
T6790
T6800
T6810
T6820
T6830
T6840
T6850
T6860
T6870
T6880
T6890
T6900
T6910
T6920
T6930
T6940
T6950
T6960
T6970
T6980
T6990
T7000
T7010
T7020
T7030
T7040
T7050
T7060
T7070
T7080
T7090
T7100
T7110
T7120
T7130
T7140
T7150
T7160
T7170
T7180
T7190
T7200
T7210
T7220
T7230
T7240
T7250
T7260
T7270
T7280
T7290
T7300
T7310
T7320
T7330
T7340
T7350
T7360
T7370
T7380
T7390
T7400
T7410
T7420
T7430
T7440
T7450
T7460
T7470
T7480
T7490
T7500
T7510
T7520
T7530
T7540
T7550
T7560
T7570
T7580
T7590
T7600
T7610
T7620
T7630
T7640
T7650
T7660
T7670
T7680
T7690
T7700
T7710
T7720
T7730
T7740
T7750
T7760
T7770
T7780
T7790
T7800
T7810
T7820
T7830
T7840
T7850
T7860
T7870
T7880
T7890
T7900
T7910
T7920
T7930
T7940
T7950
T7960
T7970
T7980
T7990
T8000
T8010
T8020
T8030
T8040
T8050
T8060
T8070
T8080
T8090
T8100
T8110
T8120
T8130
T8140
T8150
T8160
T8170
T8180
T8190
T8200
T8210
T8220
T8230
T8240
T8250
T8260
T8270
T8280
T8290
T8300
T8310
T8320
T8330
T8340
T8350
T8360
T8370
T8380
T8390
T8400
T8410
T8420
T8430
T8440
T8450
T8460
T8470
T8480
T8490
T8500
T8510
T8520
T8530
T8540
T8550
T8560
T8570
T8580
T8590
T8600
T8610
T8620
T8630
T8640
T8650
T8660
T8670
T8680
T8690
T8700
T8710
T8720
T8730
T8740
T8750
T8760
T8770
T8780
T8790
T8800
T8810
T8820
T8830
T8840
T8850
T8860
T8870
T8880
T8890
T8900
T8910
T8920
T8930
T8940
T8950
T8960
T8970
T8980
T8990
T9000
T9010
T9020
T9030
T9040
T9050
T9060
T9070
T9080
T9090
T9100
T9110
T9120
T9130
T9140
T9150
T9160
T9170
T9180
T9190
T9200
T9210
T9220
T9230
T9240
T9250
T9260
T9270
T9280
T9290
T9300
T9310
T9320
T9330
T9340
T9350
T9360
T9370
T9380
T9390
T9400
T9410
T9420
T9430
T9440
T9450
T9460
T9470
T9480
T9490
T9500
T9510
T9520
T9530
T9540
T9550
T9560
T9570
T9580
T9590
T9600
T9610
T9620
T9630
T9640
T9650
T9660
T9670
T9680
T9690
T9700
T9710
T9720
T9730
T9740
T9750
T9760
T9770
T9780
T9790
T9800
T9810
T9820
T9830
T9840
T9850
T9860
T9870
T9880
T9890
T9900
T9910
T9920
T9930
T9940
T9950
T9960
T9970
T9980
T9990
T10000
T10010
T10020
T10030
T10040
T10050
T10060
T10070
T10080
T10090
T10100
T10110
T10120
T10130
T10140
T10150
T10160
T10170
T10180
T10190
T10200
T10210
T10220
T10230
T10240
T10250
T10260
T10270
T10280
T10290
T10300
T10310
T10320
T10330
T10340
T10350
T10360
T10370
T10380
T10390
T10400
T10410
T10420
T10430
T10440
T10450
T10460
T10470
T10480
T10490
T10500
T10510
T10520
T10530
T10540
T10550
T10560
T10570
T10580
T10590
T10600
T10610
T10620
T10630
T10640
T10650
T10660
T10670
T10680
T10690
T10700
T10710
T10720
T10730
T10740
T10750
T10760
T10770
T10780
T10790
T10800
T10810
T10820
T10830
T10840
T10850
T10860
T10870
T10880
T10890
T10900
T10910
T10920
T10930
T10940
T10950
T10960
T10970
T10980
T10990
T11000
T11010
T11020
T11030
T11040
T11050
T11060
T11070
T11080
T11090
T11100
T11110
T11120
T11130
T11140
T11150
T11160
T11170
T11180
T11190
T11200
T11210
T11220
T11230
T11240
T11250
T11260
T11270
T11280
T11290
T11300
T11310
T11320
T11330
T11340
T11350
T11360
T11370
T11380
T11390
T11400
T11410
T11420
T11430
T11440
T11450
T11460
T11470
T11480
T11490
T11500
T11510
T11520
T11530
T11540
T11550
T11560
T11570
T11580
T11590
T11600
T11610
T11620
T11630
T11640
T11650
T11660
T11670
T11680
T11690
T11700
T11710
T11720
T11730
T11740
T11750
T11760
T11770
T11780
T11790
T11800
T11810
T11820
T11830
T11840
T11850
T11860
T11870
T11880
T11890
T11900
T11910
T11920
T11930
T11940
T11950
T11960
T11970
T11980
T11990
T12000
T12010
T12020
T12030
T12040
T12050
T12060
T12070
T12080
T12090
T12100
T12110
T12120
T12130
T12140
T12150
T12160
T12170
T12180
T12190
T12200
T12210
T12220
T12230
T12240
T12250
T12260
T12270
T12280
T12290
T12300
T12310
T12320
T12330
T12340
T12350
T12360
T12370
T12380
T12390
T12400
T12410
T12420
T12430
T12440
T12450
T12460
T12470
T12480
T12490
T12500
T12510
T12520
T12530
T12540
T12550
T12560
T12570
T12580
T12590
T12600
T12610
T12620
T12630
T12640
T12650
T12660
T12670
T12680
T12690
T12700
T12710
T12720
T12730
T12740
T12750
T12760
T12770
T12780
T12790
T12800
T12810
T12820
T12830
T12840
T12850
T12860
T12870
T12880
T12890
T12900
T12910
T12920
T12930
T12940
T12950
T12960
T12970
T12980
T12990
T13000
T13010
T13020
T13030
T13040
T13050
T13060
T13070
T13080
T13090
T13100
T13110
T13120
T13130
T13140
T13150
T13160
T13170
T13180
T13190
T13200
T13210
T13220
T13230
T13240
T13250
T13260
T13270
T13280
T13290
T13300
T13310
T13320
T13330
T13340
T13350
T13360
T13370
T13380
T13390
T13400
T13410
T13420
T13430
T13440
T13450
T13460
T13470
T13480
T13490
T13500
T13510
T13520
T13530
T13540
T13550
T13560
T13570
T13580
T13590
T13600
T13610
T13620
T13630
T13640
T13650
T13660
T13670
T13680
T13690
T13700
T13710
T13720
T13730
T13740
T13750
T13760
T13770
T13780
T13790
T13800
T13810
T13820
T13830
T13840
T13850
T13860
T13870
T13880
T13890
T13900
T13910
T13920
T13930
T13940
T13950
T13960
T13970
T13980
T13990
T14000
T14010
T14020
T14030
T14040
T14050
T14060
T14070
T14080
T14090
T14100
T14110
T14120
T14130
T14140
T14150
T14160
T14170
T14180
T14190
T14200
T14210
T14220
T14230
T14240
T14250
T14260
T14270
T14280
T14290
T14300
T14310
T14320
T14330
T14340
T14350
T14360
T14370
T14380
T14390
T14400
T14410
T14420
T14430
T14440
T14450
T14460
T14470
T14480
T14490
T14500
T14510
T14520
T14530
T14540
T14550
T14560
T14570
T14580
T14590
T14600
T14610
T14620
T14630
T14640
T14650
T14660
T14670
T14680
T14690
T14700
T14710
T14720
T14730
T14740
T14750
T14760
T14770
T14780
T14790
T14800
T14810
T14820
T14830
T14840
T14850
T14860
T14870
T14880
T14890
T14900
T14910
T14920
T14930
T14940
T14950
T14960
T14970
T14980
T14990
T15000
T15010
T15020
T15030
T15040
T15050
T15060
T15070
T15080
T15090
T15100
T15110
T15120
T15130
T15140
T15150
T15160
T15170
T15180
T15190
T15200
T15210
T15220
T15230
T15240
T15250
T15260
T15270
T15280
T15290
T15300
T15310
T15320
T15330
T15340
T15350
T15360
T15370
T15380
T15390
T15400
T15410
T15420
T15430
T15440
T15450
T15460
T15470
T15480
T15490
T15500
T15510
T15520
T15530
T15540
T15550
T15560
T15570
T15580
T15590
T15600
T15610
T15620
T15630
T15640
T15650
T15660
T15670
T15680
T15690
T15700
T15710
T15720
T15730
T15740
T15750
T15760
T15770
T15780
T15790
T15800
T15810
T15820
T15830
T15840
T15850
T15860
T15870
T15880
T15890
T15900
T15910
T15920
T15930
T15940
T15950
T15960
T15970
T15980
T15990
T16000
T16010
T16020
T16030
T16040
T16050
T16060
T16070
T16080
T16090
T16100
T16110
T16120
T16130
T16140
T16150
T16160
T16170
T16180
T16190
T16200
T16210
T16220
T16230
T16240
T16250
T16260
T16270
T16280
T16290
T16300
T16310
T16320
T16330
T16340
T16350
T16360
T16370
T16380
T16390
T16400
T16410
T16420
T16430
T16440
T16450
T16460
T16470
T16480
T16490
T16500
T16510
T16520
T16530
T16540
T16550
T16560
T16570
T16580
T16590
T16600
T16610
T16620
T16630
T16640
T16650
T16660
T16670
T16680
T16690
T16700
T16710
T16720
T16730
T16740
T16750
T16760
T16770
T16780
T16790
T16800
T16810
T16820
T16830
T16840
T16850
T16860
T16870
T16880
T16890
T16900
T16910
T16920
T16930
T16940
T16950
T16960
T16970
T16980
T16990
T17000
T17010
T17020
T17030
T17040
T17050
T17060
T17070
T17080
T17090
T17100
T17110
T17120
T17130
T17140
T17150
T17160
T17170
T17180
T17190
T17200
T17210
T17220
T17230
T17240
T17250
T17260
T17270
T17280
T17290
T17300
T17310
T17320
T17330
T17340
T17350
T17360
T17370
T17380
T17390
T17400
T17410
T17420
T17430
T17440
T17450
T17460
T17470
T17480
T17490
T17500
T17510
T17520
T17530
T17540
T17550
T17560
T17570
T17580
T17590
T17600
T17610
T17620
T17630
T17640
T17650
T17660
T17670
T17680
T17690
T17700
T17710
T17720
T17730
T17740
T17750
T17760
T17770
T17780
T17790
T17800
T17810
T17820
T17830
T17840
T17850
T17860
T17870
T17880
T17890
T17900
T17910
T17920
T17930
T17940
T17950
T17960
T17970
T17980
T17990
T18000
T18010
T18020
T18030
T18040
T18050
T18060
T18070
T18080
T18090
T18100
T18110
T18120
T18130
T18140
T18150
T18160
T18170
T18180
T18190
T18200
T18210
T18220
T18230
T18240
T18250
T18260
T18270
T18280
T18290
T18300
T18310
T18320
T18330
T18340
T18350
T18360
T18370
T18380
T18390
T18400
T18410
T18420
T18430
T18440
T18450
T18460
T18470
T18480
T18490
T18500
T18510
T18520
T18530
T18540
T18550
T18560
T18570
T18580
T18590
T18600
T18610
T18620
T18630
T18640
T18650
T18660
T18670
T18680
T18690
T18700
T18710
T18720
T18730
T18740
T18750
T18760
T18770
T18780
T18790
T18800
T18810
T18820
T18830
T18840
T18850
T18860
T18870
T18880
T18890
T18900
T18910
T18920
T18930
T18940
T18950
T18960
T18970
T18980
T18990
T19000
T19010
T19020
T19030
T19040
T19050
T19060
T19070
T19080
T19090
T19100
T19110
T19120
T19130
T19140
T19150
T19160
T19170
T19180
T19190
T19200
T19210
T19220
T19230
T19240
T19250
T19260
T19270
T19280
T19290
T19300
T19310
T19320
T19330
T19340
T19350
T19360
T19370
T19380
T19390
T19400
T19410
T19420
T19430
T19440
T19450
T19460
T19470
T19480
T19490
T19500
T19510
T19520
T19530
T19540
T19550
T19560
T19570
T19580
T19590
T19600
T19610
T19620
T19630
T19640
T19650
T19660
T19670
T19680
T19690
T19700
T19710
T19720
T19730
T19740
T19750
T19760
T19770
T19780
T19790
T19800
T19810
T19820
T19830
T19840
T19850
T19860
T19870
T19880
T19890
T19900
T19910
T19920
T19930
T19940
T19950
T19960
T19970
T19980
T19990
T20000
T20010
T20020
T20030
T20040
T20050
T20060
T20070
T20080
T20090
T20100
T20110
T20120
T20130
T20140
T20150
T20160
T20170
T20180
T20190
T20200
T20210
T20220
T20230
T20240
T20250
T20260
T20270
T20280
T20290
T20300
T20310
T20320
T20330
T20340
T20350
T20360
T20370
T20380
T20390
T20400
T20410
T20420
T20430
T20440
T20450
T20460
T20470
T20480
T20490
T20500
T20510
T20520
T20530
T20540
T20550
T20560
T20570
T20580
T20590
T20600
T20610
T20620
T20630
T20640
T20650
T20660
T20670
T20680
T20690
T20700
T20710
T20720
T20730
T20740
T20750
T20760
T20770
T20780
T20790
T20800
T20810
T20820
T20830
T20840
T20850
T20860
T20870
T20880
T20890
T20900
T20910
T20920
T20930
T20940
T20950
T20960
T20970
T20980
T20990
T21000
T21010
T21020
T21030
T21040
T21050
T21060
T21070
T21080
T21090
T21100
T21110
T21120
T21130
T21140
T21150
T21160
T21170
T21180
T21190
T21200
T21210
T21220
T21230
T21240
T21250
T21260
T21270
T21280
T21290
T21300
T21310
T21320
T21330
T21340
T21350
T21360
T21370
T21380
T21390
T21400
T21410
T21420
T21430
T21440
T21450
T21460
T21470
T21480
T21490
T21500
T21510
T21520
T21530
T21540
T21550
T21560
T21570
T21580
T21590
T21600
T21610
T21620
T21630
T21640
T21650
T21660
T21670
T21680
T21690
T21700
T21710
T21720
T21730
T21740
T21750
T21760
T21770
T21780
T21790
T21800
T21810
T21820
T21830
T21840
T21850
T21860
T21870
T21880
T21890
T21900
T21910
T21920
T21930
T21940
T21950
T21960
T21970
T21980
T21990
T22000
T22010
T22020
T22030
T22040
T22050
T22060
T22070
T22080
T22090
T22100
T22110
T22120
T22130
T22140
T22150
T22160
T22170
T22180
T22190
T22200
T22210
T22220
T22230
T22240
T22250
T22260
T22270
T22280
T22290
T22300
T22310
T22320
T22330
T22340
T22350
T22360
T22370
T22380
T22390
T22400
T22410
T22420
T22430
T22440
T22450
T22460
T22470
T22480
T22490
T22500
T22510
T22520
T22530
T22540
T22550
T22560
T22570
T22580
T22590
T22600
T22610
T22620
T22630
T22640
T22650
T22660
T22670
T22680
T22690
T22700
T22710
T22720
T22730
T22740
T22750
T22760
T22770
T22780
T22790
T22800
T22810
T22820
T22830
T22840
T22850
T22860
T22870
T22880
T22890
T22900
T22910
T22920
T22930
T22940
T22950
T22960
T22970
T22980
T22990
T23000
T23010
T23020
T23030
T23040
T23050
T23060
T23070
T23080
T23090
T23100
T23110
T23120
T23130
T23140
T23150
T23160
T23170
T23180
T23190
T23200
T23210
T23220
T23230
T23240
T23250
T23260
T23270
T23280
T23290
T23300
T23310
T23320
T23330
T23340
T23350
T23360
T23370
T23380
T23390
T23400
T23410
T23420
T23430
T23440
T23450
T23460
T23470
T23480
T23490
T23500
T23510
T23520
T23530
T23540
T23550
T23560
T23570
T23580
T23590
T23600
T23610
T23620
T23630
T23640
T23650
T23660
T23670
T23680
T23690
T23700
T23710
T23720
T23730
T23740
T23750
T23760
T23770
T23780
T23790
T23800
T23810
T23820
T23830
T23840
T23850
T23860
T23870
T23880
T23890
T23900
T23910
T23920
T23930
T23940
T23950
T23960
T23970
T23980
T23990
T24000
T24010
T24020
T24030
T24040
T24050
T24060
T24070
T24080
T24090
T24100
T24110
T24120
T24130
T24140
T24150
T24160
T24170
T24180
T24190
T24200
T24210
T24220
T24230
T24240
T24250
T24260
T24270
T24280
T24290
T24300
T24310
T24320
T24330
T24340
T24350
T24360
T24370
T24380
T24390
T24400
T24410
T24420
T24430
T24440
T24450
T24460
T24470
T24480
T24490
T24500
T24510
T24520
T24530
T24540
T24550
T24560
T24570
T24580
T24590
T24600
T24610
T24620
T24630
T24640
T24650
T24660
T24670
T24680
T24690
T24700
T24710
T24720
T24730
T24740
T24750
T24760
T24770
T24780
T24790
T24800
T24810
T24820
T24830
T24840
T24850
T24860
T24870
T24880
T24890
T24900
T24910
T24920
T24930
T24940
T24950
T24960
T24970
T24980
T24990
T25000
T25010
T25020
T25030
T25040
T25050
T25060
T25070
T25080
T25090
T25100
T25110
T25120
T25130
T25140
T25150
T25160
T25170
T25180
T25190
T25200
T25210
T25220
T25230
T25240
T25250
T25260
T25270
T25280
T25290
T25300
T25310
T25320
T25330
T25340
T25350
T25360
T25370
T25380
T25390
T25400
T25410
T25420
T25430
T25440
T25450
T25460
T25470
T25480
T25490
T25500
T25510
T25520
T25530
T25540
T25550
T25560
T25570
T25580
T25590
T25600
T25610
T25620
T25630
T25640
T25650
T25660
T25670
T25680
T25690
T25700
T25710
T25720
T25730
T25740
T25750
T25760
T25770
T25780
T25790
T25800
T25810
T25820
T25830
T25840
T25850
T25860
T25870
T25880
T25890
T25900
T25910
T25920
T25930
T25940
T25950
T25960
T25970
T25980
T25990
T26000
T26010
T26020
T26030
T26040
T26050
T26060
T26070
T26080
T26090
T26100
T26110
T26120
T26130
T26140
T26150
T26160
T26170
T26180
T26190
T26200
T26210
T26220
T26230
T26240
T26250
T26260
T26270
T26280
T26290
T26300
T26310
T26320
T26330
T26340
T26350
T26360
T26370
T26380
T26390
T26400
T26410
T26420
T26430
T26440
T26450
T26460
T26470
T26480
T26490
T26500
T26510
T26520
T26530
T26540
T26550
T26560
T26570
T26580
T26590
T26600
T26610
T26620
T26630
T26640
T26650
T26660
T26670
T26680
T26690
T26700
T26710
T26720
T26730
T26740
T26750
T26760
T26770
T26780
T26790
T26800
T26810
T26820
T26830
T26840
T26850
T26860
T26870
T26880
T26890
T26900
T26910
T26920
T26930
T26940
T26950
T26960
T26970
T26980
T26990
T27000
T27010
T27020
T27030
T27040
T27050
T27060
T27070
T27080
T27090
T27100
T27110
T27120
T27130
T27140
T27150
T27160
T27170
T27180
T27190
T27200
T27210
T27220
T27230
T27240
T27250
T27260
T27270
T27280
T27290
T27300
T27310
T27320
T27330
T27340
T27350
T27360
T27370
T27380
T27390
T27400
T27410
T27420
T27430
T27440
T27450
T27460
T27470
T27480
T27490
T27500
T27510
T27520
T27530
T27540
T27550
T27560
T27570
T27580
T27590
T27600
T27610
T27620
T27630
T27640
T27650
T27660
T27670
T27680
T27690
T27700
T27710
T27720
T27730
T27740
T27750
T27760
T27770
T27780
T27790
T27800
T27810
T27820
T27830
T27840
T27850
T27860
T27870
T27880
T27890
T27900
T27910
T27920
T27930
T27940
T27950
T27960
T27970
T27980
T27990
T28000
T28010
T28020
T28030
T28040
T28050
T28060
T28070
T28080
T28090
T28100
T28110
T28120
T28130
T28140
T28150
T28160
T28170
T28180
T28190
T28200
T28210
T28220
T28230
T28240
T28250
T28260
T28270
T28280
T28290
T28300
T28310
T28320
T28330
T28340
T28350
T28360
T28370
T28380
T28390
T28400
T28410
T28420
T28430
T28440
T28450
T28460
T28470
T28480
T28490
T28500
T28510
T28520
T28530
T28540
T28550
T28560
T28570
T28580
T28590
T28600
T28610
T28620
T28630
T28640
T28650
T28660
T28670
T28680
T28690
T28700
T28710
T28720
T28730
T28740
T28750
T28760
T28770
T28780
T28790
T28800
T28810
T28820
T28830
T28840
T28850
T28860
T28870
T28880
T28890
T28900
T28910
T28920
T28930
T28940
T28950
T28960
T28970
T28980
T28990
T29000
T29010
T29020
T29030
T29040
T29050
T29060
T29070
T29080
T29090
T29100
T29110
T29120
T29130
T29140
T29150
T29160
T29170
T29180
T29190
T29200
T29210
T29220
T29230
T29240
T29250
T29260
T29270
T29280
T29290
T29300
T29310
T29320
T29330
T29340
T29350
T29360
T29370
T29380
T29390
T29400
T29410
T29420
T29430
T29440
T29450
T29460
T29470
T29480
T29490
T29500
T29510
T29520
T29530
T29540
T29550
T29560
T29570
T29580
T29590
T29600
T29610
T29620
T29630
T29640
T29650
T29660
T29670
T29680
T29690
T29700
T29710
T29720
T29730
T29740
T29750
T29760
T29770
T29780
T29790
T29800
T29810
T29820
T29830
T29840
T29850
T29860
T29870
T29880
T29890
T29900
T29910
T29920
T29930
T29940
T29950
T29960
T29970
T29980
T29990
T30000
T30010
T30020
T30030
T30040
T30050
T30060
T30070
T30080
T30090
T30100
T30110
T30120
T30130
T30140
T30150
T30160
T30170
T30180
T30190
T30200
T30210
T30220
T30230
T30240
T30250
T30260
T30270
T30280
T30290
T30300
T30310
T30320
T30330
T30340
T30350
T30360
T30370
T30380
T30390
T30400
T30410
T30420
T30430
T30440
T30450
T30460
T30470
T30480
T30490
T30500
T30510
T30520
T30530
T30540
T30550
T30560
T30570
T30580
T30590
T30600
T30610
T30620
T30630
T30640
T30650
T30660
T30670
T30680
T30690
T30700
T30710
T30720
T30730
T30740
T30750
T30760
T30770
T30780
T30790
T30800
T30810
T30820
T30830
T30840
T30850
T30860
T30870
T30880
T30890
T30900
T30910
T30920
T30930
T30940
T30950
T30960
T30970
T30980
T30990
T31000
T31010
T31020
T31030
T31040
T31050
T31060
T31070
T31080
T31090
T31100
T31110
T31120
T31130
T31140
T31150
T31160
T31170
T31180
T31190
T31200
T31210
T31220
T31230
T31240
T31250
T31260
T31270
T31280
T31290
T31300
T31310
T31320
T31330
T31340
T31350
T31360
T31370
T31380
T31390
T31400
T31410
T31420
T31430
T31440
T31450
T31460
T31470
T31480
T31490
T31500
T31510
T31520
T31530
T31540
T31550
T31560
T31570
T31580
T31590
T31600
T31610
T31620
T31630
T31640
T31650
T31660
T31670
T31680
T31690
T31700
T31710
T31720
T31730
T31740
T31750
T31760
T31770
T31780
T31790
T31800
T31810
T31820
T31830
T31840
T31850
T31860
T31870
T31880
T31890
T31900
T31910
T31920
T31930
T31940
T31950
T31960
T31970
T31980
T31990
T32000
T32010
T32020
T32030
T32040
T32050
T32060
T32070
T32080
T32090
T32100
T32110
T32120
T32130
T32140
T32150
T32160
T32170
T32180
T32190
T32200
T32210
T32220
T32230
T32240
T32250
T32260
T32270
T32280
T32290
T32300
T32310
T32320
T32330
T32340
T32350
T32360
T32370
T32380
T32390
T32400
T32410
T32420
T32430
T32440
T32450
T32460
T32470
T32480
T32490
T32500
T32510
T32520
T32530
T32540
T32550
T32560
T32570
T32580
T32590
T32600
T32610
T32620
T32630
T32640
T32650
T32660
T32670
T32680
T32690
T32700
T32710
T32720
T32730
T32740
T32750
T32760
T32770
T32780
T32790
T32800
T32810
T32820
T32830
T32840
T32850
T32860
T32870
T32880
T32890
T32900
T32910
T32920
T32930
T32940
T32950
T32960
T32970
T32980
T32990
T33000
T33010
T33020
T33030
T33040
T33050
T33060
T33070
T33080
T33090
T33100
T33110
T33120
T33130
T33140
T33150
T33160
T33170
T33180
T33190
T33200
T33210
T33220
T33230
T33240
T33250
T33260
T33270
T33280
T33290
T33300
T33310
T33320
T33330
T33340
T33350
T33360
T33370
T33380
T33390
T33400
T33410
T33420
T33430
T33440
T33450
T33460
T33470
T33480
T33490
T33500
T33510
T33520
T33530
T33540
T33550
T33560
T33570
T33580
T33590
T33600
T33610
T33620
T33630
T33640
T33650
T33660
T33670
T33680
T33690
T33700
T33710
T33720
T33730
T33740
T33750
T33760
T33770
T33780
T33790
T33800
T33810
T33820
T33830
T33840
T33850
T33860
T33870
T33880
T33890
T33900
T33910
T33920
T33930
T33940
T33950
T33960
T33970
T33980
T33990
T34000
T34010
T34020
T34030
T34040
T34050
T34060
T34070
T34080
T34090
T34100
T34110
T34120
T34130
T34140
T34150
T34160
T34170
T34180
T34190
T34200
T34210
T34220
T34230
T34240
T34250
T34260
T34270
T34280
T34290
T34300
T34310
T34320
T34330
T34340
T34350
T34360
T34370
T34380
T34390
T34400
T34410
T34420
T34430
T34440
T34450
T34460
T34470
T34480
T34490
T34500
T34510
T34520
T34530
T34540
T34550
T34560
T34570
T34580
T34590
T34600
T34610
T34620
T34630
T34640
T34650
T34660
T34670
T34680
T34690
T34700
T34710
T34720
T34730
T34740
T34750
T34760
T34770
T34780
T34790
T34800
T34810
T34820
T34830
T34840
T34850
T34860
T34870
T34880
T34890
T34900
T34910
T34920
T34930
T34940
T34950
T34960
T34970
T34980
T34990
T35000
T35010
T35020
T35030
T35040
T35050
T35060
T35070
T35080
T35090
T35100
T35110
T35120
T35130
T35140
T35150
T35160
T35170
T35180
T35190
T35200
T35210
T35220
T35230
T35240
T35250
T35260
T35270
T35280
T35290
T35300
T35310
T35320
T35330
T35340
T35350
T35360
T35370
T35380
T35390
T35400
T35410
T35420
T35430
T35440
T35450
T35460
T35470
T35480
T35490
T35500
T35510
T35520
T35530
T35540
T35550
T35560
T35570
T35580
T35590
T35600
T35610
T35620
T35630
T35640
T35650
T35660
T35670
T35680
T35690
T35700
T35710
T35720
T35730
T35740
T35750
T35760
T35770
T35780
T35790
T35800
T35810
T35820
T35830
T35840
T35850
T35860
T35870
T35880
T35890
T35900
T35910
T35920
T35930
T35940
T35950
T35960
T35970
T35980
T35990
T36000
T36010
T36020
T36030
T36040
T36050
T36060
T36070
T36080
T36090
T36100
T36110
T36120
T36130
T36140
T36150
T36160
T36170
T36180
T36190
T36200
T36210
T36220
T36230
T36240
T36250
T36260
T36270
T36280
T36290
T36300
T36310
T36320
T36330
T36340
T36350
T36360
T36370
T36380
T36390
T36400
T36410
T36420
T36430
T36440
T36450
T36460
T36470
T36480
T36490
T36500
T36510
T36520
T36530
T36540
T36550
T36560
T36570
T36580
T36590
T36600
T36610
T36620
T36630
T36640
T36650
T36660
T36670
T36680
T36690
T36700
T36710
T36720
T36730
T36740
T36750
T36760
T36770
T36780
T36790
T36800
T36810
T36820
T36830
T36840
T36850
T36860
T36870
T36880
T36890
T36900
T36910
T36920
T36930
T36940
T36950
T36960
T36970
T36980
T36990
T37000
T37010
T37020
T37030
T37040
T37050
T37060
T37070
T37080
T37090
T37100
T37110
T37120
T37130
T37140
T37150
T37160
T37170
T37180
T37190
T37200
T37210
T37220
T37230
T37240
T37250
T37260
T37270
T37280
T37290
T37300
T37310
T37320
T37330
T37340
T37350
T37360
T37370
T37380
T37390
T37400
T37410
T37420
T37430
T37440
T37450
T37460
T37470
T37480
T37490
T37500
T37510
T37520
T37530
T37540
T37550
T37560
T37570
T37580
T37590
T37600
T37610
T37620
T37630
T37640
T37650
T37660
T37670
T37680
T37690
T37700
T37710
T37720
T37730
T37740
T37750
T37760
T37770
T37780
T37790
T37800
T37810
T37820
T37830
T37840
T37850
T37860
T37870
T37880
T37890
T37900
T37910
T37920
T37930
T37940
T37950
T37960
T37970
T37980
T37990
T38000
T38010
T38020
T38030
T38040
T38050
T38060
T38070
T38080
T38090
T38100
T38110
T38120
T38130
T38140
T38150
T38160
T38170
T38180
T38190
T38200
T38210
T38220
T38230
T38240
T38250
T38260
T38270
T38280
T38290
T38300
T38310
T38320
T38330
T38340
T38350
T38360
T38370
T38380
T38390
T38400
T38410
T38420
T38430
T38440
T38450
T38460
T38470
T38480
T38490
T38500
T38510
T38520
T38530
T38540
T38550
T38560
T38570
T38580
T38590
T38600
T38610
T38620
T38630
T38640
T38650
T38660
T38670
T38680
T38690
T38700
T38710
T38720
T38730
T38740
T38750
T38760
T38770
T38780
T38790
T38800
T38810
T38820
T38830
T38840
T38850
T38860
T38870
T38880
T38890
T38900
T38910
T38920
T38930
T38940
T38950
T38960
T38970
T38980
T38990
T39000
T39010
T39020
T39030

Figure F2. A–D. Schematic development of continental breakup initiated by a simple shear along a deep, low-angle fault. B–D are slightly modified from Huismans and Beaumont (2011) and illustrate modeling-based stages of extension at magma-poor, Iberia-Newfoundland type rifted margins. Key features of D are thinning of the upper crust, juxtaposition of lower crust with serpentinized mantle between the outer margin and igneous oceanic crust. UP = upper plate, LP = lower plate. The Expedition 367/368 drilling strategy was designed to sample and test whether or not these fundamental crustal units and tectonic relationships are present at the northern SCS rifted margin.

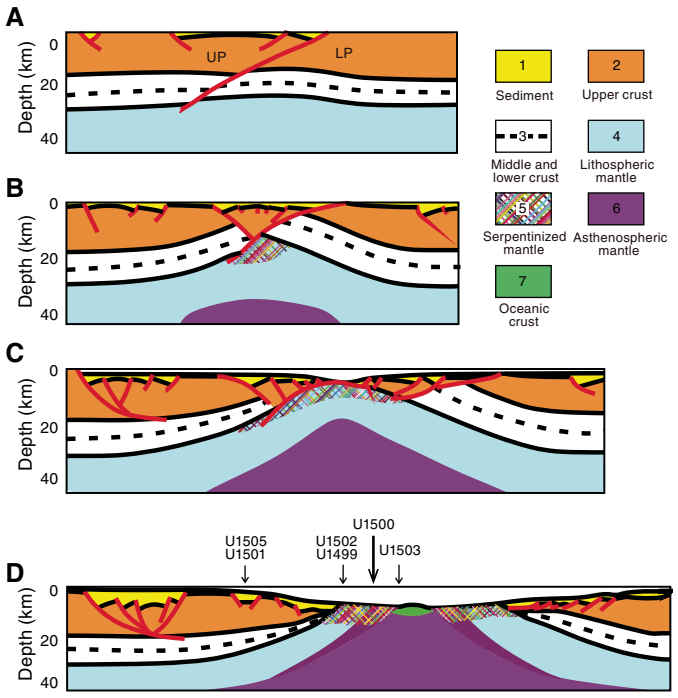

Subduction of the eastern part of the SCS basin started at or before ~15 Ma along the Manila Trench (Li et al., 2013). For a more complete review of the regional setting and tectonic development of the SCS, see Shi and Li (2012), Franke et al. (2013), Li et al. (2013), and Sun et al. (2014).

The Expedition 367/368 drilling transect is located ~50 km west of IODP Site U1435 along the northern SCS margin (Figures **F1**, **F3**) (Li et al., 2015a, 2015b). A transform fault defines a western boundary of a margin segment that exhibits a broad zone of crustal extension (Figure **F4**). This broad zone of extension (COT) may end to the east somewhere between Sites U1432 and U1435. East of this position, continental crust seems to thin into ocean crust in a much narrower COT. It is therefore conceivable that a kind of crustal transform zone is present in this location and defines an eastern end of a margin segment characterized by a high degree of crustal extension.

The segment of the SCS margin addressed by Expedition 367/368 is characterized by a relatively broader COT (~80 km) of crustal stretching and extension (Figure **F5**) prior to breakup and stretches for nearly 100 km between longitudes 115°35′E and 116°30′E. A deep sag basin (midslope basin [MSB]) of presumed Eocene to Oligocene age is present in the midslope area and is bounded seaward by an outer margin high (OMH), forming a quite persistent structure along the margin. Three distinct ridges (A, B, and C in Figure **F4**) are found seaward of the OMH in the more distal margin and on progressively thinner crust in the COT. We refer

Figure F3. Bathymetric maps showing Expedition 367/368 sites (stars), and (A) regional and (B) local coverage of multichannel seismic reflection data and OBS data. Thick blue and red lines are key seismic lines used for planning of the drilling transect. A. Magnetic isochrons (orange lines) from Briais et al. (1993). B. Magnetic picks (orange squares) from the same reference, extracted from the Seton et al. (2014) compilation. Chron labels for the picks correspond to the old edge of the normal polarity intervals (see Ogg et al. [2016] timescale for ages). Orange square = Leg 184 Site 1148, yellow squares = Expedition 349 Sites U1432 and U1435.

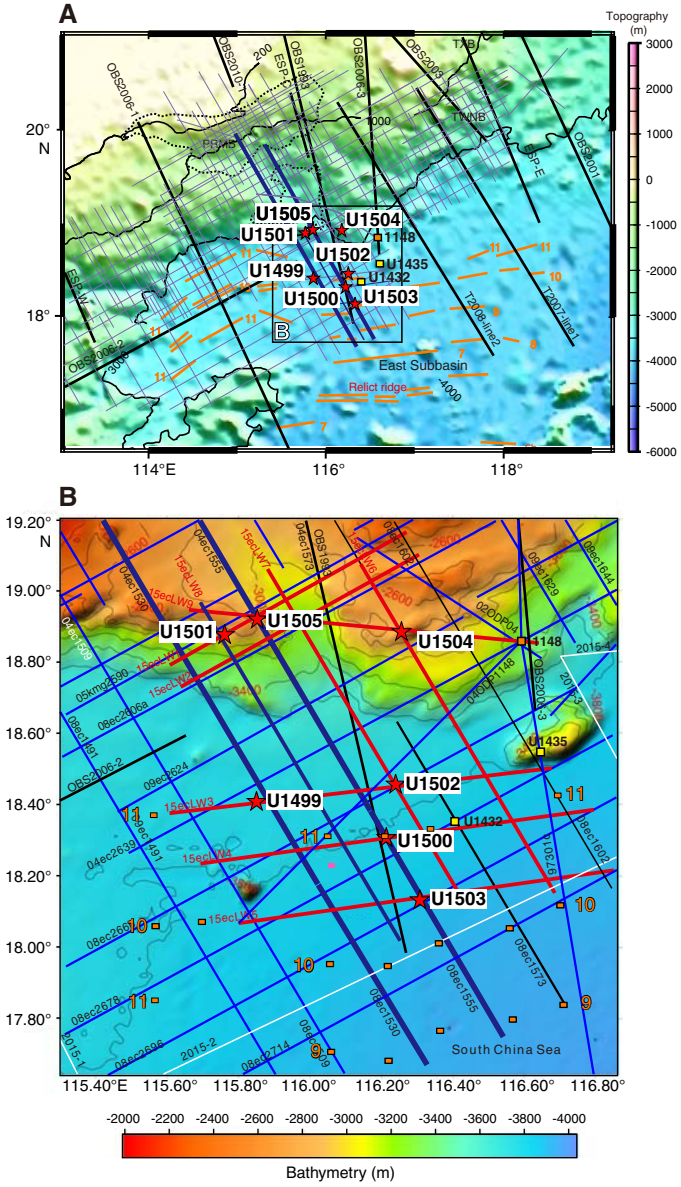

to the continent/ocean boundary (COB) as the much narrower zone in which the outermost, highly thinned continental lithosphere is replaced seaward by new crust that formed in a narrow zone at a spreading ridge in a steady-state fashion. The latter can include continuous tectonic exhumation of rising lithospheric or asthenospheric mantle (e.g., Dick et al., 2003), accretion of normal igneous oceanic crust, or a mixture of these two processes. Constraining the nature and location of the COB at the SCS will require integrated interpretation of deep crustal reflection normal and wide-angle incidence seismic data and deep sampling by drilling.

Figure F4. Two-way traveltime to (A) acoustic basement (Tg reflector) and (B) Unconformity T60 and location of Expedition 367/368 sites. Proposed drilling transect (thick black line) was located approximately at the center of a margin segment bounded to the southwest by a transform fault. Northeastern boundary of margin segment is located around Expedition 349 Site U1435. In this location, the outer margin high and Ridge A seem to coalesce, and Ridges B and C of the COT become indistinct toward the northeast within the next margin segment. Note that outer margin high is slightly east-northeast to the more parallel Ridges A, B, and C.

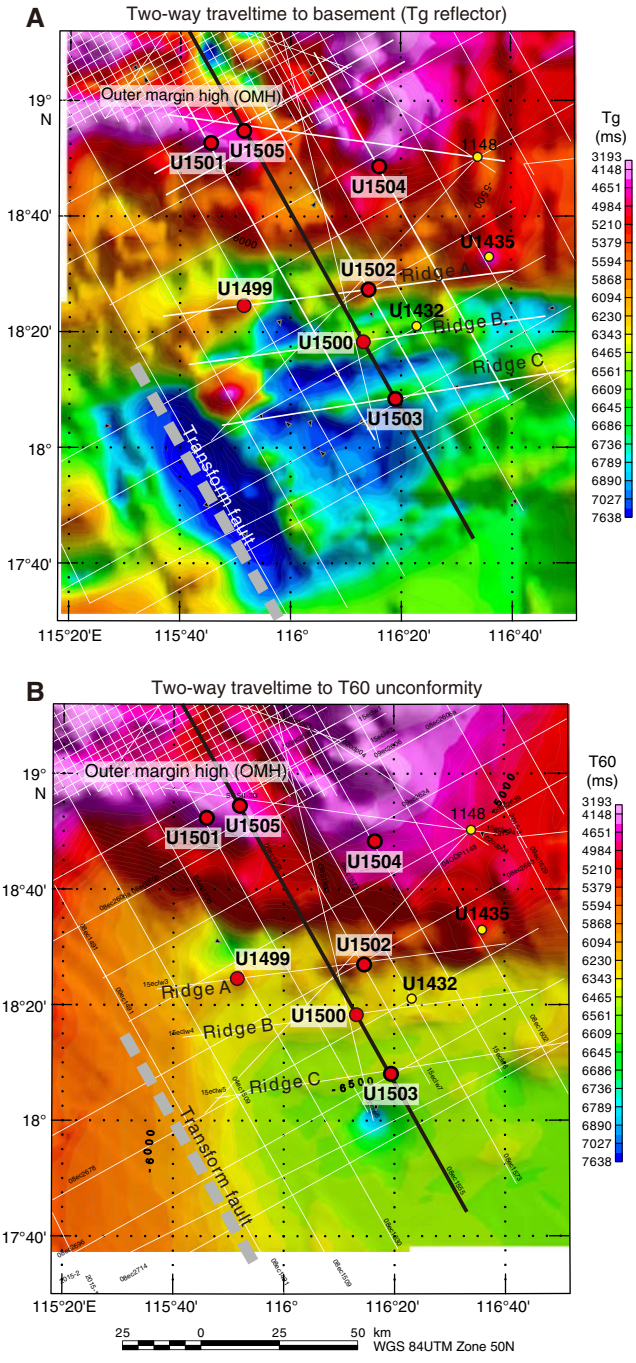

The clear seismic reflections from the Mohorovičić seismic discontinuity (Moho) show distinct thinning of the continental crust (Figure **F5**) across the COT with a thickness of ~6 km around the seaward end. Separate layers hypothesized to be upper, middle, and lower crust are present in the landward part of these seismic profiles. The lower crust is acoustically transparent and may in places be as thin as ~6 km. Lower crust with a similar thickness and seismic appearance is reported from the northeastern SCS margin (McIntosh et al., 2013, 2014; Lester et al., 2013). The seaward continuation of this crustal layering into the COB is, however, ambiguous, and prevents us from interpreting the detailed nature of the COB at this point.

The upper crust shows numerous extensional, low-angle detachment faults soling out at midcrustal levels. This fault system generated a number of deep half-grabens filled with synrift sediments that were subsequently covered by postrift sediments. The boundary between synrift and postrift sediments may follow the seismic stratigraphic unconformity named T70 (Figure **F5**). Industry data from distant wells suggest a breakup unconformity age of ~34 Ma. However, this age of T70 may be subject to revision, and in addition, the time of crustal extension is not necessarily synchronous across the margin and could be younger toward the outer margin. A younger, widely distributed unconformity (T60) is also shown in Figure **F5**. The T60 unconformity corresponds to a hiatus at ~23 Ma found at ODP Site U1148 (Shipboard Scientific Party, 2000) and IODP Site U1435. T60 is approximately synchronous with a southward jump of the SCS spreading axis (Briais et al., 1993). However, the age of T60 may also be subject to revision, and the relationship between a ridge jump and a margin-wide unconformity and seismic sequence boundary remains speculative at this point.

The OMH hosts a number of relatively shallow half-graben basins on top of this broad basement high. The stratigraphy of these smaller basins can be traced seismically into the deeper, central basin sag below the MSB (Figure **F5**). The normal faults bounding these OMH basins are clearly imaged and, for the main part, dip seaward. These small rift basins, therefore, offer an opportunity to sample the stratigraphy covering the entire period of rifting and postrift subsidence. The MSB itself is bounded landward by major, seaward-dipping normal fault(s) seemingly forming major detachments soling out at middle to lower crustal levels but not penetrating through the lower crust. This suggests decoupling between the upper and lower crust and, at least in this more landward part of the margin, faults never penetrated the lower crust, which may have remained ductile and resistant to faulting.

The lower crust in the COT may thicken seaward (lower crustal flow?), but this interpretation is not well constrained (Figure **F5**). Likewise, seismic imaging of the low-angle faults and detachments in the landward part of the COT cannot, with confidence, be traced into the distal margin regime south of the OMH. One possibility is that the main detachment zone was located above what later became Ridge A, effectively implying that Ridge A is a core complex consisting of lower continental crust or subcontinental mantle, depending on how deeply detachments exhumed the lithosphere in the distal margin. Alternatively, if the main detachment underlies Ridge A, this structure would represent upper plate material of upper crustal origin.

Ridge A is for the most part dome-like, showing neither normal faults nor clearly developed synrift half-grabens like the OMH. Excluding postrift sediments, the crust below this outermost basement high is only ~6–8 km thick using the ocean-bottom seismometer velocity constraints of Yan et al. (2001), Wang et al. (2006), and Wei et al. (2011). Seaward of Ridge A and across ridges B and C, the crust has a fairly uniform thickness of ~6 km, which could be consistent with oceanic crust (Yan et al., 2001). The oldest linear magnetic anomaly that can be confidently mapped along this margin segment is interpreted as magnetic Chron C11n based on

Figure F5. Deep crustal time-migrated seismic reflection data without and with interpretation. Note the rather thin lower crust (two layers) above a strong Mohorovičić seismic discontinuity (Moho) reflector that can be followed oceanward. Moho reflection is weak to absent seaward from around the interpreted COT. Wide-angle seismic data (Yan et al., 2001) confirm ~6 km thick ocean crust (OC) seaward of the COT. A large detachment fault ~150 km inland of the COT separates more stable crust landward from that of highly extended crust seaward. An OMH is a fairly consistent feature along this margin segment. Key seismic unconformities are shown in purple (T70; ~32 Ma breakup unconformity?) and blue (T60; ~23 Ma regional basin event). These ages are inferred from long-distance (>100 km) correlation of seismic unconformities with industry holes and ODP Leg 184 Site 1148 (T60); ages need confirmation by coring and are only tentative. Tg (black) is basement. Arrows = approximate position of seafloor magnetic anomalies with chron numbers. Seismic data are from Line 04ec1555-08ec1555 (courtesy of Chinese National Offshore Oil Corporation [CNOOC]). Location of line is shown in Figure F3. CDP = common depth point. C11n, C10n, and C9n = approximate location of normal polarity magnetic isochrons. MSB = midslope basin.

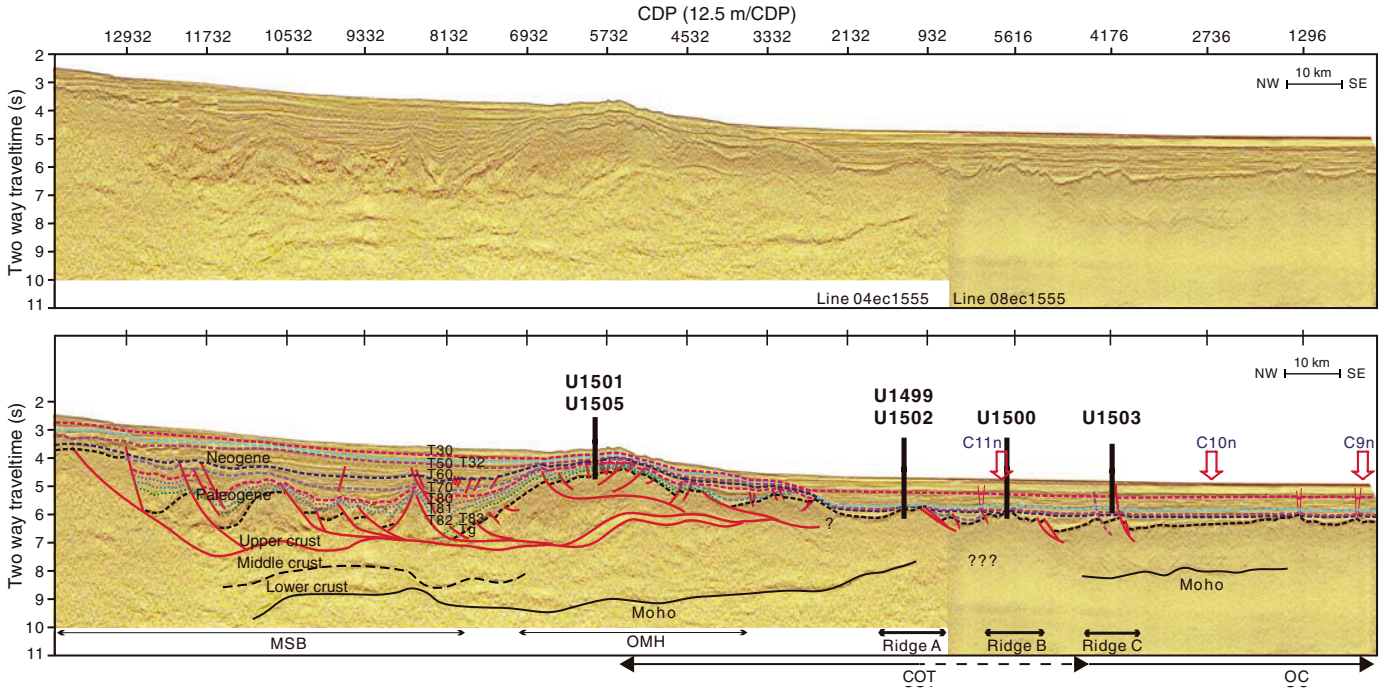

total magnetic field data; the corresponding magnetic high is located ~10 km seaward (south) of Ridge B (Figure **F5**). However, if this position is corrected by deskewing the magnetic data, the magnetic high corresponding to C11n with an age of ~29.5–30 Ma will be located more or less on top of Ridge B (Figure **F5**).

Both Ridges B and C consist of fault blocks tilted landward along seaward-dipping normal faults (Figure **F5**). Ridge B shows seismic features along strike and in the uppermost crust that could be consistent with a volcanic origin. However, without drilling constraints, these features could also be interpreted as prerift deposits below the seismic unconformity that defines the top of acoustic basement at Ridge B. Ridge C is seismically similar in many ways to Ridge B. However, an apparent reversed magnetic anomaly (C10r; ~29 Ma) strongly suggests that this ridge indeed represents close to if not full igneous oceanic crust.

Sampling the basement at Ridges A, B, and C was therefore essential for Expedition 367/368 to distinguish between different tectonic models for breakup along highly extended margins. Ridges A and B in particular help constrain the style of rifting and to determine if the SCS margin indeed succeeded to the stage of a hyperextended margin or not. Ridge C is assumed to represent the early igneous crust, and samples from this ridge will constrain the nature of early oceanic crust formation, specifically how quickly a robust igneous system was established, what mantle source was involved (e.g., composition, temperature), what conditions of mantle melting (degree and depth of melting) ruled, and, if any, type and amount of continental crustal contamination of the igneous material derived from the asthenospheric mantle.

Expedition objectives

The two-expedition drilling transect across the SCS margin set out to understand the timing and process of rifting, the eventual rupturing of the continental crust, and the onset of breakup-related magmatism at the SCS rifted margin (Figure **F2**). Four primary and sixteen alternate drill sites across a ~150 km wide COT zone were defined in the *Scientific Prospectus* (Sun et al., 2016b). The four primary sites targeted the four main tectonic features (the OMH and its small rift basins) and the nature of the three ridges in the distal margin (Ridges A, B, and C). At each of these sites, the nature of the acoustic basement and the record of synrift and postrift deposits were key targets.

Results from the OMH site (U1501) in particular will address the rifting history and provide constraints on the degree of crustal exhumation, if any, in the OMH. Located off the distal margin and in relatively thick crust, the subsidence history at this site can be compared with that of the more distal margin, which suffered a much higher degree of crustal thinning. Sampling of prerift through synrift to postrift sediments in one of the rotated fault blocks at the OMH can constrain the timing of rifting and rate of extension in a location where results can be tied to the much deeper rift basins further landward through a dense grid of high-quality 2-D seismic data provided by the Chinese National Offshore Oil and Gas Company (CNOOC). The site has the further advantage of a water depth shallower than the other three primary sites and, importantly, above the present carbonate compensation depth (CCD). It therefore has

the potential to yield a rich record of carbonate sediments for detailed paleoclimate studies using stable isotope techniques.

Ridge A in particular will be important for constraining whether this ridge is a core complex representing lower plate material (mantle of lower crust), upper plate extensional fault block, or igneous material related to breakup. Ridge B provides an option to distinguish between possible unroofed, lower plate material, upper plate extensional fault block, and igneous material related to incipient seafloor spreading. Ridge C, as described above, targeted sampling a time series of early ocean floor volcanism to establish a reference frame for understanding and modeling the igneous development of the margin.

Except for coring at Ridge C, where operations came to a halt for technical reasons, Expedition 367/368 completed all the above objectives. Expedition 367 drilled two of the primary sites (U1499 and U1500) on Ridges A and B (Figures **F2**, **F3**, **F4**, **F5**). Coring at Site U1499 on Ridge A recovered synrift or prerift sediments below the acoustic basement. Coring at Site U1500 successfully sampled 150 m of submarine basaltic lavas, including pillow lavas, below the acoustic basement at Ridge B. Expedition 368, which originally set out to drill the remaining two primary sites on Ridge C (U1503) and the OMH (Site U1501), added a second, alternate site on Ridge A (Site U1502) to improve the characterization of this ridge and recovered a 180 m thick sequence of submarine basaltic lavas. A successful drilling strategy (see **Coring and logging strategy**), however, allowed us to also pursue Site U1503 on Ridge C, but after installation of casing at this site, the hole had to be abandoned for technical reasons. This decision left time for inserting alternate Sites U1504 and U1505, both at shallower water depths on the OMH. Two of the OMH drill sites penetrated to acoustic basement and found Mesozoic prerift? sediments (Site U1501) and metamorphic schist (Site U1504). Site U1505 provided ~100 percent recovery of a very complete Oligocene to Plio–Pleistocene sediment sequence.

Coring and logging strategy

Drilling operations were designed to core and log through thick sediment sections and, significantly, into underlying basement using casing in the upper and unstable part of the sedimentary sections. Initially, the operational approach was to drill two holes per site (Figures **F6**, **F7**).

The first hole at each site would be cored with the advanced piston corer (APC) and extended core barrel (XCB) systems to refusal (or maximum casing depth) and then logged with the triple combination (triple combo) and Formation MicroScanner (FMS)-sonic tool strings. The APC/XCB hole would also document borehole and formation conditions to help determine the length of casing for drilling a second hole (B). All full APC cores were intended to be oriented, and formation temperature measurements would be made using the advanced piston corer temperature tool (APCT-3).

The second hole at each site was designed to begin by drilling in a seafloor reentry system with casing extending to ~650 m or an otherwise defined depth (Figures **F8**, **F9**, **F10**, **F11**). Casing is drilled down through the reentry cone using an extendable underreamer and mud motor technology (see **https://rosetta.iodp.tamu.edu/A/TechDoc/8250**). Following the installation of casing to the desired depth, coring using the RCB system could then extend from the base of the casing through the sediment and into the underlying basement. Multiple pipe trips to replace hard rock RCB bits would be made as required by the depth of the target in basement. Upon completion of the coring objectives, the RCB bit would be dropped either at the bottom of the hole or on the seafloor before downhole wireline logging was conducted. For this deeper logging, we planned to use the triple combo and FMS-sonic tool strings along with the Versatile Seismic Imager (VSI) tool string to conduct check shots.

During Expedition 367/368, we had to modify this general operational plan in response to borehole conditions and the need to fo-

Figure F6. Implemented Expedition 368 operations.TD = total depth.

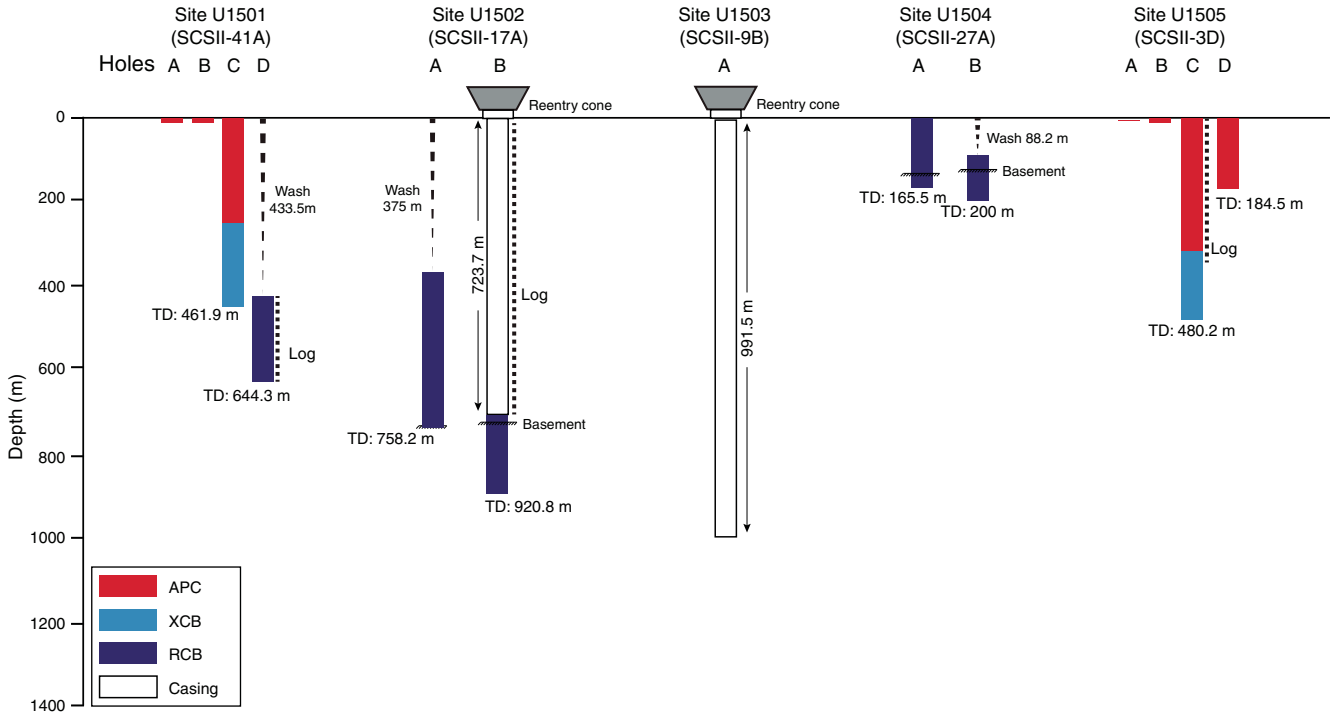

Figure F7. Planned and implemented Expedition 367 operations.

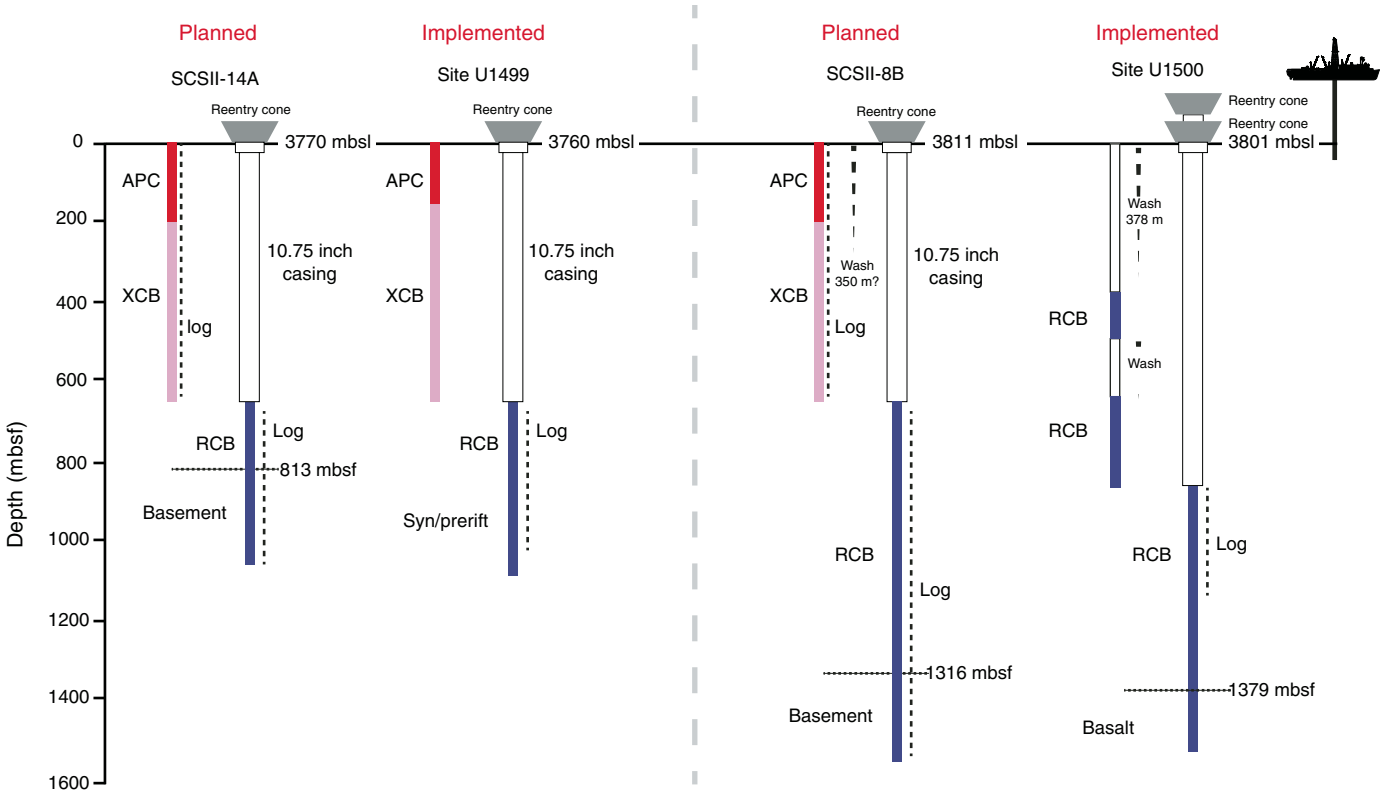

Figure F8. Reentry system and casing, Hole U1499B.

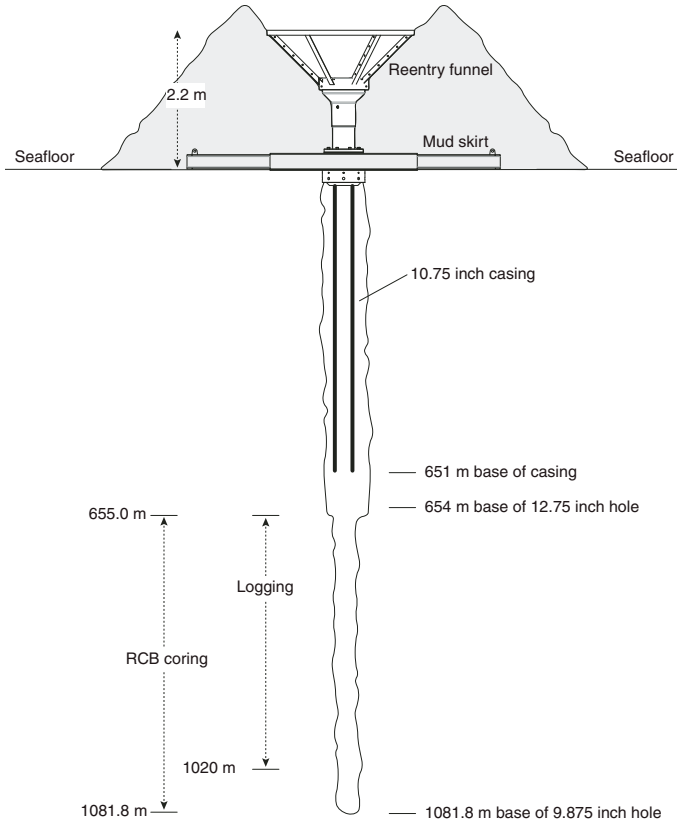

Figure F9. Reentry system and casing, Hole U1500B.

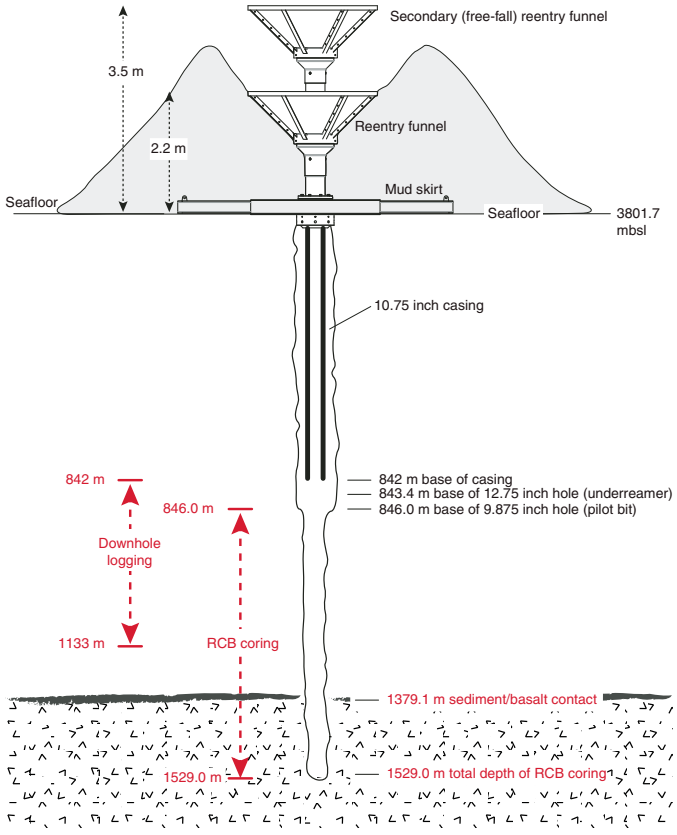

Figure F10. Reentry system and casing, Hole U1502B.

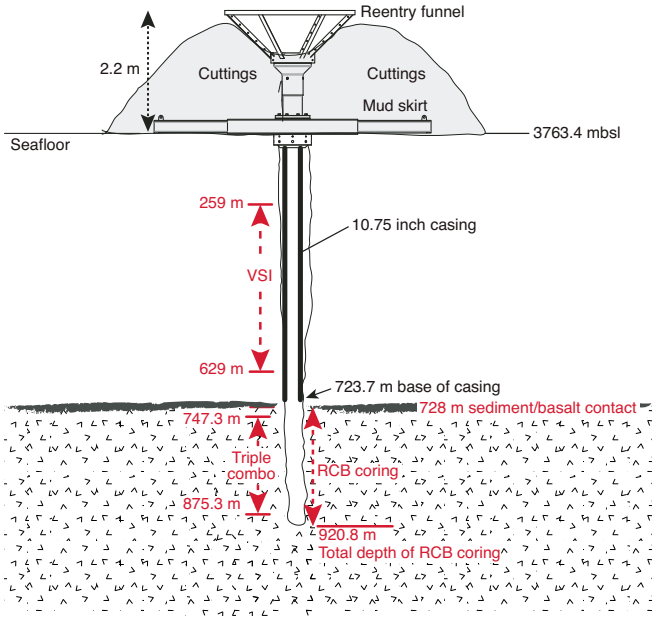

Figure F11. Reentry system and casing, Hole U1503A.

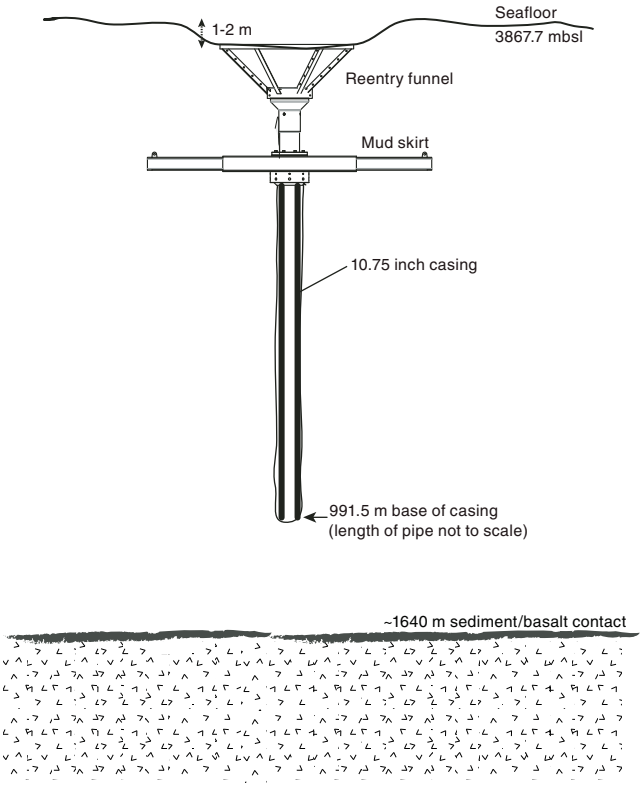

cus our operations time to achieve our highest priority basement objectives. The implemented operations are shown in Figures **F6** and **F7**.

At Site U1499, the pilot (first) hole (U1499A) consisted of APC/XCB coring until refusal. In the pilot hole (U1500A) at Site U1500, we washed down without coring in the limits of safety approval and the requirements to identify appropriate locations for setting casing in the subsequent hole. We also decided not to collect downhole log data in either of these pilot holes, partly due to poor borehole conditions that we thought would not yield good data and partly to focus more time on the deeper core and log objectives.

For the primary, deep-penetrating, cased holes at each of the first two sites, we set as much casing as possible (651 m in Hole U1499B and 842 m in Hole U1500B) to keep the upper part of the hole in stable condition for drilling and to enhance our ability to clean cuttings out of such deep holes. Casing was drilled into the seafloor to total depth as a single step at each location to minimize hole disturbance and save time. We then drilled and cored using the RCB system below the casing until we reached the basement (Hole U1500B) or until hole conditions prevented further coring (Hole U1499B). We collected downhole logging data in the deep penetration hole at each site.

At Site U1501, the pilot hole (U1501C) consisted of APC/XCB coring until refusal. From the findings, we concluded that in this location the formation might be stable enough to continue with the deeper RCB Hole U1501D to ~600 m without casing. Logging was therefore not done in Hole U1501C. Hole U1501D was drilled without coring to a slightly shallower depth than Hole U1501C and then RCB cored to the bottom of the hole. Logging was then executed. This approach saved considerable operational time. We drilled in Hole U1502A to 375 m without coring and then cored with the RCB system to identify a proper casing point. Casing was then drilled in Hole U1502B to the desired depth, followed by RCB coring to target. Single-run logging (triple combo) was then executed in the open hole below casing with VSI check shots in both open hole and casing. At Site U1503, we initially drilled in Hole U1503A without coring to a planned casing depth (990 m) estimated on the basis of drilling data from Site U1500 (~20 km away) and seismic correlation between the two sites. A free-fall reentry system was deployed, and casing was subsequently installed in the already established Hole U1503A with the assistance of the underreamer and mud motor (Figure **F12**). This approach turned out to be very efficient and saved much time. Unfortunately, mechanical problems at the rig floor (lower clutch of the drawworks) prevented us from further pursuing the site.

With an operational limit of deploying a maximum of 3400 m of drill string for the remainder of Expedition 368, no deep sites requiring casing could be pursued. Site U1504 had a primary basement target below only ~120 m of sediment cover. Hole U1504A was RCB cored to ~150 m. Hole U1504B was drilled without coring to ~90 m and continued with RCB coring to 200 m. No logging was pursued.

Four holes were cored and/or drilled at Site U1505. Hole U1505C was cored with the APC as deep as possible, further cored with the half-length advanced piston corer (HLAPC) system until refusal, extended by XCB coring until the maximum length of the drill string was reached at 480 m, and then logged. Hole U1505D was cored with the APC to 180 m.

Figure F12. (A) Reentry system on the seafloor after free fall and (B) inspection of reentry cone after casing installation, Hole U1503A. The hole remains as a legacy hole for future occupation.



Site summaries

Site U1499

Site U1499 is located on basement Ridge A in the SCS COT zone ~60 km seaward and southeast of the OMH. The goal of drilling here was to core through the sediment to sample the basement rocks and thus determine basement age and lithology, which would provide a test of different possible models for the processes and rheology controlling the extension and ultimate breakup of the continent. Ridge A was expected to have basement of either upper continental crust, lower continental crust, or exhumed mantle rocks. Coring and drilling also constrain the postrift history by determining the age, water depth, and subsidence rates of the overlying sedimentary packages.

We conducted operations in two holes at Site U1499 (proposed Site SCSII-14A; Sun et al., 2016b) (Table **T1**). Hole U1499A is located at 18°24.5698′N, 115°51.5881′E in a water depth of 3760.2 m. In Hole U1499A, APC/XCB coring penetrated from the seafloor to 659.2 m and recovered 417.05 m (63%). Hole U1499B is located at 18°24.5705′N, 115°51.5990′E in a water depth of 3758.1 m. We installed casing in Hole U1499B to 651 m followed by RCB coring that penetrated from 655.0 to 1081.8 m and recovered 150.64 m (35%). Coring terminated in gravel before deteriorating drilling conditions prevented further penetration; no crystalline basement was encountered. Despite challenging conditions in the lowermost part of Hole U1499B, two successful wireline logging runs were conducted from 652 to 1020 m.

Lithostratigraphy

The cored sediment at Site U1499 is divided into nine lithostratigraphic units (Figure **F13**). Lithostratigraphic Unit I is a 48.85 m thick middle–upper Pleistocene sequence of dark greenish gray bioclast-rich clay with thin clayey silt and sand interbeds. Fining-upward silt and fine sand intervals are abundant and interpreted as turbidite sequences. Four thin (2–7 cm) ash layers were identified in Unit I; none were observed in the deeper units. Unit II (48.85–100.04 m) is a 51.19 m thick middle–upper Pleistocene sequence of interbedded greenish gray clay-rich calcareous ooze and dark greenish gray nannofossil-rich clay. Synsedimentary deformational structures such as folds, microfaults, and inclined beds are well developed in the sediment of this unit, which is interpreted as a slump deposit. This unit is underlain by Unit III (Pliocene–middle Pleistocene), which is divided into Subunits IIIA (100.04–181.80 m) and IIIB (181.80–333.65 m). The 233.61 m of Unit III is dominated by dark greenish gray clay with thick to very thick clayey silt and calcareous sand interlaminations. Subunit IIIA contains clayey silt layers that are thick laminations (<1 cm), whereas Subunit IIIB has abundant thin beds (2–5 cm) of clayey silt and an overall increase in nannofossil and foraminifer content. Unit IV (333.65–404.90 m) is a 71.25 m thick sequence of upper Miocene–Pliocene dark greenish gray silty sand with clay interbeds. Recovery is very low throughout this unit, but the recovered intervals and physical property data suggest that the sections with no recovery may contain unconsolidated to weakly consolidated sand.

Unit V (404.90–469.45 m) is a 64.55 m thick sequence of upper Miocene dark greenish gray clay with mostly thin (<5 cm) clayey silt and foraminifer sand interbeds. Drilling disturbance in the form of biscuiting increases significantly in this unit. Similar to Unit IV, recovery in Unit VI (469.45–618.30 m) is very low. The recovered intervals in this unit include upper Miocene dark greenish gray silty sand with clay interbeds. Unit VII (618.30–761.70 m) is mainly composed of upper Miocene dark greenish gray to dark gray sandstone and claystone with siltstone interbeds. Lithification increases sharply downhole from the top of this unit, although sections with no recovery are inferred to be nonlithified sand. Unit VIII (761.70–929.02 m) comprises a 167.32 m thick interval of upper Oligocene–Miocene reddish brown to reddish gray claystone and clay-rich chalk. Based on the abundance of calcareous material, this unit is divided into two subunits. Subunit VIIIA (761.70–892.10 m) contains lower–upper Miocene dark reddish brown claystone with siltstone and foraminifer sandstone interbeds, whereas Subunit VIIIB (892.10–929.02 m) is composed of upper Oligocene–lower Miocene reddish brown to reddish gray clay-rich nannofossil chalk and clay-rich chalk. In the lowest part of Subunit VIIIB, abundant brownish black iron-manganese nodules occur in reddish brown nannofossil-rich claystone.

Unit IX (929.02–1081.80 m) is readily distinguished from the overlying units by containing Oligocene (and pre-Oligocene?) sandstone, claystone, matrix-supported breccia, and gravel. This unit is 152.78 m thick and comprises three subunits. Subunit IXA (929.02–933.28 m) is defined by dark brown and greenish gray sandstone and breccia. Subunit IXB (933.28–933.35 m) is defined by dark gray matrix-supported breccia in Core 367-U1499B-30R. Subunit IXC (933.35–1081.80 m) contains gray to dark gray gravel with silty sand intervals. The cores in Subunit IXC are completely fragmented and were recovered as pebbles and cobbles. In general,

Table T1. Expedition 367 hole summary. — = no data. **Download table in CSV format.**

Hole	Proposed site	Location	Water depth (m)	Total penetration (m)	Cored interval (m)	Drilled interval without coring (m)	Core recovery (m)	Core recovery (%)	Time on hole (days)	Cores (*N*)	Depth of 10.75 inch casing (m)
U1499A	SCSII-14A	18° 24.5698′N 115° 51.5881′E	3760.2	659.2	659.2	0.0	417.05	63	7.2	71	—
U1499B		18° 24.5705′N 115° 51.5990′E	3758.1	1081.8	426.8	655.0	150.64	35	14.9	44	651
			Site U1499 totals:	1741.0	1086.0	655.0	567.69	52	22.1	115	—
U1500A	SCSII-8B	18° 18.2762′N 116° 13.1916′E	3801.7	854.6	329.8	524.8	93.55	28	5.5	34	—
U1500B		18° 18.2707′N 116° 13.1951′E	3801.7	1529.0	683.0	846.0	278.80	41	24.8	81	842
			Site U1500 totals:	2383.6	1012.8	1370.8	372.35	37	30.3	115	—
			Expedition 367 totals:	4124.6	2098.8	2025.8	940.04	45	52.4	230	1493

the pebbles and cobbles are recycled sedimentary rocks (such as sandstone) that contain a variety of individual lithic components including igneous, sedimentary, and metamorphic clasts. Although the matrix that likely surrounded these cobbles and pebbles was not recovered, we infer that the matrix is poorly consolidated and washed away by the drilling process. Based on this description, Subunit IXC may represent synrift or prerift sediments.

Structural geology

The tilting of sedimentary beds and deformation structures observed at Site U1499 are limited to lithostratigraphic Units II, VII, VIII, and IX. The folds, faults, and tilted beds observed in Unit II are related to two slump events that reworked older sediment between younger Units I and III. Tilted beds and faults with slickensides were observed in Units VII and VIII. These faults are linked to compaction processes of the clays, and the tilted beds are associated with sandy layers. Unit IX is divided into three subunits. In Subunit IXA, tilted beds and a downhole increase in clast size, angularity, and proportion of clasts were observed. The matrix-supported breccia of Subunit IXB exhibits no clear deformation structure or tilted sedimentary bedding. Some of the sandstone and breccia clasts in Subunit IXC exhibit veins and fractures. These clasts were transported before sedimentation; therefore, their veins and fractures must have originated in a previous tectonic event.

Biostratigraphy

All core catcher samples at Site U1499 were analyzed for calcareous nannofossil and foraminiferal content, and additional samples were taken from the split-core sections when necessary to refine the ages. Preservation of microfossils varies from poor to very good, and total abundance varies from barren to abundant. Although samples exhibit some degree of reworking, 28 biostratigraphic datums are recognized, revealing that we recovered an apparently continuous succession of the Oligocene to the Pleistocene spanning nannofossil Zones NP25–NN21 and foraminifer Zones M4/M3 to Subzone PT1b. The Pleistocene/Pliocene boundary is located between Cores 367-U1499A-20X and 27X, the Pliocene/Miocene boundary is located between Cores 31X and 43X, and the Miocene/Oligocene boundary is in Section 367-U1499A-30R-2. Sedimentation rates varied from ~80 mm/ky in the late Miocene–early Pliocene and ~50 mm/ky in the early Pliocene–early Pleistocene to ~130 mm/ky in the middle–late Pleistocene. Extremely low sedimentation rates (~8 mm/ky) occurred in the early–middle Miocene during deposition of Unit VIII. Subunit IXA contains early–late Oligocene microfossils (calcareous nannofossils and foraminifers) with different preservation and abundance, probably influenced by transported and reworked materials.

Paleomagnetism

Paleomagnetic analysis was conducted on both archive-half sections and discrete samples from the working half. The archive-half sections were measured with the pass-through superconducting rock magnetometer (SRM) with demagnetization steps at 5, 15, and 25 mT. The discrete samples were subjected to alternating field (AF) and thermal demagnetization, and remanence was measured on the spinner magnetometer. We adopted a combination of stepwise AF and thermal demagnetization steps to fully demagnetize the discrete samples and obtain the characteristic remanent magnetization (ChRM).

Variations in natural remanent magnetization (NRM) intensity are well correlated to observable changes in lithology and magnetic susceptibility; for example, the low NRM intensity at ~60 m (Core 367-U1499A-7H) agrees with the carbonate-rich slump in which magnetic susceptibility values are also low. Drilling-induced remanence was identified and removed in most core sections at AF treatments of 15 mT. In addition, magnetic mineral variations were observed from the demagnetization behavior. From Core 367-U1499B-12R downhole, the drilling overprint becomes stronger and hard to remove with the relatively low AF steps used on the archive-half sections, whereas AF treatments up to 200 mT and temperatures up to 675°C could not fully demagnetize the discrete samples. These characteristics confirm the presence of higher coercivity magnetic minerals, such as hematite, compared with the predominant magnetite and/or titanomagnetite. But further rock magnetic property measurements should be conducted in a shore-based laboratory in order to better understand the compositions.

We constructed the magnetostratigraphy of Holes U1499A and U1499B based on the interpretation of the raw paleomagnetic data that show stable and clear demagnetization behaviors. Declinations from 0 to 162 m have been corrected by the Icefield MI-5 core orientation tool and therefore could help accurately define magnetic reversals. Otherwise, only inclinations are used for polarity interpretations. After correlating the magnetostratigraphy to the standard geomagnetic timescale, we confidently identified the boundary between the Brunhes and Matuyama Chrons at ~110 m. We thus conclude that the middle/early Pleistocene boundary (0.78 Ma) is at

Figure F13. Lithostratigraphic summary, Site U1499.

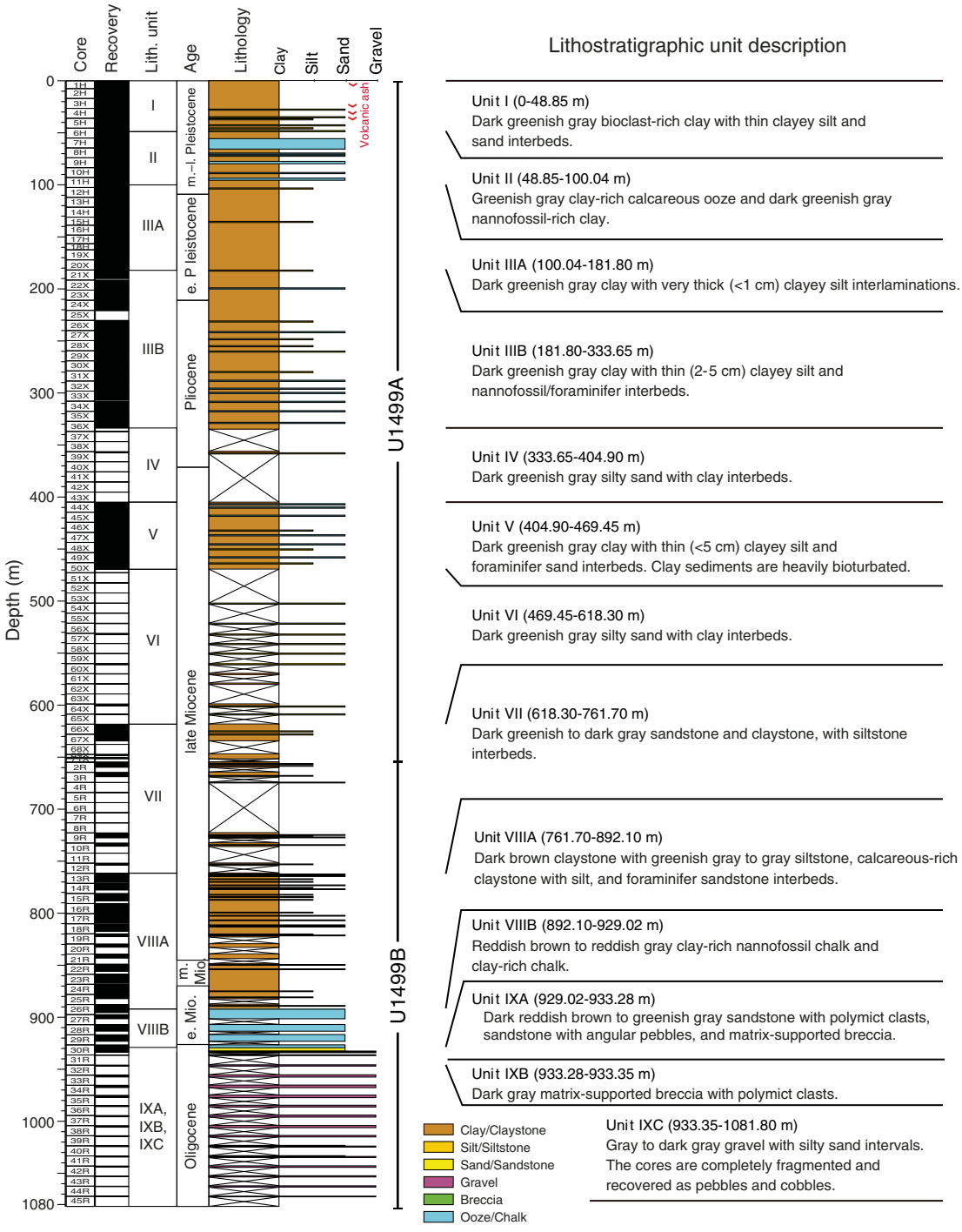

~110 m, the early Pleistocene/late Pliocene boundary is at ~220 m, the late/early Pliocene (3.6 Ma) boundary is at ~260 m, and early Pliocene/late Miocene boundary (5.33 Ma) is at ~370 m.

Geochemistry

Geochemical analyses were conducted for headspace gas safety monitoring; quantification of sediment $CaCO_3$, organic carbon, and nitrogen content; and interstitial water characterization. Calcium carbonate contents vary between 0.4 and 82 wt%, with higher values of >20 wt% corresponding to intervals of nannofossil/foraminifer ooze or chalk. Total organic carbon (TOC) contents mostly range from ~0 to ~ 1.0 wt%. TOC decreases gradually downhole from 1.0 to 0.3 wt% in the uppermost 110 m corresponding to the base of the sulfate reduction zone, reflecting active degradation of sedimentary organic matter. The TOC to total nitrogen molar ratio (TOC/TN) is mostly <8, indicating that TOC is derived dominantly from a marine source.

Hydrocarbon monitoring shows headspace gas consistently approaching zero throughout the site. Relatively higher methane contents of approximately tens to 6000 ppmv occur across the ~100–

250 m interval, just below the sulfate reduction zone. The overall low methane content indicates limited microbial methanogenesis likely caused by low TOC contents (<0.3 wt%) deeper than 110 m.

We obtained 58 interstitial water samples from Hole U1499A. The inorganic geochemistry of interstitial water is controlled by the remineralization of organic matter and carbonate and clay diagenesis. The sediment rapidly becomes suboxic, as indicated by a Mn peak of ~120 µM at ~6 m. Sulfate reduction coupled with sedimentary organic matter degradation occurs to ~110 m, with near-complete depletion to 257 m before increasing slowly to 16.9 mM at the bottom of Hole U1499A. The interval of near-complete sulfate consumption is also marked by pronounced high Ba concentrations >50 µM, suggesting the dissolution of barite ($BaSO_4$). The peak alkalinity and steady increase in NH_4^+ and Br^- in the upper 110 m are consistent with progressive remineralization of sedimentary organic matter. The gradual decrease in Ca^{2+} shallower than 80 m suggests active authigenic carbonate precipitation triggered by sulfate reduction. A subsequent downhole increase in Ca^{2+} and Sr^{2+} is likely caused by biogenic carbonate dissolution and recrystallization. Nearly parallel downhole decreases in Mg^{2+} and K^+ are mostly driven by clay mineral cation exchange and/or clay mineral authigenesis. The lower Cl^- and Na^+ concentrations compared to those of seawater at the bottom of Hole U1499A are mostly driven by the smectite–illite transformation. Elevated Si concentrations of 700–820 µM from the seafloor to 45 m suggest active dissolution of biogenic silica.

Petrophysics

At Site U1499, measurements of *P*-wave velocity, bulk density, magnetic susceptibility, and natural gamma radiation (NGR) were made on whole-round cores, and additional measurements were made on split cores and discrete samples, including thermal conductivity; caliper *P*-wave velocity on the *P*-wave caliper (PWC); porosity; and bulk, dry, and grain density. In general, bulk density, *P*-wave velocity, and thermal conductivity increase with depth, whereas porosity decreases with depth as a result of compaction and lithification. However, some properties, such as NGR or magnetic susceptibility, show local variations related to the specific lithology. The soft sediment in the upper 100 m shows rapid compaction with depth, marked by a decrease in porosity and increase in bulk density and thermal conductivity. Four thin volcanic ash layers in the uppermost 50 m are marked by peaks in magnetic susceptibility. The mass transport deposit (48.85–100.04 m) displays low magnetic susceptibility and low NGR, reflecting the high carbonate content of the calcareous ooze. Below these layers downhole to ~890 m, physical properties show small variations; bulk density, *P*-wave velocity, and thermal conductivity gradually increase, whereas porosity decreases with depth. The NGR and magnetic susceptibility data in this interval do not show much variation. From 830 to 930 m, we observed a general decrease in magnetic susceptibility and NGR where density increases slightly and *P*-wave velocity increases significantly from 2200 to 2900 m/s. These variations are associated with a significant increase in the carbonate content in the Subunit VIIIB chalks. The cobbles and pebbles in the deepest part (930–1080 m) show large variations in NGR, bulk density, and *P*-wave velocity and very low magnetic susceptibility.

Downhole measurements

Two downhole logging tool strings were run in Hole U1499B, a modified triple combo (sonic velocity, NGR, bulk density, resistivity, and caliper) tool string and the FMS-sonic tool string (FMS resistivity images and calipers, as well as NGR). We added the velocity tool to the first tool string because sonic velocities were needed for an accurate prediction of basement depth for the subsequent Site U1500 and to better constrain core-log-seismic correlation. We also did not know if hole conditions would allow a second logging run. Although stable borehole conditions in Hole U1499B allowed the second FMS logging run, we did not attempt a check shot due to time constraints and concerns about hole stability. Borehole conditions from the bottom of the casing at ~651 m to the bottom of Hole U1499B at ~1020 m were generally good, with measured diameters from ~10 to 16 inches. Washout zones were observed from 670 to 710 m, which corresponds to an interval of very low core recovery, as well as from 830 to 920 m, affecting quality of the log data in these intervals. Log and core data are generally in good agreement. Downhole logging provided information in zones of poor core recovery in Hole U1499B. The log data from 726 to 739 m exhibits high NGR and low bulk density and *P*-wave velocity, whereas the data from 820 to 840 m is characterized by a sharp increase in bulk density, a slight increase in *P*-wave velocity, and an abrupt decrease in NGR compared to average values above and below these depths. The Subunit VIIIB chalks (~890–930 m) display a sharp decrease in NGR and an increase in bulk density and *P*-wave velocity with depth, as well as only small variations in resistivity. Deeper than 930 m, bulk density, *P*-wave velocity, and resistivity show large variability, in part because of the presence of cobbles and pebbles. The quality of the acquired FMS images is strongly influenced by variations in hole diameter; they generally show alternating smooth and patchy textures with contrasting resistivity marking horizontal to slightly tilted bedding downhole to 930 m. The deepest layers of sandstones, breccias, and gravels show highly variable and oblique textures on the FMS images, possibly reflecting the varied orientation of the gravel clasts or the presence of faults and fractures in the gravel or the matrix. In general, the velocity measured with the sonic velocity logging tool match the PWC measurements taken with the caliper on the split cores. Six in situ formation temperature measurements were made in Hole U1499A and give a geothermal gradient of 93°C/km. The estimated heat flow is 110 mW/m^2, a value in agreement with the general heat flow of the area.

Correlation to seismic data

We used downhole log data and physical property measurements on cores and samples as well as other available data to correlate Site U1499 data with the available seismic reflection profiles. We also used the Site U1499 density and sonic velocity data to create synthetic seismograms that provided additional constraints on the correlation. Log sonic velocities and PWC velocities are in very good agreement, except for the deepest breccias and gravels (deeper than ~930 m) where measurement on individual pebbles leads to an overestimate of the velocity in the formation. For seismic correlation, we used the PWC and density data from moisture and density (MAD) and gamma ray attenuation (GRA) density data from Hole U1499A (0–655 m), whereas below that depth we used the downhole logging velocity and density data. We used a constant velocity of 2100 m/s in the low-recovery zones (333–406 and 531–561 m), interpreted to be sandy layers, based on the downhole logging velocity values measured at greater depth. The comparison of the time-depth relationship (TDR) obtained for Site U1499 to those for Sites 1148, U1431, and U1433 shows substantial agreement, except for the Site 1148 TDR, which shows higher velocities in the deeper layers. The comparison among the seismic reflectors and the variations in physical properties and lithology characteristics using the

computed Site U1499 TDR shows a good correlation between the main upper reflectors and the poor-recovery sandy intervals. However, the main physical property changes related to the top of the deep gravel layer do not correlate to the reflector observed at ~5.9 s in the seismic profile.

Site U1500

Site U1500 is located on basement Ridge B and is the most seaward site that Expedition 367 drilled in the SCS COT zone. Ridge B is located ~80 km seaward of the OMH and ~20 km seaward of Ridge A, where Site U1499 was drilled. The goal of drilling here was to sample and log the lowermost sediment and underlying basement rocks to determine basement age and lithology of the COT or embryonic oceanic crust, thus providing a test of different possible models for the processes and rheology controlling the breakup of the continent. Ridge B was expected to have basement of either upper continental crust, lower continental crust, mantle rocks, or oceanic crust. The coring and logging would also constrain the history of the region after rifting by determining the age, water depth, and subsidence rates of the overlying sedimentary packages.

We conducted operations in two holes at Site U1500 (proposed Site SCSII-8B; Sun et al., 2016b) (Table **T1**). Hole U1500A is located at 18°18.2762′N, 116°13.1916′E in a water depth of 3801.7 m. In Hole U1500A, we drilled without coring from the seafloor to 378.2 m and then cored with the RCB system from 378.2 to 494.6 m and recovered 26.5 m (23%). Thereafter, we drilled without coring from 494.6 to 641.2 m and cored with the RCB system from 641.2 to 854.6 m and recovered 67.2 m (31%).

Hole U1500B is located at 18°18.2707′N, 116°13.1951′E in a water depth of 3801.7 m. After installing casing, we continuously cored the sediment sequence from 846.0 to 1379.1 m (533.1 m cored; 164.7 m recovered; 31%) and then continuously cored 149.9 m into the underlying basalt from 1379.1 to 1529.0 m (114.92 m recovered; 77%). This made Hole U1500B the eighth deepest hole that the R/V *JOIDES Resolution* has drilled in ODP/Integrated Ocean Drilling Program/IODP history. Three downhole logging strings were run in Hole U1500B from 842 to 1133 m.

Lithostratigraphy

The cored sediment at Site U1500 is divided into eight lithostratigraphic units (Figure **F14**). The uppermost 378.2 m of sediment was drilled without coring. Lithostratigraphic Unit I (378.2–410.0 m) is a 31.8 m thick upper Miocene sequence of greenish gray heavily bioturbated clay with silt and sandy silt interbeds. Some of the clay intervals are nannofossil rich. Structure in the clay is mostly massive, but parallel laminations occur in the silt and sandy silt interbeds. Unit II (410.0–494.6 m) is an upper Miocene sequence of interbedded dark greenish gray clay and silt. Recovery was very low for this unit (~8%), which may indicate a change in lithology (e.g., increased abundance of nonlithified sands). This unit is underlain by another interval drilled without coring (494.6–641.2 m).

Unit III (641.2–892.4 m) is defined by upper Miocene interbedded claystone, siltstone, and sandstone. Many of the siltstone and sandstone intervals are organized into a variety of massive and stratified beds that include sedimentary structures such as parallel laminations, cross-stratification, and contorted strata. There are also several massive beds of sandstone that contain pebble-sized mud clasts. The well-organized coarser intervals fine upward into more massive claystone intervals and are interpreted as turbidite sequences. Several of the stratified beds are composed of foraminifer tests.

Unit IV (892.4–1233.3 m) also had very low recovery (15%). This unit is composed of lower upper Miocene very dark greenish gray to dark gray sandstone with dark brown to very dark gray claystone and siltstone intervals. Many of the intervals described in this unit contain interlaminations of silt or sand in a prevailing claystone lithology. Similar to Unit III, sedimentary structures in many of the sandstone and siltstone intervals are interpreted as turbidites. The claystone in some of the cores shows a distinctive color banding, which was observed as a pattern of alternating reddish brown, dark greenish gray, and brownish gray. The color banding appears to be associated with fining-upward grain sizes and varying levels of bioturbation. Sandstone intervals in this unit contain high percentages of K-feldspar, quartz, plagioclase, and mica minerals that may have been sourced from granitic rocks exposed along the southern margin of China.

Unit V (lower middle Miocene) is divided into Subunits VA (1233.30–1272.10 m) and VB (1272.10–1310.98 m) based on the abundance of calcareous material. Subunit VA consists of dark reddish brown, dark greenish gray, and dusky red homogeneous massive claystone with few sandstone and siltstone interbeds (3–12 cm thick). Subunit VB consists of dark reddish brown, reddish brown, and greenish gray intervals of claystone, nannofossil-rich claystone, claystone with biogenic carbonate, and clay-rich chalk. The greenish gray color banding in Subunits VA and VB is interpreted as diagenetic alteration.

Unit VI (1310.98–1370.33 m) is composed of Oligocene dark greenish gray massive silty claystone with biogenic carbonate and dark gray sandstone. Unit VII (1370.33–1379.10 m) comprises a thin (30 cm thick) Oligocene dusky red claystone. The lowermost 2 cm of this unit has a greenish gray color that marks a sharp horizontal contact with the igneous rocks below in Unit VIII. The basalt in Unit VIII (1379.10–1529.0 m), which is Oligocene or pre-Oligocene in age, contains some fractures that are filled with well-lithified claystone. The claystone contains authigenic carbonate, siliciclastic components, and rare nannofossils. The basalt intervals are sparsely intercalated with dusky red claystone, with the basalt/sediment contacts often associated with chilled glassy margins. Some claystone intervals in the basalt unit show evidence of dolomitization in thin section.

Igneous petrology

In Hole U1500B, we cored 149.9 m of igneous rocks below the sedimentary section and recovered a total of 114.92 m of basalt. The aphanitic to porphyritic basalts are nonvesicular to moderately vesicular and glassy to hypocrystalline, with the latter ranging from cryptocrystalline to fine grained, making up an aphyric to highly olivine-plagioclase phyric texture (microstructure). These basalts contain numerous 2–5 cm thick baked/chilled contacts and chilled margins, many of the latter with preserved fresh glass, as well as occasional hyaloclastites showing brecciated glass fragments mixed with sediment. The basalts comprise Unit VIII and are divided into igneous lithologic Subunits 1a and 1b according to flow boundaries to distinguish an upper massive lava flow sequence (27.28 m thick) from a lower, predominantly pillow lava flow succession (122.62 m thick) with subordinate thin (<6 m) interbedded lobate, sheet, and massive lava flows. The pillow lobes are well preserved and are separated by chilled, glassy margins (identifying upper and lower chilled margins of individual pillows where possible) and also claystone. Plagioclase phenocrysts are found throughout these basalts, with olivine being an occasional phenocryst. Modal abundances of olivine and plagioclase phenocrysts increase downhole, reaching a

Figure F14. Lithostratigraphic summary, Site U1500.

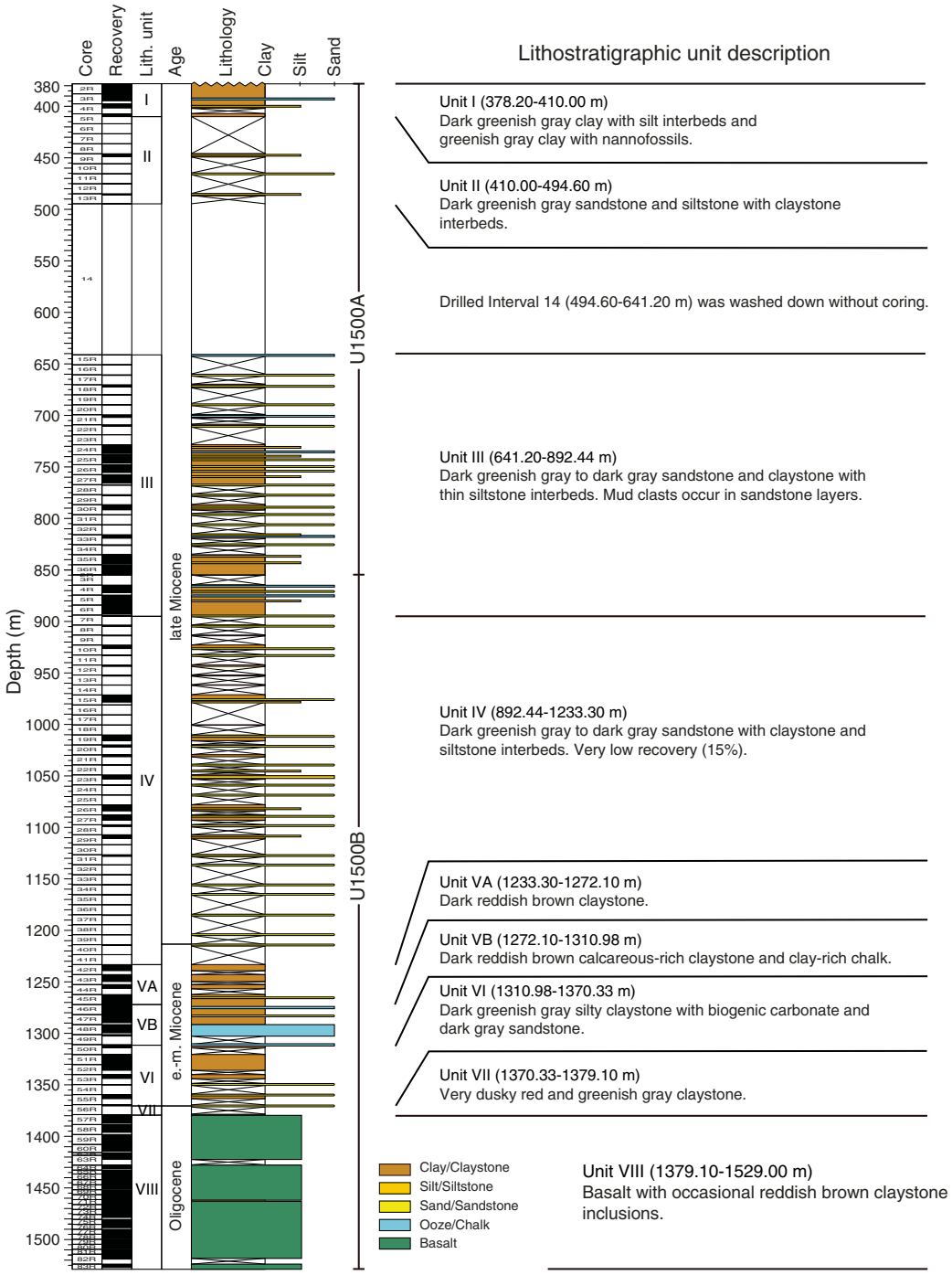

peak between 1420 and 1470 mbsf. Veins occur throughout Unit VIII and are predominantly filled with carbonates and Fe (hydr)oxides, chlorites, zeolites, and silica, as well as sediment. Veins usually show a sharp contact with the host basalt and are either polycrystalline or massive. Claystone is a ubiquitous phase in many carbonate-rich veins, especially in pillow lava flows, and is usually found as very fine aggregates in carbonate veins or as centimeter-thick veins with no preserved textures or structures. Red to green-red halos usually surround the carbonate veins, which are related to the background alteration of interstitial glass, olivine, and occasionally plagioclase and clinopyroxene. Alteration of these basalts remains slight overall, as evidenced by the minimal alteration of interstitial glass as well as the good preservation of plagioclase. Alteration intensity, however, does increase downhole.

Structural geology

Tilted sedimentary bedding and deformation structures were observed in all lithostratigraphic units. Faults, tilted beds, folds, and mud clasts observed in Units I, II, and III are likely related to gravity-controlled deposition (e.g., debris flows, slumps, slides, etc.).

Unit IV has low recovery and exhibits only a few tilted beds and compaction faults. A total of 47 centimeter-scale faults were measured in the claystone of Units V, VI, and VII. Many of these faults have slickensides and are likely related to clay compaction during lithification. Open fractures and veins are identified in the sparsely to highly plagioclase phyric basalts of Unit VIII. There are no preferred orientations of these structures. Most of the veins are filled by carbonate minerals, Fe oxides, sediment, and secondary minerals. Veins are often haloed by Fe oxide alteration. Vein connectivity is variable; single veins, branched veins, and vein networks were observed. There is no mineral-preferred orientation. Although the seismic profile across Site U1500 shows dipping reflectors in the basalt, we did not observe any clear paleohorizontal or dipping features in these lavas.

Biostratigraphy

All core catcher samples were analyzed for calcareous nannofossil and foraminifer contents. Additional samples were taken from the split-core sections when necessary to refine the ages between core catcher samples. Preservation of microfossils varies from poor to good. Overgrown and abundant broken fragments are common in the sediment sequences. The total abundance varies from barren to abundant, and most samples exhibit some degree of reworking.

Although recovery is low and ~50% of the samples are barren, the succession is apparently continuous and is tentatively assigned a late Oligocene–Miocene age. The late/middle Miocene boundary (11.6 Ma) can be placed between Samples 367-U1500B-37R-1, 40–41 cm, and 44R-CC. Both calcareous nannofossils and planktonic foraminifers indicate an early Miocene to late Oligocene succession in Cores 46R through 56R.

In the calcareous sandstone (Section 56R-1), just above the basalt, some younger species, such as *Praeorbulina circularis* (middle Miocene), *Globigerinoides subquadratus*, and *Orbulina suturalis*, are found together with the typical late Oligocene–early Miocene planktonic foraminiferal species (*Catapsydrax dissimilis*). In the same sample, the nannofossil content is represented by long-range species and cannot give a precise age. However, two samples from the veins and intrapillow fill of the basalts in Unit VIII contain poorly preserved calcareous nannofossils that indicate an Oligocene age. The resolution of the age discrepancy in Core 56R requires further postexpedition studies.

Geochemistry

At Site U1500, measurements of organic and inorganic carbon and nitrogen were conducted on one sample per sedimentary core that had relative high recovery, and headspace gas measurements were taken for all sediment cores. In addition, four basalt samples were analyzed for concentrations of major elements and several trace elements using inductively coupled plasma–atomic emission spectroscopy (ICP-AES). Headspace gas values do not exceed 15 ppmv and are mostly below the quantification limit. Carbonate contents are dominated by biogenic carbonate and vary between <1 and 40 wt%, with higher values corresponding to the calcareous-rich lithostratigraphic units. TOC and TOC/TN are low, averaging 0.14 wt% and 4.6, respectively. ICP-AES analyses of basalts from Site U1500 indicate subalkaline mid-ocean-ridge basalt (MORB)-like compositions.

Paleomagnetism

We conducted AF demagnetization of archive-half sections and AF and thermal demagnetization of representative discrete samples from both sedimentary successions and the igneous rocks. For the sedimentary samples, AF demagnetization could effectively removed the drilling-induced overprint. The polarity interpretation results based on inclination data from the sedimentary long core and discrete samples are in agreement, which supports our current preliminary polarity patten, but because of discontinuous coring and poor recovery in many cored intervals, we are not able to correlate these results to the standard geomagnetic polarity timescale. The pass-through measurements of the basalts from the archive halves using the SRM effectively removed a low-coercivity component; however, it is not clear if the ChRM or primary magnetization has been reached, partly due to the unavoidable magnetic contamination and partly due to the destructive feature and thus limited AF treatment levels (up to 25 mT).Within a single igneous subunit, basalts sometimes show both positive and negative inclinations upon stepwise AF treatments, which makes it hard to assign reliable polarities. The demagnetization behaviors of the discrete basalt samples are of high noise at higher temperatures, which is probably due to the onset of thermo-viscous remanent magnetization especially in a magnetically nonshielded environment. The close association of negative inclinations, changes in magnetic susceptibility, and demagnetization behavior with fractures in the cores points to the possibility of a secondary chemical remanent magnetization (CRM) as the source of the reversed intervals in the basalt.

Petrophysics

We conducted measurements of GRA bulk density, magnetic susceptibility, and NGR on whole-round cores and additional measurements on split cores and discrete samples, including thermal conductivity, *P*-wave velocity on the PWC, porosity, and bulk, dry, and grain density. In general, bulk density, *P*-wave velocity, and thermal conductivity increase with depth, whereas porosity decreases with depth as a result of compaction and lithification. However, some properties, such as NGR or magnetic susceptibility, show local variations related to the specific lithology. A significant increase in carbonate content in Subunit VB (1272–1311 m) causes a general decrease in NGR and only a slight decrease in magnetic susceptibility. Physical properties change significantly in the basalts of Unit VIII (1379–1529 m). Magnetic susceptibility is two orders of magnitude higher than in the sediment above and varies depending on the degree of alteration. *P*-wave velocity is also much higher, ranging between 4430 and 5710 m/s, whereas porosity and NGR are very low compared to the sediment above.

Correlation to seismic data

We used physical property data from cores and samples to correlate Site U1500 data with the available seismic reflection profile. We also used the Site U1500 density and PWC velocity data to create synthetic seismograms that provided additional constraints on the correlation. The TDR obtained for Site U1500 shows substantial agreement with that for Site U1499 and Sites U1431 and U1433; in contrast, the ODP Site 1148 TDR exhibits higher velocities in the deeper layers. The comparison between the seismic reflectors and the variations in physical properties and lithology characteristics using the computed Site U1500 TDR shows good correlation between the high-amplitude seismic reflector at ~6.4 s two-way traveltime (TWT) and the top of the basalts of Unit VIII.

Downhole measurements

Three downhole logging tool strings were run in Hole U1500B: a modified triple combo (sonic velocity, NGR, bulk density, resistivity,

Figure F15. Bathymetry at Site U1501 and location of the site in relation to seismic Lines 15ecLW1 and 15ecLW8.

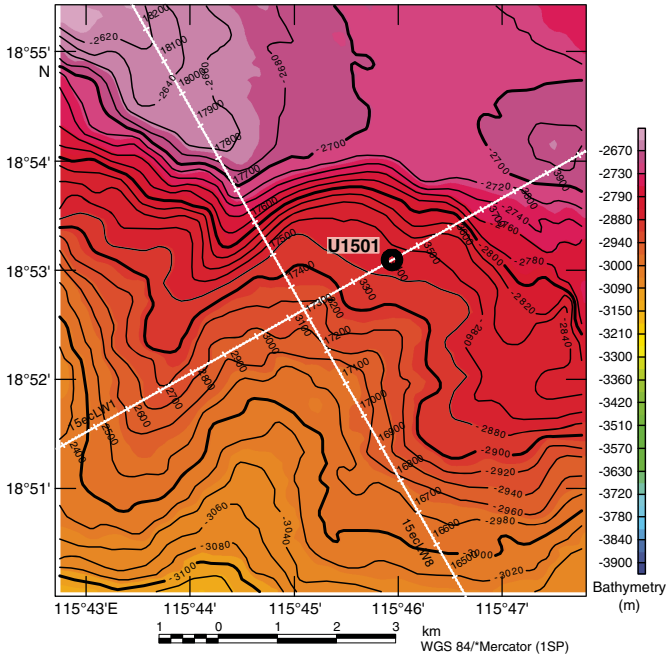

and caliper), the FMS-sonic (FMS resistivity images and calipers, as well as NGR), and the VSI (check shot and NGR). During the first run, the tool string encountered an obstruction at 4946 m wireline log depth below rig floor (WRF; ~1133 m), and we were unsuccessful in getting the tool string to pass below this depth. We collected FMS data from ~1044 m uphole to the bottom of the casing (842 m). Although the hole had many zones that were significantly enlarged, initial observations of the real-time FMS data indicate that some intervals exhibit relatively good caliper contact and should provide useful resistivity images. A seismic check shot survey with the VSI successfully collected data at one depth in the open hole and at the base of the casing. Because this was the last operation conducted during Expedition 367 and we only had a 1 day transit to Hong Kong, data processing and full evaluation of the log data will be conducted after Expedition 367.

Site U1501

Background and objectives

Site U1501 (proposed Site SCSII-41A; 18°53.0923′N, 115°45.9455′E) (Sun et al., 2016b) in the SCS northern margin (Figure **F3**) is located on a broad regional basement high (OMH). The OMH is the most landward of four distinct highs in the COT and is followed seaward by Ridges A, B, and C (Figures **F4**, **F5**, **F15**). Site U1501 is located at 2845.8 m below sea level (mbsl). Small rift basins of presumed Paleogene age are located on top of the OMH (Figure **F5**). These basins can be traced landward into much deeper half-graben basins that formed during the main phase of crustal extension. The rift basins located on the OMH, therefore, offer options to recover the stratigraphy of these basins by drilling to moderate depths, testing existing stratigraphic interpretations, and extrapolating the findings margin wide. Recovering and characterizing these sequences were key objectives at Site U1501, and the specific goal was to constrain the timing and duration of crustal extension, the tectonic vertical movements during rifting, and the subsequent postrift thermal subsidence. The crystalline basement at Site U1501 is most likely located far below the acoustic basement at ≈600 m and was not an objective for this site.

At 2846 mbsl, Site U1501 is one of the few ODP and Integrated Ocean Drilling Program sites in the SCS above the modern CCD of the SCS. Sites U1504 and U1505, also at the OMH, are situated at <3000 mbsl. The younger stratigraphy is therefore also the focus of some secondary scientific objectives related to Neogene environmental development of the SCS and adjacent landmasses of Southeast Asia. Among these secondary objectives are to (1) reconstruct the history of the east Asian monsoon evolution and of deep-water exchanges between the SCS and Pacific Ocean and (2) explore the sedimentary responses to the Cenozoic regional tectonic and environmental development of the Southeast Asia margin.

Operations

We conducted operations in four holes at Site U1501 (Table **T2**). In Holes U1501A and U1501B, Core 1H missed the sediment–water interface and retrieved full core barrels, indicating that the core was shot from below the seafloor. Hole U1501C (18°53.0919′N, 115°45.9485′E; 2846 mbsl) was cored with the APC system from the seafloor to 461.8 m and recovered 447.8 m (96.3%). Hole U1501D (18°53.0929′N, 115°45.9370′E; 2846 mbsl) was drilled without coring from the seafloor to 433.5 m and then cored with the RCB system to 644.3 m. A total of 78.8 m of core was recovered (37.4%). Hole U1501D was logged with the triple combo tool string from 113 to 299.3 m.

Lithostratigraphy

The sedimentary succession recovered at Site U1501 is composed of clay-rich nannofossil ooze, silty clay, clayey silt, sand, siltstone, sandstone with minor conglomerate, and rare volcanic ash. The succession is divided into three major lithostratigraphic units (I, II, and III) distinguished on the basis of sediment composition, particularly the relative abundance of the calcareous and siliciclastic fractions (Figure **F16**).

Lithostratigraphic Unit I is a 303 m thick, Holocene–upper Oligocene succession dominated by clay-rich nannofossil ooze and nannofossil ooze with clay, with minor amounts of nannofossil-rich foraminifer sand or silty sand. A felsic volcanic ash layer occurs in Section 368-U1501A-1H-7, and an ash pod was observed in Section 368-U1501C-3H-1. Unit I is divided into the following subunits:

- Subunit IA (0–25.47 m),
- Subunit IB (25.47–66.17 m),
- Subunit IC (66.30–156.70 m),
- Subunit ID (156.80–191.99 m),
- Subunit IE (191.99–293.09 m), and
- Subunit IF (293.90–303.01 m).

These divisions are based on changes in lithology, particularly the clay to nannofossil ratio, the presence and abundance of foraminifers, and/or physical properties. The lower contact of Unit I is erosional and marked by the emplacement of a poorly sorted sandy layer. At the boundary, marked changes in *P*-wave velocity, NGR, magnetic susceptibility, porosity, MAD, color, carbonate content, and biostratigraphy indicate a small hiatus (Figure **F16**). Unit I was deposited in a deep-marine environment, and lithologic changes between subunits likely reflect the amount of terrigenous input into a relatively open ocean setting. This input may be delivered as buoyant sediment plumes from shallower shelf environments and rarely by weak (distal) turbidity currents. Soft-sediment deformation in Subunit IB indicates slumping downslope of parts of the sequence.

Table T2. Expedition 368 hole summary. — = no data. **Download table in CSV format.**

Hole	Proposed site	Location	Water depth (m)	Total penetration (m)	Cored interval (m)	Drilled interval without coring (m)	Core recovery (m)	Core recovery (%)	Time on hole (days)	Cores (*N*)	Depth of 10.75 inch casing (m)
U1501A	SCSII-41A	18° 53.0922′N 115° 45.9483′E	2857.11	9.5	9.5	—	9.73	102.42	0.66	1	—
U1501B		18° 53.0922′N 115° 45.9483′E	2852.11	9.5	9.5	—	9.83	103.47	0.05	1	—
U1501C		18° 53.0919′N 115° 45.9485′E	2845.81	461.9	461.9	—	444.77	96.29	3.53	62	—
U1501D		18° 53.0929′N 115° 45.9370′E	2845.82	644.3	210.8	433.5	78.77	37.37	5.15	26	—
			Site U1501 totals:	1125.2	691.7	433.5	523.54	49.09	9.39	90	—
U1502A	SCSII-17A	18°27.8720′N 116°13.8381′E	3763.72	758.2	383.2	375.0	176.81	46.14	5.22	40	—
U1502B		18°27.8798′N 116°13.8409′E	3763.58	920.8	193.1	727.7	131.57	68.14	14.06	36	723.7
			Site U1502 totals:	1679.0	576.3	1102.7	308.38	53.51	19.28	76	
U1503A	SCSII-9B	18° 8.6300′N 116° 18.8456′E	3867.71	995.1		995.1	0.00	0.00	11.88	0	991.5
			Site U1503 totals:	995.1		995.1	0	0.00	11.88	0	—
U1504A	SCSII-27A	18°50.9199′N 116°14.5397′E	2816.57	165.5	165.5	—	52.93	31.98	2.17	21	—
U1504B		18°50.8213′N 116°14.5978′E	2842.97	200	111.8	88.2	21.48	19.21	3.33	19	—
			Site U1504 totals:	365.5	277.3	88.2	74.41	26.83	5.50	40	—
U1505A	SCSII-3D	18°55.0560′N 115°51.5369′E	2916.57	0.3	0.3	—	0.38	126.67	0.59	1	—
U1505B		18°55.0562′N 115°51.5370′E	2918.57	3	3	—	3.23	107.67	0.04	1	—
U1505C		18°55.0570′N 115°51.5491′E	2917.37	480.2	480.2	—	480.15	99.99	4.29	64	—
U1505D		18°55.0458′N 115°51.5501′E	2917.00	184.5	184.5	—	191.43	103.76	1.2	20	—
			Site U1505 totals:	668.0	668.0	—	675.19	101.08	6.12	86	—
			Expedition 368 totals:	4832.8	2213.3	2619.5	1601.08	138.24	52.17	292	—

Lithostratigraphic Unit II is 296 m thick and late Oligocene to late Eocene in age. The unit consists of variable amounts of clay, silt, and sand with minor nannofossil-rich clay, nannofossil ooze, and silt with organic matter. Gravel-sized grains occur, including shell fragments and glauconite, as well as carbonate and pyrite concretions. Unit II is divided into six subunits:

- Subunit IIA (303.01–385.26 m),
- Subunit IIB (388.80–452.69 m),
- Subunit IIC (452.60–482.33 m),
- Subunit IID (491.00–519.80 m),
- Subunit IIE (529.30–548.64 m), and
- Subunit IIF (548.64–598.91 m).

The uppermost two subunits define a fining-upward succession of glauconite-sand dominated to siltstone and clay overlain by clay with nannofossils. Subunits IIC and IE are dominated by sandstone with calcite; Subunit IID has more fine-grained, organic-rich lithologies; and Subunit IIF is similar to Subunit IIB but has more coarse-grained sediment and distinctive weak red and reddish gray intervals in the green glauconite-bearing sands. Coarse sand– to pebble-sized shell fragments are common in Unit II, and coral fragments were occasionally observed in the upper part of the unit. Glauconite and quartz minerals dominate the siliciclastic grain component. Diagenetic pyrite is common. Unit II most likely represents a gradual change upward from shallow-water (outer shelf or upper continental slope) to deep-water (lower slope) depositional environments. The Unit II/III boundary was not recovered but is marked by an abrupt change in magnetic susceptibility, NGR, and *P*-wave velocity. A change in the apparent dip of strata from near horizontal in Unit II to ~20° in Unit III suggests that the contact is unconformable.

Lithostratigraphic Unit III (598.91 m to the bottom of the hole) is well lithified and composed of poorly sorted, feldspar-rich sandstone interbedded with moderately to well-sorted, medium- to fine-grained sandstone and, rarely, siltstone and poorly sorted conglomerate. The age is unknown because no fossils were recognized. Unit III is divided into two subunits: IIIA (598.91–629.79 m) and IIIB (629.79–643.56 m). Subunit IIIA is composed of coarse-grained heterolithic sandstone, sandstone with calcite clasts, and minor conglomerate and siltstone. Pebble- to cobble-sized clasts include felsic intrusive and volcanic rocks, sedimentary rocks, metamorphic rocks, and rare gabbro. Subunit IIIB consists of sandstone and minor sandstone with organic matter. Subunit IIIB is finer grained than Subunit IIIA and has finely laminated intervals. We speculate that Unit III was formed in continental to littoral environments with a provenance not far from the site.

Structural geology

Unit I shows predominantly horizontal to subhorizontal bedding with local soft-sediment deformation structures such as slump folds. Unit I is devoid of any structures related to tectonic deformation, apart from some rare normal faults with minor offsets.

Unit II is characterized by subhorizontal to gently dipping bedding. Steep dips up to 40° are locally observed in close relation to

Figure F16. Lithostratigraphic, biostratigraphic, and magnetostratigraphic summary, Site U1501.

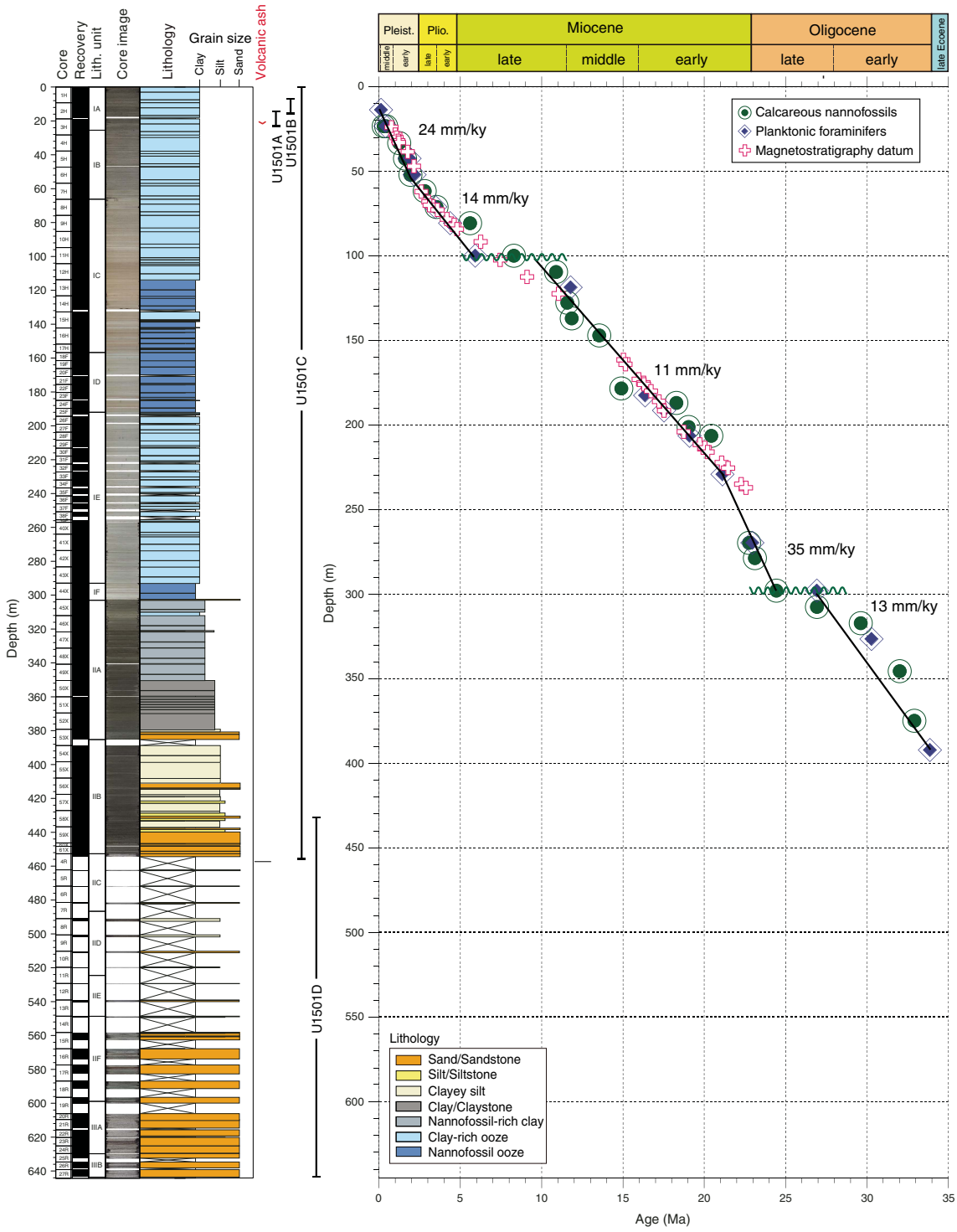

parallel lamination and are therefore interpreted as cross-laminae. In contrast to Unit I, deformation structures were observed in Unit II, although their occurrence is rather heterogeneously distributed. Planar to irregular millimeter-scale normal faults and joints were observed in Subunit IIA, typically with offsets ranging from 0.1 to 0.5 cm and apparent dips of 10°–40°. Striations and slickensides were documented locally where the surfaces of such structures are exposed. Deformation in the underlying Subunits IIC–IIF is essentially characterized by randomly distributed occurrence of single to branched uniform calcite and quartz veins. Recognition of deformational structures was difficult due to drilling disturbance throughout this unit.

The acoustic basement marks the top of Unit III. This unit shows a weak tilting of stratified beds expressed in apparent dips on split core surfaces up to ~20°. Again, deformation structures remain scarce and heterogeneously distributed in Unit III. The recognized

structures consist of veins, fractures, and local microfaults associated with cataclastic fault gouge.

In conclusion, despite the various tilting of reflectors (~5°) and the vicinity of extensional structures observed on seismic profiles, only weak evidence of bedding tilting and/or deformation structures were observed at this site, possibly due to the nature of the sediments.

Biostratigraphy

All core catcher samples at Site U1501 were analyzed for calcareous nannofossils, diatoms, and foraminifers, with select core catchers examined for ostracods. Additional samples were taken from the split working-half sections when necessary to refine the ages between core catcher samples. Preservation of calcareous microfossils varies from good in Unit I (Cores 368-U1501A-1H, 368-U1501B-1H, and 368-U1501C-1H through 44X) to poor in Units II and III (Cores 368-U1501C-45X through 62X and 368-U1501D-2R through 5R). Planktonic foraminifers and calcareous nannofossils are abundant in Unit I, common to rare in Unit II and upper Unit III, and barren in the rest of Unit III (Cores 368-U1501D-6R though 27R). Diatoms are few with moderate preservation in Samples 368-U1501A-1H-CC, 368-U1501B-1H-CC, and 368-U1501C-1H-CC and 2H-CC. The rest of the core catcher samples are barren of diatoms with the exception of Samples 368-U1501C-3H-CC, 4H-CC, 33F-CC through 35F-CC, and 46X-CC, in which diatoms are rare with poor preservation. Diatoms are common in burrows found in interval 368-U1501C-35F-1, 118–119 cm, with poor preservation.

Forty biostratigraphic datums were identified in a mostly continuous succession from the Eocene to Holocene, which indicates that Holes U1501C and U1501D penetrated late Eocene or older strata (Figure **F16**). The Pleistocene/Pliocene boundary (~2.6 Ma) was placed in Core 368-U1501C-7H, the Pliocene/Miocene boundary (~5.3 Ma) in Core 9H, the Miocene/Oligocene boundary (~23.0 Ma) between Cores 41X and 42X, and the Oligocene/Eocene boundary (~33.9 Ma) between Cores 53X and 54X. Sedimentation rates vary from ~13 mm/ky in the early Oligocene, ~11 mm/ky in the Miocene, and ~14 mm/ky in the Pliocene to 24 mm/ky in the Pleistocene. Low sediment accumulation rates (~3.6 mm/ky) during the late Eocene through the early Oligocene and in the late Miocene suggest the presence of hiatuses in the sedimentary record during these periods. In contrast, higher sediment accumulation rates (35 mm/ky) exist during the late Oligocene and the early Miocene.

Predominance of shallow-water benthic foraminifer and ostracod assemblages in Cores 368-U1501C-45X through 62X and 368-U1501D-2R through 6R indicate an upper bathyal to continental shelf paleoenvironment during the Eocene to the early Oligocene. Predominantly abyssal benthic foraminifers and ostracods above Core 368-U1501C-44X indicate that deep-water conditions existed in this part of the SCS since the early Oligocene.

Paleomagnetism

Paleomagnetic investigations combined measurement and in-line AF demagnetization of archive-half sections on the 2G Enterprises SRM with the measurement of discrete samples either AF or thermally demagnetized.

The rock magnetic experiments on six representative samples from Hole U1501C show saturation remanent magnetization (SIRM)/χ ratios between 12.8 and 14.6 kA/m, indicating the predominance of greigite in Unit I of Hole U1501C, also documented by scanning electron microscopy (SEM) in 2–10 µm grains. Thermal demagnetization behaviors show that greigite dominates the NRM, at least downhole to 83 m. However, the magnetic remanence left above 575°C suggests contributions from additional phases such as maghemite (Curie temperature [T_C] = ~590°–675°C) or hematite (T_C = ~675°C).

Both AF and thermal treatments on discrete samples successfully removed the steep low-temperature/coercivity component that represents the drilling overprint. The mean inclination gathered from the high-temperature component is 37.3° ± 6.6°, corresponding to a paleolatitude of 20.8° ± 3.3° for Unit I (see **Lithostratigraphy**). Many of the AF-demagnetized discrete samples reveal trends of reversed or normal polarity in the last step of demagnetization (50 mT) and are more difficult to interpret.

The magnetostratigraphy in Holes U1501C and U1501D is based on directions derived from the raw moments measured by the SRM after 25 mT demagnetization step and from the corroborative evidence from discrete samples. Magnetostratigraphy was correlated to the standard timescale and plotted along with the tie points from the microfossil ages from shipboard paleontologists. The paleomagnetic and paleontological age constraints match well over most of the section (Figure **F16**). A succession of eight normal and five reversed events was recognized in Hole U1501D. However, the lack of biostratigraphic constraints throughout Hole U1501D prevented even a tentative correlation of these events with the standard timescale.

Geochemistry

Interstitial water samples were obtained downcore to 450 m (Subunit IIB). In Unit I, variations are mainly the result of diagenetic and microbial processes, and measurements of alkalinity, phosphate, ammonia, and sulfate are in the typical ranges for the region (3.5–5 mM alkalinity, 250–510 µM phosphate, <30 µM ammonia, and <26 µM sulfate). However, more atypically (particularly when compared to Expedition 367 Site U1499), the main changes associated with microbial processes are notable only in the uppermost 25 m in Subunit IA and are typical of organic matter degradation. Deeper than 25 m in Unit I, changes in interstitial water chemistry appear inhibited until 300 m. These changes may be a consequence of the low organic carbon concentration and high carbonate content (~50 wt%) of Unit I. Decreases in sulfate concentrations with depth are more pronounced in Unit II (>300 m), and in this zone there is heavy pyritization and total sulfur (TS) contents are high, suggesting sulfate reduction has taken place. In the uppermost part of Unit II (300–370 m), chloride, bromide, and sodium are notably lower (chloride = 500 mM, cf. 565 mM; bromide = 0.75 mM, cf. 0.9 mM; and sodium = 410 mM, cf. 480 mM). This difference in interstitial water chemical composition is sharp and could result from pressure-isolated units retaining a distinct formation water chemistry or from the migration of chloride-poor formation water.

Headspace gas concentrations are below background laboratory levels in all samples collected from Site U1501 (<1% ppmv). TOC content is typically <0.5 wt% in Unit I, except from 0 to 50 m (Subunit IA). In this interval, a typical black marine mud has a TOC of ~1 wt%. TOC was also typically <0.5 wt% in Units II and III, except for a few carbonaceous lithologies: sandstones with plant phytoclasts associated with an ash-rich boghead coal in Unit II (interval 368-U1501D-9R-1, 10–15 cm) and a bitumen-impregnated sandstone in Unit III (interval 27R-1, 12–16 cm). TS content is low in Unit I: ~1 wt% in Subunit IA and below effective shipboard detection limits of 0.01 wt% for the rest of Unit I. TS content is higher in Unit II; >1 wt% in the muddier uppermost part of Unit II and an average of 0.5 wt% in the sandier, deeper part.

Elemental compositions primarily reflect geological units and changes in lithology. In Unit I, carbonate contents are high and exceed 50 wt% in foraminifer-rich intervals (compositionally a limestone). In Units II and III, carbonate is less common, and the units are predominantly siliciclastic with a distinction between units that are mud rich and feldspathic and sandier units toward the base of the hole. Calcium and strontium are associated with biogenic sediments in Unit I, but in deeper units they covary with aluminum. In the base of Units II and III, sodium and potassium are both high, which is consistent with the dominant presence of feldspathic sediments. The higher aluminum proportion in the uppermost part of Unit II is consistent with the muddier, clay-rich lithologies present here.

Physical properties

Hole U150A is divided into four units based on the sediment and rock physical properties. Physical properties (PP) Unit 1 (0–300 m) experienced the most evident changes in sediment compaction, which is expressed by increasing bulk density (from 1.4 to 2.0 g/cm^3) and *P*-wave velocity (from 1450 to 1930 m/s) and decreasing porosity (from 85% to 45%) with depth. Because PP Unit 1 consists mostly of calcareous ooze, it has relatively low NGR (between 20 and 40 counts/s) and magnetic susceptibility (between 10^{-6} and 10^{-5} SI). The onset of PP Unit 2 (300–450 m) is marked by a rapid increase in NGR and porosity and a rapid decrease in bulk density and *P*-wave velocity, corresponding to a shift to a different lithologic unit with sand, silt, and clay-enriched sediments. In the entire unit, NGR is persistently high (60–80 counts/s), whereas magnetic susceptibility remains as low as 10×10^{-5} SI. *P*-wave velocity and bulk density continue to increase with core depth. Most physical properties of PP Unit 3 (450–600 m) have similar values to those of Unit 2, except that *P*-wave velocity is extremely high, up to 4000–6000 m/s at some interbeds, and bulk density and porosity increase and decrease to 2.6 g/cm^3 and 2%–3%, respectively, at parallel depths. PP Unit 4 (600–657 m) is distinct from other units due to higher mean NGR (80 counts/s), bulk density (2.6 g/cm^3), magnetic susceptibility (500×10^{-5} SI), and *P*-wave velocity (4500 m/s). Throughout the hole (0–657 m), thermal conductivity values increase from 0.7 to 3.4 W/(m·K), most likely as a result of increasing sediment compaction and changes in sediment compositions. L* reflectance values are highly relevant to weight percent carbonate in sediments, which exhibit relatively high L* values between 100 and 160 in the upper 300 m and thereafter remain as low as 90.

Downhole measurements

Wireline logging was conducted in Hole U1501D using a modified triple combo tool string that included the Hostile Environment Natural Gamma Ray Sonde (HNGS), Hostile Environment Litho-Density Sonde (HLDS), High-Resolution Laterolog Array (HRLA), and magnetic susceptibility sonde (MSS). The triple combo run collected good data between 115.1 m (base of the drill pipe) and 300 m, where it encountered an impenetrable obstruction. Four logging units are defined:

- Logging Unit 1 (base of the drill pipe to 190 m wireline depth below seafloor [WSF]) is characterized by intervals of large hole diameter and relatively high variability in NGR and magnetic susceptibility.
- Logging Unit 2 (190–260 m WSF) is characterized by a relatively constant hole diameter, relatively homogeneous logs, and submeter-scale layering.
- Logging Unit 3 (260–275 m WSF) again shows a relatively large hole diameter, as well high variability in NGR, density, and resistivity logs.
- Logging Unit 4 (275–300 m WSF) exhibits relatively large values of resistivity and magnetic susceptibility.

The upward log pass indicated a collapsed hole at ~156.3 m drilling depth below seafloor (DSF) on the caliper curve, and for safety reasons no further attempts to descend deeper than that undergauge spot were made. Because the interval of the collapsed hole was located only ~40 m below the base of the pipe, the originally planned FMS-sonic tool string was not run. Four in situ formation temperature measurements were made in Hole U1501C, yielding a geothermal gradient of 81.4°C/km and a calculated heat flow of 100.1 mW/m^2. These values are comparable to the relatively high values observed at some ODP and Integrated Ocean Drilling Program sites in this part of the SCS.

Site U1502

Background and objectives

Site U1502 (proposed Site SCSII-17A; Sun et al., 2016b) in the SCS northern margin (Figures **F3**, **F17**) is located at 3764 mbsl on a prominent basement ridge (A) in the COT (Figure **F5**). Ridge A is one of four distinct basement highs found across the COT. The OMH is the most landward of these highs and is followed seaward by the nearly parallel Ridges A, B, and C. A key objective of Expeditions 367 and 368 was to examine the nature of the crust in Ridge A. This ridge is considered to be a pivotal element in the transition from continental to oceanic crust. Hence, the main objective of Site U1502 was to drill through synrift deposits overlying an interpreted shallow-dipping (~20°) fault zone and into the crystalline basement below the fault. Information on the nature and age of the synrift deposits overlying the fault, as well as the nature and age of the overly-

Figure F17. Bathymetry at Site U1502 and location of the site in relation to seismic Lines 15ecLW7, 15ecLW3, and 08ec2660. Note that the site is not at the exact crossing of Lines 15eclLW7 and 15eclLW3.

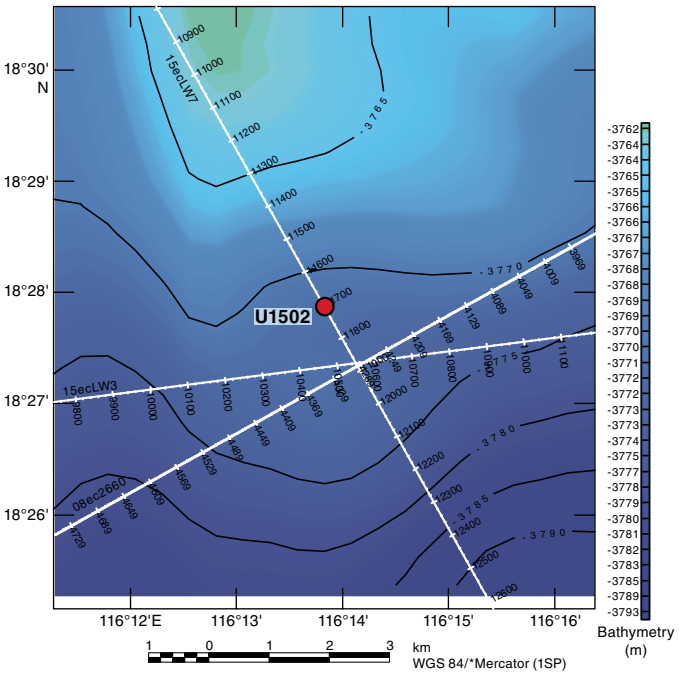

ing sediments and associated seismic unconformities, formed another target with the objective of constraining basin subsidence.

Operations

We conducted operations in two holes at Site U1502 (Table T2). Hole U1502A is located at 18°27.8720′N, 116°13.8381′E, at 3763 mbsl. Our operations in Hole U1502A were designed to provide information on formation characteristics and drilling conditions so that we could decide the length of casing to drill into the seafloor in deep-penetration Hole U1502B. Given this purpose and the amount of time to drill the second, deep hole, we did not core continuously in Hole U1502A. Instead, we drilled without coring from the seafloor to 375.0 m and cored with the RCB system from 375.0 to 758.2 m, recovering 176.81 m (46%). Hole U1502B is located at 18°27.8798′N, 116°13.8409′E, at 3763.6 mbsl. In Hole U1502B, we drilled a reentry funnel and 727.7 m of 10¾ inch casing into the seafloor; cored with the RCB system through the sediment–basalt transition (727.7–739.16 m) and 180 m into the underlying basalt (739.16–920.95 m), recovering 128 m (70%); and collected downhole log data with the triple combo tool string and a check shot with the VSI tool string.

Lithostratigraphy

The sedimentary succession recovered at Site U1502 extends from the early Oligocene (possibly late Eocene) to the late Miocene. The succession includes four sedimentary units (I and III–V) that are composed of mainly clay, nannofossil-rich clay, biosiliceous-rich clay, limestone, and clast-rich clay and two igneous units (II and VI) that are mainly composed of basalt. The base of the sedimentary succession is a sequence of clay and metasediments (dolomite marble and dolomitic limestone) that possibly forms the contact with a unit of altered basalt (Unit VI) (Figure F18).

Late Miocene to late Oligocene lithostratigraphic Unit I is divided into five subunits. Subunit IA (Hole U1502A = 375.00–486.82 m) is composed of dark gray, gray, dark greenish gray, and greenish gray silty clay, clay with nannofossils, and nannofossil-rich clay intercalated with dark grayish brown, grayish brown, and brown clay with nannofossils, with minor dark greenish gray sandy clay with calcite. Subunit IB (Hole U1502A = 490.20–599.57 m) is composed of alternating intervals of brown and greenish gray clay, silty clay, and clayey silt. Sandy intervals are rare. Recovery in Subunits IA and IB was very poor, which might be due to the occurrence of thick sand beds that were washed out. Subunit IC (Hole U1502A = 599.57–602.39 m) is composed of greenish gray and reddish gray foraminifer-rich clayey siltstone to sandstone with parallel laminations and convolute bedding, with thin layers of pinkish gray foraminiferal chalk. Subunit ID (Hole U1502A = 602.39–724.03 m) is mainly composed of alternating greenish and brownish gray and grayish brown clay, silty clay, clayey silt, and clay with silt (Cores 368-U1502A-25R through 32R), but brown colors dominate Cores 33R through 38R. Nannofossils are abundant in the lowermost ~4 m of this subunit. Subunit IE (Hole U1502A = 724.03–734.87 m; Hole U1502B; 727.79–727.96 m) is composed of brown nannofossil-rich clay with foraminifers and nannofossil-rich clay with pale green colored halos around fractures. The sediments of Unit I are interpreted as having been deposited in a deep-marine environment. Fining-upward intervals in Subunits IA–IC are interpreted as turbidites.

Unit II is a highly altered greenish gray basalt clast recovered from Hole U1502B at 727.96–728.04 m. The primary mineral phases are replaced by an alteration-mineral assemblage.

Unit III (Hole U1502A = 739.10–739.16 m; Hole U1502B = 728.04–733.82 m) is composed of brownish yellow, very hard, poorly sorted breccia. The granule- to pebble-size siliceous clasts consist of alteration minerals (Fe hydroxides) cemented by a matrix of annealed quartz in various grain sizes.

Unit IV (Hole U1502A = 739.16–747.20 m) consists of biosiliceous-rich silty clay. Diatoms, sponge spicules, and radiolarians are abundant in the upper part, but the abundance of both nannofossils and diatoms decreases rapidly downhole from Section 368-U1502A-40R-1 to Section 40R-3. Pyrite occurs as centimeter-sized patches and along cracks. The layering in Unit IV is inclined and may be slightly deformed.

Unit V (Hole U1502A = 747.20–749.01 m; Hole U1502B = 733.82–739.16 m) is an interval of alternating metasediments (dolomite marble, dolomitic limestone, and clast-rich clay). The dolomite marble is dominated by very fine grained dolomite (~95%) with minor amounts of magnetite (~3%) and calcite (~2%). The annealing texture is equigranular and crossed by fine-grained dark gray bands. The presence of magnetite explains the extraordinarily high magnetic susceptibility of this unit. The gray, fine-grained dolomitic limestone in Hole U1502B is intercalated with well-consolidated, very dark greenish gray clay with 10%–15% igneous clasts. The sediment is partially overprinted with alteration caused by secondary high-temperature processes (e.g., hydrothermal fluid sediment interaction or contact metamorphism).

Unit VI (Hole U1502A = 749.01–750.67 m; Hole U1502B = 739.16–920.95 m) consists of highly altered basaltic breccia, brecciated basalt, pillow basalt, and sheet basalt. The unit is divided into two subunits. Subunit VIA is composed of highly altered basaltic breccia and brecciated basalt with minor sheet basalt, chert, and claystone and very minor pillow basalt. Subunit VIB is dominated by altered pillow basalt and sheet flows and is less brecciated than Subunit VIA.

Igneous petrology

At Site U1502, we recovered two igneous lithologic units. Unit 1 (lithostratigraphic Unit II) is represented by just three small, aphanitic, fine-grained basalt fragments that contain rare plagioclase phenocrysts (Figure F19). Alteration of Unit 1 is intense, with most of the groundmass replaced by green clay minerals, clinozoisite, zeolites, and Fe (hydr)oxides.

Unit 2 (lithostratigraphic Unit VI) comprises a 182 m thick sequence of highly altered aphyric to highly plagioclase porphyritic basalts with minor chert (Figure F19). These basalts are divided into two igneous subunits (2a and 2b) based on flow morphology and alteration style: an upper brecciated and fractured massive lava flow sequence (Subunit 2a) and a lower sequence of interbedded pillow flows with lobate and sheet lava flows in which the alteration style is characterized by intense veining (Subunit 2b). Subunit 2a is characterized by highly altered breccia clasts of sparsely to moderately phyric basalt in a matrix of carbonates, epidote, chlorite, Fe (hydr)oxides, quartz, zeolite minerals, and clay minerals. The clasts show an alteration assemblage similar to the matrix, with remnant plagioclase and secondary pyrite. Subunit 2b consists of aphyric to highly plagioclase phyric (>30%) basalts with abundant chlorite and sulfides, as well as epidote, clay minerals, carbonates, zeolites, and opaque minerals.

All of Unit 2 has undergone some degree of hydrothermal alteration. This alteration varies from complete replacement of the rock, where the original composition and texture are difficult to determine, to replacement of mineral phases with little change to the tex-

Figure F18. Lithostratigraphic summary with simplified lithology and unit descriptions, Holes U1502A and U1502B.

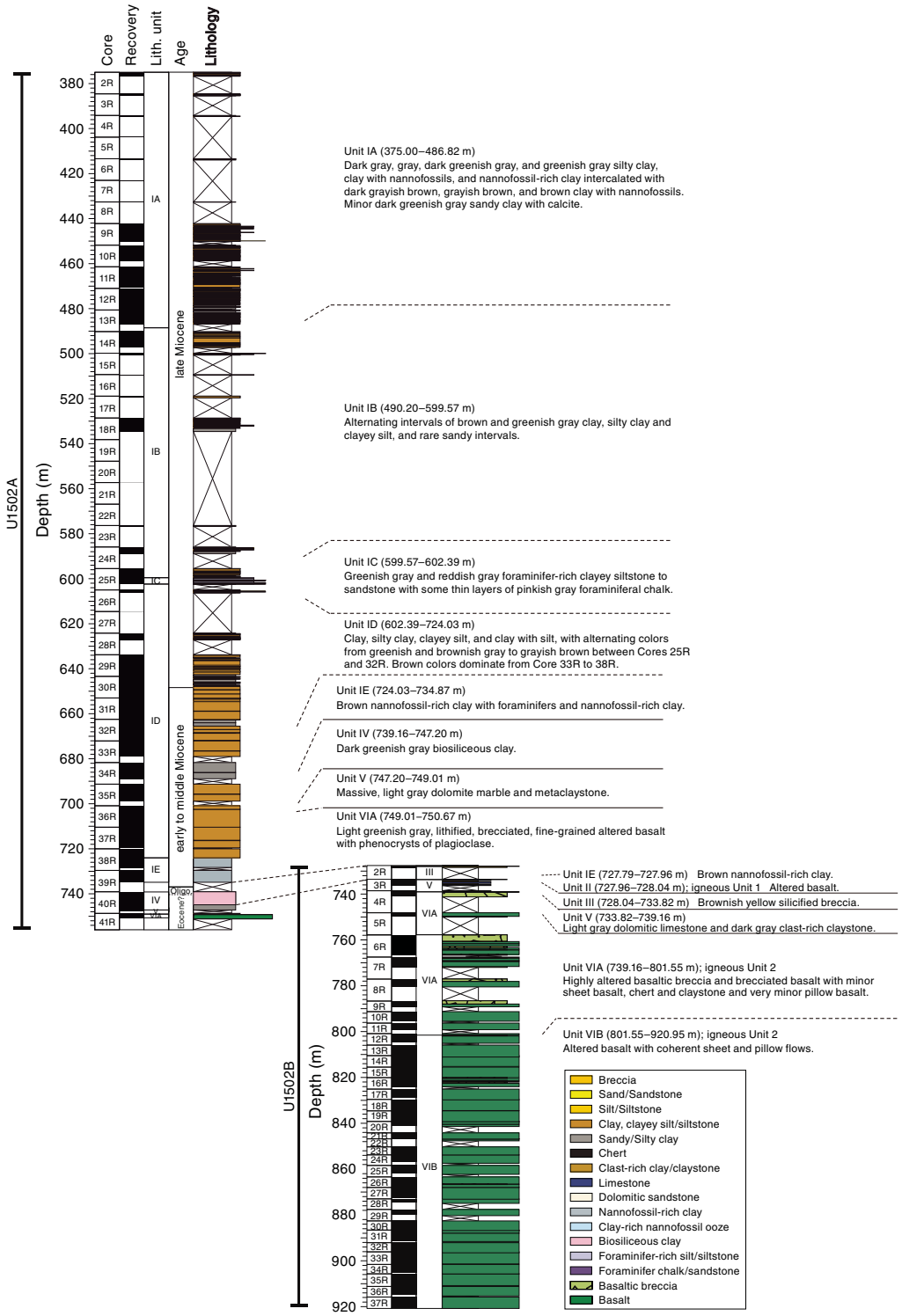

ture. Glassy pillow rinds are completely replaced, and multiple phases of veining and halos are ubiquitous throughout the rocks. Three vein types were observed: (1) white to green to black silica-epidote veins, (2) apple green pyrite-epidote veins, and (3) white silica and/or calcite veins. Sulfide mineralization (disseminated and veined) is widespread throughout Unit 2 and is dominated by pyrite, with minor sphalerite, chalcopyrite, and covellite.

Handheld portable X-ray fluorescence (pXRF) analyses show no significant differences in contents of alteration-resistant elements such as Ti and Zr in Unit 2, but Subunit 2a has lower MgO, FeO, and MnO than Subunit 2b, which is consistent with the higher degree of alteration. Subunit 2b is also strongly affected by secondary alteration, but areas of less intense alteration are indicated by higher magnetic susceptibility and high CaO and Fe_2O_3 contents. Unit 1

Figure F19. Lithostratigraphic summary with main igneous lithologies and deformation structures, Holes U1502A and U1502B. A. Highly plagioclase-phyric basalt with up to 50% plagioclase phenocrysts. B. Highly altered, sparsely plagioclase phyric pillow basalt with a well-preserved pillow. C. Moderately altered aphyric basalt flow with sparse vesicles. Note the change to a bluish gray color. D. Slump folds. E. Microfaults showing striations/slickensides on exposed surfaces. F. Distributed shear geometries with shear bands and tilted bedding. G. Brecciated basalt. H. Basaltic breccia. I. Network of composite epidote-rich veins.

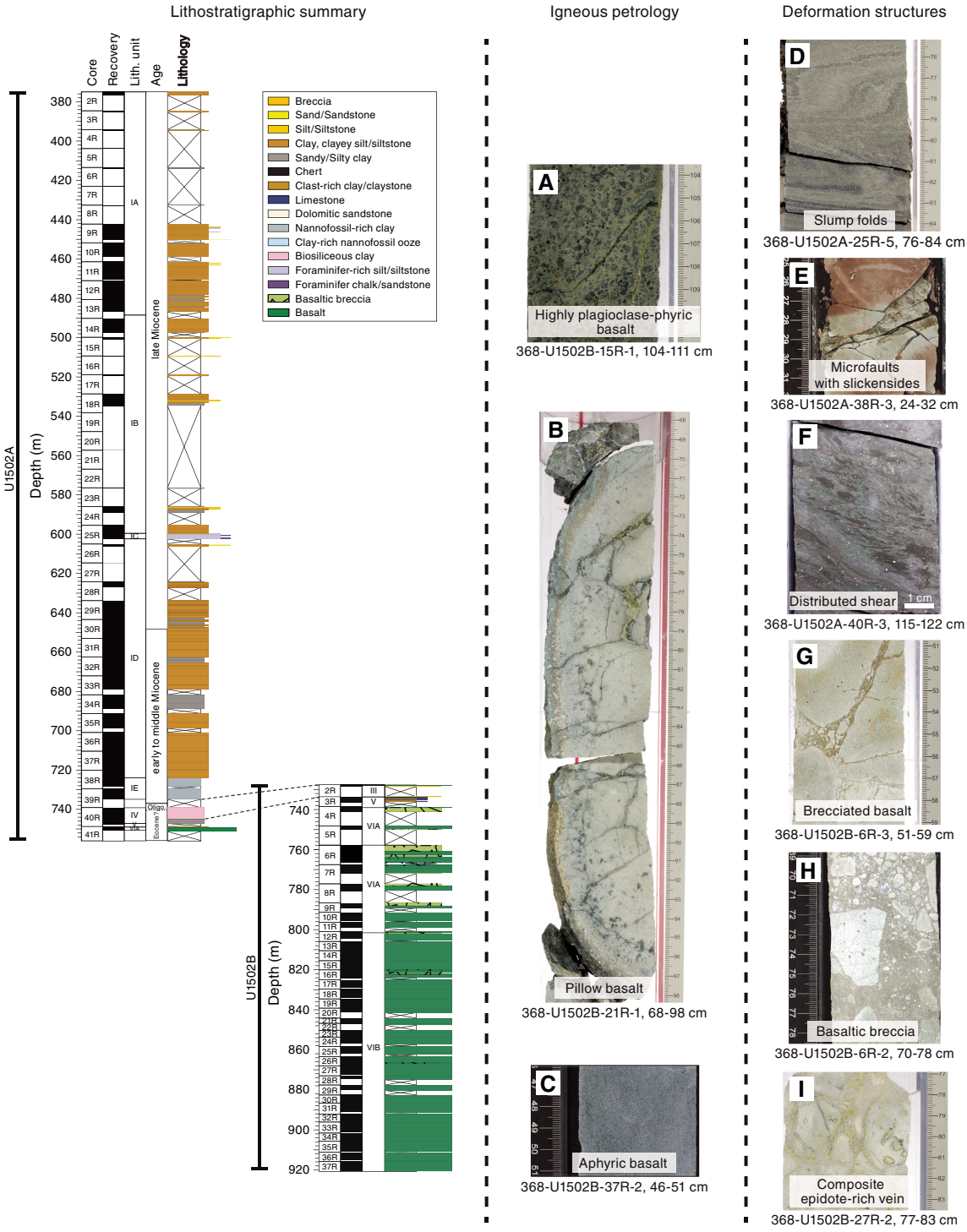

appears to be compositionally distinct from Unit 2 and has, for example, higher Ti/Zr ratios.

Structural geology

Deformation structures are scarce in Unit I above Core 368-U1502A-37R, with only a local, convolutely bedded sequence in Core 25R. Downhole from Core 37R at ~700 m, a gradual increase in deformation structures was observed (Figure F19). Cores 37R through 39R are characterized by microfaults, as evidenced by downward-dip plunging striations and slickensides on exposed fracture surfaces, systematically associated with greenish halos. No deformation structures were encountered in Unit II. Unit III con-

sists of extremely silicified breccia that was poorly recovered. The nature of this breccia, however, as sedimentary, tectonic, or hydrothermal remains unconstrained at the moment. In Unit IV, a small-scale transition from distributed to localized shear in unlithified sediments was documented. No deformation structures were encountered in Unit V.

Unit VI is essentially composed of basalts that were heterogeneously affected by brecciation and veining associated with the circulation of hydrothermal fluids. Subunit VIA is dominated by brecciated basalt/basaltic breccia, whereas Subunit VIB comprises a rather coherent series of lava flows crosscut by a multistage network of polymineralic veins. The uppermost part of Unit VI contains severely fractured and fragmented basalt locally filled by fine-grained unconsolidated greenish rock. Subunit VIA is characterized by diverse brecciation horizons associated with veins and microcracks. Depending on the intensity of fragmentation and the clast/matrix ratio, the rocks are referred to as brecciated basalt or basaltic breccia. A typically observed feature is the jigsaw-puzzle structure, suggesting possible in situ fragmentation. Macro- and microscopic observations show that the breccia-clasts consist mainly of sparsely to moderately plagioclase phyric basalts that were hydrothermally altered to variable degrees. Thus, formation of such breccias likely involved fluid-assisted fracturing of basalt. In contrast, Subunit VIB is characterized by a progressive decrease of breccia horizons and the development of different vein types, almost always polymineralic. Notably, vein composition and their orientation changes through Subunit VIB. Although numerous small-scale veins often related with major veins were observed, three first-order vein types were categorized: (1) composite silica-rich veins, (2) composite epidote-rich veins, and (3) composite carbonate- and/or silica-rich veins.

Biostratigraphy

All core catcher samples from Hole U1502A and selected samples from Hole U1502B were analyzed for calcareous nannofossils, foraminifers, diatoms, and ostracods. Additional samples were taken from the working-half core intervals when necessary to refine the ages. The preservation of calcareous microfossils is mostly good to moderate in the upper sections (Cores 368-U1502A-2R through 13R) and moderate to poor in the lower sections (Cores 14R through 41R). Planktonic foraminifers and calcareous nannofossils are abundant to common in Cores 2R through 10R, 25R, and 37R through 39R and rare to barren in all other sections. Diatoms were only observed in Sections 40R-1 through 40R-3. In Hole U1502B, foraminifers were observed only in Section 3R-1 and are represented by well-preserved agglutinated deep-water taxa. Ostracods are extremely rare; single occurrences were observed only in three samples in Hole U1502A (Samples 3R-CC, 4R-CC, and 5R-CC).

Fourteen planktonic foraminifer and calcareous nannofossil biostratigraphic events were used to provide an age-depth model for Site U1502 from the late Oligocene to the late Miocene. The Pliocene/Miocene boundary is placed tentatively in Core 368-U1502A-2R, but it may be shallower than the cored section. The Miocene/Oligocene boundary was determined to lie between Samples 39R-CC and 40R-1, 7 cm. Sedimentation rates vary from ~10 mm/ky in the early–middle Miocene to ~39 mm/ky in the late Miocene. No planktonic microfossils were found in Hole U1502B, but a sample from the sandy interval in Core 3R revealed abundant and diverse abyssal agglutinated benthic foraminifers. The composition of this agglutinated benthic foraminifer assemblage provides a possible age of late Eocene for this interval.

Figure F20. Magnetization intensity vs. inclination showing the effect of the steep drilling overprint, Holes U1502A and U1502B. Basalts have higher magnetization intensity than sediments. Green lines represent the expected normal and reversal inclination at present latitudes.

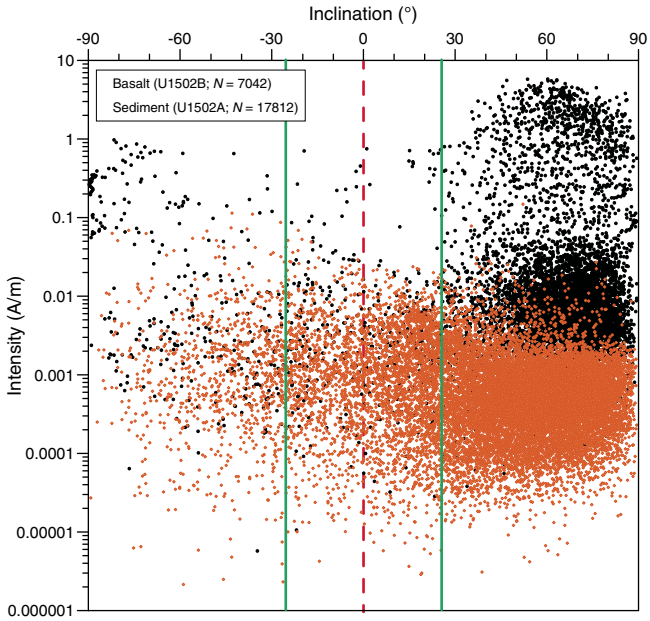

Paleomagnetism

The magnetic behavior of sediments at Site U1502 correlates with their color (greenish gray or reddish brown). Reddish brown sediment shows AF magnetization indicative of magnetite or titanomagnetite and hematite (responsible for the color). In contrast, greenish gray sediment hosts magnetite or titanomagnetite and pyrrhotite. The predominance of steep normal inclinations (~75°; Figure **F20**) across all late Oligocene to late Miocene units (375.00–750.67 m) affects the SRM section measurements and prevents any reliable magnetostratigraphy to be established for Holes U1502A and U1502B.

The basalt has NRM intensity one order of magnitude higher than sediment. The main magnetically remanent phase is titanomagnetite, but its alteration produces maghemite or hematite. Magnetic susceptibility (κ) has a bimodal distribution with a median at 327×10^{-6} SI. κ does not show any strong correlation with any chemical ($R^2 = 0.343$ for Fe_2O_3 wt%). Intervals of high κ might correspond to the bottoms of flows with a massive, less altered structure. Altered basalts have higher Koenigsberger ratios (Q_n = 1–10) than fresher basalts (Q_n = 0.001–1). The mean dip of magnetic foliation is 8°.

Cores 368-U1502B-9R and 10R show less-pervasive drilling overprint, and two discrete samples show both a normal (soft) component and a reverse (hard) component, suggesting a possible reversal.

Geochemistry

Site U1502 contains very low high-hydrocarbon gas abundances and TOC, nitrogen, and sulfur contents, likely reflecting the poor preservation of organic matter. Instances of high carbonate content are associated with siderite, and on occasion this mineral comprises >50 wt% by mass of intervals in lithostratigraphic Subunit ID. The interstitial water at Site U1502 is enriched in Ca, Mg, and K and has notably high alkalinity but is depleted in Na, Cl, and Br. The linear

Figure F21. Physical property records, Site U1502.

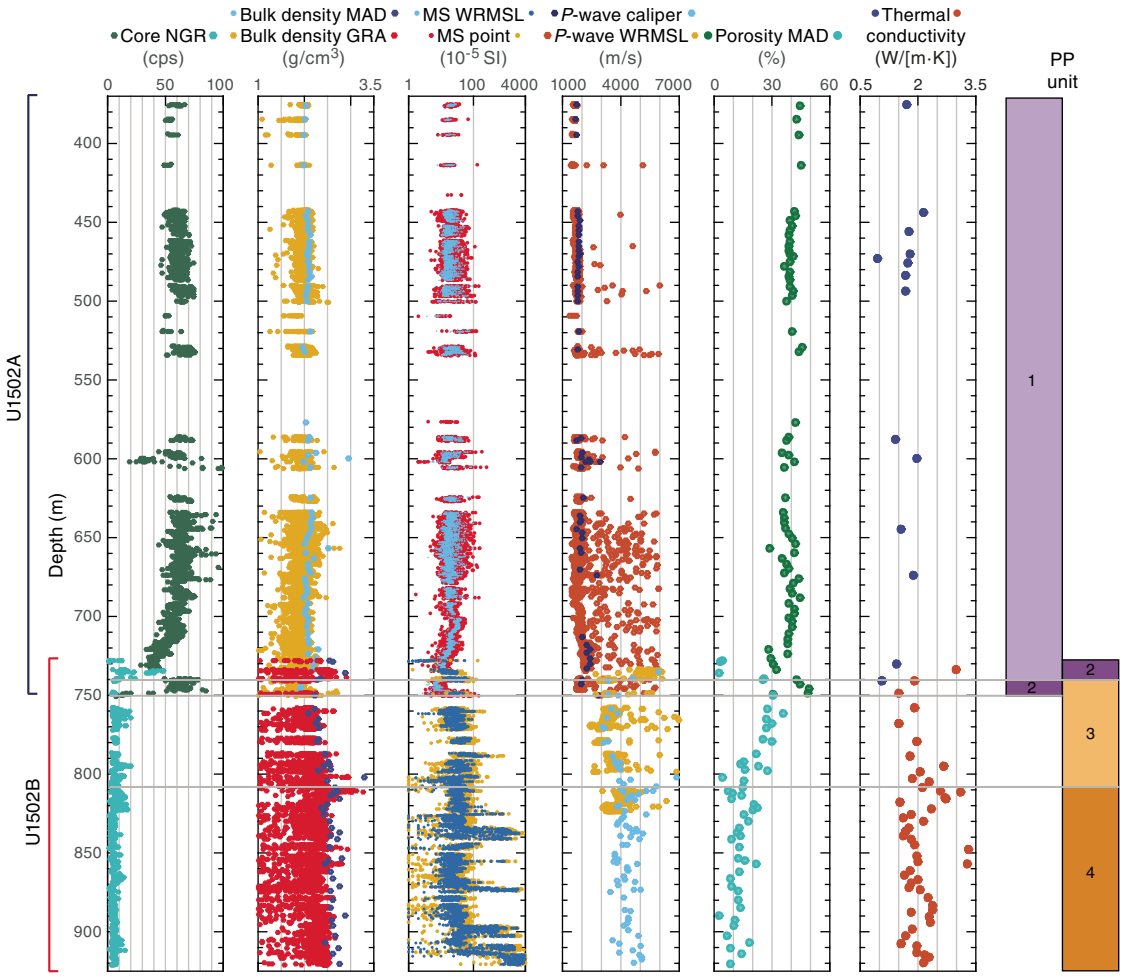

increase of major anion and cation contents implies upward movement of fluid from deeper sediments. The hemipelagic sediments in Unit I have some similarities to the geochemical characteristics of the hemipelagic and pelagic units at Sites U1501 and U1505, but Site U1502 sediments are enriched in Fe, K, and clay concentrations, likely as a result of regions of increased alteration. All of the analyzed igneous rocks from Units II–VI are heavily altered, although samples from igneous lithologic Subunit 2b are altered to a lesser degree than those from Subunit 2a.

Physical properties

Physical property data acquired at Site U1502 include density, magnetic susceptibility, *P*-wave velocity, NGR, color reflectance, and thermal conductivity (Figure **F21**). These data allow us to characterize four physical property (PP) units. PP Unit 1 (375–740 m) corresponds to the nannofossil-rich and biosiliceous-rich clay lithologies and exhibits small variations in NGR between 50 and 70 counts/s and uniformly increasing *P*-wave velocity with depth that averages <2500 m/s. Unit 1 sediments have similar porosity to those recorded at nearby Sites U1499 and U1500 in the same depth interval, suggesting the same compaction history. A significant increase in bulk density (up to 2.7 g/cm^3) in Core 368-U1502B-3R is associated with strongly lithified limestone beds. Variations of high and low magnetic susceptibility values correspond to sediment color changes in Unit 1 and may be controlled by the amount of pyrrhotite in the sediments.

PP Unit 2 (740–750 m) in Hole U1502A is characterized by lower *P*-wave velocity and bulk density and higher NGR than the strata above. Low density and *P*-wave velocity found in Unit 2 reflect the clast-rich claystone from lithostratigraphic Unit V.

PP Units 3 and 4 represent the basaltic basement and are characterized by relatively low NGR (<10 counts/s), high density, and *P*-wave velocity that vary over a broad range (3000–6000 m/s). The boundary between Units 3 and 4 is marked by an abrupt increase in density, *P*-wave velocity, and thermal conductivity and coincides with the change from igneous lithologic Subunit 2a to 2b. Prominent magnetic susceptibility peaks (up to 4000 × 10^{-5} SI) in Units 3 and 4 correspond to relatively less altered basalt. Thermal conductivity in Units 3 and 4 are variable but generally increases in line with decreasing porosity with depth.

Downhole measurements

Wireline logging was conducted in Hole U1502B using a modified triple combo tool string and the VSI tool string. The modified triple combo tool string included the HNGS, HLDS, and Dipole Sonic Imager (DSI) for acoustic velocity. The triple combo run collected good data downhole from 875.3 m (~45 m above the bottom of Hole U1502B) and allowed us to define eight logging units, which

correlate in great part to the lithostratigraphic units and core physical properties. Logging Units 1–5 are defined by data collected through the casing and drill pipe. Unit 6 data was collected outside the casing but inside the drill pipe, whereas data in Units 7 and 8 were collected in the open hole. For measurements inside the casing and/or drill pipe, only NGR and the associated K, Th, and U components provide meaningful data, although they are highly attenuated by the casing and/or drill pipe. Open borehole conditions from the bottom of the casing at 723 m to 875.3 m were generally good, with measured diameters from 12 to 14.5 inches. Log and core data generally show good agreement, and downhole measurements provide information in zones of poor core recovery in Hole U1502B. The log data exhibit increasing density and *P*-wave velocity with depth. The amplitude of NGR increases gradually with depth throughout Units 1–3 (seafloor to ~630 m), with an interval of relatively constant values between 150 and 350 m. NGR values are lowest in Units 4–8 (~630–850 m).

The VSI tool string was run only inside the casing because the tool could not pass through an obstruction encountered at the end of the casing. Eight stations were attempted. The two deepest stations (at 715.1 and 695.2 m) are associated with large noise levels, which were possibly caused by poor mechanical coupling of the casing with the surrounding formation. The remaining upper six stations, located at 290.2, 350.3, 450.3, 550.1, 590.3, and 630.3 m, recorded good quality waveforms.

Site U1503

Background and objectives

Site U1503 (proposed Site SCSII-9B; Sun et al., 2016b) is located at 3868 mbsl near the top of the structural high named Ridge C (Figures **F3**, **F22**). Ridge C is the most seaward ridge of the three margin-parallel Ridges A, B, and C that characterize the lower continental slope underlain by thin (5–7 km) crust. Ridge C is believed to represent at least partly, if not fully, igneous crust and hence the completion of continental breakup along this margin segment of the northern SCS.

A key operational objective of Site U1503 was to sample the lowermost ~300 m of sediments on top of basement to constrain the age and subsidence history of the crust at this location, the timing of normal faulting, and the environment of the early half-graben fill. The most important goal was to sample the igneous stratigraphy to at least 100 m below the basement. Because of a rig floor equipment failure (drawworks), we abandoned the site after installing casing in Hole U1503A to 991.5 m.

Deep, representative sampling of the basaltic material at this site would have provided an important reference frame for breakup modeling. With an estimated 1640 m sediment thickness overlying basement, obtaining basement samples and log data at this site represented a challenging operation.

Figure F22. Bathymetry at Site U1503 and location of the site in relation to seismic Lines 15ecLW5 and 08ec1555.

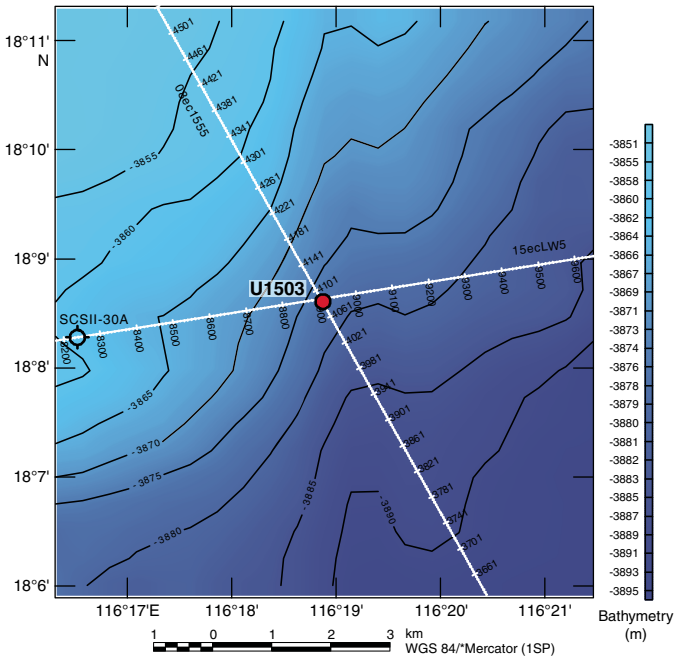

Operations

To reach our objectives, we conducted operations in one hole (U1503A; 18°08.6300′N, 116°18.8456′E; 3868 mbsl) (Table **T2**). We successfully installed a reentry system and 991.5 m of 10¾ inch casing in Hole U1503A. However, we were unable to deepen the hole below the casing because of repeated breakdowns of the low clutch diaphragm in the drawworks and concerns that we did not have enough spares to last the remainder of the expedition. Without the drawworks' low clutch, we could not conduct drilling operations deeper than 3400 m (water depth plus penetration depth). Because Site U1503 had a planned depth of 5695 m (water depth plus penetration depth), we abandoned Hole U1503A without addressing any scientific objectives. Hole U1503A remains cased and open for possible future occupation.

Site U1504

Background and objectives

Site U1504 (alternate Site SCSII-27A) was proposed during Expedition 367 and approved by the Environmental Protection and Safety Panel during Expedition 368 as an alternate site should there be time left following completion of the high-priority sites included in the *Scientific Prospectus* (Sun et al., 2016b). Expedition 368 occupied Site U1504 because of the inability to continue drilling below the 990 m deep, cased Hole U1503A. Most of our remaining approved sites were in water deeper than 3400 m and/or required deep penetration. One exception was Site U1504, which is located at 2823 mbsl ~45 km east of Site U1501 on the OMH and has a shallow coring target (Figures **F3**, **F23**) and targets the nature of basement within the COT.

Operations

Two holes were drilled at Site U1504 (Table **T2**). In Hole U1504A (18°50.9199′N, 116°14.5397′E; 2816.6 mbsl), we cored with the RCB system from the seafloor to metamorphic basement at 134.8 m and then into basement to 165.5 m, recovering 52.77 m (32%). In Hole U1504B (~200 m southeast of Hole U1504A; 18°50.8213′N, 116°14.5978′E; 2843.0 mbsl), we drilled without recovery to 88.2 m, cored with the RCB system to metamorphic basement at 107.9 m, and then cored into basement to 200 m, recovering 21.48 m (19%).

Lithostratigraphy

The succession recovered at Site U1504 includes two sedimentary units (I and II) underlain by a metamorphic unit (III). Lithostratigraphic Unit I (early Miocene–Pleistocene) is dominated by

Figure F23. Bathymetry at Site U1504 and location of the site in relation to seismic lines. Note that the clear offset in the bathymetry along the margin may indicate some transform offset in the deeper margin structure.

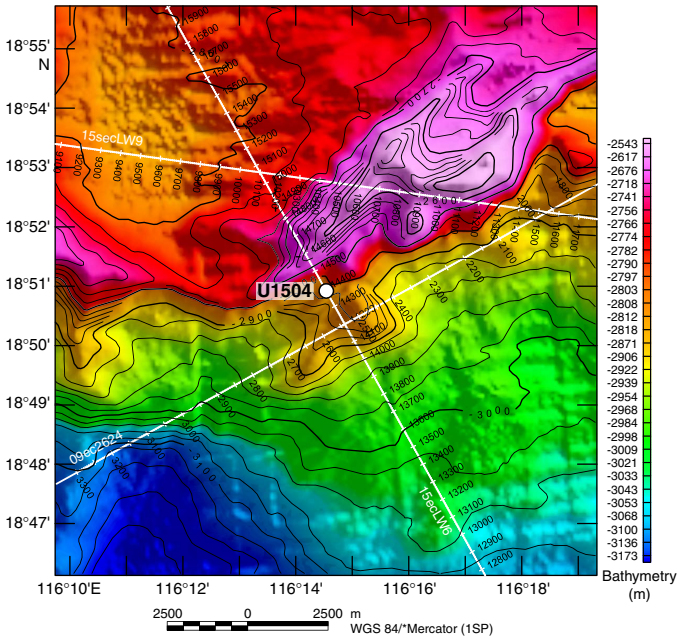

nannofossil and foraminiferal ooze and minor nannofossil-rich clay and is divided into four subunits (IA–ID). Subunit IA (Hole U1504A = 17.50–46.59 m) is composed of nannofossil-rich clay, nannofossil ooze, nannofossil ooze with biogenic silica, and clay-rich nannofossil ooze. The color of the ooze gradually changes downhole from dark greenish gray to greenish gray and gray. Distinct intervals contain more silt. Thin silt laminations are often disrupted by bioturbation. Layering is contorted at the base of the subunit. Subunit IB (Hole U1504A = 46.59–59.73 m) is composed of light brown foraminifer-rich nannofossil ooze and pale brown nannofossil ooze with foraminifers. Subunit IC (Hole U1504A = 65.80–104.99 m) is composed of light greenish gray, greenish gray, light brownish gray, pale brown, and light gray nannofossil ooze with clay and greenish gray clay-rich nannofossil ooze intercalated with light gray nannofossil-rich foraminiferal ooze with clay, light brownish gray foraminifer-rich nannofossil ooze, and foraminifer-rich nannofossil ooze with clay. Subunit ID (Hole U1504A = 104.99–112.66 m; Hole U1504B =88.20–92.31 m) is composed of light brown to yellowish brown nannofossil ooze with foraminifers intercalated with pink or brownish yellow foraminifer-rich nannofossil ooze. Unit II (possibly Eocene; Hole U1504A = 114.72–134.80 m; Hole U1504B = 97.90–107.91 m) is clast-supported, bioclast-rich limestone with larger benthic foraminifers (as large as 15 mm). Unit III (age unknown; Hole U1504A = 136.40–163.70 m; Hole U1504B = 117.40–196.28 m) is composed of fine- to coarse-grained epidote-chlorite schist (Subunit IIIA) and calc-silicate schist (Subunit IIIB) with granofels clasts.

Metamorphic petrology

We recovered 27 m (Hole U1504A) and 79 m (Hole U1504B) of a variety of mylonitic epidote-chlorite to calc-silicate schists containing granofels clasts. Recovery was <20% in metamorphic lithologic Unit 1. Lithologic changes with depth and between the two holes were observed, and Unit 1 is divided based on a change in the predominant metamorphic lithology (Figure **F24**). Metamorphic lithologic Subunit 1a was recovered in both Holes U1504A and U1504B and consists of greenish gray, microcrystalline to coarse-grained epidote-chlorite schist with dark greenish gray granofels clasts (<10 cm) and epidote-chlorite breccia. The schists show a strong mylonitic foliation, whereas the clasts have generally isotropic textures showing local weakly developed foliation. Both the schist and the granofels clasts show, in general, a comparable mineral assemblage consisting of epidote, chlorite, feldspar, and quartz ± other phyllosilicates and accessory minerals and locally isolated subhedral dark minerals (pyroxene?). The granofels clasts are often crosscut by a network of quartz veins. Subunit 1b contains an alternation of calc-silicate schist and epidote-chlorite schist with granofels clasts, epidote and/or chlorite granofels, chlorite schist with epidote, epidote-chlorite gneiss, and minor marble. The lithologies are fine grained to coarse grained with mostly an inequigranular texture and some bimodal or equigranular textures, and the schistose sections show a strong mylonitic foliation. Several of the schists show reddish brown alteration, and late calcite veins crosscut the foliation of the deepest schists recovered (e.g., in Core 368-U1504A-20R). Minerals observed are epidote, quartz, chlorite, calcite, and feldspar. Subunit 1b contains numerous clasts with variable lithologies: cryptocrystalline granofels either with or without quartz and/or calcite veins, porphyritic rocks with tabular phenocrysts (possibly altered plagioclase), brecciated (epidote, calcite, and/or quartz) veins, and foliated granofels.

Handheld pXRF analyses show an average mafic igneous composition for both the schist and the clasts but with a spread toward ultramafic (in Hole U1504B Subunit 1a) and more felsic compositions (in Subunit 1b). A clear change in sulfur contents occurs between Subunits 1a and 1b, the latter of which is below the detection limit. High Nb contents compared to MORB indicate a potentially enriched source for the protolith.

Lithostratigraphic Unit III (metamorphic lithologic Unit 1) consists of mylonitic greenschist facies metamorphic rocks, as indicated by the presence of epidote and chlorite. We infer that the protolith most likely was breccia based on the different clast sizes and types and styles of deformation. The protolith likely had a mafic igneous composition. It is, however, unclear if this breccia with mafic clasts has a sedimentary origin (e.g., volcaniclastic) or represents a potentially hydrothermally altered form of basalt, gabbro, or ultramafic protolith. At present, the metamorphic evolution of this unit and its possible connection with the opening of the SCS is unknown.

Structural geology

Lithostratigraphic Unit I shows subhorizontal bedding and locally some minor possible slump folds, as observed in Section 368-U1504A-5R-1. Unit II is devoid of any deformation structures. The metamorphic basement at Site U1504 is formed by greenschist facies mylonitic epidote-chlorite schists and calc-silicate schists (Unit III). The rocks preserve distinct deformation structures resulting from changes in the mode of deformation (brittle/ductile); the modal amount of quartz + feldspar governing the (local) rheological behavior; the amount of accumulated strain; the occurrence of variably sized (up to decimeter scale), prekinematic, heterolithic clasts that mostly form rigid (i.e., internally undeformed) bodies in the ductile foliation; and/or superimposed multiple deformation phases. The steeply dipping (up to 75°) mylonitic foliation is characterized by distinct morphologies: (1) a widely spaced anastomosing foliation associated with leucocratic bands; (2) a tight, closely

Figure F24. Lithostratigraphic, petrographic/petrological, and structural observations with strong focus on the metamorphic basement, Site U1504. A, B. Clast-supported limestone with large benthic foraminifers and coral fragments. C. Severely quartz-veined, angular clast of chlorite-epidote granofels enclosed in mylonitic foliation of a typical epidote-chlorite schist. D. Steep (~75°) widely anastomosing foliation in a quartz + feldspar-rich variety of the rock. Arrow = extensively stretched veined clast of chlorite-epidote granofels oriented parallel to the foliation. E. Epidote-chlorite schist with granofels clasts split parallel to the *x*, *y*-plane of finite strain. Large granofels clast is crosscut by a shear band in the epidote-chlorite schist. Several sigma clasts lie right above the shear band. Both deformation structures indicate normal sense of shear. A late, postkinematic vein crosscuts both the mylonitic foliation and the granofels clast. F. Tight foliation affected by crenulation cleavage in quartz-poor (i.e., more melanocratic) variety of the rock. G. Local occurrence of foliated impure calcite marble. H. Veined and altered aphyric mafic granofels clast (left side) and granofels clast interpreted as protolithic epidote vein (right side). Both clasts are internally undeformed but show synkinematic deformation together with the mylonitic fabric at their rims. I. Rigid (left) and strongly deformed (upper end) granofels clasts embedded in calc-silicate schist. Note the deflection of the mylonitic foliation at the clast boundaries. J. Long piece of core showing the characteristic morphology of the mylonitic foliation in calc-silicate schist of Subunit IIIB. Note the steep inclination and anastomosing geometry enclosing heterolithic clasts that are strongly elongated, folded, and oriented parallel to the foliation.

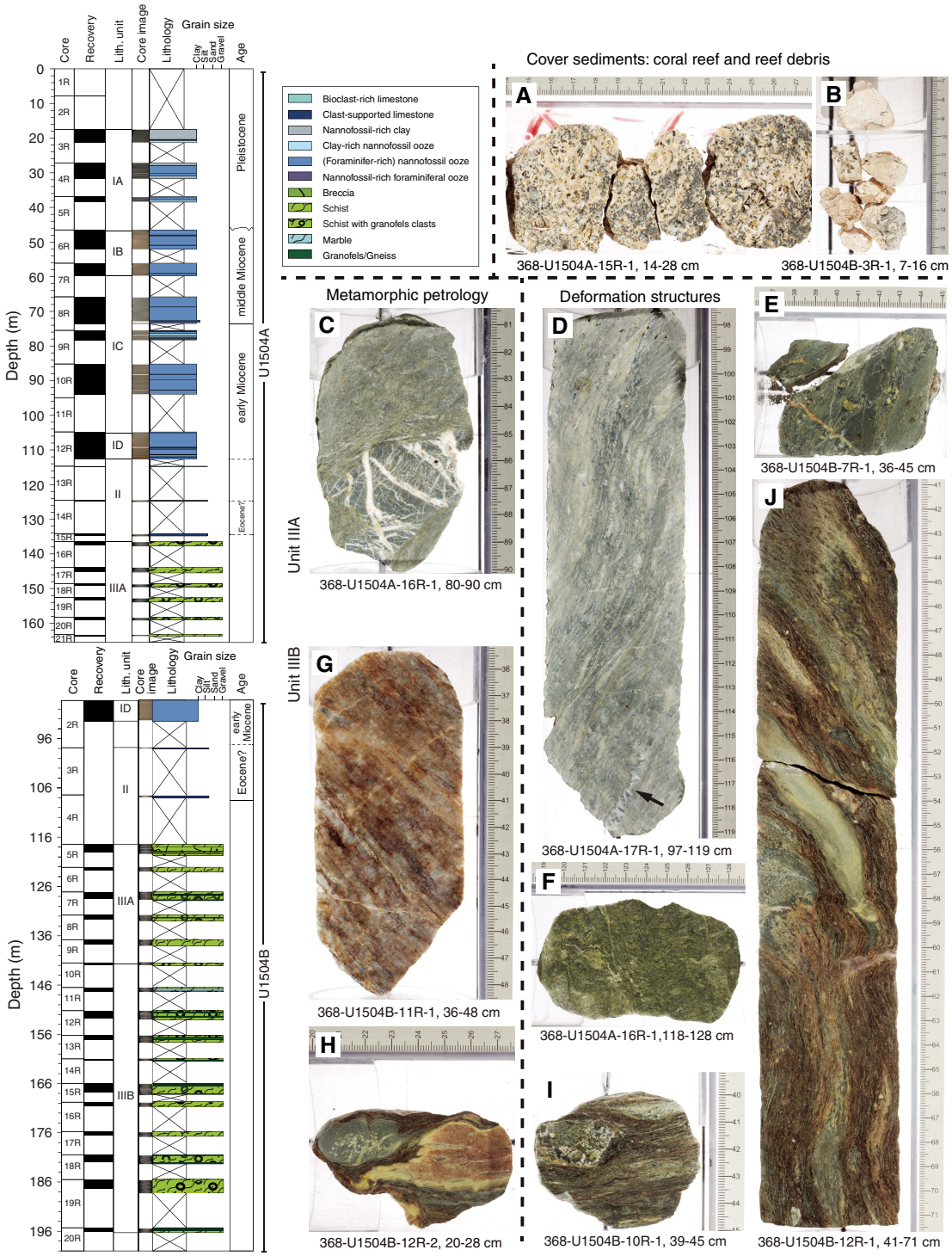

spaced, and often crenulated foliation associated with more melanocratic schist variations; and (3) a tight anastomosing foliation associated with calc-silicate schists enclosing angular to rounded heterolithic granofels clasts. Locally, the sense of shear is indicated by shear bands and sigma clasts. In metamorphic lithologic Subunit 1a (Figure **F24**), granofels clasts are consistently microcrystalline (chlorite + epidote) and dismembered by a network of mostly parallel and perpendicular quartz veins cutting each other. They often form apparently stretched, elongated bodies oriented parallel to the foliation. Subunit 1b shows a wide range of prekinematic (mostly mafic) clasts enclosed by the foliation. Encountered varieties encompass highly phyric to aphyric rocks, as well as fragmented former (epidote/calcite/quartz) vein fillings. In some cases, such clasts show ductile internal deformation. Clast boundaries can be either distinctly sharp or diffuse, the latter indicating mechanical and/or chemical interactions with the surrounding foliation. Deformation in Subunit 1b is presumably strongly controlled by an inherited (protolithic) brecciated structure.

Biostratigraphy

All core catcher samples at Site U1504 were analyzed for calcareous nannofossils, foraminifers, and diatoms. Additional samples were taken from intervals in the working-half core sections when necessary to refine the ages. Preservation of calcareous microfossils is good to very good in Cores 368-U1504A-2R through 12R, and 368-U1504B-2R and is poorly preserved (recrystallization) in the reefal limestone below Core 368-U1504A-12R. Planktonic foraminifers and calcareous nannofossils are abundant in Cores 368-U1504A-2R through 12R and 368-U1504B-2R and barren in Cores 368-U1504A-13R through 15R. Diatoms are present but poorly preserved in Cores 368-U1504A-2R through 5R and absent in rest of the samples. Twenty biostratigraphic datums were identified in a succession from the late Pleistocene to the early Miocene.

A possible hiatus between the early Pleistocene and late Miocene was determined in Core 368-U1504A-6R by abrupt planktonic foraminifer and nannofossil assemblage changes. Sedimentation rates at this site varied from ~6 mm/ky in the early middle Miocene to ~22 mm/ky during the Pleistocene.

Cores 368-U1504A-13R through 15R are mainly composed of reefal and larger benthic foraminiferal limestone. Thin section examination of these carbonate rocks indicates the presence of abundant *Nummulites*, suggesting an Eocene age. The abundant larger benthic foraminifers indicate deposition in a warm shallow-marine environment. In contrast, the abundant planktonic foraminifers and calcareous nannofossils in the carbonate ooze in the overlying sedimentary section (Cores 2R through 12R) indicate a deep-water environment since the early Miocene.

Paleomagnetism

Most of the discrete sediment samples analyzed show an initial soft magnetic behavior attributed to titanomagnetite followed by a gyroremanent magnetization (GRM) greater than 70 mT attributed to greigite, a mineral already identified in Hole U1501C. Consistently steep normal inclinations (~60°) across all sedimentary units indicate a significant drilling overprint that is removed by AF demagnetization up to 15 mT. A succession of nine normal and eight reversed polarities are defined, particularly in the upper part of the cores.

Discrete samples show low κ values, a moderate degree of magnetic anisotropy, and strongly oblate symmetry, probably of depositional origin. This subhorizontal planar fabric indicates deposition in a calm, pelagic environment with moderate traction.

NRM intensities of metamorphic rocks, measured on the SRM and on four discrete cubes, are relatively weak and indicate a complex magnetic assemblage composed of magnetite and hematite. The anisotropy of magnetic susceptibility (AMS) fabrics consistently dip steeply and show a moderate to high degree of magnetic anisotropy, oblate symmetries, and oblique magnetic lineations, possibly indicating an oblique motion in this high-strain shear zone.

Geochemistry

Hydrocarbon gases were not detected above background levels at Site U1504, and TOC, TN, and TS contents were low (<0.5 wt%). Instances of high carbonate content were associated with bioclast-rich and clast-supported limestone. The upper part of the sediment was not cored. Interstitial water data from the cored sediments are broadly comparable to other sites.

Physical properties

Four physical properties (PP) units are identified at Site U1504 according to variations in the core physical properties. Core material in PP Units 1 and 2 consists of soft sediments. In general, with respect to Unit 2, Unit 1 has a higher average NGR (~30 versus 20 counts/s), a weaker color reflectance (mean L* of ~40 versus 50), and a lower average red, green, blue (RGB) value (100 versus 150). These changes in physical properties between Units 1 and 2 correspond to a switch in sediment composition from nannofossil-rich clay to nannofossil ooze. A general increase in bulk (from ~1.4 to 1.8 g/cm^3) and dry (from ~0.7 to 1.2 g/cm^3) densities and a downhole decrease in porosity (from 75% to 56%) in Units 1 and 2 mainly indicate sediment compaction with time. The boundary between Units 1 and 2 is marked by a relatively rapid increase in *P*-wave velocity and bulk density and a rapid decrease in porosity compared with the general trends mentioned above. This physical property boundary corresponds to an unconformity in the seismic profile and to a hiatus confirmed by the biostratigraphic data.

P-wave velocity and bulk density increase from ~3800 to 5000 m/s and from ~2.4 to 2.9 g/cm^3, respectively, in Unit 3, which corresponds to a transition in lithology from coral-rich limestone to clast-supported limestone. Coral-rich limestone in the upper portion of Unit 3 is also associated with a moderately high porosity of ~23%. Unit 4 is characterized by uniformly high velocity of ~5500 m/s, high bulk density of ~2.9 g/cm^3, and low porosity of ~3%, which correspond to the epidote-chlorite schist. A large increase in both velocity and density at the Unit 2/3 and Unit 3/4 boundaries corresponds to strong reflectors in the seismic data. The gradual downhole increase in thermal conductivity values at shallow depths is likely due to progressive compaction of the sediments.

Site U1505

Background and objectives

Site U1505 (proposed Site SCSII-3D) is located at 2916.6 m water depth on a broad regional basement high (Figure **F25**). This site was an alternate to Site U1501, should time be left for drilling following completion of the high-priority sites included in the *Scientific Prospectus* (Sun et al., 2016b). Site U1505 was included in Expedition 368 because it might complement findings at Site U1501, and it was in the operational limits of the 3400 m drill string imposed by the failure of the drawworks.

Both Sites U1505 and U1501 are located on the same structural high at similar water depths and are 10.5 km apart (Figure **F2**). The seismic section at Site U1505 generally shows a more horizontal orientation of the seismic reflectors and concordant relationship of the strata than the one at Site U1501, indicating the sediment sequence

Figure F25. Bathymetry at Site U1505 and location of the site in relation to seismic Lines 04ec1555 and 15eclLW1. Note that the site is not at the exact crossing of Lines 04ec1555 and 15eclLW1.

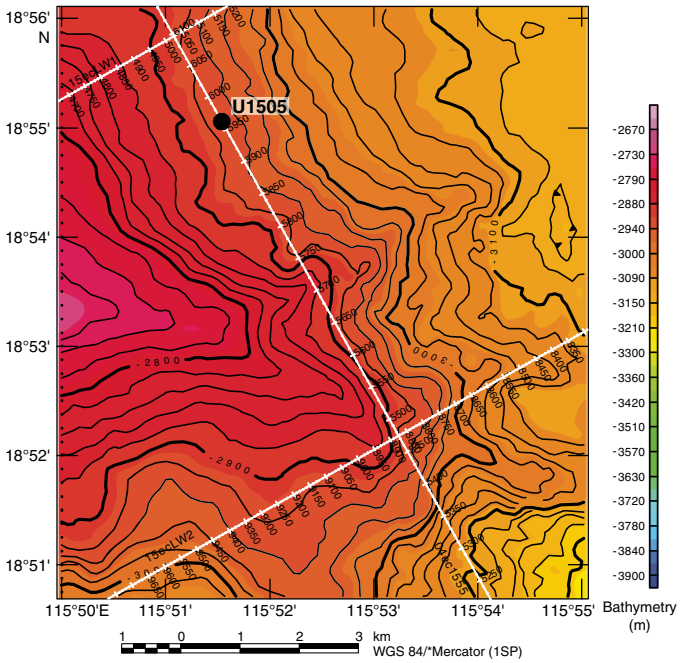

at Site U1505 should be more complete. The key objective at Site U1505 was to sample the stratigraphic record above seismic Unconformity T80 (inferred before drilling to be ~38 Ma), and specific goals were to constrain both (1) the sediment responses to the tectonic events and basin evolution since the Eocene and (2) Neogene paleoceanographic and paleoclimatological changes along the northern SCS margin.

The relatively shallow 2916.6 m water depth at Site U1505 makes it one of the few ODP/Integrated Ocean Drilling Program/IODP sites above the modern CCD of the SCS. The site's hemipelagic deposits, rich in calcareous microfossils, enable the application of stable isotopes, faunal analyses, and other multidisciplinary methods. Key objectives were to reconstruct the east Asian monsoonal climate record in the SCS and upper- and deep-water variations in the western Pacific. Site U1505 will, for the first time, provide an almost continuous sequence of paleoceanographic studies at orbital and millennial timescales since the late Eocene in the SCS. We cored two deep holes at this site with the APC/XCB system to obtain a continuous record of the Pliocene–Pleistocene interval for high-resolution paleoceanographic studies.

Operations

Four holes were cored with the APC and XCB systems at Site U1505 (Table T2). In Hole U1505A (18°55.0560′N, 115°51.5369′E; 2916.6 m water depth), Core 1H misfired and recovered only 0.3 m. In Hole U1505B (18°55.0562′N, 115°51.5370′E; 2918.6 m water depth), a 3.23 m long mudline core was recovered for future education and outreach activities. Hole U1505C (18°55.0570′N, 115°51.5370′E; 2917.4 m water depth) was cored with the APC system to 317 m and then cored with the XCB system to 480.2 m, recovering 480.15 m (100%). Hole U1505D (18°55.0485′N, 115°51.5501′E; 2917.5 m water depth) was cored with the APC system to 184.5 m and recovered 191.43 m (104%). Downhole logging with a modified triple combo tool string was conducted in Hole U1505C from 341.2 m uphole. The maximum drilling depth of 480.2 m was determined by the possible maximum total length (3400 m) of drill string deployment.

Lithostratigraphy

The sediment succession recovered at Site U1505 extends from the Oligocene to the Pleistocene. Two sedimentary units (I and II) were observed (Figure F26). Lithostratigraphic Unit I is dominated by nannofossil ooze with varying amounts of foraminifers and clay, as well as biogenic silica in the upper interval of the hole. Unit I is divided into three subunits (IA–IC). Subunit IA (Hole U1505C = 0.00–27.76 m) is composed of dark greenish gray and greenish gray biosiliceous-rich clay with nannofossils, nannofossil-rich clay with biogenic silica, and nannofossil-rich biosiliceous ooze with clay. The abundance of biogenic silica decreases downhole. A pinkish gray, ~6 cm thick, slightly fining upward ash layer occurs at 20.8 m (Hole U1505C), and ash pods were observed at 20.3 m in Hole U1505D. Subunit IB (Hole U1505C = 27.76–273.39 m) is composed of gray to brown nannofossil ooze with minor silty intervals. The color change reflects the varying abundance of foraminifers and clay. Subunit IC (Hole U1505C = 273.39–403.79 m) is composed of gray, greenish gray, and light brownish gray clay-rich nannofossil ooze (with foraminifers) and foraminifer-rich nannofossil ooze with clay and minor amounts of nannofossil-rich clay. Unit II (Hole U1505C = 403.50–480.54 m) is dominated by dark greenish gray, well-consolidated silty clay and clayey silt (with nannofossils).

Biostratigraphy

All core catcher samples from Holes U1505A–U1505C were analyzed for calcareous nannofossils, planktonic foraminifers, and diatoms. Additional samples were taken from intervals in the working-half sections when necessary to refine the ages. Hole U1505D was not sampled continuously for biostratigraphic analyses because of time constraints at the end of the expedition, but the sequence recovered spans from the late Miocene to the present (Figure F26). Preservation of calcareous microfossils is good in Cores 368-U1505C-1H through 48X and moderate to poor in Cores 49X through 64X. Planktonic foraminifers are abundant or common in Cores 1H through 56X and 59X through 62X and rare in Cores 57X, 58X, 63X, and 64X. Calcareous nannofossils are generally abundant to common in most samples from Hole U1505C, except for those from the upper part of Core 57X.

Forty-five biostratigraphic datums identified in Hole U1505C suggest a continuous succession from the early Oligocene to the Holocene (Figure F26). The Pleistocene/Pliocene boundary is placed in Core 7H, the Pliocene/Miocene boundary is placed between Cores 11H and 13H, and the Miocene/Oligocene boundary is placed between Cores 54X and 55X. Sedimentation rates are ~7 mm/ky in the Oligocene, ~15 mm/ky during the Miocene–Pliocene, and ~24 mm/ky during the Pleistocene.

Relatively low abundances of planktonic foraminifers deeper than Core 57X indicate bathyal depths during the early Oligocene, whereas much higher abundances of planktonic foraminifers shallower than Core 56X suggest a deeper water environment since the late Oligocene.

Paleomagnetism

Only NRM was measured with the SRM in Hole U1505C, except for Sections 1H-1 through 3H-1, which were in-line AF demagnetized in three steps. Most of the 55 AF demagnetized discrete samples show very soft magnetic behavior responsible for the acquisition of a strong, vertical drilling overprint (average inclina-

Figure F26. Lithostratigraphic and biostratigraphic summary, Site U1505.

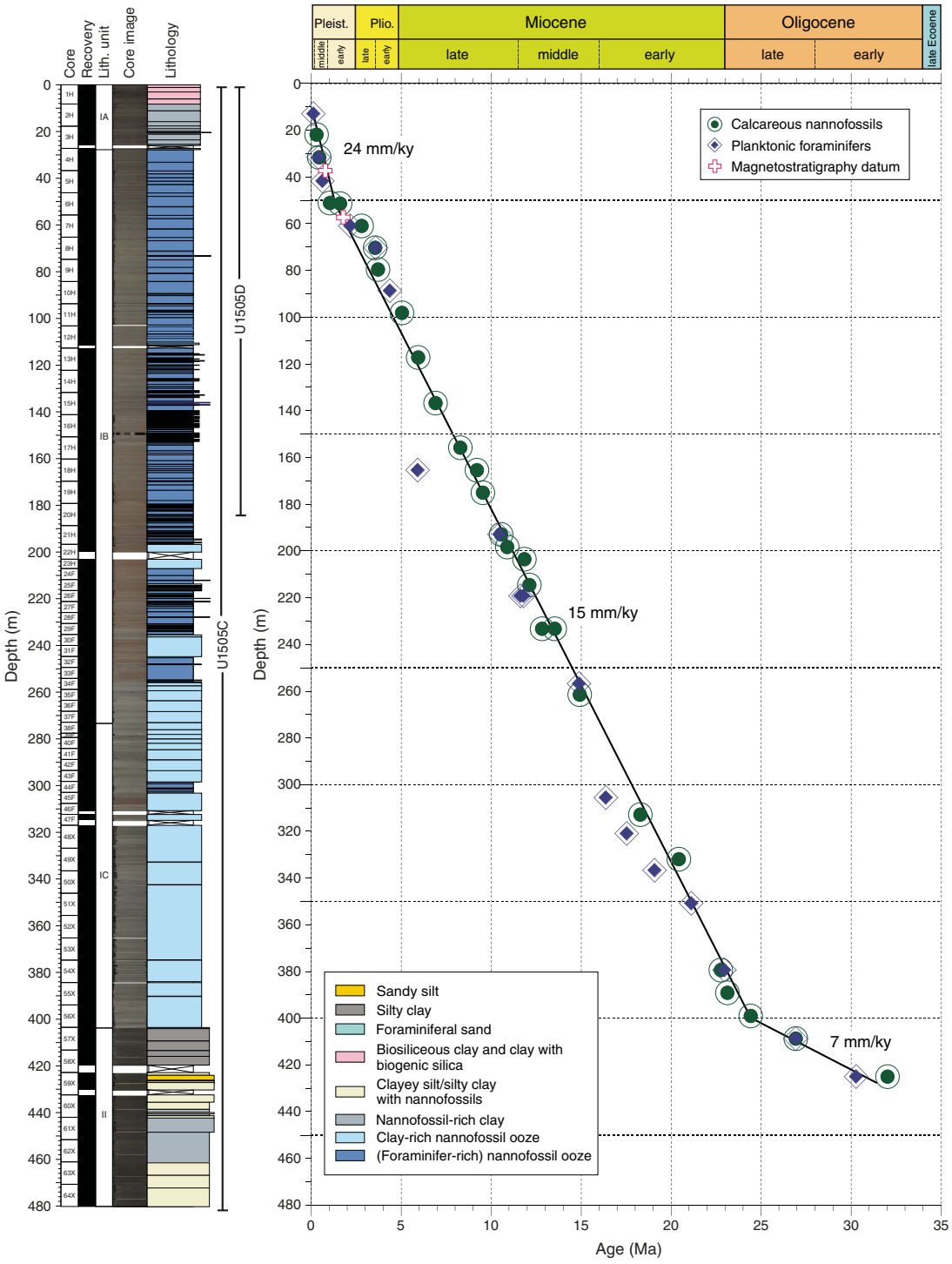

tion = ~81°) that was removed by demagnetization to 10–15 mT. This soft behavior shows that magnetic remanence is dominated by multidomain to pseudosingle-domain titanomagnetite or magnetite. The drilling overprint appears to impact discrete samples far less than core sections (Figure **F27**). The lower part of the hole (Cores 48X through 64X) is characterized by severe drilling disturbance, which causes a large scatter of NRM directions and inclinations.

Magnetostratigraphic data are based on polarities assigned to the archive-half sections and corroborated by directions obtained from oriented discrete samples. The lower boundary of the Brunhes (C1n) normal chron is at 37.4 m (0.781 Ma). The lower boundary (57.4 m) of the reverse polarity r1 is the base of Subchron C1r.3r with an age of 1.778 Ma.

Figure F27. Magnetic measurements, Hole U1505C. Inclination was used to determine polarity. AFD = AF demagnetization. Magnetostratigraphic features are referred to as n1, etc., in a sequential manner for convenience and have no bearing on chrons. Data from discrete samples are shown as yellow squares and green circles. GPTS2016 = geomagnetic polarity timescale of Ogg et al. (2016).

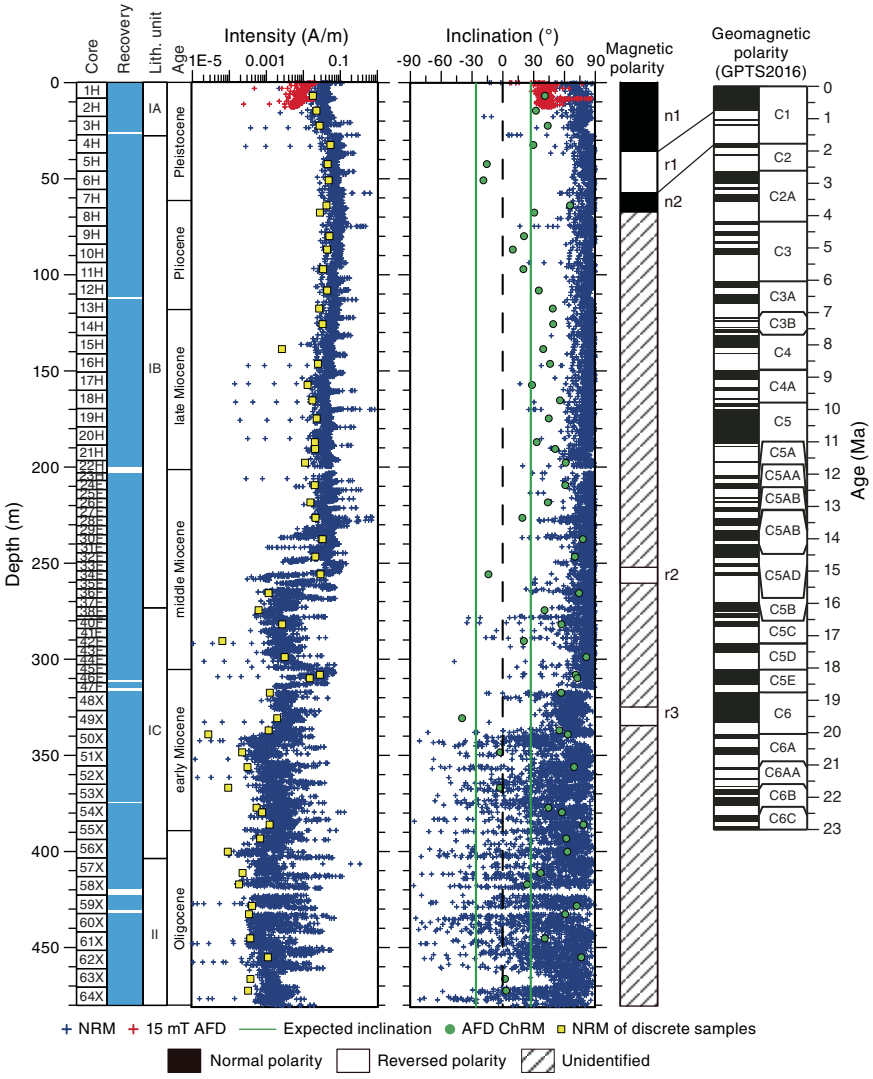

Geochemistry

Low but measurable hydrocarbon gases were detected only in Cores 368-U1505C-53X through 60X (371–438 m). The base of the hole has methane distributions similar to those at Site U1499, whereas the uppermost section is barren of methane, similar to Site U1501. Except for the shallowest 30 m of sediment, TOC, TN, and TS contents are mostly low in lithostratigraphic Unit I, but TS and TOC are slightly higher in Unit II; however, in all cases they are typically <1 wt% (Figure **F28**). Interstitial water chemistry has two important features. The upper part of the hole exhibits patterns similar to those at Site U1501; inhibited sulfate reduction and low chlorine, bromine, and salinity suggest the presence of freshwater at depth. Freshwater at >400 m coincides with the presence of low quantities of methane and the T60 regional seismic unconformity.

Physical properties and downhole measurements

Physical property data were acquired from cores from Holes U1505C (0–480.5 m) and U1505D (0–184 m), including density, magnetic susceptibility, *P*-wave velocity, NGR, color reflectance, and thermal conductivity. Physical property trends allow us to define two physical property units, PP Units 1 (0–403 m) and 2 (403–480 m). The boundary between Units 1 and 2 displays a distinct color change from greenish and light brownish gray to dark greenish gray. This boundary, which corresponds to the seismic stratigraphic T60 unconformity, is associated with a sharp change in physical properties. In Unit 1, sediments in the upper part are composed of foraminifer-rich nannofossil ooze with clay that gradually changes to clay-rich nannofossil ooze in the lower part. This change is well reflected in the NGR, which increases with depth. The higher NGR in Unit 2 is related to sediment that primarily consists of silty clay. Magnetic susceptibility overall gradually decreases with depth. The boundary between Units 1 and 2 shows that density and *P*-wave velocity drops sharply from ~2.2 to ~1.8 g/cm^3 and from ~2250 to 1750 m/s, respectively. Porosity abruptly increases from ~35% to ~50%. Thermal conductivity also shows a sharp change at the boundary. Reflectance parameter L* and RGB data are well correlated with carbonate content.

Figure F28. Data characterizing chemical anomalies associated with the T60 regional seismic marker, Site U1505.

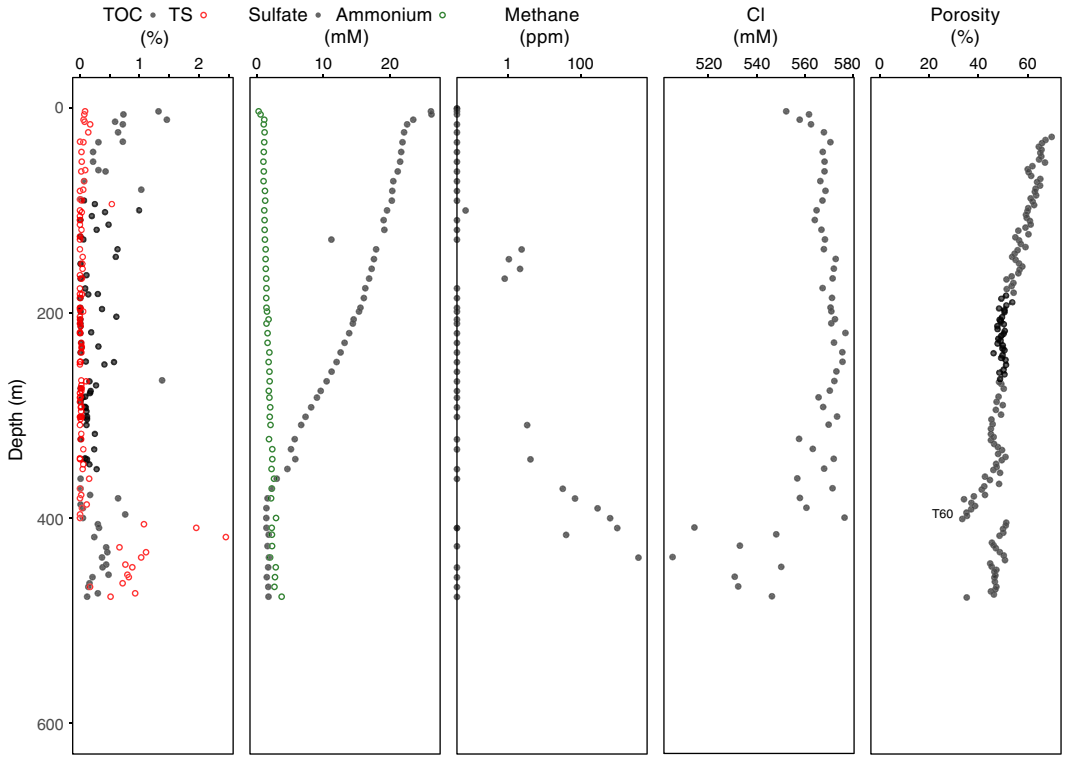

Wireline logging was conducted in Hole U1505C using the triple combo tool string, which included the HNGS, HLDS, DSI, and MSS. This logging string collected good data from 341.2 m (139.1 m above the bottom of Hole U1505C), which allows the definition of six logging units that mostly correlate with the lithostratigraphic units and core physical property data. Logging Unit 1 extends from the seafloor to the base of the drill pipe at 78 m. NGR is highly attenuated inside the drill pipe. Logging Unit 2 (base of the drill pipe to 96 m) exhibits NGR values that are ~50% lower than the underlying logging Unit 3. In Unit 3 (96–136 m), NGR increases with depth. Logging Unit 4 (136–220 m) exhibits relatively constant V_P and V_S. In logging Unit 5 (200–296 m), resistivity increases with depth, whereas most of the other physical properties are relatively constant. Logging Unit 6 (296–341.2 m) has higher magnetic susceptibility values than logging Unit 5.

Four downhole temperature measurements were conducted in Hole U1505C using the APCT-3. The temperature values range from 4.7°C at 36.7 m to 11.7°C at 122.8 m, giving a geothermal gradient of 84.6°C/km. A heat flow of 94.0 mW/m^2 was obtained from the linear fit between temperature and thermal resistance. The geothermal gradient and heat flow at Site U1505 are comparable to the relatively high values observed in a number of ODP and IODP sites in this part of the SCS.

Preliminary scientific assessment

In this section, we assess the achievements of Expedition 367/368 in the SCS toward meeting the four specific objectives as stated in the *Scientific Prospectus* (Sun et al., 2016b). Expedition 367 followed the original drilling plan and cored into acoustic basement at Ridges A and B and progressed without significant delays. However, based on Expedition 367 results, Expedition 368 followed a modified drilling plan that included a second drill site on Ridge A. Drilling plans for Expedition 368 were further modified due to serious drilling equipment failures at deep-water Site U1503 on Ridge C (see **Site U1503**). This failure limited the drilling capability of the *JOIDES Resolution* to a maximum 3400 m drill string deployment from 25 May 2017 to the end of the expedition on 11 June. Only a couple of alternate drill sites could be addressed with this limit on drill string length. Two of these, both on the OMH, were implemented (Sites U1504 and U1505). Furthermore, expedition time spent from 14 to 25 May installing casing to 990 m for primary Site U1503 was de facto time wasted for the expedition because the site could not be completed, but it left an important drill site ready for coring in the future. The overall effects of this operational constraint are that it directed efforts more toward Objective 4 (Site U1505) than originally planned and that the tectonic high-priority Site U1503 was lost for Expedition 367/368.

1. *To determine the nature of the basement in critical crustal units across the COT of the SCS rifted margin to discriminate between different competing models of breakup at magma-poor rifted margins. Specifically, to determine whether the subcontinental lithospheric mantle was exhumed during plate rupture.*

This objective was partly achieved with the potential for a higher degree of completion during postexpedition research. However, eventually Site U1503 needs to be completed, and further efforts need to be made to understand the deep nature of Ridge A.

Site U1499 at Ridge A provided important clues to the timing of tectonism but failed to provide direct evidence for its deeper crustal composition. Site U1502, originally an alternate site to Site U1499, was therefore pursued because the nature of Ridge A was considered a very high priority and the most likely place to recover either deep crust or exhumed mantle. To give this site priority was a signif-

icant decision and deviation from the drilling plan in the *Scientific Prospectus* and potentially affected our ability to address an important site on Ridge C (Site U1503).

Site U1499 on Ridge A successfully penetrated into the acoustic basement, which comprises synrift and/or postrift deposits of Oligocene or possibly older age. The clasts found in these partly coarse sediments do not contain lithologies that suggest a source of lowermost crust to exhumed mantle origin. Therefore, the nature of the deeper crust at Site U1499 remains unconstrained by direct sampling. Site U1502, also on Ridge A, recovered ~180 m of submarine basalts of possible late Eocene to Oligocene age overlain by late Eocene/Oligocene to Miocene deep-water sediments. Onboard preliminary ICP-AES element analyses indicate they are tholeiitic basalt and are comparable to samples from the ocean crust in the SCS collected during Expedition 349 and from Site U1500 at Ridge B. However, unlike the fresh basalts of Site U1500, the Site U1502 basalts show strong fracturing and alteration by high temperature hydrothermal activity, including mineralization (e.g., massive pyrite). This difference may suggest that the deeper crust comprises plutonic bodies but does not further constrain the nature of the deep crust.

Combining the findings at Site U1502 with the recovery at Site U1499 (Expedition 367; Ridge A) of potentially rift-related syntectonic or prerift sediments suggests that Ridge A is a complex structure comprising both rift-related sediments and syntectonic igneous material. The specific question of whether upper/lower crust or subcontinental lithospheric mantle is present at depth, however, remains unanswered by coring data. Detailed examination of the recovered basalts and of the gravel unit may help constrain the specific nature of the deeper crust. Future dedicated geophysical surveying and one or two more deep drill holes will be required to firmly advance our understanding of Ridge A.

The nature of the acoustic basement below Ridge B was successfully determined at Site U1500. This site recovered 150 m of fresh, submarine basalts of Oligocene age in a location where seismic imaging shows a layered structure below the acoustic basement, extending to ~2.5 km depth. The presence of a kilometer-thick carapace of basaltic lavas in the upper crust is therefore concluded. However, this carapace does not prove this ~6 km thick crust to be entirely igneous, and its lower part conceivably could contain stretched continental lithosphere.

The nature of the crust at the OMH was well addressed at Site U1501. This site drilled ~45 m into the prerift? acoustic basement beneath the Cenozoic sedimentary section and recovered lithified, coarse-grained sedimentary rocks of presumed Mesozoic age. This finding verified our predrilling interpretation of the OMH as comprising upper continental crustal material. The basement of the easternmost extension of the OMH was also sampled at Site U1504. In this location, greenschist facies metamorphic rock was found, suggesting that only a moderate amount (~5 km) of upper crust was removed prior to deposition of the thin, mainly postbreakup sediments that overlie the basement. The timing of the removal of the uppermost crust is constrained to be at least before the late Eocene. Postexpedition work on age determination and thermobarometry may constrain an exhumation history and its possible relation to the Cenozoic rifting of the SCS.

Our inability to pursue deep drilling at Site U1503 obviously prevents us from characterizing the nature of the crust at Ridge C based on in situ drilling data. Combining seismic interpretation and the observations from Ridge B (Site U1500), however, constrains this to be primarily if not entirely of igneous origin.

2. *To determine the time lag between plate rupture and asthenospheric upwelling that allowed decompression melting to generate igneous oceanic crust.*

This objective was achieved. The simple answer to Objective 2 is that there was no substantial time lag between (final) plate rupture and asthenospheric upwelling supporting the generation of igneous material with a basaltic, MORB-type composition. Submarine MORB-type basalts of early Oligocene age were recovered at Site U1500 on Ridge B, and based on geophysical evidence, Ridge C can be interpreted to be at least partly igneous. Seafloor magnetic anomalies C10r to C11n (29–30 Ma; approximately mid-Oligocene) encompass these two ridges and provide independent evidence of the age of the basalts from Site U1500 (Oligocene). Submarine basalts of similar or possibly slightly older age (early Oligocene to late Eocene) were found on Ridge A (Site U1502). These observations rule out any significant time-lag between final plate rupture and the onset of magmatism. Postexpedition work on mantle melting history may detail the thickness of residual subcontinental lithosphere of lithospheric thinning during breakup. Excellent material for this type of work, and for age determination, is available from Site U1500, but modeling efforts will lack the constraints from Ridge C (Site U1503) representing a more advanced stage of spreading. Because of the highly altered nature of Site U1502 basalts, geochemical studies will unfortunately be challenging but very important because these rocks likely represent a stage in margin development where continental lithosphere had a stronger impact on magmatism (contamination and by lithospheric thickness). Expedition 367/368 findings also rule out that the margin in this location was overprinted by late-stage magmatism as recently proposed.

Although the failure to pursue Site U1503 did not seriously affect our ability to constrain a possible time lag between plate rupture and onset of magmatism, it left us without a well-defined reference frame for assessing mantle composition and mantle melting conditions during steady-state accretion of igneous crust. Reoccupation of Site U1503 is therefore highly recommended to provide a benchmark against which the earlier breakup magmatism can be compared. Similarly, more and fresh basaltic material from Ridge A would greatly benefit the study of the SCS margin in terms of age determination of the earliest basaltic magmatism and its detailed geochemical elemental and isotopic composition evolution over time.

3. *To constrain the rate of extension and vertical crustal movements.*

This objective was partly achieved, but postexpedition work is needed to further develop our findings. Important stratigraphic control on the synrift sediments related to breakup was achieved at Sites U1499, U1501, U1502, and U1505. The findings of highly syntectonic deposits of Oligocene (and possibly older) age overlain by a very low sedimentation rate sequence of late Oligocene to early Miocene age at Ridge A (Site U1499) is strong evidence for an early Oligocene plate rupture that was completed by the latest Oligocene. This was further confirmed at Site U1501, located on the OMH. This site recovered the entire sequence of synrift sediments down to (presumed) Mesozoic basement. The sequence shows development from deltaic to shallow marine with terrigenous sedimentation (Eocene) through deepening water, yet still predominantly clastic detrital sediments (approximately early Oligocene), to deep-water marine calcareous sediments (approximately late Oligocene to Miocene). Biostratigraphic constraints on the Eocene deposits are lack-

ing below the uppermost late Eocene sediments. A very similar evolution was documented at Site U1505 for the early Oligocene to Miocene interval. Site U1504, also at the OMH and slightly shallower than at Sites U1501 and U1505, penetrated a 120 m thick postrift sedimentary sequence above crystalline basement. Deep-water conditions were established by lowermost early Miocene time. The presence of a carbonate reef debris deposit (very shallow marine water) with an approximate age of late Eocene suggests that the ~3 km subsidence experienced by these sediments was initiated post-late Eocene. Site U1502, also located on Ridge A, shows (minor) deep-water deposits of early Oligocene to perhaps late Eocene age followed exclusively by deep-water deposits of Oligocene to Miocene age. Deep-water conditions therefore developed earlier (pre-Oligocene) on Ridge A than on the OMH (approximately late Oligocene).

The inability to pursue coring at Site U1503 unfortunately prevented Expedition 368 from extending subsidence studies seaward of Ridge B (Site U1500), where the late Oligocene sediment package overlying the basalts is much better developed than at Site U1500 on Ridge B. However, the most serious lack of data needed for constraining rate of extension is the lack of biostratigraphic control in the deeper part of the Eocene section at Site U1501 and the older part of synrift or prerift deposits at Site U1499. Shallow water sediments of Eocene age similar to those at Site U1501 were found at Site U1435 (IODP Expedition 349), and, although the sediment is similarly barren of microfossils, detrital zircon is present. If also present in the Site U1501 samples, age determination on a population of these might provide maximum ages. The amount of crustal extension will be determined through a detailed tectonic interpretation of the regional seismic data (courtesy of the CNOOC) that the entire Expedition 367/368 program is based on.

4. *To improve the understanding of the Cenozoic regional tectonic and environmental development of the Southeast Asia margin and SCS by combining Expedition 367/368 results with existing ODP/IODP sediment records and regional seismic data.*

This objective was achieved, but intensive multidisciplinary postexpedition work is needed to maximize our findings. An important achievement in this regard was the recovery of a nearly continuous sequence of the prerift, synrift, and postrift sediments since the Eocene and older sediments at Site U1501. This sequence provides the sedimentary records of the SCS evolving from land to deep sea for the first time and will greatly help us to understand the sedimentary processes associated with tectonic events and paleoenvironmental development at the SCS northern margin. Together with the deep-water sediment packages from Sites U1499, U1500, U1502, and U1505, Expedition 367/368 findings provide the possible tectonic links between the SCS and the western Pacific in the aspects of the SCS formation history.

Based on the coring/drilling results of Expedition 367/368, new time-depth constraints on some of the major seismic stratigraphic unconformities are available. These unconformities were mapped regionally throughout the basin by integrating microfossil ages, petrophysics, and borehole logging data with the existing seismic reflection data. Among these seismic unconformities, the T60 unconformity is the most prominent. It is easily recognized basin-wide and is present at Sites U1500, U1501, U1502, U1503 (not sampled), and U1505. Though not resolved by seismic data, its stratigraphic position is also present at Site U1499 in an extremely condensed section. Exploring its nature (e.g., timing and duration, processes, and mechanisms) is very important for understanding the regional geological evolution, but this objective will need further postexpedition work.

The postrift sediments cored during Expedition 367/368 will contribute to our understanding of the late Cenozoic tectonic and environmental history of the SCS. An early to middle Miocene succession of red claystone was found at Sites U1499, U1500, and U1502, all located deeper than 3500 mbsl. The red claystone deposits near the acoustic basement (e.g., basalt or altered basalt or gravel) extending over all of these sites indicates that the SCS basin was deep and the sedimentation rate was extremely low at that time. These conditions may correlate with a basin-wide event related to deep circulation of oxygenated water from the western Pacific prior to the closure of the Luzon Strait.

A late Miocene succession of hemipelagic and turbidite deposits was observed at deeper Sites U1499, U1500, and U1502 and likely recorded the processes that delivered sediment from the shallow shelf or slope of the northern SCS to the deeper parts of the basin. A high sedimentation rate at the deep-water sites during the late Miocene and a nearly 10 Ma hiatus from the middle Miocene to Pleistocene observed at Site U1504 on the OMH indicate strong erosion from source areas in the upper slope and shelf region and efficient transport into the deep basin during late Miocene time.

In addition to the Oligocene to Plio–Pleistocene APC/XCB record (~100 percent) at Site U1505, the Plio–Pleistocene sequence was recovered by double APC, high-recovery holes at Site U1505 to establish a complete record for high-resolution paleoceanographic and paleoclimatic studies. The hemipelagic deposits, rich in calcareous microfossils, at this site above the modern CCD of the SCS should enable us to reconstruct the east Asian monsoonal climate and paleoceanographic changes in the SCS at orbital and millennial timescales.

Postexpedition research using samples from Expedition 367/368 together with seismic stratigraphic correlations will continue to improve the contributions to Objective 4. This research should be channeled into four general avenues:

1. To reconstruct the early stage history of the SCS, including paleoenvironmental changes from land to deep sea and new data (e.g., detrital zircon geochronology) to constrain the sedimentary provenance,
2. To explore the paleoceanographic conditions favorable for early to middle Miocene pelagic red clay and late Miocene turbidite deposition through geochemical and geophysical techniques,
3. To correlate the chronostratigraphic records between all ODP (Leg 184) and IODP drill sites from Expedition 349 and Expedition 367/368 sites in the SCS, and
4. To conduct high-resolution paleoceanographic study of Pliocene- and Pleistocene-related monsoonal climate changes and deep-water exchange between the SCS and the Pacific.

Integration of drilling results with seismic data

The large regional set of high-quality seismic data provided by the CNOOC formed an essential basis for the planning, scheduling, and implementation of Expedition 367/368. The continued availability of these data to the scientific party will be pivotal for postexpedition research on most of the scientific objectives discussed above.

References

Barckhausen, U., and Roeser, H.A., 2004. Seafloor spreading anomalies in the South China Sea revisited. *In* Clift, P., Wang, P., Kuhnt, W., and Hayes, D. (Eds.), *Continent-Ocean Interactions within East Asian Marginal Seas.* Geophysical Monograph, 149:121–125. **http://dx.doi.org/10.1029/149GM07**

Beslier, M.-O., Whitmarsh, R.B., Wallace, P.J., and Girardeau, J. (Eds.), 2001. *Proceedings of the Ocean Drilling Program, Scientific Results,* 173: College Station, TX (Ocean Drilling Program). **https://doi.org/10.2973/odp.proc.sr.173.2001**

Boillot, G., Winterer, E.L., et al., 1988. *Proceedings of the Ocean Drilling Program, Scientific Results,* 103: College Station, TX (Ocean Drilling Program). **https://doi.org/10.2973/odp.proc.sr.103.1988**

Briais, A., Patriat, P., and Tapponnier, P., 1993. Updated interpretation of magnetic anomalies and seafloor spreading stages in the South China Sea: implications for the Tertiary tectonics of Southeast Asia. *Journal of Geophysical Research: Solid Earth,* 98(B4):6299–6328. **https://doi.org/10.1029/92JB02280**

Brune, S., Heine, C., Clift, P.D., and Pérez-Gussinyé, M., 2017. Rifted margin architecture and crustal rheology: reviewing Iberia-Newfoundland, central South Atlantic, and South China Sea. *Marine and Petroleum Geology,* 79:257–281. **https://doi.org/10.1016/j.marpetgeo.2016.10.018**

Dick, H.J.B., Lin, J., and Schouten, H., 2003. An ultraslow-spreading class of ocean ridge. *Nature,* 426(6965):405–412. **https://doi.org/10.1038/nature02128**

Doré, T., and Lundin, E., 2015. Research focus: hyperextended continental margins—knowns and unknowns. *Geology,* 43(1):95–96. **https://doi.org/10.1130/focus012015.1**

Duncan, R.A., Larsen, H.C., Allan, J.F., et al., 1996. *Proceedings of the Ocean Drilling Program, Initial Reports,* 163: College Station, TX (Ocean Drilling Program). **https://doi.org/10.2973/odp.proc.sr.163.1999**

Eldholm, O., Gladczenko, T.P., Skogseid, J., and Planke, S., 2000. Atlantic volcanic margins: a comparative study. *In* Nottvedt, A. (Ed.), *Dynamics of the Norwegian Margin.* Geological Society Special Publication, *167(1):411–428.* **https://doi.org/10.1144/GSL.SP.2000.167.01.16**

Franke, D., Savva, D., Pubellier, M., Steuer, S., Mouly, B., Auxietre J.-L., Meresse, F., and Chamot-Rooke, N., 2013. The final rifting evolution in the South China Sea. *Marine and Petroleum Geology,* 58(Part B):704–720. **https://doi.org/10.1016/j.marpetgeo.2013.11.020**

Geoffroy, L., 2005. Volcanic passive margins. *Comptes Rendus Geoscience,* 337(16):1395–1408. **https://doi.org/10.1016/j.crte.2005.10.006**

Huismans, R., and Beaumont, C., 2011. Depth-dependent extension, two-stage breakup and cratonic underplating at rifted margins. *Nature,* 473(7345):74–78. **https://doi.org/10.1038/nature09988**

Huismans, R.S., and Beaumont, C., 2008. Complex rifted continental margins explained by dynamical models of depth-dependent lithospheric extension. *Geology,* 36(2):163–166. **https://doi.org/10.1130/G24231A.1**

Lester, R., McIntosh, K., Van Avendonk, H.J.A., Lavier, L., Liu, C.-S., and Wang, T.K., 2013. Crustal accretion in the Manila trench accretionary wedge at the transition from subduction to mountain-building in Taiwan. *Earth and Planetary Science Letters,* 375:430–440. **https://doi.org/10.1016/j.epsl.2013.06.007**

Li, C.-F., Lin, J., and Kulhanek, D.K., 2013. *Expedition 349 Scientific Prospectus: South China Sea Tectonics.* International Ocean Discovery Program. **https://doi.org/10.2204/iodp.sp.349.2013**

Li, C.-F., Lin, J., Kulhanek, D.K., Williams, T., Bao, R., Briais, A., Brown, E.A., Chen, Y., Clift, P.D., Colwell, F.S., Dadd, K.A., Ding, W., Hernández-Almeida, I., Huang, X.-L., Hyun, S., Jiang, T., Koppers, A.A.P., Li, Q., Liu, C., Liu, Q., Liu, Z., Nagai, R.H., Peleo-Alampay, A., Su, X., Sun, Z., Tejada, M.L.G., Trinh, H.S., Yeh, Y.-C., Zhang, C., Zhang, F., Zhang, G.-L., and Zhao, X., 2015a. Expedition 349 summary. *In* Li, C.-F., Lin, J., Kulhanek, D.K., and the Expedition 349 Scientists, *South China Sea Tectonics.* Proceedings of the International Ocean Discovery Program, 349: College Station, TX (International Ocean Discovery Program). **https://doi.org/10.14379/iodp.proc.349.101.2015**

Li, C.-F., Lin, J., Kulhanek, D.K., Williams, T., Bao, R., Briais, A., Brown, E.A., Chen, Y., Clift, P.D., Colwell, F.S., Dadd, K.A., Ding, W., Hernández-Almeida, I., Huang, X.-L., Hyun, S., Jiang, T., Koppers, A.A.P., Li, Q., Liu, C., Liu, Q., Liu, Z., Nagai, R.H., Peleo-Alampay, A., Su, X., Sun, Z., Tejada, M.L.G., Trinh, H.S., Yeh, Y.-C., Zhang, C., Zhang, F., Zhang, G.-L., and Zhao, X., 2015b. Site U1435. *In* Li, C.-F., Lin, J., Kulhanek, D.K., and the Expedition 349 Scientists, *South China Sea Tectonics.* Proceedings of the International Ocean Discovery Program, 349: College Station, TX (International Ocean Discovery Program). **https://doi.org/10.14379/iodp.proc.349.107.2015**

Li, C.-F., Wang, P., Franke, D., Lin, J., and Tian, J., 2012a. Unlocking the opening processes of the South China Sea. *Scientific Drilling,* 14:55–59. **https://doi.org/10.2204/iodp.sd.14.07.2012**

Li, C.-F., Xu, X., Lin J., Sun, Z., Zhu, J., Yao, Y., Zhao, X., Liu, Q., Kulhanek, D.K., Wang, J., Song, T., Zhao, J., Qiu, N., Guan, Y., Zhou, Z, Williams, T., Bao, R., Briais, A., Brown, E.A., Chen, Y., Clift, P.D., Colwell, F.S., Dadd, K.A., Ding, W., Hernández Almeida, I., Huang, X.-L., Hyun, S., Jiang, T., Koppers, A.A.P., Li, Q., Liu, C., Liu, Z., Nagai, R.H., Peleo-Alampay, A., Su, X., Tejada, M.L.G., Trinh, H.S., Yeh, Y.-C., Zhang, C., Zhang, F., and Zhang, G.-L., 2014. Ages and magnetic structures of the South China Sea constrained by deep tow magnetic surveys and IODP Expedition 349. *Geochemistry, Geophysics, Geosystems,* 15(12):4958–4983. **https://doi.org/10.1002/2014GC005567**

Li, J., Ding, W., Wu, Z., Zhang, J., and Dong, C., 2012b. The propagation of seafloor spreading in the southwestern subbasin, South China Sea. *Chinese Science Bulletin,* 57(24):3182–3191. **https://doi.org/10.1007/s11434-012-5329-2**

McIntosh, K., Lavier, L., van Avendonk, H., Lester, R., Eakin, D., and Liu, C.-S., 2014. Crustal structure and inferred rifting processes in the northeast South China Sea. *Marine and Petroleum Geology,* 58(Part B):612–626. **https://doi.org/10.1016/j.marpetgeo.2014.03.012**

McIntosh, K., van Avendonk, H., Lavier, L., Lester, W.R., Eakin, D., Wu, F., Liu, C.-S., and Lee, C.-S., 2013. Inversion of a hyper-extended rifted margin in the southern Central Range of Taiwan. *Geology,* 41(8):871–874. **https://doi.org/10.1130/G34402.1**

Ogg, J.G., Ogg, G., and Gradstein, F.M., 2016. *A Concise Geologic Time Scale 2016:* Boston (Elsevier).

Pérez-Gussinyé, M., Phipps Morgan, J., Reston, T.J., and Ranero, C.R., 2006. The rift to drift transition at non-volcanic margins: insights from numerical modelling. *Earth and Planetary Science Letters,* 244(1–2):458–473. **https://doi.org/10.1016/j.epsl.2006.01.059**

Pérez-Gussinyé, M., and Reston, T.J., 2001. Rheological evolution during extension at nonvolcanic rifted margins: onset of serpentinization and development of detachments leading to continental breakup. *Journal of Geophysical Research: Solid Earth,* 106(B3):3961–3975. **https://doi.org/10.1029/2000JB900325**

Reston, T.J., 2009. The structure, evolution and symmetry of the magma-poor rifted margins of the North and Central Atlantic: a synthesis. *Tectonophysics,* 468(1–4):6–27. **https://doi.org/10.1016/j.tecto.2008.09.002**

Seton, M., Whittaker, J.M., Wessel, P., Müller, R.D., DeMets, C., Merkouriev, S., Cande, S., Gaina, C., Eagles, G., Granot, R., Stock, J., Wright, N., and Williams, S.E., 2014. Community infrastructure and repository for marine magnetic identifications. *Geochemistry, Geophysics, Geosystems,* 15(4):1629–1641. **https://doi.org/10.1002/2013GC005176**

Shi, H., and Li, C.-F., 2012. Mesozoic and early Cenozoic tectonic convergence-to-rifting transition prior to opening of the South China Sea. *International Geology Review,* 54(15):1801–1828. **https://doi.org/10.1080/00206814.2012.677136**

Shipboard Scientific Party, 2000. Leg 184 summary: exploring the Asian monsoon through drilling in the South China Sea. *In* Wang, P., Prell, W.L., Blum, P., et al., *Proceedings of the Ocean Drilling Program, Initial Reports,* 184: College Station, TX (Ocean Drilling Program), 1–77. **https://doi.org/10.2973/odp.proc.ir.184.101.2000**

Sun, Z., Liu, S., Pang, X., Jiang, J., and Mao, S., 2016a. Recent research progress on the rifting-breakup process in passive continental margins. *Journal of Tropical Oceanography,* 35(1):1–16. (in Chinese with English abstract) **https://doi.org/10.11978/2015030**

Sun, Z., Stock, J., Jian, Z., McIntosh, K., Alvarez Zarikian, C.A., and Klaus, A., 2016b. *Expedition 367/368 Scientific Prospectus: South China Sea Rifted Margin.* International Ocean Discovery Program. **https://doi.org/10.14379/iodp.sp.367368.2016**

Sun, Z., Xu, Z., Sun, L., Pang, X., Yan, C., Li, Y., Zhao, Z., Wang, Z., and Zhang, C., 2014. The mechanism of post-rift fault activities in Baiyun sag, Pearl River Mouth Basin. *Journal of Asian Earth Sciences,* 89:76–87. **https://doi.org/10.1016/j.jseaes.2014.02.018**

Sutra, E., and Manatschal, G., 2012. How does the continental crust thin in a hyperextended rifted margin? Insights from the Iberia margin. *Geology,* 40(2):139–142. **https://doi.org/10.1130/G32786.1**

Wang, T.K., Chen, M.-K., Lee, C.-S., and Xia, K., 2006. Seismic imaging of the transitional crust across the northeastern margin of the South China Sea. *Tectonophysics,* 412(3–4):237–245. **https://doi.org/10.1016/j.tecto.2005.10.039**

Wei, X.-D., Ruan, A.-G., Zhao, M.-H., Qiu, X.-L., Li, J.-B., Zhu, J.-J., Wu, Z.-L., and Ding, W.-W., 2011. A wide-angle OBS profile across the Dongsha uplift and Chaoshan depression in the mid-northern South China Sea. *Chinese Journal of Geophysics,* 54(6):1149–1160. **https://doi.org/10.1002/cjg2.1691**

Whitmarsh, R.B., Manatschal, G., and Minshull, T.A., 2001. Evolution of magma-poor continental margins from rifting to seafloor spreading. *Nature,* 413(6852):150–154. **https://doi.org/10.1038/35093085**

Whitmarsh, R.B., Sawyer, D.S., Klaus, A., and Masson, D.G. (Eds.), 1996. *Proceedings of the Ocean Drilling Program, Scientific Results,* 149: College Station, TX (Ocean Drilling Program). **https://doi.org/10.2973/odp.proc.sr.149.1996**

Yan, P., Zhou, D., and Liu, Z., 2001. A crustal structure profile across the northern continental margin of the South China Sea. *Tectonophysics,* 338(1):1–21. **https://doi.org/10.1016/S0040-1951(01)00062-2**

Zhou, D., Sun, Z., Chen, H., Xu, H., Wang, W., Pang, X., Cai, D., and Hu, D., 2008. Mesozoic paleogeography and tectonic evolution of South China Sea and adjacent areas in the context of Tethyan and Paleo-Pacific interconnections. *Island Arc,* 17(2):186–207. **https://doi.org/10.1111/j.1440-1738.2008.00611.x**

Zhou, X.M., and Li, W.X., 2000. Origin of late Mesozoic igneous rocks in southeastern China: implications for lithosphere subduction and underplating of mafic magmas. *Tectonophysics,* 326(3–4):269–287. **https://doi.org/10.1016/S0040-1951(00)00120-7**

Sun, Z., Jian, Z., Stock, J.M., Larsen, H.C., Klaus, A., Alvarez Zarikian, C.A., and the Expedition 367/368 Scientists
Proceedings of the International Ocean Discovery Program Volume 367/368
publications.iodp.org

https://doi.org/10.14379/iodp.proc.367368.102.2018

Expedition 367/368 methods[1]

Zhen Sun, Zhimin Jian, Joann M. Stock, Hans Christian Larsen, Adam Klaus, Carlos A. Alvarez Zarikian, Jacopo Boaga, Stephen A. Bowden, Anne Briais, Yifeng Chen, Deniz Cukur, Kelsie A. Dadd, Weiwei Ding, Michael J. Dorais, Eric C. Ferré, Fabricio Ferreira, Akira Furusawa, Aaron J. Gewecke, Jessica L. Hinojosa, Tobias W. Höfig, Kan-Hsi Hsiung, Baoqi Huang, Enqing Huang, Xiao-Long Huang, Shijun Jiang, Haiyan Jin, Benjamin G. Johnson, Robert M. Kurzawski, Chao Lei, Baohua Li, Li Li, Yanping Li, Jian Lin, Chang Liu, Chuanlian Liu, Zhifei Liu, Antonio Luna, Claudia Lupi, Anders J. McCarthy, Geoffroy Mohn, Lachit Singh Ningthoujam, Michael Nirrengarten, Nobuaki Osono, David W. Peate, Patricia Persaud, Ning Qiu, Caroline M. Robinson, Sara Satolli, Isabel Sauermilch, Julie C. Schindlbeck, Steven M. Skinner, Susanne M. Straub, Xiang Su, Liyan Tian, Froukje M. van der Zwan, Shiming Wan, Huaichun Wu, Rong Xiang, Rajeev Yadav, Lang Yi, Cuimei Zhang, Jinchang Zhang, Yang Zhang, Ning Zhao, Guangfa Zhong, and Lifeng Zhong[2]

Keywords: International Ocean Discovery Program, IODP, *JOIDES Resolution*, Expedition 367, Expedition 368, Site U1499, Site U1500, Site U1501, Site U1502, Site U1503, Site U1504, Site U1505, northern South China Sea, rifted margin, continent–ocean transition zone, hyperextension, continental breakup, lithosphere thinning, outer margin high, embryonic ocean

Contents

1 Introduction
5 Lithostratigraphy
11 Igneous and metamorphic petrology
22 Structural geology
26 Biostratigraphy
39 Paleomagnetism
48 Geochemistry
52 Physical properties
57 Downhole measurements
62 Correlation to seismic data
63 References

Introduction

This introduction provides an overview of operations, depth conventions, core handling, curatorial procedures, and analyses performed on the R/V *JOIDES Resolution* during International Ocean Discovery Program (IODP) Expeditions 367 and 368. These two expeditions were implemented as a single science program; the methods used were intended to be the same for both expeditions. Any differences are clearly noted in this chapter. The information applies only to shipboard work described in the Expedition reports section of the Expedition 367/368 *Proceedings of the International Ocean Discovery Program* volume. Methods used by investigators for shore-based analyses of Expedition 367 and 368 data will be described in separate individual publications.

Site locations

GPS coordinates (WGS84 datum) from precruise site surveys were used to position the vessel at the Expedition 367 and 368 sites. A SyQwest Bathy 2010 CHIRP subbottom profiler was used to monitor seafloor depth on the approach to each site to confirm the depth profiles from precruise surveys. Once the vessel was positioned at a site, the thrusters were lowered and a positioning beacon was dropped to the seafloor. Dynamic positioning control of the vessel uses navigational input from the GPS system and triangulation to the seafloor beacon (Figure **F1**) weighted by the estimated positional accuracy. The final hole position was the mean position calculated from the GPS data collected over a significant portion of the time during which the hole was occupied.

[1] Sun, Z., Jian, Z., Stock, J.M., Larsen, H.C., Klaus, A., Alvarez Zarikian, C.A., Boaga, J., Bowden, S.A., Briais, A., Chen, Y., Cukur, D., Dadd, K.A., Ding, W., Dorais, M.J., Ferré, E.C., Ferreira, F., Furusawa, A., Gewecke, A.J., Hinojosa, J.L., Höfig, T.W., Hsiung, K.-H., Huang, B., Huang, E., Huang, X.-L., Jiang, S., Jin, H., Johnson, B.G., Kurzawski, R.M., Lei, C., Li, B., Li, L., Li, Y., Lin, J., Liu, C., Liu, C., Liu, Z., Luna, A., Lupi, C., McCarthy, A.J., Mohn, G., Ningthoujam, L.S., Nirrengarten, M., Osono, N., Peate, D.W., Persaud, P., Qui, N., Robinson, C.M., Satolli, S., Sauermilch, I., Schindlbeck, J.C., Skinner, S.M., Straub, S.M., Su, X., Tian, L., van der Zwan, F.M., Wan, S., Wu, H., Xiang, R., Yadav, R., Yi, L., Zhang, C., Zhang, J., Zhang, Y., Zhao, N., Zhong, G., and Zhong, L., 2018. Expedition 367/368 methods. *In* Sun, Z., Jian, Z., Stock, J.M., Larsen, H.C., Klaus, A., Alvarez Zarikian, C.A., and the Expedition 367/368 Scientists, 2018. *South China Sea Rifted Margin*. Proceedings of the International Ocean Discovery Program, 367/368: College Station, TX (International Ocean Discovery Program). https://doi.org/10.14379/iodp.proc.367368.102.2018
[2] **Expedition 367/368 Scientists' addresses.**
MS 367368-102: Published 28 September 2018
This work is distributed under the **Creative Commons Attribution 4.0 International** (CC BY 4.0) license.

Figure F1. IODP conventions for naming sites, holes, cores, sections, and samples, Expeditions 367 and 368.

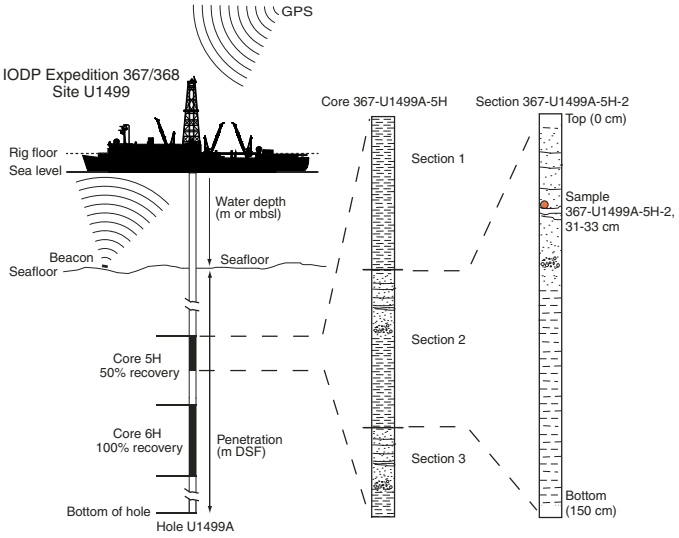

Drilling operations

The advanced piston corer (APC), half-length APC (HLAPC), extended core barrel (XCB), and rotary core barrel (RCB) systems were available during Expeditions 367 and 368. Because sampling and logging the lowermost sediments and basement were our highest priority objectives, we used the HLAPC during Expedition 368 but not during Expedition 367.

The APC and HLAPC systems cut soft-sediment cores with minimal coring disturbance relative to other IODP coring systems. After the APC/HLAPC core barrel is lowered through the drill pipe and lands above the bit, the drill pipe is pressured up until the two shear pins that hold the inner barrel attached to the outer barrel fail. The inner barrel then advances into the formation and cuts the core (Figure **F2A**). The driller can detect a successful cut, or "full stroke," by observing the pressure gauge on the rig floor because the excess pressure accumulated prior to the stroke drops rapidly. Cores collected with the APC system are denoted by the letter "H," and those collected with the HLAPC system are denoted by the letter "F."

APC refusal is conventionally defined in one of two ways: (1) the piston fails to achieve a complete stroke (as determined from the pump pressure and recovery reading) because the formation is too hard or (2) excessive force (>60,000 lb) is required to pull the core barrel out of the formation. When a full stroke could not be achieved, one or more additional attempts were typically made, and with each attempt the bit was advanced by the length of the core barrel. Note that these attempts resulted in a nominal recovery of ~100% based on the assumption that the barrel penetrated the formation by the length of core recovered. If an APC core does not achieve a full stroke, the next core can be taken after advancing to a depth determined by the recovery of the previous core (advance by recovery) or to a depth of a full APC core (typically 9.7 m). When a full or partial stroke was achieved but excessive force could not retrieve the barrel, the core barrel could be "drilled over," meaning that after the inner core barrel was successfully shot into the formation, the drill bit was advanced to total depth to free the APC barrel.

The standard APC system uses a 9.5 m long core barrel, whereas the HLAPC system uses a 4.7 m long core barrel. In most instances, the HLAPC system was deployed after the standard APC consistently had <50% recovery. During use of the HLAPC system, the same criteria were applied in terms of refusal as for the APC system. Use of the HLAPC system allowed for significantly greater APC sampling depths to be attained than would have otherwise been possible.

Figure F2. Coring systems used during Expeditions 367 and 368. A. APC system. ID = inside diameter. (Continued on next page.)

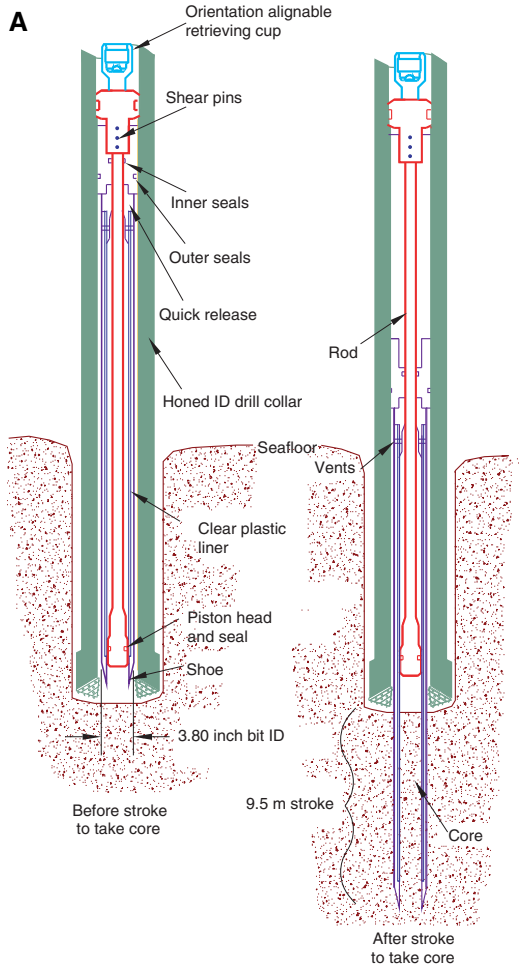

The XCB system is typically used when the APC/HLAPC system has insufficient recovery. Cores collected with the XCB system are denoted by the letter "X." In our case, however, the XCB system was not able to recover the unconsolidated sands encountered at depths where the APC/HLAPC system could not be used. The XCB system was used to advance the hole when HLAPC refusal occurred before the target depth was reached or when drilling conditions required it. The XCB system has a small cutting shoe that extends below the large rotary APC/XCB bit (Figure **F2B**). The smaller bit can cut a semi-indurated core with less torque and fluid circulation than the main bit, potentially improving recovery. The XCB cutting shoe typically extends ~30.5 cm ahead of the main bit in soft sediments but is allowed to retract into the main bit when hard formations are encountered. Shorter XCB cutting shoes can also be used. The XCB system could not recover the poorly consolidated and loose sand lithologies penetrated during Expedition 367.

The bottom-hole assembly (BHA) used for APC and XCB coring is typically composed of an 11⅞ inch (~29.05 cm) drill bit, a bit sub, a seal bore drill collar, a landing saver sub, a modified top sub, a

Figure F2 (continued). B. XCB system. C. RCB system. OD = outside diameter.

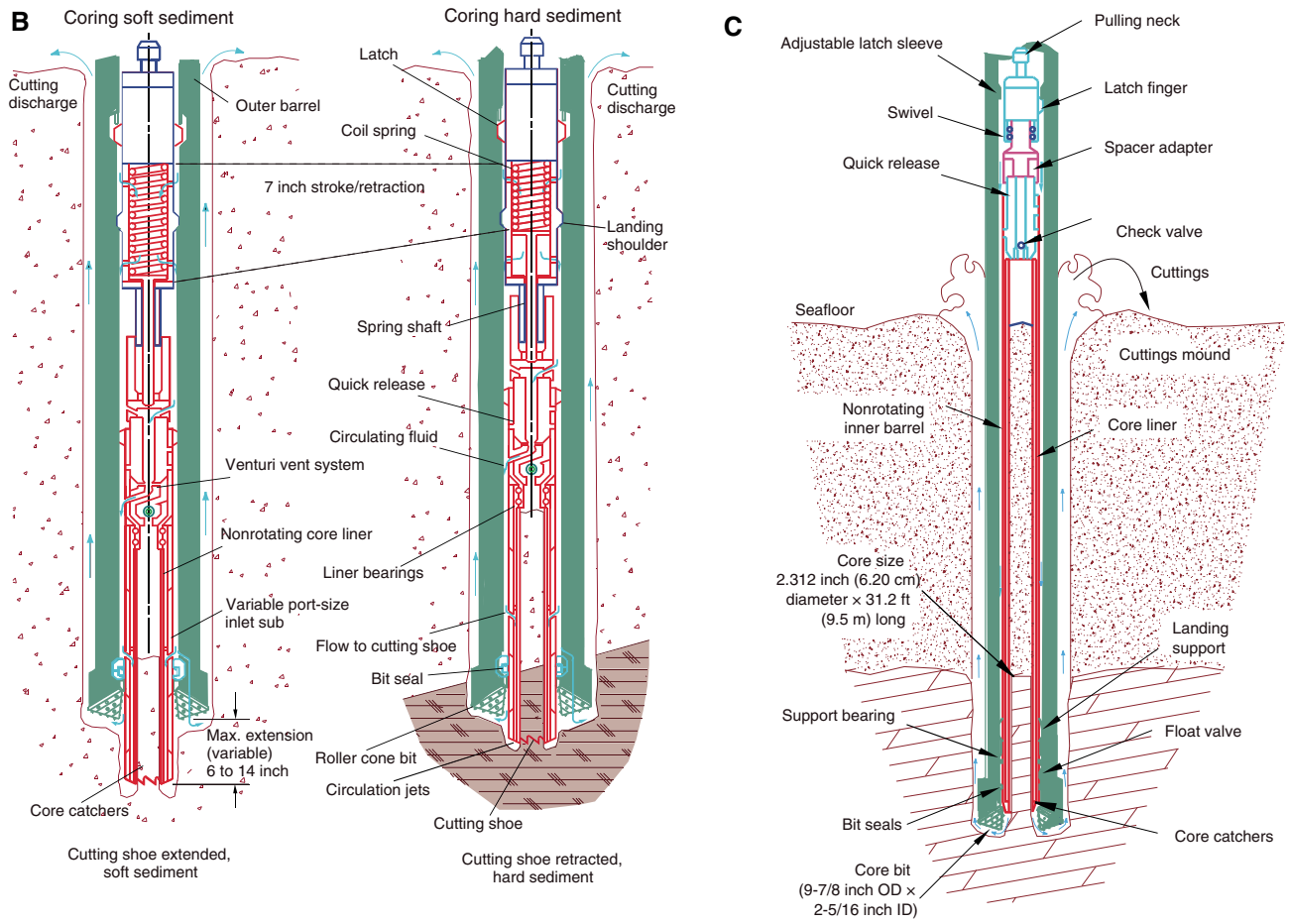

modified head sub, five 8¼ inch control length drill collars, a tapered drill collar, two stands of 5½ inch transition drill pipe, and a crossover sub to the drill pipe that extends to the surface.

The RCB system is a rotary system designed to recover firm to hard sediments and igneous basement. The BHA, including the bit and outer core barrel, is rotated with the drill string while bearings allow the inner core barrel to remain stationary (Figure **F2C**).

A typical RCB BHA includes a 9⅞ inch drill bit, a bit sub, an outer core barrel, a modified top sub, a modified head sub, a variable number of 8¼ inch control length drill collars, a tapered drill collar, two stands of 5½ inch drill pipe, and a crossover sub to the drill pipe that extends to the surface. Cores collected with the RCB system are denoted by the letter "R."

Nonmagnetic core barrels were used for all APC, HLAPC, and RCB deployments. APC cores were oriented with the Icefield MI-5 core orientation tool when coring conditions allowed. Formation temperature measurements were taken with the advanced piston corer temperature tool (APCT-3; see **Downhole measurements**). Information on recovered cores, drilled intervals, downhole tool deployments, and related information are provided in the Operations, Paleomagnetism, and Downhole measurements sections of each site chapter.

IODP depth conventions

The primary depth scales used are based on the length of the drill string deployed (e.g., drilling depth below rig floor [DRF] and drilling depth below seafloor [DSF]), the length of core recovered (e.g., core depth below seafloor [CSF] and core composite depth below seafloor [CCSF]), and the length of logging wireline deployed (e.g., wireline log depth below rig floor [WRF] and wireline log depth below seafloor [WSF]) (see IODP Depth Scales Terminology at **http://www.iodp.org/policies-and-guidelines/142-iodp-depth-scales-terminology-april-2011/file**). In cases where multiple logging passes are made, wireline log depths are mapped to one reference pass, creating the wireline log matched depth below seafloor (WMSF) scale. All units are in meters. The relationship between scales is defined either by protocol, such as the rules for computation of CSF depth from DSF depth, or by user-defined correlations, such as core-to-log correlation. The distinction in nomenclature should keep the reader aware that a nominal depth value in different depth scales usually does not refer to the exact same stratigraphic interval.

Depths of cored intervals are measured from the drill floor based on the length of drill pipe deployed beneath the rig floor (DRF scale; Figure **F1**). The depth of the cored interval is referenced to the seafloor (DSF scale) by subtracting the seafloor depth of the hole from the DRF depth of the interval. Standard depths of cores in meters below seafloor (CSF-A scale) are determined based on the assumption that (1) the top depth of a recovered core corresponds to the top depth of its cored interval (at the DSF scale) and (2) the recovered material is a contiguous section even if core segments are separated by voids when recovered. Standard depths of samples and associated measurements (CSF-A scale) are calculated by adding

the offset of the sample or measurement from the top of its section and the lengths of all higher sections in the core to the top depth of the core.

If a core has <100% recovery, for curation purposes all cored material is assumed to originate from the top of the drilled interval as a continuous section. In addition, voids in the core are closed by pushing core segments together, if possible, during core handling. Therefore, the true depth interval within the cored interval is unknown. This result should be considered a sampling uncertainty in age-depth analysis or in correlation of core data with downhole logging data.

When core recovery is >100% (the length of the recovered core exceeds that of the cored interval), the CSF depth of a sample or measurement taken from the bottom of a core will be deeper than that of a sample or measurement taken from the top of the subsequent core (i.e., the data associated with the two core intervals overlap at the CSF-A scale). This overlap can happen when a soft to semisoft sediment core recovered from a few hundred meters below the seafloor expands upon recovery (typically by a few percent to as much as 15%). Therefore, a stratigraphic interval may not have the same nominal depth on the DSF and CSF scales in the same hole.

During Expeditions 367 and 368, all core depths below seafloor were initially calculated according to the CSF-A depth scale. Unless otherwise noted, all depths presented are calculated on the CSF-A scale and reported simply in meters (m).

Curatorial procedures and sample depth calculations

Numbering of sites, holes, cores, and samples follows standard IODP procedure. A full curatorial identifier for a sample consists of the following information: expedition, site, hole, core number, core type, section number, section half, piece number (hard rocks only), and interval in centimeters measured from the top of the core section. For example, a sample identification of "367-U1499A-5H-2W, 31–33 cm" indicates a 2 cm sample removed from the interval between 31 and 33 cm below the top of Section 2 (working half) of Core 5 ("H" designates that this core was taken with the APC system) of Hole A at Site U1499 during Expedition 367 (Figure **F1**). The "U" preceding the hole number indicates the hole was drilled by the US platform, the *JOIDES Resolution*. The drilling system used to obtain a core is designated in the sample identifiers as follows: H = APC, F = HLAPC, R = RCB, and X = XCB. Integers are used to denote the "core" type of drilled intervals (e.g., a drilled interval between Cores 2H and 4H would be denoted by Core 31).

Core handling and analysis

Sediment

When the core barrel reached the rig floor, the core catcher from the bottom of the core barrel was removed and a sample was extracted for paleontological (PAL) analysis. Next, the sediment core was extracted from the core barrel in its plastic liner. The liner was carried from the rig floor to the core processing area on the catwalk outside the core laboratory, where it was split into ~1.5 m sections. Blue (uphole direction) and clear (downhole direction) liner caps were glued with acetone onto the cut liner sections.

Once the core was cut into sections, whole-round samples were taken for interstitial water chemical analyses. When a whole-round sample was removed, a yellow cap was used to denote the missing interval. Syringe samples were taken for headspace gas analyses according to the IODP hydrocarbon safety monitoring protocol.

Core sections were placed in a core rack in the laboratory. When the core sections reached equilibrium with laboratory temperature (typically after 2 h), they were run through the Whole-Round Multisensor Logger (WRMSL) for *P*-wave velocity on the *P*-wave logger (PWL), magnetic susceptibility, and gamma ray attenuation (GRA) bulk density (see **Physical properties**). The core sections were also run through the Natural Gamma Radiation Logger (NGRL), and thermal conductivity measurements were taken once per core when the material was suitable.

The core sections were then split lengthwise from bottom to top into working and archive halves. Investigators should note that older material can be transported upward on the split face of each section during splitting.

The working half of each core was described by the sedimentologists and structural geologists. Discrete samples were then taken for moisture and density (MAD) and paleomagnetic (PMAG) analyses and for remaining shipboard analyses such as X-ray diffraction (XRD) and carbonate (CARB). Samples were not collected when the lithology was a high-priority interval for expedition or postexpedition research (e.g., ash layers, etc.), there was unsuitable core material, or the core was severely deformed. During the expeditions, no samples were taken for personal postexpedition research (except for ephemeral pore water samples and five reconnaissance samples for lipids necessary to determine the appropriate sample volume/number to prepare for sensible postexpedition sampling).

The archive half of each core was scanned on the Section Half Imaging Logger (SHIL) and measured for point magnetic susceptibility (MSP), and reflectance spectroscopy and colorimetry (RSC) were measured on the Section Half Multisensor Logger (SHMSL). Labeled foam pieces were used to denote missing whole-round (WR) intervals in the SHIL images. The archive-half sections were then described visually and by means of smear slides for sedimentology. Finally, the magnetization of archive-half sections and working-half discrete pieces was measured with the cryogenic magnetometer and spinner magnetometer.

Hard rock

Pieces were extracted from the core liner on the catwalk or directly from the core barrel on the rig floor. The pieces were pushed to the bottom of 1.5 m liner sections, and the total rock length was measured. The length was entered into the database using the SampleMaster application as "created length." This number was used to calculate recovery. The liner sections were then transferred to the core splitting room.

Oriented pieces of core were marked on the bottom with a wax pencil to preserve orientation. Adjacent but broken pieces that could be fit together along fractures were curated as single pieces. The petrologists and structural geologists confirmed piece matches and marked the split line on the pieces, which defined how the pieces were to be cut into two equal halves. The aim was to maximize the expression of dipping structures on the cut face of the core while maintaining representative features in both archive and working halves. A plastic spacer was secured with acetone to the split core liner between individual pieces or reconstructed contiguous groups of subpieces. These spacers can represent substantial intervals of no recovery. The length of each section of core, including spacers, was entered into the database as "curated length," which commonly differs by several centimeters from the length measured on the catwalk. Finally, the depth of each piece in the database was recalculated based on the curated length.

Core pieces were imaged around the full 360° circumference and then placed in a core rack in the laboratory. When the core sections reached equilibrium with laboratory temperature (typically after 2 h), the whole-round core sections were run through the WRMSL (GRA and magnetic susceptibility only) and NGRL (see **Physical properties**).

Each piece of core was split with a diamond-impregnated saw into an archive half and a working half, with the positions of plastic spacers between pieces maintained in both halves. Pieces were numbered sequentially from the top of each section, beginning with 1. Separate subpieces within a single piece were assigned the same number but lettered consecutively (e.g., 1A, 1B, etc.). Pieces were labeled only on the outer cylindrical surfaces of the core. If it was evident that an individual piece had not rotated around a horizontal axis during drilling, an arrow pointing to the top of the section was added to the label. The piece's oriented character was recorded in the database using the SampleMaster application.

The working half of each core was first described by the petrologists and structural geologists. Samples were then taken for thin section preparation and shipboard paleomagnetic and physical properties analyses. The archive half of each core was scanned on the SHIL and measured for MSP and RSC on the SHMSL. Thermal conductivity measurements were made on selected archive-half samples (see **Physical properties**). After the archive halves were fully described, samples were taken for shipboard analyses (thin sections, inductively coupled plasma spectroscopy [ICP], XRD, MAD, etc). Finally, the magnetizations of archive-half sections, archive-half pieces, and discrete samples taken from the working half were measured with the cryogenic magnetometer and spinner magnetometer.

When all steps were completed, cores were wrapped, sealed in plastic tubes, and transferred to cold storage space aboard the ship. At the end of the expedition, the cores were sent to the IODP Gulf Coast Repository (Texas A&M University, College Station, Texas [USA]), where samples for postexpedition research were taken.

Drilling and handling core disturbance

Cores may be significantly disturbed and contain extraneous material as a result of the coring and core handling process (Jutzeler et al., 2014). In formations with loose sand layers, sand from intervals higher in the hole may be washed down by drilling circulation, accumulate at the bottom of the hole, and be sampled with the next core. The uppermost 10–50 cm of each core must therefore be examined critically during description for potential "fall-in." Common coring-induced deformation includes the concave-downward appearance of originally horizontal bedding. Piston action can result in fluidization ("flow-in") at the bottom of APC cores. Retrieval from depth to the surface can result in elastic rebound. Gas that is in solution at depth may become free and drive apart core segments within the liner. When gas content is high, pressure must be relieved for safety reasons before the cores are cut into segments. Holes are drilled into the liner, which forces some sediment as well as gas out of the liner. These disturbances are described in each site chapter and graphically indicated on the visual core descriptions (VCDs).

Authorship of chapters

The separate sections of the methods and site chapters were written by the following scientists (authors are listed in alphabetical order; see **Expedition 367/368 participants** for affiliation information):

Expedition 367 (Sites U1499 and U1500)

Background and objectives: J.M. Stock and Z. Sun
Operations: A. Klaus and S. Midgley
Lithostratigraphy: J.L. Hinojosa, K.-H. Hsiung, B.G. Johnson, Z. Liu, C. Robinson, C. Su, and N. Zhao
Igneous and metamorphic petrology: T.W. Höfig, X.-L. Huang, A. Luna, A.J. McCarthy, and L. Zhong
Structural geology: M.F.R. Nirrengarten and C. Zhang
Biostratigraphy: A. Furusawa, B. Huang, C. Lupi, X. Su, and R. Xiang
Paleomagnetism: S.M. Skinner, L. Yi, and Y. Zhang
Geochemistry: Y. Chen, M.J. Dorais, and L. Li
Physical properties: J. Boaga, A. Briais, C. Lei, I. Sauermilch, R. Yadav, and J. Zhang
Downhole measurements: J. Boaga, A. Briais, C. Lei, I. Sauermilch, R. Yadav, and J. Zhang
Core-log-seismic integration: J. Boaga, A. Briais, C. Lei, I. Sauermilch, R. Yadav, and J. Zhang

Expedition 368 (Sites U1501–U1505)

Background and objectives: Z. Jian and H.-C. Larsen
Operations: C.A. Alvarez Zarikian and K. Grigar
Lithostratigraphy: K.A. Dadd, C. Liu, J.C. Schindlbeck, S.M. Straub, S. Wan, and G. Zhong
Igneous and metamorphic petrology: D.W. Peate, S.M. Straub, and F.M. Van der Zwan
Structural geology: W. Ding, R.M. Kurzawski, and G.T.F. Mohn
Biostratigraphy: F. Ferreira, A.J. Gewecke, S. Jiang, H. Jin, B. Li, C. Liu, and P.-S. Yu
Paleomagnetism: E.C. Ferré, S. Satolli, and H. Wu
Geochemistry: S.A. Bowden, Y. Li, and L. Tian
Physical properties: D. Cukur, E. Huang, J. Lin, L.S. Ningthoujam, N. Osono, P. Persaud, and N. Qiu
Downhole measurements: D. Cukur, J. Lin, P. Persaud, and N. Qiu
Core-log-seismic integration: J. Lin and H.-C. Larsen

Lithostratigraphy

The lithologies of sediment and sedimentary rocks recovered during Expeditions 367 and 368 were determined using visual (macroscopic) core description, smear slides, and thin sections. Integration of data from digital core images, color reflectance spectrophotometry, magnetic susceptibility, XRD, and geochemistry provided complementary information. The methods employed during the expeditions were adapted from those used during IODP Expedition 349 (Li et al., 2015), along with those from other IODP expeditions (e.g., Expedition 339 Scientists, 2013). We used the DESClogik application to record and upload descriptive data into the Laboratory Information Management System (LIMS) database (see the DESClogik user guide at **http://iodp.tamu.edu/labs/documentation**). Spreadsheet templates were set up in DESClogik and customized for Expeditions 367 and 368 before the first core was brought on deck. The templates were used to record macroscopic core descriptions and microscopic data from smear slides and thin sections. The location of all smear slide and thin section samples taken from the core were recorded in the SampleMaster application, and descriptive data uploaded to the LIMS database were used to produce VCD standard graphic reports.

Core preparation

Standard methods for splitting core were performed either by pulling a wire lengthwise through the center of the core or by cutting the core with a rock saw. Each piece of core was split into archive and working halves, with the archive half used for visual description. When splitting the cores with a wire, we sometimes gently scraped across the cut surface of the core section using a stainless steel or glass scraper to prepare the surface for unobscured description and digital imaging, especially in the upper, poorly consolidated intervals. Most cores were imaged after they had dried; however, some cores were imaged still damp from the water used during cutting if this enhanced the features. If these cores had partially dried before they were imaged, we applied a light spray of deionized water to dampen the surface.

Visual core description

VCDs include a simplified graphical representation of each site on a core-by-core basis (Figure **F3**). The principal function of the graphic VCD is to present the physical observations of the core in a columnar format. Site, hole, core, and depth in meters CSF-A are given at the top of each VCD, with the depth and core section numbers plotted along the left margin. Next to the depth and section columns, we plotted the lithostratigraphic unit and the biostratigraphic age (see **Biostratigraphy**). The lithostratigraphic units were assigned by grouping intervals based on their lithologic similarities (see **Definition of lithostratigraphic units**). Further definition of the lithostratigraphic units and their boundaries is described in each site chapter. Additional columns correspond to either core images, physical properties (e.g., natural gamma radiation [NGR]), entries made in DESClogik, or shipboard sample locations. Data taken from DESClogik entries include core summary, principal lithology, sedimentary structures, bioturbation intensity, and drilling disturbances. The VCDs also include descriptive and lithostratigraphic information from the metamorphic and igneous rocks recovered at each site. Each VCD column is described in more detail below.

Core summary

The core summary provides a brief overview of major and minor lithologies present in the core, as well as notable features (e.g., sedimentary structures). The summary is presented at the top of the VCDs and includes sediment color determined qualitatively using Munsell soil color charts. Because sediment color may evolve during drying and subsequent oxidization, color was described shortly after the cores were split and imaged or measured by the SHIL and SHMSL. Deionized water was applied to the cut surface of lithified sedimentary rocks before determining color.

Core images

High-resolution color images were produced by scanning the flat surface of the archive-half sections with the SHIL. The cores were scanned as soon as possible after splitting and scraping to avoid color changes caused by sediment oxidation and drying. In some cases involving lithified rock, we photographed the cores both wet and dry and selected the image that best represented the lithology.

The SHIL uses three pairs of advanced illumination, high-current-focused, LED line lights to illuminate large cracks and blocks in the core surface and sidewalls. Each LED pair has a color temperature of 6500 K and emits 90,000 lx at 76.2 mm. A line-scan camera images 10 lines/mm to create a high-resolution TIFF file. The camera height is adjusted so that each pixel images a 0.1 mm^2 section of the core. However, actual core width per pixel varies because of differences in section-half surface height. High- and low-resolution JPEG files are subsequently created from the high-resolution TIFF file. Two different image types were uploaded to the LIMS database: one that includes a grayscale and ruler and one that is cropped to exclude the grayscale and ruler.

Graphic lithology

The graphic lithology column illustrates an interval-by-interval record of the primary lithologies contained within each core. The column was constructed by pairing the principal lithology name assigned to each interval in DESClogik with a predetermined set of lithology patterns (Figure **F4**). The column plots to scale all intervals that are at least 2 cm thick. Principal lithology names were not assigned to intervals thinner than 2 cm unless they were of special significance (e.g., ash layers).

Reflectance

Reflectance of visible light from the archive halves of sediment cores was measured using an Ocean Optics USB4000 spectrophotometer mounted on the automated SHMSL. Freshly split cores were covered with clear plastic wrap and placed on the SHMSL, and measurements were taken at 1, 2, or 2.5 cm spacing to provide a high-resolution stratigraphic record of color variation for visible wavelengths. Each measurement was recorded in 2 nm wide spectral bands from 400 to 900 nm. Reflectance parameters L*, a*, and b* were recorded (Balsam et al., 1997, 1998).

The SHMSL takes measurements in empty intervals and over intervals where the core surface is well below the level of the core liner, but it cannot recognize relatively small cracks, disturbed areas of core, or plastic section dividers. Thus, SHMSL data may contain spurious measurements that must be edited out of the data set by the user. When significant fragmentation and/or brecciation from drilling disturbances was evident, the SHMSL spacing was adjusted manually to avoid taking measurements in the wide spaces caused by drilling fractures. Additional detailed information about measurement and interpretation of reflectance data can be found in Balsam et al. (1997, 1998) and Balsam and Damuth (2000).

Natural gamma radiation

NGR occurs primarily by decay of ^{238}U, ^{232}Th, and ^{40}K isotopes. This radiation is measured using the NGRL (see **Physical properties**). Data generated from this instrument were used to augment geologic interpretations.

Magnetic susceptibility

We measured magnetic susceptibility with a Bartington Instruments MS2E point sensor (high-resolution surface-scanning sensor) on the SHMSL. Because the SHMSL demands direct contact between the point magnetic susceptibility sensor and the split core, measurements were made on the archive halves of split cores that were covered with clear plastic wrap. Measurements were taken at 1.0, 2.0, or 2.5 cm spacing. Measurement resolution was 1.0 SI, and each measurement integrated a volume of 10.5 mm × 3.8 mm × 4 mm, where 10.5 mm is the length perpendicular to the core axis, 3.8 mm is the width along the core axis, and 4 mm is the depth into the core.

Sedimentary structures

The location and type of stratification and sedimentary structures visible on the surface of the split cores are shown in the sedimentary structures column of the VCDs. Symbols in this column

Figure F3. Example graphic visual description form (VCD), Expeditions 367 and 368. cps = counts per second.

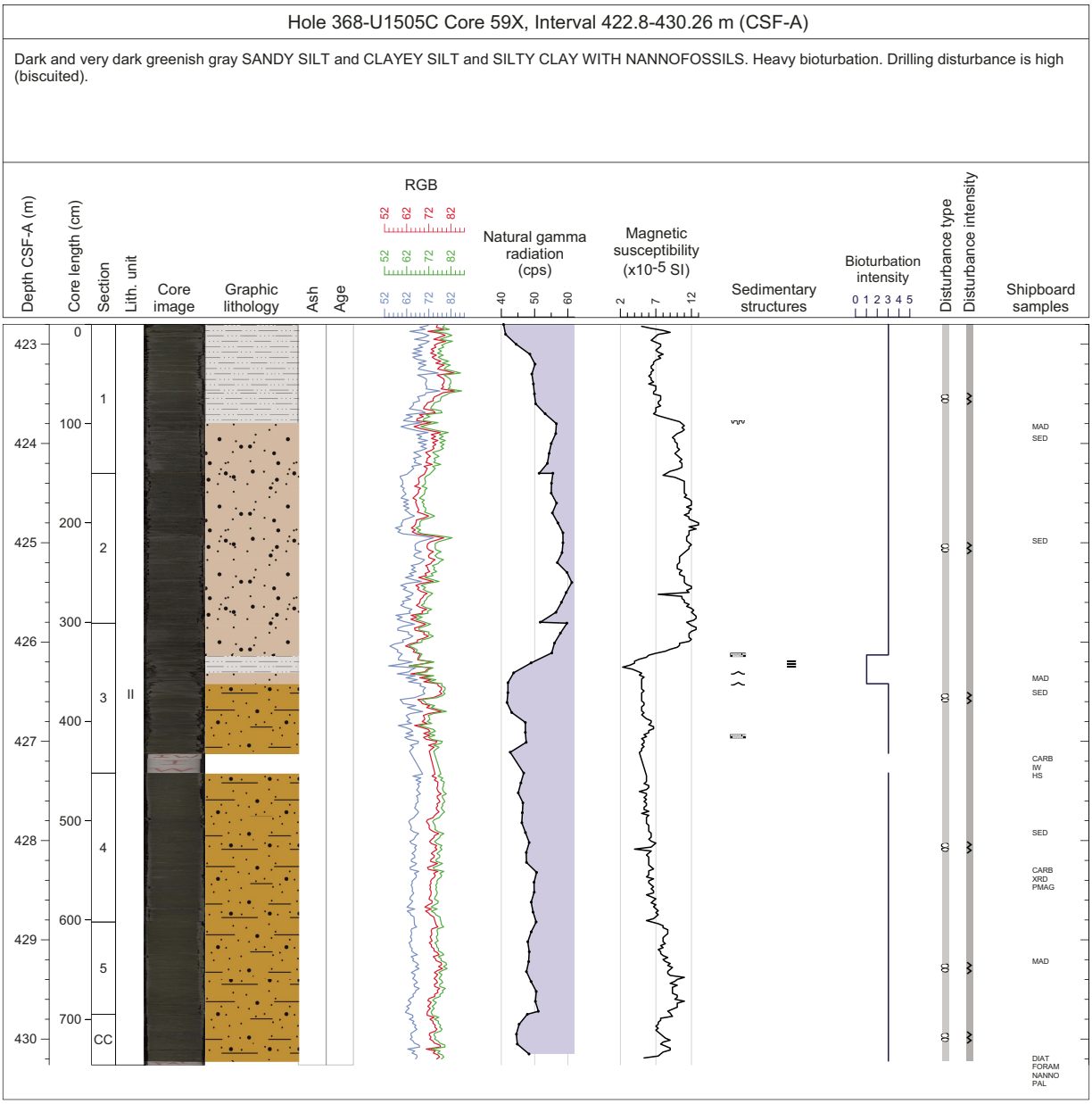

indicate the location, scale, and frequency of stratification and other sedimentary features, such as sole marks, cross-lamination, and fining-upward intervals (Figure F5).

For Expeditions 367 and 368, the following terminology (based on Stow, 2005) was used to describe the scale of stratification:

Thin lamination = <0.3 cm thick.
Medium lamination = 0.3–0.6 cm thick.
Thick lamination = 0.6–1 cm thick.
Very thin bed = 1–3 cm thick.
Thin bed = 3–10 cm thick.
Medium bed = 10–30 cm thick.
Thick bed = 30–100 cm thick.
Very thick bed = >100 cm thick.

Bioturbation intensity

Five levels of bioturbation are recognized using a scheme like that of Droser and Bottjer (1986). These levels are illustrated with a numeric scale in the bioturbation intensity column. Any identifiable trace fossils (ichnofossils) are identified in the general interval comment field in DESClogik and in the core summary.

1 = No bioturbation.
2 = Slight bioturbation (<10%–30%).
3 = Moderate bioturbation (30%–60%).
4 = Heavy bioturbation (60%–90%).
5 = Complete bioturbation (>90%).

Drilling disturbance

Drilling-related sediment disturbance is recorded in the disturbance type and intensity columns. The disturbance intensity, where

Figure F4. Lithology patterns used for visual core description, Expeditions 367 and 368.

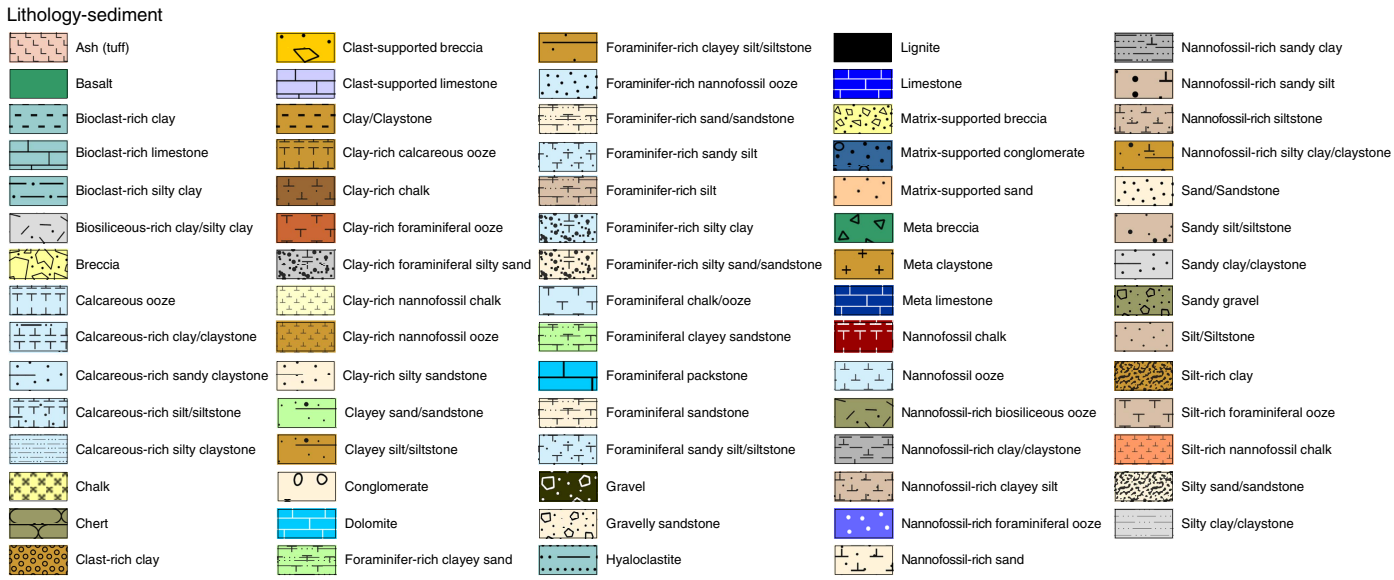

Figure F5. Symbols and nomenclature used for visual core description, Expeditions 367 and 368.

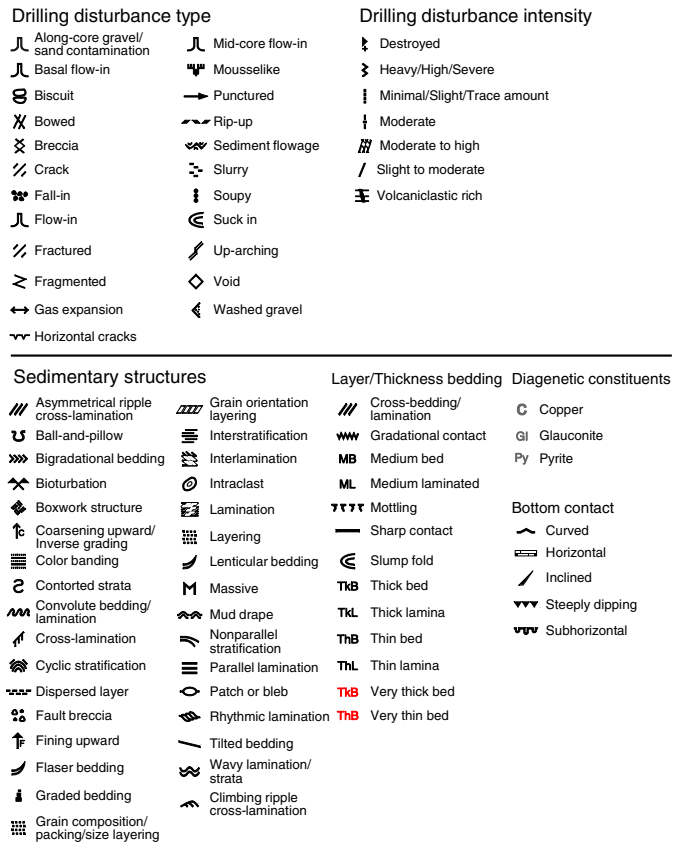

present, is ranked on a five-point scale: slight, slight to moderate, moderate, moderate to high, and high. The type of drilling disturbance is classified using the symbols shown in Figure F5. Each symbol corresponds to the following terms:

- Soupy: intervals are water-saturated and have lost all aspects of original bedding.
- Fall-in: characteristically occurs at the top of individual cores when out-of-place material from the shallower cored interval has fallen downhole onto the cored surface.
- Up-arching: bedding planes are slightly to moderately deformed but still subhorizontal and continuous across the core surface. The edges of the bedding planes typically show a concave downward shape caused by shear along the wall of the core liner.
- Flow-in: occurs in unconsolidated, sandy, or gravelly sediment, leaving a soupy texture at the base of the core. It typically occurs during APC drilling, following a partial stroke of the piston core.
- Biscuit: sediments of intermediate stiffness show vertical variations in the degree of disturbance. Softer intervals are washed and/or soupy, whereas firmer intervals are relatively undisturbed.
- Fractured: common in consolidated and lithified sediments. The core pieces are broken in places and may have been partly displaced or moved, but the correct stratigraphic sequence is maintained.
- Fragmented: complete fracturing of the core into large (>2 cm thick) pieces, where the stratigraphic order of the pieces is retained but their orientation is lost.
- Drilling breccia: core is crushed and broken into many small and angular pieces, with original orientation and stratigraphic position lost.

Samples

The shipboard samples column records the position of samples used for microscopic descriptions (i.e., smear slides and thin sections), biochronological determinations, and shipboard analyses of chemical and physical properties.

Classification of principal lithology

Types of sediment

The sediment recovered during Expeditions 367 and 368 was described and classified by measuring the relative proportions of biosiliceous, calcareous, and siliciclastic material (Figure F6). This

Figure F6. Siliciclastic-calcareous-biosiliceous ternary diagram used for sediment name classification of different compositions.

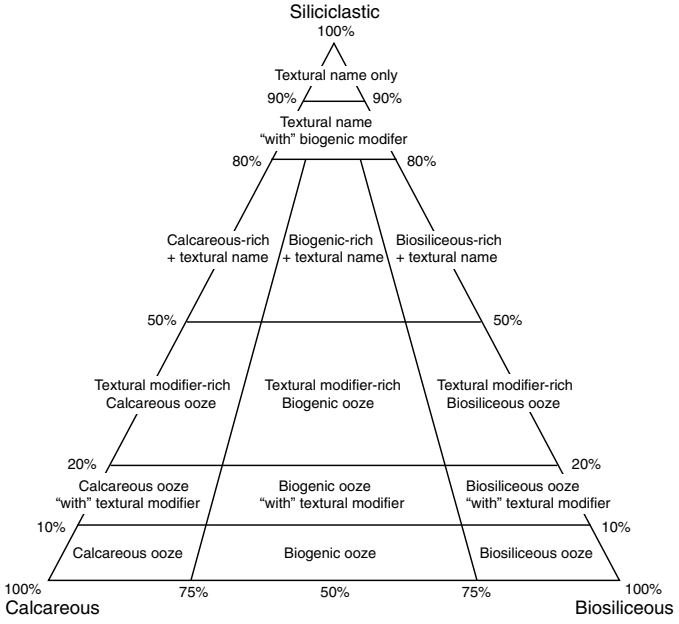

classification scheme was adapted from Integrated Ocean Drilling Program Expedition 339 (Expedition 339 Scientists, 2013), Expedition 349 (Li et al., 2015) and Stow (2005). Biosiliceous sediment is restricted to only include siliceous skeletal remains of microorganisms (e.g., radiolarians and diatoms), whereas calcareous sediment includes a wide range of grain types, such as the skeletal remains of microfauna (e.g., foraminifers) and microflora (e.g., nannofossils), macrofossil shell fragments, and fine-grained detrital carbonate. Siliciclastic sediment includes mineral and rock fragments eroded from igneous, sedimentary, and metamorphic rocks. In rare cases, sediment recovered during Expeditions 367 and 368 included grains that were directly derived from a volcanic eruption, mainly in the form of vitric material (e.g., ash and lapilli), so a separate classification scheme was applied to their description.

Naming conventions for Expeditions 367 and 368 follow the general guidelines of the Ocean Drilling Program (ODP) sediment classification scheme (Mazzullo et al., 1988), except that during Expeditions 367 and 368 a separate "mixed sediment" category was not distinguished and detrital biogenic sediment with evidence of being reworked and transported by sedimentary processes was described using the terminology for siliciclastic rocks with a prefix that describes the main biogenic component. For example, the term "foraminifer sand" defines sediment composed of >50% foraminifer tests that are >63 µm in size. A principal lithology name is assigned to each interval, and when the sediment comprises a mixture of different sediment types, modifying prefixes and suffixes are added to the principal name.

We followed the naming scheme of Shepard (1954) for the classification of siliciclastic sediment and sedimentary rock that reflects the relative proportion of sediments of different grain size (Figure F7). Sediment grain size divisions for siliciclastic and redeposited biogenic components are based on Wentworth (1922), with categories based on the relative proportions of gravel and sand-, silt-, and clay-sized particles (Figure F8). Distinguishing between some of these categories can be difficult at the macroscopic level, especially

Figure F7. Lithologic classification for textural names, Expeditions 367 and 368. A. Shepard ternary classification diagram (Shepard, 1954). B. Biogenic classification. N = nannofossil.

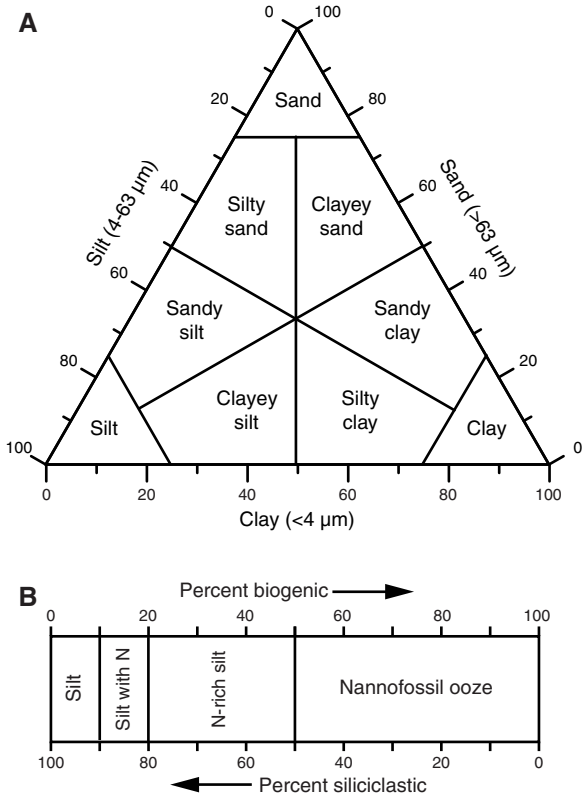

Figure F8. Udden-Wentworth grain-size classification of siliciclastic sediment (Wentworth, 1922), Expeditions 367 and 368.

Millimeters (mm)		Micrometers (µm)	Phi (ϕ)	Wentworth size class	
	4096		-12.0	Boulder	
	256		-8.0	Cobble	Gravel
	64		-6.0	Pebble	
	4		-2.0	Granule	
	2.00		-1.0	Very coarse sand	
	1.00		0.0	Coarse sand	
1/2	0.50	500	1.0	Medium sand	Sand
1/4	0.25	250	2.0	Fine sand	
1/8	0.125	125	3.0	Very fine sand	
1/16	0.0625	63	4.0	Coarse silt	
1/32	0.031	31	5.0	Medium silt	
1/64	0.0156	15.6	6.0	Fine silt	Silt
1/128	0.0078	7.8	7.0	Very fine silt	
1/256	0.0039	3.9	8.0	Clay	Clay
	0.00006	0.06	14.0		

considering the relative abundance of the fine-grained fraction (e.g., silty clay versus clayey silt); therefore, smear slides and thin sections were used in classifying fine-grained sediment abundances.

The proportions of biogenic material, both siliceous and calcareous sediment, were first macroscopically determined by observing changes in color. We used Munsell soil color charts to assign a color to different intervals within a core. Sediments that contained significant amounts of calcareous material typically had a lighter color value. Biogenic material was also determined by observing physical property changes in NGR, magnetic susceptibility, and reflectance values. Low magnetic susceptibility and high color reflectance values were two defining patterns associated with significant amounts of calcareous material. We then used smear slides and thin sections to identify and estimate the relative abundance of the different microfossils, such as nannofossils, foraminifers, and radiolarians, within unique lithologic intervals. However, smear slide observations tend to overestimate the relative proportions of calcareous microorganisms with respect to the clay-sized fraction of siliciclastic material, so we used the shipboard calcium carbonate data as a quality control. Sediment with >40 wt% calcium carbonate was classified using a calcareous principal lithology.

The lithologic names assigned to a given interval of sediment consist of a principal name and in some cases a modifying prefix and/or suffix. The assigned names are based on abundance and composition of grains determined from visual description of the core and from smear slide/thin section observations. For sediment that contains >90% of one component (either the siliciclastic or biogenic component), only the principal name was used. For sediment that contains >90% biogenic components and is not clearly reworked, the name applied indicates the most common type of biogenic grain. For example, sediment composed of >90% calcareous nannofossils was named nannofossil ooze, and sediment composed of subequal amounts of foraminifers and nannofossils was named calcareous ooze.

For sediment with >90% siliciclastic grains, the principal name is based on the textural characteristics of siliciclastic sediment particles (Figure **F7**). For sediment that contains a significant mixture of siliciclastic and biogenic components (between 10% and 90% of both siliciclastic and biogenic components), the principal name is determined by the more abundant component. If the siliciclastic component is more abundant, the principal name is based on the textural characteristics of siliciclastic fraction. If the biogenic component is more abundant, the principal name is based on the predominant microfossil group.

If a microfossil group composes 10%–50% of the sediment and this group is not included as part of the principal name, modifiers are used instead. When a microfossil group (e.g., diatom, nannofossil, or foraminifer) comprises 20%–50% of the sediment, a major modifier consisting of the component name hyphenated with the suffix "-rich" (e.g., nannofossil-rich clay) is used. When the calcareous or biosiliceous material comprises a mixture of different microfossil grain types, the major modifier "calcareous-rich" or "biosiliceous-rich" is used instead.

If the principal component forms 80%–90% of the sediment, the principal name is followed by a minor modifier (e.g., "with nannofossils"), with the minor modifier based on the most abundant component that forms 10%–20% of the sediment. If the minor component is biogenic, the modifier describes the most limited group of grains that exceeds the 10% abundance threshold. If the minor component is siliciclastic, the minor modifier is based on the texture of the siliciclastic fraction.

If the primary lithology for an interval of core has a major modifier, that major modifier is indicated in the Graphic lithology column of the VCDs using a modified version of the lithologic pattern for the primary lithology (Figure **F3**). The modified lithologic patterns are shown in Figure **F4**. The minor modifiers of sediment lithologies are not included in the graphic lithology column. Although size-texture qualifiers were used to describe siliciclastic sediment (using prefixes such as clayey or sandy), size-texture qualifiers were not typically used in the principal name for biogenic sediment.

Lithification

The degree of lithification was determined by observing the amount of deformation the sediment can accommodate and the level of sediment consolidation. Sediment was considered lithified when the sediment could not be deformed easily with a finger, toothpick, or metal scraper. Lithification was ranked using a qualitative scale with the terms slightly consolidated, moderately consolidated, well consolidated, and lithified.

Depending on the principal lithology, different lithification terms were used. For example, the name "ooze" was applied to unlithified biogenic sediment predominantly composed of calcareous or siliceous microorganisms (e.g., nannofossil ooze). The term "ooze" indicates that the sediment can be deformed by a finger. Chalk is the lithified variant of calcareous ooze that is fine grained and more compact although it can be scratched by a fingernail. Lithified sediment composed of siliceous microfossils (diatoms and radiolarians) is called "radiolarite/diatomite." Well-lithified calcareous sediment that contains evidence of shallow water deposition (e.g., skeletal macrofossils such as coral) was called "limestone" with supporting prefixes such as "bioclast-rich," "clast-supported," and "dolomitic."

For unlithified siliciclastic sediment, no lithification term was added, and the sediment was named for the dominant grain size (i.e., gravel, sand, silt, or clay). For more lithified siliciclastic material, the suffix "-stone" was appended to the dominant size classification (e.g., claystone), except for sediment of gravel size where the terms "conglomerate" or "breccia" were used for well-rounded and angular clasts, respectively. The principal names "conglomerate" and "breccia" were modified using the terms "matrix-supported" and "clast-supported," depending on the matrix to clast ratio.

When the mineralogical, chemical, or structural compositions of the sediments or sedimentary rocks have been altered or changed from their original form, the prefix "meta" is used in conjunction with principal lithology (e.g., metasandstone). These rocks are described under the Metamorphic tab in DESClogik. In many cases, however, no clear distinction of boundary between well-lithified sediments and metasedimentary rock exists. Furthermore, extensive alteration by veins, fractures, and other structural features requires special treatment, particularly when a sedimentary rock is crosscut by a mesh network of veins. For this reason, the name "breccia" is applied in several different ways (see **Igneous and metamorphic petrology**).

Ash layers (volcaniclastic sediment)

The classification of volcanic sediments followed here differs from the standard ODP and IODP classification (Mazzullo et al., 1988) in that we adopted a descriptive (nongenetic) terminology like that employed during ODP Leg 197 and Integrated Ocean Drilling Program Expedition 324 (Shipboard Scientific Party, 2002; Expedition 324 Scientists, 2010). Unless an unequivocally pyroclastic

origin for volcanogenic particles could be determined, we simply described these deposits as we did for siliciclastic sediment (i.e., sand, silt, etc.).

Where evidence for a pyroclastic origin is compelling and the sediment has >50% vitric and other primary volcanic material, we adopted the classification scheme of Fisher and Schmincke (1984). In these instances, we used the grain size terms "volcanic block or bomb" (>64 mm), "lapilli" (2–64 mm), and "ash" (<2 mm) for unconsolidated sediment and "volcanic breccia" (>64 mm), "lapillistone" (2–64 mm), and "tuff" (<2 mm) for lithified material. When the volcanic particles compose between 25% and 50% of the sediment fraction, the modifier "tuffaceous" was used as the prefix for the siliciclastic sediment (e.g., tuffaceous sandstone). The term "hyaloclastite" is used for vitroclastic (i.e., glassy) materials produced by the interaction of water and hot magma or lava.

Smear slide and thin section observation

Two or more smear slide samples of the main lithologies were typically collected from the archive half of each core. Additional samples were collected from areas of interest (e.g., laminations, ash layers, and nodules). A small amount of sediment was taken with a wooden toothpick and put on a 2.5 cm × 7.5 cm glass slide. The sediment sample was homogenized with a drop of deionized water and evenly spread across the slide to create a very thin (about <50 µm) uniform layer of sediment grains for quantification. The dispersed sample was dried on a hot plate. A drop of Norland optical adhesive was added as a mounting medium to a coverslip, which was carefully placed on the dried sample to prevent air bubbles from being trapped in the adhesive. The smear slide was then cured in an ultraviolet light box.

Thin sections were prepared by cutting 3–5 cm^3 billets of lithified sediment from the working half of the core. In some cases, the cut billet was impregnated with a clear epoxy to further consolidate the grains. They were then mounted on 2.5 cm × 4.5 cm glass slides and ground down to a thickness of ~30 µm.

Smear slides and thin sections were examined with a transmitted-light petrographic microscope equipped with a standard eyepiece micrometer. The texture of siliciclastic grains (relative abundance of sand-, silt-, and clay-sized grains) and the proportions and presence of biogenic and mineral components observed in thin sections or smear slides were recorded in DESClogik. Biogenic and mineral components were identified using IODP Technical Notes 1 and 2 (Marsaglia et al., 2013, 2015) for smear slides, and their percentage abundances were visually estimated using Rothwell (1989). The mineralogy of clay-sized grains could not be determined from smear slides. Note that smear slide analyses tend to underestimate the amount of sand-sized and larger grains because these grains are difficult to incorporate onto the slide.

Relative abundances of identified components such as mineral grains, microfossils, and biogenic fragments were assigned on a semiquantitative basis using the following abbreviations:

Tr = trace (<1% in field of view [FOV]).
R = rare (1%–5% in FOV).
C = common (>5%–25% in FOV).
A = abundant (>25%–75% in FOV).
D = dominant (>75% in FOV).

X-ray diffraction analysis

Samples for XRD analyses were selected from the working half, generally at the same depth as sampling for solid-phase geochemistry and smear slide analyses. Approximately one 5 cm^3 sample was taken of a representative lithology per core. Samples analyzed for bulk mineralogy were freeze-dried and homogenized by grinding in the metal ball mill. Prepared samples were top-mounted onto a sample holder and analyzed using a Bruker D-4 Endeavor diffractometer mounted with a Vantec-1 detector using nickel-filtered CuKα radiation. Settings for the standard locked coupled scan were as follows:

Voltage = 37 kV.
Current = 40 mA.
Goniometer scan = 4°–70°.
Step size = 0.0166°.
Scan speed = 1 s/step.
Divergence slit = 0.3 mm.

Diffractograms of bulk samples were evaluated with the aid of the Jade6 or EVA software package, which allowed for mineral identification and basic peak characterization (e.g., baseline removal and characteristic peak intensity). Files were created that contained d-spacing values, diffraction angles, and peak intensities with and without the background removed. These files were scanned by the Jade6 or EVA software to find d-spacing values characteristic of a limited range of minerals. Peak areas were further quantitatively estimated by the TOPAS software. Shipboard evaluation yielded semiquantitative results of the presence and relative abundances of the most common mineralogical components by applying correction factors (Cook et al., 1975) to the measured intensity of the characteristic reflections of minerals.

Definition of lithostratigraphic units

Sediments and sedimentary rocks were described at two levels: (1) the descriptive interval (a single descriptive line in DESClogik) and (2) the lithostratigraphic unit. Lithostratigraphic units are defined as assemblages of multiple descriptive intervals containing similar principal lithologies that are typically tens to hundreds of meters thick (e.g., Tamura et al., 2015). Lithostratigraphic units should be clearly distinguishable from each other by several characteristics, such as composition, bed thickness, grain-size class, and internal homogeneity. Following IODP tradition, they are numbered sequentially as Unit I, Unit II, and so on from the top of the core to the bottom. Subunits were defined within units that showed distinct changes in minor lithology types or bed forms but maintained continuity in the principal lithology. For instance, a unit primarily composed of clay and interbedded silt would be divided into two subunits if the interbedded lithology changed to sand and silt in the lower half of the unit's interval. Note that this distinction was interpreted differently during Expeditions 367 and 368, so a greater number of subunits were defined during Expedition 367 than during Expedition 368.

Igneous and metamorphic petrology

Expedition 367 and 368 core description procedures for igneous and metamorphic rocks are based on those from IODP Expeditions 349 and 351 (Li et al., 2015; Arculus et al., 2015) and ODP Legs 209 and 210 (Shipboard Scientific Party, 2004a, 2004b).

Core description workflow

Prior to splitting the core into working and archive halves, each core was subjected to nondestructive physical property measurements (see **Physical properties**) and imaged using the SHIL (see

Lithostratigraphy) on a wet outside surface at four different angles (0°, 90°, 180°, and 270°) that were combined to form a 360° whole-round image. The coherent hard rock sections and/or hard rock pieces were then split by a diamond-impregnated saw along lines drawn by a petrologist and/or a structural geologist in order to preserve significant compositional and structural features in both the archive and working halves. Afterward, fragmented pieces of hard rock that fit together were assigned a joint number and labeled with a letter in consecutive order downsection (e.g., 1A, 1B, 1C). Plastic spacers separate pieces with different numbers. An arrow added to the labels of single pieces that showed no evidence of rotation indicates the orientation by pointing to the top of the section. Scanning of the cut, dry archive-half surfaces by the SHIL produced high-resolution color images. Then the archive halves were analyzed for color reflectance and magnetic susceptibility at 1–2.5 cm increments by deploying the SHMSL (see **Lithostratigraphy**). Shipboard samples were taken from working halves for carrying out destructive physical properties and paleomagnetic measurements, as well as thin section, XRD, and inductively coupled plasma–atomic emission spectroscopy (ICP-AES) analysis. Because of the presence of hyaloclastic lava-sediment mixtures and sedimentary veins, working halves of igneous rock cores were also sampled for paleontological and sedimentary studies.

Initial macroscopic examination of each core section focused on petrologic and alteration features, followed by characterization of structures (see **Structural geology**). Subsequently, the texture and composition of any veins were recorded. Apart from thin sections, all descriptions were made on the archive half of each core. The DESClogik software was used to record the macroscopic and microscopic observations of primary (igneous) and secondary (alteration/metamorphic) characteristics, forming the basis of all descriptions. The use of a hand lens and binocular microscope aided the estimation of mineral modes and sizes.

Macroscopic visual core description

VCDs present and summarize macroscopic features observed in the cores. Expedition 349 VCDs were used as the basis for macroscopic descriptions for this study so they would remain as closely comparable as possible. The slightly modified VCDs display the following entries (from left to right) in terms of igneous, alteration, and metamorphic features for each core section (Figure **F9**; see Figure **F10** for VCD legend):

- CSF-A depth scale (meters below seafloor);
- Core length scale from 0 to 150 cm;
- Number and orientation of hard rock pieces;
- Interval of shipboard samples;
- Scanned digital image of the archive half;
- Graphic representation of lithology;
- Symbol "G" (for igneous rocks, next to the graphic lithology), which indicates the presence of volcanic glass either in the glassy rind of chilled margins or in hyaloclastite, if encountered; thin horizontal lines in the graphic lithology constrain the section interval containing the volcanic glass and mark the location of chilled margins/contacts;
- Igneous or metamorphic lithologic unit number;
- Vein texture, type, and connectivity;
- Line chart displaying vesicularity percentage;
- Stacked line chart displaying percent phenocryst abundance for plagioclase (PLAG; red line), olivine (OL; green line), and clinopyroxene (CPX; blue line), if present;
- Chart displaying variation in crystal size of modal groundmass (in millimeters);
- Column with variable patterns depicting alteration intensity;
- Overall grain size of the corresponding lithology and deformation intensity for metamorphic rocks, for which vesicularity, percent phenocryst abundance, groundmass grain size, and alteration intensity are not applicable;
- Plot showing whole-round magnetic susceptibility measurements (and point source for Site U1500);
- Diagram displaying color reflectance, with total reflectance (L*), red (a*), and blue (b*) (Site U1500) or individual red-green-blue color space (RGB) values (Sites U1502 and U1504); and
- Description summary of each igneous/metamorphic lithologic unit identified in the corresponding section (see below for details).

The section unit summary (presented on the right side of the VCD) for each igneous lithologic unit contains the following details:

- Expedition, site, hole, core, core type (archive or working half), section number, and interval;
- Igneous lithologic unit/subunit number(s) and representative piece (Site U1500);
- Lithology and volcanic description (e.g., massive flow);
- Color of the bulk rock determined on dry rock surfaces using standard Munsell soil color charts (Munsell Color Company, Inc., 2000);
- Texture (microstructure) based on total percentage of phenocrysts and microphenocrysts by volume;
- Percent phenocryst abundance and type based on minerals identifiable by the unaided eye, hand lens, or binocular microscope;
- Groundmass texture or mineralogy;
- Percent vesicle abundance;
- Upper and lower unit contact relations and boundaries based on physical changes observed in retrieved core material (e.g., presence of chilled margins, changes in vesicularity, and alteration), including information regarding their position within the section; the term "not recovered" was entered where no direct contact was recovered (Expedition 349 Scientists, 2015);
- Alteration intensity and vein mineralogy; and
- Comment, if applicable.

The section unit summary (presented on the right side of the VCD) for each metamorphic lithologic unit contains the following details:

- Expedition, site, hole, core, core type (archive or working half), section number, and interval;
- Metamorphic lithologic unit/subunit number(s);
- Lithology;
- Color of the bulk rock determined on dry rock surfaces using standard Munsell soil color charts (Munsell Color Company, Inc., 2000);
- Deformation intensity;
- Texture based on appearance, grain size distribution and presence of foliations, lineations, or shears;
- Mineralogy;
- Metamorphic condition, applying the metamorphic facies;
- Clast description, if applicable; and
- Comment, if applicable.

Figure F9. Example VCDs for igneous rocks from (A) Expedition 367 and (B) Expedition 368 and (C) metamorphic rocks from Expedition 368.

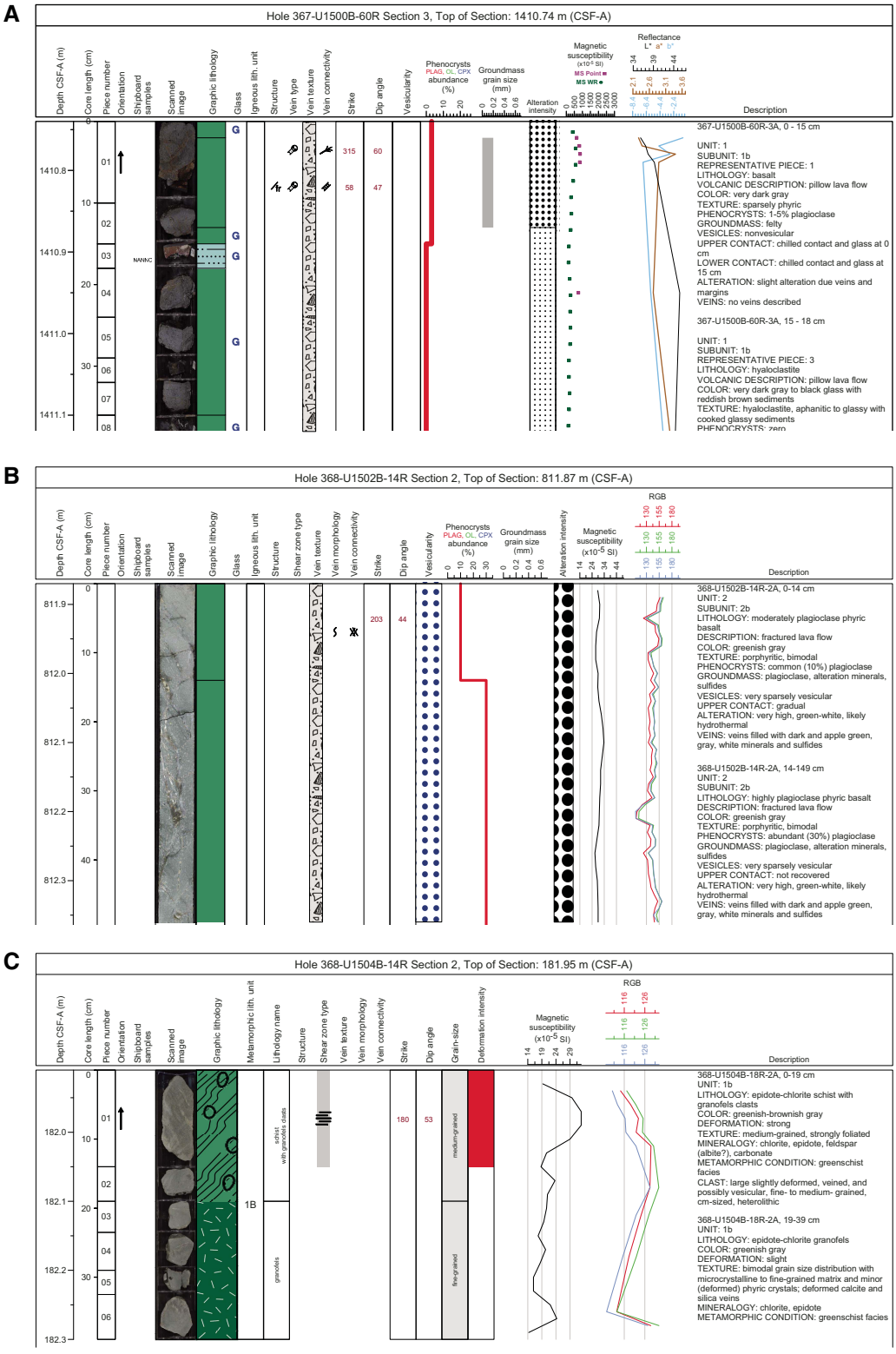

Igneous and metamorphic lithologic units and lithostratigraphic units

A hard rock lithologic unit is defined by rock type or the similarity of phenocryst/mineral assemblages within each rock type. Boundaries are defined by major changes in rock type, in phenocryst/mineral assemblages, or in the presence of a significant thickness of intervening sedimentary rocks. All igneous and metamorphic lithologic units are given consecutive downhole Ara-

Figure F10. Symbols and nomenclature used in igneous VCDs, Expeditions 367 and 368.

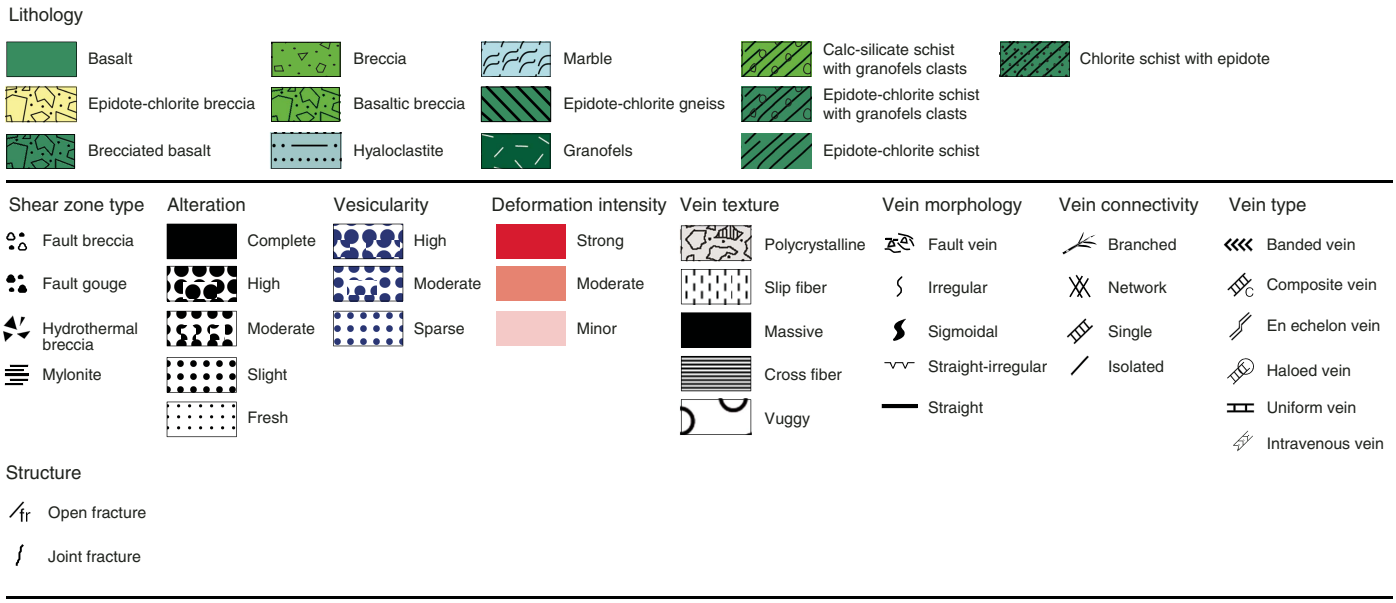

bic numerals (e.g., igneous or metamorphic lithologic Units 1, 2, 3, etc.).

To aid description of igneous and metamorphic units, it is often convenient to divide them into subunits that are named igneous or metamorphic lithologic Subunits 1a, 1b, 1c, and so on. For igneous sequences, lithologic subunits are typically used in cases where a given lithologic unit changed deposition type (e.g., massive flows changed to pillow lavas or basaltic breccia and brecciated basalt changed to massive flows). For metamorphic rocks, lithologic subunits are used when different lithologies occur intercalated with the main rock type that defines the lithologic unit, (e.g., appearance of calc-silicate schists and marble within a unit of chlorite-epidote schists). Closely intercalated intervals may be grouped as subunits to avoid repetitive entry at the small-scale level. Because of the diversity of basement rock types encountered during Expeditions 367 and 368 (fresh basalt lavas, highly altered basalt lavas, and metamorphic schists), different criteria had to be developed by the shipboard scientists to define lithologic subunits at each site. These criteria are described in detail in the relevant site chapters.

Lithostratigraphic units (as used in **Lithostratigraphy**) are defined for (1) igneous rocks in which successions of consecutive cooling or depositional units with similar volcanic characteristics could be identified based on modal compositions and matrix fabric and (2) metamorphic rocks in which successions of similar metamorphic conditions and fabric could be determined. For Expeditions 367 and 368, the lithostratigraphic units are equivalent to the igneous and metamorphic lithologic units described above. These successions are given consecutive downhole Roman numerals (e.g., lithostratigraphic Units III, IV, and V) that follow directly from the overlying sedimentary units (lithostratigraphic Units I and II, in this example).

Magmatic rock classification

Igneous rocks were classified on the basis of abundance, grain size, and texture of their primary minerals based on the International Union of Geological Sciences (IUGS) system (Le Maitre et al., 2005). This approach also applies to igneous clasts found in sedimentary lithostratigraphic units.

Grain size classification

The classification of Neuendorf et al. (2005) was used for grain size division:

- Coarse-grained (crystal diameters = 5 to ≤30 mm),
- Medium-grained (crystal diameters = 1 to <5 mm), and
- Fine-grained (crystal diameters = 0.2 to <1 mm).

Grain size distribution

Terms used to describe the grain size distribution are bimodal (two dominant mineral sizes), equigranular (principal minerals are in the same size range), inequigranular (principal minerals have different grain sizes), and seriate (continuous range in grain size).

Texture

Textures (microstructures) were described macroscopically for all igneous rock core sections and microscopically for a subset of intervals having thin sections.

Textural descriptors applied to volcanic rocks are aphyric, holocrystalline, hypocrystalline (comprising both crystals [major component] and glass), hypohyaline (comprising both crystals [minor component] and glass), holohyaline (vitric; only glass), poikilitic (larger crystals enclose smaller grains), ophitic (pyroxene encloses plagioclase laths), subophitic (pyroxene partially encloses plagioclase laths), porphyritic, phaneritic, aphanitic, trachytic, flow banding, perlite (rounded hydration fractures in glass), glomeroporphyritic (clusters of phenocrysts), "chilled" margin (a glassy or micro to cryptocrystalline margin), and layered.

Mineral shape and habit

Descriptions of mineral habits were based on Leg 209 (Shipboard Scientific Party, 2004a). The terms euhedral, subhedral, anhedral, and interstitial were used to describe the shapes of crystals interpreted to preserve their igneous morphology. The aspect ratio

of the grains was used to describe the euhedral to subhedral habit of a crystal. The aspect ratio is the ratio of the short to the long dimension of the crystal:

- Equant: aspect ratio = less than 1:2,
- Subequant: aspect ratio = 1:2 to 1:3,
- Tabular: aspect ratio = 1:3 to 1:5, and
- Elongate: aspect ratio = more than 1:5.

The description of habits for plagioclase and clinopyroxene groundmass crystals was adapted from ODP Legs 148 and 206 (Shipboard Scientific Party, 1993, 2003):

- Cryptocrystalline aggregates of fibrous crystals (fibrous),
- Comb-shaped or sheaf-like plumose crystals (fibrous),
- Granular-acicular subhedral to anhedral crystals, and
- Prismatic-stubby euhedral to subhedral crystals.

Primary lithology names of volcanic (extrusive and hypabyssal) rocks

Units and subunits were classified on the basis of groundmass texture and primary modal composition. The combined color and texture of the groundmass and the major phenocryst(s) found in hand specimens were used to give a principal lithology name to a given igneous lithologic unit. Three rock categories were defined according to Expedition 351 (Arculus et al., 2015):

- Basalt: a black to dark gray rock with a microcrystalline to cryptocrystalline groundmass that contains plagioclase and pyroxene and/or olivine,
- Andesite: a dark to light gray rock with a microcrystalline groundmass that contains pyroxenes and/or feldspar and/or amphibole but is typically devoid of olivine and quartz, and
- Rhyolite/dacite: a light gray to pale white rock with glassy to cryptocrystalline groundmass that is usually plagioclase to potassium feldspar phyric and sometimes contains quartz ± biotite.

A prefix was applied as a modifier to the primary lithology names to indicate the abundance of phenocrysts:

- Aphyric (<1% phenocrysts),
- Sparsely phyric (1%–5% phenocrysts),
- Moderately phyric (>5%–10% phenocrysts), and
- Highly phyric (>10% phenocrysts).

Moreover, the most abundant phenocryst phase was used as a mineralogical modifier for the primary lithology name of porphyritic rocks, whereas aphyric rocks were not assigned any mineralogical modifier. If present in a given sample, multiple phenocryst minerals were used as modifiers appearing in the order of increasing abundance. For example, in plagioclase-olivine phyric basalt, olivine is the more abundant phenocryst mineral.

Other volcanic rock types distinguished are fragmented rocks made up of either (1) lithic clasts associated with basaltic lava flows (basaltic breccias are defined as matrix-supported breccias with basalt clasts, whereas brecciated basalts are clast supported) or (2) hyaloclastites defined as glass-rich volcanic rocks formed by lava–water/sediment interaction where the lava is shattered into small angular glassy fragments that may be suspended in any sediment present. Breccias not related to flows are described in the Sedimentary tab in DESClogik (see DESC_WKB in **Supplementary material**). Large (>2 cm) volcanic clasts in sediments and sedimentary rocks were classified in the Volcanic tab in DESClogik.

Groundmass

For the textural description of the groundmass of volcanic rocks, we used terms and definitions modified from Expedition 349 (Li et al., 2015). The groundmass of extrusive lithologies was defined as the finer grained matrix enclosing phenocrysts.

For grain size descriptions of the groundmass, we used the following terms:

G = glassy.
cx = cryptocrystalline (<0.1 mm).
μx = microcrystalline (0.1–0.2 mm).
fg = fine grained (>0.2–1 mm).

The following nomenclature was applied to describe the groundmass, predominantly at the microscopic level (MacKenzie et al., 1982; Neuendorf et al., 2005):

- Aphanitic (crystalline but individual grains not discernable with a hand lens),
- Equigranular (similar crystal sizes),
- Glomeroporphyritic (containing clusters of phenocrysts),
- Felty (tightly irregularly interwoven feldspar microlites),
- Holohyaline (100% glass),
- Holocrystalline (100% crystals),
- Hypohyaline (glass is a major component, and crystals are a minor component),
- Inequigranular (different crystal sizes),
- Intergranular (plagioclase crystals surrounded by interstitial granular pyroxene, olivine, and/or oxide minerals),
- Intersertal (plagioclase laths surrounded by interstitial glass or cryptocrystalline material),
- Interstitial (glass, crypto-, or microcrystalline material between coarser grained crystals),
- Ophitic (total inclusion of plagioclase in clinopyroxene),
- Porphyritic (increasing presence of phenocrysts),
- Seriate (continuous range in grain size),
- Spherulitic (fan-like arrangement of divergent microlites),
- Subophitic (partial inclusion of plagioclase in clinopyroxene), and
- Vitrophyric (phenocrysts in a glassy groundmass).

Flow textures are defined below.

Glass groundmass was recorded in terms of the percentage of fresh material:

- Fresh glass (amber in transmitted plane-polarized light and isotropic in transmitted cross-polarized light [XPL]),
- Dark glass (darkness is caused by abundant crystallites; interstitial volcanic glass of basaltic composition is termed tachylite),
- Glass with spherulites (spheroid aggregates of acicular crystals forming a nucleus), and
- Altered glass (partially or completely altered to clay minerals).

Vesicularity

Vesicularity is characterized by the abundance of vesicles:

Nonvesicular = <1% vesicles.
Sparsely vesicular = 1%–5% vesicles.
Moderately vesicular = >5%–20% vesicles.
Highly vesicular = >20% vesicles.

The description of the size, shape, and roundness of vesicles is based on the classification charts from Integrated Ocean Drilling Program Expedition 330 and Expedition 349 (Expedition 330 Scien-

Figure F11. Comparison chart for describing vesicle sphericity and roundness in volcanic rocks, Expeditions 367 and 368. After Expedition 330 Scientists (2012) and Li et al. (2015), modified from Wentworth (1922).

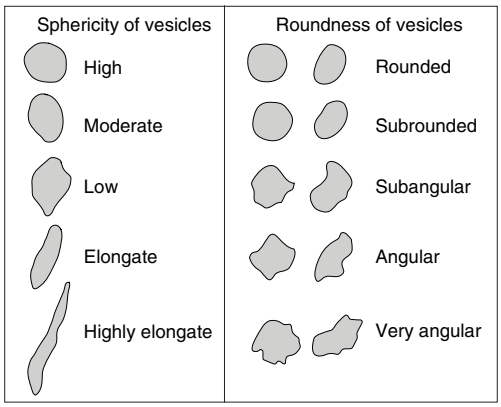

tists, 2012; Li et al., 2015), modified from Wentworth (1922) (Figure F11). An estimate of the percentage abundance of vesicles is included in the VCDs (Figure F9).

Lava flow types

The suffix of the principal lithology name indicates the nature of the volcanic body. We applied the classification scheme used for Expedition 349 (Li et al., 2015), which includes the following types:

- Pillow lava flows: 0.1–1 m in thickness and defined by curved chilled margins, spherulitic textures, glassy margins and/or hyaloclastites, and microcrystalline to cryptocrystalline groundmass grain size, as well as decreasing crystal abundances and sizes (phenocrysts, groundmass) toward the glassy rims.
- Lobate lava flows: 1–2 m thick and formed by the same inflationary process as pillow lavas. In contrast to pillow lavas, they have massive, coarser grained, and sparsely vesicular flow interiors, often with pipe vesicle domains. Vesicle zoning occurs in the upper zones of the inflation unit as a series of vesicle bands, whereas the lower zones contain sparse, poorly defined vesicle banding and/or teardrop-shaped vesicles at the basal chilled zone.
- Sheet lava flows and massive lava flows: defined as more texturally uniform, sparsely vesicular, and characterized by a gradual increase in grain size toward the center of the flow, with sheet lava flows being <3 m thick and massive lava flows being >3 m thick.

For purposes of clarity, pillow lava flows and lobate lava flows are considered to be the same subunit when they occurred together. When pillow lava and lobate lava flows occurred in succession of each other, the igneous lithologic subunit was called a "pillow lava flow." However, if a lobate lava flow had no pillow lava flow components and occurred as a separate flow either within or between massive and sheet flows, the igneous lithologic subunit was considered a "lobate lava flow" and given its own designation. Individual lobate and pillow lava flows were still recorded in DESClogik, but the lithologic subunit was not affected.

Contact types

Margins and contacts of flows were described by observing the features of the chilled sections that indicate a possible hiatus between two flows/pillows. A chilled contact, with or without glass, was recognized by observing the terminal end of the margin for sediment that was not entrenched into the rock but rather baked or cooked onto the rock, indicating a baked or chilled contact with the rock. A chilled margin was recognized through identification of a sudden change in groundmass over a very short distance. Unlike a chilled contact, sediment at the terminal end of the lobe or pillow was not required to determine its nomenclature. Several sections were described as having a chilled contact (typically with glass) in direct contact with sediments with an adjacent (or grading into) chilled margin (typically without glass) where the groundmass was determined to be cryptocrystalline and graded into a microcrystalline texture further up- or downhole. Glassy margins, chilled margins, and contact boundaries were inserted individually for the top and bottom of each section where they could be determined to discriminate individual flows and allow for a greater level of precision in the descriptions.

The following contact types were defined:

- Baked contact: contact with sediments that were baked by proximity of lava.
- Bottom (or top) chilled contact: chilled contact with sediments, with or without glass, in direct contact with sediments.
- Bottom (or top) chilled margin: chilled contact without sediments, without glass, determined by cryptocrystalline groundmass, typically found quenched adjacent to the chilled contact.
- Chilled contact: a contact that cannot be determined to be top or bottom of a flow that has sediment attached, such as a "roller."
- Chilled margin: a chilled contact without sediment or obvious glass that cannot be determined to be top or bottom of a flow.
- Glassy margin: a margin between two pillows that has no sediment and the pillows have fused together. There is no clear indication of the boundary between the pillows as originally deposited.

Alteration

Alteration minerals

Alteration minerals were recorded in DESClogik in the macroscopic template under separate tabs for alteration, veins, and halos. Primary minerals are rock-forming minerals present prior to alteration (e.g., igneous minerals), whereas secondary minerals are related to alteration (e.g., metasomatism and hydrothermal circulation). Secondary minerals found replacing primary minerals and composing vesicle fillings and veins were classified as dominant, second order, and third order.

Identified alteration minerals or mineral mixtures include carbonate (calcite, dolomite, or siderite), chlorite, clay minerals (green clay), epidote (clinozoisite), secondary feldspar (albite), iddingsite, iron hydroxides, iron oxide, mica (sericite), neptunite, silica (jasper, quartz, opal, or hydrated quartz), spinel (magnetite), sulfides (chalcopyrite, covellite, pyrite, or sphalerite), zeolites, or unknown when the mineral could not be identified.

Alteration intensity

Low-temperature and low-pressure (i.e., seafloor) mineralization, veins, and background alteration were defined as alteration. Alteration description includes primary mineralogy, groundmass, phenocryst alteration, and infilling of vesicles and halos. Textures used to define groundmass alteration are patchy, corona, pseudomorphic, and recrystallized.

Levels of background alteration were recorded as follows:

Fresh = <2 vol%.
Slight = 2–10 vol%.
Moderate = >10–50 vol%.
High = >50–95 vol%.
Complete = >95 vol%.

Veins and halos

We used the term "vein" to refer to any later crosscutting feature formed by sediment injection or precipitation from hydrothermal fluids and reserved the word "dike" to describe any later crosscutting feature that formed by introduction of magma. The term "halo" refers to alteration zones around veins or minerals identified by discoloration through change of the primary mineral assemblage. The density (i.e., the percentage of veins within a piece or an interval estimated visually), mineralogy, width, color, vein type (banded, composite, en echelon, haloed, intravenous, and uniform), connectivity (isolated, single, branched, and network), texture (cross-fiber, slip-fiber, massive, polycrystalline, and vuggy), and contacts with host rocks (diffuse, irregular, and sharp) were described, modified from the criteria from Leg 209 (Shipboard Scientific Party, 2004a) (Figures **F11**, **F12**). The length, width, and orientation of representative veins in a section were measured.

Metamorphic petrology

Primary metamorphic lithology names

The nomenclature for metamorphic rocks applied here follows the recommendations of the IUGS Subcommission on the Systematics of Metamorphic Rocks (Schmid et al., 2004). A simple but comprehensive terminology for common metamorphic rocks follows their division into three major groups on the basis of their structure (as seen in hand specimen), giving the rock its principal lithology name: schist, gneiss, or granofels. The terms essentially reflect the degree of fissility or schistosity (i.e., a preferred orientation of tabular to elongate mineral grains or grain aggregates produced by metamorphic processes) shown by the rock. If the schistosity in a metamorphic rock is well developed, the rock has a schistose texture and is termed "schist." If it is poorly developed, the rock has a gneissose texture and is termed "gneiss," and if schistosity is effectively absent, the rock has a granofelsic texture and is termed "granofels." Identified characteristic rock-forming minerals were added as a prefix. One exception to this general terminology was introduced for the specific case of mylonitic metabreccias (i.e., rocks showing an overprinted inherited fabric consisting of clasts within a matrix). To emphasize that the clasts are clearly prekinematic with respect to the mylonitic foliation, they were termed "granofels clasts."

Other standard rock names used to describe metamorphic rocks as a function of mineralogy and texture are as follows:

- Marble: dominated by carbonates (>50% calcite ± Ca-bearing silicate, such as epidote and wollastonite). If the carbonates consist of dolomite, the prefix "dolomite" was added.
- Calc-silicate schist: schistose rock consisting of silicates and carbonates (<50% calcite ± Ca-bearing silicate, such as epidote and wollastonite).

Metamorphic textures

For metamorphic rocks, textural descriptions such as ductile (pervasive, weak, strong, or mylonitic) and brittle deformation (cataclasite or fractures) were used, as well as porphyroblasts, neoblasts, and porphyroclasts. Reaction textures were categorized, including prograde and retrograde metamorphism, coronas, symplectites, and intergrowths.

For deformed rocks, characteristics include (1) fault breccia, defined as any rock composed of angular broken rock fragments held together by mineral cement or a fine-grained matrix; (2) cataclasite, defined as a rock whose mineral grains or aggregates are fractured, rotated, bent, and granulated without accompanying recrystallization; and (3) mylonites, defined as a rock from a shear zone where the dominant deformation mechanism is ductile as solid-state flow and whose mineral grain sizes are often reduced in size by dynamic recrystallization.

Figure F12. Textures used to describe veins, Expeditions 367 and 368. From Li et al. (2015), modified from Expedition 324 Scientists (2010).

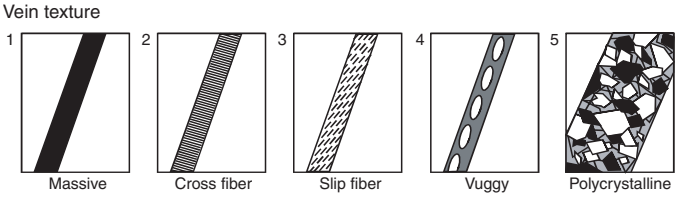

Microscopic (thin section) description

The characterization of thin sections was used to complement and refine macroscopic core observations for igneous and metamorphic rocks (Figure **F13**). All thin section observations were entered into the LIMS database through a special DESClogik thin section template (see DESC_WKB in **Supplementary material**). Thin section descriptions include both primary (igneous) rock-forming minerals (including phenocrysts, groundmass, etc.) and secondary (alteration/metamorphism) mineral phases (in veins, vesicles, groundmass, etc.). Their mineralogy, abundance (modal volume percentages), sizes, shapes, habits, textural relationships, inclusions, alteration color, intensity and style, veins (type and number), and vesicles (type and fillings) were determined, enabling verification of macroscopic observations. The percentages of the original, primary mineral phases, groundmass, and vesicles (Original [%] = Present [%] + Replaced [%]) anP when entering mineral abundances in DESClogik. Moreover, the presence of inclusions, overgrowths, zonations, and accessory minerals were documented.

Extrusive and hypabyssal thin section descriptions in the LIMS database

Thin section descriptions include the following terms:

- Sample domain: if there is more than one domain on the slide, each domain is described separately. For example, a slide that shows a large sedimentary vein (25% of the slide) in a basaltic matrix (75% of the slide) is described as two slides (samples): the first sample domain as "vein" and the second one as "host rock". Other possible domains include clast, glass, halo, lithology, and xenolith.
- Lithology prefix: lithology prefix for the described sample domain.
- Principal lithology: refers only to the lithology of the described sample domain, which includes basalt, brecciated basalt, breccia, and hyaloclastite.

Figure F13. Example of a thin section report for igneous rocks, Expeditions 367 and 368.

THIN SECTION LABEL ID: **367-U1500B-70R-2-W 120/124-TSB-TS_30** Thin section no.: 30
Observer: A. Luna Piece no.:
Unit/subunit: 1b

Thin section summary: Highly plagioclase phyric basalt with remnant olivine that has been mostly destroyed. Plagioclase and CPX are in near pristine condition. Vesciles are filled with calcite, and a green amorphous mineral that is being replaced by a zeolite. A vein bisects the slide from corner to corner and is filled with mostly calcite although there are two types of clay, one a sediment, the other is insitu weathering.

Plane-polarized: 40780541



Cross-polarized: 40780561



Igneous Petrology

Lithology: highly plagioclase phyric basalt **Groundmass grain size (avg.):** microcrystalline
Texture: porphyritic **Grain size distribution:** bimodal

Phenocrysts	Original (%)	Present (%)	Replaced (%)	Size min. (mm)	Size max. (mm)	Shape	Habit	Comments
Plagioclase	20	18	2	0.5	3.25	euhedral	elongate	
Olivine	2	1	1	0.25	0.25	euhedral	euhedral	

Groundmass	Original (%)	Present (%)	Replaced (%)	Size min. (mm)	Size max. (mm)	Shape	Habit	Comments
Plagioclase	34	29	5	0.01	0.5	euhedral	elongate	
Clinopyroxene	30	25	5	0.01	0.1	anhedral	elongate	
Fe-Ti oxide	1	1	0	0.01	0.01	interstitial	subequant	
Glass	0	0	0	N/A	N/A	N/A	N/A	

Alteration

Alteration intensity: slight **Total alteration (%):** **Recrystallization extent:** weak

Alteration mineral	Percent	Comments
Calcium carbonate	1	
Chlorite	2	chlorite appears to be infilling areas that are not vesicles but are voids possibly due to dissolution
Clay, other	5	clay mineral located within the vein crossing the slide
Zeolite	15	zeolites appear to be replacing green chlorite within the vesicles and forming acicular radiating laths
Other		olivine crystals have been replaced by iddingsite

Vesicle abundance (%): 10 **Vesicle shape:** rounded **Vesicle distribution:** moderate
Vesicle min. size (mm): 0.1 **Vesicle max. size (mm):** 1.2 **Vesicle mode size (mm):** 0.75

Vesicle fill composition	Percent
Total vesicle fill	95
Calcium carbonate	25
Zeolite	75

Veins and Halos

Vein type: composite vein **Vein boundary:** diffuse boundary or contact
Avg. thickness (cm): 2 **Vein texture:** polycrystalline

Vein fill composition	Percentage
Calcium carbonate	50
Fe oxide	15

Vein comments: filled with clays from sediment as well as a diagenic clay, calcite and iron oxide

- Average groundmass grain size modal name: grain sizes follow Neuendorf et al. (2005) using the divisions glass, cryptocrystalline, microcrystalline, fine-, medium-, and coarse-grained (as defined in **Primary lithology names of volcanic (extrusive and hypabyssal) rocks**).
- Maximum grain size modal name: analogous to "average groundmass grain size modal name."
- Grain size distribution: bimodal, equigranular, granular, inequigranular, poikilitic, and seriate (see **Texture**).
- Texture: aphanitic, aphyric, granular, glomeroporphyritic, holocrystalline, holohyaline, hypocrystalline, hypohyaline, intergranular, intersertal, interstitial, ophitic, porphyritic, seriate, spherulitic, subophitic, trachytic, and vitrophyric (see definitions above).
- Mineral phenocryst shape: the dominant (>50% of crystals) shape of the olivine (ol), plagioclase (plag), clinopyroxene (cpx), orthopyroxene (opx), and spinel (sp) crystals in euhedral, subhedral, and anhedral shapes.
- Mineral phenocryst habit: the dominant (>50% of crystals) habit of ol, plag, cpx, opx, and sp crystals in elongate, equant, subequant, and tabular habits (see definitions below).
- Plag phenocryst zoning type: continuous, discontinuous, oscillatory, and patchy zonation of the plagioclase crystals.
- Plag phenocryst zoning extent: none, scarce, abundant, and very abundant.
- Cpx and opx phenocryst exsolution: blebs and lamellae.
- Vesicle shape: see Figure **F11**.
- Mineral groundmass shape: for ol, plag, cpx, opx, sp, Fe-Ti oxides and sulfides—euhedral, subhedral, and anhedral.
- Mineral groundmass habit: for ol, plag, cpx, opx, sp, Fe-Ti oxides and sulfides—elongate, equant, subequant, and tabular.

Additional features such as dissolution/resorption textures, sieve textures, and inclusions are noted in the comments section.

Domains in DESClogik define different lithologies or textural domains inside a single lithologic unit (see **Igneous and metamorphic lithologic units and lithostratigraphic units**) within a thin section, including a diverse population of clasts, xenoliths, alteration, mingled magma, vesicular banding, and so on. Thus, thin sections encompassing a single lithologic unit might have multiple domains defined as Domain 1, Domain 2, and so on.

Metamorphic thin section description

Thin section descriptions include stable mineral parageneses, grain sizes, texture, minerals overprinting events (e.g., coronas, overgrowths, and pseudomorphs), secondary mineral assemblages, and estimation of the metamorphic facies. Such information is provided in the thin section summary in DESClogik.

Thin section descriptions include the following terms:

- Sample domain: if there is more than one domain on the slide, each domain is described separately. For example, a slide that shows a large granofels clast (25% of the slide) in an epidote-chlorite schist (75% of the slide) is described as two slides (samples): the first sample domain as "clast" and the second one as "groundmass."
- Lithology prefix: lithology prefix for the described sample domain that includes epidote-chlorite, calc-silicate, and epidote.
- Principal lithology: refers only to the lithology of the described sample domain, which includes schist and granofels.
- Average grain size modal name: grain sizes follow Neuendorf et al. (2005) using the divisions cryptocrystalline, microcrystalline, fine grained, medium grained, and coarse grained.
- Maximum grain size class: maximum grain size encountered in the thin section, which includes fine grained, medium grained, and coarse grained.
- Grain size distribution: bimodal, equigranular, granular, inequigranular.
- Texture: isotropic and foliated.

Chemical analysis

During Expedition 368, a handheld portable X-ray fluorescence spectrometer (pXRF) (Olympus Delta) was used to conduct rapid in situ chemical analysis of solid rock samples (surfaces of the archive core sections and thin section billets). Previous IODP expeditions (e.g., Reagan et al., 2015; Ryan et al., 2017) demonstrated the utility of the pXRF to provide quick chemical characterization of igneous rocks encountered in the core. Such data are invaluable in initial assessments of broad chemical variations and the nature of the igneous rocks and, in conjunction with petrographic observations, in determining unit boundaries. These compositional data also help to target sample selection for postexpedition research.

The Olympus Delta pXRF is a self-contained, energy-dispersive XRF survey instrument. The instrument setup includes several modes (e.g., Geochem and Soils) that apply different correction protocols depending on sample type and geometry. During Expedition 368, we only applied the Geochem mode, which uses two sequential beams of different energy to determine a wide range of elements. The Olympus Delta pXRF cannot determine elements lighter than Mg (such as Na). For quantitative analyses, it is important to have the sample surface parallel to and in direct contact with the face of the instrument analyzer. To ensure a consistent geometry, two different holders were used, depending on the type of sample. Long core pieces (>5 cm) were analyzed directly in the core liner using a specially made, shielded XRF holder that holds the pXRF pointed vertically downward and resting in direct contact with the flat core surface. For smaller rock pieces (<5 cm) and calibration standard powders, the pXRF was pointed vertically upward and supported in a stand, and a special shielded chamber was attached to the front of the instrument. This allowed samples to be placed directly on the face of the analyzer. Analyses were made directly on the archive half of the core. Each measurement took 60 s, and three measurements were implemented on each sample point and averaged for an individual analysis (following the protocol in Reagan et al., 2015). A basaltic powder standard reference material (BHVO-2) was analyzed approximately every 12 samples to monitor data quality and instrument performance. Raw data were exported regularly and saved to the shipboard file directory for easy access. All data processing was done using Microsoft Excel spreadsheets.

To assess how well the correction protocols of the Geochem analysis mode recovered accurate concentration data in igneous rocks, calibration curves were produced on powder mounts of a suite of international standard reference materials (JP-1, BIR-1, BE-N, BCR-2, JB-2, AGV-1, and JA-2). These standards were chosen to cover the range of compositions that were initially anticipated for Expedition 368 (basalts, andesites, and peridotites). The accepted values for these standards were taken from the GEOREM database (**http://georem.mpch-mainz.gwdg.de**). These calibration standards were analyzed at the start (11 May 2017) and end (7 June 2017) of the analysis period (Table **T1**). Drift over this time period is limited (Figure **F14**), so the data from both calibration runs were combined to calculate a single calibration curve for each element.

Table T1. Major element oxides and minor elements in reference solids, Expedition 367/368. **Download table in CSV format.**

Figure F14. Comparison plots of measured pXRF data on a suite of reference materials (JP-1, BIR-1, BE-N, BCR-2, JB-2, AGV-1, and JA-2) compared to accepted values (preferred values from GEOREM database; **http://georem.mpch-mainz.gwdg.de**). Calibration reference materials were analyzed at the start (11 May 2017; open circles) and end (7 June 2017; solid circles) of the analysis period. Drift over this time period is limited relative to the method precision, so a single calibration curve was calculated from these data for each element (solid black line). Calibration curves were then used to apply a secondary correction to the raw data (see text for details). Dashed line = 1:1 trend. (Continued on next page.)

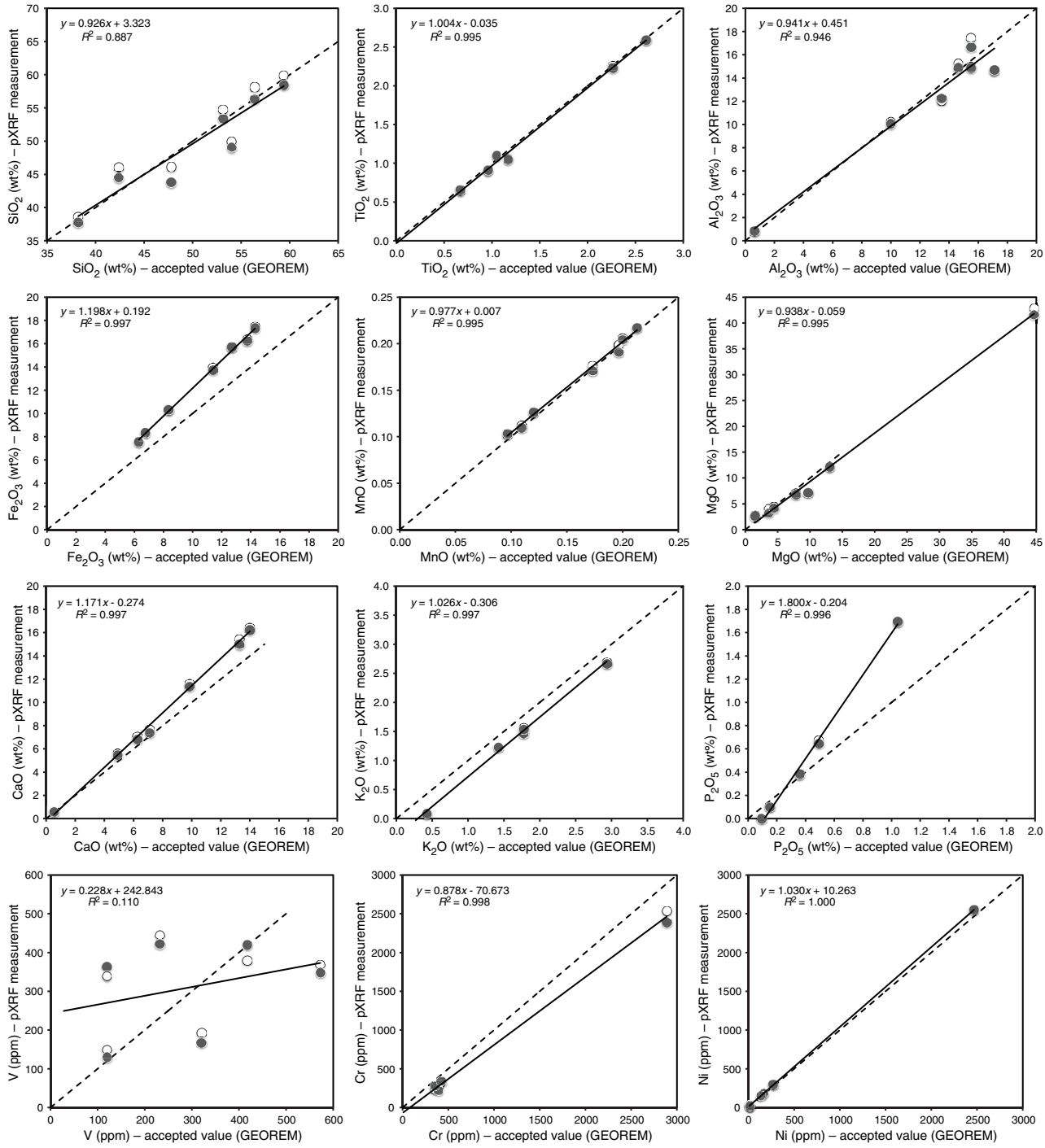

These calibrations were used to correct the raw concentration data output from the pXRF to improve the accuracy relative to the accepted values for the mafic igneous rock standards. Although these secondary calibrations were made on powders of standard materials and expedition data were measured on solid core material, previous studies have shown that this difference in method does not introduce any significant bias within the precision of the pXRF data (e.g., Ryan et al., 2017). Calibration data for 21 elements (Si, Ti, Al, Fe, Mn, Mg, Ca, K, P, V, Cr, Ni, Cu, Zn, Rb, Sr, Y, Zr, Nb, Mo, and Pb) are shown in Figure **F14**. For the remaining 13 elements measured by the pXRF (S, Co, As, Se, Ag, Cd, Sn, Sb, W, Hg, Bi, Th, and U), concentrations in the suite of standards were mostly below the instru-

Figure F14 (continued).

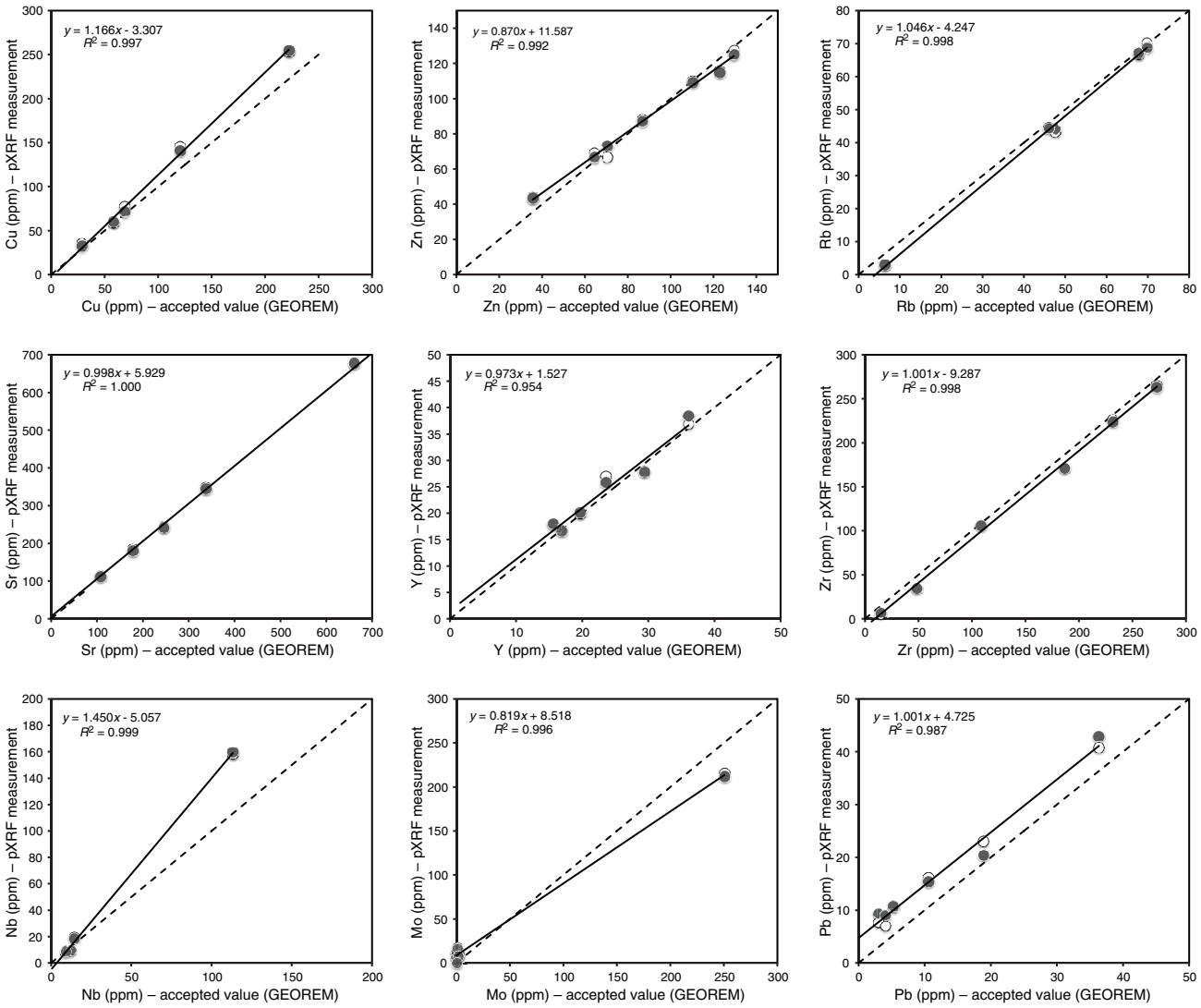

ment detection limits, so these elements were not considered further and are not reported in data tables. Although S is below detection limits in the calibration standards, it is semiquantifiable in rocks containing sulfide minerals, so raw S concentration data are reported when detected in samples. The correlation curves in Figure **F14** are of varying quality, but most give high correlation coefficient values (R^2 > 0.95). In a few cases, the high R^2 values are influenced by one standard with a significantly higher (Mg, Cr, Ni, Nb, and Mo) or lower (Al) concentration. Several elements, such as Fe and Ca, show excellent correlations but with slopes that are significantly different to 1, and for these particular elements, making the secondary calibration correction is critical to get accurate data. Although V is above the instrument detection limits in most samples, a secondary calibration could not be applied because the calibration curve is extremely poor, and V results are presented as raw data only for information.

Results for the 42 replicate analyses of the data quality standard reference material (BHVO-2) are given in Table **T1**. Two of the 42 analyses had anomalously low values (SiO_2 and Al_2O_3), perhaps indicating that the powder mount was not properly centered over the analysis window, and are thus excluded from the data analysis. Reproducibility over the course of analytical work during Expedition 368 was better than ±3% (relative standard deviation) for many elements (Si, Ti, Al, Fe, Mn, Ca, K, Ni, Cu, Zn, Sr, Y, and Zr) and better than ±10% for the remaining elements (Mg, P, Cr, Rb, Nb, and Mo), except for V (11%) and Pb (which is close to the instrument detection limit in BHVO-2). In terms of accuracy, the corrected concentrations of Si, Fe, Mn, Ca, Zn, Sr, Zr, and Nb are within 3% of the accepted values for BHVO-2 and Ti, Mg, K, Cu, and Y are within 5% of the accepted values.

To complement and considerably extend the chemical analysis made by the shipboard pXRF data set, a third-generation, energy-dispersive Avaatech XRF core scanner was used postexpedition. Onshore in situ XRF measurements were implemented for major (beyond the atomic number of Mg) and selected trace elements on Site U1500 and U1502 volcanic rock sections at the JRSO XRF Core Scanning Facility at the Gulf Coast Repository at Texas A&M University. A high standard resolution of 2 cm was applied (partially down to 0.1 cm), whereas a lower resolution had to be chosen in sections with cracks, rubble, and plastic spacers. Three runs with irradiated sample dimensions of 1.2 cm cross-core and 1 cm downcore were performed on each core section along its centerline under

different X-ray excitation conditions (defined by appropriate kV, mA, and filter settings). Several repeated runs were carried out across the entire depth range of the volcanic rock section to monitor data reproducibility. Rock standard mounts were run parallel on a regular basis for quality assurance. As part of the shipboard data set, the produced XRF core scanning data can be retrieved from the LIMS database (**http://web.iodp.tamu.edu/LORE**).

Structural geology

This section outlines the tectonic terminology used in this volume to describe the general architecture of the northern South China Sea margin and the methods and nomenclature applied to document the structural features observed in the sediments and basement rocks recovered during Expeditions 367 and 368. Such features encompass bedding dips, fractures and veins, faults and folds, and fault rocks and shear zones.

Tectonic terminology

Numerous classifications and terminologies have been proposed to describe the nature of hyperextended margins (see Peron-Pinvidic et al. [2013] and Tugend et al. [2015] for recent summaries and discussion). Although hyperextended margins are often equated with magma-poor rifted margins (e.g., Doré and Lundin, 2015), in this volume we simply refer to hyperextension as a process of profound extension (crustal stretching factor ~3 or higher) of the continental crust by normal faulting and low-angle detachments. This tectonic episode may or may not include several generations of faulting. We note that hyperextension of the continental crust and mantle lithosphere may involve different structural domains across the rifted margin. We refer in our study to the continent–ocean transition as the hyperextended domain (also referred to as distal domain) linking moderately thinned continental crust (~15 km thick) to oceanic crust. Oceanic crust in our study is 5–6 km thick crust that accretes in a steady state along a focused spreading ridge. The source of new crust can range from mantle undergoing serpentinization to form a crustal layer to upwelling of asthenospheric mantle that melts by decompression and produces new, "Penrose-type" igneous crust.

Methods

After a core was split and described by sedimentologists or petrologists, we documented structural features observed on the archive half by

- Identifying structural features and classifying their structural types,
- Determining the top and bottom location of structural features in the core,
- Measuring the orientation of a structural feature where applicable,
- Determining the sense of displacement on a structural feature where applicable,
- Determining the temporal relation between structures (especially for crosscutting structures and shear zones), and
- Assessing the role of fluids in deformation processes.

Our methods largely followed those used by structural geologists from Integrated Ocean Drilling Program Expedition 344 and Expedition 349 (Harris et al., 2013; Li et al., 2015). The types of structural measurements and key parameters (either observed or calculated) were recorded on a spreadsheet (Figure **F15**). These data were then input into the LIMS database using DESClogik. Where possible, orientation data were corrected for rotation related to drilling using paleomagnetic declination and inclination information (see **Paleomagnetism**) or by comparison to observed features in the Formation MicroScanner (FMS) log (see **Azimuth correction based on FMS log**).

Graphic symbols and terminology

A predefined set of commonly observed structural features was used in the structural description of cores. The terminology and graphic symbols used are presented in Figures **F16** and **F17**. We identified the following major structural features:

- Joints and fractures: brittle failure with no displacement and no secondary infill minerals. Breaks clearly resulting from drilling were logged separately as drilling-induced fractures in the Drilling disturbance spreadsheet in DESClogik.

Figure F15. Example structural geology observation sheet, Expeditions 367 and 368.

Site:U….

Core	Section	struct ID	top of struct	bottom of struct	Core face app.		2nd app. Dip		Calculated Orientation			P-mag pole		Corrected Orientation			note
					az	dip	az	dip	dip dir	strike	dip	Dec	Inc	dip dir	strike	dip	

Figure F16. Symbols and nomenclature used for visual core description, Expeditions 367 and 368.

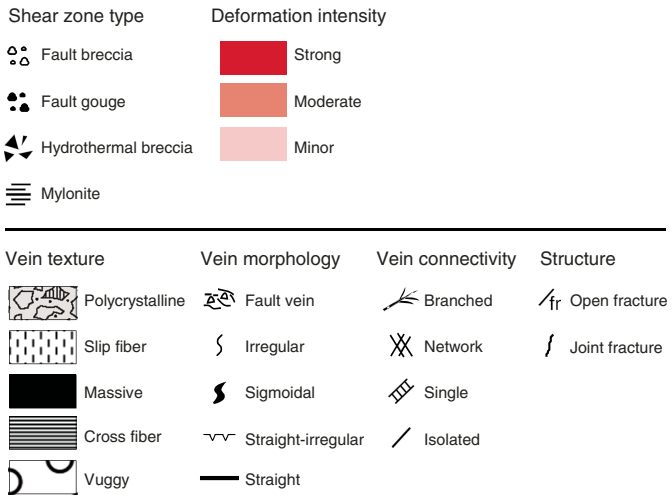

Figure F17. Vein description scheme used during Expeditions 367 and 368, modified after Expedition 324 Scientists (2010).

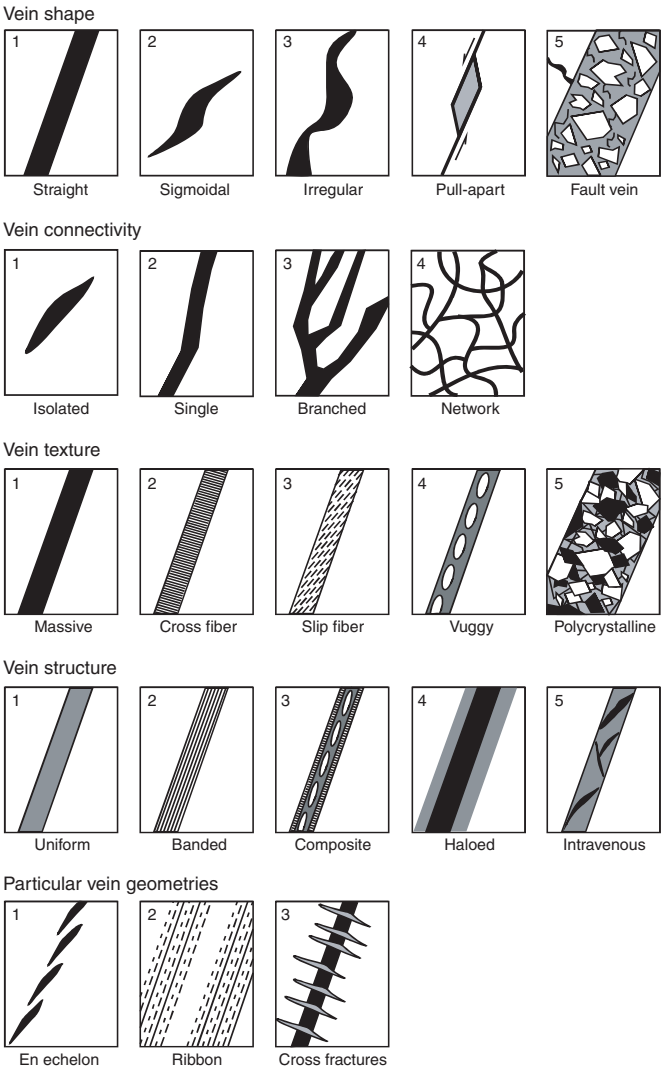

- Veins: fractures filled with secondary minerals. Veins were described in both the Structure and Veins/halos tabs in DESCLogik.
- Fault rocks: brittlely deformed rocks such as fault breccia and fault gouge. For sake of simplicity in this volume, the term "fault breccia" is defined as a clast-supported fault rock with angular clasts, and the term "fault gouge" is defined as a matrix-supported fault rock with rounded clasts.
- Hydrothermal breccia: fluid-assisted deformation leading to the fragmentation and brecciation of the rocks.
- Shear zones: zones affected by ductile crystal-plastic deformation and surrounded by less deformed rocks.
- Sedimentary bedding: layering of sediments and sedimentary rocks.
- Folds: folded sedimentary or basement rock layers.
- Igneous contacts: material contacts of extrusive or intrusive igneous rocks.
- Magmatic fabrics: magmatic foliations defined by the preferred orientations of primary minerals with no evidence of crystal-plastic deformation.

Structural observation and description

Structural features were described from the top to the bottom of each section of the core. For fractures, we examined and measured the following parameters:

- Location: where a fracture occurs in a core, measured in centimeters from the top of the section.
- Morphology and structure: morphological shape of a fracture (e.g., straight, curved, banded, irregular, composite, isolated, single or branched).
- Displacement: lateral offset and/or opening of a fracture measured in centimeters; a closed fracture with no lateral offset is recorded as 0 cm of displacement.
- Orientation: dip angle, strike, and dip direction of a fracture measured in degrees; where applicable, reorientation of a fracture to geographic coordinates (i.e., relative to true north) was done to determine the real dip direction (see **Orientation measurements and correction**).
- Frequency: occurrence frequency of fractures per section.
- Types: type of deformation of a fracture (e.g., normal, reverse, dextral, sinistral displacement, or a combination of the above).

For veins, we examined and measured several parameters:

- Location: where a vein occurs in a core, measured in centimeters from the top of the section.
- Morphology: main morphological characteristics of a vein such as shape, connectivity, texture, structure, and particular vein geometries (Figure **F17**).
- Orientation: dip angle and dipping direction of a vein.
- Frequency: occurrence frequency of veins per section.
- Mineral infill and alteration: these features are recorded as described by petrologists.

For fault rocks, hydrothermal breccias, and shear zones, we examined and measured the following parameters:

- Location: interval where a shear zone occurs in a core, measured in centimeters from the top of the section.
- Nature: type of fault rock, hydrothermal breccia, or shear zone, including fault gouge, fault breccia, cataclasite and mylonite.
- Morphology: morphological shape of the deformed zone and of the clasts.

- Orientation: dip angle and dip direction of the preferred orientation of the clasts, where applicable.
- Deformation intensity: characterization of the deformation intensity including foliation development.
- Frequency: occurrence frequency of shear zones per section.
- Mineral and alteration: matrix and clasts described by petrologists.

For sedimentary bedding, we described the following parameters:

- Location: where a nonsubhorizontal bedding occurs in a core (dip > 5°), measured in centimeters from the top of the section.
- Type of contacts: type of sedimentary contact boundary.
- Orientation: dip angle, strike, and dip direction of sedimentary bedding.

For folds, we described the following parameters:

- Location: where a fold contact occurs in a core, measured in centimeters from the top of the section.
- Type: type of fold.
- Frequency: occurrence frequency of fold axis per section.

For igneous contacts, we described the following parameters:

- Location: where an igneous contact occurs in a core, measured in centimeters from the top of the section.
- Type of contacts: type of igneous contact boundary.
- Orientation: dip angle and dip direction of an igneous contact.
- Frequency: occurrence frequency of igneous contacts per section.
- Mineral infill and alteration: as described by petrologists.

For magmatic fabrics, we measured the following parameters:

- Location: where a magmatic fabric feature occurs in a core, measured in centimeters from the top of the section.
- Morphology: morphological shape of a magmatic fabric feature.
- Orientation: dip angle, strike and dip direction of a magmatic fabric feature.
- Frequency: occurrence frequency of magmatic fabrics per section. The occurrence frequency of a structure per section is normalized on a 10 cm section.

Orientation measurements and correction

Orientation measurements

We used a plastic goniometer for orientation measurements. For sealed structures, we wrapped a transparent plastic protractor template around the core to determine the true dip (Figure **F18**). Orientations of planar and linear features in a core section were determined relative to the core reference frame (Figure **F19**). The vertical axis of the core reference frame is aligned with the upcore direction of the core section, whereas the double line marked on the core liner is defined as 180° in the cross-sectional plane perpendicular to the core vertical axis.

To determine the orientation of a planar structural element (shaded plane in Figure **F19**), two apparent dips of the element were measured in the core reference frame. The first apparent dip measures the intersection angle between the planar structural element and the split face of the core (β_1 in Figure **F19**); it is determined by measuring the dip direction and angle of the planar structural element in the core reference frame. A planar structural element could have a trend of 90° or 270° and a plunge angle ranging from 0° to 90°. The second apparent dip measures the intersection angle between the central line of the planar structural element and the split face of the core (β_2 in Figure **F19**). In most cases, this was a plane either parallel or perpendicular to the core axis. In the former case, the apparent dip would trend 0° or 180° with a plunge angle ranging from 0° to 90°; in the latter case, the trend would range from 0° to 360° with a plunge angle of 0°.

A linear feature observed in the surface of a split core is often associated with a planar structural element (e.g., a fault plane) in the core; the orientation of the planar structural element is determined by measuring either the rake (or pitch) of the associated plane or the

Figure F18. Goniometer and plastic protractor template used to measure dip and dip direction of structures, Expeditions 367 and 368.



Figure F19. Core reference frame and coordinates used in orientation data calculation, Expeditions 367 and 368. (α_1, β_1) and (α_2, β_2) = azimuths and apparent dips of traces of the plane on two sections, V_1 and V_2 = unit vectors parallel to traces of the plane on two sections, V_n = unit vector normal to plane.

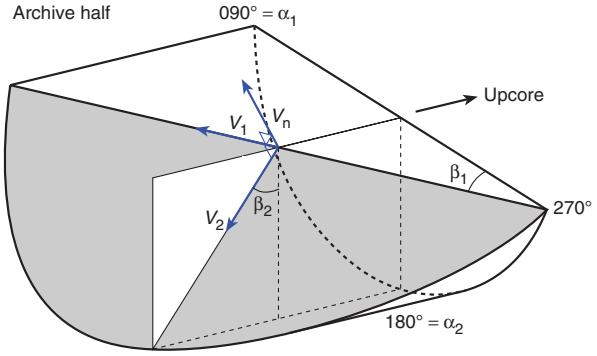

trend and plunge of the planar element in the core reference frame. All measured data were manually typed into the log sheet together with the measured depths in the core section and descriptive information (Figure **F15**).

Plane orientation calculation

For a planar structural element (e.g., a bedding or fault plane), two apparent dips on two different surfaces (e.g., one being the split core surface, which is east–west vertical, and the other being a horizontal or north–south vertical surface) were measured in the core reference frame. The two apparent dips are the azimuth (measured clockwise from north, looking down) and plunge. An *x, y, z* coordinate system was defined in such a way that the positive *x*-, *y*-, and *z*-directions coincide with north, east, and vertical downward, respectively. If the azimuths and plunges of the two apparent dips are given as (α_1, β_1) and (α_2, β_2), respectively, as in Figure **F19**, the unit vectors representing these two lines, v_1 and v_2, are given by the following expression:

$$v_1 = \begin{pmatrix} l_1 \\ m_1 \\ n_1 \end{pmatrix} = \begin{pmatrix} \cos\alpha_1 \cos\beta_1 \\ \sin\alpha_1 \cos\beta_1 \\ \sin\beta_1 \end{pmatrix} \text{ and}$$

$$v_2 = \begin{pmatrix} l_2 \\ m_2 \\ n_2 \end{pmatrix} = \begin{pmatrix} \cos\alpha_2 \cos\beta_2 \\ \sin\alpha_2 \sin\beta_2 \\ \sin\beta_2 \end{pmatrix}.$$

For any plane, the direction of the normal to the plane can be found by taking the cross product of two (nonparallel) vectors that lie within the plane. Using the above equations for v_1 and v_2, therefore, the unit vector normal to plane v_n (Figure **F20**) is defined as follows:

$$v_n = \begin{pmatrix} l_n \\ m_n \\ n_n \end{pmatrix} = \frac{v_1 \times v_2}{|v_1 \times v_2|}, \text{ where}$$

$$v_1 \times v_2 = \begin{pmatrix} \begin{vmatrix} m_1 m_2 \\ n_1 n_2 \end{vmatrix} \\ \begin{vmatrix} n_1 n_2 \\ l_1 l_2 \end{vmatrix} \\ \begin{vmatrix} l_1 l_2 \\ m_1 m_2 \end{vmatrix} \end{pmatrix} = \begin{pmatrix} m_1 n_2 - m_2 n_1 \\ n_1 l_2 - n_2 l_1 \\ l_1 m_2 - l_2 m_1 \end{pmatrix}.$$

The azimuth α_n and plunge β_n of the vector v_n are given by

$$\alpha_n = \tan^{-1}\left(\frac{m_n}{l_n}\right) \text{ and}$$

$$\beta_n = \sin^{-1} n_n.$$

Figure F20. Dip direction (α_d), right-hand rule strike (α_s), and dip (β) of a plane deduced from its normal azimuth (α_n) and dip (β_n), Expeditions 367 and 368. V_n = unit vector normal to plane. A. $\beta_n < 0°$. B. $\beta_n \geq 0°$.

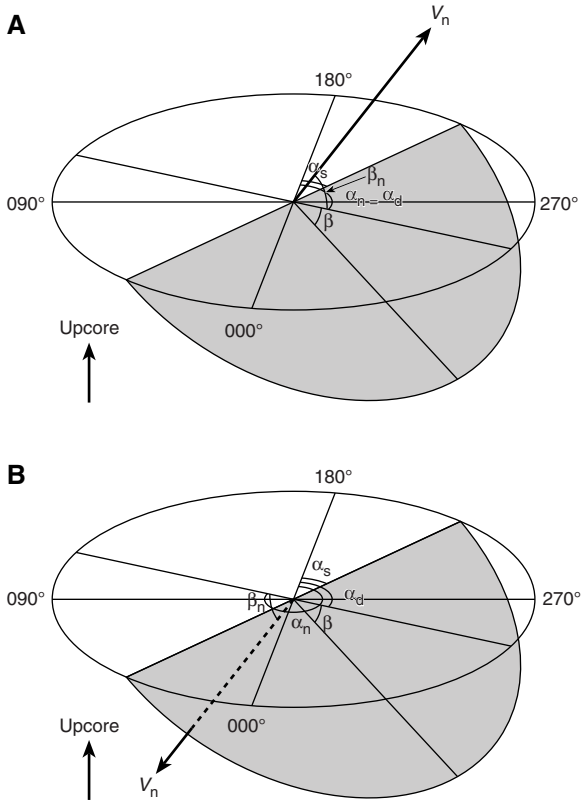

The dip direction α_d and dip angle β of this plane are $\alpha_d = \alpha_n$ and $\beta = 90° + \beta_n$, respectively, when $\beta_n < 0°$ and $\alpha_d = \alpha_n \pm 180°$ and $\beta = 90° - \beta_n$, respectively, when $\beta_n \geq 0°$. The strike of this plane, α_s, according to the right-hand rule is then given by $\alpha_s = \alpha_d - 90°$ (Figure **F20**).

Azimuth correction based on paleomagnetic data

Provided that a core is vertical, its magnetization is primary, the core was magnetized in the Northern Hemisphere, and its bedding is horizontal, its paleomagnetic declination α_p indicates the magnetic north direction when its inclination $\beta_p \geq 0°$ (Figure **F21**); in contrast, the angle α_p indicates the magnetic south direction when $\beta_p < 0°$. The dip direction and strike of a planar structural element in the geographic reference frame, α_d^* and α_s^*, are therefore $\alpha_d^* = \alpha_p - \alpha_d$ and $\alpha_s^* = \alpha_p - \alpha_s$ when $\beta_p \geq 0°$ or $\alpha_d^* = 180° + \alpha_p - \alpha_d$ and $\alpha_s^* = 180° + \alpha_p - \alpha_s$ when $\beta_p < 0°$.

If a core section was complete and continuous, one paleomagnetism sample per section (1.5 m) was deemed sufficient to determine the paleomagnetic orientation of the core section. If the core was discontinuous, one paleomagnetism sample for each subsection of the core that was continuous and structurally important was required. Paleomagnetism samples were taken as cubic or cylindrical samples close to a planar structural element of interest (usually within 5 cm) and from a coherent core interval that included the structural element of interest. In general, we avoided core fragments that were so small that potential spinning during drilling might cause significant deviation from the core axis (e.g., fragments of brecciated segments). This procedure was carefully followed, but for different reasons at each site we failed to reorient our structural measurements with respect to the paleomagnetic data.

Figure F21. Azimuth correction based on paleomagnetic data, Expeditions 367 and 368. α_p = paleomagnetic declination, α_d and α_s = dip direction and right-hand rule strike of a plane. A. $\beta_p \geq 0°$. B. $\beta_p < 0°$.

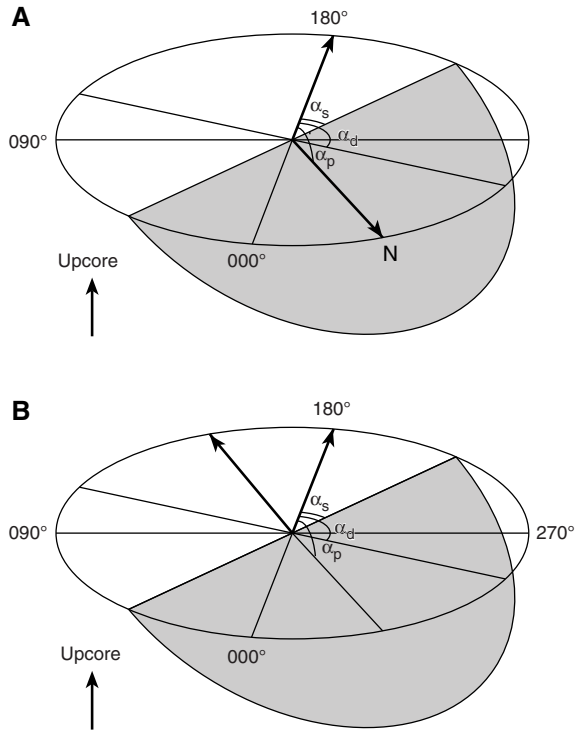

Azimuth correction based on FMS log

If an FMS log is available for the section of the drill hole that contains the core, there may be distinctive features that can be correlated from the FMS log to the core, such as bedding, fractures, folds, veins, stratification, and bioturbation. In this case, the core can be oriented with respect to geographic north. However, this orientation has to be done after the FMS log is obtained after all the cores in the hole have been collected.

Thin section description

Following ODP Leg 210 (the most recent expedition to sample basement rocks similar to those of the current expeditions), thin sections of sedimentary, igneous, and metamorphic rocks recovered were examined to

- Document each type of macroscopic deformation structure in a systematic and quantitative way,
- Characterize the microstructure of the rocks,
- Provide information on the kinematics of ductile and brittle deformation,
- Assess the role of fluids in contributing to deformation, and
- Document major structural zones and downhole variations.

For the description of microstructures, we applied the terminology of Passchier and Trouw (2005). Shipboard thin sections were oriented, except when they were made from small pieces whose orientation with respect to the rest of the core was unknown. Orientation was in the core reference frame and was marked on each thin section by an arrow pointing upward and a short tick pointing west from the base of the arrow. Marking two directions is necessary to achieve complete orientation of thin sections, which are cut parallel to the split surface of the core.

Biostratigraphy

During Expeditions 367 and 368, calcareous nannofossils, planktonic and benthic foraminifers, diatoms, and ostracods were studied in core catcher samples. Samples from core sections were examined when a more refined age determination was necessary and when time permitted. Biostratigraphic events, mainly the first appearance datum (FAD or base) and last appearance datum (LAD or top) of the age-diagnostic species are tied to the geomagnetic polarity timescale (GPTS) of Gradstein et al. (2012) (Figure **F22**).

Calcareous nannofossils

Calcareous nannofossil zonation was based on the schemes of Okada and Bukry (1980) and Martini (1971). Calibrated ages for bioevents are from Gradstein et al. (2012) and given in Table **T2**. The timescale of Gradstein et al. (2012) assigns the Pleistocene/Pliocene boundary between the Gelasian and Piacenzian stages (2.59 Ma), the Pliocene/Miocene boundary between the Zanclean and Messinian stages (5.33 Ma), the late/middle Miocene boundary between the Tortonian and Serravalian stages (11.63 Ma), the middle/early Miocene boundary between the Langhian and Burdigalian stages (15.97 Ma), the Miocene/Oligocene boundary between the Aquitanian and Chattian stages (23.03 Ma), and the Oligocene/Eocene boundary between the Rupelian and Priabonian stages (33.89 Ma). For calcareous nannofossil biostratigraphy, the Pleistocene/Pliocene boundary now falls within Zone NN16 (Martini, 1971) between the LADs of *Discoaster surculus* (2.49 Ma) and *Discoaster tamalis* (2.8 Ma). The Pliocene/Miocene boundary falls within Zone NN12 between the LAD of *Triquetrorhabdulus rugosus* (5.28 Ma) and the FAD of *Ceratolithus larrymayeri* (5.34 Ma); however, *C. larrymayeri* was not noted in our samples, so we used the FAD of *Ceratolithus acutus* (5.35 Ma) as an alternative event. The late/middle Miocene boundary is placed within Zone NN7 between the LAD of common *Discoaster kugleri* (11.58 Ma) and the FAD of common *D. kugleri* (11.90 Ma). The middle/early Miocene boundary falls within Zone NN4 between the LADs of *Helicosphaera ampliaperta* (14.91 Ma) and *Sphenolithus belemnos* (17.95 Ma). The Miocene/Oligocene boundary is placed within Zone NN1 between the FAD of *Discoaster druggii* (22.82 Ma) and the LAD of *Reticulofenestra bisecta* (>10 µm; 23.13 Ma). The Oligocene/Eocene boundary is placed within Zone NP21 between the LADs of *Coccolithus formosus* (32.92 Ma) and *Discoaster saipanensis* (34.44 Ma). In this study, the subdivision of these geologic time boundaries was mostly based on recognition of these nannofossil bioevents.

Several species of the genus *Gephyrocapsa*, which are commonly used as Pleistocene biostratigraphic markers, often show a great range of variation in sizes and other morphological features, causing problems in identification (e.g., Samtleben, 1980; Su, 1996; Bollmann, 1997). Size-defined morphological groups of this genus (Young, 1998; Maiorano and Marino, 2004; Lourens et al., 2004; Raffi et al., 2006) were used as event markers during shipboard study, including *Gephyrocapsa* sp. 3, *Gephyrocapsa* spp. medium I (≥4 µm), large *Gephyrocapsa* spp. (≥5.5 µm), *Gephyrocapsa* spp. medium II (≥4 µm; bmG event), and small *Gephyrocapsa* spp. (<3.5 µm).

Several *Reticulofenestra* species with different coccolith and central opening sizes have been used as Neogene and Quaternary biostratigraphic markers; however, these parameters show considerable variations within and between "species," making species differentiation difficult (e.g., Su, 1996; Young, 1998). In this study, we followed the definition of *Reticulofenestra pseudoumbilicus* by

Figure F22. Calcareous nannofossil, diatom, and planktonic foraminiferal events and scaled ages (Gradstein et al., 2012), Expeditions 367 and 368. B = base, Ba = base acme, Bc = base common, T = top, Ta = top acme, Tc = top common, Tr = top regular, X = crossover in abundance. This figure is available in an **oversized format**.

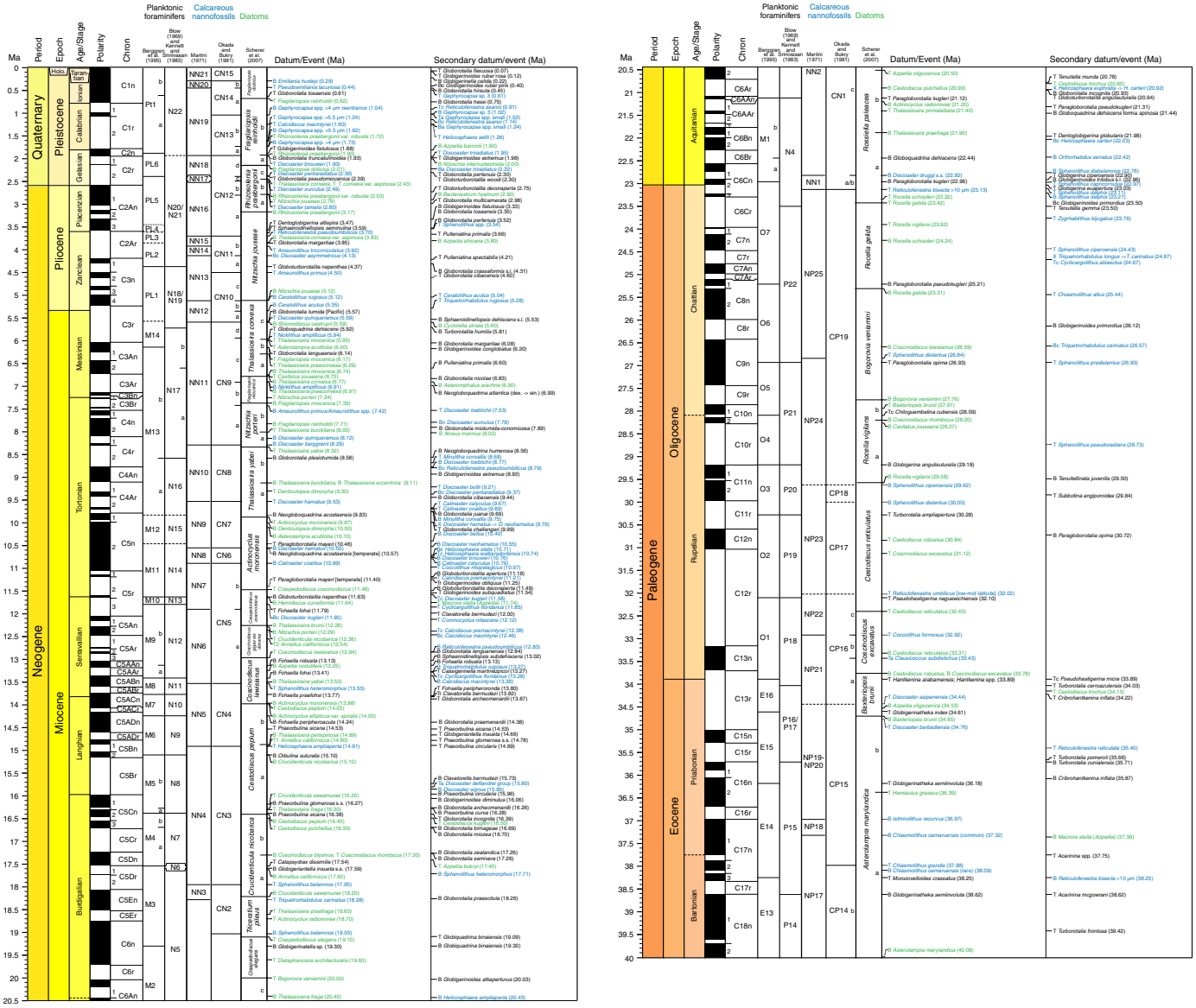

Young (1998) as having a coccolith length >7 µm (similar to the size of its holotype), especially for specimens from its uppermost range in the early Pliocene. We distinguished *Reticulofenestra asanoi* from the similarly sized *Pseudoemiliania lacunosa* by the absence of slits on the shield (Su, 1996). In addition, we further distinguished three *Reticulofenestra* morphotypes including *Reticulofenestra ampla* (5~7 µm, with central opening), *R. bisecta* (5~10 µm, with a solid central plug), and *R. bisecta* (>10 µm, with a solid central plug) following Young et al. (2014).

The LAD of *Sphenolithus* spp. (3.54 Ma) in Pliocene Zone NN16 was based on the LADs of *Sphenolithus abies* and *Sphenolithus neoabies* according to Raffi et al. (2006). Species concepts for other taxa mainly follow those of Perch-Nielsen (1985) and Bown (1998).

Methods

Calcareous nannofossil samples were prepared using standard smear slide techniques. For samples from sandy sediments, suspended aliquots of the raw sample were analyzed. Samples were examined with a Zeiss microscope under XPL and plane-transmitted or phase contrast light at 1000× to 2000× magnification. A Hitachi TM3000 tabletop scanning electron microscope (SEM) was used to confirm the presence of small forms such as *Emiliania huxleyi*, an important marker for the latest Pleistocene–Holocene. Preservation of nannofossils was defined as follows:

VG = very good (no evidence of dissolution and/or overgrowth).
G = good (slight dissolution and/or overgrowth; specimens are identifiable to the species level).
M = moderate (some etching and/or overgrowth; most specimens are identifiable to the species level).
P = poor (severely etched or overgrowth; most specimens cannot be identified at the species and/or generic level).

Table T2. Calcareous nannofossil events and scaled ages (GTS2012; Gradstein et al., 2012), Expeditions 367 and 368. T = top/last appearance datum, B = base/first appearance datum. Bold text indicates age-diagnostic datum. (Continued on next page.) **Download table in CSV format.**

GTS2012 chrono-stratigraphy	Standard tropical–subtropical biozone (biochron): CN zones (Okada and Bukry, 1980)	Standard tropical–subtropical biozone (biochron): NN zones (Martini, 1971)	Biohorizon (datum)	GTS2012 age (Ma)
0.126 Ma				
Ionian (middle Pleistocene)	**CN15/CN14b**	**NN21/NN20**	**B *Emiliania huxleyi***	**0.29**
	CN14b/CN14a	**NN20/NN19**	**T *Pseudoemiliania lacunosa***	**0.44**
	CN14a	NN19	T *Gephyrocapsa* sp. 3	0.61
0.781 Ma				
Calabrian	CN14a	NN19	T *Reticulofenestra asanoi* (common)	0.91
			T small *Gephyrocapsa* spp. dominance	1.02
			B *Gephyrocapsa* sp. 3	1.02
	CN14a/CN13b		B medium (>4 µm) *Gephyrocaps*a spp. reentrance (reenG event)	1.04
	CN13b		B *Reticulofenestra asanoi* (common)	1.14
			T large (>5.5 µm) *Gephyrocapsa* spp.	1.24
			B small *Gephyrocapsa* spp. dominance	1.24
			T *Helicosphaera sellii*	(1.26)
			T *Calcidiscus macintyrei*	1.60
			B large (>5.5 µm) *Gephyrocapsa* spp.	1.62
	CN13b/CN13a		B medium (>4 µm) *Gephyrocapsa* spp. (=bmG event)	1.73
1.806 Ma	CN13a			
Gelasian	**CN13a/CN12d**	**NN19/NN18**	**T *Discoaster brouweri***	**1.93**
	CN12d	NN18	T *Discoaster triradiatus*	1.95
			B acme *Discoaster triradiatus*	2.22
	CN12d/CN12c	**NN18/NN17**	**T *Discoaster pentaradiatus***	**2.39**
	CN12c/CN12b	**NN17/NN16**	**T *Discoaster surculus***	**2.49**
2.588 Ma	CN12b	NN16		
Piacenzian	**CN12b/CN12a**		T *Discoaster tamalis* (subtop)	2.80
	CN12a		T *Sphenolithus* spp. (subtop)	3.54
3.600 Ma				
Zanclean	**CN12a/CN11b**	**NN16/NN15**	**T *Reticulofenestra pseudoumbilicus***	**3.70**
	CN11b	**NN15/NN14**	**T *Amaurolithus tricorniculatus***	**(3.92)**
	CN11b/CN11a	**NN14/NN13**	**B common *Discoaster asymmetricus***	**4.13**
	CN11a/CN10c	NN13	T *Amaurolithus primus*	4.50
			B *Reticulofenestra pseudoumbilica, Discoaster ovata* (subbottom)	4.91
			T *Ceratolithus acutus*	5.04
	CN10c/CN10b	**NN13/NN12**	**B *Ceratolithus rugosus***	**5.12**
	CN10b	NN12	T *Triquetrorhabdulus rugosus*	5.28
5.333 Ma				
	CN10b/CN10a		B *Ceratolithus acutus*	5.35
	CN10a/CN9d	**NN12/NN11**	**T *Discoaster quinqueramus***	**5.59**
	CN9d/CN9c	NN11	T *Nicklithus amplificus*	5.94
	CN9c/CN9b		B *Nicklithus amplificus*	6.91
7.246 Ma	CN9b			
Tortonian	**CN9b/CN9a**		B *Amaurolithus primus, Amaurolithus* spp.	7.42
	CN9a		T *Discoaster loeblichii*	7.53
			B common *Discoaster surculus*	7.79
			B *Discoaster quinqueramus*	(8.12)
	CN9a/CN8	**NN11/NN10**	**B *Discoaster berggrenii***	**8.29**
	CN8	NN10	T *Minylitha convallis*	8.68
			B *Discoaster loeblichii*	8.77
			B paracme *Reticulofenestra pseudoumbilicus*	8.79
			T *Discoaster bollii*	9.21
			B common *Discoaster pentaradiatus*	9.37
	CN8/CN7	**NN10/NN9**	**T *Discoaster hamatus***	**9.53**
	CN7	NN9	T *Catinaster calyculus*	9.67
			T *Catinaster coalitus*	9.69
			B *Minylitha convallis*	9.75
			B *Discoaster bellus*	10.40
			B *Discoaster neohamatus*	10.52
	CN7/CN6	**NN9/NN8**	**B *Discoaster hamatus***	**10.55**
	CN6	NN8	B common *Helicosphaera stalis*	10.71
			T common *Helicosphaera walbersdorfensis*	10.74
			B *Discoaster brouweri*	10.76
			B *Catinaster calyculus*	10.79
	CN6/CN5b	**NN8/NN7**	**B *Catinaster coalitus***	**10.89**
	CN5b	NN7	T *Coccolithus miopelagicus*	10.97
			T *Calcidiscus premacintyrei*	11.21
			T common *Discoaster kugleri*	11.58

Table T2 (continued).

GTS2012 chrono-stratigraphy	Standard tropical–subtropical biozone (biochron): CN zones (Okada and Bukry, 1980)	Standard tropical–subtropical biozone (biochron): NN zones (Martini, 1971)	Biohorizon (datum)	GTS2012 age (Ma)
11.608 Ma	CN5b	NN7		
Serravallian			T *Cyclicargolithus floridanus*	11.85
	CN5b/CN5a	**NN7/NN6**	**B common *Discoaster kugleri***	**11.90**
	CN5a	NN6	T *Coronocyclus nitescens*	12.12
			T regular *Calcidiscus premacintyrei*	12.38
			B common *Calcidiscus macintyrei*	12.46
			B *Reticulofenestra pseudoumbilicus*	12.83
			B *Triquetrorhabdulus rugosus*	13.27
			T common *Cyclicargolithus floridanus*	13.28
			B *Calcidiscus macintyrei*	13.36
	CN5a/CN4	**NN6/NN5**	**T *Sphenolithus heteromorphus***	**13.53**
13.82 Ma	CN4	NN5		
Langhian	**CN4/CN3**	**NN5/NN4**	**T *Helicosphaera ampliaperta***	**14.91**
	CN3	NN4	T abundant *Discoaster deflandrei* group	15.80
			B *Discoaster signus*	15.85
15.97 Ma				
Burdigalian			B *Sphenolithus heteromorphus*	17.71
	CN3/CN2	**NN4/NN3**	**T *Sphenolithus belemnos***	**17.95**
	CN2/CN1c	**NN3/NN2**	**T *Triquetrorhabdulus carinatus***	**18.28**
	CN1c	NN2	B *Sphenolithus belemnos*	19.03
			B *Helicosphaera ampliaperta*	20.43
(20.44 Ma)				
Aquitanian			B common *Helicosphaera carteri*	22.03
			B *Orthorhabdus serratus*	22.42
			B *Sphenolithus disbelemnos*	22.76
	CN1c/CN1a-b	**NN2/NN1**	**B *Discoaster druggi* (sensu stricto)**	**22.82**
	CN1a–CN1b	NN1	T *Sphenolithus capricornutus*	22.97
23.03 Ma				
Chattian	CN1a–CN1b	NN1	T *Sphenolithus delphix*	23.11
	CN1a-b/CP19b	**NN1/NP25**	**T *Reticulofenestra bisecta* (>10 µm)**	**23.13**
	CP19b	NP25	B *Sphenolithus delphix*	23.21
			T *Zygrhablithus bijugatus*	23.76
			T *Sphenolithus ciperoensis*	24.43
			T *Cyclicargolithus abisectus* (common)	24.67
			T *Chiasmolithus altus*	25.44
			B *Triquetrorhabdulus carinatus* (common)	26.57
	CP19b/CP19a	**NP25/NP24**	**T *Sphenolithus distentus***	**26.84**
	CP19a	NP24	T *Sphenolithus predistentus*	26.93
(28.09)				
Rupelian			T *Sphenolithus pseudoradians*	28.73
	CP19a/CP18	**NP24/NP23**	**B *Sphenolithus ciperoensis***	**29.62**
	CP18/CP17	NP23	B *Sphenolithus distentus*	30.00
	CP17/CP16c	**NP23/NP22**	**T *Reticulofenestra umbilicus* (low-mid lat.)**	**32.02**
	CP16c/CP16b	**NP22/NP21**	**T *Coccolithus formosus***	**32.92**
	CP16b/CP16a	NP21	T *Clausicoccus subdistichus* (top of acme)	33.43
33.89	CP16a			
Priabonian	**CP16a/CP15**	**NP21/NP20–NP19**	**T *Discoaster saipanensis***	**34.44**
	CP15	NP20–NN19	T *Discoaster barbadiensis*	34.76
			T *Reticulofenestra reticulata*	35.40
		NP20–NP19/NP18	**B *Isthmolithus recurvus***	**36.97**
		NP18/NP17	**B *Chiasmolithus oamaruensis* (common)**	**37.32**
(37.75)		NP17		
Bartonian	**CP15/CP14b**		T *Chiasmolithus grandis*	37.98
	CP14b		B *Chiasmolithus oamaruensis* (rare)	38.09
			B *Reticulofenestra bisecta* (>10 µm)	38.25
	CP14b/CP14a	**NP17/NP16**	**T *Chiasmolithus solitus***	**40.40**

The relative abundance of calcareous nannofossils within the sediment was visually estimated at 1000× magnification by referring to the particle abundance charts in Rothwell (1989) and reported using the following abundance categories:

D = dominant (>90% of sediment particles).
A = abundant (>50%–90% of sediment particles).
C = common (>10%–50% of sediment particles).
F = few (1%–10% of sediment particles).
R = rare (<1% of sediment particles).
B = barren (no nannofossils present in 100 FOV).

The relative abundance of individual calcareous nannofossil species or taxa groups was estimated at 1000× magnification and defined as follows:

D = dominant (>50%, or 100 specimens/FOV).
A = abundant (10%–50%, or 10–100 specimens/FOV).
C = common (1%–10%, or 1–10 specimens/FOV).
F = few (0.1%–1%, or 1 specimen/1–10 FOV).
R = rare (<0.1%, or <1 specimen/10 FOV).

Foraminifers

Planktonic foraminifers

The planktonic foraminiferal zonation schemes of Blow (1969, 1979) and Berggren et al. (1995) as modified by Wade et al. (2011) were used in this study. Calibrated ages for bioevents are from Gradstein et al. (2012) (Table **T3**). We also adopted the use of the LAD (0.12 Ma; Thompson et al., 1979) and FAD (1.16 Ma; Li et al., 2005) of *Globigerinoides ruber* (pink) as biostratigraphic indicators. The FAD of *G. ruber* (pink) acme (0.40 Ma; Li et al., 2005) was also adopted. The age for the LAD of *Globorotalia mutlicamerata* (2.18 Ma) was adjusted based on regional stratigraphic work (Li et al., 2005).

Taxonomic concepts for Neogene and Paleogene taxa mainly follow those of Kennett and Srinivasan (1983) and Bolli and Saunders (1985).

Planktonic foraminifer species distribution and range charts are presented in each site chapter.

Benthic foraminifers

Taxonomic assignments for benthic foraminifers follow Loeblich and Tappan (1988), Kaminski and Gradstein (2005), and Holbourn et al. (2013). Paleodepth estimates were based on selected benthic foraminiferal taxa noted and described by van Morkhoven et al. (1986) using the following categories:

Neritic = <200 m.
Bathyal = 200–2000 m.
Upper bathyal = 200–600 m.
Middle bathyal = 600–1000 m.
Lower bathyal = 1000–2000 m.
Abyssal = >2000 m.
Upper abyssal = 2000–3000 m.
Lower abyssal = >3000 m.

Benthic foraminiferal assemblage composition and paleodepth estimates were based on counts of at least 100 specimens from the >150 µm size fractions, where possible.

Preparation and examination techniques

Sample preparation for foraminifer identification uses the same techniques for both planktonic and benthic foraminifers. Core catcher samples (and additional core samples as needed) were soaked in distilled water and washed over a 63 µm mesh sieve. Consolidated or lithified samples were cut in pieces and crushed to pea size, to which a hydrogen peroxide solution was added. This mixture was heated in the oven below 50°C for several hours and then sieved as above. Some samples were rewashed by additional disaggregation with the hydrogen peroxide solution. All samples were dried in a low temperature oven at ~50°C. The dried samples were sieved over a 150 µm sieve, retaining the <150 µm size fraction in a separate vial. To avoid contamination of foraminifers between samples, the sieves were thoroughly cleaned between samples, placed into a sonicator for at least 15 min, and then carefully checked. Species identifications for planktonic and benthic foraminifers were generally made on the >150 µm size fractions. The 63–150 µm size fraction was observed for distinctive taxa.

In addition, mudline (or hole top) samples were taken from selected sites and analyzed for planktonic and benthic foraminifers and ostracods. Mudline samples were collected by emptying the sediment/water material from the top core liner of a hole into a bucket and then washing it with tap water over a 63 µm sieve. Sample staining using Rose Bengal (1 g/L) was performed to confirm the presence of living foraminifers and ostracods in the mudline sample. For this, a portion of the sample was incubated for 12 h with Rose Bengal stain before being washed through a 63 µm sieve. All samples were then dried at ~50°C and subsequently examined under a binocular light microscope. Selected microfossil specimens were also examined and imaged using the shipboard SEM.

The total abundance of planktonic foraminifers was reported using the following categories:

A = abundant (>30% planktonic foraminifer specimens in total residue).
C = common (10%–30% planktonic foraminifer specimens in total residue).
R = rare (%1–10% planktonic foraminifer specimens in total residue).
P = present (<1% planktonic foraminifer specimens in total residue).
B = barren (no planktonic foraminifer specimens in total residue).

Individual planktonic foraminifers were recorded in qualitative terms based on an assessment of forms observed in a random sample of ~400 specimens from the >150 µm size fraction. Relative abundances were reported using the following categories:

D = dominant (>30% of the assemblage).
A = abundant (>10%–30%).
F = few (>5%–10%).
R = rare (1%–5%).
P = present (<1%).

Preservation of planktonic foraminifer assemblages was recorded using the following categories:

VG = very good (no evidence of breakage or dissolution).
G = good (>80% of specimens unbroken with only minor evidence of diagenetic alteration).
M = moderate (30%–80% of the specimens unbroken).
P = poor (strongly recrystallized or dominated by fragments and broken or corroded specimens).

Ostracods

Ostracods were studied at selected sites when time was available. Sample preparation for ostracod examination and illustration followed the same techniques as for foraminifers. Ostracod taxonomic assignments follow Yang et al. (1990), Zhao et al. (2000), Zhao (2005), Hu and Tao (2008), and Alvarez Zarikian (2015).

Abundance of ostracods was noted using the following definitions:

C = common (>20 specimens per sample).
X = present (<20 specimens per sample).
B = barren.

Table T3. Planktonic foraminiferal events and scaled ages (GTS2012; Gradstein et al., 2012), Expeditions 367 and 368. T = top/last appearance datum, B = base/first appearance datum. Bold text indicates age-diagnostic datum. (Continued on next two pages.) **Download table in CSV format.**

GTS2012 chronostratigraphy	Standard tropical–subtropical biozone (biochron)		Biohorizon (datum)	GTS2012 age (Ma)	Error (My)
	Indo-Pacific (Blow, 1969, 1979; Berggren et al., 1995)	Indo-Pacific (Berggren et al., 1995; Wade et al., 2011)			
Tarantian (late Pleistocene)	N22	PT1b	T *Globorotalia flexuosa*	0.07	
			T *Globigerinoides ruber* pink	0.12	
0.126 Ma					
Ionian (middle Pleistocene)			B *Globigerinella calida*	0.22	
			Bc *Globigerinoides ruber* pink	0.40	
			B *Globorotalia flexuosa*	0.40	
			B *Globorotalia hirsuta*	0.45	
		PT1b/PT1a	**T *Globorotalia tosaensis***	**0.61**	
		PT1a	B *Globorotalia hessi*	0.75	
0.781 Ma			B *Globigerinoides ruber* pink	1.16	
			T *Globigerinoides obliquus*	1.3	±0.1
			T *Neogloboquadrina acostaensis*	1.58	±0.03
			T *Globoturborotalita apertura*	1.64	±0.03
1.806 Ma					
Gelasian (early Pleistocene)		**PT1a/PL6**	**T *Globigerinoides fistulosus***	**1.88**	±0.03
			T *Globigerinoides extremus*	1.98	±0.03
			B *Pulleniatina finalis*	2.04	±0.03
			T *Globorotalia multicamerata*	2.18	
			T *Globorotalia pertenuis*	2.30	
			T *Globoturborotalita woodi*	2.30	±0.02
		PL6/PL5	**T *Globorotalia pseudomiocenica***	**2.39**	
2.588 Ma	**N22/N21**				
Piacenzian (late Pliocene)	N21		T *Globoturborotalita decoraperta*	2.75	±0.03
			B *Globigerinoides fistulosus*	3.33	
	N21/N19–N20		B *Globorotalia tosaensis*	3.35	
		PL5/PL4	**T *Dentoglobigerina altispira***	**3.47**	
		PL4	B *Globorotalia pertenuis*	3.52	±0.03
		PL4/PL3	**T *Sphaeroidinellopsis seminulina***	**3.59**	
3.600 Ma					
Zanclean (early Pliocene)		PL3	T *Pulleniatina primalis*	3.66	
			T *Globorotalia plesiotumida*	3.77	±0.02
		PL3/PL2	**T *Globorotalia margaritae***	**3.85**	±0.03
			T *Pulleniatina spectabilis*	4.21	
			B *Globorotalia crassaformis* sensu lato	4.31	±0.04
		PL2/PL1	**T *Globoturborotalita nepenthes***	**4.37**	±0.01
		PL1	B *Goblorotalia exilis*	4.45	±0.04
			T *Sphaeroidinellopsis kochi*	4.53	±0.17
			T *Globorotalia cibaoensis*	4.60	
			T *Globigerinoides seiglei*	4.72	
5.333 Ma					
Messinian (late Miocene)	**N19–N20/N18**		B *Sphaeroidinella dehiscens* sensu lato	**5.53**	±0.04
	N18/N17b	**PL1/M14**	**B *Globorotalia tumida***	**5.57**	
			B *Turborotalita humilis*	5.81	±0.17
			T *Globoquadrina dehiscens*	5.92	
			B *Globorotalia margaritae*	6.08	±0.03
		M14/M13b	**T *Globorotalia lenguaensis***	**6.14**	
		M13b	B *Globigerinoides conglobatus*	6.20	±0.41
	N17b/N17a		B *Pulleniatina primalis*	6.60	
			B *Globorotalia miotumida* (*conomiozea*)	7.89	
			B *Neogloboquadrina humerosa*	8.56	
	N17a/N16	**M13b/M13a**	**B *Globorotalia plesiotumida***	**8.58**	±0.03
	N16	M13a	B *Globigerinoides extremus*	8.93	±0.03
			B *Globorotalia cibaoensis*	9.44	±0.05
			B *Globorotalia juanai*	9.69	±0.26
	N16/N15	**M13a/M12**	**B *Neogloboquadrina acostaensis***	**9.83**	±0.06
Tortonian (late Miocene)			T *Globorotalia challengeri*	9.99	
	N15/N14	**M12/M11**	**T *Paragloborotalia mayeri/siakensis***	**10.46**	±0.02
			B *Globorotalia limbata*	10.64	±0.26
			T *Cassigerinella chipolensis*	10.89	
			B *Globoturborotalita apertura*	11.18	±0.13
			B *Globorotalia challengeri*	11.22	
			B regular *Globigerinoides obliquus*	11.25	
			B *Globoturborotalita decoraperta*	11.49	±0.04
			T *Globigerinoides subquadratus*	11.54	
11.608 Ma					

Table T3 (continued). (Continued on next page.)

GTS2012 chronostratigraphy	Standard tropical–subtropical biozone (biochron): Indo-Pacific (Blow, 1969, 1979; Berggren et al., 1995)	Standard tropical–subtropical biozone (biochron): Indo-Pacific (Berggren et al., 1995; Wade et al., 2011)	Biohorizon (datum)	GTS2012 age (Ma)	Error (My)
	N14/N13	**M11/M10**	**B *Globoturborotalita nepenthes***	**11.63**	±0.02
	N13/N12	**M10/M9b**	**T *Fohsella fohsi, Fohsella plexus***	**11.79**	±0.15
			T *Clavatorella bermudezi*	12.00	
			B *Globorotalia lenguanensis*	12.84	±0.05
			B *Sphaeroidinellopsis subdehiscens*	13.02	
Serravallian (middle Miocene)		**M9b/M9a**	**B *Fohsella robusta***	**13.13**	±0.02
		M9a	T *Cassigerinella martinezpicoi*	13.27	
	N12/N11	**M9a/M8**	**B *Fohsella fohsi***	**13.41**	±0.04
	N11	M8	B *Neogloboquadrina nympha*	13.49	
	N11/N10	**M8/M7**	**B *Fohsella praefohsi***	**13.77**	
			T *Fohsella peripheroronda*	13.80	
13.82 Ma	N10	M7			
			T regular *Clavatorella bermudezi*	13.82	
			T *Globorotalia archeomenardii*	13.87	
	N10/N9	**M7/M6**	**B *Fohsella peripheroacuta***	**14.24**	
			B *Globorotalia praemenardii*	14.38	
Langhian (middle Miocene)	N9	M6	T *Praeorbulina sicana*	14.53	
			T *Globigeriantella insueta*	14.66	
			T *Praeorbulina glomerosa* sensu stricto	14.78	
			T *Praeorbulina circularis*	14.89	
	N9/N8	**M6/M5b**	**B *Orbulina suturalis***	**15.10**	
			B *Clavatorella bermudezi*	15.73	
			B *Praeorbulina circularis*	15.96	
15.97 Ma	N8	M5b			
			B *Globigerinoides diminutus*	16.06	
			B *Globorotalia archeomenardii*	16.26	
		M5b/M5a	**B *Praeorbulina glomerosa* sensu stricto**	**16.27**	
		M5a	B *Praeorbulina curva*	16.28	
	N8/N7	**M5a/M4b**	**B *Praeorbulina sicana***	**16.38**	
		M4b	T *Globorotalia incognita*	16.39	
		M4b/M4a	**B *Fohsella birnageae***	**16.69**	
Burdigalian (early Miocene)	N7	M4a	B *Globorotalia miozea*	16.70	
			B *Globorotalia zealandica*	17.26	
			T *Globorotalia semivera*	17.26	
	N7/N6	**M4a/M3**	**T *Catapsydrax dissimilis***	**17.54**	
			B *Globigeriantella insueta* sensu stricto	17.59	
		M3	B *Globorotalia praescitula*	18.26	
			T *Globiquadrina binaiensis*	19.09	
		M3/M2	**B *Globigerinatella* sp.**	**19.30**	
	N6–N5		B *Globigerinoides altiaperturus*	20.03	
(20.44 Ma)					
			T *Tenuitella munda*	20.78	
			B *Globorotalia incognita*	20.93	
			T *Globoturborotalita angulisuturalis*	20.94	
	N5/N4b	**M2/M1b**	**T *Paragloborotalia kugleri***	**21.12**	
			T *Paragloborotalia pseudokugleri*	21.31	
Aquitanian (early Miocene)	N4b	M1b	B *Globoquadrina dehiscens* f. *spinosa*	21.44	
			T *Dentoglobigerina globularis*	21.98	
	N4b/N4a	**M1b/M1a**	**B *Globoquadrina dehiscens***	**22.44**	
			T *Globigerina ciperoensis*	22.90	
	N4a	M1a	B *Globigerinoides trilobus* sensu lato	22.96	
	N4a/P22	**M1a/O7**	**B *Paragloborotalia kugleri***	**22.96**	
23.03 Ma					
			T *Globigerina euapertura*	23.03	
		O7	T *Tenuitella gemma*	23.50	
Chattian (late Oligocene)	P22 (N3)		B common *Globigerinoides primordius*	23.50	
		O7/O6	**B *Paragloborotalia pseudokugleri***	**25.21**	
		O6	B *Globigerinoides primordius*	26.12	
	P22/P21	**O6/O5**	**T *Paragloborotalia opima* sensu stricto**	**26.93**	
(28.09 Ma)	P21 (N2)	**O5/O4**			
			T common *Chiloguembelina cubensis*	28.09	
	P21/P20	**O4/O3**	**B *Globigerina angulisuturalis***	**29.18**	
Rupelian (early Oligocene)	P20	O3	B *Tenuitellinata juvenilis*	29.50	
			T *Subbotina angiporoides*	29.84	
	P20/P19	**O3/O2**	**T *Turborotalia ampliapertura***	**30.28**	

Table T3 (continued).

GTS2012 chronostratigraphy	Standard tropical–subtropical biozone (biochron): Indo-Pacific (Blow, 1969, 1979; Berggren et al., 1995)	Standard tropical–subtropical biozone (biochron): Indo-Pacific (Berggren et al., 1995; Wade et al., 2011)	Biohorizon (datum)	GTS2012 age (Ma)	Error (My)
Rupelian (early Oligocene)	P19	O2	B *Paragloborotalia opima*	30.72	
	P19/P18	**O2/O1**	**T *Pseudohastigerina naguewichiensis***	**32.10**	
	P18	O1	B *Cassigerinella chipolensis*	33.89	
33.89 Ma					
Priabonian (late Eocene)		**O1/E16**	**T *Hantkenina* spp.**	**33.89**	
		E16	T common *Pseudohastigerina micra*	33.89	
	P18/P17		T *Turborotalia cerroazulensis*	34.03	
	P17/P16		T *Cribrohantkenina inflata*	34.22	
	P16	**E16/E15**	**T *Globigerinatheka index***	**34.61**	
		E15	T *Turborotalia pomeroli*	35.66	
			B *Turborotalia cunialensis*	35.71	
	P16/P15		B *Cribrohantkenina inflata*	35.87	
	P15	**E15/E14**	**T *Globigerinatheka semiinvoluta***	**36.18**	
(37.75 Ma)		E14			
Bartonian			T *Acarinina* spp.	37.75	

Ostracod preservation was estimated using the following definitions:

VG = very good (valves translucent; no evidence of overgrowth, dissolution, or abrasion).
G = good (valves semitranslucent; little evidence of overgrowth, dissolution, or abrasion).
M = moderate (common but minor calcite overgrowth, dissolution, or abrasion).
P = poor (substantial overgrowth, dissolution, or fragmentation of the valves).

Diatoms

Diatom zonal scheme and taxonomy

The taxonomy for diatoms studied during Expeditions 367 and 368 is taken largely from Burckle (1972), Akiba (1986), Akiba and Yanagisawa (1986), Baldauf and Iwai (1995), Barron (1981, 1985, 2005), and Barron et al. (2004). The diatom datum sequence follows Lazarus et al. (2014) with adjustments based on updates (J.A. Barron, pers. comm., 2017) and calibration to the GPTS of Gradstein et al. (2012) (Table **T4**). The diatom zonal scheme used follows the biostratigraphic study by Scherer et al. (2007). A taxonomic list of relevant diatom species is given in Table **T5**.

Methods

Strewn slides were prepared for samples examined from Expedition 368 by placing a small amount of raw sediment onto a slide and allowing the water to evaporate by heating on a hot plate for ~5 min. About 1–2 drops of optical adhesive were applied to the dry slide, which was then covered with a 22 mm × 40 mm glass coverslip. The adhesive was solidified by placing the slide under ultraviolet light for ~10 min. Strewn slides were scanned at a maximum magnification of 1250× for stratigraphic markers and other common taxa.

Abundance estimates of the diatom assemblage are qualitative estimates of the concentration of diatoms in individual sediment samples as defined by the following categories:

D = dominant (>90% of sediment particles).
A = abundant (>50%–90% of sediment particles).
C = common (>10%–50% of sediment particles).
F = few (1%–10% of sediment particles).
R = rare (<1% of sediments particles).
B = barren (none present).

Abundance of individual diatom species was recorded using the following categories:

D = dominant (>50 valves per counted transect).
A = abundant (>20–50 valves per counted transect).
C = common (>10–20 valves per counted transect).
F = few (>1–10 valves per counted transect).
R = rare (≤1 valve per counted transect).

Preservation of the diatom assemblage was recorded using the following categories:

G = good (majority of specimens complete with minor dissolution and/or breakage and no significant enlargement of the areolae or dissolution of the frustules rim detected; the sample generally has a high diatoms per gram concentration).
M = moderate (minor but common areolae enlargement and dissolution of the frustule rim with a considerable amount of breakage of specimens).
P = poor (strong dissolution or breakage, some specimens unidentifiable, strong dissolution of the frustule rim and areolae enlargement; the sample generally has lower diatoms per gram concentration).

Other microfossils

The presence of other microfossils such as pteropods, fish teeth, sponge spicules, corals, radiolarians, and other bioclasts found in the >150 µm size fractions was noted.

Table T4. Diatom events and scaled ages (Gradstein et al., 2012), Expedition 368. T = top/last appearance datum, B = base/first appearance datum. (Continued on next four pages.) **Download table in CSV format.**

Diatom zonation (Scherer et al., 2007)		Diatom bioevent	GTS2012 age (Ma)	Age reference
Fragilariopsis doliolus		T *Nitzschia aequatorialis*	0.14	Lazarus et al., 2014; Cervato and Burckle, 2003
		T *Fragilariopsis reinholdii*	0.62	Lazarus et al., 2014; Barron, 2003
Fragilariopsis reinholdii	B	T *Fragilariopsis fossilis*	0.70	Lazarus et al., 2014; Barron, 2003
		T *Thalassiosira plicata*	0.80	Lazarus et al., 2014; Barron, 2003
		T *Thalassiosira symbolophora*	0.90	Lazarus et al., 2014; Schrader, 1974
		T *Rhizosolenia matuyamai*	1.05	Lazarus et al., 2014; Barron, 2003
		B *Rhizosolenia matuyamai*	1.18	Lazarus et al., 2014; Barron, 2003
		T *Rhizosolenia praebergonii* var. *robusta*	1.72	Lazarus et al., 2014; Barron, 2003
		B *Azpeitia barronii*	1.80	Lazarus et al., 2014; Barron, 2003
		B *Nitzschia punctata*	1.80	Lazarus et al., 2014; Cervato and Burckle, 2003
		T *Rhizosolenia praebergonii*	1.90	Lazarus et al., 2014; Barron, 2003
	A	B *Actinoptychus bipunctatus*	1.90	Lazarus et al., 2014; Cervato and Burckle, 2003
		B *Asterolampra brookei*	2.00	Lazarus et al., 2014; Schrader, 1974
		B *Nitzschia interruptestriata*	2.00	Lazarus et al., 2014; Koizumi and Tanimura, 1985
		B *Fragilariopsis doliolus*	2.01	Lazarus et al., 2014; Barron, 2003
Rhizosolenia praebergonii	C	B *Nitzschia braarudii*	2.02	Lazarus et al., 2014; Cervato and Burckle, 2003
		T *Nitzschia dietrichii*	2.20	Lazarus et al., 2014; Cervato and Burckle, 2003
		T *Thalassiosira convexa*	2.43	Lazarus et al., 2014; Barron, 2003
	B	T *Thalassiosira convexa* var. *aspinosa*	2.43	Lazarus et al., 2014; Barron, 2003
		B *Rhizosolenia praebergonii* var. *robusta*	2.50	Lazarus et al., 2014; Barron, 2003
		T *Triceratium acutangulum*	2.60	Lazarus et al., 2014; Cervato and Burckle, 2003
		T *Nitzschia jouseae*	2.79	Lazarus et al., 2014; Barron, 2003
	A	B *Bacteriastrum hyalinum*	2.90	Lazarus et al., 2014; Cervato and Burckle, 2003
		B *Rhizosolenia praebergonii*	3.17	Lazarus et al., 2014; Barron, 2003
Nitzschia jouseae		B *Thalassiosira plicata*	3.30	Lazarus et al., 2014; Barron, 2003
		B *Thalassiosira symbolophora*	3.30	Lazarus et al., 2014; Schrader, 1974
		T *Actinocyclus ellipticus* f. *lanceolata*	3.40	Lazarus et al., 2014; Barron, 2003
		B *Cymatotheca weissflogii*	3.40	Lazarus et al., 2014; Cervato and Burckle, 2003
		B *Roperia tesselata*	3.60	Lazarus et al., 2014; Schrader, 1974
		T *Azpeitia vetustissima*	3.80	Lazarus et al., 2014; Schrader, 1974
		T *Roperia praetesselata*	3.80	Lazarus et al., 2014; Cervato and Burckle, 2003
		B *Azpeitia africana*	3.80	Lazarus et al., 2014; Barron, 2003
		B *Thalassiosira convexa* var. *aspinosa*	3.83	Lazarus et al., 2014; Barron, 2003
		B *Asteromphalus elegans*	4.20	Lazarus et al., 2014; Barron, 2003
		T *Fragilariopsis cylindrica*	4.30	Lazarus et al., 2014; Barron, 2003
		B *Nitzschia seriata*	4.30	Lazarus et al., 2014; Cervato and Burckle, 2003
		T *Actinocyclus ellipticus* f. *elongatus*	4.50	Lazarus et al., 2014; Schrader, 1974
		B *Nitzschia panduriformis*	4.70	Lazarus et al., 2014; Cervato and Burckle, 2003
		B *Coscinodiscus centralis*	4.80	Lazarus et al., 2014; Cervato and Burckle, 2003
		B *Asteromphalus flabellatus*	4.90	Lazarus et al., 2014; Cervato and Burckle, 2003
		B *Nitzschia jouseae*	5.12	Lazarus et al., 2014; Barron, 2003
Thalassirosira convexa	C	B *Nitzschia aequatorialis*	5.20	Lazarus et al., 2014; Cervato and Burckle, 2003
		B *Asteromphalus pettersonii*	5.40	Lazarus et al., 2014; Cervato and Burckle, 2003
		B *Shionodiscus oestrupii*	5.59	Lazarus et al., 2014; Barron, 2003
		B *Cyclotella striata*	5.60	Lazarus et al., 2014; Cervato and Burckle, 2003
		T *Thalassiosira miocenica*	5.95	Lazarus et al., 2014; Barron, 2003
	B	T *Asterolampra acutiloba*	6.00	Lazarus et al., 2014; Barron, 2003
		B *Roperia praetesselata*	6.10	Lazarus et al., 2014; Cervato and Burckle, 2003
		T *Fragilariopsis miocenica*	6.17	Lazarus et al., 2014; Barron, 2003
		T *Nitzschia miocenica* var. *elongata*	6.18	Lazarus et al., 2014; Barron, 2003
		B *Thalassiothrix frauenfeldii*	6.20	Lazarus et al., 2014; Schrader, 1974
		T *Thalassiosira praeconvexa*	6.29	Lazarus et al., 2014; Barron, 2003
	A	T *Bogorovia lancettula*	6.30	Lazarus et al., 2014; Barron, 2003
		T *Azpeitia komurae*	6.50	Lazarus et al., 2014; Yanagisawa and Akiba, 1998
		T *Bogorovia praepaleacea*	6.62	Lazarus et al., 2014; Barron, 2003
		B *Nitzschia bicapitata*	6.70	Lazarus et al., 2014; Cervato and Burckle, 2003
		B *Nitzschia dietrichii*	6.70	Lazarus et al., 2014; Cervato and Burckle, 2003
		B *Nitzschia inflatula*	6.70	Lazarus et al., 2014; Cervato and Burckle, 2003
		B *Planktoniella sol*	6.70	Lazarus et al., 2014; Cervato and Burckle, 2003
		B *Thalassiosira symmetrica*	6.70	Lazarus et al., 2014; Cervato and Burckle, 2003
		B *Thalassiosira miocenica*	6.74	Lazarus et al., 2014; Barron, 2003
		T *Cavitatus jouseana*	6.75	Lazarus et al., 2014; Barron et al., 2004
		B *Thalassiosira convexa*	6.77	Lazarus et al., 2014; Barron, 2003
Nitzschia miocenica	B	B *Thalassiosira nodulolineata*	6.80	Lazarus et al., 2014; Cervato and Burckle, 2003
		B *Asteromphalus arachne*	6.90	Lazarus et al., 2014; Cervato and Burckle, 2003
		B *Azpeitia komurae*	6.90	Lazarus et al., 2014; Yanagisawa and Akiba, 1998
		B *Nitzschia miocenica* var. *elongata*	6.90	Lazarus et al., 2014; Barron, 2003
		B *Thalassiosira praeconvexa*	6.91	Lazarus et al., 2014; Barron, 2003

Table T4 (continued). (Continued on next page.)

Diatom zonation (Scherer et al., 2007)		Diatom bioevent	GTS2012 age (Ma)	Age reference
Nitzschia miocenica	A	B *Asterolampra heptactis*	7.00	Lazarus et al., 2014; Cervato and Burckle, 2003
		B *Thalassionema bacillaris*	7.00	Lazarus et al., 2014; Cervato and Burckle, 2003
		T *Nitzschia porteri*	7.24	Lazarus et al., 2014; Barron, 2003
		B *Fragilariopsis miocenica*	7.39	Lazarus et al., 2014; Barron, 2003
Nitzschia porteri	B	B *Nitzschia interrupta*	7.40	Lazarus et al., 2014; Schrader, 1974
		B *Actinocyclus ellipticus* f. *elongatus*	7.50	Lazarus et al., 2014; Schrader, 1974
		B *Fragilariopsis cylindrica*	7.65	Lazarus et al., 2014; Barron, 2003
		T *Rossiella paleacea*	7.70	Lazarus et al., 2014; Barron, 2003
		B *Fragilariopsis reinholdii*	7.71	Lazarus et al., 2014; Barron, 2003
		T *Actinocyclus ellipticus* var. *javanica*	7.85	Lazarus et al., 2014; Barron, 1985
		T *Thalassiosira burckliana*	8.00	Lazarus et al., 2014; Barron, 2003
	A	B *Alveus marinus*	8.02	Lazarus et al., 2014; Barron, 2003
		B *Synedra indica*	8.20	Lazarus et al., 2014; Cervato and Burckle, 2003
		T *Thalassiosira yabei*	8.32	Lazarus et al., 2014; Barron, 2003
Thalassiosira yabei	B	T *Rossiella elongata*	8.40	Lazarus et al., 2014; Barron, 2003
		T *Pseudopyxilla americana*	8.70	Lazarus et al., 2014; Cervato and Burckle, 2003
		T *Triceratium condecorum*	8.70	Lazarus et al., 2014; Barron, 1976
		B *Asteromphalus robustus*	8.72	Lazarus et al., 2014; Cervato and Burckle, 2003
		T *Coscinodiscus loeblichii*	8.89	Lazarus et al., 2014; Barron, 2003
		T *Coscinodiscus yabei* var. *ellipticus*	8.90	Lazarus et al., 2014; Barron, 2003
		B *Rhizosolenia bergonii*	8.90	Lazarus et al., 2014; Cervato and Burckle, 2003
		B *Coscinodiscus yabei* var. *ellipticus*	9.01	Lazarus et al., 2014; Barron, 2003
		B *Fragilariopsis fossilis*	9.01	Lazarus et al., 2014; Barron, 2003
		T *Azpeitia endoi*	9.11	Lazarus et al., 2014; Barron, 1976
		B *Thalassiosira burckliana*	9.11	Lazarus et al., 2014; Barron, 2003
	A	B *Thalassiosira eccentrica*	9.11	Lazarus et al., 2014; Barron, 2003
		T *Denticulopsis dimorpha*	9.30	Lazarus et al., 2014; Barron, 2003
		T *Azpeitia aeginensis*	9.51	Lazarus et al., 2014; Fenner, 1985
		T *Coscinodiscus vetustissimus* var. *javanica*	9.51	Lazarus et al., 2014; Barron, 2003
		B *Coscinodiscus loeblichii*	9.64	Lazarus et al., 2014; Barron, 2003
		B *Coscinodiscus vetustissimus* var. *javanica*	9.70	Lazarus et al., 2014; Barron, 2003
		T *Actinocyclus moronensis*	9.87	Lazarus et al., 2014; Barron, 2003
Actinocyclus moronensis		B *Hemidiscus simplicissimus*	9.90	Lazarus et al., 2014; Cervato and Burckle, 2003
		B *Denticulopsis dimorpha*	10.00	Lazarus et al., 2014; Barron, 2003
		B *Asterolampra acutiloba*	10.10	Lazarus et al., 2014; Koizumi and Tanimura, 1985
		B *Actinocyclus ellipticus* f. *lanceolata*	10.46	Lazarus et al., 2014; Barron, 2003
		T *Azpeitia apiculata*	10.71	Lazarus et al., 2014; Barron, 2003
		B *Bogorovia praepaleacea*	11.13	Lazarus et al., 2014; Barron, 2003
		T *Coscinodiscus gigas* var. *diorama*	11.27	Lazarus et al., 2014; Barron, 2003
		B *Rossiella elongata*	11.27	Lazarus et al., 2014; Barron, 2003
		T *Actinocyclus ellipticus* var. *spiralis*	11.34	Lazarus et al., 2014; Barron, 2003
		T *Crucidenticula punctata*	11.44	Lazarus et al., 2014; Barron, 2003
		T *Craspedodiscus coscinodiscus*	11.48	Lazarus et al., 2014; Barron, 2005
Craspedodiscus coscinodiscus		B *Hemidiscus cuneiformis*	11.64	Lazarus et al., 2014; Barron, 2003
		T *Macrora stella* (*Azpeitia*)	11.74	Lazarus et al., 2014; Cervato and Burckle, 2003
		B *Thalassiosira brunii*	12.26	Lazarus et al., 2014; Barron, 2003
Coscinodiscus gigas var. diorama		B *Nitzschia porteri*	12.29	Lazarus et al., 2014; Barron, 2003
		T *Crucidenticula nicobarica*	12.36	Lazarus et al., 2014; Barron, 2003
		T2 *Annellus californicus*	12.54	Lazarus et al., 2014; Barron, 2005
		B *Asteromphalus imbricatus*	12.54	Lazarus et al., 2014; Cervato and Burckle, 2003
		B *Bogorovia lancettula*	12.63	Lazarus et al., 2014; Barron, 2003
		T *Azpeitia salisburyana*	12.91	Lazarus et al., 2014; Barron, 2003
		T *Coscinodiscus lewisianus*	12.94	Lazarus et al., 2014; Shackleton et al., 1995
Coscinodiscus lewisianus		T *Azpeitia vetustissima* var. *voluta*	13.02	Lazarus et al., 2014; Baldauf and Barron, 1982
		T *Thalassiosira perispinosa*	13.02	Lazarus et al., 2014; Tanimura, 1996
		B *Coscinodiscus gigas* var. *diorama*	13.02	Lazarus et al., 2014; Barron, 2003
		T *Thalassiosira tappanae*	13.20	Lazarus et al., 2014; Barron, 2003
		B *Azpeitia nodulifera*	13.25	Lazarus et al., 2014; Barron, 2003
		B *Pseudotriceratium wallichii*	13.32	Lazarus et al., 2014; Barron, 2003
		B *Coscinodiscus gigas*	13.40	Lazarus et al., 2014; Cervato and Burckle, 2003
		B *Crucidenticula punctata*	13.40	Lazarus et al., 2014; Barron, 1985
		B *Thalassiosira yabei*	13.50	Lazarus et al., 2014; Barron, 2003
		T *Cestodiscus pulchellus* var. *maculata*	13.89	Lazarus et al., 2014; Barron, 2003
		B *Azpeitia apiculata*	13.89	Lazarus et al., 2014; Barron, 2003
		B *Actinocyclus ellipticus* var. *javanica*	13.98	Lazarus et al., 2014; Barron, 1985
		B *Actinocyclus moronensis*	13.98	Lazarus et al., 2014; Barron, 2003
		B *Azpeitia aeginensis*	13.98	Lazarus et al., 2014; Fenner, 1985
		B *Actinocyclus ellipticus*	14.02	Lazarus et al., 2014; Barron, 2003
		T *Cestodiscus peplum*	14.03	Lazarus et al., 2014; Barron, 2003

Table T4 (continued). (Continued on next page.)

Diatom zonation (Scherer et al., 2007)		Diatom bioevent	GTS2012 age (Ma)	Age reference
Cestodiscus peplum	B	B *Actinocyclus ellipticus* var. *spiralis*	14.03	Lazarus et al., 2014; Barron, 2003
		T *Coscinodiscus blysmos*	14.33	Lazarus et al., 2014; Barron, 2003
		B *Thalassiosira tappanae*	14.40	Lazarus et al., 2014; Barron, 2003
		T *Actinoptychus splendens*	14.52	Lazarus et al., 2014; Cervato and Burckle, 2003
		T *Goniothecium decoratum*	14.52	Lazarus et al., 2014; Cervato and Burckle, 2003
		T *Cavitatus miocenicus*	14.63	Lazarus et al., 2014; Cody et al., 2008
		T *Crucidenticula paranicobarica*	14.79	Lazarus et al., 2014; Barron, 2003
		B *Thalassiosira perispinosa*	14.89	Lazarus et al., 2014; Tanimura, 1996
	A	T1 *Annellus californicus*	14.90	Burckle, 1978
		B *Crucidenticula nicobarica*	15.10	Lazarus et al., 2014; Barron, 2003
		T *Cavitatus lanceolatus*	15.20	Lazarus et al., 2014; Yanagisawa and Akiba, 1998
		T *Cymatogonia amblyoceras*	15.20	Lazarus et al., 2014; Barron et al, 2013
		T *Azpeitia praenodulifera*	15.40	Lazarus et al., 2014; Barron, 2003
		T *Goniothecium odontella*	15.50	Lazarus et al., 2014; Cervato and Burckle, 2003
		B *Azpeitia endoi*	15.50	Lazarus et al., 2014; Barron, 1976
		T *Cavitatus rectus*	~15.50	Lazarus et al., 2014; Fenner, 1985
		B *Cavitatus lanceolatus*	15.60	Lazarus et al., 2014; Yanagisawa and Akiba, 1998
		T *Coscinodiscus lewisianus* var. *similis*	15.70	Lazarus et al., 2014; Barron, 2003
		B *Crucidenticula paranicobarica*	16.00	Lazarus et al., 2014; Barron, 2003
		T *Crucidenticula sawamurae*	16.20	Lazarus et al., 2014; Yanagisawa and Akiba, 1990
		T *Thalassiosira fraga*	16.30	Lazarus et al., 2014; Barron, 1985
		B *Cestodiscus peplum*	16.40	Lazarus et al., 2014; Barron, 2003
Crucidenticula nicobarica	B	T *Cestodiscus kugleri*	16.50	Lazarus et al., 2014; Barron, 2005
		T *Cestodiscus ovalis*	16.50	Lazarus et al., 2014; Barron, 2005
		T *Cestodiscus pulchellus*	16.50	Lazarus et al., 2014; Barron, 2005
		T *Crucidenticula kanayae*	16.50	Lazarus et al., 2014; Barron, 2003
		T *Raphidodiscus* (*Rhaphidodiscus*) *marylandicus* (*marylandica*)	16.50	Lazarus et al., 2014; Barron, 2003
		B *Azpeitia vetustissima*	16.50	Lazarus et al., 2014; Baldauf and Barron, 1982
		B *Azpeitia vetustissima* var. *voluta*	16.50	Lazarus et al., 2014; Baldauf and Barron, 1982
		B *Crucidenticula kanayae*	16.90	Lazarus et al., 2014; Barron, 2003
		T *Cestodiscus rapax*	17.10	Lazarus et al., 2014; Barron, 2006
		B *Coscinodiscus lewisianus* var. *similis*	17.10	Lazarus et al., 2014; Barron, 2003
		T *Coscinodiscus lewisianus* var. *robustus*	17.30	Lazarus et al., 2014; Barron, 2006
		T *Coscinodiscus rhombicus*	17.30	Lazarus et al., 2014; Barron et al., 2004
		B *Coscinodiscus blysmos*	17.30	Lazarus et al., 2014; Barron, 2006
	A	T *Azpeitia bukryi*	17.40	Lazarus et al., 2014; Barron, 2006
		T *Crucidenticula ikebei*	17.40	Lazarus et al., 2014; Barron, 2006
		B *Azpeitia salisburyana*	17.40	Lazarus et al., 2014; Barron, 2006
		T *Triceratium pileus*	17.60	Lazarus et al., 2014; Barron, 2006
		B *Annellus californicus*	17.60	Lazarus et al., 2014; Barron, 2006
		B *Craspedodiscus coscinodiscus*	17.60	Lazarus et al., 2014; Barron et al., 2004
		B *Crucidenticula ikebei*	17.70	Lazarus et al., 2014; Barron, 2006
		T *Bogorovia puncticulata*	18.10	Lazarus et al., 2014; Barron, 2003
		B *Crucidenticula sawamurae*	18.20	Lazarus et al., 2014; Barron, 2003
Triceratium pileus		B *Cestodiscus kugleri*	18.40	Lazarus et al., 2014; Barron, 2006
		T *Thalassiosira praefraga*	18.60	Lazarus et al., 2014; Barron, 2006
		T *Actinocyclus barronii*	18.70	Lazarus et al., 2014; Barron, 2006
		T *Actinocyclus jouseae*	18.70	Lazarus et al., 2014; Barron, 2006
		T *Actinocyclus radionovae*	18.70	Lazarus et al., 2014; Barron, 2006
		B *Cestodiscus pulchellus* var. *maculata*	18.70	Lazarus et al., 2014; Barron, 2003
		B *Cestodiscus rapax*	18.90	Lazarus et al., 2014; Barron, 2006
		B *Triceratium pileus*	18.90	Lazarus et al., 2014; Barron, 2006
		T *Craspedodiscus barronii*	19.10	Lazarus et al., 2014; Barron, 2006
		T *Craspedodiscus elegans*	19.10	Lazarus et al., 2014; Barron, 2006
Craspedodiscus elegans		T *Dimeregramma* (*Dimerogramma*) *fossile*	19.20	Lazarus et al., 2014; Cervato and Burckle, 2003
		B *Cestodiscus ovalis*	19.20	Lazarus et al., 2014; Barron, 2006
		B *Actinocyclus barronii*	19.40	Lazarus et al., 2014; Barron, 2006
		T *Azpeitia gombosii*	19.50	Lazarus et al., 2014; Barron, 2006
		B *Coscinodiscus lewisianus* var. *robustus*	19.50	Lazarus et al., 2014; Barron, 2006
		T *Actinocyclus praellipticus*	19.60	Lazarus et al., 2014; Barron, 2006
		T *Cestodiscus japonicus*	19.60	Lazarus et al., 2014; Barron, 2006
		T *Distephanosira architecturalis*	19.60	Lazarus et al., 2014; Barron et al., 2004
		B *Actinocyclus jouseae*	19.60	Lazarus et al., 2014; Barron, 2006
		T *Actinocyclus hajosiae*	19.80	Lazarus et al., 2014; Barron, 2006
		T *Rossiella fennerae*	19.90	Lazarus et al., 2014; Barron, 2006
		T *Bogorovia veniamini*	20.00	Lazarus et al., 2014; Barron, 2006
Rossiella paleacea	C	B *Thalassiosira fraga*	20.40	Lazarus et al., 2014; Barron, 2006
		T *Azpeitia oligocenica*	20.50	Lazarus et al., 2014; Barron, 2006

Table T4 (continued). (Continued on next page.)

Diatom zonation (Scherer et al., 2007)		Diatom bioevent	GTS2012 age (Ma)	Age reference
Rossiella paleacea	B	B *Rhizosolenia alata*	20.50	Lazarus et al., 2014; Cervato and Burckle, 2003
		T *Actinocyclus mutabilis*	20.60	Lazarus et al., 2014; Barron, 2006
		B *Craspedodiscus barronii*	20.60	Lazarus et al., 2014; Barron, 2006
		B *Craspedodiscus elegans*	20.60	Lazarus et al., 2014; Barron, 2006
		T *Cestodiscus trochus*	20.80	Lazarus et al., 2014; Barron, 2006
		B *Bogorovia puncticulata*	20.80	Lazarus et al., 2014; Barron, 2003
		B *Actinocyclus praellipticus*	20.90	Lazarus et al., 2014; Barron, 2006
		B *Cestodiscus pulchellus*	20.90	Lazarus et al., 2014; Barron, 2006
		B *Rossiella paleacea*	20.90	Lazarus et al., 2014; Barron, 2003
		T *Pseudopyxilla russica* (*rossica*)	21.10	Lazarus et al., 2014; Cervato and Burckle, 2003
		B *Cymatogonia amblyoceras*	21.10	Lazarus et al., 2014; Cervato and Burckle, 2003
		B *Dimeregramma* (*Dimerogramma*) *fossile*	21.10	Lazarus et al., 2014; Cervato and Burckle, 2003
		T *Bogorovia barronii*	21.20	Lazarus et al., 2014; Barron, 2006
		B *Actinocyclus radionovae*	21.20	Lazarus et al., 2014; Barron, 2006
		T *Rossiella symmetrica*	21.40	Lazarus et al., 2014; Barron, 2006
		B *Actinocyclus hajosiae*	21.40	Lazarus et al., 2014; Barron, 2006
		T *Thalassiosira primalabiata*	21.40	Lazarus et al., 2014; Barron et al., 2004
	A	B *Actinocyclus mutabilis*	21.40	Lazarus et al., 2014; Barron, 2006
		T *Actinocyclus nigriniae*	21.50	Lazarus et al., 2014; Barron, 2006
		T *Stephanopyxis marginata*	21.60	Lazarus et al., 2014; Cervato and Burckle, 2003
		T *Cestodiscus umbonatus*	21.70	Lazarus et al., 2014; Barron, 2006
		T *Rossiella fourtanierae*	21.70	Lazarus et al., 2014; Barron, 2006
		B *Cestodiscus japonicus*	21.70	Lazarus et al., 2014; Barron, 2006
		B *Azpeitia praenodulifera*	21.80	Lazarus et al., 2014; Barron, 2003
		T *Bogorovia gombosii*	21.90	Lazarus et al., 2014; Barron, 2006
		B *Actinocyclus nigriniae*	21.90	Lazarus et al., 2014; Barron, 2006
		B *Thalassiosira praefraga*	21.90	Lazarus et al., 2014; Barron et al., 2004
		B *Bogorovia barronii*	22.20	Lazarus et al., 2014; Barron, 2006
		B *Rossiella symmetrica*	22.31	Lazarus et al., 2014; Barron, 2006
		B *Thalassiosira leptopus*	22.31	Lazarus et al., 2014; Barron, 2003
		B *Rossiella fourtanierae*	23.00	Lazarus et al., 2014; Barron et al., 2004
		B *Bogorovia gombosii*	23.26	Lazarus et al., 2014; Barron, 2006
		T *Coscinodiscus lewisianus* var. *rhomboides*	23.32	Lazarus et al., 2014; Barron et al., 2004
		T *Rocella schraderi*	23.32	Lazarus et al., 2014; Barron, 2006
		T *Rocella gelida*	23.42	Lazarus et al., 2014; Barron, 2006
Rocella gelida		B *Azpeitia tabularis*	23.42	Lazarus et al., 2014; Barron, 2003
		B *Azpeitia gombosii*	23.52	Lazarus et al., 2014; Barron, 2006
		T *Cestodiscus stokesianus*	23.62	Lazarus et al., 2014; Cervato and Burckle, 2003
		B *Raphidodiscus* (*Rhaphidodiscus*) *marylandicus* (*marylandica*)	23.82	Lazarus et al., 2014; Barron et al., 2004
		T *Rocella vigilans*	23.92	Lazarus et al., 2014; Barron et al., 2004
		T *Rocella princeps*	24.00	Lazarus et al., 2014; Barron et al., 2004
		B *Cestodiscus umbonatus*	24.24	Lazarus et al., 2014; Barron, 2006
		B *Rocella schraderi*	24.24	Lazarus et al., 2014; Barron et al., 2004
		B *Thalassiosira primalabiata*	24.87	Lazarus et al., 2014; Barron et al., 2004
		T *Cestodiscus parmula*	25.05	Lazarus et al., 2014; Cervato and Burckle, 2003
		B *Coscinodiscus lewisianus* var. *rhomboides*	25.11	Lazarus et al., 2014; Barron et al., 2004
		B *Rocella gelida*	25.31	Lazarus et al., 2014; Barron et al., 2004
Bogorovia veniamini		B *Rocella princeps*	25.42	Lazarus et al., 2014; Barron et al., 2004
		B *Rossiella fennerae*	25.73	Lazarus et al., 2014; Barron et al., 2004
		B *Coscinodiscus lewisianus*	26.59	Lazarus et al., 2014; Barron et al., 2004
		T *Coscinodiscus lewisianus* var. *levis*	26.68	Lazarus et al., 2014; Barron et al., 2004
		T *Kozloviella minor*	27.23	Lazarus et al., 2014; Barron et al., 2004
		B *Goniothecium decoratum*	27.53	Lazarus et al., 2014; Cervato and Burckle, 2003
		T *Kozloviella pacifica*	27.76	Lazarus et al., 2014; Barron et al., 2004
		T *Rocella vigilans* var. 1	27.76	Lazarus et al., 2014; Barron et al., 2004
		B *Bogorovia veniamini*	27.76	Lazarus et al., 2014; Barron et al., 2004
Rocella vigilans	B	B *Coscinodiscus lewisianus* var. *levis*	27.76	Lazarus et al., 2014; Barron et al., 2004
		T *Baxteriopsis brunii*	27.91	Lazarus et al., 2014; Barron et al., 2004
		B *Kozloviella pacifica*	28.04	Lazarus et al., 2014; Barron et al., 2004
		B *Cavitatus rectus*	28.12	Lazarus et al., 2014; Barron et al., 2004
		B *Coscinodiscus rhombicus*	28.20	Lazarus et al., 2014; Barron, 2006
	A	B *Cavitatus jouseana*	28.27	Lazarus et al., 2014; Barron et al., 2004
		B *Kozloviella minor*	28.27	Lazarus et al., 2014; Barron et al., 2004
		B *Rocella vigilans* var. 1	28.51	Lazarus et al., 2014; Barron et al., 2004
		T *Hemiaulus lyriformis*	28.63	Barron, pers. comm., 2017
		T *Rocella semigelida*	28.63	Lazarus et al., 2014; Barron et al., 2004
		B *Rocella semigelida*	28.75	Lazarus et al., 2014; Barron et al., 2004
		T *Hemiaulus polycistinorum* var. *mesolepta*	29.44	Lazarus et al., 2014; Scherer et al., 2000
		B *Rocella vigilans*	29.58	Lazarus et al., 2014; Barron et al., 2004

Table T4 (continued).

Diatom zonation (Scherer et al., 2007)		Diatom bioevent	GTS2012 age (Ma)	Age reference
Cestodiscus reticulatus		T *Hemiaulus subacutus*	29.83	Lazarus et al., 2014; Cervato and Burckle, 2003
		T *Hemiaulus exiguus*	29.95	Lazarus et al., 2014; Cervato and Burckle, 2003
		T *Cestodiscus demergitus*	30.55	Lazarus et al., 2014; Cervato and Burckle, 2003
		T *Rocella praenitida*	30.55	Lazarus et al., 2014; Scherer and Koç, 1996
		B *Azpeitia bukryi*	30.75	Lazarus et al., 2014; Barron et al., 2004
		T *Cestodiscus robustus*	30.84	Lazarus et al., 2014; Barron et al., 2004
		T *Pyxilla reticulata*	30.84	Lazarus et al., 2014; Cervato and Burckle, 2003
		T *Hemiaulus barbadensis*	30.93	Lazarus et al., 2014; Cervato and Burckle, 2003
		T *Skeletonemopsis barbadense*	30.93	Lazarus et al., 2014; Cervato and Burckle, 2003
		T *Hemiaulus altar*	31.02	Lazarus et al., 2014; Cervato and Burckle, 2003
		T *Cestodiscus convexus*	31.12	Lazarus et al., 2014; Barron et al., 2004
		T *Coscinodiscus excavatus*	31.12	Lazarus et al., 2014; Barron et al., 2004
		T *Rouxia hannae*	31.12	Barron, pers. comm., 2017
		B *Cavitatus miocenicus*	31.12	Lazarus et al., 2014; Barron et al., 2004
		B *Thalassionema nitzschioides*	31.12	Lazarus et al., 2014; Barron et al., 2004
		T *Coscinodiscus excavatus* var. *semilunaris*	31.71	Lazarus et al., 2014; Barron et al., 2004
		T *Asterolampra insignis*	32.01	Lazarus et al., 2014; Cervato and Burckle, 2003
		T *Coscinodiscus bulliens*	32.10	Lazarus et al., 2014; Gombos, 1982
		T *Pterotheca aculeifera* (*aculifera*)	32.10	Lazarus et al., 2014; Hajos, 1976
		B *Rouxia hannae*	32.10	Barron, pers. comm., 2017
		T *Trinacria subcapitata*	32.30	Lazarus et al., 2014; Cervato and Burckle, 2003
		T *Cestodiscus reticulatus*	32.40	Lazarus et al., 2014; Barron et al., 2004
		T *Coscinodiscus hajosiae*	32.40	Lazarus et al., 2014; Barron et al., 2004
		T *Hemiaulus hostilis*	32.40	Lazarus et al., 2014; Fenner, 1994
		B *Coscinodiscus excavatus* var. *semilunaris*	32.40	Lazarus et al., 2014; Barron et al., 2004
		T *Riedelia claviger*	32.70	Lazarus et al., 2014; Barron et al., 2014
		B *Thalassiothrix longissima*	32.70	Lazarus et al., 2014; Cervato and Burckle, 2003
		T *Cestodiscus* sp. 2	32.99	Lazarus et al., 2014; Barron et al., 2004
		T *Hemiaulus dubius*	33.09	Barron, pers. comm., 2017
		B *Cestodiscus reticulatus*	33.31	Lazarus et al., 2014; Barron et al., 2004
Coscinodiscus excavatus		B *Rhizosolenia styliformis*	33.31	Lazarus et al., 2014; Cervato and Burckle, 2003
		B *Cestodiscus parmula*	33.55	Lazarus et al., 2014; Cervato and Burckle, 2003
		B *Goniothecium odontella*	33.55	Lazarus et al., 2014; Cervato and Burckle, 2003
		T *Coscinodiscus decrescens*	33.66	Lazarus et al., 2014; Fenner, 1978
		B *Cestodiscus robustus*	33.78	Lazarus et al., 2014; Barron et al., 2014
		B *Coscinodiscus excavatus*	33.78	Lazarus et al., 2014; Barron et al., 2004
Baxteriopsis brunii		T *Hemiaulus gracilis*	33.91	Lazarus et al., 2014; Cervato and Burckle, 2003
		B *Cestodiscus* sp. 2	33.91	Lazarus et al., 2014; Barron et al., 2014
		B *Hemiaulus barbadensis*	33.91	Lazarus et al., 2014; Cervato and Burckle, 2003
		T *Cestodiscus fennerae*	34.09	Lazarus et al., 2014; Barron et al., 2014
		B *Cestodiscus trochus*	34.15	Lazarus et al., 2014; Barron et al., 2014
		T *Kozloviella subrotunda*	34.28	Lazarus et al., 2014; Scherer et al., 2007
		B *Rocella praenitida*	34.28	Lazarus et al., 2014; Scherer and Koç, 1996
		B *Azpeitia oligocenica*	34.53	Lazarus et al., 2014; Barron et al., 2014
		B *Cestodiscus convexus*	34.53	Lazarus et al., 2014; Barron et al., 2014
		B *Cestodiscus demergitus*	34.53	Lazarus et al., 2014; Barron et al., 2014
		B *Hemiaulus gracilis*	34.53	Lazarus et al., 2014; Cervato and Burckle, 2003
		B *Trinacria subcapitata*	34.53	Lazarus et al., 2014; Cervato and Burckle, 2003
		B *Baxteriopsis brunii*	34.65	Lazarus et al., 2014; Scherer et al., 2007
Asterolampra marylandica	B	T *Cestodiscus pulchellus* var. *novazealandica*	34.90	Lazarus et al., 2014; Barron et al., 2014
		B *Cestodiscus stokesianus*	35.13	Lazarus et al., 2014; Cervato and Burckle, 2003
		T *Azpeitia tuberculata*	35.70	Lazarus et al., 2014; Barron et al., 2014
		B *Actinocyclus octonarius*	>36.39	Lazarus et al., 2014; Hajós, 1976
		B *Triceratium acutangulum*	>36.39	Lazarus et al., 2014; Edwards, 1991
		B *Triceratium condecorum*	>36.39	Lazarus et al., 2014; Edwards, 1991
	A	T *Hemiaulus grassus*	36.39	Lazarus et al., 2014; Scherer et al., 2007
		B *Cestodiscus fennerae*	36.84	Lazarus et al., 2014; Barron et al., 2014
		T *Hemiaulus gondolaformis*	37.28	Lazarus et al., 2014; Scherer et al., 2007
		B *Hemiaulus altar*	37.39	Lazarus et al., 2014; Cervato and Burckle, 2003
		B *Macrora stella* (*Azpeitia*)	37.39	Lazarus et al., 2014; Cervato and Burckle, 2003
		B *Skeletonemopsis barbadense*	37.39	Lazarus et al., 2014; Barron et al., 2004
		B *Cestodiscus pulchellus* var. *novazealandica*	>38.36	Lazarus et al., 2014; Barron et al., 2014
		T *Triceratium kanayae*	<40.08	Lazarus et al., 2014; Scherer et al., 2007
		B *Asterolampra marylandica*	40.08	Lazarus et al., 2014; Scherer et al., 2007

Table T5. Taxonomic list of relevant diatom species, Expeditions 367 and 368. **Download table in CSV format.**

Paleomagnetism

Shipboard paleomagnetic investigations were conducted on both the archive and working halves of cores recovered during Expeditions 367 and 368. The primary objectives were to determine directions of natural remanent magnetization (NRM) components, including magnetic polarity, and downhole variation of magnetic properties.

Shipboard paleomagnetic investigations combined three complementary approaches: (1) measurement and in-line alternating field (AF) demagnetization of archive-half sections on the pass-through 2G Enterprises (model 760R-4K) superconducting rock magnetometer (SRM), (2) measurement and thermal demagnetization of oriented discrete samples on the SRM, and (3) measurement and AF demagnetization of oriented discrete samples on the spinner magnetometer (AGICO model JR6). Additionally, the anisotropy of magnetic susceptibility (AMS) was measured on discrete samples with the AGICO KLY 4 Kappabridge.

Discrete cube samples were collected from the central part of working-half sections to reduce the effect of drilling disturbance. The discrete sampling strategy was modified depending upon lithology (sediments versus basement), type of drilling used (e.g., soft sediments can be disturbed by RCB coring to the point of not being usable for magnetic inclination), and recovery rate. For basement rocks, at least one cube was collected per major lithologic unit (as defined by petrologists) to characterize the magnetic response of major units, different grain-size distributions, and deformation. These data were to be used by shipboard paleomagnetists to construct the magnetostratigraphy and by structural geologists to orient cores. Due to the low recovery in basement (<20%), samples were shared with the petrophysics team to measure porosity and moisture during Expedition 367 and until Hole U1501D of Expedition 368. The sample sharing significantly slowed down data acquisition for both teams (old protocol in Table **T6**). Furthermore, heating samples to 105°C in a magnetically unshielded oven imparts an undesirable artificial magnetization on samples. The only way to remove this artificial magnetization is to thermally demagnetize the sample to 250°/350°C, which results in the loss of all demagnetization steps between 95° and 350°C. Considering that a cube is not necessary to perform a density and porosity measurement, a new protocol was suggested that includes the use of residuals (Table **T6**). Moreover, for shared samples (cubes of hard rock) we proposed to use the magnetically shielded oven (ASC Scientific model TD-48SC), which can accommodate up to 48 samples at a time. Both teams agreed to follow this protocol and to apply it for the rest of Expedition 368.

Previous paleomagnetic studies documented a coring-induced, isothermal remanent magnetization (IRM) imparted on the core (e.g., Pinto and McWilliams, 1990; Fuller et al., 1998; de Wall and Worm, 2001).

Both section-half and discrete data, collected on the pass-through SRM and spinner magnetometer, respectively, were uploaded to the LIMS database. We then analyzed the stepwise demagnetization data of the discrete samples by principal component analysis (PCA) to define the characteristic remanent magnetization (ChRM) (Kirschvink, 1980). Data visualization (Zijderveld demagnetization plots and equal area projections) and PCA were conducted using the PuffinPlot software (version 1.03, 23 April 2015) (Lurcock and Wilson, 2012).

Magnetic measurements on archive-half sections

The remanent magnetization of archive-half sections was measured using a pass-through SRM equipped with direct-current superconducting quantum interference devices (SQUIDs) and an in-line, automated three-axis AF demagnetizer capable of reaching a peak field of 80 mT.

Measurement of archive halves was conducted using the SRM software (IMS-SRM version 9.2) assuming a sample area of 17.5 cm^2 for conversion to volume-normalized magnetization units (A/m). The interval between NRM measurement points was typically at 2.5 to 5 cm spacing for sedimentary material (depending on the expected sedimentation rate) and 2.0 cm for igneous rocks at the speed of 10 cm/s. The response functions of the pick-up coils of the SQUID sensors have a full width of 7.25–8.8 cm at half height. Therefore, data collected within ~4 cm of piece boundaries (or voids) can be significantly affected by edge effects and have to be treated with caution.

We performed successive AF demagnetizations using the SRM in-line AF demagnetizer on all split-core archive sections. The in-line AF demagnetizer applies a field to the *x*-, *y*-, and *z*-axes of the SRM in this fixed order (Figure **F23A, F23D**). Previous reports suggest that higher AF demagnetization fields have produced significant anhysteretic remanent magnetization (ARM) along the *z*-axis of the SRM (e.g., Harris et al., 2013b). Considering this limitation, we only used demagnetization steps up to 25 mT to demagnetize the sections. Depending on time constraints imposed by the rate of core recovery, for most of the sediment sections we performed 3–6 steps from NRM up to 15 or 25 mT. For basement rocks during Expedition 367, we adopted a set of narrower AF steps of 2 mT from NRM to 10 mT and steps of 5 mT from 10 to 25 mT. For Hole U1505C (starting from Section 3H-2) and for Holes U1504A, U1504B, and U1505C, only NRM was measured. This decision was

Table T6. Sampling protocols, Expeditions 367 and 368. **Download table in CSV format.**

Sample type	Team	Treatment	Time
Old protocol			
CUBE	Petrophysics	*P*-wave velocity on dry sample	10 min
CUBE	Paleomagnetism	NRM and AMS at room temperature and after heating at 95°C	3 h
CUBE	Petrophysics	Moisturized to prepare for density and porosity measured	24–48 h or more
CUBE	Petrophysics	Measure *P*-wave velocity on wet sample	10 min
CUBE	Petrophysics	Heated at 105°C	24 h
CUBE	Petrophysics	Measured for density and porosity	30 min/sample
CUBE	Paleomagnetism	Complete thermal demagnetization process	48 h
New protocol			
CUBE	Petrophysics	*P*-wave velocity on dry/wet sample	24 h
CUBE	Paleomagnetism	Complete thermal demagnetization process	48 h
Residuals	Petrophysics	Complete density and porosity treatment	48–52 h or more

Figure F23. A. IODP coordinates of paleomagnetic samples (after Richter et al., 2007). B. Natsuhara-Giken sampling cubes (7 cm³ volume) with sample coordinate system. Red hatched arrow is parallel to up arrow on sample cube and points in –*z*-direction. C. Measurement positions in JR-6A spinner magnetometer. D. Coordinate system used for the SRM on board the *JOIDES Resolution*.

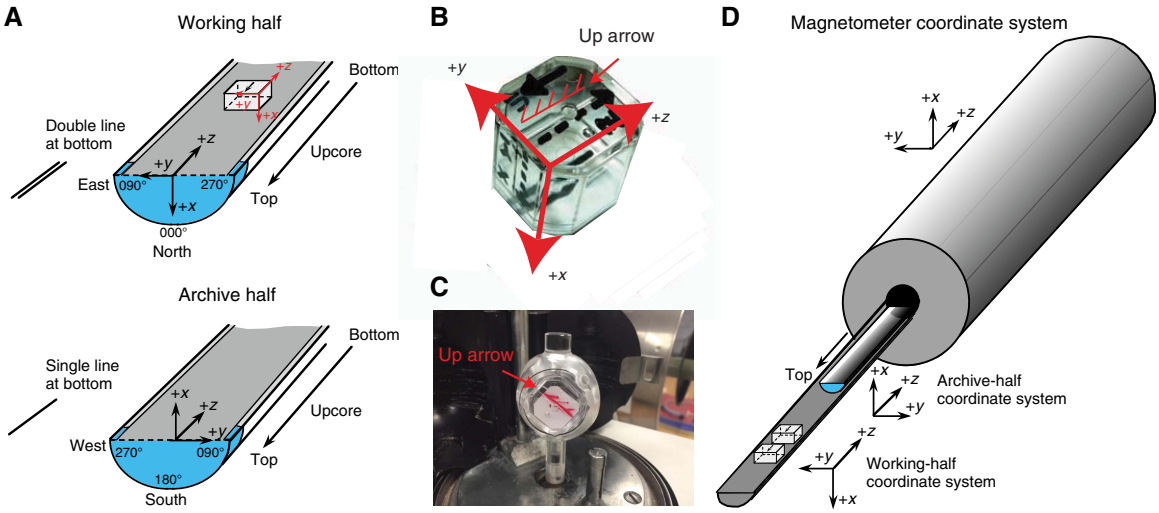

made after a comparison of magnetization intensities between discrete samples and sections led us to suspect that the SRM was not properly calibrated (geometrically) for core sections. AF demagnetization results were plotted individually as vector plots (Zijderveld, 1967)and as downhole variations with depth. We inspected the plots visually to evaluate whether the remanence after demagnetization at the highest AF step reflects the ChRM and geomagnetic polarity sequence.

Low-field magnetic susceptibility (κ), measured on whole-round core sections using the WRMSL and archive-half core sections using the SHMSL (see **Physical properties**), was used to assess the concentration of magnetic minerals and to determine the downhole relative paleointensity (NRM/κ). These whole-round records of magnetic susceptibility were compared to visual features in the split cores to flag possible artifacts.

Magnetic measurements on discrete samples

Discrete samples were initially measured on both the SRM and a spinner magnetometer. These samples were subjected to AF demagnetization treatments using both the 2G in-line AF demagnetizer (as described above) and the DTECH (model D-2000) AF demagnetizer. But the resultant demagnetization behavior of the discrete samples becomes noisy at higher AF treatments, and thus measurement on the SRM is not recommended for discrete samples. This recommendation is also confirmed by shipboard tests of the reliability of discrete measurements on the 2G SRM. The routine AF demagnetization treatment was performed using the DTECH (model D-2000) AF demagnetizer. In addition, to avoid contamination by the ambient magnetic field during shipboard measurements, two cylindrical mu-metal shields provided a suitable low-field environment for temporary sample storage.

Oriented discrete samples were taken preferentially in fine-grained intervals where drilling deformation was minimal. In soft sediment, discrete samples were taken in plastic "Japanese" Natsuhara-Giken sampling cubes (7 cm³ sample volume; Figure **F23B**). Cubes were pushed into the working half of the core with the "up" arrow on the cube pointing upsection in the core. In lithified sediments and hard rocks, 2 cm cubes (8 cm³ sample volume) were cut with the parallel saw.

Incremental AF demagnetization of discrete samples was performed with the DTECH AF demagnetizer (model D-2000) at fields up to 45 or 50 mT for lower coercivity samples and 120 or 200 mT for high-coercivity samples. We also applied progressive thermal demagnetization using a thermal specimen demagnetizer (ASC Scientific model TD-48SC) up to 700°C at steps of 25° to 50°C depending on the magnetic minerals present in the sample. During Expedition 367, a combination of stepwise AF and thermal demagnetization was applied.

AMS was measured on an AGICO KLY 4S Kappabridge instrument at a field of 300 A/m using the AMSSpin LabVIEW program designed by Gee et al. (2008) or the SUFAR (AGICO) program. The KLY 4S Kappabridge measures AMS by rotating the sample along three axes, stacking the data, and calculating the best-fit second-order tensor. It also measures the volume-normalized calibrated bulk susceptibility (χ).

Coordinates

All magnetic data are reported relative to the IODP orientation conventions: +*x* is into the face of the working half, +*y* points toward the left side of the face of the working half, and +*z* points downsection. The relationship of the SRM coordinates (*X*-, *Y*-, and *Z*-axes) to the data coordinates (*x*-, *y*-, and *z*-directions) is as follows: for archive halves, *x*-direction = *X*-axis, *y*-direction = –*Y*-axis, and *z*-direction = *Z*-axis; for working halves, *x*-direction = –*X*-axis, *y*-direction = *Y*-axis, and *z*-direction = *Z*-axis (Figure **F23**). The coordinate systems for the spinner magnetometer and Natsuhara-Giken sampling cubes are also shown in Figure **F23**.

Core orientation

Paleomagnetic study of marine sediment cores is greatly enhanced if the angle between magnetic north and the double line marked on the core liner can be determined. Core orientation of APC cores was achieved with the orientation tool (Icefield MI-5 core orientation tool) mounted on the core barrel. The Icefield MI-5

core orientation tool consists of triaxial magnetometers and accelerometers. These sensors provide an azimuthal correction for the core barrel that, combined with the local magnetic declinations, allows the measured NRM declinations to be transformed into true geographic coordinates. In the orientation deployment, the tool is connected to the core barrel with the double lines on the core liner at a fixed and known angle relative to its sensors. Previous expeditions have reported that in general these orientation tools have an accuracy of 20°–30°. Unlike earlier expeditions that reported reversed directions (i.e., 180° instead of 0°) during a period of normal polarity, the declinations (above ~160 m from the APC cores) corrected based on the Icefield data are consistent with the inclinations.

The ChRMs can also provide a reference frame to orient cores (see **Structural geology**). Provided that the reference magnetic pole is known, the orientation of the paleomagnetic vector is then used to restore the azimuth of the +*x* core axis (e.g., Fuller, 1969).

Magnetostratigraphy reference scale and interpretations

The magnetostratigraphy at each site was constructed by correlating observed polarity sequences with a reference GPTS in combination with biostratigraphic biohorizons. The GPTS used for Expeditions 367 and 368 (Table **T7**) is the GPTS2016 synthesis of astronomical tuning of Cenozoic through latest Cretaceous polarity zones updated in Ogg et al. (2016). The Cenozoic portion of GPTS2016, together with microfossil and nannofossil biozones, is plotted in Figure **F24**.

For azimuthally unoriented samples from sedimentary rocks that formed at low latitudes, such as those at the Expedition 367 and 368 drill sites, determining the polarity of sedimentary units can be difficult. The polarity ambiguity arises when the samples are azimuthally unoriented and the inclination is very shallow near the Equator (the angular distance between reversed and normal polarity inclinations is small). Because paleomagnetic inclinations from any samples will have some degree of dispersion about their mean inclination, it is likely that when the mean inclination is shallow (near zero), the sign of the inclination will not be indicative of the polarity (e.g., McFadden and Reid, 1982; Cox and Gordon, 1984). The sign of the inclination of these samples should be used carefully as a definitive estimate of magnetic polarity.

We applied the following methods to establish magnetozones:

- Observing near-180° shift in declinations and significant changes in inclinations from pass-through measurements on long coherent core sections after AF demagnetization. The observed magnetozones are then checked with the ChRM directions of the discrete samples from the corresponding intervals.
- Comparison of inclination trends with predicted paleolatitudes of the drill sites according to the absolute plate motion of the South China plate on global plate circuit reconstructions (e.g., Scotese, 2014a, 2014b). However, the reconstructed position of the drill holes through the Cenozoic has negligible displacement in paleolatitude because that plate and the adjoining main Asian landmass underwent clockwise rotation.

Whenever possible, we provide an interpretation of the magnetic polarity, with the naming convention following that of correlative chron and anomaly numbers prefaced by the letter C (e.g., Ogg et al., 2016). Normal polarity subchrons are referred to by adding suffixes (n1, n2, etc.) that increase with age. For the younger part of the timescale (Pliocene–Pleistocene), we use the traditional names to refer to the various chrons and subchrons (e.g., Brunhes, Jaramillo, Olduvai, etc.). In general, polarity reversals occurring at the end of core sections have been treated with extreme caution.

Table T7. Geomagnetic polarity timescale used during Expeditions 367 and 368. Cenozoic and latest Cretaceous magnetic polarity chron nomenclature and age model based on astronomical tuning as used in Ogg et al. (2016). GSSP = Global Boundary Stratotype Section and Points. (Continued on next three pages.) **Download table in CSV format.**

Period	Epoch	Age (stage)	Base age (Ma)	Chron	Polarity chron	Age at base of chron (Ma)	Duration (My)	Remarks
Quaternary	Holocene	late (Tarantian)	11.8 ka		Present	0		
	Pleistocene		0.126	C1	C1n (Brunhes)	0.773	0.773	Base of middle Pleistocene (Ionian) is base of Brunhes Chron.
		middle (Ionian)	0.773		C1r.1r (youngest chron within Matuyama)	1.008	0.235	
					C1r.1n (Jaramillo)	1.076	0.068	
					C1r.2r	1.189	0.113	
		early (Calabrian)			C1r.2n (Cobb Mountain)	1.221	0.032	Cobb Mountain is within early part of Matuyama (C1r).
					C1r.3r	1.775	0.554	
			1.806	C2	C2n (Olduvai)	1.934	0.159	Base of Calabrian is in lower part of Olduvai.
		early (Gelasian)			C2r.1r	2.12	0.186	
					C2r.1n (Feni)	2.155	0.035	
					C2r.2r (oldest chron within Matuyama)	2.61	0.455	Base of Pleistocene is near base of Matuyama.
			2.588					
Neogene	Pliocene	late (Piacenzian)		C2A	C2An.1n (youngest chron within Gauss)	3.032	0.422	"Gauss Normal Chron" (C2An) contains two reversed intervals; Kaena (2An.1r) and Mammoth (2An.2r).
					C2An.1r (Keana)	3.116	0.084	
					C2An.2n (Gauss)	3.207	0.091	
					C2An.2r (Mammoth)	3.33	0.123	
			3.6		C2An.3n (oldest chron within Gauss)	3.596	0.266	Base of Piacenzian is base of C2An.3n.
		early (Zanclean)	5.333		C2Ar (youngest chron within Gilbert)	4.187	0.591	"Gilbert Reversed Chron" spans C2Ar through C3r.

Table T7 (continued). (Continued on next page.)

Period	Epoch	Age (stage)	Base age (Ma)	Chron	Polarity chron	Age at base of chron (Ma)	Duration (My)	Remarks
Neogene	Pliocene	early (Zanclean)	5.333	C3	C3n.1n (Cochiti)	4.3	0.113	
					C3n.1r	4.493	0.193	
					C3n.2n (Nunivak)	4.631	0.138	
					C3n.2r	4.799	0.168	
					C3n.3n (Sidufjall)	4.896	0.097	
					C3n.3r	4.997	0.101	
					C3n.4n (Thvera)	5.235	0.238	Base of Pliocene is in uppermost C3r.
	Miocene	late (Messinian)	7.246	C3A	C3r (oldest chron within Gilbert)	6.033	0.798	
					C3An.1n	6.252	0.219	
					C3An.1r	6.436	0.184	
					C3An.2n	6.733	0.297	
				C3B	C3Ar	7.14	0.407	
					C3Bn	7.212	0.072	
					C3Br.1r	7.251	0.039	Base of Messinian is in lowermost C3Br.1r.
		late (Tortonian)	11.625		C3Br.1n	7.285	0.034	
					C3Br.2r	7.454	0.169	
					C3Br.2n	7.489	0.035	
					C3Br.3r	7.528	0.039	
				C4	C4n.1n	7.642	0.114	
					C4n.1r	7.695	0.053	
					C4n.2n	8.108	0.413	
					C4r.1r	8.254	0.146	
					C4r.1n	8.3	0.046	
					C4r.2r	8.771	0.471	C4r.2r-1 is within C4r.2r (8.661–8.699 Ma).
				C4A	C4An	9.105	0.334	
					C4Ar.1r	9.311	0.206	
					C4Ar.1n	9.426	0.115	
					C4Ar.2r	9.647	0.221	
					C4Ar.2n	9.721	0.074	
					C4Ar.3r	9.786	0.065	
				C5	C5n.1n	9.937	0.151	
					C5n.1r	9.984	0.047	
					C5n.2n	11.056	1.072	C5n.2n-1 through 3
					C5r.1r	11.146	0.09	
					C5r.1n	11.188	0.042	
					C5r.2r	11.592	0.404	C5r.2r-1 is within C5r.2r (11.263-11.308 Ma).
					C5r.2n	11.657	0.065	Base of Tortonian is near base of C5r.2n.
					C5r.3r	12.049	0.392	
		middle (Serravalian)	13.82	C5A	C5An.1n	12.174	0.125	
					C5An.1r	12.272	0.098	
					C5An.2n	12.474	0.202	
					C5Ar.1r	12.735	0.261	
					C5Ar.1n	12.77	0.035	
					C5Ar.2r	12.829	0.059	
					C5Ar.2n	12.887	0.058	
					C5Ar.3r	13.032	0.145	
				C5AA	C5AAn	13.183	0.151	
					C5AAr	13.363	0.18	
				C5AB	C5ABn	13.608	0.245	
					C5ABr	13.739	0.131	
				C5AC	C5ACn	14.07	0.331	Base of Serravalian is upper C5ACn.
		middle (Langhian)	15.97		C5ACr	14.163	0.093	
				C5AD	C5ADn	14.609	0.446	
					C5ADr	14.775	0.166	
				C5B	C5Bn.1n	14.87	0.095	
					C5Bn.1r	15.032	0.162	
					C5Bn.2n	15.16	0.128	
					C5Br	15.974	0.814	Base of Langhian is base of C5Br.
		early (Burdigalian)	20.44	C5C	C5Cn.1n	16.268	0.294	
					C5Cn.1r	16.303	0.035	
					C5Cn.2n	16.472	0.169	
					C5Cn.2r	16.543	0.071	
					C5Cn.3n	16.721	0.178	
					C5Cr	17.235	0.514	
				C5D	C5Dn	17.533	0.298	
					C5Dr.1r	17.717	0.184	
					C5Dr.1n	17.74	0.023	Cryptochron in C5Dr
					C5Dr.2r	18.056	0.316	

Table T7 (continued). (Continued on next page.)

Period	Epoch	Age (stage)	Base age (Ma)	Chron	Polarity chron	Age at base of chron (Ma)	Duration (My)	Remarks
Neogene	Miocene	early (Burdigalian)	20.44	C5E	C5En	18.524	0.468	
					C5Er	18.748	0.224	
				C6	C6n	19.722	0.974	
					C6r	20.04	0.318	Cryptochron C6r-1
				C6A	C6An.1n	20.213	0.173	
					C6An.1r	20.439	0.226	Base of Burdigalian (working version) is approximate base of C6An.1r (used here) or of C6An.1n.
		early (Aquitanian)	23.03		C6An.2n	20.709	0.27	
					C6Ar	21.083	0.374	
				C6AA	C6AAn	21.159	0.076	
					C6AAr.1r	21.403	0.244	
					C6AAr.1n	21.483	0.08	
					C6AAr.2r	21.659	0.176	
					C6AAr.2n	21.688	0.029	
					C6AAr.3r	21.767	0.079	
				C6B	C6Bn.1n	21.936	0.169	
					C6Bn.1r	21.992	0.056	
					C6Bn.2n	22.268	0.276	
					C6Br	22.564	0.296	
				C6C	C6Cn.1n	22.754	0.19	
					C6Cn.1r	22.902	0.148	
					C6Cn.2n	23.03	0.128	Base of Miocene is base of C6Cn.2n.
Paleogene	Oligocene	late (Chattian)	28.09		C6Cn.2r	23.233	0.203	
					C6Cn.3n	23.295	0.062	
					C6Cr	23.962	0.667	
				C7	C7n.1n	24	0.038	
					C7n.1r	24.109	0.109	
					C7n.2n	24.474	0.365	
					C7r	24.761	0.287	Cryptochron C7r-1
				C7A	C7An	24.984	0.223	
					C7Ar	25.099	0.115	
				C8	C8n.1n	25.264	0.165	
					C8n.1r	25.304	0.04	
					C8n.2n	25.987	0.683	Cryptochron C8n.2n-1
					C8r	26.42	0.433	
				C9	C9n	27.439	1.019	Cryptochrons C9n-1; C9n-2
					C9r	27.859	0.42	Cryptochron C9r-1
				C10	C10n.1n	28.087	0.228	Base of Chattian (working version) is base of C10n.1n. Note: base is potentially at ~70% up in "undifferentiated Chron C10n" in candidate GSSP in Italy (Coccioni et al.; 2008); which would project as equivalent to C10n.1n.4.
		early (Rupelian)	33.89		C10n.1r	28.141	0.054	
					C10n.2n	28.278	0.137	
					C10r	29.183	0.905	Cryptochrons C10r-1; C10r-2
				C11	C11n.1n	29.477	0.294	
					C11n.1r	29.527	0.05	
					C11n.2n	29.97	0.443	
					C11r	30.591	0.621	Cryptochron C11r-1
				C12	C12n	31.034	0.443	
					C12r	33.157	2.123	Cryptochrons C12r-1 through C12r-8
				C13	C13n	33.705	0.548	Cryptochron C13n-1
					C13r	35.102	1.397	Base of Rupellian is at C13r.86. Cryptochrons C13r-1 through C13r-4
	Eocene	late (Priabonian)	37.99	C15	C15n	35.336	0.234	"C14" does not exist.
					C15r	35.58	0.244	
				C16	C16n.1n	35.718	0.138	
					C16n.1r	35.774	0.056	
					C16n.2n	36.351	0.577	
					C16r	36.573	0.222	
				C17	C17n.1n	37.385	0.812	Base of Priabonian (working version) assigned as base of C17n.1n.
		middle (Bartonian)	41.03		C17n.1r	37.53	0.145	
					C17n.2n	37.781	0.251	
					C17n.2r	37.858	0.077	
					C17n.3n	38.081	0.223	
					C17r	38.398	0.317	

Table T7 (continued).

Period	Epoch	Age (stage)	Base age (Ma)	Chron	Polarity chron	Age at base of chron (Ma)	Duration (My)	Remarks
Paleogene	Eocene	middle (Bartonian)	41.03	C18	C18n.1n	39.582	1.184	Cryptochron C18n.1n-1
					C18n.1r	39.666	0.084	
					C18n.2n	40.073	0.407	
					C18r	41.03	0.957	Base of Bartonian (working version) assigned as base of C18r.
		middle (Lutetian)	47.84	C19	C19n	41.18	0.15	
					C19r	42.124	0.944	
				C20	C20n	43.426	1.302	
					C20r	45.724	2.298	
				C21	C21n	47.349	1.625	
					C21r	48.566	1.217	Base of Lutetian (GSSP ratified Feb 2011) is base of nannofossil *Blackites inflatus* at Gorrondatxe section in Spain.
		early (Ypresian)	55.96	C22	C22n	49.344	0.778	
					C22r	50.628	1.284	
				C23	C23n.1n	50.835	0.207	
					C23n.1r	50.961	0.126	
					C23n.2n	51.833	0.872	
					C23r	52.62	0.787	
				C24	C24n.1n	53.074	0.454	
					C24n.1r	53.199	0.125	
					C24n.2n	53.274	0.075	
					C24n.2r	53.416	0.142	
					C24n.3n	53.983	0.567	This is NOT tied proportionally within C24r, but some indicate it as C24r.36 (e.g., used in Agnini et al., 2007, for calibrating nannofossil datums near boundary). Age used here is from U-Pb ≥ 0.05 My lower. Base of Eocene is 0.94 My (0.98 in another table) above top C25n according to cycle stratigraphy.
	Paleocene	late (Thanetian)	59.24	C24	C24r	57.101	3.118	
				C25	C25n	57.656	0.555	
					C25r	58.959	1.303	
				C26	C26n	59.237	0.278	Base of C26n = same as temporary assignment in GTS2004 (GSSP in Zumaya, Spain), as in Berggren et al., 1995.
		middle (Selandian)	61.61		C26r	62.221	2.984	Onset of a carbon isotope shift and sea level drop (Exxon/Hardenbol sequence boundary "Sel1"); near diversification of the Fasciculith group of calcareous nannoplankton, preceding the lowest *Fasciculithus tympaniformis* (base of nannoplankton Zone NP5).
		early (Danian)	66.04	C27	C27n	62.517	0.296	
					C27r	63.494	0.977	
				C28	C28n	64.667	1.173	
					C28r	64.958	0.291	
				C29	C29n	65.688	0.73	
					C29r	66.398	0.71	Mesozoic/Cenozoic boundary event is ~C29r.5 in total C29r span of ~710 ky, according to cycles; Husson et al., 2012.
Cretaceous	Late	Masstrichtian		C30	C30n	68.196		

Figure F24. Selected Cenozoic marine and terrestrial biostratigraphic zonations. Age is the time equivalent of the rock-record stage. Subepoch groupings of these ages into "late" or "early" are informal common usage. Magnetic polarity zones are scaled to astronomical cycles (e.g., Hilgen et al., 2012; Vandenberghe et al., 2012; Westerhold et al., 2015). Planktonic foraminifer zones and main markers are from GPTS2012 (Hilgen et al., 2012; Anthonissen and Ogg, 2012) with Paleogene modified from Wade et al. (2011), but late Pliocene details for Zones PL4–PL5 between Atlantic (Atl.) and Pacific (Pac.) basins are omitted. Placement of proposed base Chattian marker of last common occurrence (LCO) of *Chiloguembelina cubensis* is relative to Oligocene magnetic polarity chrons; hence, the assigned age to the Rupelian/Chattian boundary is uncertain. Calcareous nannofossil (CN) zones and markers from Backman et al. (2012) and Agnini et al. (2014) are shown with commonly used NN and NP zonations of Martini (1971). Major sea level sequence boundaries and highstands are from Hardenbol et al. (1998). Additional zonations, biostratigraphic markers, geochemical trends, sea level curves, and details on calibrations are compiled in Hilgen et al. (2012) and Vandenberghe et al. (2012) and in internal data sets within the TimeScale Creator visualization system (free at **https://engineering.purdue.edu/Stratigraphy/tscreator/index/index.php**). Modified from Ogg et al. (2016). LGM = last glacial maximum. Megacycles: T = transgression, R = regression. (Continued on next two pages.)

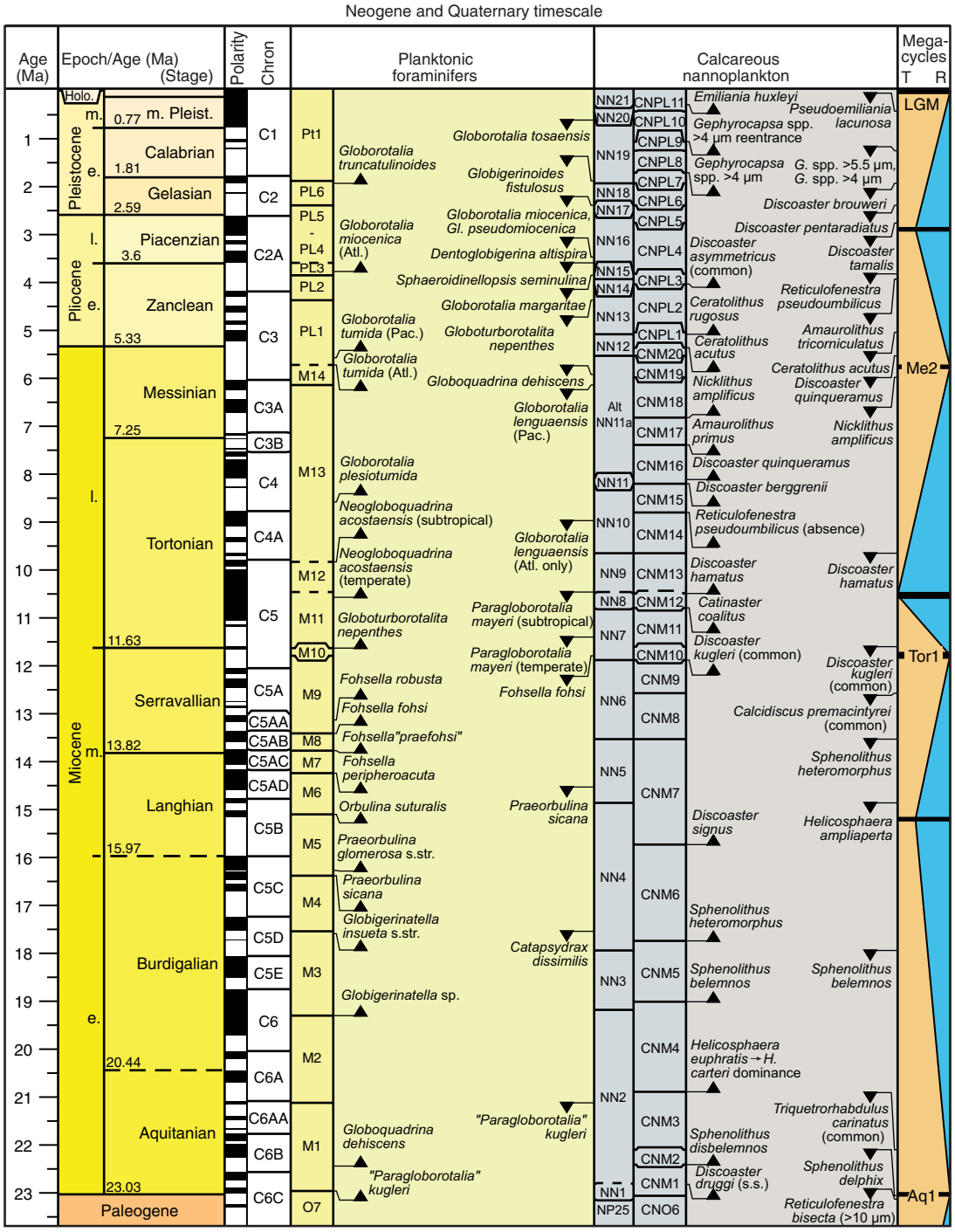

Figure F24 (continued). (Continued on next page.)

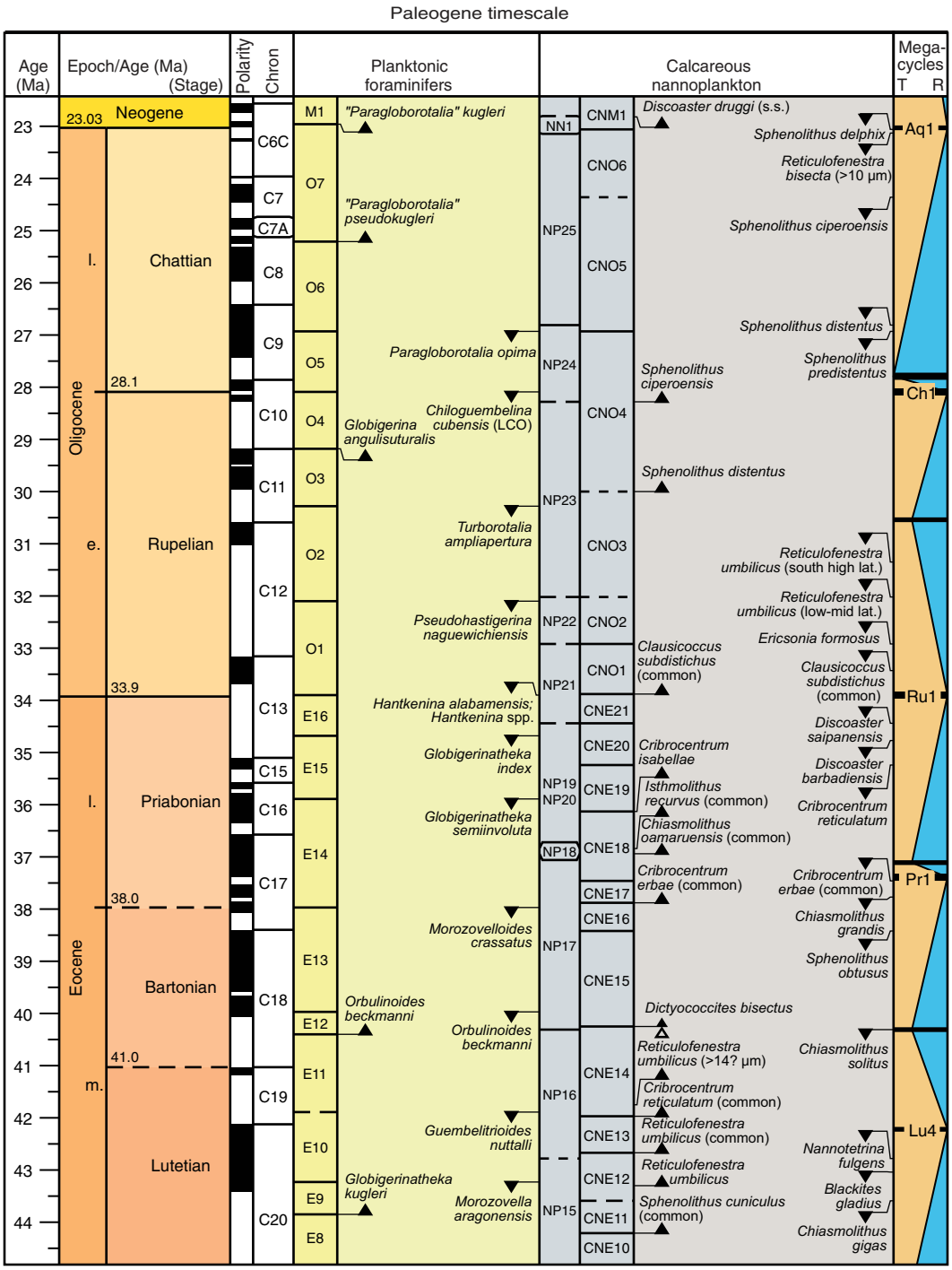

Figure F24 (continued).

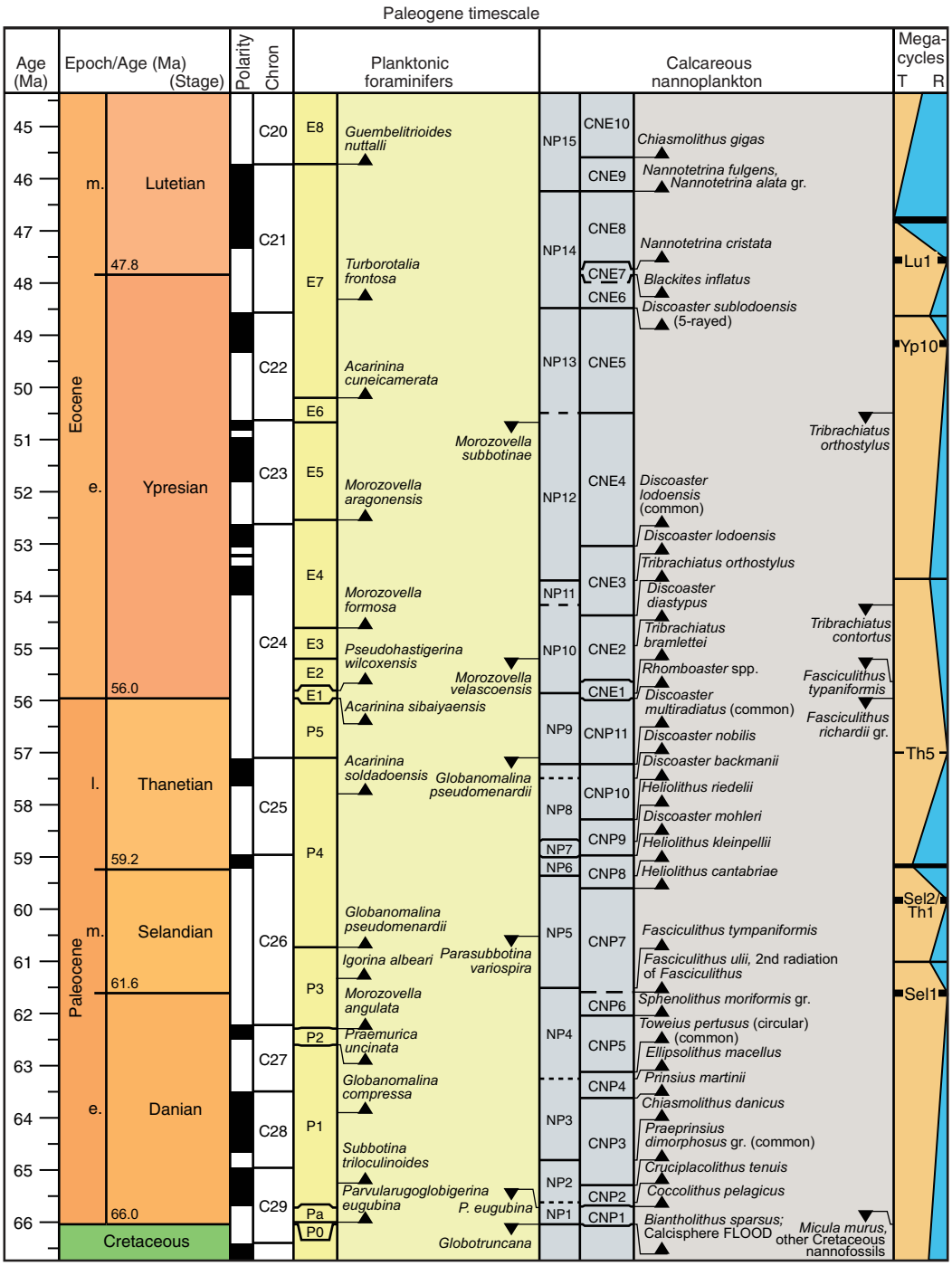

Geochemistry

The shipboard geochemistry program for Expeditions 367 and 368 included the following measurements:

- Headspace gas content;
- Interstitial water composition;
- Sedimentary geochemistry, including total inorganic carbon, total carbon, total nitrogen, and major and minor element content; and
- Igneous and metamorphic rock geochemistry (major and minor element content).

Our analytical procedures follow those described by Integrated Ocean Drilling Program Expedition 345 and IODP Expeditions 349, and 352 (Gillis et al., 2014; Li et al., 2015; Reagan et al., 2015). Our analyses were conducted to satisfy routine shipboard safety and pollution prevention requirements; characterize interstitial water, sediment, and rock geochemistry for shipboard interpretation; and provide a basis for sampling for subsequent shore-based research.

Headspace gas analysis

For headspace gas analysis, 5 cm^3 samples were collected immediately after core retrieval on deck, placed in a 20 cm^3 glass vial, sealed with a septum, and crimped with a metal cap. When consolidated or lithified samples were encountered, chips of material were placed in the vial and sealed and soft-sediment samples were collected with a sawn-off syringe or with a scoop. If an interstitial water sample was obtained, the headspace sample was taken from the top of the section immediately next to the interstitial water sample whenever possible. Otherwise, the headspace sample was taken from the top of the third section. The vial was labeled with the core, section, and interval from which the sample was taken and then placed in an oven at 70°C for 30 min. A 5 cm^3 aliquot of gas was extracted through the septum with a gas-tight glass syringe and then injected into a gas chromatograph (GC).

An Agilent 6890 GC equipped with a flame ionization detector (FID) was used to measure the concentrations of methane (C_1), ethane (C_2), ethylene ($C_{2=}$), propane (C_3), and propylene ($C_{3=}$). A 2.4 m × 2.0 mm stainless steel column packed with 80/100 mesh HayeSep "R" was installed in the GC oven. The injector consists of a 1/16 inch Valco union with a 7 µm screen connected to a Valco-to-Luer lock syringe adapter. This injector connects to a 10-port Valco valve that is switched pneumatically by a digital valve interface. The injector temperature was set at 120°C throughout each run. Samples were introduced into the GC through a 0.25 cm^3 sample loop connected to the Valco valve. The valve can be switched automatically to backflush the column. The oven temperature was programmed to start at 80°C for 8.25 min and then increase to 150°C at a rate of 40°C/min and hold for 5 min. Helium was used as the carrier gas. Initial helium flow in the column was 30 mL/min. Flow was then ramped up to 60 mL/min after 8.25 min to accelerate elution of C_3 and $C_{3=}$. The run time was 15 min. The GC was also equipped with an electronic pressure control module to control the overall gas flow. The FID was set at 250°C. Data were collected and evaluated with an Agilent Chemstation data handling program. Chromatographic response was calibrated against known standards provided by Scott Specialty Gases.

No accurate measurement of the sediment mass was carried out. As such, measured concentrations are semiquantitative (likely carrying a ±25% relative uncertainty, mainly reflecting variations in the sediment mass around the target mass) and are only indicative for safety monitoring. However, gas ratios (e.g., C_1/C_2) are not affected by the uncertainty on the sediment mass.

Interstitial water chemistry

Interstitial water collection

Routine interstitial water samples were obtained by squeezing whole-round sections cut from cores. Standard whole-round samples were 5 cm long, but as water content decreased downhole, the size of the whole-round samples was increased to 15 cm to enable extraction of ~30 mL of water needed for shipboard and shore-based analyses. Interstitial water collection stopped when it was no longer possible to obtain ~10 mL for shipboard analyses by squeezing 15–20 cm long whole-round sediments. Whole-round samples were cut and capped as quickly as possible after the core arrived on deck and immediately moved to the chemistry laboratory for squeezing. Whole-round samples were typically collected at a frequency of ~3 samples per core in the first 5 cores, 2 samples per core for cores 5–10, and subsequently 1 sample per core. Samples of basement were not collected for squeezing interstitial water.

The exterior of the whole-round sample was carefully scraped with a spatula to remove potential contamination from drilling fluid and sediment smearing in the borehole. In APC cores, ~0.5 cm of material from outside of the whole round was removed, whereas in XCB and RCB cores, where borehole contamination is higher, as much as two-thirds of the sediment was removed from each whole round. The cleaned sediment was placed into a 9 cm diameter titanium squeezer that was then placed in a Carver hydraulic press (Manheim and Sayles, 1974) and squeezed at pressures no higher than 30,000 lb (~20.3 MPa) to extract interstitial water. The squeezed interstitial water was collected in precleaned high-density polyethylene syringes attached to the squeezing assembly. Subsequently, the interstitial water was filtered through a 0.45 µm polyethersulfone membrane disc filter into various sample containers, except for aliquots taken for dissolved organic carbon (DOC) analysis, which were filtered through a 0.2 µm polyethersulfone membrane disc filter.

Sample allocation was determined based on the pore fluid volume obtained and analytical priorities based on the objectives of the expedition. Aliquots for major and minor elements by ICP-AES were acidified by adding ~10 µL of trace metal–grade concentrated HNO_3 and placed in 2 mL cryovials. Aliquots for chloride and alkalinity titration, ammonium and phosphate spectrophotometry analyses, and ion chromatography analyses were put in 8 mL glass vials. Aliquots for isotopic analyses of oxygen and hydrogen were placed in zero-headspace 2 mL septum screw-lid glass vials. Aliquots for Sr, B, and Li isotopes were acidified by adding ~10 µL of trace metal–grade concentrated HNO_3 and placed in two 5 mL cryovials. Aliquots for dissolved inorganic carbon (DIC) and DOC and their $\delta^{13}C$ were treated with 10 µL of a saturated $HgCl_2$ solution and placed in zero-headspace 2 mL and 5 mL septum screw-lid glass vials, respectively. Aliquots for TH_2S were placed in 2 mL septum screw-lid glass vials with 0.5 mL of ~50 mM zinc acetate solution. The samples were stored at 4°C after collection.

Alkalinity, pH, and salinity were analyzed immediately after interstitial water was obtained. Other shipboard analyses were carried out in batches. Dissolved sodium, calcium, magnesium, chloride, bromide, and sulfate were analyzed by ion chromatography. Ammonium and phosphate were analyzed by UV-VIS spectrophotometry. Minor element concentrations were analyzed by ICP-AES.

After interstitial water extraction was complete, sediment squeeze cakes were divided and sealed in plastic bags for shipboard

and shore-based analyses. Squeeze cake samples for shore-based organic analysis were stored at −20°C. All other squeeze cake samples were refrigerated at 4°C.

Shipboard interstitial water analysis

Interstitial water samples were analyzed on board following the protocols in Gieskes et al. (1991), Murray et al. (2000), and the Integrated Ocean Drilling Program user manual for shipboard instrumentation, which was updated during Expedition 344 (Harris et al., 2013).

Salinity, alkalinity, and pH

Salinity, alkalinity, and pH were measured immediately after squeezing, following the procedures in Gieskes et al. (1991). Salinity was measured using a Fisher temperature-compensated handheld refractometer. The pH was measured with a combined glass electrode, and alkalinity was determined by Gran titration with an autotitrator (Metrohm 794 basic Titrino). Three milliliters of interstitial water sample was titrated against 0.1 M HCl at 25°C. International Association for the Physical Sciences of the Oceans (IAPSO) standard seawater was used for calibration and was analyzed at the beginning and end of a set of samples for each site and also every 5–10 samples. Both the analytical precision and accuracy of alkalinity titrations were better than 3% based on repeated analysis of IAPSO standard seawater.

Chloride by titration

High-precision chloride concentrations were acquired using a Metrohm 785 DMP autotitrator and silver nitrate ($AgNO_3$) solution calibrated against repeated titrations of IAPSO standard. A 0.5 mL aliquot of sample was diluted with 30 mL of 0.32 M HNO_3 solution and titrated with 0.1 M $AgNO_3$. Repeated analyses of an IAPSO standard yielded a precision better than 0.06%; however, the chloride concentrations yielded by titration includes not only dissolved chloride but also all of the other halide elements and bisulfide. The *JOIDES Resolution* is equipped with a Metrohm 850 Professional ion chromatograph that can analyze anions and cations simultaneously. The chloride concentration was analyzed by both titration and ion chromatography for Holes U1499A, U1501C, U1501D, U1502A, U1504A, and U1505C. Chloride concentrations analyzed by ion chromatography were not greater than those by titration, indicating that ion chromatography can provide mostly reliable chloride data. As a result, chloride concentration was analyzed by both titration and ion chromatography only for the upper 50 m section for all sites during Expeditions 367 and 368.

Sulfate, chloride, bromide, calcium, magnesium, potassium, and sodium

Sulfate, chloride, bromide, calcium, magnesium, and sodium concentrations were analyzed by ion chromatography (Metrohm 850 Professional IC) using aliquots of 100 µL that were diluted 1:100 with deionized water (18 MΩ/cm). At the beginning and end of each run, different dilutions (1:80 to 1:500) of IAPSO standard seawater were analyzed to create a six point calibration curve. The r^2 for the calibration curve was always >0.99, and relative standard deviation varied from 0.8% to 3.4%. The 1:100 diluted IAPSO standard seawater was also analyzed every ~10 samples for quality control and to determine accuracy and precision. A new calibration curve was run if measured concentrations deviated from the expected values (28.9 mM for SO_4^{2-} and 0.865 mM for Br^-). Based on measurements of IAPSO standard seawater, analytical precision (2σ) was within 1% for chloride, 5% for bromide, 2% for sulfate, 5% for calcium, 3% for magnesium, and 1% for sodium.

Ammonium and phosphate

Ammonium and phosphate concentrations were determined using an Agilent Technologies Cary Series SPS3 spectrophotometer with a sipper sample introduction system following the protocol in Gieskes et al. (1991). For ammonium concentration analysis, a 0.2 mL sample aliquot was diluted with 2 mL reagent water to which 1 mL phenol ethanol, 1 mL sodium nitroprusside, and 2 mL oxidizing solution of sodium hypochlorite were added in a 15 mL capped plastic tube (Gieskes et al., 1991). The solution was kept at room temperature for ~6.5 h to develop color. Ammonium concentrations were determined at an absorbance of 640 nm. Precision and accuracy of the ammonium analyses of a standard were within 4% and 10%, respectively.

For phosphate analysis, a 0.6 mL sample was diluted with 2 mL deionized water (18 MΩ/cm) and 4 mL mixed reagent solution of ammonium molybdate, sulfuric acid, ascorbic acid, and antimony potassium tartrate in a 15 mL plastic tube. Then 2 mL of mixed reagent (ammonium molybdate, sulfuric acid, ascorbic acid, and potassium antimonyl tartrate) was added to the vial (Gieskes et al., 1991), which was capped and kept at room temperature for at least several minutes to develop color. The phosphate concentration was determined at an absorbance of 885 nm ~30 min after adding the mixed reagent solution. At beginning of each run, different concentrations (0–300 µM) of phosphorus standards were analyzed to create an 11-point calibration curve. Based on the measurements of 100 µM phosphorus standard during the expedition, precision (1σ) and accuracy of the phosphate analyses were better than 2% and 0.3%, respectively.

Minor elements

Dissolved minor elements were determined by Teledyne Leeman Prodigy ICP-AES. The general method for shipboard ICP-AES analysis of samples is described in Murray et al. (2000) and the user manuals for shipboard instrumentation.

For minor element (B, Ba^{2+}, Fe^{2+}, Mn^{2+}, Li^+, Si, and Sr^{2+}) analyses, interstitial water samples were diluted 1:20 (v/v) using 2% HNO_3 solution with 10 ppm Y (the interstitial water matrix solution) as an internal standard. Because the high concentration of salt in interstitial water samples at the 1:20 dilution demands matrix matching of standards and samples, standards were prepared with an acidified synthetic seawater of 35‰ NaCl with 2% HNO_3 to have an ionic strength similar to seawater. A stock multielement synthetic standard solution was gravimetrically prepared from ultrapure primary standards (SPC Science PlasmaCAL) diluted in the acidified synthetic seawater. An eight-point calibration curve was created through diluting the stock multielement standard in the acidified synthetic seawater at various degrees. Drift correction was made using the factor from a drift monitor solution of 100% stock standard solution, which was analyzed every 8–10 samples. The ICP-AES autosampler and analysis chamber were rinsed with a 3% (by volume) HNO_3 solution between samples. Multiple wavelengths were measured for each element, and the best were selected for reporting element concentrations. Wavelengths were selected based on possible interferences, the linearity of calibration curves, and the precision and accuracy of measurements of several standards. The selected wavelengths were Ba = 493.409 nm, B = 249.772 nm, Li = 670.784 nm, Fe = 259.940 nm, Si = 288.158 nm, Mn = 257.610 nm, and Sr = 460.733 nm.

Sediment geochemistry

Sediment nitrogen and inorganic and organic carbon content

Samples (~50 mg) for carbon, sulfur and nitrogen analyses were collected from squeeze cakes from interstitial water analyses and taken from intervals of distinct lithologic importance for expedition aims. Samples were freeze-dried for ~24 h, crushed using an agate pestle and mortar, and then analyzed for total carbon (TC), total inorganic carbon (TIC), total sulfur (TS) and total nitrogen (TN).

TC, TS, and TN of the bulk sediment samples were determined with a ThermoElectron Corporation Flash EA 1112 CHNS elemental analyzer equipped with a ThermoElectron packed column CHNS/NCS GC and a thermal conductivity detector (TCD). Approximately 12–13 mg of dry sediment was weighed into a tin cup, and 5–10 mg of vanadium pentoxide was added. Samples were then combusted at 950°C in a stream of oxygen. The reaction gases were passed through a reduction chamber to reduce nitrogen oxides to N_2, and then the evolved N_2, CO_2, and SO_2 were separated by the GC column before detection by the TCD. All measurements were calibrated to a set of reference standards covering the range in expected TC, TS, and TN values (Soil Reference Material: Buffalo River Sediments PWDR7837591) that was run every 9 samples. Peak areas from the TCD were calculated to determine the TC, TS, and TN of the samples. Blank levels were determined by analyzing empty tin cups and were subtracted from each measurement. Blank contributions for C is on the order of 1 µg. Given the typical sample mass used (12.5 mg on average) and using a signal/blank threshold of 10, this translates into a detection limit of ~0.04 wt%. For N, blanks were also estimated from the intercept of the calibration curve, which gave results similar to direct blank determination (i.e., empty tin cup blank). Blank contribution for N is on the order of 12 µg, unsurprisingly high considering the use of a sampler open to the atmosphere. This translates into a detection limit of ~0.06 wt%. Accuracy of TC determination was estimated using repeated measurements of reference material and was found to be better than 5% of the TC value (i.e., <0.05 wt% for the vast majority of samples analyzed). Precision of TC determination was estimated from limited duplicate measurements and was systematically within estimated accuracy. TS determination was less accurate than for nitrogen or carbon, and based on the analysis of both blank cups and minimum detection limits obtained from calibration curves, this equates to a TS of 0.1 wt%.

Sulfur analyses were only carried out for Expedition 368. TIC was determined using a Coulometrics 5015 CO_2 coulometer. Approximately 13 mg (10 mg for lithologies dominated by carbonates) of sediment was weighed into a glass vial and acidified with 2 M HCl. The liberated CO_2 was titrated, and the corresponding change in light transmittance in the coulometric cell was monitored using a photodetection cell. The weight percent of calcium carbonate was calculated from the inorganic carbon content using the following equation:

$$CaCO_3\ (wt\%) = TIC\ (wt\%) \times 100/12.$$

Blank levels were determined by analyzing empty reactors, were found to vary between 3 and 7 µg C, and were subtracted from each measurement. Repeated measurements of pure $CaCO_3$ (several times at the beginning and every 10 samples) were used to estimate accuracy, which was <2% of the TIC. TOC content was calculated by subtraction of TIC from TC.

Surface-enhanced Raman spectroscopy of solvent extractable sedimentary organic matter

Samples for surface-enhanced Raman spectroscopy (SERS) of solvent extractable organic matter were only collected during Expedition 368. They were obtained from freeze-dried residues used for TC analysis or collected from locations of lithologic interest to expedition goals. Powdered samples were placed in 10 mL extraction vials and sonicated for 15 min in 3:1 DCM/MeOH (dichloromethane/methanol) to obtain a solvent extract. The extract was decanted into a separate vial; more DCM was added to the sediment-residue before sonication was repeated for another 15 min. The solvent was again decanted, and the process was repeated to produce three extraction stages. The combined extract was reduced to dryness.

The extract was dissolved in DCM, and 4 µL of it was introduced in small increments to the sample wells of a gold-coated SERS-substrate. Introducing samples as small increments allowed the solvent to evaporate under ambient conditions until the entire volume had been loaded. When the solvent had evaporated, 4 µL of dilute nitric acid (1 M concentration) was dispensed into the pit and allowed to stand for ~2–3 min. The aqueous phase remaining within the pit was then removed to aid focusing of the microscope on the base of the pit. Raman spectroscopic measurements were performed using a BWTek i-Raman Pro fitted with a 532 nm light source and mounted on 20× video-microscope. Spectra were collected by accumulating 20 spectra over 20 s; spectral acquisition was in the range 200–2000 per centimeter. Laser spot size was approximately 1–2 µm, and laser power was 50% (<13 mW delivered to the sample). Identification of key bands was made with reference spectra presented in Alabi et al., 2015.

Elemental analysis of bulk sediment/sedimentary rock by ICP-AES

Elemental composition of bulk sediment was determined using a Leeman ICP-AES. Our analytical approach followed the general procedure outlined by Murray et al. (2000) and the constraints indicated by Quintin et al. (2002). Analytical blanks were prepared using 400 mg of lithium metaborate ($LiBO_2$) flux to ensure matrix matching. Samples analyzed by ICP-AES were ignited before dissolution by heating 5 g of oven-dried (600°C for 12 h) ground sediment at 1025°C for 5 h to determine weight loss on ignition (LOI), release volatile phases (H_2O, CO_2, and S), and fully oxidize all iron to ferric iron.

Aliquots of 100 mg of ignited sediment and standards were mixed with 400 mg of $LiBO_2$ flux. Subsequently, 10 µL of a wetting agent, 0.172 mM lithium bromide (LiBr), was added to the samples, standards, and blanks. This mixture was fused at 1050°C for 5 min in a Bead Sampler NT-4100 prior to dissolution in 50 mL of 10% HNO_3. For complete dissolution, 1 h of shaking with a Burrell wrist-action shaker was required. Aliquots of 5 mL of the resulting solutions were filtered (0.45 µm) and diluted with 35 mL of 10% HNO_3, resulting in a 4000× dilution of the original sediment.

A range of standards was selected to cover the entire range of expected sediment compositions, with their suitability monitored during the expedition. These standards were: STSD1, STSD2, STSD4, SO-1, SO-2, SO-3, SO-4, NBS-1c, JR-2, and BCR-2. BHVO-2 was also selected as both the drift and consistency standard. A range of major and trace elements was analyzed. Major elements included Al, Ca, Fe, K, Mg, Mn, Na, Si, and Ti, and trace elements included Ba, Co, Cr, Cu, Sc, Sr, V, Zn, and Zr. Major elements were expressed as weight percent oxide, and trace elements were expressed as parts per million. LOI values were determined routinely.

Samples were analyzed in duplicate. The procedures used to process the data are outlined in **Data reduction**, below.

The elemental compositions of sediment/sedimentary rock were only determined during Expedition 368 because the bead maker for the ICP did not work during Expedition 367.

Igneous and metamorphic rock geochemistry

Sample preparation

Representative samples of igneous and metamorphic rocks were analyzed for major and trace element concentrations during Expeditions 367 and 368 using the Leeman ICP-AES.

Samples ranging in size from ~2 to ~8 cm^3 were cut from the core with a diamond saw blade. A thin section billet was taken from the same or adjacent interval for petrographic analysis and alteration determination (see **Igneous and metamorphic petrology** and **Alteration**). All outer surfaces were ground on a diamond-impregnated disk to remove altered rinds and surface contamination derived from the drill or saw. Each sample was then placed in a beaker containing acetone and washed ultrasonically for 15 min. The acetone was decanted, and the samples were sonicated in deionized water (18 MΩ/cm) twice for 10 min. The cleaned pieces were dried for 10–12 h at 110°C.

The cleaned, dried samples were crushed to <1 cm chips between two disks of Delrin plastic in a hydraulic press. The rock chips were then ground to a fine powder in tungsten carbide in a SPEX 8515 Shatterbox. After grinding, a 5.0 ± 0.5 g aliquot of the sample powder was weighed on a Mettler Toledo balance and ignited at 1025°C for 4 h to determine LOI.

Murray et al. (2000) describes in detail the shipboard procedure for digestion of rocks and ICP-AES analysis of samples. The following protocol is an abbreviated form of this procedure with minor modifications. After determination of LOI, 100.0 ± 0.2 mg splits of the ignited whole-rock powders were weighed and mixed with 400.0 ± 0.5 mg of $LiBO_2$ flux that had been preweighed on shore. Standard rock powders and full procedural blanks were included with unknowns in each ICP-AES run (note that among the elements analyzed, contamination from the tungsten carbide mills is negligible; Shipboard Scientific Party, 2003). All samples and standards were weighed on a microbalance with weighing errors estimated to be ±0.05 mg under relatively smooth sea-surface conditions.

To prevent the cooled bead from sticking to the crucible, 10 mL of 0.172 mM aqueous LiBr solution was added to the mixture of flux and rock powder as a nonwetting agent. Samples were then fused individually in Pt-Au (95:5) crucibles for ~12 min at a maximum temperature of 1050°C in an internally rotating induction furnace (Bead Sampler NT-4100).

After cooling, beads were transferred to high-density polypropylene bottles and dissolved in 50 mL of 10% (by volume) HNO_3, aided by shaking with a Burrell wrist-action bottle shaker for 1 h. Following digestion of the bead, the solution was passed through a 0.45 µm filter into a clean 60 mL wide-mouth high-density polypropylene bottle. Next, 1.25 mL of this solution was transferred to a plastic vial and diluted with 10% HNO_3 to a total volume of 10 mL. The final solution-to-sample dilution factor was ~4000×.

Analyses of igneous and metamorphic rocks

Major (Al, Ca, Fe, K, Mg, Mn, Na, Si, and Ti) and trace (Ba, Co, Cr, Cu, Sc, Sr, V, Zn, and Zr) element concentrations of standards and samples were determined with a Leeman ICP-AES instrument. The plasma was ignited at least 30 min before each run of samples to allow the instrument to warm up and stabilize.

The ICP-AES data presented in the Geochemistry section of each site chapter were acquired using the Gaussian mode of the Prodigy software. This mode fits a curve to points across a peak and integrates the area under the curve for each element measured. Each sample was analyzed four times from the same dilute solution (i.e., in quadruplicate) within a given sample run. For elements measured at more than one wavelength, we either used the wavelength giving the best calibration line in a given run or, if the calibration lines for more than one wavelength were of similar quality, used the data from all wavelengths and reported the average concentration.

The ICP-AES run included the following:

- Certified rock standards, analyzed twice during each run, chosen to cover a wide range of compositions in order to calibrate the analyses (peridotite: JP-1; basalt: BIR-1, BHVO-2, and BCR-2; gabbro: MRG-1; andesite: AGV-1; and granodiorite: JG-1A);
- Samples (unknowns) analyzed in quadruplicate;
- A drift-correcting standard (BHVO-2) analyzed in every eighth sample position and at the beginning and end of each run;
- A blank solution analyzed near the beginning;
- Two or three "check" standards run as unknowns, each also analyzed in quadruplicate; check standards were chosen for their compositions similar to that of the analyzed material (ultramafic: DTS-1, basalt: JB-1a, JB-2, felsic rocks: JG-2, JG-3, etc.); and
- A 10% HNO_3 wash solution run for 60 s between each analysis.

Data reduction

Following each run of the instrument, the measured raw intensity values were transferred to a data file, corrected for instrument drift, and then corrected for the procedural blank. Drift correction was applied to each element by linear interpolation between the drift-monitoring solutions run in every eighth sample position.

After drift correction and blank subtraction, a calibration line for each element was calculated using the results for the certified rock standards. Element concentrations in the samples were then calculated from the relevant calibration lines.

Individual analyses of both standards and samples produced total volatile-free major element weight percentages that vary from 100 wt% by as much as several percent. Possible causes include some combination of errors in weighing the sample (particularly in rougher seas) and/or flux powders (although even when weighed on land, weighing errors are possible), variability in the dilutions (which were done volumetrically), and the duration and relatively low temperature of ignition. To facilitate comparison of Expedition 367 and 368 results with each other and with data from the literature, the measured major element values were normalized to 100 wt% totals.

Estimates of accuracy and precision of major and trace element analyses were based on replicate analyses of check standards compared to values published in Govindaraju (1994) and the GeoReM database (**http://georem.mpch-mainz.gwdg.de**) for international rock standards and to values published in Puchelt et al. (1996). Results are presented in Table **T1**. During Expeditions 367 and 368, run-to-run relative standard deviation by ICP-AES was generally ±1% for major elements except for MgO (±5%) and ±10% for trace elements. Accuracy was better than 2% for major elements and better than 5% for most trace elements, with the exception of low-concentration data for Cr and Zr.

Physical properties

High-resolution physical property measurements were made during Expeditions 367 and 368 mainly to aid lithostratigraphic characterization and to tie core descriptions to borehole data and seismic profiles. In particular, physical property data play a major role in hole-to-hole and site-to-site stratigraphic correlation, detection of discontinuities and inhomogeneities, collection of information about differences in the composition and texture of sediment, identification of major seismic reflectors, and construction of synthetic seismic profiles. A variety of techniques and methods were used to characterize Expedition 367 and 368 cores on whole-round, split section-half, and discrete samples. Core sections are generally 1.5 m in length, so a typical coring length (stroke) of 9.5 m yields six sections plus a shorter seventh section. Procedures for measuring sediment or hard rock cores differed slightly.

Sedimentary cores

Recovered whole-round sections were first allowed to equilibrate to ambient room temperature (~20°C) and pressure for ~4 h. After thermally equilibrating, core sections were run through the WRMSL for measurement of density by GRA, magnetic susceptibility, and compressional wave velocity on the PWL. Cores recovered with the XCB or the RCB coring systems are slightly smaller in diameter than those cored with the APC system. As a result, sections cored with the XCB or RCB systems typically have gaps between the liner and the core, so *P*-wave velocity was not measured with he WRMSL. Sections were then measured with the NGRL. Thermal conductivity was measured on one whole-round section per sediment core (typically Section 3) by a needle probe inserted into the section through a small hole drilled through the plastic core liner close to the middle of the section. When the sediment cores were too hard to insert the needle probe, a contact probe was used instead to measure the thermal conductivity later on the section half after core splitting. Cores were split longitudinally, with one half designated as archive and one as working half for sampling and analysis. The archive half of the core was passed through the SHMSL for measurement of point magnetic susceptibility and color reflectance. *P*-wave velocity measurements on split cores were made on the working halves at least for every section that had been sampled for MAD, or on other sections according to the lithology, employing the transducers oriented in *x*- and *z*-axis directions (see directions defined in Figure **F23**). Discrete samples were collected from the working halves (every other section) to measure wet bulk density, dry bulk density, water content, porosity, and grain density with MAD procedures.

Hard rock cores

Recovered hard rock sections were shaken onto sterile liners in the core splitting room for examination by a petrologist and/or a structural geologist, who decided where the pieces should be split between working and archive halves. The pieces were then put back into liners and run through the WRMSL and NGRL. *P*-wave velocity was not measured because the spaces between the liner and the rock core pieces make these measurements meaningless. After physical property measurements on whole-round cores, the core sections were split into working and archive halves and all rock pieces were labeled. The archive half of the core was passed through the SHMSL for measurement of point magnetic susceptibility and color reflectance. Thermal conductivity was measured once per core using a contact probe on a piece of section half in a bath of seawater for igneous rock pieces. Samples were taken from the working half of the core at a sampling interval of ~1 m depending on lithologic variability. Samples from igneous basement were shared for both paleomagnetic and MAD measurements. *P*-wave velocity measurements were made on these discrete samples.

A full discussion of all methodologies and calculations used aboard the *JOIDES Resolution* in the Physical Properties Laboratory is available in Blum (1997). Details and procedures for each physical property measurement are described below.

Whole-Round Multisensor Logger measurements

GRA-derived bulk density, *P*-wave velocity, and magnetic susceptibility were measured nondestructively with the WRMSL (Figure **F25**). To optimize the measurement process, sampling intervals and measurement integration times were set to be uniform for all sensors. Sampling intervals were set at 2 cm with an integration time of 5 s for each measurement. These sampling intervals are common denominators of the distances between the sensors installed on the WRMSL (30–50 cm), which allows sequential and simultaneous measurements. After every core, quality assurance/quality control (QA/QC) was monitored by passing a single core liner filled with deionized water through the WRMSL; if deviations from expected values were observed, recalibrations could be conducted if needed.

GRA bulk density

Bulk density can be used to estimate the pore volume in sediment and evaluate the consolidation state of sediment. GRA density is an estimate of bulk density based on the attenuation of a gamma ray beam. The beam is produced by a ^{137}Cs gamma ray source at a radiation level of 370 MBq within a lead shield with a 5 mm collimator that is directed through the whole-round core. The gamma ray detector on the opposite side of the core from the source includes a scintillation detector and an integral photomultiplier tube to record the gamma radiation that passes through the core. The attenuation of gamma rays occurs primarily by Compton scattering, in which gamma rays are scattered by electrons in the formation; the degree of scattering is related to the material bulk density. Therefore, for a known thickness of sample, the density (ρ) is related to the intensity of the attenuated gamma rays and can be expressed as follows:

Figure F25. WRMSL (measures GRA bulk density, magnetic susceptibility, and *P*-wave velocity), Expeditions 367 and 368. Water standard is measured at end of each core to control measurement quality.

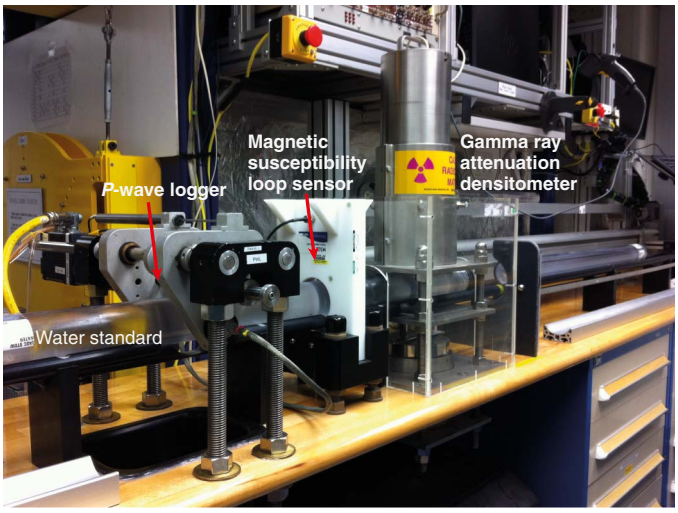

$$\rho = \ln(I_0/I)/(\mu d),$$

where

I = the measured intensity of gamma rays passing through the sample,
I_0 = gamma ray source intensity,
μ = Compton attenuation coefficient, and
d = sample diameter.

The μ and I_0 are treated as constants, such that ρ can be calculated from I. Note that this equation differs from the equation (5) in Blum (1997) in order to correct a typo.

In general, WRMSL measurements are most accurate when taken on a completely filled core liner with minimal drilling disturbance; otherwise, measurements tend to underestimate true values. By default, the instrument reports measurements using the internal diameter of the core liner (66 mm) as the assumed sample diameter. This assumption is suitable for most sediment cores obtained by the APC system; however, for sediment and/or hard rock cored by the XCB or RCB systems, core diameter is usually about 58 mm or less. Following Jarrard and Kerneklian (2007), the density measurements of cores obtained by XCB or RCB may be corrected by multiplying the density values by $^{66}/_{58}$ = 1.138 to account for this bias. We chose not to correct the raw values but to mention the offset in the description of the measurements. The spatial resolution of the GRA densitometer is less than ±1 cm. The gamma ray detector is calibrated with sealed calibration cores (one standard core liner filled with distilled water and aluminum cylinders of various diameters). To establish the calibration curves, gamma ray counts were taken through each aluminum cylinder for 60 s. Each aluminum cylinder has a density of 2.7 g/cm^3, and d is 1, 2, 3, 4, 5, or 6 cm. The relationship between I and μd is

$$\ln(I) = A(\mu d)^2 + B(\mu d) + C,$$

where A, B, and C are coefficients determined from the calibration.

Recalibration was performed as needed when the deionized water QA/QC standard density deviated significantly (more than a few percent) from 1 g/cm^3.

Magnetic susceptibility

Magnetic susceptibility (χ) is a dimensionless measure of the degree to which a material can be magnetized by an external magnetic field:

$$\chi = M/H,$$

where M is the magnetization induced in the material by an external field of strength H. Magnetic susceptibility is primarily sensitive to the concentration of ferrimagnetic minerals (e.g., magnetite and maghemite). It is also sensitive to magnetic mineralogy and can be related to the origin of the materials in the core and their subsequent diagenesis. Igneous materials typically have magnetic susceptibility a couple of orders of magnitude greater than their alteration products, such as clay.

The measurements were made using a Bartington MS2C loop sensor with a 9 cm diameter. An oscillator circuit in the sensor, which operates at a frequency of 0.565 kHz and an AF of ~140 A/m, produces a low-intensity, nonsaturating alternating magnetic field. Sediment or hard rock core sections passing through the influence of this field cause a change in oscillator frequency. Frequency information returned in pulse form to the susceptibility meter is converted into magnetic susceptibility. The loop sensor has a spatial resolution of 23–27 mm, and it is accurate to within 2%.

P-wave velocity

P-wave velocity data can be used to evaluate small-strain moduli, correlate downhole logging and core data, and evaluate porosity and cementation. *P*-wave (compressional) velocity (V_P) is defined by the time required for a compressional wave to travel a specific distance:

$$V_P = d/t_{core},$$

where d is the path length of the wave across the core and t_{core} is the traveltime through the core.

The PWL measures the traveltime of 500 kHz ultrasonic waves horizontally across the core at 2 cm intervals while it remains in the core liner. Waves are transmitted to the core by plastic transducer contacts connected to linear actuators. Pressure is applied to the actuators to ensure coupling between the transducers and the core liner. *P*-wave velocity transducers measure total traveltime of the compressional wave between transducers. The wave travels horizontally across the whole core and core liner. The total observed traveltime, t_{core}, is composed of

t_{delay} = time delay related to transducer faces and electronic circuitry,
t_{pulse} = delay related to the peak detection procedure,
t_{liner} = transit time through the core liner, and
t_{core} = traveltime through the sediment.

The system is calibrated using a core liner filled with distilled water, which provides control for t_{delay}, t_{pulse}, and t_{liner}. From these calibrations, V_P can be calculated for the whole-round specimens in core liners as

$$V_P = (d_{cl} - 2d_{liner})/(t_o - t_{pulse} - t_{delay} - 2t_{liner}),$$

where

d_{cl} = measured diameter of core and liner,
d_{liner} = liner wall thickness, and
t_o = measured total traveltime.

The above equation assumes that the core completely fills the core liner. The PWL of the WRMSL was turned off for cores recovered with the XCB and RCB systems, which often do not fill the core liner.

Natural Gamma Radiation Logger measurements

Gamma radiation is emitted from the decay of mineral-hosted ^{238}U, ^{232}Th, and ^{40}K. The NGRL measures this natural emission on whole-round cores using a system designed and built at the Integrated Ocean Drilling Program US Implementing Organization (USIO) (Texas A&M University) (Vasiliev et al., 2011; Dunlea et al., 2013) (Figure **F26**). When ^{238}U, ^{232}Th, and ^{40}K radioisotopes decay, they and their daughter products emit gamma radiation at specific energy levels unique to each isotope. NGR spectroscopy measures a wide energy spectrum that can be used to estimate the abundance of each isotope based on the strength of the signal at characteristic energies (Blum, 1997; Gilmore, 2008). Spectral data were collected and can be used for postcruise processing for U, Th, and K abundance. We estimated concentrations of K, U, and Th using NGR and

Figure F26. NGRL for whole-round cores (conducts 8 measurements at a time in 2 positions, resulting in 16 measurements per core), Expedition 367 and 368. During Expedition 367, scintillation Detector 7 was deficient, so only 14 measurements per core were performed.



Figure F27. NGRL detectors (from Vasiliev et al., 2011), Expeditions 367 and 368. The main NGR scintillation detector unit consists of 8 sodium iodide (NaI) scintillometers arranged along core measurement axis at 20 cm intervals surrounding the lower half of the core section.

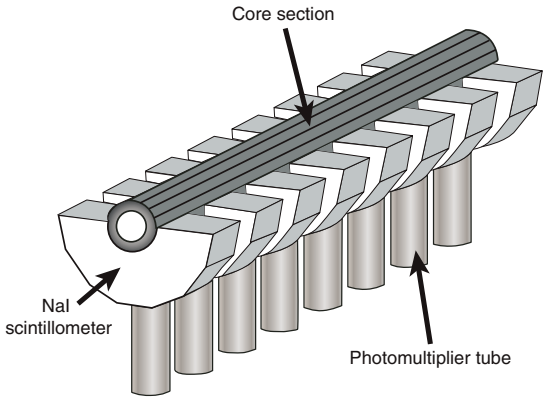

bulk density measurements (see Figure **F26**), based on a study and Matlab scripts from De Vleeschouwer et al. (2017). High total counts usually identify fine-grained deposits containing K-rich clay minerals and their absorbed U and Th isotopes. NGR data thus reveal stratigraphic details that aid in core-to-core correlations. The system was initially installed on the renovated *JOIDES Resolution* in 2009 and has been used during every Integrated Ocean Drilling Program USIO and IODP *JOIDES Resolution* Science Operator (JRSO) expedition starting with Expedition 320. The main NGR detector unit consists of 8 sodium iodide (NaI) detectors arranged along the core measurement axis at 20 cm intervals surrounding the lower half of the section (Figure **F27**). During Expedition 367, scintillation Detector 7 was deficient, which led to a small gap in the measurements. Before Expedition 368, the deficient scintillation detector was fixed by the IODP technicians, and all detectors performed well during Expedition 368. The detector array has passive (layers of lead) and active (plastic scintillometers) shielding to reduce the background environmental and cosmic radiation. The overlying plastic scintillometers detect incoming high-energy gamma and muon cosmic radiation and cancel this signal from the total counted by the NaI detectors.

A measurement run consisted of two sample positions, 10 cm apart, for a total of 16 (14 during Expedition 367) measurements per 150 cm section. During Expedition 367, measurements at distances of 20 and 30 cm in each section have no measured values because of the scintillation detector failure. The quality of the energy spectrum measured in a core depends on the concentration of radionuclides in the sample but also on the counting time, with higher times yielding better spectra. Counting times were chosen as 5 min per position, or ~10 min per core, yielding statistically significant energy spectra (Vasiliev et al., 2011).

Thermal conductivity measurements

After NGR measurements were completed, thermal conductivity was measured with the TK-04 (Teka Bolin) system using a needle-probe method in full-space configuration for whole-round sediment cores (Von Herzen and Maxwell, 1959) or a contact-probe method in half-space configuration on split cores for hard rock. The probes contain a heater wire and calibrated thermistor.

For soft sediment, the needle probe was inserted into a 2 mm diameter hole drilled through the liner along one of the lines that later guided core splitting. To avoid interference from air flow in the laboratory, the core was placed into an enclosed box outfitted with foam.

For hard rock cores, samples were selected from the working half and returned unaltered to the core liner upon completion of the measurements. The contact probe embedded in the surface of an epoxy block with a low thermal conductivity (Vacquier, 1985) was maintained in contact with the sample. For igneous rock pieces, both rock and probe were equilibrated together in a bath of seawater at room temperature in a cooler insulated with extruded polystyrene foam. The calibrated heat source of the probe was then turned on, and the increase in temperature was recorded over 80 s. A heating power of 1.5 to 1.8 W/m was typically used in soft sediment and for indurated material. In cases when this heating power did not lead to reliable measurements, we used a higher value, up to 2.0 W/m. The solution to the heat conduction equation with a line source of heat was then fit to the temperature measurements to obtain the thermal conductivity. Because the probe is much more conductive than sediment or hard rock, the probe is assumed to be a perfect conductor. Under this assumption, the temperature of the superconductive probe has a linear relationship with the natural logarithm of the time after the initiation of the heat:

$$T(t) = (q/4\pi k) \times \ln(t) + C,$$

where

T = temperature (K),
q = heat input per unit length per unit time (J/m/s),
k = thermal conductivity (W/[m·K]),
t = time after the initiation of the heat (s), and
C = instrumental constant.

Three measuring cycles were automatically performed to calculate average conductivity. A self-test, which included a drift study, was conducted at the beginning of each measurement cycle. Once the probe temperature stabilized, the heater circuit was closed and the temperature rise in the probe was recorded. Thermal conductivity was calculated from the rate of temperature rise while the heater current was flowing. Temperatures measured during the first 80 s of

the heating cycle were fitted to an approximate solution of a constantly heated line source (for details, see Kristiansen, 1982; Blum, 1997). Measurement errors were 5%–10%. Thermal conductivity measurements were routinely taken in one section per core (usually the third section of each core). Some cores retrieved by the XCB system did not yield results for thermal conductivity because cracks in the hard sediment caused bad coupling of the probe to the sediment.

Section Half Multisensor Logger measurements

We measured color reflectance and magnetic susceptibility on archive section halves using the SHMSL. The archive half of the split core was placed on the core holder, above which an electronic platform moves along a track, recording the height of the split-core surface with a laser sensor. The laser establishes the location of the bottom of the section, and then the platform reverses the direction of movement, moving from bottom to top making measurements of point magnetic susceptibility and color reflectance. All foam inserts were removed from the section-half cores before measurement, so the measured range of values represents that of the core material only. During Expeditions 367 and 368, point magnetic susceptibility and color reflectance data were collected at constant intervals for each core but varied between 0.5 and 2.0 cm for different cores, depending on the available time for processing and the type of rock recovered. These measurements have a sufficient resolution for comparing with the results obtained from the magnetic susceptibility loop of the WRMSL.

Color reflectance spectrometry

The color reflectance spectrometer uses an Ocean Optics 30 mm integrating sphere and both halogen and LED light sources, which cover wavelengths from ultraviolet through visible to near infrared. The measurements were taken from 380 to 900 nm wavelengths at 2 nm intervals. The approximate 3 s data acquisition offset was applied for the entire scan of the archive section half. The data are reported using the L*a*b* color system, in which L* is lightness, a* is redness (positive) versus greenness (negative), and b* is yellowness (positive) versus blueness (negative) of the rock. The color reflectance spectrometer calibrates on two spectra, pure white (reference) and pure black (dark). Color calibration was conducted automatically approximately once every 6 h (twice per shift).

Point magnetic susceptibility

Point magnetic susceptibility was measured with a Bartington MS2 meter and an MS2K contact probe with a flat 15 mm diameter round sensor with a field of influence of 25 mm and an operation frequency of 930 Hz. The instrument averages three measurements from the sensor for each offset, leading to an accuracy of ~5%. The spatial resolution of the point magnetic susceptibility instrument is ~3.8 mm, higher than that of the whole-round magnetic susceptibility (23–27 mm), making it especially useful for sections containing broken pieces <4 cm in length. As with whole-round measurements, the output displayed by the point magnetic susceptibility sensor must be converted to dimensionless SI units by multiplying by 10^{-5}. The probe is zeroed in air before each measurement location to avoid influence from the metal track. The point magnetic susceptibility meter was calibrated by the manufacturer before installation on the ship and is quality checked every ~6 h at the same time as color reflectance sensor calibration.

Figure F28. SHMG showing *x*-axis caliper and *y*- and *z*-axis bayonets used to measure *P*-wave velocity on split core sections of soft sediments or discrete samples of indurated sediment or hard rock, Expeditions 367 and 368. Insert shows measurement of *P*-wave velocity on a hard rock discrete sample using *x*-axis caliper.

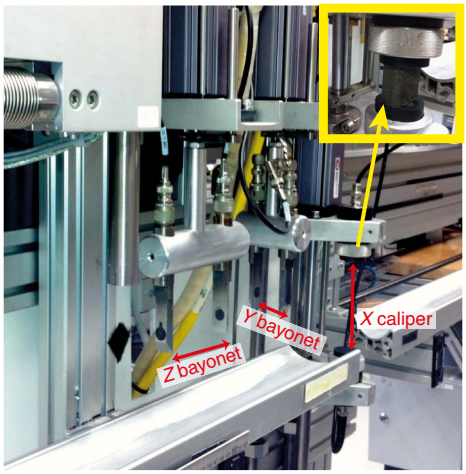

Section Half Measurement Gantry measurements

For soft-sediment cores, *P*-wave velocity measurements were performed on the working half of split cores before any samples were taken. *P*-wave velocity measurements used the *x*-axis caliper and *z*-axis bayonet contact probe transducers on the Section Half Measurement Gantry (SHMG) (Figure **F28**) with one analysis completed every other section. Measurements were usually taken at ~75 cm in the section; however, if this interval lacked good sediment/transducer coupling (e.g., caused by high amounts of sand or cracks), different positions were chosen to generate viable data. Cores drilled with the XCB sometimes did not provide usable data because of bad sediment/liner contact and disturbed sediment. For hard rock cores, *P*-wave velocity was measured on the discrete samples chosen for both physical property and paleomagnetic measurements.

P-wave velocity

The *P*-wave velocity system uses Panametrics-NDT Microscan delay line transducers, which transmit at 0.5 MHz. The signal received through the section half or the discrete sample was recorded by the computer attached to the system, with the peak (*P*-wave arrival) usually chosen by autopicking software. In case of a weak signal, the first arrival was manually picked. The distance between transducers was measured with a built-in linear voltage displacement transformer. Calibration was performed with a series of acrylic cylinders of differing thicknesses and a known *P*-wave velocity of 2750 ± 20 m/s. The determined system time delay from calibration was subtracted from the picked arrival time to give a traveltime of the *P*-wave through the sample. The thickness of the sample (calculated by the linear voltage displacement transformer, in meters) was divided by the traveltime (in seconds) to calculate *P*-wave velocity in meters per second.

Discrete sample MAD measurements

Discrete samples were collected from the working halves to determine wet and dry bulk density, grain density, water content, and

porosity. In soft sediment, samples of ~10 cm^3 volume were collected with a plastic syringe, the diameter of which fits that of the glass vials. We sampled every other section of core (usually Sections 1, 3, and 5). In indurated sediment and hard rock, minicores or pieces were extracted from the working halves for physical property measurements. Samples from igneous basement were shared for paleomagnetic measurements.

Sample preparation

Soft-sediment samples were placed in numbered, preweighed ~16 mL Wheaton glass vials for wet and dry sediment weighing, drying, and dry volume measurements. Determination of an accurate wet mass of the minicore samples of indurated sediment and hard rock first required that the pore space of the samples be completely saturated with seawater. To do this, we placed the samples in individual plastic vials filled with seawater and used a vacuum chamber. A vacuum pump removed the air from the chamber to a pressure of ~40–50 kPa below the atmospheric pressure, forcing seawater into the samples. The samples were kept under saturation for at least 24 h, with the vacuum maintained in the chamber by turning the pump on for 30 min every 5 h. After removal from the saturator, the minicores were patted dry with a paper towel, and wet mass was immediately determined using the dual balance system. *P*-wave velocities were then measured on the wet samples. Following the velocity measurements, the samples were dried in a convection oven for at least 24 h at 105° ± 5°C. Dried samples were then cooled in a desiccator for at least 4 h before the dry mass and the volume were measured.

Dual balance mass measurement

The weights of wet and dry sample masses were determined to a precision of 0.005 g using two Mettler Toledo electronic balances, with one acting as a reference. A standard weight of similar value to the sample was placed upon the reference balance to increase accuracy. A computer averaging system was used to compensate for the ship's motion. The default setting of the balances is 300 measurements (taking ~1.5 min).

Pycnometer volume measurement

Dry sample volume was determined using a hexapycnometer system of a six-celled, custom-configured Micrometrics AccuPyc 1330TC helium-displacement pycnometer (Figure **F29**). The precision of each cell is 1% of the full-scale volume. Volume measurement was preceded by three purges of the sample chamber with helium warmed to ~28°C. Three measurement cycles were run for each sample. A reference volume (a set of two calibration spheres) was placed sequentially in one of the chambers to check for instrument drift and systematic error. The volumes occupied by the numbered Wheaton vials were calculated before the cruise by multiplying each vial's weight against the average density of the vial glass. The procedures for the determination of these physical properties comply with the American Society for Testing and Materials (ASTM) designation (D) 2216 (ASTM International, 1990). The fundamental relation and assumptions for the calculations of all physical property parameters are discussed by Blum (1997) and summarized below.

Mass and volume calculation

We measured wet mass (M_{wet}), dry mass (M_{dry}), and dry volume (V_{dry}). The ratio of mass (rm) is a computational constant of 0.965 (i.e., 0.965 g of freshwater per 1 g of seawater). Salt precipitated in sediment pores during the drying process is included in the M_{dry} and V_{dry} values. The mass of the evaporated water (M_{water}) and salt (M_{salt}) in the sample are given by

Figure F29. Pycnometer used to measure volume of dry samples, either in small vials for soft sediments or as discrete samples, Expeditions 367 and 368.

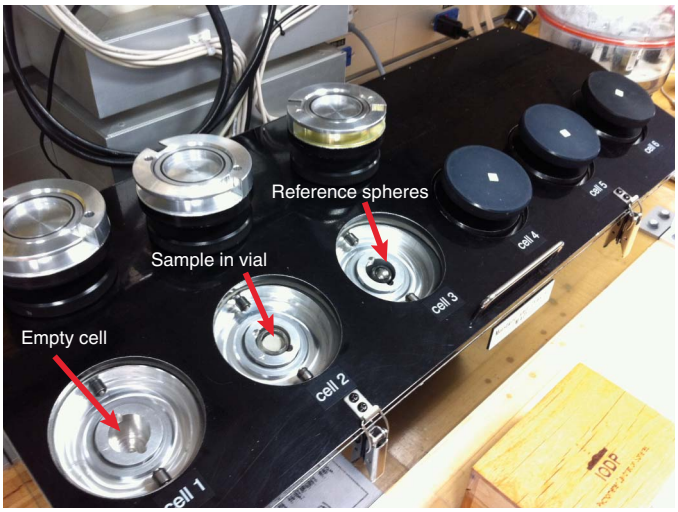

$$M_{water} = M_{wet} - M_{dry} \text{ and}$$

$$M_{salt} = M_{water}[s/(1 - s)],$$

where s is the assumed saltwater salinity (0.035%) corresponding to a pore water density (ρ_{pw}) of 1.024 g/cm^3 and a salt density (ρ_{salt}) of 2.22 g/cm^3. The corrected mass of pore water (M_{pw}), volume of pore water (V_{pw}), mass of solids excluding salt (M_{solid}), volume of salt (V_{salt}), volume of solids excluding salt (V_{solid}), and wet volume (V_{wet}) are

$$M_{pw} = (M_{wet} - M_{dry})/\text{rm},$$

$$V_{pw} = M_{pw}/\rho_{pw},$$

$$M_{solid} = M_{wet} - M_{pw},$$

$$M_{salt} = M_{pw} - (M_{wet} - M_{dry}),$$

$$V_{salt} = M_{salt}/\rho_{salt},$$

$$V_{wet} = V_{dry} - V_{salt} + V_{pw}, \text{ and}$$

$$V_{solid} = V_{wet} - V_{pw}.$$

Calculation of bulk properties

For all sediment samples, water content (w) is expressed as the ratio of mass of pore water to wet sediment (total) mass:

$$w = M_{pw}/M_{wet}.$$

Wet bulk density (ρ_{wet}), dry bulk density (ρ_{dry}), sediment grain density (ρ_{solid}), porosity (ϕ), and void ratio (VR) are calculated as follows:

$$\rho_{wet} = M_{wet}/V_{wet},$$

$$\rho_{dry} = M_{solid}/V_{solid},$$

$$\rho_{solid} = M_{solid}/V_{solid},$$

$$\phi = V_{pw}/V_{wet}, \text{ and}$$

$$VR = V_{pw}/V_{solid}.$$

MAD properties reported and plotted in the Physical properties sections of all site chapters were calculated with the MADMax shipboard program set with the "method C" calculation process.

Downhole measurements

Downhole logs are used to determine physical, chemical, and structural properties of the formation penetrated by a borehole. The data are rapidly collected, continuous with depth, and measured in situ; they can be interpreted in terms of the stratigraphy, lithology, mineralogy, magnetic characteristics, and geochemical composition of the penetrated formation. Where core recovery is incomplete or disturbed, log data may provide the only way to characterize the borehole section. Where core recovery is good, log and core data complement one another and may be interpreted jointly.

Downhole logs measure formation properties on a scale that is intermediate between those obtained from laboratory measurements on core samples and those from geophysical surveys. They are useful in calibrating the interpretation of geophysical survey data (e.g., through the use of synthetic seismograms) and provide a necessary link for the integrated understanding of physical and chemical properties on different scales.

During Expeditions 367 and 368, downhole wireline log data was collected at Sites U1499–U1501, and U1503. In addition, a total of 14 downhole temperature measurements were acquired using the APCT-3 in Holes U1499A (6), U1501C (4), and U1505C (4).

Wireline logging

During wireline logging operations, logs were recorded with Schlumberger logging tools combined into several tool strings that were lowered into the hole after completion of coring operations. Three standard IODP tool string configurations were used during Expeditions 367 and 368 (Figure **F30**; Table **T8**). The first was a variant of the triple combo tool string, which measures borehole fluid temperature, NGR, porosity, density, electrical resistivity, and magnetic susceptibility. The second was the FMS-sonic tool string, which measures NGR, sonic velocity, and FMS resistivity images of the borehole wall. The third was the Versatile Seismic Imager (VSI) tool string, which measures a vertical seismic profile in order to integrate well and seismic data. Each tool string also contains an Enhanced Digital Telemetry Cartridge (EDTC) for communicating through the wireline to the Schlumberger data acquisition system (i.e., multitasking acquisition and imaging system [MAXIS]) on the drillship. See the site chapters for detailed lists of which tools were run in which combinations in each hole.

In preparation for logging, the boreholes were reamed in their lower sections, flushed of debris by circulating drilling fluid, and filled with seawater-based logging gel (i.e., sepiolite mud mixed with seawater and weighted with barite; approximate density = 10.5 lb/gal) to help stabilize the borehole walls in sections where instability would be expected based on drilling and coring results. The BHA was pulled up to a logging depth determined by the borehole conditions. Although log data can be collected while lowering the tool string to the bottom of the hole, the primary data set is collected while raising the tool strings upward at a constant speed, typically ~300 m/h for the triple combo and 600 m/h for the FMS-sonic.

Each tool string deployment is termed a logging "run." During each run, tool strings can be lowered and pulled up in the hole several times to check repeatability and increase coverage of the FMS borehole images. Each lowering or hauling-up of the tool string while collecting data constitutes a "pass." Incoming data were recorded and monitored in real time on the Schlumberger Minimum Configuration MAXIS logging computer. A wireline heave compensator (WHC) was typically used to minimize the effect of ship's heave on the tool position in the borehole (see below).

Logged sediment properties and tool measurement principles

The logged properties and the principles used with the tools that measure them are briefly described below. The main tools are listed in Tables **T8** and **T9**. More detailed information on individual tools and their geological applications may be found in Serra (1984, 1986, 1989), Schlumberger (1989, 1994), Rider (1996), Goldberg (1997), Lovell et al. (1998), and Ellis and Singer (2007). A complete list of acronyms for the Schlumberger tools and measurement curves is available at **http://www.apps.slb.com/cmd**. The complete list of downhole logging tools used during Integrated Ocean Drilling Program and IODP expeditions and additional information about tool physics are available at **http://iodp.ldeo.columbia.edu/TOOLS_LABS/tools.html** and **http://iodp.tamu.edu/tools/logging/index.html**.

Natural gamma radiation

The Hostile Environment Natural Gamma Ray Sonde (HNGS) was used on both the triple combo and FMS-sonic tool strings to measure NGR in the formation. The HNGS uses two bismuth germanate scintillation detectors and five-window spectroscopy to determine concentrations of potassium (in weight percent), thorium (in parts per million), and uranium (in parts per million) from the characteristic gamma ray energies of isotopes in the ^{40}K, ^{232}Th, and ^{238}U radioactive decay series, which dominate the natural radiation spectrum. The computation of the elemental abundances uses a least-squares method of extracting U, Th, and K elemental concentrations from the spectral measurements. The HNGS filters out gamma ray energies below 500 keV, eliminating sensitivity to bentonite or KCl in the drilling mud and improving measurement accuracy. The HNGS also provides a measure of the total spectral gamma ray (HSGR) and computed gamma ray (HCGR) that are measured in American Petroleum Institute gamma radiation units (gAPI). The HNGS response is influenced by the borehole diameter; therefore, the HNGS data are corrected for borehole diameter variations during acquisition.

An additional NGR sensor was housed in the EDTC to communicate data to the surface. The sensor includes a sodium iodide scintillation detector that also measures the total NGR emission of the formation. It is not a spectral tool (i.e., it does not provide U, Th, and K concentrations), but it provides total gamma radiation for each pass.

The inclusion of the HNGS in every tool string allows use of the gamma ray data for precise depth match processing between logging strings and passes and for core-log integration.

Figure F30. Wireline tool strings, Expeditions 367 and 368. Triple combo tool string takes downhole measurements of hole diameter, NGR, bulk density, electrical resistivity, and magnetic susceptibility of the borehole. FMS-sonic tool string measures borehole resistivity images, NGR, and *P*- and *S*-wave velocities. VSI tool string acquires seismic waveform data in a check shot experiment. LEH-MT = logging equipment head-mud temperature, EDTC = Enhanced Digital Telemetry Cartridge, HNGS = Hostile Environment Natural Gamma Ray Sonde, APS = Accelerator Porosity Sonde, HLDS = Hostile Environment Litho-Density Sonde, HRLA = High-Resolution Laterolog Array, MSS = magnetic susceptibility sonde, DSI = Dipole Sonic Imager, GPIT = General Purpose Inclinometry Tool. Except for MSS, all acronyms are trademarks of Schlumberger. Also see Tables T8 and T9.

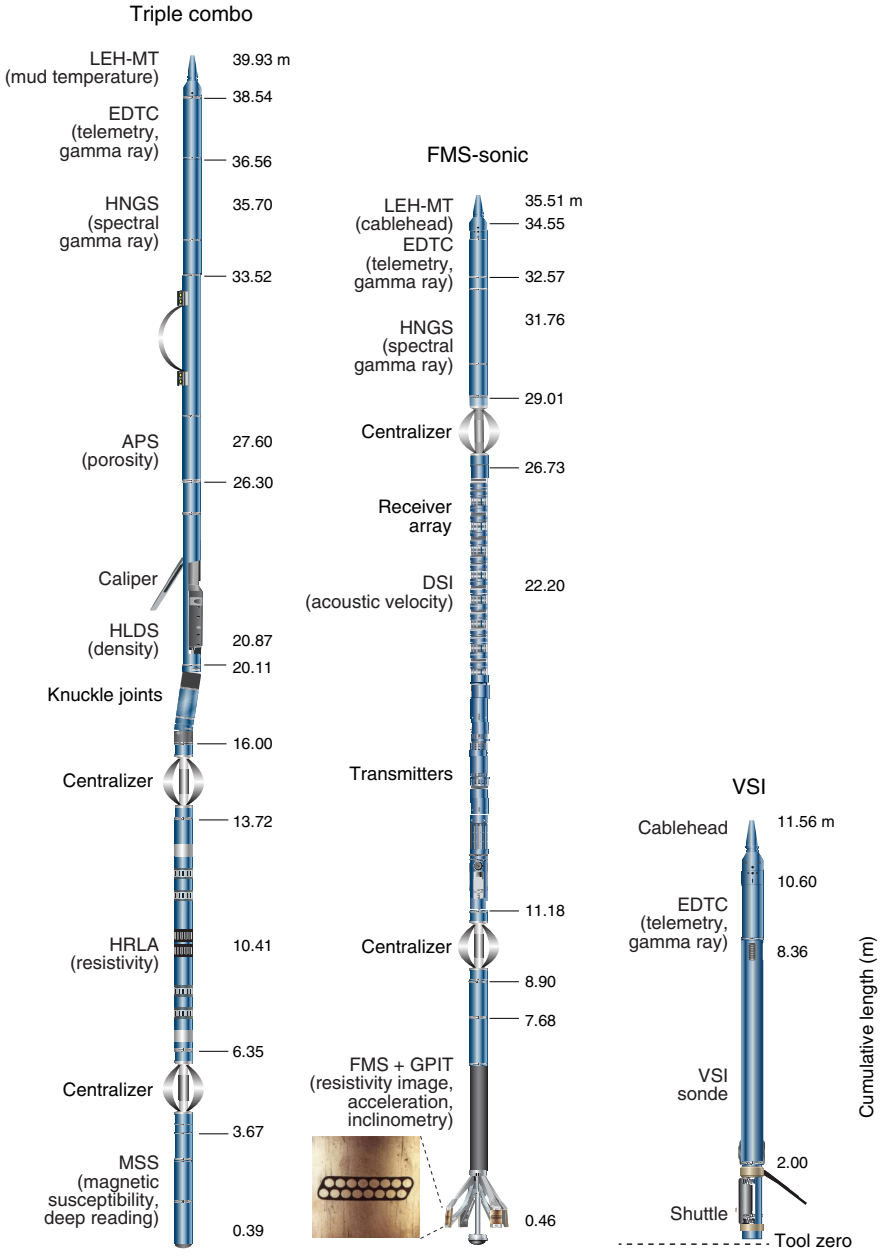

Density and photoelectric factor

Formation density was measured with the Hostile Environment Litho-Density Sonde (HLDS). The sonde contains a radioactive cesium (^{137}Cs) gamma ray source (622 keV) and far and near gamma ray detectors mounted on a shielded skid that is pressed against the borehole wall by a hydraulically activated decentralizing arm. Gamma radiation emitted by the source undergoes Compton scattering, in which gamma rays are scattered by electrons in the formation. The number of scattered gamma rays that reach the detectors is proportional to the density of electrons in the formation, which is in turn related to bulk density. Porosity may also be derived from this bulk density if the matrix (grain) density is known.

The HLDS also measures the photoelectric effect factor (PEF), a measure of the photoelectric absorption of low-energy gamma radiation. Photoelectric absorption occurs when the energy of the gamma rays falls below 150 keV as a result of being repeatedly scattered by electrons in the formation. PEF is determined by comparing the counts from the far detector in the high-energy region, where only Compton scattering occurs, to those in the low-energy region, where count rates depend on both reactions. Because PEF

Table T8. Downhole measurements made by wireline tool strings, Expeditions 367 and 368. For definitions of tool acronyms, see Table T9. All tool and tool string names except the MSS are trademarks of Schlumberger. **Download table in CSV format.**

Tool string	Tool	Measurement	Sampling interval (cm)	Approximate vertical resolution (cm)
Triple combo	EDTC	Total gamma ray	5 and 15	30
	HNGS	Spectral gamma ray	15	20–30
	APS	Porosity	15	38
	HLDS	Bulk density and caliper	2.5 and 15	38
	HRLA	Resistivity	15	30
	MSS	Magnetic susceptibility	4	12–36
FMS-sonic	EDTC	Total gamma ray	5 and 15	30
	GPIT	Tool orientation and acceleration	3.8	15
	DSI	Acoustic velocity	15	107
	FMS	Microresistivity and caliper	0.25	1

Table T9. Acronyms and units used for downhole wireline tools and measurements, Expeditions 367 and 368. For the complete list of acronyms used in IODP and for additional information about tool physics, consult IODP-USIO Science Services, LDEO, at **http://iodp.ldeo.columbia.edu/TOOLS_LABS/tools.html**. **Download table in CSV format.**

Tool	Output	Description	Unit
EDTC		Enhanced Digital Telemetry Cartridge	
	GR	Total gamma ray	gAPI
	ECGR	Environmentally-corrected gamma ray	gAPI
	EHGR	High-resolution environmentally corrected gamma ray	gAPI
HNGS		Hostile Environment Gamma Ray Sonde	
	HSGR	Standard (total) gamma ray	gAPI
	HCGR	Computed gamma ray (HSGR minus uranium contribution)	gAPI
	HFK	Potassium	wt%
	HTHO	Thorium	PPM
	HURA	Uranium	PPM
APS		Accelerator Porosity Sonde	
	APLC	Near/array limestone corrected porosity	Dec. fraction
	STOF	Computed standoff	Inches
	SIGF	Formation capture cross section	Capture units
HLDS		Hostile Environment Litho-Density Sonde	
	RHOM	Bulk density	g/cm^3
	PEFL	Photoelectric effect	barn/e$^-$
	LCAL	Caliper (measure of borehole diameter)	Inches
	DRH	Bulk density correction	g/cm^3
HRLA		High Resolution Laterolog Array Tool	
	RLA1–5	Apparent Resistivity from Computed Focusing Mode 1–5	Ωm
	RT	True resistivity	Ωm
	MRES	Borehole fluid resistivity	Ωm
MSS		Magnetic susceptibility sonde	
	LSUS	Magnetic susceptibility, deep reading	Uncalibrated units
FMS		Formation MicroScanner	
	C1, C2	Orthogonal hole diameters	Inches
	P1AZ	Pad 1 azimuth	°
		Spatially oriented resistivity images of borehole wall	
GPIT		General-purpose inclinometer tool	
	DEVI	Hole deviation	°
	HAZI	Hole azimuth	°
	F_x, F_y, F_z	Earth's magnetic field (three orthogonal components)	°
	A_x, A_y, A_z	Acceleration (three orthogonal components)	m/s^2
DSI		Dipole Sonic Imager	
	DTCO	Compressional wave slowness	µs/ft
	DTSM	Shear wave slowness	µs/ft
	DT1	Shear wave slowness, lower dipole	µs/ft
	DT2	Shear wave slowness, upper dipole	µs/ft

depends on the atomic number of the elements in the formation (heavier elements have higher PEF), it also varies according to the chemical composition of the minerals present and can be used for the identification of the overall mineral makeup of the formation. For example, the PEF of calcite is 5.08 barn/e$^-$, illite is 3.03 barn/e$^-$, quartz is 1.81 barn/e$^-$, and hematite is 21 barn/e$^-$. Good contact between the tool and the borehole wall is essential for good HLDS logs; poor contact results in underestimation of density values. Both the density correction and caliper measurement of the hole are used to check the contact quality. In the deeper parts of the hole, the PEF

log should be used with caution, especially in washouts, because barium in the logging mud swamps the signal despite correction for mud effect.

Electrical resistivity

The High-Resolution Laterolog Array (HRLA) provides six resistivity measurements with different depths of investigation (including the borehole or mud resistivity and five measurements of formation resistivity with increasing penetration into the formation). The tool sends a focused current into the formation and measures the intensity necessary to maintain a constant drop in voltage across a fixed interval, providing direct resistivity measurements. The array has one central (source) electrode and six electrodes above and below it, which serve alternatively as focusing and returning current electrodes. By rapidly changing the role of these electrodes, a simultaneous resistivity measurement at six penetration depths is achieved. The tool is designed to ensure that all signals are measured at exactly the same time and tool position and to reduce the sensitivity to "shoulder bed" effects when crossing sharp beds thinner than the electrode spacing. The design of the HRLA, which eliminates the need for a surface reference electrode, improves formation resistivity evaluation compared to traditional dual induction and allows the full range of resistivity to be measured from low (e.g., in high-porosity sediments) to high (e.g., in basalt). The HRLA needs to be run centralized in the borehole for optimal results, so knuckle joints were used to centralize the HRLA while allowing the density and porosity tools to maintain good contact with the borehole wall (Figure **F30**).

Calcite, silica, and hydrocarbons are electrical insulators, whereas ionic solutions like interstitial water are conductors. Electrical resistivity, therefore, can be used to evaluate porosity for a given salinity and resistivity of the interstitial water. Clay surface conduction also contributes to the resistivity values, but at high porosities, this effect is relatively minor.

Acoustic velocity

The Dipole Shear Sonic Imager (DSI) measures the transit times between sonic transmitters and an array of eight receivers. It combines replicate measurements, thus providing a direct measurement of sound velocity through formations that is relatively free from the effects of formation damage and an enlarged borehole (Schlumberger, 1989). Along with the monopole transmitters found on most sonic tools, it also has two crossed-dipole transmitters that allow the measurement of shear wave velocity in addition to compressional wave velocity. Dipole measurements are necessary to measure shear velocities in slow formations with shear velocity less than the velocity of sound in the borehole fluid. Such slow formations are typically encountered in deep-ocean drilling.

Formation MicroScanner

The FMS provides high-resolution electrical resistivity–based images of borehole walls. The tool has four orthogonal arms and pads, each containing 16 button electrodes that are pressed against the borehole wall during logging (Figure **F30**). The electrodes are arranged in two diagonally offset rows of 8 electrodes each. A focused current is emitted from the button electrodes into the formation, with a return electrode near the top of the tool. Resistivity of the formation at the button electrodes is derived from the intensity of current passing through the button electrodes.

Processing transforms the resistivity measurements into oriented high-resolution images that reveal geologic structures of the borehole wall. Features such as bedding, stratification, fracturing, slump folding, and bioturbation can be resolved (Luthi, 1990; Salimullah and Stow, 1992; Lovell et al., 1998). Because the images are oriented to magnetic north, further analysis can provide measurement of the dip and direction (azimuth) of planar features in the formation. In addition, when the corresponding planar features can be identified in the recovered core samples, individual core pieces can be reoriented with respect to true north.

Approximately 30% of a borehole with a diameter of 25 cm (9⅞ inches) is imaged during a single pass. Standard procedure is to make two full upward passes with the FMS to maximize the chance of getting full borehole coverage with the pads. The maximum extension of the caliper arms is 40.6 cm (16 inches). In holes with a diameter greater than this maximum, the pad contact at the end of the caliper arms is inconsistent, and the FMS images may appear out of focus and too conductive. Irregular (rough) borehole walls will also adversely affect the images if contact with the wall is poor.

Magnetic susceptibility

The magnetic susceptibility sonde (MSS) is a nonstandard wireline tool designed by the Lamont-Doherty Earth Observatory (LDEO). It measures the ease with which formations are magnetized when subjected to a magnetic field. The ease of magnetization is ultimately related to the concentration and composition (size, shape, and mineralogy) of magnetic minerals (principally magnetite) in the formation. These measurements provide one of the best methods for investigating stratigraphic changes in mineralogy and lithology because the measurement is quick, repeatable, and nondestructive and because different lithologies often have strongly contrasting susceptibilities.

The MSS dual-coil sensor provides ~40 cm resolution measurements, with ~20 cm depth of horizontal investigation. The MSS was run as the lowermost tool in the triple combo tool string using a specially developed data translation cartridge to enable the MSS to be run in combination with the Schlumberger tools. The MSS also has an optional single-coil sensor to provide high-resolution measurements (~10 cm), but this sensor was not used during Expeditions 367 and 368 because it has a large bowspring that requires the MSS to be run higher up in the tool string and because it is very sensitive to separation from the borehole wall.

Magnetic susceptibility data from both the high-resolution and deep-reading sensors are plotted as uncalibrated units. The MSS reading responses are affected by temperature and borehole size (higher temperatures lead to higher susceptibility measurements). Preliminary processing was performed offshore to remove the temperature drift by calculating a least-squares polynomial fit to the data and subtracting the calculated trend from the data set. When the magnetic susceptibility signal in sediment is very low, the detection limits of the tool may be reached. For quality control and environmental correction, the MSS also measures internal tool temperature, *z*-axis acceleration, and low-resolution borehole conductivity.

Acceleration and inclinometry

The General Purpose Inclinometry Tool (GPIT) was included in the FMS-sonic tool string to calculate tool acceleration and orientation during logging. Tool orientation is defined by three parameters: tool deviation, tool azimuth, and relative bearing. The GPIT utilizes a three-axis inclinometer and a three-axis fluxgate magnetometer to record the orientation of the FMS as the magnetometer records the magnetic field components (F*x*, F*y*, and F*z*). Thus, the FMS im-

ages can be corrected for irregular tool motion, and the dip and direction (azimuth) of features in the FMS image can be determined.

Versatile Seismic Imager

Borehole seismic tools are used in wells to detect the acoustic signal generated at the surface. The VSI is used to determine the time–depth relation and to produce a zero-offset vertical seismic profile and/or check shots in the borehole. The VSI (Figure **F30**) uses three-axis single sensor seismic hardware and software and advanced wireline telemetry for efficient data delivery from the borehole to the surface. Each sensor package delivers high-fidelity wave fields through the use of a three-axis geophone accelerometer that is acoustically isolated from the main body of the tool (Figure **F30**). The geophone accelerometer detects particle motion and provides a linear and flat response from 3 to 200 Hz. The VSI maximal operational temperature is 177°C, or 350°F.

During Expeditions 367 and 368, the VSI was anchored against the borehole wall or the casing at ~50 m intervals, and 5–10 recordings were typically taken at each station. The recorded waveforms were stacked, and a one-way traveltime was determined from the first breaks for each station. The seismic source was a Sercel G-gun parallel cluster composed of two 250 inch^3 air guns separated by 1 m. It was positioned by one of the ship cranes off the port side of the ship at a total horizontal offset of ~30 m from the top of the wellhead and was maintained at a fixed water depth (typically between 2 and 7 m; see Figure **F50** in the Site U1500 chapter [Stock et al., 2018]).

Log data quality

The main influence on log data quality is the condition of the borehole wall. Where the borehole diameter varies over short intervals because of washouts of softer material or ledges of harder material, the logs from tools that require good contact with the borehole wall (i.e., FMS, density, and porosity) may be degraded. Deep investigation measurements such as gamma radiation, resistivity, and sonic velocity, which do not require contact with the borehole wall, are generally less sensitive to borehole conditions. "Bridged" sections, where borehole diameter is much below the bit size, also cause irregular log results. The quality of the borehole is improved by minimizing the circulation of drilling fluid while drilling, flushing the borehole to remove debris, and logging as soon as possible after drilling and conditioning are completed. During Expeditions 367 and 368, the necessity of flushing loose material from sandy formations up and out of the borehole required heavy circulation.

The quality of the wireline depth determination depends on several factors. The depth of the logging measurements is determined from the length of the cable payed out from the winch on the ship. The seafloor is identified on the NGR log by the abrupt reduction in gamma ray count at the water/sediment interface (mudline). Discrepancies between the drilling depth and the wireline log depth may occur. In the case of drilling depth, discrepancies are due to core expansion, incomplete core recovery, or incomplete heave compensation. In the case of log depth, discrepancies between successive runs occur because of incomplete heave compensation, incomplete correction for cable stretch, and cable slip. Tidal changes in sea level affect both drilling and logging depths, although these were <1 m in the South China Sea.

Wireline heave compensator

During wireline logging operations, the up-and-down motion of the ship (heave) causes a similar motion of the downhole logging tools. If the amplitude of this motion is large, depth discrepancies can be introduced into the logging data. The risk of damaging downhole instruments is also increased. A WHC system was thus designed to compensate for the vertical motion of the ship and maintain a steady motion of the logging tools to ensure high-quality logging data acquisition (Liu et al., 2013; Iturrino et al., 2013). The WHC uses a vertical accelerometer (motion reference unit [MRU]) positioned under the rig floor near the ship's center of gravity to calculate the vertical motion of the ship with respect to the seafloor. It then adjusts the length of the wireline by varying the distance between two sets of pulleys through which the cable passes in order to minimize downhole tool motion. Real-time measurements of uphole (surface) and downhole acceleration are made simultaneously by the MRU and the EDTC, respectively. An LDEO-developed software package allows these data to be analyzed and compared in real time, displaying the actual motion of the logging tool string and enabling monitoring of the efficiency of the compensator.

Logging data flow and log depth scales

Data for each wireline logging run were monitored in real time and recorded using the Schlumberger MAXIS 500 system. Initial logging data were referenced to the rig floor (wireline depth below rig floor [WRF]). After logging was completed, the data were shifted to a seafloor reference (WSF) that is based on the step in gamma radiation at the sediment/water interface.

Data were transferred onshore to LDEO, where standardized data processing takes place. The main part of the processing is depth matching to remove depth offsets between logs from different logging runs, which results in a new depth scale: wireline log matched depth below seafloor (WMSF). Also, corrections are made to certain tools and logs (e.g., FMS imagery is corrected for tool acceleration, including "stick and slip"), documentation for the logs (with an assessment of log quality) is prepared, and the data are converted to ASCII for the conventional logs and GIF for the FMS images. The Schlumberger Geo-Quest GeoFrame software package is used for most of the processing of the collected wireline logging data. The data were transferred back to the ship within a few days after logging, and this processed data set was made available to the science party (in ASCII and DLIS formats) through the shipboard IODP logging database and shipboard servers.

In situ temperature measurements and heat flow calculation

During Expeditions 367 and 368, in situ temperature measurements were made with the APCT-3 (Figure **F31**) at each site when the APC was deployed. The APCT-3 fits directly into the coring shoe of the APC and consists of a battery pack, data logger, and platinum resistance-temperature device calibrated over a temperature range from 0° to 30°C. Before entering the borehole, the tool is first stopped at the mudline for 5 min to thermally equilibrate with bottom water. However, the lowest temperature recorded during the run is occasionally used instead of the average temperature at the mudline as an estimate of the bottom water temperature because (1) it is more repeatable and (2) the bottom water is expected to have the lowest temperature in the profile. When the APC is plunged into the formation, there is an instantaneous temperature rise from frictional heating. This heat gradually dissipates into the surrounding sediment as the temperature at the APCT-3 equilibrates toward the temperature of the sediment. After the APC penetrates the sediment, it is held in place for 5 min while the APCT-3 records the temperature of the cutting shoe every second.

Figure F31. APCT-3 for in situ temperature measurements, Expeditions 367 and 368.



The equilibrium temperature of the sediment is estimated by applying a mathematical heat-conduction model to the temperature decay record (Horai and Von Herzen, 1985). The synthetic thermal decay curve for the APCT-3 is a function of the geometry and thermal properties of the probe and the sediment (Bullard, 1954; Horai and Von Herzen, 1985). Equilibrium temperature is estimated by applying a fitting procedure (Pribnow et al., 2000). However, where the APC does not achieve a full stroke or where ship heave pulls the APC up from full penetration, the temperature equilibration curve is disturbed and temperature determination is less accurate. The nominal accuracy of the APCT-3 temperature measurements is ±0.05°C.

APCT-3 temperature data is combined with thermal conductivity measurements obtained from whole-round core sections to retrieve heat flow values. Heat flow and geothermal gradient are calculated according to the Bullard (1939) method to be consistent with the synthesis of ODP heat flow data by Pribnow et al. (2000). This method assumes a linear relation between temperature T and thermal resistance of the sediments:

$$T(z) = T_0 + Q \times \Omega(z),$$

where

T = temperature,
z = depth,
T_0 = surface temperature (z = 0),
Q = is heat flow, and
$\Omega(z)$ = thermal resistance, expressed as

$$\Omega(z) = \int_0^z \{dz/[\lambda(z)]\} \approx \sum_{i=1}^{I} [(z_i - z_{i-1})/\lambda_i],$$

with z_i and z_{i-1} as bottom and top depths, respectively, of a horizontal layer with thermal conductivity λ_i. I is the number of layers between the surface and depth z.

Plotting $\Omega(z)$ as a function of T(z), the Bullard plot allows estimation of the surface temperature (T_0) from the intercept with z = 0 and of the heat flow (Q) from the slope. The conditions for the linearity of the plot are affected by conductive conditions, steady state, and absence of internal heat source.

To obtain the thermal conductivity at the depth of the temperature measurements, we estimated a continuous profile of $\lambda(z)$, assuming that there is a linear variation of thermal conductivity with depth (Pribnow et al., 2000):

$$\lambda_{LIN}(z) = \lambda_0 + \Gamma \times z.$$

The linear trend was confirmed at each site. The thermal resistance $\Omega_{LIN,j}$ for the depth $z_{T,j}$ of the jth temperature value T_j was calculated using the results of the linear regression, λ_0 and Γ (slope) with

$$\Omega_{LIN,j} = [\ln(\lambda_0 + \Gamma \times z_{T,j}) - \ln(\lambda_0)]/\Gamma,$$

which allows the calculation of the heat flow.

Correlation to seismic data

The Chinese National Offshore Oil and Gas Company (CNOOC) holds an extensive database of 2-D and 3-D reflection seismic data covering the northern South China Sea margin. Interpretations of these data by CNOOC allow a suite of regional seismic unconformities to be identified. These are named by CNOOC with the capital letter T followed by a number (e.g., T30, T50, etc.). The ages of these seismic stratigraphic unconformities are constrained by industry wells located significantly landward of our study area.

During this expedition, we tried to extend the regional seismic unconformities mapped by CNOOC within the northern SCS continental slope (e.g., Dai et al., 2015) into our more southerly located study area of the slope and deep SCS basin. We applied the principle of seismic stratigraphy established by Vail et al. (1977) in the mapping of these horizons. That is, each unconformity and its correlative conformity are determined by recognizing systematic reflection terminations (including onlap, downlap, truncation, etc.). We expect there to be ten horizons tied to the CNOOC scheme in our area (Table **T10**), although at some of our sites one or more of these could not be identified due to lack of age control and/or disruption by faulting. Following the seismic stratigraphic principle, these can all be considered time markers, but only where they have a true conformal relationship to strata above and below will they represent a specific age. In all other settings, they represent a hiatus of a shorter or longer time interval.

We follow the convention established by CNOOC to name the base of the Cenozoic sedimentary succession Reflector Tg. This horizon is also often referred to as the "acoustic basement." By this we mean a strong reflector that to a large but variable degree masks the underlying reflectors and does not allow any regional seismic stratigraphic mapping below it. Importantly, Tg is not a seismic stratigraphically defined horizon, nor does it represent any particular age or lithology. In our study area, it can represent the top of anything from volcanic basement of Neogene age to Mesozoic sediments or continental crystalline crust.

Table T10. Chinese National Offshore Oil and Gas Company (Shenzhen Branch) scheme for correlation between the regional seismic stratigraphic unconformities and the chrono- and lithostratigraphy in the Pearl River Mouth Basin, northern South China Sea margin (Shi et al., 2014; Dai et al., 2015). Modified with regard to Reflector Tg. **Download table in CSV format.**

Seismic horizon	Age (Ma)	Corresponding lithostratigraphic boundaries
T20	2.6	Base of Quaternary
T30	5.3	Base of Pliocene Wanshan Formation
T32	10	Base of upper Miocene Yuehai Formation
T40	16	Base of middle Miocene Hanjiang Formation
T50	19.1	Upper/lower Zhujiang Formation
T60	23	Base of lower Miocene Zhujiang Formation
T70	33.9	Base of Oligocene Zhuhai Formation
T80	38	Base of upper Eocene Enping Formation, underlain by lower Eocene Wenchang Formation
T83	Unknown	
Tg	No specific age	Acoustic basement

References

Agnini, C., Fornaciari, E., Raffi, I., Catanzariti., R., Pälike, H., Backman, J., and Rio, D., 2014. Biozonation and biochronology of Paleogene calcareous nannofossils from low and middle latitudes. *Newsletters on Stratigraphy,* 47(2):131–181. **https://doi.org/10.1127/0078-0421/2014/0042**

Akiba, F., 1986. Middle Miocene to Quaternary diatom biostratigraphy in the Nankai Trough and Japan Trench, and modified lower Miocene through Quaternary diatom zones for middle-to-high latitudes of the north Pacific. *In* Kagami, H., Karig, D.E., Coulbourn, W.T., et al., *Initial Reports of the Deep Sea Drilling Project,* 87: Washington, DC (U.S. Government Printing Office), 393–481. **https://doi.org/10.2973/dsdp.proc.87.106.1986**

Akiba, F., and Yanagisawa, Y., 1986. Taxonomy, morphology and phylogeny of the Neogene diatom zonal marker species in the middle-to-high latitudes of the North Pacific. *In* Kagami, H., Karig, D.E., Coulbourn, W.T., et al., *Initial Reports of the Deep Sea Drilling Project,* 87: Washington, DC (U.S. Government Printing Office), 483–554. **https://doi.org/10.2973/dsdp.proc.87.107.1986**

Alabi, O.O., Edilbi, A.N.F., Brolly, C., Muirhead, D., Parnell, J., Stacey, R., and Bowden, S.A., 2015. Asphaltene detection using surface enhanced Raman scattering (SERS). *Chemical Communications,* 51(33):7152–7155. **http://pubs.rsc.org/en/content/articlehtml/2015/cc/c5cc00676g**

Alvarez Zarikian, C.A., 2015. Cenozoic bathyal and abyssal ostracods beneath the South Pacific Gyre (IODP Expedition 329 Sites U1367, U1368 and U1370). *Palaeogeography, Palaeoclimatology, Palaeoecology,* 419:115–142. **https://doi.org/10.1016/j.palaeo.2014.07.024**

Anthonissen, D.E., and Ogg, J.G., 2012. Appendix 3—Cenozoic and Cretaceous biochronology of planktonic foraminifera and calcareous nannofossils. *In* Gradstein, F.M., Ogg, J.G., Schmitz, M.D., and Ogg, G.M., (Eds.), *The Geologic Time Scale 2012:* Amsterdam (Elsevier), 1083–1127. **https://doi.org/10.1016/B978-0-444-59425-9.15003-6**

Arculus, R.J., Ishizuka, O., Bogus, K., Aljahdali, M.H., Bandini-Maeder, A.N., Barth, A.P., Brandl, P.A., do Monte Guerra, R., Drab, L., Gurnis, M.C., Hamada, M., Hickey-Vargas, R.L., Jiang, F., Kanayama, K., Kender, S., Kusano, Y., Li, H., Loudin, L.C., Maffione, M., Marsaglia, K.M., McCarthy, A., Meffre, S., Morris, A., Neuhaus, M., Savov, I.P., Sena Da Silva, C.A., Tepley, F.J., III, van der Land, C., Yogodzinski, G.M., and Zhang, Z., 2015. Expedition 351 methods. *In* Arculus, R.J., Ishizuka, O., Bogus, K., and the Expedition 351 Scientists, *Izu-Bonin-Mariana Arc Origins.* Proceedings of the International Ocean Discovery Program, 351: College Station, TX (International Ocean Discovery Program). **https://doi.org/10.14379/iodp.proc.351.102.2015**

ASTM International, 1990. Standard method for laboratory determination of water (moisture) content of soil and rock (Standard D2216–90). In *Annual Book of ASTM Standards for Soil and Rock* (Volume 04.08): Philadelphia (American Society for Testing Materials). [revision of D2216-63, D2216-80]

Backman, J., Raffi, I., Rio, D., Fornaciari, E., and Pälike, H., 2012. Biozonation and biochronology of Miocene through Pleistocene calcareous nannofossils from low and middle latitudes. *Newsletters on Stratigraphy,* 45(3):221–244. **https://doi.org/10.1127/0078-0421/2012/0022**

Baldauf, J.G., and Iwai, M., 1995. Neogene diatom biostratigraphy for the eastern equatorial Pacific Ocean, Leg 138. *In* Pisias, N.G., Mayer, L.A., Janecek, T.R., Palmer-Julson, A., and van Andel, T.H. (Eds.), *Proceedings of the Ocean Drilling Program, Scientific Results,* 138: College Station, TX (Ocean Drilling Program), 105–128. **https://doi.org/10.2973/odp.proc.sr.138.107.1995**

Balsam, W.L., and Damuth, J.E., 2000. Further investigations of shipboard vs. shore-based spectral data: implications for interpreting Leg 164 sediment composition. *In* Paull, C.K., Matsumoto, R., Wallace, P., and Dillon, W.P. (Eds.), *Proceedings of the Ocean Drilling Program, Scientific Results,* 164: College Station, TX (Ocean Drilling Program), 313–324. **https://doi.org/10.2973/odp.proc.sr.164.222.2000**

Balsam, W.L., Damuth, J.E., and Schneider, R.R., 1997. Comparison of shipboard vs. shore-based spectral data from Amazon Fan cores: implications for interpreting sediment composition. *In* Flood, R.D., Piper, D.J.W., Klaus, A., and Peterson, L.C. (Eds.), *Proceedings of the Ocean Drilling Program, Scientific Results,* 155: College Station, TX (Ocean Drilling Program), 193–215. **https://doi.org/10.2973/odp.proc.sr.155.210.1997**

Balsam, W.L., Deaton, B.C., and Damuth, J.E., 1998. The effects of water content on diffuse reflectance spectrophotometry studies of deep-sea sediment cores. *Marine Geology,* 149(1–4):177–189. **https://doi.org/10.1016/S0025-3227(98)00033-4**

Barron, J.A., 1981. Late Cenozoic diatom biostratigraphy and paleoceanography of the middle-latitude eastern North Pacific, Deep Sea Drilling Project Leg 63. *In* Yeats, R.S., Haq, B.U., et al., *Initial Reports of the Deep Sea Drilling Project,* 63: Washington, DC (U.S. Government Printing Office), 507–538. **https://doi.org/10.2973/dsdp.proc.63.113.1981**

Barron, J.A., 1985. Late Eocene to Holocene diatom biostratigraphy of the equatorial Pacific Ocean, Deep Sea Drilling Project Leg 85. *In* Mayer, L., Theyer, F., Thomas, E., et al., *Initial Reports of the Deep Sea Drilling Project,* 85: Washington, DC (U.S. Government Printing Office), 413–456. **https://doi.org/10.2973/dsdp.proc.85.108.1985**

Barron, J.A., 2003. Planktonic marine diatom record of the past 18 m.y.: appearances and extinctions in the Pacific and Southern Oceans. *Diatom Research,* 18(2):203–224. **https://doi.org/10.1080/0269249X.2003.9705588**

Barron, J.A., 2006. Diatom biochronology for the early Miocene of the equatorial Pacific. *Stratigraphy,* 2(4):281–309. **http://www.micropress.org/micropen2/articles/1/4/3987_articles_article_file_1443.pdf**

Barron, J.A., Fourtanier, E., and Bohaty, S.M., 2004. Oligocene and earliest Miocene diatom biostratigraphy of ODP Leg 199 Site 1220, equatorial Pacific. *In* Wilson, P.A., Lyle, M., Janecek, T.R., and Firth, J.V. (Eds.), *Proceedings of the Ocean Drilling Program, Scientific Results,* 199: College

Station, TX (Ocean Drilling Program), 1–25. **https://doi.org/10.2973/odp.proc.sr.199.204.2004**

Berggren, W.A., Kent, D.V., Swisher, C.C., III, and Aubry, M.-P., 1995. A revised Cenozoic geochronology and chronostratigraphy. *In* Berggren, W.A., Kent, D.V., Aubry, M.-P., and Hardenbol, J. (Eds.), *Geochronology, Time Scales and Global Stratigraphic Correlation.* Special Publication - SEPM (Society for Sedimentary Geology), 54:129–212. **https://doi.org/10.7916/D8XD1B1H**

Blow, W.H., 1969. Late middle Eocene to recent planktonic foraminiferal biostratigraphy. *Proceedings of the International Conference on Planktonic Microfossils,* 1:199–422.

Blow, W.H., 1979. *The Cainozoic Foraminifera* (Volumes 1–3): Leiden, The Netherlands (E.J. Brill).

Blum, P., 1997. *Technical Note 26: Physical Properties Handbook—A Guide to the Shipboard Measurement of Physical Properties of Deep-Sea Cores*. Ocean Drilling Program. **https://doi.org/10.2973/odp.tn.26.1997**

Bolli, H.M., and Saunders, J.B., 1985. Oligocene to Holocene low latitude planktic foraminifera. *In* Bolli, H.M., Saunders, J.B., and Perch-Nielsen, K. (Eds.), *Plankton Stratigraphy* (Volume 1): *Planktic Foraminifera, Calcareous Nannofossils and Calpionellids:* Cambridge, United Kingdom (Cambridge University Press), 155–262.

Bollmann, J., 1997. Morphology and biogeography of *Gephyrocapsa* coccoliths in Holocene sediments. *Marine Micropaleontology,* 29(3–4):319–350. **https://doi.org/10.1016/S0377-8398(96)00028-X**

Bown, P.R. (Ed.), 1998. *Calcareous Nannofossil Biostratigraphy:* Dordrecht, The Netherlands (Kluwer Academic Publishing).

Bullard, E.C., 1939. Heat flow in South Africa. *Proceedings of the Royal Society of London, Series A,* 173(955):474–502. **https://doi.org/10.1098/rspa.1939.0159**

Bullard, E.C., 1954. The flow of heat through the floor of the Atlantic Ocean. *Proceedings of the Royal Society of London, Series A: Mathematical, Physical and Engineering Sciences,* 222(1150):408–429. **https://doi.org/10.1098/rspa.1954.0085**

Burckle, L.H., 1972. Late Cenozoic planktonic diatom zones from the eastern equatorial Pacific. *In* Simonsen, R. (Ed.), *First Symposium on Recent and Fossil Marine Diatoms* (Bremenhaven, Germany, 21–26 September 1970). Beihefte zur Nova Hedwigia, 39:217–249.

Cervato, C., and Burckle, L., 2003. Pattern of first and last appearance in diatoms: Oceanic circulation and the position of polar fronts during the Cenozoic. *Paleoceanography,* 18(2). **https://doi.org/10.1029/2002PA000805**

Coccioni, R., Marsili, A., Montanari, A., Bellanca, A., Neri, R., Bice, D.M., Brinkhuis, H., Church, N., Macalady, A., McDaniel, A., Deino, A., Lirer, F., Sprovieri, M., Maiorano, P., Monechi, S., Nini, C., Nocchi, M., Pross, J., Rochette, P., Sagnotti, L., Tateo, F., Touchard, Y., Van Simaeys, S., and Williams, G.L., 2008. Integrated stratigraphy of the Oligocene pelagic sequence in the Umbria-Marche Basin (northeastern Apennines, Italy): a potential Global Stratotype Section and Point (GSSP) for the Rupelian/Chattian boundary. *Geological Society of America Bulletin,* 120(3–4):487–511. **https://doi.org/10.1130/B25988.1**

Cook, H.E., Johnson, P.D., Matti, J.C., and Zemmels, I., 1975. Methods of sample preparation and X-ray diffraction data analysis, X-ray Mineralogy Laboratory, Deep Sea Drilling Project, University of California, Riverside. *In* Hayes, D.E., Frakes, L.A., et al., *Initial Reports of the Deep Sea Drilling Project,* 28: Washington (U.S. Government Printing Office), 999–1007. **http://dx.doi.org/10.2973/dsdp.proc.28.app4.1975**

Cox, A., and Gordon, R.G., 1984. Paleolatitudes determined from paleomagnetic data from vertical cores. *Reviews of Geophysics and Space Physics,* 22(1):47–71. **https://doi.org/10.1029/RG022i001p00047**

Dai, Y., Yu, Q., Li, H., Wang, Z., Bai, J., and Peng, H., 2015. Threshold conditions and reservoir-controlling characteristics of source kitchen in Zhu I depression, Pearl River Mouth Basin. *Acta Petrolei Sinica,* 36(S2):145–155. (in Chinese with English abstract) **https://doi.org/10.7623/syxb2015S2013**

De Vleeschouwer, D., Dunlea, A.G., Auer, G., Anderson, C.H., Brumsack, H., de Loach, A., Gurnis, M., Huh, Y., Ishiwa, T., Jang, K., Kominz, M.A., März, C., Schnetger, B., Murray, R.W., Pälike, H., and Expedition 356 Shipboard Scientists, 2017. Quantifying K, U, and Th contents of marine sediments using shipboard natural gamma radiation spectra measured on DV *JOIDES Resolution*. *Geochemistry, Geophysics, Geosystems,* 18(3):1053–1064. **https://doi.org/10.1002/2016GC006715**

de Wall, H., and Worm, H.-U., 2001. Recognition of drilling-induced remanent magnetization by *Q*-factor analysis: a case study from the KTB-drillholes. *Journal of Applied Geophysics,* 46(1):55–64. **https://doi.org/10.1016/S0926-9851(00)00039-2**

Doré, T., and Lundin, E., 2015. Research focus: hyperextended continental margins—knowns and unknowns. *Geology,* 43(1):95–96. **https://doi.org/10.1130/focus012015.1**

Droser, M.L., and Bottjer, D.J., 1986. A semiquantitative field classification of ichnofabric. *Journal of Sedimentary Research,* 56(4):558–559. **https://doi.org/10.1306/212F89C2-2B24-11D7-8648000102C1865D**

Dunlea, A.G., Murray, R.W., Harris, R.N., Vasiliev, M.A., Evans, H., Spivack, A.J., and D'Hondt, S., 2013. Assessment and use of NGR instrumentation on the *JOIDES Resolution* to quantify U, Th, and K concentrations in marine sediment. *Scientific Drilling,* 15:57–63. **https://doi.org/10.2204/iodp.sd.15.05.2013**

Edwards, A.R., 1991. The Oamaru diatomite. *New Zealand Geological Survey Paleontological Bulletin*, 64.

Ellis, D.V., and Singer, J.M., 2007. *Well Logging for Earth Scientists* (2nd edition): New York (Elsevier).

Expedition 324 Scientists, 2010. Methods. *In* Sager, W.W., Sano, T., Geldmacher, J., and the Expedition 324 Scientists, *Proceedings of the Integrated Ocean Drilling Program,* 324: Tokyo (Integrated Ocean Drilling Program Management International, Inc.). **https://doi.org/10.2204/iodp.proc.324.102.2010**

Expedition 330 Scientists, 2012. Methods. *In* Koppers, A.A.P., Yamazaki, T., Geldmacher, J., and the Expedition 330 Scientists, *Proceedings of the Integrated Ocean Drilling Program,* 330: Tokyo (Integrated Ocean Drilling Program Management International, Inc.). **https://doi.org/10.2204/iodp.proc.330.102.2012**

Expedition 339 Scientists, 2013. Methods. *In* Stow, D.A.V., Hernández-Molina, F.J., Alvarez Zarikian, C.A., and the Expedition 339 Scientists, *Proceedings of the Integrated Ocean Drilling Program,* 339: Tokyo (Integrated Ocean Drilling Program Management International, Inc.). **https://doi.org/10.2204/iodp.proc.339.102.2013**

Fenner, J., 1978. Cenozoic diatom biostratigraphy of the equatorial and southern Atlantic Ocean. *In* Perch-Nielsen, K., Supko, P.R., et al., *Initial Reports of the Deep Sea Drilling Project,* 38, 39, 40, 41 (Suppl.): Washington, DC (U.S. Government Printing Office), 491–624. **https://doi.org/10.2973/dsdp.proc.38394041s.201.1978**

Fenner, J., 1985. Late Cretaceous to Oligocene planktic diatoms. *In* Bolli, H.M., Saunders, J.B., and Perch-Nielsen, K. (Eds.), *Plankton Stratigraphy:* Cambridge, United Kingdom (Cambridge University Press), 713–762.

Fenner, J., 1994. Diatoms of the Fur Formation, their taxonomy and biostratigraphic interpretation: results from the Harre borehole, Denmark. *Aarhus Geoscience,* 1:99–163.

Fisher, R.V., and Schmincke, H.-U., 1984. *Pyroclastic Rocks:* Berlin (Springer-Verlag). **https://doi.org/10.1007/978-3-642-74864-6**

Fuller, M., 1969. Magnetic orientation of borehole cores. *Geophysics,* 34(5):772–774. **https://doi.org/10.1190/1.1440047**

Fuller, M., Hastedt, M., and Herr, B., 1998. Coring-induced magnetization of recovered sediment. *In* Weaver, P.P.E., Schmincke, H.-U., Firth, J.V., and Duffield, W. (Eds.), *Proceedings of the Ocean Drilling Program, Scientific Results,* 157: College Station, TX (Ocean Drilling Program), 47–56. **https://doi.org/10.2973/odp.proc.sr.157.103.1998**

Gee, J.S., Tauxe, L., and Constable, C., 2008. AMSSpin: a LabVIEW program for measuring the anisotropy of magnetic susceptibility with the Kappabridge KLY-4S. *Geochemistry, Geophysics, Geosystems,* 9(8):Q08Y02. **https://doi.org/10.1029/2008GC001976**

Gieskes, J.M., Gamo, T., and Brumsack, H., 1991. *Technical Note 15: Chemical Methods for Interstitial Water Analysis Aboard JOIDES Resolution.* Ocean Drilling Program. **https://doi.org/10.2973/odp.tn.15.1991**

Gillis, K.M., Snow, J.E., Klaus, A., Guerin, G., Abe, N., Akizawa, N., Ceuleneer, G., Cheadle, M.J., Adrião, Á., Faak, K., Falloon, T.J., Friedman, S.A., Godard, M.M., Harigane, Y., Horst, A.J., Hoshide, T., Ildefonse, B., Jean, M.M., John, B.E., Koepke, J.H., Machi, S., Maeda, J., Marks, N.E., McCaig, A.M., Meyer, R., Morris, A., Nozaka, T., Python, M., Saha, A., and Wintsch, R.P., 2014. Methods. *In* Gillis, K.M., Snow, J.E., Klaus, A., and the Expedition 345 Scientists, *Proceedings of the Integrated Ocean Drilling Program,* 345: College Station, TX (Integrated Ocean Drilling Program). **https://doi.org/10.2204/iodp.proc.345.102.2014**

Gilmore, G.R., 2008. *Practical Gamma-ray Spectrometry* (2nd edition): Hoboken, NJ (John Wiley & Sons). **https://doi.org/10.1002/9780470861981**

Goldberg, D., 1997. The role of downhole measurements in marine geology and geophysics. *Reviews of Geophysics,* 35(3):315–342. **https://doi.org/10.1029/97RG00221**

Gombos, A.M., Jr., 1982. Early and middle Eocene diatom evolutionary events. *Bacillaria,* 5:225–242.

Govindaraju, K., 1994. 1994 compilation of working values and sample description for 383 geostandards. *Geostandards Newsletter,* 18(1). **https://doi.org/10.1111/j.1751-908X.1994.tb00502.x**

Gradstein, F.M., Ogg, J.G., Schmitz, M.D., and Ogg, G.M. (Eds.), 2012. *The Geological Time Scale 2012:* Oxford, United Kingdom (Elsevier).

Hajós, M., 1976. Upper Eocene and lower Oligocene diatomaceae, archaeomonadaceae, and silicoflagellatae in southwestern Pacific sediments, DSDP Leg 29. *In* Hollister, C.D., Craddock, C., et al., *Initial Reports of the Deep Sea Drilling Project,* 35: Washington, DC (U.S. Government Printing Office), 817–883. **https://doi.org/10.2973/dsdp.proc.35.29chap1.1976**

Hardenbol, J., Thierry, J., Farley, M.B., Jacquin, T., de Graciansky, P.-C., and Vail, P.R., 1998. Mesozoic and Cenozoic sequence chronostratigraphic framework of European basins. *In* de Graciansky, P.-C., Hardenbol, J., Jacquin, T., and Vail, P.R. (Eds.), *Mesozoic and Cenozoic Sequence Stratigraphy of European Basins.* Special Publication - SEPM (Society for Sedimentary Geology), 60:3–13. **http://archives.datapages.com/data/sepm_sp/SP60/Mesozoic_and_Cenozoic_Sequence_Chronostratigraphic.pdf**

Harris, R.N., Sakaguchi, A., Petronotis, K., Baxter, A.T., Berg, R., Burkett, A., Charpentier, D., Choi, J., Diz Ferreiro, P., Hamahashi, M., Hashimoto, Y., Heydolph, K., Jovane, L., Kastner, M., Kurz, W., Kutterolf, S.O., Li, Y., Malinverno, A., Martin, K.M., Millan, C., Nascimento, D.B., Saito, S., Sandoval Gutierrez, M.I., Screaton, E.J., Smith-Duque, C.E., Solomon, E.A., Straub, S.M., Tanikawa, W., Torres, M.E., Uchimura, H., Vannucchi, P., Yamamoto, Y., Yan, Q., and Zhao, X., 2013. Methods. *In* Harris, R.N., Sakaguchi, A., Petronotis, K., and the Expedition 344 Scientists, *Proceedings of the Integrated Ocean Drilling Program,* 344: College Station, TX (Integrated Ocean Drilling Program). **https://doi.org/10.2204/iodp.proc.344.102.2013**

Hilgen, F.J., Lourens, L.J., and Van Dam, J.A., 2012. The Neogene period. With contributions by A.G. Beu, A.F. Boyes, R.A. Cooper, W. Krijgsman, J.G. Ogg, W.E. Piller, and D.S. Wilson. *In* Gradstein, F.M., Ogg, J.G., Schmitz, M.D., and Ogg, G.M. (Eds.), *The Geologic Time Scale:* Oxford, United Kingdom (Elsevier), 923–978. **https://doi.org/10.1016/B978-0-444-59425-9.00029-9**

Holbourn, A., Henderson, A.S., and MacLeod, N., 2013. *Atlas of Benthic Foraminifera:* Chichester, United Kingdom (John Wiley & Sons, Ltd.). **https://doi.org/10.1002/9781118452493**

Horai, K., and Von Herzen, R.P., 1985. Measurement of heat flow on Leg 86 of the Deep Sea Drilling Project. *In* Heath, G.R., Burckle, L.H., et al., *Initial Reports of the Deep Sea Drilling Project,* 86: Washington, DC (U.S. Government Printing Office), 759–777. **https://doi.org/10.2973/dsdp.proc.86.135.1985**

Hu, C.-H., and Tao, H.-J., 2008. Studies on the ostracod fauna of Taiwan and it adjacent seas, Part 1 and 2. *Journal of the National Taiwan Museum, Special Publication Series*, 13. (in Chinese)

Husson, D., Galbrun, B., Laskar, J., Hinnov, L.A., Thibault, N., Gardin, S., and Lockair, R.E., 2011. Astronomical calibration of the Maastrichtian (Late Cretaceous). *Earth and Planetary Science Letters,* 305(3–4):328–340. **https://doi.org/10.1016/j.epsl.2011.03.008**

Iturrino, G., Liu, T., Goldberg, D., Anderson, L., Evans, H., Fehr, A., Guerin, G., Inwood, J., Lofi, J., Malinverno, A., Morgan, S., Mrozewski, S., Slagle, A., and Williams, T., 2013. Performance of the wireline heave compensation system onboard D/V *JOIDES Resolution. Scientific Drilling,* 15:46–50. **https://doi.org/10.2204/iodp.sd.15.08.2013**

Jarrard, R.D., and Kerneklian, M.J., 2007. Data report: physical properties of the upper oceanic crust of ODP Site 1256: multisensor track and moisture and density measurements. *In* Teagle, D.A.H., Wilson, D.S., Acton, G.D., and Vanko, D.A. (Eds.), *Proceedings of the Ocean Drilling Program, Scientific Results,* 206: College Station, TX (Ocean Drilling Program), 1–11. **https://doi.org/10.2973/odp.proc.sr.206.011.2007**

Jutzeler, M., White, J.D.L., Talling, P.J., McCanta, M., Morgan, S., Le Friant, A., and Ishizuka, O., 2014. Coring disturbances in IODP piston cores with implications for offshore record of volcanic events and the Missoula megafloods. *Geochemistry, Geophysics, Geosystems,* 15(9):3572–3590. **https://doi.org/10.1002/2014GC005447**

Kaminski, M.A., and Gradstein, F.M., 2005. Atlas of Paleogene cosmopolitan deep-water agglutinated foraminifera. *Grzybowski Foundation Special Publication,* 10. **http://www.foraminifera.eu/atlas.html**

Kennett, J.P., and Srinivasan, M.S., 1983. *Neogene Planktonic Foraminifera: A Phylogenetic Atlas:* Stroudsburg, PA (Hutchinson Ross).

Kirschvink, J.L., 1980. The least-squares line and plane and the analysis of palaeomagnetic data. *Geophysical Journal of the Royal Astronomical Society,* 62(3):699–718. **https://doi.org/10.1111/j.1365-246X.1980.tb02601.x**

Koizumi, I., and Tanimura, Y., 1985. Neogene diatom biostratigraphy of the middle latitude western North Pacific, Deep Sea Drilling Project Leg 86. *In* Heath, G.R., Burckle, L.H., et al., *Initial Reports of the Deep Sea Drilling Project,* 86: Washington, DC (U.S. Government Printing Office), 269–300. **https://doi.org/10.2973/dsdp.proc.86.109.1985**

Kristiansen, J.I., 1982. The transient cylindrical probe method for determination of thermal parameters of earth materials [Ph.D. dissertation]. Åarhus University, Åarhus, Denmark.

Lazarus, D., Barron, J., Renaudie, J., Diver, P., and Türke, A., 2014. Cenozoic planktonic marine diatom diversity and correlation to climate change. *PLoS ONE,* 9(1):e84857. **https://doi.org/10.1371/journal.pone.0084857**

Le Maitre, R.W., Steckeisen, A., Zanettin, B., Le Bas, M.J., Bonin, B., and Bateman, P. (Eds.), 2002. *Igneous rocks: A Classification and Glossary of Terms* (2nd edition.): Cambridge, United Kingdom (Cambridge University Press).

Li, B., Jian, Z., Li, Q., Tian, J., and Wang, P., 2005. Paleoceanography of the South China Sea since the middle Miocene: evidence from planktonic foraminifera. *In* Wang, P., and Lipps, J. (Eds.), *Marine Micropaleontology of the South China Sea.* Marine Micropaleontology, 54(1–2):49–62. **https://doi.org/10.1016/j.marmicro.2004.09.003**

Li, C.-F., Lin, J., Kulhanek, D.K., Williams, T., Bao, R., Briais, A., Brown, E.A., Chen, Y., Clift, P.D., Colwell, F.S., Dadd, K.A., Ding, W., Hernández-Almeida, I., Huang, X.-L., Hyun, S., Jiang, T., Koppers, A.A.P., Li, Q., Liu, C., Liu, Q., Liu, Z., Nagai, R.H., Peleo-Alampay, A., Su, X., Sun, Z., Tejada, M.L.G., Trinh, H.S., Yeh, Y.-C., Zhang, C., Zhang, F., Zhang, G.-L., and Zhao, X., 2015. Methods. *In* Li, C.-F., Lin, J., Kulhanek, D.K., and the Expedition 349 Scientists, *South China Sea Tectonics.* Proceedings of the International Ocean Discovery Program, 349: College Station, TX (International Ocean Discovery Program). **https://doi.org/10.14379/iodp.proc.349.102.2015**

Liu, T., Iturrino, G., Goldberg, D., Meissner, E., Swain, K., Furman, C., Fitzgerald, P., Frisbee, N., Chlimoun, J., Van Hyfte, J., and Beyer, R., 2013. Performance evaluation of active wireline heave compensation systems in marine well logging environments. *Geo-Marine Letters,* 33(1):83–93. **https://doi.org/10.1007/s00367-012-0309-8**

Loeblich, A.R., Jr., and Tappan, H., 1988. *Foraminiferal Genera and Their Classification:* New York (Van Nostrand Reinhold). **https://doi.org/1007/978-1-4899-5760-3**

Lourens, L., Hilgen, F., Shackleton, N.J., Laskar, J., and Wilson, D., 2004. The Neogene period. *In* Gradstein, F.M., Ogg, J.G., and Smith, A. (Eds.), *A Geologic Time Scale 2004:* Cambridge, United Kingdom (Cambridge Uni-

versity Press), 409–440. **https://doi.org/10.1017/CBO9780511536045.022**

Lovell, M.A., Harvey, P.K., Brewer, T.S., Williams, C., Jackson, P.D., and Williamson, G., 1998. Application of FMS images in the Ocean Drilling Program: an overview. *In* Cramp, A., MacLeod, C.J., Lee, S.V., and Jones, E.J.W. (Eds.), *Geological Evolution of Ocean Basins: Results from the Ocean Drilling Program.* Geological Society Special Publication, 131(1):287–303. **https://doi.org/10.1144/GSL.SP.1998.131.01.18**

Lurcock, P.C., and Wilson, G.S., 2012. PuffinPlot: a versatile, user-friendly program for paleomagnetic analysis. *Geochemistry, Geophysics, Geosystems,* 13(6):Q06Z45. **https://doi.org/10.1029/2012GC004098**

Luthi, S.M., 1990. Sedimentary structures of clastic rocks identified from electrical borehole images. *In* Hurst, A., Lovell, M.A., and Morton, A.C. (Eds.), *Geological Applications of Wireline Logs.* Geological Society Special Publication, 48:3–10. **https://doi.org/10.1144/GSL.SP.1990.048.01.02**

MacKenzie, W.S., Donaldson, C.H., and Guilford, C., 1982. *Atlas of Igneous Rocks and Their Textures:* Essex, United Kingdom (Longman Group UK Limited).

Maiorano, P., and Marino, M., 2004. Calcareous nannofossil bioevents and environmental control on temporal and spatial patterns at the early–middle Pleistocene. *Marine Micropaleontology*, 53(3–4):405–422. **https://doi.org/10.1016/j.marmicro.2004.08.003**

Manheim, F.T., and Sayles, F.L., 1974. Composition and origin of interstitial waters of marine sediments, based on deep sea drill cores. *In* Goldberg, E.D. (Ed.), *The Sea* (Volume 5): *Marine Chemistry: The Sedimentary Cycle:* New York (Wiley), 527–568.

Marsaglia, K., Milliken, K., and Doran, L., 2013. *Technical Note 1: IODP digital reference for smear slide analysis of marine mud—Part 1: Methodology and atlas of siliciclastic and volcanogenic components.* Integrated Ocean Drilling Program. **https://doi.org/10.2204/iodp.tn.1.2013**

Marsaglia, K., Milliken, K., Leckie, R.M., Tentori, D., and Doran, L., 2015. *Technical Note 2: IODP smear slide digital reference for sediment analysis of marine mud, Part 2: Methodology and atlas of biogenic components.* International Ocean Discovery Program. **https://doi.org/10.2204/iodp.tn.2.2015**

Martini, E., 1971. Standard Tertiary and Quaternary calcareous nannoplankton zonation. *In* Farinacci, A. (Ed.), *Proceedings of the Second Planktonic Conference, Roma 1970:* Rome (Edizioni Tecnoscienza), 2:739–785.

Mazzullo, J.M., Meyer, A., and Kidd, R.B., 1988. New sediment classification scheme for the Ocean Drilling Program. *In* Mazzullo, J., and Graham, A.G. (Eds.), *Technical Note 8: Handbook for Shipboard Sedimentologists.* Ocean Drilling Program, 44–67. **https://doi.org/10.2973/odp.tn.8.1988**

McFadden, P.L., and Reid, A.B., 1982. Analysis of paleomagnetic inclination data. *Geophysical Journal of the Royal Astronomical Society,* 69(2):307–319. **https://doi.org/10.1111/j.1365-246X.1982.tb04950.x**

Munsell Color Company, Inc., 2000. *Munsell Soil Color Charts: Year 2000 Revised Washable Edition:* Grand Rapids, MI (GretagMacbeth).

Murray, R.W., Miller, D.J., and Kryc, K.A., 2000. *Technical Note 29: Analysis of Major and Trace Elements in Rocks, Sediments, and Interstitial Waters by Inductively Coupled Plasma–Atomic Emission Spectrometry (ICP-AES).* Ocean Drilling Program. **https://doi.org/10.2973/odp.tn.29.2000**

Neuendorf, K.K.E., Mehl, J.P., Jr., and Jackson, J.A., 2005. *Glossary of Geology* (5th edition, revised): Alexandria, VA (American Geological Institute).

Ogg, J.G., Ogg, G., and Gradstein, F.M., 2016. *A Concise Geologic Time Scale 2016:* Boston (Elsevier).

Okada, H., and Bukry, D., 1980. Supplementary modification and introduction of code numbers to the low-latitude coccolith biostratigraphic zonation (Bukry, 1973; 1975). *Marine Micropaleontology,* 5:321–325. **https://doi.org/10.1016/0377-8398(80)90016-X**

Passchier, C.W., and Trouw, R.A.J., 2005. *Microtectonics* (2nd edition): Berlin (Springer).

Perch-Nielsen, K., 1985. Cenozoic calcareous nannofossils. *In* Bolli, H.M., Saunders, J.B., and Perch-Nielsen, K. (Eds.), *Plankton Stratigraphy:* Cambridge, United Kingdom (Cambridge University Press), 427–554.

Peron-Pinvidic, G., Manatschal, G., and Osmundsen, P.T., 2013. Structural comparison of archetypal Atlantic rifted margins: a review of observations and concepts. *Marine and Petroleum Geology,* 43:21–47. **https://doi.org/10.1016/j.marpetgeo.2013.02.002**

Pinto, M.J., and McWilliams, M., 1990. Drilling-induced isothermal remanent magnetization. *Geophysics,* 55(1):111–115. **https://doi.org/10.1190/1.1442765**

Pribnow, D., Kinoshita, M., and Stein, C., 2000. *Thermal Data Collection and Heat Flow Recalculations for Ocean Drilling Program Legs 101–180:* Hanover, Germany (Institute for Joint Geoscientific Research, Institut für Geowissenschaftliche Gemeinschaftsaufgaben [GGA]). **http://www-odp.tamu.edu/publications/heatflow/ODPReprt.pdf**

Puchelt, H., Prichard, H.M., Berner, Z., and Maynard, J., 1996. Sulfide mineralogy, sulfur content, and sulfur isotope composition of mafic and ultramafic rocks from Leg 147. *In* Mével, C., Gillis, K.M., Allan, J.F., and Meyer, P.S. (Eds.), *Proceedings of the Ocean Drilling Program, Scientific Results,* 147: College Station, TX (Ocean Drilling Program), 91–101. **https://doi.org/10.2973/odp.proc.sr.147.005.1996**

Quintin, L.L., Faul, K.L., Lear, C., Graham, D., Peng, C., Murray, R.W., and Shipboard Scientific Party, 2002. Geochemical analysis of bulk marine sediment by inductively coupled plasma–atomic emission spectroscopy on board the *JOIDES Resolution. In* Lyle, M., Wilson, P.A., Janecek, T.R., et al., *Proceedings of the Ocean Drilling Program, Initial Reports,* 199: College Station, TX (Ocean Drilling Program), 1–14. **https://doi.org/10.2973/odp.proc.ir.199.107.2002**

Raffi, I., Backman, J., Fornaciari, E., Pälike, H., Rio, D., Lourens, L., and Hilgen, F., 2006. A review of calcareous nannofossil astrobiochronology encompassing the past 25 million years. *Quaternary Science Reviews,* 25(23–24):3113–3137. **https://doi.org/10.1016/j.quascirev.2006.07.007**

Reagan, M.K., Pearce, J.A., Petronotis, K., Almeev, R., Avery, A.A., Carvallo, C., Chapman, T., Christeson, G.L., Ferré, E.C., Godard, M., Heaton, D.E., Kirchenbaur, M., Kurz, W., Kutterolf, S., Li, H.Y., Li, Y., Michibayashi, K., Morgan, S., Nelson, W.R., Prytulak, J., Python, M., Robertson, A.H.F., Ryan, J.G., Sager, W.W., Sakuyama, T., Shervais, J.W., Shimizu, K., and Whattam, S.A., 2015. Expedition 352 methods. *In* Reagan, M.K., Pearce, J.A., Petronotis, K., and the Expedition 352 Scientists, *Izu-Bonin-Mariana Fore Arc.* Proceedings of the International Ocean Discovery Program, 352: College Station, TX (International Ocean Discovery Program). **https://doi.org/10.14379/iodp.proc.352.102.2015**

Richter, C., Acton, G., Endris, C., and Radsted, M., 2007. *Technical Note 34: Handbook for Shipboard Paleomagnetists.* Ocean Drilling Program. **https://doi.org/10.2973/odp.tn.34.2007**

Rider, M.H., 1996. *The Geological Interpretation of Well Logs* (2nd edition): Caithness, Scotland (Whittles Publishing).

Rothwell, R.G., 1989. *Minerals and Mineraloids in Marine Sediments: An Optical Identification Guide:* London (Elsevier). **https://doi.org/10.1007/978-94-009-1133-8**

Ryan, J.G., Shervais, J.W., Li, Y., Reagan, M.K., Li, H.Y., Heaton, D., Godard, M., Kirchenbauer, M., Whattam, S.A., Pearce, J.A., Chapman, T., Nelson, W., Prytulak, J., Shimizu, K., Petronotis, K., and the IODP Expedition 352 Scientific Team, 2017. Application of a handheld X-ray fluorescence spectrometer for real-time, high-density quantitative analysis of drilled igneous rocks and sediments during IODP Expedition 352. *Chemical Geology,* 451:55–66. **https://doi.org/10.1016/j.chemgeo.2017.01.007**

Salimullah, A.R.M., and Stow, D.A.V., 1992. Application of FMS images in poorly recovered coring intervals: examples from ODP Leg 129. *In* Hurst, A., Griffiths, C.M., and Worthington, P.F. (Eds.), *Geological Application of Wireline Logs II.* Geological Society Special Publication, 65(1):71–86. **https://doi.org/10.1144/GSL.SP.1992.065.01.06**

Samtleben, C., 1980. Die Evolution der Coccolithophoriden-Gattung *Gephyrocapsa* nach Befunden im Atlantik. *Paläontologische Zeitschrift,* 54(1–2):91–127. **https://doi.org/10.1007/BF02985885**

Scherer, R.P., Bohaty, S.M., and Harwood, D.M., 2000. Oligocene and lower Miocene siliceous microfossil biostratigraphy of Cape Roberts Project core CRP-2/2A, Victoria Land Basin, Antarctica. *Terra Antartica,* 7(4):417–442.

Scherer, R.P., Gladenkov, A.Y., and Barron, J.A., 2007. Methods and applications of Cenozoic marine diatom biostratigraphy. *In* Starratt, S.W. (Ed.), *Pond Scum to Carbon Sink: Geological and Environmental Applications of the Diatoms.* Paleontological Society Papers, 13:61–83.

Schlumberger, 1989. *Log Interpretation Principles/Applications:* Houston (Schlumberger Education Services), SMP–7017.

Scherer, R.P., and Koç, N., 1996. Late Paleogene diatom biostratigraphy and paleoenvironments of the northern Norwegian-Greenland Sea. *In* Thiede, J., Myhre, A.M., Firth, J.V., Johnson, G.L., and Ruddiman, W.F. (Eds.), *Proceedings of the Ocean Drilling Program, Scientific Results,* 151: College Station, TX (Ocean Drilling Program), 75–99. **https://doi.org/10.2973/odp.proc.sr.151.155.1996**

Schlumberger, 1994. *IPL Integrated Porosity Lithology:* Houston (Schlumberger Education Services), SMP-9270.

Schmid, R., Fettes, D., Harte, B., Davis, E., Desmons, J., Meyer-Marsilius, H.J., and Siivola, J., 2004. A systematic nomenclature for metamorphic rocks: 1. How to name a metamorphic rock. Recommendations by the IUGS Subcommission on the Systematics of Metamorphic Rocks. *Recommendations,* web version of 2004.

Schrader, H.-J., 1974. Cenozoic marine planktonic diatom stratigraphy of the tropical Indian Ocean. *In* Fisher, R.L., Bunce, E.T., et al., *Initial Reports of the Deep Sea Drilling Project,* 24: Washington, DC (U.S. Government Printing Office), 887–967. **https://doi.org/10.2973/dsdp.proc.24.122.1974**

Scotese, C.R., 2014a. Atlas of Neogene Paleogeographic Maps (Mollweide Projection), Maps 1–7, Volume 1, The Cenozoic, PALEOMAP Atlas for ArcGIS, PALEOMAP Project, Evanston, IL. **https://www.academia.edu/11082185/Atlas_of_Neogene_Paleogeographic_Maps**

Scotese, C.R., 2014b. Atlas of Paleogene Paleogeographic Maps (Mollweide Projection), Maps 8–15, Volume 1, The Cenozoic, PALEOMAP Atlas for ArcGIS, PALEOMAP Project, Evanston, IL. **https://www.academia.edu/11099001/Atlas_of_Paleogene_Paleogeographic_Maps**

Serra, O., 1984. *Fundamentals of Well-Log Interpretation* (Volume 1): *The Acquisition of Logging Data:* Amsterdam (Elsevier).

Serra, O., 1986. *Fundamentals of Well-Log Interpretation* (Volume 2): *The Interpretation of Logging Data:* Amsterdam (Elsevier).

Serra, O., 1989. *Formation MicroScanner Image Interpretation:* Houston (Schlumberger Education Services), SMP-7028.

Shepard, F.P., 1954. Nomenclature based on sand-silt-clay ratios. *Journal of Sedimentary Research,* 24(3):151–158. **https://doi.org/10.1306/D4269774-2B26-11D7-8648000102C1865D**

Shi, H., He, M., and Zhang, L., 2014. Hydrocarbon geology, accumulation pattern and the next exploration strategy in the eastern Pearl River Mouth basin. *China Offshore Oil and Gas,* 26(3):11–22. (in Chinese with English abstracts)

Shipboard Scientific Party, 1993. Explanatory notes. *In* Alt, J.C., Kinoshita, H., Stokking, L.B., et al., *Proceedings of the Ocean Drilling Program, Initial Reports,* 148: College Station, TX (Ocean Drilling Program), 5–24. **https://doi.org/10.2973/odp.proc.ir.148.101.1993**

Shipboard Scientific Party, 2002. Explanatory notes. *In* Tarduno, J.A., Duncan, R.A., Scholl, D.W., et al., *Proceedings of the Ocean Drilling Program, Initial Reports,* 197: College Station, TX (Ocean Drilling Program), 1–89. **https://doi.org/10.2973/odp.proc.ir.197.102.2002**

Shipboard Scientific Party, 2003. Explanatory notes. *In* Wilson, D.S., Teagle, D.A.H., Acton, G.D. et al., *Proceedings of the Ocean Drilling Program, Initial Reports,* 206: College Station, TX (Ocean Drilling Program), 1–94. **https://doi.org/10.2973/odp.proc.ir.206.102.2003**

Shipboard Scientific Party, 2004a. Explanatory notes. *In* Kelemen, P.B., Kikawa, E., Miller, D.J., et al., *Proceedings of the Ocean Drilling Program, Initial Reports,* 209: College Station, TX (Ocean Drilling Program), 1–75. **https://doi.org/10.2973/odp.proc.ir.209.102.2004**

Shipboard Scientific Party, 2004b. Explanatory notes. *In* Tucholke, B.E., Sibuet, J.-C., Klaus, A., et al., *Proceedings of the Ocean Drilling Program, Initial Reports,* 210: College Station, TX (Ocean Drilling Program), 1–69. **https://doi.org/10.2973/odp.proc.ir.210.102.2004**

Stock, J.M., Sun, Z., Klaus, A., Larsen, H.C., Jian, Z., Alvarez Zarikian, C.A., Boaga, J., Bowden, S.A., Briais, A., Chen, Y., Cukur, D., Dadd, K.A., Ding, W., Dorais, M.J., Ferré, E.C., Ferreira, F., Furusawa, A., Gewecke, A.J., Hinojosa, J.L., Höfig, T.W., Hsiung, K.-H., Huang, B., Huang, E., Huang, X.-L., Jiang, S., Jin, H., Johnson, B.G., Kurzawski, R.M., Lei, C., Li, B., Li, L., Li, Y., Lin, J., Liu, C., Liu, Z., Luna, A., Lupi, C., McCarthy, A.J., Mohn, G., Ningthoujam, L.S., Nirrengarten, M., Osono, N., Peate, D.W., Persaud, P., Qui, N., Robinson, C.M., Satolli, S., Sauermilch, I., Schindlbeck, J.C., Skinner, S.M., Straub, S.M., Su, X., Tian, L., van der Zwan, F.M., Wan, S., Wu, H., Xiang, R., Yadav, R., Yi, L., Zhang, C., Zhang, J., Zhang, Y., Zhao, N., Zhong, G., and Zhong, L., 2018. Site U1500. *In* Sun, Z., Jian, Z. Stock, J.M., Larsen, H.C., Klaus, A., Alvarez Zarikian, C.A., and the Expedition 367/368 Scientists, 2018. *South China Sea Rifted Margin.* Proceedings of the International Ocean Discovery Program, 367/368: College Station, TX (International Ocean Discovery Program). **https://doi.org/10.14379/iodp.proc.367368.104.2018**

Stow, D.A.V., 2005. *Sedimentary Rocks in the Field: A Colour Guide:* London (Manson Publishing)

Su, X., 1996. Development of late Tertiary and Quaternary coccolith assemblages in the northeast Atlantic. *GEOMAR Report,* 48. **https://doi.org/10.3289/GEOMAR_Report_48_1996**

Tamura, Y., Busby, C.J., Blum, P., Guèrin, G., Andrews, G.D.M., Barker, A.K., Berger, J.L.R., Bongiolo, E.M., Bordiga, M., DeBari, S.M., Gill, J.B., Hamelin, C., Jia, J., John, E.H., Jonas, A.-S., Jutzeler, M., Kars, M.A.C., Kita, Z.A., Konrad, K., Mahony, S.H., Martini, M., Miyazaki, T., Musgrave, R.J., Nascimento, D.B., Nichols, A.R.L., Ribeiro, J.M., Sato, T., Schindlbeck, J.C., Schmitt, A.K., Straub, S.M., Vautravers, M.J., and Yang, Y., 2015. Expedition 350 summary. *In* Tamura, Y., Busby, C.J., Blum, P., and the Expedition 350 Scientists, *Izu-Bonin-Mariana Rear Arc.* Proceedings of the International Ocean Discovery Program, 350: College Station, TX (International Ocean Discovery Program). **https://doi.org/10.14379/iodp.proc.350.101.2015**

Thompson, P.R., Bé, A.W.H., Duplessy, J.-C., and Shackleton, N.J., 1979. Disappearance of pink-pigmented *Globigerinoides ruber* at 120,000 yr BP in the Indian and Pacific Oceans. *Nature,* 280(5723):554–558. **https://doi.org/10.1038/280554a0**

Tugend, J., Manatschal, G., Kusznir, N.J., and Masini, E., 2015. Characterizing and identifying structural domains at rifted continental margins: application to the Bay of Biscay margins and its Western Pyrenean fossil remnants. *In* Gibson, G.M., Roure, F., and Manatschal, G. (Eds.), *Sedimentary Basins and Crustal Processes at Continental Margins: From Modern Hyper-extended Margins to Deformed Ancient Analogues*. Geological Society Special Publication, 413:171–203. **https://doi.org/10.1144/SP413.3**

Vacquier, V., 1985. The measurement of thermal conductivity of solids with a transient linear heat source on the plane surface of a poorly conducting body. *Earth and Planetary Science Letters,* 74(2–3):275–279. **https://doi.org/10.1016/0012-821X(85)90027-5**

Vail, P.R., Mitchum, R.M., Jr., Todd, R.G., Widmier, J.M., Thompson, S.I., Sangree, J.B., Bubb, J.N., and Hatlelid, W.G., 1977. Seismic stratigraphy and global changes of sea level, Parts 1–11. *In* Payton, C.E. (Ed.), *Seismic Stratigraphy: Applications to Hydrocarbon Exploration.* AAPG Memoir, 26:51–212.

van Morkhoven, F.P.C.M., Berggren, W.A., Edwards, A.S.,and Oertli, H.J., 1986. Cenozoic cosmopolitan deep-water benthic foraminifera. *Bulletin des Centres de Recherches Exploration-Production Elf-Aquitaine,* 11.

Vandenberghe, N., Hilgen, F.J., and Speijer, R.P., 2012. The Paleogene period. With contributions by J.G. Ogg, F.M. Gradstein, O. Hammer, C.J. Hollis, and J.J. Hooker. *In* Gradstein, F.M., Ogg, J.G., Schmitz, M.D., and Ogg, G.M. (Eds.), *The Geological Time Scale 2012:* Amsterdam (Elsevier), 855–921. **https://doi.org/10.1016/B978-0-444-59425-9.00028-7**

Vasiliev, M.A., Blum, P., Chubarian, G., Olsen, R., Bennight, C., Cobine, T., Fackler, D., Hastedt, M., Houpt, D., Mateo, Z., and Vasilieva, Y.B., 2011. A new natural gamma radiation measurement system for marine sediment and rock analysis. *Journal of Applied Geophysics,* 75:455–463. **https://doi.org/10.1016/j.jappgeo.2011.08.008**

Von Herzen, R., and Maxwell, A.E., 1959. The measurement of thermal conductivity of deep-sea sediments by a needle-probe method. *Journal of Geophysical Research,* 64(10):1557–1563. **https://doi.org/10.1029/JZ064i010p01557**

Wade, B.S., Pearson, P.N., Berggren, W.A., and Pälike, H., 2011. Review and revision of Cenozoic tropical planktonic foraminiferal biostratigraphy and calibration to the geomagnetic polarity and astronomical time scale. *Earth-Science Reviews,* 104(1–3):111–142. **https://doi.org/10.1016/j.earscirev.2010.09.003**

Wentworth, C.K., 1922. A scale of grade and class terms for clastic sediments. *Journal of Geology,* 30(5):377–392. **https://doi.org/10.1086/622910**

Westerhold, T., Röhl, U., Frederichs, T., Bohaty, S.M., and Zachos, J.C., 2015. Astronomical calibration of the geological timescale: closing the middle Eocene gap. *Climate of the Past,* 11:1181–1195. **https://doi.org/10.5194/cp-11-1181-2015**

Yanagisawa, Y., and Akiba, F., 1998. Refined Neogene diatom biostratigraphy for the northwest Pacific around Japan, with an introduction of code numbers for selected diatom biohorizons. *Chishitsugaku Zasshi,* 104(6):395–414. **http://dx.doi.org/10.5575/geosoc.104.395**

Yang, H., Chen, D., and Wang, J., 1990. Eocene ostracoda from the southwestern continental shelf basin of the East China Sea. *Acta Micropaleontologica Sinica,* 7(4):367–388. **http://caod.oriprobe.com/articles/35018830/dong_hai_lu_jia_pen_di_xi_nan_bu_shi_xin_shi_hai_xiang_jie_xing_lei_.htm**

Young, J.R., 1998. Neogene. *In* Bown, P.R. (Ed.), *Calcareous Nannofossil Biostratigraphy:* Dordrecht, The Netherlands (Kluwer Academic Publishing), 225–265.

Young, J.R., Bown, P.R., and Lees, J.A. (Eds.). Nannotax3. **http://ina.tmsoc.org/Nannotax3** (accessed 24 September 2014).

Zhao, Q., Whatley, R., and Zhou, B., 2000. The taxonomy and distribution of recent species of the ostracod genus *Cytheropteron* in the South China Sea. *Revista Espanola de Micropaleontologia,* 32(2):259–281.

Zhao, Q., 2005. Late Cainozoic ostracod faunas and paleoenvironmental changes at ODP Site 1148, South China Sea. *In* Wang, P., and Lipps, J. (Eds.), *Marine Micropaleonotology of the South China Sea.* Marine Micropaleontology, 54(1–2):27–47. **https://doi.org/10.1016/j.marmicro.2004.09.002**

Zijderveld, J.D.A., 1967. AC demagnetization of rocks: analysis of results. *In* Collinson, D.W., Creer, K.M., and Runcorn, S.K. (Eds.), *Methods in Palaeomagnetism:* Amsterdam (Elsevier), 254–286.

Sun, Z., Jian, Z., Stock, J.M., Larsen, H.C., Klaus, A., Alvarez Zarikian, C.A., and the Expedition 367/368 Scientists
Proceedings of the International Ocean Discovery Program Volume 367/368
publications.iodp.org

https://doi.org/10.14379/iodp.proc.367368.103.2018

Site U1499[1]

Check for updates

Zhen Sun, Joann M. Stock, Adam Klaus, Hans Christian Larsen, Zhimin Jian, Carlos A. Alvarez Zarikian, Jacopo Boaga, Stephen A. Bowden, Anne Briais, Yifeng Chen, Deniz Cukur, Kelsie A. Dadd, Weiwei Ding, Michael J. Dorais, Eric C. Ferré, Fabricio Ferreira, Akira Furusawa, Aaron J. Gewecke, Jessica L. Hinojosa, Tobias W. Höfig, Kan-Hsi Hsiung, Baoqi Huang, Enqing Huang, Xiao-Long Huang, Shijun Jiang, Haiyan Jin, Benjamin G. Johnson, Robert M. Kurzawski, Chao Lei, Baohua Li, Li Li, Yanping Li, Jian Lin, Chang Liu, Chuanlian Liu, Zhifei Liu, Antonio Luna, Claudia Lupi, Anders J. McCarthy, Geoffroy Mohn, Lachit Singh Ningthoujam, Michael Nirrengarten, Nobuaki Osono, David W. Peate, Patricia Persaud, Ning Qiu, Caroline M. Robinson, Sara Satolli, Isabel Sauermilch, Julie C. Schindlbeck, Steven M. Skinner, Susanne M. Straub, Xiang Su, Liyan Tian, Froukje M. van der Zwan, Shiming Wan, Huaichun Wu, Rong Xiang, Rajeev Yadav, Liang Yi, Cuimei Zhang, Jinchang Zhang, Yang Zhang, Ning Zhao, Guangfa Zhong, and Lifeng Zhong[2]

Keywords: International Ocean Discovery Program, IODP, *JOIDES Resolution*, Expedition 367, Expedition 368, Site U1499, northern South China Sea, continent–ocean transition zone, Ridge A, hyperextension, continental breakup, lithosphere thinning, rifting, gravel, Cenozoic, red clay, manganese nodules, turbidite

Contents

1 Site summary
4 Background and objectives
8 Operations
13 Lithostratigraphy
27 Structural geology
30 Biostratigraphy
35 Paleomagnetism
39 Geochemistry
44 Physical properties
48 Downhole measurements
54 Correlation to seismic data
59 References

Site summary

International Ocean Discovery (IODP) Expedition 367 Site U1499 (proposed Site SCSII-14A; Sun et al., 2016) is located on basement Ridge A within the South China Sea (SCS) continent–ocean transition (COT) zone ~60 km seaward and southeast of the outer margin high. The goal of drilling here was to core through the sediment to sample the basement rocks and thus determine basement age and lithology, which would provide a test of different possible models for the processes and rheology controlling the extension and ultimate breakup of the continent. Ridge A was expected to have basement of either upper continental crust, lower continental crust, or exhumed mantle rocks. Coring and drilling also constrain the postrift history by determining the age, water depth, and subsidence rates of the overlying sedimentary packages.

We conducted operations in two holes at Site U1499. Hole U1499A is located at 18°24.5698′N, 115°51.5881′E in a water depth of 3760.2 m. In Hole U1499A, advance piston corer/extended core barrel (APC/XCB) coring penetrated from the seafloor to 659.2 m and recovered 417.05 m (63%). Hole U1499B is located at 18°24.5705′N, 115°51.5990′E in a water depth of 3758.1 m. We installed casing in Hole U1499B to 651 m followed by rotary core barrel (RCB) coring that penetrated from 655.0 to 1081.8 m and recovered 150.64 m (35%). Coring terminated in gravel before deteriorating drilling conditions prevented further penetration; no crystalline basement was encountered. Despite challenging conditions in the lowermost part of Hole U1499B, two successful wireline logging runs were conducted from 652 to 1020 m.

Lithostratigraphy

The cored sediment at Site U1499 is divided into nine lithostratigraphic units (Figure **F8**). Lithostratigraphic Unit I is a 48.85 m thick middle–upper Pleistocene sequence of dark greenish gray bioclast-rich clay with thin clayey silt and sand interbeds. Fining-upward silt and fine sand intervals are abundant and interpreted as turbidite sequences. Four thin (2–7 cm) ash layers were identified in

[1] Sun, Z., Stock, J.M., Klaus, A., Larsen, H.C., Jian, Z., Alvarez Zarikian, C.A., Boaga, J., Bowden, S.A., Briais, A., Chen, Y., Cukur, D., Dadd, K.A., Ding, W., Dorais, M.J., Ferré, E.C., Ferreira, F., Furusawa, A., Gewecke, A.J., Hinojosa, J.L., Höfig, T.W., Hsiung, K.-H., Huang, B., Huang, E., Huang, X.-L., Jiang, S., Jin, H., Johnson, B.G., Kurzawski, R.M., Lei, C., Li, B., Li, L., Li, Y., Lin, J., Liu, C., Liu, C., Liu, Z., Luna, A., Lupi, C., McCarthy, A.J., Mohn, G., Ningthoujam, L.S., Nirrengarten, M., Osono, N., Peate, D.W., Persaud, P., Qui, N., Robinson, C.M., Satolli, S., Sauermilch, I., Schindlbeck, J.C., Skinner, S.M., Straub, S.M., Su, X., Tian, L., van der Zwan, F.M., Wan, S., Wu, H., Xiang, R., Yadav, R., Yi, L., Zhang, C., Zhang, J., Zhang, Y., Zhao, N., Zhong, G., and Zhong, L., 2018. Site U1499. *In* Sun, Z., Jian, Z., Stock, J.M., Larsen, H.C., Klaus, A., Alvarez Zarikian, C.A., and the Expedition 367/368 Scientists, *South China Sea Rifted Margin*. Proceedings of the International Ocean Discovery Program, 367/368: College Station, TX (International Ocean Discovery Program). https://doi.org/10.14379/iodp.proc.367368.103.2018

[2] **Expedition 367/368 Scientists' addresses.**

MS 367368-103: Published 28 September 2018

This work is distributed under the **Creative Commons Attribution 4.0 International** (CC BY 4.0) license.

Unit I; none were observed in the deeper units. Unit II (48.85–100.04 m) is a 51.19 m thick middle–upper Pleistocene sequence of interbedded greenish gray clay-rich calcareous ooze and dark greenish gray nannofossil-rich clay. Synsedimentary deformational structures such as folds, microfaults, and inclined beds are well developed in the sediment of this unit, which is interpreted as a slump deposit. This unit is underlain by Unit III (Pliocene–middle Pleistocene), which is divided into Subunits IIIA (100.04–181.80 m) and IIIB (181.80–333.65 m). The 233.61 m of Unit III is dominated by dark greenish gray clay with thick to very thick clayey silt and calcareous sand interlaminations. Subunit IIIA contains clayey silt layers that are thick laminations (<1 cm), whereas Subunit IIIB has abundant thin beds (2–5 cm) of clayey silt and an overall increase in nannofossil and foraminifer content. Unit IV (333.65–404.90 m) is a 71.25 m thick sequence of upper Miocene–Pliocene dark greenish gray silty sand with clay interbeds. Recovery is very low throughout this unit, but the recovered intervals and physical property data suggest that the sections with no recovery may contain unconsolidated to weakly consolidated sand.

Unit V (404.90–469.45 m) is a 64.55 m thick sequence of upper Miocene dark greenish gray clay with mostly thin (<5 cm) clayey silt and foraminifer sand interbeds. Drilling disturbance in the form of biscuiting increases significantly in this unit. Similar to Unit IV, recovery in Unit VI (469.45–618.30 m) is very low. The recovered intervals in this unit include upper Miocene dark greenish gray silty sand with clay interbeds. Unit VII (618.30–761.70 m) is mainly composed of upper Miocene dark greenish gray to dark gray sandstone and claystone with siltstone interbeds. Lithification increases sharply downhole from the top of this unit, although sections with no recovery are inferred to be nonlithified sand. Unit VIII (761.70–929.02 m) comprises a 167.32 m thick interval of upper Oligocene–Miocene reddish brown to reddish gray claystone and clay-rich chalk. Based on the abundance of calcareous material, this unit is divided into two subunits. Subunit VIIIA (761.70–892.10 m) contains lower–upper Miocene dark reddish brown claystone with siltstone and foraminifer sandstone interbeds, whereas Subunit VIIIB (892.10–929.02 m) is composed of upper Oligocene–lower Miocene reddish brown to reddish gray clay-rich nannofossil chalk and clay-rich chalk. In the lowest part of Subunit VIIIB, abundant brownish black iron-manganese nodules occur within reddish brown nannofossil-rich claystone.

Unit IX (929.02–1081.80 m) is readily distinguished from the overlying units by containing Oligocene (and pre-Oligocene?) sandstone, claystone, matrix-supported breccia, and gravel. This unit is 152.78 m thick and comprises three subunits. Subunit IXA (929.02–933.28 m) is defined by dark brown and greenish gray sandstone and breccia. Subunit IXB (933.28–933.35 m) is defined by dark gray matrix-supported breccia in Core 367-U1499B-30R. Subunit IXC (933.35–1081.80 m) contains gray to dark gray gravel with silty sand intervals. The cores in Subunit IXC are completely fragmented and were recovered as pebbles and cobbles. In general, the pebbles and cobbles are recycled sedimentary rocks (such as sandstone) that contain a variety of individual lithic components including igneous, sedimentary, and metamorphic clasts. Although the matrix that likely surrounded these cobbles and pebbles was not recovered, we infer that the matrix is poorly consolidated and washed away by the drilling process. Based on this description, Subunit IXC may represent synrift or prerift sediments.

Structural geology

The tilting of sedimentary beds and deformation structures observed at Site U1499 are limited to lithostratigraphic Units II, VII, VIII, and IX. The folds, faults, and tilted beds observed in Unit II are related to two slump events that reworked older sediment between younger Units I and III. Tilted beds and faults with slickensides were observed in Units VII and VIII. These faults are linked to compaction processes of the clays, and the tilted beds are associated with sandy layers. Unit IX is divided into three subunits. In Subunit IXA, tilted beds and a downhole increase in clast size, angularity, and proportion of clasts were observed. The matrix-supported breccia of Subunit IXB exhibits no clear deformation structure or tilted sedimentary bedding. Some of the sandstone and breccia clasts in Subunit IXC exhibit veins and fractures. These clasts were transported before sedimentation; therefore, their veins and fractures must have originated in a previous tectonic event.

Biostratigraphy

All core catcher samples at Site U1499 were analyzed for calcareous nannofossil and foraminiferal content, and additional samples were taken from the split-core sections when necessary to refine the ages. Preservation of microfossils varies from poor to very good, and total abundance varies from barren to abundant. Although samples exhibit some degree of reworking, 28 biostratigraphic datums are recognized, revealing that we recovered an apparently continuous succession of the Oligocene to the Pleistocene spanning nannofossil Zones NP25–NN21 and foraminifer Zones M4/M3 to Subzone PT1b. The Pleistocene/Pliocene boundary is located between Cores 367-U1499A-20X and 27X, the Pliocene/Miocene boundary is located between Cores 31X and 43X, and the Miocene/Oligocene boundary is in Section 367-U1499A-30R-2. Sedimentation rates varied from ~80 mm/ky in the late Miocene–early Pliocene and ~50 mm/ky in the early Pliocene–early Pleistocene to ~130 mm/ky in the middle–late Pleistocene. Extremely low sedimentation rates (~8 mm/ky) occurred in the early–middle Miocene during deposition of Unit VIII. Subunit IXA contains early–late Oligocene microfossils (calcareous nannofossils and foraminifers) with different preservation and abundance, probably influenced by transported and reworked materials.

Paleomagnetism

Paleomagnetic analysis was conducted on both archive-half sections and discrete samples from the working half. The archive-half sections were measured with the pass-through superconducting rock magnetometer (SRM) with demagnetization steps at 5, 15, and 25 mT. The discrete samples were subjected to alternating field (AF) and thermal demagnetization, and remanence was measured on the spinner magnetometer. We adopted a combination of stepwise AF and thermal demagnetization steps to fully demagnetize the discrete samples and obtain the characteristic remanent magnetization (ChRM).

Variations in natural remanent magnetization (NRM) intensity are well correlated to observable changes in lithology and magnetic susceptibility; for example, the low NRM intensity at ~60 m (Core 367-U1499A-7H) agrees with the carbonate-rich slump in which magnetic susceptibility values are also low. Drilling-induced remanence was identified and removed in most core sections at AF treatments of 15 mT. In addition, magnetic mineral variations were observed from the demagnetization behavior. From Core 367-U1499B-12R downhole, the drilling overprint becomes stronger and hard to remove with the relatively low AF steps used on the archive-half sections, whereas AF treatments up to 200 mT and temperatures up to 675°C could not fully demagnetize the discrete samples. These characteristics confirm the presence of higher coercivity magnetic minerals, such as hematite, compared with the pre-

dominant magnetite and/or titanomagnetite. But further rock magnetic property measurements should be conducted in a shore-based lab in order to better understand the compositions.

We constructed the magnetostratigraphy of Holes U1499A and U1499B based on the interpretation of the raw paleomagnetic data that show stable and clear demagnetization behaviors. Declinations from 0 to 162 m have been corrected by the Icefield MI-5 core orientation tool and therefore could help accurately define magnetic reversals. Otherwise, only inclinations are used for polarity interpretations. After correlating the magnetostratigraphy to the standard geomagnetic timescale, we confidently identified the boundary between the Brunhes and Matuyama Chrons at ~110 m. We thus conclude that the middle/early Pleistocene boundary (0.78 Ma) is at ~110 m, the early Pleistocene/late Pliocene boundary is at ~220 m, the late/early Pliocene (3.6 Ma) boundary is at ~260 m, and early Pliocene/late Miocene boundary (5.33 Ma) is at ~370 m.

Geochemistry

Geochemical analyses were conducted for headspace gas safety monitoring; quantification of sediment $CaCO_3$, organic carbon, and nitrogen content; and interstitial water characterization. Calcium carbonate contents vary between 0.4 and 82 wt%, with higher values of >20 wt% corresponding to intervals of nannofossil/foraminifer ooze or chalk. Total organic carbon (TOC) contents mostly range from ~0 to ~ 1.0 wt%. TOC decreases gradually downhole from 1.0 to 0.3 wt% in the uppermost 110 m corresponding to the base of the sulfate reduction zone, reflecting active degradation of sedimentary organic matter. The TOC to total nitrogen molar ratio (TOC/TN) is mostly <8, indicating that TOC is derived dominantly from a marine source.

Hydrocarbon monitoring shows headspace gas consistently approaching zero throughout the site. Relatively higher methane contents of approximately tens to 6000 ppmv occur across the ~100–250 m interval, just below the sulfate reduction zone. The overall low methane content indicates limited microbial methanogenesis likely caused by low TOC contents (<0.3 wt%) deeper than 110 m.

We obtained 58 interstitial water samples from Hole U1499A. The inorganic geochemistry of interstitial water is controlled by the remineralization of organic matter and carbonate and clay diagenesis. The sediment rapidly becomes suboxic, as indicated by a Mn peak of ~120 µM at ~6 m. Sulfate reduction coupled with sedimentary organic matter degradation occurs to ~110 m, with near-complete depletion to 257 m before increasing slowly to 16.9 mM at the bottom of Hole U1499A. The interval of near-complete sulfate consumption is also marked by pronounced high Ba concentrations >50 µM, suggesting the dissolution of barite ($BaSO_4$). The peak alkalinity and steady increase in NH_4^+ and Br^- in the upper 110 m are consistent with progressive remineralization of sedimentary organic matter. The gradual decrease in Ca^{2+} shallower than 80 m suggests active authigenic carbonate precipitation triggered by sulfate reduction. A subsequent downhole increase in Ca^{2+} and Sr^{2+} is likely caused by biogenic carbonate dissolution and recrystallization. Nearly parallel downhole decreases in Mg^{2+} and K^+ are mostly driven by clay mineral cation exchange and/or clay mineral authigenesis. The lower Cl^- and Na^+ concentrations compared to those of seawater at the bottom of Hole U1499A are mostly driven by the smectite–illite transformation. Elevated Si concentrations of 700–820 µM from the seafloor to 45 m suggest active dissolution of biogenic silica.

Petrophysics

At Site U1499, measurements of *P*-wave velocity, bulk density, magnetic susceptibility, and natural gamma radiation (NGR) were made on whole-round cores, and additional measurements were made on split cores and discrete samples, including thermal conductivity; caliper *P*-wave velocity on the *P*-wave caliper (PWC); porosity; and bulk, dry, and grain density. In general, bulk density, *P*-wave velocity, and thermal conductivity increase with depth, whereas porosity decreases with depth as a result of compaction and lithification. However, some properties, such as NGR or magnetic susceptibility, show local variations related to the specific lithology. The soft sediment in the upper 100 m shows rapid compaction with depth, marked by a decrease in porosity and increase in bulk density and thermal conductivity. Four thin volcanic ash layers in the uppermost 50 m are marked by peaks in magnetic susceptibility. The mass transport deposit (48.85–100.04 m) displays low magnetic susceptibility and low NGR counts, reflecting the high carbonate content of the calcareous ooze. Below these layers downhole to ~890 m, physical properties show small variations; bulk density, *P*-wave velocity, and thermal conductivity gradually increase, whereas porosity decreases with depth. The NGR and magnetic susceptibility data in this interval do not show much variation. From 830 to 930 m, we observed a general decrease in magnetic susceptibility values and NGR counts where densities increase slightly and *P*-wave velocities increase significantly from 2200 to 2900 m/s. These variations are associated with a significant increase in the carbonate content in the Subunit VIIIB chalks. The cobbles and pebbles in the deepest part (930–1080 m) show large variations in NGR, bulk density, and *P*-wave velocity and very low magnetic susceptibility.

Downhole measurements

Two downhole logging tool strings were run in Hole U1499B, a modified triple combo (sonic velocity, NGR, bulk density, resistivity, and caliper) tool string and the Formation MicroScanner (FMS)-sonic tool string (FMS resistivity images and calipers, as well as NGR). We added the velocity tool to the first tool string because sonic velocities were needed for an accurate prediction of basement depth for the subsequent Site U1500 and to better constrain core-log-seismic correlation. We also did not know if hole conditions would allow a second logging run. Although stable borehole conditions in Hole U1499B allowed the second FMS logging run, we did not attempt a check shot due to time constraints and concerns about hole stability. Borehole conditions from the bottom of the casing at ~651 m to the bottom of Hole U1499B at ~1020 m were generally good, with measured diameters from ~10 to 16 inches. Washout zones were observed from 670 to 710 m, which corresponds to an interval of very low core recovery, as well as from 830 to 920 m, affecting quality of the log data in these intervals. Log and core data are generally in good agreement. Downhole logging provided information in zones of poor core recovery in Hole U1499B. The log data from 726 to 739 m exhibits high NGR values and low bulk densities and *P*-wave velocities, whereas the data from 820 to 840 m is characterized by a sharp increase in bulk densities, a slight increase in *P*-wave velocities, and an abrupt decrease in NGR values compared to average values above and below these depths. The Subunit VIIIB chalks (~890–930 m) display a sharp decrease in NGR and an increase in bulk density and *P*-wave velocity with

depth, as well as only small variations in resistivity. Deeper than 930 m, bulk densities, *P*-wave velocities, and resistivities show large variability, in part because of the presence of cobbles and pebbles. The quality of the acquired FMS images is strongly influenced by variations in hole diameter; they generally show alternating smooth and patchy textures with contrasting resistivity values marking horizontal to slightly tilted bedding downhole to 930 m. The deepest layers of sandstones, breccias, and gravels show highly variable and oblique textures on the FMS images, possibly reflecting the varied orientation of the gravel clasts or the presence of faults and fractures in the gravel or the matrix. In general, the velocities measured with the sonic velocity logging tool match the PWC measurements taken with the caliper on the split cores. Six in situ formation temperature measurements were made in Hole U1499A and give a geothermal gradient of 93°C/km. The estimated heat flow is 110 mW/m^2, a value in agreement with the general heat flow of the area.

Correlation to seismic data

We used downhole log data and physical property measurements on cores and samples as well as other available data to correlate Site U1499 data with the available seismic reflection profiles. We also used the Site U1499 density and sonic velocity data to create synthetic seismograms that provided additional constraints on the correlation. Log sonic velocities and PWC velocities are in very good agreement, except for the deepest breccias and gravels (deeper than ~930 m) where measurement on individual pebbles leads to an overestimate of the velocity in the formation. For seismic correlation, we use the PWC and density values from moisture and density (MAD) and gamma ray attenuation (GRA) measurements from Hole U1499A (0–655 m), whereas below that depth we used the downhole logging velocity and density data. We used a constant velocity of 2100 m/s in the low-recovery zones (333–406 and 531–561 m), interpreted to be sandy layers, based on the downhole logging velocity values measured at greater depth. The comparison of the time-depth relationship (TDR) obtained for Site U1499 to those for Ocean Drilling Program (ODP) Site 1148 and IODP Sites U1431 and U1433 shows substantial agreement, except for the Site 1148 TDR, which shows higher velocities in the deeper layers. The comparison among the seismic reflectors and the variations in physical properties and lithology characteristics using the computed Site U1499 TDR shows a good correlation between the main upper reflectors and the poor-recovery sandy intervals. However, the main physical property changes related to the top of the deep gravel layer do not correlate to the reflector observed at ~5.9 s in the seismic profile.

Background and objectives

Site U1499 (Figures **F1**, **F2**) is located on a basement high (Ridge A) clearly visible in the map of two-way traveltime (TWT) to basement (Figure **F3**) and is well imaged on seismic Line 15ecLW3 (Figure **F4**). This site is a high priority for Objectives 1–4 as listed in **Expedition objectives** in the Expedition 367/368 summary chapter (Larsen et al., 2018). Seismic Unconformity T30 (inferred to correlate to the Miocene/Pliocene boundary [Reflector Tmp]) (Li et al., 2015a) is seen at ~5.5 s TWT within the sedimentary sequence that overlies the basement target location. Seismic Unconformities T32, T40, and T60 pinch out against the basement high. Site U1499 was originally an alternate for primary proposed Site SCSII-1A. Site SCSII-1A would have penetrated these deeper reflectors but could not be used due to an undersea cable that had recently been installed close to the site's coordinates. Although Site U1499 could not sample these deeper reflectors, we did reach the interpreted top of acoustic basement (Reflector Tg) at a shallower depth.

The primary objective at Site U1499 was to sample basement in a region of the COT where the basement composition is not known so that rifting models could be constrained. Basement at Site U1499 could have been upper or lower continental crust, exhumed mantle (serpentinized or not), or, less likely, igneous oceanic rock (e.g., basalt and gabbro). The model in Figure **F5** shows the basement at Site U1499 as possibly corresponding to serpentinized lithospheric mantle, but it could also be lower continental crust or upper continental crust, depending on the rheological differences among these various units during the rifting process. Figure **F6** shows that there is a broad spectrum of possible magma-poor rifted-margin structures that may form, depending on the initial rheologic structure of the extending lithosphere.

We expected the upper sedimentary section shallower than Unconformity T30 to be deep-marine clay, silt, or fine-grained sand based on Site 1148 data (e.g., Shipboard Scientific Party, 2000; Clift et al., 2001) and seismic stratigraphic correlation. Sediments below Unconformity T30 and above the basement reflection appear to have more sandy layers or thin interlayered sand and clay (Figure **F4**). On the seismic cross Line 04ec1530, some channel-like reflections are associated with the inferred sandy layers. However, the na-

Figure F1. Seismic data coverage and magnetic anomalies of the SCS Basin, Expedition 367/368. Black lines = ocean-bottom seismometer refraction data. Other seismic lines are mostly multichannel seismic reflection data. White stars = Expedition 367/368 sites, red squares = Leg 184 sites, red circles = Expedition 349 sites. For more detail, see Figure F2.

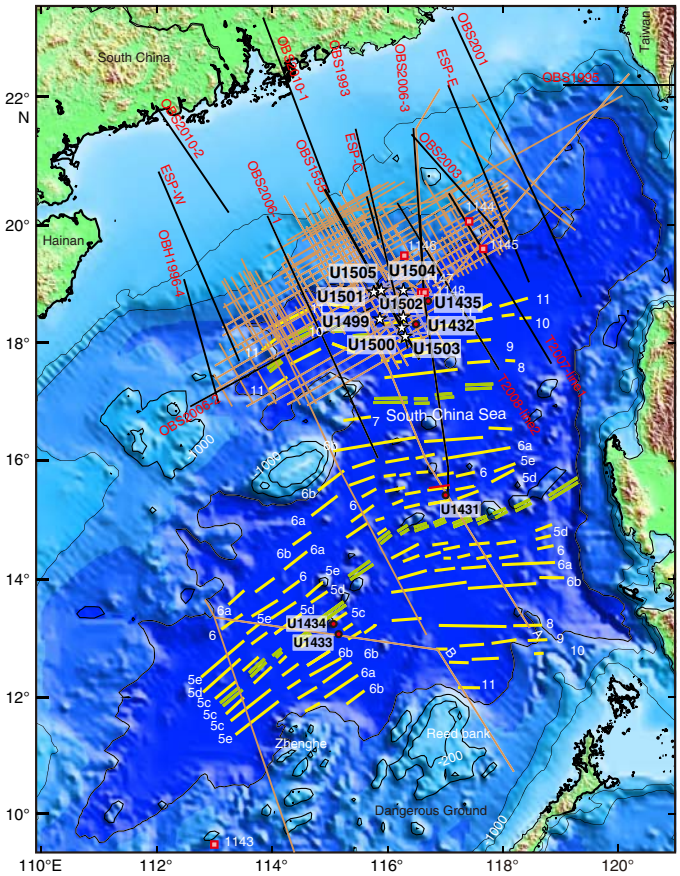

Figure F2. Bathymetric maps showing Expedition 367/368 sites (stars), and (A) regional and (B) local coverage of multichannel seismic reflection data and OBS data. Thick blue and red lines are key seismic lines used for planning of the drilling transect. A. Magnetic isochrons (orange lines) from Briais et al. (1993). B. Magnetic picks (orange squares) from the same reference, extracted from the Seton et al. (2014) compilation. Chron labels for the picks correspond to the old edge of the normal polarity intervals (see Ogg et al. [2016] timescale for ages). Orange square = Leg 184 Site 1148, yellow squares = Expedition 349 Sites U1432 and U1435.

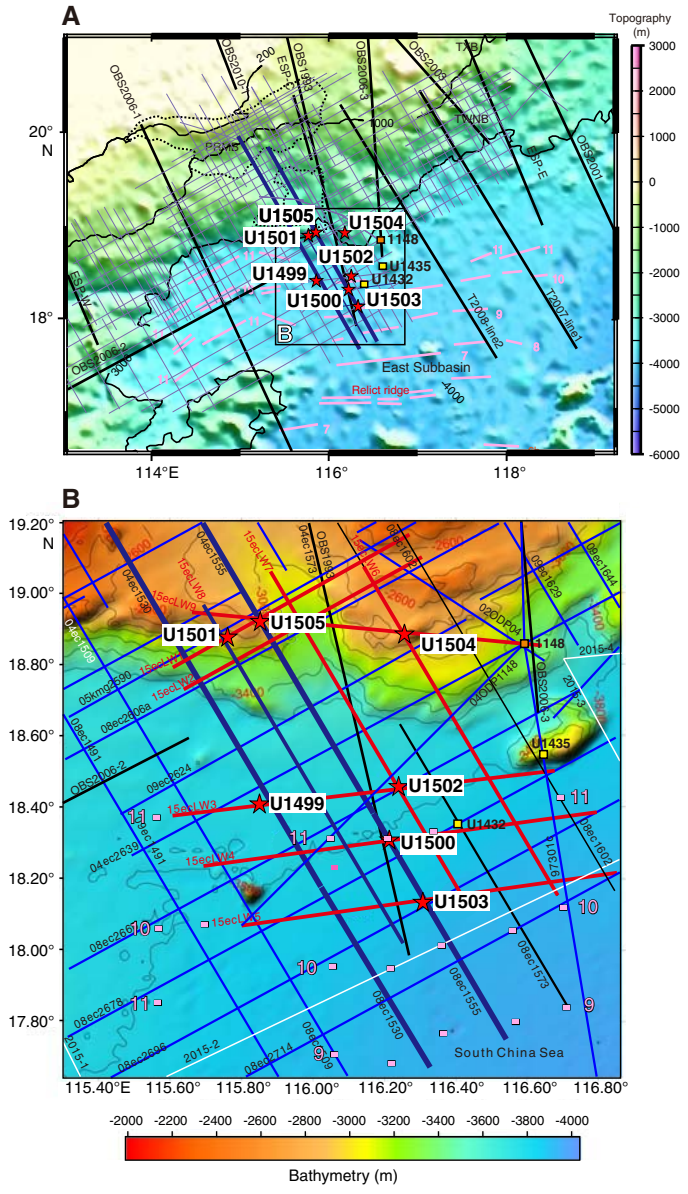

ture of the lower sedimentary section, including Paleogene synrift and possible prerift strata, is poorly constrained and may be shallow- to deep-marine rocks. Recovery of core from the lower synrift sedimentary section is important here because this constrains the timing and depositional environment of final breakup as well as the subsidence history.

Figure F3. Two-way traveltime to (A) acoustic basement (Tg reflector) and (B) Unconformity T60 and location of Expedition 367/368 sites. Proposed drilling transect (thick black line) was located approximately at the center of a margin segment bounded to the southwest by a transform fault. Northeastern boundary of margin segment is located around Expedition 349 Site U1435. In this location, the outer margin high and Ridge A seem to coalesce, and Ridges B and C of the COT become indistinct toward the northeast within the next margin segment. Note that outer margin high is slightly east-northeast to the more parallel Ridges A, B, and C.

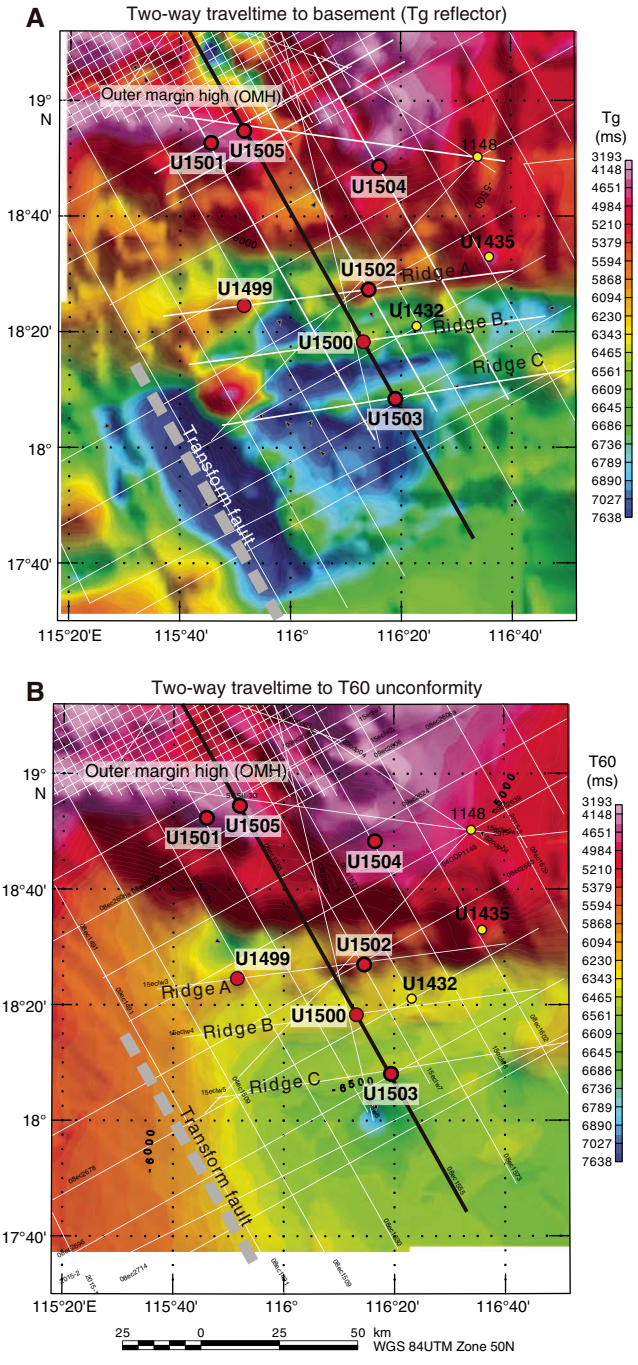

Figure F4. Original and interpreted seismic profiles across Site U1499. Seismic profile locations are shown in Figures F1, F2, and F3. Site U1499 is located on seismic Profile 15ecLW3 and projected onto seismic Profile 04ec1530. Red text and tick marks = locations of crossing seismic lines. CDP = common depth point. All seismic profiles are courtesy of the Chinese National Offshore Oil Corporation [CNOOC]).

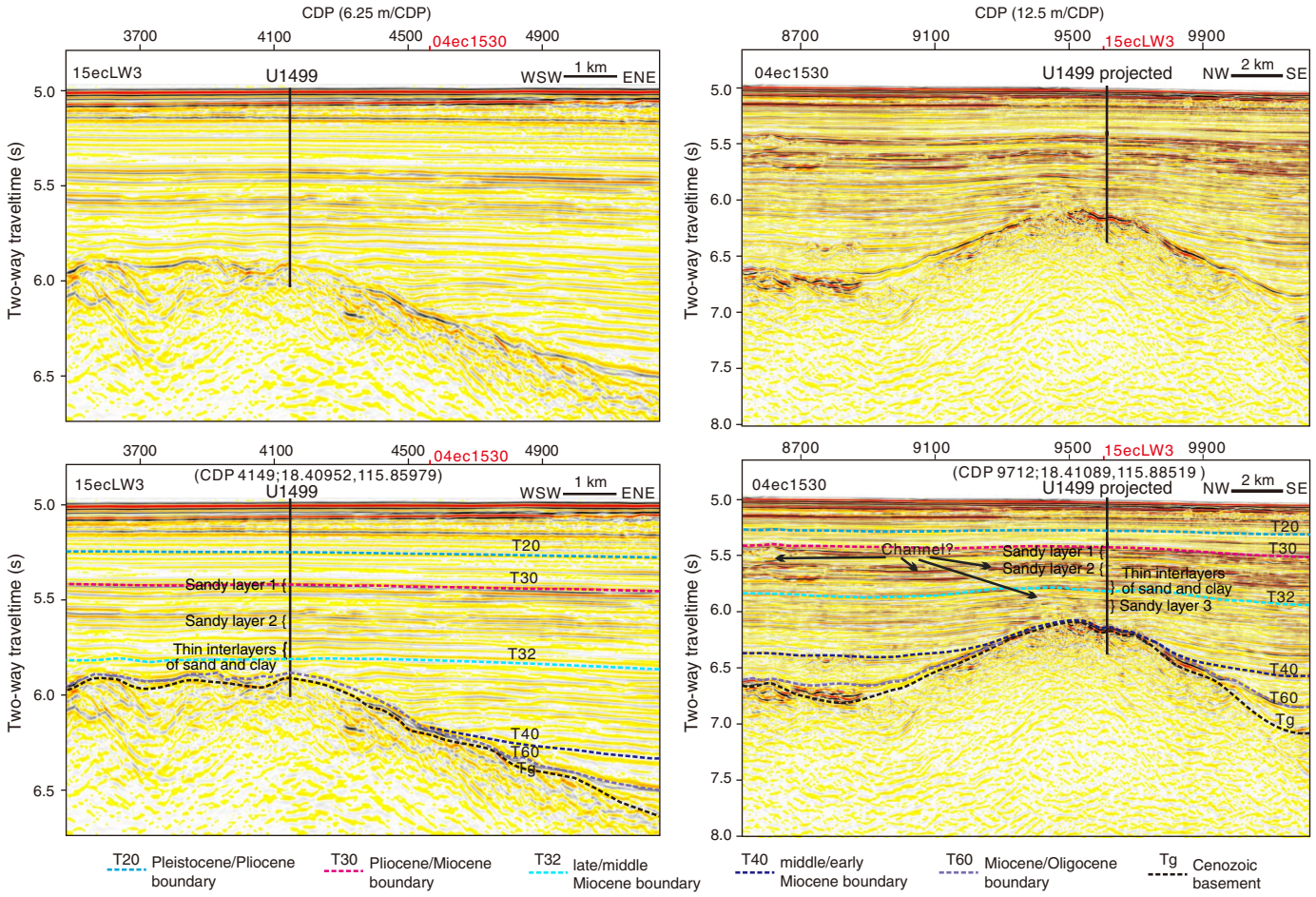

Figure F5. A–D. Schematic development of continental breakup initiated by a simple shear along a deep, low-angle fault. B–D are slightly modified from Huismans and Beaumont (2011) and illustrate modeling-based stages of extension at magma-poor rifted margins of the Iberia-Newfoundland type. Key features of D are thinning of upper crust, juxtaposition of lower crust (e.g., Site U1499), and serpentinized mantle (Site U1500) between outer margin and igneous oceanic crust. UP = upper plate, LP = lower plate.

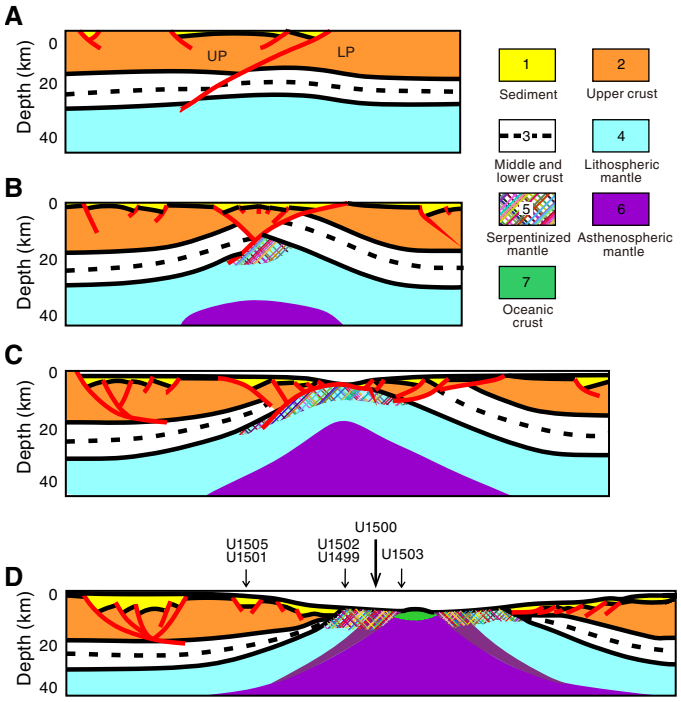

Figure F6. A–E. Composite figures redrawn from models in Huismans and Beaumont (2011), Sibuet and Tucholke (2012), Makris et al. (2012), and Sun et al. (2016) showing spectrum of possible magma-poor rifted margin models based on rheological differences. These models suggest that lithospheric layers with relatively lower strength will tend to stretch and thin more than other layers. Thus, the continent–ocean transition (COT) may be dominated by these weaker layers. D features a strong lower crust overlying a weak, wet upper mantle, resulting in upper subcontinental (serpentinized) mantle dominating the COT. C shows a particularly interesting alternative in which moderately weaker lower crust leads to its exhumation in the COT. UCC = upper continental crust, LCC = lower continental crust, UCM = upper continental mantle, UOM = upper oceanic mantle, OC = oceanic crust.

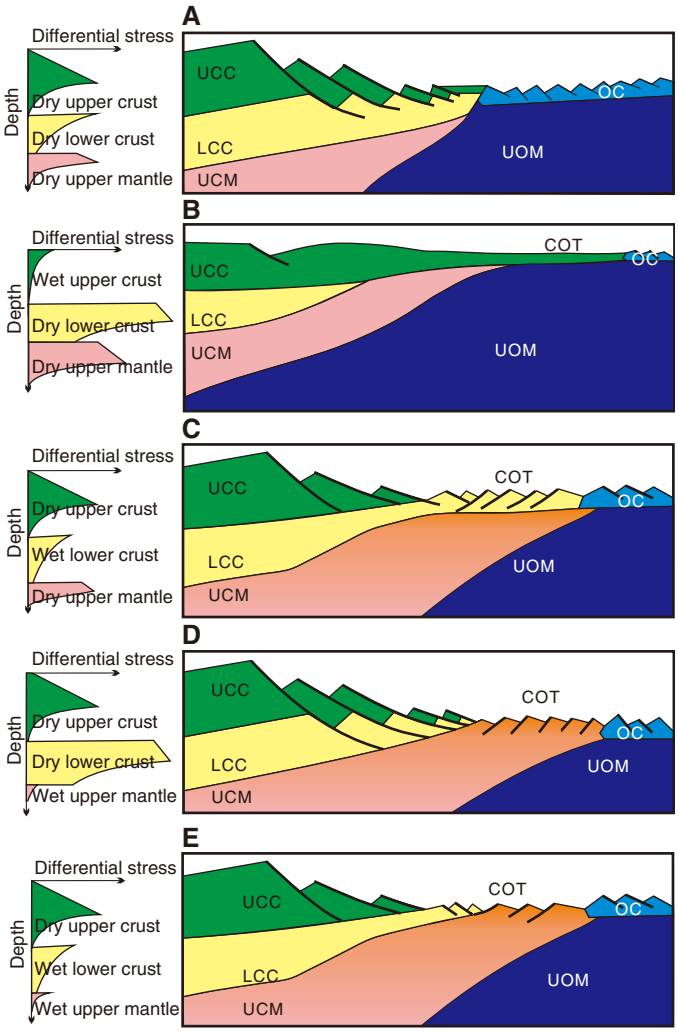

Operations

We conducted operations in two holes at Site U1499. We APC/XCB cored in Hole U1499A (18°24.5698′N, 115°51.5881′E; 3760.2 m water depth) from the seafloor to 659.2 m and recovered 417.05 m of core (63%). We installed 651 m of casing in Hole U1499B (18°24.5705′N, 115°51.5990′E; 3758.1 m water depth) (Figure **F7**), RCB cored from 655.0 to 1081.8 m (recovering 150.64 m, or 35%), and conducted two wireline logging runs from ~65 m above the base of the hole upward to the casing. Coring summaries of Holes U1499A and U1499B are in Table **T1**. In this section we also document the first part of the expedition leading up to Site U1499.

Figure F7. Hole U1499B reentry system and casing.

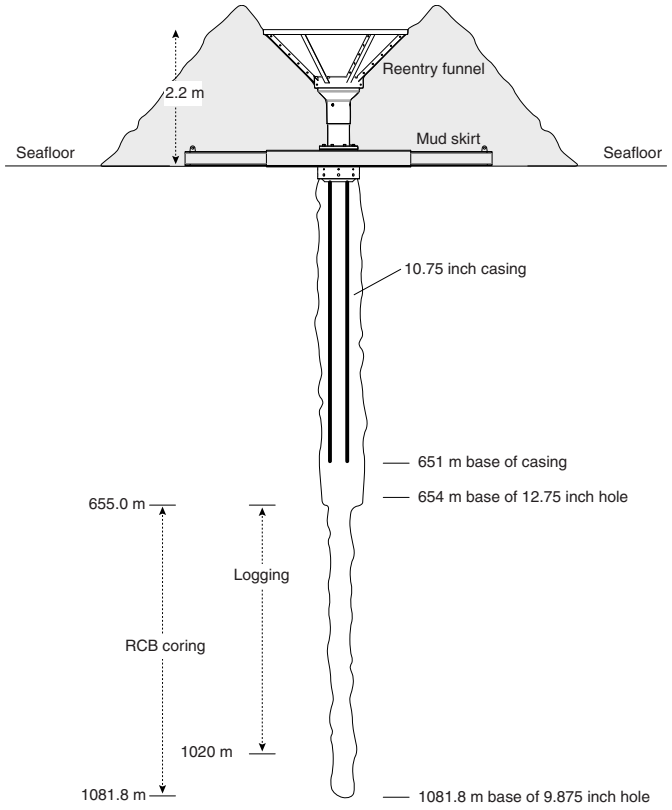

Hong Kong port call

Expedition 367, South China Sea Rifted Margin, started at 0812 h (all times are UTC + 8 h) on 7 February 2017 with the first line ashore at the China Merchants Wharf in Hong Kong. The Co-Chief Scientists and IODP staff moved onto the ship and started crossover with their Expedition 366 counterparts. Initial loading of incoming shipments began. The Expedition 367 scientists boarded the ship on the morning of 8 February. After they got settled in their rooms, the scientists were introduced to life on board the R/V *JOIDES Resolution* and participated in an initial laboratory and ship safety tour. The scientists were then introduced to the information technology on board the ship and started to connect their computers to the shipboard network, and half of the science party went on a core-flow tour. Transfer of incoming and outgoing shipments continued throughout the day. Arriving sea freight was partially loaded, along with fresh and refrigerated food products and 300 metric tons of potable water. All departing freight was moved to the pier. On 9 February, the day began with introductions of the Expedition 367 scientists and *JOIDES Resolution* Science Operator (JRSO) shipboard staff followed by a presentation of the expedition scientific objectives by the Co-Chief Scientists. The rest of the day's science meetings were postponed until the next day so that seven scientists could address issues with their travel documents. Major port call activities on 9 February included loading of 40 short tons of drilling mud, 987.3 metric tons of marine gas oil, sea freight, and frozen food, as well as offloading frozen shipments from the previous expedition. Because of a missed boat transfer in Shanghai, China, a shipment of essential hardware (reentry cones, casing, and mud motors) was delayed until 10 February. Because of the time required to load this essential hardware, our departure was delayed by 1 day to 13 February.

On 10 February, scientists were introduced to shipboard deliverables, met in laboratory groups with their JRSO technical staff team members, and underwent the Captain's introduction and safety orientation. The other half of the science party went on a core-flow tour. A Texas A&M University System film crew spent the day filming some promotional videos and was escorted around the ship. In addition to routine loading/offloading, the trucks with our delayed shipment of essential hardware started arriving in the late afternoon on 10 February. After carefully calculating the remaining work, arrangements were made with the agent and immigration authorities for a departure at 1200 h on 13 February.

Table T1. Site U1499 core summary. * = base of 10.75 inch casing at 651 m; drilled in with pilot bit and underreamer that extended 2.71 m below the end of the casing. † = not including casing drilled into 651 m. DRF = drilling depth below rig floor, DSF = drilling depth below sea floor. NA = not applicable. Core type: H = advanced piston corer, X = extended core barrel (XCB), R = rotary core barrel, numeric core type = drilled interval. APCT-3 = advanced piston corer temperature tool, WOB = weight on bit. (Continued on next two pages.) **Download table in CSV format.**

Hole U1499A	
Latitude:	18°24.5698′N
Longitude:	115°51.5881′E
Time on hole (d):	7.2
Seafloor (drill pipe measurement below rig floor, m DRF):	3771
Distance between rig floor and sea level (m):	10.8
Water depth (drill pipe measurement from sea level, mbsl):	3760.2
Total penetration (drilling depth below seafloor, m DSF):	659.2
Total depth (drill pipe measurement from rig floor, m DRF):	4430.2
Total length of cored section (m):	659.2
Total core recovered (m):	417.05
Core recovery (%):	63
Drilled interval (m):	NA
Total number of cores:	71

Hole U1499B	
Latitude:	18°24.5705′N
Longitude:	115°51.5990′E
Time on hole (d):	14.9
Seafloor (drill pipe measurement below rig floor, m DRF):	3769
Distance between rig floor and sea level (m):	10.9
Water depth (drill pipe measurement from sea level, mbsl):	3758.1
Total penetration (drilling depth below seafloor, m DSF):	4850.8
Total depth (drill pipe measurement from rig floor, m DRF):	1081.8
Total length of cored section (m):	426.8
Total core recovered (m):	150.64
Core recovery (%):	35
Drilled interval (m):	4†
Total number of cores:	44

Table T1 (continued). (Continued on next page.)

Core	Type	Top of interval DSF (m)	Bottom of interval DSF (m)	Interval advanced (m)	Core recovered length (m)	Curated length (m)	Recovery (%)	Time on deck UTC (h)	Time on deck (ship local time; UTC + 8 h)	Time to cut core (min)	Mud pumped (bbl)	Driller's notes
367-U1499A-												
1	H	0.0	7.5	7.5	7.50	7.50	100	2/15/2017 01:50	2/15/2017 09:50			
2	H	7.5	17.0	9.5	9.88	9.88	104	2/15/2017 02:55	2/15/2017 10:55	5		
3	H	17.0	26.5	9.5	9.89	9.89	104	2/15/2017 04:05	2/15/2017 12:05	5		
4	H	26.5	36.0	9.5	9.91	9.91	104	2/15/2017 05:20	2/15/2017 13:20	5		APCT-3
5	H	36.0	45.5	9.5	9.70	9.70	102	2/15/2017 07:20	2/15/2017 15:20	5		
6	H	45.5	55.0	9.5	10.14	10.14	107	2/15/2017 09:20	2/15/2017 17:20	5		APCT-3
7	H	55.0	64.5	9.5	10.15	10.15	107	2/15/2017 10:25	2/15/2017 18:25	5		
8	H	64.5	74.0	9.5	9.99	9.99	105	2/15/2017 11:50	2/15/2017 19:50	5		APCT-3
9	H	74.0	83.5	9.5	9.52	9.52	100	2/15/2017 13:00	2/15/2017 21:00	5		
10	H	83.5	93.0	9.5	9.93	9.93	105	2/15/2017 14:20	2/15/2017 22:20	5		APCT-3
11	H	93.0	102.5	9.5	10.14	10.14	107	2/15/2017 15:30	2/15/2017 23:30	5		
12	H	102.5	112.0	9.5	10.11	10.11	106	2/15/2017 17:00	2/16/2017 01:00	5		APCT-3
13	H	112.0	121.5	9.5	9.33	9.33	98	2/15/2017 18:00	2/16/2017 02:00	5		
14	H	121.5	131.0	9.5	9.74	9.74	103	2/15/2017 19:15	2/16/2017 03:15	5		APCT-3
15	H	131.0	138.8	7.8	7.85	7.85	101	2/15/2017 20:15	2/16/2017 04:15	5		
16	H	138.8	148.3	9.5	9.53	9.53	100	2/15/2017 21:40	2/16/2017 05:40	5		
17	H	148.3	156.5	8.2	8.28	8.28	101	2/15/2017 22:55	2/16/2017 06:55	5		
18	H	156.5	162.4	5.9	5.92	5.92	100	2/16/2017 00:15	2/16/2017 08:15	5		
19	X	162.4	172.1	9.7	8.58	8.58	88	2/16/2017 02:00	2/16/2017 10:00	15		
20	X	172.1	181.8	9.7	9.65	9.65	99	2/16/2017 03:05	2/16/2017 11:05	15		
21	X	181.8	191.5	9.7	8.36	8.36	86	2/16/2017 04:20	2/16/2017 12:20	15		
22	X	191.5	201.2	9.7	9.61	9.61	99	2/16/2017 05:30	2/16/2017 13:30	15		
23	X	201.2	210.9	9.7	9.79	9.79	101	2/16/2017 06:35	2/16/2017 14:35	15		
24	X	210.9	220.6	9.7	9.87	9.87	102	2/16/2017 07:40	2/16/2017 15:40	15		
25	X	220.6	230.3	9.7	0.02	0.02	0	2/16/2017 08:45	2/16/2017 16:45	15		
26	X	230.3	240.0	9.7	9.89	9.89	102	2/16/2017 09:55	2/16/2017 17:55	15		
27	X	240.0	249.7	9.7	9.82	9.82	101	2/16/2017 11:55	2/16/2017 19:55	15		Sheared overshot
28	X	249.7	259.4	9.7	9.58	9.58	99	2/16/2017 13:15	2/16/2017 21:15	15		
29	X	259.4	269.1	9.7	9.75	9.75	101	2/16/2017 14:35	2/16/2017 22:35	20		
30	X	269.1	278.8	9.7	9.86	9.86	102	2/16/2017 15:45	2/16/2017 23:45	20		
31	X	278.8	288.5	9.7	9.88	9.88	102	2/16/2017 17:05	2/17/2017 01:05	25		
32	X	288.5	298.2	9.7	9.85	9.85	102	2/16/2017 18:25	2/17/2017 02:25	25		
33	X	298.2	307.9	9.7	8.69	8.69	90	2/16/2017 19:45	2/17/2017 03:45	30		
34	X	307.9	317.6	9.7	9.55	9.55	98	2/16/2017 21:00	2/17/2017 05:00	25		
35	X	317.6	327.3	9.7	9.79	9.79	101	2/16/2017 22:10	2/17/2017 06:10	25		
36	X	327.3	337.0	9.7	6.45	6.45	66	2/16/2017 23:15	2/17/2017 07:15	15		Drilling break last 2 m
37	X	337.0	346.7	9.7	0.06	0.06	1	2/17/2017 00:10	2/17/2017 08:10	5	30	Drilling break
38	X	346.7	356.4	9.7	0.05	0.10	1	2/17/2017 01:55	2/17/2017 09:55	15	30	Firmed up at 349 m
39	X	356.4	366.1	9.7	1.19	1.19	12	2/17/2017 02:50	2/17/2017 10:50	10		Drilling break at 359 m
40	X	366.1	375.8	9.7	0.00	0.00	0	2/17/2017 03:50	2/17/2017 11:50	10		
41	X	375.8	385.5	9.7	0.00	0.00	0	2/17/2017 06:45	2/17/2017 14:45	5	30	Could not maintain WOB; formation unstable
42	X	385.5	395.2	9.7	0.00	0.00	0	2/17/2017 08:45	2/17/2017 16:45	5		Drilling break sands; could not maintain WOB
43	X	395.2	404.9	9.7	0.07	0.07	1	2/17/2017 10:45	2/17/2017 18:45	10		
44	X	404.9	414.6	9.7	9.20	9.20	95	2/17/2017 13:15	2/17/2017 21:15	10	30	
45	X	414.6	424.3	9.7	9.90	9.90	102	2/17/2017 15:20	2/17/2017 23:20	20		
46	X	424.3	434.0	9.7	9.83	9.83	101	2/17/2017 17:25	2/18/2017 01:25	30		
47	X	434.0	443.7	9.7	9.86	9.86	102	2/17/2017 19:35	2/18/2017 03:35	30	30	
48	X	443.7	453.4	9.7	9.96	9.96	103	2/17/2017 21:35	2/18/2017 05:35	30		
49	X	453.4	463.1	9.7	10.03	10.03	103	2/17/2017 23:40	2/18/2017 07:40	30		
50	X	463.1	472.8	9.7	6.41	6.41	66	2/18/2017 01:30	2/18/2017 09:30	20	30	Drilling break at 468 m
51	X	472.8	482.5	9.7	0.00	0.00	0	2/18/2017 03:00	2/18/2017 11:00	5		Could not mainain WOB; drilling break
52	X	482.5	492.2	9.7	0.00	0.00	0	2/18/2017 04:35	2/18/2017 12:35	5		
53	X	492.2	501.9	9.7	0.00	0.00	0	2/18/2017 07:10	2/18/2017 15:10	10	80	No rotation
54	X	501.9	511.6	9.7	0.24	0.24	2	2/18/2017 08:50	2/18/2017 16:50	5		Could not maintain WOB; drilling break 8 m
55	X	511.6	521.3	9.7	0.00	0.00	0	2/18/2017 10:50	2/18/2017 18:50	5	30	Could not maintain WOB; drilling break 8 m
56	X	521.3	531.0	9.7	0.43	0.43	4	2/18/2017 12:50	2/18/2017 20:50	10		
57	X	531.0	540.7	9.7	1.15	1.15	12	2/18/2017 15:20	2/18/2017 23:20	5	30	Could not maintain WOB; drilling break
58	X	540.7	550.4	9.7	0.13	0.13	1	2/18/2017 17:00	2/19/2017 01:00	10		XCB shoe missing
59	X	550.4	560.1	9.7	0.15	0.15	2	2/18/2017 19:10	2/19/2017 03:10	20	30	
60	X	560.1	569.8	9.7	1.20	1.20	12	2/18/2017 21:10	2/19/2017 05:10	30		XCB shoe missing
61	X	569.8	579.5	9.7	0.30	0.30	3	2/18/2017 23:50	2/19/2017 07:50	30	30	
62	X	579.5	589.2	9.7	0.13	0.13	1	2/19/2017 02:00	2/19/2017 10:00	25		

Table T1 (continued).

Core	Type	Top of interval DSF (m)	Bottom of interval DSF (m)	Interval advanced (m)	Core recovered length (m)	Curated length (m)	Recovery (%)	Time on deck UTC (h)	Time on deck (ship local time; UTC + 8 h)	Time to cut core (min)	Mud pumped (bbl)	Driller's notes
63	X	589.2	598.9	9.7	0.00	0.00	0	2/19/2017 03:50	2/19/2017 11:50	20	30	
64	X	598.9	608.6	9.7	1.86	1.86	19	2/19/2017 05:45	2/19/2017 13:45	15		Drilling break at 605–607 m
65	X	608.6	618.3	9.7	0.39	0.39	4	2/19/2017 07:55	2/19/2017 15:55	25	30	Destroyed XCB shoe, spacer sub
66	X	618.3	628.0	9.7	9.84	9.84	101	2/19/2017 10:30	2/19/2017 18:30	45		
67	X	628.0	637.7	9.7	6.37	6.37	66	2/19/2017 12:50	2/19/2017 20:50	20	30	
68	X	637.7	647.4	9.7	0.00	0.00	0	2/20/2017 15:20	2/20/2017 23:20	5	555	Could not maintain WOB; drawworks repair took 24.5 h
69	X	647.4	650.2	2.8	1.16	1.16	41	2/20/2017 17:40	2/21/2017 01:40	40		
70	X	650.2	651.2	1.0	0.38	0.38	38	2/20/2017 20:10	2/21/2017 04:10	35		
71	X	651.2	659.2	8.0	0.26	0.26	3	2/20/2017 22:50	2/21/2017 06:50	50	70	
		Hole U1499 totals:		659.20	417.05	417.10	63					
367-U1499B-												
1	1	651.0*	655.0	4.0	*****Drilled interval *****			2/24/2017 15:00	2/24/2017 23:00			Drilled in 651 m of 10.75 inch casing
2	R	655.0	664.7	9.7	4.81	4.81	50	2/26/2017 12:10	2/26/2017 20:10	50	30	
3	R	664.7	674.4	9.7	4.16	4.16	43	2/26/2017 14:30	2/26/2017 22:30	30		Penetration changed last 1.5 m
4	R	674.4	684.1	9.7	0.15	0.15	2	2/26/2017 16:20	2/27/2017 00:20	5		Fast penetration, 9 m; sands?
5	R	684.1	693.8	9.7	0.05	0.05	0.50	2/26/2017 18:10	2/27/2017 02:10	10	30	Formation firmed up last 2 m
6	R	693.8	703.5	9.7	0.02	0.02	0.20	2/26/2017 19:50	2/27/2017 03:50	10		Ratty formation
7	R	703.5	713.2	9.7	0.02	0.02	0.20	2/26/2017 21:35	2/27/2017 05:35	5		Fast penetration
8	R	713.2	722.9	9.7	0.08	0.08	0.80	2/26/2017 23:30	2/27/2017 07:30	10	30	
9	R	722.9	732.6	9.7	4.77	4.77	49	2/27/2017 01:20	2/27/2017 09:20	25		Formation firmed up at 727.6 m
10	R	732.6	742.3	9.7	3.07	3.07	32	2/27/2017 03:10	2/27/2017 11:10	25		Drilling break, last 3 m
11	R	742.3	752.0	9.7	0.08	0.08	0.80	2/27/2017 05:05	2/27/2017 13:05	5	30	Drilling break, 9 m; sands
12	R	752.0	761.7	9.7	1.95	1.95	20	2/27/2017 07:10	2/27/2017 15:10	10		Drilling break, first 7.7 m; firmed up last 2 m
13	R	761.7	771.4	9.7	8.84	8.84	91	2/27/2017 09:35	2/27/2017 17:35	50	30	
14	R	771.4	781.1	9.7	6.38	6.38	66	2/27/2017 12:05	2/27/2017 20:05	45		
15	R	781.1	790.8	9.7	7.06	7.06	73	2/27/2017 14:40	2/27/2017 22:40	40	30	
16	R	790.8	800.5	9.7	9.41	9.41	97	2/27/2017 17:00	2/28/2017 01:00	45		
17	R	800.5	810.2	9.7	8.53	8.53	88	2/27/2017 19:00	2/28/2017 03:00	30		
18	R	810.2	819.9	9.7	7.27	7.27	75	2/27/2017 20:55	2/28/2017 04:55	30	30	
19	R	819.9	829.6	9.7	2.67	2.67	28	2/27/2017 22:40	2/28/2017 06:40	20		Drilling break at 825 m
20	R	829.6	839.3	9.7	3.09	3.09	32	2/28/2017 00:30	2/28/2017 08:30	20		Formation firmed up at 834 m
21	R	839.3	849.0	9.7	3.93	3.93	41	2/28/2017 03:00	2/28/2017 11:00	60	30	
22	R	849.0	858.7	9.7	6.75	6.75	70	2/28/2017 05:20	2/28/2017 13:20	40		
23	R	858.7	868.4	9.7	8.76	8.76	90	2/28/2017 07:45	2/28/2017 15:45	40		
24	R	868.4	878.1	9.7	10.09	10.09	104	2/28/2017 10:20	2/28/2017 18:20	40		
25	R	878.1	887.8	9.7	4.09	4.09	42	2/28/2017 13:05	2/28/2017 21:05	45	30	
26	R	887.8	897.5	9.7	7.74	7.74	80	2/28/2017 15:35	2/28/2017 23:35	50		
27	R	897.5	907.2	9.7	3.99	3.99	41	2/28/2017 22:00	3/1/2017 06:00	205		Firm formation at 898 m; stuck core barrel; sheared overshot
28	R	907.2	916.9	9.7	6.24	6.24	64	3/1/2017 02:00	3/1/2017 10:00	130		
29	R	916.9	926.6	9.7	6.20	6.20	64	3/1/2017 05:35	3/1/2017 13:35	120	30	
30	R	926.6	936.3	9.7	7.17	7.17	74	3/1/2017 08:50	3/1/2017 16:50	45	30	Formation change from 931 to 936 m; high torque
31	R	936.3	946.0	9.7	0.36	0.42	4	3/1/2017 15:25	3/1/2017 23:25	130	90	Work tight hole from 931 to 939 m; high torque
32	R	946.0	955.7	9.7	0.79	0.92	8	3/1/2017 21:10	3/2/2017 05:10	190	30	
33	R	955.7	965.4	9.7	1.50	1.74	15	3/2/2017 01:50	3/2/2017 09:50	165		Pipe stuck
34	R	965.4	975.1	9.7	1.50	2.22	15	3/2/2017 05:50	3/2/2017 13:50	115		
35	R	975.1	984.8	9.7	1.26	1.87	13	3/2/2017 10:50	3/2/2017 18:50	155	30	
36	R	984.8	994.5	9.7	1.00	1.12	10	3/2/2017 15:40	3/2/2017 23:40	145	30	
37	R	994.5	1004.2	9.7	1.00	1.21	10	3/2/2017 20:25	3/3/2017 04:25	165	30	
38	R	1004.2	1013.9	9.7	1.25	1.50	13	3/3/2017 00:35	3/3/2017 08:35	135	70	Plugged bit jet nozzle
Bit change												
39	R	1013.9	1023.6	9.7	0.80	0.88	8	3/4/2017 22:15	3/5/2017 06:15	190	30	
40	R	1023.6	1033.3	9.7	0.84	0.82	9	3/5/2017 02:00	3/5/2017 10:00	120	30	
41	R	1033.3	1043.0	9.7	1.10	1.07	11	3/5/2017 05:35	3/5/2017 13:35	100	30	
42	R	1043.0	1052.7	9.7	0.85	0.88	9	3/5/2017 09:55	3/5/2017 17:55	140	30	
43	R	1052.7	1062.4	9.7	0.48	0.54	5	3/5/2017 13:45	3/5/2017 21:45	110	30	
44	R	1062.4	1072.1	9.7	0.45	0.50	5	3/5/2017 17:00	3/6/2017 01:00	65	60	
45	R	1072.1	1081.8	9.7	0.09	0.09	0.90	3/6/2017 03:50	3/6/2017 11:50	100	100	High pressure and torque; pipe stuck
		Hole U1499B totals:		426.80	150.64	153.15	35					

On 11 February, the scientists were introduced to drilling/coring/logging operations, our shipboard Educator and Journalist gave an overview of their plans for the expedition, and the Captain held the first fire and boat safety drill. In the afternoon, the scientists shared their individual research interests for the expedition with each other. Loading of essential hardware continued throughout the

day, and by the end of the day all casing had been secured in the riser hold. All that remained of port call activities was to load five flats of drill pipe and final securing of cargo prior to departure.

We finished loading all remaining operations hardware on 12 February, including 288 joints of drill pipe. We also spooled new coring line onto the forward coring winch, offloaded trash prior to sailing, secured all cargo and equipment for heading out to sea, and made necessary arrangements with port authorities for departing the next day.

At 1000 h on 13 February, immigration authorities boarded the ship and cleared the vessel for departure. The harbor pilot arrived on board just before noon, and the last line was released at 1215 h on 13 February. We proceeded to the pilot station, and after a 7 nmi transit the pilot disembarked at 1248 h. Our 277 nmi transit to Site U1499 took 28.0 h with an average speed of 9.8 kt.

Hole U1499A

After arriving at Site U1499 at 1615 h on 14 February 2017, we lowered the thrusters, deployed a seafloor beacon, assembled two extra stands for RCB coring later in the expedition, put together the APC/XCB bottom-hole assembly (BHA), and lowered it to 3749.4 m below rig floor (mbrf) in preparation for coring. As each piece of the drill string was assembled, its length was measured and its interior was verified to be unobstructed. The top drive was picked up, the entire string was spaced out to place in preparation for starting coring, and a wiper pig was pumped through the drill string to clean rust and debris from the inside of the drill string. The calculated precision depth recorder (PDR) depth for the seafloor at Hole U1499A was 3774.4 mbrf; we chose to place the bit at 3769 mbrf to take the first core. An APC core barrel was lowered to the bit, and coring in Hole U1499A started at 0930 h on 15 February. Based on a mudline core recovery of 7.5 m, we calculated the seafloor to be at 3771.0 mbrf (3760.2 m below sea level [mbsl]). APC Cores 367-U1499A-1H through 18H penetrated to 162.4 m and recovered 167.51 m (103%). All APC cores used nonmagnetic core barrels and were orientated. Formation temperature measurements with the advanced piston corer temperature tool (APCT-3) were made while taking Cores 4H, 6H, 8H, 10H, 12H, and 14H.

APC Cores 12H through 18H (102.5–162.4 m) encountered increasingly firm formation, and the core barrel did not fully penetrate the formation for many of them. Because of our primary expedition objectives, we switched to XCB coring instead of first using the half-length APC (HLAPC) system, which would have taken twice as long to penetrate the formation.

XCB Cores 19X through 57X penetrated from 162.4 to 540.7 m and recovered 227.37 m (60%). XCB core recovery was highly bimodal. We had quite high core recovery in the fine-grained intervals (Cores 19X through 36X from 162.4 to 337.0 m with 158.99 m recovered [91%] and Cores 44X through 50X from 404.9 to 472.8 m with 65.19 m recovered [96%]). We had very fast penetration rates and extremely low recovery in unconsolidated sands (Cores 37X through 43X from 337.0 to 404.9 m with 1.37 m recovered [2%] and Cores 51X through 57X from 472.8 to 540.7 m with 1.82 m recovered [3%]). One exception was Core 25X, which came back with only 2 cm of core, but the core liner appeared to have had sediment in it, so we inferred that the sediment was fine grained and that it fell out of the core barrel while it was being retrieved.

Once we encountered unconsolidated sand, we started circulating mud sweeps (30 bbl at 337.0, 346.7, 375.8, 404.9, 443.7, 472.8, 492.2, 511.6, and 531.0 m). While making a connection at 492.2 m, the drill string became stuck and could not be rotated. We circulated an additional 50 bbl of mud, were able to regain rotation, and resumed XCB coring in Hole U1499A. Cores 58X through 67X penetrated from 540.7 to 637.7 m (20.37 m recovered; 21%). For the first eight cores (58X through 65X), the bit penetrated very quickly through 77.6 m and recovered only 4.16 m (5%), so we inferred that the sediment is predominantly unconsolidated sand. Core 66X had slower penetration and 100% recovery in the finer grained formation. However, the penetration rate increased again in Core 67X, indicating that we had encountered sand again. The last core on 19 February (Core 68X) also cut very quickly and had almost arrived back on the rig floor (~100 mbrf) when the low-clutch diaphragm in the drawworks failed at 2245 h; we could not raise the drill string. We secured the drill string and circulated, rotated, and pumped a mud sweep every hour to keep the drill string from getting stuck while repairing the ruptured diaphragm. After the 24.5 h it took to repair the drawworks, we were finally able to open the drill string and get Core 68X out of it at 2320 h on 20 February. We had suspected it would be empty because it cored very quickly through inferred sand, but it also had been sitting in the drill string for a full day. Although coring recovery was quite variable, we were very close to XCB coring refusal, and the finer grained formation we did recover was getting quite hard, we wanted to penetrate a few more cores to verify an appropriate formation to set the base of the casing to be deployed in our next hole (firm formation, not sand).

Cores 69X through 71X penetrated quite slowly from 647.4 to 659.2 m and recovered 1.8 m of hard sedimentary rock; we decided this was an appropriate interval for the base of the casing. The driller then circulated the entire hole with mud to minimize risks of hole problems as we pulled the drill string out of the hole. We started pulling the drill string out of Hole U1499A at 0815 h on 21 February. We kept the top drive installed until the bit was at 299 m, above the uppermost interval of unconsolidated sand. The bit cleared the seafloor at 1230 h on 21 February and arrived on the rig floor at 2015 h, ending Hole U1499A. APC/XCB coring in Hole U1499A penetrated 659.2 m. As mentioned above, core recovery was highly variable (formation dependent), and core recovery totaled 417.05 m (63%). We suspect that unconsolidated sand accounted for the poor recovery. The overall drilling, coring, and formation information from Hole U1499A was used for planning the casing installation for the second hole to achieve our deep-coring and logging objectives.

Hole U1499B

We offset the ship 20 m east of Hole U1499A and conducted required routine rig servicing (drill line slip and cut). At 2345 h on 21 February 2017, we started preparing the rig floor for assembling the reentry cone and 651 m long casing to be drilled into the seafloor in Hole U1499B.

We spent all of 22 February and the first part of 23 February assembling the 10.75 inch casing and the drill string we would use to drill it into the seafloor. This included

- Moving the mud skirt over the moonpool;
- Assembling 651 m of 10.75 inch casing, lowering it through, and latching it into the mud skirt; and
- Assembling a 9.875 inch tricone bit, underreamer set to 12.75 inches, and mud motor and lowering them through the casing hung off in the moonpool.

At 0430 h on 23 February, we finished putting together the final parts of the drilling assembly. This included attaching the upper part of the casing running tool (which contains the hydraulic release tool [HRT]) and attaching the reentry funnel. We started lowering the entire 651 m long casing string and drilling assembly to the seafloor and deployed the camera system at 1115 h on 23 February to monitor the reentry funnel while the casing was being drilled into the seafloor. When the pilot bit that extends 2.71 m below the casing shoe was just above the seafloor, the drillers measured the pressures at various pump rates to get information to compare to measurements when we would start penetrating the formation. Drilling in Hole U1499B started at 1535 h on 23 February. While drilling the casing into the seafloor, we circulated 25 bbl mud sweeps at 152.6, 327.8, 356.98, 493.1, and 619.8 m. We continued to drill the casing into the seafloor until the mud skirt landed on the seafloor.

We deployed the go-devil to activate the casing running tool, which released the casing at 2300 h on 24 February. We retrieved the entire drilling assembly, with the bit clearing the seafloor at 0230 h on 25 February, and the bit arrived back on the rig floor at 1230 h on 25 February. After taking apart the drilling assembly and flushing the mud motor, underreamer, and bit with freshwater, we began preparing the rig floor for RCB coring. We started assembling the RCB BHA at 1430 h on 25 February, and the rest of the day was spent lowering it to the seafloor. At 2230 h on 25 February, the subsea camera was deployed. Once the RCB bit and camera reached the seafloor, we started searching for the Hole U1499B reentry funnel at 0215 h on 26 February. After we were unable to find it relatively quickly (as is usual), we initiated an expanding 5 m grid search. After just over 6 h, we eventually found the reentry funnel cone. It was clearly visible inside a small crater of sediment located about half-way (~10 m) back toward and a little south of Hole U1499A to the west. Also, the top of the reentry funnel appeared to be close to level with the top of the cuttings pile. After only 10 min of maneuvering, we reentered Hole U1499B at 0825 h on 26 February, started lowering the RCB bit down through the casing, and recovered the camera system. As the bit was being lowered, it encountered sediment inside the casing at 571 m, 80 m above the casing shoe. This sediment was assumed to be sand that entered the casing as the drilling stinger assembly (with pilot bit, underreamer, and mud motor), used to drill the casing in, was withdrawn from the casing. We picked up the top drive, deployed a core barrel at 1230 h, and washed back to the bottom of the hole at 655 m (4 m below the base of the casing). We circulated 30 bbl of mud, retrieved the core barrel (empty), and started RCB coring in Hole U1499B at 2230 h on 26 February.

On 27 February, RCB coring in Hole U1499B penetrated from 655.0 to 790.8 m with an overall recovery of 41.44 m (Cores 367-U1499B-2R through 15R; 31%). However, recovery continued to be highly variable and formation dependent. In fine-grained intervals, we had higher recovery (53%) and steady, relatively slow penetration rates (Cores 2R through 3R from 655.0 to 674.4 m, Cores 9R through 10R from 722.9 to 742.3 m, and Cores 13R through 15R from 752.0 to 790.8 m). In other intervals, inferred to consist of loosely consolidated coarse-grained sand, we had very low recovery (0.7%) and very quick penetration rates. The drillers noted these intervals at 672.9–727.6 and 739.3–759.7 m, which correspond mostly with Cores 4R through 8R (674.4–722.0 m) and 11R (742.3–752.0 m). We circulated 30 bbl mud sweeps at 684.1, 713.2, 742.3, 761.7, and 781.1 m. At first light on 27 February, a boat (M/V *Taikoo*) with critical spares for the drawworks clutch arrived on site, and the transfer was completed.

We continued RCB coring from 790.8 to 897.5 m (Cores 16R through 26R; 72.33 m recovered; 68%) and circulated 30 bbl mud sweeps at 810.2, 839.3, and 878.1 m. Each of these cores (16R through 26R) took from 20 to 60 min to cut. Another fast-drilling zone from 825.0 to 834.0 m was also noted by the drillers. After Core 26R, however, we encountered a substantial formation when Core 27R took over 2 h (205 min) to cut. RCB Cores 27R through 29R continued in very hard formation. These cores took 120–205 min to cut, penetrated 29.1 m from 897.5 to 926.6 m, and recovered 16.43 m (56%). However, Core 30R took only 45 min to cut (as opposed to 205, 130, and 120 min for the cores just above). In addition, when the bit was being raised off bottom to recover the core, the drill string became stuck momentarily, so we circulated 30 bbl of mud, and hole conditions improved. The penetration time for Core 31R went back up (130 min), but the drill string became temporarily stuck again. This time we circulated 90 bbl of mud and were able to continue coring.

RCB Cores 31R through 38R penetrated 77.6 m from 936.3 to 1013.9 m and recovered 8.66 m (11%). It took from 2 to >3 h to cut each core. The drill string became stuck momentarily while cutting Core 33R. We circulated 30 bbl of mud after cutting Cores 32R and 35R through 37R.

Because we decided to stop coring to change the RCB bit to core deeper and the bit had accumulated 40.6 rotating hours, we circulated the cuttings out of the hole with 70 bbl of mud after Core 38R. Before pulling the bit up into the casing and out of the hole, we first raised the bit up to 780 m, circulated the hole with 35 bbl of mud, and then filled the uncased (open) part of the hole with 235 bbl of heavy mud (11.0 lb/gal; barite). This process was intended to help stabilize the hole while we changed the bit and to reduce the amount of fill we might encounter when we reentered the hole to resume RCB coring. It was also expected to give us some indication of the hole conditions we might encounter for planned downhole logging after coring had finished. Because we had some challenges locating the hole the first time we reentered, we lowered the subsea camera system to observe the reentry funnel as we pulled the bit out of the hole. While we were still in the hole, we could see the drill pipe clearly in the center of the crater created by the cuttings mound. Although the reentry funnel's concentric black and white stripes were not visible, we didn't anticipate problems finding and reentering the hole. The bit was pulled out of the hole at 1655 h on 3 March, and we spent the rest of the day recovering the drill string (except for a 0.5 h repair of the pipe racker).

We finished recovering the drill string at 0215 h on 4 March, attached a new RCB bit (C-7), lowered it to the seafloor, and then deployed the subsea camera system at 0915 h. We paused rig floor operations from 0915 to 1045 h to conduct required routine rig servicing (drill line slip and cut) before we resumed lowering the drill bit to the seafloor. At 1345 h on 4 March, the bit and camera were in position, and we were able to immediately see the reentry funnel in the center of the cuttings pile caldera. It took us 22 min to position the bit over the funnel and reenter Hole U1499B at 1407 h on 4 March. We retrieved the camera and lowered the bit down through the 651 m of casing to 848.1 m in the open hole. We installed the top drive and circulated/rotated to 987 m, only ~27 m from the bottom of the hole, before the bit encountered any resistance. This resistance was easily penetrated, and we only encountered 1 m of fill on the bottom of the hole. At the end of the day, we pumped 40 bbl of mud to clear cuttings from the hole and retrieved the core barrel that was in place while getting back to the bottom of the hole. We resumed RCB coring from 1013.9 m at 0115 h on 5 March. Cores

39R through 43R penetrated from 1013.9 to 1062.4 m and recovered 4.1 m (4%). We pumped 30 bbl of mud after each of these cores.

At 0100 h on 6 March, Core 44R arrived on the rig floor (1062.4–1072.1 m; 0.45 m recovered; 5%), and we dropped the next core barrel to start cutting Core 45R. While this core was being cut, there were periods of erratic torque and high pump pressure, as well as some short times when the drill string could not be rotated. The driller raised and lowered the drill string and was able to keep coring. Just after we put the core line into the drill string to retrieve Core 45R, the pipe became stuck. For ~45 min, we worked the drill string until it was freed at 0615 h on 6 March. We then removed the core line from the drill string. We raised the bit back up to 994 m and worked to clean out the hole. Eventually at 1045 h, conditions had improved enough that we retrieved Core 45R at 1150 h (1072.1–1081.8 m; 0.09 m recovered; 0.9%). We spent the next 9 h attempting to wash, ream, drill, and circulate our way back to bottom. However, we never were able to get below ~1053 m (~30 m above the bottom of the hole) without the drill string getting stuck. At 2045 h on 6 March, we decided that further attempts to get back to the bottom of the hole and core deeper were not reasonable, so we started to prepare the hole for wireline logging. We circulated 50 bbl of mud to clean cuttings out of the hole, retrieved the core (wash) barrel that was in place during the hole remediation efforts, and lowered the rotary shifting tool on the coring line to release the bit in the hole.

After the bit was released in the bottom of the hole at 0000 h on 7 March, we raised the end of the pipe from 1052.7 to 877.3 m and shifted the mechanical bit release sleeve back into the circulating position. We then raised the end of the pipe to 780 m and pumped 235 bbl of heavy mud into the hole to help maintain good hole conditions for logging. By 1030 h on 7 March, we had raised the end of pipe back inside the casing to 85.1 m and started to prepare the rig floor for logging. Our first logging tool string consisted of the resistivity, velocity, density, and NGR tools. We started lowering it at 1345 h on 7 March. The tool string was able to reach 1020 m, and we successfully logged from that depth up to the base of the casing at 651 m. Log data were also collected up the casing and drill pipe to the seafloor. The tool string arrived back at the rig floor at 2215 h on 7 March. Based on the first logging run results, we decided to conduct a second logging run with the FMS and NGR tools.

We assembled the FMS and NGR tools and started lowering them at 0130 h on 8 March. The tool string was able to reach 1010 m, and we were able to make two passes of the open hole up to the base of the casing at 651 m. Initial results showed that we collected some excellent data in intervals with good borehole diameter. The tool string arrived back on the rig floor at 0925 h, and all of the logging equipment was off the rig floor at 1030 h on 8 March. We pulled the end of the drill string out of Hole U1499B at 1120 h, recovered the seafloor beacon, and started the transit to Site U1500 in dynamic positioning mode just before 1300 h on 8 March. While in transit, we continued to recover the drill string (arrived back on the rig floor at 1830 h on 8 March) and assembled a new RCB bit and started lowering it to the seafloor. We spent a total of 22.1 days at Site U1499.

Lithostratigraphy

We defined nine lithostratigraphic units at Site U1499 based on visual core description, smear slide and thin section inspection, physical property measurements (e.g., magnetic susceptibility and color spectra), geochemistry data, and X-ray diffraction (XRD) (see **Lithostratigraphy** and **Physical properties** in the Expedition 367/368 methods chapter [Sun et al., 2018]). We constructed a composite lithostratigraphy by combining data from Holes U1499A and U1499B (Figure **F8**). The lithostratigraphy for all of Site U1499 is divided into three dominant lithologic sections. The dominant lithologies in the upper part of the stratigraphy (Units I–VII) are composed of clay, clayey silt, silty sand, claystone, sandstone, and calcareous ooze with minor intervals of volcanic ash. The second dominant lithologic section consists of dark brown to reddish brown claystone in Unit VIII. The lower part of the stratigraphy (Unit IX) marks the third main lithologic section and contains gravelly sandstone, matrix supported breccia, and gravel. The transition from Unit VIII to Unit IX (the lowermost unit) is marked by a stark change from manganese nodule–bearing reddish brown chalk to matrix-supported breccia and gravel.

Unit I is composed of dark greenish gray bioclast-rich clay with thin clayey silt and sand interbeds. Unit II contains interbedded greenish gray clay-rich calcareous ooze and dark greenish gray nannofossil-rich clay. Unit III contains dark greenish gray clay with very thick (<1 cm) clayey silt interlaminations in the upper part (Subunit IIIA) and thin (2–5 cm) clayey silt and nannofossil/foraminifer interbeds in the lower part (Subunit IIIB). Unit IV is dominated by dark greenish gray silty sand with clay interbeds. Recovery was very low in this unit, but limited recovery in core catcher samples, fast drilling penetration rates, and seismic reflection data suggest that the unrecovered sections are primarily composed of loose sand. Unit V is composed of dark greenish gray clay with thin (<5 cm) clayey silt and foraminifer sand interbeds. Unit VI contains dark greenish gray silty sand with clay interbeds but has limited recovery. Similar to Unit IV, we infer that the low-recovery sections in Unit VI are composed of loose sand. Unit VII is composed mainly of dark greenish gray to dark gray sandstone and claystone with siltstone interbeds. Lithification increases sharply downhole from the top of this unit, although sections with very low recovery are assumed to be primarily composed of nonlithified sand.

Unit VIII comprises two subunits. Subunit VIIIA contains dark brown claystone with greenish gray to gray siltstone, calcareous-rich claystone with silt, and foraminifer sandstone interbeds in the upper part. Subunit VIIIB contains reddish brown to reddish gray clay-rich nannofossil chalk. Unit IX comprises three subunits, predominately composed of polymict breccia and gravel. Subunit IXA is defined by dark reddish brown to greenish gray sandstone and breccia and Subunit IXB is defined by dark gray matrix-supported breccia in Core 367-U1499B-30R. Subunit IXC contains gray to dark gray gravel with silty sand intervals. The cores in Subunit IXC are completely fragmented and recovered as pebbles and cobbles. Unit boundaries are also recognized in magnetic susceptibility, color reflectance spectroscopy, and bulk mineralogy compositions (Figures **F9**, **F10**).

Unit descriptions

Unit I

Interval: 367-U1499A-1H-1, 0 cm, to 6H-3, 35 cm
Depth: 0–48.85 m
Age: middle–late Pleistocene

Unit I spans the uppermost 48.85 m and is dominated by a sequence comprising dark greenish gray bioclast-rich clay with thin clayey silt and sand interbeds. The clay is generally massive and homogeneous, sometimes marked by faint color banding of more intense green against the background of greenish gray. Most of the

Figure F8. Lithostratigraphic summary of Site U1499 with simplified lithology and unit description of combined Holes U1499A and U1499B.

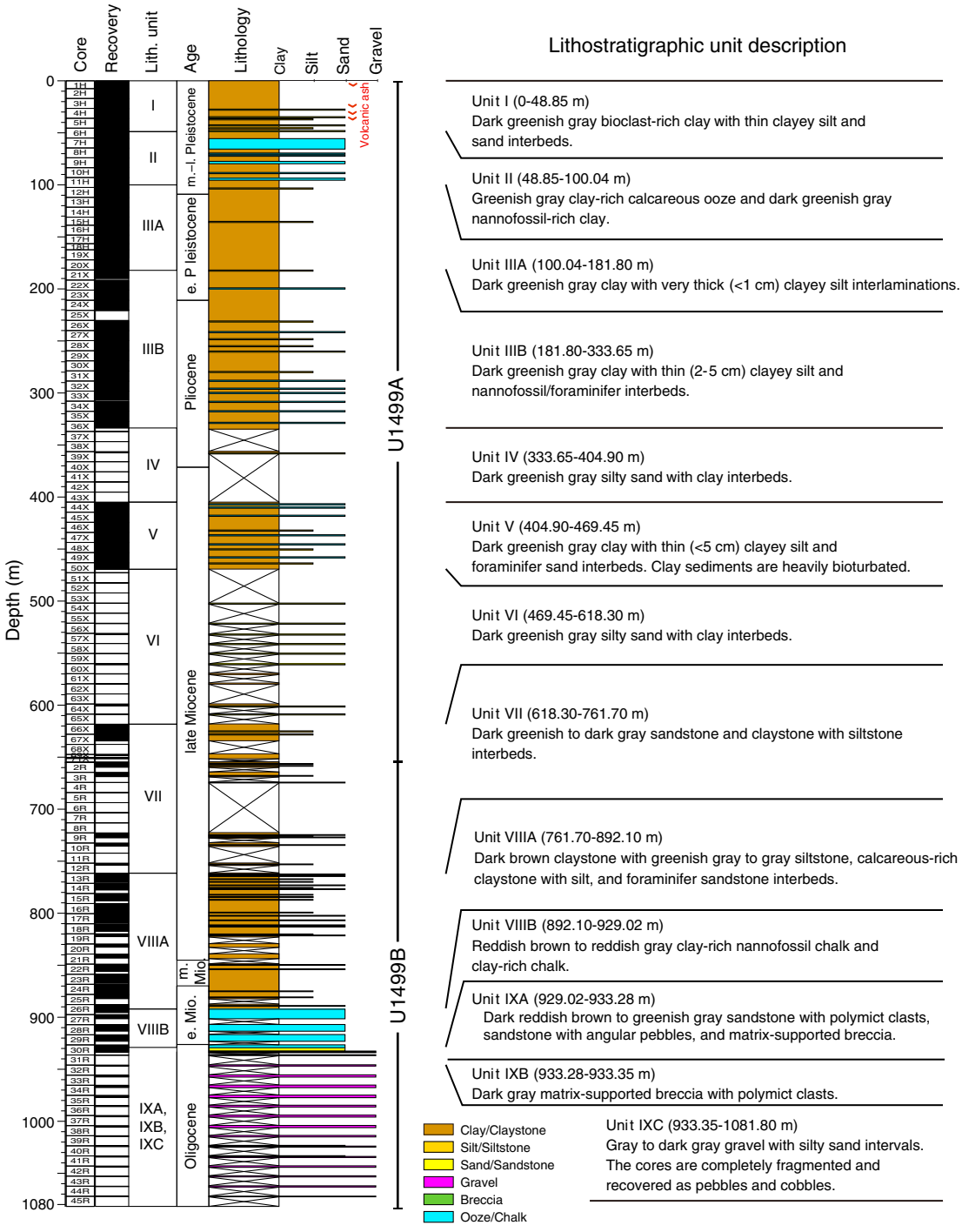

clay intervals have heavy bioturbation. Some light-colored intervals have higher biogenic content, mostly including foraminifer, nannofossil, diatom, and radiolarian particles (Figure **F11**). A distinct oxidized layer (dark yellowish brown) occurs in the top of this unit. The silt and fine sand layers, varying from 2–5 to 15–20 cm in thickness, occur as dark greenish gray interbeds within a finer grained primary lithology. We interpret these graded, fining-upward cycles as distal turbidite sequences. At the base of each coarse-grained bed is a sharp erosive contact between the overlying silty and fine sand layer and the underlying clay layer. Fine to medium sand layers can be occasionally as thick as 50–70 cm in Cores 4H, 5H, and 6H. The erosive base of a medium-grained sand interval in Section 6H-7 marks the boundary between Units I and II.

Unit I has four thin volcanic ash layers (2–6 cm thick) that are not present in any other unit. They occur in Cores 1H, 3H, 4H, and 5H. The ash layers are pale brown and comprise unaltered pumice and ash shards (Figure **F12B**). This unit is characterized by relatively low magnetic susceptibility (<40 × 10^{-5} SI) but with several abrupt peaks (>100 × 10^{-5} SI) that correspond to the ash layers (Figures **F9**, **F12A**). However, the magnetic susceptibility data are not

Figure F9. Correlation of lithostratigraphic units with magnetic susceptibility, reflectance spectroscopy, and carbonate content, Site U1499. Magnetic susceptibility and reflectance spectroscopy are displayed with a 10-point running average.

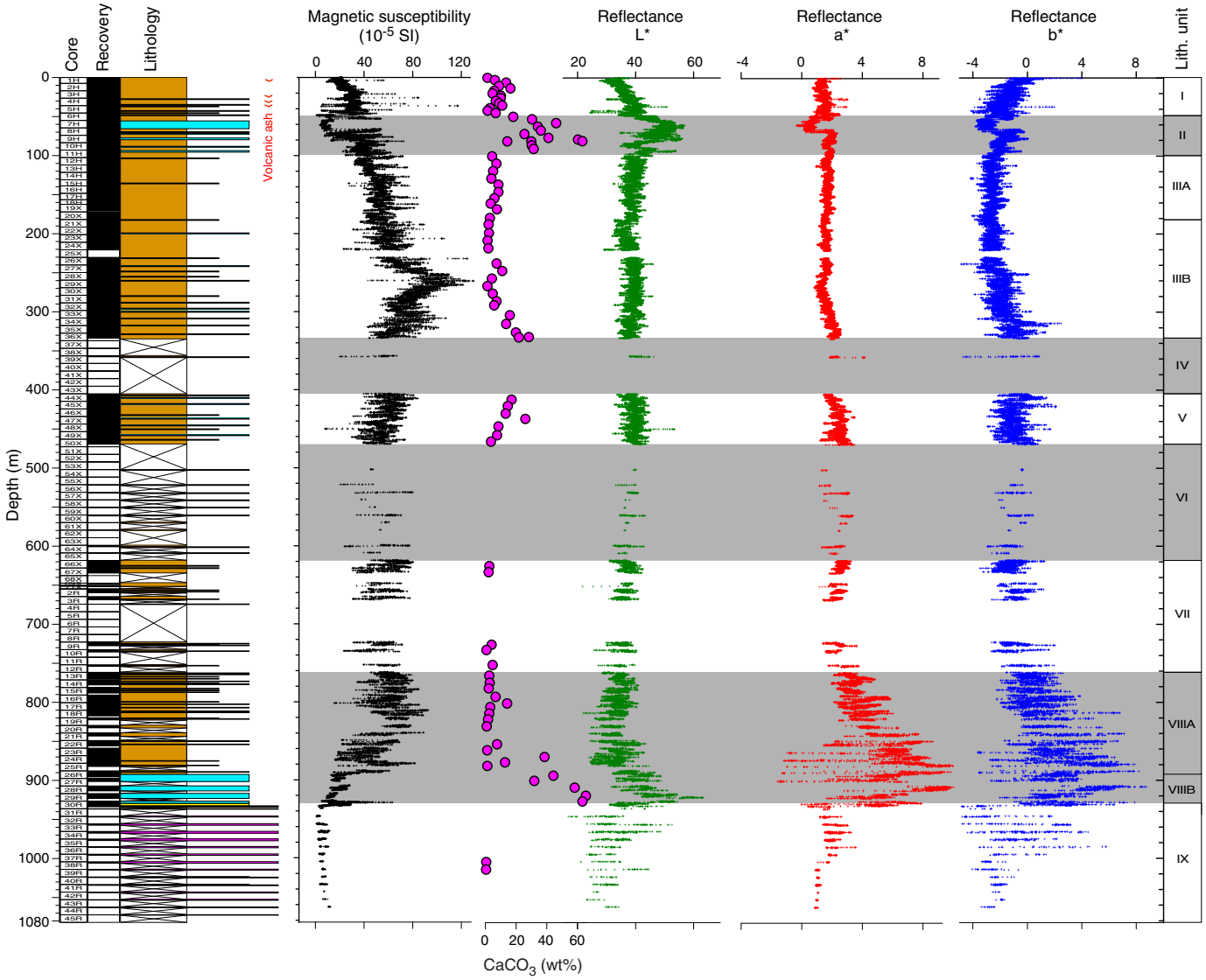

density-normalized, which can cause artificially low values in shallower intervals because of low degrees of sediment compaction. Bulk light reflectance (L*) slightly increases downhole, whereas b* (blue) slightly decreases, suggesting gradually decreasing sediment oxidation. The bulk mineralogy of this unit, measured by XRD, consists mainly of quartz (31%–52%), plagioclase (9%–15%), muscovite (11%–18%), kaolinite + chlorite (17%–30%), and halite (7%–24%) (Figure **F10**). Mineralogy does not vary strongly with depth, except in the uppermost sample, which has the highest halite concentration (24%) as a result of high seawater content (Table **T2**).

Unit II

Interval: 367-U1499A-6H-3, 35 cm, to 11H-5, 104 cm
Depth: 48.85–100.04 m
Age: early–middle Pleistocene

Unit II is composed of alternating greenish gray clay-rich calcareous ooze and dark greenish gray nannofossil-rich clay. The two colors usually form alternating bands with gradational contacts. Sand-sized foraminifers and clay-sized nannofossils are common in both calcareous ooze and clay intervals (Figure **F13**). Foraminifer grains are observable on the core surface and are usually more abundant in light greenish gray intervals. Very thin beds (<3 cm thick) of dark gray sandy silt occur occasionally in the nannofossil-rich clay layers.

This unit has erosive upper and lower contacts (Figure **F31A**). The dark greenish gray medium-grained sand of Unit I in Core 6H overlies Unit II, and the dark greenish gray clay of Unit III in Core 11H underlies it. Intervals in Unit II, especially in Cores 6H, 8H, 10H, and 11H, exhibit synsedimentary deformation with distinct folds, faults, and inclined bedding (Figures **F14**, **F15**). Based on the erosive contacts and deformation structures, we interpret this unit as a slump deposit. The age of foraminifers and nannofossils preserved in the ooze and clay layers are mainly Pliocene (see **Biostratigraphy**), which is older than the underlying Pleistocene sediments of Unit III, further supporting the slump deposit interpretation.

Figure F10. Bulk mineralogy by XRD with major mineral compositions and correlation of calcite with carbonate content, Site U1499.

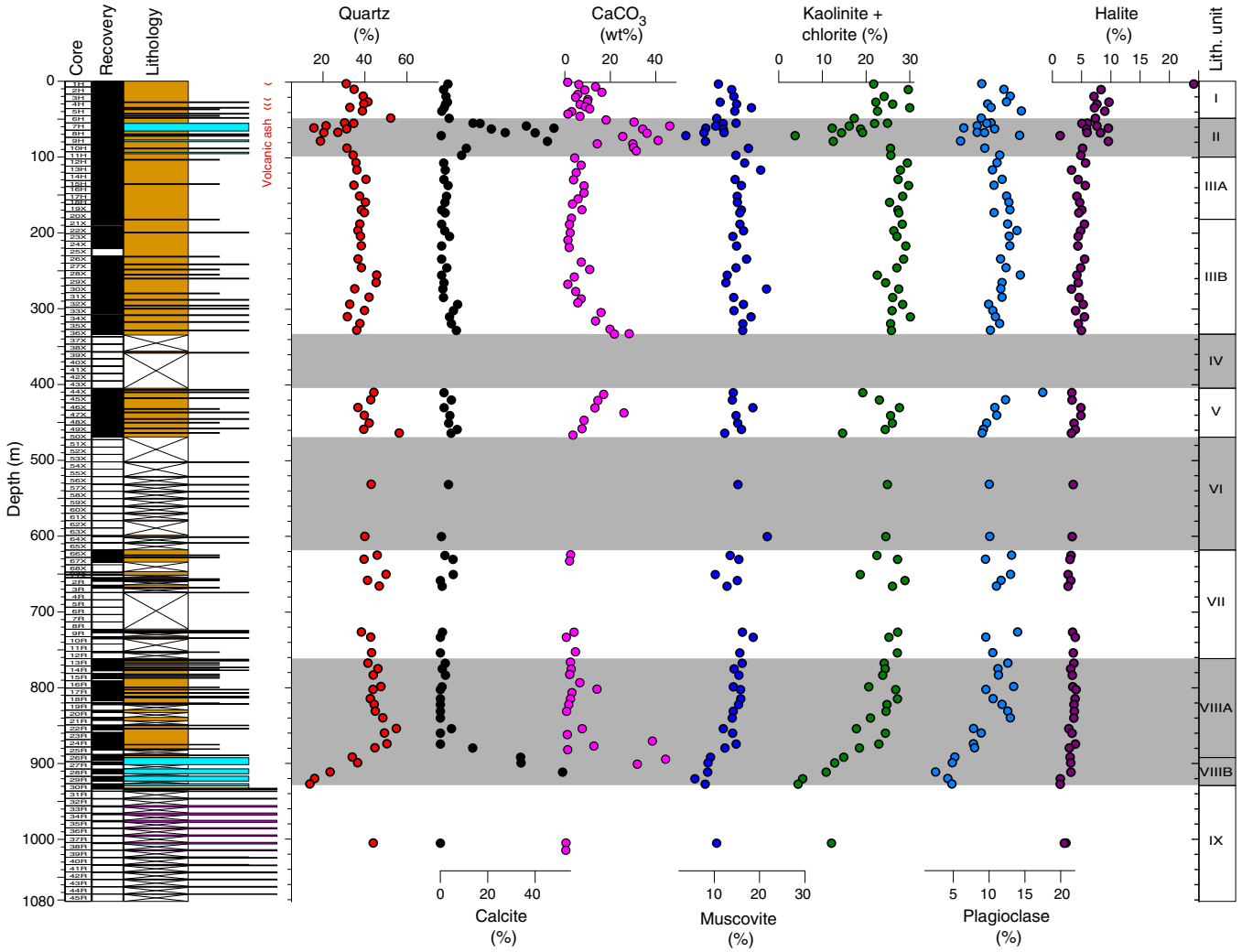

Greenish gray clay-rich calcareous ooze layers (mainly in Core 7H) in Unit II exhibit very low magnetic susceptibility (~10 × 10^{-5} SI), high bulk reflectance, and low a* (red) (Figure F9). These layers correlate to high carbonate content (30–45 wt%) and calcite abundance (20%–48%) (Figure F10). Accordingly, quartz (15%–35%), plagioclase (7%–11%), muscovite (8%–12%), and kaolinite + chlorite (14%–22%) concentrations largely decrease through dilution by high calcite content.

Unit III

Interval: 367-U1499A-11H-5, 104 cm, to 36X-CC, 30 cm
Depth: 100.04–333.65 m
Age: middle Pleistocene–Pliocene

Unit III contains dark greenish gray clay with thick laminations, very thin beds of clayey silt, and calcareous-rich intervals. This unit is divided into two subunits based on relative thickness and recurrence of silt interbeds and abundance of calcareous-rich intervals. Subunit IIIA contains thick laminations of clayey silt (<1 cm), whereas Subunit IIIB has abundant thin beds (2–5 cm) of clayey silt and increased occurrence of nannofossil- or foraminifer-rich intervals.

Subunit IIIA

Interval: 367-U1499A-11H-5, 104 cm, to 21X-1, 0 cm
Depth: 100.04–181.80 m
Age: early–middle Pleistocene

The dominant lithology of Subunit IIIA is greenish gray and dark gray clay, with thick (<1 cm) clayey silt interlaminations. The silt interlaminations generally occur every 20–50 cm and have erosive bases (Figure F15). We interpret the recurring silt interbeds fining upward into clays as distal turbidites. At one interval in the subunit (15H-3, 141–145 cm), the coarser interbed contains foraminiferal silty sand, but presence of other biogenic material is low in the rest of the subunit. Correspondingly, no distinct bioturbation was observed.

Color reflectance, magnetic susceptibility, and mineralogy remain fairly constant throughout Subunit IIIA (Figures F9, F10). The dominant mineralogical components are quartz (35%–40%) and kaolinite + chlorite (25%–30%), whereas calcite content is low (<8 wt%).

In Subunit IIIA, we transitioned from APC to XCB coring (at 162.4 m), which led to increased drilling disturbance starting at Core 19X. Presence of drilling biscuits increased at Core 21X.

Subunit IIIB

Interval: 367-U1499A-21X-1, 0 cm, to 36X-CC, 30 cm
Depth: 181.80–333.65 m
Age: early Pleistocene–Pliocene

Subunit IIIB is a thick interval of primarily dark greenish gray clay with thin (2–5 cm) clayey silt and nannofossil/foraminifer-rich interbeds. Although clay is the dominant grain size in both subunits, Subunit IIIB contains more calcareous bioclasts and bioturbation than Subunit IIIA (Figure F16). Similar to Subunit IIIA, the coarser grained interbeds have erosive bases and fining-upward sequences, implying deposition by turbidity currents.

Magnetic susceptibility increases downhole from values near 45–50 × 10^{-5} SI at the top of the subunit to a peak interval of 120 × 10^{-5} SI in Section 28X-6 (Figure F9). Values then decrease back to the 40–50 × 10^{-5} SI range at the bottom of the subunit. Carbonate content also varies downhole, with concentration increasing from <2 wt% in Section 21X-4 to 28 wt% in Section 36X-4. The steepest increase of carbonate content occurs in Cores 30X through 36X. Despite this change in composition, color reflectance data remain mostly invariant throughout Subunit IIIB. XRD analysis of Subunit IIIB shows similar mineralogy to Subunit IIIA (Figure F10). The dominant components of the clays are quartz (32%–46%) and kaolinite + chlorite (23%–30%), both of which decrease slightly as carbonate increases.

Figure F11. Dark greenish gray bioclast-rich clay of Unit I, consisting mainly of silty terrigenous clay with mixed biogenic grains, including foraminifers, nannofossils, radiolarians, and diatoms.

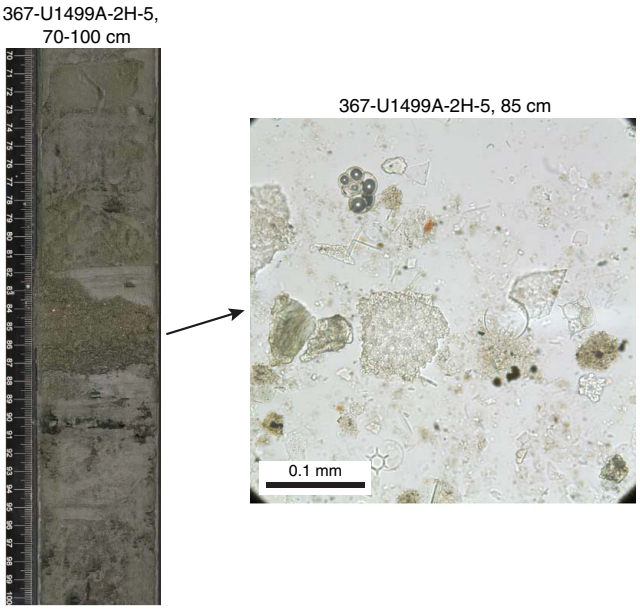

Unit IV

Interval: 367-U1499A-36X-CC, 30 cm, to 44X-1, 0 cm
Depth: 333.65–404.90 m
Age: early Pliocene–late Miocene

Recovery in Unit IV is very low (2%). Most lithostratigraphic information comes from Core 39X, which had 12% recovery of dark greenish gray clay and silty sand. Because of poor recovery, fast drilling penetration rates, and seismic reflection data, we infer most of this unit to contain unconsolidated sand similar to that found in the Section 39X-CC. Because of low recovery, we have no measurements of sediment composition from this unit (XRD and carbonate) and limited magnetic susceptibility and color reflectance data (Figure F9).

Table T2. Mineral percentages, Site U1499. **View table in PDF format. Download table in CSV format.**

Figure F12. (A) Magnetic susceptibility, core image, and (B) smear slide image of pale brownish volcanic ash layer (plane-polarized light [PPL]), Unit I.

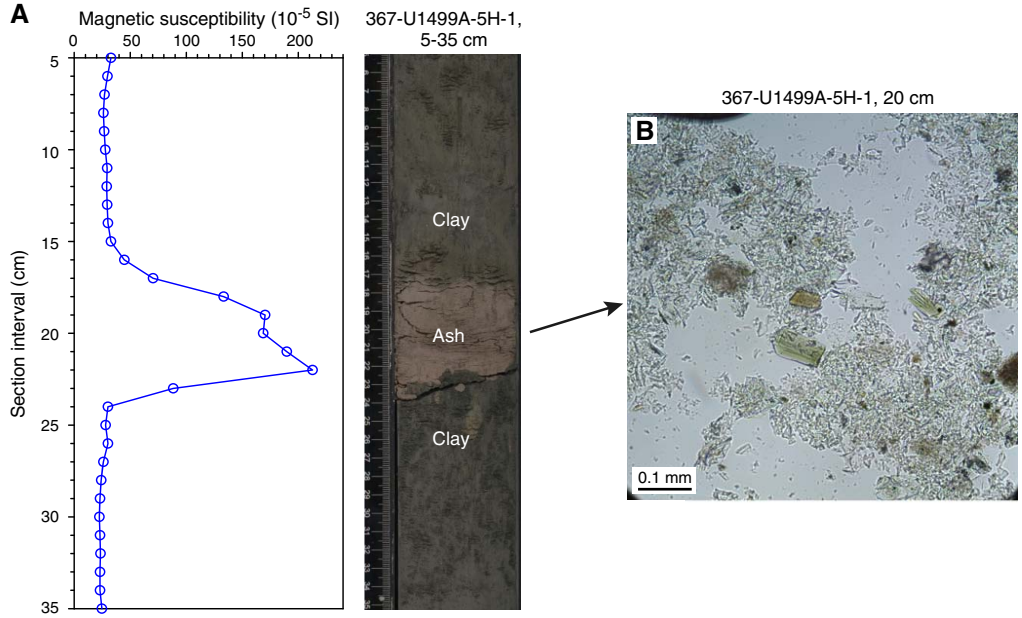

Figure F13. (A) Greenish gray clay-rich calcareous ooze and (B) dark greenish gray nannofossil-rich clay showing abundant foraminifers and nannofossils (cross-polarized light [XPL]), Unit II.

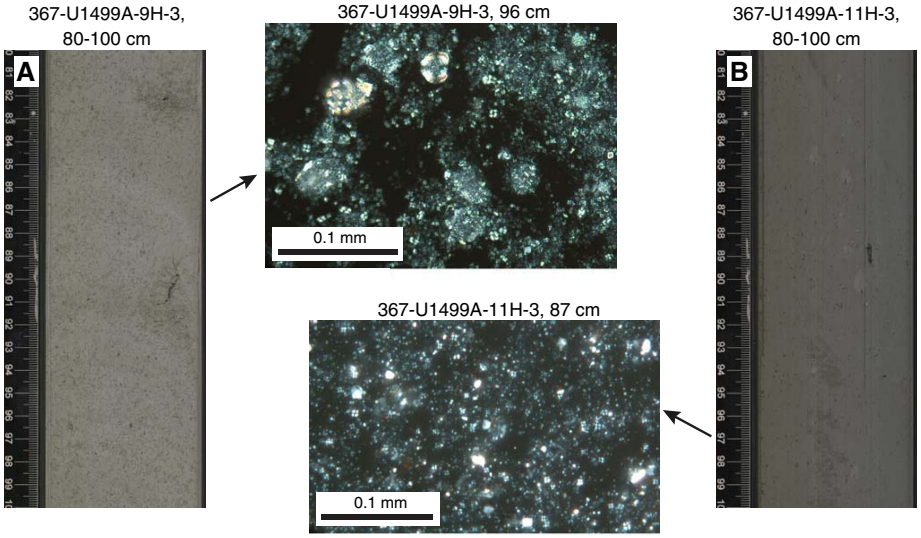

Figure F14. Core composite image showing synsedimentary deformation with distinct fold, fault, and inclined bedding structures.

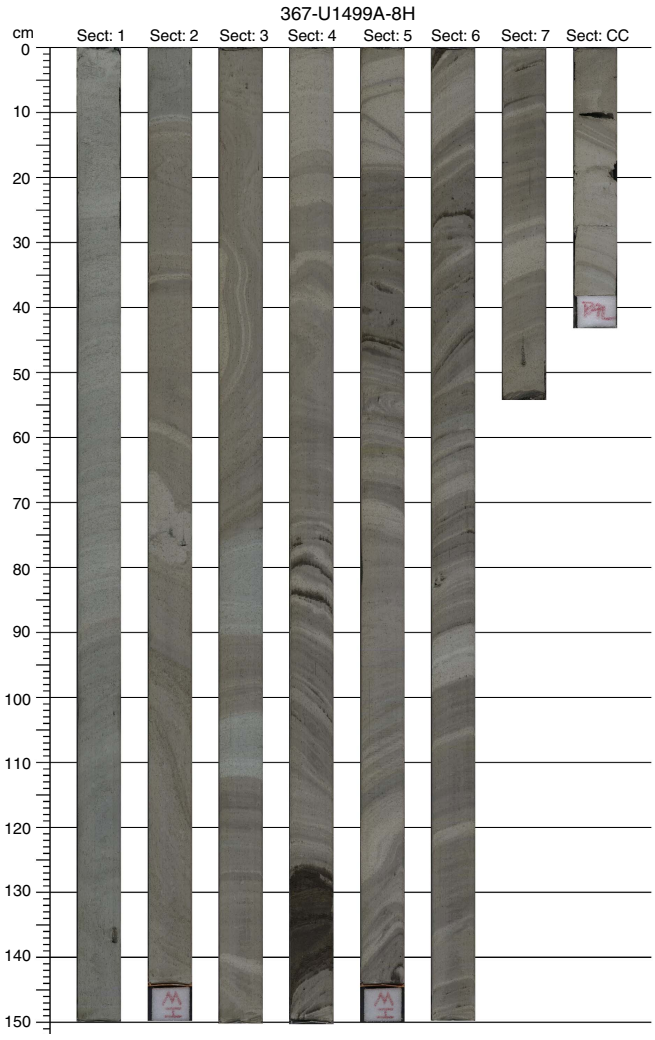

Figure F15. Representative section of clay with silt interbeds, Subunit IIIA. A. Very thin silt interbed showing mostly siliciclastic silt and clay. B. Dominant clay lithology showing mostly siliciclastic clay material (PPL).

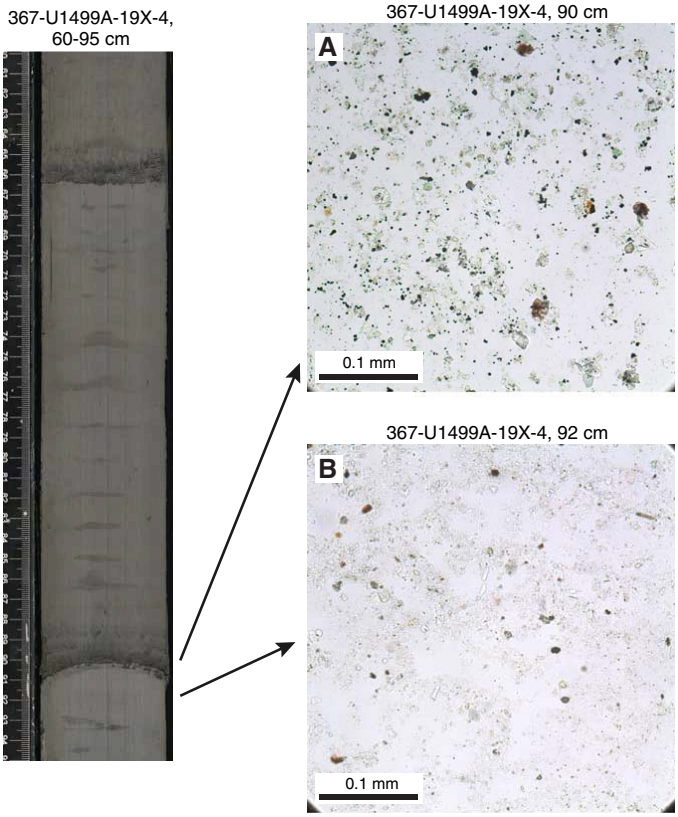

Unit V

Interval: 367-U1499A-44X-1, 0 cm, to 50X-CC, 39 cm
Depth: 404.90–469.45 m
Age: late Miocene

Figure F16. Increased carbonate content and bioturbation, Subunit VIIIB. A. Foraminiferal sand interbed showing an erosive contact with underlying clay (PPL). B. Nannofossil-rich clay showing heavy bioturbation and lighter clay intervals with abundant nannofossils (XPL).

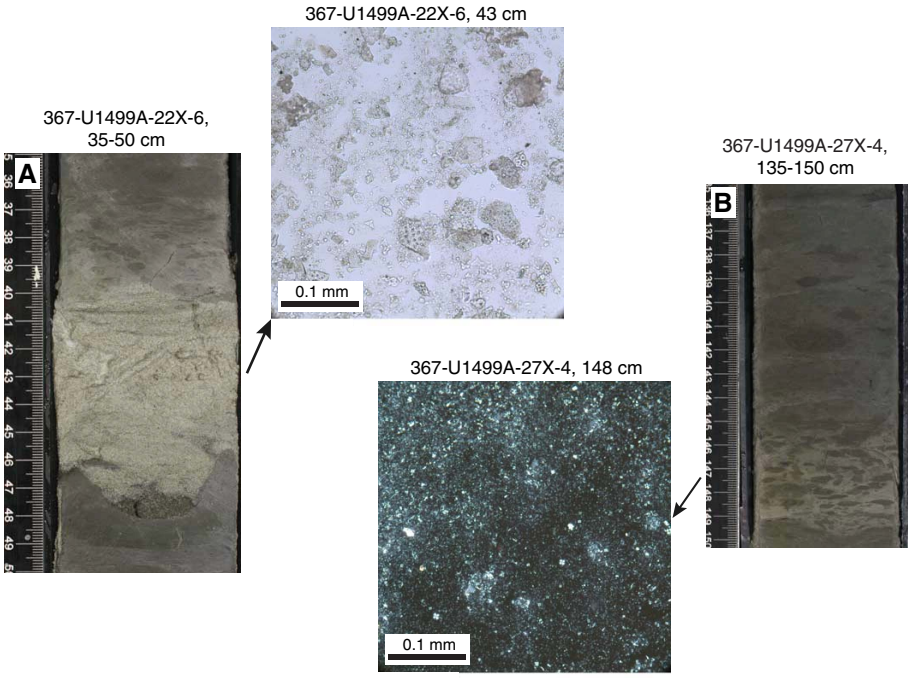

Higher recovery resumed in Core 44X, and the primary lithologies of Unit V are similar to those of Subunit IIIB. The dominant component is dark greenish gray clay with mostly thin (<5 cm) clayey silt and foraminifer sand interbeds. However, some coarser foraminifer sand intervals are much thicker (e.g., interval 48X-5, 18–54 cm; Figure **F17**). Clay sediments are heavily bioturbated. Drilling disturbance, in the form of biscuiting, increases significantly in this unit.

Carbonate content and magnetic susceptibility both decrease downhole, whereas color reflectance data stay within a narrow range (Figure **F9**). XRD analysis shows concentrations of quartz from 37% to 56% with kaolinite + chlorite between 15% and 28% (Figure **F10**). Plagioclase contents decrease downhole from 18% to 9%.

Figure F17. Thick interval of well-sorted foraminiferal sand with an erosive base and fining-upward sequence. Foraminifers consist mainly of planktonic *Sphaeroidinellopsis seminulina* (detailed image from sieved paleontology sample).

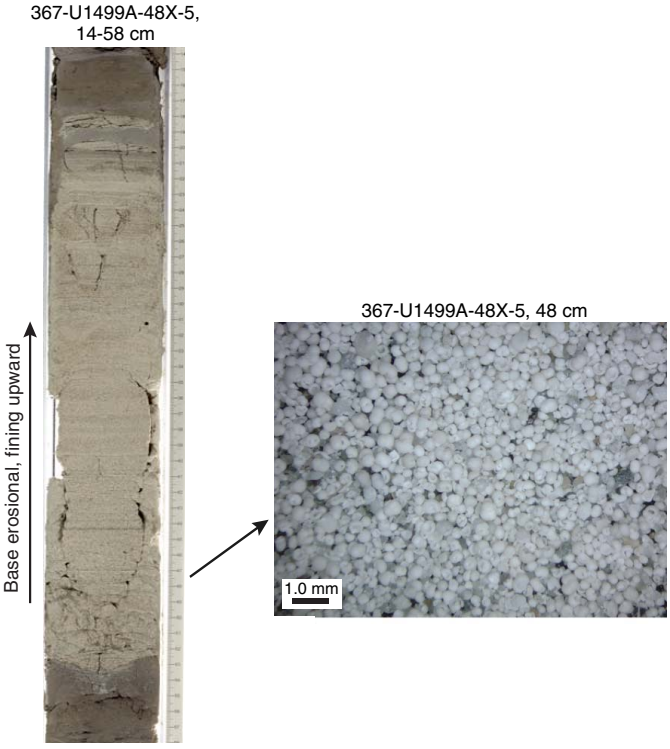

Unit VI

Interval: 367-U1499A-50X-CC, 39 cm, to 66X-1, 0 cm
Depth: 469.45–618.30 m
Age: late Miocene

Recovery in Unit VI was very low (0%–20%). Similar to Unit IV, the fast rates of drilling penetration, seismic reflection data, and recovered sand intervals in the core catchers of Cores 57X, 60X, and 64X imply that this unit predominantly consists of unconsolidated sand. The recovered intervals include dark greenish gray fine- to medium-grained sand (Figure **F18**) interbedded with clay and foraminifer-rich intervals.

Limited measurements of magnetic susceptibility and color reflectance do not show distinct differences from the previous unit (Figure **F9**). The major minerals include quartz (average = 41%), kaolinite + chlorite (25%), muscovite (18%), and plagioclase (10%) (Figure **F10**).

Figure F18. Unconsolidated medium-grained sand showing the dominant siliciclastic composition (PPL), Unit VI.

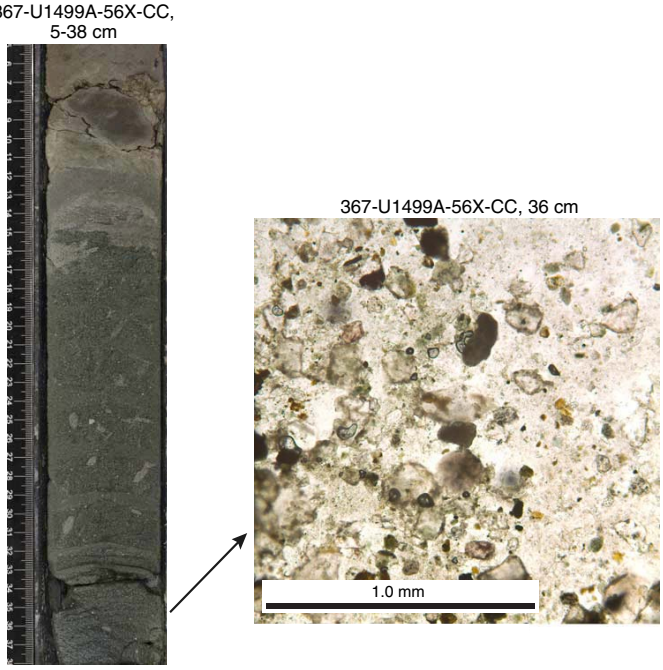

Figure F19. Foraminifer siltstone layer showing erosive base, parallel lamination, and fining-upward sequence, Unit VII. The clay at the top of the interval has *Planolites* and *Zoophycos* trace fossils.

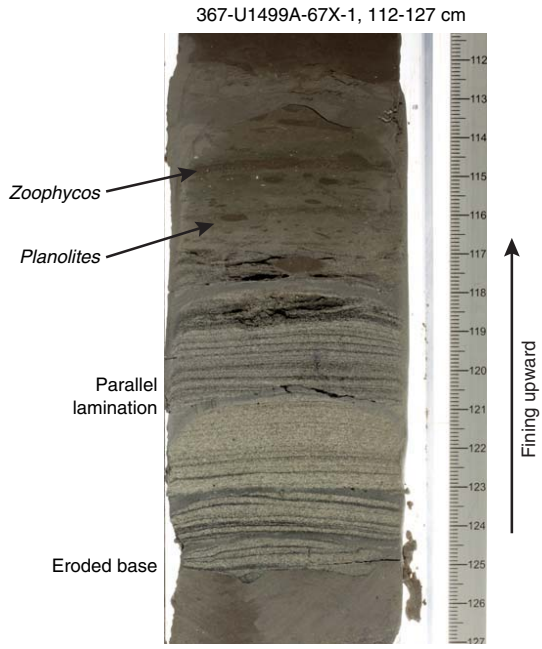

Unit VII

Intervals: 367-U1499A-66X-1, 0 cm, to 71X-CC, 26 cm; 367-U1499B-2R-1, 0 cm, to 13R-1, 0 cm
Depths: Hole U1499A = 618.30–659.20 m; Hole U1499B = 655.00–761.70 m
Age: late Miocene

Unit VII comprises dark greenish gray to dark gray sandstone and claystone with siltstone and foraminifer sandstone interbeds. This unit was recovered in the lower part of Hole U1499A and the upper part of Hole U1499B (Figure **F8**). Lithification increases sharply downhole, although sections with very low recovery are assumed to be primarily composed of nonlithified sand. The recovered siltstone and sandstone layers are generally 3–10 cm thick, have erosive bases, contain parallel laminations, and fine upward into fine-grained claystone intervals (Figure **F19**). Thus, we interpret these intervals as turbidite sequences. Dark greenish gray sandstone intervals usually contain abundant biogenic carbonate clasts and blue-green material that we infer to be a result of alteration from sulfide-rich fluids based on the increased presence of authigenic pyrite near these zones. The claystone is mostly heavily bioturbated with distinctive trace fossils (e.g., *Zoophycos* and *Planolites*).

Measurements of magnetic susceptibility, color reflectance, and bulk mineralogy are fairly consistent downhole (Figures **F9**, **F10**). Quartz (38%–46%), kaolinite + chlorite (18%–27%), muscovite (10%–19%), and plagioclase (10%–14%) dominate the mineralogy.

Unit VIII

Interval: 367-U1499B-13R-1, 0 cm, to 30R-2, 103 cm
Depth: 761.70–929.02 m
Age: early–late Miocene

In Unit VIII, the sediments become lithified, although the transition between well-consolidated and fully lithified sediments is not clear. The unit primarily includes dark brown claystone and reddish brown to reddish gray clay-rich nannofossil chalk. Based on the abundance of calcareous material, we divided this unit into two subunits. Subunit VIIIA contains dark brown claystone with siltstone and foraminifer sandstone interbeds, whereas Subunit VIIIB comprises reddish brown to reddish gray clay-rich nannofossil chalk and clay-rich chalk.

Subunit VIIIA

Interval: 367-U1499B-13R-1, 0 cm, to 26R-4, 12 cm
Depth: 761.70–892.10 m
Age: early–late Miocene

Subunit VIIIA is characterized by dark brown claystone with greenish gray to gray siltstone, calcareous-rich claystone with silt, and foraminifer sandstone interbeds. The top of the subunit, in Section 13R-1, marks the first occurrence of dark brown claystone. The color gradually becomes lighter from dark brown to reddish brown downhole, and the siltstone interbeds occur less frequently (Figure **F20**). The color and minor lithology transition happens in Cores 20R and 21R. Gray, thin (<10 cm) interbeds of foraminifer silty sandstone occur frequently in the upper part of this subunit and usually have an erosive base, parallel laminations, and fining-upward bed forms. The reddish brown claystone is usually massive with moderate bioturbation, and abundant calcareous grains are observable in smear slides. Some thin to medium-thick green intervals occur in the sections of reddish brown claystone in the lower part of this subunit, and green alteration halos around foraminifer tests are common in the reddish brown clay intervals. The green intervals and alteration halos are interpreted as a diagenetic response of formation of glauconite or other secondary minerals.

Magnetic susceptibility values are relatively high (60×10^{-5} SI) in the upper part of this subunit and rapidly decrease along with the minor lithology change in Cores 20R and 21R (Figure **F9**). Reflectance parameters a* and b* generally increase toward the lower por-

Figure F20. Lithology and color change from dark brown claystone with siltstone interbeds to reddish brown nannofossil chalk with occasional greenish claystone interbeds downhole from Subunits VIIIA and VIIIB.

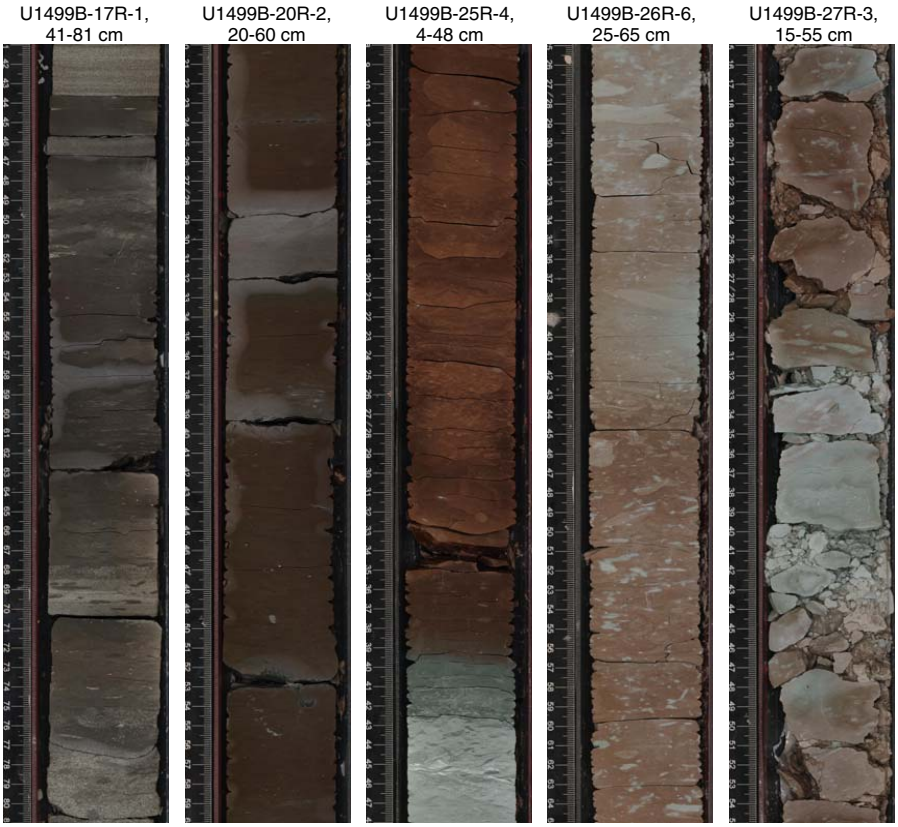

tion of the subunit. Accordingly, the majority of mineralogical components also change downhole in this subunit, showing a decrease in plagioclase, kaolinite + chlorite, and muscovite and an increase in quartz (Figure **F10**).

Subunit VIIIB

Interval: 367-U1499B-26R-4, 12 cm, to 30R-2, 103 cm
Depth: 892.10–929.02 m
Age: early Miocene

Subunit VIIIB features pelagic reddish brown to reddish gray clay-rich nannofossil chalk and clay-rich chalk. The transition from overlying dark brown claystone (Subunit VIIIA) to underlying reddish clay-rich chalk (Subunit VIIIB) is gradual and occurs in the middle of Core 26R. The reddish brown nannofossil chalk is massive with moderate bioturbation. Greenish gray alteration or diagenesis occurs within discrete intervals or as small halos around individual bioclasts (foraminifer tests), fractures, and bioturbated lenses (Figure **F21**).

Abundant brownish black iron-manganese nodules occur in the lowest part of Subunit VIIIB (interval 30R-2, 39–103 cm) within a reddish brown nannofossil-rich claystone matrix (Figure **F22**). The composition of these nodules was later confirmed with postexpedition XRF analysis. The round, concentric nodules are 2–5 cm in diameter. Small to medium, angular to subrounded pebbles form the core of each nodule, providing a nucleation site. The boundary between this nodule-bearing claystone and the underlying sandstone of Unit IX is gradational (Figures **F22**, **F23**).

Figure F21. Greenish gray claystone interbedded in brown claystone sections showing abundant calcareous grains, Subunit VIIIB. A. XPL. B. PPL.

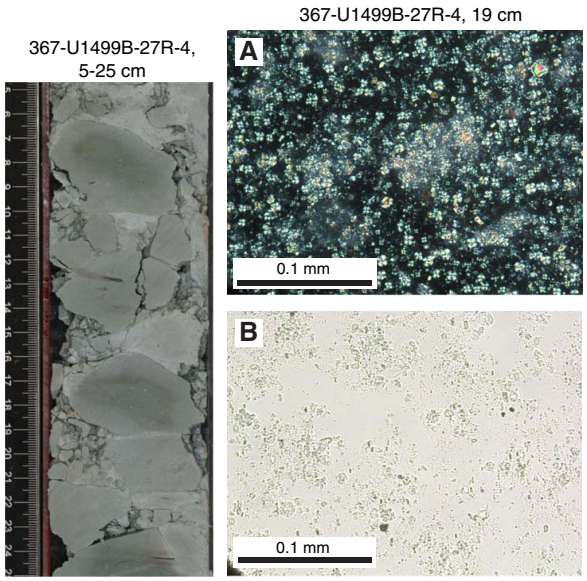

Because the majority of Subunit VIIIB is pelagic nannofossil chalk, it has very low magnetic susceptibility (~10 × 10^{-5} SI) and the highest reflectance values (L*, a*, and b*) at Site U1499 (Figure **F9**). The deviations in a* and b* to negative values occur within the

Figure F22. A. Black-brownish iron-manganese (composition confirmed by postcruise XRF scanning) nodules in lowest part of Subunit VIIIB. Angular to subrounded pebbles form center of nodules. B. Gradational contact with Subunit IXA below nodules.

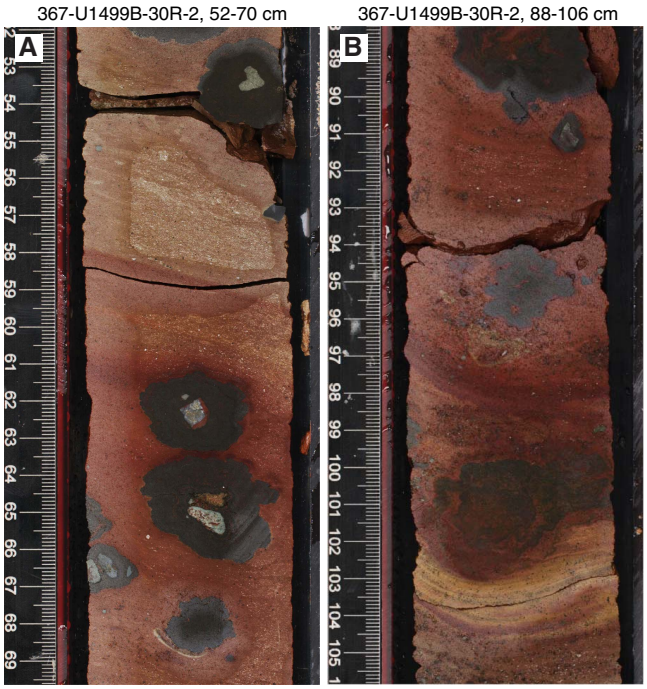

green alteration zones. The major lithology change is also reflected in bulk mineralogical compositions, with increased calcite (34%–68%) and decreased quartz (13%–37%), kaolinite + chlorite (4%–13%), plagioclase (3%–5%), and muscovite (6%–9%) (Figure F10).

Unit IX

Interval: 367-U1499B-30R-2, 103 cm, to 45R-1, 9 cm
Depth: 929.02–1081.80 m
Age: Oligocene (and pre-Oligocene?)

Unit IX contains sandstone, claystone, matrix-supported breccia, and gravel. The unit is broken into three subunits (Figure F23) based on the presence or absence of recovered matrix, matrix composition, and the size and shape of clasts embedded in the matrix material.

Subunit IXA

Interval: 367-U1499B-30R-2, 103 cm, to 30R-6, 55 cm
Depth: 929.02–933.28 m
Age: Oligocene

Subunit IXA is a short but important interval entirely contained within Sections 30R-2 through 30R-6. The contact between the clay-rich chalk of Subunit VIIIB and the gravelly sandstone of Subunit IXA is inclined and gradational. Below the contact is 3.8 m of greenish gray and reddish brown sandstone and claystone with gravel, some of which shows inclined bedding (see **Structural geology** for more details). The bottom of the subunit comprises 45 cm of matrix-supported breccia. Sorting of the subunit decreases from moderate to very poor downhole. Also downhole, the maximum clast size increases from granule to pebble. Throughout the subunit, clasts are angular and of variable lithologic composition (Figures F23, F24), with angularity increasing downhole. The large clasts were identified as claystone, siltstone, sandstone, and conglomerate.

Magnetic susceptibility in Subunit IXA ranges from 10×10^{-5} to 50×10^{-5} SI and is much lower than the overlying, nodule-bearing portion of Subunit VIIIB (Figure F9). Reflectance L* and a* shift to more negative values as a result of darker and greener core material. Because of the limited material in this section, no samples were taken for XRD or carbonate analysis.

Subunit IXB

Interval: 367-U1499B-30R-6, 55 cm, to 30R-6, 62 cm
Depth: 933.28–933.35 m
Age: Oligocene (and pre-Oligocene?)

Subunit IXB is 7 cm thick with textural properties similar to the matrix-supported breccia at the base of Subunit IXA (Figure F25). The subunit is entirely composed of dark gray matrix-supported breccia that includes pebble- and granule-sized polymict clasts of sandstone, siltstone, and claystone. Subunit IXB is distinguished from Subunit IXA because (1) its fine-grained matrix is barren of nannofossils; (2) the matrix changes from greenish gray in Subunit IXA to dark gray in Subunit IXB; (3) the pebble-sized clasts of Subunit IXB are subangular to rounded, which is in contrast to the angular to subrounded pebbles at the base of Subunit IXA; and (4) sand-sized pyrite clasts are common in Subunit IXB. The contact between Subunits IXA and IXB may be obscured by drilling disturbances; however, it has an irregular geometry and could be erosive.

Subunit IXC

Interval: 367-U1499B-30R-6, 62 cm, to 45R-1, 9 cm
Depth: 933.35–1081.80 m
Age: Oligocene (and pre-Oligocene)

Subunit IXC comprises mostly gravel with some intervals of nonlithified clayey silt or silty sand. The gravel was recovered as pebbles and cobbles without matrix, which we infer was lost during the RCB drilling process. The overall recovery was very low for the subunit (~9%), indicating the difficulty in coring this formation. Thus, our information on the lithology and mineralogy of this subunit is biased toward the clasts we recovered, with little information about remaining constituents of this interval (such as the matrix).

Based on visual identification and thin section analysis, gravels as pebbles or cobbles consist of various kinds of grayish fine- to coarse-grained sandstone. The sandstone is well lithified, poorly to well sorted, and grain supported (Figure F26). See **Discussion** for more details on this classification.

We measured magnetic susceptibility on cobble-sized clasts, which were determined to be sedimentary rocks. Values were very low ($<30 \times 10^{-5}$ SI) regardless of clast lithology (Figure F9). The color reflectance data show large amounts of scatter, except for a*, which remains slightly positive but low. These values may be a result of very low levels of green/red hues in the clasts, which are mostly gray, black, and bluish gray.

Carbonate content remains low throughout Subunit IXC, although only four samples were taken. All samples contained <0.5 wt% carbonate (Figure F9). However, one sample did have a relatively high organic carbon content of 4.9 wt% (Sample 38R-1, 74–77 cm; see **Geochemistry**). XRD analysis of a clast from Core 38R

Figure F23. Core 367-U1499B-30R and top of 31R showing contacts between Subunits VIIIB, IXA, IXB, and IXC.



shows dominant quartz (44%) and plagioclase (21%) (Figure F10), although that is not representative of all clasts in the subunit.

Discussion

The lithostratigraphic units observed at Site U1499 characterize deposition in a deep-marine setting. However, lithologic and stratigraphic differences between units likely reflect changes in transport mechanisms, sediment sources, and/or rates of sedimentation. The depositional changes recorded in the stratigraphy at Site U1499 provide important information about the regional climatic and tectonic evolution of the SCS.

Modern day deposition in the SCS consists of several types of sediment, including sand, calcareous silt and clay, and clay progressing in that order as distance from the coast and water depth increase (Wang et al., 1995). Site U1499 sits close to the boundary between deposition of calcareous silt and clay and deep-sea clay, meaning the site will be particularly sensitive to changes in sea level and energy of sediment transport from more proximal environments.

Characteristic fining-upward sequence types

Sequences that have erosive bases and fining-upward transitions from sand to clay are pervasive throughout the cores, but they are more frequent in Units I, III, and V–VII. The coarse-grained basal beds are often >5 cm thick. Sometimes these beds are composed of siliciclastic material, whereas other intervals contain calcareous bioclasts, especially foraminifers (Figure F27). In almost all cases, grains are moderately sorted and subrounded to subangular. As the sequences fine upward, they move into clay-sized particles, which are the dominant size fraction throughout all units. The overlying clay varies in content. Siliciclastic material is almost always the dominant component, but the relative amount of biocalcareous material, particularly nannofossils, changes. Often, the overlying clay intervals are heavily bioturbated.

In Subunits IIIA and IIIB, fining-upward sequences are also present. However, the coarsest material present is generally silt-sized (Figure F27), and silt layers are mostly <2 cm thick. The transition between the deposition of fining-upward silt interbeds and overlying background sediment could not be resolved, has import-

Figure F24. Poorly sorted angular clasts of sedimentary rocks within a reddish brown sandstone matrix, Subunit IXA.



Figure F25. Breccia intervals showing matrix composition changes between subunits: reddish brown to greenish gray sandstone in Subunit IXA and brownish gray sandstone in Subunit IXB. Subunit IXA contains a higher concentration of calcareous microfossils compared to Subunit IXB. Yellow stars = locations of smear slides (XPL) taken from supporting matrix of the breccia intervals.

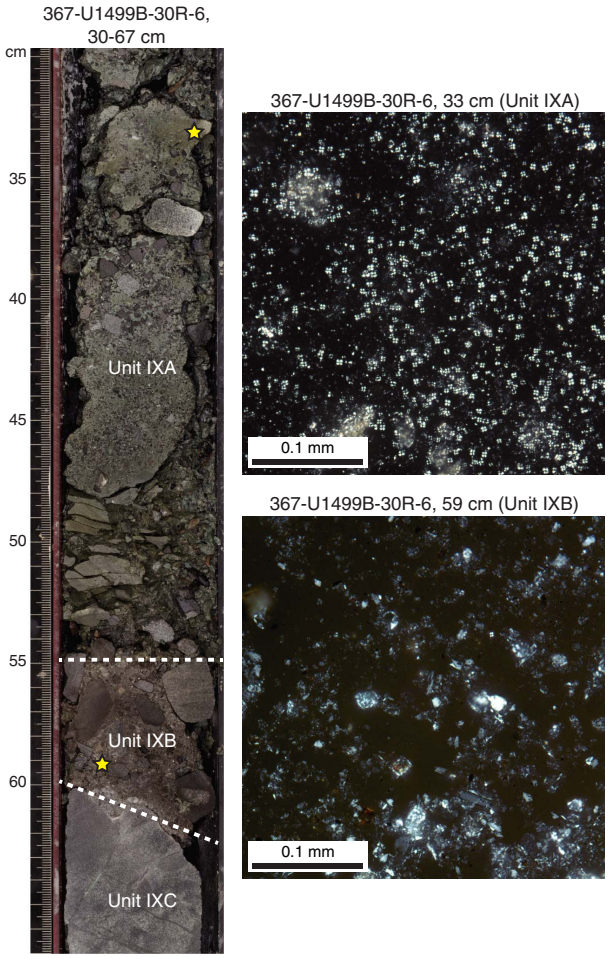

ant implications for accumulation rates at Site U1499. If the series of interpreted distal turbidites stack on top of one another, each represents a relatively short event in geologic time. However, if the deposit fines into clay and then background clay sedimentation occurs, potentially at rates as low as 1 cm/ky (see **Biostratigraphy**; Li et al., 2015b), then the 20–30 cm between recurring thin silt beds could represent 20–30 ky.

Mechanisms of mass transport

Tectonics

The South China Sea Basin formed as a result of continental breakup and rifting, followed by seafloor spreading through the middle Miocene (Briais et al., 1993; Sibuet et al., 2016; Yan et al., 2006). The depositional setting of the sediment at Site U1499 was not strongly influenced by regional tectonics because most of the sediments (middle of Subunit VIIIA and above) were deposited during the late Miocene or later. However, later Neogene and Quaternary tectonic activity, including the collision of the Luzon Arc with Eurasia, subduction in the eastern SCS, and/or the uplift of Taiwan (Li et al., 2015a) could have influenced sediment transport to Site U1499 through the early to middle Miocene (Subunits VIIIB and VIIIA).

Climate

The East Asian monsoon system and its temporal variability is another potential cause of episodic sediment delivery to the SCS. The summer monsoon is characterized by strong rainfall and warm winds from the southwest, whereas the winter monsoon brings strong, dry winds from the north/northeast (Jian et al., 2009). Although the East Asian monsoon was established by the early Miocene (Jia et al., 2003), predating most of the sediments at Site U1499, the intensity of the monsoon system is thought to have increased during the Pliocene–Pleistocene as a response to growing Northern Hemisphere ice sheets and higher amplitude glacial cycles (Clemens et al., 1996; Zachos et al., 2001). Thus, changes in the monsoon system through the Neogene and Quaternary could influence the amount of sediment being delivered to Site U1499, particularly as increased precipitation and glaciation increase continental weathering (Liu et al., 2007).

Slope instability

Because Site U1499 is located on the outer slope, close to the abyssal plain, it is likely to receive sediments transported from upslope. These sediments could be terrigenous in origin or derived from a higher location on the shelf/slope. For example, Unit II contains apparent slump deposits containing high amounts (up to ~50%) of biogenic carbonate (Figure **F9**), indicating shallow water production and transport downslope. Other fining-upward sequences also include biogenic carbonate that was most likely produced higher on the shelf and transported downslope. A potential trigger for this movement could be overloading of weak sediments (Pickering et al., 1989b).

Figure F26. Sandstone cobbles from Subunit IXC, Hole U1499B. Qtz = quartz, Ms = muscovite, Fsp = feldspar, v = lithic volcanic, m = lithic metamorphic, s = lithic sedimentary, p = lithic plutonic. A. Silty sandstone (30R-CC). B. Gravelly sandstone (34R-2). C. Sandy siltstone (38R-1). D–F. Gravelly sandstone (39R-1).

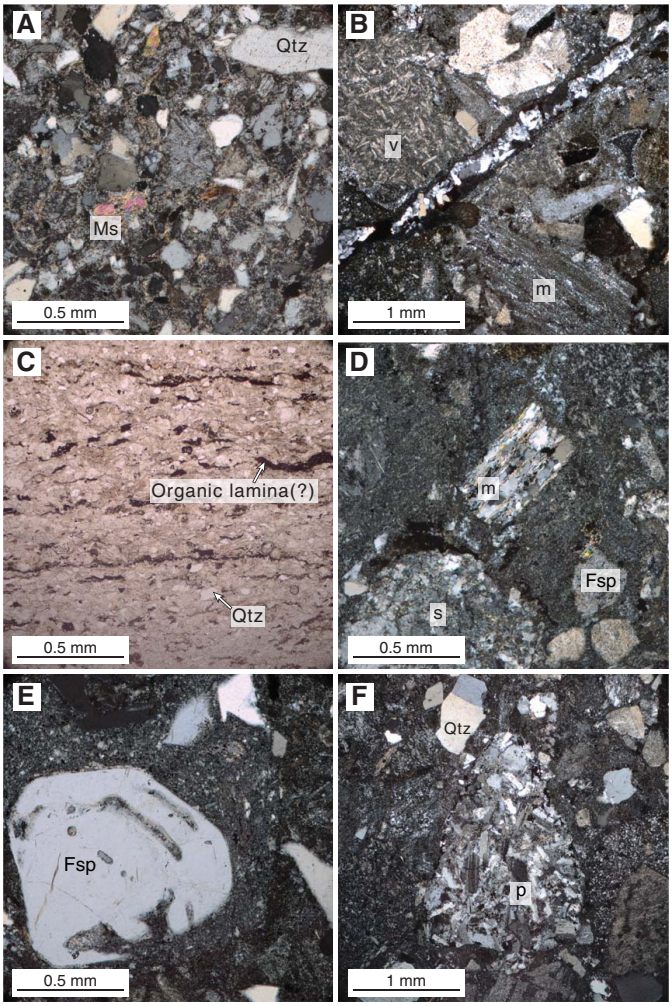

Lateral transport

Site U1499 is susceptible to lateral transport of sediment due to the South China Sea Contour Current, which is a deep-water cyclonic current that may transport sediments sourced from Taiwan and/or the Red River outflow as well as other southern sources (Figure **F28**) to Site U1499 (Liu et al., 2016). Importantly, deposition through this mechanism may lead to the preservation of contourite deposits in the sedimentary record, which can have similar characteristics to turbidites (e.g., fining upward) but a different depositional mechanism (Pickering et al., 1989a). Although the majority of sediment transported downslope is from episodic mass transport, the lateral redistribution of this material is an important and often underappreciated influence on the ultimate burial and preservation of sedimentary sequences.

Ash layers

Four thin ash layers, 2–7 cm thick each, were identified in Cores 367-U1499A-1H through 5H of lithostratigraphic Unit I; no ash layers were observed in any of the underlying units. These ash layers are defined by bioturbated and gradational upper contacts as well as sharp to irregular basal contacts (Figure **F12A**). They show an intermediate to felsic composition with an increasing content of mafic minerals (rare to abundant) downhole from the uppermost to the lowermost layer. The major mafic constituent is amphibole and subordinate accessory clinopyroxene. Amphibole is euhedral to subhedral and appears brown-green in plane-polarized light (Figure **F12B**). Overall, the well-sorted ash layers contain up to ~75% fresh colorless glass shards that range in size from silt to fine sand (0.01–1 mm). Opaque inclusions (presumably oxides) are present in glass shards. Tabular plagioclase crystals as large as 0.1 mm occur throughout the ashes in rare to common abundances.

Red claystone

In Unit VIII, red coloration increases in the claystone and chalk that makes up the dominant lithologies. The transition from gray/brown to reddish brown clay is gradual and can be seen in both core images and color reflectance data. In particular, a* represents psychometric red–green values, where more positive values indicate increasing red content and more negative values indicate greener colors. The shift to more positive values as depth increases in Unit VIII can be seen in Figure **F9**. Based on the interpretation of similar pelagic red clays in the Pacific Ocean, we interpret the increased red content to be a result of deposition in a pelagic environment where accumulation rates are low and bottom waters are oxygenated (Bryant and Bennett, 1988).

Biostratigraphic evidence supports a decrease in sedimentation rates (see **Biostratigraphy**) during deposition of Unit VIII. These environmental conditions allow for oxidation of Fe-bearing siliciclastic minerals from land, producing Fe oxides that have a characteristic red color. Smear slides from Unit VIII confirm the presence of abundant Fe oxides (Figure **F29**). Although the overall trend in a* is toward more positive values, there is also increased scatter in Unit VIII. The shifts to more negative a* values correspond to greenish layers within the red clay, which we interpret to be related to diagenesis from reducing fluids flowing through fractures in the clays.

In Subunit VIIIA, carbonate content is very low (Figure **F9**). Three possible scenarios could lead to this. First, there may have been production of biogenic carbonate in the water column that fell below the carbonate compensation depth (CCD), leading to dissolution of carbonate. Slow sedimentation rates would aid in this process because sediments sit at or near the sediment–water interface for longer periods of time, allowing for more dissolution. A second scenario involves reduced primary productivity, leading to no or little biogenic carbonate production during the deposition of Subunit VIIIA.

A third scenario involves the geographic location of the site. Site U1499 is positioned on top of a structural high bounded by two sedimentary basins. Sediments coming from the continent could have been trapped in the continent-side basin, causing a reduced and finer sedimentary input at the site location and reducing siliciclastic sedimentation rates on the structural high, allowing for higher carbonate deposition (shown in the abundance of calcareous sediment in Subunit VIIIB). When the basin was filled, the site would no longer be isolated, and siliciclastic sedimentation would dilute the carbonate deposition.

Regardless of which scenario actually occurred, Subunits VIIIA and VIIIB are markedly different. In Subunit VIIIB (starting at Section 367-U1499B-26R-4), carbonate content drastically increases to a maximum of 65%. The dominant components of these cores are nannofossils, suggesting high primary productivity and/or conditions favorable to preservation. The reddish color remains in the

Figure F27. Fining-upward sequences seen throughout Site U1499 intervals. A. Sand-based fining-upward sequence. B. Silt-based fining-upward sequence. C. Fining-upward sequence with laminated foraminiferal sand at the base. The uppermost clay contains bioturbation, including *Zoophycos* and *Planolites* trace fossils. Note biscuiting drilling disturbance.

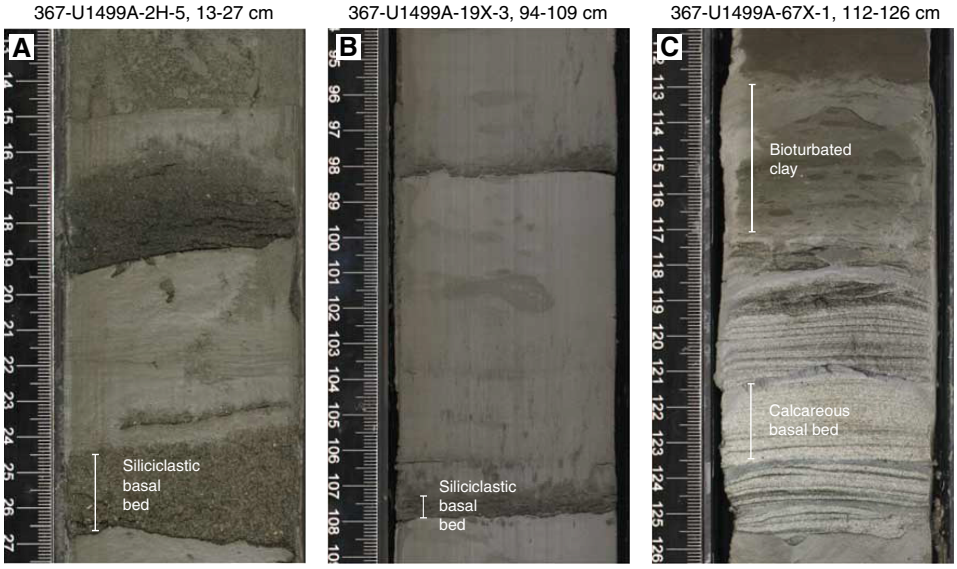

Figure F28. South China Sea and surrounding region. Redrawn from Liu et al. (2016).

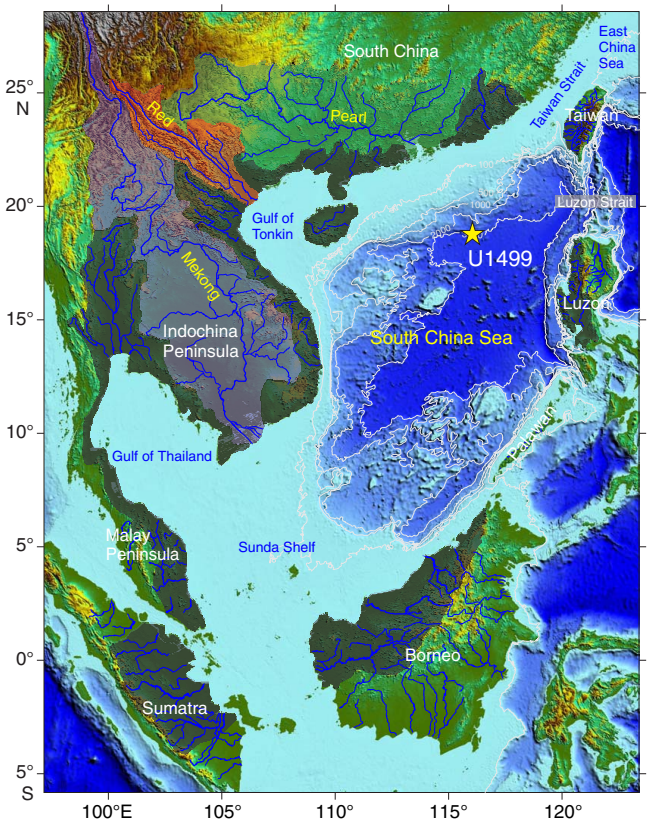

Figure F29. A. Red claystone. B. Abundant iron oxides that glow orange under XPL (top) and appear brownish orange in PPL (bottom).

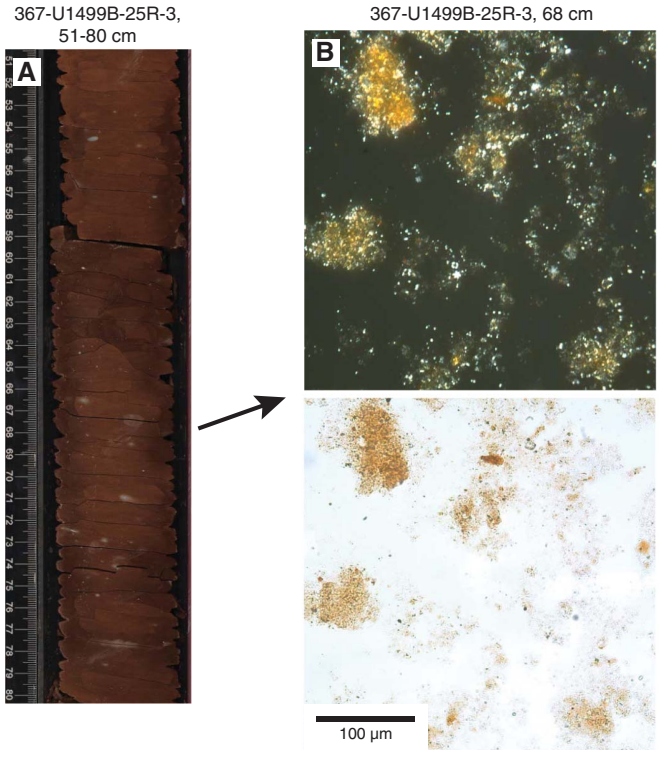

minor clays associated with the chalks, indicative of an oxygenated environment similar to Subunit VIIIA. However, it is possible that this site was above the CCD during deposition of Subunit VIIIB, leading to enhanced preservation of carbonate.

Interpretation of Unit IX

The gravel and breccia intervals of Unit IX (Section 367-U1499B-30R-2 through Core 45R) are divided into three subunits based on the compositional changes in the fine-grained supporting matrix and changes in clast shape and size (Figures **F24**, **F25**). However, the clasts have similar lithologies throughout Unit IX.

Subunit IXA

Subunit IXA is composed of sandstone and claystone clasts in a pelagic matrix. Clast concentration and clast size increase downsection. The clasts are angular. Oblique bedding was observed in the upper part of the subunit, whereas the lower part is more chaotic. Identifiable bioclasts in Core 367-U1499B-30R suggest reworking (see **Biostratigraphy**), and the base of Subunit IXA is irregular and could be erosive (Figure **F25**). The massive structure, poor sorting, and matrix-supported character of this unit suggest deposition by gravity-flow processes.

Subunit IXB

Subunit IXB was defined based on (1) increased rounding of pebble-sized clasts compared to the angular to subrounded clasts of Subunit IXA, (2) change in color of the matrix, (3) poor sorting, (4) presence of detrital pyrite grains in the matrix, (5) lack of nannofossils in the matrix, and (6) irregular and potentially erosive contact with Subunit IXA (Figure **F25**).

The base of Subunit IXB is inclined above a large sandstone cobble of Subunit IXC. Four scenarios are proposed for this subunit:

1. It was formed in the same environment as Subunit IXA.
2. It corresponds to the matrix of Subunit IXC, which was washed out during drilling.
3. It has a distinct primary origin different than that of Subunits IXA and IXC.
4. The matrix is distinct from Subunits IXA and IXC because of contamination by drilling slurry.

Subunit IXC

The depositional setting and source of the gravel of Subunit IXC is unknown, but the angularity and size of many of the clasts suggest that transport distances likely were short. The clasts are composed of sedimentary rock, mostly sandstone similar to the clasts of Subunits IXA and IXB. The composition and stratigraphic architecture of the Subunit IXC matrix is also uncertain because recovery was low (<10%) and drilling disturbance was high in the cored intervals (Cores 367-U1499B-30R through 45R). *P*-wave velocity values from measurements of individual cobbles from Subunit IXC range from 2.7 to 5.5 km/s, whereas downhole logging sonic velocity measurements range from 2.3 to 4.1 km/s (see **Downhole measurements**). The reduced velocity measurements from the downhole logging imply that the cobbles of Subunit IXC are supported by a finer grained, lower velocity matrix.

Although Subunit IXC cores are heavily fragmented and were recovered only as cobbles due to drilling disturbances, the gravel fragments can be studied to further understand provenance and transport mechanisms. Thin sections of the cobbles were made and analyzed for each major cobble lithology type (Figure **F26**). Five major cobble lithology types were identified for Subunit IXC, as well as several other minor lithologies. The major lithologies include gray fine-grained sandstone, gray medium-grained gravelly sandstone, very dark gray fine-grained sandy siltstone, layered gray/very dark gray medium-grained sandstone, and gray medium-grained (low-grade) metasandstone.

A variety of framework grains were identified and photographed for each thin section in this subunit (Figure **F26**). The framework grains include abundant mono- and polycrystalline quartz, feldspar, muscovite, and lithic grains of igneous, metamorphic, and sedimentary origin. Small inclusions of apatite and zircon were also identified within some of these grains (as shown in the feldspar grain in Figure **F26E**). Thin sections made of the gray medium-grained gravelly sandstone included volcanic grains with plagioclase-phyric texture, plutonic grains, metamorphic grains with gneissic texture, and sandstone fragments containing quartz and feldspar (Figure **F26B, F26D, F26F**). Thin sections made of the other main cobble lithologies have similar compositions with varying grain size. The thin section made of the fine-grained very dark gray sandy siltstone, shown in Figure **F26C**, contains abundant silt- to fine sand–sized quartz and mica grains, along with common lithic and chert fragments. It also contains strands of opaque sediment inferred to be organic or sulfide-rich lamina. The pervasive fine-grained mica in the clay matrix of the sandstone cobbles could have formed in response to low-grade metamorphism that occurred prior to deposition of the gravel of Subunit IXC.

The pervasive presence of lithic grains in most of the sandstone cobbles highlight a complex sedimentological history that occurred before the transport and deposition of the gravel (Figure **F26**). The lithic grains that compose the cobbles were sourced from a variety of sedimentary, metamorphic, and igneous rocks. Their presence also indicates multiple sedimentary cycles. Qualitatively applying the provenance fields of Dickinson et al. (1983), we infer that the sediments within the cobbles were sourced from a magmatic arc or recycled orogen. The angularity and coarseness of some of the grains within the cobbles implies that the sediments accumulated in proximity to their source and were not transported over long distances.

Well-lithified cobbles represent most of the recovery in Subunit IXC. However, moderately consolidated dark clayey silt to sandy gravel was also recovered in some intervals (e.g., Cores 367-U1499B-38R, 39R, 41R, 42R, and 43R). This material could potentially correspond to the matrix of Subunit IXC, which was mostly unrecovered. This moderately consolidated lithology is barren of microfossils. The high organic carbon content of 4.9 wt% in some black, fissile clasts (interval 38R-1, 74–77 cm) could mark an important terrigenous component in the sedimentation of Subunit IXC.

Structural geology

Site U1499 is located on the northwestern flank of Ridge A at the COT of the northern SCS margin. Drilling at Site U1499 penetrated a sedimentary sequence reaching Oligocene deposits followed by polymict gravels of unknown age and undetermined thickness. The tilting of sedimentary bedding (Figure **F30**) and deformation structures observed at Site U1499 are limited to lithostratigraphic Units II and VII–IX.

Unit II

Unit II is bounded by two erosive contacts (Figure **F31**) and is composed of greenish gray clay-rich calcareous ooze and dark greenish gray nannofossil-rich clay beginning at Section 367-U1499A-6H-3, 35 cm. The color variations of Unit II highlight the deformation structures. The top of Unit II is slightly deformed with few inclined beds. In Sections 6H-5, 100 cm, to 8H-1, 90 cm, the bedding is flat, and no deformation structures were observed. Variations of the bedding dip and centimeter-scale synsedimentary folds (Figure **F32**) were observed in Sections 8H-1, 90 cm, to 8H-4, 126 cm, where a 17 cm thick dark clayey silt layer (Figure **F31**) occurs. Below this layer, the cores present several bedding-dip variations and synsedimentary folds downhole to the base of Unit II (Section 11H-5, 104 cm). However, we note that the deformation in-

Figure F30. Lithostratigraphic summary of Site U1499 with bedding dips in Holes U1499A and U1499B. Flat-lying bedding and bedding dips <5° were not measured.

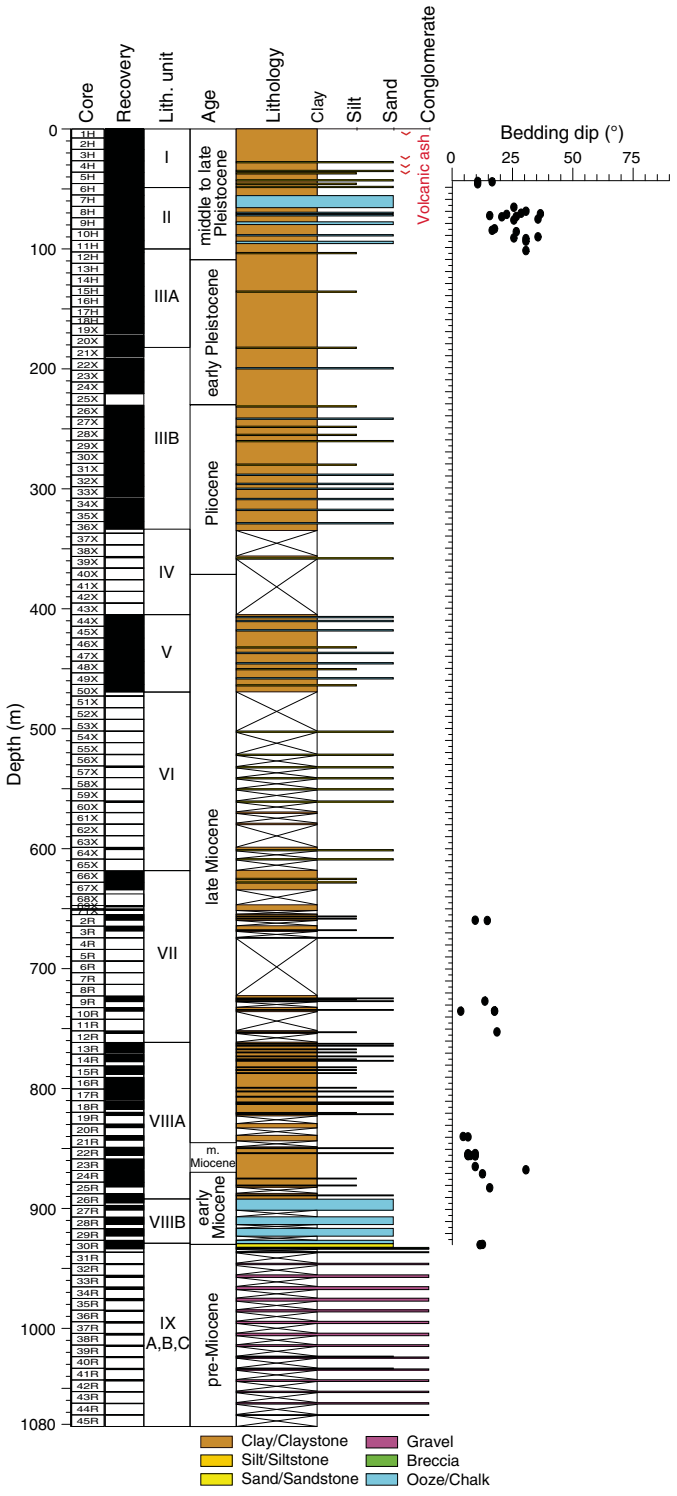

tensity is not homogeneous throughout Unit II. Additionally, one subvertical normal fault was observed (Figure **F32**).

Interpretation

The deformation structures observed in Unit II indicate slump activity. Paleontological correlations show that Unit II contains older microfossils than Unit III, but within Unit II the ages of the species are still increasing with depth (Figure **F31**). This observation suggests that slumping moved the strata from upslope into the sedimentary basins with limited internal deformation or sediment reworking. Unit II may correspond to two slump events separated by the 17 cm thick dark clayey silt layer.

Units VII and VIII

Units VII and VIII are mainly composed of claystones and sandstones. Tilted bedding observed in Cores 367-U1499B-2R through 25R has an average dip of 11° with a standard deviation of 6°. Only six normal, one strike slip, and eight undetermined faults were observed in Cores 12R through 30R. The mean dip of these faults is 48° with a standard deviation of 24°. Some of these faults have slickenside surfaces (Figure **F32**); however, the offset can rarely be determined and never exceeds 2 cm. Reorientation to the geographical reference frame using paleomagnetic measurements was attempted, but the shipboard demagnetization process was not effective deeper than Unit VI due to the presence of hematite. Lithification in Units VII and VIII is more developed than in shallower units; therefore, these faults likely may be related to compaction and lithification of the claystones (Figure **F33**). Tilted bedding is often related to contacts with sandy layers or associated with layers containing a significant proportion of coarser sand-sized material. Veins 1–2 mm thick filled by magnetite or other Fe oxide showing single vein connectivity appear in Unit VIII. Interval 14R-3, 31–49 cm, revealed a subrounded triangular sandy structure occupying one side of the core (Figure **F32**). The surrounding claystone is deformed, in particular above the sandy formation, which suggests that the deformation took place in soft sediments below the seafloor.

Unit IX

Unit IX is composed of three subunits (IXA, IXB, and IXC). Subunit IXA consists of matrix-supported breccia and sandstone with polymict clasts. Subunit IXB is nannofossil-barren dark gray matrix-supported breccia. Subunit IXC is formed by polymict gravel (Figure **F24**). A bedding dip of 11° was observed in the upper part of Subunit IXA (Sections 367-U1499B-30R-2, 105 cm, to 30R-3, 110 cm). The subunit's lower part contains pebble-sized clasts. The alignment of some of these clasts may reflect sedimentary bedding, but the overall organization is chaotic. Clast proportion and angularity generally increase downhole. The paleontological record of Subunit IXA indicates reworking of foraminifers and nannofossils; however, older species were observed at the bottom of this subunit (Figure **F37**). Although the biostratigraphy of this section is not clear, the time gap between the older and younger species is ~5 My in only 4.3 m (see **Biostratigraphy**), which may suggest that the deposition was discontinuous. Subunit IXA is interpreted as a gravity flow deposit accumulated on a slope showing a succession of several deposition events. Subunit IXA may show an erosive basal contact boundary (Figure **F24**). Subunit IXB does not exhibit any clear structures or sedimentary bedding. Subunit IXB was distinguished from the two other subunits, but it could also belong to Subunit IXA, be the washed matrix of Subunit IXC, be a different subunit, or be induced by drilling. The gravel of Subunit IXC comprises pebble- to boulder-sized sandstones, siltstones, and breccias, but no matrix was recovered. Several types of sandstone have sedimentary bedding, and some contain vein networks principally filled by quartz, pyrite, and/or Fe oxides (in altered parts). In addition, fractures were observed in the gravel clasts. However, their orientations cannot be related to a tectonic event because the age of the

Figure F31. Lithostratigraphic summary correlated to biostratigraphic ages and slump events in Unit II, Site U1499. Age estimates are based on age correlation of foraminifers and nannofossils. A. Erosive contact separating Units I and II. B. Dark clayey silt layer separating two slump events. C. Erosive contact separating Units II and III.

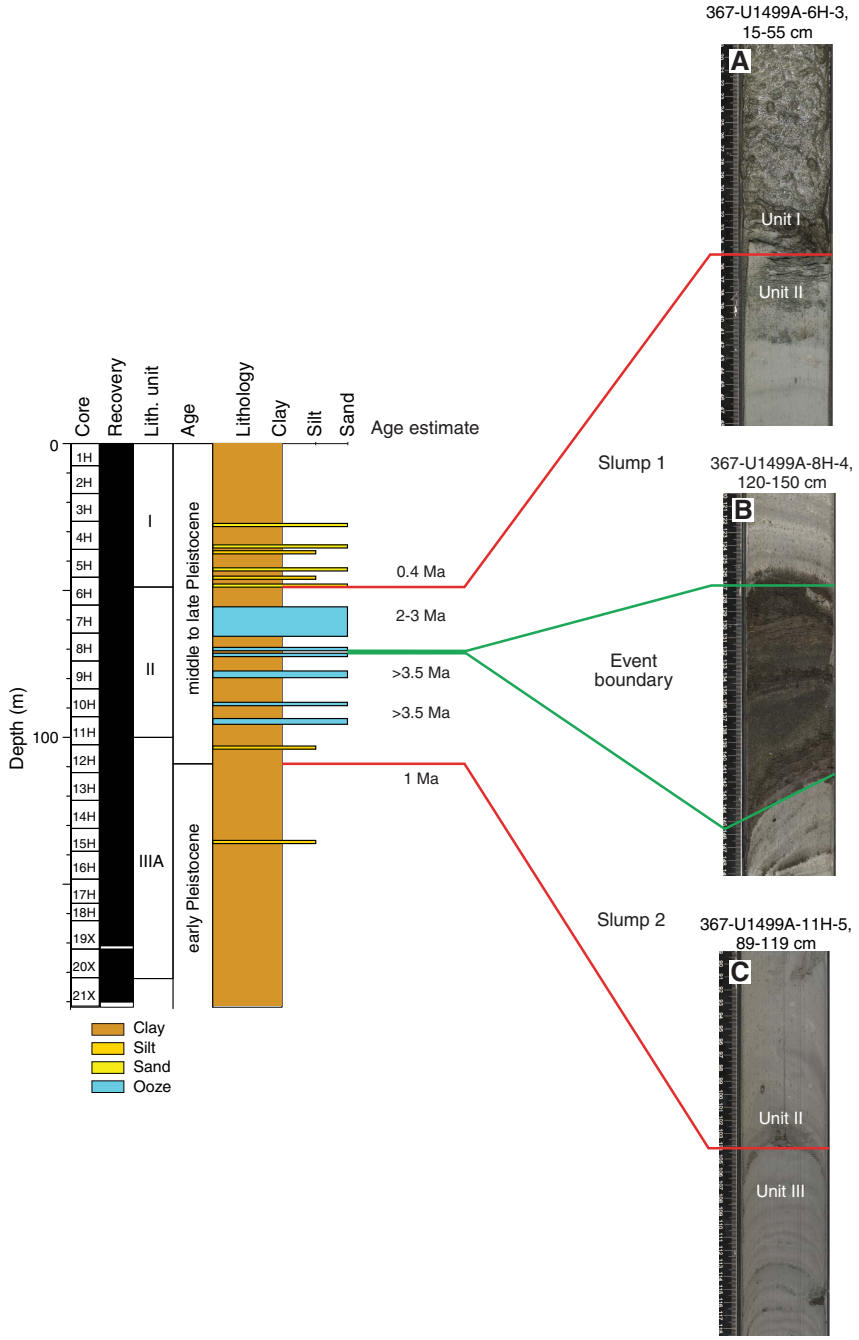

first deposition, the lithification, and the age of resedimentation of the pebble- to cobble-sized clasts remain unknown. Paleomagnetic inclination data from these clasts show a large scatter, which also suggests that these cobbles were not formed in situ but were transported (see **Paleomagnetism**). In addition, only a weak (low-grade) metamorphic imprint is found in a few clasts of Subunit IXC.

Comparison and interpretation

The determination of pre-, syn-, and postrift sequences and their relative ages is key for characterizing the tectonic evolution of the SCS margin. At Site U1499, the significance of Unit IX is not clear due to the lack of a complete stratigraphy, clear structural information, and unequivocal biostratigraphic data. However, the major sedimentological differences between Subunits IXA and IXC may suggest a drastic change in the depositional environment from potentially more continental to pelagic environment; this change may be consistent with a sedimentation hiatus.

Interestingly, the ODP Iberia margin Site 1069 shows sedimentation patterns (Shipboard Scientific Party, 1998) that are strikingly similar to Unit IX at Site U1499. At Site 1069, the 2.3 m thick Unit IV, which contains slump deposits that rework clasts of deeper units into hemipelagic material, lies between hemipelagic sediments and

Figure F32. Structures in Unit II, Hole U1499A. A. Contorted subvertical beds. B. Centimeter-scale synsedimentary fold. C. Synsedimentary fold. D. Normal subvertical fault.

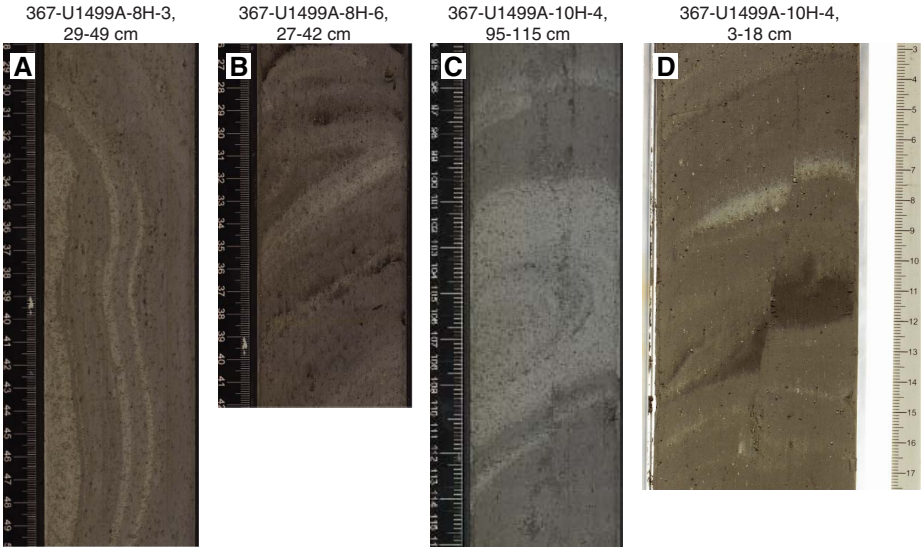

Figure F33. Structures in Subunit VIIIA, Hole U1499B. A. Compaction-related fault. B. Perpendicular view of compaction-related fault. C. Sedimentary structure with a mass of sand with deformed finer grained claystones above.

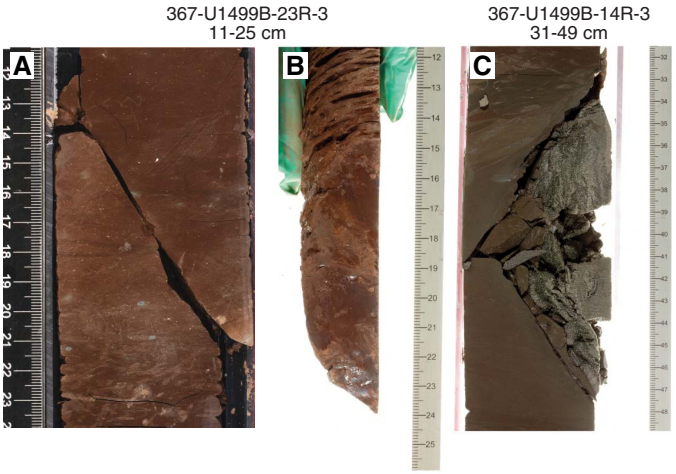

a deeper Unit V (Shipboard Scientific Party, 1998). This deeper Unit V has very low recovery (<3%) and is characterized by an extremely fragmented Subunit VA that contains limestone clasts and an Upper Jurassic (Tithonian) fossil assemblage. In contrast, the lower Subunit VB is composed of fossil-barren, polymict conglomerates with rounded pebble- to boulder-sized gravel of igneous, sedimentary (sandstones), and metamorphic (gneiss) origin. Because the Upper Jurassic age corresponds to the initiation of rifting on the Iberia margin, Subunit VB was interpreted as prerift (Shipboard Scientific Party, 1998). Based on such analogy with Site 1069, Subunit IXA might correspond to syn- to early postrift sedimentation, whereas Subunit IXC may represent prerift sediments containing pebbles and boulders of an older eroded sedimentary basin. Following this interpretation, the presence of prerift sedimentary rock would imply that the targeted high is a tectonic block composed of upper continental crust. However, due to the lack of age and deformation constraints at Site U1499, such interpretation remains speculative. Another interpretation is that the detrital facies of Subunit IXC corresponds to a synrift sequence related to tectonic activity during the rifting of the SCS.

Biostratigraphy

All core catcher samples from Holes U1499A and U1499B were analyzed for calcareous nannofossil and foraminiferal content. Additional samples were taken from the split-core sections when necessary to refine the ages between core catcher samples. Preservation of microfossils varies from poor to very good. Overgrown and abundant broken fragments are common in the sediment sequences. The total abundance varies from barren to abundant, but most samples exhibit some reworking.

Twenty-eight biostratigraphic datums were recognized from Holes U1499A and U1499B, revealing an apparently continuous succession of Oligocene to Pleistocene age at Site U1499 (Table **T3**; Figures **F34**, **F35**). No nannofossils or foraminifers were found in Sample 367-U1499B-30R-CC through Section 38R-1 (933.66 m to the bottom of the Hole U1499B). An age-depth plot based on the biostratigraphic and paleomagnetic data (see **Paleomagnetism**) allows a direct comparison of the data (Figure **F35**).

Cores 367-U1499A-1H through 5H (0 to ~45 m) represent the middle–late Pleistocene sequence. Preservation of calcareous nannofossils is moderate, but planktonic foraminifers are poorly preserved. The estimated sedimentation rate is ~130 mm/ky.

Cores 367-U1499A-6H through 11H (45 to ~112 m) correspond to lithostratigraphic Unit II and are defined as the slump deposit. Preservation is very good for all calcareous microfossils. The reworked microfossil assemblages are dominated by the Pliocene–early Pleistocene species.

Cores 367-U1499A-11H through 31X (112 to ~288 m) represent the Pliocene–early Pleistocene sequence with a sedimentation rate of ~50 mm/ky. Fossil preservation is moderate to good. Several events could be placed with a high degree of certainty to define the boundaries. The last appearance datum (LAD) of *Discoaster brouweri* (1.93 Ma) and the first appearance datum (FAD) of *Globorotalia tosaensis* (3.35 Ma) indicate the Pleistocene/Pliocene boundary

Table T3. Biostratigraphic events, Site U1499. PF = planktonic foraminifer, CN = calcareous nannofossil. T = top/last appearance datum, B = bottom/first appearance datum, Bc = bottom/first common appearance datum (acme). **Download table in CSV format.**

Epoch		Fossil group	Zone	Event	Core, section, interval (cm)	Top depth CSF-A (m)	Age (Ma)
					367-U1499A-		
Pleistocene		PF	PT1b	T *Globigerinoides ruber pink*	2H-CC	17.33	0.12
		CN	NN21/NN20	B *Emiliania huxleyi*	2H-CC	17.33	0.29
		PF	PT1b	Bc *Globigerinoides ruber pink*	5H-CC	45.68	0.40
		CN	NN20/NN19	T *Pseudoemiliania lacunosa*	5H-CC	45.68	0.44
		PF	PT1a	T *Globigerinoides obliquus*	13H-CC	121.28	1.30
		CN	NN19/NN18	T *Discoaster brouweri*	20X-CC	181.70	1.93
Pliocene		PF	PL5	B *Globorotalia tosaensis*	27X-CC	249.77	3.35
		CN	NN16	T *Sphenolithus* spp.	29X-CC	269.10	3.54
		PF	PL4/PL3	T *Sphaeroidinellopsis seminulina*	29X-CC	269.10	3.59
		CN	NN16/NN15	T *Reticulofenestra pseudoumbilica*	30X-5, 72	275.82	3.70
		CN	NN15/NN14	T *Amaurolithus tricorniculatus*	31X-CC	288.54	3.92
		PF	PL2/PL1	T *Globoturborotalita nepenthes*	31X-CC	288.54	4.37
Miocene	late	CN	NN12/NN11	T *Discoaster quinqueramus*	43X-CC	395.20	5.59
		PF	M14	T *Globoquadrina dehiscens*	48X-CC	453.61	5.92
		PF	M13b	B *Pulleniatina primalis*	50X-CC	469.32	6.60
					367-U1499B-		
		CN	NN11/NN10	B *Discoaster quinqueramus*	2R-1, 128	656.28	8.12
		PF	M13b/M13a	B *Globorotalia plesiotumida*	2R-CC	659.76	8.58
		CN	NN10	T *Discoaster bollii*	9R-2, 12	724.42	9.21
		CN	NN9	T *Catinaster coalitus*	10R-CC	735.62	9.69
		PF	M12/M11	T *Paragloborotalia mayeri/siakensis*	17R-CC	808.97	10.46
		CN	NN8/NN7	B *Catinaster coalitus*	18R-2, 94	812.64	10.89
	middle	CN	NN6/NN5	T *Sphenolithus heteromorphus*	22R-5, 98	855.24	13.53
		CN	NN4	T abundant *Discoaster deflandrei* group	23R-CC	867.41	15.80
	early	PF	M4a/M3	T *Catapsydrax dissimilis*	25R-CC	882.13	17.54
		CN	NN4	B *Sphenolithus heteromorphus*	26R-2, 89	890.09	17.71
Oligocene		CN	NN1/NP25	T *Reticulofenestra bisecta* (>10 µm)	30R-2, 34	928.33	23.13
		CN	NP25	T *Sphenolithus distentus*	30R-3, 79	930.10	26.84

(2.58 Ma) lies between Samples 20X-CC and 27X-CC. The FAD of *Sphaeroidinellopsis seminulina* (3.59 Ma) indicates the late/early Pliocene boundary is in Sample 29X-CC (269.15 m).

Cores 367-U1499A-31X through 367-U1499B-18R (288 to ~812 m) correspond to the late Miocene–early Pliocene sequence and have a sedimentation rate of ~80 mm/ky. The microfossils are generally sparse and poorly to moderately preserved throughout the succession. Five nannofossil and four foraminiferal datum events are identified in this interval. The Pliocene/Miocene boundary (5.33 Ma) is close to the LAD of *Discoaster quinqueramus* (5.59 Ma) in Sample 367-U1499A-43X-CC (395.15 m).

Cores 367-U1499B-18R through 30R (812 to ~928 m) correspond to lithostratigraphic Unit VIII and were assigned to the early–middle Miocene. Microfossils are moderately abundant and preserved in this interval. Eight biostratigraphic events constrain this interval well, and calibrated biohorizons allow us to estimate extremely low sedimentation rates (~8 mm/ky) during the early to late Miocene.

Based on the LADs of *Reticulofenestra bisecta* (>10 µm; 23.13 Ma) and *Globigerina ciperoensis* (22.9 Ma) in Sample 367-U1499B-30R-2, 35–37 cm (928.34 m), the Miocene/Oligocene boundary is tentatively placed within Section 30R-2. This placement is also supported by the regional correlation of the early to middle Miocene red claystone in this site with Sites U1500 and U1502.

Sections 367-U1499B-30R-3 through 30R-6 (~928 to ~933 m) were studied by analyzing 12 additional samples for nannofossil and foraminiferal biostratigraphy (Figure **F36**). This succession comprises microfossils from the early Oligocene to the late Oligocene. Compared to the generally moderate preservation at Site U1499, the well-preserved and abundant calcareous nannofossils in Sections 30R-3 through 30R-6 indicate that they are probably transported and reworked, a theory that is also supported by the sorted foraminifers at this succession. This theory makes the age determination less reliable, and only one nannofossil event is given. Hence, it is difficult to calculate the sedimentation rate. The resolution of the age discrepancy between foraminiferal and nannofossil bioevents given for this interval (question mark in Figure **F35**) awaits further post-cruise studies.

Calcareous nannofossils

Calcareous nannofossil biostratigraphy at Site U1499 is based on the analyses of all core catcher samples and additional split-core samples from Holes U1499A and U1499B (Tables **T4**, **T5**). Calcareous nannofossil zonation is based on the scheme of Martini (1971), and calibrated ages for bioevents are from Gradstein et al. (2012). Calcareous nannofossil abundances vary in the succession; they are more abundant in the upper portion within bioclastic- and nannofossil-rich clay beds and rare or absent in the more lithified units below Core 367-U1499B-30R (~933 m). Various overgrowths on nannofossils, reworked specimens, and abundant broken fragments, especially among discoasters, are common in the whole sediment sequences.

In general, the calcareous nannofossil assemblages and preservation at Site U1499 are variably affected by carbonate dissolution and turbidites. Sixteen nannofossil biostratigraphic datums were recognized in the Oligocene to Pleistocene sediment sequence (Table **T3**). The oldest nannofossil event identified, the LAD of *Spheno-*

Figure F34. Biostratigraphic and paleoenvironmental summary, Site U1499. Calcareous nannofossil and planktonic foraminifer biozonal assignments with paleoenvironmental information are provided by benthic foraminifers (BF).

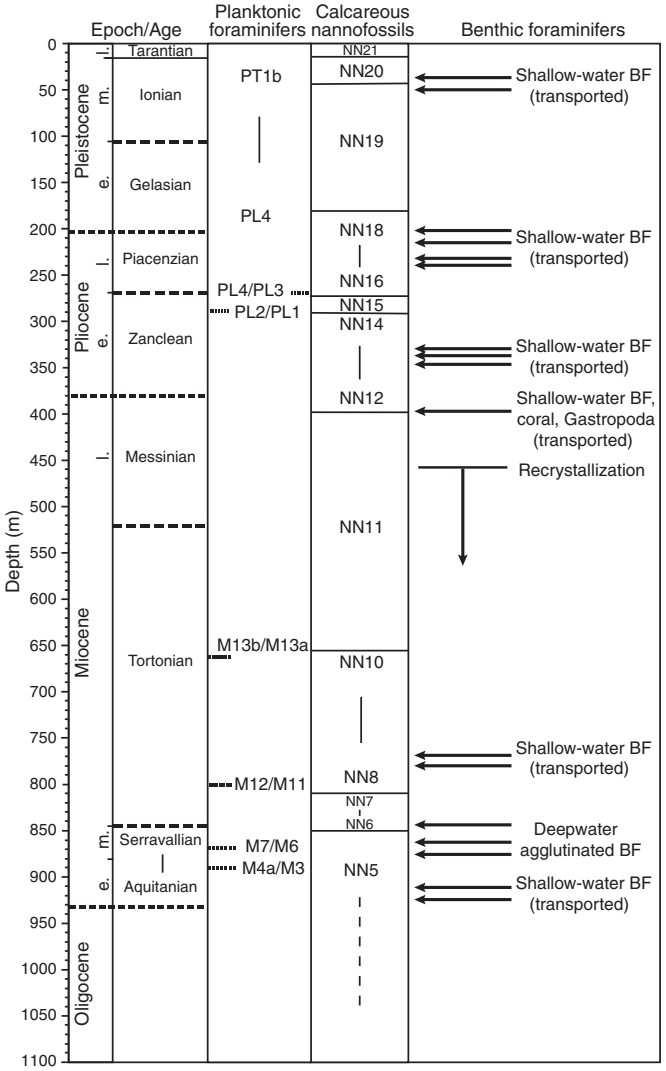

lithus distentus, occurs at 930.1 m, indicating an age <26.84 Ma for most of the sedimentary sequence at Site U1499.

Pleistocene

The top of Hole U1499A is dated as the middle–late Pleistocene (<0.29 Ma) based on the presence of *Emiliania huxleyi* (marker species for Zone NN21) in Samples 1H-CC through 2H-CC. Recognition of the FAD of *E. huxleyi* (0.29 Ma) in Sample 2H-CC defines the base of Zone NN21. Samples 3H-CC and 4H-CC were assigned to Zone NN20 based on the absence of both *E. huxleyi* and *Pseudoemiliania lacunosa*. The LAD of *P. lacunosa* (0.44 Ma) in Sample 5H-CC (45.68 m) defines the top of Zone NN19. The interval from Cores 6H through 11H (48.85–100.04 m) consists of calcareous ooze and nannofossil-rich clay. Nannofossils are exceptionally well preserved, and the assemblage is mostly represented by *P. lacunosa, Calcidiscus macintyrei, D. brouweri, Discoaster pentaradiatus, Discoaster tamalis*, and *Sphenolithus abies*. Based on the occurrence of these species, this interval could be assigned to the Pliocene–early Pleistocene.

In Samples 11H-CC through 19X-CC (103.09–170.93 m), however, the nannofossil assemblage is dominated by typical middle–early Pleistocene taxa such as *Gephyrocapsa* spp. and *P. lacunosa*. For this reason, the interval between Cores 6H and 11H is considered as reworked and related to the occurrence of a slumping deposit (see **Lithostratigraphy**), and Samples 11X-CC through 19X-CC are assigned to Zone NN19. Because of the poor preservation, many specimens of *Gephyrocapsa* spp. are lacking in clear bridges, which makes their identification difficult; moreover, specimens of large *Gephyrocapsa* spp. (>5.5 µm), *C. macintyrei,* and *Reticulofenestra asanoi* are very rare and occur discontinuously, preventing the recognition of the subsidiary events that divided Zone NN19.

Zone NN18 is marked by the LAD of *D. brouweri* (1.93 Ma) in Sample 20X-CC (181.70 m). However, because of the poor preservation of Samples 20X-CC through 26X-CC (181.70–240.14 m), these events could not be identified until Sample 27X-2, 75 cm (242.25 m), making it difficult to recognize the true depths of Zone NN17. Some subsidiary events such as the LADs of *Discoaster tri-radiatus* (1.95 Ma) and *D. tamalis* (2.80 Ma) could add information to distinguish the Zone NN18–NN16 interval, but these species are too rare and occur too discontinuously in the sample to allow clear identification of their last occurrences.

Pliocene

The bottom of Zone NN16 is defined by the LAD of *Sphenolithus* spp. (3.54 Ma) in Sample 367-U1499A-29X-CC (269.10 m). The Zone NN16/NN15 boundary was assigned in Sample 30X-5, 72 cm (275.8 m), based on the LAD of *Reticulofenestra pseudoumbilicus* (3.70 Ma). The LAD of *Amaurolithus tricorniculatus* (3.92 Ma) in Sample 31X-CC (288.54 m) marks the top of Zone NN14. The interval between Cores 36X and 43X (327.64–395.20 m) is predominantly a long sequence of assemblages with very similar nannofossil composition. Poor preservation and rare occurrence of large coccoliths/nannoliths such as *Ceratolithus, Amaurolithus*, and *Triquetrorhabdulus* make it difficult to identify the boundaries from Zones NN15 to NN12.

Miocene

Eight events occur in the Miocene strata of Holes U1499A and U1499B (Table **T3**). The LAD of *D. quinqueramus* (5.59 Ma) marks the top of Zone NN11 in Sample 367-U1499A-43X-CC (395.20 m), which corresponds to the top of the upper Miocene (Pliocene/Miocene boundary at 5.33 Ma). *D. quinqueramus* occurs continually until Sample 367-U1499B-2R-1, 128 cm (656.28 m), which is the uppermost core taken in Hole U1499B, allowing reliable biostratigraphic correlation between the deep part of Hole U1499A and the uppermost section of Hole U1499B (Tables **T4**, **T5**). The FAD of *D. quinqueramus* (8.12 Ma) in Sample 367-U1499B-2R-1, 128 cm, defines the bottom of Zone NN11. Zones NN11–NN9 could not be reliably identified in samples from Cores 2R through 17R (656.76–808.97 m) due to the poor preservation, the absence of nannofossils in several core catchers, or very low recovery.

The LAD of *Discoaster bollii* (9.21 Ma) within Zone NN10 occurs in Sample 9R-2, 12 cm (724.42 m). The LAD of *Catinaster coalitus* (9.69 Ma) within Zone NN9 occurs in Sample 10R-CC (735.62 m). The FAD of *C. coalitus* (10.89 Ma) defines the top of Zone NN7 in Sample 18R-2, 94 cm (812.64 m). Low abundance and barren samples between Cores 19R and 21R prevented identification of the boundary between Zones NN7 and NN6 and make the last common appearance (LCA) of *Cyclicargolithus floridanus* event (13.28 Ma) less reliable at Site U1499. The LAD of *Sphenolithus hetero-*

Figure F35. Age-depth model, Site U1499. Plotted event data are in Tables T4 and T8 (see Paleomagnetism). Top = last appearance datum, bottom = first appearance datum.

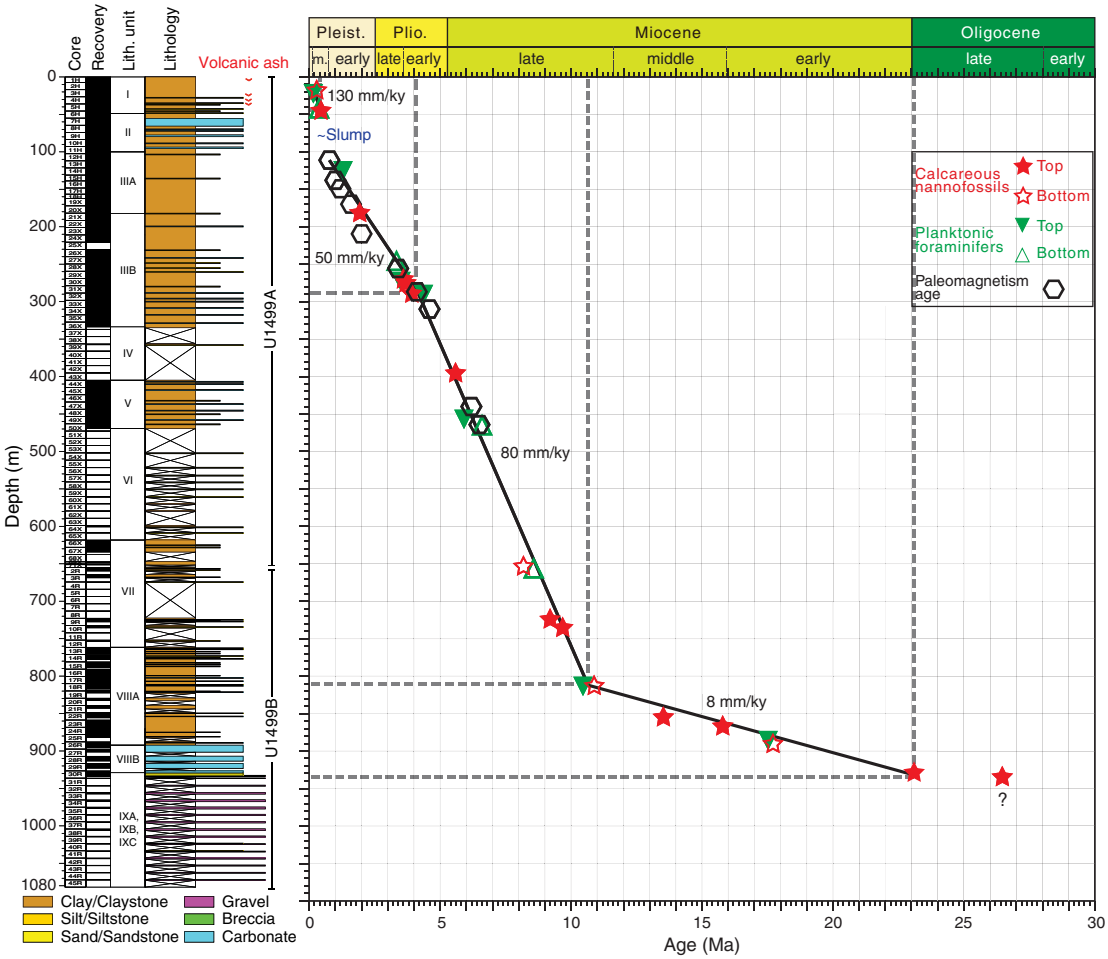

morphus (13.53 Ma), which defines the top of Zone NN5, occurs in Sample 22R-5, 98 cm (855.24 m).

The boundaries between Zones NN5 and NN2 could not be identified; however, the LAD of *Discoaster deflandrei* group (15.80 Ma) and the FAD of *S. heteromorphus* (17.81 Ma) within Zone NN4 occur in Samples 23R-CC (867.41 m) and 26R-2, 89 cm (890.09 m), respectively. The middle/early Miocene boundary falls between the last aforementioned datums.

Oligocene

The LAD of *R. bisecta* (>10 µm; 23.13 Ma), which corresponds to the Zone NN1/NP25 boundary, occurs in Sample 367-U1499B-30R-2, 34 cm (928.33 m). The Miocene/Oligocene boundary should thus be placed between Samples 30R-1, 59 cm, and 30R-2, 34 cm. Throughout Sections 30R-3 through 30R-6, an early late Oligocene assemblage composed of *Sphenolithus ciperoensis, Sphenolithus predistentus, S. distentus,* and *R. bisecta* was found from the brownish to greenish matrix-supported breccia. The LAD of *S. distentus* (26.84 Ma) is found in Sample 30R-3, 79 cm (930.10 m). The nannofossil preservation in this interval is much better than in the upper parts. Considering the features of the sediments, the occurrence of these species in these sections could be attributed to reworking; therefore, they are not taken into account for stratigraphic purposes (Figure **F35**). Samples from the bottom of the sequence recovered in Hole U1499B (Cores 30R through 45R; 933.6–1081.8 m) are gray gravel with silty sand intervals that were recovered as pebbles and cobbles. No nannofossils were observed in this section, so no age could be assigned to the lowermost section at Site U1499.

Planktonic foraminifers

Planktonic foraminiferal biostratigraphy was constructed by analyzing planktonic foraminifers in all core catcher samples from Holes U1499 and samples from selected core sections in Hole U1499B, especially within Core 30R (Table **T6**). Planktonic foraminifers were additionally checked in the fine fraction >63 µm for samples from Core 30R.

The preservation of planktonic foraminifers varies from poor to very good. Based on the evaluation of the percentage of planktonic foraminiferal fragmentation and the distinct microstructure of foraminiferal shells, there is evident foraminiferal dissolution (e.g., *Globigerinoides*) and recrystallization in the lower part of Hole U1499A (cores below Core 50X). In general, most core catcher samples from Holes U1499A and U1499B show poor to moderate preservation of foraminifers, except for Samples 367-U1499A-6H-CC through 10H-CC, where they are well preserved and the planktonic foraminiferal assemblage indicates a mixture of late Pliocene and early Pleistocene components. In addition, some shallow-water species of ostracods were found in Section 5H. Therefore, the interval be-

Figure F36. Additional samples, Core 367-U1499B-30R. The oldest age range estimate for Section 30R-6 is based on the last occurrence of *S. predistentus* (26.93 Ma) and the presence of *S. distentus*.

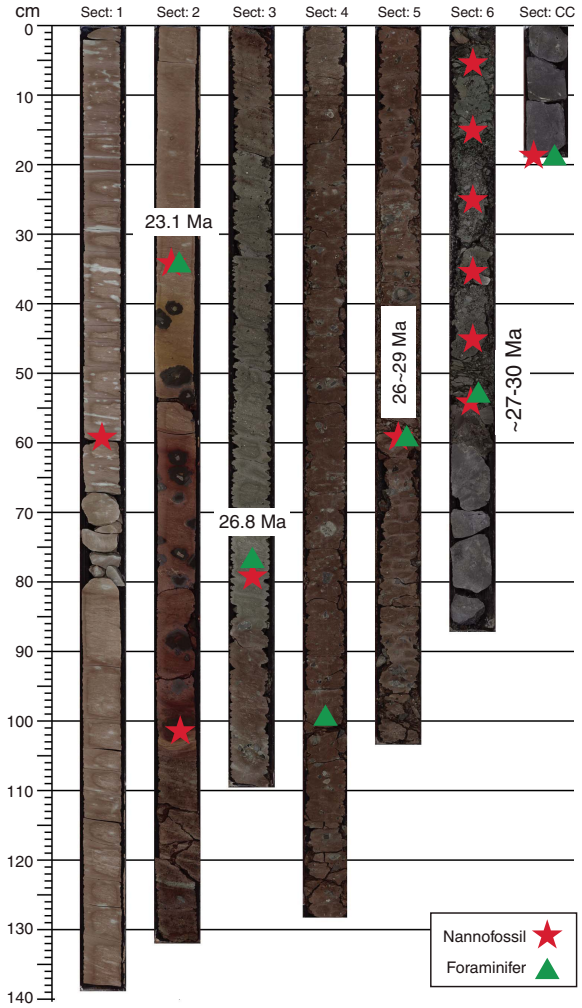

tween Samples 5H-CC and 10H-CC is considered to be a turbidite or slump deposit. In some deeper cores, planktonic foraminifers are rare to common with moderate to good preservation; however, most of them are reworked and possibly transported from the shallow water as indicated by common occurrence of shallow-water benthic foraminifers and coral debris (e.g., Samples 43X-CC and 54X-CC). In samples from Hole U1499B, preservation of planktonic foraminifers varies from poor to good, and reworking and recrystallization are common.

The Site U1499 planktonic foraminiferal biostratigraphy was established by the planktonic foraminiferal evolution events and assemblages. Because most foraminifers are reworked, we distinguished in situ bioevents from reworked occurrences by relying more heavily on FADs than LADs.

The sediment sequence recovered in Hole U1499A is continuous and spans the upper Miocene (Zone M13) through the Pleistocene (Subzone Pt1b) based on eight planktonic foraminiferal bioevents (Table **T3**). Within Subzone PT1b, the FAD (0.12 Ma) of pink *Globigerinoides ruber* and LAD (0.40 Ma) of pink *Globigerinoides ruber* acme provide two biostratigraphic control points that are present in Samples 367-U1499A-2H-CC (17.33 m) and 5H-CC

Table T4. Distribution of calcareous nannofossils, Hole U1499A. **View table in PDF format. Download table in CSV format.**

Table T5. Distribution of calcareous nannofossils, Hole U1499B. **View table in PDF format. Download table in CSV format.**

Table T6. Distribution of planktonic foraminifers, Site U1499. **View table in PDF format. Download table in CSV format.**

(45.68 m), respectively. The LAD of *Globigerinoides obliquus* (1.3 Ma) in Sample 13H-CC (121.33 m) indicates Subzone PT1a. The Pleistocene/Pliocene boundary could not be determined due to the absence of the zonal marker species. Through comparison with nearby Site 1148 (Wang et al., 2000), we observed the FAD of *Globorotalia inflata* in Sample 22H-CC (201.11 m), which is near the Pleistocene/Pliocene boundary.

For Zone PL5, the FAD of *G. tosaensis* (3.35 Ma) was found in Sample 27X-CC (249.82 m). The FAD of *S. seminulina* (3.59 Ma) appears in Sample 29X-CC (269.15 m) and was used as a marker for the bottom of Zone PL4. The LAD of *Globoturborotalia nepenthes* (4.36 Ma) was assigned in Sample 31X-CC (288.59 m), which marks the bottom of Zone PL2. The LAD of *Globoquadrina dehiscens* (5.92 Ma) was observed in Sample 48X-CC (453.66 m), marking Zone M14. The FAD of *Pulleniatina primalis* (6.6 Ma) occurs in Sample 50X-CC (469.37 m) and indicates Zone M13b. The lowermost part of Hole U1499A is still in the late Miocene.

Five planktonic foraminiferal bioevents (Table **T3**) were discerned in Hole U1499B. The FAD of *Globoratalia plesiotumida* (8.58 Ma) in Sample 2R-CC (659.76 m) marks the boundary of Subzones M13b and M13a. The LAD of *Paragloborotalia mayeri* (10.46 Ma) in Sample 17R-CC (808.97 m) constrains the boundary of Zones M12 and M11. *Fohsella peripheroacuta* is present in Sample 24R-CC, but because it was only found in this sample, we did not use it as the FAD of *F. peripheroacuta* (14.24 Ma). However, the LAD of *Catapsydrax dissimilis* (17.54 Ma) in Sample 25R-CC (882.13 m) marks the boundary of Subzone M4a and Zone M3. Therefore, the middle/early Miocene boundary occurs between Samples 24R-CC and 25R-CC.

Foraminifers were only observed above Core 30R. Five additional samples were analyzed from Sections 30R-2 through 30R-6, and the LAD of *Globigerina ciperoensis* (22.9 Ma) in Sample 30R-2, 35–37 cm (928.34 m) indicates the possible Miocene/Oligocene boundary. Foraminifers from Sections 30R-3 and 30R-4 are deformed and sorted distinctly, which implies that foraminifers were transported. The early–late Oligocene assemblage of planktonic foraminifers (such as *Globigerina euapertura, Tenuitella gemma, Chiloguembelina cubensis,* and *Globigerina angulisuturalis*) is present in Sections 30R-5 and 30R-6; however, any accurate age or age boundary cannot be provided due to the poor preservation and low abundance (almost barren) of foraminifers.

Benthic foraminifers

Shallow-water (shelf) benthic foraminifers (e.g., *Ammonia* and *Florius*) and upper slope benthic foraminifers (e.g., *Bulimina* and *Globocassidulina*) are present in some of the core catchers of Hole U1499A. They are especially common in turbidite and slump deposits (e.g., from Core 367-U1499A-5H and Samples 37X-CC through 43X-CC and 54X-CC), suggesting that downslope transportation/reworked foraminifers from the shallow shelf to slope is a common phenomenon at this site. In the red clay deposit (litho-

Figure F37. Deepwater agglutinated benthic foraminifers (367-U1499B-23R-CC; 867.41 m; reflected light). Scale bars = 1 mm. A. *Ammodiscus* sp. B. *Glomospira* sp.

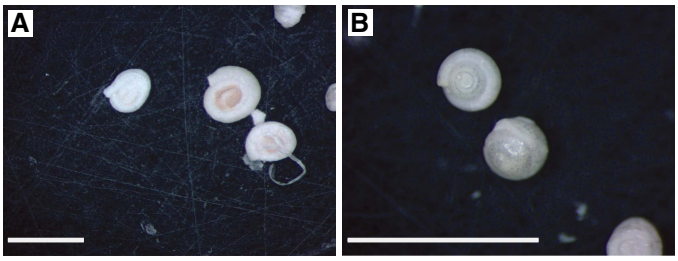

stratigraphic Unit VIII) in Hole U1499B, deep-water agglutinated foraminifers (e.g., *Glomospira* and *Ammodiscus*; Figure **F37**) were observed and are abundant in Samples CC, 23R-CC, 24R-CC, and 26R-CC), suggesting a deep-water environment.

Paleomagnetism

Shipboard measurements

Shipboard paleomagnetic studies consisted of two complementary approaches (see **Paleomagnetism** in the Expedition 367/368 methods chapter [Sun et al., 2018]): (1) measurement and in-line AF demagnetization of archive-half sections on the pass-through 2G Enterprises SRM and (2) measurement and AF and thermal demagnetization of oriented discrete samples on the spinner magnetometer (Agico JR-6A). Representative discrete samples were collected from every core section (1.5 m), except those that were severely disturbed or contained unique sediments or structures deemed important for other research.

We used the remanent magnetization of archive-half sections, measured after the maximum AF treatment, to determine the polarity along the core (Figure **F38**). Discrete samples were analyzed using Zijderveld diagrams (Zijderveld, 1967), and ChRM direction were calculated by principal component analysis (PCA) (Kirschvink, 1980) using PuffinPlot (version 1.03, 23 April 2015) (Lurcock and Wilson, 2012).

Demagnetization behavior

The drilling-induced remanence was removed in most core sections with an AF treatment of 15 mT. Changes in magnetic remanence with depth can be correlated to observable changes in lithology. Low values of NRM near ~60 m (Core 367-U1499A-7H) correlate with a carbonate-rich layer that also has low magnetic susceptibility values (Figure **F48**). A decrease in the moment of the NRM and in our ability to effectively demagnetize the archive-half cores deeper than ~800 m (Core 367-U1499B-17R and below) correlates with an increase in the red color of the sediments and the presence of hematite.

The maximum field strength of in-line AF demagnetization used on the archive-half sections is limited because of the destructive nature of the treatments and our limited ability to measure weak magnetizations in the magnetically noisy shipboard environment. As a consequence, the maximum AF treatment used on the long-core sections is usually not sufficient to isolate a stable ChRM vector. When we did not have enough data to quantitatively solve for the ChRM but the demagnetization path suggests normal or reversed polarity, we then used the term potential normal or potential

Figure F38. Remanent magnetization of archive-half sections, Site U1499. Declinations shallower than 162 m (APC coring) are corrected using orientation from Icefield MI-5 core orientation tool. Red = data determined by maximum AF treatment, blue = NRM, yellow = discrete samples.

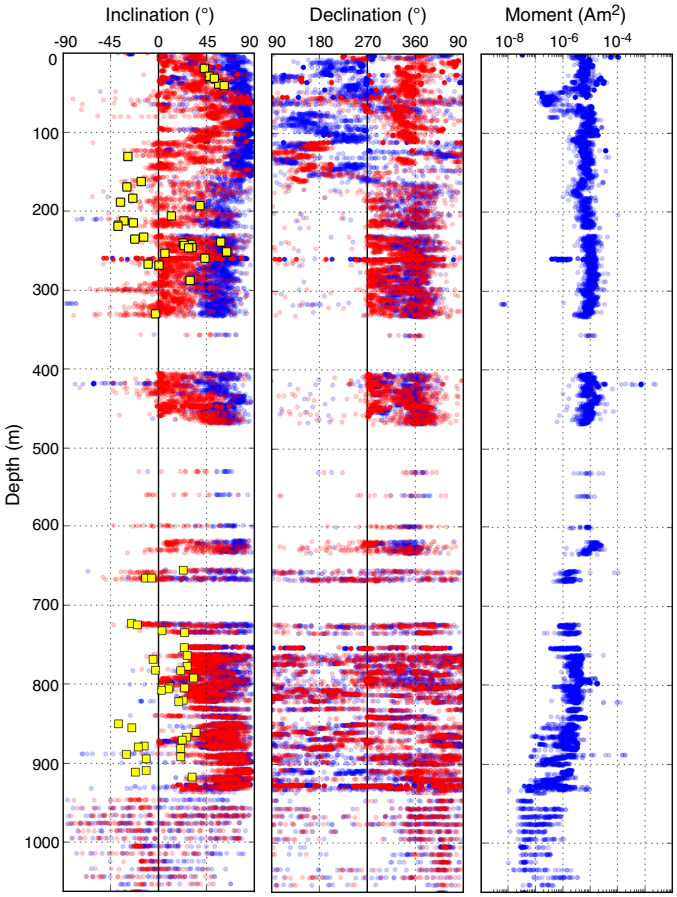

reversed. A typical example of potential normal from the archive-half section of Hole U1499A is illustrated in Figure **F39A**.

The typical behavior of discrete samples from Hole U1499A are shown in Figure **F39**. AF demagnetization of these samples produces demagnetization paths that are easier to interpret than the results of samples subjected to thermal demagnetization. Both treatments show removal of a steep low-temperature/low-coercivity component that represents the drilling overprint. Thermal demagnetization at higher temperatures becomes noisy and thus not reliable, possibly due to the remagnetization of weak samples in the magnetically unshielded environment. The magnetization level of some samples subjected to thermal demagnetization decreased below what we could reliably resolve on the ship. Further thermal demagnetization will take place on shore. Many of the AF demagnetized discrete samples reveal robust trends showing clear normal or reversed polarity. During AF demagnetization, many samples show an anomalous increase in magnetization at fields greater than 60 mT, which indicates the existence of greigite (e.g., Roberts et al., 2011).

We have very low (0%–30%) recovery in Cores 367-U1499B-2R through 11R. From Core 12R downhole, color changes from greenish gray to dark brownish with relatively higher magnetic susceptibility (Figure **F48**). Deeper than Core 27R, magnetic susceptibility

Figure F39. Demagnetization plots of (A) archive-half section and (B–D) discrete samples, Hole U1499A. Stereographic plots: solid squares = positive (down) inclination, open squares = negative (up) inclination. A. Normal polarity. B. Normal polarity; PCA calculated ChRM (blue line; red squares = measurements used in calculation) has 51° declination and 21° inclination. C. Reversed polarity with ChRM declination of 156° and inclination of −16°. D. Potential reversed polarity.

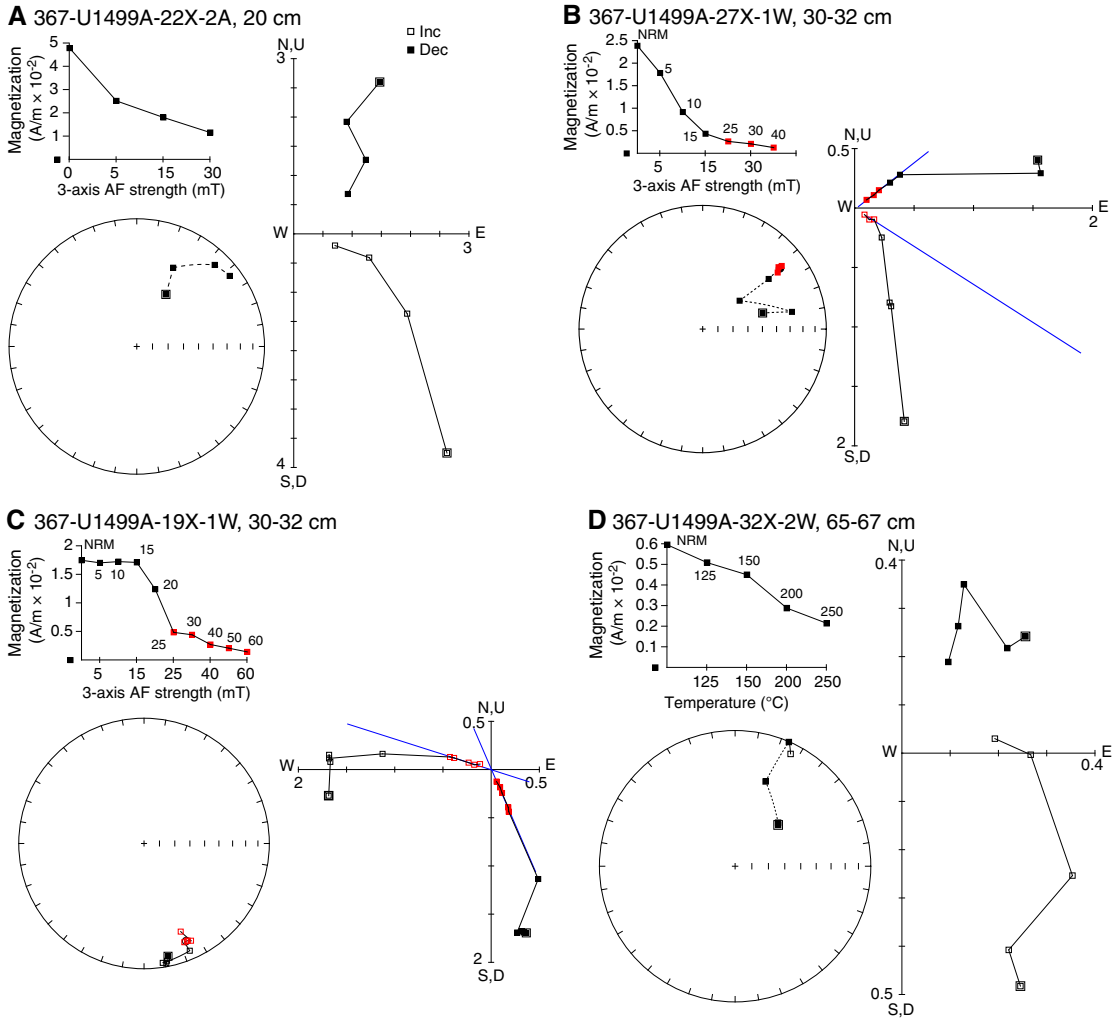

decreases by an order of magnitude, whereas the drilling overprint becomes stronger and drilling disturbance intensifies. All of these factors hampered a reliable identification of possible magnetic reversals in Hole U1499B. The number of discrete samples was also reduced and limited only to the most intact pieces. The change in AF and thermal demagnetization behaviors indicates the presence of high-coercivity and high–blocking temperature hematite rather than the previous dominating low-coercivity and low–blocking temperature components (e.g., titanomagnetite) that could be easily demagnetized (Figure **F40C, F40D**).

Magnetostratigraphy

We constructed the magnetostratigraphy of Site U1499 (Figures **F41**, **F42**) based on the polarity assigned to the archive-half cores where they exhibit stable demagnetization paths (e.g., Figures **F38**, **F39A**, **F40A, F40B**). We do not use the paleomagnetic data from ~50 to 100 m where sediments are interpreted as slumps. Declinations from the archive-half sections from the seafloor to 162 m (APC Cores 367-U1499A-1H through 18H) were corrected using the Icefield MI-5 core orientation tool. Our interpretation of polarity deeper than 162 m is based only on the inclination data because the XCB and RCB coring processes disturb the geographic core orientation. Our interpretations of inclination are based on directions derived from the raw moments measured on the SRM.

The first reversal for the interval shallower than 162 m, where we have constraints based on both inclination and declination, is at ~110 m and interpreted to be the boundary between the Brunhes and Matuyama Chrons. For intervals of poor recovery or poor data quality, the polarity is difficult to determine and thus denoted by question marks (Figure **F43**). The recovery in Hole U1499B is poor (35%), making it challenging to correlate the polarity patterns to the standard geomagnetic polarity timescale.

We correlate the magnetostratigraphy of Hole U1499A to the standard timescale (Ogg et al., 2016) and plot it along with tie points from the microfossil ages from the shipboard paleontologists (Figure **F43**). The paleomagnetic and paleontological age constraints match well over most of the section.

Based on our shipboard paleomagnetic age model (Figure **F43**; Table **T7**), the middle/early Pleistocene boundary (0.78 Ma) is at ~110 m, the late/early Pliocene (3.6 Ma) boundary is at ~260 m, and the early Pliocene/late Miocene boundary (5.33 Ma) is at ~370 m. Considering only the paleomagnetic data, the early Pleistocene/late Pliocene boundary might be at ~220 m.

Figure F40. Demagnetization plots of (A, B) archive-half sections and (C, D) discrete samples, Hole U1499B. PCA calculated ChRM (blue line; red squares = measurements used in calculation) is also shown. Note the high coercivity of samples in A and B.

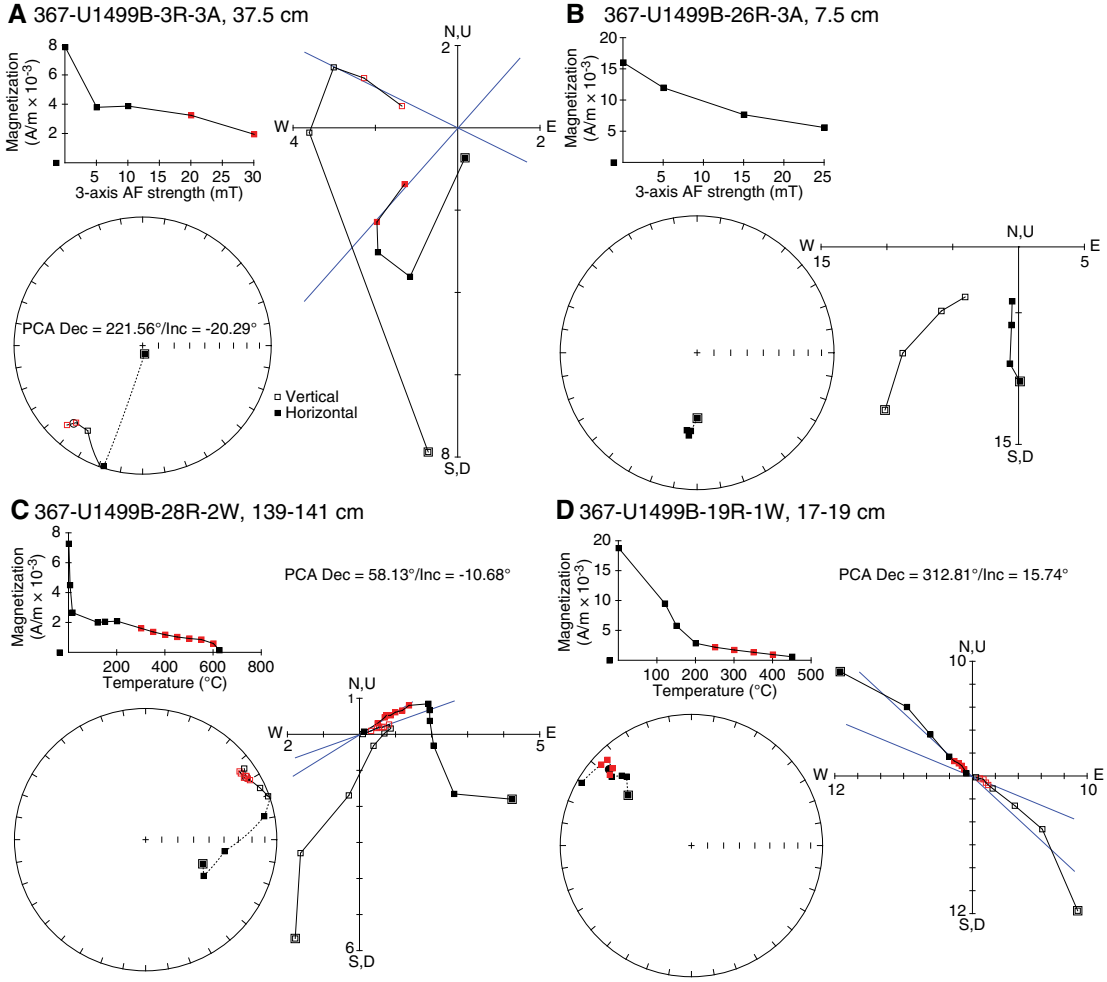

Figure F41. Magnetostratigraphy, Hole U1499A. Lithology column is simplified from the shipboard core description (see Figure F8).

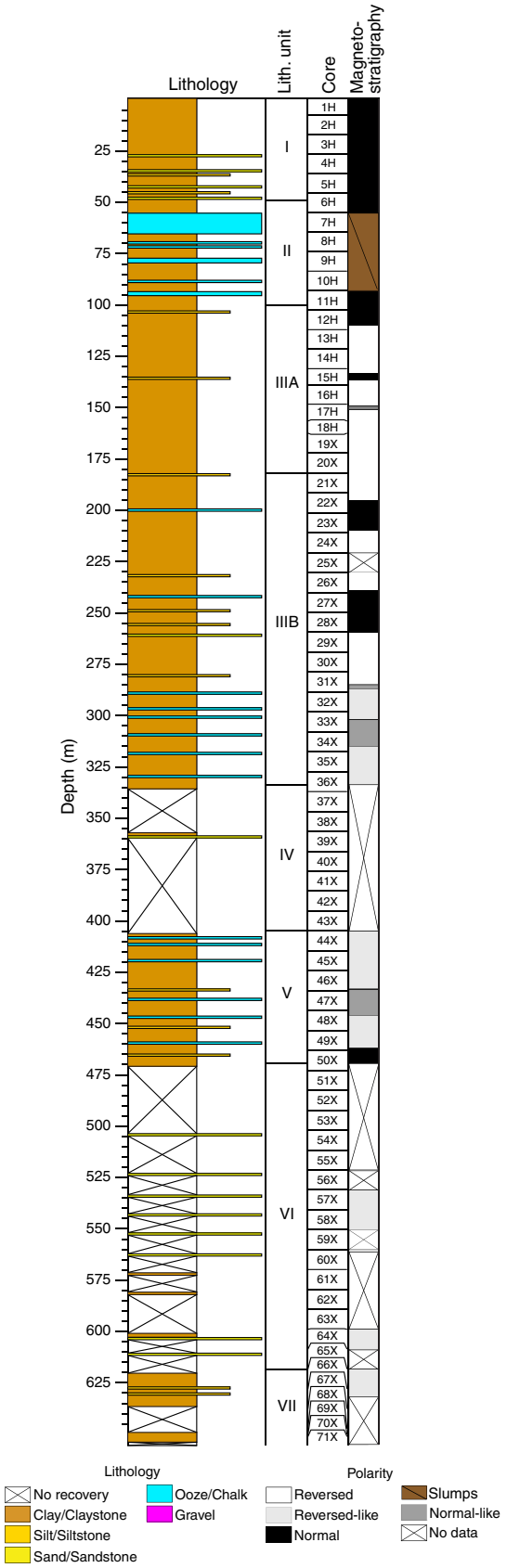

Figure F42. Magnetostratigraphy, Hole U1499B. Lithology column is simplified from shipboard core description (see Figure F8).

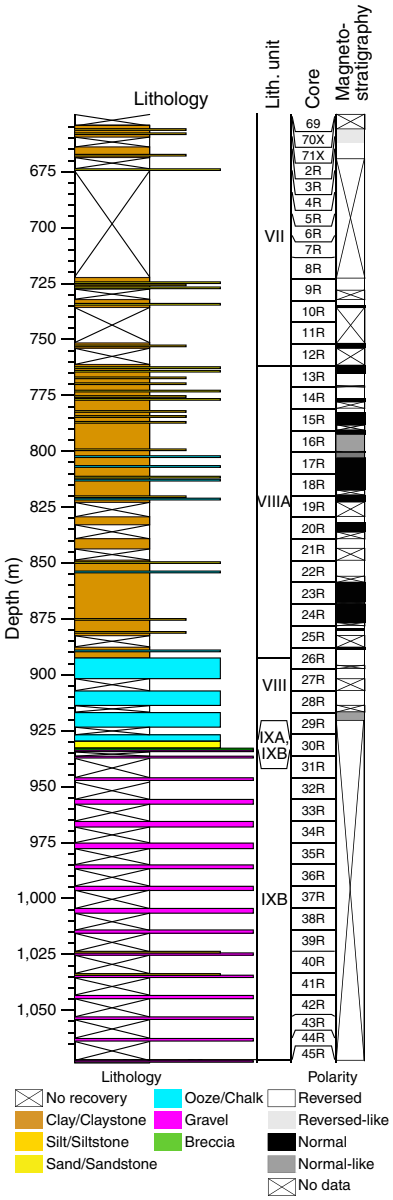

Figure F43. Age-depth model constructed from shipboard paleomagnetic analysis, Site U1499. A possible change in age-depth model was observed during late Pliocene and earliest early Pleistocene (dashed orange line). B/M = Brunhes/Matuyama Chron boundary, M/G = Matuyama/Gauss Chron boundary. GPTS2016 = geomagnetic polarity timescale of Ogg et al. (2016).

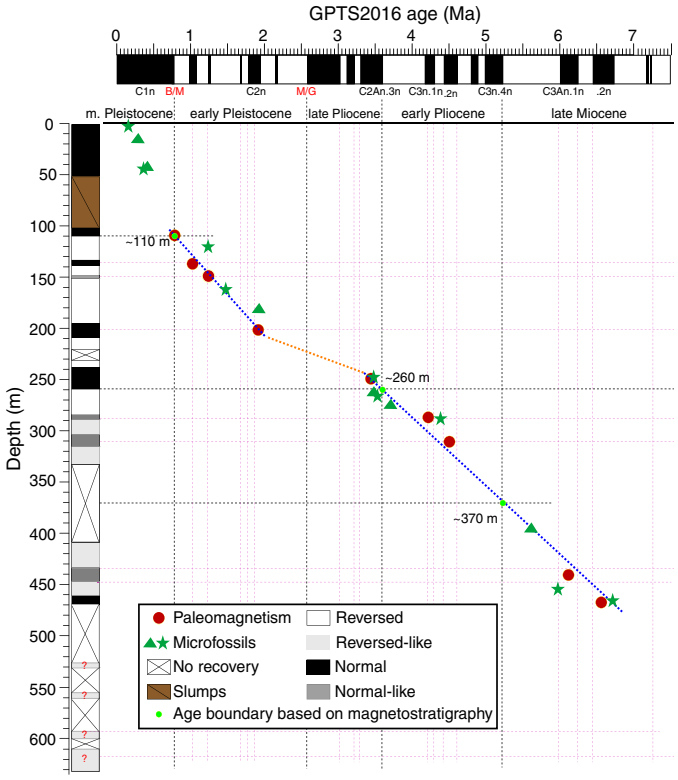

Table T7. Magnetostratigraphy, Site U1499. **Download table in CSV format.**

Base age (Ma)	Duration (My)	Base depth (m)	Core	Thickness (m)
0.78		110	12H	
1.08	0.3	137	15H	27
1.22	0.14	151	17H	14
1.93	0.71	210	24X	59
3.6	1.67	260	28X	50
4.3	0.7	287	31X	27
4.63	0.33	315	34X	28
6.25	1.62	446	48X	131
6.73	0.48	469	49X	23

Geochemistry

At Site U1499, measurements of headspace gas, organic and inorganic carbon, nitrogen, and interstitial water were made in Hole U1499A, and the same measurements, except for interstitial water, were made in Hole U1499B. The headspace gas consistently approaches zero throughout the site, with approximately tens to 6000 ppmv of methane across ~100–250 m, indicating limited microbial methanogenesis because of low TOC content <0.3 wt%. Bulk sediment geochemistry is controlled by lithology. Calcium carbonate contents are predominantly the result of biogenic carbonate abundance. TOC decreases downhole, reflecting the mineralization of sedimentary organic matter. The interstitial water concentration-depth profiles show typical redox zones in marine sediments: oxic seawater, manganese reduction, iron reduction, and sulfate reduction. The interstitial water chemistry also reflects various diagenetic processes: organic matter degradation, carbonate diagenesis, and clay diagenesis occurring in sediments.

Table T8. Headspace gas data, Site U1499. **View table in PDF format. Download table in CSV format.**

Headspace gas

Headspace gas samples (99 samples) were taken at a frequency of one sample per core in Holes U1499A and U1499B for routine safety monitoring (Table **T8**). Methane concentrations were extremely low (<4 ppmv) in the upper 81 m in Hole U1499A. They increased to 1819 ppmv at 100 m, reached a maximum of ~4000–6000 ppmv from 110 to 180 m, and then reduced to 96 ppmv at 257 m. Below this depth, methane concentrations are quite low (<200 ppmv) to the base of Holes U1499A (651 m) and U1499B (1062 m). The distinct higher methane between ~100 and 250 m (Figure **F44**) correlates with the reduction of sulfate concentrations in the upper 100 m in the interstitial water profile (Figure **F45**), suggesting a transition from sulfate reduction to methanogenesis. Ethane, ethene, propane, and propene were below the detection limits in the majority of the samples investigated with concentrations <12 ppmv in only a few samples (12 samples).

Bulk sediment geochemistry

Total carbon, total inorganic carbon (TIC), calcium carbonate, TOC, and TN were determined on 89 sediment samples from interstitial water squeeze cakes (58 samples from Hole U1499A) and discrete samples selected by scientists describing the cores (5 samples from Hole U1499A and 26 samples from Hole U1499B; Table **T9**; Figure **F44**). The downhole profile of carbonate content was also indicated by the reflectance L* and calcite contents as measured by XRD (Figures **F45**, **F46**).

TIC content ranges from <0.1 to 9.9 wt% (average = 1.8 wt%). TIC is expressed as weight percent $CaCO_3$, assuming inorganic carbon is exclusively present as $CaCO_3$, and varies between 0.4 and 82 wt% (average = 14.8 wt%). Carbonate content varies from 1 to 18 wt% in the upper 50 m in Hole U1499A, reaching the highest values (25–63 wt%) between 50 and 91 m and then decreasing to <10 wt% to 291 m. Below this depth, carbonate content slightly increases to 13–28 wt% at 300–436 m and then increases to 2 wt% at the bottom of the hole. Low carbonate content continues (<10 wt%) in the upper part of Hole U1499B (726–861 m), and then carbonate increases to 65 wt% from 870 to 927 m before finally decreasing to extremely low values in the gravels of lithostratigraphic Subunit IXB.

The two intervals with the highest carbonate content (50–91 and 870–927 m) correspond well to lithostratigraphic Unit II and the lower part of Unit VIII, which are characterized by abundant nannofossil oozes and clay-rich chalk, respectively. An interval between has relatively high carbonate content (300–436 m) and contains clay, clayey silt, and sand with nannofossil/foraminifer interbeds; this interval also had very poor core recovery. One sample (367-U1499A-48X-5, 33–34 cm; 450 m) is characterized by very high carbonate content, reaching 82 wt% (Table **T9**). This sample was taken from a foraminifer sand layer.

Total carbon concentrations vary between 0.1 and 10.2 wt% (Table **T9**). TOC, calculated as the difference between total carbon and

Figure F44. Lithology, methane, calcium carbonate, TOC, and TOC/TN profiles, Site U1499.

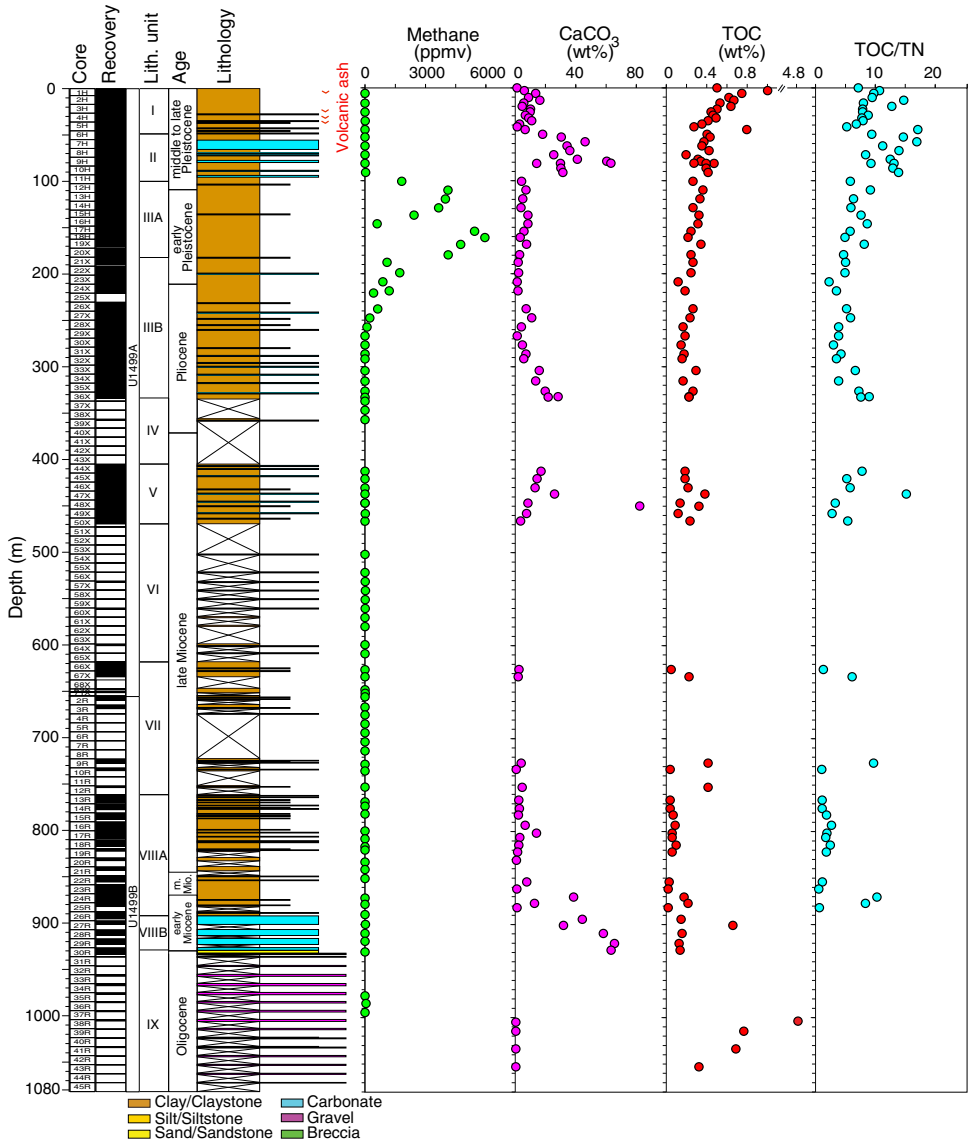

TIC, decreases gradually in the upper 100 m from 1 to 0.2 wt%, possibly because of the early postdepositional degradation of organic matter. TOC generally varies between 0 and 0.3 wt% with increasing depth (Figure **F44**). One sample in Hole U1499B (38R-1, 74–77 cm; 1005 m) exhibited extremely high TOC content (4.8 wt%). The high TOC in this sample from the gravel of lithostratigraphic Subunit IXC may not be representative of the unit as a whole because it was selected due to its dark color, which is scarce in this unit.

TOC/TN is generally used as a preliminary estimate for the source of organic material with high values (TOC/TN > 12) typically attributed to a predominantly terrestrial source, whereas lower values (TOC/TN < 8) are indicative of dominant marine contributions (Müller and Mathesius, 1999). TOC/TN values range from 1 to 17 in Hole U1499A (Table **T9**; Figure **F44**), indicating mixed marine/terrestrial organic input in this site. The higher values in the upper 100 m (Figure **F44**) imply relatively high contributions from terrestrial sources during this time interval compared to the following deeper sections where marine sources appear to dominate.

Interstitial water chemistry

A total of 58 whole-round core sections were collected from Hole U1499A for interstitial water analyses, including 32 samples from near the seafloor to ~160.9 m that were taken from APC cores and 26 samples from 168.3 to ~633.4 m taken from XCB cores. A mudline bottom seawater sample was also taken from Hole U1499A. No interstitial water samples were available from Hole U1499B.

Sulfate, alkalinity, ammonium, phosphate, bromide, and barium

Sulfate concentration decreases gradually from the seawater-like value of 28.8 mM at the mudline to ~1 mM at ~110 m. Sulfate maintains near-complete depletion values of <2 mM to 257 m and thereafter increases slowly to 16.9 mM at ~633 m, near the bottom of Hole U1499A (Table **T10**; Figure **F45**). The curvature of sulfate profile shallower than ~110 m suggests that sulfate reduction is pre-

Figure F45. Interstitial water sulfate, alkalinity, ammonium, phosphate, bromide, and barium concentration profiles, Hole U1499A. Black diamonds = typical seawater values.

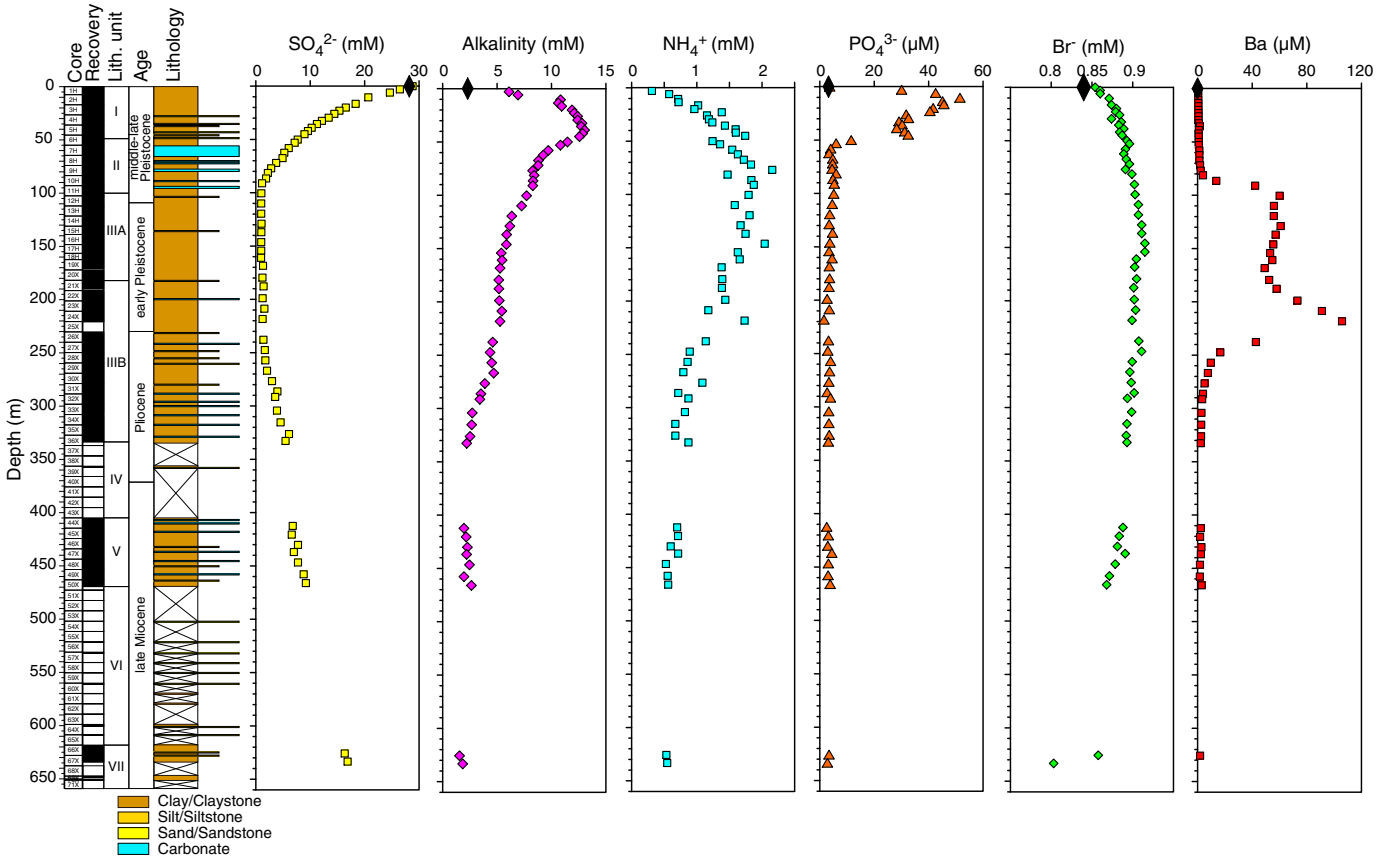

Table T9. Carbon and nitrogen, Site U1499. **View table in PDF format. Download table in CSV format.**

dominantly mediated by sedimentary organic matter degradation (Chen et al., 2010) with a net simplified equation:

$$2CH_2O + SO_4^{2-} = 2HCO_3^- + H_2S.$$

As shown in the equation, sulfate reduction coupled with organic matter oxidation produces bicarbonates and increases the alkalinity of interstitial water in the sulfate reduction zone. Consequently, alkalinity increases from a seawater-like value of 2.38 mM at the mudline to a maximum of 13.1 mM at ~39 m before decreasing steadily with depth to a minimum of 1.5 mM at ~625 m (Figure **F45**). The last two samples near the bottom of the hole have alkalinity values <2.0 mM, lower than a typical seawater value of 2.3 mM. These values are likely caused by the pure water released during the smectite-illite transformation (see **Chloride, sodium, and salinity**).

During sedimentary organic matter degradation, ammonium, phosphate, and bromide are released into the pore fluids. Dissolved NH_4^+ increases from the mudline to a peak of 2.16 mM at ~77 m and then decreases gradually to 0.55 mM at 633.4 m approaching the bottom of Hole U1499A (Figure **F45**). The decrease in NH_4^+ below the sulfate reduction zone reflects diffusion and/or clay mineral ion exchange. The dissolved PO_4^{3-} concentration increases sharply from 3.7 μM at the mudline to a maximum of 51.5 μM at ~10 m and then declines quickly to a local background value of 3.4 μM at ~62 m. Phosphate increases slightly to concentrations between 3.7 and 6.0 μM between ~67 and 146 m before staying fairly stable at ~3.0 μM to the bottom of the hole. The slight increase in PO_4^{3-} in the short interval from ~67 to 146 m is likely controlled by the geochemistry of slump deposits there (see **Lithostratigraphy**). The overall downhole decrease in PO_4^{3-} is likely the result of its adsorption onto Fe/Mn oxyhydroxides.

Bromide concentrations increase from 0.85 mM at the mudline to a maximum of 0.92 mM at ~154 m and then remain constant at ~0.90 mM to ~304 m before declining downhole to a minimum of 0.80 mM near the bottom of the hole. The minimal concentrations in bromide near the bottom of the hole are mostly caused by dilution from pure water released from the smectite-illite transformation (see **Chloride, sodium, and salinity**).

Barium concentrations remain consistently low (<2 μM) shallower than ~72 m and then sharply increase from 2.3 to 60.0 μM from ~77 to 100 m. Ba varies from 55 to 61 μM in the ~109–146 m interval and thereafter quickly increases from 53.2 to 105.8 μM from 154 to 218 m, followed by a sharp decrease from 42.7 μM at ~238 m to 1.8 μM at 633 m near the bottom of the hole. The interval of high Ba concentrations >50 μM corresponds to the interval of near-complete consumption of SO_4^{2-}, suggesting the dissolution of barite ($BaSO_4$), a mineral that precipitates in highly productive surface ocean water (Dymond et al., 1992). The two Ba concentration peaks possibly mark two barite fronts existing in sediments.

Figure F46. Interstitial water calcium, strontium, manganese, iron, and silica concentration profiles, Hole U1499A. Black diamonds = typical seawater values.

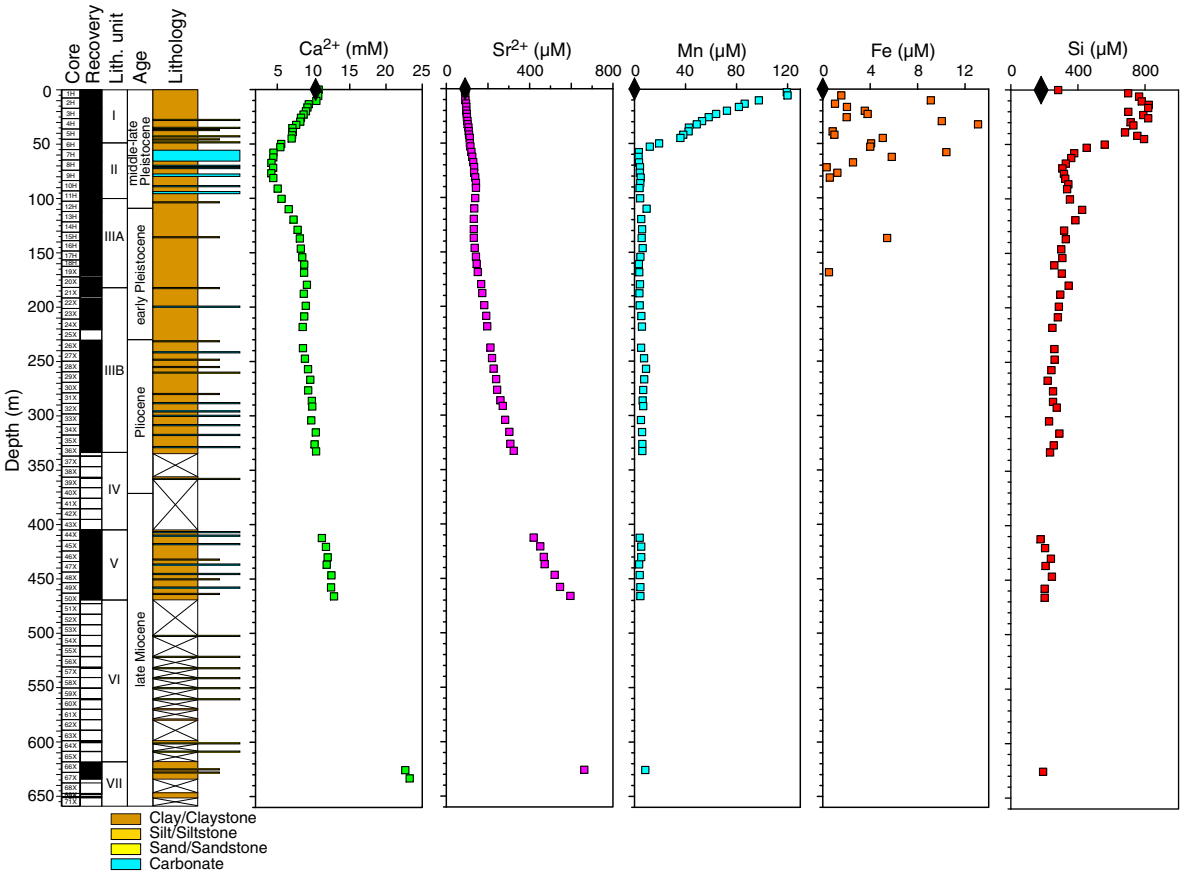

Table T10. Interstitial water chemistry data, Hole U1499A. **View table in PDF format. Download table in CSV format.**

Calcium and strontium

Calcium concentrations decrease from 10.7 mM at the mudline to a minimum of 4.2 mM at ~77 m and then increase gradually to 12.5 mM at ~466 m before increasing sharply to >22 mM in the 626–633 m interval near the bottom of the hole (Figure **F46**). The minimum calcium concentration occurring at ~77 m correlates with the sulfate reduction zone (Figure **F45**), indicating that authigenic carbonate precipitation driven by active sulfate reduction coupled with sedimentary organic matter decomposition is actively ongoing ($2HCO_3^- + Ca^{2+} \leftrightarrow CaCO_3 = \downarrow H_2O + CO_2$). It also suggests that the calcium profile shallower than 77 m is mainly controlled by authigenic carbonate precipitation with minor calcareous microfossil dissolution (see **Biostratigraphy**); this suggestion is further supported by the Sr data. The downhole increase in calcium is likely caused by biogenic carbonate dissolution and recrystallization, which is evidenced by the poorer downhole preservation of calcareous microfossils and clear overgrowth of calcareous fossils deeper than 450 m (see **Biostratigraphy**).

Strontium concentrations monotonically increase downhole from a seawater-like value of 90.7 μM at the mudline to 662.3 μM at ~633 m near the bottom of the hole. Biogenic calcite dissolution and recrystallization release Sr into fluids, leading to an overall Sr increase with depth. Therefore, the Sr profile suggests that biogenic carbonate has experienced dissolution throughout the hole, particularly through lithostratigraphic Units V–VII (see **Lithostratigraphy**) since the late Miocene. This suggestion is supported by the variability in preservation of calcareous microfossils (see **Biostratigraphy**). Less dissolution of biogenic carbonate in the sulfate reduction zone suggests that the high alkalinity produced by sulfate reduction and organic matter oxidation might help preserve calcareous microfossils.

Chloride, sodium, and salinity

Chloride concentrations increase from 555.5 mM at the mudline to a maximum value of 565.7 mM at 35.5 m and then decrease gradually to an average downhole value of ~558.5 mM at 81.3 m (Figure **F47**). Thereafter, chloride concentrations are consistent, with an average value of 558.3 ± 2.9 mM to ~466 m. However, near the bottom of Hole U1499A, chloride concentrations sharply decrease to 542.7 mM at ~626 m and 533.6 mM at ~633.4 m. The maximum chloride concentration at 35.5 m was possibly caused either by the imprint of bottom seawater chloride of the Last Glacial Maximum and/or by water uptake during the alteration of kaolinite to smectite or illite in sediments. Pure water released from the smectite-illite transformation may be responsible for the lower chloride concentrations near the bottom of the hole. The transformation is mostly caused by the relatively high temperature of ~60°C in sediments at ~630 m because the optimal temperature for the smectite-illite transformation is between 50° and 120°C (Kastner and Rudnicki, 2004). Sediment temperature was calculated based on a bottom seawater temperature of 2.5°C and the geothermal gradient (91°C/km) found in Hole U1499A (see **Physical properties** and **Downhole measurements**).

Figure F47. Interstitial water chloride, sodium, magnesium, potassium, boron, and lithium concentration profiles, Hole U1499A. Black diamonds = typical seawater values.

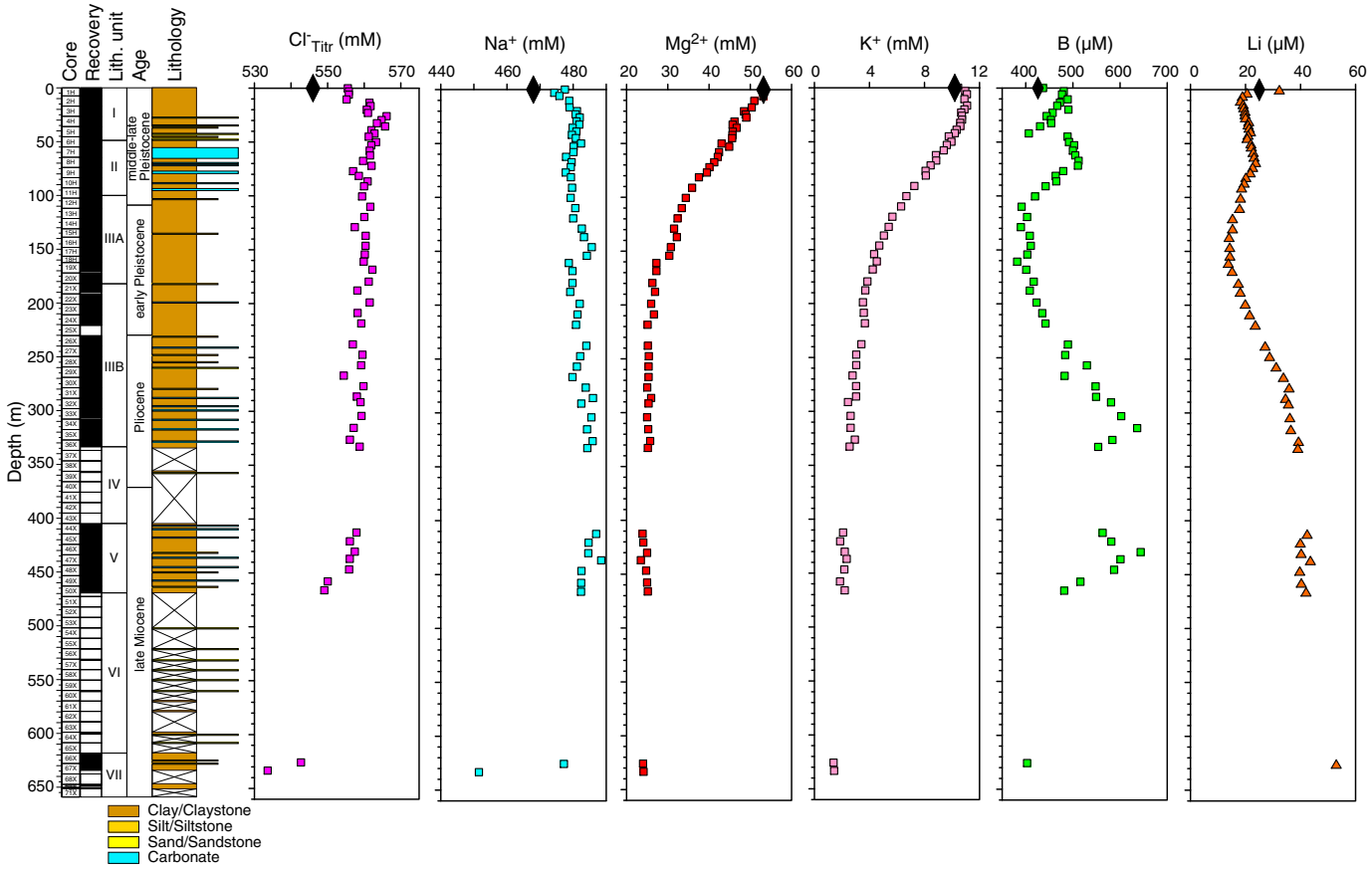

Sodium concentrations are nearly constant with a seawater-like value of 481 ± 2.8 mM shallower than 466 m before sharply decreasing to 452 mM at ~633 m near the bottom of the hole. The lower sodium concentrate at the bottom of the hole is mostly driven by the smectite-illite transformation (see **Chloride, sodium, and salinity**).

Salinity decreases from 36.5 at the mudline to 35 at 62.4 m and then varies between 34 and 33 to the bottom of Hole U1499A. Decreasing salinity is likely driven by the downhole decreases in calcium, magnesium, potassium, and sulfate.

Silica

Dissolved silica concentrations increase sharply from ~282 μM at the mudline to >700 μM with a maximum of 822 μM between ~3 and 45 m. Deeper than this, Si decreases from 560 μM at ~50 m to 192 μM at 626 m near the bottom of the hole. Elevated Si concentrations (>700 μM) in the uppermost 45 m suggest active dissolution of biogenic silica in these sediments, consistent with the presence of siliceous microfossils such as diatoms and radiolarians in the uppermost 19 m. Below this depth, the sediments are barren of siliceous microfossils (see **Biostratigraphy**).

Manganese and iron

Downhole distributions of manganese and iron in interstitial waters are shown in Figure **F46**, and concentrations of both elements are given in Table **T10**. Manganese concentrations increase sharply from below the detection limit of ~0.8 μM at the mudline to a maximum of ~120 μM at ~6 m and then decline gradually to a minimum value of ~3 μM at ~62 m. Thereafter, manganese varies between 3 and 10 μM to the bottom of Hole U1499A. This trend reflects the transition from oxic bottom seawater to suboxic sediments at a shallow depth, which is consistent with the relatively high organic carbon contents (~0.6–1.0 wt%) at shallow depths (see **Bulk sediment geochemistry**). Iron concentrations increase from the mudline to a peak of 13.1 μM at ~33 m and quickly decrease to ~1.0 μM at 42 m. Concentrations then increase to a high value of 10.43 μM at ~58 m before decreasing to a background value of ~0.59 μM at ~81 m. The second peak of iron concentration (10.43 μM) at ~58 m is within the slump deposit between 36.0 and 103.1 m (see **Lithostratigraphy**), which must have carried more iron rich sediments. Iron concentrations are mostly below the detection limit of 0.3 μM, particularly from ~90 m to the bottom of Hole U1499A, suggesting a limited supply of available iron in sediments and/or efficient removal of ferrous iron by hydrogen sulfide produced by sulfate reduction to form pyrite ($Fe^{2+} + S^{2-} \rightarrow FeS_2\downarrow$).

Magnesium and potassium

Magnesium concentrations gradually decrease from a seawater-like value of 53.4 mM at the mudline to ~23.9 mM at ~412 m (Figure **F47**) and remain fairly constant at ~24.0 mM to the bottom of the hole. Potassium concentrations are nearly constant at a seawater-like value of 10.8 ± 0.2 mM in the uppermost ~35 m and then decrease steadily downhole to ~1.4 mM at 626–633 m near the bottom of the hole. The nearly identical Mg^{2+} and K^+ profiles indicate that a common process influenced their concentrations, such as clay

mineral cation exchange and/or clay mineral authigenesis as kaolinite is transformed to smectite/illite with Mg^{2+} and/or K^{+} being incorporated into newly formed clay minerals.

Boron and lithium

Boron concentrations exhibit considerable variation with depth (Figure **F47**). B first decreases from 481 to 407 µM in the 3–42 m interval and then increases from 489 to 511 µM through the 45–72 m interval. Thereafter, B decreases from 480 to 390 µM from 77 to 129 m followed by a gradual increase from 409 µM at 137 m to a maximum of 636 µM at 315 m. Finally, B concentrations decrease from 584 µM at 326 m to 482 µM at 466 m before sharply decreasing to 403 µM at ~633 m near the bottom of the hole. This erratic B profile is likely driven by clay mineral cation exchange, its adsorption onto clay minerals, and desorption from clay minerals.

The lithium profile mimics that of boron because of the similar behavior of these two ions. Li concentrations are 19 ± 3 µM, less than the modern seawater value of 25 µM shallower than 218 m, likely because of adsorption of Li onto clay minerals such as kaolinite and smectite and/or onto other terrigenous sediments. Thereafter, Li concentrations increase gradually from 27 µM at 238 m to 53 µM at 626 m toward the bottom of the hole, possibly a result of diagenetic release of Li from clay minerals and/or diffusion from Li-enriched deep fluid.

In general, interstitial water chemistry at Site U1499 is controlled by sediment input and organic matter degradation, sulfate reduction, carbonate diagenesis, and clay diagenesis.

Physical properties

We measured physical properties on whole-round cores and working-half sections from Holes U1499A and U1499B for lithostratigraphic characterization and correlation between core description, borehole data, and seismic profiles. These measurements included GRA bulk density, magnetic susceptibility, NGR, *P*-wave velocity, MAD porosity, and thermal conductivity. We used the Whole-Round Multisensor Logger (WRMSL) to measure GRA bulk density, magnetic susceptibility, and *P*-wave velocity. NGR was measured on whole-round cores with the Natural Gamma Radiation Logger (NGRL). After the cores were split into section halves, *P*-wave velocity was measured with the Section Half Measurement Gantry (SHMG) using the caliper for measurements through the split core and bayonets inserted into the sediment for measurements along and across the core. Discrete samples were taken for MAD measurements, including mass measurement with dual balances and volume measurement with a pycnometer. Resulting values were used to calculate bulk properties (wet bulk density, dry bulk density, sediment grain density, porosity, and void ratio).

We measured *P*-wave velocities using the WRMSL for Hole U1499A cores collected with the APC system (367-U1499A-1H through 18H; 0–162 m). Cores recovered with the XCB or the RCB systems are slightly smaller in diameter than those cored with the APC system. As a result, sections cored with the XCB or RCB systems typically have gaps between the liner and the core, so we did not measure *P*-wave velocity with the WRMSL on these cores (i.e., from Core 19X to the bottom of Hole U1499A and all RCB cores from Hole U1499B). Velocity measurements with the *X*-caliper on the SHMG were performed on section halves for all cores from Holes U1499A and U1499B (usually 3 per core). *Y*- and *Z*-bayonet velocity measurements on the SHMG were stopped after Section 367-U1499A-9H-6 (~82 m) because the sediment was too hard for the bayonets to penetrate without disrupting and introducing cracks.

In Hole U1499B, we performed whole-round measurements of magnetic susceptibility, GRA bulk density, and NGR along with *P*-wave measurements on half cores using the PWC on Cores 2R through 38R and MAD measurements on discrete samples downhole to Core 30R. As the sediment in the cores became harder in Hole U1499B, we changed the sampling method and either cut small pieces or drilled minicores from the working-half sections for MAD measurements. For Cores 30R through 38R, *P*-wave measurements were made with the PWC on individual core pieces without the core liner.

For cores containing soft material in Hole U1499A (lithostratigraphic Units I–VI; to ~530 m), thermal conductivity was measured with the TK-04 (Teka Bolin) system with a needle probe inserted into whole-round cores. Because of the increased compaction, thermal conductivity on cores from deeper formations (Cores 367-U1499A-60X through 71X and all RCB cores from Hole U1499B) was measured on split section halves with a puck probe. For each core, three measurements were conducted in the middle section (usually Section 3). The puck probe measurements showed unstable results, presenting notable differences between the three measurements. The contact probe values likely overestimate the average in situ thermal conductivity.

In addition, downhole formation temperature measurements were made in Hole U1499A, and wireline log data were acquired from the bottom of the casing (651 m) to ~1020 m in Hole U1499B (see **Downhole measurements**).

Data cleaning and depth correction

Data measured using automatic systems such as the WRMSL, NGRL, and Section Half Multisensor Logger (SHMSL; point magnetic susceptibility) can contain data outliers (e.g., data from voids in core, unrealistic high values, etc.) that must be removed. This cleaning is required before the integration of these data into the models (e.g., computation of synthetic scenario seismograms).

We defined values exceeding $\mu \pm N\sigma$ (with $N = 2$), where µ is the mean and σ is the standard deviation of the entire data set (Table **T11**), as outliers and removed them from the data set. We also smoothed the data when used for modeling computation by applying a moving average filter. SHMG data were usually considered to be reliable because the operator checks the result as it is acquired. For MAD data, we observed very few outliers with values exceeding $\mu \pm 2\sigma$.

We tested the accuracy of the PWC measurements by performing several measurements in the same sample. Table **T12** presents

Table T11. Mean and standard deviation (SD) of all physical property measurements, Site U1499. **Download table in CSV format.**

NGR mean (cps)	NGR SD (cps)	Density mean (g/cm³)	Density SD (g/cm³)	MS mean (10^{-5} SI)	MS SD (10^{-5} SI)	*P*-wave velocity mean (m/s)	*P*-wave velocity SD (m/s)	Porosity mean (%)	Porosity SD (%)	Thermal conductivity mean (W/[m·K])	Thermal conductivity SD (W/[m·K])
52.7	11.0	1.85	0.12	45.8	16.1	1522	45	53.7	8.3	1.22	0.4

the results of one test on Core 367-U1499B-14H. Error in the PWC measurements is <3%. For computation of synthetic seismograms to be compared to the real seismic data (e.g., with Petrel software), we chose to use the downhole logging velocity data (available deeper than 650 m) and the PWC data (in the uppermost 650 m) because the quality of the latter is manually checked at each measurement. Choosing the highest quality data is important because they can change the estimation of the reflectivity of the layers and thus have major impact on the computation.

To insure the homogeneity of the descriptions and the comparisons of our measurements with other core characteristics collected in other laboratories, we used sample depths below seafloor calculated by the CSF-A method (see **http://www.iodp.org/policies-and-guidelines/142-iodp-depth-scales-terminology-april-2011/file**). It is important to note that depths calculated this way do not account for core expansion, including cores that have >100% recovery.

Table T12. SHMG velocity caliper accuracy test on sample from Section 367-U1499A-14H. **Download table in CSV format.**

Measurement	*P*-wave velocity (m/s)	*P*-wave velocity SD (m/s)	*P*-wave velocity mean (m/s)
1	2003.8	52.5	2064
2	2087.6	52.5	2064
3	2100.6	52.5	2064

Density

GRA bulk density was measured automatically every 2 cm by the WRMSL. In addition, bulk density was measured on discrete core samples with the MAD system (~10 cm^3 volume each; usually three samples per core according to recovery). Both types of density measurements show similar variations (Figure **F48**). A clear shift can be observed in the GRA bulk density from ~1.90 to ~1.75 g/cm^3 at ~160 m. This shift coincides with the change from the APC to XCB. The reduced diameter of the XCB cores does not completely fill the core liner and causes lower density values during WRMSL measurements. No data were collected for the sandy layers within lithostratigraphic Units IV and VI and the lower part of Unit VII because of the poor core recovery in these intervals. No MAD samples were collected from Core 367-U1499B-31R to the bottom of Hole U1499B because the cores contained mostly small pieces of hard sandstone similar to the sample collected from Core 30R, which likely were not individually representative of the properties of the section penetrated.

Bulk densities increase quickly with depth from 1.4 g/cm^3 to nearly 2 g/cm^3 in the uppermost 100 m in Units I and II. Bulk densities then exhibit a slower increase from 2.0 g/cm^3 near 100 m to 2.3

Figure F48. Petrophysics data summary, Holes U1499A and U1499B. Red arrows = magnetic susceptibility (MS) peaks associated with ash layers, black arrow = MS peak in layer of Core 367-U1499B-30R containing Fe-Mn nodule, yellow line = APC/XCB coring boundary where some physical properties values change, blue box = Unit II slump layer, gray box = gravel layer in Subunit IXC. cps = counts per second.

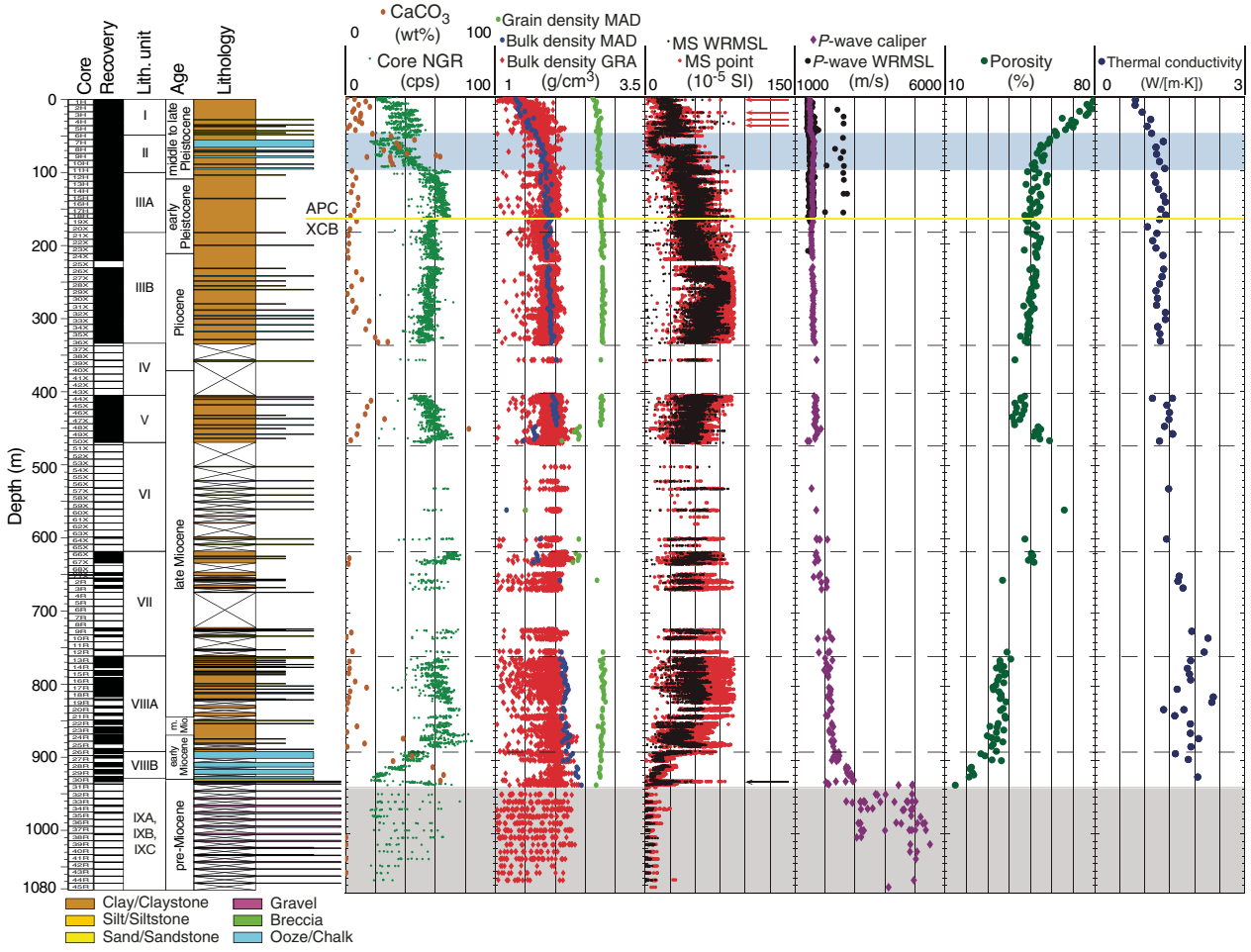

g/cm^3 near the bottom of Hole U1499B. GRA bulk density data show high scatter in the indurated sediment deeper than ~650 m due to the fact that some of the measurements are made on partly empty liners when the recovered rocks are relatively small. The only discrete MAD sample taken from this unit was in the core catcher of Core 367-U1499B-30R and has a bulk density of 2.4 g/cm^3 (higher than the ~2.3 g/cm^3 average of lithostratigraphic Subunit VIIIB above) and a porosity of 15% (lower than the ~22% average of the unit above). Grain densities are almost constant (2.7 g/cm^3) to ~450 m (Units I–V). Below that depth, grain densities are lower (~2.4 g/cm^3), which can be related to the sandy layer of Unit VI.

Porosities sharply decrease from 80% at the seafloor to ~50% at 100 m in Hole U1499A and are relatively constant (53%) through Subunit IIIA and the upper part of Subunit IIIB. Porosities then slowly decrease to 45% at 470 m (base of Unit V). The sand in Units VI and VII between 450 and 650 m has a higher porosity (50%–55%). Porosities decrease again slowly from ~40% to 30% between 760 and 890 m. The deepest sample measured for MAD in Hole U1499B is a piece of sandstone from Subunit IXA (Core 367-U1499B-30R) with a porosity of only 15%.

Magnetic susceptibility

Magnetic susceptibility was measured on the WRMSL and the SHMSL (point magnetic susceptibility). Magnetic susceptibility is sensitive to magnetic mineral content and the mineralogy of the formation. After Clark and Emerson (1991), magnetic susceptibility varies between 0 and 2000 × 10^{-5} SI for sandstone and between 20 and 200 × 10^{-5} SI for clay material. Magnetic susceptibility data were collected every 2 cm, whereas point magnetic susceptibility data were collected every 1 cm through Section 367-U1499A-11H-4 (~95 m) and every 2 cm downsection to the bottom of Hole U1499A and throughout Hole U1499B. Magnetic susceptibility and point magnetic susceptibility values are in very good agreement along the entire profile of Site U1499.

Magnetic susceptibility displays four distinct peaks in Cores 1H through 5H (~30–50 m) that correspond with volcanic ash layers containing an increased amount of magnetic minerals. An abrupt decrease from ~30 × 10^{-5} to ~5 × 10^{-5} SI was observed in Cores 6H and 7H (~50 to ~70 m) and corresponds to a mass transport deposit composed of calcareous ooze and nannofossil-rich clay in Unit II. A local increase in magnetic susceptibility values from ~60 × 10^{-5} to 80 × 10^{-5} SI was observed from ~240 to 290 m (Cores 27H through 31H). This increase is associated with a slight decrease in reflectance a* values (Figure **F9**) and likely reflects higher Fe-rich mineral content. Between 300 and 830 m, magnetic susceptibility values are relatively constant around 50 × 10^{-5} SI and then significantly decrease with depth to 0–20 × 10^{-5} SI at 930 m. In Core 30R near the base of Subunit VIIIB (~930 m), a unique layer of reddish brown claystone with Fe-Mn nodules has high magnetic susceptibility values and NGR counts. Deeper than ~933 m, magnetic susceptibility values are very low in the gravel and sandstone of Subunit IXC.

P-wave velocity

P-wave velocities for the uppermost sediment are close to the seawater velocity, ~1500 m/s, for the uppermost 50 m, reflecting the high porosity of the sediment near the surface. WRMSL *P*-wave velocity values are slightly lower than the SHMG caliper values, probably because the WRMSL has a looser contact between measuring sensors and core material being measured. Some WRMSL *P*-wave velocity values, however, are much larger than the caliper measurements (2700 versus 1500 m/s, respectively; Figure **F48**). This might be related either to material in the core not measured with the caliper or to other unidentified factors. The caliper values were considered more accurate for the computation of synthetic seismograms (see **Correlation to seismic data**). *P*-wave velocity gradually increases with depth from 1500 m/s near 50 m to values around 2300 m/s at ~930 m. Some slightly higher *P*-wave velocity values (2000 m/s compared to 1800 m/s in the layers above) were observed in the partially recovered cores of Units IV and V around 350 and 450 m, corresponding to coarser sands. Deeper than 930 m, the gravels of Subunit IXC measured individually yielded relatively high velocities (~5500 m/s), whereas the silty sand interbeds give lower values (~3060 m/s).

Natural gamma radiation

NGR counts vary with lithology, with higher values in sediments rich in clay, silt, and mud (40–70 counts/s; Russell, 1944) and lower values in sand or sandstone (0–25 counts/s; Russell, 1944). NGR values in Hole U1499A present an increase in counts for the uppermost 60 m (Figures **F48**, **F49**). Below this depth, values decrease abruptly to ~20 counts/s near 60 m and then increase again to ~60 counts/s at ~100 m. This anomaly coincides with the drop in magnetic susceptibility and is correlated with the lithology in the slump deposits in lithostratigraphic Unit II. A clear decrease can be observed in NGR counts at ~160 m from ~65 to ~55 counts/s when coring switched from the APC system to the XCB system, resulting in a reduced volume of material being measured in the core liner. Between 100 and 830 m, NGR values only show small variations between 50 and 70 counts/s. From ~830 to 920 m, a sharp decrease in NGR from 70 to 20 counts/s is associated with a decrease in magnetic susceptibility values and an increase in carbonate content. This change corresponds to the chalks of lithostratigraphic Subunit VIIIB (Cores 367-U1499B-26R through 29R). In Core 30R, a sharp increase in NGR values corresponds to the clay with Fe-Mn nodules; this increase continues into the breccia of Subunits IXB and IXC.

We estimated concentrations of K, U, and Th using NGR and bulk density measurements (Figure **F49**) based on a study from De Vleeschouwer et al. (2017). The general trend of each element concentration is similar to the total count values.

Thermal conductivity

Thermal conductivity presents an almost linear increase from the seafloor, with values from 0.8 to ~2 W/(m·K) at ~900 m. The trend of increasing thermal conductivity with depth is used to calculate a heat flow of 110 mW/m^2 (see **Downhole measurements**). This relatively high value is consistent with previous estimates in the area.

Data interpretation and lithology correlation

Correlation with lithology

The variations of magnetic susceptibility and NGR data show some interesting and variable correlations with lithology. For example, low NGR values are associated with the high carbonate content of lithostratigraphic Unit II and Subunit VIIIA, whereas clay/silt has relatively low NGR but high magnetic susceptibility from 260 to 350 m, and an opposite correlation occurs at 420–480 m. The content of magnetic mineral and its mineralogy is reflected in magnetic susceptibility measurements of the formation of clay/silt/sand. Meanwhile, NGR values vary not only with lithology but also within the same sediment type.

Figure F49. Core NGR measurements, Holes U1499A and U1499B. Estimates of K, U, and Th concentrations are derived from NGR measurements using method of De Vleeschouwer et al. (2017).

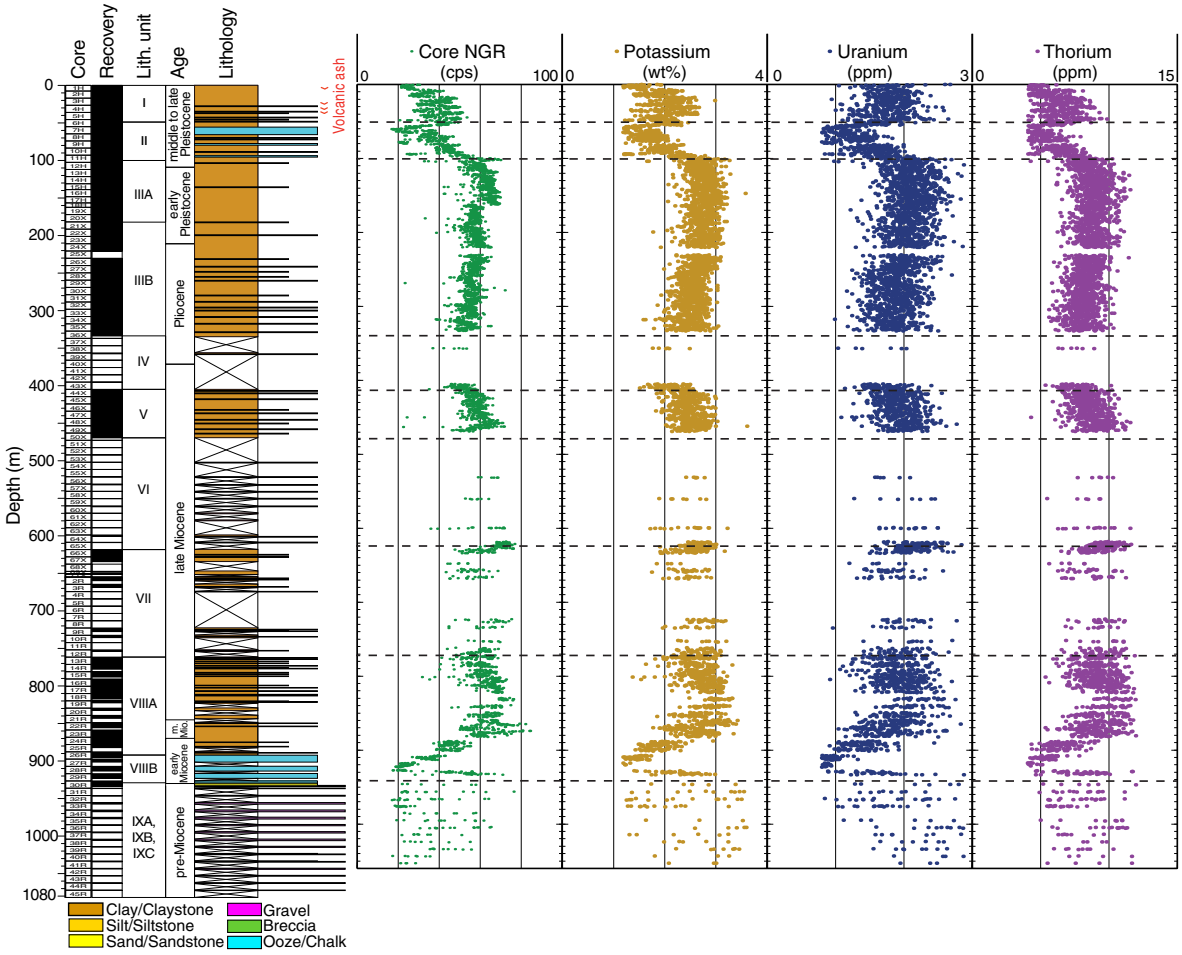

Sediment compaction

The compaction of the sediments is reflected by the variation with depth of most of the physical properties in the uppermost 100 m. Density, *P*-wave velocity, NGR, magnetic susceptibility, and thermal conductivity increase gradually, whereas porosity drops from ~80% to ~50%. For the lower part of Hole U1499A (>170 m) and in Hole U1499B downsection to 930 m (top of the gravel layer in Subunit IXC), density, *P*-wave velocity, and thermal conductivity keep increasing with depth but to a lower extent, whereas NGR and magnetic susceptibility show undulations with opposite variations, reflecting other controlling factors such as the carbonate content.

Ash layers

In Hole U1499A, several peaks in magnetic susceptibility values in the uppermost cores (~5, 20, and 40 m) appear to be associated with ash layers observed in the lithology. Ash layers are characterized by relatively high magnetic susceptibility values in WRMSL and SHMSL measurements. However, although additional ash layers were not identified during core description, others may be present but too thin or dispersed to be observed within the resolution of magnetic susceptibility measurements.

Mass transport deposit in Unit II

The mass transport deposit observed in Sections 367-U1499A-6H-3 through 11H-5 (48.85–100.04 m; 51.19 m thick) coincides with a prominent decrease in magnetic susceptibility and NGR values. The very low values of magnetic susceptibility are likely due to the high concentration of carbonate (see **Lithostratigraphy** and **Geochemistry**). The deposit is also well detected by the decrease in NGR values (Figure **F48**).

Carbonate layer in Subunit VIIIB

From 830 to 930 m (Cores 367-U1499B-26R through 29R), magnetic susceptibility values and NGR counts generally decrease where density increases slightly and *P*-wave velocity increases significantly from 2200 to 2900 m/s. These variations are associated with a significant increase in the carbonate content from ~1 to ~65 wt% in the lowermost part of Subunit VIIIA and in the chalks of Subunit VIIIB.

Gravel layer in Subunit IXC

Section 367-U1499B-30R-6 through Core 45R recovered predominantly pebbles and cobbles with a few limited intervals of clayey silt or silty sand. The *P*-wave velocity of the pebbles/cobbles ranges from ~3000 to ~5500 m/s. The pebbles with the lowest *P*-wave velocity values are mainly the rocks showing fractures or weathering. Because of the low recovery in Subunit IXC, we are not able to determine a trend in velocity.

Downhole measurements

Wireline downhole logging

Logging operations and tools

Downhole log data was acquired after RCB coring in Hole U1499B penetrated to 1081.8 m. Hole conditions in the lowermost part of the hole significantly deteriorated after cutting the last core. The drillers were able to free the stuck drill string, pumped 100 bbl of mud, and raised the bit to 994 m but were never able to get the bit back deeper than ~1053 m. After circulating another 50 bbl of mud to clean cuttings out of the hole, the core (wash) barrel was recovered, and the bit was released in the hole. The end of the pipe was then raised to 877.3 m, where the mechanical bit release sleeve was shifted back into the circulating position. The end of the pipe was raised again to 780 m, and 235 bbl of heavy mud (11 lb/gal barite weighted) were pumped into the borehole to stabilize the hole for the downhole measurements. Finally, the end of the pipe was raised back inside the casing to 85.1 m, and the rig floor was prepared for the logging.

Borehole conditions from end of casing at 651 m to bottom of hole that could be logged at 1020 m were sufficiently good to run two different logging tool strings (Figure **F50**).

The first tool string, a modified triple combo tool string, included the following tools:

- Dipole Sonic Imager (DSI) for acoustic velocity,
- High-Resolution Laterolog Array (HRLA)/Phasor Dual Induction-Spherically Focused Resistivity Tool (DIT) for electrical resistivity,
- Hostile Environment Litho-Density Sonde (HLDS) for bulk density, and
- Hostile Environment Natural Gamma Ray Sonde (HNGS)/Enhanced Digital Telemetry Cartridge (EDTC-B) for NGR.

The first tool run was conducted downward (downlog), collecting data with all the string tools (DSI, HRLA, DIT, HLDS, HNGS, and EDTC-B) with the HLDS caliper closed. An uplog run ("repeat") was then collected with the same recording tools but with the caliper open to ensure the HLDS tool was against the borehole wall and for borehole diameter measurements. Finally, the upward (uplog) main pass collected data with all the string tools (DSI, HRLA, DIT, HLDS, HNGS, and EDTC-B) and with the caliper open as before.

The second tool string was set up with a FMS to collect borehole resistivity images and the HNGS and EDTC-B for correlating with the previous logging runs. The FMS provides geographically orientated images and caliper measurements for both sets of arms. During the first pass, HNGS data were collected while lowering the tools into the borehole (downlog) without collecting FMS data and with the calipers closed (Figure **F51**). We collected FMS and HNGS data during two complete (uplog) runs over the entire open borehole.

The focus of our data analysis is primarily on the uplog main pass measurements. However, in general, measurements during down- and uplogging match well for all data types. Average heave conditions were ~0.5 m just prior to logging. The heave compensator was utilized whenever the tools were in open hole.

Log data processing

After we collected downhole logging information, the raw data were sent to Lamont-Doherty Earth Observatory for processing. Depth corrections were made to the data to account for the offset between rig floor and seafloor and for depth matching between each logging pass. For each logging run, the NGR information was used to define the water–sediment transition (water-casing; seafloor). The original logs were first shifted to the seafloor determined by the step in NGR values at 3770 m wireline log depth below rig floor (WRF) on the FMS/General Purpose Inclinometry Tool (GPIT)/EDTC-B/HNGS main pass. This differs by 1 m from the seafloor depth given by the drillers. Afterward, depth offsets between measurements taken during different logging runs were ad-

Figure F50. Downhole logging tool strings, Site U1499. A. Run 1. B. Run 2. LEH-MT = logging equipment head-mud temperature, EDTC = Enhanced Digital Telemetry Cartridge, HNGS = Hostile Environment Natural Gamma Ray Sonde, HLDS = Hostile Environment Litho-Density Sonde, HRLA = High-Resolution Laterolog Array, DSI = Dipole Sonic Imager, GPIT = General Purpose Inclinometry Tool, FMS = Formation MicroScanner.

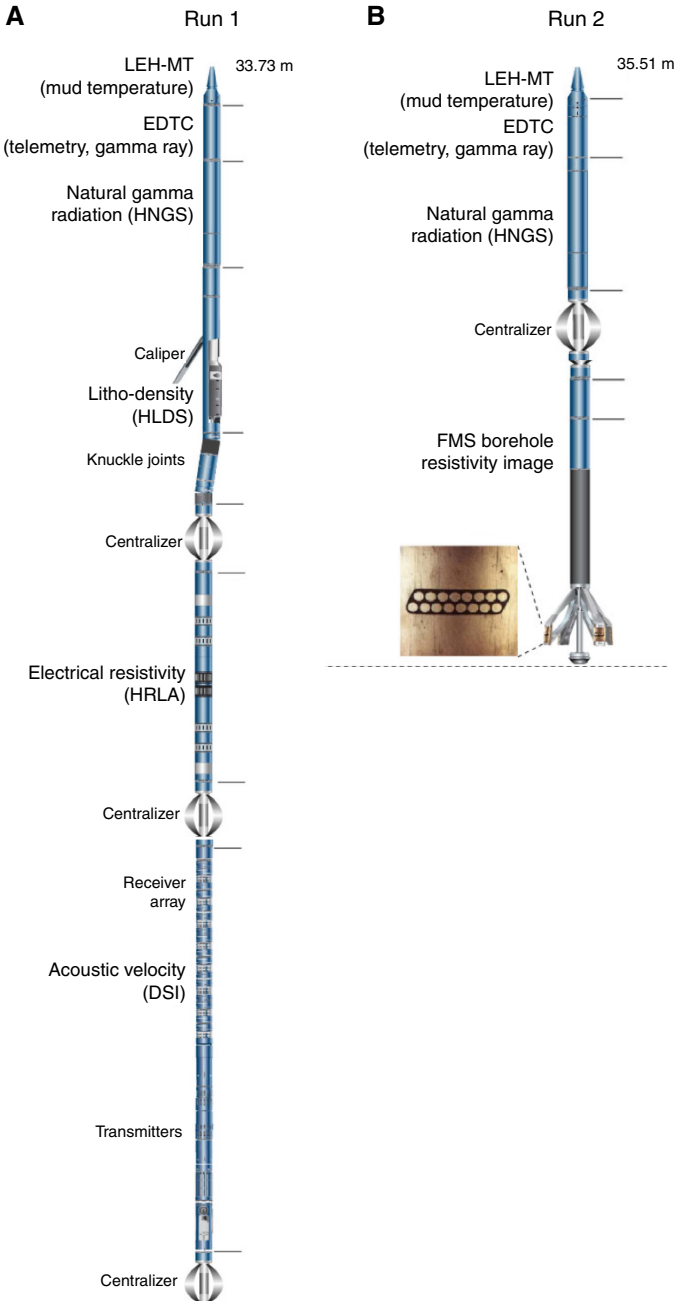

Figure F51. Logging operations summary, Hole U1499B.

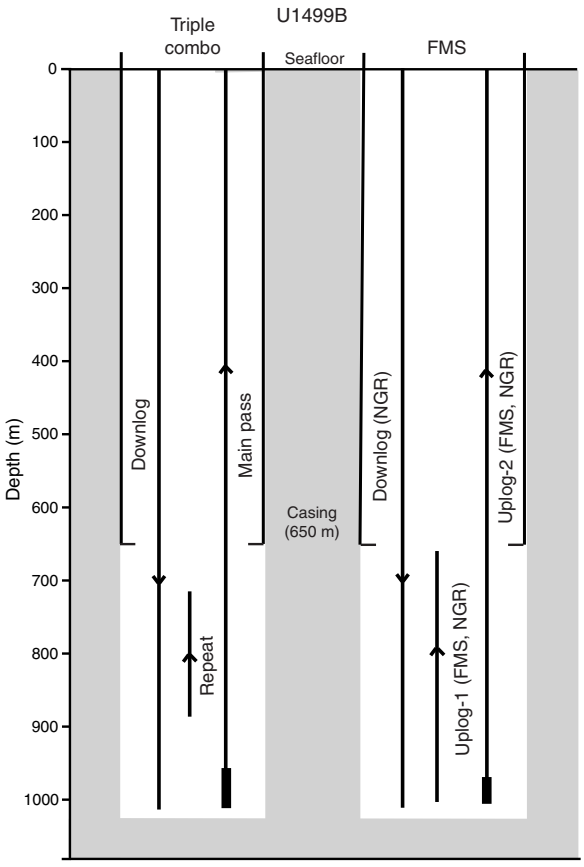

Figure F52. Hole U1499B diameter. Yellow box with dashed lines = size of drill bit (9.875 inches). Left: measurements from triple combo caliper (LCAL). Middle: measurements in two FMS directions. Right: three examples of borehole deformation.

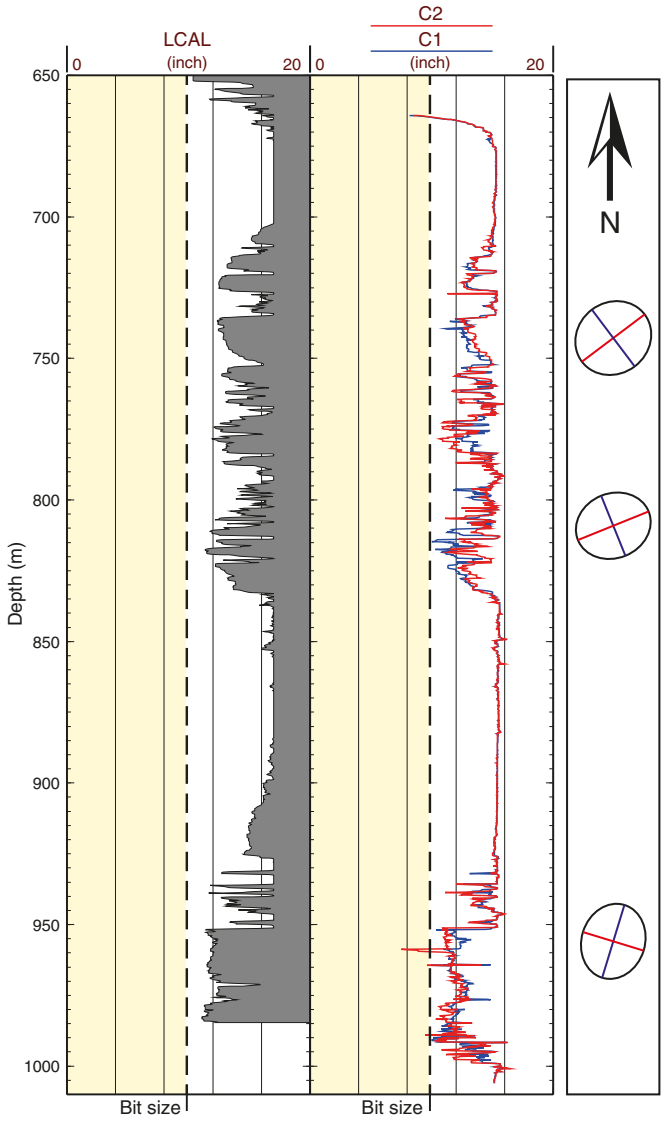

justed. The HLDS and HRLA data were corrected for hole size, and the HNGS data were corrected for hole size and mud weight during the recording. Sonic data were a high priority, and the Schlumberger engineer reprocessed the labeling for both compressional and shear data to improve the data quality. FMS images were processed to convert the electrical signals recorded by the FMS sensors to color-scaled images with both static and dynamic normalization. After this shore-based processing, the resulting data were sent back to the ship a few days later in a variety of formats (ASCII for conventional logs, GIF for FMS images, binary for acoustic waveforms, and SEGY for velocity data).

The collected log data are shown in DOWNHOLE in **Supplementary material**.

Log data quality

The borehole was generally in good condition, with measured diameters from ~10 inches at 664.15 m to >16 inches in the washout areas (Figure **F52**). Log data quality can be affected by the large borehole diameter in the washout zones. These zones were observed from 670 to 710 m, which corresponds to an interval of very low core recovery, and from 830 to 920 m, which spans a variety of lithologies in the lower half of lithostratigraphic Subunit VIIIA and relatively well recovered claystones and chalks in Subunit VIIIB. The borehole diameter decreases to 8 inches in the lowermost formation of the borehole (sandstones, breccias, and gravels of Unit IX) and in some intervals between 705 and 830 m. The FMS resistivity images are generally of good quality, except where large borehole diameters do not allow good contact of the FMS sensors to the borehole wall, resulting in dark (conductive) images. The two FMS passes followed nearly the same track over most parts of the borehole. The sonic velocities are very consistent with the shipboard laboratory measurements on the recovered cores, suggesting a general good quality of the DSI measurements.

Logging units

Downhole logging data for Hole U1499B are summarized in Figures **F52** and **F53**. The logged interval is divided into 10 logging units, which are described below and are shown in Figure **F53**.

Logging Unit 1

Logging Unit 1 spans from 651 m (end of casing) to 726 m and is characterized by small-scale variations in NGR, bulk density, *P*-wave velocity, and borehole size. Within the uppermost part of the unit (~651–697 m), NGR gradually increases from ~60 to ~80 gAPI and then gradually decreases with depth from ~80 to ~55 gAPI

Figure F53. Downhole logs, Hole U1499B. Downhole logs are on the logging depth scale (WSF) and MAD discrete samples, PWC, and core recovery data are on the core depth scale (CSF-A). Small differences between these depth scales are usually <2 m. HCGR = computed gamma ray.

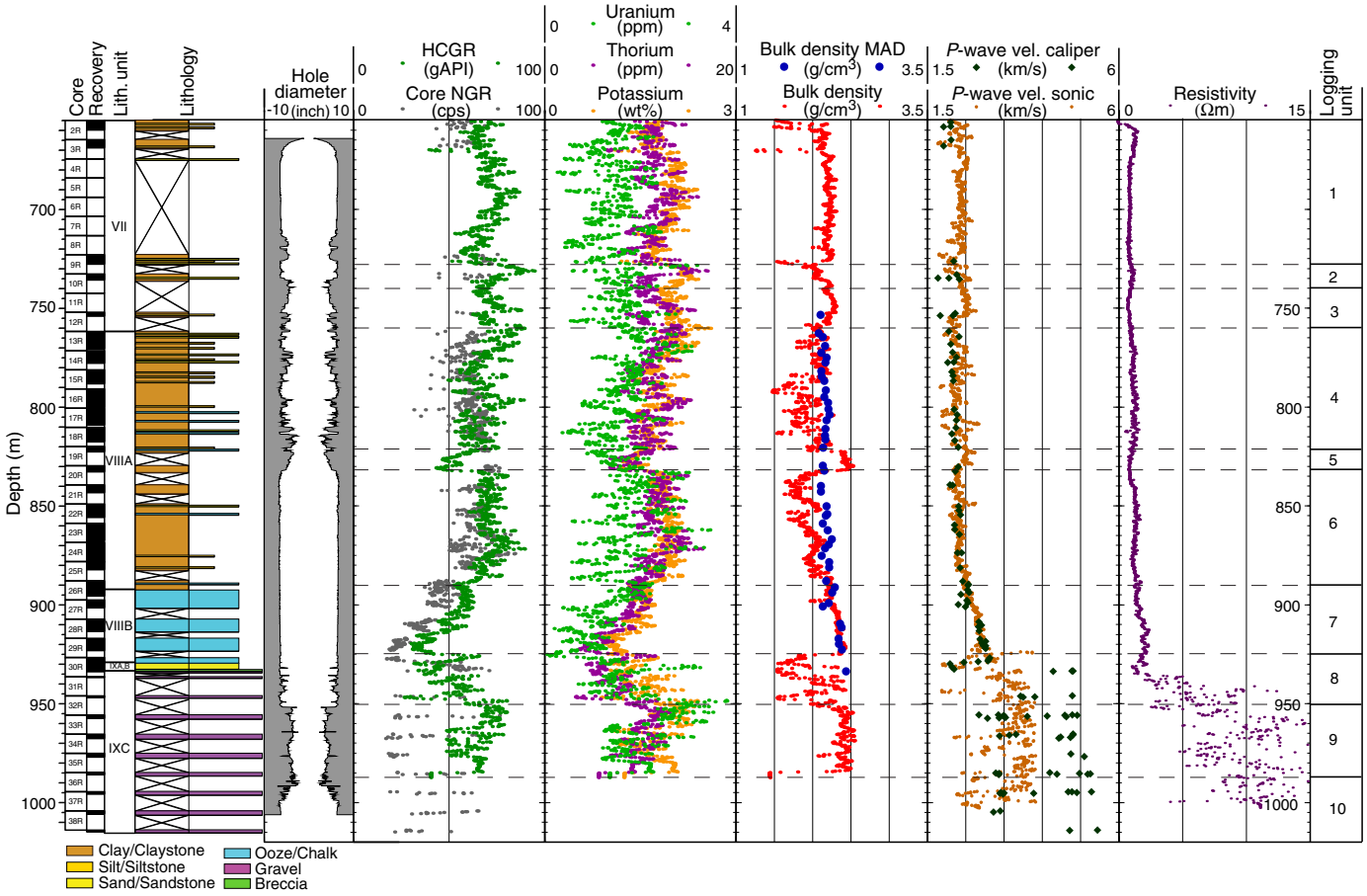

within the underlying part (~697–726 m). Consequently, Th, K, and U concentrations follow this trend. However, bulk density, *P*-wave velocity, and resistivity are relatively homogeneous within logging Unit 1. FMS images show many interlayers with high resistivity and nearly horizontal bedding (e.g., 675, 685, 690, and 720 m; see DOWNHOLE in **Supplementary material**).

Logging Unit 2

Logging Unit 2 spans from 726 to 739 m and is characterized by high NGR values and relatively low bulk density and *P*-wave velocity. Resistivity is relatively homogeneous. Around 730 m, a high NGR peak coincides with a low in bulk density and *P*-wave velocity (~2.0 g/cm^3 and 2.2 km/s, respectively). In the FMS images, horizontal bedding continues in this unit. Notably, a relatively thick interlayer with low resistivity was observed from ~734 to 735 m.

Logging Unit 3

Logging Unit 3 spans from 740 to 760 m and is characterized by relatively high NGR values and *P*-wave velocity, whereas density and resistivity are in the same range as Unit 1. The FMS images show a slightly scattered pattern within the unit.

Logging Unit 4

Logging Unit 4 spans from 760 to 820 m and presents a constant character and trend of most of the log values (e.g., density, resistivity, and *P*-wave velocity). Caliper measurements indicate that the borehole is relatively narrow in this zone (Figure **F52**). The FMS data show continuous, horizontal layering within this unit, even though the lower part (~788–813 m) presents poor quality in logging imagery.

Logging Unit 5

Logging Unit 5 spans from 820 to 840 m and is characterized by a sharp increase in bulk density, a slight increase in *P*-wave velocity, and an abrupt decrease in NGR values. This unit, especially at ~823–833 m, is characterized by scattered pattern in the FMS images, except for the lowermost part (~833–840 m), which shows horizontal bedding.

Logging Unit 6

Logging Unit 6 spans from 840 to 890 m and is characterized by relatively constant values of NGR, *P*-wave velocity, and bulk density. The FMS data are of poor quality; the variation in bedding, however, increases with depth throughout this unit.

Logging Unit 7

Logging Unit 7 spans from 890 to 925 m and is characterized by increasing values in density, *P*-wave velocity, and resistivity combined with NGR values decreasing from ~ 62 to ~30 gAPI with depth. The FMS images show many short-interval variations resulting in thin, horizontal layering in the upper part (~890–905 m), whereas scattered patterns were observed in the lower part (~905–925 m).

Figure F54. FMS images, Hole U1499B. These images use a 2 m interval dynamic normalization to enhance local contrast between conductive and resistive material. A. Contrasting smooth and irregular layers possibly reflecting claystones and sandstones in an interval of low core recovery, logging Unit 1/lithostratigraphic Unit VII. B. 10 cm relatively horizontal bedding in claystones and sandstones, logging Unit 1/lithostratigraphic Unit VII. C. Irregular, oblique, and chaotic structures or bedding in gravel/breccia, logging Unit 3 corresponding to lithostratigraphic Subunit IXC.

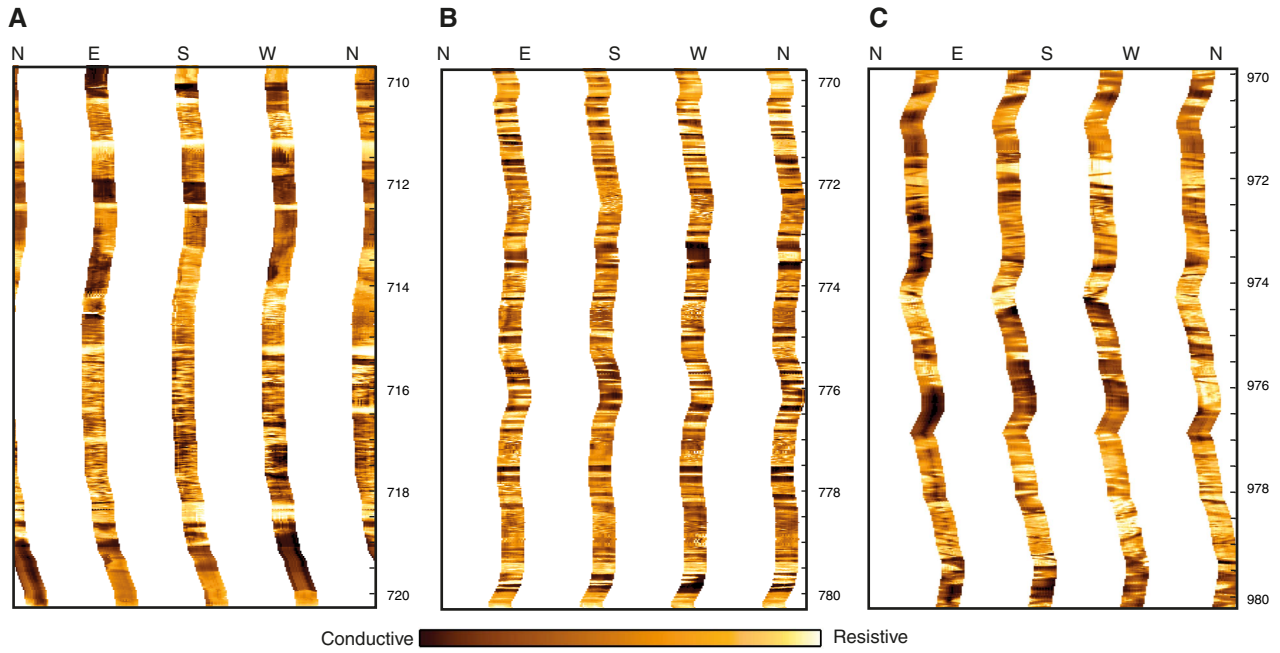

Logging Unit 8

Logging Unit 8 spans from 925 to 950 m and shows a change in the character and trend of most of the log curves. In general, NGR, density, *P*-wave velocity, and resistivity show very scattered values. *P*-wave velocity, NGR, and resistivity with generally increase with depth, and bulk density decreases. The FMS data are poor quality and show thicker beds than the unit above.

Logging Unit 9

The data set in logging Unit 9 shows very scattered values. This deeper unit (950–990 m) presents a NGR mean value of 63 gAPI and a relatively high resistivity value (mean value = 12 Ωm). *P*-wave velocity is highly variable, ranging from 2.1 to 4.0 km/s (mean value = 3.4 km/s). The FMS images show highly variable and oblique textures (Figure **F54**).

Logging Unit 10

In the bottom part of the hole (990 m to bottom of hole) in logging Unit 10, we observed scattered data with relatively high values of *P*-wave velocity and resistivity. As in logging Unit 9, the FMS images present variable and oblique textures.

Downhole logs and lithology

Downhole logs and FMS images provide important constraints on the lithology at Site U1499. Lithostratigraphic Subunit VIIIA is ~130 m of claystones and siltstones with variable amounts of carbonate, as well as interbeds of silt and foraminifer-rich sandstone. In this zone, the log data show relatively constant values of NGR, density, and *P*-wave velocity. The only observable change is in logging Unit 5, in an interval from which there was no recovery in lithostratigraphic Subunit VIIIA. Low NGR values and high density values in this no-recovery zone can be tentatively ascribed to a richer carbonate content.

Within the chalks of lithostratigraphic Subunit VIIIB, NGR values clearly decrease and density and velocity increase with depth, which likely reflects the increase of carbonate content with depth, as confirmed by geochemical analyses. The transition from carbonate to sandstone, breccia, and gravel at the boundary between lithostratigraphic Units VIII and IX corresponds to an increase in NGR and velocity and a notable decrease in density. All the log values in lithostratigraphic Unit IX are very scattered, confirming the heterogeneity of this deepest unit cored and logged in Hole U1499B.

NGR measurements from downhole logging generally agree with laboratory NGR measurements. A decrease to ~50 gAPI was observed in the formation of lithostratigraphic Subunit VIIIB (high carbonate) between 870 and 925 m.

Resistivity measurements from downhole logging show relatively constant values throughout logging Units 1–7 (downhole to 925 m). Resistivity increases sharply and exhibits more variability in the sandstones, breccias, and gravels of lithostratigraphic Unit IX.

The acquired FMS images provide constraints on the formation characteristics in addition to contributing to constraining the nature of the formation in zones where core recovery was poor (Figure **F53**), but they are strongly influenced by the hole diameter variations. The FMS images from the low-recovery zones in the lower part of lithostratigraphic Unit VII (~660–665, ~669–723, and ~727–761 m) generally show alternating smooth and patchy textures (Figure **F54**). Images from the no-recovery zone within lithostratigraphic Subunit VIIIA (~823–849 m) are similar. The sandstones, breccias, and gravels of lithostratigraphic Unit IX (logging Units 9 and 10) show highly variable and oblique textures on the FMS images (Figure **F54**), possibly reflecting the scattered orientation of the gravel clasts or the presence of faults and fractures in the gravel or the matrix (see DOWNHOLE in **Supplementary material**).

Figure F55. APCT-3 temperature-time series with extrapolated formation temperature estimates, Hole U1499A (see Table T13).

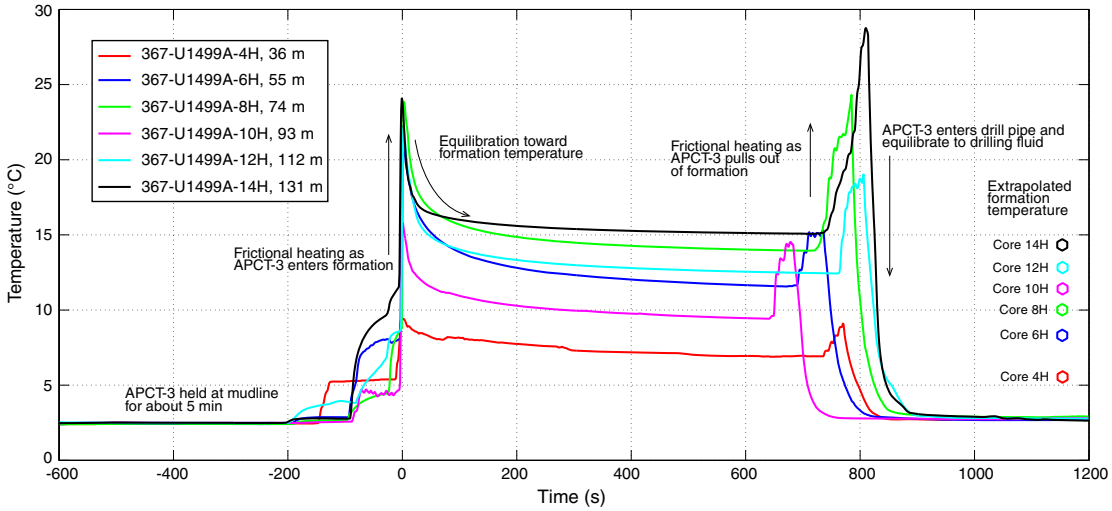

Table T13. APCT-3 measurements, Hole U1499A. **Download table in CSV format.**

Core	Depth of APCT-3 measurement (m)	Temperature (°C)
367-U1499A-		
Seafloor	0	2.50
4H	36	5.46
6H	55	8.09
8H	74	10.04
10H	93	11.45
12H	112	12.90
14H	131	14.42

Comparison of sonic velocity and PWC measurements

In general, the velocities measured with the Versatile Seismic Imager (VSI) tool match the PWC measurements taken with the *x*-axis caliper on the SHMSL on the split cores. In the lowermost lithostratigraphic Unit IX, PWC velocities are higher than those measured in situ downhole with the DSI. In this unit, core recovery was very low, and the PWC velocity could only be measured on the cobbles and pebbles recovered. Thus, the PWC velocities are clearly higher than and not representative of the overall formation velocity.

Downhole temperature measurement and heat flow calculation

Six in situ formation temperature measurements were conducted using the APCT-3 (Figure **F55**). Extrapolated formation temperature values range from 5.46°C at 36 m (Core 367-U1499A-4H) to 14.42°C at 131 m (Core 14H) (Table **T13**). These values, with a seafloor temperature of 2.5°C, indicate a linear increase of the temperature with depth and give a geothermal gradient of 93°C/km (Figure **F56**). Thermal resistance was calculated in the upper 131 m using the "linear approach" (Pribnow et al., 2000; see **Downhole measurements** in the Expedition 367/368 methods chapter [Sun et al., 2018]). The slope of the linear fit between temperature and thermal resistance indicates a heat flow estimation of 110 mW/m^2. This value is in agreement with the general high heat flow of the area (Figure **F57**).

Figure F56. Heat flow calculations, Hole U1499A. A. Formation temperature measurements. B. Thermal conductivity data from core measurements and calculated thermal resistance. C. Thermal resistance plotted against formation temperature, providing heat flow estimate for Hole U1499A of 110 mW/m^2.

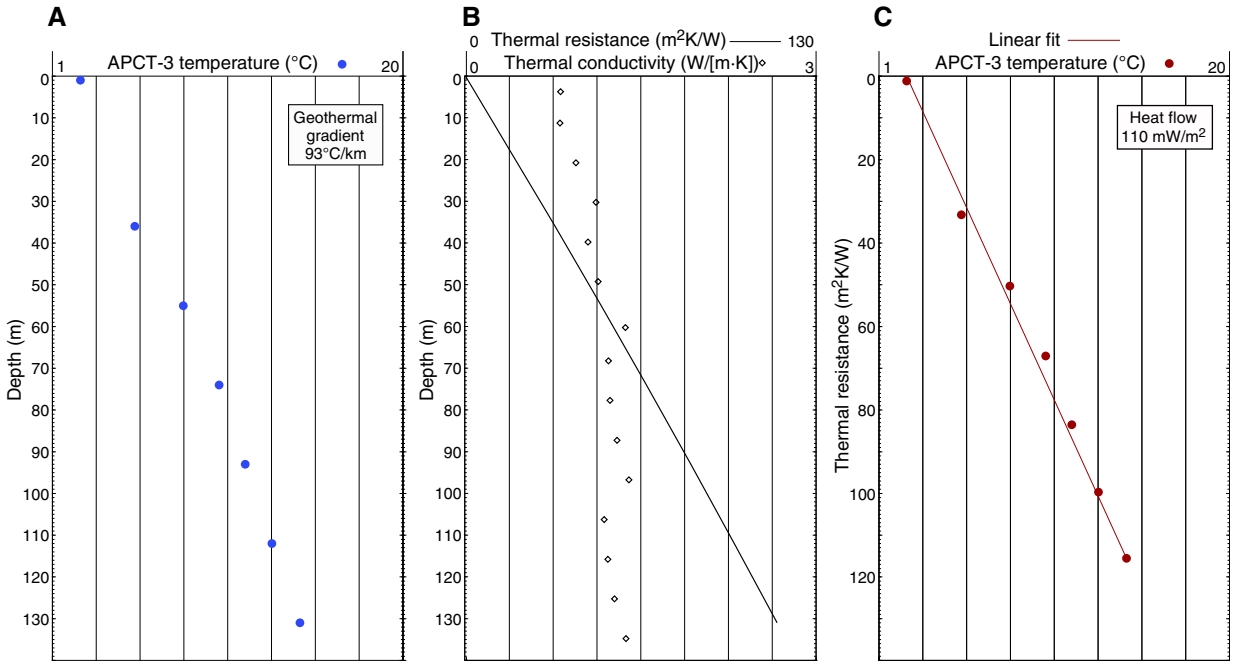

Figure F57. Seafloor heat flow values, South China Sea. Large circle = value calculated based on Site U1499 data, smaller circles = previous measurements compiled in Li et al. (2010, 2015c).

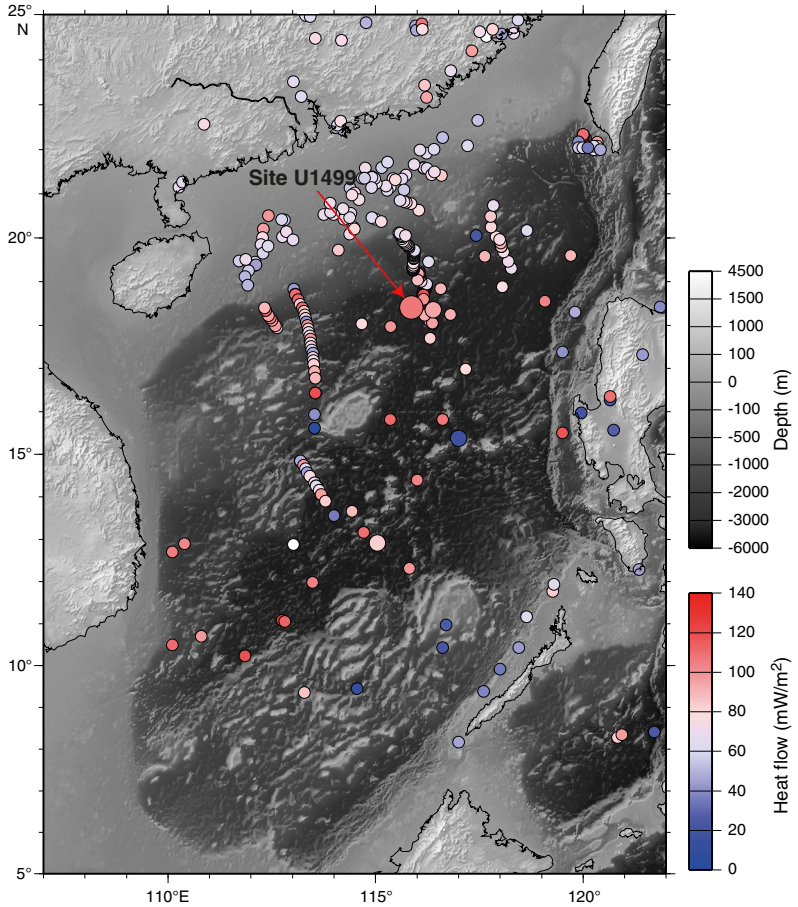

Correlation to seismic data

We used downhole log data, physical property measurements on cores and samples, and other available data to correlate Site U1499 data to the available seismic reflection profiles. We also used the Site U1499 density and sonic velocity data to create synthetic seismograms that provided additional constraints on the correlation. All correlations of the seismic reflection data with the Site U1499 core and log data, as well as the synthetic seismogram tests, were performed onboard using the Petrel software.

Velocity and density data

Velocity and density data were acquired in the laboratory (whole-round core sections [*P*-wave logger; PWL] and split-core sections [PWC]) in Holes U1499A and U1499B and from downhole logging between 655 and ~1020 m in Hole U1499B (see **Physical properties** and **Downhole measurements**).

The PWL data were measured only for whole-round APC core sections from the upper part of Hole U1499A (0–162 m). PWL data, once cleaned of the outliers resulting from automatic WRMSL data acquisition (see **Physical properties** in the Expedition 367/368 methods chapter [Sun et al., 2018]), are in substantial agreement with the PWC velocity data acquired from split-core sections.

Downhole log velocity data were collected using the DSI tool, and downhole density data were collected using the HDSL. Log-sonic velocities and PWC velocities are in very good agreement except for the deepest breccias and gravels of lithostratigraphic Subunit IXC. In Subunit IXC, PWC overestimates the velocities; they could only be measured on the cobbles and pebbles of the matrix-supported formation. In addition, core recovery in this unit was very poor. DSI log-velocity is considered to be more representative of the true formation velocity in this section. For seismic correlation, we used PWC values and density values from MAD and GRA from Hole U1499A (0–655 m), whereas below we used the downhole logging velocity and density data (Table **T14**).

Time-depth relations from the velocity data

TDRs are generally assumed to be quadratic polynomial functions from the interpolation of depth-velocity data. From the depth-velocity data, we computed the incremental TWT (Ti_n) as

$$Ti_n = [(d_n - d_{n-1})/V_n] \times 2 \times 1000,$$

where d_n is the depth of the nth layer and V_n is the relative velocity. The incremental Ti is multiplied by 2000 for conversion into TWT expressed in milliseconds.

From Ti_n we derived the cumulative TWT (Tc_n) expressed as

$$Tc_n = Tc_{n-1} + Ti_n$$

Table T14. Velocity and density information used for TDR computation, Site U1499. **Download table in CSV format.**

Depth (m)	*P*-wave velocity information	Depth (m)	Density information
0–655	*P*-wave caliper	0–655	GRA and MAD
333–406	Poor recovery; estimated velocity = 2.1 km/s	655–1020	HLSD density (downhole measurement)
531–561	Poor recovery; estimated velocity = 2.1 km/s		
655–1020	*P*-wave sonic (downhole measurement)		

and finally the TWT adjusted from the seafloor (Ta) as

$$Ta_n = Tc_n + Ta,$$

where Ta is the TWT at the seafloor expressed in milliseconds.

If the TDR is referred to the seafloor, the intercept of the interpolated quadratic polynomial functions is set to 0.

Figure **F58** shows the velocity and density values collected with the PWC and the downhole measurements at Site U1499. TDR is computed relative to the seafloor and assuming a constant velocity of 2.1 km/s for the poor-recovery intervals that are inferred to be predominantly loosely consolidated sands/silts and for which no downhole log data were acquired (Table **T14**). We considered these poor-recovery zones as our seismic upper reflectors. Because we had no meaningful core recovery to make PWC velocity measurements on cores and no log data in these intervals, we assumed a velocity of 2.1 km/s based on velocity values measured with the DSI in the deeper poor-recovery sandy part (670–720 m; see **Downhole measurements** and Inderbitzen, 1974).

The resulting quadratic polynomial function is

$$d = 0.0003t^2 + 0.5659t,$$

where d is the depth in meters and t the TWT in milliseconds.

Comparison of time-depth relations

We compared our Site U1499 TDR with others collected during previous expeditions in the SCS (Wang et al. 2000; Li et al. 2008, 2015c). Figure **F59** shows the comparison of the Site U1499 TDR to those for Sites 1148, U1431, and U1433. The TDRs are in substantial agreement, except for the Site 1148 TDR, which shows higher velocities in the deeper layers.

Data correlations with Petrel

We correlated the site survey seismic reflection data with the data collected from whole-round cores (GRA density), split cores (MAD and PWC velocity), and log data (HDSL density and SVEL-

Figure F58. HLDS density and DSI velocity collected during logging, PWC velocity data, and TDR adjusted to seafloor, Site U1499. PWC velocity data were used from the seafloor to 655 m, and DSI velocity data were used below that depth (see Table T14).

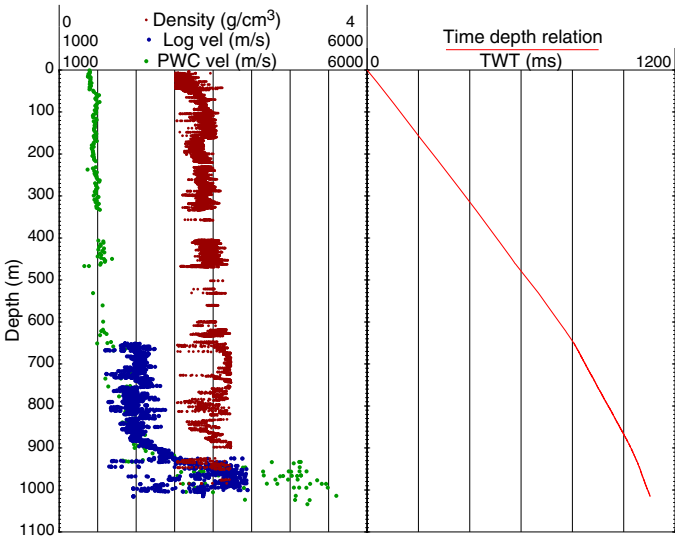

Figure F59. Site U1499 TDR curve compared to Sites U1431, U1433, and 1148 (Li et al., 2008).

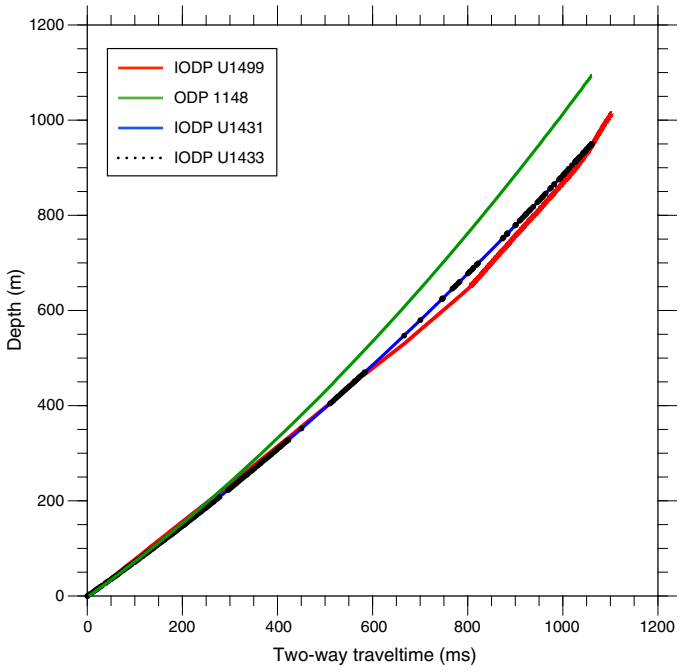

DSI velocity). We also considered other data collected on board such as NGR, magnetic susceptibility, lithostratigraphic unit descriptions, and carbonate content. All of these properties were plotted over the seismic section with Petrel (Figure **F60**).

The following import flow process was used:

1. The coordinate system of the project was set (for Expedition 367: WGS1984_UTM50N),
2. A new seismic folder and a new survey were created,
3. SEGY data were imported with presettings (after the check of the Trace Header Information with the SeiSee software),
4. The "Well" was created,
5. The TDR file was imported (the file must have the depth-TWT adjusted with respect to the seafloor; we first chose the raw caliper and PWL V_P curve to generate it), and
6. Well logs (ASCII files) for all the properties of interest were imported (the file must be tab delimited and can be directly imported from the LIMS database; we chose to import CSF-B depths and values of interest).

We cleaned the data to remove the outliers before importing the values in Petrel (see **Physical properties**). An additional moving smoothing filter was also applied for GRA density. For the velocity data, more cleaning was applied; we manually checked the differences that might be created by manual or automatic picking of the first break for the caliper data.

The physical properties were displayed over the seismic data to allow a direct comparison between the reflectors and the property trends. The data shown in Figure **F60** use the computed Site U1499 TDR (Figure **F58**) and show a good correlation between the main upper reflectors and the poor-recovery sandy intervals. In contrast, the main sedimentological and physical property changes related to the boundary between lithostratigraphic Units VIII and IX do not correlate to the reflector observed at ~5.9 s if the latter is interpreted to be the acoustic basement Tg reflector. The Tg reflector in this region is a distinct unconformity onto which seismic Unconformities T60 and T40 onlap, and younger strata above these show undisturbed and parallel bedding. Below the Tg reflector, seismic data indicate the presence of discontinuous and partly dipping reflectors strongly suggesting the presence of tectonically disturbed beds. Within the cored section, the boundary between undisrupted sedimentary layers (top) and syntectonic sediments (below) form the boundary between lithostratigraphic Units VIII and IX within Core 367-U1499B-30R at ~930 m, which contains an extremely large age span of supposedly early Oligocene to lowermost early Miocene.

Locally on the seismic profile, the acoustic basement is less clear than on other sections of the profiles, and the reflector at 5.9 s TWT has a relatively low amplitude (Figure **F61**). Moreover, although the correlation between the Tg reflector at ~ 5.9 s TWT and the boundary between lithostratigraphic Units VIII and IX would be intuitively obvious, this interpretation is difficult to reconcile with the observed physical properties and logging data. The only way for the top of lithostratigraphic Unit IX (~930 m) to fit with both the ~5.9 s Tg reflector and the ~5.42 s reflector (upper sandy layers; ~330 m) would be to apply a 30% velocity increase in the deeper part of the TDR from 300 to 930 m (Figure **F62**). This velocity increase seems unrealistic and led to much discussion on how to resolve the apparent discrepancy (see discussion on alternate TDR, below).

Evaluation of alternative time-depth relations

We performed tests of alternative velocity assumptions. Two of them help characterize the effects of the TDR on the fit with the available seismic data.

The first test included the use of PWC velocity and downhole measurements data without imposing a constant velocity for the sandy poor-recovery zones (333–406 and 531–561 m). In this case, the TDR equation is

$$d = 0.0003t^2 + 0.5715t,$$

where d is the depth in meters and t is the TWT in milliseconds.

The resulting seismic correlation with this equation is shown in Figure **F63**. In this case, the velocity in the poor-recovery zone at 333–406 m is likely underestimated; there is a misfit between the relatively strong reflectors near 5.55–5.70 s TWT and the poor-recovery zones.

The second test was aimed to fit the top of lithostratigraphic Unit IX (~930 m) with the ~5.9 s TWT Tg reflector and to fit the upper sandy layers (~330 m) with the ~5.42 s TWT. To reach these constraints, we needed to compute an alternative TDR with a 30% increase in velocity in the deeper part from 300 to 930 m with respect to the original TDR (Figure **F62**). The resulting polynomial interpolation is

$$d = 0.0004t^2 + 0.63678t.$$

The resulting seismic correlation with this equation is shown in Figure **F64**. Despite the intervals of low recovery, the data quality and the good match between laboratory and downhole data seems to exclude such overall velocity values as being too far from the observations. So although the correlation with lithologic variations could be made to match the Tg reflector at ~5.9 s TWT, this model conflicts with both caliper and log velocity data in the deeper parts of the section. In contrast, the model in Figure **F60** honors the velocity data from core and logging and includes reasonable assumptions about the velocities in sandy layers of low recovery. Postcruise

Figure F60. Seismic section across Site U1499. Site is located at lithostratigraphic unit plot (gray = Unit I, light brown = Unit II, light blue = Subunit IIIA, yellow = Subunit IIIB, pink = Unit IV, blue = Unit V, purple = Unit VI, violet = Unit VII, medium blue = Subunit VIIIA, cyan = Subunit VIIIB, orange = Unit IX). Other Site U1499 data are offset from site location: magnetic susceptibility logger (MSL), NGR, PWC velocity and VSI shear velocity (SVEL) logging data, GRA density, and $CaCO_3$ content.

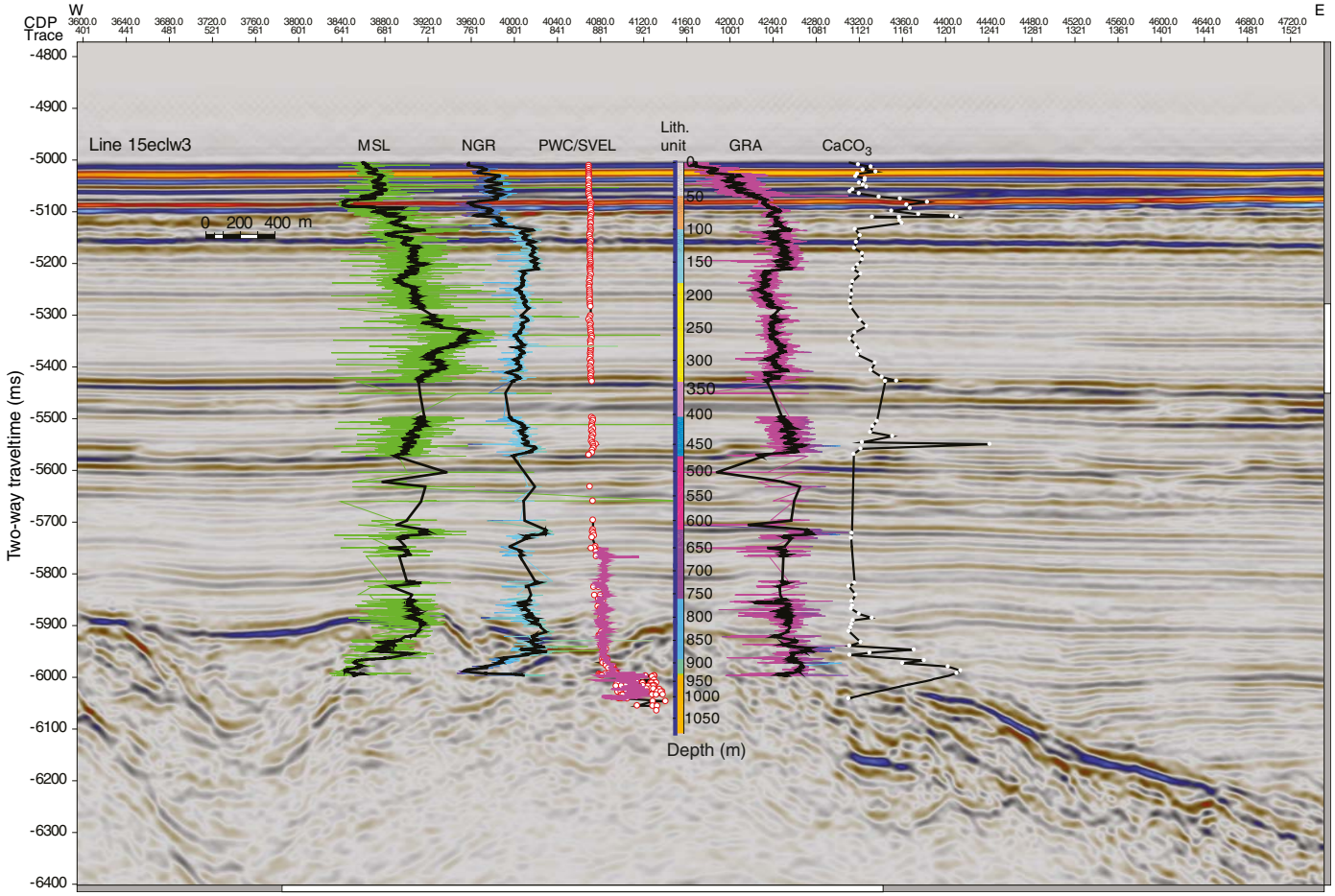

research, including the analysis of FMS images from Site U1499, detailed interpretations of seismic profiles close to Site U1499, and comparisons with TDR profiles from nearby Sites U1501, U1502, and U1505, will all be necessary to further address this issue and could possibly result in a unique model.

Synthetic seismograms with Petrel

We used the Seismic interpretation module in Petrel to compute synthetic seismograms to further constrain the TDR. The parameters that need to be defined to compute synthetic seismograms are the seismic source signature, density curve, and velocity curve.

We performed several trials comparing the synthetic seismograms with the seismic reflection data. Petrel allows the choice of single frequency–centered sources. We chose Ricker wavelets centered at the mean values of the frequency content in our seismograms. For Hole U1499A (from the seafloor to 655 m), we used the density data derived from the MAD and GRA density data, whereas deeper than that (Hole U1499B) we used the HDSL density log data (Table **T14**). Similarly, we used the PWC velocity data from 0 to 655 m and the DSI logging velocity data below that. We conducted several trials with binning density and velocity data over different depth intervals. Our best fit was obtained with a 5 m binning for both density and velocity, which did not decimate the data. The resulting synthetic seismogram is shown in Figure **F61**.

Figure F61. Synthetic seismogram computed for Site U1499. Panels from left to right: density (blue) and velocity (black) values, reflection coefficient (RC), seismic source properties, and real seismic traces with synthetic seismogram inserted in the center.

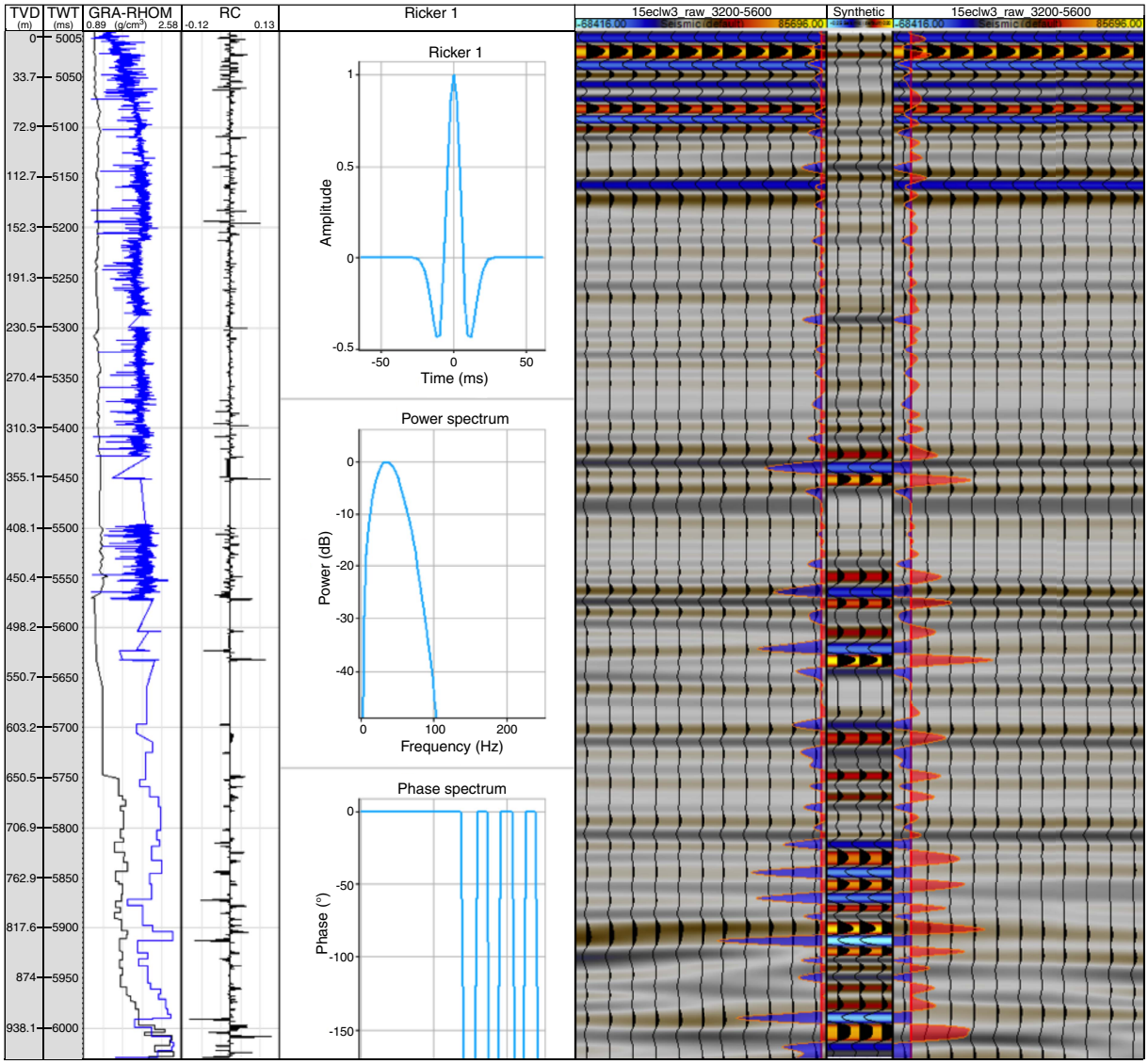

Figure F62. Preferred Site U1499 TDR and modified TDR required to fit the top of lithostratigraphic Unit IX with the reflector at 5.9 s (see Figure F60).

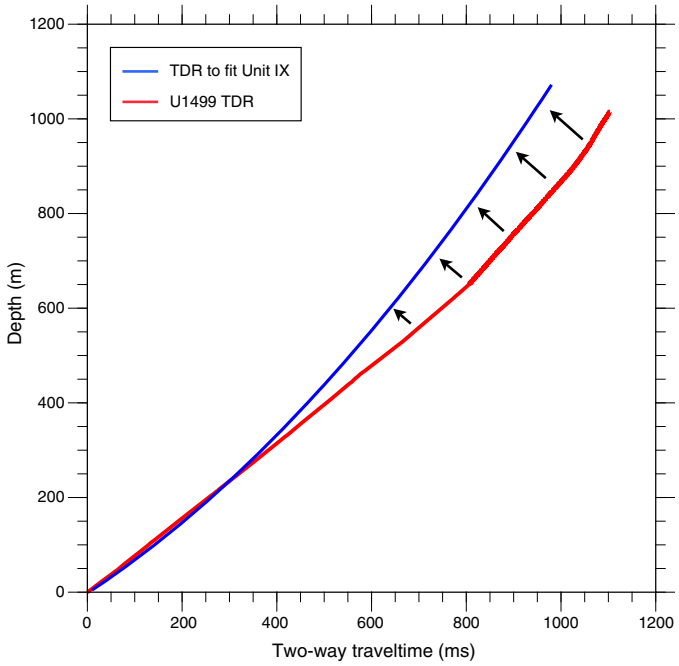

Figure F63. Seismic section across Site U1499 using alternative TDRs without constant velocity for sandy no-recovery zones. Site is located at lithostratigraphic unit plot (see Figure F60). Other Site U1499 data are offset from site location: MSL, NGR, PWC velocity and VSI shear velocity logging data, GRA density, and $CaCO_3$ content.

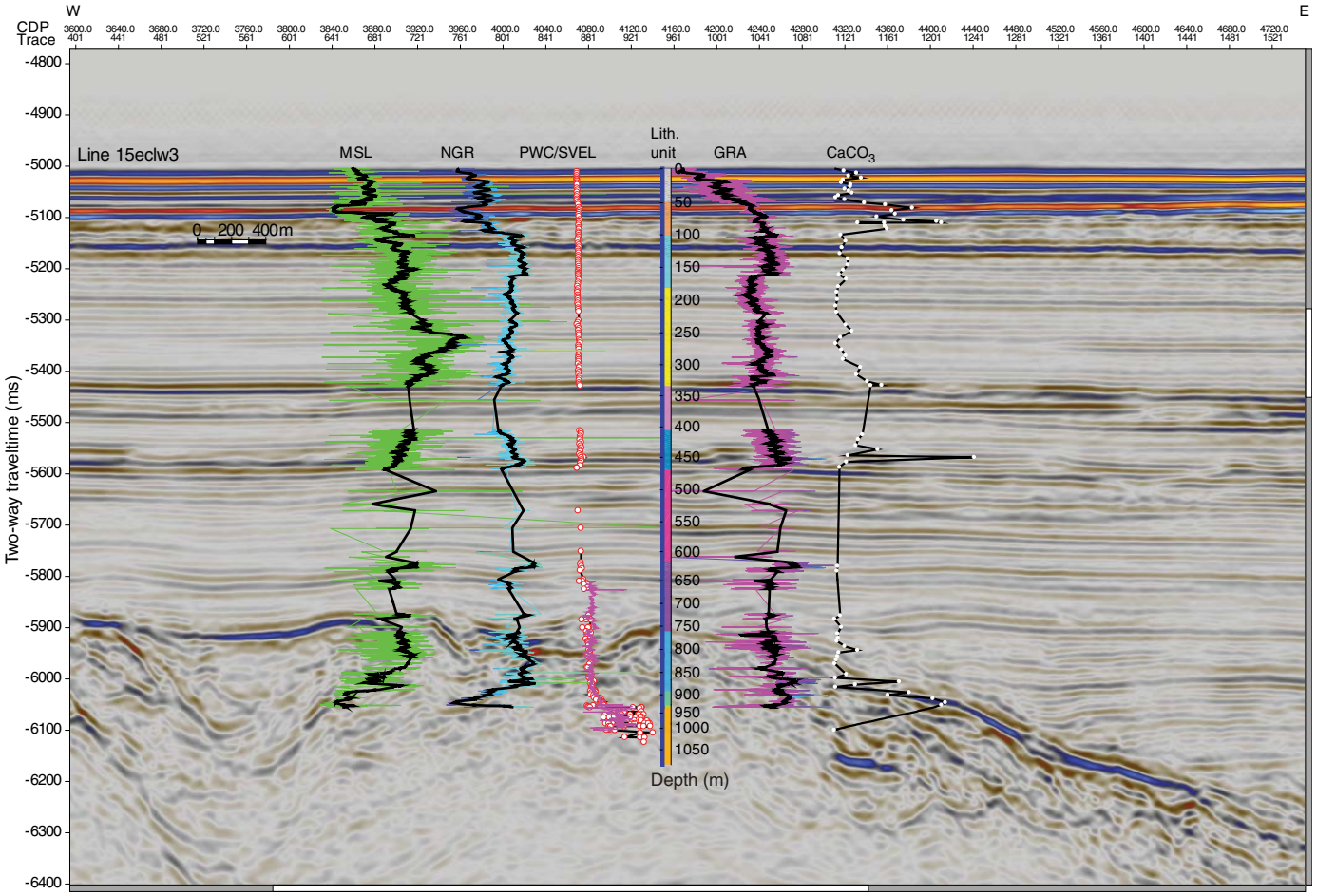

Figure F64. Seismic section across Site U1499 using alternative TDRs with an increase in velocity (blue line in Figure F62). Site is located at lithostratigraphic unit plot (see Figure F60). Other Site U1499 data are offset from site location: MSL, NGR, PWC velocity and VSI shear velocity logging data, GRA density, and $CaCO_3$ content.

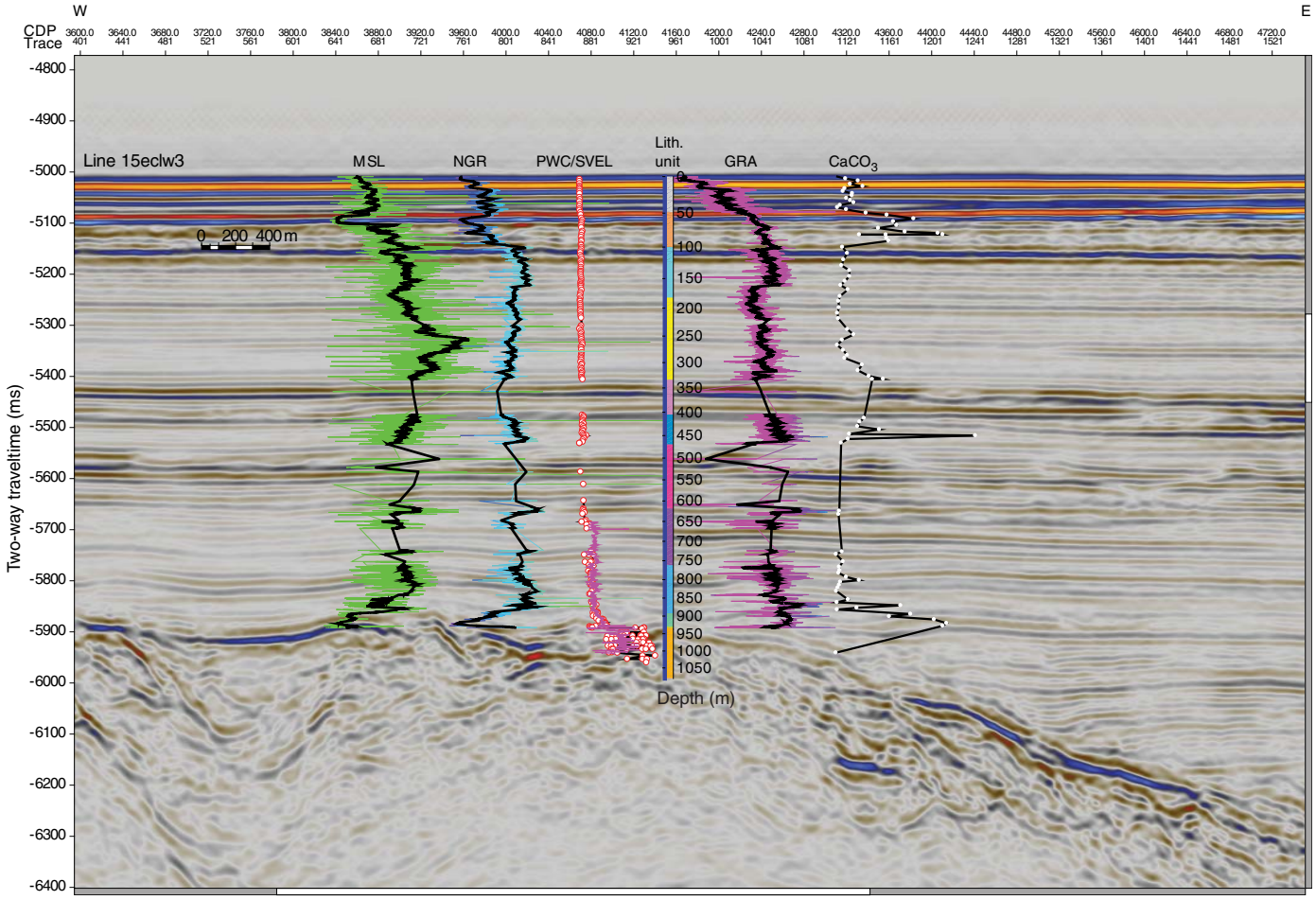

References

Briais, A., Patriat, P., and Tapponnier, P., 1993. Updated interpretation of magnetic anomalies and seafloor spreading stages in the South China Sea: implications for the Tertiary tectonics of Southeast Asia. *Journal of Geophysical Research: Solid Earth,* 98(B4):6299–6328. **http://dx.doi.org/10.1029/92JB02280**

Bryant, W.R., and Bennett, R.H., 1988. Origin, physical, and mineralogical nature of red clays: the Pacific Ocean Basin as a model. *Geo-Marine Letters,* 8(4):189–249. **http://dx.doi.org/10.1007/BF02281640**

Chen, Y., Ussler, W., III, Haflidason, H., Lepland, A., Leif, R., Hovland, M., and Hjelstuen, B.O., 2010. Sources of methane inferred from pore water $\delta^{13}C$ of dissolved inorganic carbon in Pockmark G11, offshore Mid-Norway. *Chemical Geology,* 275(3–4):127–138. **https://doi.org/10.1016/j.chemgeo.2010.04.013**

Clark, D.A., and Emerson, D.W., 1991. Notes on rock magnetization characteristics in applied geophysical studies. *Exploration Geophysics,* 22(3):547–555. **http://dx.doi.org/10.1071/EG991547**

Clemens, S.C., Murray, D.W., and Prell, W.L., 1996. Nonstationary phase of the Plio-Pleistocene Asian monsoon. *Science,* 274(5289):943–948. **http://dx.doi.org/10.1126/science.274.5289.943**

Clift, P.D., Lin, J., and ODP Leg 184 Scientific Party, 2001. Patterns of extension and magmatism along the continent-ocean boundary, South China margin. *In* Wilson, R.C.L., Beslier, M.-O., Whitmarsh, R.B., Froitzheim, N., and Taylor, B. (Eds.), *Non-Volcanic Rifting of Continental Margins: A Comparison of Evidence from Land and Sea.* Geological Society Special Publication, 187:489–510. **http://dx.doi.org/10.1144/GSL.SP.2001.187.01.24**

De Vleeschouwer, D., Dunlea, A.G., Auer, G., Anderson, C.H., Brumsack, H., de Loach, A., Gurnis, M., et al., 2017. Quantifying K, U, and Th contents of marine sediments using shipboard natural gamma radiation spectra measured on DV *JOIDES Resolution*. *Geochemistry, Geophysics, Geosystems,* 18(3):1053–1064. **https://doi.org/10.1002/2016GC006715**

Dickinson, W.R., Beard, L.S., Brakenridge, G.R., Erjavec, J.L., Ferguson, R.C., Inman, K.F., Knepp, R.A., Lindberg, F.A., and Ryberg, P.T., 1983. Provenance of North American Phanerozoic sandstones in relation to tectonic setting. *Geological Society of America Bulletin,* 94(2):222–235. **http://dx.doi.org/10.1130/0016-7606(1983)94<222:PONAPS>2.0.CO;2**

Dymond, J., Suess, E., and Lyle, M., 1992. Barium in deep-sea sediment: a geochemical proxy for paleoproductivity. *Paleoceanography,* 7(2):163–181. **https://doi.org/10.1029/92PA00181**

Gradstein, F.M., Ogg, J.G., Schmitz, M.D., and Ogg, G.M. (Eds.), 2012. *The Geological Time Scale 2012:* Amsterdam (Elsevier).

Huismans, R., and Beaumont, C., 2011. Depth-dependent extension, two-stage breakup and cratonic underplating at rifted margins. *Nature,* 473(7345):74–78. **https://dx.doi.org/10.1038/nature09988**

Inderbitzen, A. (Ed.), 1974. *Marine Science* (Volume 2): *Deep-Sea Sediments: Physical and Mechanical Properties:* New York (Springer US). **https:/doi.org/10.1007/978-1-4684-2754-7**

Jia, G., Peng, P., Zhao, Q., and Jian, Z., 2003. Changes in terrestrial ecosystem since 30 Ma in East Asia: stable isotope evidence from black carbon in the

South China Sea. *Geology,* 31(12):1093–1096. **http://dx.doi.org/10.1130/G19992.1**

Jian, Z., Tian, J., and Sun, X., 2009. Upper water structure and paleo-monsoon. *In* Wang, P., and Li, Q. (Eds.), *Developments in Paleoenvironmental Research* (Volume 13): *The South China Sea.* Smol, J.P. (Series Ed.): Dordrecht, Netherlands (Springer), 297–394. **https://doi.org/10.1007/978-1-4020-9745-4_5**

Kastner, M., and Rudnicki, M.D., 2004. Ridge flank sediment-fluid interactions. *In* Davis, E., and Elderfield, H. (Eds.), *Hydrogeology of the Oceanic Lithosphere:* Cambridge, UK (Cambridge University Press), 534–571.

Kirschvink, J.L., 1980. The least-squares line and plane and the analysis of palaeomagnetic data. *Geophysical Journal of the Royal Astronomical Society,* 62(3):699–718. **https://doi.org/10.1111/j.1365-246X.1980.tb02601.x**

Larsen, H.C., Sun, Z., Stock, J.M., Jian, Z., Alvarez Zarikian, C.A., Klaus, A., Boaga, J., Bowden, S.A., Briais, A., Chen, Y., Cukur, D., Dadd, K.A., Ding, W., Dorais, M.J., Ferré, E.C., Ferreira, F., Furusawa, A., Gewecke, A.J., Hinojosa, J.L., Höfig, T.W., Hsiung, K.-H., Huang, B., Huang, E., Huang, X.-L., Jiang, S., Jin, H., Johnson, B.G., Kurzawski, R.M., Lei, C., Li, B., Li, L., Li, Y., Lin, J., Liu, C., Liu, C., Liu, Z., Luna, A., Lupi, C., McCarthy, A.J., Mohn, G., Ningthoujam, L.S., Nirrengarten, M., Osono, N., Peate, D.W., Persaud, P., Qui, N., Robinson, C.M., Satolli, S., Sauermilch, I., Schindlbeck, J.C., Skinner, S.M., Straub, S.M., Su, X., Tian, L., van der Zwan, F.M., Wan, S., Wu, H., Xiang, R., Yadav, R., Yi, L., Zhang, C., Zhang, J., Zhang, Y., Zhao, N., Zhong, G., and Zhong, L., 2018. Expedition 367/368 summary. *In* Sun, Z., Jian, Z., Stock, J.M., Larsen, H.C., Klaus, A., Alvarez Zarikian, C.A., and the Expedition 367/368 Scientists, *South China Sea Rifted Margin*. Proceedings of the International Ocean Discovery Program, 367/368: College Station, TX (International Ocean Discovery Program). **https://doi.org/10.14379/iodp.proc.367368.101.2018**

Li, C.-F., Li, J., Ding, W., Franke, D., Yao, Y., Shi, H., Pang, X., et al., 2015a. Seismic stratigraphy of the central South China Sea basin and implications for neotectonics. *Journal of Geophysical Research: Solid Earth,* 120(3):1377–1399. **https://doi.org/10.1002/2014JB011686**

Li, C.-F., Lin, J., Kulhanek, D.K., Williams, T., Bao, R., Briais, A., Brown, E.A., Chen, Y., Clift, P.D., Colwell, F.S., Dadd, K.A., Ding, W., Hernández-Almeida, I., Huang, X.-L., Hyun, S., Jiang, T., Koppers, A.A.P., Li, Q., Liu, C., Liu, Q., Liu, Z., Nagai, R.H., Peleo-Alampay, A., Su, X., Sun, Z., Tejada, M.L.G., Trinh, H.S., Yeh, Y.-C., Zhang, C., Zhang, F., Zhang, G.-L., and Zhao, X., 2015b. Expedition 349 summary. *In* Li, C.-F., Lin, J., Kulhanek, D.K., and the Expedition 349 Scientists, *South China Sea Tectonics.* Proceedings of the International Ocean Discovery Program, 349: College Station, TX (International Ocean Discovery Program). **https://doi.org/10.14379/iodp.proc.349.101.2015**

Li, C.-F., Lin, J., Kulhanek, D.K., Williams, T., Bao, R., Briais, A., Brown, E.A., Chen, Y., Clift, P.D., Colwell, F.S., Dadd, K.A., Ding, W., Hernández-Almeida, I., Huang, X.-L., Hyun, S., Jiang, T., Koppers, A.A.P., Li, Q., Liu, C., Liu, Q., Liu, Z., Nagai, R.H., Peleo-Alampay, A., Su, X., Sun, Z., Tejada, M.L.G., Trinh, H.S., Yeh, Y.-C., Zhang, C., Zhang, F., Zhang, G.-L., and Zhao, X., 2015c. Site U1435. *In* Li, C.-F., Lin, J., Kulhanek, D.K., and the Expedition 349 Scientists, *South China Sea Tectonics.* Proceedings of the International Ocean Discovery Program, 349: College Station, TX (International Ocean Discovery Program). **http://dx.doi.org/10.14379/iodp.proc.349.107.2015**

Li, C.-F., Shi, X., Zhou, Z., Li, J., Geng, J., and Chen, B., 2010. Depths to the magnetic layer bottom in the South China Sea area and their tectonic implications. *Geophysical Journal International,* 182(3):1229–1247. **https://doi.org/10.1111/j.1365-246X.2010.04702.x**

Li, C.-F., Zhou, Z., Li, J., Chen, B., and Geng, J., 2008. Magnetic zoning and seismic structure of the South China Sea ocean basin. *Marine Geophysical Research,* 29(4):223–238. **https://doi.org/10.1007/s11001-008-9059-4**

Liu, Z., Colin, C., Huang, W., Le, K.P., Tong, S., Chen, Z., and Trentesaux, A., 2007. Climatic and tectonic controls on weathering in south China and Indochina Peninsula: clay mineralogical and geochemical investigations from the Pearl, Red, and Mekong drainage basins. *Geochemistry, Geophysics, Geosystems,* 8(5):Q05005. **https://doi.org/10.1029/2006GC001490**

Liu, Z., Zhao, Y., Colin, C., Stattegger, K., Wiesner, M.G., Huh, C.-A., Zhang, Y., et al., 2016. Source-to-sink transport processes of fluvial sediments in the South China Sea. *Earth-Science Reviews,* 153:238–273. **https://doi.org/10.1016/j.earscirev.2015.08.005**

Lurcock, P.C., and Wilson, G.S., 2012. PuffinPlot: a versatile, user-friendly program for paleomagnetic analysis. *Geochemistry, Geophysics, Geosystems,* 13(6):Q06Z45. **https://doi.org/10.1029/2012GC004098**

Makris, J., Papoulia, J., McPherson, S., and Warner, L., 2012. Mapping of sediments and crust offshore Kenya, East Africa: a wide aperture refraction/reflection Survey. In *SEG Technical Program Expanded Abstracts 2012:* Tulsa, OK (Society of Exploration Geophysicists). **https://doi.org/10.1190/segam2012-0426.1**

Martini, E., 1971. Standard Tertiary and Quaternary calcareous nannoplankton zonation. *In* Farinacci, A. (Ed.), *Proceedings of the Second Planktonic Conference, Roma 1970:* Rome (Edizioni Tecnoscienza), 2:739–785.

Müller, A., and Mathesius, U., 1999. The palaeoenvironments of coastal lagoons in the southern Baltic Sea, I. The application of sedimentary C_{org}/N ratios as source indicators of organic matter. *Palaeogeography, Palaeoclimatology, Palaeoecology,* 145(1–3):1–16. **https://doi.org/10.1016/S0031-0182(98)00094-7**

Ogg, J.G., Ogg, G., and Gradstein, F.M., 2016. *A Concise Geologic Time Scale 2016:* Boston (Elsevier).

Pickering, K.T., Hiscott, R.N., and Hein, F.J., 1989a. Contourite drifts. *In* Pickering, K.T., Hiscott, R.N., and Hein, F.J., (Eds.), *Deep-Marine Environments: Clastic Sedimentation and Tectonics:* London (Unwin Hyman), 219–245.

Pickering, K.T., Hiscott, R.N., and Hein, F.J., 1989b. Facies, processes, sequences and controls. *In* Pickering, K.T., Hiscott, R.N., and Hein, F.J., (Eds.), *Deep-Marine Environments: Clastic Sedimentation and Tectonics:* London (Unwin Hyman), 13–40.

Pribnow, D., Kinoshita, M., and Stein, C., 2000. *Thermal Data Collection and Heat Flow Recalculations for Ocean Drilling Program Legs 101–180:* Hanover, Germany (Institute for Joint Geoscientific Research, Institut für Geowissenschaftliche Gemeinschaftsaufgaben [GGA]). **http://www-odp.tamu.edu/publications/heatflow/ODPReprt.pdf**

Roberts, A.P., Chang, L., Rowan, C.J., Horng, C.-S., and Florindo, F., 2011. Magnetic properties of sedimentary greigite (Fe_3S_4): an update. *Reviews of Geophysics,* 49(1):RG1002. **https://doi.org/10.1029/2010RG000336**

Russell, W.L., 1944. The total gamma ray activity of sedimentary rocks as indicated by Geiger counter determinations. *Geophysics,* 9(2):180–216. **https://doi.org/10.1190/1.1445076**

Shipboard Scientific Party, 1998. Site 1069. *In* Whitmarsh, R.B., Beslier, M.-O., Wallace, P.J., et al., *Proceedings of the Ocean Drilling Program, Initial Reports,* 173: College Station, TX (Ocean Drilling Program), 219–263. **http://doi.org/10.2973/odp.proc.ir.173.107.1998**

Shipboard Scientific Party, 2000. Site 1148. *In* Wang, P., Prell, W.L., Blum, P., et al., *Proceedings of the Ocean Drilling Program, Initial Reports,* 184: College Station, TX (Ocean Drilling Program), 1–122. **https://doi.org/10.2973/odp.proc.ir.184.109.2000**

Sibuet, J.-C., and Tucholke, B.E., 2012. The geodynamic province of transitional lithosphere adjacent to magma-poor continental margins. *Geological Society Special Publication,* 369:429–452. **https://doi.org/10.1144/SP369.15**

Sibuet, J.-C., Yeh, Y.-C., and Lee, C.-S., 2016. Geodynamics of the South China Sea. *Tectonophysics,* 692(B):87–119. **https://doi.org/10.1016/j.tecto.2016.02.022**

Sun, Z., Jian, Z., Stock, J.M., Larsen, H.C., Klaus, A., Alvarez Zarikian, C.A., Boaga, J., Bowden, S.A., Briais, A., Chen, Y., Cukur, D., Dadd, K.A., Ding, W., Dorais, M.J., Ferré, E.C., Ferreira, F., Furusawa, A., Gewecke, A.J., Hinojosa, J.L., Höfig, T.W., Hsiung, K.-H., Huang, B., Huang, E., Huang, X.-L., Jiang, S., Jin, H., Johnson, B.G., Kurzawski, R.M., Lei, C., Li, B., Li, L., Li, Y., Lin, J., Liu, C., Liu, C., Liu, Z., Luna, A., Lupi, C., McCarthy, A.J., Mohn, G., Ningthoujam, L.S., Nirrengarten, M., Osono, N., Peate, D.W., Persaud, P., Qui, N., Robinson, C.M., Satolli, S., Sauermilch, I., Schindl-

beck, J.C., Skinner, S.M., Straub, S.M., Su, X., Tian, L., van der Zwan, F.M., Wan, S., Wu, H., Xiang, R., Yadav, R., Yi, L., Zhang, C., Zhang, J., Zhang, Y., Zhao, N., Zhong, G., and Zhong, L., 2018. Expedition 367/368 methods. *In* Sun, Z., Jian, Z., Stock, J.M., Larsen, H.C., Klaus, A., Alvarez Zarikian, C.A., and the Expedition 367/368 Scientists, *South China Sea Rifted Margin*. Proceedings of the International Ocean Discovery Program, 367/368: College Station, TX (International Ocean Discovery Program). **https://doi.org/10.14379/iodp.proc.367368.102.2018**

Sun, Z., Stock, J., Jian, Z., McIntosh, K., Alvarez Zarikian, C.A., and Klaus, A., 2016. *Expedition 367/368 Scientific Prospectus: South China Sea Rifted Margin.* International Ocean Discovery Program. **https://doi.org/10.14379/iodp.sp.367368.2016**

Wang, P., Prell, W.L., Blum, P., et al., 2000. *Proceedings of the Ocean Drilling Program, Initial Reports,* 184: College Station, TX (Ocean Drilling Program). **https://doi.org/10.2973/odp.proc.ir.184.2000**

Wang, P., Wang, L., Bian, Y., and Jian, Z., 1995. Late Quaternary paleoceanography of the South China Sea: surface circulation and carbonate cycles. *In* Tokuyama, H., Taira, A., and Kuramoto, S. (Eds.), *Asian Marine Geology.* Marine Geology, 127(1–4):145–165. **https://doi.org/10.1016/0025-3227(95)00008-M**

Yan, P., Deng, H., Liu, H., Zhang, Z., and Jiang, Y., 2006. The temporal and spatial distribution of volcanism in the South China Sea region. *Journal of Asian Earth Sciences,* 27(5):647–659. **https://doi.org/10.1016/j.jseaes.2005.06.005**

Zachos, J., Pagani, M., Sloan, L., Thomas, E., and Billups, K., 2001. Trends, rhythms, and aberrations in global climate 65 Ma to present. *Science,* 292(5517):686–693. **https://doi.org/10.1126/science.1059412**

Zijderveld, J.D.A., 1967. AC demagnetization of rocks: analysis of results. *In* Collinson, D.W., Creer, K.M., and Runcorn, S.K. (Eds.), *Methods in Palaeomagnetism:* Amsterdam (Elsevier), 254–286.

Sun, Z., Jian, Z., Stock, J.M., Larsen, H.C., Klaus, A., Alvarez Zarikian, C.A., and the Expedition 367/368 Scientists
Proceedings of the International Ocean Discovery Program Volume 367/368
publications.iodp.org

https://doi.org/10.14379/iodp.proc.367368.104.2018

Site U1500[1]

Check for updates

Joann M. Stock, Zhen Sun, Adam Klaus, Hans Christian Larsen, Zhimin Jian, Carlos A. Alvarez Zarikian, Jacopo Boaga, Stephen A. Bowden, Anne Briais, Yifeng Chen, Deniz Cukur, Kelsie A. Dadd, Weiwei Ding, Michael J. Dorais, Eric C. Ferré, Fabricio Ferreira, Akira Furusawa, Aaron J. Gewecke, Jessica L. Hinojosa, Tobias W. Höfig, Kan-Hsi Hsiung, Baoqi Huang, Enqing Huang, Xiao-Long Huang, Shijun Jiang, Haiyan Jin, Benjamin G. Johnson, Robert M. Kurzawski, Chao Lei, Baohua Li, Li Li, Yanping Li, Jian Lin, Chang Liu, Chuanlian Liu, Zhifei Liu, Antonio Luna, Claudia Lupi, Anders J. McCarthy, Geoffroy Mohn, Lachit Singh Ningthoujam, Michael Nirrengarten, Nobuaki Osono, David W. Peate, Patricia Persaud, Ning Qiu, Caroline M. Robinson, Sara Satolli, Isabel Sauermilch, Julie C. Schindlbeck, Steven M. Skinner, Susanne M. Straub, Xiang Su, Liyan Tian, Froukje M. van der Zwan, Shiming Wan, Huaichun Wu, Rong Xiang, Rajeev Yadav, Liang Yi, Cuimei Zhang, Jinchang Zhang, Yang Zhang, Ning Zhao, Guangfa Zhong, and Lifeng Zhong[2]

Keywords: International Ocean Discovery Program, IODP, *JOIDES Resolution*, Expedition 367, Expedition 368, Site U1500, northern South China Sea, continent–ocean transition zone, Ridge B, hyperextension, continental breakup, thinning, rifting, basalt, Cenozoic, red clay, turbidite, reworked microfossils

Contents

1 Site summary
6 Background and objectives
11 Operations
15 Lithostratigraphy
25 Igneous and metamorphic petrology
32 Structural geology
37 Biostratigraphy
39 Paleomagnetism
44 Geochemistry
46 Physical properties
50 Downhole measurements
53 Correlation to seismic data
55 References

Site summary

International Ocean Discovery Program (IODP) Expedition 367 Site U1500 is located on basement Ridge B and is the most seaward site that Expedition 367 drilled within the South China Sea (SCS) continent–ocean transition (COT) zone. Ridge B is located ~80 km seaward of the outer margin high and ~20 km seaward of Ridge A, where Site U1499 was drilled. The goal of drilling here was to sample and log the lowermost sediment and underlying basement rocks to determine basement age and lithology of the COT or embryonic oceanic crust, thus providing a test of different possible models for the processes and rheology controlling the breakup of the continent. Ridge B was expected to have basement of either upper continental crust, lower continental crust, mantle rocks, or oceanic crust. The coring and logging would also constrain the history of the region after rifting by determining the age, water depth, and subsidence rates of the overlying sedimentary packages.

We conducted operations in two holes at Site U1500 (proposed Site SCSII-8B; Sun et al., 2016) (Table **T1**). Hole U1500A is located at 18°18.2762′N, 116°13.1916′E in a water depth of 3801.7 m. In Hole U1500A, we drilled without coring from the seafloor to 378.2 m and then cored with the rotary core barrel (RCB) system from 378.2 to 494.6 m and recovered 26.5 m (23%). Thereafter, we drilled without coring from 494.6 to 641.2 m and cored with the RCB system from 641.2 to 854.6 m and recovered 67.2 m (31%).

Hole U1500B is located at 18°18.2707′N, 116°13.1951′E in a water depth of 3801.7 m. After installing casing, we continuously cored the sediment sequence from 846.0 to 1379.1 m (533.1 m cored; 164.7 m recovered; 31%) and then continuously cored 149.9 m into the underlying basalt from 1379.1 to 1529.0 m (114.92 m recovered; 77%). This made Hole U1500B the eighth deepest hole that the R/V *JOIDES Resolution* has drilled in Ocean Drilling Program (ODP)/Integrated Ocean Drilling Program/IODP history. Three downhole logging strings were run in Hole U1500B from 842 to 1133 m.

[1] Stock, J.M., Sun, Z., Klaus, A., Larsen, H.C., Jian, Z., Alvarez Zarikian, C.A., Boaga, J., Bowden, S.A., Briais, A., Chen, Y., Cukur, D., Dadd, K.A., Ding, W., Dorais, M.J., Ferré, E.C., Ferreira, F., Furusawa, A., Gewecke, A.J., Hinojosa, J.L., Höfig, T.W., Hsiung, K.-H., Huang, B., Huang, E., Huang, X.-L., Jiang, S., Jin, H., Johnson, B.G., Kurzawski, R.M., Lei, C., Li, B., Li, L., Li, Y., Lin, J., Liu, C., Liu, C., Liu, Z., Luna, A., Lupi, C., McCarthy, A.J., Mohn, G., Ningthoujam, L.S., Nirrengarten, M., Osono, N., Peate, D.W., Persaud, P., Qui, N., Robinson, C.M., Satolli, S., Sauermilch, I., Schindlbeck, J.C., Skinner, S.M., Straub, S.M., Su, X., Tian, L., van der Zwan, F.M., Wan, S., Wu, H., Xiang, R., Yadav, R., Yi, L., Zhang, C., Zhang, J., Zhang, Y., Zhao, N., Zhong, G., and Zhong, L., 2018. Site U1500. *In* Sun, Z., Jian, Z., Stock, J.M., Larsen, H.C., Klaus, A., Alvarez Zarikian, C.A., and the Expedition 367/368 Scientists, 2018. *South China Sea Rifted Margin*. Proceedings of the International Ocean Discovery Program, 367/368: College Station, TX (International Ocean Discovery Program). https://doi.org/10.14379/iodp.proc.367368.104.2018

[2] **Expedition 367/368 Scientists' addresses.**

MS 367368-104: Published 28 September 2018

This work is distributed under the **Creative Commons Attribution 4.0 International** (CC BY 4.0) license.

Table T1. Site U1500 core summary. * = base of 10.75 inch casing at 842 m; drilled in with pilot bit and underreamer that extended below the end of the casing. † = excludes core recovered during hole cleaning (ghost core). DRF = drilling depth below rig floor, DSF = drilling depth below seafloor. Core type: numeric core type = drilled interval, R = rotary core barrel, G = ghost core. WOB = weight on bit. Drilling break = fast penetration, unable to maintain any WOB. (Continued on next two pages.) **Download table in CSV format.**

Hole U1500A

Latitude:	18°18.2762′N
Longitude:	116°13.1916′E
Time on hole (d):	5.51
Seafloor (drill pipe measurement below rig floor, m DRF):	3812.8
Distance between rig floor and sea level (m):	11.11
Water depth (drill pipe measurement from sea level, mbsl):	3801.7
Total penetration (drilling depth below seafloor, m DSF):	854.6
Total depth (drill pipe measurement from rig floor, m DRF):	4656.3
Total length of cored section (m):	329.8
Total core recovered (m):	93.55
Core recovery (%):	28
Drilled interval (m):	524.8
Total number of cores:	34

Hole U1500B

Latitude:	18°18.2707′N
Longitude:	116°13.1951′E
Time on hole (d):	
Seafloor (drill pipe measurement below rig floor, m DRF):	3812.8
Distance between rig floor and sea level (m):	11.1
Water depth (drill pipe measurement from sea level, mbsl):	3801.7
Total penetration (drilling depth below seafloor, m DSF):	1529
Total depth (drill pipe measurement from rig floor, m DRF):	5341.8
Total length of cored section (m):	683
Total core recovered (m):	278.8
Core recovery (%):	41
Drilled interval (m):	846
Total number of cores:	81

Core	Type	Top of interval DSF (m)	Bottom of interval DSF (m)	Interval advanced (m)	Core recovered† (m)	Core curated† (m)	Recovery† (%)	Time on deck UTC (h)	Time on deck (ship local time; UTC + 8 h)	Time to cut core (min)	Mud pumped (bbl)	Driller's notes
367-U1500A-												
1	1	0.0	378.2	378.2	*****Drilled interval*****			3/10/2017 3:00	3/10/2017 11:00			
2	R	378.2	387.9	9.7	8.82	8.82	91	3/10/2017 6:55	3/10/2017 14:55	30		
3	R	387.9	397.6	9.7	6.78	6.78	70	3/10/2017 8:55	3/10/2017 16:55	20		Drilling break from 393.2 to 395.2 m
4	R	397.6	407.3	9.7	4.11	4.11	42	3/10/2017 11:00	3/10/2017 19:00	15	30	Drilling break from 406.2 to 407.2 m
5	R	407.3	417.0	9.7	2.70	2.70	28	3/10/2017 13:00	3/10/2017 21:00	10		Drilling break from 413.2 to 416.2 m
6	R	417	426.7	9.7	0.00	0.00	0	3/10/2017 15:10	3/10/2017 23:10	5	30	Drilling break over entire interval
7	R	426.7	436.4	9.7	0.00	0.00	0	3/10/2017 16:55	3/11/2017 0:55	5		Drilling break over entire interval
8	R	436.4	446.1	9.7	0.00	0.00	0	3/10/2017 18:35	3/11/2017 2:35	5	30	Drilling break over entire interval
9	R	446.1	455.8	9.7	2.86	2.86	29	3/10/2017 20:10	3/11/2017 4:10	10	30	Firmed up from 449.0 to 453.0 m
10	R	455.8	465.5	9.7	0.07	0.07	0.70	3/10/2017 21:40	3/11/2017 5:40	5	30	Drilling break over entire interval
11	R	465.5	475.2	9.7	0.05	0.05	0.50	3/10/2017 23:05	3/11/2017 7:05	5	30	Drilling break over entire interval
12	R	475.2	484.9	9.7	0.00	0.00	0	3/11/2017 0:25	3/11/2017 8:25	5	30	Drilling break over entire interval
13	R	484.9	494.6	9.7	1.06	1.06	11	3/11/2017 2:00	3/11/2017 10:00	5	30	Drilling break over entire interval
14	1	494.6	641.2	146.6	*****Drilled interval*****			3/11/2017 11:40	3/11/2017 19:40			
15	R	641.2	650.9	9.7	0.14	0.14	1.40	3/11/2017 13:50	3/11/2017 21:50	10		Drilling break over entire interval
16	R	650.9	660.6	9.7	0.00	0.00	0	3/11/2017 15:55	3/11/2017 23:55	5	30	Drilling break over entire interval
17	R	660.6	670.3	9.7	0.45	0.58	5	3/11/2017 17:30	3/12/2017 1:30	5		Drilling break over entire interval
18	R	670.3	680.0	9.7	2.07	2.07	21	3/11/2017 19:15	3/12/2017 3:15	10	30	
19	R	680.0	689.7	9.7	0.03	0.03	0.30	3/11/2017 20:45	3/12/2017 4:45	5		Drilling break over entire interval
20	R	689.7	699.4	9.7	0.10	0.10	1	3/11/2017 22:15	3/12/2017 6:15	5		Drilling break over entire interval
21	R	699.4	709.1	9.7	2.57	2.57	26	3/11/2017 23:55	3/12/2017 7:55	10		Firmed up at 704 m
22	R	709.1	718.8	9.7	1.45	1.45	15	3/12/2017 2:05	3/12/2017 10:05	40	30	Drilling break at 714 m
23	R	718.8	728.5	9.7	0.00	0.00	0	3/12/2017 3:30	3/12/2017 11:30	5		Drilling break over entire interval
24	R	728.5	738.2	9.7	8.51	8.51	88	3/12/2017 6:10	3/12/2017 14:10	60	30	
25	R	738.2	747.9	9.7	8.13	8.13	84	3/12/2017 8:25	3/12/2017 16:25	30		
26	R	747.9	757.6	9.7	7.54	7.54	78	3/12/2017 10:40	3/12/2017 18:40	35	30	
27	R	757.6	767.3	9.7	7.94	7.94	82	3/12/2017 12:55	3/12/2017 20:55	35		
28	R	767.3	777.0	9.7	0.61	0.61	6	3/12/2017 15:10	3/12/2017 23:10	10	30	Drilling break over entire interval
29	R	777.0	786.7	9.7	0.90	0.90	9	3/12/2017 17:00	3/13/2017 1:00	15		Drilling break over entire interval
30	R	786.7	796.4	9.7	4.98	4.98	51	3/12/2017 19:10	3/13/2017 3:10	30	30	Drilling break from 794 m
31	R	796.4	806.1	9.7	0.29	0.29	3	3/12/2017 21:40	3/13/2017 5:40	5	30	Drilling break over entire interval
32	R	806.1	815.8	9.7	0.20	0.20	2	3/13/2017 0:10	3/13/2017 8:10	10	30	Drilling breaks off/on over entire interval
33	R	815.8	825.5	9.7	3.41	3.41	35	3/13/2017 2:45	3/13/2017 10:45	15	30	Firmed up from 820 to 824 m
34	R	825.5	835.2	9.7	0.88	0.88	9	3/13/2017 5:15	3/13/2017 13:15	15	30	Drilling break entire core
35	R	835.2	844.9	9.7	8.93	8.93	92	3/13/2017 7:45	3/13/2017 15:45	35	30	Firm formation able to maintain 10 klb WOB
36	R	844.9	854.6	9.7	7.97	7.97	82	3/13/2017 10:50	3/13/2017 18:50	45	30	Last 1 m could not maintain WOB
		Hole U1500A totals:		329.8	93.55	93.68	28					
		Core 2R–13R totals:		116.4	26.50	26.50	23					
		Core 15R–36R totals:		213.4	67.10	67.20	31					
367-U1500B-												
1	1	0.0	846.0*	846.0	*****Drilled interval*****			3/17/2017 9:45	3/17/2017 17:45			
2	R	846.0	855.0	9.0	8.54	8.54	95	3/18/2017 19:05	3/19/2017 3:05	60		
3	R	855.0	864.7	9.7	0.05	0.05	1	3/18/2017 21:10	3/19/2017 5:10	20		Drilling break
4	R	864.7	874.4	9.7	7.14	7.14	74	3/18/2017 23:30	3/19/2017 7:30	50		
5	R	874.4	884.1	9.7	9.18	9.18	95	3/19/2017 1:55	3/19/2017 9:55	50	30	
6	R	884.1	893.8	9.7	8.34	8.34	86	3/19/2017 4:10	3/19/2017 12:10	45		

Table T1 (continued). (Continued on next page.)

Core	Type	Top of interval DSF (m)	Bottom of interval DSF (m)	Interval advanced (m)	Core recovered† (m)	Core curated† (m)	Recovery† (%)	Time on deck UTC (h)	Time on deck (ship local time; UTC + 8 h)	Time to cut core (min)	Mud pumped (bbl)	Driller's notes
7	R	893.8	903.5	9.7	1.31	1.31	14	3/19/2017 6:10	3/19/2017 14:10	15		Drilling break from 895 to 903 m, 0 klb WOB
8	R	903.5	913.2	9.7	1.17	1.17	12	3/19/2017 8:30	3/19/2017 16:30	10	30	Drilling break from 903 to 913 m, 0 klb WOB
9	R	913.2	922.9	9.7	0.84	0.84	9	3/19/2017 10:35	3/19/2017 18:35	15		Drilling break from 913 to 917 and 919 to 920 m, 0 klb WOB; 8 klb WOB 917–919 and 920–922 m
10	R	922.9	932.6	9.7	3.38	3.38	35	3/19/2017 12:50	3/19/2017 20:50	15	30	Drilling break from 922 to 925 and 930 to 931 m, 0 klb WOB; 8 klb WOB 925–930 and 931–932 m
11	R	932.6	942.3	9.7	0.53	0.53	5	3/19/2017 15:10	3/19/2017 23:10	15	30	Drilling break 935-939 m, 0 klb WOB; 8 klb WOB 932–935 and 939–942 m
12	R	942.3	952.0	9.7	1.40	1.40	14	3/19/2017 17:10	3/20/2017 1:10	15	30	Drilling break
13	R	952.0	961.7	9.7	1.04	1.04	11	3/19/2017 19:00	3/20/2017 3:00	10	30	Drilling break
14	R	961.7	971.4	9.7	0.21	0.21	2	3/19/2017 20:45	3/20/2017 4:45	5	30	Drilling break
15	R	971.4	981.1	9.7	6.93	6.93	71	3/19/2017 23:10	3/20/2017 7:10	55	30	Firmed up at 973 m
16	R	981.1	990.8	9.7	0.00	0.00	0	3/20/2017 0:50	3/20/2017 8:50	5		Drilling break
17	R	990.8	1000.5	9.7	0.00	0.00	0	3/20/2017 2:40	3/20/2017 10:40	5	30	Drilling break
18	R	1000.5	1010.2	9.7	0.20	0.20	2	3/20/2017 4:40	3/20/2017 12:40	10	30	Drilling break
19	R	1010.2	1019.9	9.7	5.65	5.65	58	3/20/2017 6:55	3/20/2017 14:55	25	30	Drilling break 1010-1012 and 1015-1016 m, 0 klb WOB; 1012–1015 and 1016–1020 m, 8 klb WOB
20	R	1019.9	1029.6	9.7	1.94	1.94	20	3/20/2017 9:00	3/20/2017 17:00	15	30	Drilling Break 1023–1029 m, 0 klb WOB; 8 klb WOB 1020–1023 m
21	R	1029.6	1039.3	9.7	1.79	1.79	18	3/20/2017 11:10	3/20/2017 19:10	15	30	Drilling break 1029–1037 m, 0 klb WOB; 8 klb WOB 1037–1039 m
22	R	1039.3	1049.0	9.7	0.12	0.14	1.20	3/20/2017 13:25	3/20/2017 21:25	10	30	Drilling break 1039–1049 m, 0 klb WOB
23	R	1049.0	1058.7	9.7	4.04	4.04	42	3/20/2017 15:30	3/20/2017 23:30	20	30	Drilling break 1049–1052 and 1057–1058 m, 0 klb WOB; 8 klb WOB 1052–1057 m
24	R	1058.7	1068.4	9.7	0.44	0.44	5	3/20/2017 17:25	3/21/2017 1:25	15	30	Drilling break
25	R	1068.4	1078.1	9.7	0.29	0.29	3	3/20/2017 19:30	3/21/2017 3:30	25	30	Drilling break, irregular penetration
26	R	1078.1	1087.8	9.7	5.94	5.94	61	3/20/2017 21:45	3/21/2017 5:45	45	30	Firmed up at 1083 m
27	R	1087.8	1097.5	9.7	5.23	5.23	54	3/21/2017 0:05	3/21/2017 8:05	45	30	Drilling break
28	R	1097.5	1107.2	9.7	1.75	1.75	18	3/21/2017 1:55	3/21/2017 9:55	15	30	Drilling break, firmed up 1105–1107 m
29	R	1107.2	1116.9	9.7	3.60	3.60	37	3/21/2017 3:55	3/21/2017 11:55	30	30	Drilling break
30	R	1116.9	1126.6	9.7	0.00	0.00	0	3/21/2017 5:55	3/21/2017 13:55	10	30	Drilling break 1126–1131 and 11135–1136 m, 0 klb WOB; 8 klb WOB 1131–1135 m
31	R	1126.6	1136.3	9.7	1.57	1.57	16	3/21/2017 8:00	3/21/2017 16:00	15	30	Drilling break 1138–1140 and 1141–1146 m, 0 klb WOB; 8 klb WOB 1136–1138 and 1140–1141 m
32	R	1136.3	1146.0	9.7	0.25	0.25	3	3/21/2017 10:05	3/21/2017 18:05	15	30	Drilling break
33	R	1146.0	1155.7	9.7	0.03	0.03	0.30	3/21/2017 12:15	3/21/2017 20:15	10	30	Drilling break 1155–1163 and 1164–1165 m, 0 klb WOB; 8 klb WOB 1163–1164 m
34	R	1155.7	1165.4	9.7	0.09	0.09	0.90	3/21/2017 14:30	3/21/2017 22:30	15	30	Drilling break 1165–1170 and 1171–1175 m, 0 klb WOB; 8 klb WOB 1170–1171 m
35	R	1165.4	1175.1	9.7	0.05	0.05	0.50	3/21/2017 16:25	3/22/2017 0:25	15	30	Drilling break
36	R	1175.1	1184.8	9.7	0.00	0.00	0	3/21/2017 18:25	3/22/2017 2:25	20	30	Drilling break
37	R	1184.8	1194.5	9.7	0.66	0.66	7	3/21/2017 20:20	3/22/2017 4:20	15	30	Drilling break
38	R	1194.5	1204.2	9.7	0.00	0.00	0	3/21/2017 22:20	3/22/2017 6:20	5	30	Drilling break
39	R	1204.2	1213.9	9.7	0.16	0.16	2	3/22/2017 0:25	3/22/2017 8:25	15	30	Drilling break
40	R	1213.9	1223.6	9.7	0.67	0.67	7	3/22/2017 2:20	3/22/2017 10:20	10	30	Drilling break
41	R	1223.6	1233.3	9.7	0.00	0.00	0	3/22/2017 4:35	3/22/2017 12:35	5	30	Drilling break
42	R	1233.3	1243.0	9.7	5.84	5.84	60	3/22/2017 7:20	3/22/2017 15:20	40	30	Experienced increase in torque and pump pressure; 1233–1235 m, 0 klb WOB; 10 klb WOB, 1235–1243 m
43	R	1243.0	1252.7	9.7	6.65	6.65	69	3/22/2017 10:00	3/22/2017 18:00	40	30	
44	R	1252.7	1262.4	9.7	3.52	3.52	36	3/22/2017 13:10	3/22/2017 21:10	80	30	
45	R	1262.4	1272.1	9.7	9.63	9.63	99	3/22/2017 15:50	3/22/2017 23:50	50	30	
46	R	1272.1	1281.8	9.7	10.01	10.01	103	3/22/2017 19:50	3/23/2017 3:50	140	30	
47	R	1281.8	1291.5	9.7	7.76	7.76	80	3/23/2017 0:05	3/23/2017 8:05	140	30	
48	R	1291.5	1301.2	9.7	7.96	7.96	82	3/23/2017 5:45	3/23/2017 13:45	225	30	
49	R	1301.2	1310.9	9.7	1.44	1.44	15	3/23/2017 10:05	3/23/2017 18:05	150	30	
50	R	1310.9	1320.6	9.7	3.00	3.00	31	3/23/2017 14:05	3/23/2017 22:05	110	30	Drilling Break 1314–1318 m
51	R	1320.6	1330.3	9.7	8.91	8.97	92	3/23/2017 17:30	3/24/2017 1:30	100	30	

Table T1 (continued).

Core	Type	Top of interval DSF (m)	Bottom of interval DSF (m)	Interval advanced (m)	Core recovered† (m)	Core curated† (m)	Recovery† (%)	Time on deck UTC (h)	Time on deck (ship local time; UTC + 8 h)	Time to cut core (min)	Mud pumped (bbl)	Driller's notes
52	R	1330.3	1340.0	9.7	5.57	5.57	57	3/23/2017 20:10	3/24/2017 4:10	65	30	
53	R	1340.0	1349.7	9.7	3.84	3.84	40	3/23/2017 22:20	3/24/2017 6:20	25	30	Drilling break 1345.5–1349.7 m
54	R	1349.7	1359.4	9.7	0.47	0.47	5	3/24/2017 0:25	3/24/2017 8:25	5	30	Drilling break
55	R	1359.4	1369.1	9.7	3.96	3.96	41	3/24/2017 2:30	3/24/2017 10:30	20	30	Drilling break
56	R	1369.1	1378.8	9.7	1.28	1.28	13	3/24/2017 4:50	3/24/2017 12:50	25	30	Drilling break
57	R	1378.8	1388.5	9.7	8.34	8.37	86	3/24/2017 10:15	3/24/2017 18:15	215	30	Sediment/basement contact at 1379.1 m
58	R	1388.5	1398.2	9.7	6.50	7.51	67	3/24/2017 17:25	3/25/2017 1:25	325	30	
59	R	1398.2	1407.9	9.7	8.04	9.17	83	3/25/2017 0:20	3/25/2017 8:20	310	30	
60	R	1407.9	1415.9	8.0	5.39	5.39	67	3/25/2017 7:10	3/25/2017 15:10	255	35	Final core with 1st RCB bit
61	G	1066.0	1415.9	—	0.80	0.54	—	3/29/2017 9:35	3/29/2017 17:35			Ghost core recovered while reaming back to bottom
62	R	1415.9	1418.4	2.5	2.36	2.62	94	3/29/2017 14:30	3/29/2017 22:30	155	35	Weighted 11.0 lb/gal mud
63	R	1418.4	1428.0	9.6	3.60	3.60	38	3/30/2017 0:15	3/30/2017 8:15	480	70	Core jammed in liner, switch to half cores; weighted 11.0 lb/gal mud
64	R	1428.0	1432.8	4.8	3.20	3.56	67	3/30/2017 4:15	3/30/2017 12:15	135	35	
65	R	1432.8	1436.6	3.8	3.52	3.94	93	3/30/2017 10:00	3/30/2017 18:00	240		
66	R	1436.6	1442.1	5.5	3.85	4.45	70	3/30/2017 15:05	3/30/2017 23:05	195	35	Weighted 11.0 lb/gal mud
67	R	1442.1	1447.1	5.0	4.50	4.94	90	3/30/2017 21:40	3/31/2017 5:40	280		
68	R	1447.1	1451.9	4.8	4.05	4.06	84	3/31/2017 2:00	3/31/2017 10:00	160	35	
69	R	1451.9	1456.7	4.8	4.95	5.07	103	3/31/2017 7:35	3/31/2017 15:35	230	40	
70	R	1456.7	1461.5	4.8	5.17	5.40	108	3/31/2017 12:45	3/31/2017 20:45	190	40	
71	R	1461.5	1466.3	4.8	4.00	4.50	83	3/31/2017 17:15	4/1/2017 1:15	170	40	
72	R	1466.3	1471.1	4.8	3.24	3.87	68	3/31/2017 21:55	4/1/2017 5:55	170	40	
73	R	1471.1	1475.9	4.8	3.95	3.95	82	4/1/2017 3:40	4/1/2017 11:40	220	70	Final core with 2nd RCB bit; weighted 11.0 lb/gal mud
74	R	1475.9	1480.7	4.8	2.70	2.94	56	4/4/2021 15:50	4/4/2021 23:50	260	25	
75	R	1480.7	1485.5	4.8	4.95	5.05	103	4/4/2021 20:35	4/5/2021 4:35	190	40	
76	R	1485.5	1490.3	4.8	3.00	3.00	63	4/4/2017 0:15	4/4/2017 8:15	130	40	
77	R	1490.3	1495.1	4.8	4.73	4.77	99	4/5/2021 4:05	4/5/2021 12:05	135	40	
78	R	1495.1	1500.0	4.9	4.15	4.15	85	4/5/2021 8:35	4/5/2021 16:35	160	40	
79	R	1500.0	1504.8	4.8	4.52	5.14	94	4/4/2017 14:00	4/4/2017 22:00	175	40	
80	R	1504.8	1509.6	4.8	4.10	4.37	85	4/4/2017 17:45	4/5/2017 1:45	135	40	Weighted 11.0 lb/gal mud
81	R	1509.6	1514.4	4.8	3.75	3.98	78	4/4/2017 21:25	4/5/2017 5:25	125	40	
82	R	1514.4	1524.0	9.6	4.50	4.73	47	4/5/2017 3:30	4/5/2017 11:30	250	40	
83	R	1524.0	1529.0	5.0	3.36	3.36	67	4/5/2017 7:30	4/5/2017 15:30	105	70	Weighted 11.0 lb/gal mud
Hole U1500B totals:			683.0	683.0	278.80	286.90	41					
Sedimentary section totals:			533.1	533.1	164.70	164.80	31					
Basalt section totals:			149.9	149.9	114.92	122.13	77					

Lithostratigraphy

The cored sediment at Site U1500 is divided into eight lithostratigraphic units (Figure **F11**). The uppermost 378.2 m of sediment was drilled without coring. Lithostratigraphic Unit I (378.2–410.0 m) is a 31.8 m thick upper Miocene sequence of greenish gray heavily bioturbated clay with silt and sandy silt interbeds. Some of the clay intervals are nannofossil rich. Structure in the clay is mostly massive, but parallel laminations occur in the silt and sandy silt interbeds. Unit II (410.0–494.6 m) is an upper Miocene sequence of interbedded dark greenish gray clay and silt. Recovery was very low for this unit (~8%), which may indicate a change in lithology (e.g., increased abundance of nonlithified sands). This unit is underlain by another interval drilled without coring (494.6–641.2 m).

Unit III (641.2–892.4 m) is defined by upper Miocene interbedded claystone, siltstone, and sandstone. Many of the siltstone and sandstone intervals are organized into a variety of massive and stratified beds that include sedimentary structures such as parallel laminations, cross-stratification, and contorted strata. There are also several massive beds of sandstone that contain pebble-sized mud clasts. The well-organized coarser intervals fine upward into more massive claystone intervals and are interpreted as turbidite sequences. Several of the stratified beds are composed of foraminifer tests.

Unit IV (892.4–1233.3 m) also had very low recovery (15%). This unit is composed of lower upper Miocene very dark greenish gray to dark gray sandstone with dark brown to very dark gray claystone and siltstone intervals. Many of the intervals described in this unit contain interlaminations of silt or sand within a prevailing claystone lithology. Similar to Unit III, sedimentary structures in many of the sandstone and siltstone intervals are interpreted as turbidites. The claystone in some of the cores shows a distinctive color banding, which was observed as a pattern of alternating reddish brown, dark greenish gray, and brownish gray. The color banding appears to be associated with fining-upward grain sizes and varying levels of bioturbation. Sandstone intervals within this unit contain high percentages of K-feldspar, quartz, plagioclase, and mica minerals that may have been sourced from granitic rocks exposed along the southern margin of China.

Unit V (lower middle Miocene) is divided into Subunits VA (1233.30–1272.10 m) and VB (1272.10–1310.98 m) based on the abundance of calcareous material. Subunit VA consists of dark reddish brown, dark greenish gray, and dusky red homogeneous massive claystone with few sandstone and siltstone interbeds (3–12 cm thick). Subunit VB consists of dark reddish brown, reddish brown, and greenish gray intervals of claystone, nannofossil-rich claystone, claystone with biogenic carbonate, and clay-rich chalk. The green-

ish gray color banding within Subunits VA and VB is interpreted as diagenetic alteration.

Unit VI (1310.98–1370.33 m) is composed of Oligocene dark greenish gray massive silty claystone with biogenic carbonate and dark gray sandstone. Unit VII (1370.33–1379.10 m) comprises a thin (30 cm thick) Oligocene dusky red claystone. The lowermost 2 cm of this unit has a greenish gray color that marks a sharp horizontal contact with the igneous rocks below in Unit VIII. The basalt in Unit VIII (1379.10–1529.0 m), which is Oligocene or pre-Oligocene in age, contains some fractures that are filled with well-lithified claystone. The claystone contains authigenic carbonate, siliciclastic components, and rare nannofossils. The basalt intervals are sparsely intercalated with dusky red claystone, with the basalt/sediment contacts often associated with chilled glassy margins. Some claystone intervals within the basalt unit show evidence of dolomitization in thin section.

Igneous petrology

In Hole U1500B, we cored 149.9 m of igneous rocks below the sedimentary section and recovered a total of 114.92 m of basalt. The aphanitic to porphyritic basalts are nonvesicular to moderately vesicular and glassy to hypocrystalline, with the latter ranging from cryptocrystalline to fine grained, making up an aphyric to highly olivine-plagioclase phyric texture (microstructure). These basalts contain numerous 2–5 cm thick baked/chilled contacts and chilled margins, many of the latter with preserved fresh glass, as well as occasional hyaloclastites showing brecciated glass fragments mixed with sediment. The basalts comprise Unit VIII and are divided into igneous lithologic Subunits 1a and 1b according to flow boundaries to distinguish an upper massive lava flow sequence (27.28 m thick) from a lower, predominantly pillow lava flow succession (122.62 m thick) with subordinate thin (<6 m) interbedded lobate, sheet, and massive lava flows. The pillow lobes are well preserved and are separated by chilled, glassy margins (identifying upper and lower chilled margins of individual pillows where possible) and also claystone. Plagioclase phenocrysts are found throughout these basalts, with olivine being an occasional phenocryst. Modal abundances of olivine and plagioclase phenocrysts increase downhole, reaching a peak between 1420 and 1470 mbsf. Veins occur throughout Unit VIII and are predominantly filled with carbonates and Fe (hydr)oxides, chlorites, zeolites, and silica, as well as sediment. Veins usually show a sharp contact with the host basalt and are either polycrystalline or massive. Claystone is a ubiquitous phase in many carbonate-rich veins, especially in pillow lava flows, and is usually found as very fine aggregates within carbonate veins or as centimeter-thick veins with no preserved textures or structures. Red to green-red halos usually surround the carbonate veins, which are related to the background alteration of interstitial glass, olivine, and occasionally plagioclase and clinopyroxene. Alteration of these basalts remains slight overall, as evidenced by the minimal alteration of interstitial glass as well as the good preservation of plagioclase. Alteration intensity, however, does increase downhole.

Structural geology

Tilted sedimentary bedding and deformation structures were observed in all lithostratigraphic units. Faults, tilted beds, folds, and mud clasts observed in Units I, II, and III are likely related to gravity-controlled deposition (e.g., debris flows, slumps, slides, etc.). Unit IV has low recovery and exhibits only a few tilted beds and compaction faults. A total of 47 centimeter-scale faults were measured in the claystone of Units V, VI, and VII. Many of these faults have slickensides and are likely related to clay compaction during lithification. Open fractures and veins are identified in the sparsely to highly plagioclase phyric basalts of Unit VIII. There are no preferred orientations of these structures. Most of the veins are filled by carbonate minerals, Fe oxides, sediment, and secondary minerals. Veins are often haloed by Fe oxide alteration. Vein connectivity is variable; single veins, branched veins, and vein networks were observed. There is no mineral-preferred orientation. Although the seismic profile across Site U1500 shows dipping reflectors in the basalt, we did not observe any clear paleohorizontal or dipping features within these lavas.

Biostratigraphy

All core catcher samples were analyzed for calcareous nannofossil and foraminifer contents. Additional samples were taken from the split-core sections when necessary to refine the ages between core catcher samples. Preservation of microfossils varies from poor to good. Overgrown and abundant broken fragments are common in the sediment sequences. The total abundance varies from barren to abundant, and most samples exhibit some degree of reworking.

Although recovery is low and ~50% of the samples are barren, the succession is apparently continuous and is tentatively assigned a late Oligocene–Miocene age. The late/middle Miocene boundary (11.6 Ma) can be placed between Samples 367-U1500B-37R-1, 40–41 cm, and 44R-CC. Both calcareous nannofossils and planktonic foraminifers indicate an early Miocene to late Oligocene succession in Cores 46R through 56R.

In the calcareous sandstone (Section 56R-1), just above the basalt, some younger species, such as *Praeorbulina circularis* (middle Miocene), *Globigerinoides subquadratus*, and *Orbulina suturalis*, are found together with the typical late Oligocene–early Miocene planktonic foraminiferal species (*Catapsydrax dissimilis*). In the same sample, the nannofossil content is represented by long-range species and cannot give a precise age. However, two samples from the veins and intrapillow fill of the basalts in Unit VIII contain poorly preserved calcareous nannofossils that indicate an Oligocene age. The resolution of the age discrepancy in Core 56R requires further postcruise studies.

Geochemistry

At Site U1500, measurements of organic and inorganic carbon and nitrogen were conducted on one sample per sedimentary core that had relative high recovery, and headspace gas measurements were taken for all sediment cores. In addition, four basalt samples were analyzed for concentrations of major elements and several trace elements using inductively coupled plasma–atomic emission spectroscopy (ICP-AES). Headspace gas values do not exceed 15 ppmv and are mostly below the quantification limit. Carbonate contents are dominated by biogenic carbonate and vary between <1 and 40 wt%, with higher values corresponding to the calcareous-rich lithostratigraphic units. Total organic carbon (TOC) and TOC/total nitrogen (TN) are low, averaging 0.14 wt% and 4.6, respectively. ICP-AES analyses of basalts from Site U1500 indicate subalkaline mid-ocean-ridge basalt (MORB)-like compositions.

Paleomagnetism

We conducted alternating field (AF) demagnetization of archive-half sections and AF and thermal demagnetization of representative discrete samples from both sedimentary successions and the igneous rocks. For the sedimentary samples, AF demagnetization effectively removed the drilling-induced overprint. The polar-

ity interpretation results based on inclination data from the sedimentary long core and discrete samples are in agreement, which supports our current preliminary polarity pattern, but because of discontinuous coring and poor recovery in many cored intervals, we are not able to correlate these results to the standard geomagnetic polarity timescale. The pass-through measurements of the basalts from the archive halves using the SRM effectively removed a low-coercivity component; however, it is not clear if the characteristic remanent magnetization (ChRM) or primary magnetization has been reached, partly due to the unavoidable magnetic contamination and partly due to the destructive feature and thus limited AF treatment levels (up to 25 mT). Within a single igneous subunit, basalts sometimes show both positive and negative inclinations upon stepwise AF treatments, which makes it hard to assign reliable polarities. The demagnetization behaviors of the discrete basalt samples are of high noise at higher temperatures, which is probably due to the onset of thermo-viscous remanent magnetization especially in a magnetically nonshielded environment. The close association of negative inclinations, changes in magnetic susceptibility, and demagnetization behavior with fractures in the cores points to the possibility of a secondary chemical remanent magnetization (CRM) as the source of the reversed intervals in the basalt.

Petrophysics

We conducted measurements of gamma ray attenuation (GRA) bulk density, magnetic susceptibility, and natural gamma radiation (NGR) on whole-round cores and additional measurements on split cores and discrete samples, including thermal conductivity, *P*-wave velocity on the *P*-wave caliper (PWC), porosity, and bulk, dry, and grain density. In general, bulk densities, *P*-wave velocities, and thermal conductivities increase with depth, whereas porosities decrease with depth as a result of compaction and lithification. However, some properties, such as NGR or magnetic susceptibility, show local variations related to the specific lithology. A significant increase in carbonate content in Subunit VB (1272–1311 m) causes a general decrease in NGR counts and only a slight decrease in magnetic susceptibility. Physical properties change significantly in the basalts of Unit VIII (1379–1529 m). Magnetic susceptibility values are two orders of magnitude higher than in the sediment above and vary depending on the degree of alteration. *P*-wave velocity values are also much higher, ranging between 4430 and 5710 m/s, whereas porosity and NGR values are very low compared to the sediment above.

Correlation to seismic data

We used physical property measurements on cores and samples to correlate Site U1500 data with the available seismic reflection profile. We also used the Site U1500 density and PWC velocity data to create synthetic seismograms that provided additional constraints on the correlation. The time-depth relationship (TDR) obtained for Site U1500 shows substantial agreement with that for Site U1499 and Sites U1431 and U1433; in contrast, the ODP Site 1148 TDR exhibits higher velocities in the deeper layers. The comparison between the seismic reflectors and the variations in physical properties and lithology characteristics using the computed Site U1500 TDR shows good correlation between the high-amplitude seismic reflector at ~6.4 s two-way traveltime (TWT) and the top of the basalts of Unit VIII.

Downhole measurements

Three downhole logging tool strings were run in Hole U1500B: a modified triple combo (sonic velocity, NGR, bulk density, resistivity, and caliper), the Formation MicroScanner (FMS)-sonic (FMS resistivity images and calipers, as well as NGR), and the Versatile Seismic Imager (VSI; check shot and NGR). During the first run, the tool string encountered an obstruction at 4946 m wireline log depth below rig floor (WRF; ~1133 m), and we were unsuccessful in getting the tool string to pass below this depth. We collected FMS data from ~1044 m uphole to the bottom of the casing (842 m). Although the hole had many zones that were significantly enlarged, initial observations of the real-time FMS data indicate that some intervals exhibit relatively good caliper contact and should provide useful resistivity images. A seismic check shot survey with the VSI successfully collected data at one depth in the open hole and at the base of the casing. Because this was the last operation conducted during Expedition 367 and we only had a 1 day transit to Hong Kong, data processing and full evaluation of the log data will be conducted after Expedition 367.

Background and objectives

Site U1500 (Figures **F1**, **F2**) is located on a basement high (Ridge B) clearly visible in the map of TWT to basement (Figure **F3**) and is well imaged on seismic Lines 08ec1555 and 15ecLW4 (Figure **F4**). The primary objectives at this site were to document the nature of

Figure F1. Seismic data coverage and magnetic anomalies of the SCS Basin, Expeditions 367 and 368. Black lines = ocean-bottom seismometer refraction data. Other seismic lines are mostly multichannel seismic reflection data. White stars = Expedition 367/368 sites, red squares = Leg 184 sites, red circles = Expedition 349 sites. For more detail, see Figure F2.

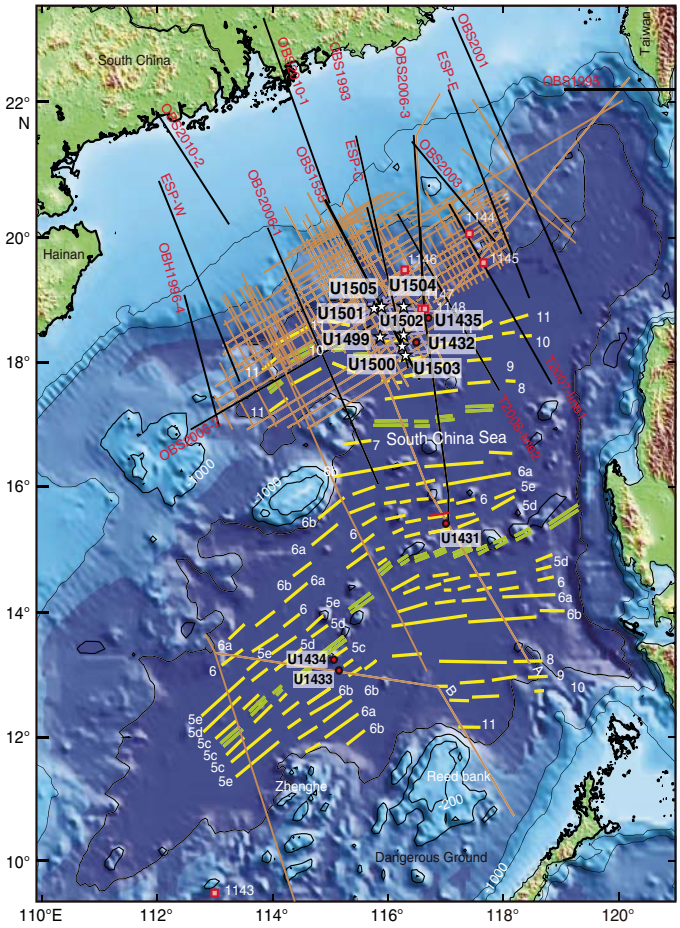

Figure F2. Bathymetric maps showing Expedition 367/368 sites (stars), and (A) regional and (B) local coverage of multichannel seismic reflection data and OBS data. Thick blue and red lines are key seismic lines used for planning of the drilling transect. A. Magnetic isochrons (orange lines) from Briais et al. (1993). B. Magnetic picks (orange squares) from the same reference, extracted from the Seton et al. (2014) compilation. Chron labels for the picks correspond to the old edge of the normal polarity intervals (see Ogg et al. [2016] timescale for ages). Orange square = Leg 184 Site 1148, yellow squares = Expedition 349 Sites U1432 and U1435.

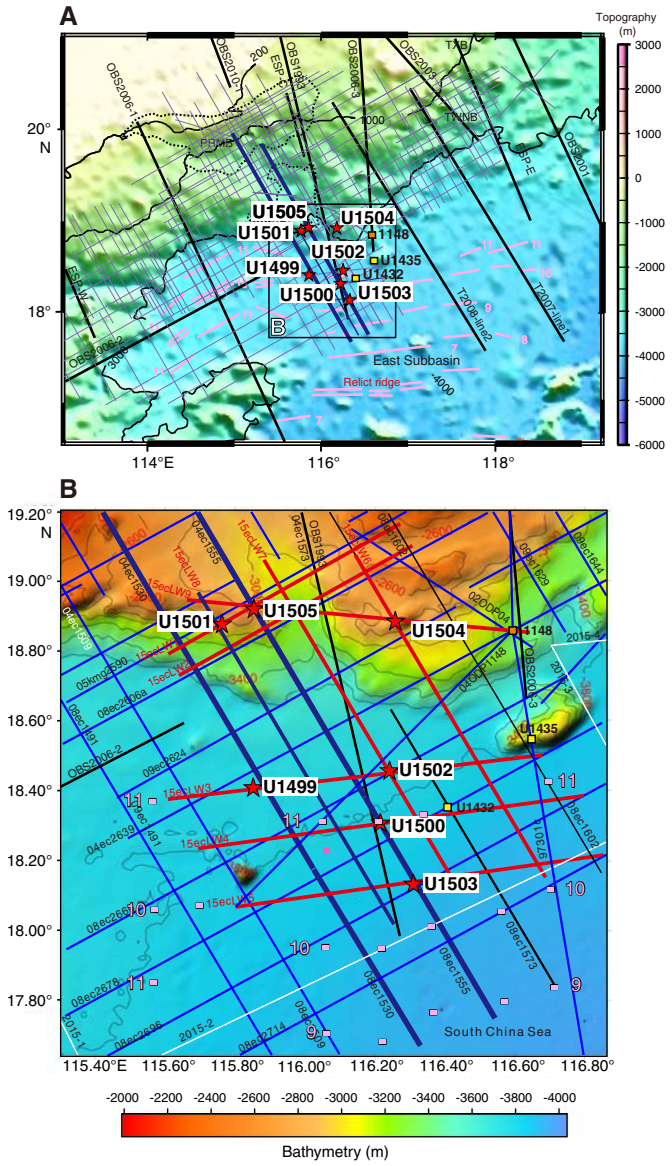

Figure F3. Two-way traveltime to (A) basement (Tg reflector) and (B) Unconformity T60 with the location of Expedition 367/368 sites indicated. Proposed drilling transect (thick black line) was located approximately at the center of a margin segment bounded to the southwest by a transform fault. Northeastern boundary of margin segment is located around Expedition 349 Site U1435. In this location, the outer margin high and Ridge A seem to coalesce, and Ridges B and C of the COT become indistinct toward the northeast within the next margin segment. Note that outer margin high is slightly oblique to the more parallel Ridges A, B, and C.

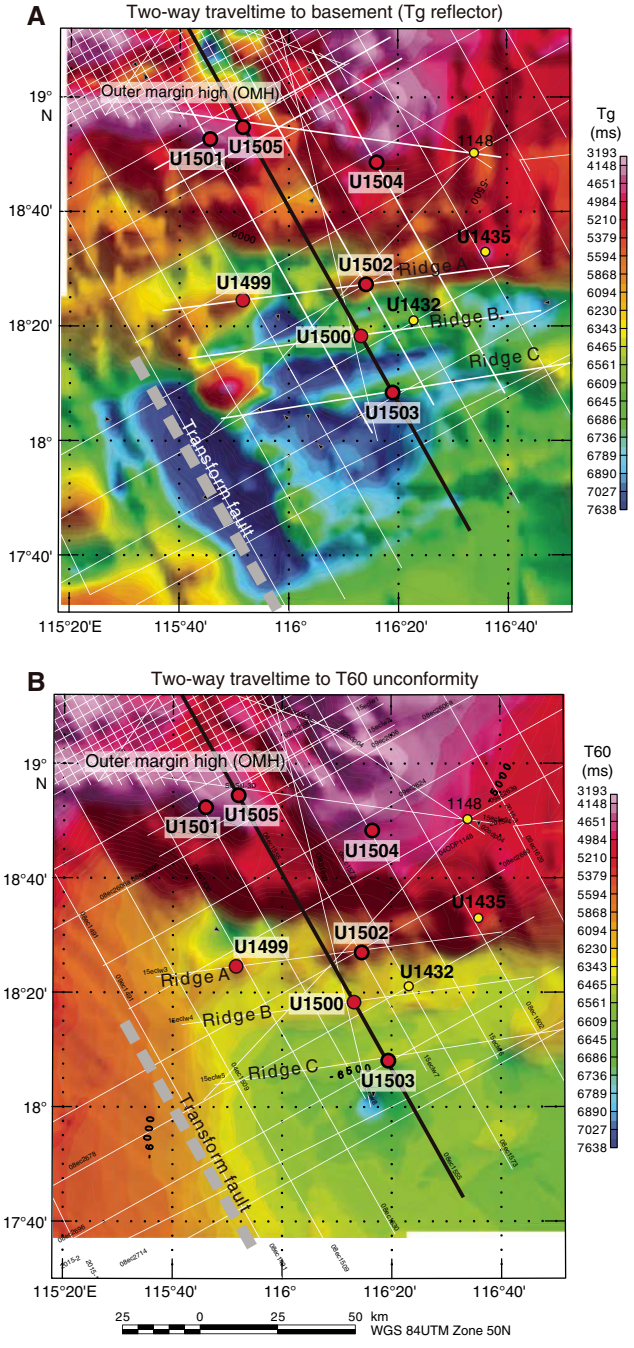

the basement and relative timing of processes of basement formation in this part of the COT (see Objectives 1 and 2 in **Preliminary scientific assessment** in the Expedition 367/368 summary chapter [Larsen et al., 2018]).

The Ridge B basement high is seaward of Ridge A, where Site U1499 was cored and logged. The sedimentary section at Ridge B is similar to that seen covering and pinching out against Ridge A (Figure **F5**) and is interpreted to be sand/sandstone, clay/claystone, and silt/siltstone containing major seismic reflectors in the postrift sequence (seismic stratigraphic Unconformities T32–T60), with a variable thickness of sedimentary rock below Unconformity T60 and above acoustic basement Reflector Tg (see **Correlation to seismic data** in the Expedition 367/368 summary chapter [Larsen et al., 2018]). The site is located along the part of Ridge B where the basement is shallowest and the sedimentary rocks older than Unconformity T60 are relatively thin, so basement can be reached most easily.

Figure F4. Original and interpreted multichannel seismic reflection profiles across Site U1500. Site U1500 is located on seismic Profile 08ec1555 and projected 75 m onto seismic Profile 15ecLW4. Red text and tick marks = locations of crossing seismic lines, red lines = faults interpreted from the seismic data. CDP = common depth point. All seismic profiles are courtesy of the Chinese National Offshore Oil Corporation [CNOOC]).

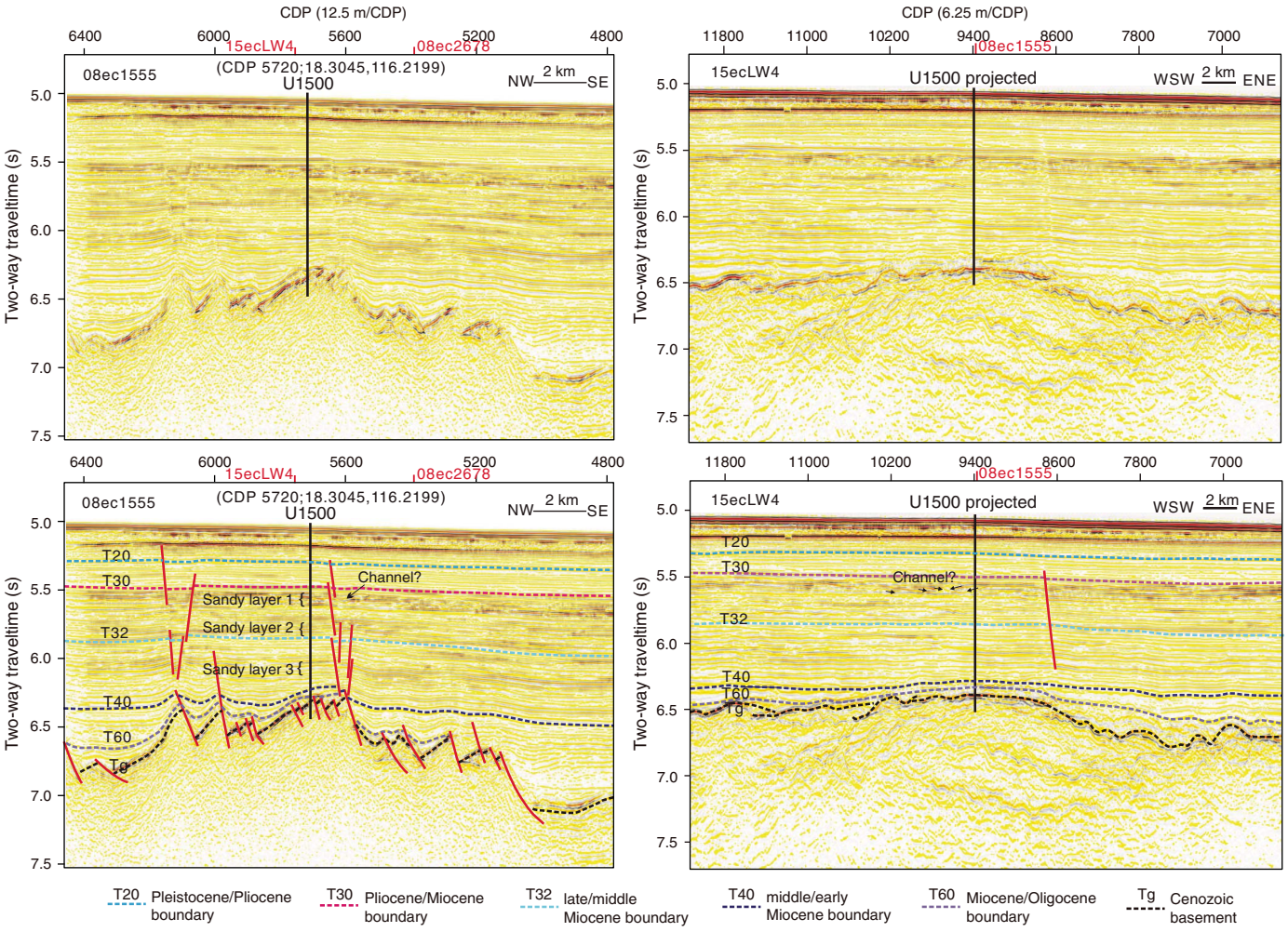

This basement high is cut by a series of generally southeast-dipping faults. As seen clearly on seismic Line 08ec1555 (Figure **F4**), the surface interpreted as acoustic basement (Reflector Tg) is tilted northwest in a series of fault blocks. Some of the bounding faults only affect older strata (deeper than Unconformity T60), whereas other faults can be seen to cut Unconformities T60, T40, and T32; a few faults also cut Unconformity T30 (inferred to correlate with the Miocene/Pliocene boundary [Reflector Tmp]; Li et al., 2015a) and extend nearly to the seafloor before terminating at a shallow, strong reflector at ~0.1 ms TWT below the seafloor. The faults show minor offset after Unconformity T60 suggesting that they might be caused mainly by differential compaction. The spacing of these faults varies from 200 to 600 m. Because the basement surface is dipping, the drill hole was in an optimal position to avoid the nearby faults while reaching the basement at the shallowest feasible location.

This site will help to distinguish among various models for the nature of the basement at this part of the COT. The basement might be serpentinized subcontinental or asthenospheric mantle, as shown in the evolutionary model in Figure **F6**. However, it could also be upper or lower continental crust or oceanic igneous rock such as basalt and/or gabbro (Figure **F7**). Because the Mohorovicic seismic discontinuity is not clearly imaged here on the seismic profile (Figure **F8**) and crustal reflectors suggestive of detachment faults are not seen in this area (Figure **F9**), several possible models are left open, including diverse combinations of continental or oceanic lithosphere with or without magmatic intrusions or serpentinization.

Figure F5. Uninterpreted and interpreted seismic profiles and sequence correlation between Sites U1499 and U1500.

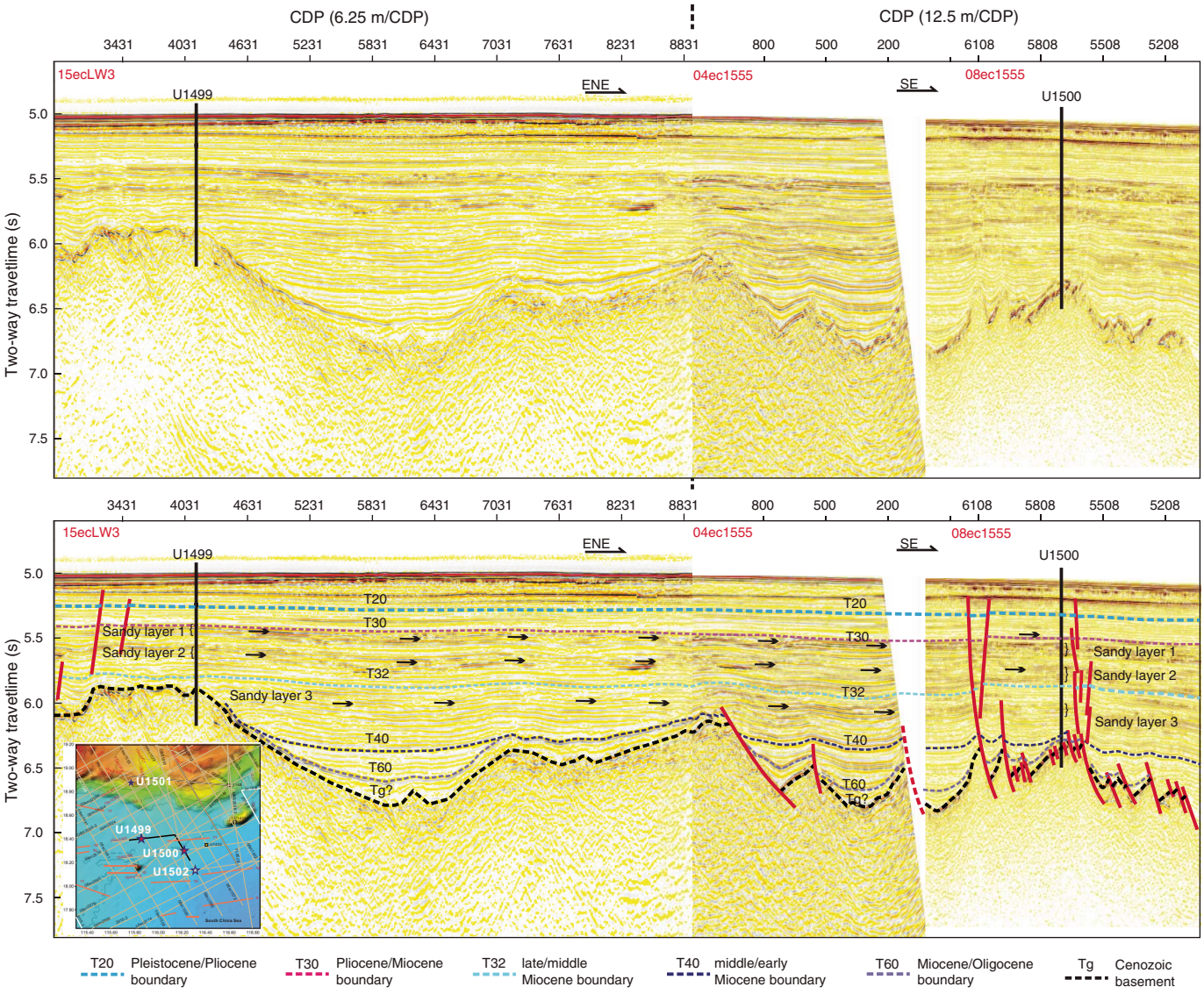

Figure F6. A–D. Schematic development of continental breakup initiated by a simple shear along a deep, low-angle fault. B–D are slightly modified from Huismans and Beaumont (2011) and illustrate modeling-based stages of extension at magma-poor rifted margins of the Iberia-Newfoundland type. Key features of D are thinning of upper crust, juxtaposition of lower crust (e.g., Site U1499), and serpentinized mantle (Site U1500) between outer margin and igneous oceanic crust. UP = upper plate, LP = lower plate.

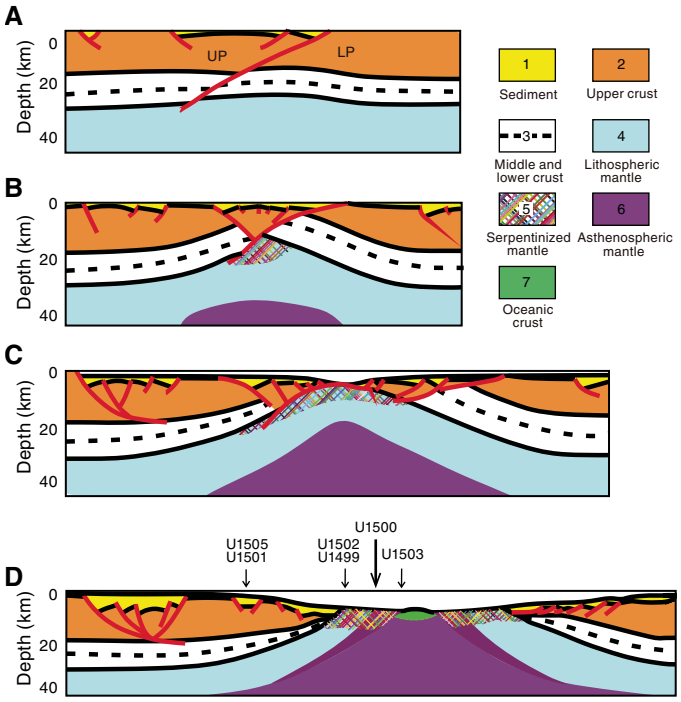

Figure F7. A–E. Composite figures redrawn from models in Huismans and Beaumont (2011), Sibuet and Tucholke (2012), Makris et al. (2012), and Sun et al. (2016) showing spectrum of possible magma-poor rifted margin models based on rheological differences. These models suggest that lithospheric layers with relatively lower strength will tend to stretch and thin more than other layers. Thus, COT may be dominated by these weaker layers. D features a strong lower crust overlying a weak, wet upper mantle, resulting in upper subcontinental (serpentinized) mantle dominating the COT. C shows a particularly interesting alternative in which moderately weaker lower crust leads to its exhumation in the COT. UCC = upper continental crust, LCC = lower continental crust, UCM = upper continental mantle, UOM = upper oceanic mantle, OC = oceanic crust.

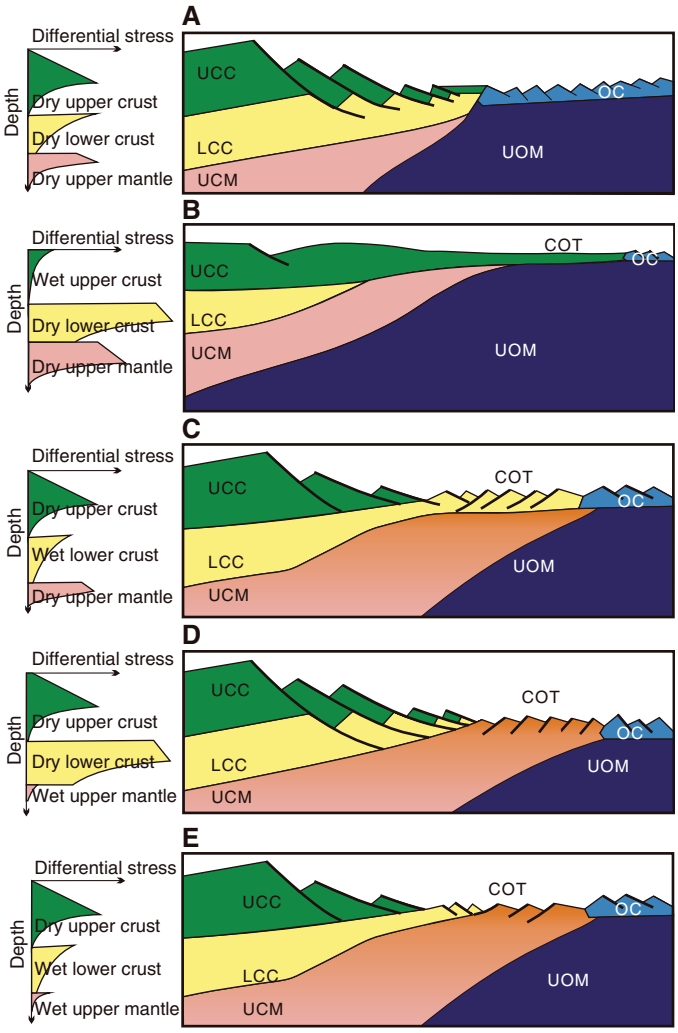

Figure F8. Uninterpreted and simplified interpretation of seismic Profile 1555. Note the seaward shallowing of interpreted Mohorovicic seismic discontinuity (Moho) seismic reflection and presence of major detachment faults that seem to sole out between the upper and middle/lower crust. Although general location of the COT (question marks) is well constrained by both this seismic profile and Figure F9, details of crustal structure within the COT are not well constrained. Seismic line in Figure F9 images this zone slightly better, in particular the Moho. Location of ocean floor magnetic Lineations C11n to C9n are projected from Figure F2B. MSB = midslope basin.

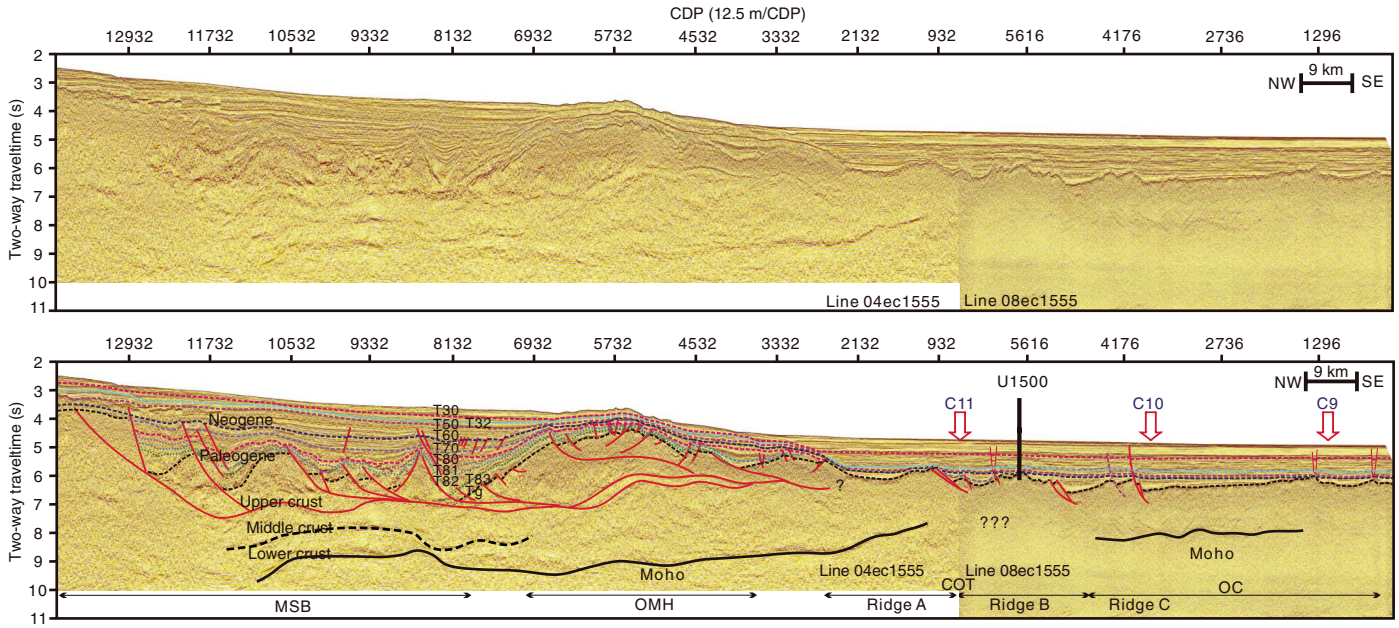

Figure F9. Uninterpreted and simplified interpretation of seismic Profile 1530. Note the presence of reflectors interpreted as major detachment faults that seem to sole out between the upper and middle/lower crust in the outer margin high. Location of ocean floor magnetic lineations C11n to C9n are projected from maps in Figure F2B.

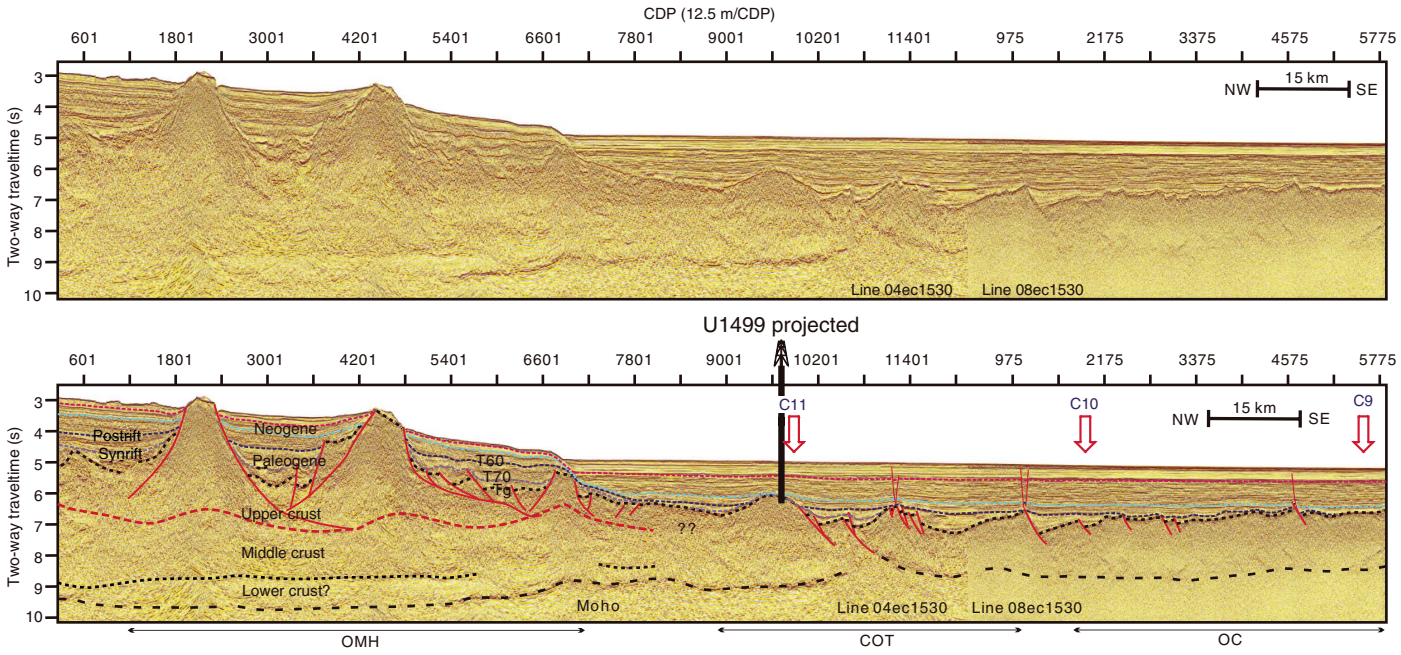

Operations

We conducted operations in two holes at Site U1500 with the primary objective of sampling and logging the lowermost sediments and underlying basalt. We successfully penetrated from the seafloor to the sediment/basalt contact at 1379 m and 150 m into the underlying basalt. The sedimentary section was not continuously cored, and recovery in the cored intervals was highly variable and rather poor (30%). In contrast, core recovery in the basalt was excellent (77%).

Hole U1500A is located at 18°18.2762′N, 116°13.1916′E in a water depth of 3801.7 m. We knew we would have to install casing to

achieve our deep objectives at this site, so our operations in Hole U1500A were designed to provide information on the formation characteristics and drilling conditions so that we could decide the length of casing to drill into the seafloor at deep-penetration Hole U1500B. Given this purpose and the amount of time to drill the second, deep hole, we did not core continuously in Hole U1500A. In Hole U1500A, we

1. Drilled without coring from the seafloor to 378.2 m,
2. RCB cored from 378.2 to 494.6 m and recovered 26.5 m (23%),
3. Drilled without coring from 494.6 to 641.2 m, and
4. RCB cored from 641.2 to 854.6 m and recovered 67.2 m (31%).

Hole U1500B is located at 18°18.2707′N, 116°13.1951′E in a water depth of 3801.7 m. In Hole U1500B, we

1. Drilled a reentry funnel and 842 m of 10¾ inch casing into the seafloor,
2. Continuously RCB-cored the sediment sequence from 846.0 to 1379.1 m (533.1 m cored; 164.7 m recovered; 31%),
3. Continuously RCB-cored 150 m into the underlying basalt from 1379.1 to 1529.0 m (114.92 m recovered; 77%), and
4. Collected downhole log data with three tool strings from 842 m (base of casing) to a total depth of 1133 m (~400 m above the base of the hole).

Core summaries for Holes U1500A and U1500B are presented in Table **T1**, and a summary of the casing installation and operations in Hole U1500B is shown in Figure **F10**.

Figure F10. Hole U1500B reentry system and casing.

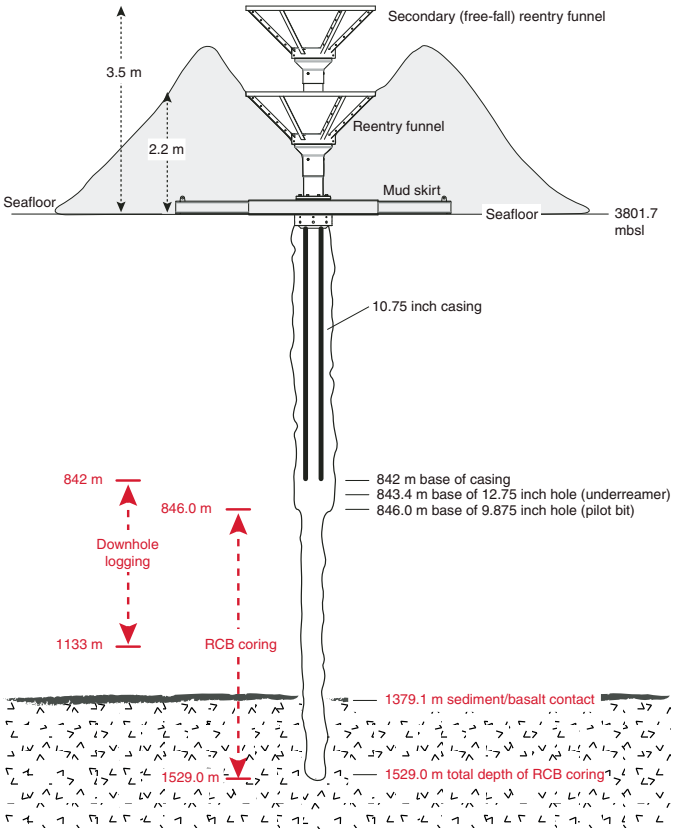

Hole U1500A

After pulling the drill string out of Hole U1499B at 1120 h on 8 March 2017, we recovered the seafloor positioning beacon and started the transit to Site U1500 in dynamic positioning mode just before 1300 h. While in transit, we continued to recover the drill string (which was completed at 1830 h) and then assembled a new RCB bit and started lowering it to the seafloor.

At 0415 h on 9 March, we deployed the subsea camera system and observed the bit tag the seafloor to establish the water depth (3801.7 meters below sea level [mbsl]). After recovering the camera system, we started drilling without coring in Hole U1500A at 0935 h. Unfortunately, at 1930 h with the bit at 340.5 m, the drawworks clutch diaphragm that was replaced earlier in the expedition failed. The clutch diaphragm was repaired with one of the new diaphragms that had been delivered to the ship by boat on 27 February. As soon as it was fixed (0930 h on 10 March), we resumed drilling without coring from 340.5 to 378.2 m. While drilling down, we pumped 30 bbl mud sweeps at 350.2 and 378.2 m. We recovered the center bit and started RCB coring at 1245 h on 10 March. Cores 2R through 13R penetrated from 378.2 to 494.6 m and recovered 26.5 m (23%). We drilled without coring from 494.6 to 641.2 m and then resumed RCB coring to the total depth of 854.6 m.

Except for a few short intervals (Cores 2R through 4R from 378.2 to 407.3 m, Cores 24R through 27R from 728.5 to 767.3 m, and Cores 35R through 36R from 835.2 to 844.9 m), core recovery was quite poor. In contrast, the cores that took 15 min or more to cut had better recovery (from 0.88 to 8.93 m; average recovery = 59%). We pumped frequent mud sweeps through the entire cored interval.

A formation change occurred at 728.5 m with Cores 24R through 27R (728.5–767.3 m), taking 30–50 min to cut with substantially improved recovery (32.1 m; 83%) of clay/claystone. We thought this would be a good formation for the base of our planned Hole U1500B casing until Core 28R once again reentered a fast-penetrating, low-recovery interval inferred to be sand. Following this, Cores 29R through 36R penetrated from 770.0 to 854.6 m and recovered 27.6 m (36%). The majority of the core recovered was in Cores 30R, 33R, 35R, and 36R (25.29 m). For the other cores, penetration rates were, once again, very fast and recovery was very low (2%–9%; inferred to be less consolidated silt/sand). When the last two cores (35R and 36R) encountered stable, well-consolidated formation, we decided we had met our primary objective of determining formation conditions at Site U1500 and an appropriate casing set point for our next hole at this site. We pulled the bit out of the hole, and it cleared the seafloor at 2330 h on 13 March. Based on the Hole U1500A information (cores, drilling, and borehole conditions), we decided that to achieve our deep-coring and logging objectives at this site, we would drill 842 m of casing into the seafloor at Hole U1500B. This placed the base of the casing in the relatively fine grained stable formation recovered in the last two cores and would isolate the multiple intervals of unstable formation above (inferred sand/silt). After the bit arrived back on the rig floor at 0640 h on 14 March, we disassembled the bit, cleared the rig floor, and conducted required routine rig servicing (drill line slip and cut).

Hole U1500B

From 0900 on 14 March 2017 to 0400 h on 15 March we prepared the casing running tool (HRT), assembled 842 m of 10.5 inch casing, and latched it into the mud skirt sitting on the moonpool doors. We then assembled and tested a 846 m long drilling assembly

composed of a 9.875 inch tricone bit, underreamer (set to 12.75 inches), and mud motor. This drilling assembly was lowered through the casing, the HRT was attached to the top of it, and then it was secured to the mud skirt/casing. At 1130 h on 15 March, the entire system was lowered through the moonpool and to the seafloor. We deployed the subsea camera system at 2015 h on 15 March and installed the top drive shortly thereafter (2315 h).

At 0035 h on 16 March, we started drilling the casing into the seafloor at Hole U1500B. Along the way, we circulated 30 bbl of mud at multiple depths (335.6, 374.6, 394.0, 423.1, 452.2, 481.4, 510.6, 539.6, 568.8, 597, 627, 656, 685, 714, 744, 774, 802, and 832 m). Drilling the casing into the seafloor proceeded smoothly until ~779 m (0800 h on 17 March) when we observed the mud skirt and reentry funnel rotate very quickly, indicating that torque had built up in the drill string and then suddenly released. At the same time, we also observed that the penetration rate slowed down substantially. We suspected that one or more of the underreamer arms had lost its cutting structure (roller cone). Our options at this point were limited. We could continue to drill the bit in to the full depth or pull it back to the ship, shorten the casing string, and try to drill that in. We had only ~63 m more of penetration until the casing was fully installed. Based on the coring information from Hole U1500A, much of this interval was expected to be loosely consolidated fast-penetration formation with only a couple of short intervals of firm formation, so we continued to drill in. Although penetration rates slowed quite a bit, we were able to continue advancing the entire system until a reduction in drill string weight indicated that the mud skirt had landed on the seafloor at 1740 h on 17 March (Figure **F10**). This fact led us to suspect that if the underreamer cutters had come off, they likely had been pushed off into the borehole wall behind the casing. We dropped the go-devil to activate the HRT, and the drilling assembly released from the casing at ~1833 h on 17 March. We raised the bit and underreamer back up to 841.4 m, inside the casing, and filled the annulus between the casing and the drill pipe with 100 bbl of mud to inhibit sand from being sucked back up into the casing as we pulled the drilling assembly out of the hole (as previously happened at Hole U1499B). We then pulled the drill string out of the hole. After the bit cleared the seafloor (2220 h on 17 March), we conducted a short survey of the reentry system, which was barely visible in the cutting mound.

Once we finished recovering the drilling assembly and the underreamer arrived back on the rig floor (0730 h on 18 March), we observed that all of its cutting structures were still attached. However, one of them was clearly damaged (failed bearing assembly) and likely the cause of the torque event and subsequent reduction in penetration rate. We started assembling the RCB bottom-hole assembly (BHA) at 0915 h on 18 March and lowered it to the seafloor. We deployed the subsea camera system at 1615 h, started searching for the Hole U1500B reentry funnel, and after only 6 min of maneuvering, we reentered Hole U1500B at 1845 h on 18 March. We recovered the camera system, lowered the bit through the casing, and installed the top drive in preparation for RCB coring. We lowered the bit into the open hole below the end of the casing (842 m), found only 1 m of fill, circulated 25 bbl of mud and displaced the heavy mud out of the hole, and started RCB coring at 0115 h on 19 March. The uppermost 5.3 m of the first core taken after installing the casing (Core 2R) was composed primarily of heavy mud mixed with some cuttings.

Overall core recovery in Hole U1500B was very poor over a significant interval of the sedimentary section, particularly from 893.8 to 1233.3 m (lithostratigraphic Unit IV). Cores from this interval (Cores 7R through 41R) penetrated 339.5 m and recovered only 51.3 m (15%). For cores in this interval that cut quickly (≤15 min), core recovery was only 7%, and we inferred the formation is likely dominated by unconsolidated sand/silt. In contrast, recovery in cores that took longer to penetrate (20–55 min) was higher (41%) and recovered sandstone with claystone and siltstone interbeds.

While cutting Core 42R, we encountered a substantial formation change at 1235 m, and core recovery increased to 66% for Cores 42R through 45R. The time to cut Cores 43R through 45R also increased to 40–80 min. The formation change is also reflected in the recovered cores, which are dusky red claystones with greenish alteration zones and a few interbedded sandstone layers. Cores 46R through 50R penetrated from 1272.1 to 1320.6 m and recovered 30.2 m (62%). Although it took quite a long time to cut each of these cores (1.8–3.8 h), the penetration rate was very smooth and hole conditions were quite good. Cores 51R through 57R then penetrated from 1320.6 to 1388.5 m and recovered 32.4 m (48%). After Core 51R took 100 min to cut, the next five cores (52R through 56R) penetrated quite quickly; all but one took only 5–25 min and had relatively lower recovery (31%). Core 57R cut slowly (3.6 h) but smoothly and consistently and recovered 8.34 m that is almost entirely basalt. Cores 58R through 60R continued in basalt, penetrating from 1388.5 to 1415.9 m and recovering 19.9 m (73%). These cores also cut slowly (4.3–5.4 h) but mostly smoothly and consistently. Because we had 52 rotating hours on the bit and we wanted to core and log deeper in Hole U1500B, we decided to retrieve the drill string to change the RCB bit. We circulated cuttings out of the hole, raised the bit up to 1242 m, and pumped 235 bbl of weighted (11.0 lb/gal) mud into the hole to stabilize it while we changed the bit. We then pulled the drill string out of the hole (removing the top drive at 1066.0 m), and the bit cleared the seafloor at 2340 h on 25 March.

Before we recovered the drill string, we paused operations for 2 h to conduct routine rig servicing (drill line slip and cut). The bit arrived on the rig floor in good shape at 0845 h on 26 March. We attached a new RCB bit for basement coring (C-7) and lowered it toward the seafloor. Once the bit was at the seafloor along with the camera system, we started searching for the reentry funnel at 1730 h on 26 March. After a short search, we saw streaks of cuttings on the outside of the mound of drill cuttings around the hole. We moved the bit over the clearly visible reentry funnel and reentered Hole U1500B at 1755 h. We lowered the bit through the casing and into the open hole below. As we were doing this, we had the float valve shifted into the open position, which allows water to easily pass through the bit. If it's in the closed position we have to stop periodically to fill the drill string with water as we lower it. As we lowered the bit, it encountered a bridge at ~1067 m, and sediment appeared to block flow through the bit. We then pulled up a little bit and deployed a core barrel to try to clear the obstruction in the bit and to close the float valve so we could wash/drill back down the hole to resume RCB coring.

The core barrel that we dropped to clear the obstruction in the bit did not land properly at the bottom of the drill string. We deployed the core line to retrieve the core barrel and found that it had landed ~42 m above the bottom of the drill string. We made three unsuccessful attempts to pull the core barrel back out. We then raised the bit from 1018 to 454 m inside the casing (above the top of the weighted mud) and still could not free the core barrel and reestablish circulation. We made two more unsuccessful attempts with the bit at 249 m and then above the seafloor. At 1530 h on 27 March, we decided the only way to fix this problem was to retrieve the en-

tire drill string. At 0000 on 28 March, the bit had reached 58 m below the rig floor, and we spent most of the early morning of 28 March recovering the final parts of the BHA on the rig floor and cleaning out sediment (cuttings, sand, etc.) that filled the lowermost ~40 m of it. The sediment had worked its way above the core barrel. At 0700 h on 28 March, we started reassembling the RCB BHA and lowering it to the seafloor. We deployed the camera system, dropped a core barrel to close the float valve, and started to position the bit over the reentry funnel at 1830 h on 28 March. We reentered Hole U1500B at 1930 h, recovered the camera system, and lowered the bit down to 804.3 m in the casing. At 2315 h on 28 March, we started to install the top drive in preparation for lowering the bit through the base of the casing (842 m) and into the open hole below. At 0045 h on 29 March, however, we discovered a problem with the top drive (one of the counter-balance cylinders). After fixing it, we resumed lowering the bit at 0400 h on 29 March. After exiting the base of the casing and moving down into the open hole, the bit started encountering some resistance at ~1066 m. We washed from there back down to the bottom of the hole at 1415.9 m, pumping 30 bbl of mud at 1008, 1115, 1203, 1232.4, and 1300.52 m. At the bottom of the hole, we pumped 35 bbl of weighted (11.0 lb/gal) mud to clean the cuttings out of this deep hole. We planned to continue using weighted mud in Hole U1500B as we penetrated deeper. We recovered the core barrel that was in place while getting the bit back to bottom (ghost Core 61G; 2.36 m recovered), deployed a fresh core barrel at 1745 h on 29 March, and resumed RCB coring. Core 62R arrived on the rig floor at 2230 h on 29 March after penetrating 2.5 m (1415.9–1418.4 m) and recovering 2.36 m (94%). This shorter penetration was necessary to adjust pipe connections at the rig floor.

Although Core 63R recovered 3.6 m of very nice basalt, it took much longer to cut (8 h) and the core pieces became stuck inside the plastic core liner and in the core catcher sub. It is likely that the recovered material came from the upper part of the cored interval, then jammed, and the rest of the core got ground up, washed away, and never entered the core barrel. These conditions may have also contributed to the slow penetration rate (at least after the core jammed off), so we decided to cut only half-length cores. Cores 64R through 73R then penetrated from 1428.0 to 1475.9 m and recovered 40.0 m (84%). Although the cores took from 2.3 to 4.7 h to cut, the recovery and core quality of the basalts was excellent.

Because the bit had accumulated 44 h of rotating time, hole conditions remained good, and we planned to continue to core deeper into basement and collect downhole logs, we decided to stop coring to change the bit. After cutting Core 73R, we circulated cuttings out of the hole with two 35 bbl weighted mud sweeps and raised the bit to 1387.8 m where we removed the top drive. We then raised the bit to 1242.1 m and filled the hole with 235 bbl of weighted mud to stabilize it while we changed the bit. Once the mud was in place, we raised the bit to just below the seafloor (45.7 m) and deployed a secondary reentry (free-fall) funnel on top of the first one that we previously drilled into the seafloor with the casing (Figure **F10**). This secondary reentry funnel was intended to block the large pile of cuttings around the hole from falling back in while we continued our Hole U1500B operations. After the funnel was dropped at 2208 h on 1 April, we continued to circulate to minimize the amount of cuttings in the seafloor structure while the secondary funnel landed. We deployed the subsea camera system at 2330 h on 1 April so that we could observe the bit being withdrawn from Hole U1500B.

At 0100 h on 2 April, we observed the bit being pulled out of the hole with the subsea camera system and then recovered the drill string with the bit arriving back on the rig floor at 0840 h. We installed a new bit more appropriate for hard formations (C-9), lowered it to the seafloor, and started positioning the ship to reenter Hole U1500B at 2000 h on 2 April. We reentered the hole at 2100 h, recovered the camera system, and lowered the bit down through the casing.

Before lowering the new RCB bit into the open hole below the casing, we paused for 2 h to conduct routine rig servicing (drill line slip and cut; lubricate the rig). Once in the open hole, the bit encountered some resistance (bridge/ledge) at ~947 m and we reamed from there to ~950 m. The bit passed quite easily from there to the bottom of the hole, where ~0.5 m of hard fill was drilled out. After circulating two 35 bbl mud sweeps, we recovered the core barrel that was in place while getting back to the bottom of the hole. We resumed RCB coring from 1475.9 m at 1730 h on 3 April. Cores 74R through 83R penetrated from 1475.9 to 1529.0 m and recovered 39.8 m (75%).

The last core of Expedition 367 (Core 83R) arrived on the rig floor at 1530 h on 5 April. We stopped coring so that we would have time to collect downhole log data with three different tool strings (triple combo, FMS-sonic, and VSI). In preparation for logging, we circulated cuttings out of the hole (two 35 bbl mud sweeps) and raised the bit to 1416 m, where we removed the top drive. We then continued to raise the bit to 1242 m and spent 1 h (1730–1830 h on 5 April) filling the borehole (and well up into the casing) with 300 bbl of weighted (11.0 lb/gal) mud to improve our chances that the hole would stay open for collecting the log data. When this was finished, the drill string had become stuck and we were unable to raise it. We spent the next 2.75 h trying to free the drill string (installed the top drive, pumped, and applied overpull). Finally, at 2115 h on 5 April, we were able to resume raising the bit up the hole with the top drive.

We deployed the subsea camera system as we finished pulling the drill string out of Hole U1500B; the bit cleared the seafloor at 0430 h on 6 April. We offset the ship 20 m to the west, released the bit on the seafloor at 0600 h, reentered Hole U1500B at 0840 h, and set the end of the pipe at a logging depth of 35.4 m (inside casing). After the camera system was recovered at 1100 h on 6 April, we prepared the rig floor for logging. We assembled a modified triple combo tool string that contained the following tools:

- Dipole Sonic Imager (DSI) for acoustic velocity,
- High-Resolution Laterolog Array (HRLA)/Phasor Dual Induction-Spherically Focused Resistivity Tool (DIT) for electrical resistivity,
- Hostile Environment Litho-Density Sonde (HLDS) without the source for caliper data, and
- Hostile Environment Natural Gamma Ray Sonde (HNGS)/Enhanced Digital Telemetry Cartridge (EDTC-B) for NGR.

At 1345 h on 6 April, we started lowering to the seafloor. The tool passed through the base of the casing at 842 m and into the open hole. It was unable to pass an obstruction at 1133 m, and log data were collected from there up to the base of the casing. The modified triple combo tool string arrived back on the rig floor at 2145 h on 6 April.

We assembled an FMS tool string consisting of the FMS to collect borehole resistivity images and the HNGS and EDTC-B to collect NGR data and for correlating with the previous logging runs. This second tool string was only able to reach 1044 m, 89 m shallower than the first logging string. We opened the FMS arms and collected data from that depth up to the bottom of the casing at 842

m. Our last operation for Expedition 367 was to conduct a check shot experiment with the VSI (geophone). We started assembling the VSI tool string at 0700 on 7 April. It consisted of the VSI sonde and ETDC-B. Routine IODP protected-species procedures were implemented leading up to and throughout use of the seismic source. The VSI tool string reached a total depth of 1031 m, and data were collected at that depth as well as at one station in the bottom of the casing at 783 m. The VSI tool string arrived back on the rig floor at 1430 h on 7 April. After the rig floor was cleared of logging equipment at 1530 h on 7 April, we pulled the end of the pipe out of the hole (1523 h on 7 April) and recovered the drill string. We conducted operations at Site U1500 for a total of 30.3 days (5.5 days in Hole U1500A; 24.8 days in Hole U1500B).

At 0100 h on 8 April, we started our transit to Hong Kong. Expedition 367 ended with the first line ashore at 0800 h on 9 April.

Lithostratigraphy

Two holes were drilled at Site U1500, reaching a total depth of 1529.0 m below seafloor. Both Holes U1500A and U1500B were cored using the RCB drilling assembly. We penetrated from the seafloor through 1379.1 m of unconsolidated to lithified sediment and sedimentary rock and into the underlying basalt (see **Igneous petrology**). However, we only cored 862.9 m of the sedimentary section, from which we recovered 258.22 m of core. The overall sedimentary penetration included two intervals that we drilled without coring (0–378.2 and 494.6–641.2 m) (Table **T1**).

From the recovered intervals at Site U1500, we organized the lithostratigraphy into eight units (Figure **F11**) grouped into three main lithologic sections. The uppermost four units (I–IV) comprise interbedded greenish gray clay(stone), silt(stone), and sand(stone), with some intervals containing increased biogenic carbonate. Units V–VII comprise the second main lithologic section composed of reddish brown and greenish gray claystone. More specifically, Unit V is dark reddish brown claystone that transitions into a clay-rich chalk. Unit VI contains massive greenish gray silty claystone and dark gray sandstone. Unit VII is a short interval of very dusky red and greenish gray claystone. Unit VIII is the third main lithologic section recovered at this site and is composed of basalt with occasional gray and reddish brown sandy claystone inclusions (see **Igneous and metamorphic petrology**).

Lithostratigraphic units and subunits were primarily defined by principal lithology and by the repetitive assemblages of facies that occur in each unit (see **Lithostratigraphy** in the Expedition 367/368 methods chapter [Sun et al., 2018a]). The boundaries between units and subunits were initially chosen based on these criteria and then corroborated using physical property measurements (Figure **F12**), mineralogical data by X-ray diffraction (XRD) (Figure **F13**), and calcium carbonate concentrations. Because core recovery was poor across most of the boundaries that separate individual lithostratigraphic units, their precise depth can only be inferred. Like many of the lithostratigraphic units defined at Site U1499, the units at Site U1500 exhibit gradual changes downhole, further complicating the definition of unit boundaries.

Unit descriptions

Unit I

Interval: 367-U1500A-2R-1, 0 cm, to 5R-CC, 17 cm
Depth: 378.20–410.00 m (0–378.20 m drilled without coring)
Age: late Miocene

Unit I consists of greenish gray clay with silt and sandy silt interbeds. Some of the clay intervals are nannofossil rich (Figure **F14**). The clays are well consolidated and exhibit heavy bioturbation. Based on visual and smear slide analysis, we observed subrounded grains that are well sorted. Structure in the clay is mostly massive, but parallel laminations occur in the silt and sandy silt interbeds. Contacts between lithologic intervals are bioturbated higher in the unit (Core 2R), whereas in Cores 4R and 5R the contacts are erosive and planar.

Calcium carbonate concentrations range from 4 to 19 wt% (Figure **F12**), with nannofossil-rich clay intervals containing higher amounts of carbonate. L* values measured on the Section Half Multisensor Logger (SHMSL), which are positively correlated to carbonate concentrations, increase from Cores 2R through 4R (L* = 30–40) to Core 5R (L* = 40–50), indicating increasing carbonate concentrations toward the bottom of the unit. Magnetic susceptibility decreases from a peak of 167×10^{-5} SI at the top of Unit I to values between 30×10^{-5} and 40×10^{-5} SI at the bottom of the unit (Figure **F12**). Three XRD samples from Unit I provide preliminary mineralogical information. The dominant components are quartz (27%–31%) and kaolinite + chlorite (25%–34%) (Figure **F13**).

Unit II

Interval: 367-U1500A-5R-CC, 17 cm, to 13R-CC, 18 cm
Depth: 410.00–494.60 m
Age: late Miocene

In Unit II, recovery was very low (~8%). The recovered sediment contains interbedded dark greenish gray clay and silt. The clay and silt intervals are well consolidated and heavily bioturbated. Classifying Unit II was difficult due to low recovery. For example, Core 11R only contains 3 cm of lithified sandstone (Figure **F15A**) that could have been fall-in from higher in the hole. However, the intervals of no recovery may indicate a change in lithology (e.g., increased abundance of nonlithified sands). Based on this inference, we separated this interval (Cores 9R through 13R) into a distinct unit.

Some clay intervals contain >10% biogenic carbonate, based on carbonate concentrations (Figure **F12**), smear slide analysis, and visual analysis of color change. These intervals are classified as clay with nannofossils and range from 4 to 65 cm thick. There is one interval of foraminiferal silt in Section 13R-1 (Figure **F15B**). Contacts between the silt and underlying clay are generally erosive, and silt intervals often exhibit parallel laminations.

Two XRD samples from Unit II clay intervals contain dominant quartz (26%–42%) and kaolinite + chlorite (24%–31%) (Figure **F13**). Magnetic susceptibility exhibits relatively high variance between 45×10^{-5} and 100×10^{-5} SI, but there is no significant trend throughout the unit. Similarly, color reflectance data (L*, a*, b*) lack trends downunit (Figure **F12**).

The drilled interval from 494.60 to 641.20 m was washed down without coring.

Unit III

Intervals: 367-U1500A-15R-1, 0 cm, to 36R-CC, 17 cm; 367-U1500B-2R-1, 0 cm, to 6R-CC, 17 cm
Depths: Hole U1500A = 641.20–854.60 m; Hole U1500B = 846.00–892.44 m
Age: late Miocene

Unit III spans the bottom of Hole U1500A and the top of Hole U1500B and is composed of interbedded claystone, siltstone, and

Figure F11. Lithostratigraphic summary of Site U1500 with simplified lithology and unit description of combined Holes U1500A and U1500B.

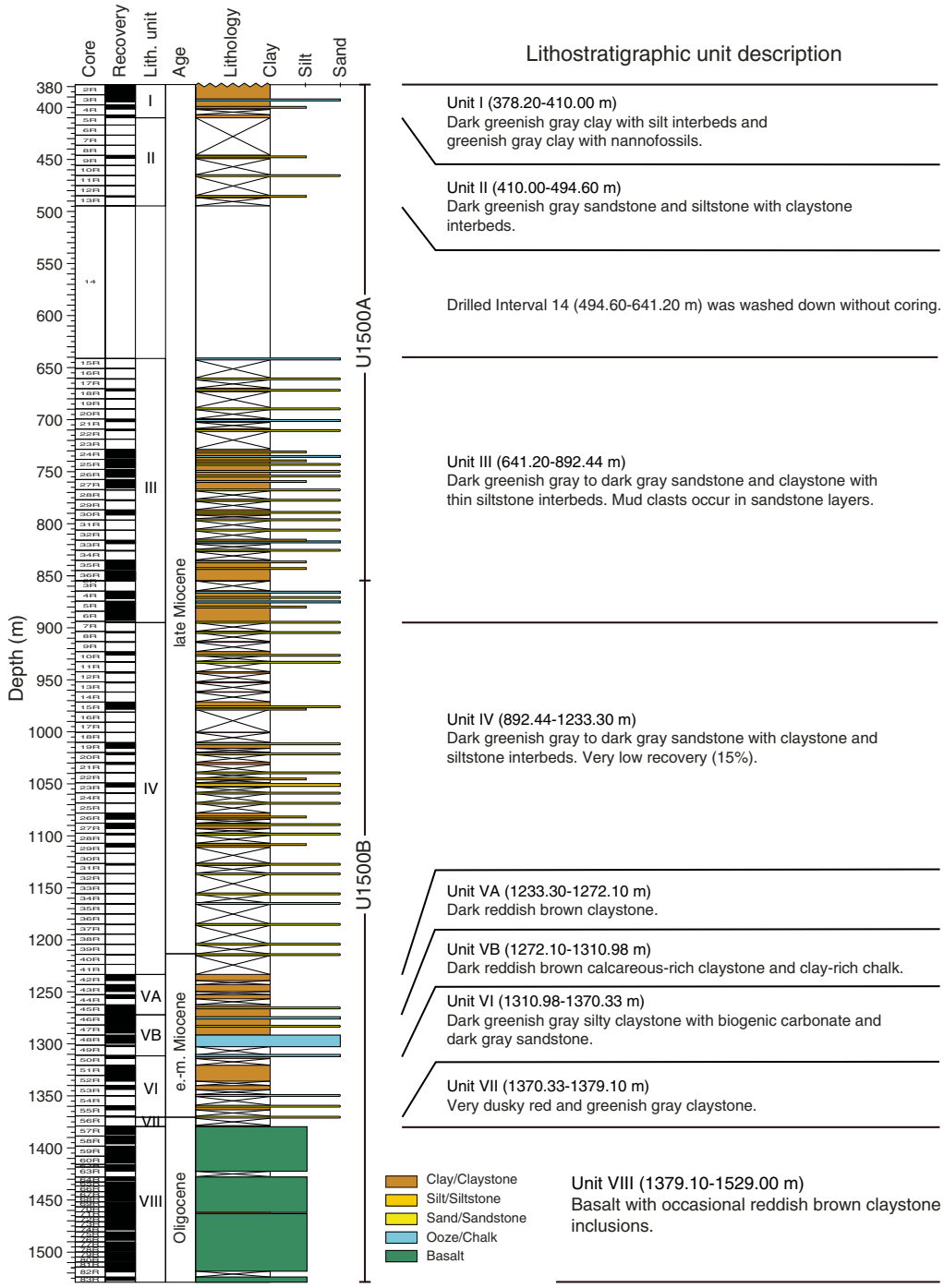

sandstone. Many of the contacts between siltstone or sandstone and underlying claystone are erosive, and some are slightly inclined. Color transitions from dark greenish gray into dark gray and grayish brown. Bioturbation increases downhole from slight to heavy.

The siltstone and sandstone intervals include both massive and stratified beds with parallel lamination, cross-stratification, contorted strata, and mud clasts (Figure **F16**).

Similar to Units I and II, the dominant mineralogical components of Unit III are quartz (33%–62%) and kaolinite + chlorite (17%–31%) (Figure **F13**). However, two samples contain minerals that may be diagenetic. Interval 367-U1500A-21R-1, 105–106 cm, contains 29% siderite, which is an order of magnitude higher than any other sample measured at Site U1500. Interval 22R-1, 106–108 cm, contains 9% ankerite, which is again an order of magnitude greater than all other samples at Site U1500. This interval also has the lowest measured concentrations of muscovite (5%; unit average = 16%) and kaolinite + chlorite (4%; unit average = 25%).

Magnetic susceptibility increases from between 25×10^{-5} and 30×10^{-5} SI to a midunit peak between 100×10^{-5} and 110×10^{-5} SI and then decreases toward the bottom of the unit to between 40×10^{-5}

Figure F12. Correlation of lithostratigraphic units with magnetic susceptibility, reflectance spectroscopy, and carbonate contents, Site U1500. Magnetic susceptibility and reflectance spectroscopy are displayed as a 10-point running average.

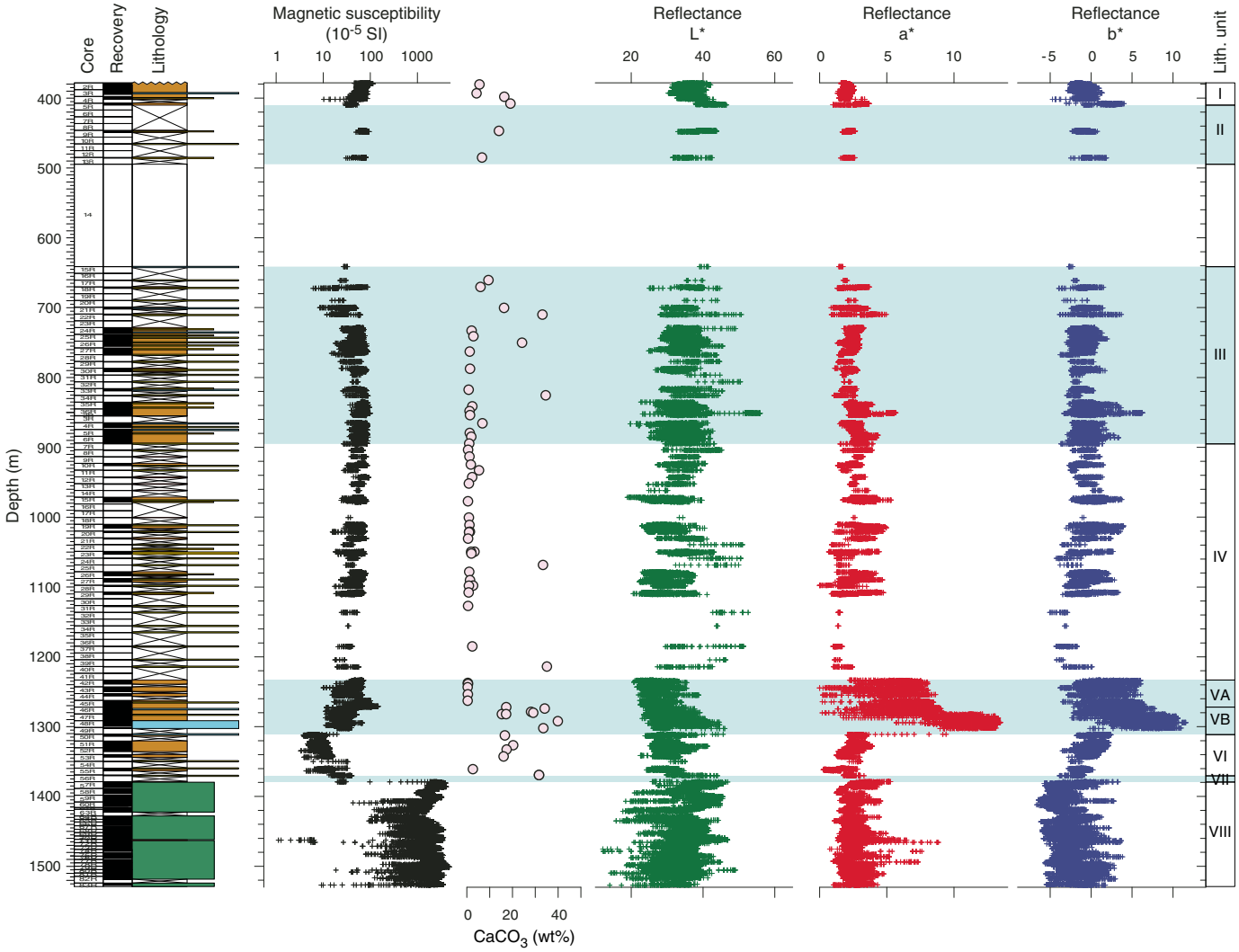

and 50 × 10^{-5} SI. Color reflectance data vary within a small range throughout the unit. Carbonate contents in the claystone intervals range from <1 to 16 wt%, whereas siltstone and sandstone intervals contain up to 35 wt% carbonate (Figure **F12**).

Unit IV

Interval: 367-U1500B-6R-CC, 17 cm, to 42R-1, 0 cm
Depth: 892.44–1233.30 m
Age: late Miocene

Recovery in Unit IV was very low with an average of 15%. The dominant lithology is very dark greenish gray to dark gray sandstone with dark brown to very dark gray claystone and siltstone intervals. Many of the intervals described in this unit contain interlaminations of silt or sand within a prevailing claystone lithology. Some of the sandstone and siltstone intervals contain interlaminations of clay and are typically organized into a variety of stratified and massive beds (Figure **F17**). We observed parallel lamination, cross-stratification, fining-upward sequences, interlamination, contorted strata, and mud clasts. Mud clasts, similar to those observed in Unit III, were observed within massive sandstone intervals in Cores 10R, 11R, and 23R. Parallel laminations are present in siltstone and claystone intervals in sections where color banding is also abundant.

The claystone in some cores shows distinctive color banding, which was observed as a pattern of alternating reddish brown, dark greenish gray, and brownish gray (Figure **F17**). The color banding appears to be associated with varying levels of bioturbation and fining-upward intervals. Contacts between different lithologies are more varied than in previous units, including planar, gradational, erosive, and bioturbated geometries. Bioturbation is also highly variable from none to heavy throughout the unit. Bioturbation cannot be easily observed within sandstone intervals but is very abundant within claystone intervals.

The dominant mineralogical components from Cores 7R through 21R are quartz (29%–50%) and kaolinite + chlorite (17%–38%) with lesser plagioclase (10%–22%) and muscovite (8%–17%) (Figure **F13**). The top of the unit has slightly higher amounts (0%–3%) of calcite and siderite. Samples from sandstone intervals generally contain higher amounts of K-feldspar and calcite and lower amounts of muscovite and kaolinite + chlorite. Thin sections cut

Figure F13. Bulk mineralogy with major mineral compositions and correlation of calcite with carbonate contents, Site U1500.

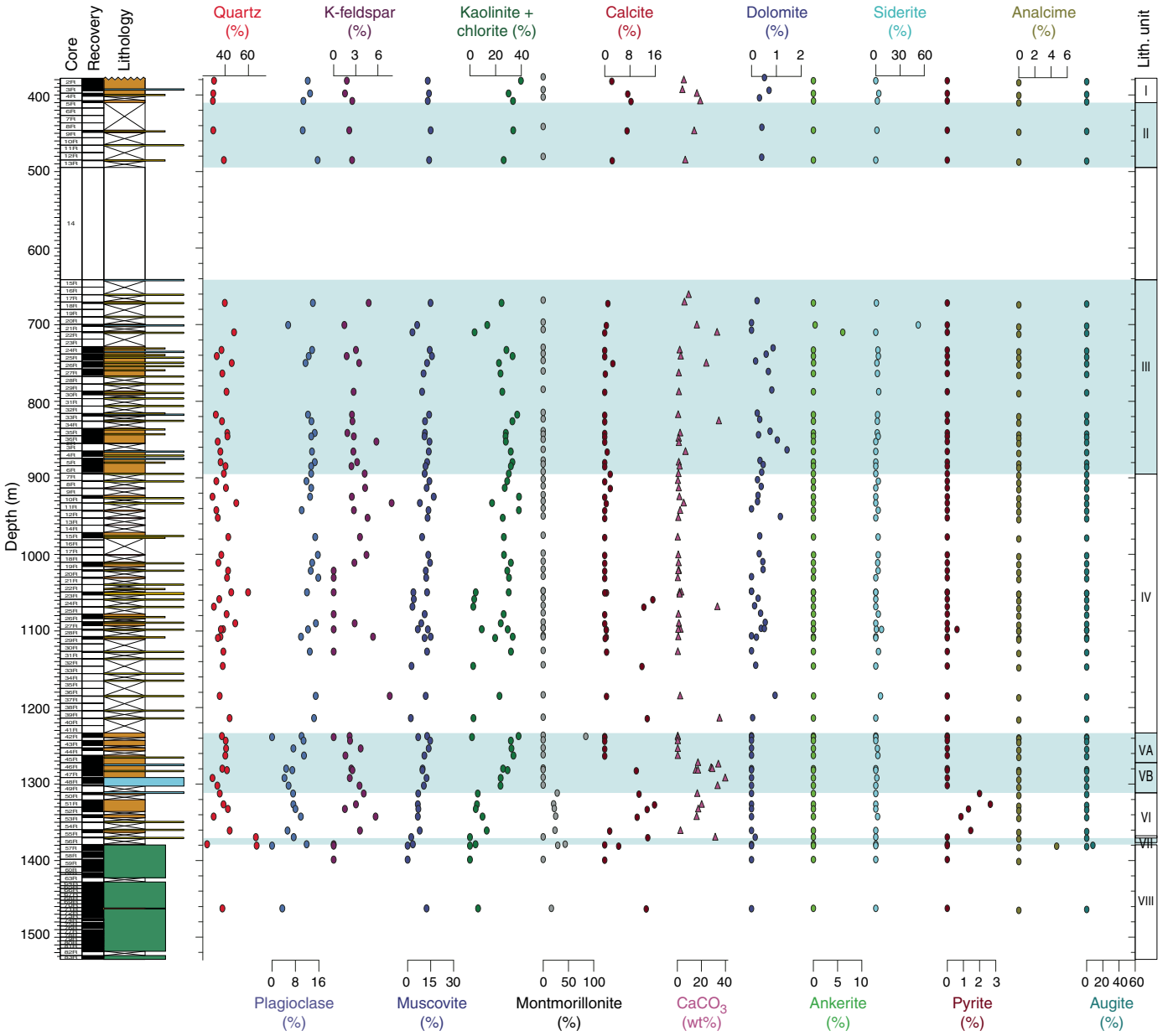

from well-lithified sandstone intervals show that many of the framework grains coincide with the results from the XRD analysis (Figure F18). Samples that have high amounts of muscovite and kaolinite + chlorite and low amounts of K-feldspar and calcite are from claystone intervals.

Carbonate contents for Unit IV are typically very low and range from <1 to 5 wt%, with two samples containing very high abundances of calcium carbonate (>30 wt%) (Figure F12). Both samples are from sandstone intervals; one is from Section 25R-CC (33 wt% calcium carbonate), and one is from Section 40R-1 (35 wt% calcium carbonate). The high carbonate contents in the sandstone intervals are likely due to the pervasive carbonate cement that occupies the interstitial spaces between grains (Figure F18). Magnetic susceptibility exhibits relatively high variance between 5×10^{-5} and 99×10^{-5} SI, but there are no significant peaks within the unit (Figure F12). Values appear to slightly decrease from a maximum value of 99×10^{-5} SI at the top of the unit to a maximum value of 67×10^{-5} SI at the bottom of the unit. Color reflectance data show an increase in L* around Cores 24R and 25R (L* = 52) and then a short decrease. The L* data also have a positive peak around Cores 39R and 40R (L* = 58). These two peaks in L* occur in the same core sections as the two high values of calcium carbonate, showing a positive correlation of L* values and calcium carbonate abundance. Overall, L* varies throughout the unit from 10 to 58.

Unit V

Interval: 367-U1500B-42R-1, 0 cm, to 50R-1, 8 cm
Depth: 1233.30–1310.98 m
Age: early–middle Miocene

Figure F14. Heavily bioturbated nannofossil-rich clay between two darker clay intervals, Unit I. Abundant (A) discoasters (plane-polarized light [PPL]) and (B) coccolithophores (cross-polarized light [XPL]).

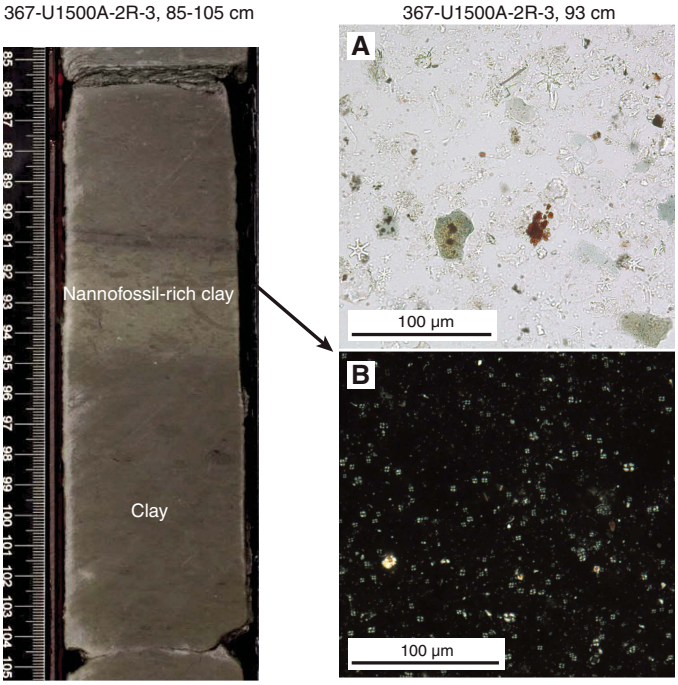

Figure F15. A. Entire recovered interval from Core 367-U1500A-11R (5 cm), Unit II. Well-lithified greenish gray sandstone fragments with mud clasts. B. Foraminiferal siltstone, Unit II.



Unit V contains dark reddish brown claystone and reddish brown clay-rich chalk. The unit is divided into two subunits based on carbonate contents (Figure F12). Subunit VA consists of dark reddish brown claystone with few sandstone and siltstone intervals, whereas Subunit VB consists of dark reddish brown to reddish brown calcareous-rich claystone and clay-rich chalk. In Core 48R, the calcareous-rich claystone transitions into a clay-rich chalk. There are also thin (<5 cm) sandstone intervals in Subunit VB.

Subunit VA

Interval: 367-U1500B-42R-1, 0 cm, to 46R-1, 0 cm
Depth: 1233.30–1272.10 m
Age: early–middle Miocene

A gradational contact (Sections 34R-1 through 42R-1) marks the boundary between the very dark gray to dark brown claystone with sandstone and siltstone interbeds in Unit IV and the more homogeneous red claystone of Unit V (Figure F19). Subunit VA consists of dark reddish brown, dark greenish gray, and dusky red homogeneous claystone with few sandstone and siltstone interbeds (3–12 cm thick). Bioturbation throughout these cores is mostly moderate. Although the overall structure is massive, we observed parallel laminations in some of the claystone and sandstone intervals. Bottom contacts between intervals are mostly gradational, with some planar and bioturbated contacts. One interval in Section 42R-1 (72–78 cm) contains contorted strata within an altered section of yellow to greenish gray claystone (see leftmost core image in Figure F19). Intervals of greenish gray color within the unit are interpreted as diagenetic because they were observed surrounding fractures in the core and as halos surrounding foraminifer tests and other fossil fragments.

Similar to the first four units, the dominant mineralogical components for most of Subunit VA are quartz (40%–41%) and kaolinite + chlorite (32%–34%) (Figure F13). However, one sample contains a completely different mineral assemblage. The sample taken from Section 42R-5 (67–68 cm) contains 84% montmorillonite, 7% quartz, and 7% muscovite. This is the only sample measured for XRD analysis in this subunit that contains montmorillonite. This is also the largest percentage of montmorillonite observed in any XRD sample at Site U1500. Samples measured at the base of the subunit contain small amounts of siderite (2%–3%), and samples at the top do not contain any siderite.

Carbonate contents for the claystone in this subunit are very low, all <0.5 wt% (Figure F12). Although the laboratory-measured carbonate values for this unit are low overall, a smear slide taken of a foraminifer-rich sandstone interval in Section 45R-3 was observed to have >20% biogenic carbonate. This variability in carbonate contents is the result of sampling from different lithology intervals within a core. Thus, a smear slide may indicate high carbonate contents from one interval and geochemical analysis from another interval may show low carbonate contents. Magnetic susceptibility is variable throughout the unit, with lower values at the top of the unit (0×10^{-5} to 87×10^{-5} SI) increasing in range lower in the unit (0×10^{-5} to 154×10^{-5} SI) (Figure F12). A large peak within the massive claystone at Section 45R-6 could be caused by the diagenesis and alteration of red clay to green clay. L* reflectance data range from 10 to 47 throughout the subunit. The top of Core 43R (Sections 1–3) shows a slight increase in L* and a decrease in a* and b*, possibly suggesting an increase of calcium carbonate in those sections.

Subunit VB

Interval: 367-U1500B-46R-1, 0 cm, to 50R-1, 8 cm
Depth: 1272.10–1310.98 m
Age: early–middle Miocene

Subunit VB consists of dark reddish brown, reddish brown, and greenish gray intervals of claystone, nannofossil-rich claystone, claystone with biogenic carbonate, and clay-rich chalk. Bottom contacts between these claystone and clay-rich chalk intervals are

Figure F16. Turbidite sequences and sedimentary structures within claystone and sandstone intervals, Unit III. A. Cross-stratification and climbing ripple beds in foraminiferal sandstone. B. Sandstone with biogenic carbonate containing mud clasts. C. Parallel laminations in foraminiferal sandstone. D. Contorted strata within carbonate-rich, coarse-grained interval highlighted by folded light and dark laminations.

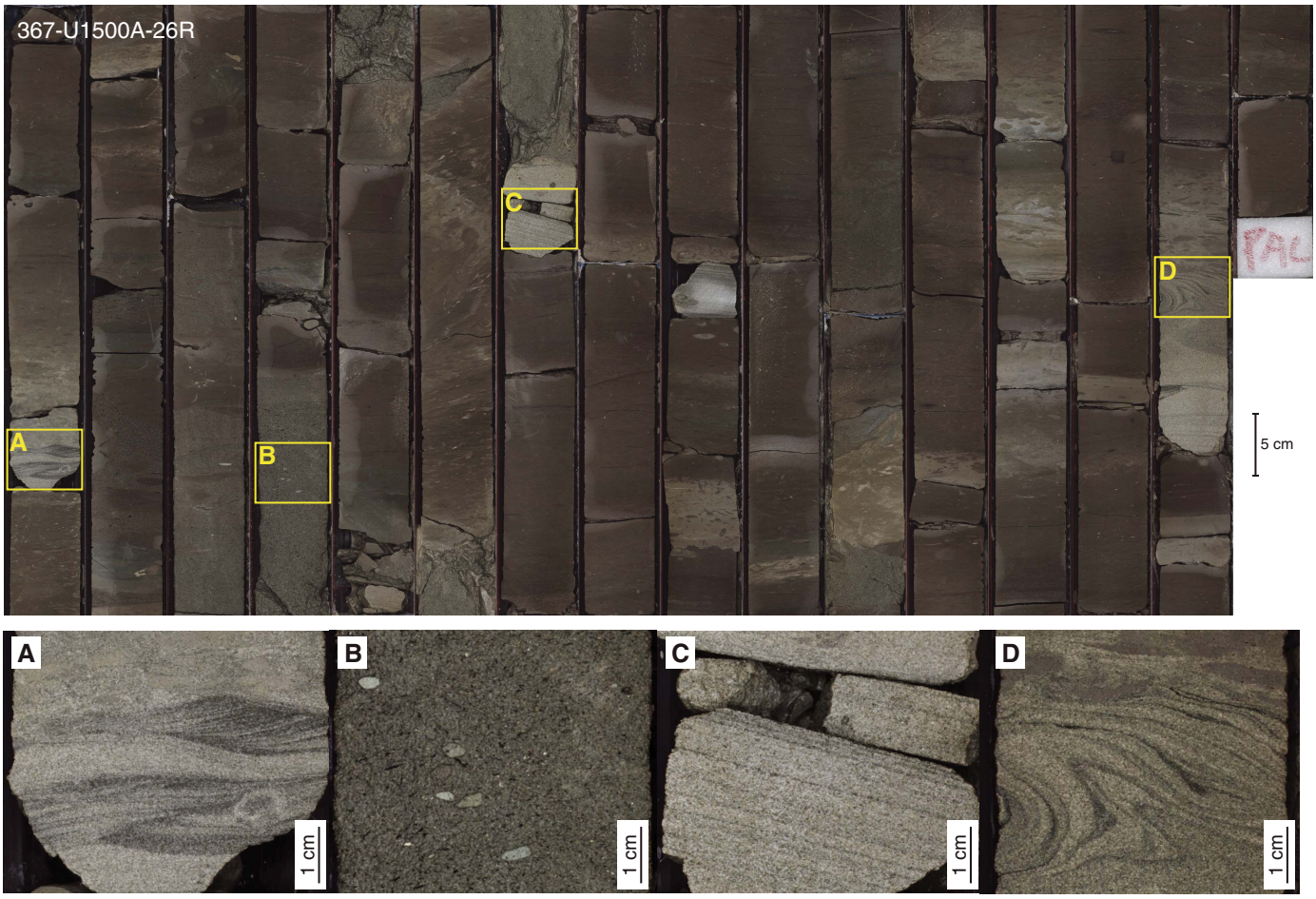

mostly gradational, with few planar and irregular contacts. There are two 3–4 cm thick intervals of greenish gray clayey sandstone within Core 47R, one of which contains mud clasts. Bioturbation throughout these cores is mostly heavy. Similar to Subunit VA, diagenetic greenish gray intervals were observed within the core in the form of halos around foraminifer tests and surrounding fractures. We analyzed smear slides from three intervals within the subunit. All three have abundant to dominant calcareous nannofossils, making two of the samples chalk and one a nannofossil-rich claystone (Figure **F19**). This analysis correlates well with the macroscopic description.

Subunit VB is constrained by a significant change in carbonate concentration from <1 wt% in Section 45R-1 of Subunit VA to 17 wt% in Section 46R-1 of Subunit VB. Carbonate contents ranged from 15 to 40 wt% in Subunit VB, which is higher than in Subunit VA. The dominant mineralogical components for most of Subunit VB are quartz (29%–42%), kaolinite + chlorite (24%–29%), and calcite (10%–27%) (Figure **F13**). This subunit has the largest percentage of calcite observed at Site U1500; other samples outside of this subunit that were measured for XRD contain 0%–16% calcite.

Magnetic susceptibility decreases with depth to Section 47R-1, where there is a small increase to ~55 × 10^{-5} SI (Figure **F12**). Magnetic susceptibility data also show a large peak in Section 48R-3, with a maximum of 131 × 10^{-5} SI compared to a subunit average of 29 × 10^{-5} SI. L* reflectance shows a small range of values; however, it does increase slightly downhole (Figure **F12**).

Unit VI

Interval: 367-U1500B-50R-1, 8 cm, to 56R-1, 123 cm
Depth: 1310.98–1370.33 m
Age: Oligocene

Unit VI contains dark greenish gray silty claystone with biogenic carbonate and dark gray sandstone (Figure **F20**). Recovery rate varies significantly from sandstone-dominated (e.g., Core 54R; 5% recovery) to claystone-dominated (e.g., Core 51R; 92% recovery) cores. Bioturbation is heavy within the claystone intervals, whereas sandstone intervals show almost no bioturbation.

Magnetic susceptibility drops significantly from Unit V to <10 × 10^{-5} SI in the upper part of Unit VI (Figure **F12**). Color reflectance a* decreases significantly from Subunit VB, and b* shifts to ~0, which corresponds to the color change from dark brownish gray to dark greenish gray. The changes in magnetic susceptibility and color reflectance data are consistent with a decrease of magnetic minerals from Unit V to VI. Generally, magnetic susceptibility migrates to higher values within Unit VI, shifting to an average value of 25 × 10^{-5} SI in Core 56R.

Figure F17. Patterns of color banding and sedimentary structures, Unit IV. A. Coarser grained sediment organized into parallel laminations with heavy bioturbation at the base of the fragmented interval. B. Small fining-upward sequence that transitions from light-colored sand to heavily bioturbated clay. C. Heavily bioturbated clay transitioning to clay-rich parallel laminations that are overlain by cross-stratified sandstone that fines upward into clay-rich wavy lamination.

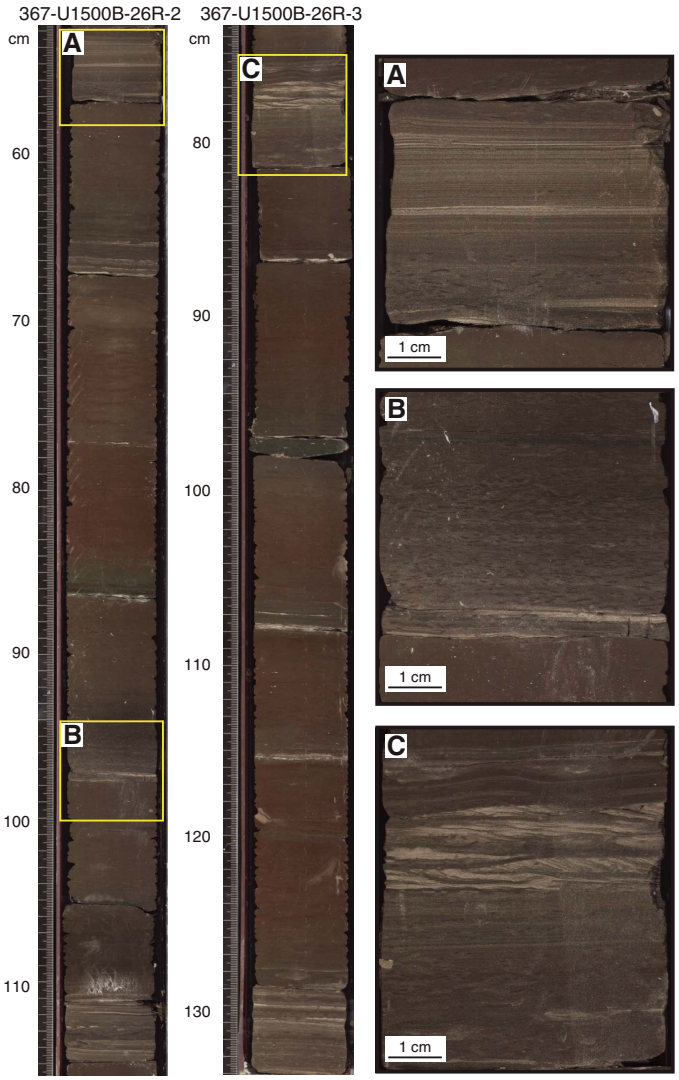

Figure F18. Sandstone intervals in Unit IV with feldspar (Fld), foraminifer shells (Foram), quartz (Qtz), glauconite (Glc), and carbonate cement, Hole U1500B. A. 23R-1, 69–71 cm. B. 24R-1, 16–18 cm. The sediment within the possible bryozoan microfossil is altering to glauconite. C, D. 33R-CC, 0–3 cm. Sample in C contains chert lithic grains, quartz, feldspar, carbonate cement, and mica (another common mineral in these sandstones). Sample in D contains a foraminifer shell filled with glauconite, quartz and feldspar grains, and carbonate cement.

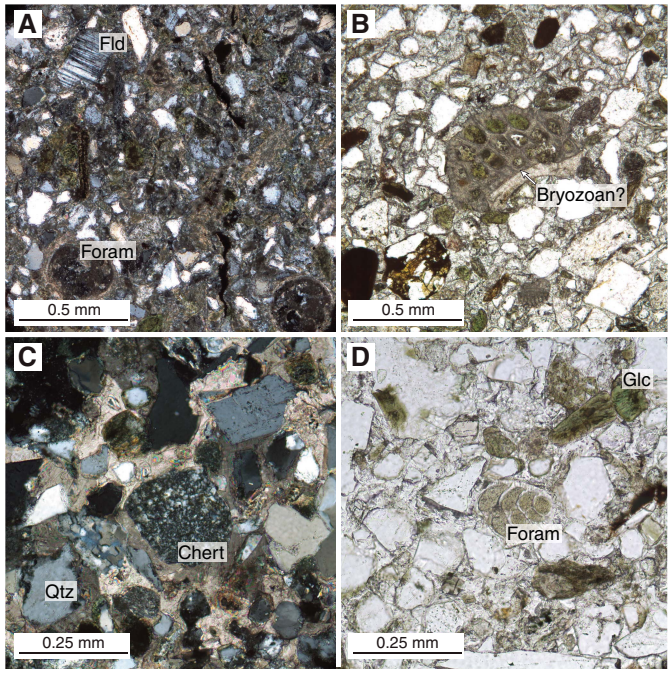

Calcium carbonate contents in the upper part of Unit VI (in and above Sample 53R-3, 18–19 cm) are ~20 wt%, dropping significantly in a claystone interval downcore (3 wt% in Sample 55R-2, 13–14 cm) and increasing again in a deeper sandstone interval (32 wt% in Sample 56R-1, 46–47 cm). The trend is corroborated by XRD data (Figure **F13**). The most significant mineralogical changes are the increase of montmorillonite (from 0% in Subunit VB to >20% in the claystone intervals of Unit VI) and the decrease of kaolinite + chlorite (from >20% in Subunit VB to mostly <10% in Unit VI).

Unit VII

Interval: 367-U1500B-56R-1, 123 cm, to 57R-1, 30 cm
Depth: 1370.33–1379.10 m
Age: Oligocene

Unit VII comprises a short (30 cm thick) dusky red claystone interval (Figure **F20**). Because the recovery of the sandstone layer above this unit is low (13%), the upper boundary of Unit VII is uncertain. However, the dusky red claystone was observed in the core catcher of Core 56R, indicating a change in lithology unrelated to fall-in. The lower boundary of Unit VII is in horizontal contact with igneous rocks (Unit VIII). The lowermost 2 cm of this unit has a greenish gray color. Bioturbation is slight throughout the unit.

The average magnetic susceptibility of Unit VII is similar to the lowermost section (Core 56R) of Unit VI (Figure **F12**). Carbonate contents were not measured within Unit VII due to the limited material. One XRD sample from this unit shows that the montmorillonite content is 43%, even higher than in Unit VI, and the calcite content is almost zero (Figure **F13**).

Unit VIII

Interval: 367-U1500B-57R-1, 30 cm, to 83R-3, 150 cm
Depth: 1379.10–1529.0 m
Age: Oligocene

Unit VIII comprises basalt (see **Igneous and metamorphic petrology** for description of principal composition); however, some fractures within the basalt are filled with very well lithified claystone. Based on smear slide analysis, the claystone contains authigenic carbonate, siliciclastic components, and rare nannofossils (Figure **F21**). The basalt intervals contain rare dusky red claystone

Figure F19. Transitions between subunits, Unit V. A. Silty clay with clay minerals, rare calcite, and no nannofossils. B. Foraminifer-rich sandstone with foraminifer fragments, quartz, feldspar, chlorite, and glauconite. C. Nannofossil-rich claystone with abundant discoasters, clay minerals, and unknown opaque material. D. Nannofossil-rich claystone with abundant nannofossils, clay minerals, and Fe oxides. E. Clay-rich chalk with clay-sized carbonate material, clay minerals, and Fe oxides.

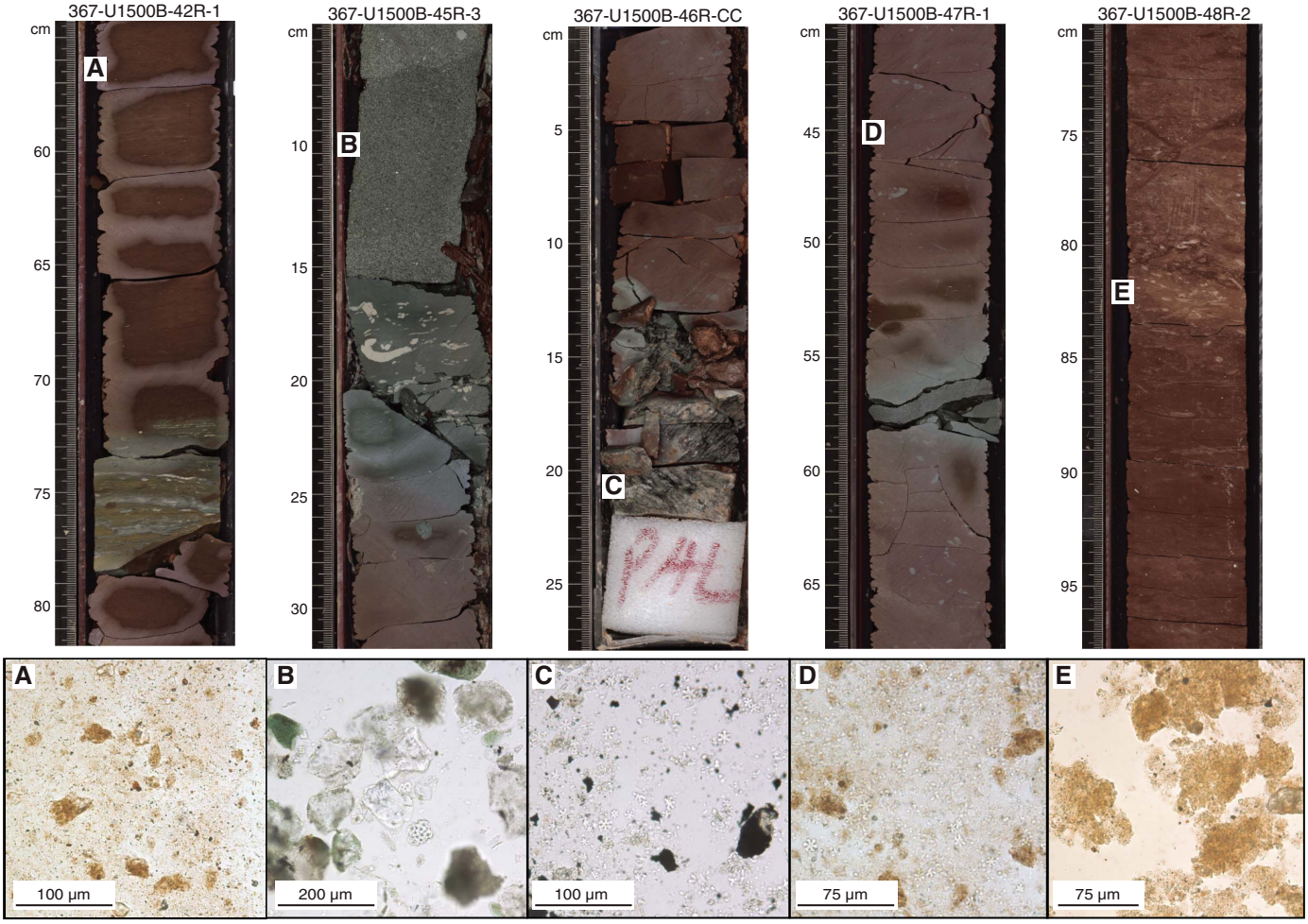

inclusions where the basalt is typically bound with chilled, glassy margins (Figure **F24**). Section 71R-1 contains 31 cm of gray to reddish brown claystone, silty claystone, and calcareous-rich sandy claystone. Parts of the sedimentary intervals have undergone extensive dolomitization, possibly by the recrystallization of calcium carbonate microfossil fragments (e.g., foraminifer tests). Additionally, Section 71R-3 contains 15 cm of calcareous-rich sandy claystone with a 1.8 cm long angular clast of altered basalt.

Discussion

Sandstone deposition

Sandstone intervals are common in almost all of the lithostratigraphic units cored at Site U1500. However, they are most prevalent in Units III and IV. In addition to the recovered sedimentary intervals, most of the unrecovered intervals are inferred to represent weakly consolidated sand because of fast drilling penetration rates and high amplitudes in the seismic reflection data. A similar interpretation was drawn at Site U1499. The amount of sandstone recovered from each core likely depends on the degree of lithification and the presence of interbedded clay.

The depositional setting of the sand intervals from Site U1500 is uncertain, but the sand intervals all share similar characteristics. The sand intervals are organized into both massive and stratified beds, which likely suggests that a variety of transport processes were responsible for sediment delivery to Site U1500. The stratified beds include a range of parallel, cross, and convolute laminations, together with fining-upward sequences (Figures **F16**, **F17**), which implies that deposition occurred through suspension-load transport, potentially by turbidity currents (e.g., Pickering et al., 1989). The massive beds at Site U1500 typically contain pebble-sized mud clasts, which are particularly common in Unit III. Unlike stratified beds, massive beds are most commonly deposited in sediment-laden gravity flows where intergranular friction is high (e.g., Pickering et al., 1989). Massive beds can form in high-concentration turbidity currents or in sand–clay debris flows (e.g., Lowe, 1982; Stow and Shanmugam, 1980).

Grain size in the sand intervals ranges from fine- to coarse-grained sand, with the maximum grain size rarely exceeding 1 mm (Figure **F18**). The grains have subangular and subrounded shapes and are either surrounded by a clay matrix or cemented with calcium carbonate. The size and shape of the grains implies that the sand was not transported over long distances or significantly reworked by bottom currents. The composition of the sand grains

Figure F20. Contacts between Units VI, VII, and VIII, Hole U1500B. A. Nannofossil-rich claystone with abundant nannofossils, quartz, feldspar, organic material, and clay minerals (55R-3). B. Sandstone with quartz, glauconite, feldspar, foraminifer fragments, and calcite cement (56R-1). C. Claystone with abundant clay minerals, lithic grains, and Fe oxides but no nannofossils (57R-1). D. Abrupt contact between claystone in Unit VII and basalt in Unit VIII. E. Clay-filled fracture within basalt of Unit VIII.

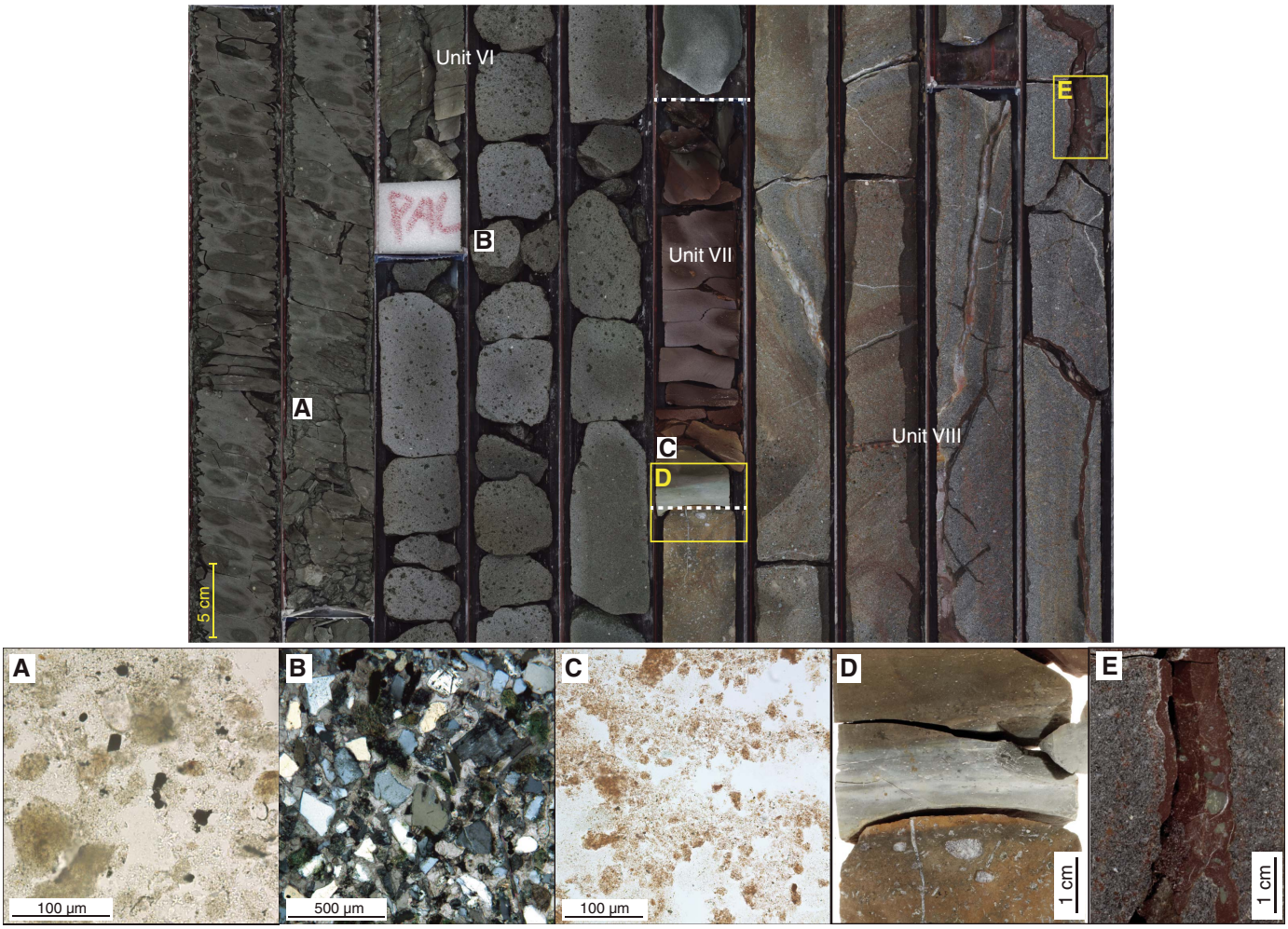

from each lithostratigraphic unit is similar. The siliciclastic component includes quartz, plagioclase, K-feldspar, mica, chert, and other sedimentary rock fragments. Fragmented bioclasts of benthic and planktonic foraminifers (see **Biostratigraphy**) also make up significant proportions of the sand, and in some cases their proportions exceed 50% of all grains found within a single interval (e.g., foraminiferal sandstone intervals from Unit III) (Figure **F16**).

Petrographic observations from thin sections and smear slides corroborate the results from XRD analysis (Figure **F13**). The combination of K-feldspar, quartz, plagioclase, and mica indicates a plutonic source of felsic composition (e.g., granite). Abundant Jurassic and Cretaceous granitic rocks are exposed along the margin of southern China (e.g., Zhou and Li, 2000). Additionally, the majority of these sediments were deposited prior to the uplift of Taiwan, eliminating that as a potential source region. It is therefore likely that the large rivers of southern China, namely the Pearl River and its analogous rivers, delivered sediments from the plutonic rocks of the southern margin of China to the SCS.

Diagenesis

Sediments recovered from Site U1500 are mainly composed of quartz, carbonate minerals (including calcite, dolomite, ankerite, and siderite), clay minerals (including illite-muscovite, kaolinite, and chlorite), plagioclase, and K-feldspar. Minor minerals include montmorillonite-beidellite and pyrite (Table **T2**; Figure **F13**). The variation of mineral compositions with depth is well correlated to the lithology. For example, most of the samples collected from chalk and nannofossil-rich claystone intervals are accompanied by higher calcite abundance. On the contrary, the sandstone samples usually contain less clay minerals and more K-feldspar. Besides the trend between lithology and mineral composition of sediments, some subtle changes between different species of carbonate minerals and secondary minerals reveal that the sediments have undergone different diagenetic processes.

Comparing analytical results between carbonate species (measured by XRD analysis) and total calcium carbonate concentration, the XRD data are systematically lower than the measured total calcium carbonate. In some cases, samples with lower calcium carbonate abundances (measured by geochemical analysis) show elevated values of other carbonate species such as dolomite, siderite, and ankerite (measured by XRD analysis), which all have possible diagenetic origin. In carbonates at surface temperatures, dominant cations (Ca^{2+}) are strongly hydrated, preventing Mg^{2+} and Fe^{2+} cations in interstitial water of marine sediments from entering the

Figure F21. Claystone-filled fracture/vein within basalt. Star = location of smear slide images in A and B. A. Discoaster nannofossil and other siliciclastic components (PPL). B. Authigenic calcite and rare calcareous nannofossils (XPL).

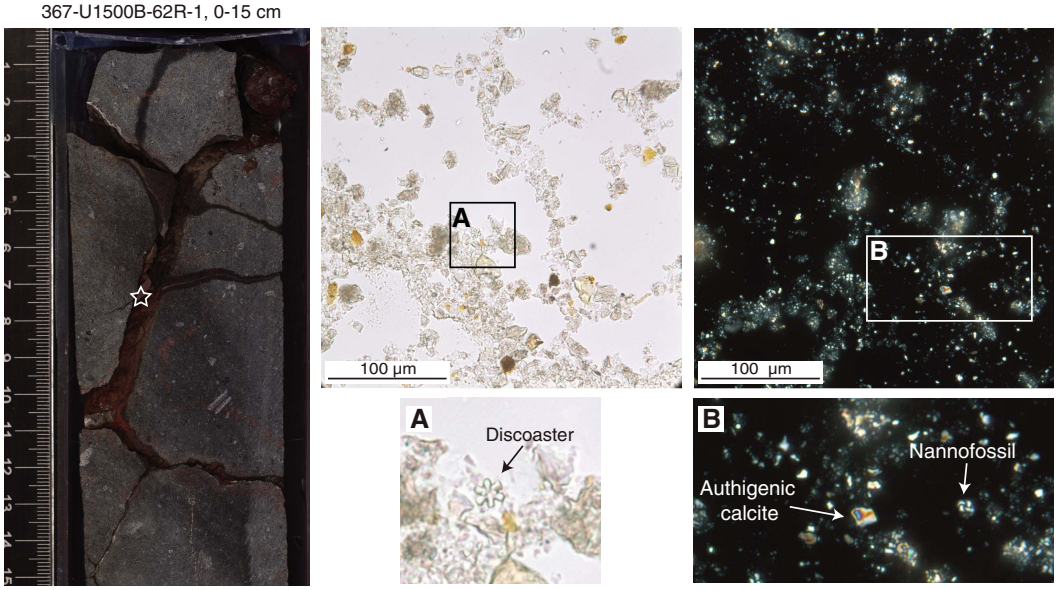

Table T2. Mineral percentages, Site U1500. **View table in PDF format. Download table in CSV format.**

mineral lattice. Ca ions will be less hydrated with increasing temperature (60°–100°C), allowing Mg and Fe to replace Ca in the lattice. When this occurs, dolomite, ankerite, or siderite may form (Bjørlykke, 1983; Larsen and Chilingar, 1979). In addition to thermal regulation, mechanical compaction may also influence the solubility of minerals and precipitation in open pores (De Boer, 1977; De Boer et al., 1977; Hendry et al., 2000; Weyl, 1959). Although we did not use the advanced piston corer temperature tool (APCT-3) for geothermal gradient measurements at Site U1500, the general heat flow of the area (see Figure **F57** in the Site U1499 chapter [Sun et al., 2018b]) and the thermal gradient at Site U1499 (93°C/km; Figure **F56** in the Site U1499 chapter [Sun et al., 2018b]) suggest conditions favorable to the formation of ankerite and siderite. At Site U1500, we also identified Mg-calcite as cement in multiple sandstone intervals from Sections 367-U1500B-24R-1, 25R-CC, 33R-1, 40R-1, and 56R-1 (Figure **F13**). This cementation process may be linked to the high *P*-wave velocities observed in Sections 24R-1 and 25R-CC (4468 and 4550 m/s, respectively).

In Unit V, which is composed of dark reddish brown claystone and clay-rich chalk, some greenish gray intervals were observed. One sample taken from the greenish gray interval (Sample 42R-5, 67–68 cm) for XRD analysis contains >80% montmorillonite-beidellite (Figure **F13**), which is of diagenetic origin (Larsen and Chilingar, 1979; Sato et al., 1996). The existence of beidellite also implies the sample may have undergone hydrothermal alteration (Guisseau et al., 2007).

Pyrite was identified by XRD in Sections 28R-1, 50R-2, 51R-5, 52R-2, 53R-3, and 55R-2. Especially for samples from Sections 50R-2 through 55R-2, pyritization of foraminifers, radiolarians, diatoms, and sea urchin spines were observed in addition to authigenic pyrite grains (Figure **F13**). However, because these pyritized biogenic grains occurred alongside pristine biogenic material, it is possible they were pyritized elsewhere before being transported to this site.

In summary, the variation of mineral composition in Site U1500 can be divided into three zones. In the first zone, encompassing lithostratigraphic Units I and II, little evidence of diagenetic activity was observed, and the carbonates are dominated by calcite. In the second zone, which includes lithostratigraphic Units III and IV, most of the carbonate in sediments with low fossil abundance is composed of dolomite, ankerite, and siderite. In calcareous-rich clay and chalk intervals, the dominant carbonate species is calcite. In sandstone intervals, the cementation by Mg-calcite increases the lithification of Sections 367-U1500B-24R-1 and 25R-CC and leads to high *P*-wave velocity. We interpreted the no recovery zones in Units III and IV to contain nonlithified sands. These intervals could provide a pathway for basin-scale transport of fluid or hydrothermal flow, which could drive diagenesis in adjacent lithologies. The third zone includes lithostratigraphic Units V–VII. Close to the contact with underlying basalt, the most characteristic features include the appearance of montmorillonite-beidellite in greenish gray silty sandstone and the pyritization of foraminifers, radiolarians, diatoms, and sea urchin spines in Sections 50R-2 through 55R-2. Both diagenetic minerals suggest potential hydrothermal alteration related to the emplacement or alteration of basalt below the sediments.

Trace fossils

Recovered sediments and sedimentary rocks at Site U1500 are heavily bioturbated, especially in intervals of both dark greenish gray and brownish gray claystone and dark reddish brown clay-rich chalk. Trace fossils preserved in deep-sea sediments represent the burrows that are imposed on sediment beneath the mixed surface layer, which spans the uppermost 5–7 cm of the seafloor (Ekdale et al., 1984). The occurrence of trace fossil assemblages or even a single ichnogenus in deep-sea sediments can provide information about the depositional environment. They have been increasingly used as paleoceanographic tools to infer the sedimentary and ecological setting (e.g., Knaust and Bromley, 2012; Dorador et al., 2016).

Investigations of modern seafloor sediments of the SCS reveal that postdepositional trace fossils are extensively distributed in

Figure F22. Trace fossils in claystone and chalk intervals. A. Gray chalk interval within dark gray-brown claystone with *Scolicia* and *Nereites* trace fossils (367-U1500B-5R-2, 98–106 cm). B. Greenish gray claystone with biogenic carbonate with *Chondrites* trace fossils (367-U1500A-26R-4, 66–72 cm). C. Dusky red claystone with *Planolites* trace fossils (367-U1500B-45R-3, 90–102 cm). D. Dark reddish gray calcareous-rich claystone with *Zoophycos* trace fossils (46R-2, 55–64 cm).

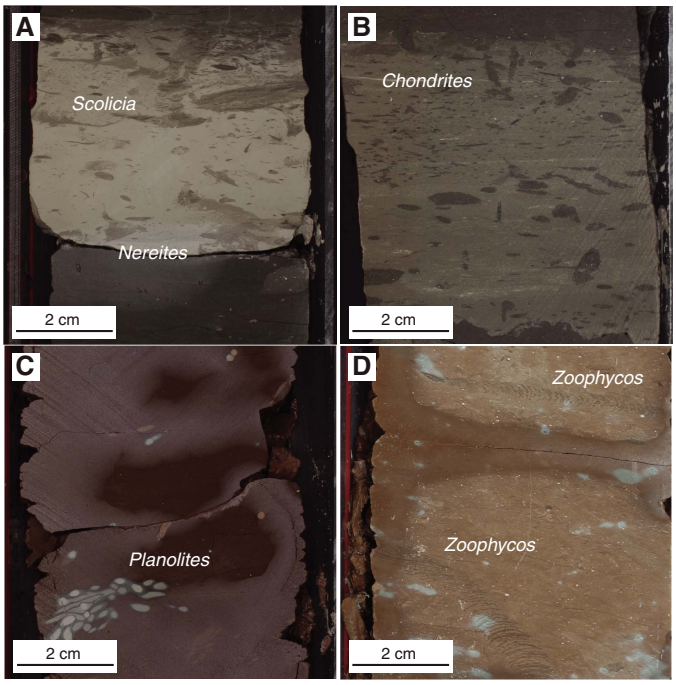

brown, oxidized, soft to soupy, and uniformly fine grained deep-sea sediments (Wetzel, 2002; 2009). These trace fossils were also observed in the long sedimentary sequences dating back to the middle Miocene in the central SCS during IODP Expedition 349 (Li et al., 2015b). Similarly, trace fossils identified in our cores are typical of very deep water sedimentary environments in distal clastic settings. They mainly include *Nereites, Planolites, Thalassinoides, Scolicia, Chondrites,* and *Zoophycos* (Figure **F22**). Modern observation shows that *Nereites* exclusively occurs above the redox boundary, with water depths mostly exceeding 4000 m (Wetzel, 2002). Although relatively less frequent at Site U1500, *Nereites* was observed at the base of Unit III (Core 367-U1500B-5R), which could reflect the limit of oxygenation depth during the deposition period. *Zoophycos* occurs in environments experiencing high but seasonal organic matter deposition on the seafloor. In Cenozoic hemipelagic sediments, the presence of *Zoophycos* is used to interpret deep-sea environmental conditions related to energy variation, sedimentation rate change, and food availability (e.g., Löwemark, 2015). A study from Site U1385 on the West Iberian margin shows that *Zoophycos* is most common in sediments deposited during glacial times, when the sedimentation rate was intermediate and primary production was high and seasonal, suggesting a relationship with seasonal organic matter deposition (Dorador et al., 2016). *Zoophycos* was frequently observed in dark reddish gray calcareous-rich claystone in Subunit VB (Figure **F22D**).

Igneous and metamorphic petrology

In Hole U1500B, basalt was drilled from 1379.1 to 1529.0 m with a total recovered core length of 114.92 m. The aphanitic to porphyritic basalts are nonvesicular to moderately vesicular and glassy to hypocrystalline, with the latter ranging from cryptocrystalline to fine grained in grain size, making up an aphyric to highly (olivine-) plagioclase phyric texture (microstructure). The basalt comprises lithostratigraphic Unit VIII, which corresponds to igneous lithologic Unit 1. Unit 1 is further divided into two subunits (1a and 1b) to separate an upper sequence of massive flows (Subunit 1a) and a lower sequence dominated by pillow lava flows and occasionally interbedded massive, sheet, and lobate flows (Subunit 1b). Pillow lobes are well preserved with chilled and/or glassy margins, occasionally associated with claystone. Plagioclase phenocrysts are present throughout the basalts, with occasional olivine phenocrysts. Modal abundances of olivine and plagioclase phenocrysts increase downhole, reaching a peak between 1420 and 1470 m.

Veins found throughout the lava flows usually show a sharp contact with the host basalt. The veins are either polycrystalline or massive and predominantly filled with carbonates and Fe (hydr)oxides, as well as subordinate chlorites, zeolites, silica, and clay sediment. Very fine claystone aggregates are ubiquitous in several carbonate-rich veins, particularly in those hosted by pillow lava flows. Alteration of the basaltic flows is slight overall; however, the alteration intensity increases to a moderate level downhole.

Igneous lithologic Unit 1 (lithostratigraphic Unit VIII)

Interval: 367-U1500B-57R-1, 30 cm, to 83R-3, 67 cm
Depth: 1379.1–1529.0 m
Thickness: 149.9 m
Recovery: 76%
Lithology: basalt with minor hyaloclastite and claystone
Age: late Oligocene or older

The boundary between the pelagic sediment of Unit VII and the underlying basalt of Unit VIII was identified at 1379.1 m (Figure **F23**). Lithostratigraphic Unit VIII extends throughout the remainder of the hole to the bottom at 1529.0 m. The sediment/volcanic contact is sharp with a ~0.5 cm thick basaltic chilled margin and is overlain by claystone, gradually changing from greenish gray to dark reddish brown closer to the contact (Figure **F20**). Although this color change might suggest a baked contact, no other mineralogical or textural observations could be made to confirm this hypothesis. Throughout Unit VIII, the recovered basaltic rocks remain texturally and mineralogically similar, ranging from nonvesicular to moderately vesicular, cryptocrystalline to fine grained, and aphyric to highly (olivine-)plagioclase phyric with a hypocrystalline groundmass (Figure **F24**). The basaltic flows contain 2–5 cm thick hypohyaline to holohyaline chilled margins (Figures **F24C**, **F25**), with preserved fresh glass and occasional hyaloclastites with brecciated glass fragments mixed with clayey sediments. All basalts are grouped as lithostratigraphic Unit VIII (see **Lithostratigraphy**)/lithologic igneous Unit 1 due to the lack of significant change in mineralogy, texture, composition, or emplacement mechanism but are separated into two igneous lithologic subunits (1a and 1b) based on the change from massive (Subunit 1a; 27.28 m) to predominantly pillow lava flows (Subunit 1b; 122.62 m) (Figures **F23**, **F25**). Sparsely vesicular massive and sheet lava flows are texturally uniform and gradually increase in grain size toward the center of the flow. Pillow lobes are well preserved and separated by chilled, glassy margins (distinguishing upper from lower chilled margins of individual pillows where possible) and occasionally admixed claystone (Figures **F24**, **F26**). Core 71R contains two sequences of reddish gray to reddish calcareous claystone locally showing fining-upward

Figure F23. Lithostratigraphic summary of Unit VIII basalts showing lithology, lava flow types, and igneous Subunits 1a and 1b, Hole U1500B.

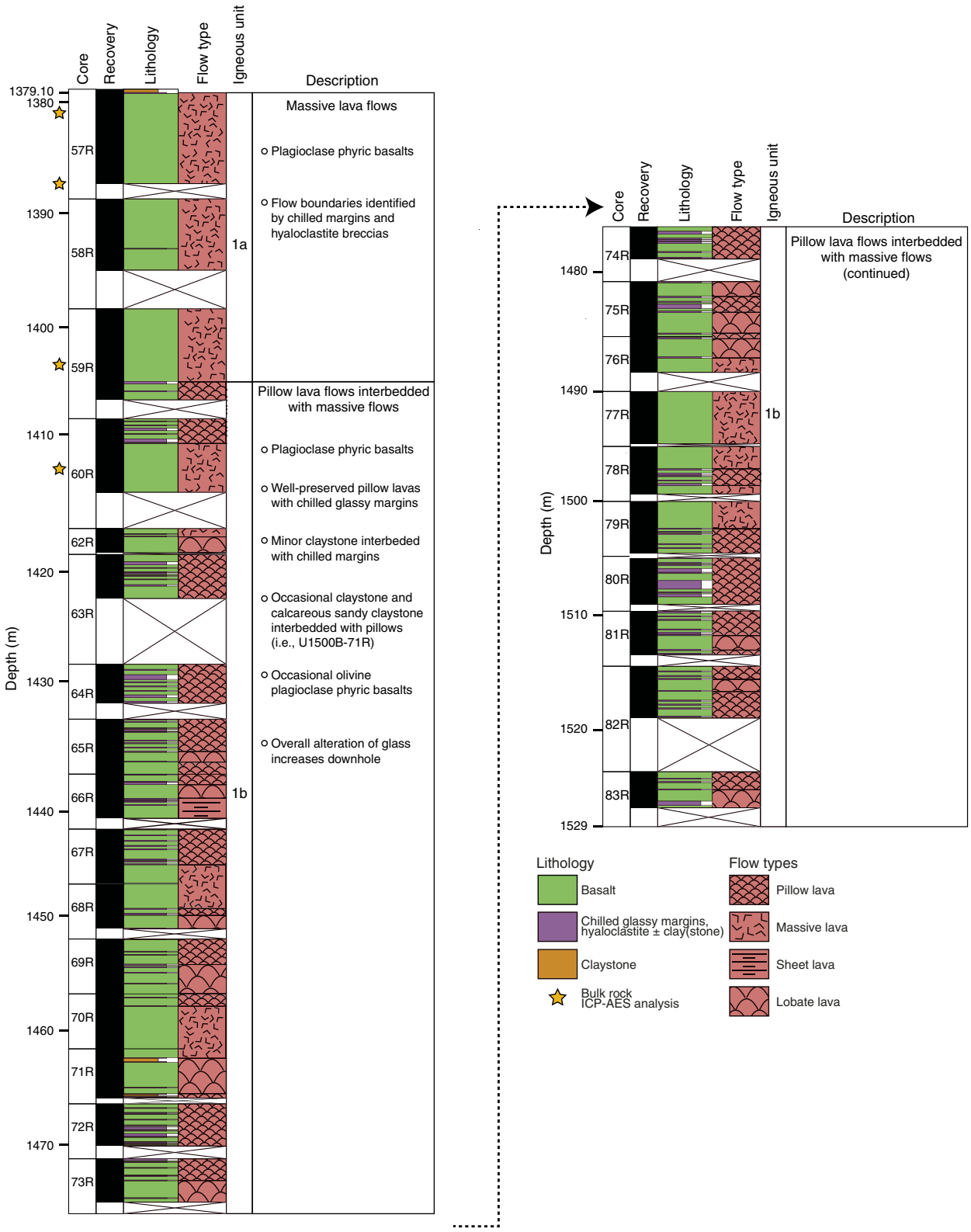

sequences in direct contact with chilled margins of basalt pillows (Figure **F24F**). Plagioclase phenocrysts are found throughout the basalts, with olivine being usually a sparse phenocryst mineral. The modal abundance of olivine phenocrysts increases downhole, reaching a peak of 5%–10% between 1420 and 1470 m. The plagioclase phenocryst abundance also increases downhole, reaching a peak at 1440–1460 m (20%–35%; referring to highly plagioclase phyric basalts).

Figure F24. Homogeneous sparsely vesicular and sparsely to moderately plagioclase phyric basalts spanning 27 m in Hole U1500B interspersed with minor chilled margins (from left to right: 57R-5, 0–50 cm, 58R-4, 0–50 cm, 59R-4, 60–110 cm, and 59R-7, 30–90 cm), grading downhole into moderately to highly plagioclase phyric basalts with a higher abundance of glassy chilled margins and baked sediments (pillow lava flows; from left to right: 60R-1, 60–110 cm, 60R-2, 0–50 cm, 69R-5, 1–50 cm, and 71R-1, 75–125 cm). A. Sparsely plagioclase phyric basalt with sparse vesicularity (57R-5, 33–38 cm). B. Haloed vein containing carbonates and Fe (hydr)oxides with 2 cm thick alteration halo (59R-4, 91–96 cm). Alteration of host basalt is predominantly focused on groundmass alteration of glass to low-temperature green-yellow alteration minerals (e.g., zeolites or chlorite) and localized replacement of plagioclase by carbonate. C. Upper rim of sample with a black glassy chilled margin grading into aphyric basalt (dark gray) and a joint perpendicular to the glassy margin (60R-1, 90–95 cm). D. Hyaloclastite with mixing of rounded to angular quenched basaltic glass shards with baked claystone (69R-5, 6–13 cm). E. Highly plagioclase phyric basalt with sparse vesicles (69R-5, 4–9 cm). F. Basaltic chilled margin with a sharp contact to a baked reddish calcareous sandy claystone (top of section to the left; 71R-1, 106–120 cm).

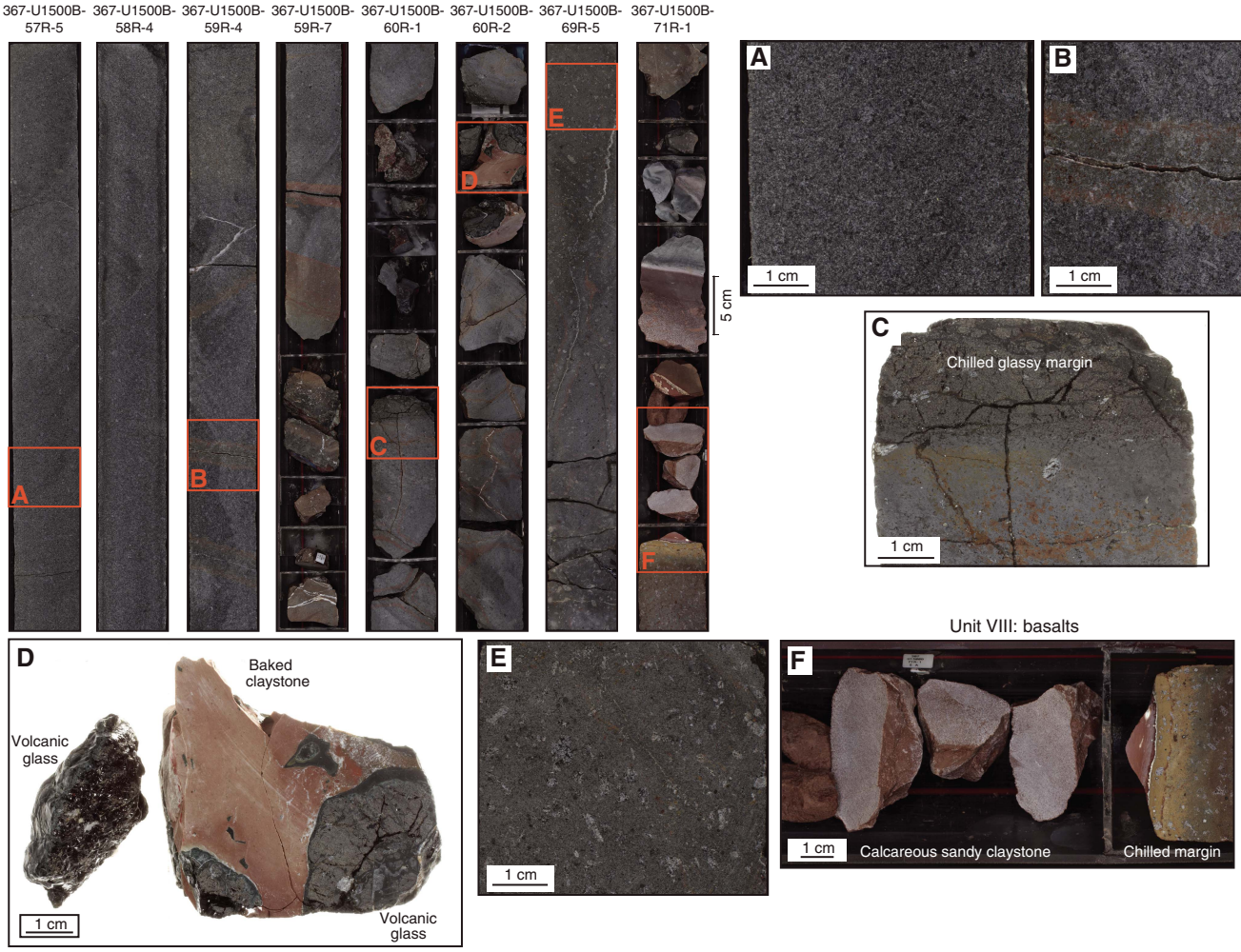

Petrographic description

At the microscopic scale, these hypohyaline to hypocrystalline, cryptocrystalline to fine-grained porphyritic basalts show a well-preserved primary igneous mineral assemblage (olivine, plagioclase, clinopyroxene, and Fe-Ti oxides) and microtextures (such as aphyric, [glomero]porphyritic, vitrophyric, dendritic, [sub]ophitic, and intersertal) (Figure F27). Stubby or elongated prismatic subhedral plagioclase is the dominant phenocryst mineral (1%–35%; 1–20 mm in size), showing well-defined oscillatory zoning and resorption textures (Figure F28). Plagioclase glomerocrysts are found throughout these flows. Olivine (≤10%; 0.5–2.5 mm in size) remains an occasional phenocryst mineral throughout Unit VIII and is either fresh (Figures F27, F28) or recognizable by olivine pseudomorphs composed of iddingsite, chlorite, and mesh textures of serpentine and fine-grained magnetite. Rare clinopyroxene phenocrysts were identified at the macroscopic scale.

The hypocrystalline groundmass is composed primarily of glass, plagioclase, clinopyroxene, and Fe-Ti oxide, as well as rare pyrite. Plagioclase mostly occurs as narrow, elongated prismatic crystals in subophitic to ophitic relationships with clinopyroxene and occasionally in swallow-tail textures containing inclusions of Fe-Ti oxide, clinopyroxene, and altered glass. Clinopyroxene mostly occurs as narrow, elongated prismatic crystals within poikilitic textures or occasional comb textures (Figure F28). Clinopyroxene is partially slightly altered to chlorite. Fresh glass is only preserved in chilled margins and is altered to chlorite in the groundmass. Glass and groundmass alteration does increase downhole.

Veins and alteration

Veins are found throughout lithostratigraphic Unit VIII and are predominantly filled with carbonates and Fe (hydr)oxides, chlorite, zeolites, and silica, giving them a white, red, or greenish color. Veins

Figure F25. Unit VIII basalts highlighting all observed chilled contacts and (glassy) margins (dashed yellow lines), Hole U1500B. (Continued on next two pages.)

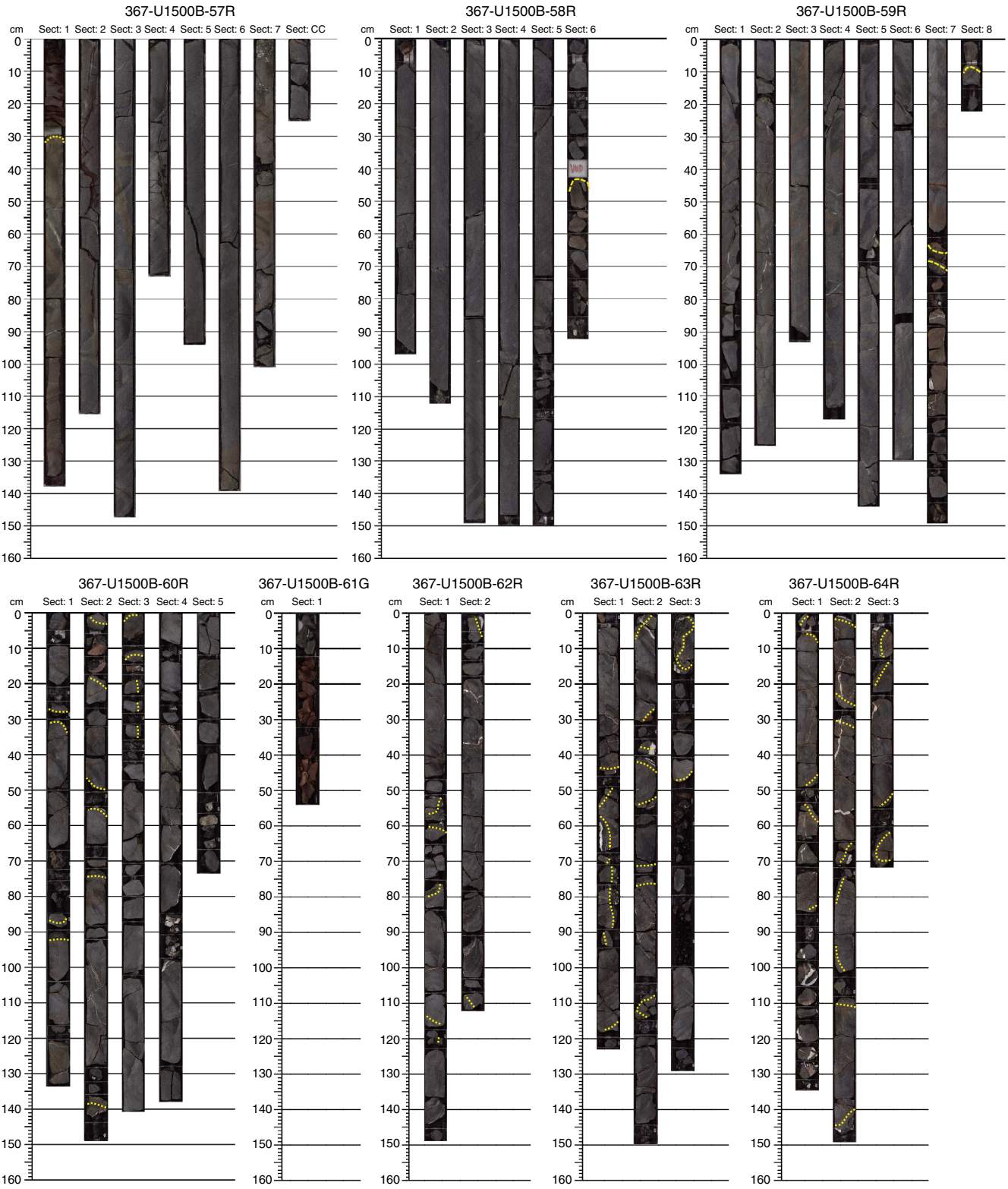

usually have a sharp contact with the host basalt and are either polycrystalline or massive. Clay-rich margins in veins, as well as clay aggregates, are ubiquitous in many carbonate-rich veins, particularly in pillow lava flows, being usually found as very fine aggregates within carbonate veins or as centimeter-thick claystone layers with no preserved textures or structures. Red to green-red halos related to the background alteration of interstitial glass, olivine, and occasionally plagioclase (Figure **F24**) usually surround these veins. The halos consist of carbonates, Fe (hydr)oxides, zeolites, and chlorite. The remainder of the background alteration predominantly com-

Figure F25 (continued). (Continued on next page.)

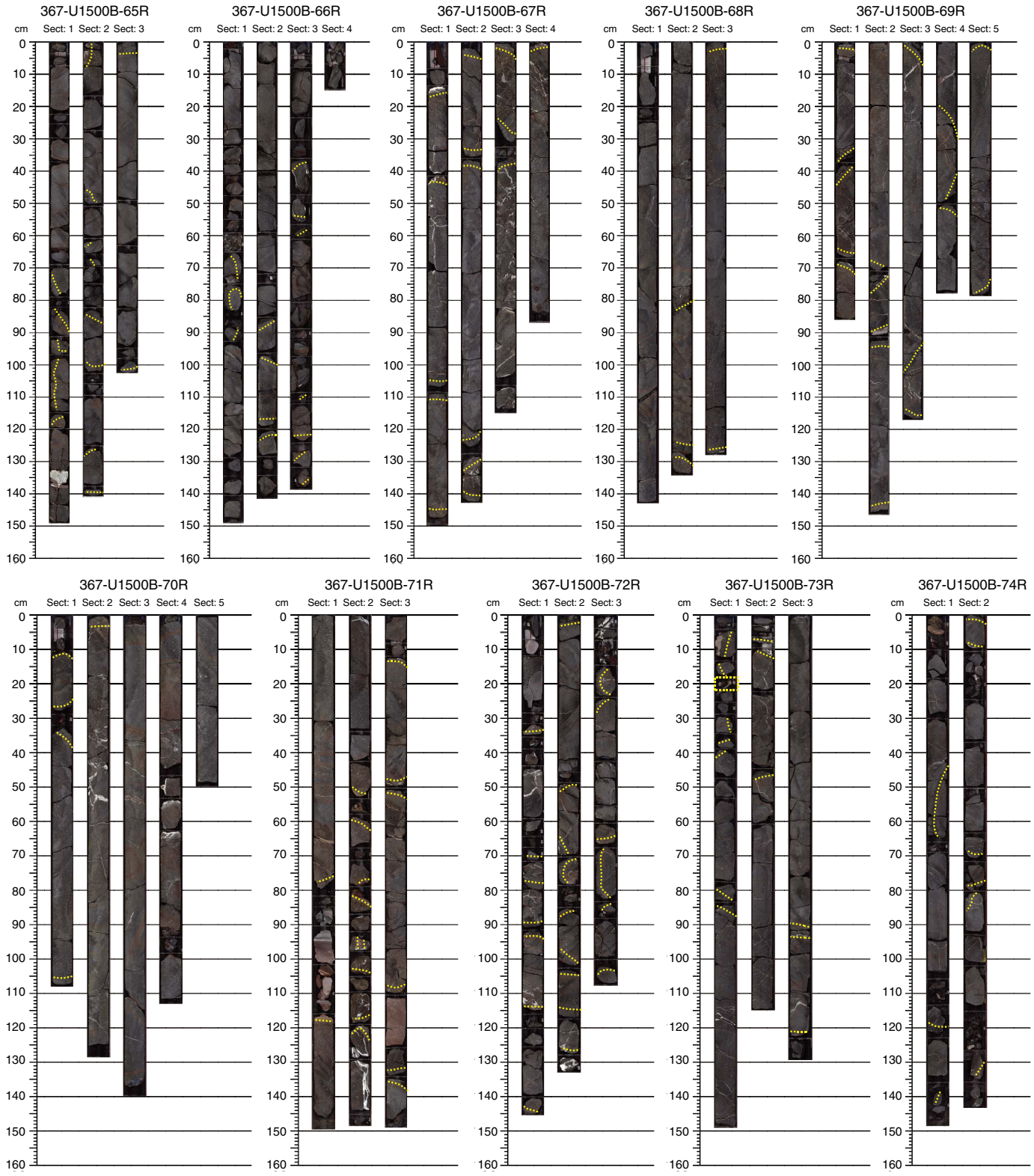

prises iddingsite, partially to fully replacing olivine phenocrysts. Background alteration varies from a fresh to moderate intensity throughout Unit VIII and is mostly related to vein halos. Occasionally, opal- or hydrated quartz–bearing veins are found in carbonate-rich veins, whereas sulfides are commonly absent and only rarely preserved. Vesicles in these flows are overall moderately to highly spherical and rounded and are usually filled with zeolites, chlorite, and carbonates. Alteration of Unit VIII basalts is slight overall, consistent with the alteration of interstitial glass and with the good preservation of plagioclase. Average alteration intensity increases

Figure F25 (continued).

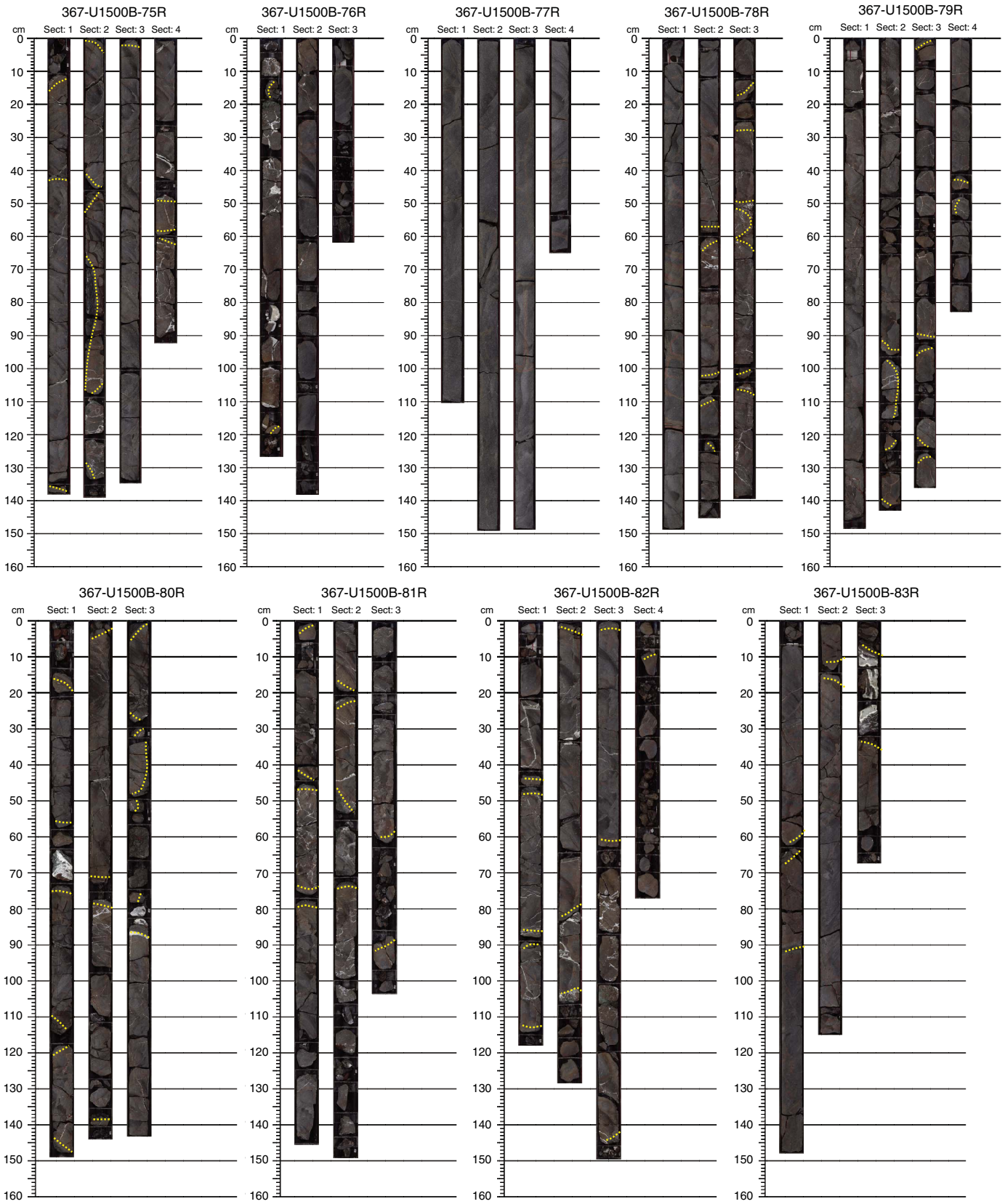

downhole (changing from slight to moderate), which is compatible with decreasing preservation of glass within the chilled margins and background color of Unit VIII grading from black (fresh glass) and very dark gray (fresh basalt) to greenish (altered glass) and reddish-grayish brown (moderately altered basalt), respectively.

Figure F26. Pillow basalts with glassy chilled rims and hypocrystalline interiors, Hole U1500B. Polycrystalline carbonate veins and Fe (hydr)oxide halos were observed within the pillow basalt. A. 69R-4, 19–50 cm. B. 66R-1A, 75–84 cm. C. 64R-3A, 61–71 cm.

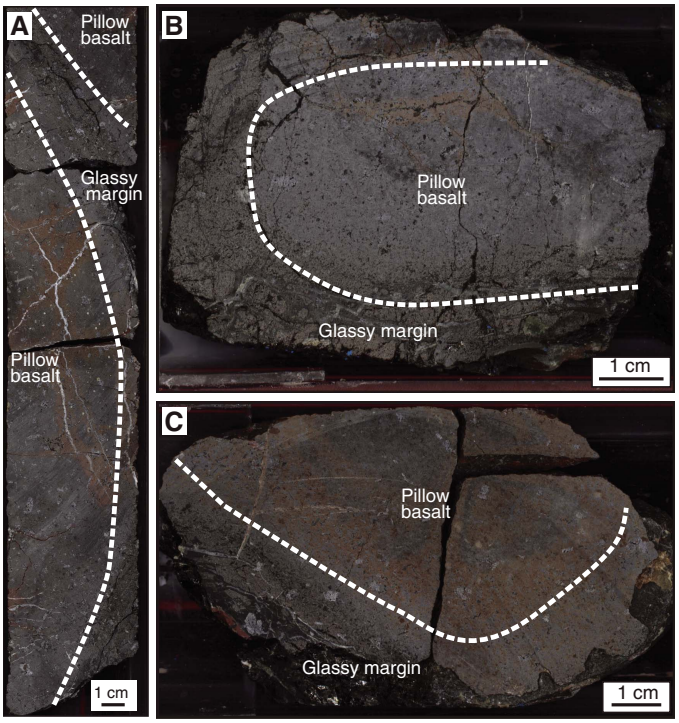

Chemical composition (pXRF and XRF core scanning)

Four samples from Subunit 1a and the uppermost core of Subunit 1b were analyzed for major elements and selected trace elements by ICP-AES, and these data are discussed in **Geochemistry**. During Expedition 368, additional compositional analyses were made on the 14 thin section billets of the Site U1500 basalts using the handheld portable X-ray fluorescence spectrometer (pXRF; see **Igneous and metamorphic petrology** in the Expedition 367/368 methods chapter [Sun et al., 2018a]). The results of these reconnaissance pXRF analyses are given in Table **T3**, and they were made to see if there were any significant compositional changes with depth (the ICP-AES analyses cover Cores 367-U1500B-57R to 60R, and the pXRF analyses cover Cores 57R to 74R). The pXRF analyses show limited compositional variability (TiO_2 = 1.5 ± 0.1 wt%; Zr = 97 ± 10 ppm; Sr = 161 ± 17 ppm), with concentrations similar to the ICP-AES analyses. Ratios of immobile incompatible elements, such as Ti and Zr, also show limited variability (Ti/Zr = 94 ± 8), which suggests that there were no significant changes in parental magma composition at Site U1500.

A high-resolution XRF core scanning data set for the Site U1500 volcanic rock section was produced onshore (see **Igneous and metamorphic petrology** in the Expedition 367/368 methods chapter [Sun et al., 2018a]) and can be retrieved as shipboard data from the LORE database (**http://web.iodp.tamu.edu/LORE**). At the time of this publication, assessment and discussion of this data set have not been concluded yet.

Interpretation

Because of the lack of well-defined age constraints from the immediately overlying sediments (lithostratigraphic Unit VII) and

Figure F27. Representative textures observed in hypocrystalline basalts, Hole U1500B (XPL). A. Fine-grained basalt with plagioclase (Plg) phenocrysts embedded in microcrystalline groundmass of plagioclase microphenocrysts, interstitial clinopyroxene, and altered interstitial glass (interstitial dark green) (68R-3, 56–60 cm). Note the presence of a filled round vesicle (Ves). B. Medium-grained basalt with plagioclase phenocrysts embedded in a groundmass of subophitic texture showing plagioclase laths intergrown with clinopyroxene (Cpx) (59R-5, 112–114 cm). Note the presence of altered interstitial glass (Gl). C. Holohyaline to hypohyaline chilled margin with preserved basaltic glass (brown in PPL) and plagioclase phenocrysts increasingly nucleating away from the holohyaline rim (74R-1, 117–121 cm). Chilled margin is crosscut by calcite-bearing veins (Cc).

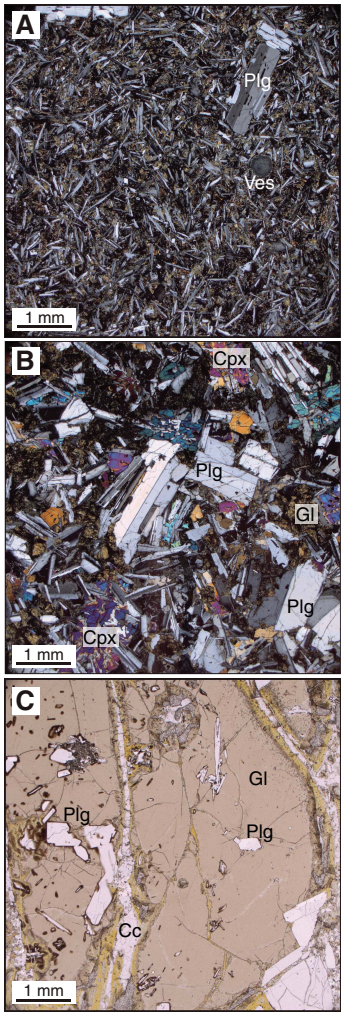

interbedded calcareous claystone within the pillow lava flows, the age of Unit VIII can only be estimated as being Oligocene or older, based on the late Oligocene age of lithostratigraphic Unit VI. The presence of pillow structures, quenched mineral textures, hyaloclastites, and chilled margins mixed or associated with claystone containing deep-water agglutinated foraminifers (see **Biostratigraphy**) indicates subaqueous eruptions. The presence of zoned plagioclase phenocrysts and subordinate olivine phenocrysts suggests that these basalts had already fractionated at depth and are thus not "primitive," which is consistent with a moderately low Mg# (see **Geochemistry**). Moreover, the lack of significant clinopyroxene phenocrysts, up to 35% plagioclase, and a crystallization sequence of olivine → plagioclase → clinopyroxene + Fe-Ti oxides indicates shallow-level crystallization of relatively dry melts, which is consis-

Figure F28. Representative primary rock-forming minerals and textures of basalts, Hole U1500B (XPL). A. Subhedral to euhedral plagioclase phenocrysts (Plg) found throughout Unit VIII basalts show resorption textures, inherited cores, and oscillatory zoning (59R-1, 67–70 cm). B. Olivine phenocryst (Ol) (59R-5, 112–114 cm). C. Subophitic texture showing poikilitic clinopyroxene (Cpx) enclosing laths of plagioclase (59R-5, 112–114 cm). D. Quenched texture showing plagioclase phenocrysts within radially oriented, dendritic intergrowths of plagioclase and clinopyroxene (59R-1, 67–70 cm). E. Intersertal texture in groundmass showing swallow-tail plagioclase with radially oriented, dendritic clinopyroxene (60R-4, 135–138 cm). F. Intersertal texture of swallow-tail plagioclase and comb-texture clinopyroxene with altered interstitial glass (60R-4, 135–138 cm).

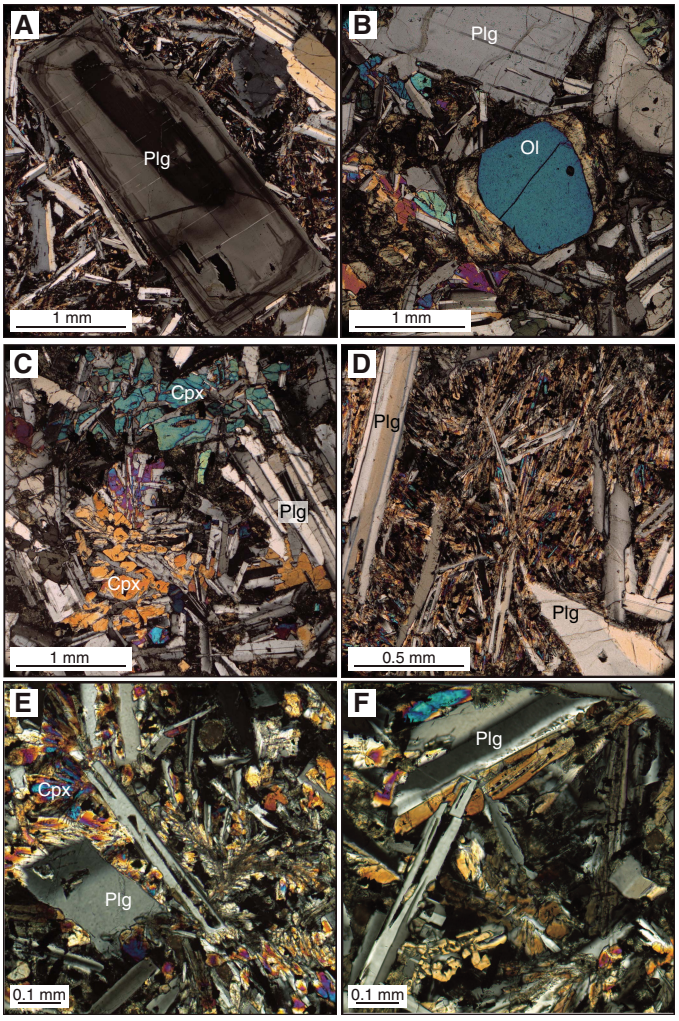

Table T3. Major element oxides and minor elements in rocks, Site U1500.
View table in PDF format. Download table in CSV format.

tent with a general tholeiitic trend and MORB-like affinity shown by initial shipboard chemical bulk rock analysis (Figures **F3**, **F44**).

Structural geology

Site U1500 is located on Ridge B at the northern COT of the SCS margin and ~39 km southeast of Site U1499. Coring at Site U1500 did not start until 378 m below the seafloor. Tilted bedding (Figure **F29**) and deformation structures were observed in all lithostratigraphic units. Several units present similar deformation structures and are described together.

Figure F29. Lithostratigraphic summary with bedding dips, Site U1500.

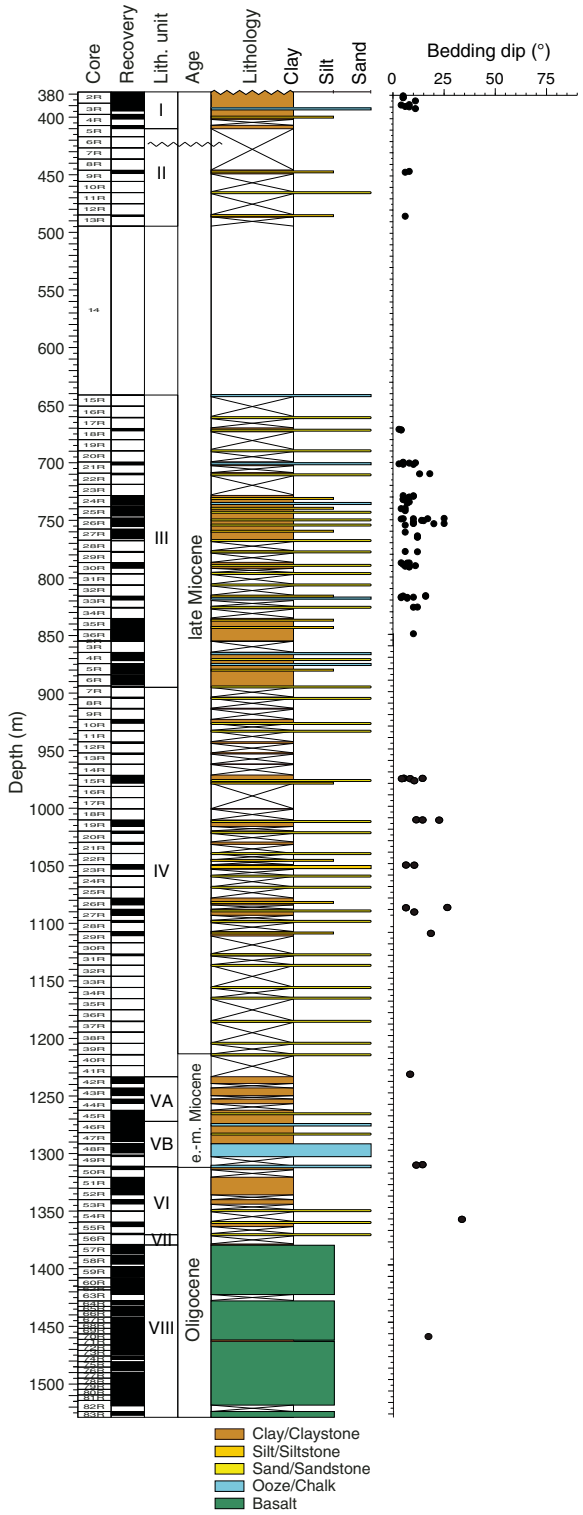

Units I–III

Units I–III are mainly composed of dark greenish to dark gray clay, sandstone, and claystone. Only six faults (five normal and one indeterminate) were measured in these units, four of them in the unlithified Unit I (Figure **F30**) and two in Unit III (Figure **F31**). The centimeter-scale faults have 0–2 cm offsets and 35°–62° dips. A series of millimeter-scale faults appear to crosscut thin sand layers

Figure F30. Sedimentary and deformation structures in Units I–III, Hole U1500A. A. Normal fault. B. Millimeter-scale faults and contorted beds. C. Synsedimentary folds. D. Oriented claystone clasts in sandstone with clay. E. Synsedimentary folds in sandstone. F. Subrounded mud clasts in sandstone.

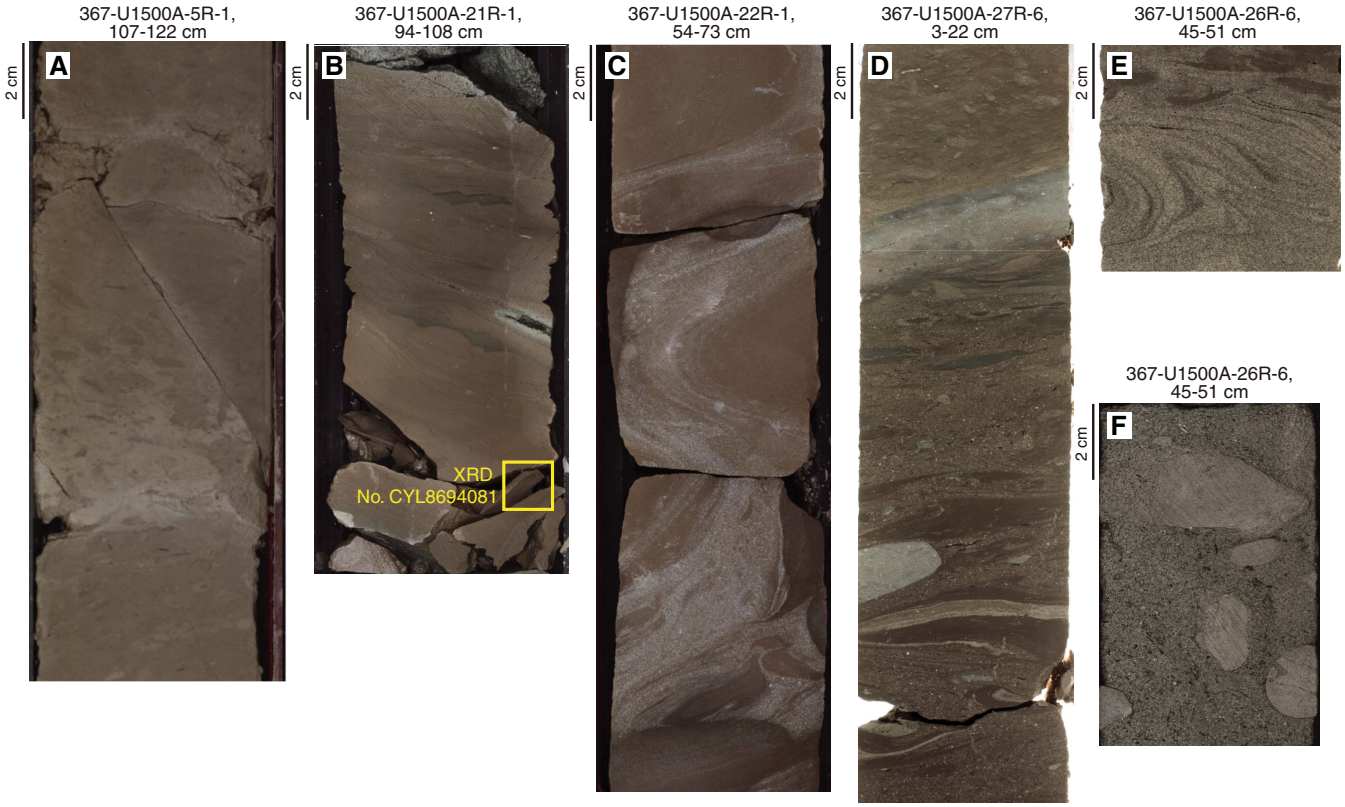

Figure F31. Sedimentary and deformation structures in Units IV–VII, Hole U1500B. A. Compaction fault in Unit IV with a slickenside. B. Synsedimentary fold. C. Pyrite vein. D. Slickenside of one fault in Unit VI.

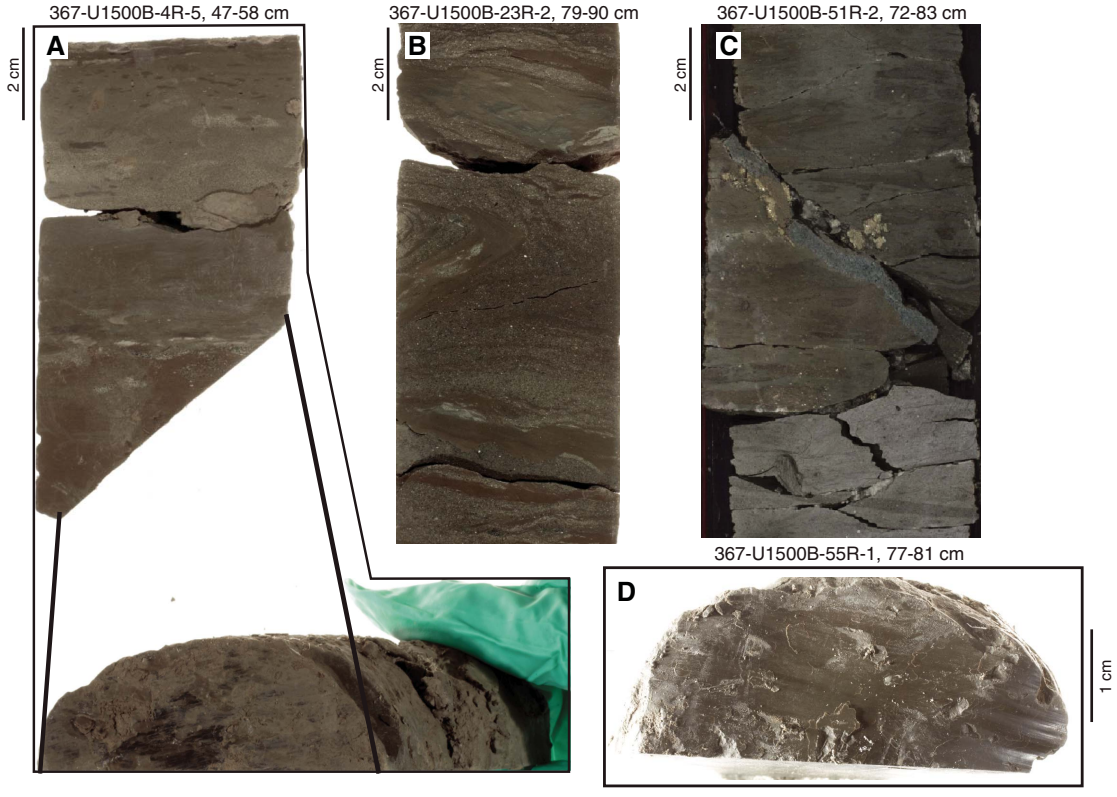

with an offset of less than 5 mm. In addition, the surrounding claystone contains contorted beds in interval 367-U1500A-21R-1, 94–108 cm (Figure **F30**). Four synsedimentary folds are identified in Units II and III. The variations of color and lithology highlight the fold morphologies. For instance, folds from Section 22R-1 occur with coarse sand within a grayish brown claystone. Tilted bedding in Units I–III has an average dip of 9° with a standard deviation of 5° (Figure **F29**). Tilted beds are more frequent in Cores 21R through 30R. Additionally, mud clasts occur in Sections 26R-1, 100 cm, to 33R-1, 87 cm. These clasts sometimes show preferred orientation (interval 27R-6, 8–15 cm) or subrounded shape (interval 33R-1, 79–86 cm; Figure **F30**).

Interpretation

Synsedimentary folds are formed in poorly consolidated sediments before lithification. The millimeter-scale faults, together with the contorted beds in Section 364-U1500A-21R-1, indicate synsedimentary deformation. Interestingly, the XRD sample (CYL8694081) located at the bottom of the deformed zone presents anomalously high contents of siderite. We interpret this deformation zone as a potential pathway for hydrothermal fluid. Mud clasts present throughout Unit III (Cores 15R through 33R) suggest erosion and transport of these clasts before their sedimentation within coarser material, likely caused by gravity-controlled deposition (e.g., debris flows, slumps, etc).

Unit IV

Unit IV has low recovery and is composed of dark greenish to dark gray sandstone with claystone and siltstone interbeds. Fourteen tilted beds in localized sandstone intervals were measured. The average bedding dip is 11°, and the standard deviation is 6°. A single centimeter-scale synsedimentary fold was recorded in an interval of sandstone with foraminifers (interval 367-U1500B-23R-2, 83–86; Figure **F31**). Six centimeter-scale faults with indeterminate motion were measured in the different lithologies of Unit IV. These faults are likely related to differential compaction.

Units V–VII

Units V–VII are composed of claystone with variations of color, carbonate contents, and frequency of sandstone intervals. Only four tilted beds were measured in these three units. In all cases, tilted bedding occurs within bioturbated claystone. The average bedding dip is 16°, and the standard deviation is 11° (Figure **F29**). Forty-seven centimeter-scale faults were measured in Units V–VII. Most of these faults (92%) are in Unit V, and >80% have well-defined slickensides (Figure **F31**). Only five faults are defined as normal faults; no clear shearing direction can be determined on the others. All of the faults occur in claystone intervals, which suggests the faulting is linked to differential compaction during clay lithification. Three single, uniform veins appear in silty claystone or claystone in Unit VI and are filled with pyrite (Figure **F31**).

Unit VIII

Unit VIII is composed of sparsely to highly plagioclase phyric basalts. Petrologists defined two subunits composed of sheet flow, massive flow, and pillow lava/lobate flow. A total of 819 measurements were taken on structures, including open fractures and veins (some fractures present mineral infill and were counted in both categories). Half of the veins are haloed, but uniform and composite veins were also observed (Figure **F32**). Forty-nine percent of the veins are single; the other veins present branched or network connectivity. Vein dips range from 1° to 90°; the average dip is 41° with a standard deviation of 24°. Haloed-vein thicknesses vary from 0.2 to 11 cm and are composed of carbonate, Fe oxide, and other secondary minerals. From interval 367-U1500B-57R-2, 27–55 cm, neptunian dikes filled with dark red claystone were observed throughout Unit VIII.

Digital imaging of the whole-round external core surface was conducted for sufficiently intact/unbroken core pieces of basalt before splitting. The resulting images and structural analysis of these 360° images from Cores 59R through 83R are shown in Figure **F33**. These images are complementary and similar to the logging FMS resistivity data; therefore, the position and amplitude of a sinusoid can indicate the strike and dip angle of a plane. The stereographic projections in the core reference frame of veins and fractures (Figure **F34**) and the 360° images of these cores indicate that there is no preferred orientation of the structures (Figure **F33**). Some single veins are almost perpendicular to the chilled glassy margin, whereas a vein network filled by carbonate mineral is often observed parallel to the glassy margin (Figure **F32**). Carbonate vein networks were observed, sometimes containing individualized angular basalt or sediment clasts (Section 71R-2). These fractures and veins are likely generated by cracking and fluid circulation during or after cooling of the basalt. There are no macroscopic or microscopic mineral preferred orientations in the basalts, which could indicate a flow direction. The silty and sandy claystone interbedded with the basalt in interval 71R-1, 91–101 cm, has a dip of 20°; however, because it is the only tilted bed, we cannot assess the origin of the tilting.

Figure F32. Igneous structures in Unit VIII, Hole U1500B. A. Open fracture with a halo. B. Vein perpendicular to chilled glassy selvage. C. Haloed carbonate and Fe oxide vein. D. Haloed vein. E. Neptunian dike. F. Carbonate vein network within a glassy margin. G. Tilted sedimentary bedding. H. Angular basalt and sediment clasts in a carbonate vein.

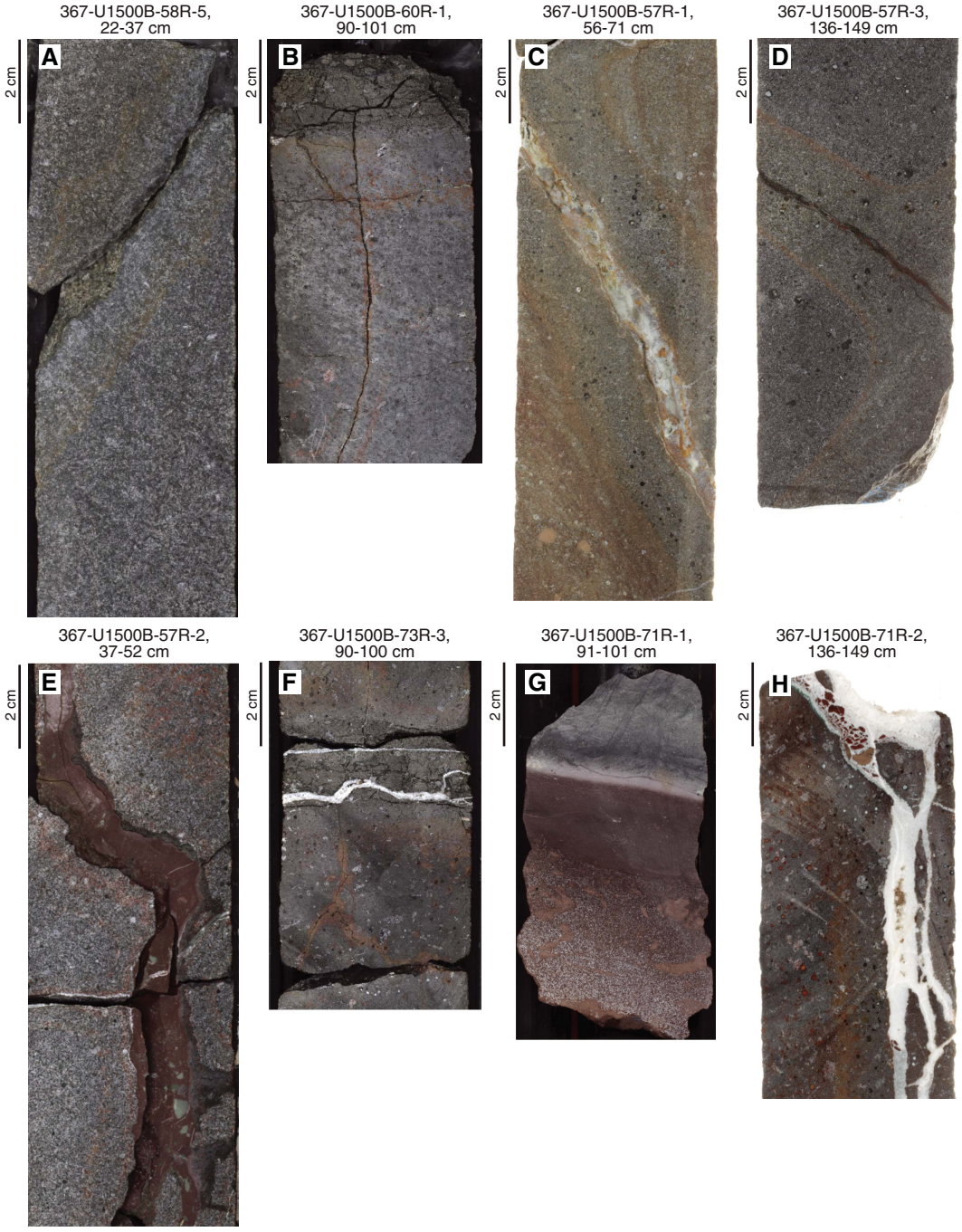

Figure F33. Whole-round images, Hole U1500B.



Figure F34. Stereographic projection of Unit VIII fractures and veins in core reference frame, Site U1500. Note random orientations of the fractures and veins.

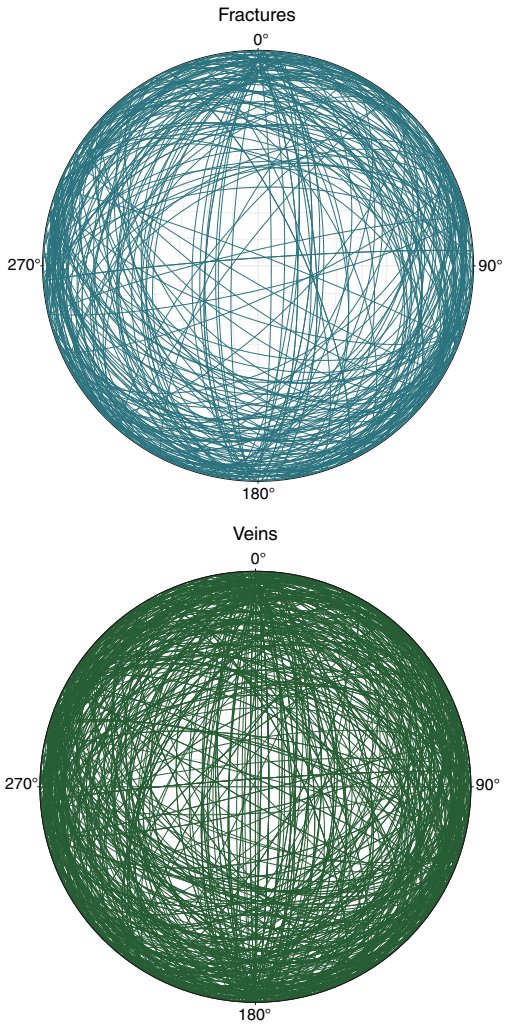

Biostratigraphy

All core catcher samples in Holes U1500A and U1500B were analyzed for calcareous nannofossil and foraminiferal content. Additional samples were taken from the split-core sections when necessary to refine the ages between core catcher samples. Preservation of microfossils varies from poor to good. Overgrown or broken fragments are common for the calcareous fossils in the sediment sequences. Both calcareous nannofossils and foraminifers vary from barren to abundant and exhibit some degree of reworking in most samples.

Although core recovery is low or even barren for half of the cores, 12 biostratigraphic datums were recognized from Cores 367-U1500A-2R through 367-U1500B-56R, revealing that we recovered an apparently continuous succession from the late Oligocene to the late Miocene. The biostratigraphic events are listed in Table **T4**, and an age-depth plot using these events is shown in Figure **F35**.

Cores 367-U1500A-2R through 367-U1500B-10R (380 to ~930 m) were assigned to the upper portion of the late Miocene. Preservation of the calcareous nannofossils is moderate, whereas the planktonic foraminifers are poorly preserved. The sedimentation rate is ~120 mm/ky for the late late Miocene at this site.

Cores 367-U1500B-10R through 37R (930 to ~1200 m) were assigned to the lower portion of the late Miocene. Both calcareous nannofossils and planktonic foraminifers are poorly preserved at this interval. The estimated sedimentation rate is ~270 mm/ky for the early late Miocene.

Cores 37R through 50R (1200 to ~1313.85 m) were assigned to the middle Miocene–late Oligocene with a sedimentation rate of ~10 mm/ky. Fossil preservation is moderate to poor. The first appearance datums (FADs) of *Globoturborotalita decoraperta* (11.46 Ma) and *Reticulofenestra pseudoumbilicus* (12.83 Ma) indicate the late/middle Miocene boundary (11.60 Ma) can be confidently placed between Samples 37R-1, 40–41 cm, and 44R-CC. The last appearance datums (LADs) of *Globigerina ciperoensis* (22.9 Ma) and *Reticulofenestra bisecta* (23.13 Ma) occur in Core 50R and possibly indicate the Miocene/Oligocene boundary. Both calcareous nannofossils and planktonic foraminifers indicate a late Oligocene succession from Cores 51R through 55R. Two samples from the veins and intrapillow fill of the basalts in Unit VIII contain poorly preserved calcareous nannofossils and indicate an Oligocene age. However, in the calcareous sandstone from Section 56R-1, *P. circularis, G. subquadratus,* and *O. suturalis*, which are commonly present in the middle Miocene, are found together with early Miocene to late Oligocene typical planktonic foraminiferal species (*C. dissimilis*). In the same sample, the nannofossil content is represented by long-range species and cannot give a precise age for Core 56R. The accurate age of Core 56R requires further studies.

Calcareous nannofossils

Calcareous nannofossil biostratigraphy at Site U1500 is based on analysis of all core catcher samples and additional split-core samples (Tables **T5**, **T6**). A total of 148 samples were analyzed, 71 of which were barren of calcareous nannofossils. Nannofossils are rare to common in most of the fossiliferous samples and abundant in samples from the dark brownish calcareous-rich claystone of lithostratigraphic Unit VB. Preservation of nannofossils is poor to moderate with varying degrees of overgrowth on nannofossils, as well as reworked specimens and abundant broken fragments, especially among discoasters.

Seven nannofossil biostratigraphic datums indicate an age of late Oligocene to late Miocene for the sediment sequence recovered at Site U1500 (Table **T4**). The LAD of *Discoaster quinqueramus* (5.59 Ma) marks the top of Zone NN11, which corresponds to the Pliocene/Miocene boundary. *D. quinqueramus* was found in Sample 367-U1500A-2R-CC (386.97 m), which suggests that the Pliocene/Miocene boundary is shallower than 386.97 m. The FAD of *D. quinqueramus* (8.12 Ma) in Sample 17R-1 (660.89 m) defines the bottom of Zone NN11. Zones NN11–NN9 could not be reliably identified due to poor preservation or the absence of nannofossils in several core catchers. The LAD of *Discoaster bollii* (9.21 Ma) within Zone NN10 occurs in Sample 25R-5, 54 cm (743.96 m). The LAD of *Catinaster coalitus* (9.69 Ma) within Zone NN9 occurs in Sample 30R-3, 86 cm (790.18 m). The occurrences of *C. coalitus* and *D. bollii* in Sample 367-U1500B-4R-3, 28 cm (867.80 m), allow reliable biostratigraphic correlation between the deep part of Hole U1500A and the uppermost section of Hole U1500B (Tables **T5**, **T6**). Low or barren nannofossil abundance between Cores 367-U1500B-4R and 40R prevent the identification of boundaries between Zones NN9 and NN6. The LAD of *Discoaster brouweri* (10.76 Ma) within Zone NN8 occurs in Sample 40R-CC (1214.5 m), and the FAD of *R. pseudoumbilicus* (12.83 Ma) within Zone NN6 occurs in Sample 44R-CC (1256.1 m). The Zone NN1/NP25 boundary occurs in Sample 50R-1, 8 cm (1310.98 m), based on the LAD of *R. bisecta* (23.13 Ma), which corresponds to the top of the late Oligocene. Samples from Core 51R through 55R present a typical late Oligocene associ-

Table T4. Biostratigraphic events, Site U1500. T = top/last appearance datum, B = bottom/first appearance datum. PF = planktonic foraminifers, CN = calcareous nannofossils. **Download table in CSV format.**

Epoch	Fossil group	Zone	Event	Hole, core, section, interval (cm)	Top depth CSF-A (m)	Age (Ma)
				367-		
Miocene	CN	NN11	T *Discoaster quinqueramus*	U1500A-2R-CC	386.97	>5.59
			B *Discoaster quinqueramus*	U1500A-17R-1	660.89	8.12
		NN10	T *Discoaster bollii*	U1500A-25R-5, 54	743.96	9.21
		NN9	T *Catinaster coalitus*	U1500A-30R-3, 86	790.18	9.69
		NN8	B *Discoaster brouweri*	U1500B-40R-CC	1214.50	10.76
		NN6	B *Reticulofenestra pseudoumbilicus*	U1500B-44R-CC	1256.10	12.83
Oligocene		NN1/NP25	T *Reticulofenestra bisecta* >10 µm	U1500B-50R-1, 8	1310.98	23.13
late Miocene		M14	B *Turborotalita humilis*	U1500A-2R-CC	386.97	5.81
		M13b/M13a	B *Globorotalia plesiotumida*	U1500A-29R-CC	777.79	8.58
	PF	M12/M11	T *Paragloborotalia mayeri/siakensis*	U1500B-10R-CC	926.23	10.46
		M9b	B *Globoturborotalita decoraperta*	U1500B-37R-1, 40–41	1185.20	11.49
early Miocene		M1a	T *Globigerina ciperoensis*	U1500B-50R-CC	1313.85	22.90

Figure F35. Age-depth model, Site U1500. Plotted event data are in Table T5.

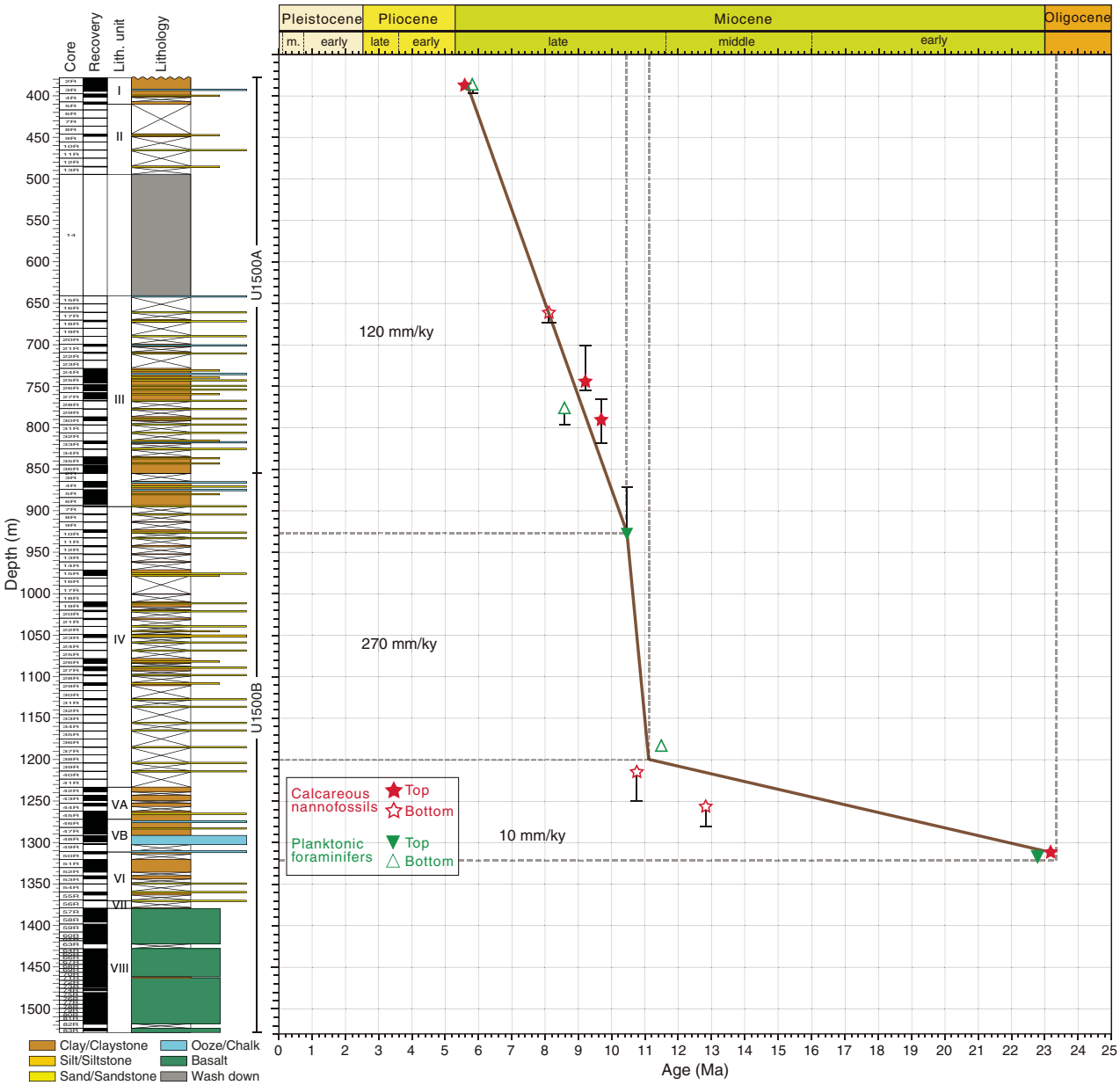

Table T5. Distribution of calcareous nannofossils, Hole U1500A. **View table in PDF format. Download table in CSV format.**

Table T6. Distribution of calcareous nannofossils, Hole U1500B. **View table in PDF format. Download table in CSV format.**

ation, such as *Sphenolithus predistentus, Sphenolithus distentus, Sphenolithus ciperoensis,* and *R. bisecta*. However, this portion of the succession is considered with caution because the nannofossils became surprisingly abundant and well preserved.

Eighteen sediment samples were analyzed from the veins and intrapillow fill of the basalts of lithostratigraphic Unit VIII. Only two samples contain poorly preserved calcareous nannofossils (Samples 62R-1, 7 cm, and 66R-3, 90–92 cm; Table **T6**). Sample 62R-1, 7 cm (1415.97 m), contains *R. bisecta* (LAD at 23.13 Ma), *Cyclicargolithus floridanus, Cyclicargolithus abisectus* (FAD at 32.02 Ma in Young et al., 2014), and *S. predistentus* (LAD at 26.93 Ma), which indicates an age range of ~27–32 Ma. In Sample 66R-3, 90–92 cm (1440.4 m), nannofossils are poorly preserved and strongly overgrown; only some specimens of *R. bisecta, C. floridanus,* and *C. abisectus* were recognized, indicating an Oligocene age.

Table T7. Distribution of planktonic foraminifers, Site U1500. **View table in PDF format. Download table in CSV format.**

Planktonic foraminifers

We analyzed all core catcher samples and several additional samples from selected split cores in Holes U1500A and U1500B (Table **T7**) for planktonic foraminifers. The preservation of planktonic foraminifers varies from good to poor. Recrystallization, dissolution, and deformation of planktonic foraminifers were often observed in most of the samples. The abundance of planktonic

foraminifers is generally low. More samples in the upper part of Hole U1500B (880–1270 m) are barren of planktonic foraminifers, which makes the identification of foraminiferal bioevents difficult.

The Site U1500 planktonic foraminiferal biostratigraphy was established by planktonic foraminiferal evolution events and assemblages. Because many planktonic foraminifers are reworked, we distinguished bioevents from reworked occurrences by relying more heavily on FADs rather than LADs.

Our results indicate that the recovered sediment sequence spans the early Miocene/late Oligocene to the late Miocene (Zone M14) based on four bioevents and one assemblage of planktonic foraminifers. Samples from Core 367-U1500A-2R-CC (378.2 m) through Sample 367-U1500B-37R-1, 40–41 cm (1185.3 m), are assigned to the late Miocene. Sediments from Cores 367-U1500B-37R-CC (1184.8 mbsf) through 50R-CC (1313.85 m) are assigned to the middle Miocene to early Miocene/late Oligocene.

Within Zone M14, the FAD of *Tuborotalita humilis* (5.81 Ma) was found in Sample 367-U1500A-2R-CC (386.97 m). The FAD of *Globorotalia plesiotumida* (8.58 Ma) in Sample 29R-CC (777.79 m) and LAD of *Paragloborotalia mayeri/siakensis* (10.46 Ma) in Sample 367-U1500B-10R-CC (926.23 m) provide two biostratigraphic control points for the boundary of Subzones M13b/M13a and Zones M12/M11, respectively.

Several specimens of *Fohsella robusta* found in Sample 29R-CC (1110.75 m) suggest an age from 11.75 to 13.13 Ma. The LAD of *G. decoraperta* (11.49 Ma) was assigned in Sample 37R-1, 40–41 cm (1185.20 m).

In Sections 46R-2 (1274.2 m) through 55R-CC (1363.3 m), planktonic foraminifers are dominated by *C. dissimilis* and *Catapsydrax unicavus* and contain abundant deformed planktonic foraminifer shells. The LAD of *G. ciperoensis* (22.9 Ma) in Sample 50R-CC (1313.85 m) implies the Miocene/Oligocene boundary. In addition, the late Oligocene species *Paragloborotalia nana* was observed in Samples 48R-CC through 53R-CC, suggesting these planktonic foraminiferal assemblages belong to early Miocene to late Oligocene.

Sample 56R-CC (red claystone) is barren of planktonic foraminifers. However, the middle Miocene or younger components, such as *Globigerinoides sacculifer, G. subquadratus, P. circularis,* and *Orbulina suturlaris*, together with the early Miocene to late Oligocene species (*C. dissimilis*), were observed in two samples from Section 56R-1. Further studies are needed to clarify the stratigraphy of this section.

Benthic foraminifers

Shallow-water benthic foraminifers (e.g., *Ammonia* and *Florius*) were observed in some sandstone samples (e.g., interval 367-U1500B-56R-1, 72–74 cm), indicating downslope transport. Deep-water agglutinated benthic foraminifers (e.g., *Glomospira, Trochamminopsis*, and *Recurvoides*) are common in Samples 40R-CC through 56R-CC and in sediments interbedded within lithostratigraphic Unit VIII basalt (Section 71R-1), suggesting it was a deep-water environment at that time.

Paleomagnetism

Shipboard paleomagnetic studies consisted of two complementary approaches (see **Paleomagnetism** in the Expedition 367/368 methods chapter [Sun et al., 2018a]): (1) measurement and in-line AF demagnetization of archive-half sections on the pass-through 2G Enterprises superconducting rock magnetometer (SRM) and (2) measurement and AF and thermal demagnetization of discrete samples on the spinner magnetometer (Agico JR-6A). Representative discrete samples were collected from each sedimentary core section (1.5 m) except those that were severely disturbed or contained unique sediments or structures deemed important for other research. Three discrete samples were collected from the basalt in lithostratigraphic Unit VIII.

We use the remanent magnetization of archive-half sections, measured after the maximum AF treatment (25 mT), to determine the polarity along the core (Figure **F36**). Discrete samples were analyzed using Zijderveld diagrams (Zijderveld, 1967), and the ChRM direction was calculated by principal component analysis (PCA) (Kirschvink, 1980) using PuffinPlot (version 1.03, 23 April 2015) (Lurcock and Wilson, 2012).

Demagnetization behavior

The archive halves of sedimentary cores were measured at 2.5 cm intervals through in-line AF demagnetization steps of 0, 5, 15, and 25 mT. The sedimentary cores exhibited a steep drilling-induced overprint that was removed with a field of 15 mT. Discrete samples were measured on the SRM with 11 AF demagnetization steps from 0 to 45 mT. The sedimentary cores, including both archive halves and discrete samples, had an average initial intensity of magnetization on the order of 10^{-2} A/m. We were able to remove on average 70% of the initial intensity of magnetization (Figure **F36**). The sediments recovered in Cores 367-U1500B-50R through 53R had an initial intensity of magnetization that was an order of magnitude weaker than the sediments above. The average magnetization of these cores after demagnetization to 25 mT is on the order of 10^{-4} A/m, which is of same level as the background noise and thus beyond the shipboard SRM resolution. Typical examples of normal (and reversed) polarity interpretation are shown in Figure **F37**. In cases where the data are insufficient to quantitatively solve for the ChRM yet the demagnetization path suggests a trend toward normal or reversed polarity, we use the terms "potential normal" or "potential reversed" (Figure **F37A, F37B**).

The archive halves of basalt cores from Site U1500 were measured at 2 cm intervals after nine in-line AF demagnetization steps from 0 to 25 mT. The average initial intensity of magnetization of the basalts was on the order of 10 A/m. The stepwise AF demagnetization of the archive halves usually reveals two components: the first component is closely related to the drilling overprint, whereas the second is directed toward the origin but needs further demagnetization to determine the ChRM. To elucidate the demagnetization behavior, three representative discrete samples were taken from the basalts of Cores 57R, 59R, and 60R (Figure **F38**). Discrete samples have a 50%–90% loss of initial intensity of magnetization after an AF treatment of 10 mT. A combination of AF and thermal demagnetization of the discrete basalt samples reveals multiple components with overlapping coercivity. The first component (AF treatments < 5–7 mT) is related to the drilling overprint; the second component (AF treatments of 8–10 mT and low-temperature steps < 300°C) is marked by a "plateau" in demagnetization with a slight directional shift toward the origin; the third component (300°–450°C) is then interpreted as the ChRM; for higher steps, the samples often become noisy and exhibit a scattered distribution. AF demagnetization of the archive-half sections is insufficient to reveal the multiple components contributing to the remanent magnetization. Thermal demagnetization on shore is therefore required to fully characterize the magnetic remanence of the basalts and the magnetic minerals contributing to the various components.

Figure F36. Inclination of remanent magnetization, fraction of magnetization remaining after 25 mT AF treatment, magnitude of initial magnetization, and point magnetic susceptibility, Site U1500. Yellow squares = discrete sample ChRM inclination.

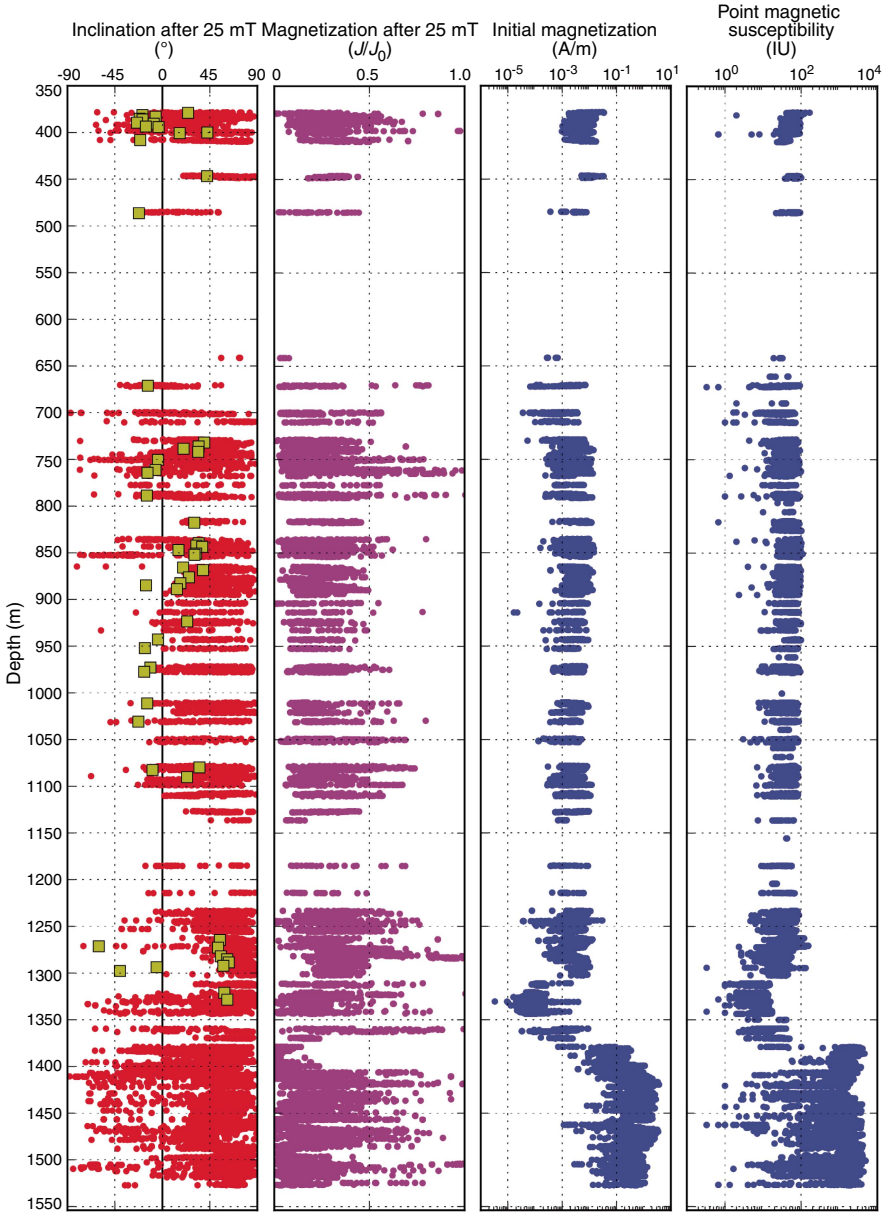

Magnetostratigraphy

For the sedimentary cores shallower than Core 57R, we constructed the magnetostratigraphy (Figure **F39**) based on the demagnetization behavior of both the archive halves and discrete samples. However, robust correlation to the standard geomagnetic polarity timescale is not possible because of coring gaps, the very poor core recovery, and the noisy demagnetization behavior.

The basalts show predominately positive inclinations with sporadic negative inclinations upon stepwise AF treatments within a single cooling unit, such as in igneous lithologic Subunit 1a (1379.1–1395.52 m), described by shipboard petrologists (e.g., Figure **F23**). Therefore, we infer that these inclinations are likely CRM and not useful for determining magnetic polarity (e.g., Channell and Xuan, 2009; Doubrovine and Tarduno, 2004). Additionally, the negative inclinations in the basalt are sometimes closely associated with fractures and intervals of alteration, which also correlate with changes in the effectiveness of AF demagnetization and changes in magnetic susceptibility (Figure **F40**). All these might indicate the presence of magnetic mineralogical changes and a corresponding secondary CRM after the basalt cooled. To clarify this, postcruise analysis of rock magnetic properties should be conducted (Zhao et al., 2006).

Figure F37. Demagnetization plots of (A, B) archive-half sections and (C–F) discrete samples. Stereographic plots: solid squares = positive (down) inclination, open squares = negative (up) inclination. A. Potential normal polarity. B. Potential reversed polarity. C. Normal polarity. Blue line = PCA calculated ChRM, red squares = measurements used in calculation. D, F. Reversed polarity. E. Normal polarity.

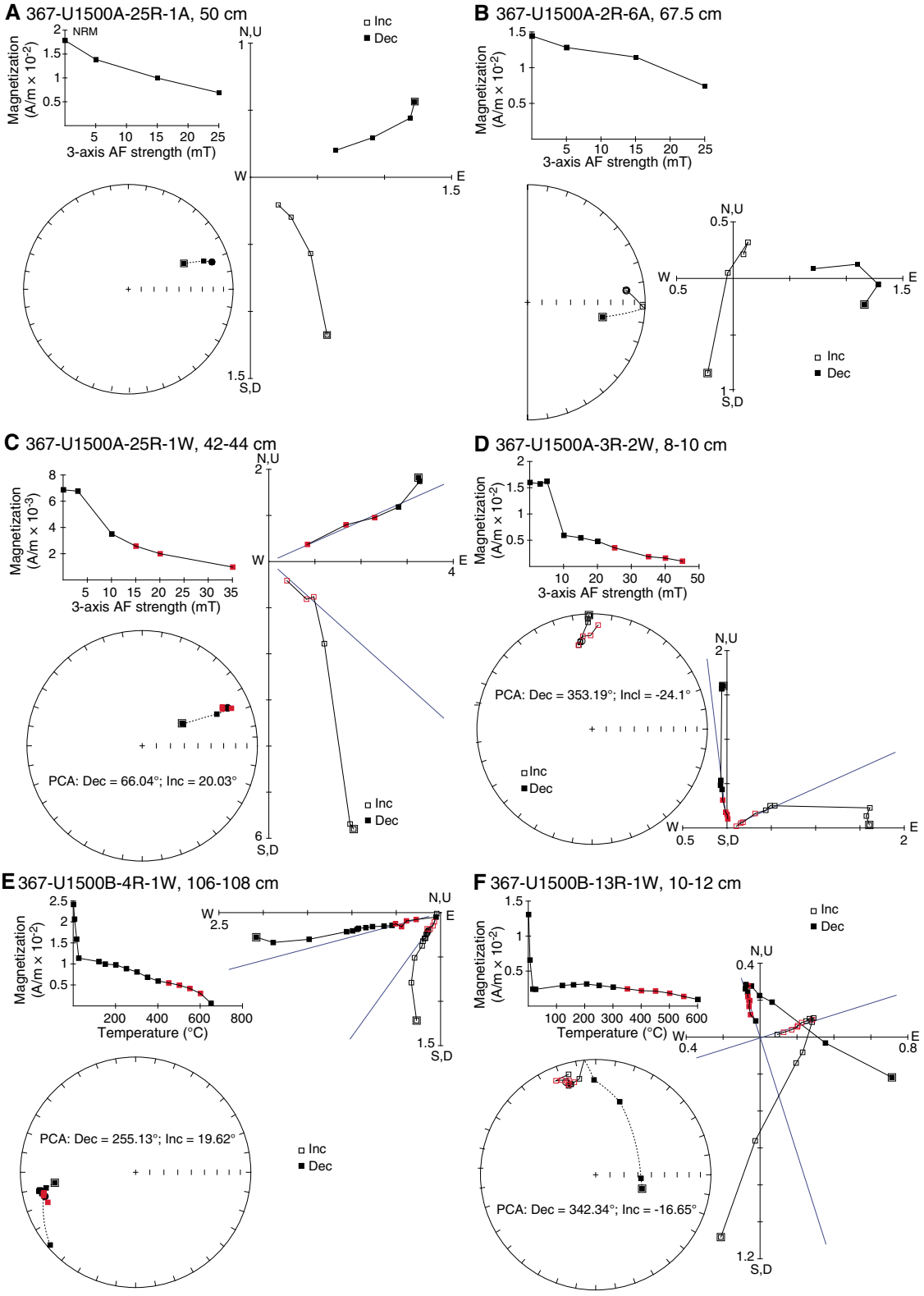

Figure F38. Demagnetization plots of (A, B) archive-half sections and (C, D) discrete samples, Hole U1500B basalts. Blue line = PCA calculated ChRM, red squares = measurements used in calculation. A, C. Normal polarity. B, D. Reversed polarity.

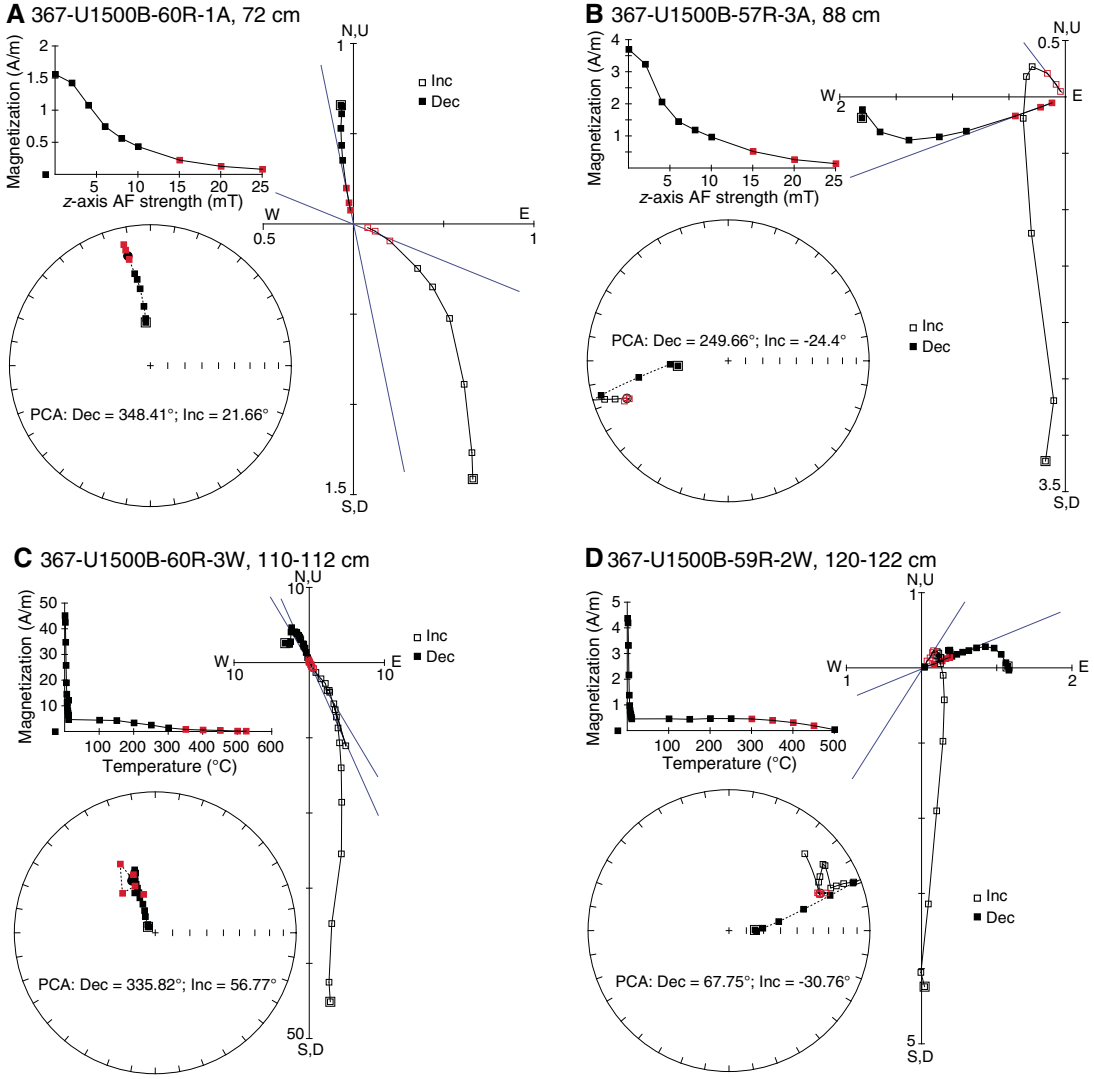

Figure F39. Magnetostratigraphy. Inclination: red = archive-half measurements after 25 mT treatment, yellow = discrete sample ChRM. Lithology column is simplified from shipboard core description (see Figure F11).

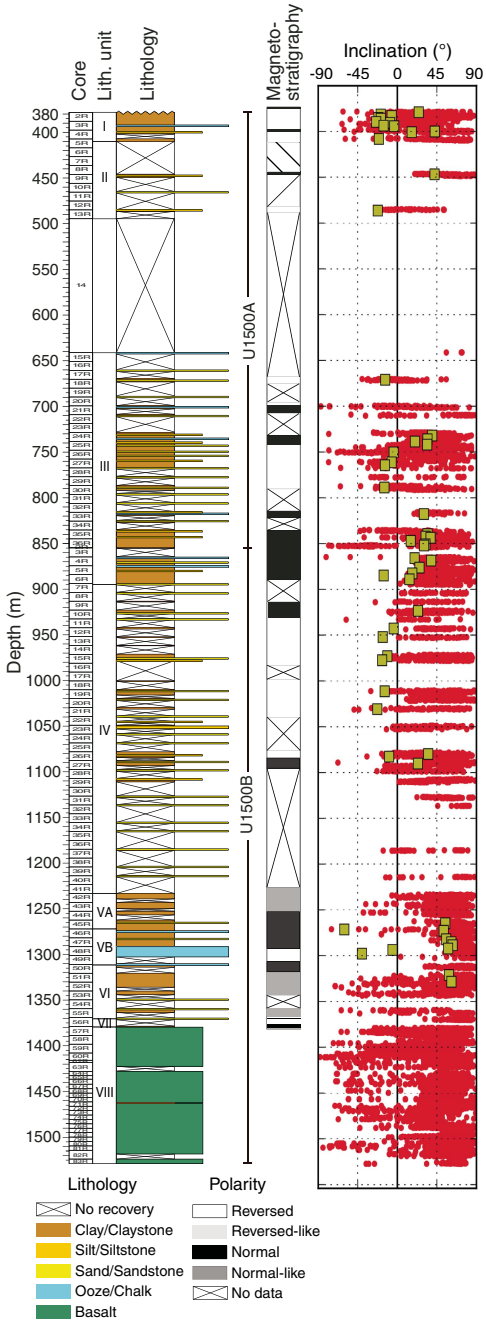

Figure F40. Magnetic property variation (367-U1500B-57R-2). Archive-half section inclination after 25 mT demagnetization, magnitude of magnetization, and point magnetic susceptibility. Note that the negative inclination at 1380.75 m correlates to fractures in core, higher magnetization remaining after 25 mT treatment, and a low in magnetic susceptibility.

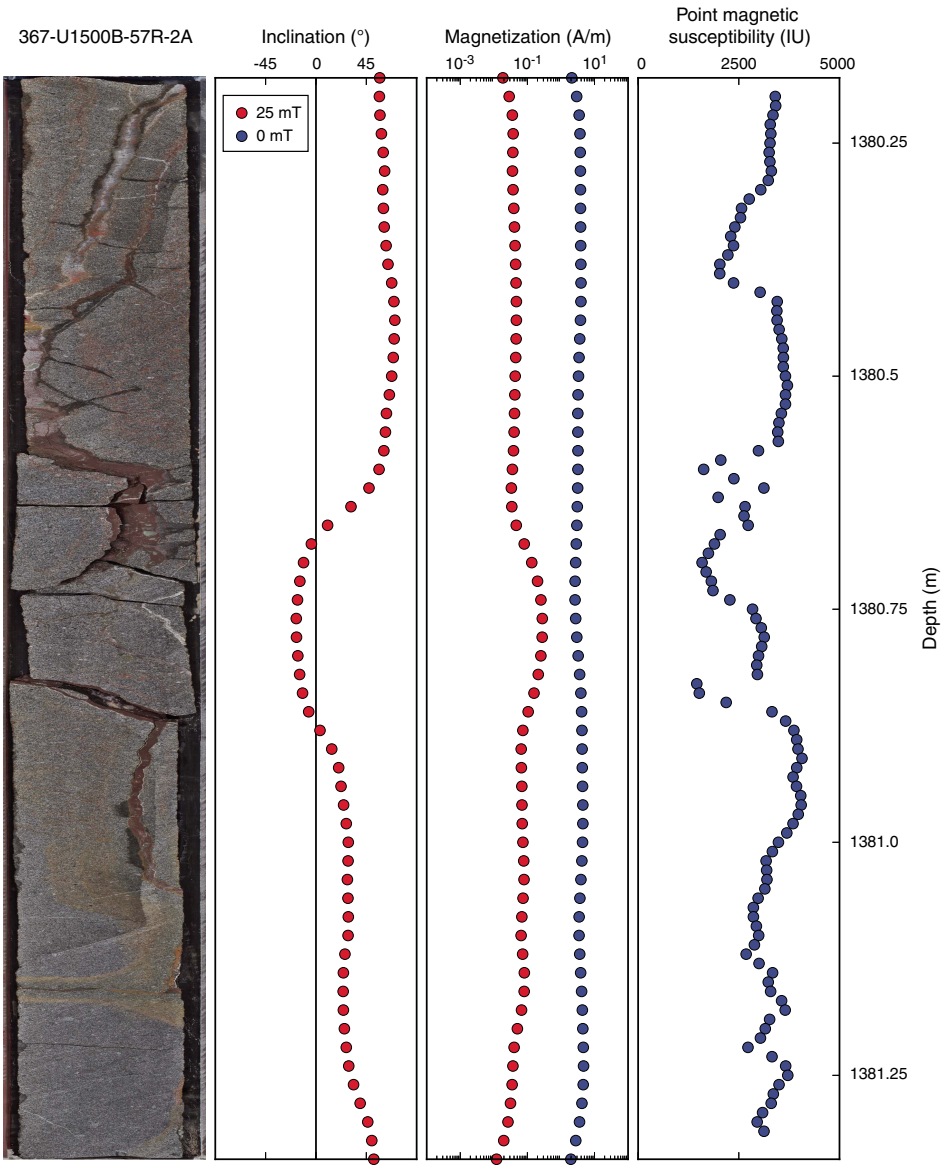

Geochemistry

At Site U1500, headspace gas measurements were taken for all cores, with values not exceeding 15 ppmv and mostly below the detection limit. Total organic and inorganic carbon and nitrogen were conducted on one sample per sedimentary core that had relative high recovery. Carbonate contents are dominated by biogenic carbonate and vary between <1 and 40 wt%, with higher values corresponding to the calcareous-rich lithostratigraphic units. TOC and TOC/TN ratios are low, averaging 0.14 wt% and 4.6, respectively. In addition, four basalt samples were analyzed for concentrations of major elements and several trace elements using ICP-AES. The ICP-AES analyses of basalts from Site U1500 indicate a subalkaline, MORB composition.

Headspace gas

Headspace gas analyses (78 samples) were performed on one sample per core throughout the sedimentary section (upper 1378 m) for routine safety monitoring. Methane and ethane concentrations are generally below detection limits except for 14 samples with low values (<15 ppmv) occurring from 1250 to 1378 m (Table T8). Ethene was detected only in one sample; its presence is probably the result of coring contamination.

Table T8. Headspace gas data, Site U1500. **View table in PDF format. Download table in CSV format.**

Table T9. Carbon and nitrogen, Site U1500. **View table in PDF format. Download table in CSV format.**

Bulk sediment geochemistry

Total carbon, total inorganic carbon (TIC), calcium carbonate, TOC, and TN were determined on 68 discrete sediment samples (Table T9; Figure F41). Bulk sediment total carbon and TN were determined by elemental analysis, and TIC was determined by coulo-

Figure F41. Lithology, methane, calcium carbonate, TOC, and TOC/TN profiles, Site U1500.

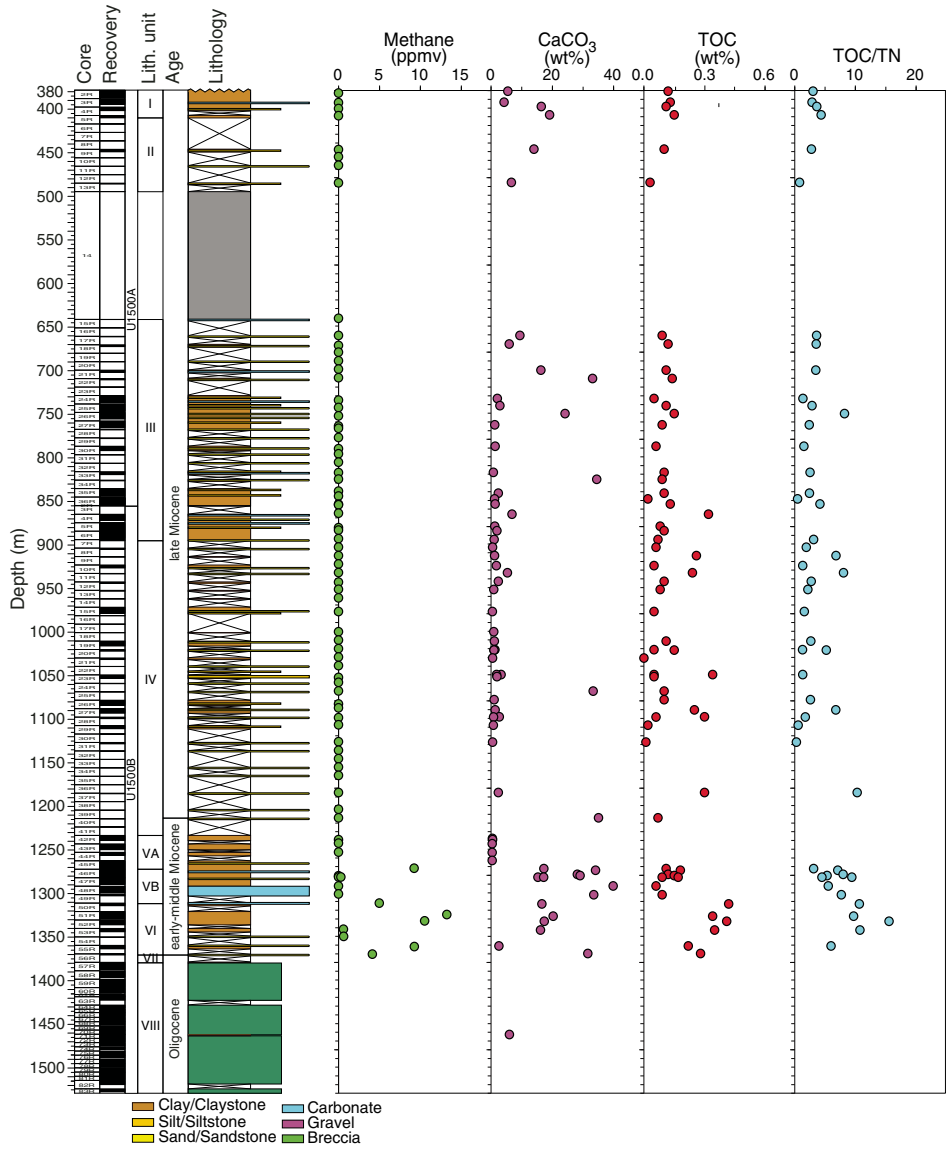

meter (see **Geochemistry** in the Expedition 367/368 methods chapter [Sun et al., 2018a]).

TIC contents range from <0.1 to 4.79 wt% (average = 1.13 wt%). Weight percent calcium carbonate, assuming inorganic carbon is exclusively present as $CaCO_3$, varies between 0.34 and 39.9 wt% (average = 9.4 wt%). From 380 to 485 m, carbonate contents vary from 4 to 19 wt%. Between 660 and 1263 m, carbonate contents fluctuate greatly from <1% to >30%; the higher values correspond to nannofossil- and/or foraminifer-rich intervals. High carbonate contents of up to ~40 wt% (average = 23 wt%; 1272–1370 m) occur in the calcareous-rich claystone and sandstone of lithostratigraphic Subunit VB and Unit VI.

Total carbon contents vary between <0.1 and 4.85 wt%. TOC is <0.2 wt% from 380 to 848 m (Table **T9**; Figure **F41**), varies between <0.1 and 0.34 wt% without a consistent pattern between 854 and 1312 m, and finally increases to relatively higher contents (up to 0.41 wt%) in the dark greenish claystone/sandstone of lithostratigraphic Unit VI. The relatively higher TOC in this deepest unit coincides with the presence of very small concentrations of hydrocarbon gases, suggesting that a slightly higher concentration of organic matter has facilitated methanogenesis.

The elemental TOC/TN ratio is generally used as a preliminary estimate for the source of organic material, with high values (TOC/TN > 12) typically attributed to a predominantly terrestrial source and lower values (TOC/TN < 8) being indicative of dominant marine contributions (Müller and Mathesius, 1999). TOC/TN values range from <1 to 15 (average = 4.6), with most values <8 at Site U1500 (Table **T9**; Figure **F41**), suggesting that the majority of the organic matter is likely from a marine source.

Table T10. Inductively coupled atomic–emission spectroscopy analyses of basalts, Hole U1500B. **View table in PDF format. Download table in CSV format.**

Igneous rock geochemistry

Four samples of igneous rocks from three different basaltic lava flows in lithostratigraphic Unit VIII in Hole U1500B (igneous lithologic Subunits 1a and 1b) were analyzed for concentrations of major

Figure F42. Total alkalis ($Na_2O + K_2O$) vs. SiO_2 diagram (Le Maitre et al., 1989) showing analyses of samples from Sites U1500, U1431, U1433, and U1434 (Li et al., 2015b). All samples plot in subalkaline basalt field.

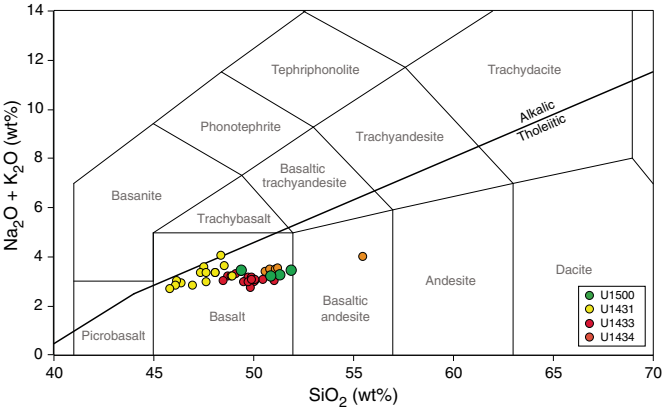

Figure F43. V vs. Ti (Shervais, 1982) diagram for basalts from Site U1500 compared to samples from Expedition 349 Sites U1431, U1433, and U1434 (Li et al., 2015b). All samples plot in MORB/back-arc basalt (BAB) field. OIB = ocean-island basalt.

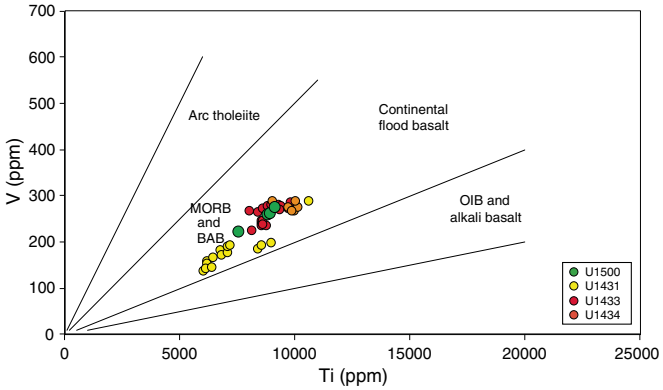

Figure F44. Zr vs. Ti (Pearce and Cann, 1973) diagram showing analyses of basalts from Site U1500 compared to samples from Expedition 349 Sites U1431, U1433, U1434 (Li et al., 2015b). All samples plot in MORB field.

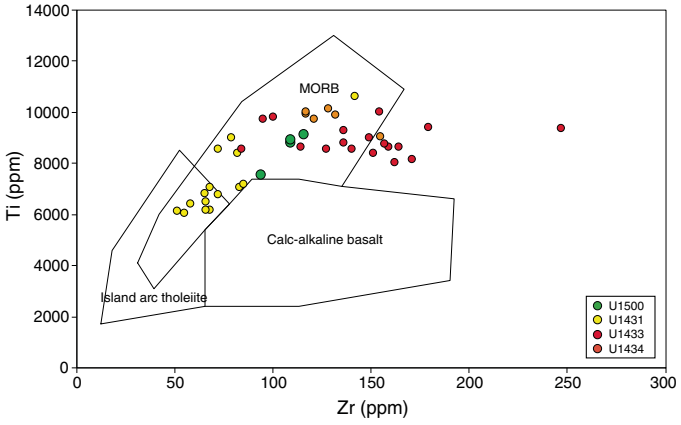

elements and several trace elements (Table **T10**) by ICP-AES (see **Geochemistry** in the Expedition 367/368 methods chapter [Sun et al., 2018a] for information on analytical procedures, instrumentation, and data quality). Total contents for the major element oxides vary from 97.31 to 99.72 wt%. Possible reasons for such totals are discussed in **Geochemistry** in the Expedition 367/368 methods chapter (Sun et al., 2018a). To enable a better comparison of our results between each another and with data from the literature, we normalized raw major element values to 100 wt% totals.

Weight loss on ignition (LOI) serves as a rough indicator of the overall level of alteration in these rocks. LOI values for unaltered basalt are typically <1 wt% (Rhodes, 1996). With the exception of Sample 367-U1500B-57R-2, 36–39 cm, which has an LOI of 2.55 wt%, the other three samples from Hole U1500B have LOI values of <1.6 wt%. The principal effects of alteration on the suite of elements measured appear to be strongest on the K_2O contents. Potassium contents of Sample 57R-2, 36–39 cm, are the highest of the four samples from this site, reaching 0.49 wt%, whereas the other three samples with low LOI values have K_2O contents of 0.23 wt% or less.

In a total alkalis ($Na_2O + K_2O$) versus SiO_2 diagram (Le Maitre et al., 1989; Figure **F42**), the obtained data plot in the subalkaline basalt field shows normalized SiO_2 concentrations ranging from 49 to 53 wt%. Hole U1500B samples overlap the compositional range of other SCS basalts recovered during Expedition 349 (Li et al., 2015b), especially rocks from Sites U1433 and U1434. Samples from Site U1431 are poorer in silica than other igneous rocks obtained during Expedition 349 and those from Hole U1500B. Mg# (Mg# = 100 × (MgO/[MgO + FeO*] calculated on a molar basis; FeO* = Fe_2O_3 × 0.8998) varies from moderately low values of 51.9 to 65.5 in the Site U1500 basalts, indicating some fractionation at depth.

On the V versus Ti diagram (Shervais, 1982) Figure **F43**), Hole U1500B samples plot in the MORB and back-arc basalt field and overlap the compositional range of Site U1433 and U1434 samples. Likewise, in the Ti versus Zr diagram (Pearce and Cann, 1973) of Figure **F44**, all samples from Expeditions 349 and 367 plot in the MORB field (with some samples from Site U1431 plotting in the overlap region of several basalt types), and Hole U1500B samples overlap the compositional range defined by samples from Sites U1433 and U1434. These relationships suggest that the basalts drilled at Site U1500 are very similar to MORB obtained from the previous SCS expedition.

Physical properties

We measured physical properties on whole-round cores and on working-half sections for lithostratigraphic characterization and correlation between core description, borehole data, and seismic profiles. These measurements included GRA bulk density, magnetic susceptibility, NGR, *P*-wave velocity, moisture and density (MAD; porosity), and thermal conductivity. We used the Whole-Round Multisensor Logger (WRMSL) to measure GRA bulk density and magnetic susceptibility. No *P*-wave velocity was measured using the WRMSL because of the large gap between sample and core liner produced during RCB coring. NGR was measured on whole-round cores with the Natural Gamma Radiation Logger (NGRL). After the cores were split into section halves, *P*-wave velocity was measured with the Section Half Measurement Gantry (SHMG) using the *X*-caliper for measurements through the split core, usually at least one measurement per section. No velocity measurements were performed with the *Y*- and *Z*-bayonet on the SHMG because the sample material was too hard for the bayonets to penetrate without disrupting and introducing cracks. Discrete samples were taken for MAD measurements, including mass measurement with dual balances and volume measurement with a pycnometer. For this, small pieces were cut from the working-half sections in the hard sediment or in the basalt. Resulting MAD values were used to calculate bulk

Table T11. Mean and standard deviation (SD) of the data sets of physical property measurements for sediment (0–1379.1 m) and underlying basalt, Site U1500. High SDs for magnetic MS and NGR in basalt reflect the presence of voids in the core liner between rock pieces. **Download table in CSV format.**

	NGR mean (cps)	NGR SD (cps)	Density mean (g/cm³)	Density SD (g/cm³)	MS mean (10^{-5} SI)	MS SD (10^{-5} SI)	*P*-wave velocity mean (m/s)	*P*-wave velocity SD (m/s)	Porosity mean (%)	Porosity SD (%)	Thermal conductivity mean (W/[m·K])	Thermal conductivity SD (W/[m·K])
Sediment	54.67	20.69	1.88	0.33	40.64	23.68	2456	707	31.9	9.8	2.35	0.79
Basalt	3.45	1.84	1.74	1.07	992.8	695.6	5177	353.4	9.1	5.8	1.62	0.05

properties (wet bulk density, dry bulk density, sediment grain density, porosity, and void ratio).

For Cores 367-U1500B-57R through 82R, *P*-wave measurements were made with the caliper on individual basalt core pieces without the core liner. For Cores 57R through 60R within the basalt, discrete samples were shared between paleomagnetism and physical property analyses. First, samples were measured for paleomagnetism using AF demagnetization but no heating. Afterwards, we soaked the same samples in salt water for 24 h under a vacuum and then performed *P*-wave and MAD measurements (see **Physical properties** in the Expedition 367/368 methods chapter [Sun et al., 2018a]). The samples were then returned for further paleomagnetic measurements that included thermal demagnetization.

Throughout all cores, thermal conductivity was measured on section halves with a puck probe. For each core, three measurements were conducted on the same piece, usually in the middle section. The small puck probe measurements showed unstable results and notable differences between the three measurements on samples with high amounts of fractures. Therefore, no measurement was implemented on some of the cores (e.g., Cores 49R through 53R). Hard rock pieces from Cores 57R through 73R were placed in a seawater bath for 4 h before thermal conductivity was measured with a large puck in the bath.

In addition, wireline log data were acquired below the bottom of the casing (846 m) in Hole U1500B (see **Downhole measurements**).

Data cleaning and depth correction

Data measured using automatic systems such as the WRSML, NGRL, and SHMSL (point magnetic susceptibility) can contain data outliers (e.g., data from voids in the core, unrealistic high values, etc.) that must be removed. This cleaning is required before the integration of these data into the models (e.g., synthetic seismograms).

We defined values exceeding $\mu \pm N\sigma$ (with $N = 2$), where μ is the mean and σ is the standard deviation of the data set, as outliers and removed them from the data set. Because the values in the basalt layer are very different from those in the sediment, we estimated the mean and standard deviation for the two data sets separately and cleaned the data accordingly (Table **T11**). The WRMSL measurements on the basalt cores (from Core 367-U1500B-57R to the bottom of the hole) show very scattered values due to voids in the liner between rock pieces. The corresponding standard deviation is very high. We also smoothed the data when it was used for modeling computation by applying a moving-average filter. SHMG data were usually considered to be reliable because the operator checks the result as it is acquired. For the MAD data, we observed very few outliers with values exceeding $\mu \pm 2\sigma$.

To insure the homogeneity of the descriptions and the comparisons of our measurements to other core characteristics collected in other laboratories, we used sample depths below seafloor calculated by core depth below seafloor, Method A (CSF-A; see **http://www.iodp.org/top-resources/program-documents/policies-and-guidelines/142-iodp-depth-scales-terminology-april-2011/file**). It is important to note that depths calculated this way do not account for core expansion, including cores that have >100% recovery.

Density

GRA bulk density was measured automatically every 2 cm by the WRMSL. In addition, bulk density was measured on discrete core samples with the MAD system (~10 cm³ volume each, usually three samples per core according to recovery). Both types of density measurements show similar variations (Figure **F45**). It should be noted that the reduced diameter of the RCB cores does not completely fill the core liner and causes lower density values during WRMSL measurements. No data could be collected for intervals penetrated without coring (0–378 and 495–641 m) or for intervals of poor core recovery within lithostratigraphic Unit IV that are presumed to be sand/sandstone. A few MAD samples were collected in the basalt of Unit VIII. No MAD samples were collected from Core 367-U1500B-61R to the bottom of the hole because we did not expect much variability in the MAD values in the relatively uniform basalts recovered and because these cores should mostly be preserved for higher priority postcruise research.

In Unit I (378–410 m), GRA bulk density decreases slightly with depth, ranging between 2.1 and 1.4 g/cm³ (Figure **F45**). Unit II has such low recovery that no trend can be observed. However, the shallowest part (446–449 m) has slightly higher density values (up to 2.04 g/cm³) than the deeper part (485–487 m), which has values only up to ~1.96 g/cm³. MAD bulk density in Units I and II shows similar trends and generally increases from 1.86 to 1.99 g/cm³. Below the second interval penetrated without coring, GRA bulk density data are highly scattered because of the presence of cracks and gaps in the more lithified core pieces, with values ranging between 1.5 and 2.5 g/cm³. Within Unit III through Subunit VA (641–1272 m), MAD bulk density increases slightly with depth from ~2.0 to 2.3 g/cm³, with some measurements as high as 2.9 g/cm³. In Subunit VB (1272–1311 m), MAD bulk density significantly increases with depth from ~2.3 to 2.5 g/cm³, whereas in lithostratigraphic Units VI and VII (1311–1379 m), it decreases with depth from 2.3 to 2.0 g/cm³. Grain densities of discrete samples from Units I–VII (378–1370 m) stay relatively constant, ranging between 2.7 and 2.85 g/cm³. The basalts in Unit VIII (1370 m to the bottom of the hole) have much higher GRA bulk density values, ranging mainly between 2.3 and 2.6 g/cm³. Three discrete samples were taken in Unit VIII, yielding MAD bulk density values between 2.67 and 2.75 g/cm³. Grain densities of these samples range between 2.84 and 2.86 g/cm³.

Porosity decreases with depth within the upper two lithostratigraphic units (378–495 m), ranging between 45% and 52%. From 641 to 1370 m, porosity shows a less steep decrease with depth from

Figure F45. Physical property measurements, Holes U1500A and U1500B. Solid black line = boundary between sediment and basalt, dashed lines = lithostratigraphic unit boundaries (see Lithostratigraphy). Note that magnetic susceptibility (MS) plot has a log scale.

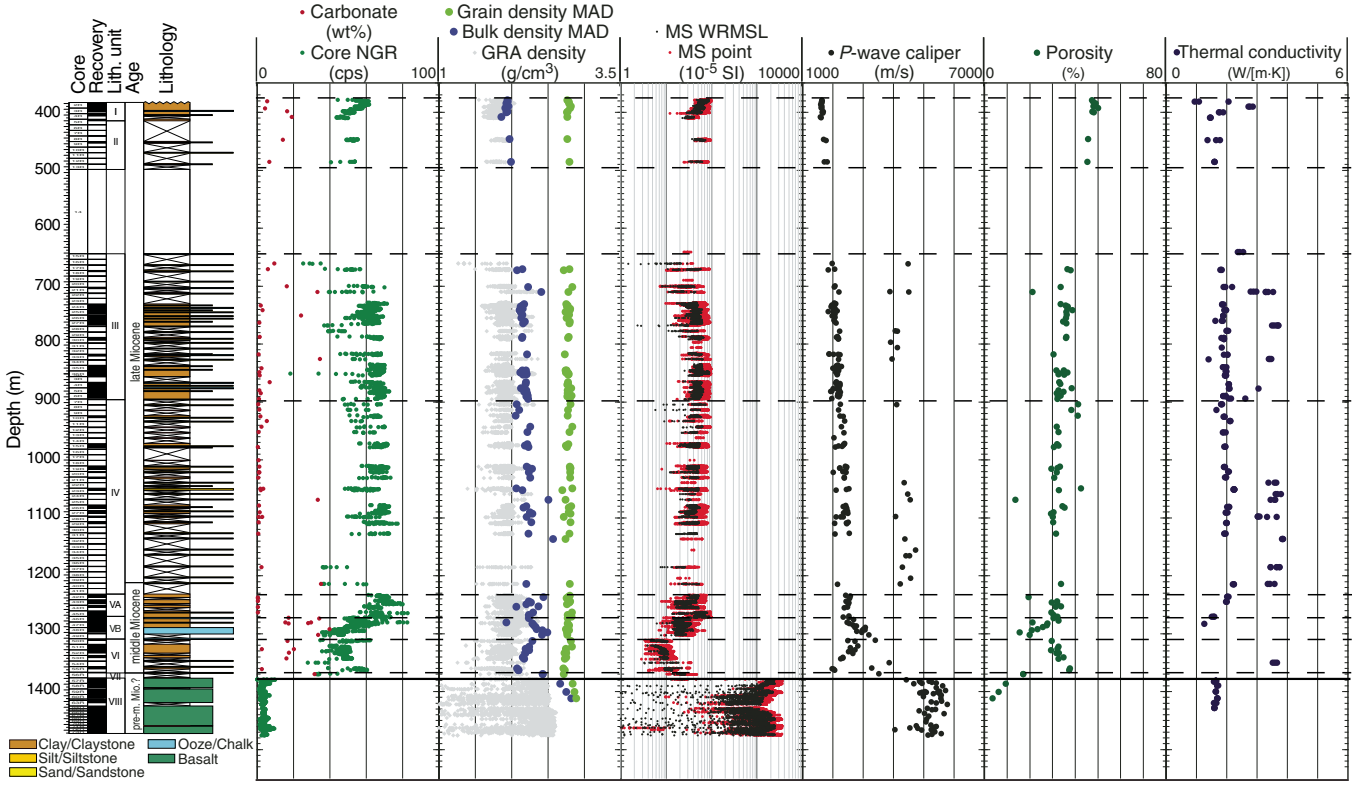

42% to ~20%. In carbonate-rich Subunit VB (1272–1311 m), there is a significant drop in porosity data from 33% to 20%. Porosity data from the basalts show very low values between 2% and 9%.

Magnetic susceptibility

Magnetic susceptibility was measured on the WRMSL and the SHMSL (point). Magnetic susceptibility is sensitive to magnetic mineral content and mineralogy of the formation (e.g., Clark and Emerson, 1991). Magnetic susceptibility data were collected every 2 cm, and point magnetic susceptibility data were collected every 1 cm. Magnetic susceptibility and point magnetic susceptibility values are in very good agreement throughout the entire cored section (Figure **F45**).

Magnetic susceptibility values show a strong decrease with depth within Unit I (378–410 m) from 95 × 10^{-5} to 15 × 10^{-5} SI (Figure **F45**). Deeper values show much smaller variability from ~410 to ~1233 m, around 30 × 10^{-5} to 40 × 10^{-5} SI on average. The lowermost part of lithostratigraphic Subunit VA (~1260–1272 m) has magnetic susceptibility values of ~60 × 10^{-5} SI that are higher than in the sediment above and include a local high of up to 150 × 10^{-5} SI (Core 367-U1500B-45R; ~1270–1272 m). Within Subunit VB (1272–1311 m), magnetic susceptibility exhibits relatively lower values, ~20 × 10^{-5} SI on average. Still significantly lower magnetic susceptibility values were measured in Unit VI (1311–1370 m); they increased with depth between ~5 × 10^{-5} and 15 × 10^{-5} SI. In the basalt of Unit VIII, magnetic susceptibility values are two orders of magnitude higher than in the sediment units and increase to about 2390 × 10^{-5} to 2980 × 10^{-5} SI. The data are very scattered but appear to correlate with alteration reactions in new fractures and veins (Figure **F46**; see **Paleomagnetism**).

P-wave velocity

P-wave velocity was not measured with the WRMSL on Site U1500 cores due to the gap between liner and sample but was measured directly on the split cores with the *X*-caliper. The values show a gradual increase with depth from 1630 m/s near 360 m to 2570 m/s at 1270 m (Figure **F45**). Some isolated measurements in lithostratigraphic Units III and IV show significantly higher values ranging between ~3880–4720 m/s, corresponding either to sandstone layers interbedded with claystone in Unit III or to single pieces in the low-recovery cores of Unit IV. In carbonate-rich Subunit VB (1270–1310 m), *P*-wave velocity increases with depth from 2380 to 3400 m/s, which is higher than the over and underlying sediment units. There is a steep increase in *P*-wave velocity values (4430–5710 m/s) in the basalt of Unit VIII.

Natural gamma radiation

In lithostratigraphic Unit I (378–410 m), NGR values decrease with depth from ~60 to ~40 counts/s, coinciding with a decrease in magnetic susceptibility within this unit (Figure **F45**). NGR values show very low variability, remaining around 60–70 counts/s between 410 and 1272 m. In Unit II, NGR values range between 45–60 counts/s with no clear trend due to the low recovery. NGR slightly increases with depth in Units III and IV (641–1233 m), ranging from ~20 to 80 counts/s. NGR significantly decreases from ~80 counts/s near 1270 m to 25 counts/s at 1310 m, coinciding with an increase in carbonate contents at the boundary between Subunits VA and VB. Basalts in Unit VIII have very low NGR values, almost entirely <10 counts/s, as expected for basalt.

Figure F46. Physical properties measurements of Unit VIII basalts, Hole U1500B. Alteration rank observed by petrologists. Note that MS plot has a log scale.

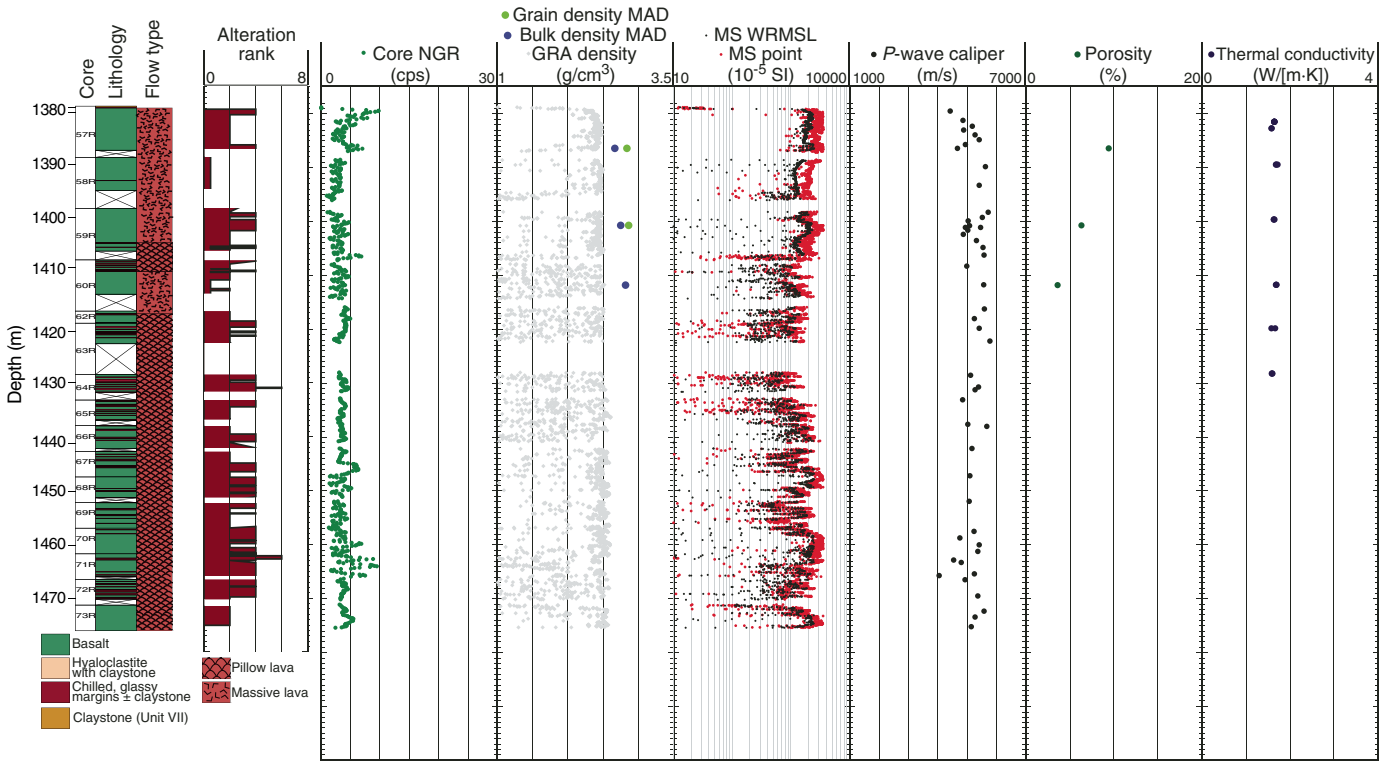

We estimated concentrations of K, U, and Th using NGR and bulk density measurements (Figure **F47**), based on a study from De Vleeschouwer et al. (2017). The general trend of each element concentration is similar to the total NGR count values.

Thermal conductivity

Thermal conductivity increases slightly with depth from 1.1 W/(m·K) at 381 m to 2.2 W/(m·K) at 1214 m (Figure **F45**). Some measurements in lithified pieces from lithostratigraphic Units III and IV have significantly higher values between ~2.8 and 3.8 W/(m·K). These very high values could be spurious and related to measurement problems with the contact probe. Thermal conductivity decreases significantly to 1.5 W/(m·K) in the chalks of Subunit VB. Values measured in the basalt of Unit VIII are relatively uniform around 1.6 W/(m·K) (Figure **F46**).

Data interpretation and lithology correlation

Correlation with lithology

The claystones, siltstones, and sandstones of lithostratigraphic Units II–IV (410–1233 m) do not display large contrasts (Figure **F45**). However, some deeper layers exhibit variations that can be correlated to the lithology. For example, clear changes in NGR (low), density (high), velocity (as high as 3400 m/s), porosity (low), and thermal conductivity (low) are associated with the high carbonate contents (up to 40 wt%) in Subunit VB (1272–1311 m). However, no significant increase in magnetic susceptibility data could be observed, similar to the carbonate-rich layer at Site U1499 (Subunit VIIIB). The content in magnetic minerals and their mineralogy are reflected in magnetic susceptibility measurements in claystone, siltstone, or sandstone, which likely explains the variations in depth of magnetic susceptibility and NGR in Unit I and the relatively high magnetic susceptibility values in the lower part of the brownish claystone in Subunit VA. Meanwhile, NGR values vary not only with lithology but also within the same sediment type. Unit VIII, which consists mainly of basalt, causes a significant change in the physical property measurements.

Unit VIII basalt

Cores 367-U1500B-57R through 73R recovered basalt. Magnetic susceptibility values are very high in Unit VIII but vary depending on the alteration grade within the basalt (Figure **F46**). Zones where alteration is significant generally have lower magnetic susceptibility. However, some variations do not appear to be directly related to alteration and might correspond to changes in the nature of the magnetized minerals or the grain size (see **Paleomagnetism**). Compared to the sedimentary rocks above, the *P*-wave velocities of the basalts are quite high (~4430–5710 m/s.). NGR and porosity are quite low, whereas density is much higher.

Figure F47. Core NGR measurements, Holes U1500A and U1500B. Estimates of K, U, and Th concentrations are derived from NGR and GRA density measurements using the method of De Vleeschouwer et al. (2017).

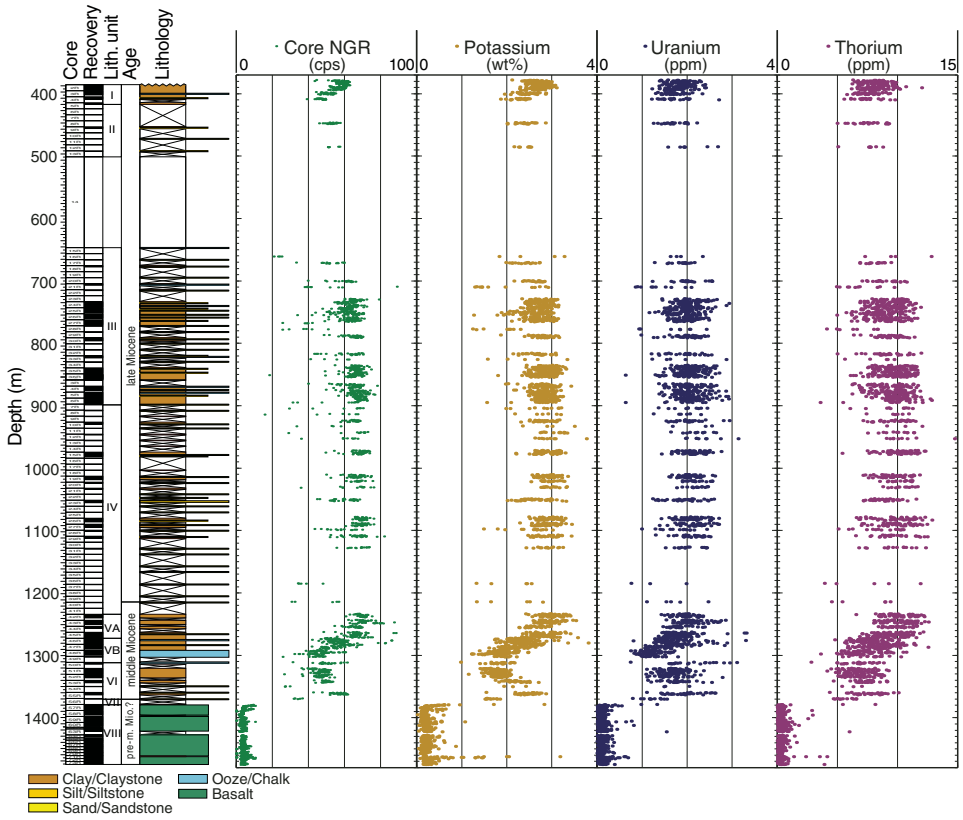

Downhole measurements

Wireline downhole logging

Downhole logging measurements at Site U1500 were performed as the last operations of Expedition 367 and ended just before the 1 day transit to Hong Kong. The collected raw data were sent to Lamont-Doherty Earth Observatory for postprocessing and were not available before the end of the expedition. Therefore, the following chapter focuses mainly on logging operations and tool setups, as well as preliminary results based on real-time observations (e.g., caliper measurements for description of borehole conditions) that were not depth corrected. The processed data were made available online to the Expedition 367 scientists immediately following the expedition and were also sent back to the ship during the port call for the Expedition 368 scientists to use.

Logging operations and tools

Downhole logging operations started at 1400 h on 6 April 2017 after finishing RCB coring to 1529 m. Three logging string tools were run in Hole U1500B (Figure **F48**). The first tool string was a modified triple combo tool string that included the following tools:

- DSI for acoustic velocity,
- HRLA/DIT for electrical resistivity,
- HLDS for caliper data (no source was included to acquire density data due to unstable borehole conditions experienced when raising the drill string out of hole), and
- HNGS/EDTC-B for NGR.

At 1630 h, the modified triple combo tool string reached the end of casing at 4655 m WRF at a speed of ~600 m/h (Figure **F49**). The end of casing is easily detected by a substantial change in resistivity and sonic velocity. The tool string was lowered out of the end of the casing at 842 m drilling depth below seafloor (DSF) and into the open hole (previously RCB cored to a total depth of 1529 m DSF). The tool string encountered an obstruction at 4946 m WRF (~1133 m). We were unsuccessful in getting the tool string to pass below this depth. We opened the caliper and collected data from 4946 m WRF (~1133 m) up to 4800 m WRF (~987 m). We then closed the caliper arm and lowered it back down, but it could not get back to the previous depth and this time reached 4925 m WRF (~1112 m), ~21 m shallower than the first run. We then opened the caliper arm and collected log data at a speed of ~600 m/h over the entire open hole from 4925 m WRF (~1112 m) up to the base of the casing (4655 m WRF; 842 m).

The second tool string run started at ~0300 h 7 April. This tool string included the FMS to collect borehole resistivity images and the HNGS and EDTC-B for NGR and correlating with the previous logging runs.

HNGS data were collected while lowering the tools into the borehole (Figures **F48**, **F49**). The tool string could only reach a total depth of 4857 m WRF (~1044 m), and we opened the FMS arms and collected FMS and HNGS data from that depth up to the bottom of the casing at 4655 m WRF (842 m).

We started assembling our third logging string at 0700 on 7 April. The third tool string consisted of the EDTC-B and VSI. Routine IODP protected-species procedures were implemented leading

Figure F48. A–C. Downhole logging tool string configurations for logging Runs 1–3, Hole U1500B. LEH-MT = logging equipment head-mud temperature. HLDS is without nuclear source.

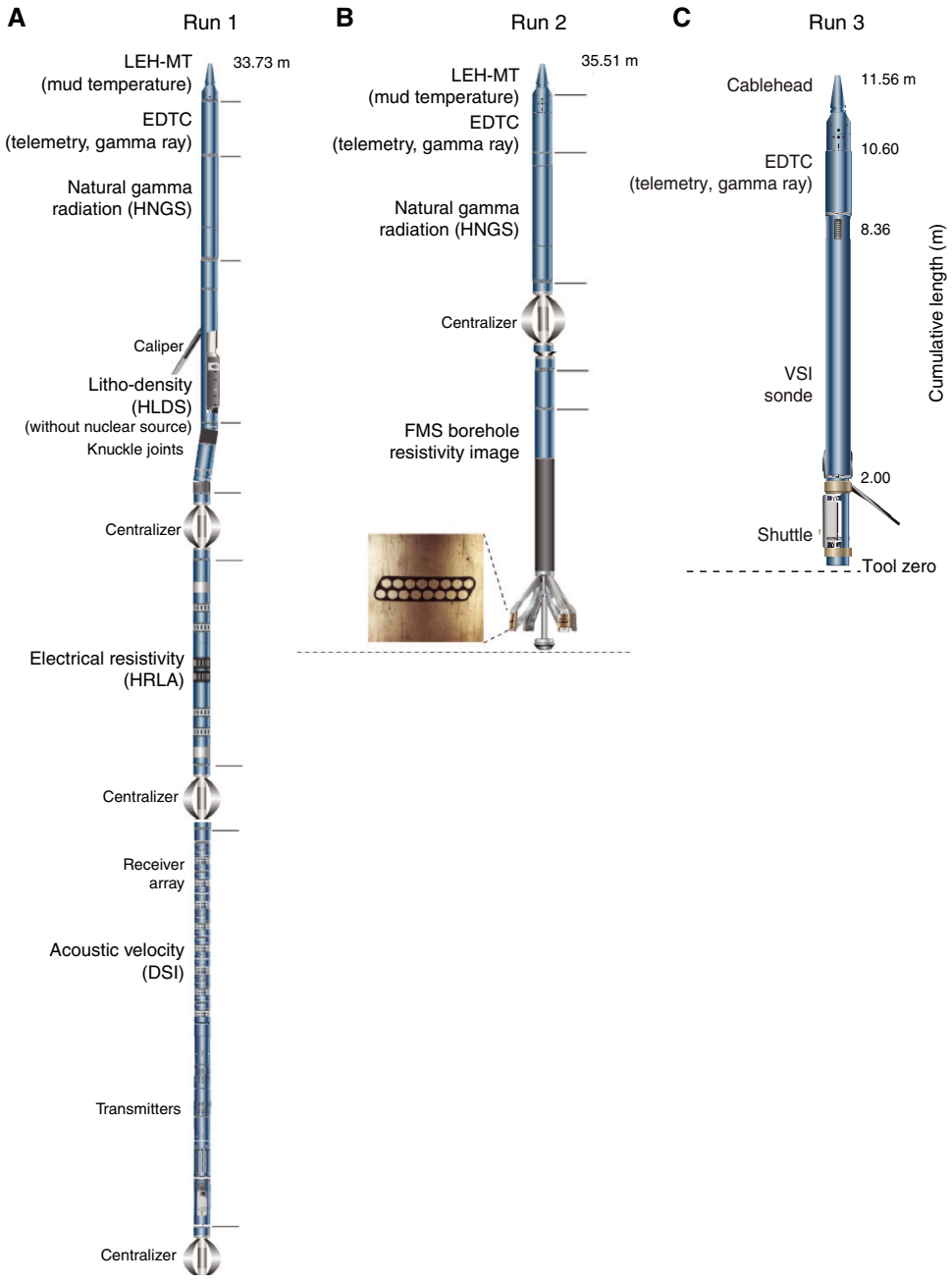

up to and throughout use of the seismic source. The seismic source was deployed 38 m from the moon pool and 7 m below the sea surface using the aft port crane (Figure **F50**). No protected species were observed, and a soft ramp-up of the gun was performed to a maximum pressure of 2000 psi. The VSI tool string reached a total depth of 4843 m WRF (~1031 m). We set the VSI tool at that depth, activated the seismic source four times, and acquired two good data records for stacking. No other good location in the open hole was found in the restricted time left for the experiment. We set the VSI tool again at 4595 m WRF (~783 m; in the casing) and got two good data records. After the VSI station, the tool was brought back to the surface and rigged down. The rig floor was then cleared of logging equipment at 1430 h on 7 April for a total of ~24 h for logging operations.

Borehole conditions and expected data quality

Before starting the downhole measurements, conditions in the deeper part of the hole deteriorated significantly while pulling out of the hole to release the drill bit on the seafloor. For the details of hole preparation, see **Operations**. While pulling the bit out of the hole, the drill string became stuck at ~1240 m. Unfortunately, during these operations the weighted (11.0 lb/gal) mud that had been pumped into the hole to help stabilize it for downhole measurements was displaced out of the hole. There were no other prob-

Figure F49. Logging operations summary, Site U1500.

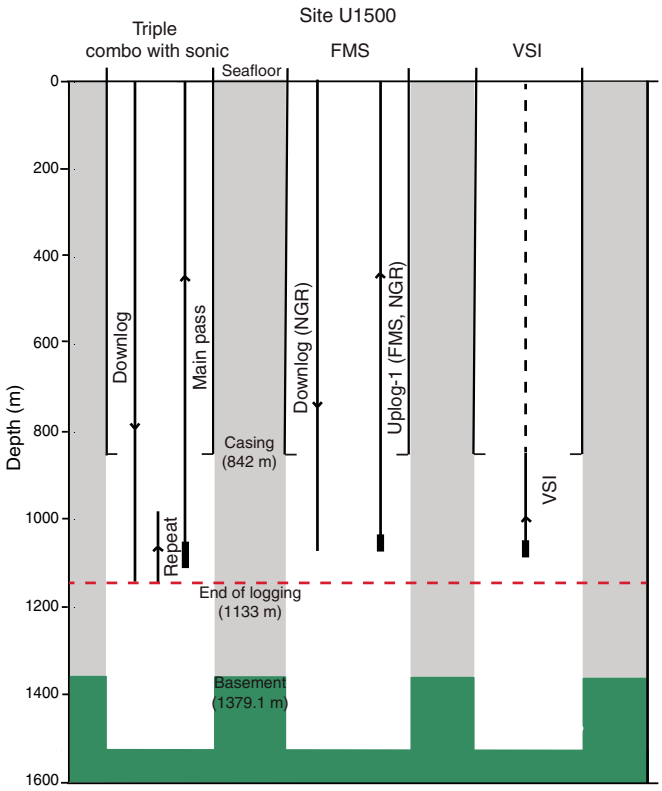

Figure F50. Deployment scheme of seismic source used during VSI tool string logging run.

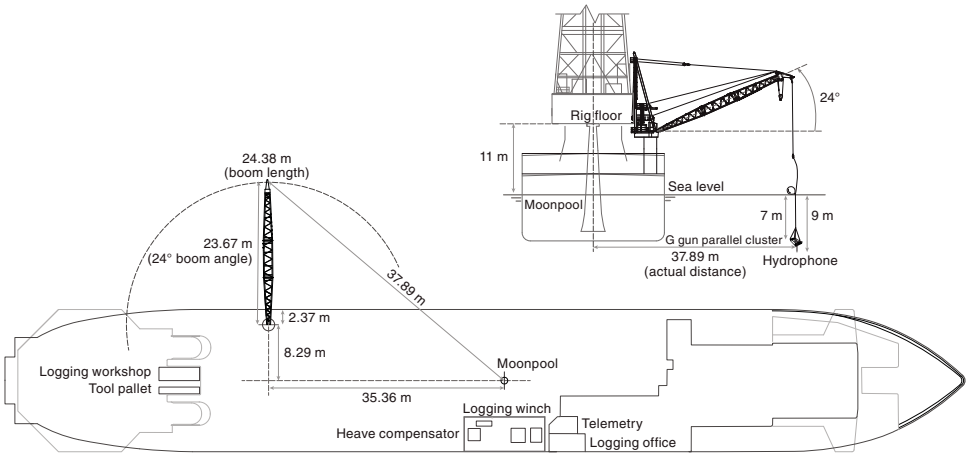

lems pulling the bit out of the hole; however, we suspected that the borehole conditions were not ideal for logging. We released the bit on the seafloor, reentered Hole U1500B, set the end of the pipe at 30 m (inside the casing), and prepared the rig floor for logging.

During the first logging run, low tension was noticed at 4907 m WRF (1094 m), which most probably was caused by a ledge or bridge. Subsequently, caliper data in this region show that the hole is enlarged from 4892 to 4901 m WRF (1079–1088 m) and at 4902 m WRF (1089 m), the hole diameter narrows to ~6 inches, less than the bit size. We were able to get the tool string through this barrier after hitting it a second time. However, the tool string could not pass below 4946 m WRF (1133 m), and log data could only be collected to that depth. It appears that this depth correlates to the top of a low-recovery zone that only returned sandstones with a high *P*-wave velocity (~4.5 km/s). The total depth of the hole kept decreasing for each subsequent logging run.

The quality of the collected FMS images could be estimated only on the screen during their acquisition. The images are of variable quality due to large variations in borehole diameter, but there are at least three intervals that are several tens of meters thick where the FMS pads had good contact with the borehole walls and we obtained good quality images. The collected log data are in DOWNHOLE in **Supplementary material**.

Correlation to seismic data

We used physical property measurements on cores and samples and other available data to correlate Site U1500 data with the available seismic reflection profiles. We also used the Site U1500 density and velocity data to create synthetic seismograms that provided additional constraints on the correlation. All correlations of the seismic reflection data with the Site U1500 core data, as well as the synthetic seismogram tests, were performed onboard using the Petrel software.

Velocity and density data

Velocity data in Holes U1500A and U1500B were acquired in the laboratory from split-core sections (PWC), and density data were acquired both in whole-round core sections (GRA density) and split-core sections (MAD; see **Physical properties**). For seismic correlation, we used PWC velocity and MAD density values.

Time-depth relations from the velocity data

TDRs are generally assumed to be quadratic polynomial functions from the interpolation of depth-velocity data. From the depth-velocity data, we computed the incremental TWT (Ti_n) as

$$Ti_n = [(d_n - d_{n-1})/V_n] \times 2 \times 1000,$$

where d_n is the depth of the nth layer and V_n is the relative velocity. The incremental Ti is multiplied by 2000 for conversion into TWT expressed in milliseconds.

From Ti_n we derived the cumulative TWT (Tc_n) expressed as

$$Tc_n = Tc_{n-1} + Ti_n,$$

and finally, the TWT adjusted from the seafloor (Ta) was calculated as

$$Ta_n = Tc_n + Ta,$$

where Ta is the TWT of the seafloor expressed in milliseconds.

If the TDR is referred to the seafloor, the intercept of the interpolated quadratic polynomial functions is set to 0.

Figure **F51** shows the Site U1500 velocity and density values collected with the PWC and MAD measurements and the TDR computed relative to the seafloor.

The resulting quadratic polynomial function is

$$d = 0.0003t^2 + 0.6204t,$$

where d is the depth in meters and t is the TWT in milliseconds.

Comparison of time-depth relations

We compared our Site U1500 TDR with the Site U1499 TDR and other relations collected in previous expeditions in the SCS (Shipboard Scientific Party, 2000; Li et al., 2008, 2015a). Figure **F52** shows the comparison of Site U1500 TDR to those for IODP Sites U1499, U1431, and U1433 and Site 1148. Our Site U1500 and U1499 TDRs are in substantial agreement with each other. The analyzed TDRs collected during previous SCS expeditions are in general agreement for the upper sediments (0–400 m). However, the TDR from Site 1148 shows higher velocities in the deeper layers.

Figure F51. MAD density and PWC velocity laboratory measurements and TDR adjusted to seafloor, Site U1500.

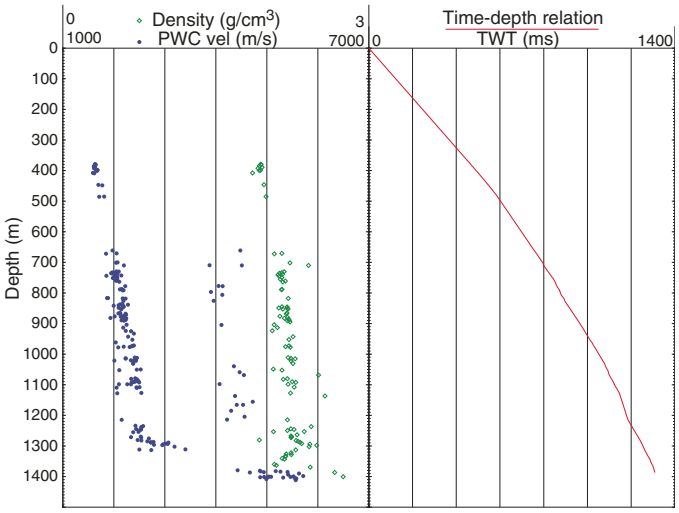

Figure F52. Site U1500 TDR compared to Sites U1499, U1431, U1433, and 1148 (Li et al., 2008).

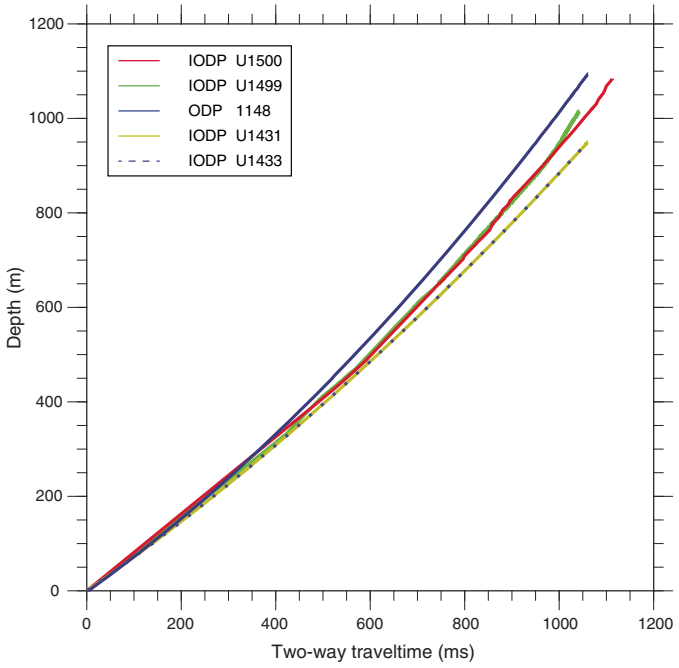

Data correlations with Petrel

Using the TDR based on Site U1500 data, we correlated the site survey seismic reflection data with the data collected from the whole-round cores (GRA density, magnetic susceptibility, and NGR) and split cores (MAD and PWC). We also plotted other data collected on board, such as core recovery, lithostratigraphic unit description, and carbonate contents. All of these properties were plotted over the seismic section with Petrel (Figure **F53**).

The following import flow process was used:

1. The coordinate system of the project was set (for Expedition 367: WGS1984_UTM50N),
2. A new seismic folder and a new survey were created,

Figure F53. Seismic section across Site U1500 (northwest–southeast). The site is located where the lithostratigraphic column is plotted (black = Unit I, yellow = Unit II, light blue = Unit III, blue = Unit IV, pink = Subunit VA, purple = Subunit VB, cyan = Unit VI, green = Unit VIII). Hole U1500A and U1500B core recovery is also shown (black = 100%, white = 0%). Other Site U1500 data are offset from site location. See CORRELATION in Supplementary material for original profile from Petrel software in the reversed direction.

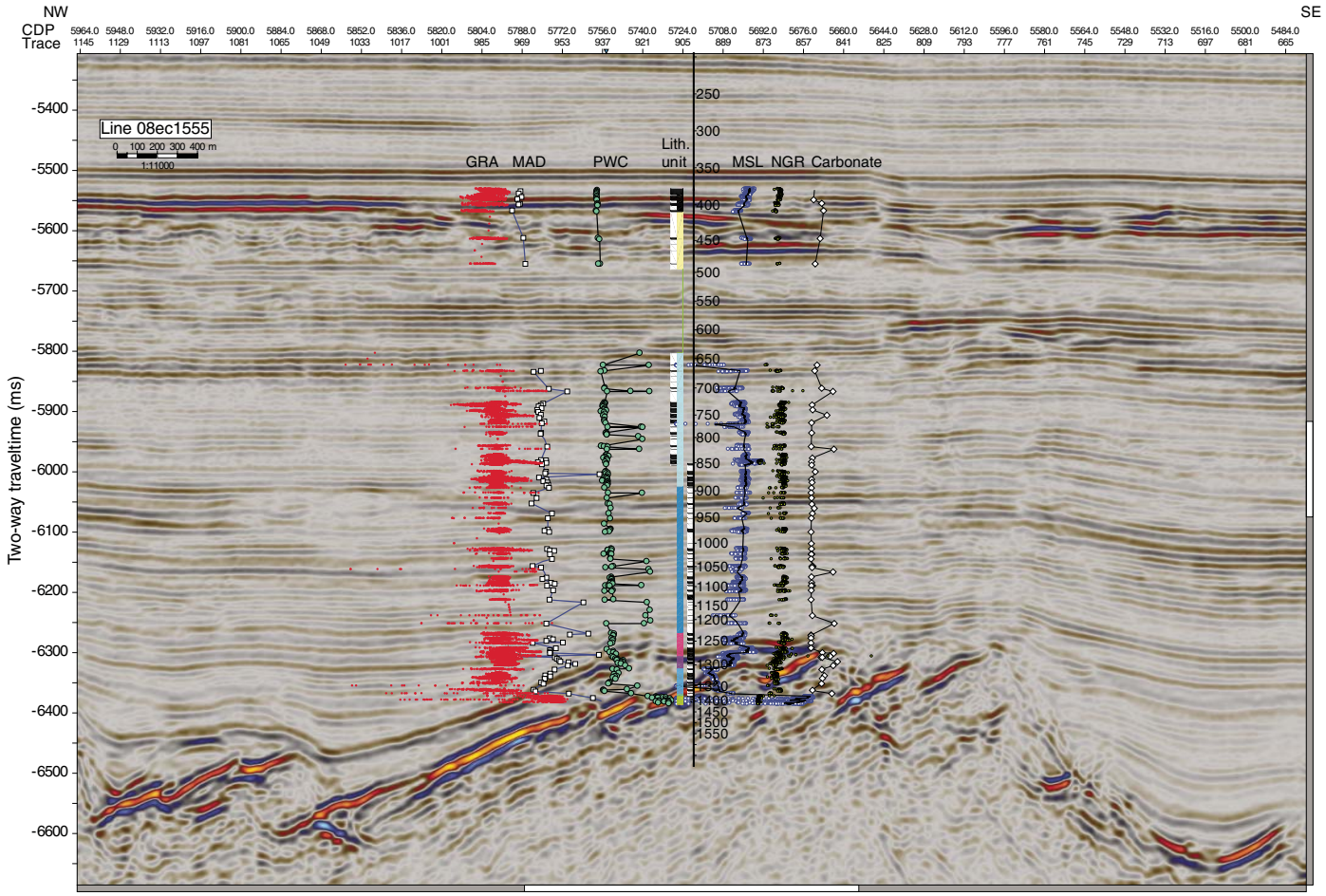

3. SEGY data were imported with presettings (after the check of the Trace Header Information with the SeisSee software),
4. The "Well" was created,
5. The TDR file was imported (the file must have the depth-TWT adjusted with respect to the seafloor), and
6. Well logs (ASCII files) for all the properties of interest were imported (the file must be tab delimited and can be directly imported from the Laboratory Information Management System database; we chose to import CSF-B depths and the values of interest).

We cleaned the data to remove the outliers before importing the values in Petrel (see **Physical properties**). An additional moving-average smoothing filter was also applied for GRA density. For the velocity data, more cleaning was applied. We manually checked the differences that might be created by manual or automatic picking of the first break for the caliper data and discarded the manually picked values that appeared doubtful because of a large difference from the surrounding values.

The physical properties are displayed over the seismic data to allow a direct comparison between the reflectors and the properties trends. Figure **F53** shows the data using the computed Site U1500 TDR (Figure **F51**). The figure shows good correlation between the main reflectors and the measured physical properties. In particular, there is an abrupt decrease in magnetic susceptibility and NGR values and a corresponding increase in carbonate contents, density, and *P*-wave velocity at ~1280 m, in agreement with the high-amplitude reflector at ~6.3 s TWT. This reflector seems to be related to the carbonate-rich interval within lithostratigraphic Unit V; a similar correlation was observed between the core and seismic data at Site U1499. At ~1380 m, abrupt changes can be observed in all the physical properties, especially the steep increase in magnetic susceptibility, density, and *P*-wave velocity values (the boundary between the sediments of Unit VII and the basalt of Unit VIII; see **Physical properties**). This depth is well correlated with the main seismic reflector at ~6.4 s TWT.

Synthetic seismograms with Petrel

We used the seismic interpretation module in Petrel to compute synthetic seismograms to further constrain the TDR relation. The parameters that need to be defined to compute synthetic seismograms are the seismic source signature, density values, and velocity values. Petrel allows the choice of single frequency–centered sources. We chose Ricker wavelets centered at the mean values of the frequency content in our seismograms. For Site U1500, we used the density data derived from the MAD measurements and the PWC velocity. The resulting synthetic seismogram for the main deep reflectors (900–1400 m) is shown in Figure **F54**.

Figure F54. Synthetic seismogram computed for the deeper part (800–1400 m) of Site U1500 (southeast–northwest). Panels from left to right: density (blue) and velocity (black) values, reflection coefficient (RC), and real seismic traces with synthetic seismogram inserted in the center. TVD = true vertical depth computed by Petrel program based on TDR quadratic equation given in TDRs from the velocity data and plotted in Figure F51.

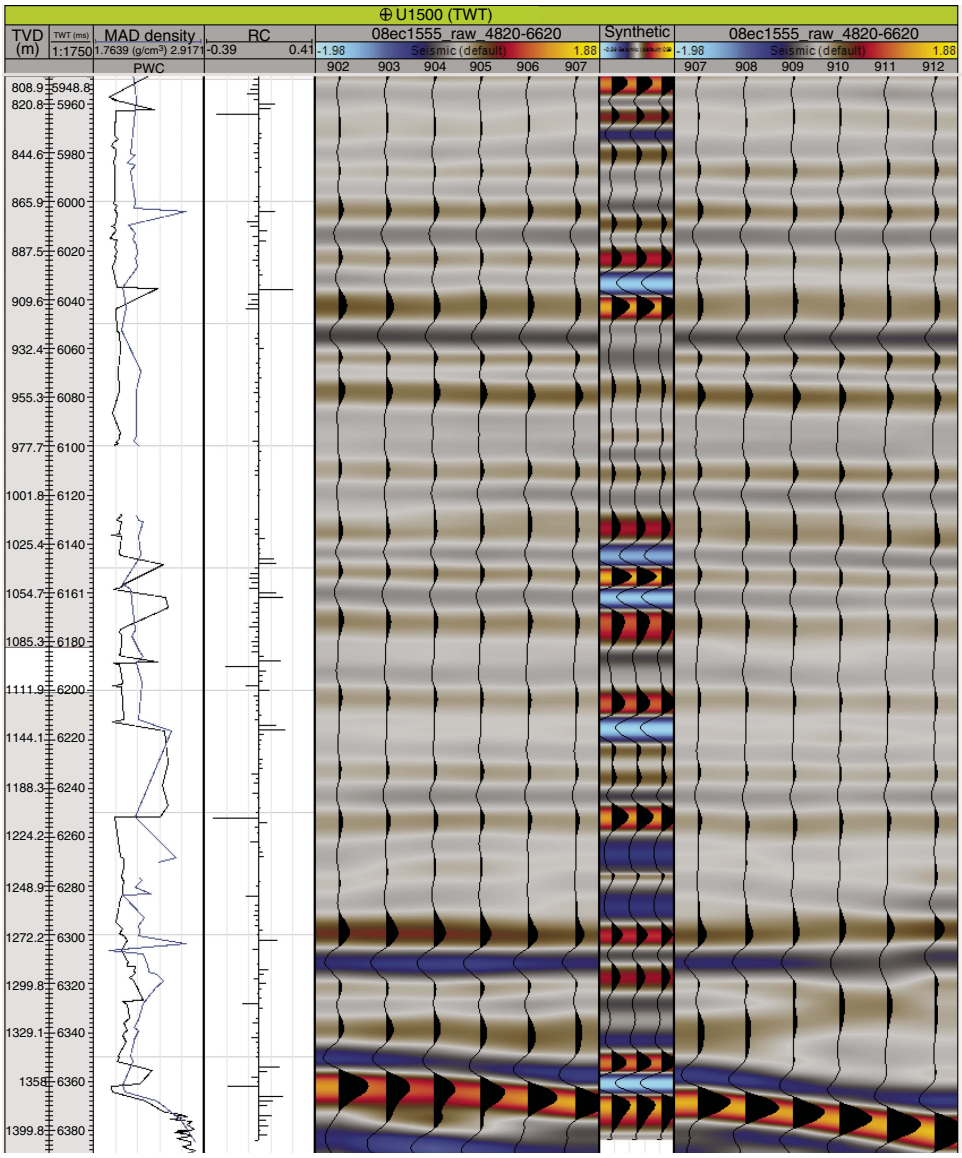

References

Bjørlykke, K., 1983. Diagenetic reactions in sandstones. *In* Parker, A., and Sellwood, B.W. (Eds.), *Sediment Diagenesis:* Dordrecht, Netherlands (Springer), 169–213. **https://doi.org/10.1007/978-94-009-7259-9_3**

Briais, A., Patriat, P., and Tapponnier, P., 1993. Updated interpretation of magnetic anomalies and seafloor spreading stages in the South China Sea: implications for the Tertiary tectonics of Southeast Asia. *Journal of Geophysical Research: Solid Earth,* 98(B4):6299–6328. **https://doi.org/10.1029/92JB02280**

Channell, J.E.T., and Xuan, C., 2009. Self-reversal and apparent magnetic excursions in Arctic sediments. *Earth and Planetary Science Letters,* 284(1–2):124–131. **https://doi.org/10.1016/j.epsl.2009.04.020**

Clark, D.A., and Emerson, D.W., 1991. Notes on rock magnetization characteristics in applied geophysical studies. *Exploration Geophysics,* 22(3):547–555. **https://doi.org/10.1071/EG991547**

De Boer, R.B., 1977. On the thermodynamics of pressure solution—interaction between chemical and mechanical forces. *Geochimica et Cosmochimica Acta*, 41(2):249–256. **https://doi.org/10.1016/0016-7037(77)90232-0**

De Boer, R.B., Nagtegaal, P.J.C., and Duyvis, E.M., 1977. Pressure solution experiments on quartz sand. *Geochimica et Cosmochimica Acta*, 41(2):257–264. **https://doi.org/10.1016/0016-7037(77)90233-2**

De Vleeschouwer, D., Dunlea, A.G., Auer, G., Anderson, C.H., Brumsack, H., de Loach, A., Gurnis, M., et al., 2017. Quantifying K, U, and Th contents of marine sediments using shipboard natural gamma radiation spectra measured on DV *JOIDES Resolution*. *Geochemistry, Geophysics, Geosystems,* 18(3):1053–1064. **https://doi.org/10.1002/2016GC006715**

Dorador, J., Wetzel, A., and Rodríguez-Tovar, F.J., 2016. *Zoophycos* in deep-sea sediments indicates high and seasonal primary productivity: Ichnology as a proxy in palaeoceanography during glacial–interglacial variations. *Terra Nova,* 28(5):323–328. **https://doi.org/10.1111/ter.12224**

Doubrovine, P.V., and Tarduno, J.A., 2004. Self-reversed magnetization carried by titanomaghemite in oceanic basalts. *Earth and Planetary Science Letters,* 222(3–4):959–969. **https://doi.org/10.1016/j.epsl.2004.04.009**

Ekdale, A.A., Bromley, R.G., and Pemberton, S.G. (Eds.), 1984. *Ichnology: The Use of Trace Fossils in Sedimentology and Stratigraphy.* SEPM Short Course, 15.

Guisseau, D., Mas, P.P., Beaufort, D., Girard, J.-P., Inoue, A., Sanjuan, B., Petit, S., Lens, A., and Genter, A., 2007. Significance of the depth-related transition montmorillonite-beidellite in the geothermal field of Bouillante (Guadeloupe, Lesser Antilles). *American Mineralogist,* 92(11):1800–1813. **https://doi.org/10.2138/am.2007.2398**

Hendry, J.P., Wilkinson, M., Fallick, A.E., and Haszeldine, R.S., 2000. Ankerite cementation in deeply buried Jurassic sandstone reservoirs of the central North Sea. *Journal of Sedimentary Research,* 70(1):227–239. **https://doi.org/10.1306/2DC4090D-0E47-11D7-8643000102C1865D**

Huismans, R., and Beaumont, C., 2011. Depth-dependent extension, two-stage breakup and cratonic underplating at rifted margins. *Nature,* 473(7345):74–78. **https://doi.org/10.1038/nature09988**

Kirschvink, J.L., 1980. The least-squares line and plane and the analysis of palaeomagnetic data. *Geophysical Journal of the Royal Astronomical Society,* 62(3):699–718. **https://doi.org/10.1111/j.1365-246X.1980.tb02601.x**

Knaust, D., and Bromley, R.G. (Eds.), 2012. *Developments in Sedimentology* (Volume 64): *Trace Fossils as Indicators of Sedimentary Environments.* van Loon, A.J. (Series Ed.): Amsterdam (Elsevier).

Larsen, G., and Chilingar, G.V. (Eds.), 1979. *Developments in Sedimentology* (Volume 25A): *Diagenesis in Sediments and Sedimentary Rocks:* New York (Elsevier).

Larsen, H.C., Sun, Z., Stock, J.M., Jian, Z., Alvarez Zarikian, C.A., Klaus, A., Boaga, J., Bowden, S.A., Briais, A., Chen, Y., Cukur, D., Dadd, K.A., Ding, W., Dorais, M.J., Ferré, E.C., Ferreira, F., Furusawa, A., Gewecke, A.J., Hinojosa, J.L., Höfig, T.W., Hsiung, K.-H., Huang, B., Huang, E., Huang, X.-L., Jiang, S., Jin, H., Johnson, B.G., Kurzawski, R.M., Lei, C., Li, B., Li, L., Li, Y., Lin, J., Liu, C., Liu, C., Liu, Z., Luna, A., Lupi, C., McCarthy, A.J., Mohn, G., Ningthoujam, L.S., Nirrengarten, M., Osono, N., Peate, D.W., Persaud, P., Qui, N., Robinson, C.M., Satolli, S., Sauermilch, I., Schindlbeck, J.C., Skinner, S.M., Straub, S.M., Su, X., Tian, L., van der Zwan, F.M., Wan, S., Wu, H., Xiang, R., Yadav, R., Yi, L., Zhang, C., Zhang, J., Zhang, Y., Zhao, N., Zhong, G., and Zhong, L., 2018. Expedition 367/368 summary. *In* Sun, Z., Jian, Z., Stock, J.M., Larsen, H.C., Klaus, A., Alvarez Zarikian, C.A., and the Expedition 367/368 Scientists, *South China Sea Rifted Margin*. Proceedings of the International Ocean Discovery Program, 367/368: College Station, TX (International Ocean Discovery Program). **https://doi.org/10.14379/iodp.proc.367368.101.2018**

Le Maitre, R.W., Bateman, P., Dudek, A., Keller, J., Lameyre, J., Le Bas, M.J., Sabine, P.A., Schmid, R., Sorensen, H., Streckeisen, A., Woolley, A.R., and Zanettin, B., 1989. *A Classification of Igneous Rocks and Glossary of Terms:* Oxford, United Kingdom (Blackwell Science Publishing).

Li, C.-F., Li, J., Ding, W., Franke, D., Yao, Y., Shi, H., Pang, X., et al., 2015a. Seismic stratigraphy of the central South China Sea Basin and implications for neotectonics. *Journal of Geophysical Research: Solid Earth,* 120(3):1377–1399. **https://doi.org/10.1002/2014JB011686**

Li, C.-F., Lin, J., Kulhanek, D.K., Williams, T., Bao, R., Briais, A., Brown, E.A., Chen, Y., Clift, P.D., Colwell, F.S., Dadd, K.A., Ding, W., Hernández-Almeida, I., Huang, X.-L., Hyun, S., Jiang, T., Koppers, A.A.P., Li, Q., Liu, C., Liu, Q., Liu, Z., Nagai, R.H., Peleo-Alampay, A., Su, X., Sun, Z., Tejada, M.L.G., Trinh, H.S., Yeh, Y.-C., Zhang, C., Zhang, F., Zhang, G.-L., and Zhao, X., 2015b. Expedition 349 summary. *In* Li, C.-F., Lin, J., Kulhanek, D.K., and the Expedition 349 Scientists, *South China Sea Tectonics.* Proceedings of the International Ocean Discovery Program, 349: College Station, TX (International Ocean Discovery Program). **https://doi.org/10.14379/iodp.proc.349.101.2015**

Li, C.-F., Zhou, Z., Li, J., Chen, B., and Geng, J., 2008. Magnetic zoning and seismic structure of the South China Sea ocean basin. *Marine Geophysical Researches,* 29(4):223–238. **https://doi.org/10.1007/s11001-008-9059-4**

Lowe, D.R., 1982. Sediment gravity flows, II. Depositional models with special reference to the deposits of high-density turbidity currents. *Journal of Sedimentary Petrology,* 52(1):279–297. **https://doi.org/10.1306/212F7F31-2B24-11D7-8648000102C1865D**

Löwemark, L., 2015. Testing ethological hypotheses of the trace fossil *Zoophycos* based on Quaternary material from the Greenland and Norwegian Seas. *Palaeogeography, Palaeoclimatology, Palaeoecology,* 425:1–13. **https://doi.org/10.1016/j.palaeo.2015.02.025**

Lurcock, P.C., and Wilson, G.S., 2012. PuffinPlot: a versatile, user-friendly program for paleomagnetic analysis. *Geochemistry, Geophysics, Geosystems,* 13(6):Q06Z45. **https://doi.org/10.1029/2012GC004098**

Makris, J., Papoulia, J., McPherson, S., and Warner, L., 2012. Mapping of sediments and crust offshore Kenya, East Africa: a wide aperture refraction/reflection Survey. In *SEG Technical Program Expanded Abstracts 2012:* Tulsa, OK (Society of Exploration Geophysicists). **https://doi.org/10.1190/segam2012-0426.1**

Müller, A., and Mathesius, U., 1999. The palaeoenvironments of coastal lagoons in the southern Baltic Sea, I. The application of sedimentary C_{org}/N ratios as source indicators of organic matter. *Palaeogeography, Palaeoclimatology, Palaeoecology,* 145(1–3):1–16. **https://doi.org/10.1016/S0031-0182(98)00094-7**

Pearce, J.A., and Cann, J.R., 1973. Tectonic setting of basic volcanic rocks determined using trace element analyses. *Earth and Planetary Science Letters,* 19(2):290–300. **https://doi.org/10.1016/0012-821X(73)90129-5**

Pickering, K.T., Hiscott, R.N., and Hein, F.J., 1989. Facies, processes, sequences and controls. *In* Pickering, K.T., Hiscott, R.N., and Hein, F.J., (Eds.), *Deep-Marine Environments: Clastic Sedimentation and Tectonics:* London (Unwin Hyman), 13–40.

Rhodes, J.M., 1996. Geochemical stratigraphy of lava flows sampled by the Hawaii Scientific Drilling Project. *Journal of Geophysical Research: Solid Earth,* 101(B5):11729–11746. **https://doi.org/10.1029/95JB03704**

Sato, T., Murakami, T., and Watanabe, T., 1996. Change in layer charge of smectites and smectite layers in illite/smectite during diagenetic alteration. *Clays and Clay Minerals,* 44(4):460–469. **https://doi.org/10.1346/CCMN.1996.0440403**

Shervais, J.W., 1982. Ti-V plots and the petrogenesis of modern and ophiolitic lavas. *Earth and Planetary Science Letters,* 59(1):101–118. **https://doi.org/10.1016/0012-821X(82)90120-0**

Shipboard Scientific Party, 2000. Leg 184 summary: exploring the Asian monsoon through drilling in the South China Sea. *In* Wang, P., Prell, W.L., Blum, P., et al., *Proceedings of the Ocean Drilling Program, Initial Reports,* 184: College Station, TX (Ocean Drilling Program), 1–77. **https://doi.org/10.2973/odp.proc.ir.184.101.2000**

Sibuet, J.-C., and Tucholke, B.E., 2012. The geodynamic province of transitional lithosphere adjacent to magma-poor continental margins. *Geological Society Special Publication,* 369:429–452. **https://doi.org/10.1144/SP369.15**

Stow, D.A.V., and Shanmugam, G., 1980. Sequences of structures in fine-grained turbidites: comparison of recent deep-sea and ancient flysch sediments. *Sedimentary Geology,* 25(1–2):23–42. **https://doi.org/10.1016/0037-0738(80)90052-4**

Sun, Z., Jian, Z., Stock, J.M., Larsen, H.C., Klaus, A., Alvarez Zarikian, C.A., Boaga, J., Bowden, S.A., Briais, A., Chen, Y., Cukur, D., Dadd, K.A., Ding, W., Dorais, M.J., Ferré, E.C., Ferreira, F., Furusawa, A., Gewecke, A.J., Hinojosa, J.L., Höfig, T.W., Hsiung, K.-H., Huang, B., Huang, E., Huang, X.-L., Jiang, S., Jin, H., Johnson, B.G., Kurzawski, R.M., Lei, C., Li, B., Li, L., Li, Y., Lin, J., Liu, C., Liu, C., Liu, Z., Luna, A., Lupi, C., McCarthy, A.J., Mohn, G., Ningthoujam, L.S., Nirrengarten, M., Osono, N., Peate, D.W., Persaud, P., Qui, N., Robinson, C.M., Satolli, S., Sauermilch, I., Schindlbeck, J.C., Skinner, S.M., Straub, S.M., Su, X., Tian, L., van der Zwan, F.M., Wan, S., Wu, H., Xiang, R., Yadav, R., Yi, L., Zhang, C., Zhang, J., Zhang, Y., Zhao, N., Zhong, G., and Zhong, L., 2018a. Expedition 367/368 methods. *In* Sun, Z., Jian, Z., Stock, J.M., Larsen, H.C., Klaus, A., Alvarez Zarikian, C.A., and the Expedition 367/368 Scientists, *South China Sea Rifted Margin*. Proceedings of the International Ocean Discovery Program, 367/368: College Station, TX (International Ocean Discovery Program). **https://doi.org/10.14379/iodp.proc.367368.102.2018**

Sun, Z., Stock, J.M., Klaus, A., Larsen, H.C., Jian, Z., Alvarez Zarikian, C.A., Boaga, J., Bowden, S.A., Briais, A., Chen, Y., Cukur, D., Dadd, K.A., Ding, W., Dorais, M.J., Ferré, E.C., Ferreira, F., Furusawa, A., Gewecke, A.J.,

Hinojosa, J.L., Höfig, T.W., Hsiung, K.-H., Huang, B., Huang, E., Huang, X.-L., Jiang, S., Jin, H., Johnson, B.G., Kurzawski, R.M., Lei, C., Li, B., Li, L., Li, Y., Lin, J., Liu, C., Liu, C., Liu, Z., Luna, A., Lupi, C., McCarthy, A.J., Mohn, G., Ningthoujam, L.S., Nirrengarten, M., Osono, N., Peate, D.W., Persaud, P., Qui, N., Robinson, C.M., Satolli, S., Sauermilch, I., Schindlbeck, J.C., Skinner, S.M., Straub, S.M., Su, X., Tian, L., van der Zwan, F.M., Wan, S., Wu, H., Xiang, R., Yadav, R., Yi, L., Zhang, C., Zhang, J., Zhang, Y., Zhao, N., Zhong, G., and Zhong, L., 2018b. Site U1499. *In* Sun, Z., Jian, Z., Stock, J.M., Larsen, H.C., Klaus, A., Alvarez Zarikian, C.A., and the Expedition 367/368 Scientists, *South China Sea Rifted Margin*. Proceedings of the International Ocean Discovery Program, 367/368: College Station, TX (International Ocean Discovery Program). **https://doi.org/10.14379/iodp.proc.367368.103.2018**

Sun, Z., Stock, J., Jian, Z., McIntosh, K., Alvarez Zarikian, C.A., and Klaus, A., 2016. *Expedition 367/368 Scientific Prospectus: South China Sea Rifted Margin.* International Ocean Discovery Program. **https://doi.org/10.14379/iodp.sp.367368.2016**

Wetzel, A., 2002. Modern *Nereites* in the South China Sea—ecological association with redox conditions in the sediment. *Palaios,* 17(5):507–515. **https://doi.org/10.1669/0883-1351(2002)017<0507:MNITSC>2.0.CO;2**

Wetzel, A., 2009. The preservation potential of ash layers in the deep-sea: the example of the 1991-Pinatubo ash in the South China Sea. *Sedimentology,* 56(7):1992–2009. **https://doi.org/10.1111/j.1365-3091.2009.01066.x**

Weyl, P.K., 1959. Pressure solution and the force of crystallization—a phenomenological theory. *Journal of Geophysical Research,* 64(11):2001–2025. **https://doi.org/10.1029/JZ064i011p02001**

Young, J.R., Bown, P.R., and Lees, J.A. (Eds.). Nannotax3. **http://ina.tmsoc.org/Nannotax3**

Zhao, X., Riisager, P., Antretter, M., Carlut, J., Lippert, P., Liu, Q., Galbrun, B., Hall, S., Delius, H., and Kanamatsu, T., 2006. Unraveling the magnetic carriers of igneous cores from the Atlantic, Pacific, and the southern Indian oceans with rock magnetic characterization. *In* Sager, W.W., Acton, G.D., Clement, B.M., and Fuller, M. (Eds.), *ODP Contributions to Paleomagnetism.* Physics of The Earth and Planetary Interiors, 156(3–4):294–328. **https://doi.org/10.1016/j.pepi.2005.08.005**

Zhou, X.M., and Li, W.X., 2000. Origin of late Mesozoic igneous rocks in southeastern China: implications for lithosphere subduction and underplating of mafic magmas. *Tectonophysics,* 326(3–4):269–287. **https://doi.org/10.1016/S0040-1951(00)00120-7**

Zijderveld, J.D.A., 1967. AC demagnetization of rocks: analysis of results. *In* Collinson, D.W., Creer, K.M., and Runcorn, S.K. (Eds.), *Developments in Solid Earth Geophysics* (Volume 3): *Methods in Palaeomagnetism:* Amsterdam (Elsevier), 254–286. **https://doi.org/10.1016/B978-1-4832-2894-5.50049-5**

Sun, Z., Jian, Z., Stock, J.M., Larsen, H.C., Klaus, A., Alvarez Zarikian, C.A., and the Expedition 367/368 Scientists
Proceedings of the International Ocean Discovery Program Volume 367/368
publications.iodp.org

https://doi.org/10.14379/iodp.proc.367368.105.2018

Site U1501[1]

Check for updates

Hans Christian Larsen, Zhimin Jian, Carlos A. Alvarez Zarikian, Zhen Sun, Joann M. Stock, Adam Klaus, Jacopo Boaga, Stephen A. Bowden, Anne Briais, Yifeng Chen, Deniz Cukur, Kelsie A. Dadd, Weiwei Ding, Michael J. Dorais, Eric C. Ferré, Fabricio Ferreira, Akira Furusawa, Aaron J. Gewecke, Jessica L. Hinojosa, Tobias W. Höfig, Kan-Hsi Hsiung, Baoqi Huang, Enqing Huang, Xiao-Long Huang, Shijun Jiang, Haiyan Jin, Benjamin G. Johnson, Robert M. Kurzawski, Chao Lei, Baohua Li, Li Li, Yanping Li, Jian Lin, Chang Liu, Chuanlian Liu, Zhifei Liu, Antonio Luna, Claudia Lupi, Anders J. McCarthy, Geoffroy Mohn, Lachit Singh Ningthoujam, Michael Nirrengarten, Nobuaki Osono, David W. Peate, Patricia Persaud, Ning Qiu, Caroline M. Robinson, Sara Satolli, Isabel Sauermilch, Julie C. Schindlbeck, Steven M. Skinner, Susanne M. Straub, Xiang Su, Liyan Tian, Froukje M. van der Zwan, Shiming Wan, Huaichun Wu, Rong Xiang, Rajeev Yadav, Liang Yi, Cuimei Zhang, Jinchang Zhang, Yang Zhang, Ning Zhao, Guangfa Zhong, and Lifeng Zhong[2]

Keywords: International Ocean Discovery Program, IODP, *JOIDES Resolution*, Expedition 367, Expedition 368, Site U1501, northern South China Sea, continent–ocean transition zone, outer margin high, hyperextension, continental breakup, thinning, rifting, basement, Cenozoic, Mesozoic, prerift, land facies, Eocene marine deposition, subsidence

Contents

1 Site summary
6 Background and objectives
7 Operations
11 Lithostratigraphy
24 Structural geology
26 Biostratigraphy
33 Paleomagnetism
41 Geochemistry
49 Physical properties
53 Downhole measurements
56 Correlation to seismic data
61 References

Site summary

Background and objectives

Site U1501 (proposed Site SCSII-41A; 18°53.0923′N, 115°45.9455′E) (Sun et al., 2016) within the South China Sea (SCS) northern margin (Figure **F1**) is located on a broad regional basement high (outer margin high [OMH]). The OMH is the most landward of four distinct highs within the continent–ocean transition (COT) and is followed seaward by Ridges A, B, and C (Figures **F2**, **F3**, **F4**). Site U1501 is located at 2845.8 m below sea level (mbsl). Small rift basins of presumed Paleogene age are located on top of the OMH (Figure **F2**). These basins can be traced landward into much deeper half-graben basins that formed during the main phase of crustal extension. The rift basins located on the OMH, therefore, offer options to recover the stratigraphy of these basins by drilling to moderate depths, testing existing stratigraphic interpretations, and extrapolating the findings margin wide. Recovering and characterizing these sequences were key objectives at Site U1501, and the specific goal was to constrain the timing and duration of crustal extension, the tectonic vertical movements during rifting, and the subsequent postrift thermal subsidence. The crystalline basement at Site U1501 is most likely located far below the acoustic basement at ≈600 m and was not an objective for this site.

At 2846 mbsl, Site U1501 is one of the few Ocean Drilling Program (ODP) and Integrated Ocean Drilling Program sites in the SCS above the modern carbonate compensation depth (CCD) of the SCS. Sites U1504 and U1505, also at the OMH, are situated at <3000 mbsl. The younger stratigraphy is therefore also the focus of some secondary scientific objectives related to Neogene environmental development of the SCS and adjacent landmasses of Southeast Asia. Among these secondary objectives are to (1) reconstruct the history of the east Asian monsoon evolution and of deepwater exchanges between the SCS and Pacific Ocean and (2) explore the sedimentary responses to the Cenozoic regional tectonic and environmental development of the Southeast Asia margin.

[1] Larsen, H.C., Jian, Z., Alvarez Zarikian, C.A., Sun, Z., Stock, J.M., Klaus, A., Boaga, J., Bowden, S.A., Briais, A., Chen, Y., Cukur, D., Dadd, K.A., Ding, W., Dorais, M.J., Ferré, E.C., Ferreira, F., Furusawa, A., Gewecke, A.J., Hinojosa, J.L., Höfig, T.W., Hsiung, K.-H., Huang, B., Huang, E., Huang, X.-L., Jiang, S., Jin, H., Johnson, B.G., Kurzawski, R.M., Lei, C., Li, B., Li, L., Li, Y., Lin, J., Liu, C., Liu, C., Liu, Z., Luna, A., Lupi, C., McCarthy, A.J., Mohn, G., Ningthoujam, L.S., Nirrengarten, M., Osono, N., Peate, D.W., Persaud, P., Qui, N., Robinson, C.M., Satolli, S., Sauermilch, I., Schindlbeck, J.C., Skinner, S.M., Straub, S.M., Su, X., Tian, L., van der Zwan, F.M., Wan, S., Wu, H., Xiang, R., Yadav, R., Yi, L., Zhang, C., Zhang, J., Zhang, Y., Zhao, N., Zhong, G., and Zhong, L., 2018. Site U1501. *In* Sun, Z., Jian, Z., Stock, J.M., Larsen, H.C., Klaus, A., Alvarez Zarikian, C.A., and the Expedition 367/368 Scientists, *South China Sea Rifted Margin*. Proceedings of the International Ocean Discovery Program, 367/368: College Station, TX (International Ocean Discovery Program). https://doi.org/10.14379/iodp.proc.367368.105.2018

[2] **Expedition 367/368 Scientists' addresses.**

MS 367368-105: Published 28 September 2018

This work is distributed under the **Creative Commons Attribution 4.0 International** (CC BY 4.0) license.

Figure F1. Bathymetric maps showing Expedition 367/368 sites (stars), and (A) regional and (B) local coverage of multichannel seismic reflection data and OBS data. Thick blue and red lines are key seismic lines used for planning of the drilling transect. A. Magnetic isochrons (orange lines) from Briais et al. (1993). B. Magnetic picks (orange squares) from the same reference, extracted from the Seton et al. (2014) compilation. Chron labels for the picks correspond to the old edge of the normal polarity intervals (see Ogg et al. [2016] timescale for ages). Orange square = Leg 184 Site 1148, yellow squares = Expedition 349 Sites U1432 and U1435.

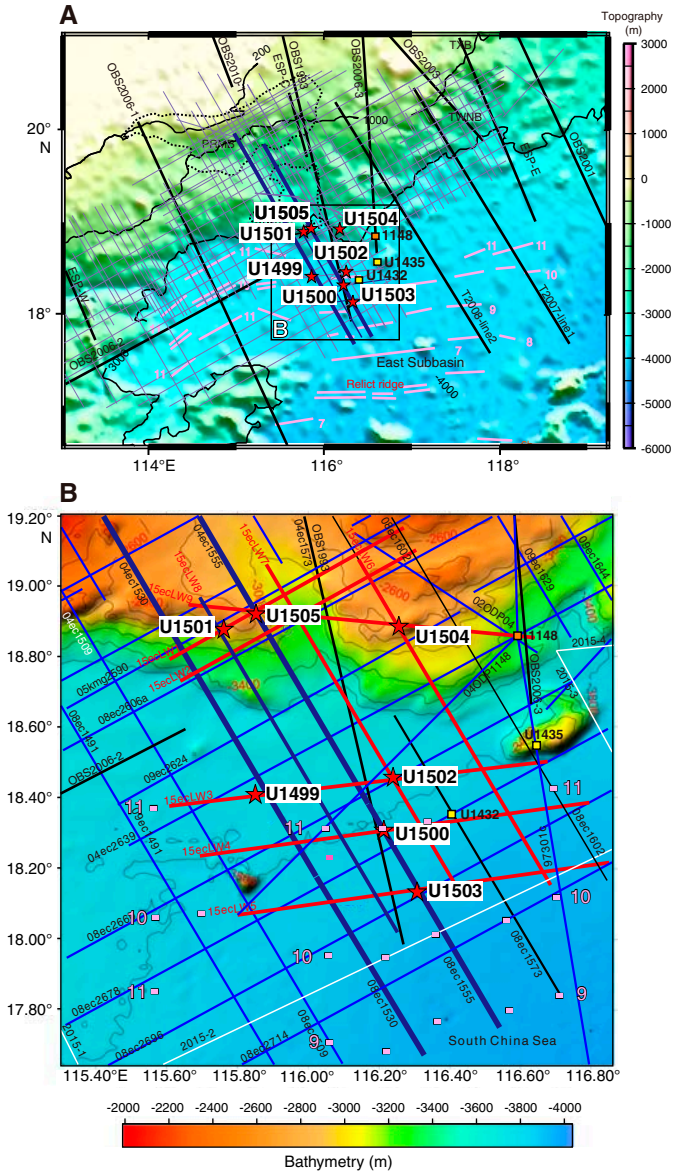

Operations

We conducted operations in four holes at Site U1501. In Holes U1501A and U1501B, Core 1H missed the sediment–water interface and retrieved full core barrels, indicating that the core was shot from below the seafloor. Hole U1501C (18°53.0919′N, 115°45.9485′E; 2846 mbsl) was cored with the advanced piston corer (APC) system from the seafloor to 461.8 m and recovered 447.8 m (96.3%). Hole U1501D (18°53.0929′N, 115°45.9370′E; 2846 mbsl) was drilled without coring from the seafloor to 433.5 m and then cored with the rotary core barrel (RCB) system to 644.3 m. A total of 78.8 m of core was recovered (37.4%). Hole U1501D was logged with the triple combo tool string from 113 to 299.3 m.

Lithostratigraphy

The sedimentary succession recovered at Site U1501 is composed of clay-rich nannofossil ooze, silty clay, clayey silt, sand, siltstone, sandstone with minor conglomerate, and rare volcanic ash. The succession is divided into three major lithostratigraphic units (I, II, and III) distinguished on the basis of sediment composition, particularly the relative abundance of the calcareous and siliciclastic fractions (Figure **F30**).

Lithostratigraphic Unit I is a 303 m thick, Holocene–upper Oligocene succession dominated by clay-rich nannofossil ooze and nannofossil ooze with clay, with minor amounts of nannofossil-rich foraminifer sand or silty sand. A felsic volcanic ash layer occurs in Section 368-U1501A-1H-7, and an ash pod was observed in Section 368-U1501C-3H-1. Unit I is divided into the following subunits:

- Subunit IA (0–25.47 m),
- Subunit IB (25.47–66.17 m),
- Subunit IC (66.30–156.70 m),
- Subunit ID (156.80–191.99 m),
- Subunit IE (191.99–293.09 m), and
- Subunit IF (293.90–303.01 m).

These divisions are based on changes in lithology, particularly the clay to nannofossil ratio, the presence and abundance of foraminifers, and/or physical properties. The lower contact of Unit I is erosional and marked by the emplacement of a poorly sorted sandy layer. At the boundary, marked changes in *P*-wave velocity, natural gamma radiation (NGR), magnetic susceptibility, porosity, moisture and density (MAD), color, carbonate content, and biostratigraphy indicate a small hiatus (Figure **F30**). Unit I was deposited in a deep-marine environment, and lithologic changes between subunits likely reflect the amount of terrigenous input into a relatively open ocean setting. This input may be delivered as buoyant sediment plumes from shallower shelf environments and rarely by weak (distal) turbidity currents. Soft-sediment deformation in Subunit IB indicates slumping downslope of parts of the sequence.

Lithostratigraphic Unit II is 296 m thick and late Oligocene to late Eocene in age. The unit consists of variable amounts of clay, silt, and sand with minor nannofossil-rich clay, nannofossil ooze, and silt with organic matter. Gravel-sized grains occur, including shell fragments and glauconite, as well as carbonate and pyrite concretions. Unit II is divided into six subunits:

- Subunit IIA (303.01–385.26 m),
- Subunit IIB (388.80–452.69 m),
- Subunit IIC (452.60–482.33 m),
- Subunit IID (491.00–519.80 m),
- Subunit IIE (529.30–548.64 m), and
- Subunit IIF (548.64–598.91 m).

The uppermost two subunits define a fining-upward succession of glauconite-sand dominated to siltstone and clay overlain by clay with nannofossils. Subunits IIC and IE are dominated by sandstone with calcite; Subunit IID has more fine-grained, organic-rich lithologies; and Subunit IIF is similar to Subunit IIB but has more coarse-grained sediment and distinctive weak red and reddish gray intervals within the green glauconite-bearing sands. Coarse sand–to pebble-sized shell fragments are common in Unit II, and coral fragments were occasionally observed in the upper part of the unit.

Figure F2. Deep crustal time-migrated seismic reflection data without and with interpretation. Note the rather thin lower crust (two layers) above a strong Mohorovičić seismic discontinuity (Moho) reflector that can be followed oceanward. Moho reflection is weak to absent seaward from around the interpreted COT. Wide-angle seismic data (Yan et al., 2001) confirm ~6 km thick ocean crust (OC) seaward of COT. Large detachment fault ~150 km inland of COT separates more stable crust landward from that of highly extended crust seaward. OMH is a fairly consistent feature margin along this margin segment. Key seismic unconformities are shown in purple (T70; ~32 Ma breakup unconformity?) and blue (T60; ~23 Ma regional basin event). These ages are inferred from long distance (>100 km) correlation of seismic unconformities with industry holes and ODP Leg 184 Site 1148 (T60); ages need confirmation by coring and are only tentative. Tg reflector (green) is basement. Arrows = approximate positions of seafloor magnetic anomalies with chron numbers. Seismic data are from Line 04ec1555-08ec1555 (courtesy of Chinese National Offshore Oil Corporation [CNOOC]). Location of line is shown in Figure F1. C11n, C10n, and C9n = possible chrons. MSB = midslope basin.

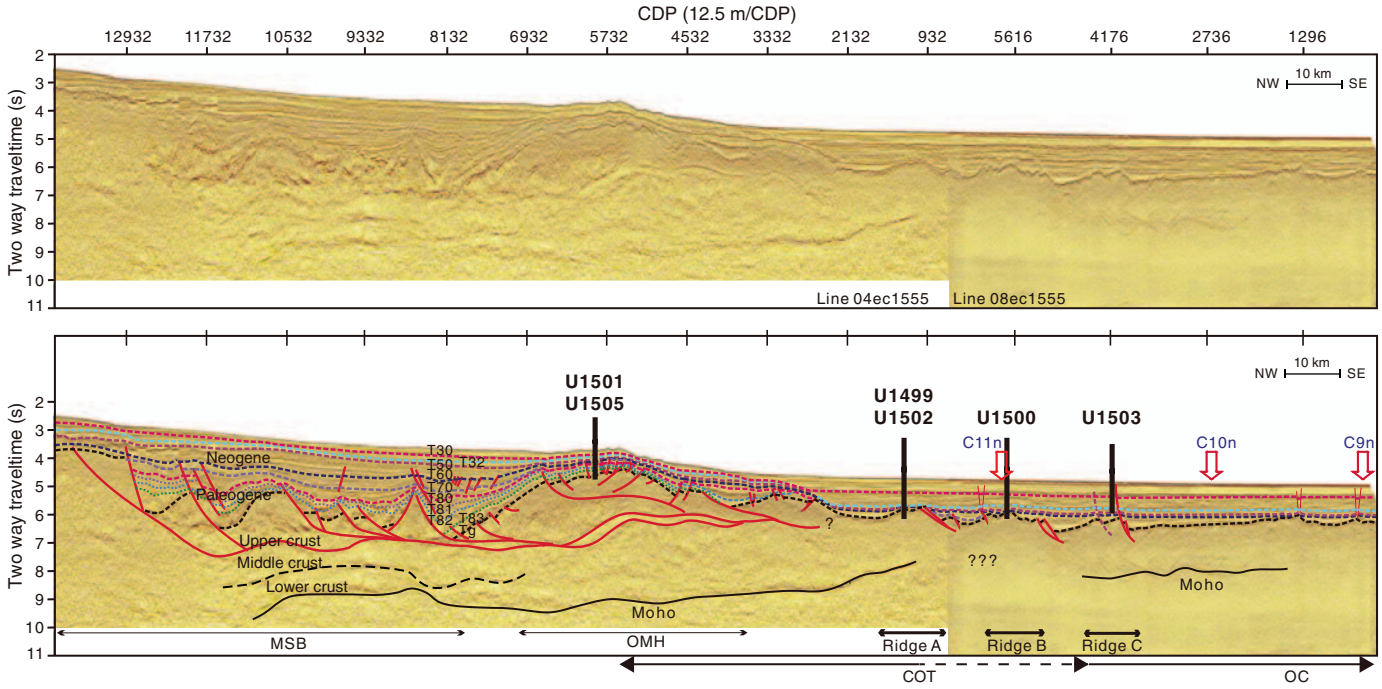

Glauconite and quartz minerals dominate the siliciclastic grain component. Diagenetic pyrite is common. Unit II most likely represents a gradual change upward from shallow-water (outer shelf or upper continental slope) to deepwater (lower slope) depositional environments. The Unit II/III boundary was not recovered but is marked by an abrupt change in magnetic susceptibility, NGR, and *P*-wave velocity. A change in the apparent dip of strata from near horizontal in Unit II to ~20° in Unit III suggests that the contact is unconformable.

Lithostratigraphic Unit III (598.91 m to the bottom of the hole) is well lithified and composed of poorly sorted, feldspar-rich sandstone interbedded with moderately to well-sorted, medium- to fine-grained sandstone and, rarely, siltstone and poorly sorted conglomerate. The age is unknown because no fossils were recognized. Unit III is divided into two subunits: IIIA (598.91–629.79 m) and IIIB (629.79–643.56 m). Subunit IIIA is composed of coarse-grained heterolithic sandstone, sandstone with calcite clasts, and minor conglomerate and siltstone. Pebble- to cobble-sized clasts include felsic intrusive and volcanic rocks, sedimentary rocks, metamorphic rocks, and rare gabbro. Subunit IIIB consists of sandstone and minor sandstone with organic matter. Subunit IIIB is finer grained than Subunit IIIA and has finely laminated intervals. We speculate that Unit III was formed in continental to littoral environments with a provenance not far from the site.

Structural geology

Unit I shows predominantly horizontal to subhorizontal bedding with local soft-sediment deformation structures such as slump folds. Unit I is devoid of any structures related to tectonic deformation, apart from some rare normal faults with minor offsets.

Unit II is characterized by subhorizontal to gently dipping bedding. Steep dips up to 40° are locally observed in close relation to parallel lamination and are therefore interpreted as cross-laminae. In contrast to Unit I, deformation structures were observed within Unit II, although their occurrence is rather heterogeneously distributed. Planar to irregular millimeter-scale normal faults and joints were observed in Subunit IIA, typically with offsets ranging from 0.1 to 0.5 cm and apparent dips of 10°–40°. Striations and slickensides were documented locally where the surfaces of such structures are exposed. Deformation in the underlying Subunits IIC–IIF is essentially characterized by randomly distributed occurrence of single to branched uniform calcite and quartz veins. Recognition of deformational structures was difficult due to drilling disturbance throughout this unit.

The acoustic basement marks the top of Unit III. This unit shows a weak tilting of stratified beds expressed in apparent dips on split core surfaces up to ~20°. Again, deformation structures remain scarce and heterogeneously distributed in Unit III. The recognized

Figure F3. Two-way traveltime to (A) basement (Tg reflector) and (B) T60 unconformity. Proposed drilling transect (thick black line) is approximately at the center of a margin segment bounded to the southwest by a transform fault. Northeastern boundary of margin segment around Site U1435. At this location, OMH and Ridge A seem to coalesce, and Ridges B and C in COT become indistinct toward the northeast within the next margin segment. Note that OMH is slightly oblique to more parallel Ridges A, B, and C.

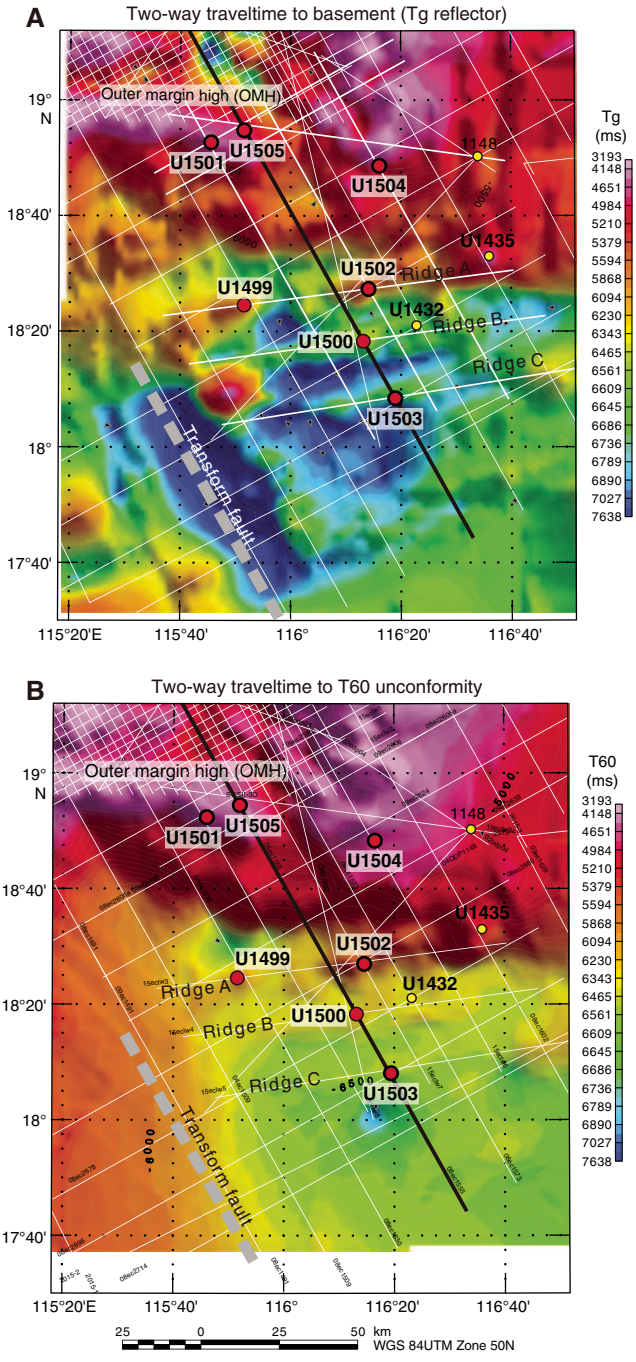

structures consist of veins, fractures, and local microfaults associated with cataclastic fault gouge.

In conclusion, despite the various tilting of reflectors (~5°) and the proximity of extensional structures observed on seismic profiles, only weak evidence of bedding tilting and/or deformation

Figure F4. Bathymetry with seismic lines, Site U1501. Note that site is not at the exact crossing of seismic Lines 15ecLW8 and 15ecLW1.

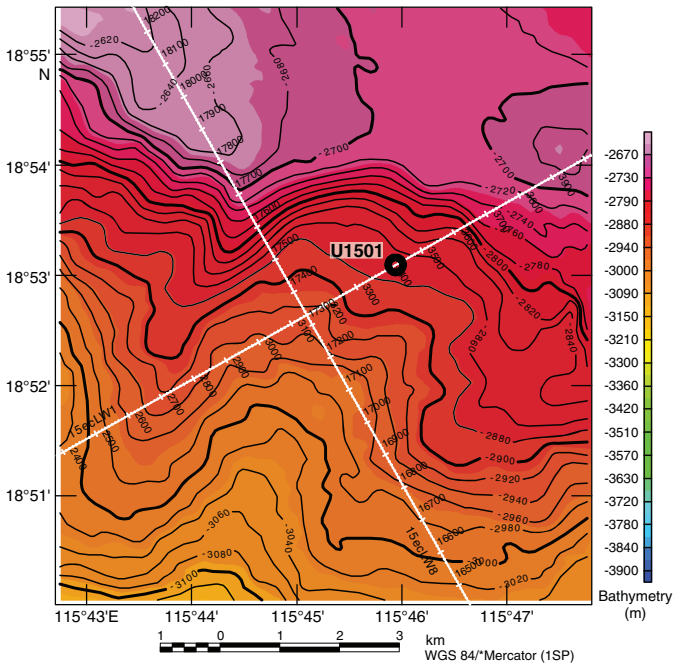

structures was observed at this site, possibly due to the nature of the sediments.

Biostratigraphy

All core catcher samples at Site U1501 were analyzed for calcareous nannofossils, diatoms, and foraminifers, with select core catchers examined for ostracods. Additional samples were taken from the split working-half sections when necessary to refine the ages between core catcher samples. Preservation of calcareous microfossils varies from good in Unit I (Cores 368-U1501A-1H, 368-U1501B-1H, and 368-U1501C-1H through 44X) to poor in Units II and III (Cores 368-U1501C-45X through 62X and 368-U1501D-2R through 5R). Planktonic foraminifers and calcareous nannofossils are abundant in Unit I, common to rare in Unit II and upper Unit III, and barren in the rest of Unit III (Cores 368-U1501D-6R though 27R). Diatoms are few with moderate preservation in Samples 368-U1501A-1H-CC, 368-U1501B-1H-CC, and 368-U1501C-1H-CC and 2H-CC. The rest of the core catcher samples are barren of diatoms with the exception of Samples 368-U1501C-3H-CC, 4H-CC, 33F-CC through 35F-CC, and 46X-CC, in which diatoms are rare with poor preservation. Diatoms are common in burrows found in interval 368-U1501C-35F-1, 118–119 cm, with poor preservation.

Forty biostratigraphic datums were identified in a mostly continuous succession from the Eocene to Holocene, which indicates that Holes U1501C and U1501D penetrated late Eocene or older strata (Figure **F30**). The Pleistocene/Pliocene boundary (~2.6 Ma) was placed within Core 368-U1501C-7H, the Pliocene/Miocene boundary (~5.3 Ma) within Core 9H, the Miocene/Oligocene boundary (~23.0 Ma) between Cores 41X and 42X, and the Oligocene/Eocene boundary (~33.9 Ma) between Cores 53X and 54X. Sedimentation rates vary from ~13 mm/ky in the early Oligocene, ~11 mm/ky in the Miocene, and ~14 mm/ky in the Pliocene to 24 mm/ky in the Pleistocene. Low sediment accumulation rates (~3.6

mm/ky) during the late Eocene through the early Oligocene and in the late Miocene suggest the presence of hiatuses in the sedimentary record during these periods. In contrast, higher sediment accumulation rates (35 mm/ky) exist during the late Oligocene and the early Miocene.

Predominance of shallow-water benthic foraminifer and ostracod assemblages in Cores 368-U1501C-45X through 62X and 368-U1501D-2R through 6R indicate an upper bathyal to continental shelf paleoenvironment during the Eocene to the early Oligocene. Predominantly abyssal benthic foraminifers and ostracods above Core 368-U1501C-44X indicate that deepwater conditions existed in this part of the SCS since the early Oligocene.

Paleomagnetism

Paleomagnetic investigations combined measurement and in-line alternating field (AF) demagnetization of archive-half sections on the 2G Enterprises superconducting rock magnetometer (SRM) with the measurement of discrete samples either AF or thermally demagnetized.

The rock magnetic experiments on six representative samples from Hole U1501C show saturation remanent magnetization (SIRM)/χ ratios between 12.8 and 14.6 kA/m, indicating the predominance of greigite in Unit I of Hole U1501C, also documented by scanning electron microscopy (SEM) in 2–10 µm grains. Thermal demagnetization behaviors show that greigite dominates the natural remanent magnetization (NRM), at least downhole to 83 m. However, the magnetic remanence left above 575°C suggests contributions from additional phases such as maghemite (Curie temperature [T_C] = ~590°–675°C) or hematite (T_C = ~675°C).

Both AF and thermal treatments on discrete samples successfully removed the steep low-temperature/coercivity component that represents the drilling overprint. The mean inclination gathered from the high-temperature component is 37.3° ± 6.6°, corresponding to a paleolatitude of 20.8° ± 3.3° for Unit I (see **Lithostratigraphy**). Many of the AF-demagnetized discrete samples reveal trends of reversed or normal polarity in the last step of demagnetization (50 mT) and are more difficult to interpret.

The magnetostratigraphy in Holes U1501C and U1501D is based on directions derived from the raw moments measured by the SRM after 25 mT demagnetization step and from the corroborative evidence from discrete samples. Magnetostratigraphy was correlated to the standard timescale and plotted along with the tie points from the microfossil ages from shipboard paleontologists. The paleomagnetic and paleontological age constraints match well over most of the section (Figure **F30**). A succession of eight normal and five reversed events was recognized in Hole U1501D. However, the lack of biostratigraphic constraints throughout Hole U1501D prevented even a tentative correlation of these events with the standard timescale.

Geochemistry

Interstitial water samples were obtained downcore to 450 m (Subunit IIB). Within Unit I, variations are mainly the result of diagenetic and microbial processes, and measurements of alkalinity, phosphate, ammonia, and sulfate are within the typical ranges for the region (3.5–5 mM alkalinity, 250–510 µM phosphate, <30 µM ammonia, and <26 µM sulfate). However, more atypically (particularly when compared to Expedition 367 Site U1499), the main changes associated with microbial processes are notable only within the uppermost 25 m in Subunit IA and are typical of organic matter degradation. Deeper than 25 m within Unit I, changes in interstitial water chemistry appear inhibited until 300 m. These changes may be a consequence of the low organic carbon concentration and high carbonate content (~50 wt%) of Unit I. Decreases in sulfate concentrations with depth are more pronounced in Unit II (>300 m), and within this zone there is heavy pyritization and total sulfur (TS) contents are high, suggesting sulfate reduction has taken place. Within the uppermost part of Unit II (300–370 m), chloride, bromide, and sodium are notably lower (chloride = 500 mM, cf. 565 mM; bromide = 0.75 mM, cf. 0.9 mM; and sodium = 410 mM, cf. 480 mM). This difference in interstitial water chemical composition is sharp and could result from pressure-isolated units retaining a distinct formation water chemistry or from the migration of chloride-poor formation water.

Headspace gas concentrations are below background laboratory levels in all samples collected from Site U1501 (<1% ppmv). Total organic carbon (TOC) content is typically <0.5 wt% in Unit I, except from 0 to 50 m (Subunit IA). Within this interval, a typical black marine mud has a TOC of ~1 wt%. TOC was also typically <0.5 wt% in Units II and III, except for a few carbonaceous lithologies: sandstones with plant phytoclasts associated with an ash-rich boghead coal in Unit II (interval 368-U1501D-9R-1, 10–15 cm) and a bitumen-impregnated sandstone in Unit III (interval 27R-1, 12–16 cm). TS content is low in Unit I: ~1 wt% in Subunit IA and below effective shipboard detection limits of 0.01 wt% for the rest of Unit I. TS content is higher in Unit II; >1 wt% in the muddier uppermost part of Unit II and an average of 0.5 wt% in the sandier, deeper part.

Elemental compositions primarily reflect geological units and changes in lithology. Within Unit I, carbonate contents are high and exceed 50 wt% within foraminifer-rich intervals (compositionally a limestone). Within Units II and III, carbonate is less common, and the units are predominantly siliciclastic with a distinction between units that are mud rich and feldspathic and sandier units toward the base of the hole. Calcium and strontium are associated with biogenic sediments in Unit I, but in deeper units they covary with aluminum. Within the base of Units II and III, sodium and potassium are both high, which is consistent with the dominant presence of feldspathic sediments. The higher aluminum proportion within the uppermost part of Unit II is consistent with the muddier, clay-rich lithologies present here.

Physical properties

Hole U150A is divided into four units based on the sediment and rock physical properties. Physical properties (PP) Unit 1 (0–300 m) experienced the most evident changes in sediment compaction, which is expressed by increasing bulk density (from 1.4 to 2.0 g/cm^3) and *P*-wave velocities (from 1450 to 1930 m/s) and decreasing porosity (from 85% to 45%) with depth. Because PP Unit 1 consists mostly of calcareous ooze, it has relatively low NGR (between 20 and 40 counts/s) and magnetic susceptibility (between 10^{-6} and 10^{-5} SI). The onset of PP Unit 2 (300–450 m) is marked by a rapid increase in NGR and porosity values and a rapid decrease in bulk densities and *P*-wave velocities, corresponding to a shift to a different lithologic unit with sand, silt, and clay-enriched sediments. Within the entire unit, NGR is persistently high (60–80 counts/s), whereas magnetic susceptibility remains as low as 10×10^{-5} SI. *P*-wave velocities and bulk densities continue to increase with core depth. Most physical properties of PP Unit 3 (450–600 m) have similar values to those of Unit 2, except that *P*-wave velocities are extremely high, up to 4000–6000 m/s at some interbeds, and bulk densities and porosities increase and decrease to 2.6 g/cm^3 and 2%–3%, respectively, at parallel depths. PP Unit 4 (600–657 m) is dis-

tinct from other units due to higher mean values of NGR (80 counts/s), bulk density (2.6 g/cm^3), magnetic susceptibility (500 × 10^{-5} SI), and *P*-wave velocity (4500 m/s). Throughout the hole (0–657 m), thermal conductivities increase from 0.7 to 3.4 W/(m·K), most likely as a result of increasing sediment compaction and changes in sediment compositions. L* reflectance values are highly relevant to weight percent carbonate in sediments, which exhibit relatively high L* values between 100 and 160 in the upper 300 m and thereafter remain as low as 90.

Downhole measurements

Wireline logging was conducted in Hole U1501D using a modified triple combo tool string that included the Hostile Environment Natural Gamma Ray Sonde (HNGS), Hostile Environment Litho-Density Sonde (HLDS), High-Resolution Laterolog Array (HRLA), and magnetic susceptibility sonde (MSS). The triple combo run collected good data between 115.1 m (base of the drill pipe) and 300 m, where it encountered an impenetrable obstruction. Four logging units are defined:

- Logging Unit 1 (base of the drill pipe to 190 m wireline depth below seafloor [WSF]) is characterized by intervals of large hole diameter and relatively high variability in NGR and magnetic susceptibility.
- Logging Unit 2 (190–260 m WSF) is characterized by a relatively constant hole diameter, relatively homogeneous logs, and sub-meter-scale layering.
- Logging Unit 3 (260–275 m WSF) again shows a relatively large hole diameter, as well high variability in NGR, density, and resistivity logs.
- Logging Unit 4 (275–300 m WSF) exhibits relatively large values of resistivity and magnetic susceptibility.

The upward log pass indicated a collapsed hole at ~156.3 m drilling depth below seafloor (DSF) on the caliper curve, and for safety reasons no further attempts to descend deeper than that undergauge spot were made. Because the interval of the collapsed hole was located only ~40 m below the base of the pipe, the originally planned Formation MicroScanner (FMS)-sonic tool string was not run. Four in situ formation temperature measurements were made in Hole U1501C, yielding a geothermal gradient of 81.4°C/km and a calculated heat flow of 100.1 mW/m^2. These values are comparable to the relatively high values observed at some ODP and Integrated Ocean Drilling Program sites in this part of the SCS.

Background and objectives

Site U1501 is located at 2845.8 mbsl on a broad, regional basement high (OMH) within the SCS northern margin (Figures **F2**, **F4**). The OMH features prominently in the two-way traveltime (TWT) depth to basement map and is one of four distinct basement highs found across the COT. The OMH is the most landward of these highs within the COT and is followed seaward by Ridges A, B, and C (Figure **F3**). The crustal thickness below the OMH is significantly greater than that of the ridges located more seaward within the COT. Site U1501 is located near the crossing of seismic Lines 15ecLW8 and 15ecLW1 (Figures **F5**, **F6**).

Small rift basins are located on top of the OMH (Figure **F3**). An important feature of these OMH basins is that they can be traced landward on seismic data into much deeper half-graben basins that formed during the main phase of crustal extension. The sediment fill of these basins shows development from initial rifting and half-graben fill to subsequent postrift subsidence (Figure **F2**). The seismic stratigraphy established on industry seismic data (with well control) from the inner margin is extrapolated into these deep fault basins, including those located on the OMH (Figure **F5**). Therefore, the latter offers options to recover the stratigraphy of these basins by moderately deep drilling, testing existing stratigraphic interpretations, and extrapolating the findings margin wide. The key objective of Site U1501 is to sample the stratigraphic record from one of the small rift basins on top of the OMH. Ideally, the sequence targeted by Site U1501 would represent all stages from prerift sediments through synrift to postrift fill. To recover and characterize these sequences are key objectives of Site U1501, with the specific goal of constraining the timing and duration of crustal extension, the tectonic vertical movements during rifting, and the subsequent postrift thermal subsidence. Unlike the basement at Ridges A, B, and C, the nature of the crystalline basement below the OMH is not an objective at Site U1501 and is most likely located far below the Tg horizon planned as the deepest target at the site.

The predrilling interpretation of the seismic unconformities (T30 to T83 and Tg; see **Correlation to seismic data** in the Expedition 367/368 methods chapter [Sun et al., 2018a]) around Site U1501 is shown in Figure **F5**. There are clear indications of seismic reflectors below the Tg reflector in this location, so it is not interpreted as crystalline basement. Poorly constrained seismic velocities of these strata (stacking velocities; CNOOC, unpubl. data)

Figure F5. Original and predrilling interpretation of seismic dip Line 15ecLW1 crossing with seismic Line 15ecLW8 (red tick mark) and CDPs (CDP distance = 6.25 m). Seismic stratigraphic Unconformities T20 (2.6 Ma), T30 (5.3 Ma), T32 (10.0 Ma), T40 (16 Ma), T50 (19.1 Ma), T60 (23.0), T80 (38.0 Ma), and T83 (unknown age) and acoustic basement Reflector Tg are shown. The clear but not extensively coherent seismic reflectors below Tg to ~4.7 s TWT are semiconcordant to highly discordant to Tg and interpreted as pre-Cenozoic sediments. Origin of deep, quite strong reflectors (~5 s TWT) is not interpreted.

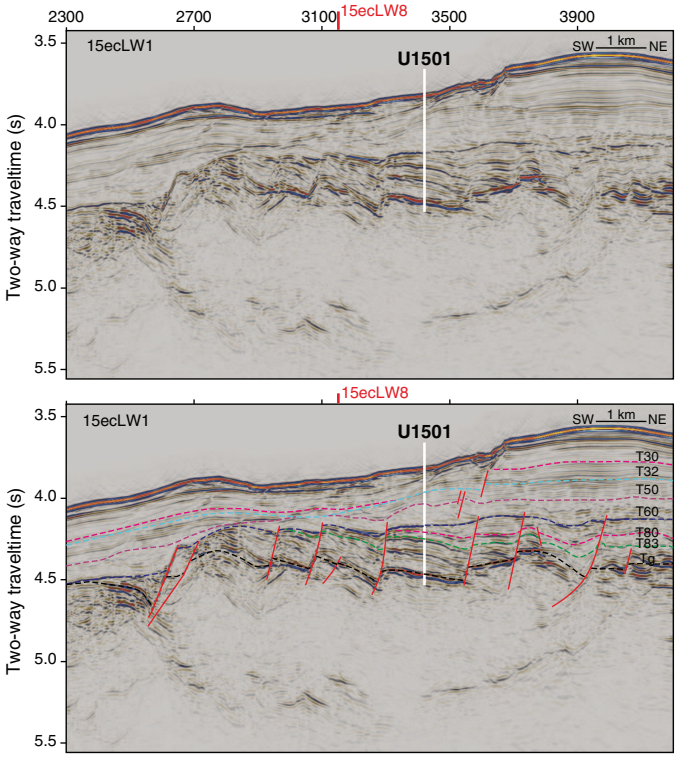

Figure F6. Original and predrilling interpretation of seismic strike Line 15ecLW8 crossing with seismic Line 15ecLW1 (red tick mark) and CDPs (CDP distance = 6.25 m). See Figure F5 for description of seismic interpretations. Dashed lines = unconformities, red solid lines = faults.

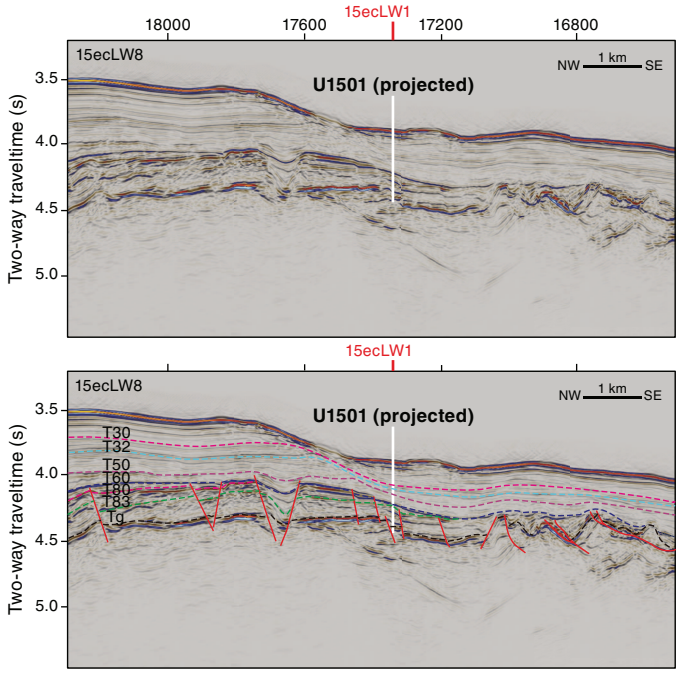

suggest that older sediments could be present. The sub-Tg reflectors seem to be approximately conformal with the overlying package of sediments just around Site U1501. However, further to the southwest of the site around common depth point (CDP) 2800, the seismic data suggest that sub-Tg strata form a tight, synclinal structure truncated by the Tg reflector (Figure **F5**). The nature and age of the strata represented by these deeper sub-Tg reflectors are completely unknown but are generally considered to be of pre-Cenozoic age in this location.

Site U1501 is located on seismic Line 15ecLW1 at CDP 3421 (Figure **F5**). This seismic line is interpreted to be close to a true dip line with regard to the tilted faults blocks (tilted northeast) because crossing seismic Line 15ecLW8 (Figure **F6**) generally shows more horizontal orientation of the strata (i.e., strike line) within the fault blocks. Note, however, that the position of Site U1501 is projected ~1700 m from the northeast into Line 15ecLW8. This projection in a structurally complex area like the OMH must therefore be accounted for in any interpretation. Nevertheless, using the velocity structure obtained from drilling for depth conversion, the dip of the post-Tg strata within the fault block drilled at Site U1501 is estimated to be ~5° toward the northeast and likely to be close to the actual dip. Using the same velocity model (see **Physical properties** and **Correlation to seismic data**), the normal faults associated with the block rotation are estimated to dip 55°–65° southwest.

The faults offset the Tg reflector as much as 75 ms TWT (90–120 m pending seismic velocities). The faults also affect the interpreted T60 unconformity, but in most places these offsets are interpreted to be more like drape structures over a tectonically generated relief with only minor fault offsets, possibly generated by differential compaction. In some places, however, the T60 unconformity can be interpreted as having been significantly faulted (e.g., around CDP 2600 at Line 15ecLW1). Nevertheless, the main faulting is interpreted to be between the age of the lowermost post-Tg strata and the age of the T60 unconformity. This entire interval is therefore an important objective with regard to the timing and environment of rifting, including vertical crustal movements.

The predrilling interpretation of the seismic stratigraphy of this critical interval shows the T83 (unknown age) and T80 (38.0 Ma) unconformities to be present above the Tg reflector and below the T60 unconformity (23.0 Ma). Sampling this interval will help us determine the environment before the SCS ocean basin formed, possibly including its earliest transgression history. However, the T70 unconformity (33.9 Ma), interpreted to represent final breakup and the approximate start of seafloor spreading, is interpreted (predrilling) to have been eroded away at the OMH by the younger T60 unconformity (Figure **F5**). However, enough of the rift-to-drift sequence would likely be in place at Site U1501 to meet our objectives, and despite several alternate drill sites that were identified, none held better prospects to recover the T70 unconformity than Site U1501. The basin-wide T60 unconformity is prominently present at Site U1501. The nature of this profound unconformity is an objective together with the post-T60 unconformity stratigraphic interval. This upper interval is expected to provide information on paleowater depth changes within the lower to middle Miocene deposits and thereby constrain the rate of thermal subsidence following initial tectonic subsidence.

The younger stratigraphy is the focus of some secondary scientific objectives related to Neogene environmental development of the SCS and adjacent landmasses of Southeast Asia. Among these objectives are (1) to reconstruct the history of the East Asian monsoon evolution and of deepwater exchanges between the SCS and Pacific Ocean and (2) to explore the sedimentary responses to the Cenozoic regional tectonic and environmental development of the Southeast Asia margin.

The water depth (2850 m) at Site U1501 makes it one of the few ODP and Integrated Ocean Drilling Program sites within the SCS above the modern CCD. Its hemipelagic deposits, rich in calcareous microfossils, enable the application of stable isotopes and faunal analyses. Key objectives were reconstructions of the monsoonal climate changes of the SCS and surrounding land and upper and deep water variations in the western Pacific Ocean. Particularly, through a comparative study with ODP Leg 184 and IODP Expedition 349 sites, Site U1501, with its sequence of prerift, synrift, and postrift sediments, will greatly help us to understand the sedimentary and paleoenvironmental responses to the tectonic events and the basin evolution experienced by the SCS.

Operations

We conducted operations in four holes at Site U1501. The original plan included two holes. The first hole was to be cored to ~650 m with the APC/extended core barrel (XCB) system, followed by downhole measurements with the triple combo and FMS-sonic tool strings. The second hole was to have a reentry system to ~640 m followed by coring to ~1063 m and logging with the triple combo, FMS-sonic, and Versatile Seismic Imager (VSI) tool strings. Actual operations differed significantly from the original plan. Mudlines were missed in Holes U1501A and U1501B, with Core 1H for each hole retrieving a full core barrel. Hole U1501C (18°53.0919′N, 115°45.9485′E; 2845.8 m water depth) was cored from the seafloor to 461.8 m and recovered 447.8 m (96%). Hole U1501D (18°53.0929′N, 115°45.9370′E; 2845.8 m water depth) was drilled without coring from the seafloor to 433.5 m and cored to 644.3 m,

recovering 78.8 m of core (37%). Coring summaries for Holes U1501A–U1501D are presented in Table T1. We also document our port call activities at the start of the expedition in this section.

Hong Kong port call

Expedition 368 South China Sea Rifted Margin started at 0754 h (all times presented are UTC + 8 h) on 9 April 2017 with the first line ashore at the China Merchants Wharf in Hong Kong. After the ship cleared immigration and customs, the Expedition 368 Co-Chief Scientists, IODP staff, and a group of 11 scientists representing each ship laboratory moved onto the ship and started crossover with their Expedition 367 counterparts. Loading and offloading operations began after clearance was issued. Sixty tons of barite were loaded. The rig crew began breaking down 68 stands of 5½ inch drill pipe and laying them out on the riser hold hatch. All life rafts were offloaded for inspection and returned prior to sailing.

The rest of the Expedition 368 scientists boarded the ship on the morning of 10 April and settled into their rooms. Later that morn-

Table T1. Site U1501 core summary. DRF = drilling depth below rig floor, DSF = drilling depth below seafloor. NA = not applicable. Core type: H = advanced piston corer, F = half-length advanced piston corer, X = extended core barrel, R = rotary core barrel, numeric core type = drilled interval. APCT-3 = advanced piston corer temperature tool. (Continued on next two pages.) **Download table in CSV format.**

Hole U1501A	
Latitude:	18°53.0922′N
Longitude:	115°45.9483′E
Seafloor (drill pipe measurement below rig floor, m DRF):	2857.11
Time on hole (days):	0.66
Total depth (drill pipe measurement from rig floor, m DRF):	2868
Distance between rig floor and sea level (m):	10.89
Total penetration (drilling depth below seafloor, m DSF):	9.5
Total length of cored section (m):	9.5
Total core recovered (m):	9.73
Core recovery (%):	102.42
Drilled interval (m):	NA
Total cores (no.):	1

Hole U1501B	
Latitude:	18°53.0922′N
Longitude:	115°45.9483′E
Seafloor (drill pipe measurement below rig floor, m DRF):	2852.11
Time on hole (days):	0.05
Total depth (drill pipe measurement from rig floor, m DRF):	2863
Distance between rig floor and sea level (m):	10.89
Total penetration (drilling depth below seafloor, m DSF):	9.5
Total length of cored section (m):	9.5
Total core recovered (m):	9.83
Core recovery (%):	103.47
Drilled interval (m):	NA
Total cores (no.):	1

Hole U1501C	
Latitude:	18°53.0919′N
Longitude:	115°45.9485′E
Seafloor (drill pipe measurement below rig floor, m DRF):	2845.81
Time on hole (days):	3.53
Total depth (drill pipe measurement from rig floor, m DRF):	2856.7
Distance between rig floor and sea level (m):	10.89
Total penetration (drilling depth below seafloor, m DSF):	461.9
Total length of cored section (m):	461.9
Total core recovered (m):	444.77
Core recovery (%):	96.29
Drilled interval (m):	NA
Total cores (no.):	62

Hole U1501D	
Latitude	18°53.0929′N
Longitude	115°45.9370′E
Seafloor (drill pipe measurement below rig floor, m DRF):	2845.82
Time on hole (days)	5.15
Total depth (drill pipe measurement from rig floor, m DRF):	2856.7
Distance between rig floor and sea level (m):	10.88
Total penetration (drilling depth below seafloor, m DSF):	644.3
Total length of cored section (m):	210.8
Total core recovered (m):	78.77
Core recovery (%):	37.37
Drilled interval (m)	433.5
Total cores (no.)	26

Core	Type	Top of interval DSF (m)	Bottom of interval DSF (m)	Interval advanced (m)	Core recovered length (m)	Curated length (m)	Recovery (%)	Time on deck UTC (h)	Time to cut core (min)	Core barrel	Mud pumped (bbl)	Driller's notes
368-U1501A-												
1	H	0.00	9.5	9.5	9.73	9.73	102	4/15/2017 16:10		Nonmagnetic		
			Hole U1501A totals:	9.5	9.73	9.73	102					
368-U1501B-												
1	H	0.00	9.5	9.5	9.83	9.83	103	4/15/2017 17:25		Nonmagnetic		
			Hole U1501B totals:	9.5	9.83	9.83	103					
368-U1501C-												
1	H	0.0	9.3	9.3	9.24	9.24	99	4/15/2017 21:30		Nonmagnetic		
2	H	9.3	18.8	9.5	8.68	8.68	91	4/15/2017 22:35	5	Nonmagnetic		
3	H	18.8	28.3	9.5	9.76	9.76	103	4/15/2017 23:35	5	Nonmagnetic		
4	H	28.3	37.8	9.5	9.78	9.78	103	4/16/2017 00:20	5	Nonmagnetic		
5	H	37.8	47.3	9.5	9.15	9.15	96	4/16/2017 01:30	5	Nonmagnetic		APCT-3
6	H	47.3	56.8	9.5	9.77	9.77	103	4/16/2017 02:25	5	Nonmagnetic		
7	H	56.8	66.3	9.5	9.42	9.42	99	4/16/2017 03:30	5	Nonmagnetic		
8	H	66.3	75.8	9.5	9.51	9.51	100	4/16/2017 04:45	5	Nonmagnetic		APCT-3
9	H	75.8	85.3	9.5	9.70	9.70	102	4/16/2017 05:40	5	Nonmagnetic		
10	H	85.3	94.8	9.5	9.61	9.61	101	4/16/2017 06:25	5	Nonmagnetic		
11	H	94.8	104.3	9.5	10.11	10.11	106	4/16/2017 07:50	5	Nonmagnetic		APCT-3
12	H	104.3	113.8	9.5	9.67	9.67	102	4/16/2017 09:00	5	Nonmagnetic		
13	H	113.8	123.3	9.5	10.03	10.03	106	4/16/2017 09:50	5	Nonmagnetic		
14	H	123.3	132.8	9.5	8.23	8.23	87	4/16/2017 11:05	10	Nonmagnetic		APCT-3
15	H	132.8	142.3	9.5	9.39	9.39	99	4/16/2017 12:10	10	Nonmagnetic		
16	H	142.3	151.8	9.5	9.50	9.50	100		10	Nonmagnetic		
17	H	151.8	156.8	5.0	4.95	4.95	99	4/16/2017 14:15	10	Nonmagnetic		

Table T1 (continued). (Continued on next page.)

Core	Type	Top of interval DSF (m)	Bottom of interval DSF (m)	Interval advanced (m)	Core recovered length (m)	Curated length (m)	Recovery (%)	Time on deck UTC (h)	Time to cut core (min)	Core barrel	Mud pumped (bbl)	Driller's notes
18	F	156.8	161.5	4.7	4.92	4.92	105	4/16/2017 15:40	5	Nonmagnetic		
19	F	161.5	166.2	4.7	4.80	4.80	102	4/16/2017 16:30	10	Nonmagnetic		
20	F	166.2	170.9	4.7	3.77	3.77	80	4/16/2017 17:20	5	Nonmagnetic		
21	F	170.9	175.6	4.7	5.07	5.07	108	4/16/2017 18:10	10	Nonmagnetic		
22	F	175.6	180.3	4.7	5.00	5.00	106	4/16/2017 19:00	5	Nonmagnetic		
23	F	180.3	185.0	4.7	4.15	4.15	88	4/16/2017 19:50	10	Nonmagnetic		
24	F	185.0	189.7	4.7	4.47	4.47	95	4/16/2017 20:45	5	Nonmagnetic		
25	F	189.7	194.4	4.7	3.65	3.65	78	4/16/2017 21:35	10	Nonmagnetic		
26	F	194.4	199.1	4.7	3.98	3.98	85	4/16/2017 22:20	5	Nonmagnetic		
27	F	199.1	203.8	4.7	4.98	4.98	106	4/16/2017 23:20	10	Nonmagnetic	15	
28	F	203.8	208.5	4.7	4.90	4.90	104	4/17/2017 00:10	5	Nonmagnetic		
29	F	208.5	213.2	4.7	4.22	4.22	90	4/17/2017 01:05	10	Nonmagnetic		
30	F	213.2	217.9	4.7	4.39	4.39	93	4/17/2017 01:50	5	Nonmagnetic		
31	F	217.9	222.6	4.7	3.68	3.68	78	4/17/2017 02:40	10	Nonmagnetic		
32	F	222.6	227.3	4.7	3.87	3.87	82	4/17/2017 03:30	5	Nonmagnetic		
33	F	227.3	232.0	4.7	4.53	4.53	96	4/17/2017 04:20	10	Nonmagnetic		
34	F	232.0	236.7	4.7	3.72	3.72	79	4/17/2017 05:15	5	Nonmagnetic		
35	F	236.7	241.4	4.7	3.43	3.43	73	4/17/2017 06:05	10	Nonmagnetic		
36	F	241.4	246.1	4.7	3.88	3.88	83	4/17/2017 06:55	10	Nonmagnetic		
37	F	246.1	250.8	4.7	3.25	3.25	69	4/17/2017 07:45	10	Nonmagnetic		
38	F	250.8	255.5	4.7	2.72	2.72	58	4/17/2017 08:45	10	Nonmagnetic		
39	F	255.5	257.0	1.5	1.36	1.36	91	4/17/2017 09:30	10	Nonmagnetic		
40	X	257.0	264.0	7.0	8.35	8.35	119	4/17/2017 11:20	35			
41	X	264.0	273.7	9.7	9.91	9.91	102	4/17/2017 12:45	40			
42	X	273.7	283.3	9.6	9.76	9.76	102	4/17/2017 14:05	30			
43	X	283.3	292.9	9.6	9.85	9.85	103	4/17/2017 15:30	35			
44	X	292.9	302.5	9.6	9.66	9.66	101	4/17/2017 16:50	30			
45	X	302.5	312.1	9.6	9.70	9.70	101	4/17/2017 18:15	40			
46	X	312.1	321.7	9.6	9.71	9.71	101	4/17/2017 19:40	30			
47	X	321.7	331.3	9.6	9.48	9.48	99	4/17/2017 21:15	45			
48	X	331.3	340.8	9.5	9.13	9.16	96	4/17/2017 23:10	40		15	
49	X	340.8	350.4	9.6	9.65	9.69	101	4/18/2017 00:50	40			
50	X	350.4	360.0	9.6	9.21	9.28	96	4/18/2017 02:20	40			
51	X	360.0	369.6	9.6	9.88	9.98	103	4/18/2017 03:40	35			
52	X	369.6	379.2	9.6	9.97	10.04	104	4/18/2017 05:10	45			
53	X	379.2	388.8	9.6	6.13	6.13	64	4/18/2017 06:50	50			
54	X	388.8	398.4	9.6	9.99	9.99	104	4/18/2017 08:40	50		20	
55	X	398.4	408.0	9.6	9.90	9.90	103	4/18/2017 10:25	45			
56	X	408.0	417.6	9.6	9.85	9.85	103	4/18/2017 12:45	55			
57	X	417.6	427.2	9.6	9.99	10.02	104	4/18/2017 14:35	50		20	
58	X	427.2	436.8	9.6	9.92	9.92	103	4/18/2017 16:10	45			
59	X	436.8	446.3	9.5	9.90	9.90	104	4/18/2017 17:35	35			
60	X	446.3	448.3	2.0	1.67	1.67	84	4/18/2017 18:50	15			
61	X	448.3	454.9	6.6	4.72	4.72	72	4/18/2017 20:50	60			
62	X	454.9	461.9	7.0	3.20	3.20	46	4/18/2017 22:50	60			
		Hole U1501C totals:		461.9	444.77	445.11	96.37					
368-U1501D-												
1	1	0.0	433.5	433.5	*****Drilled interval*****			4/20/2017 22:45	540	Nonmagnetic	150	
2	R	433.5	443.1	9.6	7.62	7.62	79	4/21/2017 00:35	30	Nonmagnetic		
3	R	443.1	452.6	9.5	5.19	5.19	55	4/21/2017 02:10	50	Nonmagnetic		
4	R	452.6	462.2	9.6	1.84	1.84	19	4/21/2017 03:45	50	Nonmagnetic	15	
5	R	462.2	471.8	9.6	0.48	0.48	5	4/21/2017 04:55	25	Nonmagnetic		
6	R	471.8	481.4	9.6	0.15	0.15	2	4/21/2017 06:00	5	Nonmagnetic		
7	R	481.4	491.0	9.6	0.95	0.95	10	4/21/2017 07:40	45	Nonmagnetic	15	
8	R	491.0	500.6	9.6	1.64	1.64	17	4/21/2017 08:35	5	Nonmagnetic		
9	R	500.6	510.2	9.6	1.22	1.22	13	4/21/2017 09:25	5	Nonmagnetic		
10	R	510.2	519.7	9.5	0.94	0.94	10	4/21/2017 11:25	75	Nonmagnetic	15	
11	R	519.7	529.3	9.6	0.12	0.12	1	4/21/2017 12:35	10	Nonmagnetic		
12	R	529.3	539.0	9.7	0.13	0.13	1	4/21/2017 14:10	20	Nonmagnetic	20	
13	R	539.0	548.6	9.6	1.05	1.05	11	4/21/2017 15:50	45	Nonmagnetic		
14	R	548.6	558.2	9.6	0.74	0.74	8	4/21/2017 18:30	20	Nonmagnetic	20	
15	R	558.2	567.8	9.6	4.44	4.44	46	4/21/2017 19:35	15	Nonmagnetic		
16	R	567.8	577.4	9.6	6.08	6.08	63	4/21/2017 20:50	25	Nonmagnetic		
17	R	577.4	586.9	9.5	5.39	5.39	57	4/21/2017 22:20	40	Nonmagnetic	20	
18	R	586.9	596.5	9.6	4.51	4.51	47	4/21/2017 23:25	20	Nonmagnetic		
19	R	596.5	606.1	9.6	3.45	3.45	36	4/22/2017 01:15	75	Nonmagnetic		
20	R	606.1	609.6	3.5	4.11	4.11	117	4/22/2017 04:20	100	Nonmagnetic	20	

Table T1 (continued).

Core	Type	Top of interval DSF (m)	Bottom of interval DSF (m)	Interval advanced (m)	Core recovered length (m)	Curated length (m)	Recovery (%)	Time on deck UTC (h)	Time to cut core (min)	Core barrel	Mud pumped (bbl)	Driller's notes
21	R	609.6	615.7	6.1	5.07	5.07	83	4/22/2017 07:15	140	Nonmagnetic		
22	R	615.7	620.2	4.5	3.98	3.98	88	4/22/2017 11:15	150	Nonmagnetic		
23	R	620.2	625.2	5.0	4.94	4.94	99	4/22/2017 17:05	255	Nonmagnetic		
24	R	625.2	629.7	4.5	4.23	4.23	94	4/22/2017 21:30	180	Nonmagnetic		
25	R	629.7	634.7	5.0	2.68	2.68	54	4/23/2017 01:15	140	Nonmagnetic		
26	R	634.7	639.2	4.5	3.46	3.46	77	4/23/2017 05:50	190	Nonmagnetic	20	
27	R	639.2	644.3	5.1	4.36	4.36	85	4/23/2017 09:50	110	Nonmagnetic	40	
Hole U1501D totals including drilled interval:				644.3	78.77	78.77	12.23					
Hole U1501D totals excluding drilled interval:				210.8	78.77	78.77	37.37					

ing, they were introduced to life on board the R/V *JOIDES Resolution* and participated in the laboratory and ship safety tours. Loading and offloading operations continued with the loading of 40 short tons of sepiolite and the containerized science ocean freight, along with fresh and refrigerated food products and 300 metric tons of potable water. Cores from the two previous expeditions (366 and 367) were offloaded from the vessel and loaded into refrigerated containers for shipment to the Kochi Core Center (Japan) and Gulf Coast Repository (US), respectively. Ninety joints of 5½ inch drill pipe were offloaded to the pier, and another 72 were broken down and stowed on the riser hold hatch.

On 11 April, major port call activities included loading of 1212 metric tons of marine gas oil and 40 short tons of sepiolite mud (total = ~80 short tons). All dry food for Expedition 368 was loaded. The rest of the 204 joints of 5½ inch drill pipe were broken down and offloaded to the pier to be returned for inspection and refurbishment. The vessel continued conducting annual class, radio, and lifeboat surveys. Tours were conducted for members of the Hong Kong Sea Cadet Corps and Hong Kong Baptist University.

On 12 April, casing-loading operations were initiated and tours were conducted for students and faculty from the Southern University of Science and Technology. On 13 April, casing-loading operations were completed. Mud motors, underreamers, and reentry equipment were all loaded and stowed for transit. Annual lifeboat inspections and all other certifications were completed. All equipment was secured for sailing.

At 0600 h on 14 April, Hong Kong immigration authorities boarded the ship and cleared the personnel and vessel for departure. The harbor pilot arrived on board shortly after 0900 h, and with assistance from two harbor tugs, the *JOIDES Resolution* was underway, with the last line released at 0912 h. We proceeded to the pilot station, and after a 6 nmi transit, the pilot disembarked the ship at 0954 h. The sea voyage continued for the next 24 h. During the transit, the Co-Chief Scientists presented the scientific objectives for Site U1501 and the Captain held the first fire and boat safety drill. Later that day, the Co-Chief Scientists, key *JOIDES Resolution* Science Operator staff, and ship's crew met to review the coring and logging plan for Site U1501. The scientists moved into their working shifts, and the noon-to-midnight shift resumed laboratory activities. The 255 nmi transit from Hong Kong to Site U1501 was completed at 0837 h on 15 April at an average speed of 10.6 kt.

Holes U1501A–U1501C

After arriving at Site U1501, we lowered the thrusters, deployed a seafloor beacon, and put together the APC/XCB bottom-hole assembly (BHA) and started lowering it to the seafloor (2857 mbsl) in preparation for coring. The calculated precision depth recorder (PDR) depth for the seafloor at Site U1501 was 2873.4 meters below rig floor (mbrf), and we chose to place the bit at 2868 mbrf to take the first core. An APC core barrel was lowered to the bit, and coring in Hole U1501A started at 2345 h on 15 April 2017. The mudline core recovered 9.5 m of sediment, and the seafloor depth was calculated to be 2868 mbrf (2857.1 mbsl). Hole U1501A was terminated at 0025 h on 16 April, and the drill string was repositioned to attempt to core a better mudline at the site. With the bit at 2863 mbrf, we started Hole U1501B at 0100 h and again recovered a full core barrel, indicating once again that the APC was fired at or below the seafloor, and Hole U1501B was terminated. The vessel was offset 10 m east. The bit was raised to 2843 mbrf in an attempt to start Hole U1501C, but the core barrel was retrieved empty. We then lowered the bit to 2848 mbrf for a second spud attempt at 0300 h and retrieved another empty core barrel. We then lowered the bit to 2856.4 mbrf and successfully spudded Hole U1501C at 0510 h, recovering 9.3 m of core and establishing a seafloor depth at 2856.7 mbrf (2845.8 mbsl).

Hole U1501C was cored to 156.8 m using the full-length APC coring system. The half-length APC (HLAPC) was deployed to deepen the hole to HLAPC refusal at 257 m. We changed to the XCB system and deepened the hole to a final depth of 469.1 m. Nonmagnetic core barrels were used on all cores. All full-length APC cores were oriented using the Icefield MI-5 core orientation tool. The APC system recovered 156.5 m of core (100%). Temperature measurements were taken on Cores 5H (47.3 m), 8H (75.8 m), 11H (104.3 m), and 14H (132.8 m). Partial strokes were recorded on Cores 16H and 17H (151.8 and 156.8 m, respectively). The HLAPC system penetrated 100.2 m and recovered 88.54 m (88%). Partial strokes were recorded on Cores 22F (180.3 m) and 25F through 39F (189.7–257.0 m). The bit was advanced 4.7 m after each core despite the partial strokes and 1.5 m after Core 39F.

The XCB system was deployed to core to refusal, recovering 199.5 m (97%). A hard layer was met at 383.5 m (Core 53X), and a small piece of sandstone was recovered in the cutting shoe after retrieving the core barrel. Core recovery after that consisted of mudstone. Three more hard layers were found at 447.1, 454, and 460 m. Refusal was reached after no advancement was accomplished for ~10 min at 469.1 m. There were no indications that casing would be needed to core deeper using the RCB system at this site. The bit was then retrieved to the rig floor, clearing the seafloor at 0935 h and clearing the rotary table at 1420 h on 19 April. Overall, 62 cores were taken over a 461.9 m interval with 444.8 m of recovery (96%). Time spent in Hole U1501C was 84.75 h (3.5 days).

Hole U1501D

The vessel was offset 20 m west for Hole U1501D. The RCB outer core barrel was set up in the rotary table, and the core barrels were spaced out. While making up the BHA, at 1600 h on 19 April 2017 a leak was detected in the low clutch diaphragm. The diaphragm was replaced and back on line by 0500 h on 20 April. The core barrels were prepared and spaced out, the remainder of the RCB BHA was made up, and the drill string was run in the hole to 2816 mbrf. The top drive was picked up, and the bit was spaced out to start Hole U1501D.

Hole U1501D was drilled without coring to 433.5 m, and then RCB coring penetrated from that depth to 644.3 m. The hole was conditioned for logging, the rotary shifting tool was run to release the bit, heavy mud was spotted at the bottom of the hole, the top drive was set back, and the bit was raised to 113 m for logging.

With an average heave of <1 m, the rig floor was set up for logging, and a modified triple combo tool string was made up and run into the open hole. During its descent, the tool string hung up at ~3030 mbrf (173.3 m). After six attempts, the tool string finally passed through the obstruction with significant drag and then continued downhole smoothly until it reached 3156 mbrf (299.3 m). At that depth, the full weight of the tool hung up, and it would no longer advance. The consensus between the wireline engineer and the drilling and operations personnel was that the hole was collapsed and logging would have to be conducted from that depth upward.

During the logging run, there was significant overpull at ~173.3 m. The caliper log indicated that the hole was collapsed to approximately the same diameter as the tool itself. It was deemed unsafe to go below that depth with any subsequent passes; therefore, the rest of the logging program was terminated. The drill pipe was recovered to the rig floor, clearing the seafloor at 1225 h on 24 April and the rotary table at 1715 h.

A total of 90 cores were recorded for the site. The full-length APC system was deployed 19 times. The HLAPC system was deployed 22 times, the XCB coring system was deployed 23 times, and the RCB coring system was deployed 26 times. The total drilled interval was 433.5 m without recovery. The interval cored with the APC system was 175.8 m with a recovery of 176.6 m (100%). The interval cored with the HLAPC system was 100.2 m with a recovery of 88.54 m (88%). The interval cored with the XCB system was 204.9 m with a recovery of 199.53 m (97%). The RCB system cored 210.8 m and recovered 78.77 m (37%). Total core recovered at Site U1501 was 543.10 m, and the overall recovery was 79%. Total time spent at Site U1501 was 224.75 h (9.4 days).

Lithostratigraphy

We constructed a composite lithostratigraphy by combining Holes U1501A–U1501D (Figure **F7**). We defined three lithostratigraphic units at Site U1501 based on visual core description, smear slide and thin section inspection, and X-ray diffraction (XRD) analysis (see **Lithostratigraphy** in the Expedition 367/368 methods chapter [Sun et al., 2018a]). The lithostratigraphic units and subunits are primarily defined by principal lithology. Several of the subunits exhibit gradual changes, complicating a sharp definition of their boundaries. The precise depth of boundaries between certain lithostratigraphic subunits in intervals of poor core recovery was difficult to determine; therefore, the boundaries were refined using physical property measurements (e.g., magnetic susceptibility, color reflectance spectroscopy, and seismic velocity) (see **Physical properties**; also see **Physical properties** in the Expedition 367/368 methods chapter [Sun et al., 2018a]) and $CaCO_3$ measurements in Figure **F8**.

The sedimentary succession recovered at Site U1501 extends from the pre-Cenozoic(?) to the Holocene and is dominated by clay-rich nannofossil ooze, silty clay, clayey silt, sand, and sandstone. The succession is divided into three major lithostratigraphic units (I, II, and III) that are distinguished on the basis of sediment composition, particularly the relative abundance of calcareous and siliciclastic fractions. Unit I is dominated by clay-rich nannofossil ooze and nannofossil ooze with clay. The transition from Unit I to Unit II is abrupt and erosive and marked by a change from nannofossil-rich sediment in Unit I to siliciclastic-dominated clay, silt, and sand in Unit II.

The Unit II/III boundary was not recovered, but it is marked by an abrupt change in magnetic susceptibility, NGR, and *P*-wave velocity. Unit III is well lithified and comprises sandstone, sandstone with gravel, and minor conglomerate and laminated siltstone. Units I–III are further divided into several subunits.

Unit descriptions

Unit I

Intervals: 368-U1501A-1H-1, 0 cm, to 1H-CC, 14 cm;
368-U1501B-1H-1, 0 cm, to 1H-7, 14 cm;
368-U1501C-1H-1, 0 cm, to 45X-1, 51 cm
Depths: Hole U1501A = 0–9.73 m; Hole U1501B = 0–9.77 m;
Hole U1501C = 0–303.01 m
Age: Holocene to Oligocene

Lithology and sedimentary structures

Lithostratigraphic Unit I, in the upper part of the stratigraphy, was fully recovered in Hole U1501C. The top of Unit I was also recovered in Holes U1501A and U1501B. The dominant lithologies are clay-rich nannofossil ooze and nannofossil ooze with clay. Both lithologies can additionally have foraminifers, silt, or ash (e.g., "with foraminifers" as suffix) and minor amounts of nannofossil-rich foraminifer sand or silty sand. One discrete volcanic ash layer was found in Section 368-U1501A-1H-7, and an ash pod was found in Section 368-U1501C-3H-1. Ash is present in small amounts in some smear slides taken from other cores (e.g., Samples 368-U1501C-6H-5, 88 cm, and 6H-6, 78 cm). Unit I is divided into six subunits (IA–IF) based on minor changes in lithology and/or physical properties (Figure **F9**).

Bulk mineralogy and chemistry

The bulk mineralogy results of XRD analyses are listed in Table **T2**. Unit I sediments are composed mainly of calcite; halite; quartz; plagioclase; K-feldspar; clay minerals including smectite, illite, kaolinite, and/or chlorite; and minor amounts of pyrite. Calcite is present throughout Unit I (mostly in the form of nannofossils and foraminifers). Other minor minerals were observed in smear slides, but it was not possible to detect them through XRD analysis of bulk samples.

Figure **F8** shows the downcore variations in the relative abundance of minerals identified by XRD in bulk sediments at Site U1501. The percentages of most terrigenous minerals in Unit I (quartz, plagioclase, authigenic halite, and clay minerals such as illite, kaolinite, and/or chlorite) decrease downcore, whereas calcite and pyrite increase. In contrast, K-feldspar decreases downcore for the upper 60 m, increases between 60 and 140 m, and then de-

Figure F7. Lithostratigraphic summary of Site U1501 with simplified lithology and unit description of combined Holes U1501A–U1501C and U1501D. Upper cores are from Hole U1501C (1H through 61X); lower cores are from Hole U1501D (4R through 27R).

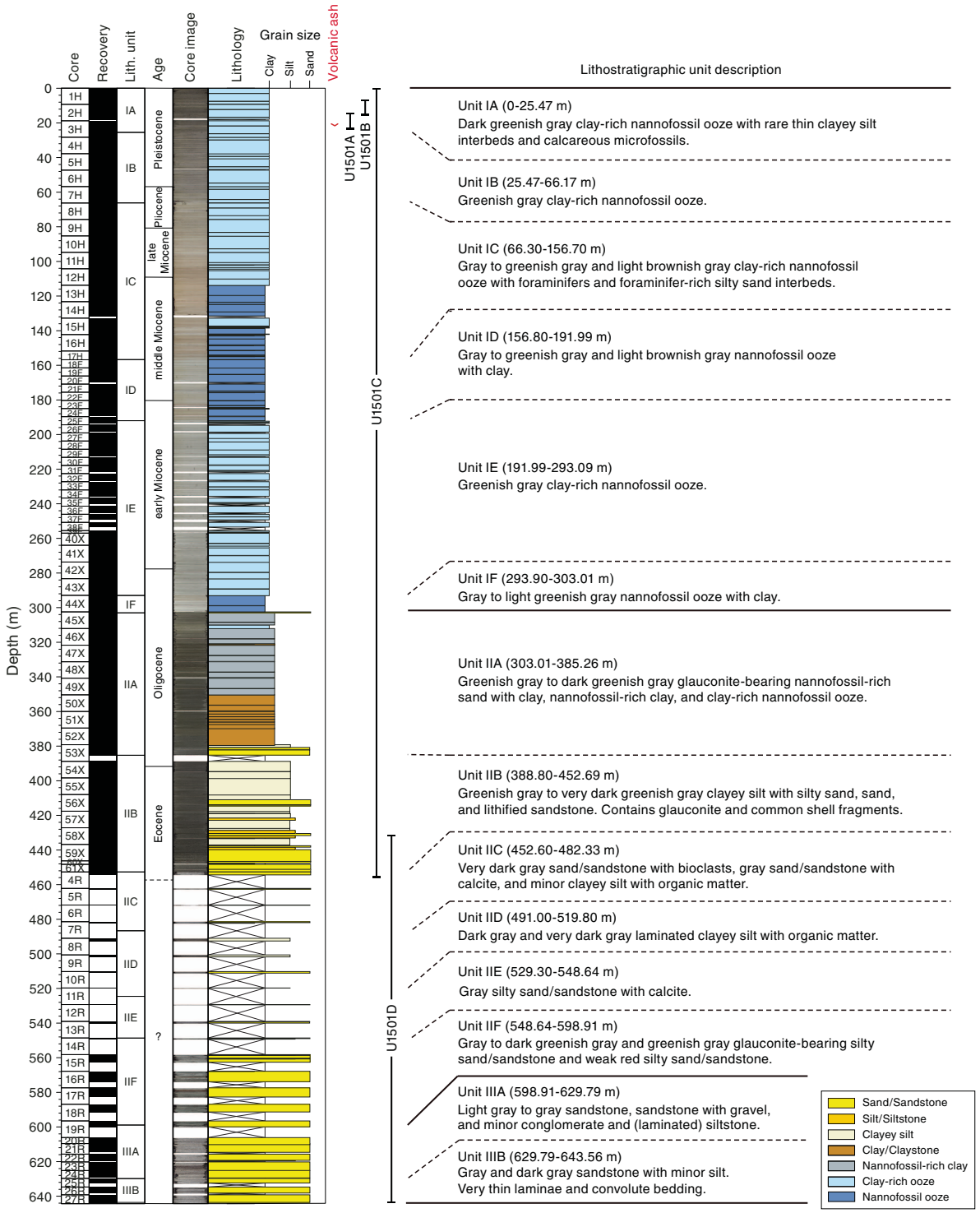

creases again from 140 to 280 m. These general characteristics are consistent with the observed lithologic change from clay-rich nannofossil ooze to nannofossil ooze with clay.

Compositional analyses of the nannofossil ooze in Sections 368-U1501C-44X-7, 44X-CC, and 45X-1 (Subunit IF) were made directly on the archive half of the core using the handheld portable X-ray fluorescence spectrometer (pXRF) (see **Igneous and metamorphic petrology** in the Expedition 367/368 methods chapter [Sun et al., 2018a]). The pXRF data are shown in Table **T3**. Eleven intervals of the nannofossil ooze show no variation in composition (CaO = 25–28 wt%, SiO_2 = ~20 wt% and lower, Al_2O_3 = 4–5 wt%, Fe_2O_3 < 2 wt%, and MgO < 2 wt%). The lowermost few centimeters of Subunit

Figure F8. (A) Bulk mineralogy (XRD) and (B) carbonate content, Holes U1501C and U1501D.

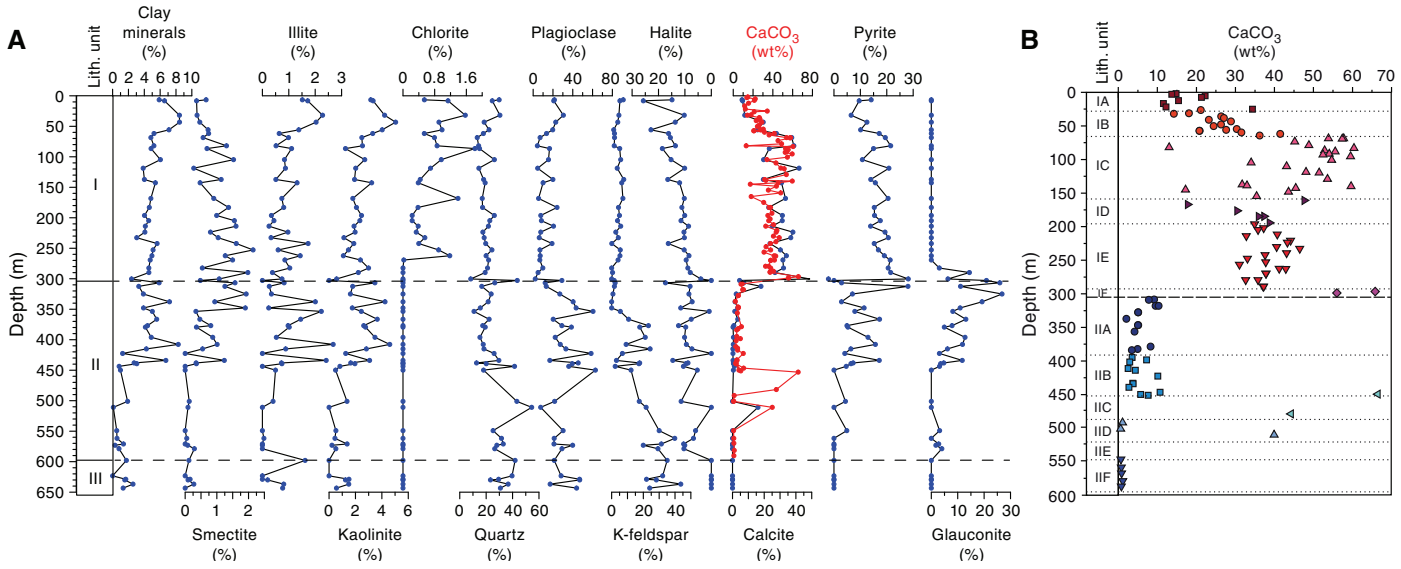

IF close to the contact with Unit II contain black sand and have lower CaO (~18 wt%) and higher SiO_2, Al_2O_3, and Fe_2O_3 (~25 wt%, ~5 wt%, and ~3 wt%, respectively). The dark nodules at the base of Subunit IF are iron and silica rich (Fe_2O_3 = ~10 wt% and SiO_2 = 26 wt%). The Zr content of Subunit IF varies between 50 and 75 ppm. The ooze has high Sr (>750 ppm) and low Ni (<20 ppm) contents, whereas the nodules have low Sr (<100 ppm) and higher Ni (100 ppm) contents.

Subunit IA

Intervals: 368-U1501A-1H-1, 0 cm, to 1H-CC, 14 cm;
368-U1501B-1H-1, 0 cm, to 1H-7, 14 cm;
368-U1501C-1H-1, 0 cm, to 3H-5, 84 cm
Depths: Hole U1501A = 0–9.73 m; Hole U1501B = 0–9.77 m;
Hole U1501C = 0–25.47 m
Age: Holocene to late Pleistocene

Subunit IA spans the uppermost 25.47 m of Unit I and is dominated by clay-rich calcareous ooze and clay-rich nannofossil ooze. The color of the ooze gradually changes from dark greenish gray to greenish gray. A distinct light-brown oxidized layer occurs at the top of this unit. The ooze comprises calcareous nannofossils and foraminifers, siliceous diatoms, sponge spicules, radiolarians, rare silicoflagellates, and terrigenous grains, including quartz, feldspar, clay minerals, and rare ferromagnesian minerals.

Bioturbation is moderate to heavy (apart from the slightly bioturbated top layer) with no clear layering visible. Individual burrows are difficult to distinguish but are mostly horizontal to inclined with recognizable *Planolites*, *Thalassinoides,* and *Ophiomorpha* (Figure **F10**). Distinct intervals (368-U1501C-1H-5, 6.0–6.5 cm, and 1H-5, 7.5–8.5 cm) contain more silt, and thin silt laminations are often disrupted by bioturbation (interval 3H-3, 89–133 cm).

Subunit IA has a discrete light gray silt-sized volcanic ash layer in interval 368-U1501A-1H-7A, 45–51 cm, and a centimeter-sized pod of volcanic ash in interval 368-U1501C-3H-1A, 29 cm. The ash is composed of silicic, platy, bubble wall, and lesser pumiceous glass shards and rare (1%–5%) plagioclase crystals (Figure **F11**). Although the mudline was not recovered in Hole U1501A, the drilling log indicates that the drill string was raised by 10 m before drilling of Hole U1501C commenced. The ash layer is found at 9.05 m in Hole U1501A, which is consistent with the depth of the ash patch in Hole U1501C (19.08 m). Furthermore, because the ash texture and composition is similar in the two holes, we assume that both intervals are the deposit of the same eruption. No other discrete ash intervals were observed at Site U1501.

Subunit IA shows a gradual lithologic transition into Subunit IB but with a clear change in magnetic susceptibility, porosity, density, and seismic velocity. From this boundary, there is an upward increase in biogenic silica, including diatoms, sponge spicules, and radiolarians.

Subunit IB

Interval: 368-U1501C-3H-5, 84 cm, to 7H-CC, 11 cm
Depth: 25.47–66.17 m
Age: late Pleistocene to Pliocene

Subunit IB comprises a monotonous sequence of greenish gray and minor gray and dark greenish gray clay-rich nannofossil ooze. Minor dark greenish gray clay-rich nannofossil ooze with ash was found in Sections 6H-5 and 6H-6. The ooze comprises mainly calcareous nannofossils and foraminifers with minor quartz and clay minerals. Single foraminifer tests are visible on the core surface and become more abundant below Section 7H-3. Diagenetic pyrite grains are common.

The upper part of the subunit (Sections 3H-5 through 3H-7) is marked by slumping with inclined and convolute lamination and patchy color changes. Below these sections, bedding is difficult to determine due to lack of grain size or color variation and moderate bioturbation. Individual burrows are difficult to distinguish but are mostly horizontal to inclined with recognizable *Planolites* and *Thalassinoides* (Figure **F10**).

The base of Subunit IB is marked by both a color change to brown and light brownish sediment in Subunit IC and a lithologic change that reflects an increase in the percentage of foraminifers. This unit change is also seen in the progressive increase in measured carbonate content from ~20 wt% at the top of Subunit IB to ~40 wt% at the base (Figure **F8**).

Figure F9. Simplified lithology and unit description overview, Unit I.

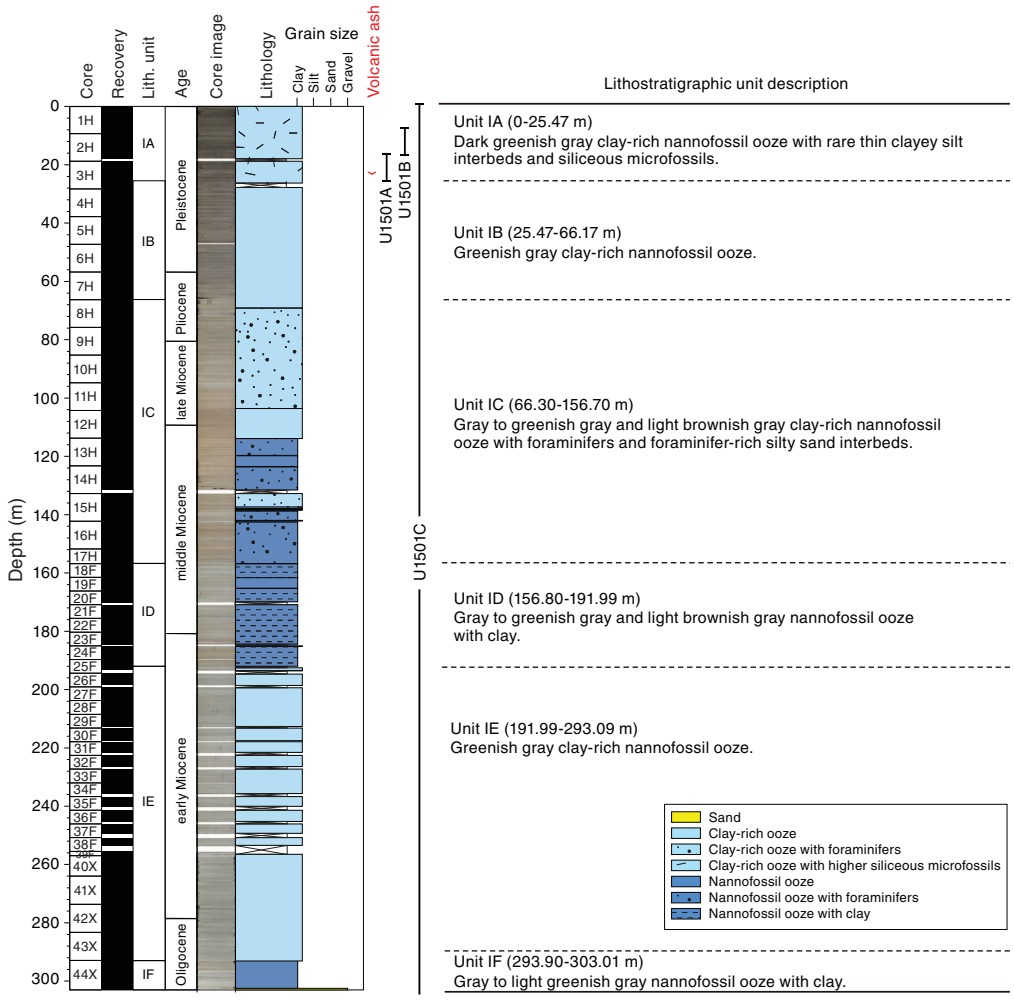

Table T2. Mineral percentages, Site U1501. **View table in PDF format. Download table in CSV format.**

Table T3. Major element oxides and minor elements in sediments, Site U1501. **View table in PDF format. Download table in CSV format.**

Subunit IC

Interval: 368-U1501C-8H-1, 0 cm, to 17H-4, 60 cm
Depth: 66.30–156.70 m
Age: Pliocene to middle Miocene

Subunit IC comprises an alternating sequence of gray, light gray, light brownish gray, greenish gray, and light greenish gray clay-rich nannofossil ooze with foraminifers; brown clay-rich nannofossil ooze with calcite; light brownish gray clay-rich nannofossil ooze and nannofossil ooze; light brownish gray silty sand; and greenish gray foraminifer-rich silty sand. The proportion of foraminifer-rich silty sand intervals increases from Core 16H to the base of the subunit.

Vague layering in the core is defined by color change. Boundaries between brownish and grayish intervals are mostly gradational, such as the color changes in Core 16H (Figure **F12A**), but sharp boundaries also occur, such as the one at Section 11H-6, 135 cm. Variation in color may indicate grading with fining-upward intervals recognized in Cores 11H, 14H, 16H, and 17H (Figure **F12**). Boundaries are usually horizontal but are inclined in Sections 10H-3 and 10H-4, possibly indicating intraformational slumping. The number of sand-sized fining-upward laminations increases from Core 15H to Core 17H.

Bioturbation varies from slight to heavy, but more intense bioturbation may be masked by the homogeneous sediment composition. Some burrows are filled with silty sand that consists mainly of foraminifers (Figure **F10**). Burrows are mostly horizontal to inclined, but some are vertical with recognizable *Planolites*.

The boundary between Subunits IC and ID is defined by a change in lithology from foraminifer-rich silty sand and nannofossil ooze with foraminifers (Subunit IC) to nannofossil ooze with clay (Subunit ID).

Subunit ID

Interval: 368-U1501C-18F-1A, 0 cm, to 25F-2, 78 cm
Depth: 156.80–191.99 m
Age: middle to early Miocene

Subunit ID is dominated by nannofossil ooze with clay. The color changes gradually from the top of the subunit to the bottom from gray to light greenish gray to greenish gray to light brownish gray and gray. The sediment is well sorted and well consolidated.

Figure F10. Diverse burrows, Hole U1501C. A. *Thalassinoides*. B, C. Pyritized burrows. D. *Ophiomorpha* or *Cylindrichnus concentricus*. E. Burrow filled with coarser sand.

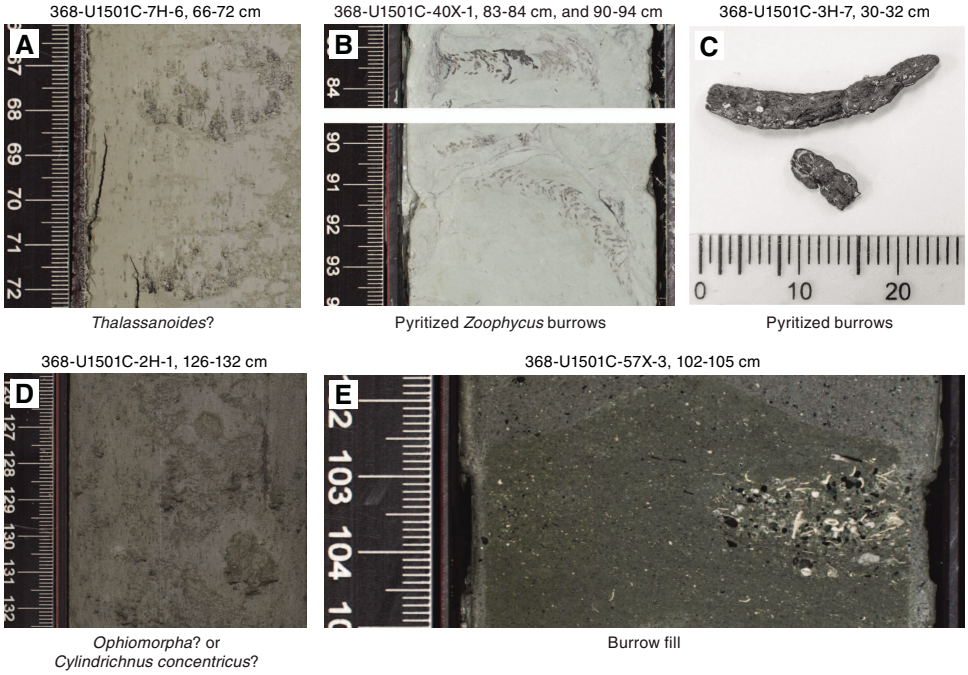

Figure F11. A. Pale brownish ash layer (368-U1501A-1H-7, 45–51 cm), Subunit IA. B. Magnetic susceptibility of core interval with ash layer, Hole U1501A. The ash layer has a significantly higher magnetic susceptibility than the nannofossil ooze. C. Smear slide image of ash layer. The ash is compositionally dominated by transparent glass shards and rare colored minerals (feldspar and ferromagnesian minerals). D. Pale brownish ash patch (368-U1501C-3H-1, 29 cm), Subunit IA.

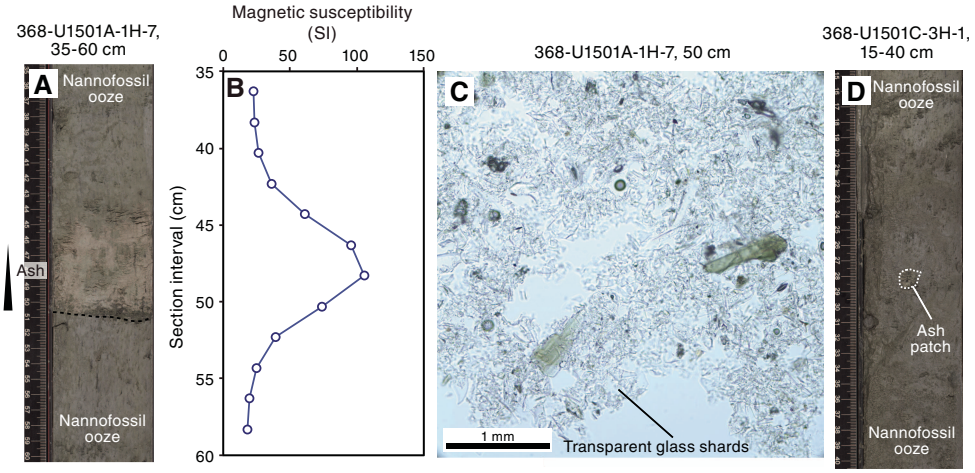

The average grain size is clay, and fine sand is the maximum grain size.

Contacts between layers are planar or irregular inclined and gradational horizontal. Some contacts between layers are also bioturbated. Bioturbation in Subunit ID is moderate to heavy.

The sediment is dominated by clay minerals and calcareous nannofossils, but quartz crystals are common and rare foraminifers are present, as well as traces of organic matter and pyrite. Measured carbonate content ranges from 18 to 48 wt% (Figure **F8**).

The lower boundary between Subunits ID and IE is characterized by a change in color and lithology, with more clay minerals in Subunit IE. A distinct increase in magnetic susceptibility and a slight decrease in NGR were observed at the transition.

Subunit IE

Interval: 368-U1501C-25F-2, 78 cm, to 43X-CC, 38 cm
Depth: 191.99–293.09 m
Age: early Miocene to Oligocene

Subunit IE is composed of monotonous greenish gray clay-rich nannofossil ooze (Figure **F13**) that is well consolidated and well sorted with either silt or very fine sand as the maximum grain size. There is little perceptible variation in grain size, with only minor thin silt laminations. Contacts are horizontal and gradational. One thick (~1 cm) lamination with upward fining was observed. Light-colored foraminifer grains and pyrite were observed on the core surface. Pyrite also forms rare laminae. Another diagenetic feature

Figure F12. Subunit IC. A. Core composite image. Red stars = thin fining-upward intervals. These intervals are interpreted as distal turbidites. B. Fining-upward interval with sharp bottom contact and diffuse top.

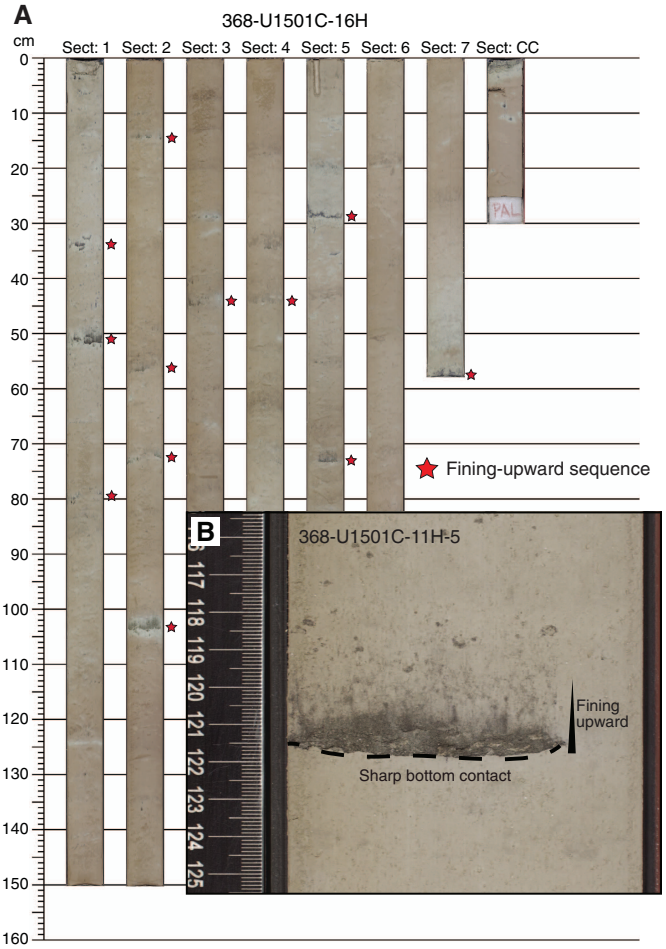

Figure F13. A. Clay-rich nannofossil ooze, Subunit IE. Monotonous sedimentation with pyrite patches. B. Close-up image (red square in A) of pyrite patches. C. Smear slide image of clay-rich nannofossil ooze with pyrite grains.

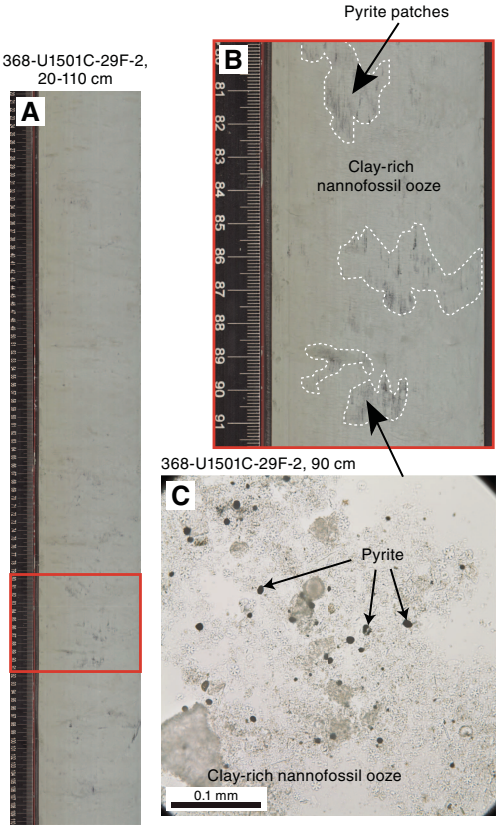

is a 1 cm wide patch of calcite or dolomite (interval 27F-1, 29–30 cm). Bioturbation is moderate to high throughout the sequence, causing lens- and podlike textures.

The nannofossil ooze of Subunit IE exhibits consistently low magnetic susceptibility (less than -20×10^{-5} SI), low NGR (<50 counts/s), high bulk reflectance, and low red color (reflectance a*), which is consistent with dilution by high carbonate content (31–46 wt%; Figure **F8**). Accordingly, nannofossils and foraminifers are common to abundant (50%–75%), whereas the amounts of quartz (<5%) and feldspar (<5%) are low.

The lower contact to Subunit IF is marked by the occurrence of nannofossil ooze with clay and a color change to gray and light greenish gray. Drilling disturbance varies from slight to high, and "biscuits" are the most common disturbance type.

Subunit IF

Interval: 368-U1501C-44X-1, 0 cm, to 45X-1, 51 cm
Depth: 293.90–303.01 m
Age: Oligocene

Subunit IF is a short interval (~11 m) of mainly gray to light greenish gray and greenish gray, well-sorted, well-consolidated nannofossil ooze with clay. The lowermost ~51 cm (interval 45X-CC, 0–51 cm) of this subunit is poorly sorted, matrix-supported sand with gravel. The lithologic components are heterogeneous and include cobble-sized rip-up clasts of nannofossil ooze with clay, pebble-sized botryoidal concretions (Figure **F14**), and sand-sized grains of glauconite and quartz embedded in a matrix of biogenic silt and clay (measured carbonate content = ~60 wt%; Figure **F8**). Subunit IF sediment fines upward in grain size and is heavily bioturbated. The cores are slightly to moderately biscuited or fractured due to drilling disturbances.

The lower contact of Subunit IF, which is also the base of lithostratigraphic Unit I, is erosional and marked by the emplacement of a poorly sorted sandy layer (Figure **F14**). The lower Subunit IF boundary is also marked by distinct discontinuities in *P*-wave velocity, NGR, magnetic susceptibility, porosity, MAD, red-green-blue color space (RGB) colors, and blue color (reflectance b*; see **Igneous and metamorphic petrology** in the Expedition 367/368 methods chapter [Sun et al., 2018a]) but does not represent a major gap in sediment age (all Oligocene; see **Biostratigraphy**). Measured carbonate contents markedly decrease from 56–66 wt% in Subunit IF to 2–10 wt% in Subunit IIA.

Unit II

Intervals: 368-U1501C-45X-1, 51 cm, to 62X, 39 cm; 368-U1501D-2R-1, 0 cm, to 19R-2, 135 cm
Depths: Hole U1501C = 303.01–458.09 m (base of Unit II not recovered); Hole U1501D = 433.5–598.91 m (top of Unit II not recovered)
Age: Oligocene to Eocene

Figure F14. Contact between Units I and II (368-U1501C-45X-1, 50 cm). Nannofossil ooze with clay dominates Subunit IF with centimeter-sized concretions at the lower boundary and rip-up clasts. Subunit IIA is dominated by nannofossil-rich clay. Photomicrographs show (top) nannofossil ooze with clay, (middle) concretions, and (bottom) nannofossil-rich clay.

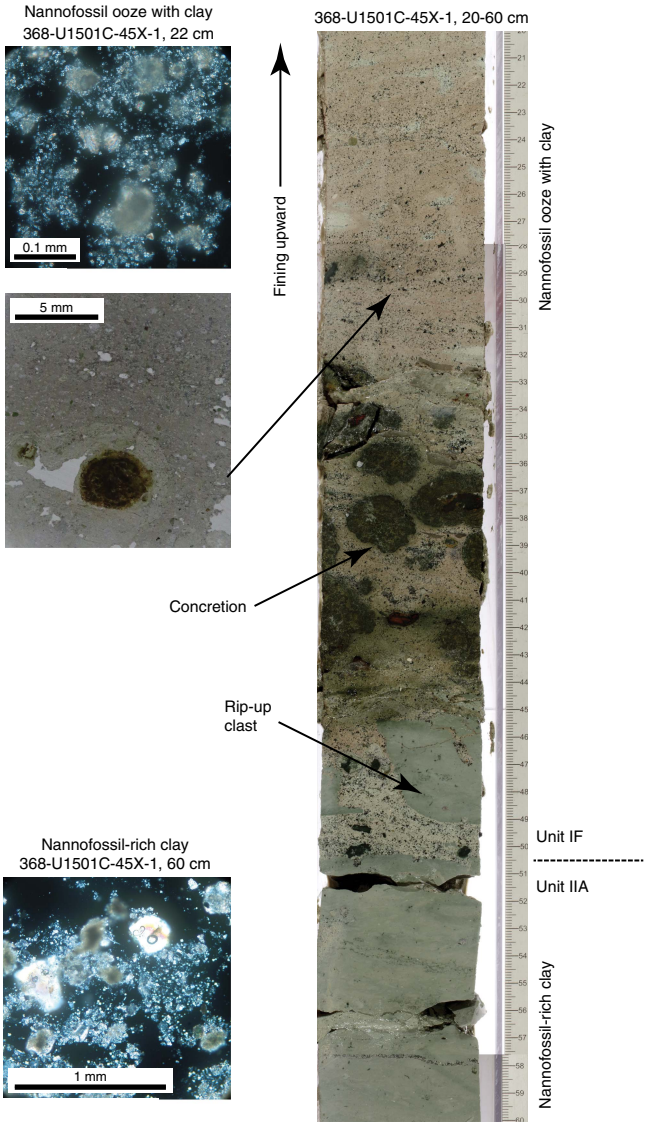

Lithology and sedimentary structures

Lithostratigraphic Unit II was recovered in Holes U1501C and U1501D. It consists of variable amounts of clay, silt, and sand (clay, silty clay, clayey silt, sandy silt, silty sand, and sand, which may be clay rich, with sand or with clay) with some nannofossil-rich clay (Figure **F14**), clay with nannofossils and minor nannofossil ooze, and clayey silt and silt with organic matter. In addition, gravel-sized grains include shell fragments and glauconite, as well as carbonate and pyrite concretions. The overall carbonate contents of Unit II is significantly lower (2–10 wt%) than that of Unit I (12–66 wt%) (Figure **F8**). Unit II is divided into six subunits (Figure **F15**) based on minor changes in lithology and grain size.

Bulk mineralogy and chemistry

The bulk mineralogy results of XRD analyses are listed in Table **T2**. Unit II sediments are composed mainly of glauconite, quartz, plagioclase, K-feldspar, clay minerals (including smectite, illite, and kaolinite), and minor amounts of pyrite and halite.

Figure **F8** shows the downcore variations in the relative contents of minerals identified by XRD in bulk sediments at Site U1501. Compared to Unit I, Unit II has distinct higher percentages of authigenic glauconite and terrigenous minerals, including quartz, plagioclase, K-feldspar, and clay minerals (illite and kaolinite). Unit II sediments have lower contents of calcite, pyrite, chlorite, and smectite. Most of the terrigenous minerals (illite, kaolinite, K-feldspar, and plagioclase) increase downcore in Unit II. We can only trace the downcore trend of glauconite content, rather than its precise abundance, because of its very poor crystallinity (wide peak around 7–8.9°Δ2θ) at the study site and the lack of a shipboard standard for calibration.

Compositional analyses of the clay in Sections 368-U1501C-45X-1 and 45X-2 were made directly on the archive half of the core using the handheld pXRF instrument (see **Igneous and metamorphic petrology** in the Expedition 367/368 methods chapter [Sun et al., 2018a]). The pXRF data are shown in Table **T3**. The nine analyzed intervals show no significant trends downhole. The clay has SiO_2 contents between 30 and 38 wt%, Al_2O_3 contents between 8 and 11 wt%, and low CaO contents (<5 wt%). The intervals in Section 45X-2 have sulfur contents between 690 and 4600 ppm. Zr contents are constant at ~70 ppm.

The uppermost two subunits of Unit II define a fining-upward succession from glauconite sand dominated in Sections 61X-CC through 59X-5 to siltstone and clay in Sections 59X-5 through 53X-1 (Subunit IIB) and clay with nannofossils in Core 53X through Section 45X-1 (Subunit IIA). Subunit IIC is dominated by sandstone with calcite but shows poor recovery. Subunit IID is distinctive with more fine grained, organic-rich lithologies. Subunit IIE is similar to Subunit IIC, whereas Subunit IIF repeats Subunit IIB but has more coarse-grained sediment and distinctive weak red and reddish gray intervals between the green glauconite-bearing sands.

The sediment in Unit II is matrix supported and moderately to poorly sorted. Coarse sand- to pebble-sized shell fragments are common. Coral fragments occur occasionally in the upper part of the unit. Glauconite and quartz minerals dominate the siliciclastic grain component. Diagenetic pyrite concretions, patches, or laminae are common throughout Unit II (Figure **F16**). Locally, carbonate and clay concretions are found. The measured carbonate content of Subunits IIA and IIB ranges from 2 to 10 wt% (Figure **F8**).

Horizontal lamination and ripple lamination can be recognized even though the entire interval is variably affected by drilling disturbance. Cross-bedding is present, as well as occasional fining-upward lamination, mostly in Subunit IIB. Bioturbation in Unit II is moderate. Burrows are horizontal to gently dipping and belong to the *Zoophycos* ichnofacies in Subunit IIA.

Drilling disturbance within Unit II varies from slight to high. Cores are slightly to heavily biscuited and partly fractured. Core 368-U1501C-62X has basal flow-in, and Cores 368-U1501D-2R, 8R, and 15R have soupy intervals.

Subunit IIA

Interval: 368-U1501C-45X-1, 51 cm, to 53X-CC, 26 cm
Depth: 303.01–385.26 m
Age: Oligocene to late Eocene

Subunit IIA is characterized by an overall fining-upward sequence from sand with clay to nannofossil-rich clay and clay-rich

Figure F15. Simplified lithology and unit description overview, Unit II.

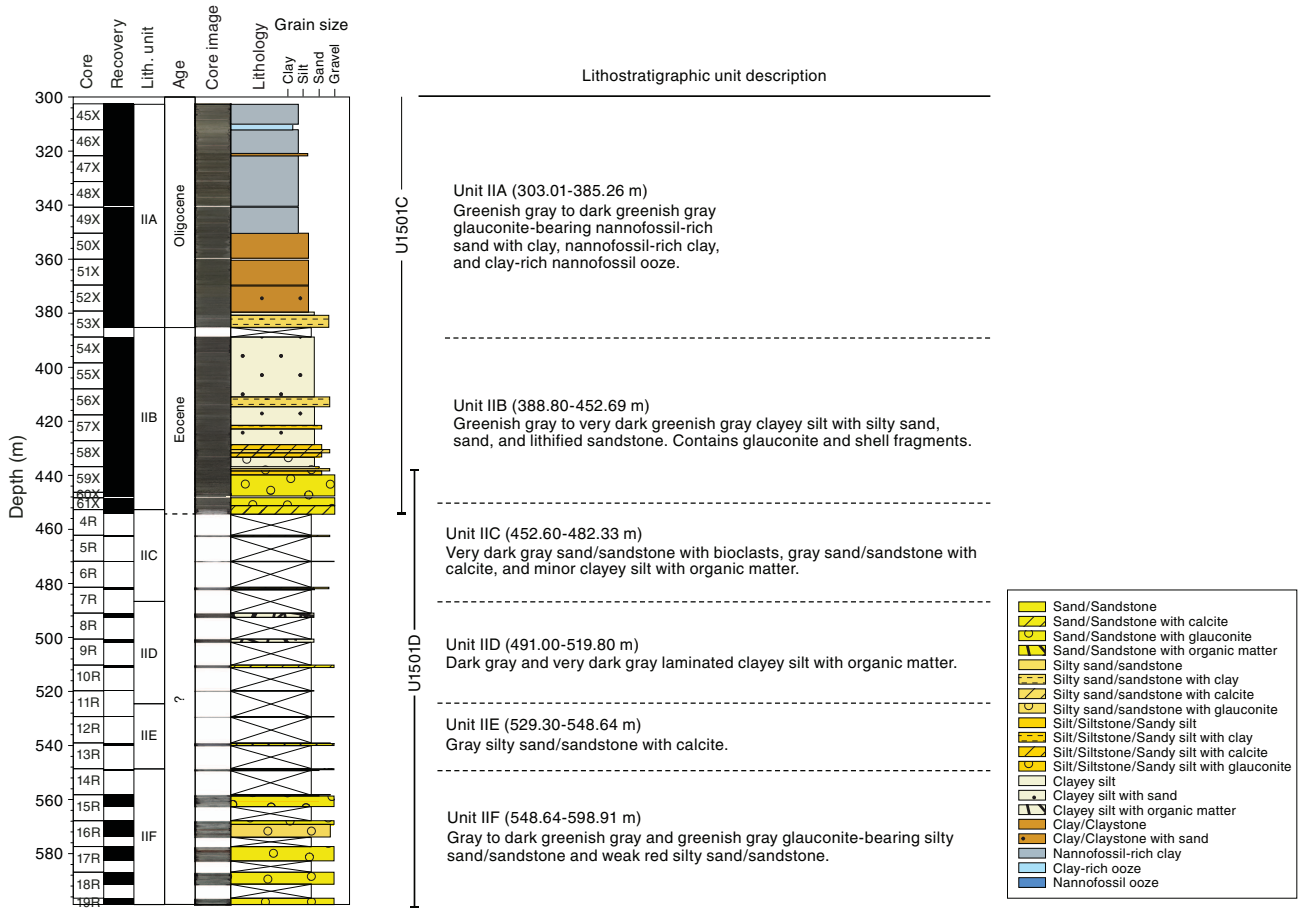

nannofossil ooze. The sediments are well consolidated and well sorted. Sections 45X-1, 51 cm, to 49X-CC, 39 cm, are composed of greenish gray to very dark greenish gray nannofossil clay and clay-rich nannofossil ooze with a maximum grain size of silt to fine sand. Several intervals fine upward from coarse sand to clay (e.g., intervals 48X-2, 103–151 cm, and 48X-3, 136–151 cm). Boundaries between sediment layers are horizontal and gradational. Very dark greenish gray silty clay with nannofossils was recovered from Section 50X-1, 0 cm, to 51X-CC, 34 cm. This interval shows cross-bedding, lamination, and a maximum grain size of fine sand. Grain size changes to silty clay with sand in Sections 52X-1, 0 cm, to 52X-CC, 45 cm. From Section 53X-1, 0 cm, to 53X-CC, 26 cm, the grain size increases from clayey silt with sand to silty sand and sand with clay (Figure **F17**). Boundaries between layers are gradational and horizontal, and lenticular bedding was observed in interval 53X-3A, 124–134 cm. The sediment is greenish gray and rich in sand-sized glauconite and quartz crystals. Shell fragments as large as 1 cm and foraminifers are common. Pyrite patches a few centimeters in size (Figure **F16**) occur throughout Subunit IIA. Bioturbation is moderate in the lower part of Subunit IIA (Sections 53X-1, 0 cm, to 53X-CC, 26 cm) and heavy in the upper part. The Subunit IIA/IIB boundary is characterized by a change in grain size. The recovered sediments are slightly to moderately disturbed with biscuits and fractures.

Subunit IIB

Intervals: 368-U1501C-54X-1, 0 cm, to 61X-CC, 7 cm; 368-U1501D-2R-1, 0 cm, to 3R-CC, 40 cm
Depths: Hole U1501C = 388.80–452.69 m; U1501D = 433.5–448.24 m (top of Subunit IIB not recovered)
Age: Eocene

Subunit IIB has well-consolidated sediment with fining-upward intervals that vary in grain size from clayey silt with sand to silty sand with clay to sand. The color changes from greenish gray (Core 368-U1501C-54X) to dark greenish gray (Sections 55X-1 through 57X-5) to very dark greenish gray (Sections 57X-6 through 58X-CC). The average grain size is silt to coarse sand, with a maximum grain size of granule and pebble. The sorting of the intervals in this subunit is moderate to poor.

Boundaries between sediment layers are gradational and horizontal, and layers fine upward (e.g., Section 59X-3). The sediment is rich in sand-sized glauconite and quartz crystals (Figure **F17**). There are pyrite patches throughout the subunit, especially in Sections 55X-1, 55X-2, 55X-5, 59X-3, 59X-5, 59X-6, and 60X-1 and in all sections of Core 61X. Shell fragments are common and horizontally oriented within the sediment (Figure **F16**). Calcite concretions occur in Section 58X-1, 42 cm, and interval 58X-CC, 16–18 cm. Bioturbation in Subunit IIB is moderate.

The Subunit IIB/IIC boundary is characterized by a change from glauconite-rich sand/sandstone to sandstone with calcite.

Figure F16. Special features, Subunits IIA and IIB. A. Thin parallel laminations. B. Gastropod shell filled with pyrite. C. Calcite concretion. D. Pyrite nodule. E. Coral fragment.

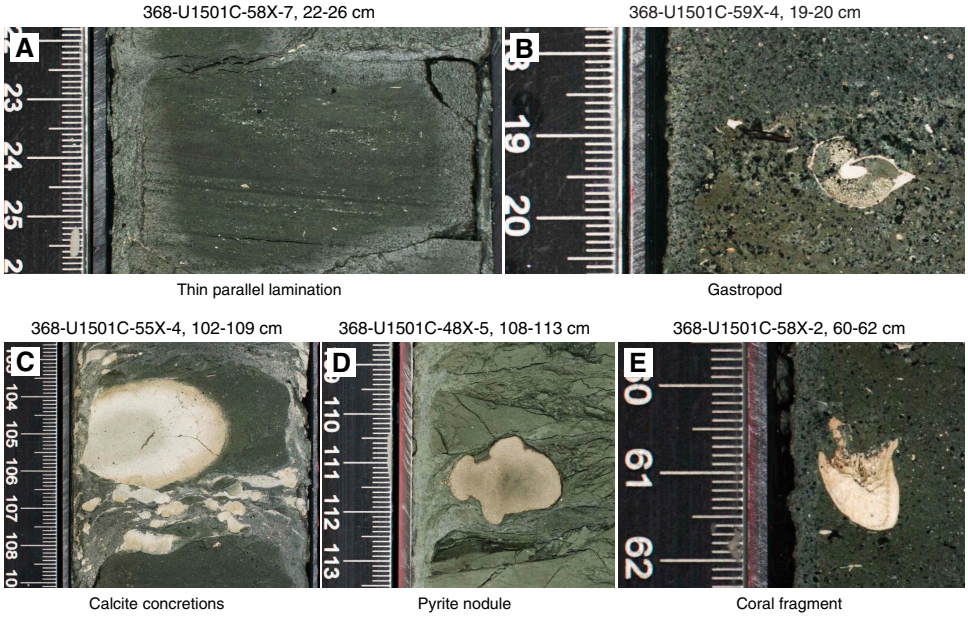

NGR values decrease at the transition from Subunit IIB to IIC (see **Physical properties**). The sediment in Subunit IIB is biscuited due to drilling, with disturbance intensities from moderate to high.

Subunit IIC

Intervals: 368-U1501C-61X-CC, 7 cm, to 62X-CC, 39 cm; 368-U1501D-4R-1, 0 cm, to 7R-1, 93 cm
Depths: Hole U1501C = 452.69–458.09 m (base of subunit IIC not recovered); Hole U1501D = 452.60–482.33 m
Age: Eocene

Subunit IIC is composed of gray sandstone with calcite, silty sandstone with calcite, and minor gray clayey silt with organic matter (Figure **F18**). The average grain size is coarse sand with a maximum of granule and pebble sizes, and the sediment is well to moderately sorted. Boundaries between sediment layers are planar and horizontal or erosive and curved. Recovery was very low (<10%) in this subunit (Figure **F7**). Shell fragments are abundant, and pyrite patches and calcite veins occur. The lithified sandstone is slightly bioturbated.

Drilling disturbance is moderate to high throughout Cores 368-U1501C-61X through 62X. The sediment is biscuited, fractured, and brecciated. Soft sediment recovered in Core 62X is interpreted as fall-in and basal flow-in and is therefore not described in any detail.

The boundary between Subunits IIC and IID is marked by a distinctive change from calcite-rich sandstone to more fine grained clay and organic-rich lithologies in Subunit IID.

Subunit IID

Interval: 368-U1501D-8R-1, 0 cm, to 11R-CC, 10 cm
Depth: 491.00–519.80 m
Age: Eocene

Subunit IID is composed of alternating laminae of dark gray to very dark gray clayey silt with organic matter or lignite (Figure **F19**).

Figure F17. Glauconite sand, Unit II. A. Glauconite-rich sand, Subunit IIA. Rounded green glauconite grains in smear slide image. B. Glauconite-rich sand, Subunit IIB. Thin section is dominated by quartz and glauconite grains.

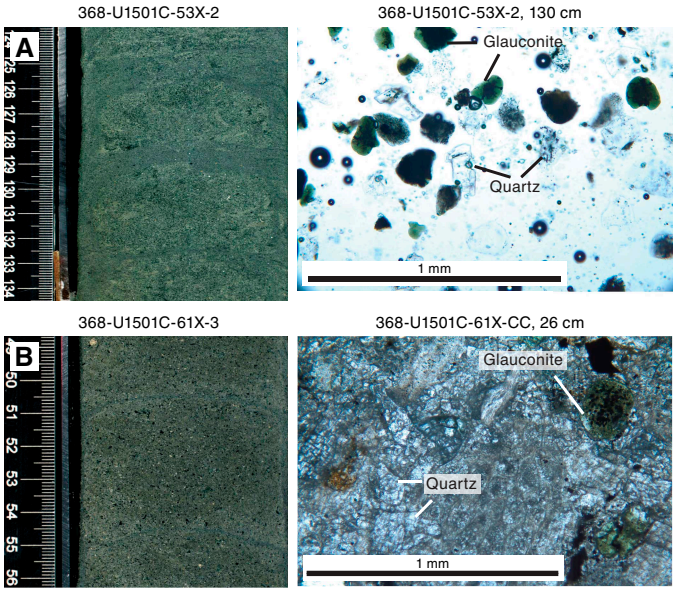

The sediment is slightly consolidated with an average grain size of silt and a maximum grain size of medium sand. The sediment is well to moderately sorted and characterized by very fine laminations and minor pebble-sized wood fragments. The organic matter occurs in clasts, lenses, or laminae. There is no bioturbation. The sediment is slightly soupy. Sandstone layers, similar to those described in Subunit IIC, are intercalated with the clayey silt.

Similar to Subunit IIC, recovery in this unit is also very low (<10%). The boundary between Subunits IID and IIE is characterized by a lack of organic-rich layers and a change to calcite-rich sandstone in Subunit IIE.

Figure F18. A. Calcite-rich sandstone with calcite-filled veins, Subunits IIC and IIE. B. Close-up image (red square in A) of calcite veins. C. Smear slide image of sandstone that is dominated by quartz crystals and calcite matrix.

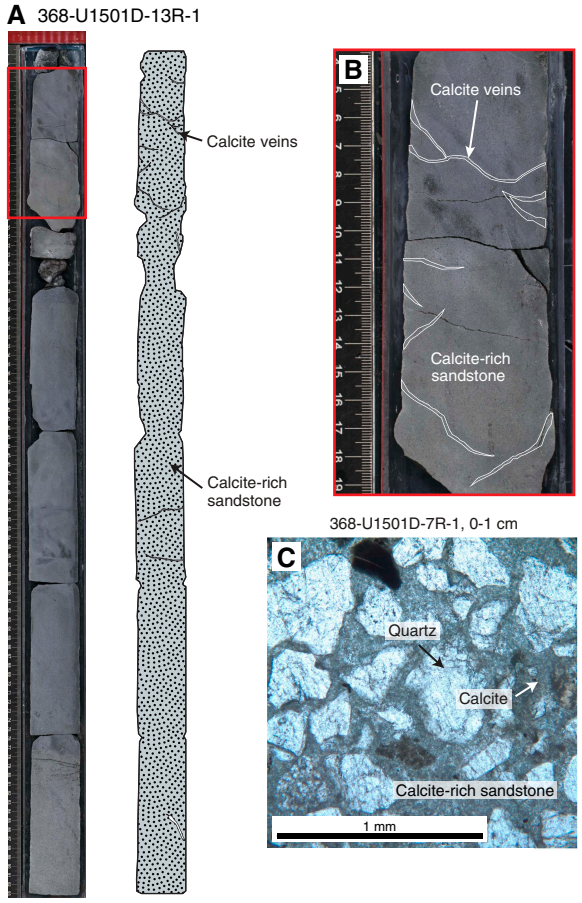

Figure F19. A. Subunit IID is characterized by the presence of thin layers of organic matter within a clayey silt. Red square = location of B. B, C. Close-up images of organic-rich layers and bedding structures. Layers of organic-rich material are intercalated with clayey silt layers. D. 5 cm of lignite-rich silt.

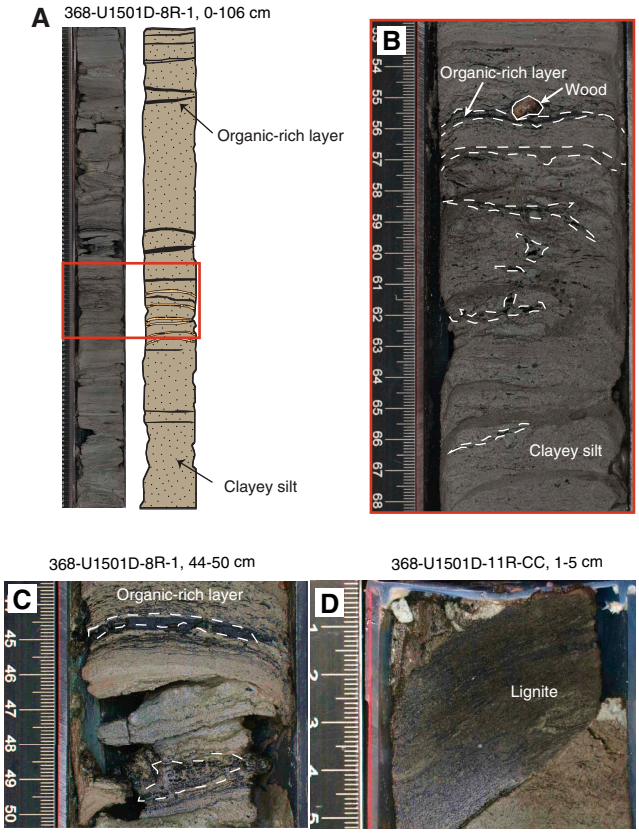

Subunit IIE

Interval: 368-U1501D-12R-CC, 0 cm, to 14R-1, 4 cm
Depth: 529.30–548.64 m
Age: Eocene

Subunit IIE is composed of gray silty sand with calcite, silty sandstone with calcite, and sandstone with calcite. The sediment is well consolidated to lithified, and the average grain size is fine to medium sand. The sediment is well sorted. Bioturbation is slight to moderate. The sediment is slightly fragmented due to drilling. This subunit appears similar to Subunit IIC (Figure **F18**).

Recovery in this subunit is extremely low (<6%). Subunit IIE is similar to Subunit IIC, whereas Subunit IIF repeats Subunit IIB. The boundary between Subunits IIE and IIF is marked by a change from sandstone with calcite to gray and dark greenish gray glauconite-bearing silty sand and silty sandstone.

Subunit IIF

Interval: 368-U1501D-14R-1, 4 cm, to 19R-2, 135 cm
Depth: 548.64–598.91 m
Age: Eocene

Subunit IIF is composed of gray, dark greenish gray, greenish gray silty sand, sandy silt and sand, and silty sandstone, as well as weak red silty sand and silty sandstone. A color change to weak red is observed in Sections 17R-1, 101 cm, to 17R-2, 47 cm. The consolidation varies from well consolidated to lithified. The average grain size is from fine to coarse sand to a maximum of granule, and the sediment is well to moderately sorted. The bedding thickness is medium to thick (see **Lithostratigraphy** in the Expedition 367/368 methods chapter [Sun et al., 2018a]), and contacts between the beds are planar to gradational and horizontal to curved. The majority of the beds fine upward or are massive (Figure **F20**). The sands are rich in glauconite and quartz minerals. Pyrite is common, and patches are as large as centimeter sized (e.g., interval 16R-2, 77–129 cm). The sediment and lithified sandstone are slightly to moderately bioturbated. The sandstone is slightly fractured due to drilling disturbance. The contact with Unit III was not recovered, but Subunit IIF has marked brown- to ochre-colored alteration patches at the base (Figure **F21**).

Unit III

Interval: 368-U1501D-19R-3, 0 cm, to 27R-4, 71 cm
Depth: 598.91–643.56 m
Age: pre-Eocene

Lithology and sedimentary structures

Unit III was only recovered in Hole U1501D and consists of lithified sandstone, sandstone with gravel, and minor conglomerate and laminated siltstone. Unit III is divided into two subunits (Figure **F22**). Pebble- to cobble-sized clasts include felsic volcanic and plutonic rocks, sedimentary rocks, metamorphic rocks, and rare gabbro (Figure **F23**).

Figure F20. A. Glauconite-rich coarse sandstone, Subunit IIF. The interval fines upward from very coarse sand to medium sand. B. Thin section image of glauconite sandstone dominated by quartz and glauconite. C. Glauconite-rich sandstone with burrows and blotches.

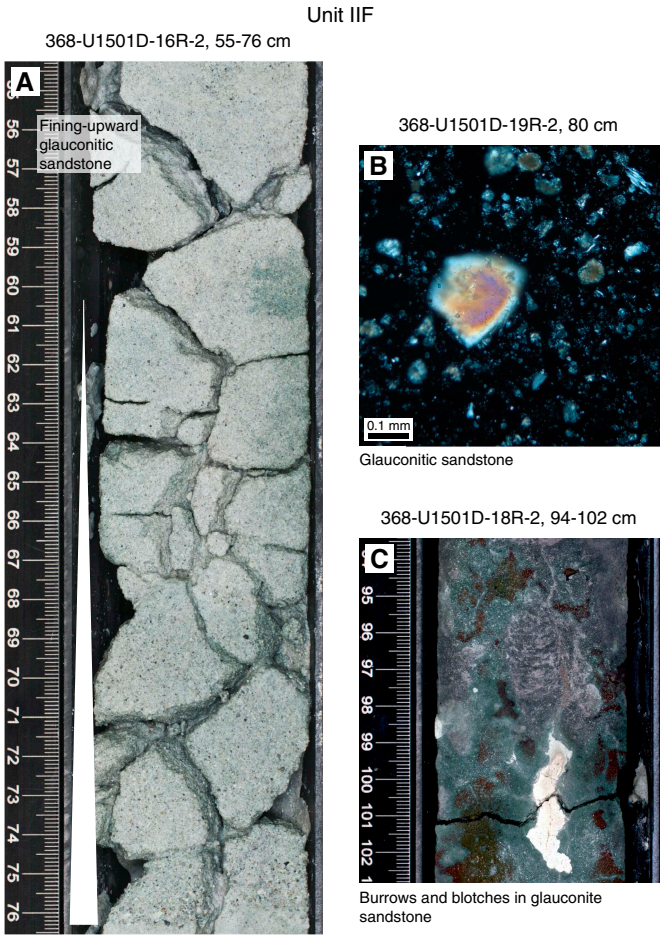

Figure F21. Composite of core section images showing the lithologic change from greenish gray medium coarse sand with glauconite in Subunit IIF to gray lithified coarse sandstone in Subunit IIIA, Hole U1501D. Lower part of Subunit IIF (19R-2) shows irregular brown to ochre and purple patches inferred to be related to diagenetic alteration.

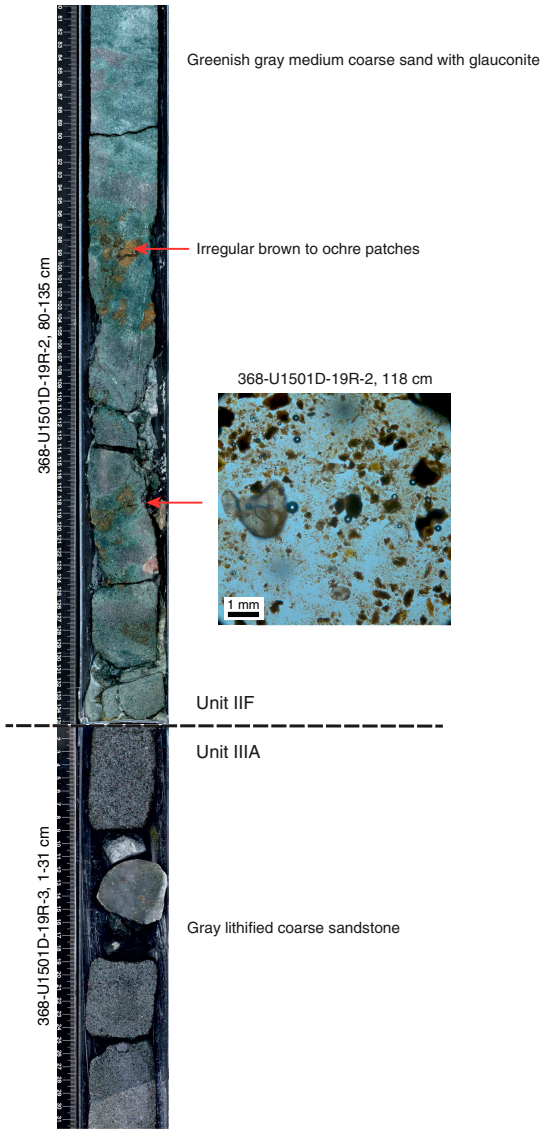

The contact between Units II and III was not recovered. The base of Section 19R-2 represents Unit II, and the top of Section 19R-3 is in Unit III (Figure **F21**). However, the low recovery (26%) indicates that intervals are missing. The boundary is marked by an abrupt downhole increase in magnetic susceptibility, NGR, and *P*-wave velocity, so it is assumed that this boundary is sharp. A change in the apparent dip of strata from approximately horizontal (seismics show ~5°) in Unit II to ~20° in Unit III (see **Structural geology**) suggests that the contact is unconformable.

Bulk mineralogy

The bulk mineralogy results of XRD analyses are given in Table **T2** and Figure **F8**. Unit III sediments are composed mainly of quartz, plagioclase, and K-feldspar, as well as minor amounts of kaolinite and mica. Compared to Units I and II, Unit III sediments have much higher K-feldspar and plagioclase abundances but almost no calcite, glauconite, or pyrite.

Subunit IIIA

Interval: 368-U1501D-19R-3, 0 cm, to 25R-1, 9 cm
Depth: 598.91–629.79 m
Age: pre-Eocene

Subunit IIIA is composed of light gray to gray lithified sandstone, sandstone with gravel, and sandstone with calcite clasts (Figure **F24**), along with minor conglomerate and siltstone. The average grain size is medium to very coarse sand, and the maximum grain size is as large as cobble sized. The sorting is well to moderate, but some intervals are poorly sorted because of large pebbles or cobbles. The pebble- to cobble-sized clasts consist of felsic volcanic and plutonic rocks (granite), sedimentary rocks, and rare gabbro. The bottom contacts of beds are planar, erosional, gradational, and horizontal. The sandstone layers are massive or fine upward. Interval 22R-3, 80–102 cm, contains an ~22 cm thick interval of dark gray siltstone. The contact with the overlying sandstone was not recovered, but the bottom contact with the underlying conglomerate is erosive and inclined. Intervals 22R-3, 102–105 cm, and 22R-CC, 0–19 cm, are composed of poorly sorted conglomerate.

This subunit consists of heterolithic, densely packed, moderately sorted siltstone to coarse-grained heterolithic sandstone rich in quartz, feldspar, and sedimentary lithoclasts (mudstone) (Figure F24). The grains are cemented with a mixture of clay and calcite. There are minor amounts of mica, amphibole, and opaque minerals, as well as traces of glauconite pellets. Igneous (volcanic and plutonic) and metamorphic lithoclasts (quartzite) are rare. Alteration is pervasive, and most feldspar grains have been pseudomorphed by clay minerals. A cobble of slightly recrystallized granite was recovered in interval 19R-3, 13–28 cm, and is composed of quartz, feldspar, mica, and amphibole with traces of apatite and zircon.

A distinctive thick bed of dark brown clay-rich silty sandstone and clay-rich silty sandstone with gravel occurs in Sections 23R-2 (Figure F24) and 23R-3. This bed has a massive base and grades into gray silty sandstone with gravel in Section 23R-4. The fine-grained upper interval of the bed is poorly sorted with millimeter-sized feldspar grains in a fine-grained red clayey matrix.

The transition to Subunit IIIB is sharp and marked by a change from sandstone and sandstone with gravel to sandstone and sandstone with silt. Magnetic susceptibility decreases toward the base of Subunit IIIA.

Figure F22. Simplified lithology and unit description overview, Unit III.

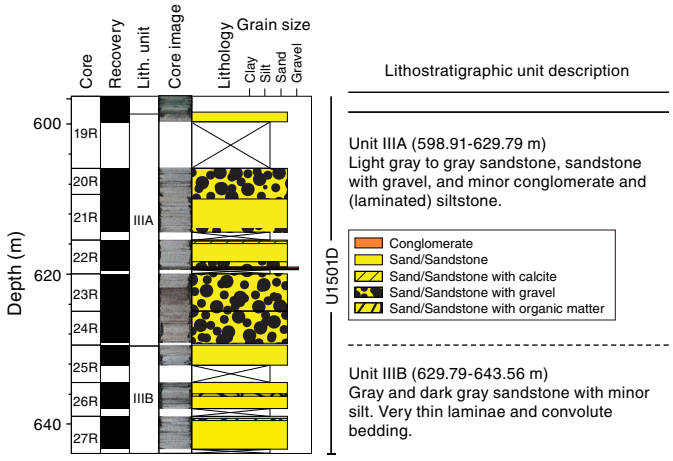

Subunit IIIB

Interval: 368-U1501D-25R-1, 9 cm, to 27R-4, 71 cm
Depth: 629.79–643.56 m
Age: pre-Eocene

Subunit IIIB consists of light gray, gray, and minor dark gray sandstone, sandstone with silt, and minor sandstone with organic matter (Figure F24). This subunit is different from Subunit IIIA in that it is finer grained overall and has finely laminated intervals. The average grain size is fine to very coarse sand, and the maximum grain size is as large as pebble sized. The sediment is very well to moderately sorted, but some intervals are poorly sorted because of pebbles. The pebble-sized clasts consist of felsic volcanic rocks and fine-grained quartzite. The bottom contacts of the beds are planar to erosional to gradational and subhorizontal to horizontal. The sandstone layers are massive or fine upward.

Interval 26R-3, 7–54 cm, has convolute lamination intercalated between planar laminated intervals that is interpreted as soft-sediment deformation. Some intervals of fine sandstone and siltstone have plane and ripple cross-lamination. However, most beds are fairly massive or show weak grading. A bituminous clast was recovered in Section 27R-1 (Figure F24).

Discussion

Depositional environment of Unit III

Unit III consists of poorly sorted, feldspar-rich, coarse-grained sandstone with pebbles or cobbles that is interbedded with light gray and gray to dark gray moderately to well-sorted medium- to fine-grained sandstone and rarely siltstone and poorly sorted conglomerate. Both massive bedding and fining-upward grading is common in the coarse-grained sandstone and conglomerate, whereas the relatively well sorted medium- to fine-grained sandstone intervals have thin parallel bedding. Finely rippled cross-lamination, convolute bedding, pyrite patches, and organic-rich laminae and lenses were found in the fine-grained interbeds. In addition, glauconite particles occur in some thin sections. No fossils were found. In general, we speculate that Unit III was formed in a terrestrial to littoral environment with a provenance not far from the site (Figure F25). The well-sorted sandstone with parallel to low-angle cross-lamination could have been formed by wave re-

Figure F23. A–D. Diverse lithologies of pebble- to cobble-sized clasts in Unit III sandstone.

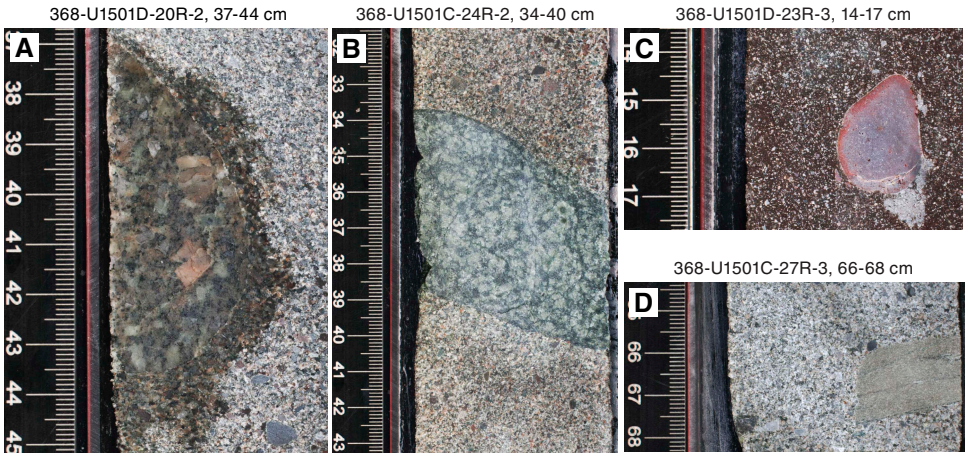

Figure F24. Sandstone, Unit III. A. Subunit IIIA is dominated by gray coarse-grained sandstone rich in feldspar. B. Thin section image of heterolithic feldspar-rich sandstone showing rounded sedimentary, volcanic, and metamorphic (mica-bearing quartzite) lithic grains. Subunit IIIB is dominated by gray sandstone with (C) very thin laminae, (D) calcite clasts, and (E) bituminous clasts.

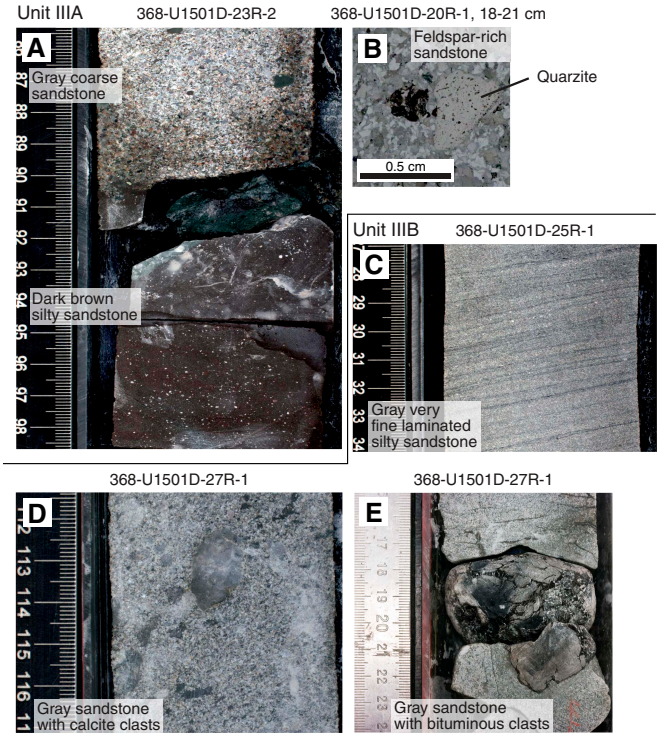

Figure F25. Preliminary model for deposition and sedimentary environments at Site U1501 showing deposition of prerift sediment and formation of the different units during and after rifting of the SCS.

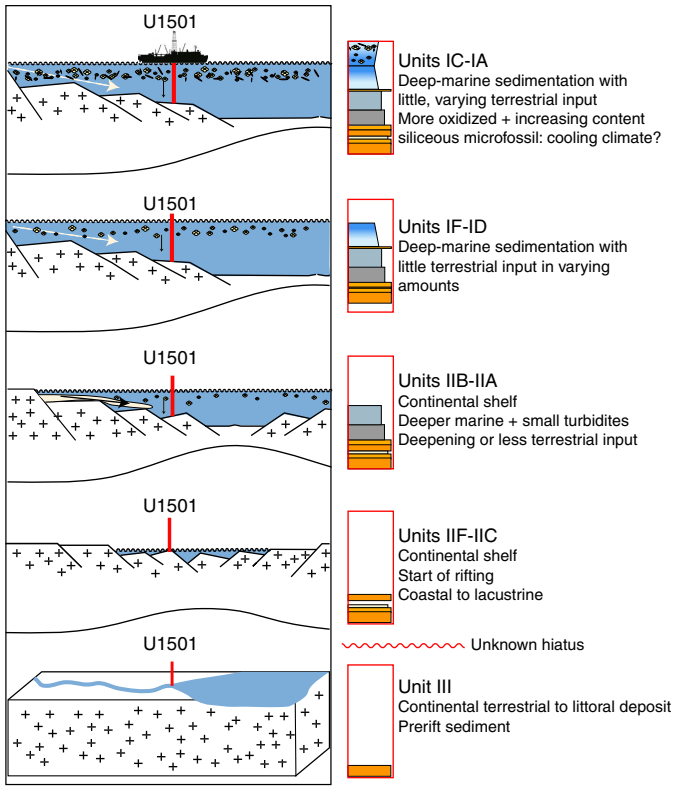

working in a littoral environment. Overall, the downhole color change from more or less brownish to grayish rock and the decrease in average grain size may indicate a change to a deeper water environment.

Transition between Units II and III

The boundary between Units II and III is in Core 368-U1501D-19R at around 598.91 m. The boundary separates the overlying greenish to dark greenish and less consolidated glauconite-bearing silty sand/sandstone of Unit II from the underlying dark brownish to gray and well-lithified sandstone with minor conglomerate and siltstone interbeds. The Unit II/III boundary is marked by an abrupt change in magnetic susceptibility, NGR, and *P*-wave velocity. In the seismic data, the boundary is tied to the acoustic basement (Tg), a high-amplitude reflector separating the overlying high-amplitude reflections in Unit II from the underlying low-amplitude reflections in Unit III (see **Background and objectives**).

We speculate if the Tg reflector between Units II and III might represent a boundary between possible early synrift (Paleocene?) deposits and the Eocene synrift sediments of Unit II or simply a hiatus between the Eocene synrift deposits of Unit II and a pre-Cenozoic basement (Unit III) (Shi et al., 2014; Dai et al., 2015). In the first case, Unit III could be similar to the Paleocene nonmarine sandstone and conglomerate successions common in the petroleum-bearing basins of eastern China. However, we found glauconite particles in the Unit III sandstone, which is commonly an indicator of marine environments (McRae, 1972; Wigley and Compton, 2007; Harris and Whiting, 2000). Most importantly, the sandstone in Unit III is quite different from the overlying sand/sandstone in Unit II in terms of color, composition of clastic components, degree of lithification, and physical properties, including seismic velocity (see **Physical properties**). Therefore, we suggest the transition from Unit II to III represents a significant hiatus that formed in late Mesozoic to perhaps early Cenozoic time and that the sand-dominated terrigenous clastic rocks of Unit III represent a pre-Cenozoic basement succession. Regional geologic research (e.g., Yao et al., 1994; Zhou et al., 1995, 2006) indicates that in the late Mesozoic there was an active continental margin in eastern Asia, including the northern SCS margin, where the paleo-Pacific Ocean plate was subducted under the Eurasia plate. Therefore, the Unit II/III boundary could represent the transition from an active margin to a passive margin setting. Obviously, postexpedition research is needed to further constrain the age and nature of the boundary between Units II and III.

Depositional environment of Unit II

Unit II most likely represents a gradual change from shallow-water (outer shelf or upper continental slope) to deepwater (lower slope) depositional environments (Figure **F25**). In general, the sediments of the lower part, including Subunits IIB–IIF, are dominated by terrigenous materials (quartz and clay minerals) and/or authigenic minerals (glauconite and calcite), with very rare calcareous nannofossils or foraminifer tests. Moreover, the glauconite (Figure **F17**) and large shell fragments become more common downhole and are even abundant in these subunits.

Glauconite is a clay- or mica-like mineral that usually forms from the absorption of potassium and iron by a degraded-layer sili-

cate lattice. Glauconite formation appears related to organic activity because grains are often found with decaying organic matter or the tests of marine organisms (McRae, 1972). Glauconite grains may form as clasts or fecal pellets or by accretionary growth, leading to a wide range of external morphologies (McRae, 1972). Glauconite clasts in Unit II have a range of morphologies from angular to well rounded and equant to more elongate. Some well-rounded glauconite grains occur mixed with subangular terrigenous quartz grains (Figure **F17**), suggesting that the rounded morphology is not a result of reworking but due to their formation as fecal pellets.

Modern deposits typically occur at low latitudes (temperatures ranging from 7° to 15°C) (Margielewski et al., 2017) and where there are low oxygen contents, mostly in the shelf to lower-slope environments from 20 to 700 mbsl (e.g., Drzewiecki and Simó, 2002; Margielewski et al., 2017) but also (less common) in anoxic and salty lake or marginal sea environments such as the Black Sea (Suttill, 2009). Glauconite forms where sedimentation rates are low and the formation can be stopped by rapid sedimentation. Glauconite grains are often associated with marine transgressions, unconformities, condensed sections, or transgressive systems tracts (McRae, 1972; Wigley and Compton, 2007; Harris and Whiting, 2000). However, because glauconite can form in a wide range of environments, it may not be a good tool for use in paleoenvironmental studies (McRae, 1972). Margielewski et al. (2017) found that glauconite grains are not destroyed when transported for short distances but break down to become part of the finer sediment fraction in high-energy environments. Glauconite grains could therefore be found in redeposited sediment sequences but only if mechanical abrasion and chemical destruction is limited.

A remarkably similar Tertiary sequence was described by Exon et al. (2002) for sites drilled during ODP Leg 189 offshore Tasmania. The glauconite-bearing silty claystone and clayey siltstone was deposited very slowly, representing a condensed sequence with sedimentation rates of <1 cm/ky. The comparable sediment at Site U1501 was deposited at an approximate rate of 2.5–3 cm/ky based on a preliminary shipboard age/depth curve. This rate is much greater than expected for a sediment-starved glauconite sand shelf and supports redeposition of the glauconite-bearing silts and sands in Subunits IIA, IIB, and IIF.

Subunit IID, between the calcite-rich sandstones of Subunits IIC and IIE, is different than other parts of Unit II and is characterized by alternating laminae of dark gray clayey silt with organic matter or lignite. The lack of marine fossils and authigenic glauconite and the frequent thin organic-rich laminae with pyrite and very fine grained clayey silt sediment likely indicate a very low sedimentation rate and a reducing, coastal brackish environment. A similar depositional environment was observed in a petroleum well of the eastern Pearl River Mouth Basin (Shao et al., 2016). Therefore, this unit may represent a temporary switch from shallow-marine environment to brackish facies.

The upper section of Unit II fines upward from sandy, silty, and clayey sediment in Subunit IIB to clayey sediment in Subunit IIA. This trend is accompanied by an upward increase in bioturbation intensity. The occurrence of a *Zoophycos* trace fossil assemblage in Subunit IIA indicates a moderate- to deepwater environment. We propose that this gradual transition is the result of a deepening of the basin. Benthic foraminifers from Subunit IIA suggest water depths of 300–800 m.

The coexistence of deepwater nannofossils and shallow-water shell and coral clasts suggests that the sediment was deposited by resedimentation processes. This idea is supported by the matrix-supported texture of the sediment and structures such as fining-upward strata and cross-bedding. These features indicate that the sediment may have been deposited by turbidity currents (Figure **F20**). We interpret the sediment intervals with horizontal and ripple laminations in Unit II as representing the Tc and Td divisions of a Bouma sequence.

Transition between Units I and II

The boundary between Units I and II is located at Section 368-U1501C-45X-1, 51 cm, and corresponds to a high-amplitude seismic unconformity. The boundary is dated at 24–27 Ma by the shipboard paleontologists based on foraminifer and nannofossil assemblages. We suggest this boundary can be correlated with the T60 unconformity at ODP Site 1148 (Li et al., 2005) (Figure **F5**). Above the boundary, Unit I is dominated by carbonate sediment, whereas Unit II is dominated by terrigenous material. The color of the sediment also varies abruptly from light brown in Unit I to dark and very dark greenish gray in Unit II.

Depositional environment of Unit I

Unit I was deposited in a deep-marine environment (Figure **F25**). The dominant lithologies are clay-rich nannofossil ooze and nannofossil ooze with clay. There are variable amounts of foraminifers. Lithologic changes between subunits likely reflect the amount of terrigenous input into a relatively open ocean setting. This input may be delivered as buoyant plumes from shallower shelf environments and rarely by weak (distal) turbidity currents. There is little change in the composition of the terrigenous grains, so we envisage a similar source for these grains throughout Unit I. Thin laminae of silt are found rarely but throughout Unit I. Some are graded, and all have sharp bases; however, many are disrupted by bioturbation and are interpreted as distal turbidites.

Soft-sediment deformation in Subunit IB, including inclined and convolute bedding, indicates slumping downslope of parts of the sequence. Bedding above and below this interval is consistently horizontal, indicating the deformation was synsedimentary.

Structural geology

Site U1501 is located on the OMH in a water depth of 2846 m. The southwest–northeast-oriented seismic profile (Figure **F5**) across the OMH reveals the occurrence of extensional structures controlled by steeply dipping southwest-normal faults with obvious offset and tilting of seismic reflectors (~5°). The T60 seismic unconformity is supposed to represent the Oligocene/Miocene boundary. Downsection, the Tg reflector may mark the base of the Cenozoic sediments (Pang et al., 2007). This site was considered a high-priority target to recover pre- (below Tg), syn-, and postrift sediments (see also **Background and objectives**).

Lithostratigraphic Unit I structures

Lithostratigraphic Unit I, which essentially consists of nannofossil oozes, has predominantly horizontal to subhorizontal bedding that in most cases is erased due to moderate to strong bioturbation. This unit is devoid of any structures related to tectonic deformation, apart from some rare normal faults, such as the one observed in interval 368-U1501C-19F-1, 109–127 cm (Figure **F26**), which preserves a high-angle planar normal fault with an apparent dip of 65° and an offset of 6 cm. In addition, local soft-sediment deformation structures such as slump folds were observed in Subunits IB and IC.

Lithostratigraphic Unit II structures

Lithostratigraphic Unit II is characterized by subhorizontal to gently dipping bedding. Dips as steep as 40° were locally observed in close relation to parallel lamination and therefore interpreted as cross-laminae (see **Lithostratigraphy**). In contrast to Unit I, deformation structures were observed within Unit II, although their occurrence is rather heterogeneously distributed. Subunit IIA is affected by millimeter-scale normal faults and joints, especially across Cores 368-U1501C-47X and 48X (Figure **F27**). In these cores, normal faults are typically planar to irregular with small apparent offsets as large as 0.5 cm and apparent dips of 10°–40°. They form semiregular arrays with millimeter- to centimeter-scale spacing, often arranged in an "en echelon" geometry (e.g., interval 47X-6, 126–129 cm). Striations and slickensides were observed locally where the surfaces of such structures are exposed. The occurrence of slickensides and the overall polished appearance of such planes are clear evidence for a natural deformation process. However, the recognition of these original deformation structures remains locally difficult due to drilling disturbances caused by the XCB and RCB coring systems. Deformation in the underlying Subunits IIC–IIF is essentially characterized by the variably distributed occurrence of single to branched uniform calcite and quartz veins (Figure **F28**).

Lithostratigraphic Unit III structures

The prominent Tg reflector marks the top of lithostratigraphic Unit III, which is composed of lithified sandstone, sandstone with gravel, and minor conglomerate and laminated siltstone. This unit shows weak tilting of stratified beds expressed in apparent dips on split core surfaces as shallow as approximately 20°, which are best observed in the two last cores (368-U1501D-26R and 27R). Again, deformation structures remain scarce and heterogeneously distributed in Unit III. The recognized structures consist of veins, fractures, and local microfaults associated with cataclastic fault gouge. Locally structures associated with soft-sediment deformation are preserved. Single, branched, and en echelon uniform veins are filled by calcite or quartz (e.g., Cores 25R and 27R) (Figure **F29**). Planar and straight fractures were also observed with various dips from 40° to 55° showing locally striations and slickensides. In the sandstones, these fractures are often associated with alteration zones and filled by green fine-grained minerals likely resulting from diffusion-controlled chemical reactions between the matrix and a migrating reducing fluid (Figure **F29A**, **F29D**). Finally, slump folds were recovered in Core 26R (Figure **F29F**), providing evidence for soft-sediment deformation during mass movements.

Interpretation

Despite the various tilting of seismic reflectors in the proximity of extensional structures, especially between the T60 seismic unconformity and the Tg reflector observed on the seismic profile (Figure **F5**), no evidence of significant bedding tilting and/or deformation structures was observed at this site. However, the observed millimeter-scale normal faults in Unit II may be related to an extensional event during or soon after its deposition. In seismic data, the top of Unit II describes a wedge geometry controlled by southwest-dipping normal faults (Figure **F5**). The end of this extensional event may correspond to the marked decrease of terrigenous input and the transition from clays, silts, and sands in Unit II to clearly pelagic nannofossil oozes in Unit I. In line with lithostratigraphic observations and physical properties, the boundary between Units I and II is extremely sharp, reflecting a switch from bathyal marine depositional conditions in Subunit IIA to deep-sea depositional conditions in Unit I.

Figure F26. Deformation structures, Unit I. Normal fault affecting nannofossil oozes (368-U1501C-19F-1, 108-127 cm).

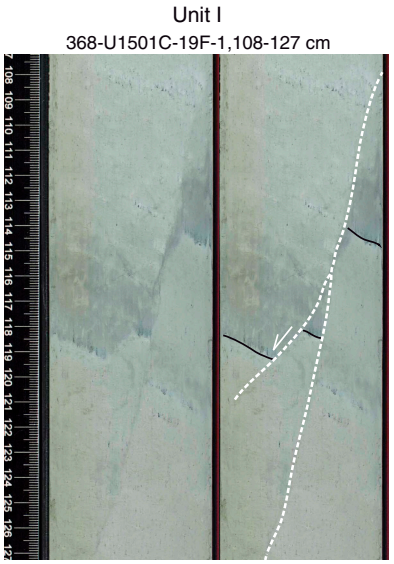

Figure F27. Deformation structures, Subunits IIA and IIB. A. Millimeter-scale normal faults and fractures. B. En echelon millimeter-scale normal faults and fractures. C. Millimeter-scale normal fault offsetting black layers from about 5 mm within the nannofossil-rich clay. D. Slickenslide on an exposed polished fault surface.

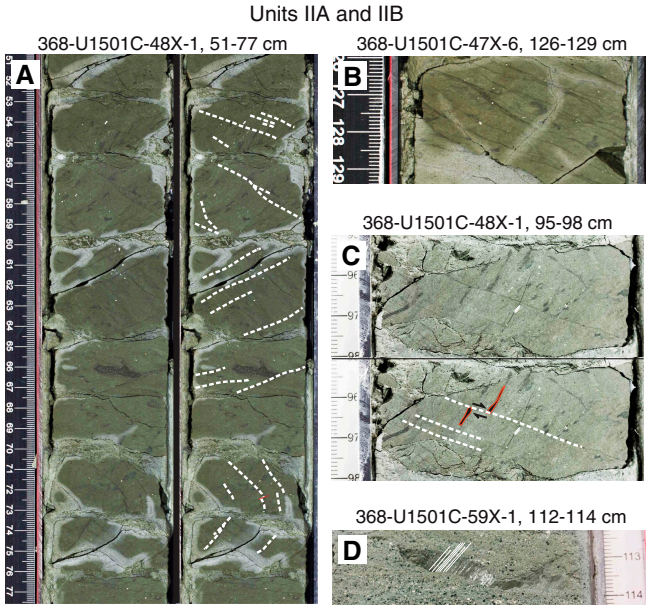

Unit III records a slight tilting compared to Units I and II, suggesting an unconformable relationship between them. This unit was likely deposited before the main Cenozoic rifting of the SCS continental margin. Despite relatively minor evidence for internal deformation, the tilting of beds, the soft-sediment deformations, and the nature of the lithostratigraphic succession may suggest that this unit was deposited during active tectonic processes. Mesozoic basins documented onshore (e.g., Nanni et al., 2017) may represent a possible analog for the tectonic setting during Unit III deposition.

Figure F28. Distinct uniform calcite and quartz vein shapes and structures, Subunit IIC. A, D. Single. B, C. Branched.

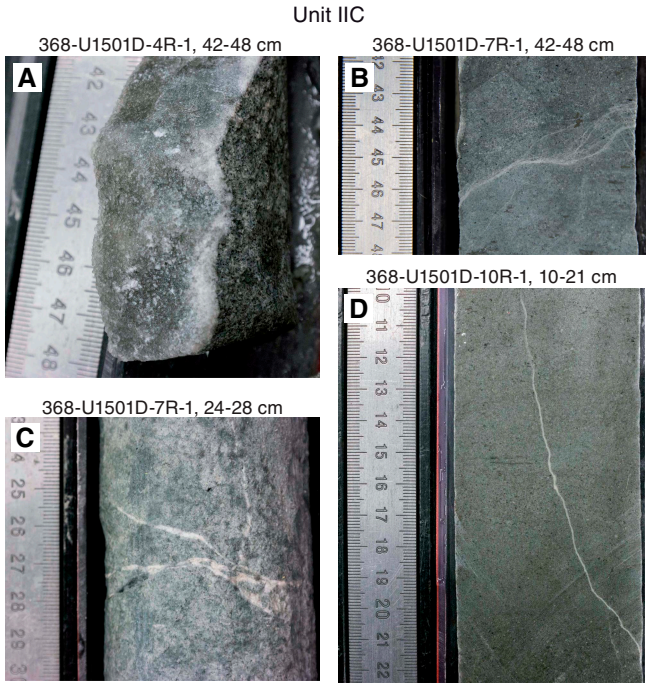

Figure F29. Deformation structures, Unit III. A. Straight fracture associated with a green alteration pattern. B. Fine-grained cataclastic fault gouge developing along a straight fracture. C. Single uniform quartz vein. D. Straight fracture associated with an alteration zone. E. En echelon uniform calcite vein. F. Convolute bedding associated with centimeter-scale slump fold.

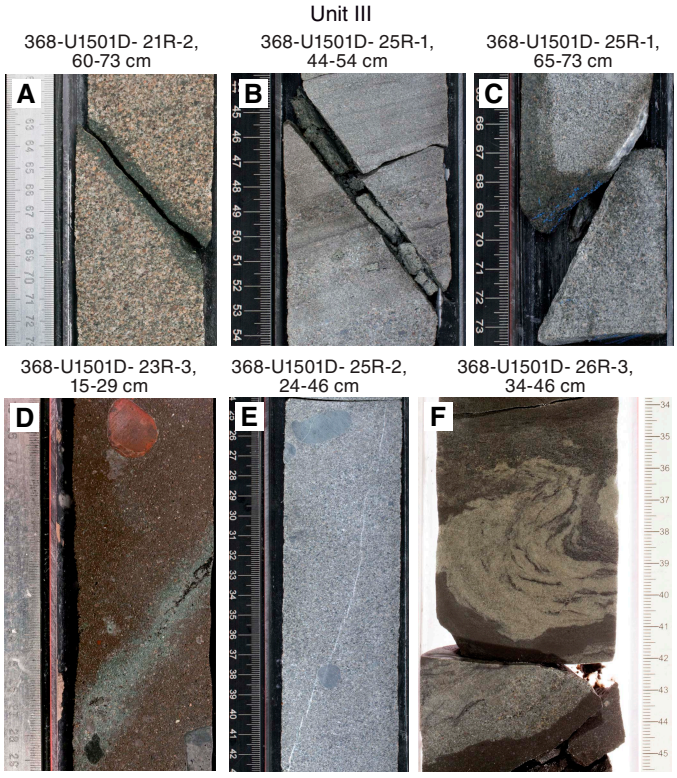

Biostratigraphy

All core catcher samples at Site U1501 were analyzed for calcareous nannofossils, planktonic and benthic foraminifers, diatoms, and ostracods. Additional samples were taken from intervals in the working-half cores when necessary to refine the ages. Preservation of calcareous microfossils is good to very good in samples from Cores 368-U1501A-1H, 368-U1501B-1H, and 368-U1501C-1H through 44X and moderate to poor in Cores 368-U1501C-45X through 62X and 368-U1501D-2R through 5R. Samples 368-U1501A-1H-CC, 368-U1501B-1H-CC, and 368-U1501C-1H-CC and 2H-CC are composed of as much as 10% diatoms with moderate preservation, whereas other core catcher samples are rare or barren of diatoms (Table **T4**). Planktonic foraminifers and calcareous nannofossils are abundant in Cores 368-U1501A-1H, 368-U1501B-1H, and 368-U1501C-1H through 44X; rare to common in Cores 368-U1501C-45X through 62X and 368-U1501D-2R through 5R; and barren in Cores 368-U1501D-6R through 27R.

Forty biostratigraphic datums were identified in a generally continuous succession from the Holocene to the late Eocene (Tables **T5**, **T6**; Figure **F30**).

The Pleistocene/Pliocene boundary is placed within Core 368-U1501C-7H, the Pliocene/Miocene boundary is placed within Core 9H, the Miocene/Oligocene boundary is placed between Cores 41X and 42X, and the Oligocene/Eocene boundary is placed between Cores 53X and 54X. Sedimentation rates varied from ~13 mm/ky in the early Oligocene to ~11 mm/ky in the early–middle Miocene, ~14 mm/ky in the Pliocene, and 24 mm/ky in the Pleistocene. Sedimentation rates during the late Oligocene and late Miocene were much lower (~36 mm/ky), suggesting hiatuses may be present during these periods, whereas a relatively higher sedimentation rate (35 mm/ky) existed during the upper late Oligocene to the lower early Miocene.

Relatively higher abundances of benthic foraminifers with dominant shallow-water marker species in Cores 368-U1501C-45X through 62X and 368-U1501D-2R through 5R indicate an upper-slope environment during the Eocene to early Oligocene, whereas there is a higher abundance of planktonic foraminifers above Core 368-U1501C-44X, suggesting a deep ocean environment since the late Oligocene.

Calcareous nannofossils

Core catchers from Holes U1501A–U1501D were examined (Table **T7**). Calcareous nannofossil biostratigraphy for Site U1501 was based mainly on the analysis of all core catcher samples from Hole U1501C. To better constrain biostratigraphic events, a number of samples from intervals within cores were analyzed.

Calcareous nannofossils are very abundant and well preserved in the upper part of the succession (Cores 368-U1501C-1H through 45X). Nannofossils in samples below Section 46X-CC (321.81 m) generally degrade to low abundance and moderate preservation with intermittent abundance increases down to the bottom of Hole U1501C. In Cores 368-U1501D-2R through 5R, nannofossils are rare to common with moderate preservation. Nannofossils are barren below Section 6R-CC (471.99 m) to the bottom of Hole U1501D. Some of the samples from Hole U1501C exhibit signs of slight reworking, overgrowth, and fragmentation.

Twenty-four nannofossil biostratigraphic datums were recognized in the Oligocene through Pleistocene sediment sequence at Site U1501 (Table **T5**). The oldest nannofossil event identified at Site U1501 is the last appearance datum (LAD) of *Coccolithus for-*

mosus at 379.64 m (Sample 368-U1501C-52X-CC), which indicates an age older than 32.92 Ma.

Pleistocene

The top of Hole U1501C (Samples 1H-CC to 2H-CC; 0–17.98 m) is dated as late Pleistocene based on the presence of *Emiliania huxleyi* (marker species for Zone NN21). The LAD of *Pseudoemiliania lacunosa* in Sample 3H-CC (28.56 m) defines the top of Zone NN19. Zone NN19 is further divided by two nannofossil events: the LAD of large *Gephyrocapsa* spp. (>5.5 µm) in Sample 4H-CC (38.08 m) and the LAD of *Calcidiscus macintyrei* in Sample 5H-CC (46.95 m). The top of Zone NN18 is marked by the LAD of *Discoaster brouweri* in Sample 6H-CC (57.07 m).

Pliocene

Pliocene nannofossil Zone NN16 was recognized in Hole U1501C. Two events occur in the lower part of Zone NN16: the LAD of *Discoaster tamalis* (2.8 Ma) in Sample 7H-CC (66.22 m) and the LAD of *Sphenolithus* spp. (3.54 Ma) in Sample 8H-CC (75.81

Table T4. Distribution of diatom species, Site U1501. **View table in PDF format. Download table in CSV format.**

Table T5. Calcareous nannofossil biostratigraphic events, Site U1501. T = top/last appearance datum, B = bottom/first appearance datum. **Download table in CSV format.**

Epoch		Biozone (Martini, 1971)	Calcareous nannofossil event	Top		Bottom		Age model	
				Core, section	Depth CSF-A (m)	Core, section	Depth CSF-A (m)	Depth (m)	Age (Ma)
				368-U1501C-		368-U1501C-			
Pleistocene		NN21	B *Emiliania huxleyi*	2H-CC	17.98	3H-CC	28.56	23.27	0.29
		NN19	T *Pseudoemiliania lacunosa*	2H-CC	17.98	3H-CC	28.56	23.27	0.44
			T *Gephyrocapsa* spp. >5.5 µm	3H-CC	28.56	4H-CC	38.08	33.32	1.24
			T *Calcidiscus macintyrei*	4H-CC	38.08	5H-CC	46.95	42.52	1.60
		NN18	T *Discoaster brouweri*	5H-CC	46.95	6H-CC	57.07	52.01	1.93
Pliocene		NN16	T *Discoaster tamalis*	6H-CC	57.07	7H-CC	66.22	61.65	2.80
			T *Sphenolithus* spp.	7H-CC	66.22	8H-CC	75.81	71.02	3.54
Miocene	late	NN11	T *Discoaster quinqueramus*	8H-CC	75.81	9H-CC	85.50	80.66	5.59
		NN11	B *Discoaster berggrenii*	10H-CC	94.91	11H-CC	104.91	99.91	8.29
		NN8	B *Catinaster coalitus*	11H-CC	104.91	12H-CC	113.97	109.44	10.89
	middle	NN7	T *Discoaster kugleri*	13H-CC	123.83	14H-CC	131.53	127.68	11.58
		NN6	T *Cyclicargolithus floridanus*	14H-CC	131.53	15H-CC	142.19	136.86	11.85
		NN5	T *Sphenolithus heteromorphus*	15H-CC	142.19	16H-CC	151.80	147.00	13.53
		NN4	T *Helicosphaera ampliaperta*	21F-CC	175.97	22F-CC	180.60	178.29	14.91
	early	NN2	T *Triquetrorhabdulus carinatus*	23F-CC	184.45	24F-CC	189.47	186.96	18.28
			B *Sphenolithus belemnos*	26F-CC	198.38	27F-CC	204.08	201.23	19.03
			B *Helicosphaera ampliaperta*	27F-CC	204.08	28F-CC	208.70	206.39	20.43
			B *Sphenolithus disbelemnos*	40X-CC	265.35	41X-CC	273.91	269.63	22.76
Oligocene		NN1	T *Sphenolithus delphix*	41X-CC	273.91	42X-CC	283.46	278.69	23.11
		NP25	T *Sphenolithus ciperoensis*	43X-CC	293.15	44X-CC	302.56	297.86	24.43
		NP24	T *Sphenolithus predistentus*	44X-CC	302.56	45X-CC	312.20	307.38	26.93
		NP24	B *Sphenolithus ciperoensis*	45X-CC	312.20	46X-CC	321.81	317.01	29.62
		NP22	T *Reticulofenestra umbilicus*	48X-CC	340.46	49X-CC	350.49	345.48	32.02
		NP21	T *Coccolithus formosus*	51X-CC	369.98	52X-CC	379.64	374.81	32.92

Table T6. Planktonic foraminifer events, Site U1501. T = top/last appearance datum, B = bottom/first appearance datum, Bc = bottom/first common appearance datum (acme). **Download table in CSV format.**

Epoch	Biozone (Blow, 1969)	Events	Top		Bottom		Age model	
			Core, section	Depth CSF-A (m)	Core, section	Depth CSF-A (m)	Depth (m)	Age (Ma)
			368-U1501C-		368-U1501C-			
Pleistocene	N22	T *Globigerinoides ruber* (pink)	1H-CC	9.24	2H-CC	17.98	13.61	0.12
	N22	Bc *Globigerinoides ruber* (pink)	2H-CC	17.98	3H-CC	28.56	23.27	0.40
	N22	T *Globigerinoides fistulosus*	4H-CC	38.08	5H-CC	46.95	42.52	1.88
	N20–N21	T *Globorotalia multicamerata*	5H-CC	46.95	6H-CC	57.07	52.01	2.18
Pliocene	N20–N21	T *Dentoglobigerina altispira*	7H-CC	66.22	8H-CC	75.81	71.02	3.47
	N19	T *Globoturborotalita nepenthes*	8H-CC	75.81	9H-CC	85.05	80.66	4.37
Miocene	N17	T *Globoquadrina dehiscens*	10H-CC	94.91	11H-CC	104.91	99.91	5.92
	N12	T *Fohsella fohsi*	12H-CC	113.48	13H-CC	123.83	118.66	11.79
	N8	B *Praeorbulina sicana*	22F-CC	180.60	23F-CC	184.45	182.53	16.38
	N6	T *Catapsydrax dissimilis*	24F-CC	189.47	25F-CC	193.35	191.41	17.54
	N5	T *Globoquadrina binaiensis*	27F-CC	204.08	28F-CC	208.70	206.39	19.09
	N4	T *Paragloborotalia kugleri*	32F-CC	226.47	33F-CC	231.83	229.15	21.12
Oligocene	N4	T *Globigerina ciperoensis*	40X-CC	265.35	41X-CC	273.91	269.63	22.90
	P21	T *Paragloborotalia opima*	43X-CC	293.15	44X-CC	302.56	297.86	26.93
	P19	T *Turborotalia ampliapertura*	46X-CC	321.81	47X-CC	331.18	326.50	30.28
Eocene	P18	T *Globigerinatheka subconglobata*	53X-CC	385.33	54X-CC	398.79	392.06	33.89

Figure F30. Age-depth model, Site U1501. Plotted event data are in Tables T6, T7, and T13 (see Paleomagnetism; Figure F40).

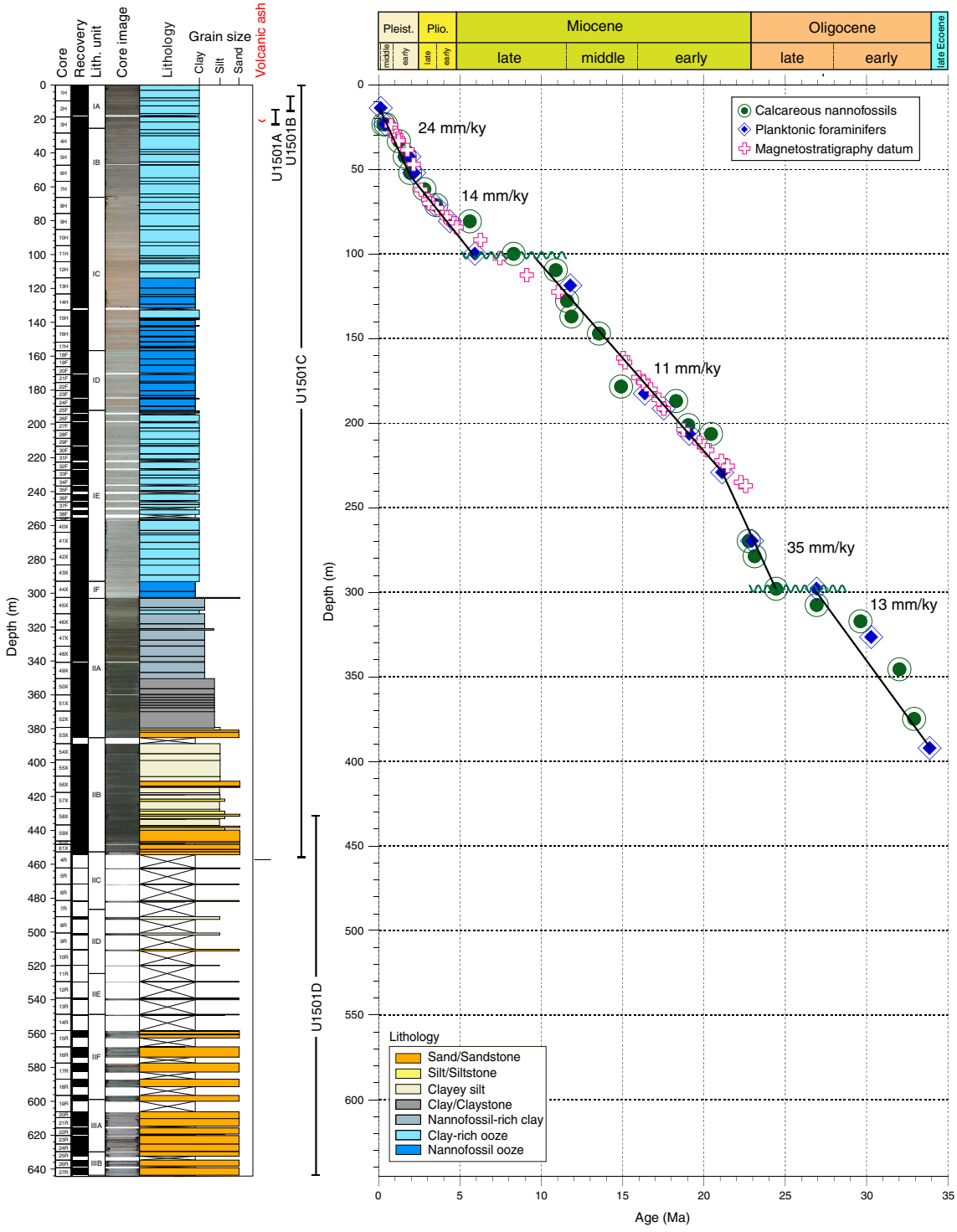

m). The Miocene/Pliocene boundary in Hole U1501C is placed between Samples 8H-CC (75.81 m) and 9H-CC (85.5 m) based on the LADs of *Sphenolithus* spp. (3.54 Ma) and *Discoaster quinqueramus* (5.59 Ma), respectively.

Miocene

Three events occur in the upper Miocene strata of Hole U1501C. The top of Zone NN11 is defined by the LAD of *D. quinqueramus* (5.59 Ma) in Sample 9H-CC (85.5 m). The first appearance datum (FAD) of *Discoaster berggrenii* (8.29 Ma) was found in Sample 10H-CC (94.91 m). The FAD of *Catinaster coalitus* was used to mark the base of Zone NN8 (10.89 Ma) in Sample 11H-CC (104.91 m). The late/middle Miocene boundary in Hole U1501C was assigned between Samples 11H-CC (104.91 m) and 14H-CC (131.53 m) based on the FAD of *C. coalitus* (10.89 Ma) and the LAD of *Discoaster kugleri* (11.58 Ma), respectively.

Table T7. Nannofossil abundance, Site U1501. **View table in PDF format. Download table in CSV format.**

Table T8. Distribution of planktonic foraminifers, Site U1501. **View table in PDF format. Download table in CSV format.**

Four events occur in the middle Miocene strata of Hole U1501C. The LAD of *D. kugleri* (11.58 Ma) within Zone NN7 occurs in Sample 14H-CC (131.53 m). The top of Zone NN6 is marked by the LAD of *Cyclicargolithus floridanus* (11.85 Ma) in Sample 15H-CC (142.19 m). The top of Zone NN5 is marked by the LAD of *Sphenolithus heteromorphus* (13.53 Ma) in Sample 16H-CC (151.8 m). The top of Zone NN4 is defined by the LAD of *Helicosphaera ampliaperta* (14.91 Ma) in Sample 22F-CC (180.6 m). The middle/early Miocene boundary was assigned between Samples 22F-CC (180.6 m) and 24F-CC (189.47 m).

Four events occur in the lower Miocene strata of Hole U1501C. The top of Zone NN2 is marked by the LAD of *Triquetrorhabdulus carinatus* (18.28 Ma) in Sample 24F-CC (189.47 m). The bottom of Zone NN2 is approximated by the FAD of *Sphenolithus disbelemnos* (22.76 Ma) in Sample 40X-CC (265.35 m). Two additional events were found in Zone NN2: the FAD of *Sphenolithus belemnos* (19.03 Ma) in Sample 26F-CC (198.38 m) and the FAD of *H. ampliaperta* (20.43 Ma) in Sample 27F-CC (204.08 m). The Miocene/Oligocene boundary was assigned between Samples 40X-CC (265.35 m) and 42X-CC (283.46 m) based on the FAD of *S. disbelemnos* (22.76 Ma) and the LAD of *Sphenolithus delphix* (23.11 Ma), respectively.

Oligocene

Six events were identified in the Oligocene strata of Hole U1501C. The LAD of *S. delphix* (23.11 Ma) within Zone NN1 occurs in Sample 42X-CC (283.46 m), the LAD of *Sphenolithus ciperoensis* (24.43 Ma) within Zone NP25 occurs in Sample 44X-CC (302.56 m), and the LAD of *Sphenolithus predistentus* (26.93 Ma) and FAD of *S. ciperoensis* (29.62 Ma) within Zone NP24 occur in Sample 45X-CC (312.2 m). The top of Zone NP22 is marked by the LAD of *Reticulofenestra umbilicus* (32.02 Ma) in Sample 49X-CC (350.49 m). The top of Zone NP21 is marked by the LAD of *C. formosus* (32.92 Ma) in Sample 52X-CC (379.64 m).

From Sample 52X-CC (379.64 m) to the bottom of Hole U1501C (Sample 62X-CC, 457.83 m), the nannofossil assemblage includes *Chiasmolithus altus, C. formosus, Discoaster nodifer, Discoaster tani, Discoaster williamsii, Helicosphaera bramlettei, Helicosphaera recta, Helicosphaera compacta, Lanternithus minutus, Pontosphaera exilis, Pontosphaera punctosa, Reticulofenestra circus, Reticulofenestra, R. umbilicus, Reticulofenestra erbae,* and *Reticulofenestra lockeri*. Such a nannofossil assemblage indicates a late Eocene age for the base of Hole U1501C.

The nannofossil assemblages in Cores 368-U1501D-2R through 5R are similar to those in samples from the bottom part of Hole U1501C, so they were also assigned to the late Eocene. Nannofossils are barren from Sample 6R-CC (471.99 m) to the bottom of Hole U1501D, so we cannot determine the age of these samples.

Planktonic foraminifers

All core catcher samples and several additional samples from the split cores in Holes U1501A–U1501D were processed for planktonic foraminiferal analyses (Table **T8**). Planktonic foraminifers are well preserved and abundant for samples from Cores 368-U1501A-1H, 368-U1501B-1H, and 368-U1501C-1H through 44X and moderate to poorly preserved or even recrystallized and less abundant in Cores 368-U1501C-45X through 62X.

Only one core was drilled in Holes U1501A and U1501B. Abundant pink *Globigerinoides ruber* specimens were observed in the core catcher samples, indicating an age between 0.12 and 0.4 Ma for the bottom of these two holes. No planktonic foraminifer was observed in Hole U1501D.

Sixteen planktonic foraminiferal datums were recognized in Hole U1501C, spanning the late Eocene (<37.75 Ma) to the late Pleistocene (Plate **P1**; Table **T6**). The planktonic foraminiferal biostratigraphy for Hole U1501C was established by these events and the planktonic foraminiferal assemblages at successive depth intervals.

The Pleistocene planktonic foraminifers are composed of *G. ruber, Globigerinoides sacculifer, Globorotalia menardii, Pulleniatina obliquiloculata,* and *Neogloboquadrina dutertrei*. The LAD of pink *G. ruber* (0.12 Ma) and FAD of pink *G. ruber* acme (0.40 Ma) are placed between Samples 1H-CC and 2H-CC and Samples 2H-CC and 3H-CC, respectively. The LAD of *Globigerinoides fistulosus* (1.88 Ma) is located between Samples 4H-CC and 5H-CC and marks the Zone N22/N21 boundary. The LAD of *Globorotalia multicamerata* (2.18 Ma) is located between Samples 5H-CC and 6H-CC.

The Pliocene planktonic foraminiferal assemblage is characterized by the higher content of *Dentoglobigerina altispira* and *Sphaeroidinellopsis seminulina*. The LAD of *D. altispira* (3.47 Ma) is located between Samples 7H-CC and 8H-CC. The LAD of *Globoturborotalita nepenthes* (4.37 Ma) is located between Samples 8H-CC and 9H-CC and defines the Zone N20/N19 boundary.

The middle–late Miocene foraminiferal assemblage is dominated by *D. altispira, Globoquadrina dehiscens,* and *Praeorbulina circularis/glomerosa*. The LAD of *G. dehiscens* (5.92 Ma) is located between Samples 10H-CC and 11H-CC and defines the boundary of Zones N18/N17. The LAD of *Fohsella fohsi* (11.79 Ma) is located between Samples 12H-CC and 13H-CC and defines the boundary of Zones N13/N12. The FAD of *Praeorbulina sicana* (16.38 Ma) is located between Samples 22F-CC and 23F-CC and marks the boundary of Zones N8/N7.

The late Oligocene–early Miocene planktonic foraminifers are characterized by *G. dehiscens, Globoquadrina venezuelana,* and *Paragloborotalia mayeri*. The LAD of *Catapsydrax dissimilis* (17.54 Ma) is located between Samples 24F-CC and 25F-CC and defines the boundary of Zones N7/N6. The LAD of *Globoquadrina binaiensis* (19.09 Ma) is located between Samples 27F-CC and 28F-CC. The LAD of *Paragloborotalia kugleri* (21.12 Ma) is located between Samples 32F-CC and 33F-CC as the boundary of Zones N5/N4. The LAD of *Globigerina ciperoensis* (22.90 Ma) is located between Samples 40X-CC and 41X-CC and represents the Miocene/Oligocene boundary.

Compared to the large planktonic foraminiferal components during the late Oligocene–early Miocene, the early Oligocene planktonic foraminifers are characterized by small *Paragloborotalia nana* and *Paragloborotalia opima*. The LAD of *P. opima* (26.93 Ma) is located between Samples 43X-CC and 44X-CC as the boundary of Zones P22/P21. The LAD of *Turborotalia ampliapertura* (30.28 Ma) is located between Samples 46X-CC and 47X-CC as the boundary of Zones P20/P19.

Plate P1. Principal planktonic foraminifers from Hole U1501C used in biostratigraphy analyses for Site U1501. 1: optical; 2–14: SEM. Scale bar = 100 µm. 1. *Globigerinoides ruber* pink (1H-CC). 2. *Globigerinoides fistulosus* (5H-CC). 3. *Globorotalia multicamerata* (7H-CC). 4. *Dentoglobigerina altispira* (9H-CC). 5. *Globoturborotalita nepenthes* (8H-CC). 6. *Globoquadrina dehiscens* (11H-CC). 7. *Fohsella fohsi* (15H-CC). 8. *Praeorbulina sicana* (23F-CC). 9. *Catapsydrax dissimilis* (26F-CC). 10. *Globoquadrina binaiensis* (28H-CC). 11. *Paragloborotalia kugleri* (32F-CC). 12. *Globigerina ciperoensis* (51X-CC). 13. *Paragloborotalia opima* (44X-CC). 14. *Globigerinatheka subconglobata* (54X-CC).

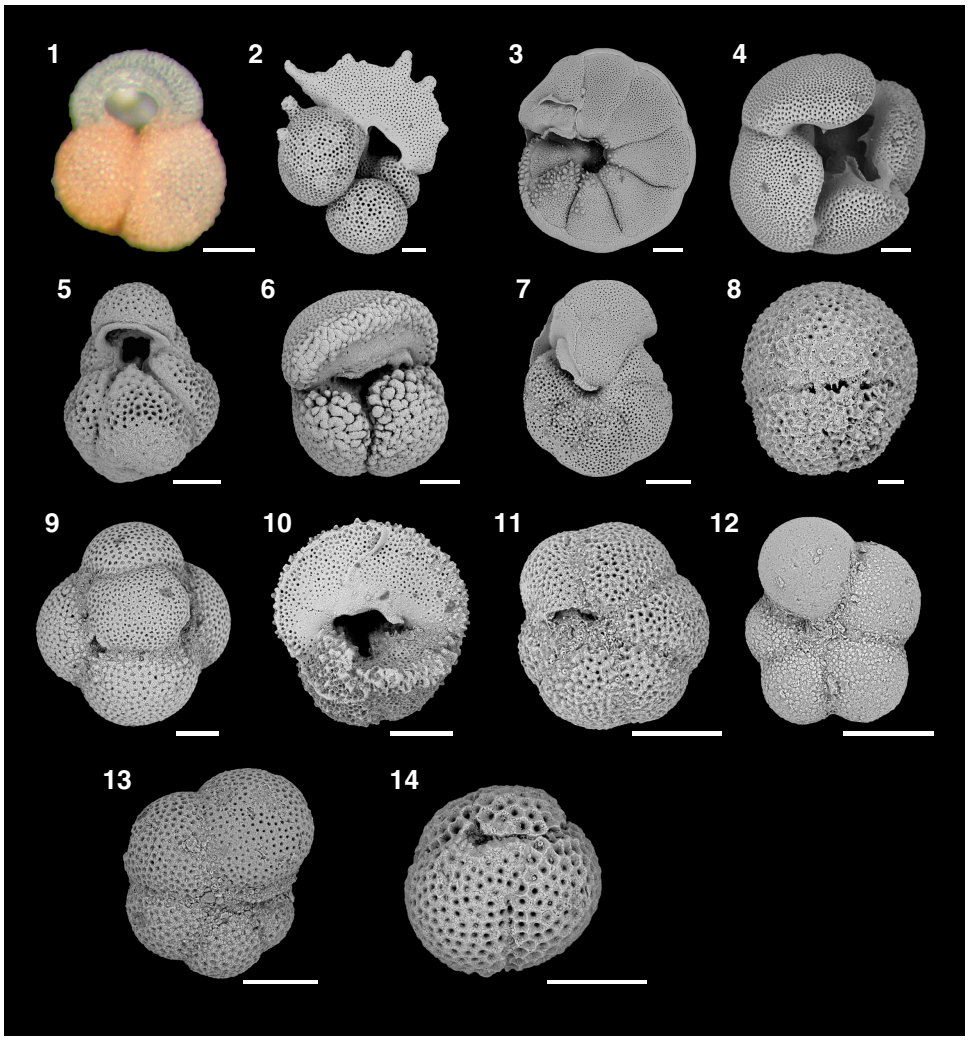

In Sample 54X-CC, late Eocene planktonic foraminiferal components such as *Globigerinatheka subconglobata* and *Globigerinatheka index rubriformis* were observed, suggesting a late Eocene age. Because of the low abundance and poor preservation of the planktonic foraminifers in Samples 368-U1501C-55X-CC to 62X-CC and their absence from Samples 368-U1501D-2R-CC to 27R-CC, a definite age for the lowest part of Holes U1501C and U1501D could not be determined.

Benthic foraminifers

Benthic foraminifers in Samples 368-U1501C-41X-CC to 62X-CC and 368-U1501D-2R-CC to 4R-CC were counted (~300 random specimens) from the >150 µm size fraction (Figure **F31**). Benthic foraminifers are abundant in Samples 368-U1501C-46X-CC and 368-U1501D-4R-CC and are more abundant than planktonic foraminifers in samples deeper than Sample 368-U1501C-54X-CC. *Bulimina* spp., *Melonis* spp., *Cibicidoides* spp., *Lenticulina* spp., and some agglutinated benthic foraminifers were observed in these samples. From the planktonic foraminifer/total foraminifer ratios, it is inferred that the paleoenvironment at this site changed from shelf (Samples 368-U1501C-54X-CC and 368-U1501D-4R-CC) to upper slope (Samples U1501C-46X-CC to 53X-CC) and then to deep sea (Samples 41X-CC to 45X-CC), clearly indicating an increasing water depth.

Diatoms

Core catcher samples from Holes U1501A–U1501D were processed into smear and strewn slides for diatom analysis. An additional 21 toothpick samples were taken from selected intervals of the working-half cores for better resolution. Samples 368-U1501A-1H-CC, 368-U1501B-1H-CC, and 368-U1501C-1H-CC and 2H-CC are composed of as much as 10% diatoms with moderate preservation. Smear slides from Samples 368-U1501C-3H-CC, 4H-CC, 35F-CC, 45X-CC, and 46X-CC contain <1% diatoms with poor preservation. The rest of the core catcher samples from Cores 368-U1501C-5H through 62X and 368-U1501D-2R through 27R are barren of diatoms (Table **T4**).

Figure F31. Statistics of benthic foraminifers (368-U1501C-41X-CC to 62X-CC and 368-U1501D-2R-CC to 4R-CC). B = barren, P = present, R = rare, F = few, A = abundant, D = dominant.

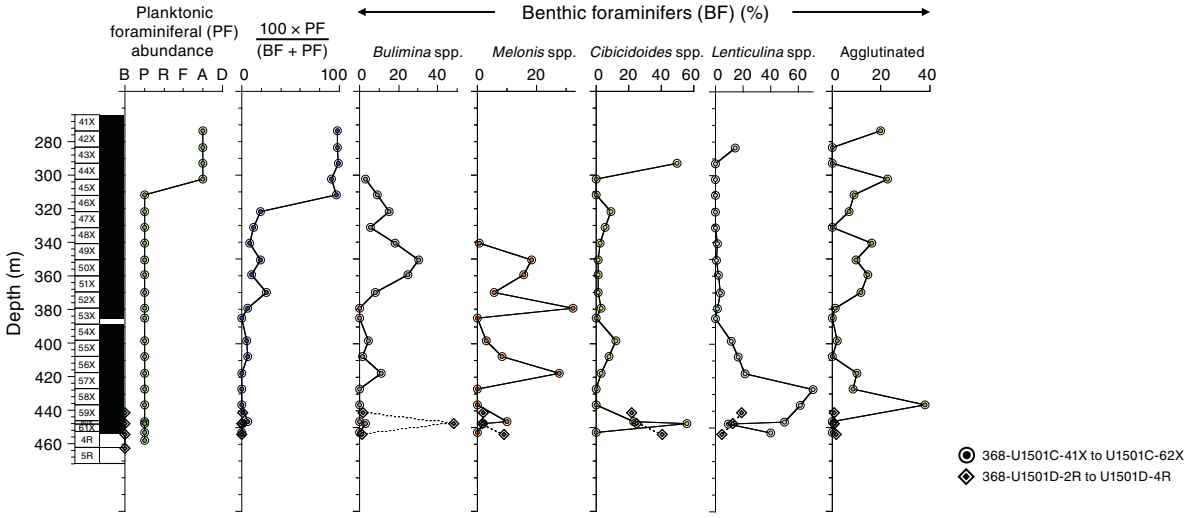

Toothpick samples of burrows in the working-half sections of Holes U1501C and U1501D were found to contain between 0% and 60% diatoms with poor to moderate preservations. Samples 368-U1501A-1H-CC, 368-U1501B-1H-CC, and 368-U1501C-1H-CC and 2H-CC contain a few specimens of *Fragilariopsis doliolus*, indicating an age of 2.0–0.6 Ma. A smear slide of a partially pyritized burrow in Sample 368-U1501C-35F-1, 118 cm, contains a few specimens of *Azpetia bukryi* with *Cestodiscus trochus* commonly observed, indicating an age range between 20.8 and 30.8 Ma (Table **T9**).

Ostracods

A preliminary examination of ostracods was conducted in core catcher samples from Holes U1501C and U1501D (Table **T10**) to characterize the assemblage variability through time and to reconstruct paleoenvironmental changes throughout the Cenozoic. Ostracod abundance ranges from absent to >60 valves per sample, and preservation varies from good (mostly in the Pleistocene section) to poor, although most specimens are moderately preserved. The highest incidences of ostracods were observed in Samples 368-U1501C-10H-CC to 16H-CC (94–151 m), 27F-CC to 31F-CC (204–221 m), 40X-CC to 43X-CC (265–293 m), and in particular Samples 49X-CC to 51X-CC (350.44–369.9 m) and 60X-CC (447.92 m). In Hole U1501D, ostracods are only present in Samples 2R-CC to 6R-CC.

In Hole U1501C, lower bathyal to abyssal genera (*Krithe, Legitimocythere, Henryhowella, Bradleya, Abyssocythereis, Argilloecia, Pennyella, Poseidonamicus, Pelecocythere, Arcacythere, Cytheropteron, Eucythere, Abyssocythere,* and *Parakrithe*) dominate the Oligocene through Pleistocene assemblage, indicating that deepwater conditions have existed in the SCS since the early Oligocene. Below 349 m (Sample 50X-CC, 40–45 cm, estimated to be of late Eocene age), the assemblage is characterized by upper bathyal and continental shelf taxa (e.g., *Heinia, Cytheropteron, Xestoleberis, Abrocythereis, Neomonoceratina, Trachyleberis, Cytherelloidea,* and *Cytherella*), although deep-sea genus *Krithe* remains present. In Hole U1501D, Samples 2R-2, 111–114 cm, and 4R-CC to 6R-CC (estimated to be middle to late Eocene in age) are composed of *Paranesidea* sp., *Cytherelloidea* cf. *Cytherelloidea asatoensis* Nohara, *Coquimba* sp., *Schizocythere*? sp., and *Paijenborchella sinensis*, among others. Paleoecologically, the absence of abyssal to upper bathyal or brackish water taxa in the assemblage indicates a shallow-marine environment (Plates **P2**, **P3**).

Table T9. Diatom biostratigraphic events, Site U1501. T = top/last appearance datum, B = bottom/first appearance datum. **Download table in CSV format.**

Epoch	Biozone (Scherer et al., 2007)	Diatom event	Top		Bottom		
			Core, section	Depth CSF-A (m)	Core, section, interval (cm)	Depth CSF-A (m)	Age model range (Ma)
Pleistocene	*Fragilariopsis reinholdii*	T *Fragilariopsis reinholdii* and B *Fragilariopsis doliolus*	1H-CC	9.05	3H-CC	28.56	2.01–0.61
Pliocene	Barren						
late Miocene							
middle Miocene							
early Miocene							
Oligocene	*Rossiella paleacea–Rocella vigilans*	T *Cestodiscus trochus*	34F-CC	234.45	35F-1, 118	237.88	20.8–30.8
		B *Azpetia bukryi*					
Eocene	Barren						

Table T10. Distribution of ostracods, Holes U1501C and U1501D. **View table in PDF format. Download table in CSV format.**

Plate P2. Representative Miocene to Pleistocene abyssal ostracods, Hole U1501C. 1. *Henryhowella* sp. (1H-CC). 2. *Legitimocythere* sp. (1H-CC). 3. *Krithe* sp. (3H-CC). 4. *Poseidonamicus* cf. *Poseidonamicus pintoi* Benson, 1972 (6H-CC). 5. *Pennyella* sp. (12H-CC). 6. *Cytheropteron* cf. *Cytheropteron uchioi* Hanai, 1957 (13H-CC). 7. *Bradleya* cf. *Bradleya metamorphica* Whatley et al. (14H-CC). 8. *Arcacythere* sp. (43X-CC).

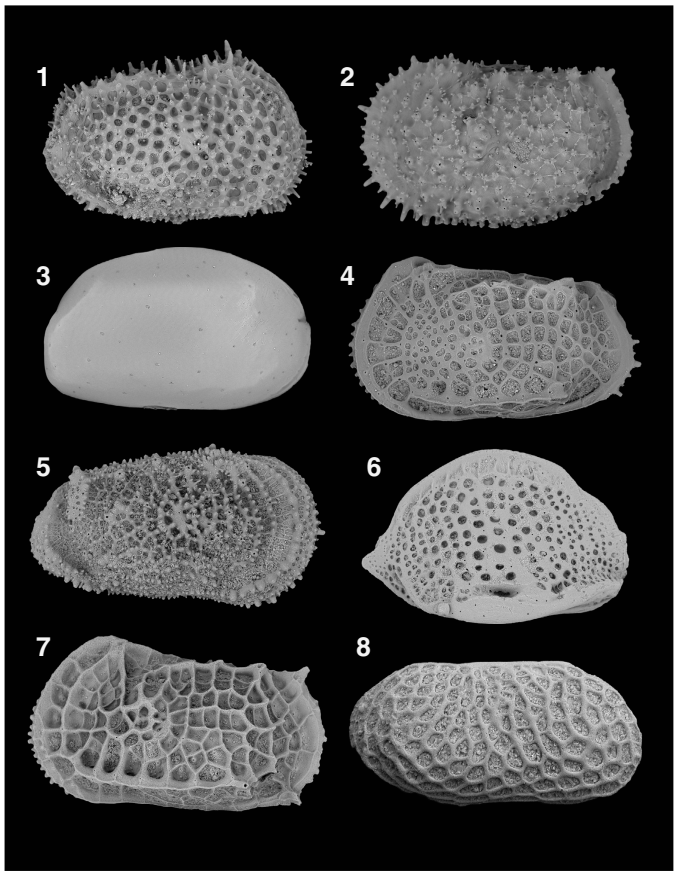

Plate P3. Representative late Eocene shallow-water marine ostracods, Hole U1501D. 1. *Cytherelloidea* sp. C (4R-CC). 2. *Cytherelloidea* cf. *Cytherelloidea asatoensis* Nohara (4R-CC). 3. *Schizocythere*? sp. (4R-CC). 4. *Paijenborchella sinensis* (Liu, 1989) (4R-CC). 5. *Paranesidea* sp. (4R-CC). 6. *Coquimba* sp. (4R-CC).

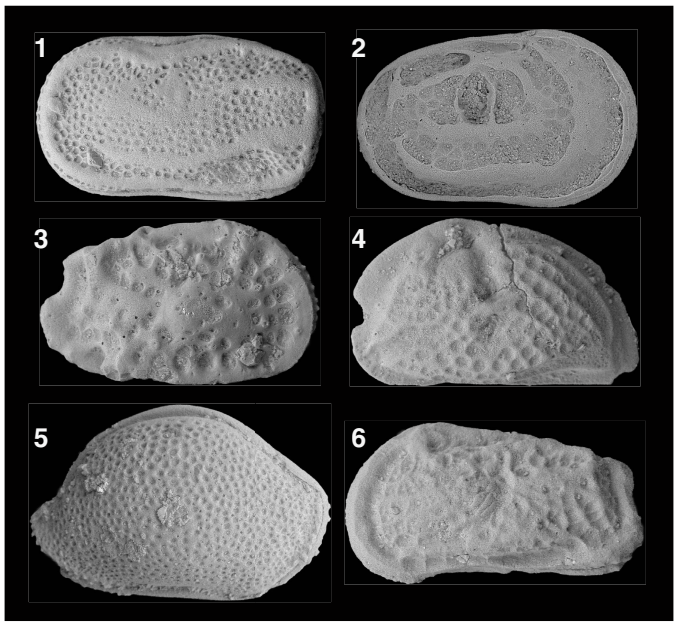

Paleomagnetism

Shipboard measurements

Shipboard paleomagnetic investigations combined three complementary approaches (see **Paleomagnetism** in the Expedition 367/368 methods chapter [Sun et al., 2018a]): (1) measurement and in-line AF demagnetization of archive-half sections on the pass-through 2G Enterprises SRM, (2) measurement and thermal demagnetization of oriented discrete samples on the SRM, and (3) measurement and AF demagnetization of oriented discrete samples on the spinner magnetometer (Agico JR-6A). Representative discrete samples were collected from every two sections (3 m), except where drilling disturbance was high or where core recovery was low.

First, we used scalar data from AF demagnetization up to 50 mT and thermal demagnetization on discrete samples to constrain the nature of the magnetic assemblage. Second, we used the directional and intensity data of archive-half sections, measured after the highest in-line AF demagnetization step (25 mT), to determine magnetic polarity along the core. Third, we used the directional and intensity data from discrete samples to validate the polarities inferred from section measurements. Directional data were analyzed using Zijderveld diagrams (Zijderveld, 1967), and the characteristic remanent magnetization (ChRM) direction(s) were calculated by principal component analysis (PCA) (Kirschvink, 1980) using the software PuffinPlot (version 1.03, 23 April, 2015) (Lurcock and Wilson, 2012).

Demagnetization behavior and implications for magnetic assemblages

Stepwise demagnetization of the NRM shows that 91% of analyzed samples lost the bulk of their magnetic remanence between 200° and 300°C. For all steps of thermal demagnetization, the cumulative behavior of all samples was analyzed (each sample having the same statistical weight). The loss of remanent magnetization was normalized to NRM and expressed as a percentage (Figure **F32**). This behavior shows that one or several phases with low T_C, such as pyrrhotite ($T_C \approx 325$°C; Tauxe, 2010) or greigite ($T_C \approx 330$°C; Tauxe, 2010), dominate the NRM. High SIRM/χ ratios are widely considered characteristic of greigite in sediments (e.g., Snowball, 1991; Roberts, 1995; Roberts et al., 2011). The rock magnetic experiments on six representative samples from Hole U1501C (Table **T11**), after magnetic saturation at 2.3 T, show SIRM/χ between 12.8 and 14.6 kA/m. These values rule out pyrrhotite and confirm the predominance of greigite in lithostratigraphic Unit I of Hole U1501C. Using a rare-earth magnet on a slurry from Section 368-U1501A-1H-CC (PAL), greigite was separated and concentrated. The grains observed with an optical binocular microscope are subhedral, pale yellow, partially corroded metallic cubes (≤10 µm in length). These grains, documented with SEM (Figure **F33**), have physical sizes in the 2–10 µm range, which corresponds to pseudosingle to multidomain magnetic grain sizes (Roberts et al., 2011). Overall, thermal demagnetization behaviors suggest that greigite dominates the NRM, at least to 83 m. However, the magnetic remanence remaining above 575°C (Figure **F34**) strongly suggests contributions from additional phases such as maghemite ($T_C \approx 590$°–675°C; Tauxe, 2010) or hematite ($T_C \approx 675$°C; Tauxe, 2010). The NRM remaining above 575°C increases notably in the 50–85 m interval in Hole U1501C. The maximum field strength of in-line AF demagnetization used on the archive-half sections is limited because of the destructive nature of the treatments and our limited ability to measure weak magnetizations in the magnetically noisy shipboard environment. To evaluate the effectiveness of AF demagnetization of the NRM, experiments were performed on six discrete samples from Hole U1501C (Table **T11**). These experiments reveal the existence of a high-coercivity phase characterized by self-reversal behavior (Figure **F35**). This self-reversal behavior is typical of greigite (Krs et al., 1992; Horng et al., 1998) and has recently been reported in Pleistocene sediments of the South Yellow Sea (Liu et al., 2014).

Typical behaviors of demagnetization from the three complementary approaches are shown in Figure **F36**. AF demagnetization of these samples with in-line AF produces demagnetization paths that are easier to interpret than the results of discrete samples subjected to AF demagnetization. Both AF and thermal treatments on discrete samples effectively remove a steep low-temperature/low-coercivity component, which represents the drilling overprint. However, thermal demagnetization is more effective at isolating ChRM, as evident by comparing results from twin samples collected from the same core and section (e.g., Figure **F36C**). The mean inclination gathered from the high-temperature component is 37.3° ± 6.6°, corresponding to a paleolatitude of 20.85° ± 3.3° for Unit I (see **Lithostratigraphy**).

Figure F32. Percentage of NRM loss between stepwise thermal demagnetization of NRM as a function of demagnetization temperature. Magnetization normalized to NRM (78 samples from Hole U1501C) carry the same statistical weight. Samples from Holes U1501A and U1501B were excluded to avoid statistically over representing the upper part of Unit I. Most magnetization is lost between 200° and 300°C, which shows that either greigite or pyrrhotite carry the NRM.

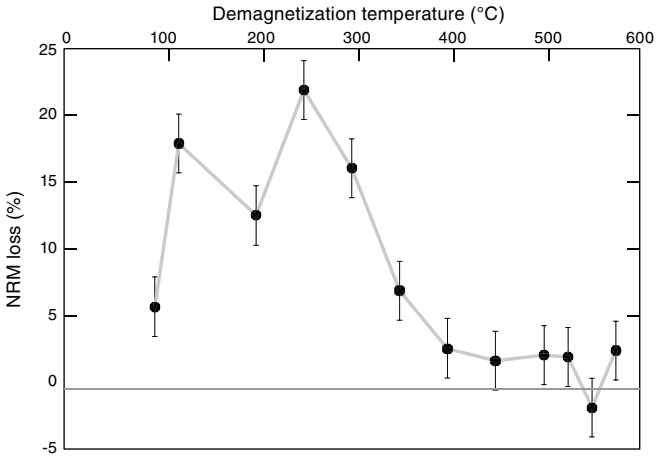

Table T11. Rock magnetic properties of representative samples, Hole U1501C. **Download table in CSV format.**

Core, section, interval (cm)	$SIRM_{2.3T}$ (A/m)	χ (10^{-6}), at 300 A/m	SIRM/χ (kA/m)
368-U1501C-			
3H-7, 30–32	4.91	338	14.6
4H-1, 36–38	6.53	462	14.1
4H-5, 27–29	4.87	345	14.1
6H-3, 26–28	5.03	362	13.9
7H-3, 30–32	5.32	416	12.8
8H-2, 90–92	4.33	313	13.8

Figure F33. SEM image of greigite cube (3 µm length), Hole U1501A. Material was magnetically separated with a rare earth magnet from a slurry prepared from core catcher sample.

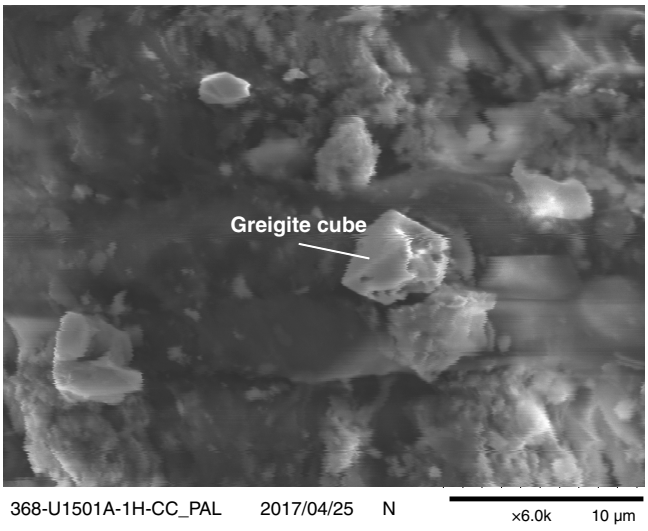

Many of the AF-demagnetized discrete samples reveal trends showing reversed or normal polarity in the last step of demagnetization (50 mT).

Thermal demagnetization shows removal of a steep low-temperature normal component which is carried up to 300°C.

Magnetostratigraphy

Inclination, declination, and intensity for Holes U1501A–U1501D are reported in Figures **F37**, **F38**, and **F39**. We constructed the magnetostratigraphy of Site U1501 based on the polarity assigned to the archive-half cores and recognized polarity reversals in Hole U1501D (Figures **F39**, **F40**, **F41**; Tables **T12**, **T13**). We did not use data from Hole U1501C from ~240 m to the bottom of the hole (Cores 35F through 62X) because a decrease in NRM moment hampers the determination of magnetic polarity.

Declinations from Holes U1501A and U1501B and Cores 368-U1501C-1H through 17H were corrected using the Icefield MI-5 core orientation tool (see **Paleomagnetism** in the Expedition 367/368 methods chapter [Sun et al., 2018a]). In Holes U1501C and U1501D, the interpretation of polarity deeper than 156.8 m is based only on the inclination data because the XCB and RCB coring processes disturb the geographic core orientation. Our interpretations of inclination are based on directions derived from the raw moments measured by the SRM at 25 mT and from the corroborative evidence from AF demagnetization of discrete samples.

We then correlated the magnetostratigraphic data of Site U1501 to the standard timescale (Ogg et al., 2016) and plotted them along with the tie points from the microfossil ages from shipboard paleontologists (Figures **F40**, **F41**). The paleomagnetic and paleontological age constraints match well over most of the section. A succession of eight normal and five reversed intervals was recognized in Hole U1501D (Table **T13**; Figure **F39**). The lack of fossils in Unit III prevents correlation of magnetostratigraphic features (n1 to n8 in Figure **F39**) to the geologic timescale. The apparently long n8 interval (~37.45 m thick) may only represent a relatively short duration (0.37 My) if the sedimentation rate was high (~100 mm/ky) at that time.

Figure F34. Variation of percentage of NRM left above 575°C, upper part of Hole U1501C (1H through 9H). Note the significant increase in the percentage below 60 m, which suggests an increasing contribution of maghemite or hematite.

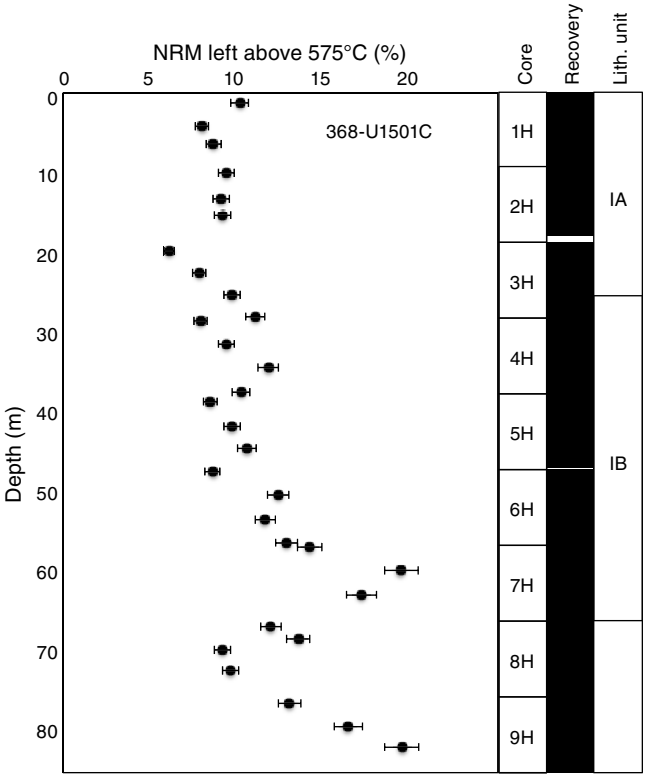

Figure F35. Magnetization normalized to NRM as a function of AF demagnetization, Hole U1501C. This behavior shows initially low coercivity below 30 mT followed by coercivity inversion (or plateau), generally attributed to magnetic self-reversal of greigite (e.g., Krs et al., 1992; Horng et al., 1998). Complete demagnetization requires AF fields >100 mT.

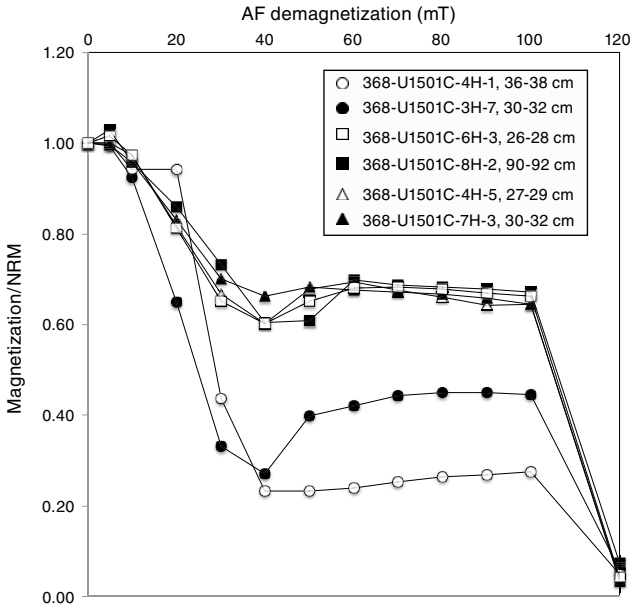

Figure F36. Demagnetization plots of (A, D, E, G, H) archive-half sections and (B, C, F, I) discrete samples, Holes U1501C and U1501D. A, B, D, E, F, G, H: AF demagnetized; C, I: thermally demagnetized. Zijderveld plots: solid squares = declination, open squares = inclination. Stereographic plots: solid squares = positive (down) inclination, open squares = negative (up) inclination. Calculated ChRM (blue line; red squares = measurements used in calculation) using PCA are in good agreement for samples coming from same section and subjected to different treatments. Unit I: (A) reversed polarity, (B) normal polarity but with last step indicating a tendency to reversal, (C) reversed polarity. Unit II: (D) normal polarity, (E) reversed polarity, (F) normal polarity. Unit III: (G) normal polarity, (H) reversed polarity, (I) normal polarity.

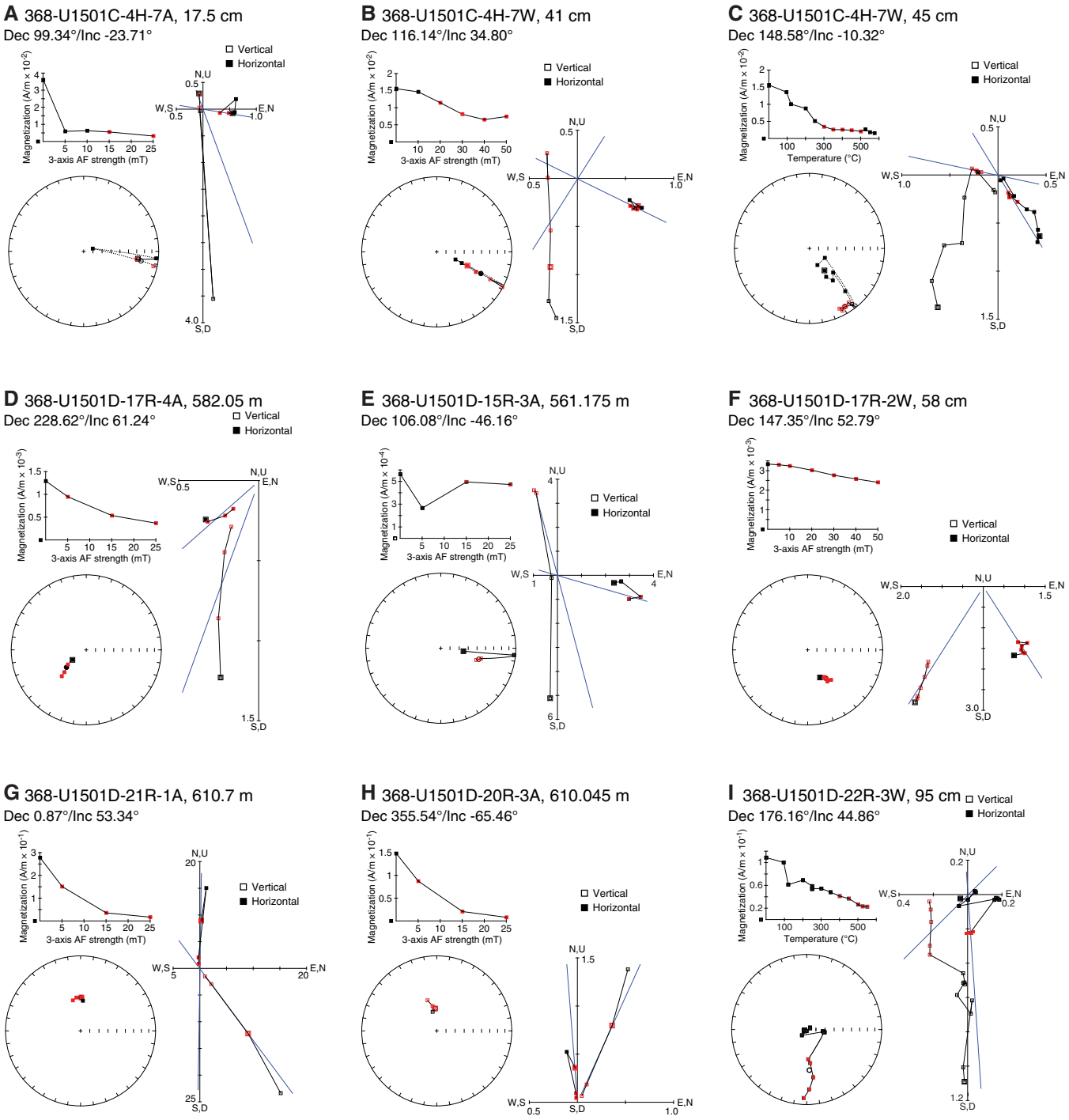

Based on both inclination and declination, we placed the boundary between the Brunhes and Matuyama Chrons at ~24 m in Hole U1501C. Based on our shipboard paleomagnetic age model, the middle/early Pleistocene boundary (0.78 Ma) is at ~24 m, the Pleistocene/ Pliocene (2.58 Ma) boundary is at ~62 m, and the Pliocene/ Miocene boundary (5.33 Ma) is at ~90 m (Table **T12**).

Figure F37. Magnetic measurements, Holes (A) U1501A and (B) U1501B. Inclination was used to determine polarity. AFD = AF demagnetization, TD = thermal demagnetization. Discrete samples are yellow and green.

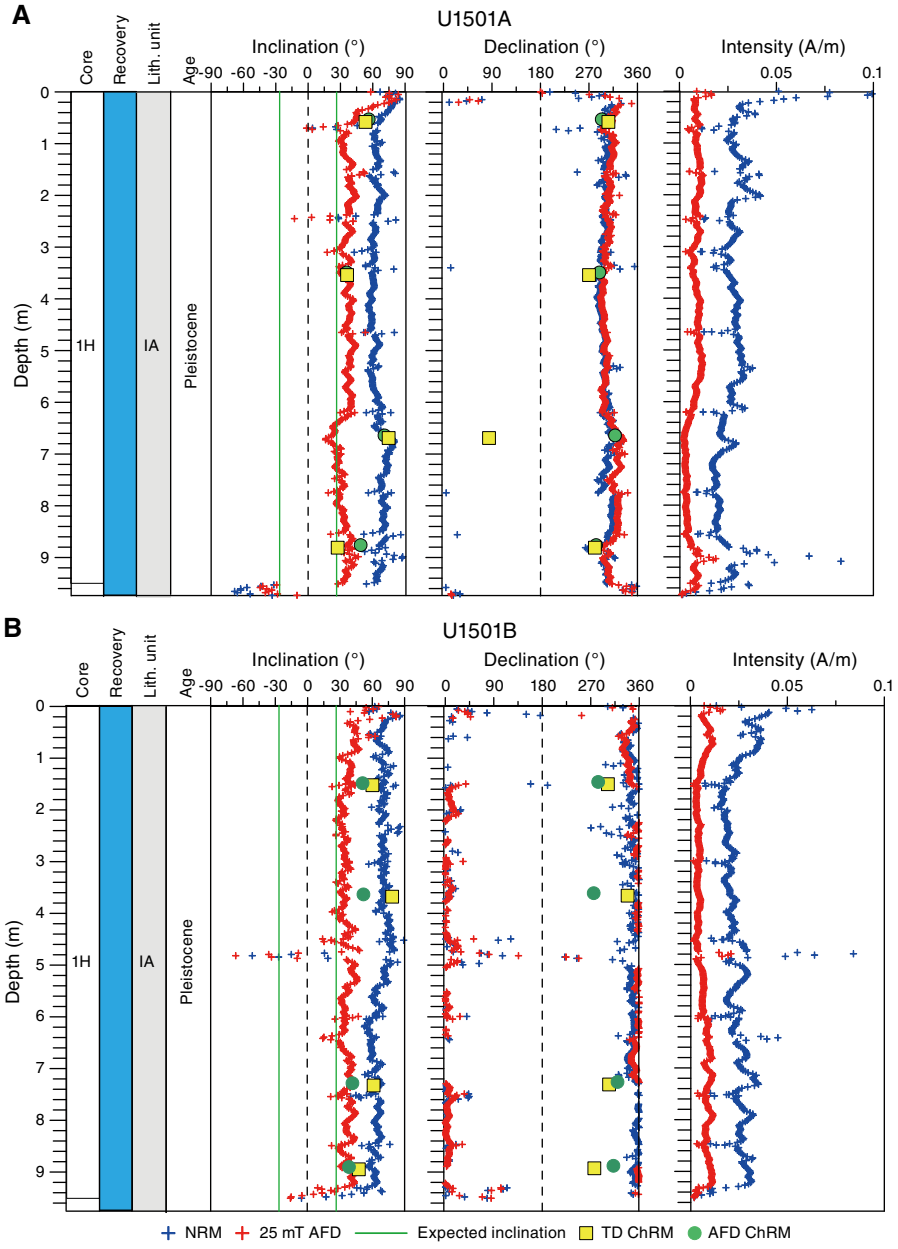

Figure F38. Magnetic measurements, Hole U1501C. Inclination was used to determine polarity. Discrete samples are yellow and green.

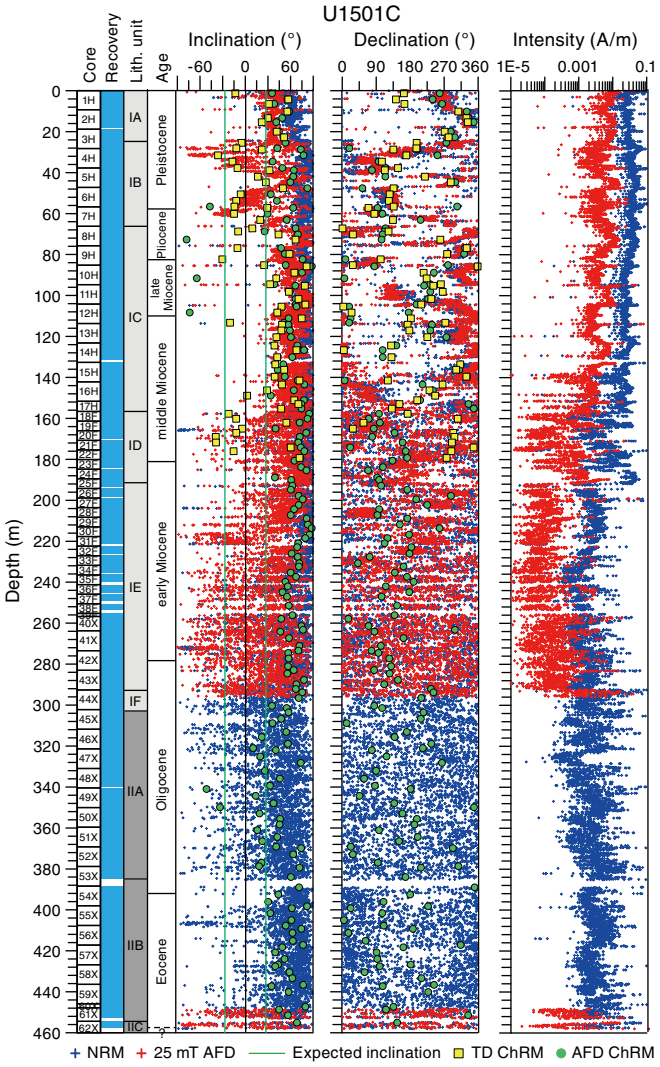

Figure F39. Magnetic measurements, Hole U1501D. Inclination was used to determine polarity. Magnetostratigraphic features are referred to as n1, etc., in a sequential manner for convenience and have no bearing on chrons. GTS2016 = geomagnetic polarity timescale of Ogg et al. (2016). Green circles = discrete samples.

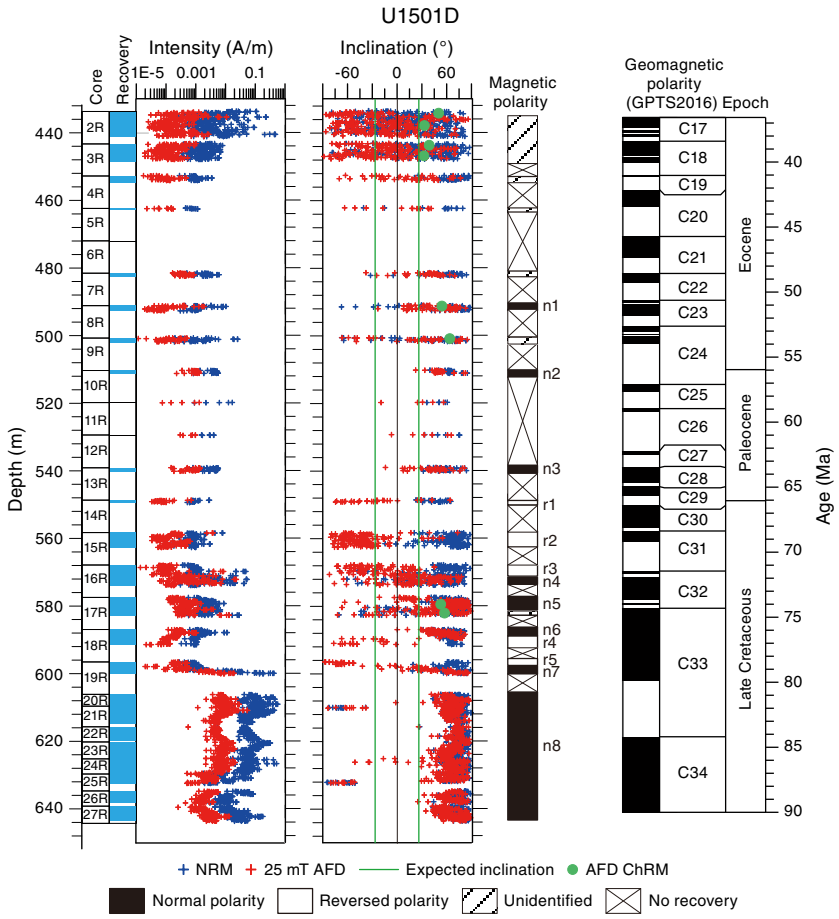

Figure F40. Magnetic measurements and correlation to magnetostratigraphy (368-U1501C-1H through 17H). Age-depth model constructed from shipboard paleomagnetic analysis. Magnetostratigraphy converted to time and plotted against standard geologic timescale (GPTS2016; Ogg et al., 2016). Magnetostratigraphic features are referred to as n1, etc., in a sequential manner for convenience and have no bearing on chrons. B/M = Brunhes/Matuyama Chron boundary, M/G = Matuyama/Gauss Chron boundary. Discrete samples are yellow and green.

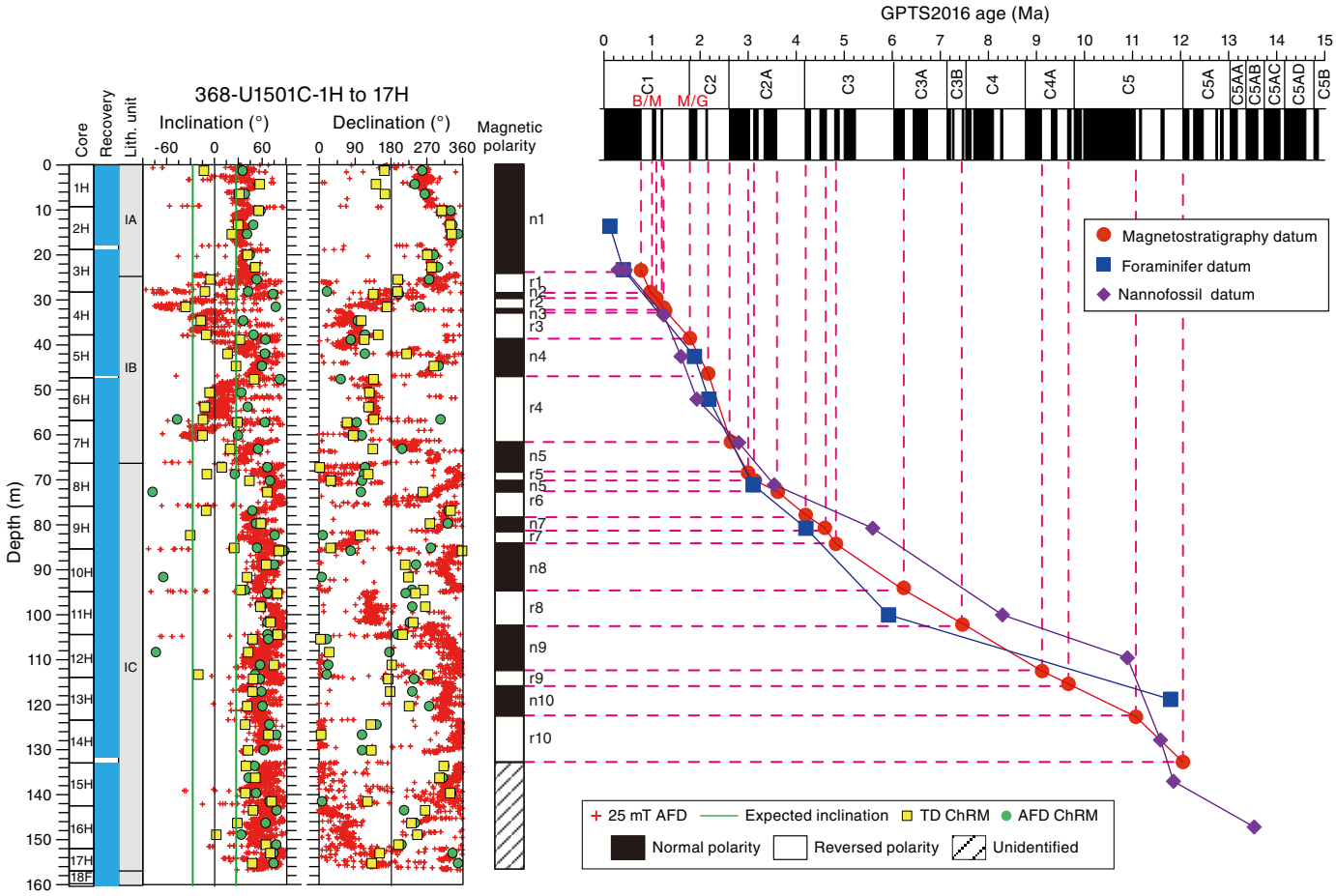

Figure F41. Magnetic measurements and correlation to magnetostratigraphy (U1501C-18F through 40X-2). Age-depth model constructed from shipboard paleomagnetic analysis. Magnetostratigraphy converted to time and plotted against standard geologic timescale (GPTS2016; Ogg et al., 2016). Magnetostratigraphic features are referred to as n1, etc., in a sequential manner for convenience and have no bearing on chrons. Discrete samples are yellow and green.

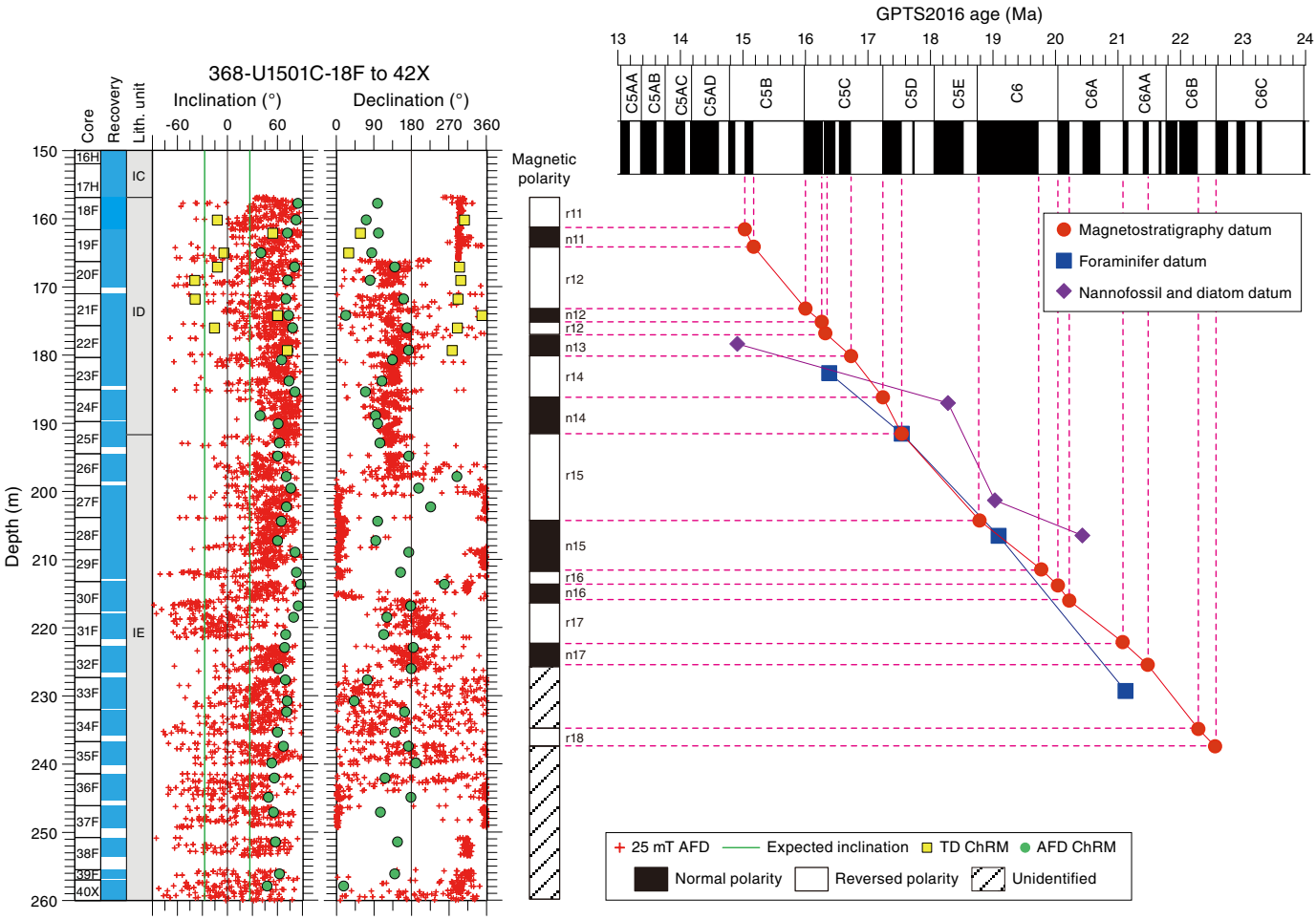

Table T12. Paleomagnetic age datums, Hole U1501C. **Download table in CSV format.**

Polarity chron	Age of chron base (Ma)	Depth CSF-A (m)
C1n (Brunhes)	0.773	24.00
C1r.1r	1.008	28.40
C1r.1n (Jaramillo)	1.076	30.00
C1r.2r	1.189	32.10
C1r.2n (Cobb Mountain)	1.221	33.05
C1r.3r	1.775	38.50
C2r.1n (Feni)	2.155	47.00
C2r.2r	2.61	61.90
C2An.1n	3.032	68.05
C2An.1r (Keana)	3.116	70.10
C2An.3n	3.596	72.80
C2Ar	4.187	78.20
C3n.2n (Nunivak)	4.631	81.70
C3n.2r	4.799	84.20
C3An.1n	6.252	91.60
C3Br.2r	7.454	102.40
C4An	9.105	112.45
C5n.2n	11.056	122.35
C5Bn.1r	15.032	161.40
C5Bn.2n	15.16	164.20
C5Br	15.974	173.14
C5Cn.1n	16.268	174.80
C5Cn.1r	16.303	176.12
C5Cn.3n	16.721	180.04
C5Cr	17.235	186.06
C5Dn	17.533	191.50
C5Er	18.748	204.25
C6n	19.722	211.50
C6r	20.04	213.50
C6An.1n	20.213	216.24
C6Ar	21.083	222.25
C6AAr.1n	21.483	225.52
C6Bn.2n	22.268	234.97
C6Br	22.564	237.08

Table T13. Interpreted possible magnetic polarity sequence, Hole U1501D. **Download table in CSV format.**

Possible magnetic polarity	Depth CSF-A (m)	
	Upper boundary	Lower boundary
n1	491.000	492.285
n2	510.200	511.125
n3	539.000	539.925
r1	548.700	549.275
r2	558.275	562.575
r3	564.000	570.725
n4	570.725	573.805
n5	577.400	582.505
n6	586.900	589.590
r4	589.625	591.355
r5	596.500	597.860
n7	598.805	599.940
n8	606.100	643.550

Geochemistry

Headspace gas concentrations were below detection due to low TOC contents <0.25 wt% and low levels of thermal alteration within underlying units. The bulk sediment geochemistry was controlled by lithology. High calcium carbonate content in lithostratigraphic Unit I reflects its high biogenic carbonate content. TOC and sulfur are mostly low in Unit I, with higher sulfur concentrations observed in lithostratigraphic Unit II. The low TOC concentrations in much of Unit I likely reflect poor preservation under aerobic conditions. The interstitial water concentration depth profiles show atypical redox zones for marine sediments with rates of sulfate reduction appearing to be inhibited, much as methanogenesis has likely been inhibited at this site. Sulfate reduction is more pronounced in Unit II (>300 m), and within this interval there is also heavy pyritization. Raman spectroscopy was applied shipboard to organic materials and indicates a mild thermal history for Units I and II. Surface-enhanced Raman spectroscopy yielded Raman bands diagnostic of asphaltene within the sediments of Unit I.

Headspace gas

Headspace gas samples were taken at a frequency of one sample per core or per 10 m of drilling advance for routine safety monitoring. Where possible, samples were collected from sections adjacent to interstitial water samples. At no point did hydrocarbon gas levels exceed a 12 ppmv detection limit—a limit corresponding to background values in air. Methane was detected in standard reference materials and within a paleomagnetism sample obtained from the core catcher of Core 368-U1501C-62X that evidenced drilling disturbance (frictional heating induced by rotation). A typical safety gas chromatogram is shown in Figure **F42**, in which hydrocarbons up to propane (C_4H_{10}) can be seen in the drilling-disturbed sample (propane is the highest carbon number that is quantified by the method used). Also shown are data for the analysis of a paleomagnetism sample obtained from the core catcher that was altered by drilling disturbance and contains light hydrocarbon gases. Analytical methods were capable of detecting light hydrocarbon gases, but none were present at significantly high concentrations within safety gas samples. Traces of propene were also detected, particularly from headspace samples collected close to the core liner and from RCB cores.

Figure F42. Gas chromatograms showing low levels of methane present in headspace samples, Hole U1501C. Detection of hydrocarbon gases in a drilling-disturbed sample obtained from a core catcher is shown for comparison. Relatively high proportions of ethene are consistent with generation of hydrocarbons by frictionally induced flash pyrolysis.

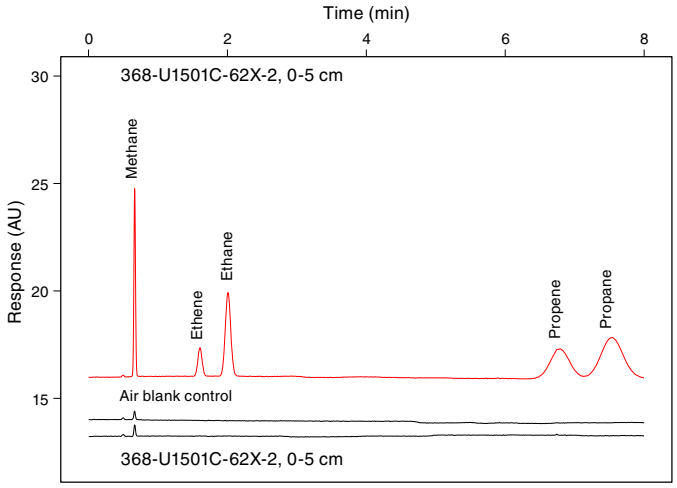

Bulk sediment organic geochemistry

Bulk sediment organic geochemical parameters are presented by depth in Figure **F43** and Table **T14** and cross-plotted by unit in Figure **F44**.

Lithostratigraphic Unit I

Sediments from the uppermost 30 m of lithostratigraphic Unit I (seafloor to Core 368-U1501C-5H) generally have high TOC and low carbonate contents. The top of the section to ~25 m has low but measurable sulfur contents. Otherwise, lithostratigraphic Subunits IB–IF have very low sulfur values. This is distinct from the underlying members of Unit I that have an average carbonate content of ~40 wt% and low TOC, typically <0.25 wt%. Given the fossiliferous nature of the lithologies (nannofossil ooze with foraminifers), it is unlikely that these carbon results represent low levels of biological productivity. More likely, they represent poor preservation of organic matter, which is typical of accumulation under aerobic rather than anaerobic conditions (Demaison and Moore, 1980). The preservation of sulfur in sediments is biologically mediated by sulfate reduction to form sulfide, which in turn forms pyrite (Berner and Raiswell, 1984). Under aerobic conditions, this process is inhibited and would not occur as readily, although organic matter starvation also inhibits sulfate reduction because organic matter forms part of the vital redox couple for sulfate reduction. Whatever the cause, dissolved sulfate concentrations within interstitial water, as described later, did not decline markedly within Subunits IB–IF, supporting the notion that TS levels are low because sulfur has not been reduced during early diagenesis and fixed as pyrite. The instances of very high TOC/total nitrogen (TN) ratios (>10) may reflect an autochthonous input of terrestrial-derived organic matter to the sediments but may also be produced by a lower detection limit for organic carbon than for nitrogen (Hedges et al. 1988).

Lithostratigraphic Unit II

Lithologies within lithostratigraphic Unit II include both high and low TOC members that likely reflect sandy and mud-rich litho-

Figure F43. (A) Methane, (B) TOC and TS, and (C) carbon/nitrogen ratio and carbonate.

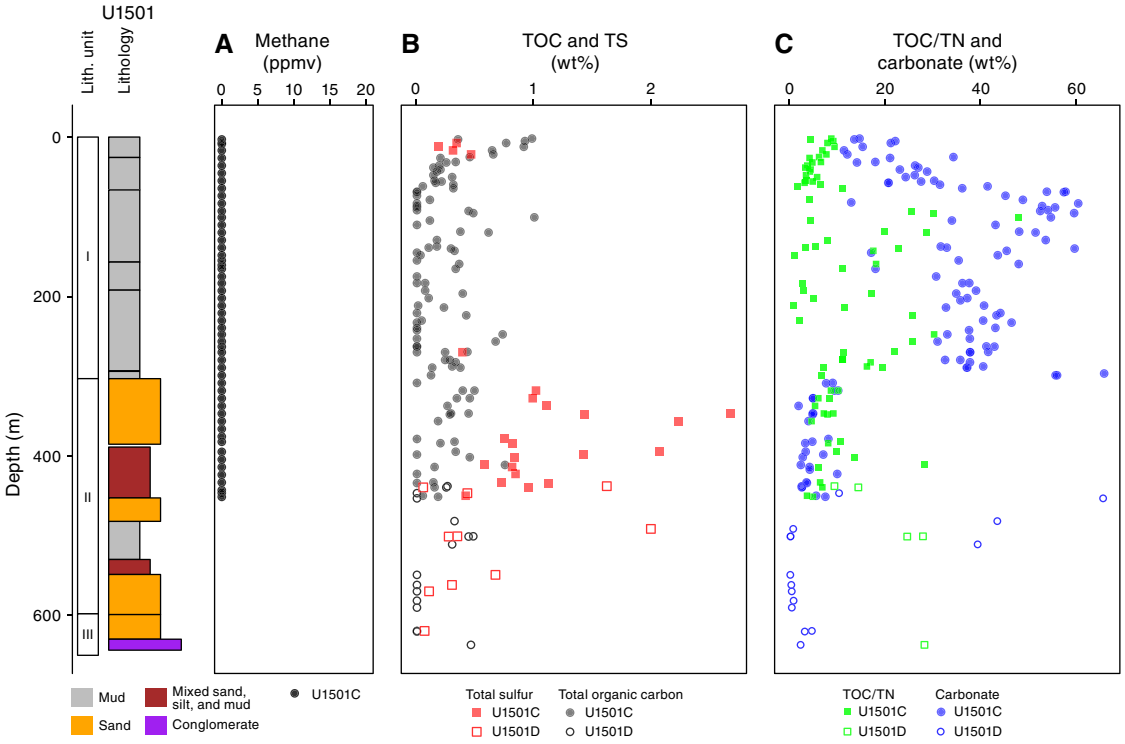

Table T14. Carbon, nitrogen, and sulfur, Holes U1501C and U1501D. **View table in PDF format. Download table in CSV format.**

Figure F44. Crossplot of organic geochemical parameters: carbonate vs. carbon/nitrogen ratio and TS vs. TOC. Black circles = lithostratigraphic Subunit IA, open triangles = Subunits IB–IF, crosses = Unit II, green circles = Unit III.

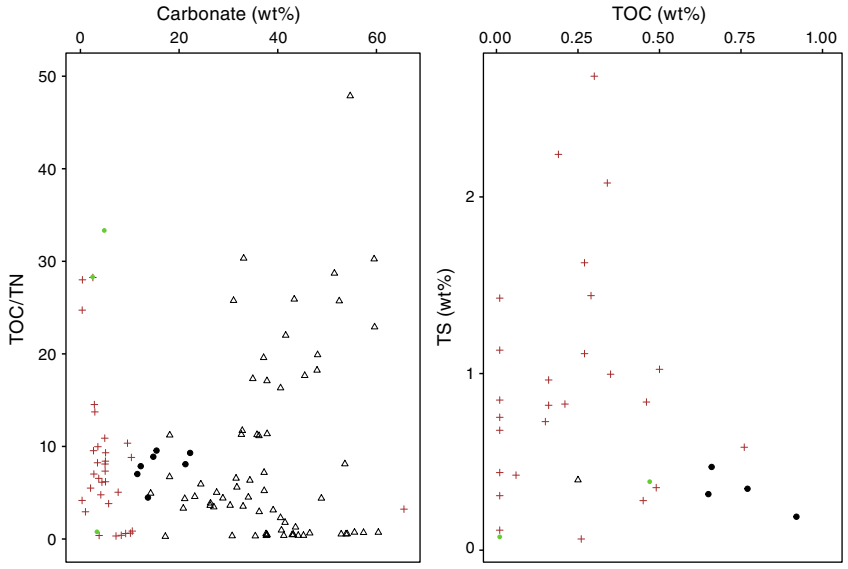

logies. The highest TOC values have the highest TOC/TN ratio, consistent with organic carbon being derived from terrestrial organic matter (Hedges et al., 1988). This unit also has high sulfur content, likely reflecting the fixation of interstitial water sulfate as sulfide that becomes incorporated within sulfide minerals during diagenesis (Raiswell and Berner, 1984). The unit has low carbonate contents relative to Unit I, but overall an 8–10 wt% carbonate content is still significant and must represent either a bioclastic or authigenic component.

Lithostratigraphic Unit III

Only a few lithologies within lithostratigraphic Unit III were analyzed (three samples in all). A TOC content of 0.5 wt% was obtained for gray mudstone, but otherwise Unit III sediments have

very low TOC and carbonate contents. The sulfur content of <0.5 wt% is low but higher than might be expected given the unit's lithologic associations (gravel) and when compared to Unit I (see **Lithostratigraphy**).

Raman and surface-enhanced Raman spectroscopy

Conventional Raman spectroscopy was applied to organic materials, including samples of amber, ash-rich lignite, and bitumen. For reference purposes, they are compared to a sample of Midlothian bituminous coal from the Midlothian coalfields (Scotland) and a sample of pre-oil-window oil-shale from the Brora Coal Member (Caithness, Scotland). Raman spectra are shown in Figure **F45**. Raman spectra obtained from solid carbon-rich fossil organic matter typically have two broad composite bands (or peaks). The first is centered at 1460 cm^{-1}, is relatively broad and wide, and is termed the disordered band (D-peak). Another band at 1600 cm^{-1} is produced by vibrational modes generated by aromatic sheets with a graphite-like structural ordering (Pasteris and Wopenka, 2003) and is termed the graphite (G) or ordered (O) peak.

Fluorescence dominates the spectra obtained for the amber sample (368-U1501C-61X-1, 70 cm), with no clear band distinguished at 1460 or 1600 cm^{-1}, although the broad band observed around 1550 cm^{-1} likely derives from the ordering of π-bonded aromatic sheets with graphite-like structures. A D-peak is also present, but is so broad it cannot be reasonably interpreted. Thus, the sample can be shown to contain organic carbon, but beyond this no other information can be obtained. Relative to the high molecular weight aromatic compounds within humic organic macerals or kerogen, amber comprises plant resins that are highly aliphatic, lack strong aromatic cores, and fluoresce strongly. These qualities make these materials poorly suited for analysis by Raman spectroscopy using a 532 nm light source.

The sample of lignite (light brown streak, no cleats, and partial humification; Sample 368-U1501D-9R-1, 78 cm) yielded broad D and G bands characteristic of levels of thermal maturation typical of brown coal (preoil and gas generation) and levels of thermal alteration that indicate heating at temperatures <40°C.

In most cases, the bitumen impregnating a sandstone clast from Section 368-U1501D-27R-1, 10–15 cm, yielded fluorescence only, but Raman spectra were obtained from a solvent-insoluble component present on the clast's exterior and within a fracture. The D band for these spectra was shrouded by fluorescence, but a G peak could be observed, and the Raman shift was notably high (equal to or greater than that of the coal, ~1600 cm^{-1}), possibly indicating a higher level of thermal maturity than observed for the lignite. This higher level would be consistent with the insolubility of the bitumen in solvent.

Surface-enhanced Raman spectroscopy detected 0.2–2 ng asphaltene/g sediment in lithostratigraphic Units I and II. Detection required deconvolution of surface-enhanced Raman spectra (Figure **F46**). Primarily, two components were considered: solvent extracts of sedimentary organic matter (SOM) that exhibited relatively narrow Raman bands at shifts of 1310, 1448, and 1650 cm^{-1} and asphaltene that exhibited broad Raman bands at 1380 and 1575–1585 cm^{-1} (Alabi et al., 2015). A small Raman band at ~1522 cm^{-1} was often left as a residual. The two broad Raman bands are at positions consistent with previous studies of asphaltene and are similar to the D and G bands of solid carbonaceous materials, whereas the band at ~1522 cm^{-1} is a position, based on previous surface-enhanced Raman scattering studies, that likely corresponds to carotenoids (Wilson et al., 2007), which are also a likely component of marine SOM. The detection of surface-enhanced Raman scattering bands diagnostic for asphaltene and thereby residual petroleum (asphaltene is the most resistant component of petroleum and bitumen and accumulates as residues) is important given the context of the SOM. There is no evidence of recent petroleum migration at Site U1501, and indeed headspace hydrocarbon gases remained below detection. The single instance of bitumen was a highly thermally matured solid component, unlikely to have migrated in recent geological history.

Figure F45. Raman spectra of carbonaceous materials collected from reference materials and Holes U1501C and U1501D. AU = arbitrary units.

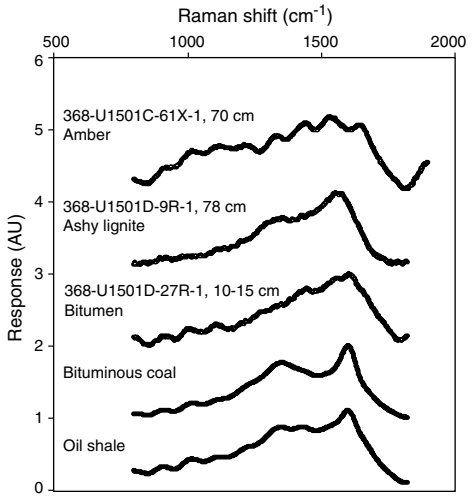

Interstitial water chemistry

Shipboard analyses were performed on interstitial water squeezed from 5–15 cm long whole-round sediment samples from Hole U1501C. For Cores 1H through 10H, 5 cm long interstitial water samples were squeezed and yielded >40 mL of interstitial water per sample. For Cores 11H through 37F, 10 cm long whole-round sediment cores were squeezed and yielded ~30 mL of interstitial water. For Cores 39F through 61X, 15 cm long whole-round interstitial water samples yielded <15 mL of interstitial water per sample. In Hole U1501D, only one sample from Core 2R yielded water on squeezing and then only at a maximum pressure of 30,000 lb for 6 h.

Interstitial water geochemical parameters are listed in Table **T15** and presented by depth in Figures **F47** and **F48**.

We defined four geochemical interstitial water zones at Site U1501 based on the variation of geochemical parameters (listed in Table **T15**). Interstitial water Zone 1 (interval 368-U1501C-1H-2, 0–5 cm, through 2H-5, 0–5 cm) comprises samples obtained close to the mudline (sediment/water interface). Within this interval, maximum sulfate, alkalinity, phosphate, ammonium, boron, silica, lithium, and manganese concentrations are likely related to degradation of organic matter. In interstitial water Zone 2 (interval 3H-2, 0–5 cm, through 43X-4, 0–15 cm), sulfate slightly decreases and alkalinity is buffered by high carbonate concentrations within foraminifer-rich oozes. Atypically for this marine setting (Li et al., 2015a), in which sulfate reduction is prevalent in marine sediments, diffusion processes dominate the sulfate profile. Decreasing K and Mg and increasing Ca and Li reflect the typical diffusion-formed profile of interstitial water, but in interval 19F-3, 0–15 cm, and Section 27F-2, there is an obvious increase in Fe, Si, and Mn and a slight

Figure F46. Surface-enhanced Raman spectra of sediment extracts: asphaltene (residual oil), a core sample rich in SOM, a blank, and a sample containing both SOM and residual petroleum.

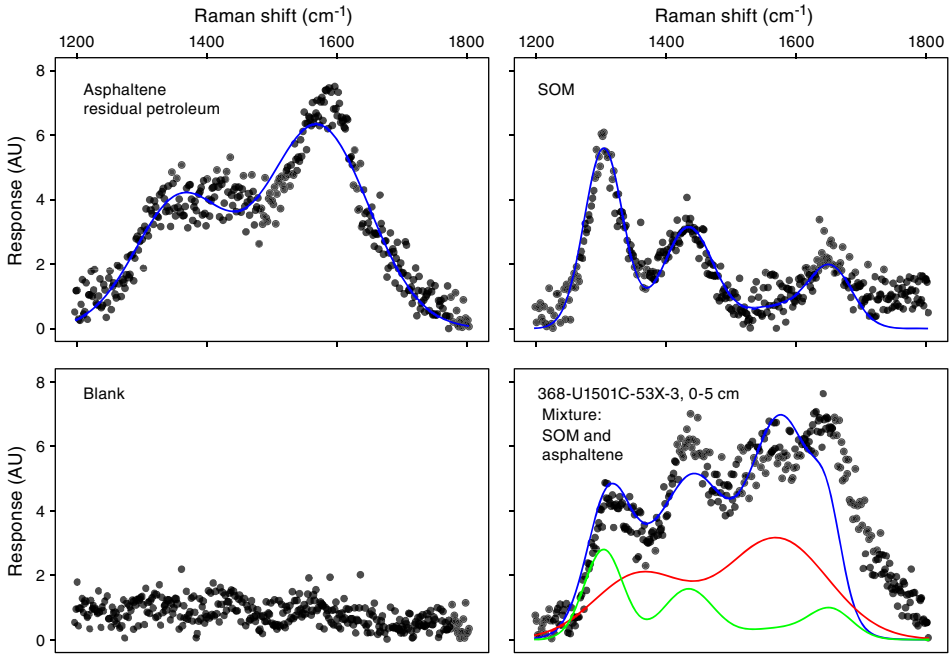

Table T15. Interstitial water analyses, Hole U1501C and U1501D. **View table in PDF format. Download table in CSV format.**

decrease in Na, Cl, and Br. This atypical profile is similar to that of the deep fluids in Hole U1502A, which are suggested to derive from basalt. In interstitial water Zone 3 (interval 44X-4, 0–15 cm, through 50X-4, 0–15 cm) sulfate, chloride, and bromide concentrations are anomalously low. One possible origin for this fluid migration is along sand and silt layers in which a fluid depleted in Cl, Br, and Na migrates. Alternatively, the chemical composition may be explained by a sand body or sand-rich unit being isolated by differential compaction within a hydraulically sealed mudstone; in such a case, the water would represent relict formation water. In interstitial water Zone 4 (interval 53X-4, 0–15 cm, through 61X-2, 0–15 cm), all major anion and cation concentrations are normal for that depth and the region (Li et al., 2015a).

Alkalinity varies within Hole U1501C, ranging from 1.5 to 8.8 mM (shown in Figure **F47**). In interstitial water Zone 1, alkalinity increases to a peak concentration of 7.1 mM at 16.72 m (Sample 2H-5, 0–5 cm). This change in alkalinity is most likely caused by degradation of organic matter. In interstitial water Zone 2, alkalinity decreases to ~3.5 mM at 59 m and remains constant at ~3.5 mM to 100 m. Alkalinity increases again to a peak concentration of 8.8 mM at 230 m and then decreases downhole to the base of interstitial water Zone 2. The changes of alkalinity in interstitial water Zone 2 are similar to those of carbonate, suggesting that alkalinity might be influenced by the dissolution of carbonate. The pH value decreases slowly from the seafloor to the bottom of interstitial water Zone 2 and then increases to a maximum (pH = 7.94) at the bottom of interstitial water Zone 4 (Sample 61X-2, 0–15 cm).

In interstitial water Zones 1 and 2, interstitial water chlorinity values are mostly ~560 mM, similar to the standard seawater value (559 mM; Figure **F47**). In interstitial water Zone 3, chlorinity values decrease to the minimum (498 mM) at 356 m. About 10% decreased chlorinity implies that a "freshwater" component might be present. The bromide depth profile is similar to the variation observed for chlorinity but with a maximum that occurs at a different depth. Bromide concentration also decreases to a minimum in interstitial water Zone 3. It is worth noting that slightly decreased chlorinity and bromide concentrations were observed in Cores 19X-3 and 21X-3.

The dissolved sulfate profile decreases from 27.2 mM at the seafloor to 3.7 mM at the bottom of Hole U1501C (Figure **F47**). In interstitial water Zone 1, sulfate concentrations decrease sharply, most likely caused by bacterially mediated organic matter diagenesis in upper sediments. Downhole, this decline is more gradual and can best be explained by diffusion processes. The interstitial water contains significant amounts of sulfate (3.7 mM) to the bottom of the hole, indicating that sulfate is not completely consumed in Hole U1501C. A similar case was observed at IODP Site U1431 (Li et al., 2015b), but otherwise this lack of sulfate reduction is unusual. Dissolved NH_4^+ concentrations increase from 336 µM at 7.5 m to a maximum of 492 µM at 16 m in interstitial water Zone 1. Interstitial water Zones 2–4 have slight variations in NH_4^+ concentrations. A maximum in dissolved phosphate concentrations is 30.6 µM at 3 m in interstitial water Zone 1. In interstitial water Zones 2–4, phosphate concentrations are generally low, just about several micromolars.

The Na^+ profile is similar to Cl^- and Br^- (Figure **F47**). Sodium concentrations are mostly constant (~480 mM) in interstitial water Zones 1 and 4, decrease to a minimum (399 mM) in interstitial water Zone 3, and increase to standard seawater value (~480 mM) in interstitial water Zone 4 (likely representing contamination). Sodium concentrations in interstitial water Zone 3 are about 20% of that in other units. The K^+ and Mg^{2+} profiles decrease in a similar way to each other from the surface to the bottom of the hole. Decreases in potassium and magnesium are possibly due to diagenetic reactions occurring in sediment, such as clay ion exchange. Contrary to the potassium and magnesium pore water profiles, the Ca^{2+}

Figure F47. Interstitial water alkalinity, pH, chloride, bromide, sulfate, phosphate, ammonium, sodium, potassium, calcium, and magnesium concentration profiles.

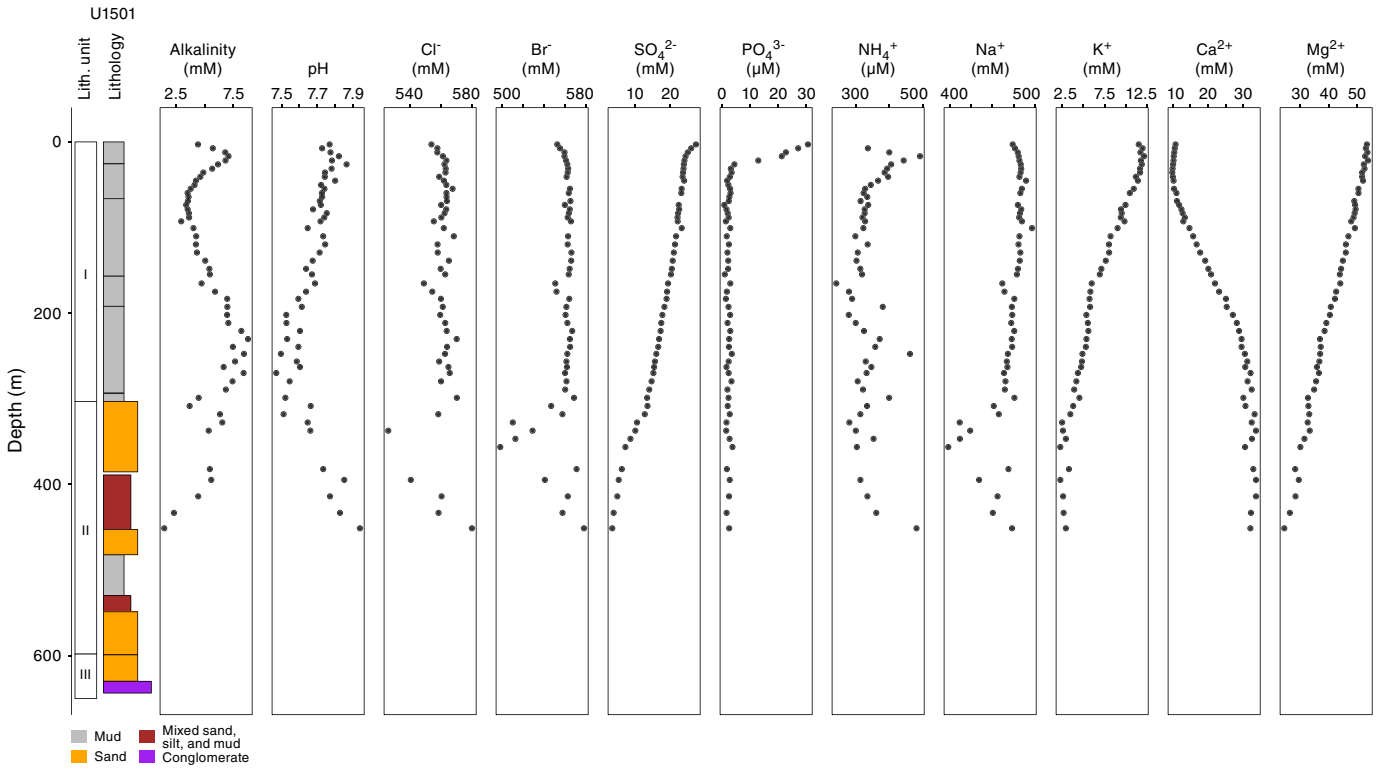

profile increases from the surface to a maximum concentration (33.7 mM) at 337 m, and below this depth calcium has a near-constant concentration. Changes in calcium concentration are mostly caused by carbonate diagenesis (i.e., dissolution and recrystallization of biogenic carbonate). The strontium profile in interstitial water is controlled by the dissolution of biogenic carbonate, so it is similar to the profile of calcium. Strontium concentrations increase from the subsurface to the maximum (440 µM) at 269 m and remain around 400 µM until the bottom of the hole (Table **T16**).

Dissolved Ba concentrations in the interstitial water are controlled by the formation and stability of the mineral barite ($BaSO_4$). Barium and sulfate concentrations are negatively correlated. In interstitial water Zone 1, the dissolved Ba concentration is very low (0.05 µM) and corresponds with the maximum in sulfate. In interstitial water Zones 2–4, Ba concentrations increase linearly to a maximum (2.49 µM) at the bottom of Hole U1501C at the same time sulfate concentrations decrease to a minimum.

In interstitial water Zone 1, degradation of organic matter releases B into the interstitial water (Li and Jiang, 2010), so the dissolved B concentrations increase with depth (Figure **F48**). In interstitial water Zone 2, the B profile is likely driven by clay mineral cation exchange (e.g., adsorption onto and desorption from clay minerals). Decreased B concentrations are observed in interstitial water Zones 2 and 3. Lithium is also easily adsorbed onto clay minerals such as kaolinite and smectite and/or other terrigenous sediments. Thereafter, in interstitial water Zone 1, the concentration of Li is lower than modern seawater (25 µM). In interstitial water Zone 2, Li concentrations increase gradually from 27 µM to a maximum (499 µM) and then decrease to lower concentrations in interstitial water Zones 3 and 4. The increases in Li concentration are possibly due to the diagenetic release of Li from clay minerals and/or diffusion from Li-enriched deep fluids.

Silica concentrations in interstitial water Zone 1 are controlled by the dissolution of siliceous microfossils that release silica into interstitial water. In interstitial water Zone 2, peaks in Si, Fe, and Mn concentrations were observed between Sample 368-U1501C-21F-3, 0–10 cm, and Section 27F-2 at the same time as decreased Na, Cl, and Br concentrations. The changes in geochemical parameters are similar in character to those of the deeper fluids in Hole U1502A. The profiles of dissolved Fe and Mn change in a way similar to that of Si, perhaps because Fe and Mn are affected by the degradation of organic matter, which also occurs in surface sediments. At Site U1502, there was enrichment in Mg and Ca, but in Hole U1501C changes in Ca and Mg do not appear to be off-trend.

In summary, the most obvious changes in interstitial water chemical composition occur in Sections 368-U1501C-19F-3 through 27F-2 and deeper than 300 m. Fluid from these sections have similar geochemical parameters to the deep fluid from Hole U1502A, which is suggested to be influenced by the dissolution of mafic minerals within basalt. The fluid below 300 m corresponds to a boundary between lithostratigraphic Units I and Unit II. A sharp change in interstitial water chemistry at very shallow subseafloor depths suggests very rapid degradation of organic matter within the uppermost 16 m.

Bulk sediment and rock geochemistry

We analyzed a total of 64 sediment samples from Holes U1501B, U1501C, and U1501D for major and minor element concentrations by inductively coupled plasma–atomic emission spectroscopy (ICP-AES) (Table **T17**).

Figure F48. ICP-AES iron, manganese, silica, strontium, boron, and lithium concentration profiles.

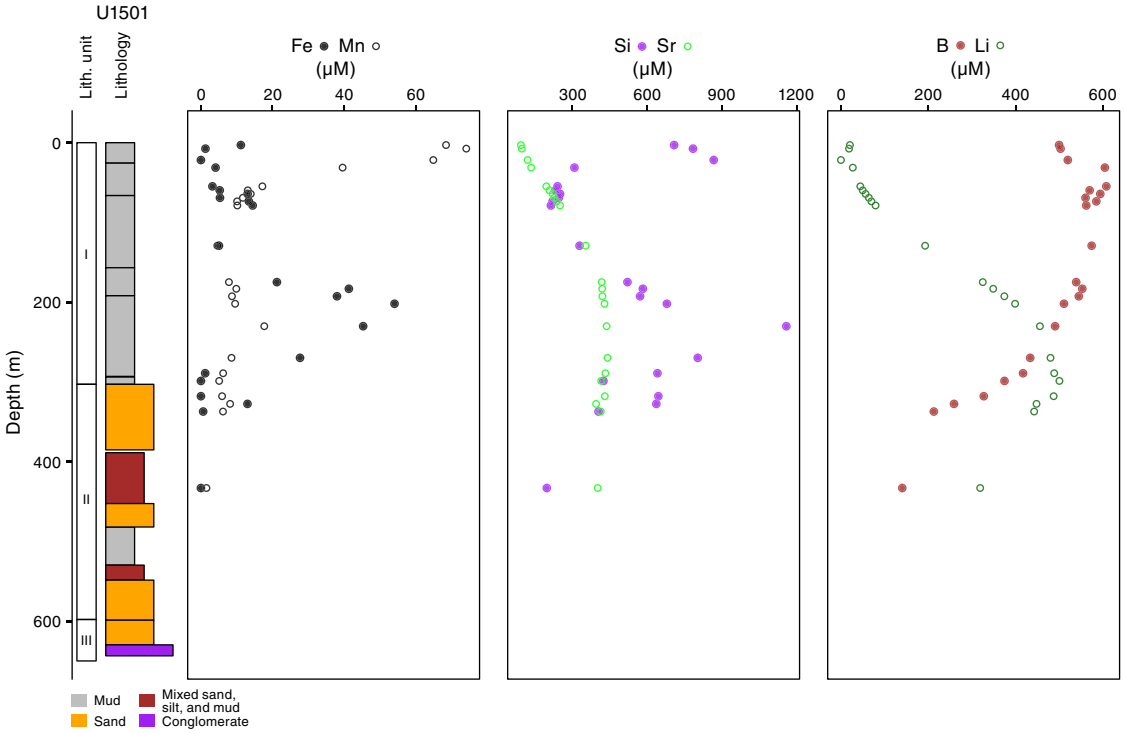

Table T16. Interstitial water minor elements, Hole U1501C. **View table in PDF format. Download table in CSV format.**

Table T17. Major element oxide and minor element contents of sedimentary samples, Site U1501. **View table in PDF format. Download table in CSV format.**

Elemental compositions primarily reflect geological units and changes in lithology. Silica, aluminum, and calcium oxides are the major elements and typically account for greater than 90 wt% of the elemental composition of most lithologies (Figure **F49**). In lithostratigraphic Unit I, calcium oxide contents are high, and within the foraminifer-rich interval they exceed 40 wt% (consistent with the unit being a high-carbonate ooze, e.g., >50% carbonate). Within lithostratigraphic Units II and III, calcium (as carbonate) is less common and the units are predominantly siliciclastic with sharp distinctions between units that are mud-rich and the feldspathic, sandier lithologies toward the base of the hole. In lithostratigraphic Unit III, a steady decrease in potassium content reflects the upward transition from an orthoclase-rich to less orthoclase-rich sandstone. Sandstones at the top of lithostratigraphic Unit II are far muddier than those beneath, and the relatively increased potassium content is associated with increased aluminum content. Likely, these changes reflect an upward increase in clay content in lithostratigraphic Unit II. Such a progression is consistent with increased compositional maturity within the sediment, brought on by the transition from first- to second-cycle sediments (Suttner et al., 1981) (e.g., the breakdown and conversion of orthoclase to clay minerals during weathering in the sediment source). Within the basal part of lithostratigraphic Unit II, sodium and potassium are both high, which is also consistent with the presence of first-cycle feldspathic sediments.

Parameters previously proposed to represent sedimentological processes for the SCS were also evaluated (Clift et al., 2014). In detail, Figure **F50** shows the depth profile of a parameter based on the major cations in smectite (Mg and Na) and illite (K). The variation of (Mg + Na)/K values reflects the different clay assemblages in the lithostratigraphic units. The Ti/Ca parameter has previously been used as a proxy of clastic flux (Clift et al., 2014), with Ti being dominated by the presence of heavy detrital minerals (e.g., rutile and titanite) and Ca by biogenic carbonate. The high peak in Ti/Ca depth profile (lithostratigraphic Subunit IA) is most possibly correlated with intensified clastic delivery from continents; furthermore, the high Ti/Ca with low Al/Si (low ratios of clay and quartz sand) values in Subunit IA (Figure **F49**) may indicate a high-energy transport regime during this period.

Discussion of organic, formation water, and inorganic chemical results

The following synthesis is based on the geochemical data presented in the preceding sections. Based on the lack of methane generation and sulfate reduction and the fixation of sulfur as pyrite within sediments, aspects of early diagenetic environments at Site U1501 are atypical in comparison to other sites in the region (Li et al., 2015a). Deepwater marine mudstones do not regularly have high TOC values, largely because their depositional environments in general do not favor high rates of organic carbon preservation (Demaison and Moore, 1980). However, the low TOC values (<0.5 wt%) found in lithostratigraphic Subunit IIA are also at odds with nearby sites such as Site U1499. The low methane content of sediments and sulfate reduction profiles also differ markedly between the two sites; there is no evidence of a present-day sulfate–methane transition zone (SMTZ) at Site U1501 (Barnes and Goldberg, 1976). Figure **F51** summarizes these features. Within lithostratigraphic Unit II,

Figure F49. (A) Major element oxide abundances and lithostratigraphic unit–normalized (B) CaO/SiO_2, (C) K_2O/SiO_2, and (D) Al_2O_3/SiO_2. B–D: solid black circles = Subunit IA, open circles = Subunits IB–IF, red circles = Unit II, green circles = Unit III.

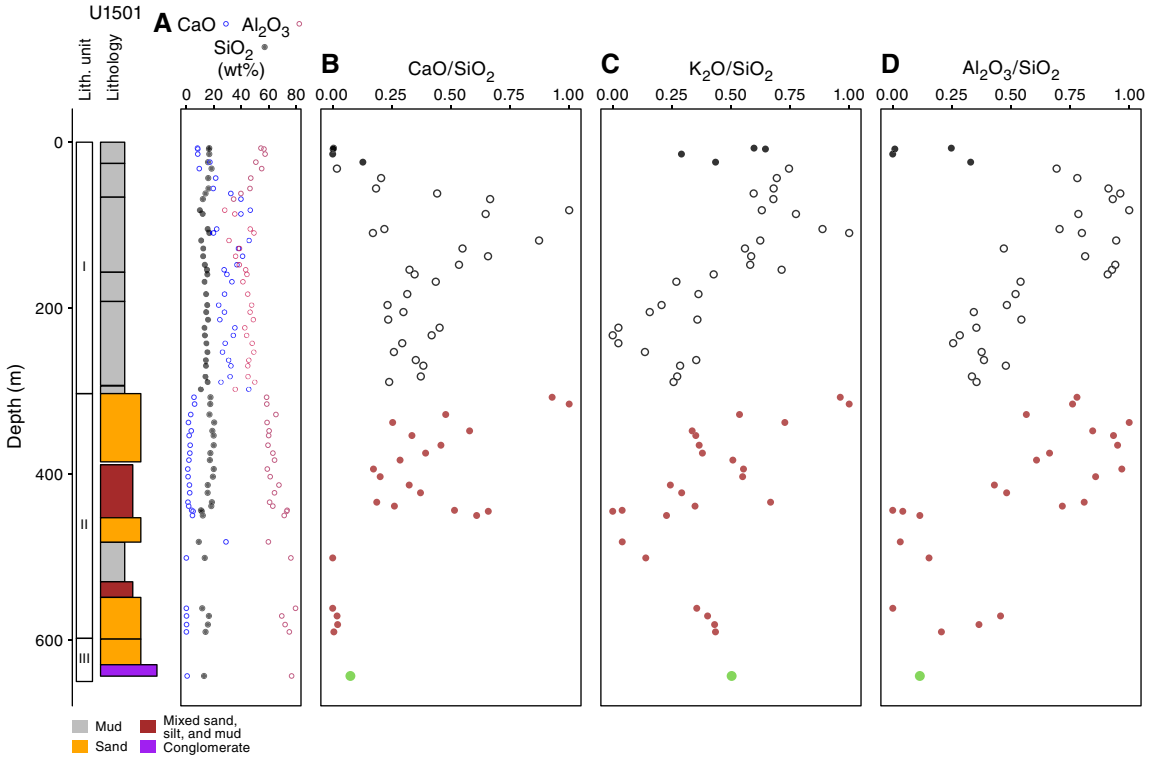

sulfate reduction is inhibited relative to Site U1499. Perhaps unsurprisingly, because sulfate is ultimately converted to pyrite, the main form in which pyrite is stabilized within sediments, the TS content of Unit I is mostly low, except for the topmost interval, where both iron and organic carbon contents are high.

Causes for inhibited pyrite formation and sulfate reduction might include a lack of iron, low organic matter content (organic matter serves as a reductant), and a dysoxic environment (Berner and Raiswell, 1984). Both factors are present at Site U1501, as can be seen in Figure **F51**. Iron, which is particularly noticeable in this regard, has an inverse correlation to barite. Barite and thereby Ba can also serve as indicators for past redox boundaries in sediments (Torres et al., 1996). Barite precipitates and is fixed in sediment where sulfate is stable under oxic conditions, generally found above the SMTZ where sulfate is most abundant. The inversely varied Ba and Fe thus likely denote varying diagenetic conditions within the sediment column. Overall, this strongly indicates that Site U1501, situated at a basement high, has seen a substantial change in early diagenesis conditions during recent geological history.

Figure F50. Geochemical parameters correlated with sedimentological processes. A. (Mg + Na)/K ratio as proxy for smectite and illite. B. Ti/Ca ratio normalized by lithostratigraphic unit. Solid black circles = Subunit IA, open circles = Subunits IB–IF, red circles = Unit II, green circles = Unit III.

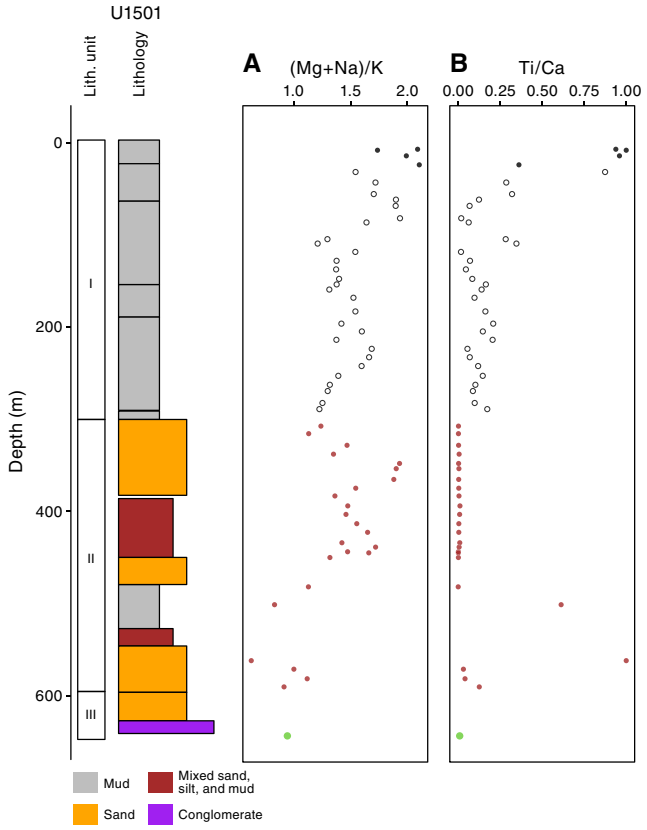

Figure F51. Variations in diagenetic history, Site U1501. A. Interstitial water Zones 1–4 and redox state of early stage diagenesis (green = reducing, red = dysoxic). B. Rescaled (from 0 to 1) interstitial water sulfate concentrations. AU = arbitrary units. C. Elemental and oxide abundances (Fe as Fe_2O_3). D. TOC and TS.

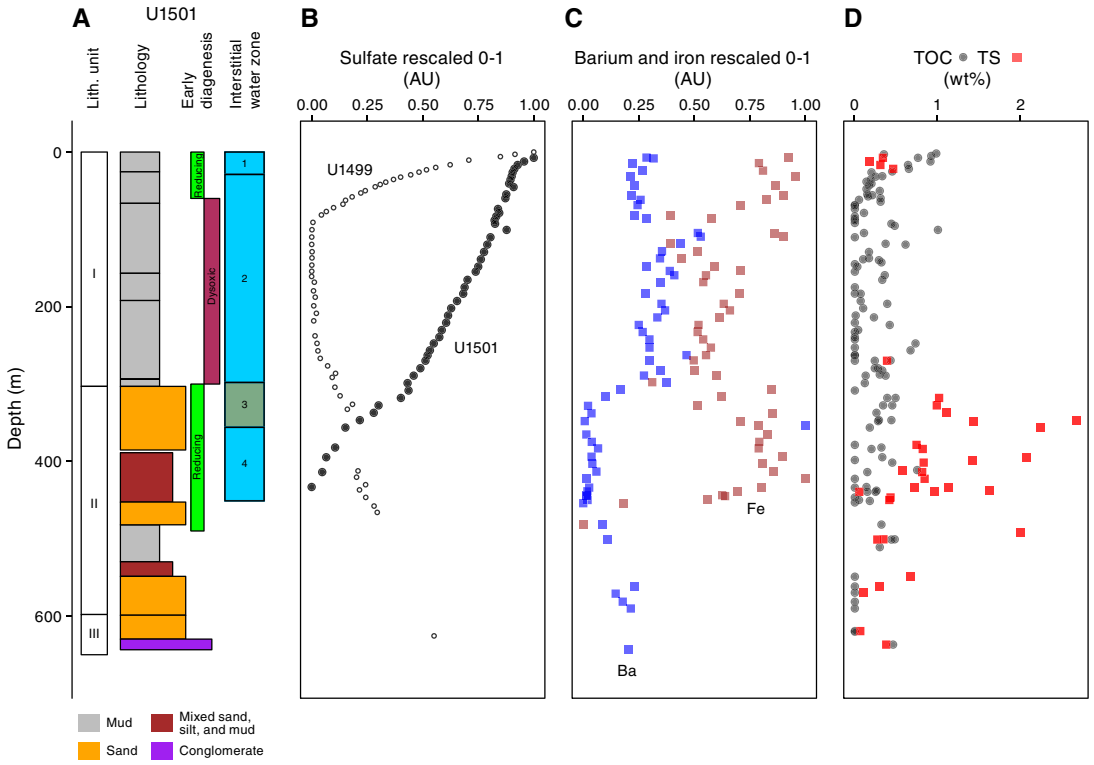

Physical properties

Sediment and rock physical properties were measured on cores from Holes U1501A (0–9.5 m), U1501B (0–9.5 m), U1501C (0–461.9 m), and U1501D (433.5–644.3 m). After cores reached thermal equilibrium with ambient temperature at ~20°C, gamma ray attenuation (GRA) density, magnetic susceptibility, and *P*-wave velocity were measured every 2 cm using the Whole-Round Multisensor Logger (WRMSL). After WRMSL scanning, NGR was measured on the whole-round sections with a counting period of 10 min and a measurement spacing of 10 cm. Thermal conductivity was measured next with a needle probe inserted into whole-round cores on unconsolidated sediments and with a puck probe on split section halves on hard rocks. Following core splitting, color reflectance and magnetic susceptibility measurements were taken from the archive halves using the point magnetic susceptibility (MSP) sensor on the Section Half Multisensor Logger (SHMSL). Discrete MAD measurements were obtained on every other section of the working halves. *P*-wave velocity was also measured on the working halves with the *P*-wave caliper (PWC) and *P*-wave bayonet (PWB) pulser-receiver systems of the Section Half Measurement Gantry (SHMG).

The following major physical property units were distinguished at Site U1501:

- PP Unit 1 (0–300 m),
- PP Unit 2 (300–450 m),
- PP Unit 3 (450–600 m), and
- PP Unit 4 (600–657 m).

These units are described below. The results from the WRMSL, SHMSL, SHMG, and discrete sample measurements are shown in Figure **F52**.

Natural gamma radiation

The NGR intensity measured at an energy level characteristic for K, U, or Th is proportional to the content of that element in the sediment. These elemental proportions can help improve stratigraphic correlation and may be indicative of the geochemistry and mineralogy of the sediments (e.g., De Vleeschouwer et al., 2017). In general, the NGR count of sandstones increases with silt and shale content and a higher percentage of minerals other than quartz (Russell, 1944).

NGR values in PP Unit 1 are represented by two major intervals (Figure **F53**). The upper interval from the seafloor to ~65 m ranges from ~20 to ~50 counts/s and is associated with NGR values that peak around the middle of this depth range. The lower interval of PP Unit 1 has a similar but broader trend and ends at an abrupt increase in NGR values to ~60 counts/s at ~300 m. In PP Unit 2, NGR values vary rapidly, showing an overall increase followed by a decrease in values with depth to the top of PP Unit 3 at ~450 m. PP Unit 3 has a steady rise in NGR values and a sharp increase at ~600 m to ~80 counts/s that characterizes PP Unit 4.

Concentrations of K, U, and Th were estimated using the NGR counts and bulk density measurements for Hole U1501C according to the methods by De Vleeschouwer et al. (2017). The trends in the NGR counts are not as clearly expressed in the Th concentrations as

Figure F52. Physical properties, Holes U1501A and U1501B. cps = counts per second.

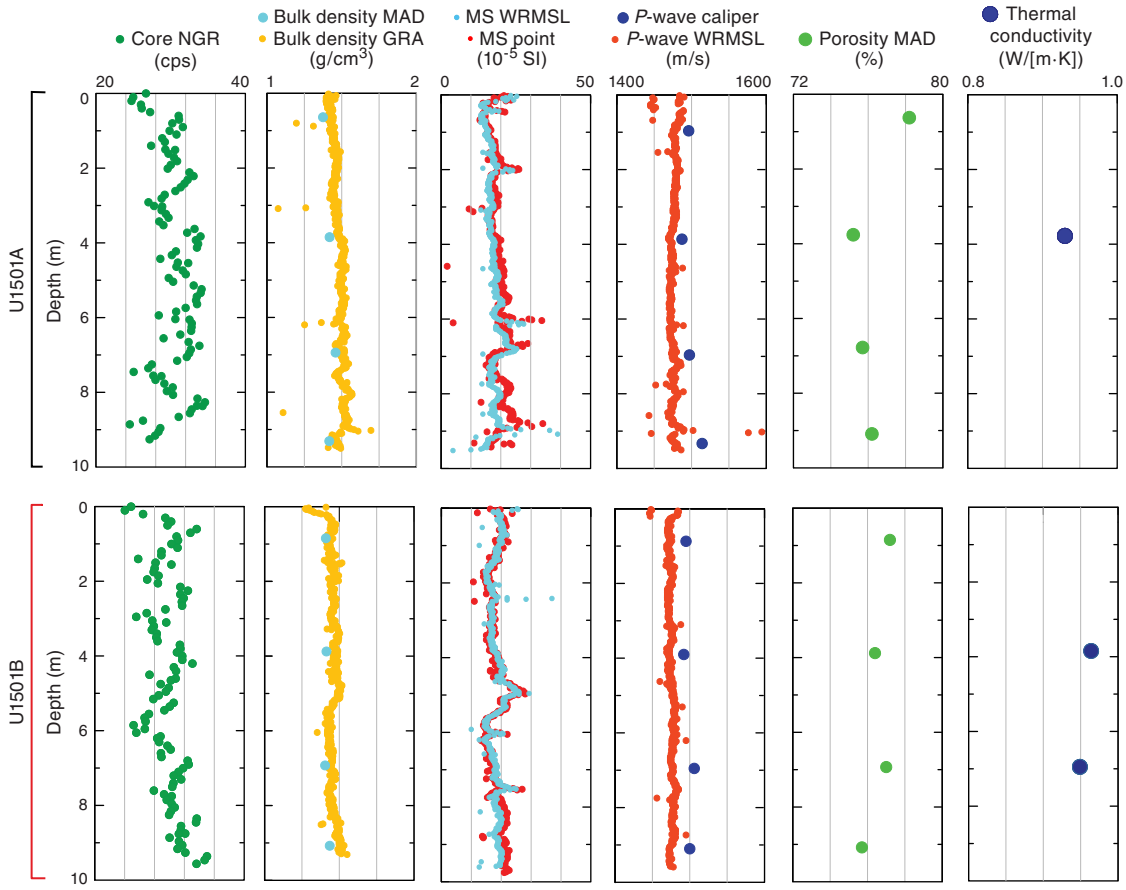

Figure F53. Physical properties, Holes U1501C and U1501D. Note logarithmic scales used for magnetic susceptibility and *P*-wave velocity.

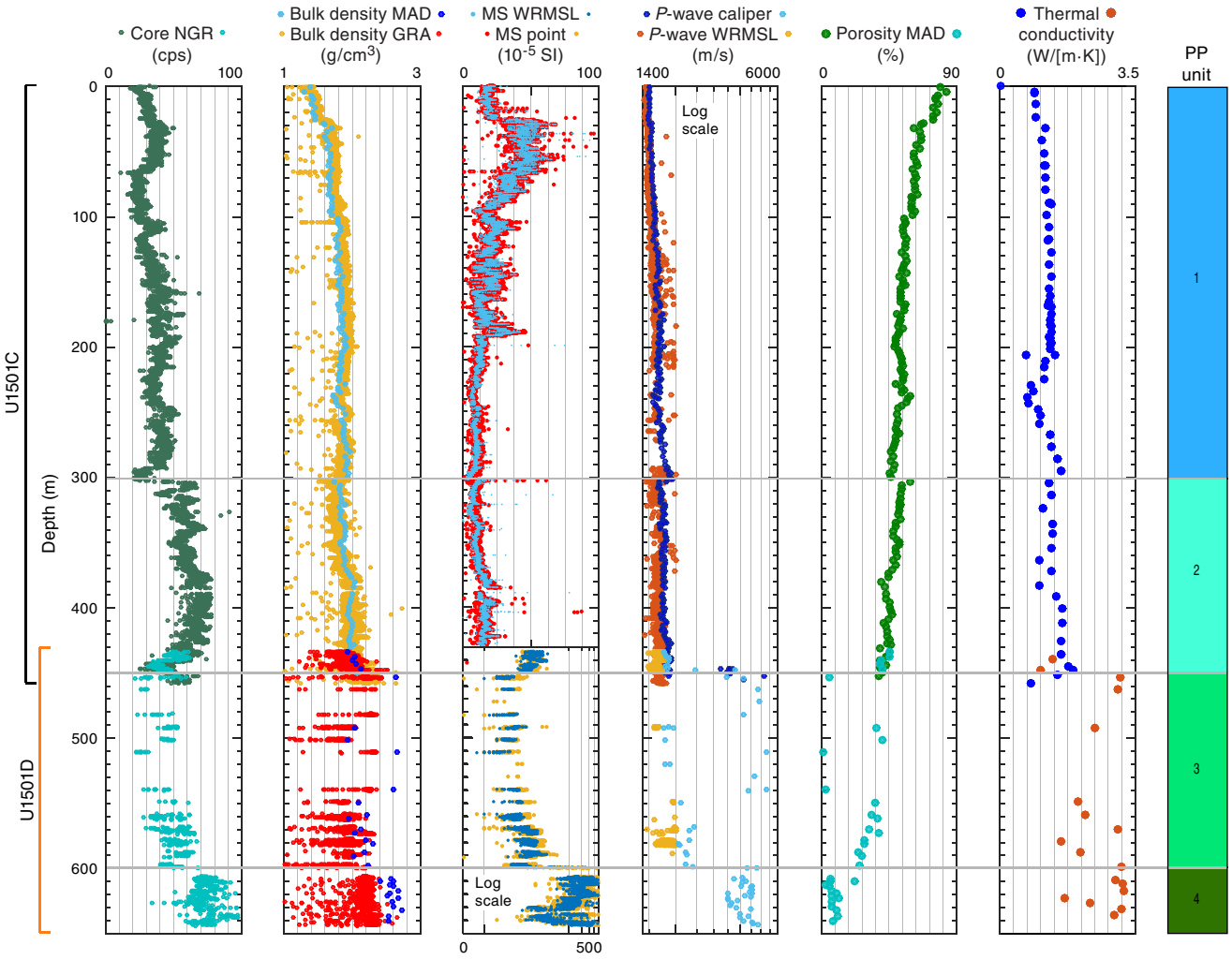

they are in the K percent weight and U concentrations, which show very similar variations to the total NGR count values (Figure **F54**).

P-wave velocity

In PP Unit 1, *P*-wave velocities gradually increase with depth from ~1450 to 1931 m/s, reflecting sediment compaction (Figure **F53**). *P*-wave velocities decrease sharply at the boundary between PP Units 1 and 2 to 1650 m/s. In PP Unit 2 (300–450 m), velocities increase again with depth but remain lower than 2000 m/s downhole to ~450 m, where they spike to values of ~3500 m/s and higher. Scattered high velocity measurements continue to the bottom of PP Unit 3 (450–600 m), but they become the norm in PP Unit 4 (600–657 m), where they generally exceed ~3500 m/s.

Thermal conductivity

In PP Unit 1, thermal conductivity increases gradually with depth from ~0.88 W/(m·K) near the seafloor to ~1.64 W/(m·K) at ~300 m (Figure **F53**). The increasing trend is interrupted at ~265 m by a slight reduction in thermal conductivity caused by poor connection between the core and the probe. Reliable measurements resumed below 267 m. A drop in thermal conductivity from 1.576 to 1.255 W/(m·K) occurs at the boundary between PP Units 1 and 2 (~300 m), followed by increasing trends in PP Unit 2. Thermal conductivity is more variable in the lowermost section of PP Unit 2 and in PP Units 3 and 4 (440–622 m), where it ranges from ~1.350 to 3.600 W/(m·K).

Density and porosity

In PP Unit 1, GRA and MAD bulk densities increase gradually from ~1.3 g/cm^3 just below the seafloor to ~1.9 g/cm^3 (Figure **F55**) at ~300 m. Dry density increases with depth from ~0.6 to ~1.5 g/cm^3, and porosity decreases with depth from 80% to 45%, consistent with increasing compaction. At the boundary with PP Unit 2 (~300 m), bulk and dry densities abruptly decrease, whereas porosity increases up to 60%. Grain density remains constant at 2.7 g/cm^3.

In PP Unit 2, bulk and dry densities slightly increase with depth from 1.7 to 2.0 g/cm^3 and from 1.1 to 1.7 g/cm^3, respectively. Scattered grain density values range from 2.6 to 2.9 g/cm^3. Porosity decreases with depth from 60% to 40%. The boundary between PP Units 2 and 3 (450 m) is marked by an abrupt increase in bulk (2.0 to 2.7 g/cm^3) and dry (1.7 to 2.7 g/cm^3) densities. In PP Unit 3, densities vary, with an overall increasing trend toward the bottom of the unit. At ~600 m, corresponding to the transition between PP Units 3 and 4, bulk and dry densities increase rapidly from ~2.2 to >2.6 g/cm^3 and from 2.0 to 2.5 g/cm^3, respectively. In contrast, porosity at this depth decreases sharply from 20% to 5%.

Figure F54. NGR measurements, Hole U1501C. K, U, and Th concentrations are derived from NGR and GRA density measurements using method of De Vleeschouwer et al. (2017).

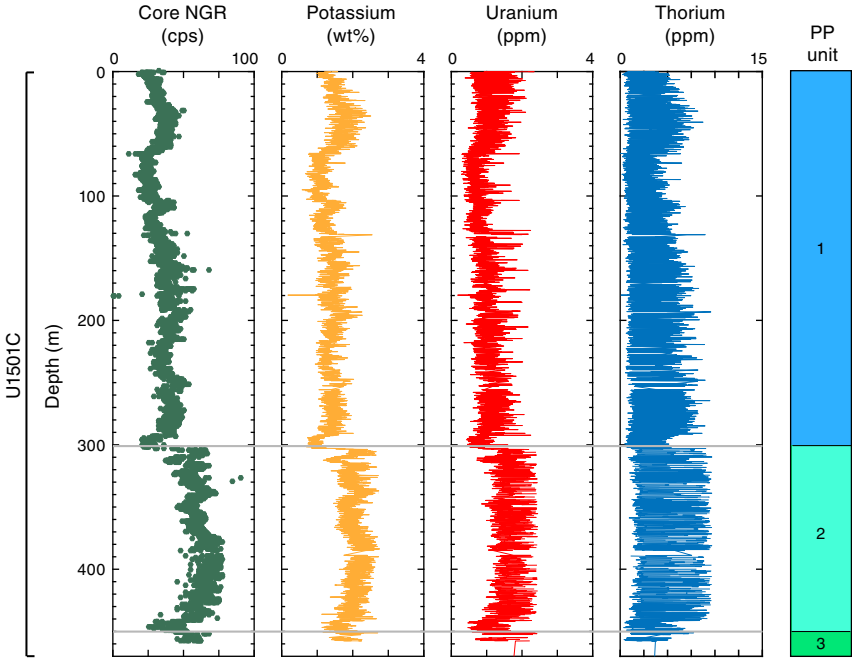

Figure F55. GRA bulk density and MAD bulk density, dry density, grain density, and porosity, Holes U1501C and U1501D.

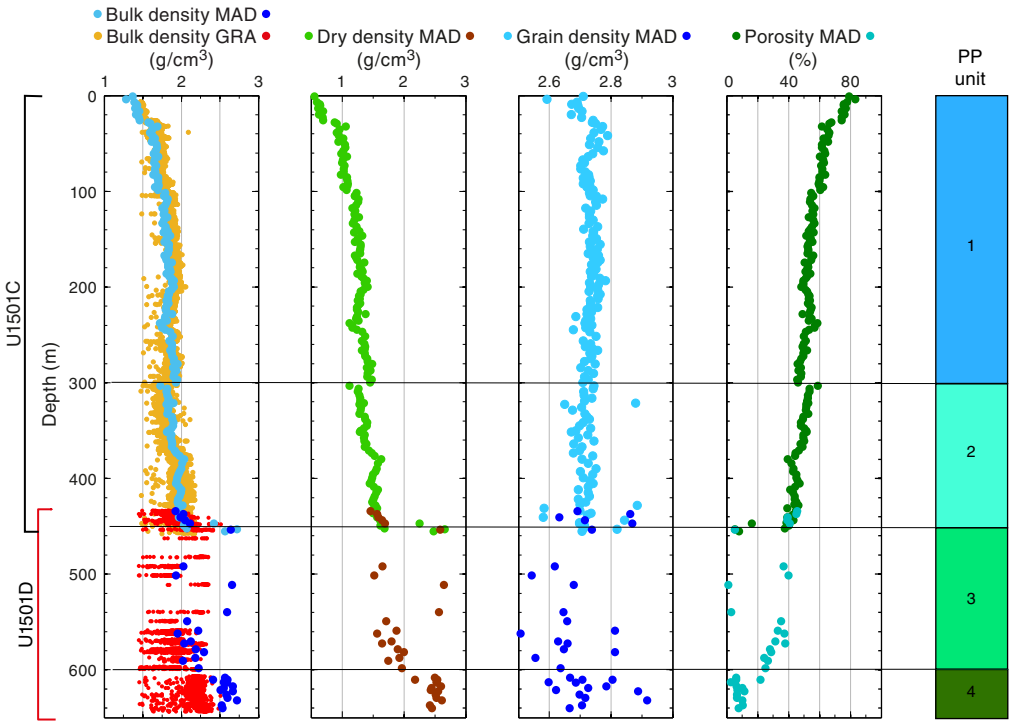

PP Unit 4 has an average bulk density of 2.6 g/cm^3 and dry density of 2.5 g/cm^3 (Figure F55). Grain densities and porosities in this unit fluctuate between 2.5 and 2.9 g/cm^3 and 3% and 10%, respectively.

Color reflectance spectrophotometry

L* values are higher in PP Unit 1, reflecting the higher concentration of biogenic carbonate in the uppermost 300 m. Reflectance parameters a* and b* increase sharply from the seafloor to ~120 m to their highest values and then drop in similar fashion before ~180 m. Values remain low thereafter to the boundary with PP Unit 2. L* drops sharply at the boundary at ~300 m, marking the transition between PP Units 1 and 2 and reflecting the increase in clay in the formation (Figure F56). L*, a*, and b* values in PP Unit 2 show relatively constant trends with a variable range. The transition between PP Units 2 and 3 is characterized by a slight increase of L*

Figure F56. Sediment color reflectance parameters L*, a*, and b* and $CaCO_3$ content, Holes U1501C and U1501D.

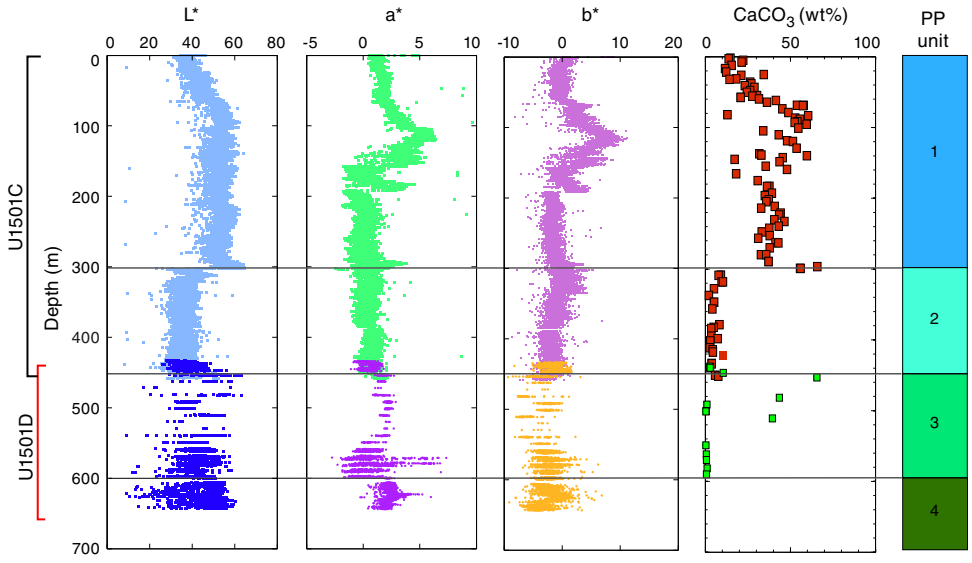

and b*. An abrupt increase in a* occurs at 600 m, coinciding with the change from glauconite sand to sandstone (see **Lithostratigraphy**). Below this depth, all reflectance values remain relatively constant.

Magnetic susceptibility

Magnetic susceptibility rapidly increases from the seafloor to ~50 m and then gradually decreases downhole throughout the lower section of PP Unit 1 until abruptly increasing at the boundary between PP Units 1 and 2, coinciding with the change from nannofossil ooze to nannofossil-rich clay (see **Lithostratigraphy**). Magnetic susceptibility remains constant in PP Unit 2, with a slight decrease at the boundary between PP Units 2 and 3 (450 m) from 15 × 10^{-5} SI to 5 × 10^{-5} SI that is followed by an abrupt increase at the transition between PP Units 3 and 4. Magnetic susceptibility values in PP Unit 4 are relatively high, locally exceeding 500 × 10^{-5} SI (Figure **F53**).

Red, green, blue

Red, green, blue (RGB) values show similar trends to the L* values throughout Holes U1501A–U1501D (Figures **F56**, **F57**). From the seafloor through the upper portion of PP Unit 1 (~95 m), RGB values increase from 100 to 160, whereas they remain constant and vary between ~140 and 160 in the lower portion of PP Unit 1. A marked decrease in RGB from 170 to 100 was observed at the boundary between PP Units 1 and 2 (Figure **F57**). RGB values in PP Unit 2 remain relatively constant at ~100, followed by another increase from 70 to 150 in PP Unit 4.

Discussion and summary

Sediments recovered from Site U1501 are generally composed of both biogenic (calcareous or siliceous ooze) and terrigenous material dominated by either quartz or clay. Changes in sediment physical properties not only reflect relative amounts of these components but also their compaction/lithification state and may also be related to depositional environments. Overall, we found a strong correlation between the sediment physical properties and the designated lithostratigraphic units (Figure **F53**; see **Lithostratigraphy**). The GRA and bulk densities increase with depth, reflecting the increasing compaction of sediments with depth. Porosity values are consistent with this trend and have an inverse relationship with density (Figure **F55**). The lowest porosities (about 5%) were encountered in sandstones from the lowermost section of Holes U1501C and U1501D and are related to diagenetic processes (i.e., lithification and cementation).

Figure F57. RGB values, Holes U1501C and U1501D.

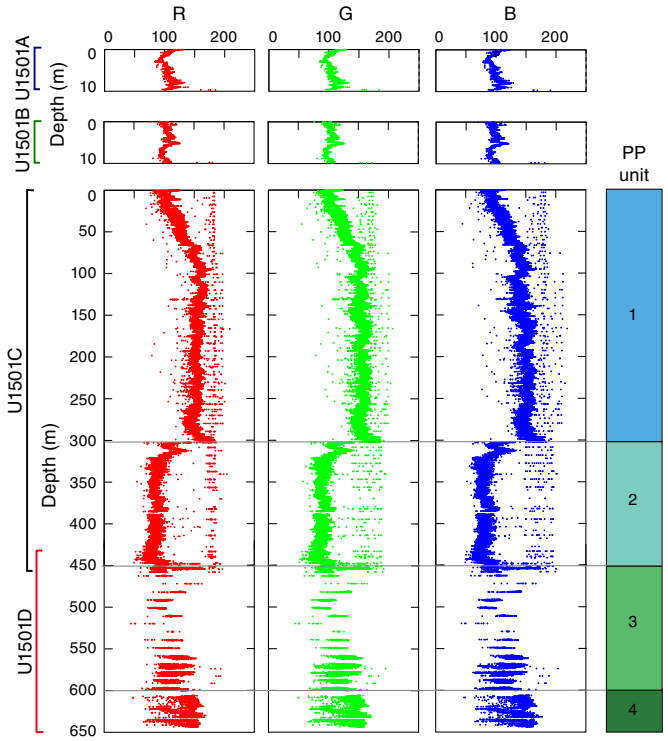

Similarly, a general increase in *P*-wave velocity at Site U1501 from 1451 m/s at the seafloor to 1931 m/s at 302 m (Figure **F53**) reflects sediment compaction. This increase is followed by a sharp decrease in velocity at 302.9 m to 1796 m/s, marking a distinct lithologic transition from nannofossil ooze to a sand layer overlying clays

(lithostratigraphic Units I to II; see **Lithostratigraphy**). Below this depth, *P*-wave velocities show a continuous trend of increasing values, with a second abrupt change from 1824 m/s at 446.7 m to 2453 m/s at 447.4 m that marks the change from an unconsolidated sand layer to a thin layer of sandstone (lithostratigraphic Subunits IIB to IIC). Rapid changes in velocities occur below this depth due to changes in lithology, with values ranging between 1760 and 5330 m/s. Below ~600 m, velocities lie in a narrower range and fluctuate between two sets of values, from as low as ~3491 m/s in a sand or silty sandstone layer to 4814 m/s in a grayish sandstone.

Thermal conductivity values show a general increase from ~0.88 W/(m·K) near the seafloor to ~3.60 W/(m·K) at ~662 m (Figure **F53**). The gradual increase in value at shallow depths is likely due to sediment compaction. A significant decrease in thermal conductivity between 294 and 304 m is associated with a major change from lithostratigraphic Subunits IE–IF to IIA.

Changes in NGR values are associated with the major lithologic boundaries, but there are also significant, well defined fluctuations at a much finer scale (Figure **F53**). NGR values are low in lithostratigraphic subunits with high calcium carbonate content such as Subunit IC, and values are high in subunits with low carbonate content such as Subunits IIA and IIB. NGR values show some of the strongest fluctuations of all of the physical properties measurements and reflect rapid changes in lithostratigraphic subunits below ~300 m.

Comparison between L* values and lithologic content (Figure **F56**; see **Lithostratigraphy**) indicates that low L* values (darker intervals) are well correlated with clay-rich strata, whereas high L* values (lighter intervals) match well with carbonate-rich layers. There is also a close match between NGR and L*; low L* values (dark intervals) correlate with high NGR values and vice-versa because they both reflect the amount of clay minerals.

In Hole U1501C, the highest magnetic susceptibility values are between 25 and 95 m (Figure **F53**), corresponding to lithostratigraphic Subunits IB and IC, which are dominated by calcite-rich minerals. We suspect that the weak trend representing changes in paramagnetic clay minerals, compared to diamagnetic calcite, is overprinted by the presence of ferromagnetic minerals. One of the prominent peaks in magnetic susceptibility correlates with the ash layer found in the uppermost section of Hole U1501A. In Hole U1501D, extremely high magnetic susceptibility values within lithostratigraphic Subunits IIIA and IIIB correspond to layers of sandstone or sandstone with gravels.

Downhole measurements

Logging operations

After recovering the last RCB core from 644.3 m in Hole U1501D, a wiper trip was made to condition the hole for logging operations and the RCB drill bit was released at the bottom of the hole. The bottom of the drill pipe was raised to logging depth at 2971.8 m drilling depth below rig floor (DRF [I give the scale whether it's used again or not because some people will know the acronym better]), or 115.1 m below the seafloor (Figure **F58**). Rig-up for downhole logging started at 0400 h (local time; UTC – 8 h) on 24 April 2017. The modified triple combo tool string started downhole at 0705 h on 24 April. The upward pass of the triple combo run began at 0815 h and ended at 0905 h. Because a section of collapsed hole was identified during the triple combo run, the logging operation ended after completion of the run. Logging tools were rigged down at 1200 h. Heave conditions were less than ~0.2 m for the triple combo run; therefore, the active heave compensator was not used.

Figure F58. Logging operations summary, Hole U1501D.

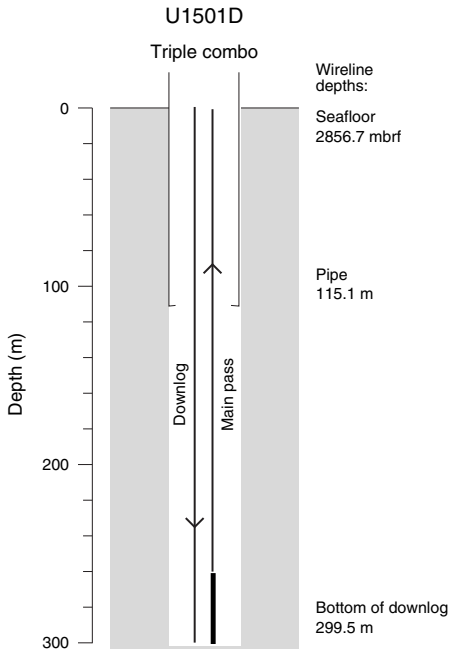

The modified triple combo tool string included the HNGS, HLDS, HRLA, and MSS (Figure **F59**). The centralized tools were run in the lower part of the tool string so it would be easier to lower the tool string past ledges than with an eccentralized tool (see **Downhole measurements** in the Expedition 367/368 methods chapter [Sun et al., 2018a]). The tool string encountered difficulty going down at approximately 173.3 m DSF and was unable to pass below 299.3 m DSF. The uphole log pass indicated a collapsed hole at ~156.3 m DSF based on the caliper curve. For safety reasons, no further attempts to descend below that undergauge spot were made. Because the interval of the collapsed hole was located only ~40 m below the bottom of the pipe, the originally planned FMS-sonic tool string was not run.

Logging units

The triple combo run in Hole U1501D allowed us to define four logging units that are correlated with lithostratigraphic units (see **Lithostratigraphy**), lithology, and physical properties (see **Physical properties**) (Figure **F60**).

Logging Unit 1: base of drill pipe to 190 m WSF

Logging Unit 1 is characterized by relatively high variability in the logs. For example, NGR values vary from ~38 to 70 gAPI. Excursions to lower and higher values also punctuate the magnetic susceptibility log. This logging unit corresponds to lithostratigraphic Subunits IA–ID.

Logging Unit 2: 190–260 m WSF

Logging Unit 2 is characterized by relative homogeneity in the logs, without major excursions to higher or lower log values (e.g., magnetic susceptibility logs). It is also characterized by submeter-scale layering, which is particularly evident in the caliper and resistivity logs. This logging unit corresponds to the lowest part of lithostratigraphic Subunit ID and the upper part of Subunit IE.

Figure F59. Tools used in triple combo run, Site U1501. LEH-QT = logging equipment head-q tension, EDTC = Enhanced Digital Telemetry Cartridge.

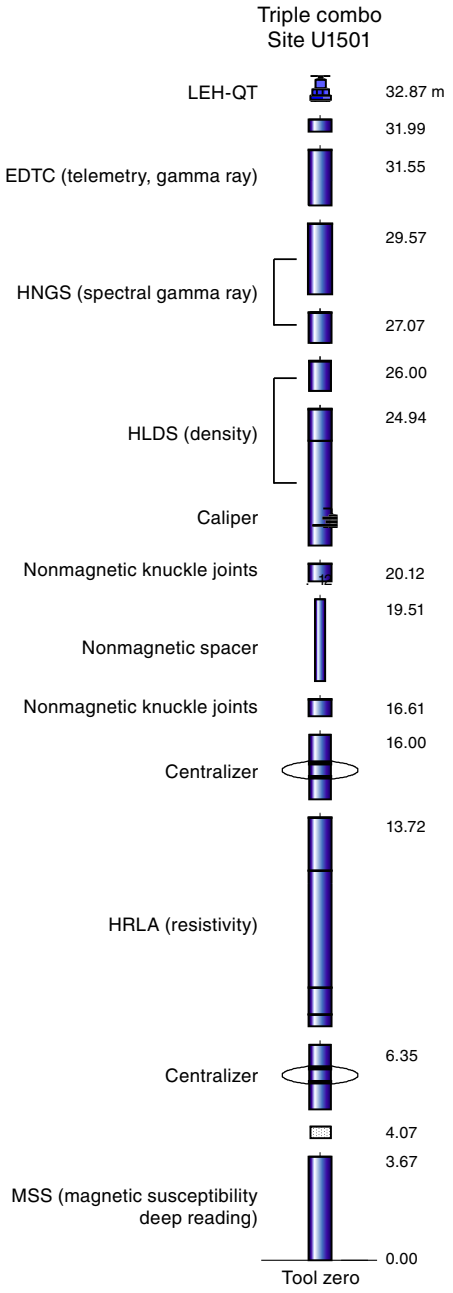

Logging Unit 3: 260–275 m WSF

Logging Unit 3 shows relatively high variability in the logs similar to that in logging Unit 1. The NGR, density, and resistivity logs reveal higher amplitude variations than those in logging Unit 2. This logging unit corresponds to lithostratigraphic Subunit IE.

Logging Unit 4: 275–300 m WSF

The upper part of logging Unit 4 (275–285 m WSF) corresponds to a section in the lower part of lithostratigraphic Subunit IE. This logging unit does not exhibit any major excursions, similar to logging Unit 2. Although the bottom of the triple combo string reached 300 m WSF, the sensors did not reach the lower part of logging Unit 4 (285–300 m WSF), which corresponds to parts of lithostratigraphic Subunits IE and IF.

Log data quality and lithology

Log data quality was affected by the large borehole diameter, which exceeded the 17 inch limit of the HLDS caliper arm for about half of the logged interval (Figure **F60**). Some particularly large caving was inferred at 115–190 and 260–275 m WSF, leading to uncertainty in some of the log values in those intervals. A major thin-bridged (narrow diameter) interval occurred at ~156.3 m WSF.

The downhole logs reflect the lithology at Site U1501. The clay-dominated sediments have high NGR readings because of high concentrations of K and Th in clay minerals, whereas the calcareous sediments have lower NGR and magnetic susceptibility because of a relative lack of radioactive and magnetic minerals. The same NGR and magnetic susceptibility signatures are also seen in the physical property measurements made on cores from Hole U1501C, which enables the downhole logs from Hole U1501D to be correlated to the core data from Hole U1501C.

Contrasts in NGR and magnetic susceptibility can be seen in the logs as a whole. In particular, the calcareous beds can be readily identified in the downhole logs with low NGR. Sand-rich beds can be difficult to identify because they tend to be only partially recovered in the cores and because they become easily washed out in the borehole, resulting in anomalous log data values. In fact, the best indication of sand layers in the logs may be the diameter of the borehole. Such washouts also have very low NGR values.

Downhole temperature and heat flow

Four downhole temperature measurements were conducted in Hole U1501C using the advanced piston corer temperature tool (APCT-3). Temperatures range from 5.5°C at 47.3 m DSF to 12.4°C at 132.8 m DSF, giving a geothermal gradient of 81.4°C/km (Figure **F61A**). These measurements, together with the seafloor temperature of 1.2°C, indicate that temperatures increase linearly with depth.

Thermal conductivity under in situ conditions was estimated from laboratory-determined thermal conductivity from Hole U1501C using the method in Hyndman et al. (1974) (see **Physical properties** in the Expedition 367/368 methods chapter [Sun et al., 2018a]). Thermal resistance (Figure **F61C**) was then calculated by integrating the inverse of the in situ thermal conductivity over depth (Figure **F61B**). A heat flow of 100.1 mW/m^2 was obtained from the linear fit between temperature and thermal resistance (Figure **F61D**) (Pribnow et al., 2000). The geothermal gradient and heat flow at Site U1501 are comparable to the relatively high values observed in some ODP, Integrated Ocean Drilling Program, and IODP sites in this part of the SCS, including Sites U1432 (100.1 mW/m^2) and U1499 (114 mW/m^2). Together, these sites show that parts of the northern SCS margin have relatively high heat flow values (Li et al., 2010).

Figure F60. Downhole logs, Hole U1501D. HSGR = total spectral gamma ray, HCGR = computed gamma ray (U-free). Downhole logs were taken in Hole U1501D, and lithology and core recovery data are from Hole U1501C.

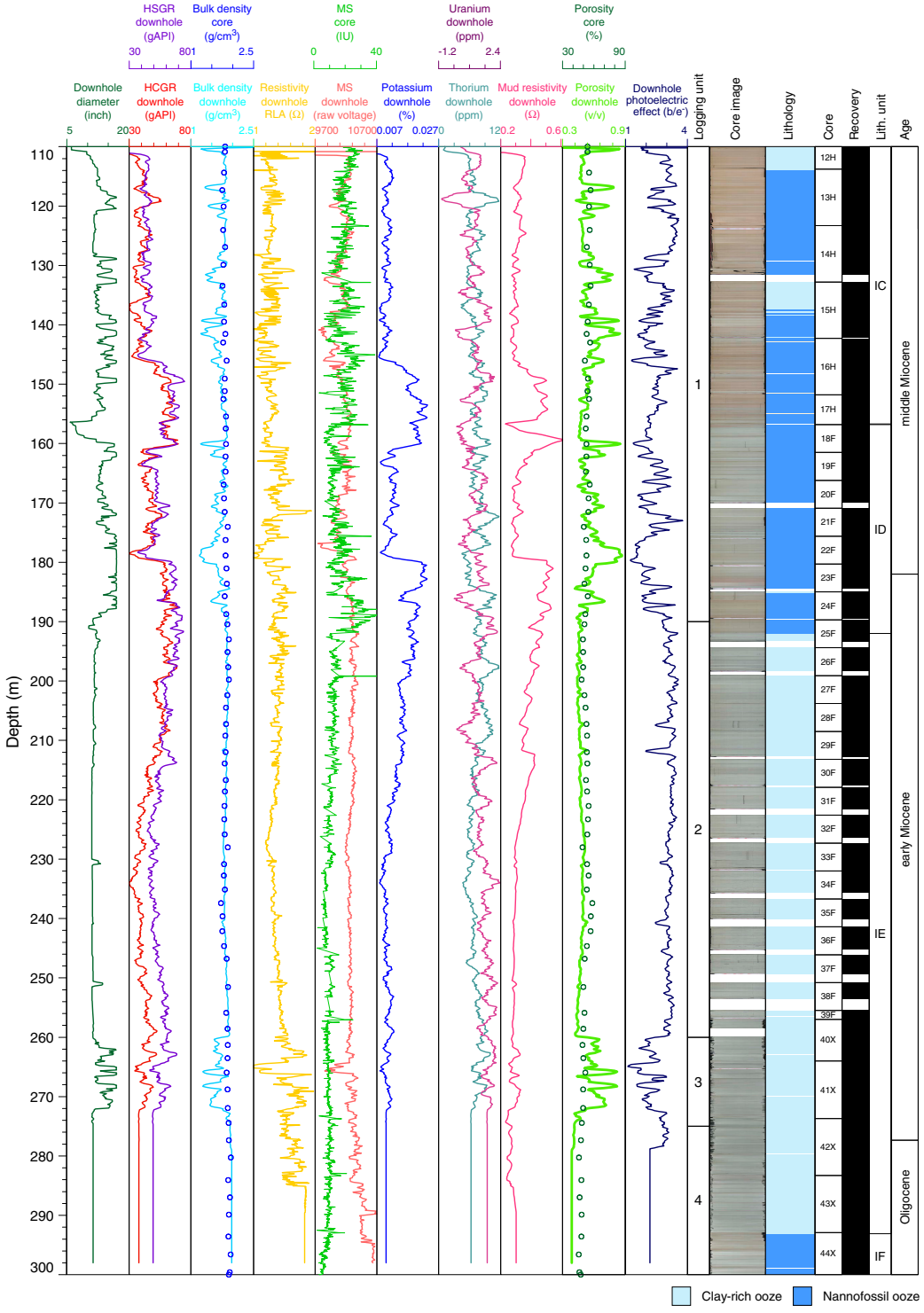

Figure F61. Heat flow calculations, Site U1501. A. Sediment temperatures. B. Thermal conductivity data, Hole U1501C. C. Calculated thermal resistance. D. Bullard plot of heat flow calculated from a linear fit of temperature data.

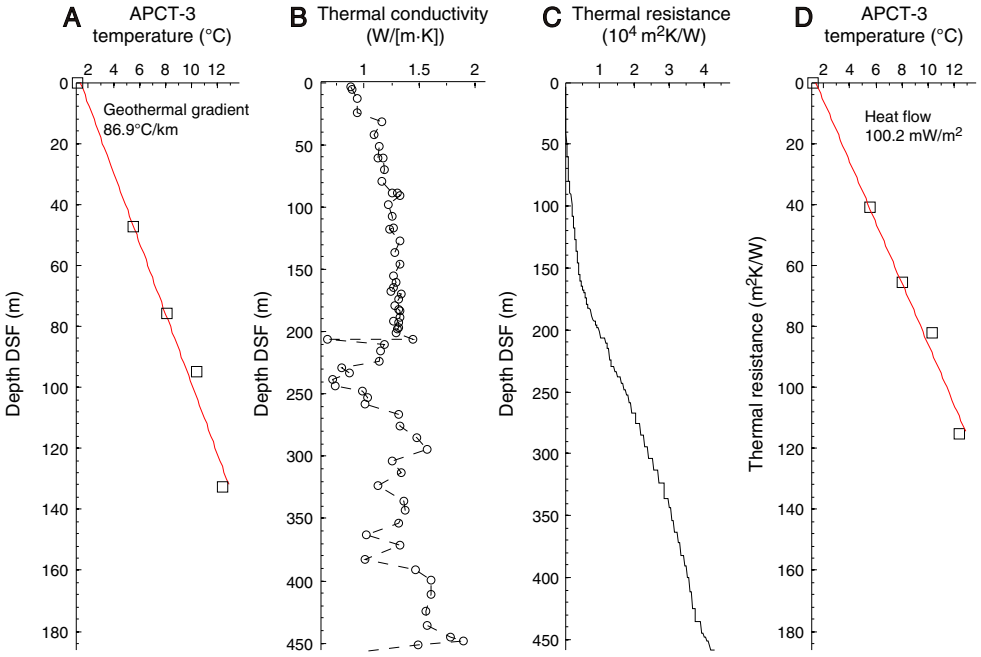

Correlation to seismic data

We conducted two sets of analyses to correlate core measurements to the time-based seismic data at Site U1501. First, we analyzed core data and made a direct comparison with the seismic reflection profile. Second, we constructed synthetic seismograms using the Site U1501 core data and compared the results with the traces in seismic profiles. Preliminary calculations were done during the expedition using a combination of Matlab scripts and Petrel software.

Velocity and density data and comparison with seismic reflectors

Whole-round core measurements, including *P*-wave velocity (PWL) and GRA density, were conducted from 0 to 457.7 m in Hole U1501C and from 433.5 to 643.5 m in Hole U1501D (Figure **F62**). *P*-wave velocity was also measured along the *x*-axis with the PWC system on working-half sections. MAD measurements were performed on discrete samples, one every other section. In addition, HLDS density measurements were obtained from downhole logging in Hole U1501D from 115 to 300 m (see **Physical properties** and **Downhole measurements**). After outliers were cleaned, the whole-round PWL data are in good agreement with the PWC velocities of core samples. The HLDS density values from downhole logging are also in good agreement with MAD data for intervals away from borehole enlargements (Figure **F60**).

Seismic velocity and density show significant variations in quality with depth, affecting calculations of TWT and synthetic seismograms. From 0 to ~450 m, PWC velocity is of excellent quality. From ~450 to ~608 m, PWC velocity is highly scattered. From ~608 to ~643.5 m, the number of PWC measurements is very limited, whereas the PWL data provide some constraints. For the density data, both the whole-round and discrete sample measurements provide excellent constraints in the 0–450 and 608–643.5 m intervals, respectively. However, data recovery is poor at 450–608 m (Figure **F62**).

Site U1501 core measurements show distinct changes in physical properties and lithology in a number of depth intervals (see **Physical properties**). In general, these intervals correlate well with the depth intervals of strong amplitudes in the seismic reflection profile (Figure **F62**). Intervals with increasing velocity and density with depth often correlate with strong positive amplitudes in the seismic reflection profile, whereas decreases correspond to negative amplitudes. Such correlations are especially clear between the velocity and density profiles and the depth-converted seismic trace at Site U1501.

Time-depth relationship

The PWC velocity measurements from Holes U1501C and U1501D were used to calculate the time-depth relationship (TDR) model of seismic waves. We first calculated a preliminary model of TDR that best fits the observed PWC velocity data, called "U1501_Preliminary_Model" (Figure **F63**). This model was calculated using data for the 0–450 m interval only, where PWC data are available. For the 450–608 m interval, the highly scattered PWC data do not provide reliable constraints on the TDR models.

At least three depth intervals at Site U1501 are associated with major changes in velocity and/or density and are assigned as reference points for correlation with the seismic reflection profile. The three depth intervals of the most prominent changes are at ~303 m (RP1), ~450 m (RP2), and ~600 m (RP3). RP1 and RP3 also correlate with the seismic sequence T60 boundary and with the seismic Tg reflector, respectively. These reference points are readily recognized in the drill core, lending further support to our models. With the additional constraints from these reference points and fitting the TDR using a polynomial function with depth, we constructed a new TDR model for Site U1501 called "U1501_modified_model" (Figure

Figure F62. Comparison of a subset of physical properties with seismic waveform (converted to depth scale using best-fitting TDR model) and seismic image (in timescale).

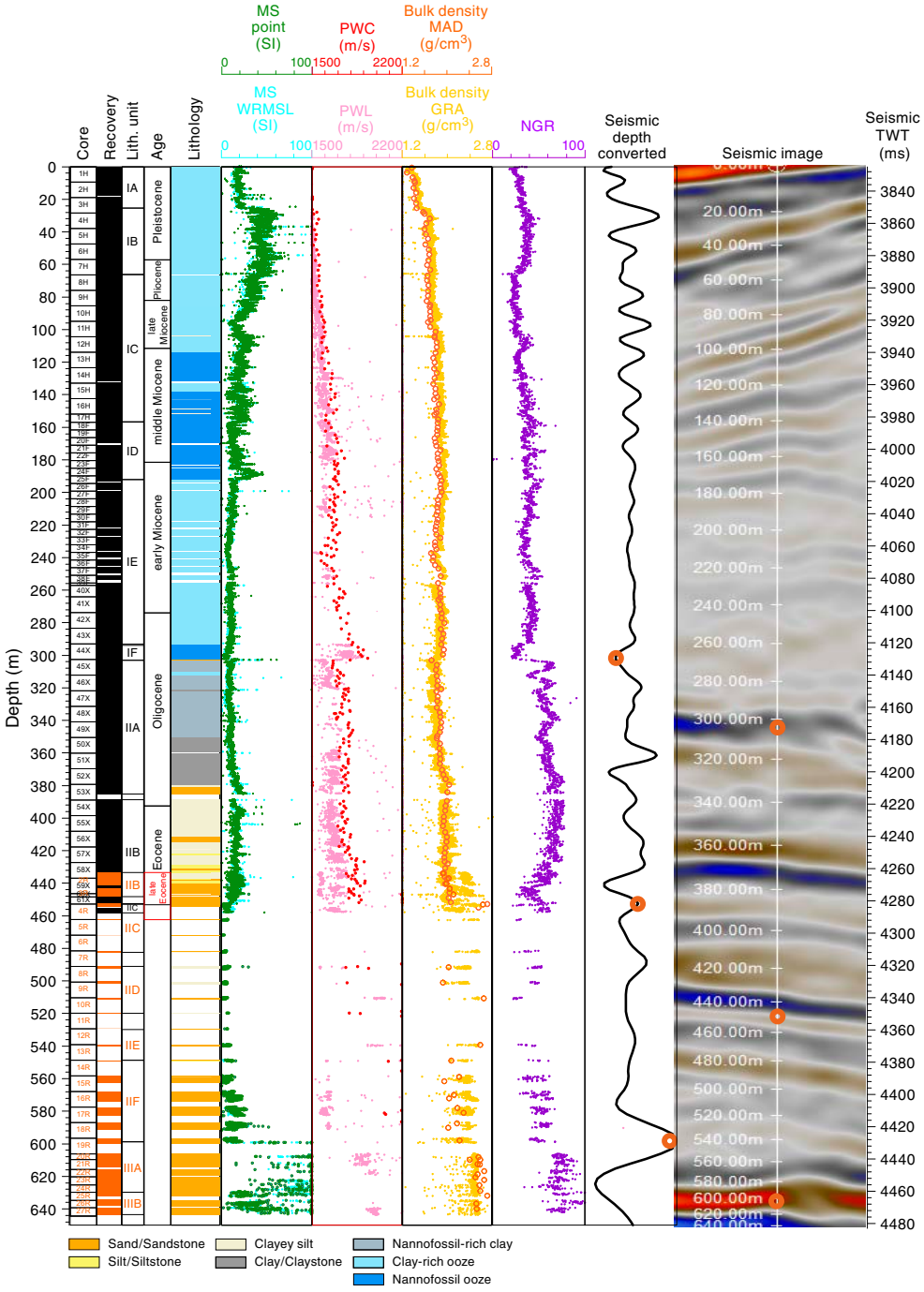

F63). The modified TDR model with constraints of the three reference points is, in general, in line with the preliminary TDR model.

We also compared our TDR models of Site U1501 with those of Sites 1148 (Shipboard Scientific Party, 2000), U1431 (Li et al., 2015b), U1499, and U1500 (see the **Site U1499** and **Site U1500** chapters [Sun et al., 2018b; Stock et al., 2018]). Our calculated TDR models for Site U1501 show substantial agreement with the TDR models of most of these drill sites, especially with the model of Site 1148 (Figure F64).

Using the best-fitting TDR model (U1501_modified_model), we were able to convert depth scale to timescale for all core measurements. Such conversion enabled us to display the core measurements directly on top of the time-based seismic sections, facilitating identification of correlated features, as illustrated in the example in Figure F65.

Figure F63. TDR curves, Site U1501. U1501_preliminary_model was primarily based on PWC velocity data for depths shallower than ~450 m, an interval where PWC data are available. U1501_modified_model was based on the preliminary model with additional constraints from three reference points (RP1–RP3).

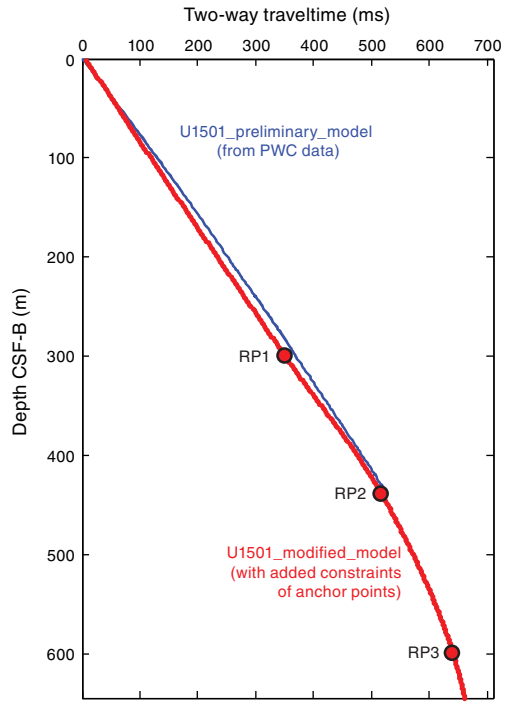

Figure F64. Site U1501 TDR curves, including U1501_preliminary_model and U1501_modified_model, compared to TDRs for Sites U1499, U1500, and 1148 (Li et al., 2008).

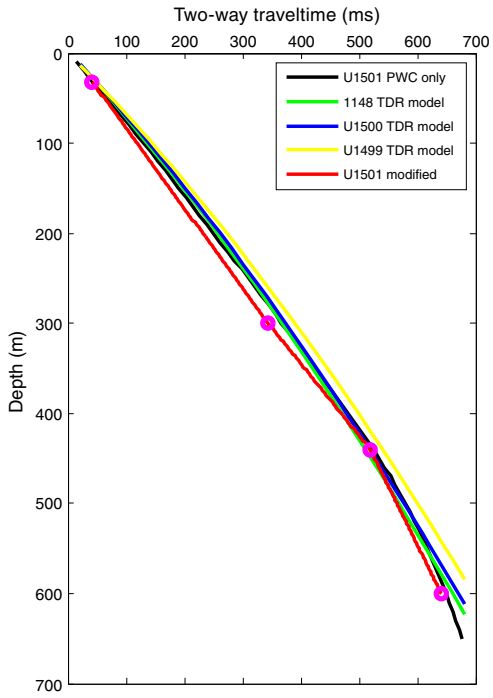

Synthetic seismograms

To further illustrate the relationship between the core measurements at Site U1501 and the seismic reflection profile, the Seismic interpretation module in Petrel was used to compute synthetic seismograms based on the relevant core measurements. Synthetic traces were generated by convolving the reflectivity from the density of core samples and the smoothed velocities from the PWC together with the source wavelet that best fits the seismic data (Ricker 2_30 Hz; Figure **F66**).

Seismic impedance (SI) of a rock layer is the product of its average seismic velocity (V_P) and density (ρ) (i.e., SI = V_P × ρ). The seismic reflection coefficient (RC), in turns, measures the change in the seismic impedance between two adjacent rock layers. Thus, we can expect greater amplitudes in the modeled seismogram for rock layers with larger RC values. The resulting synthetic seismogram shows strong reflectors at several depth intervals, including ~303 and 600 m, that are consistent with the observed seismic unconformities. The transition between lithostratigraphic Units II and III at 600 m, for instance, is marked by a sharp increase in density and velocity; the net result is a strong positive increase in impedance (Figure **F66**).

Figure F65. Seismic section at Site U1501 with thin strip of synthetic seismogram and lithostratigraphic units overlain at drill hole location. Also shown are selected core and downhole logging measurements converted to depth scale using best-fitting TDR model, including magnetic susceptibility (core), thorium (logging), uranium (logging), PWL (core), density (core and logging), and NGR (core and logging).

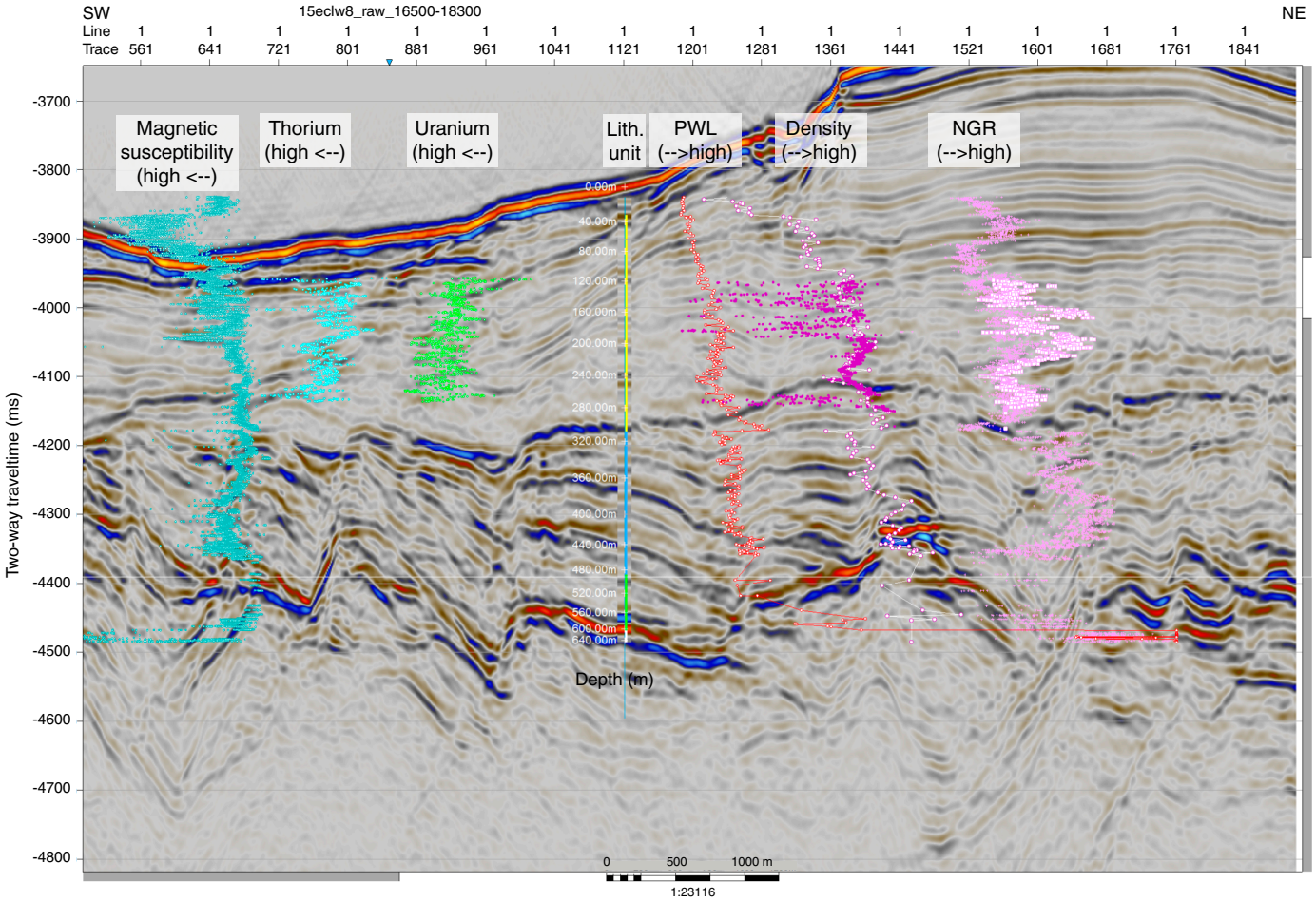

Figure F66. Synthetic seismogram, Site U1501. Left to right: smoothed velocity and MAD density used in the calculation, resultant RC, real seismic traces with synthetic seismogram inserted in the center, and seismic source function "Ricker 2_30 Hz" used in modeling. TVD = true vertical depth from Petrel software.

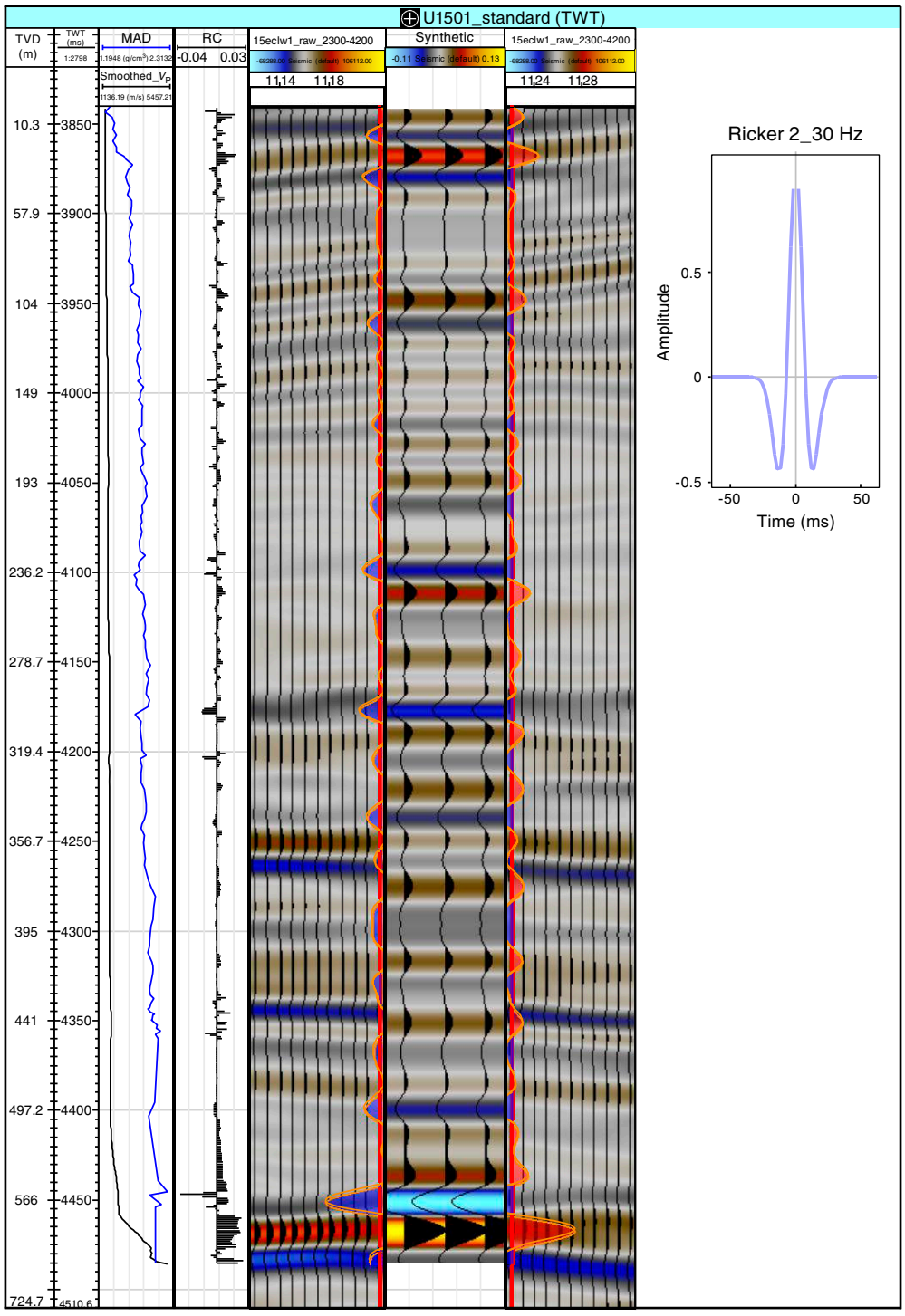

References

Alabi, O.O., Edilbi, A.N.F., Brolly, C., Muirhead, D., Parnell, J., Stacey, R., and Bowden, S.A., 2015. Asphaltene detection using surface enhanced Raman scattering (SERS). *Chemical Communications,* 51(33):7152–7155. **http://pubs.rsc.org/en/content/articlehtml/2015/cc/c5cc00676g**

Barnes, R.O., and Goldberg, E.D., 1976. Methane production and consumption in anoxic marine sediments. *Geology,* 4(5):297–300. **https://doi.org/10.1130/0091-7613(1976)4<297:MPACIA>2.0.CO;2**

Berner, R.A., and Raiswell, R., 1984. C/S method for distinguishing freshwater from marine sedimentary rocks. *Geology,* 12(6):365–368. **https://doi.org/10.1130/0091-7613(1984)12<365:CMFDFF>2.0.CO;2**

Briais, A., Patriat, P., and Tapponnier, P., 1993. Updated interpretation of magnetic anomalies and seafloor spreading stages in the South China Sea: implications for the Tertiary tectonics of Southeast Asia. *Journal of Geophysical Research: Solid Earth,* 98(B4):6299–6328. **https://doi.org/10.1029/92JB02280**

Clift, P.D., Wan, S., and Blusztajn, J., 2014. Reconstructing chemical weathering, physical erosion and monsoon intensity since 25 Ma in the northern South China Sea: a review of competing proxies. *Earth-Science Reviews,* 130:86–102. **https://doi.org/10.1016/j.earscirev.2014.01.002**

Dai, Y., Yu, Q., Li, H., Wang, Z., Bai, J., and Peng, H., 2015. Threshold conditions and reservoir-controlling characteristics of source kitchen in Zhu I depression, Pearl River Mouth Basin. *Acta Petrolei Sinica,* 36(S2):145–155. (in Chinese with English abstract) **https://doi.org/10.7623/syxb2015S2013**

De Vleeschouwer, D., Dunlea, A.G., Auer, G., Anderson, C.H., Brumsack, H., de Loach, A., Gurnis, M., et al., 2017. Quantifying K, U, and Th contents of marine sediments using shipboard natural gamma radiation spectra measured on DV *JOIDES Resolution*. *Geochemistry, Geophysics, Geosystems,* 18(3):1053–1064. **https://doi.org/10.1002/2016GC006715**

Demaison, G.J., and Moore, G.T., 1980. Anoxic environments and oil source bed genesis. *AAPG Bulletin,* 64:1179–1209.

Drzewiecki, P.A., and Simó, J.A., 2002. Depositional processes, triggering mechanisms and sediment composition of carbonate gravity flow deposits: examples from the Late Cretaceous of the south-central Pyrenees, Spain. *Sedimentary Geology,* 146(1–2):155–189. **https://doi.org/10.1016/S0037-0738(01)00171-3**

Exon, N.F., Kennett, J.P., Malone, M.J., Brinkhuis, H., Chaproniere, G., Ennyo, A., Fothergill, P., et al., 2002. Drilling reveals climatic consequences of Tasmanian Gateway opening. *Eos, Transactions of the American Geophysical Union,* 83(23):253–259. **https://doi.org/10.1029/2002EO000176**

Hanai, T., 1957. Studies on the Ostracoda from Japan: 3. Subfamilies Cytherurinae G.W. Müller (emend. G.O. Sars, 1925) and Cytheropterinae n. subfam. *Journal of the Faculty of Science, University of Tokyo, Section 2,* 11:11–36.

Harris, L.C., and Whiting, B.M., 2000. Sequence-stratigraphic significance of Miocene to Pliocene glauconite-rich layers, on- and offshore of the US Mid-Atlantic margin. *Sedimentary Geology,* 134(1–2):129–147. **https://doi.org/10.1016/S0037-0738(00)00017-8**

Hedges, J.I., Clark, W.A., and Come, G.L., 1988. Organic matter sources to the water column and surficial sediments of a marine bay. *Limnology and Oceanography,* 33(5):1116–1136. **https://doi.org/10.4319/lo.1988.33.5.1116**

Horng, C.-S., Torii, M., Shea, K.-S., and Kao, S.-J., 1998. Inconsistent magnetic polarities between greigite- and pyrrhotite/magnetite-bearing marine sediments from the Tsailiao-chi section, southwestern Taiwan. *Earth and Planetary Science Letters,* 164(3–4):467–481. **https://doi.org/10.1016/S0012-821X(98)00239-8**

Hyndman, R.D., Erickson, A.J., and Von Herzen, R.P., 1974. Geothermal measurements on DSDP Leg 26. *In* Davies, T.A., Luyendyk, B.P., et al., *Initial Reports of the Deep Sea Drilling Project,* 26: Washington, DC (U.S. Govt. Printing Office), 451–463. **https://doi.org/10.2973/dsdp.proc.26.113.1974**

Kirschvink, J.L., 1980. The least-squares line and plane and the analysis of palaeomagnetic data. *Geophysical Journal of the Royal Astronomical Society,* 62(3):699–718. **https://doi.org/10.1111/j.1365-246X.1980.tb02601.x**

Krs, M., Novák, F., Krsová, M., Pruner, P., Kouklíková, L., and Jansa, J., 1992. Magnetic properties and metastability of greigite-smythite mineralization in brown-coal basins of the Krušné hory Piedmont, Bohemia. *Physics of the Earth and Planetary Interiors,* 70(3–4):273–287. **https://doi.org/10.1016/0031-9201(92)90194-Z**

Li, C.-F., Li, J., Ding, W., Franke, D., Yao, Y., Shi, H., Pang, X., et al., 2015a. Seismic stratigraphy of the central South China Sea basin and implications for neotectonics. *Journal of Geophysical Research: Solid Earth,* 120(3):1377–1399. **https://doi.org/10.1002/2014JB011686**

Li, C.-F., Lin, J., Kulhanek, D.K., Williams, T., Bao, R., Briais, A., Brown, E.A., Chen, Y., Clift, P.D., Colwell, F.S., Dadd, K.A., Ding, W., Hernández-Almeida, I., Huang, X.-L., Hyun, S., Jiang, T., Koppers, A.A.P., Li, Q., Liu, C., Liu, Q., Liu, Z., Nagai, R.H., Peleo-Alampay, A., Su, X., Sun, Z., Tejada, M.L.G., Trinh, H.S., Yeh, Y.-C., Zhang, C., Zhang, F., Zhang, G.-L., and Zhao, X., 2015b. Site U1431. *In* Li, C.-F., Lin, J., Kulhanek, D.K., and the Expedition 349 Scientists, *South China Sea Tectonics.* Proceedings of the International Ocean Discovery Program, 349: College Station, TX (International Ocean Discovery Program). **http://dx.doi.org/10.14379/iodp.proc.349.103.2015**

Li, C.-F., Shi, X., Zhou, Z., Li, J., Geng, J., and Chen, B., 2010. Depths to the magnetic layer bottom in the South China Sea area and their tectonic implications. *Geophysical Journal International,* 182(3):1229–1247. **https://doi.org/10.1111/j.1365-246X.2010.04702.x**

Li, C.-F., Zhou, Z., Li, J., Chen, B., and Geng, J., 2008. Magnetic zoning and seismic structure of the South China Sea ocean basin. *Marine Geophysical Research,* 29(4):223–238. **https://doi.org/10.1007/s11001-008-9059-4**

Li, Q., Zheng, H., Zhong, G., and Wang, P., 2005. Tectonic events indicated by late Oligocene slumped deposits from the South China Sea. *Earth Science-Journal of China University of Geosciences,* 30:19–24. **http://en.cnki.com.cn/Article_en/CJFDTOTAL-DQKX200501001.htm**

Li, Y.-P., and Jiang, S.Y., 2010. Boron concentration and isotopic constraints on processes affecting the chemistry of interstitial water in normal- and over-pressured basins, Gulf of Mexico. *Marine Geology,* 275(1–4):230–243. **https://doi.org/10.1016/j.margeo.2010.06.004**

Liu, J., Shi, X., Liu, Q., Ge, S., Liu, Y., Yao, Z., Zhao, Q., et al., 2014. Magnetostratigraphy of a greigite-bearing core from the South Yellow Sea: implications for remagnetization and sedimentation. *Journal of Geophysical Research: Solid Earth,* 119(10):7425–7441. **https://doi.org/10.1002/2014JB011206**

Lurcock, P.C., and Wilson, G.S., 2012. PuffinPlot: a versatile, user-friendly program for paleomagnetic analysis. *Geochemistry, Geophysics, Geosystems,* 13(6):Q06Z45. **https://doi.org/10.1029/2012GC004098**

Margielewski, W., Jankowski, L., Krapiec, M., Garecka, M., Hałas, S., and Urban, J., 2017. Analysis of reworked sediments as a basis of the Palaeogene-Neogene palaeogeography reinterpretation: case study of the Roztocze region (SE Poland). *Sedimentary Geology,* 352:14–29. **https://doi.org/10.1016/j.sedgeo.2017.02.009**

McRae, S.G., 1972. Glauconite. *Earth-Science Reviews,* 8(4):397–440. **https://doi.org/10.1016/0012-8252(72)90063-3**

Nanni, U., Pubellier, M., Sang Chan, L., and Sewell, R.J., 2017. Rifting and reactivation of a Cretaceous structural belt at the northern margin of the South China Sea. *Journal of Asian Earth Sciences,* 136:110–123. **https://doi.org/10.1016/j.jseaes.2017.01.008**

Ogg, J.G., Ogg, G., and Gradstein, F.M., 2016. *A Concise Geologic Time Scale 2016:* Boston (Elsevier).

Pang, X., Chen, C.M., Peng, D.J., Zhu, M., Shu, Y., He, M., Shen, J., and Liu, B., 2007. Sequence stratigraphy of deep-water fan system of Pearl River, South China Sea. *Earth Science Frontiers,* 14(1):220–229. (in Chinese with English abstract) **https://doi.org/10.1016/S1872-5791(07)60010-4**

Pasteris, J.D., and Wopenka, B., 2003. Necessary, but not sufficient: Raman identification of disordered carbon as a signature of ancient life. *Astrobiology,* 3(4):727–738. **https://www.ncbi.nlm.nih.gov/pubmed/14987478**

Pribnow, D., Kinoshita, M., and Stein, C., 2000. *Thermal Data Collection and Heat Flow Recalculations for Ocean Drilling Program Legs 101–180:* Hanover, Germany (Institute for Joint Geoscientific Research, Institut für Geowissenschaftliche Gemeinschaftsaufgaben [GGA]). **http://www-odp.tamu.edu/publications/heatflow/ODPReprt.pdf**

Roberts, A.P., 1995. Magnetic properties of sedimentary greigite (Fe_3S_4). *Earth and Planetary Science Letters,* 134(3–4):227–236. **https://doi.org/10.1016/0012-821X(95)00131-U**

Roberts, A.P., Chang, L., Rowan, C.J., Horng, C.-S., and Florindo, F., 2011. Magnetic properties of sedimentary greigite (Fe_3S_4): an update. *Reviews of Geophysics,* 49(1):RG1002. **https://doi.org/10.1029/2010RG000336**

Russell, W.L., 1944. The total gamma ray activity of sedimentary rocks as indicated by Geiger counter determinations. *Geophysics,* 9(2):180–216. **https://doi.org/10.1190/1.1445076**

Shao, L., Cao, L., Pang, X., Jiang, T., Qiao, P., and Zhao, M., 2016. Detrital zircon provenance of the Paleogene syn-rift sediments in the northern South China Sea. *Geochemistry, Geophysics, Geosystems,* 17(2):255–269. **https://doi.org/10.1002/2015GC006113**

Shi, H., He, M., and Zhang, L., 2014. Hydrocarbon geology, accumulation pattern and the next exploration strategy in the eastern Pearl River Mouth basin. *China Offshore Oil and Gas,* 26(3):11–22. (in Chinese with English abstracts)

Shipboard Scientific Party, 2000. Site 1148. *In* Wang, P., Prell, W.L., Blum, P., et al., *Proceedings of the Ocean Drilling Program, Initial Reports,* 184: College Station, TX (Ocean Drilling Program), 1–122. **https://doi.org/10.2973/odp.proc.ir.184.109.2000**

Snowball, I.F., 1991. Magnetic hysteresis properties of greigite (Fe_3S_4) and a new occurrence in Holocene sediments from Swedish Lappland. *Physics of the Earth and Planetary Interiors,* 68(1–2):32–40. **https://doi.org/10.1016/0031-9201(91)90004-2**

Stock, J.M., Sun, Z., Klaus, A., Larsen, H.C., Jian, Z., Alvarez Zarikian, C.A., Boaga, J., Bowden, S.A., Briais, A., Chen, Y., Cukur, D., Dadd, K.A., Ding, W., Dorais, M.J., Ferré, E.C., Ferreira, F., Furusawa, A., Gewecke, A.J., Hinojosa, J.L., Höfig, T.W., Hsiung, K.-H., Huang, B., Huang, E., Huang, X.-L., Jiang, S., Jin, H., Johnson, B.G., Kurzawski, R.M., Lei, C., Li, B., Li, L., Li, Y., Lin, J., Liu, C., Liu, Z., Luna, A., Lupi, C., McCarthy, A.J., Mohn, G., Ningthoujam, L.S., Nirrengarten, M., Osono, N., Peate, D.W., Persaud, P., Qui, N., Robinson, C.M., Satolli, S., Sauermilch, I., Schindlbeck, J.C., Skinner, S.M., Straub, S.M., Su, X., Tian, L., van der Zwan, F.M., Wan, S., Wu, H., Xiang, R., Yadav, R., Yi, L., Zhang, C., Zhang, J., Zhang, Y., Zhao, N., Zhong, G., and Zhong, L., 2018. Site U1500. *In* Sun, Z., Jian, Z. Stock, J.M., Larsen, H.C., Klaus, A., Alvarez Zarikian, C.A., and the Expedition 367/368 Scientists, 2018. *South China Sea Rifted Margin*. Proceedings of the International Ocean Discovery Program, 367/368: College Station, TX (International Ocean Discovery Program). **https://doi.org/10.14379/iodp.proc.367368.104.2018**

Sun, Z., Jian, Z., Stock, J.M., Larsen, H.C., Klaus, A., Alvarez Zarikian, C.A., Boaga, J., Bowden, S.A., Briais, A., Chen, Y., Cukur, D., Dadd, K.A., Ding, W., Dorais, M.J., Ferré, E.C., Ferreira, F., Furusawa, A., Gewecke, A.J., Hinojosa, J.L., Höfig, T.W., Hsiung, K.-H., Huang, B., Huang, E., Huang, X.-L., Jiang, S., Jin, H., Johnson, B.G., Kurzawski, R.M., Lei, C., Li, B., Li, L., Li, Y., Lin, J., Liu, C., Liu, C., Liu, Z., Luna, A., Lupi, C., McCarthy, A.J., Mohn, G., Ningthoujam, L.S., Nirrengarten, M., Osono, N., Peate, D.W., Persaud, P., Qui, N., Robinson, C.M., Satolli, S., Sauermilch, I., Schindlbeck, J.C., Skinner, S.M., Straub, S.M., Su, X., Tian, L., van der Zwan, F.M., Wan, S., Wu, H., Xiang, R., Yadav, R., Yi, L., Zhang, C., Zhang, J., Zhang, Y., Zhao, N., Zhong, G., and Zhong, L., 2018a. Expedition 367/368 methods. *In* Sun, Z., Jian, Z., Stock, J.M., Larsen, H.C., Klaus, A., Alvarez Zarikian, C.A., and the Expedition 367/368 Scientists, *South China Sea Rifted Margin*. Proceedings of the International Ocean Discovery Program, 367/368: College Station, TX (International Ocean Discovery Program). **https://doi.org/10.14379/iodp.proc.367368.102.2018**

Sun, Z., Stock, J.M., Klaus, A., Larsen, H.C., Jian, Z., Alvarez Zarikian, C.A., Boaga, J., Bowden, S.A., Briais, A., Chen, Y., Cukur, D., Dadd, K.A., Ding, W., Dorais, M.J., Ferré, E.C., Ferreira, F., Furusawa, A., Gewecke, A.J., Hinojosa, J.L., Höfig, T.W., Hsiung, K.-H., Huang, B., Huang, E., Huang, X.-L., Jiang, S., Jin, H., Johnson, B.G., Kurzawski, R.M., Lei, C., Li, B., Li, L., Li, Y., Lin, J., Liu, C., Liu, C., Liu, Z., Luna, A., Lupi, C., McCarthy, A.J., Mohn, G., Ningthoujam, L.S., Nirrengarten, M., Osono, N., Peate, D.W., Persaud, P., Qui, N., Robinson, C.M., Satolli, S., Sauermilch, I., Schindlbeck, J.C., Skinner, S.M., Straub, S.M., Su, X., Tian, L., van der Zwan, F.M., Wan, S., Wu, H., Xiang, R., Yadav, R., Yi, L., Zhang, C., Zhang, J., Zhang, Y., Zhao, N., Zhong, G., and Zhong, L., 2018b. Site U1499. *In* Sun, Z., Jian, Z., Stock, J.M., Larsen, H.C., Klaus, A., Alvarez Zarikian, C.A., and the Expedition 367/368 Scientists, *South China Sea Rifted Margin*. Proceedings of the International Ocean Discovery Program, 367/368: College Station, TX (International Ocean Discovery Program). **https://doi.org/10.14379/iodp.proc.367368.103.2018**

Suttill, H.L., 2009. Sedimentological evolution of the Emine and Kamchia Basins, eastern Bulgaria [Ph.D. thesis]. University of Edinburgh. **https://www.era.lib.ed.ac.uk/handle/1842/4919**

Suttner, L.J., Basu, A., and Mack, G.H., 1981. Climate and the origin of quartz arenites. *Journal of Sedimentary Research,* 51(4):1235–1246. **https://doi.org/10.1306/212F7E73-2B24-11D7-8648000102C1865D**

Tauxe, L., 2010. *Essentials of Paleomagnetism:* Berkeley, California (University of California Press).

Torres, M.E., Brumsack, H.-J., Bohrmann, G., and Emeis, K.C., 1996. Barite fronts in continental margin sediments: a new look at barium remobilization in the zone of sulfate reduction and formation of heavy barites in diagenetic fronts. *Chemical Geology,* 127(1–3):125–139. **https://doi.org/10.1016/0009-2541(95)00090-9**

Wigley, R., and Compton, J.S., 2007. Oligocene to Holocene glauconite–phosphorite grains from the head of the Cape Canyon on the western margin of South Africa. *Deep-Sea Research Part II: Topical Studies in Oceanography,* 54(11–13):1375–1395. **https://doi.org/10.1016/j.dsr2.2007.04.004**

Wilson, R., Monaghan, P., Bowden, S.A., Parnell, P., and Cooper, J.M., 2007. Surface-enhanced Raman signatures of pigmentation of cyanobacteria from within geological samples in a spectroscopic-microfluidic flow cell. *Analytical Chemistry,* 79(18):7036–7041. **https://doi.org/10.1021/ac070994c**

Yan, P., Zhou, D., and Liu, Z., 2001. A crustal structure profile across the northern continental margin of the South China Sea. *Tectonophysics,* 338(1):1–21. **https://doi.org/10.1016/S0040-1951(01)00062-2**

Yao, B., Zeng, W., Chen, Y., and Zhang, X., 1994. The crustal structure in the eastern part of the northern margin of the South China Sea. *Acta Geophysica Sinica,* 37:27–35.

Zhou, D., Ru, K., and Chen, H., 1995. Kinematics of Cenozoic extension on the South China Sea continental margin and its implications for the tectonic evolution of the region. *Tectonophysics,* 251(1–4):161–177. **https://doi.org/10.1016/0040-1951(95)00018-6**

Zhou, D., Wang, W., Wang, J., Pang, X., Cai, D., and Sun, Z., 2006. Mesozoic subduction-accretion zone in northeastern South China Sea inferred from geophysical interpretations. *Science in China, Series D: Earth Sciences,* 49(5):471–482. **https://doi.org/10.1007/s11430-006-0471-9**

Zijderveld, J.D.A., 1967. AC demagnetization of rocks: analysis of results. *In* Collinson, D.W., Creer, K.M., and Runcorn, S.K. (Eds.), *Developments in Solid Earth Geophysics* (Volume 3): *Methods in Palaeomagnetism:* Amsterdam (Elsevier), 254–286. **https://doi.org/10.1016/B978-1-4832-2894-5.50049-5**

Sun, Z., Jian, Z., Stock, J.M., Larsen, H.C., Klaus, A., Alvarez Zarikian, C.A., and the Expedition 367/368 Scientists
Proceedings of the International Ocean Discovery Program Volume 367/368
publications.iodp.org

https://doi.org/10.14379/iodp.proc.367368.106.2018

Site U1502[1]

Check for updates

Hans Christian Larsen, Zhimin Jian, Carlos A. Alvarez Zarikian, Zhen Sun, Joann M. Stock, Adam Klaus, Jacopo Boaga, Stephen A. Bowden, Anne Briais, Yifeng Chen, Deniz Cukur, Kelsie A. Dadd, Weiwei Ding, Michael J. Dorais, Eric C. Ferré, Fabricio Ferreira, Akira Furusawa, Aaron J. Gewecke, Jessica L. Hinojosa, Tobias W. Höfig, Kan-Hsi Hsiung, Baoqi Huang, Enqing Huang, Xiao-Long Huang, Shijun Jiang, Haiyan Jin, Benjamin G. Johnson, Robert M. Kurzawski, Chao Lei, Baohua Li, Li Li, Yanping Li, Jian Lin, Chang Liu, Chuanlian Liu, Zhifei Liu, Antonio Luna, Claudia Lupi, Anders J. McCarthy, Geoffroy Mohn, Lachit Singh Ningthoujam, Michael Nirrengarten, Nobuaki Osono, David W. Peate, Patricia Persaud, Ning Qiu, Caroline M. Robinson, Sara Satolli, Isabel Sauermilch, Julie C. Schindlbeck, Steven M. Skinner, Susanne M. Straub, Xiang Su, Liyan Tian, Froukje M. van der Zwan, Shiming Wan, Huaichun Wu, Rong Xiang, Rajeev Yadav, Liang Yi, Cuimei Zhang, Jinchang Zhang, Yang Zhang, Ning Zhao, Guangfa Zhong, and Lifeng Zhong[2]

Keywords: International Ocean Discovery Program, IODP, *JOIDES Resolution*, Expedition 367, Expedition 368, Site U1502, northern South China Sea, continent–ocean transition zone, Ridge A, hyperextension, continental breakup, thinning, rifting, altered basalt, Cenozoic, prerift, red clay, greigite, agglutinated benthic foraminifers

Contents

1 Site summary
7 Background and objectives
9 Operations
13 Lithostratigraphy
23 Igneous and metamorphic petrology
37 Structural geology
45 Biostratigraphy
49 Paleomagnetism
57 Geochemistry
62 Physical properties
67 Downhole measurements
71 Correlation to seismic data
75 References

Site summary

Background and objectives

Site U1502 (proposed Site SCSII-17A; Sun et al., 2016) within the South China Sea (SCS) northern margin (Figures **F1**, **F2**) is located at 3764 meters below sea level (mbsl) on a prominent basement ridge (A) within the continent–ocean transition (COT) (Figure **F3**). Ridge A is one of four distinct basement highs found across the COT. The outer margin high (OMH) is the most landward of these highs and is followed seaward by the nearly parallel Ridges A, B, and C. A key objective of Expeditions 367 and 368 was to examine the nature of the crust within Ridge A. This ridge is considered to be a pivotal element in the transition from continental to oceanic crust. Hence, the main objective of Site U1502 was to drill through synrift deposits overlying an interpreted shallow-dipping (~20°) fault zone and into the crystalline basement below the fault. Information on the nature and age of the synrift deposits overlying the fault, as well as the nature and age of the overlying sediments and associated seismic unconformities, formed another target with the objective of constraining basin subsidence.

Operations

We conducted operations in two holes at Site U1502. Hole U1502A is located at 18°27.8720′N, 116°13.8381′E, at 3763 mbsl. Our operations in Hole U1502A were designed to provide information on formation characteristics and drilling conditions so that we could decide the length of casing to drill into the seafloor in deep-penetration Hole U1502B. Given this purpose and the amount of time to drill the second, deep hole, we did not core continuously in Hole U1502A. Instead, we drilled without coring from the seafloor to 375.0 m and cored with the rotary core barrel (RCB) system from 375.0 to 758.2 m, recovering 176.81 m (46%). Hole U1502B is located at 18°27.8798′N, 116°13.8409′E, at 3763.6 mbsl. In Hole U1502B, we drilled a reentry funnel and 727.7 m of 10¾ inch casing into the seafloor; cored with the RCB system through the sediment–basalt transition (727.7–739.16 m) and 180 m into the underlying basalt (739.16–920.95 m), recovering 128 m (70%); and collected downhole log data with the triple combo tool string and a check shot with the Versatile Sonic Imager (VSI) tool string.

[1] Larsen, H.C., Jian, Z., Alvarez Zarikian, C.A., Sun, Z., Stock, J.M., Klaus, A., Boaga, J., Bowden, S.A., Briais, A., Chen, Y., Cukur, D., Dadd, K.A., Ding, W., Dorais, M.J., Ferré, E.C., Ferreira, F., Furusawa, A., Gewecke, A.J., Hinojosa, J.L., Höfig, T.W., Hsiung, K.-H., Huang, B., Huang, E., Huang, X.-L., Jiang, S., Jin, H., Johnson, B.G., Kurzawski, R.M., Lei, C., Li, B., Li, L., Li, Y., Lin, J., Liu, C., Liu, C., Liu, Z., Luna, A., Lupi, C., McCarthy, A.J., Mohn, G., Ningthoujam, L.S., Nirrengarten, M., Osono, N., Peate, D.W., Persaud, P., Qui, N., Robinson, C.M., Satolli, S., Sauermilch, I., Schindlbeck, J.C., Skinner, S.M., Straub, S.M., Su, X., Tian, L., van der Zwan, F.M., Wan, S., Wu, H., Xiang, R., Yadav, R., Yi, L., Zhang, C., Zhang, J., Zhang, Y., Zhao, N., Zhong, G., and Zhong, L., 2018. Site U1502. *In* Sun, Z., Jian, Z., Stock, J.M., Larsen, H.C., Klaus, A., Alvarez Zarikian, C.A., and the Expedition 367/368 Scientists, *South China Sea Rifted Margin*. Proceedings of the International Ocean Discovery Program, 367/368: College Station, TX (International Ocean Discovery Program). https://doi.org/10.14379/iodp.proc.367368.106.2018

[2] **Expedition 367/368 Scientists' addresses.**

MS 367368-106: Published 28 September 2018

This work is distributed under the **Creative Commons Attribution 4.0 International** (CC BY 4.0) license.

Figure F1. Bathymetric maps showing Expedition 367/368 sites (stars), and (A) regional and (B) local coverage of multichannel seismic reflection data and OBS data. Thick blue and red lines are key seismic lines used for planning of the drilling transect. A. Magnetic isochrons (orange lines) from Briais et al. (1993). B. Magnetic picks (orange squares) from the same reference, extracted from the Seton et al. (2014) compilation. Chron labels for the picks correspond to the old edge of the normal polarity intervals (see Ogg et al. [2016] timescale for ages). Orange square = Leg 184 Site 1148, yellow squares = Expedition 349 Sites U1432 and U1435.

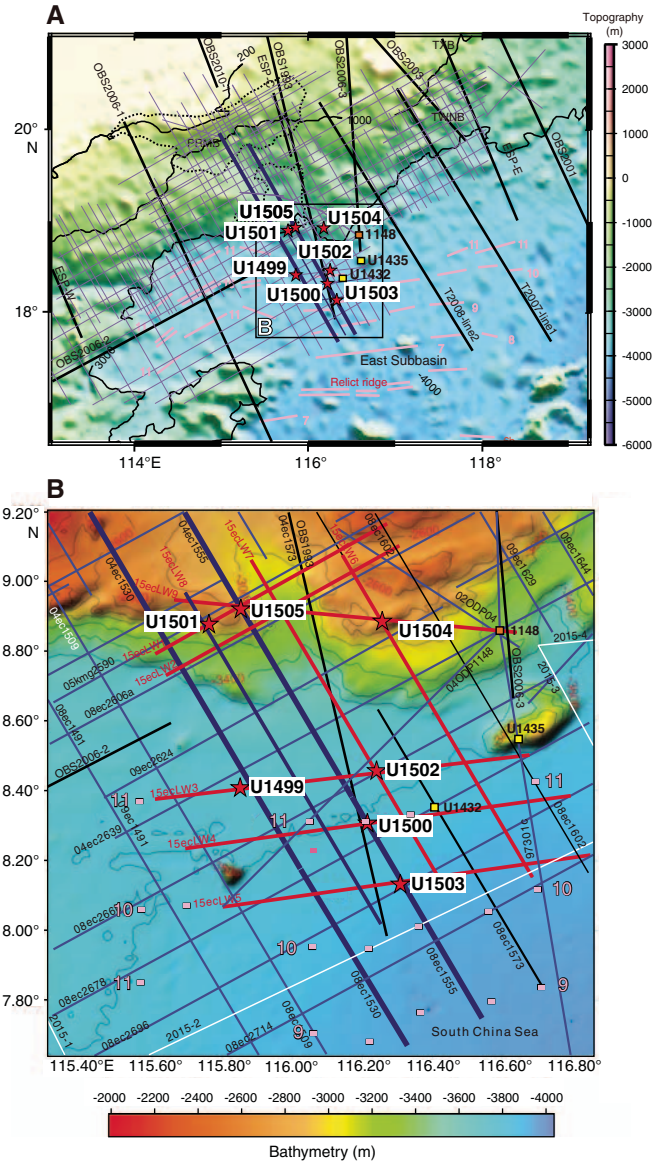

Lithostratigraphy

The sedimentary succession recovered at Site U1502 extends from the late Eocene to the late Miocene. The succession includes four sedimentary units (I and III–V) that are composed of mainly clay, nannofossil-rich clay, biosiliceous-rich clay, limestone, and clast-rich clay and two igneous units (II and VI) that are mainly composed of basalt. The base of the sedimentary succession is a sequence of clay and metasediments (dolomite marble and dolomitic limestone) that possibly forms the contact with a unit of altered basalt (Unit VI) (Figure **F4**).

Late Miocene to late Oligocene lithostratigraphic Unit I is divided into five subunits. Subunit IA (Hole U1502A = 375.00–486.82 m) is composed of dark gray, gray, dark greenish gray, and greenish gray silty clay, clay with nannofossils, and nannofossil-rich clay intercalated with dark grayish brown, grayish brown, and brown clay with nannofossils, with minor dark greenish gray sandy clay with calcite. Subunit IB (Hole U1502A = 490.20–599.57 m) is composed of alternating intervals of brown and greenish gray clay, silty clay, and clayey silt. Sandy intervals are rare. Recovery in Subunits IA and IB was very poor, which might be due to the occurrence of thick sand beds that were washed out. Subunit IC (Hole U1502A = 599.57–602.39 m) is composed of greenish gray and reddish gray foraminifer-rich clayey siltstone to sandstone with parallel laminations and convolute bedding, with thin layers of pinkish gray foraminiferal chalk. Subunit ID (Hole U1502A = 602.39–724.03 m) is mainly composed of alternating greenish and brownish gray and grayish brown clay, silty clay, clayey silt, and clay with silt (Cores 368-U1502A-25R through 32R), but brown colors dominate Cores 33R through 38R. Nannofossils are abundant within the lowermost ~4 m of this subunit. Subunit IE (Hole U1502A = 724.03–734.87 m; Hole U1502B; 727.79–727.96 m) is composed of brown nannofossil-rich clay with foraminifers and nannofossil-rich clay with pale green colored halos around fractures. The sediments of Unit I are interpreted as having been deposited in a deep-marine environment. Fining-upward intervals in Subunits IA–IC are interpreted as turbidites.

Unit II is a highly altered greenish gray basalt clast recovered from Hole U1502B at 727.96–728.04 m. The primary mineral phases are replaced by an alteration-mineral assemblage.

Unit III (Hole U1502A = 739.10–739.16 m; Hole U1502B = 728.04–733.82 m) is composed of brownish yellow, very hard, poorly sorted breccia. The granule- to pebble-size siliceous clasts consist of alteration minerals (Fe hydroxides) cemented by a matrix of annealed quartz in various grain sizes.

Unit IV (Hole U1502A = 739.16–747.20 m) consists of biosiliceous-rich silty clay. Diatoms, sponge spicules, and radiolarians are

Figure F2. Bathymetry with seismic lines, Site U1502. Site is not at exact crossing of seismic Lines 15ecLW7 and 15ecLW3. Common depth point (CDP) numbers are shown along seismic lines.

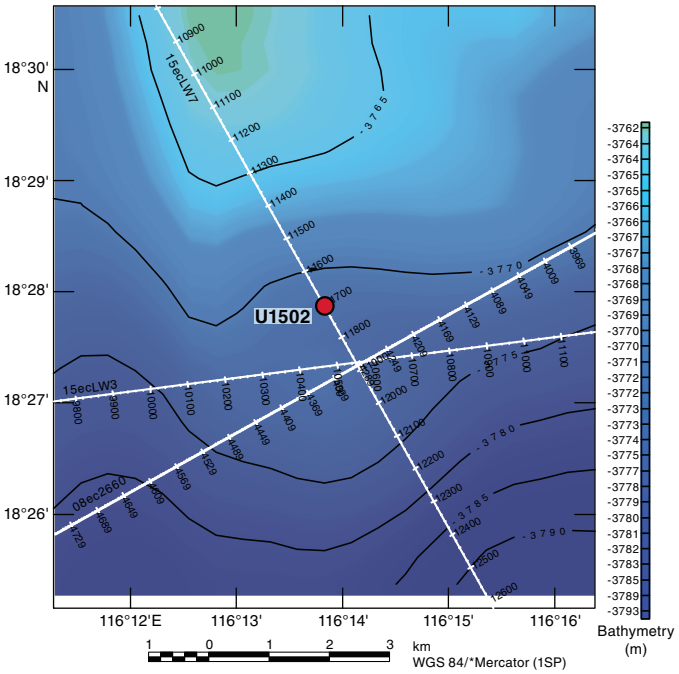

Figure F3. Deep crustal time-migrated seismic reflection data without and with interpretation. Note the rather thin lower crust (two layers) above a strong Mohorovičić seismic discontinuity (Moho) reflector that can be followed oceanward. Moho reflection is weak to absent seaward from around the interpreted COT. Wide-angle seismic data (Yan et al., 2001) confirm ~6 km thick ocean crust (OC) seaward of the COT. A large detachment fault ~150 km inland of the COT separates more stable crust landward from that of highly extended crust seaward. An OMH is a fairly consistent feature along this margin segment. Key seismic unconformities are shown in purple (T70; ~32 Ma breakup unconformity?) and blue (T60; ~23 Ma regional basin event). These ages are inferred from long-distance (>100 km) correlation of seismic unconformities with industry holes and ODP Leg 184 Site 1148 (T60); ages need confirmation by coring and are only tentative. Tg (black) is basement. Arrows = approximate positions of seafloor magnetic anomalies with chron numbers. Seismic data are from Line 04ec1555-08ec1555 (courtesy of Chinese National Offshore Oil Corporation [CNOOC]). Location of line is shown in Figure F1. C11n, C10n, and C9n = approximate location of normal polarity magnetic isochrons. MSB = midslope basin.

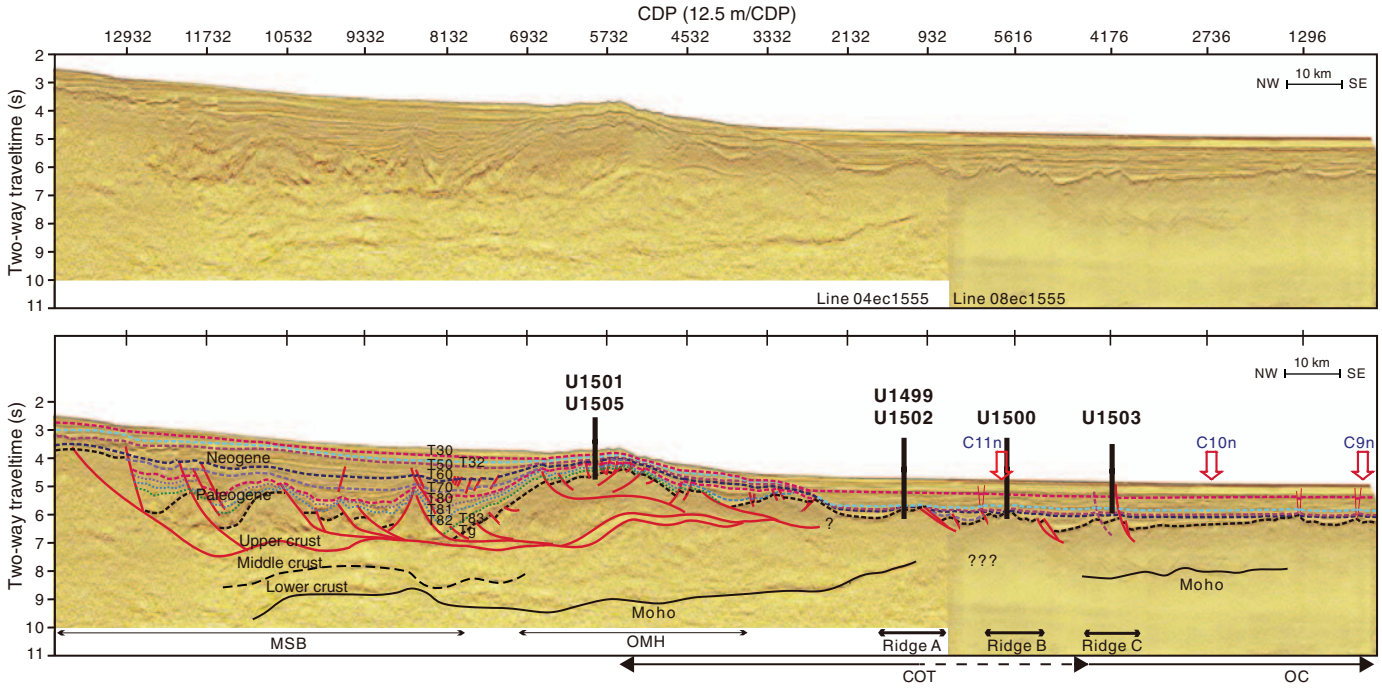

abundant in the upper part, but the abundance of both nannofossils and diatoms decreases rapidly downhole from Section 368-U1502A-40R-1 to Section 40R-3. Pyrite occurs as centimeter-sized patches and along cracks. The layering in Unit IV is inclined and may be slightly deformed.

Unit V (Hole U1502A = 747.20–749.01 m; Hole U1502B = 733.82–739.16 m) is an interval of alternating metasediments (dolomite marble, dolomitic limestone, and clast-rich clay). The dolomite marble is dominated by very fine grained dolomite (~95%) with minor amounts of magnetite (~3%) and calcite (~2%). The annealing texture is equigranular and crossed by fine-grained dark gray bands. The presence of magnetite explains the extraordinarily high magnetic susceptibility of this unit. The gray, fine-grained dolomitic limestone in Hole U1502B is intercalated with well-consolidated, very dark greenish gray clay with 10%–15% igneous clasts. The sediment is partially overprinted with alteration caused by secondary high-temperature processes (e.g., hydrothermal fluid sediment interaction or contact metamorphism).

Unit VI (Hole U1502A = 749.01–750.67 m; Hole U1502B = 739.16–920.95 m) consists of highly altered basaltic breccia, brecciated basalt, pillow basalt, and sheet basalt. The unit is divided into two subunits. Subunit VIA is composed of highly altered basaltic breccia and brecciated basalt with minor sheet basalt, chert, and claystone and very minor pillow basalt. Subunit VIB is dominated by altered pillow basalt and sheet flows and is less brecciated than Subunit VIA.

Igneous petrology

At Site U1502, we recovered two igneous lithologic units. Unit 1 (lithostratigraphic Unit II) is represented by just three small, aphanitic, fine-grained basalt fragments that contain rare plagioclase phenocrysts (Figure **F5**). Alteration of Unit 1 is intense, with most of the groundmass replaced by green clay minerals, clinozoisite, zeolites, and Fe (hydr)oxides.

Unit 2 (lithostratigraphic Unit VI) comprises a 182 m thick sequence of highly altered aphyric to highly plagioclase porphyritic basalts with minor chert (Figure **F5**). These basalts are divided into two igneous subunits (2a and 2b) based on flow morphology and alteration style: an upper brecciated and fractured massive lava flow sequence (Subunit 2a) and a lower sequence of interbedded pillow flows with lobate and sheet lava flows in which the alteration style is characterized by intense veining (Subunit 2b). Subunit 2a is characterized by highly altered breccia clasts of sparsely to moderately phyric basalt in a matrix of carbonates, epidote, chlorite, Fe (hydr)oxides, quartz, zeolite minerals, and clay minerals. The clasts show an alteration assemblage similar to the matrix, with remnant plagioclase and secondary pyrite. Subunit 2b consists of aphyric to highly plagioclase phyric (>30%) basalts with abundant chlorite and sulfides, as well as epidote, clay minerals, carbonates, zeolites, and opaque minerals.

All of Unit 2 has undergone some degree of hydrothermal alteration. This alteration varies from complete replacement of the rock,

Figure F4. Lithostratigraphic summary with simplified lithology and unit descriptions, Holes U1502A and U1502B.

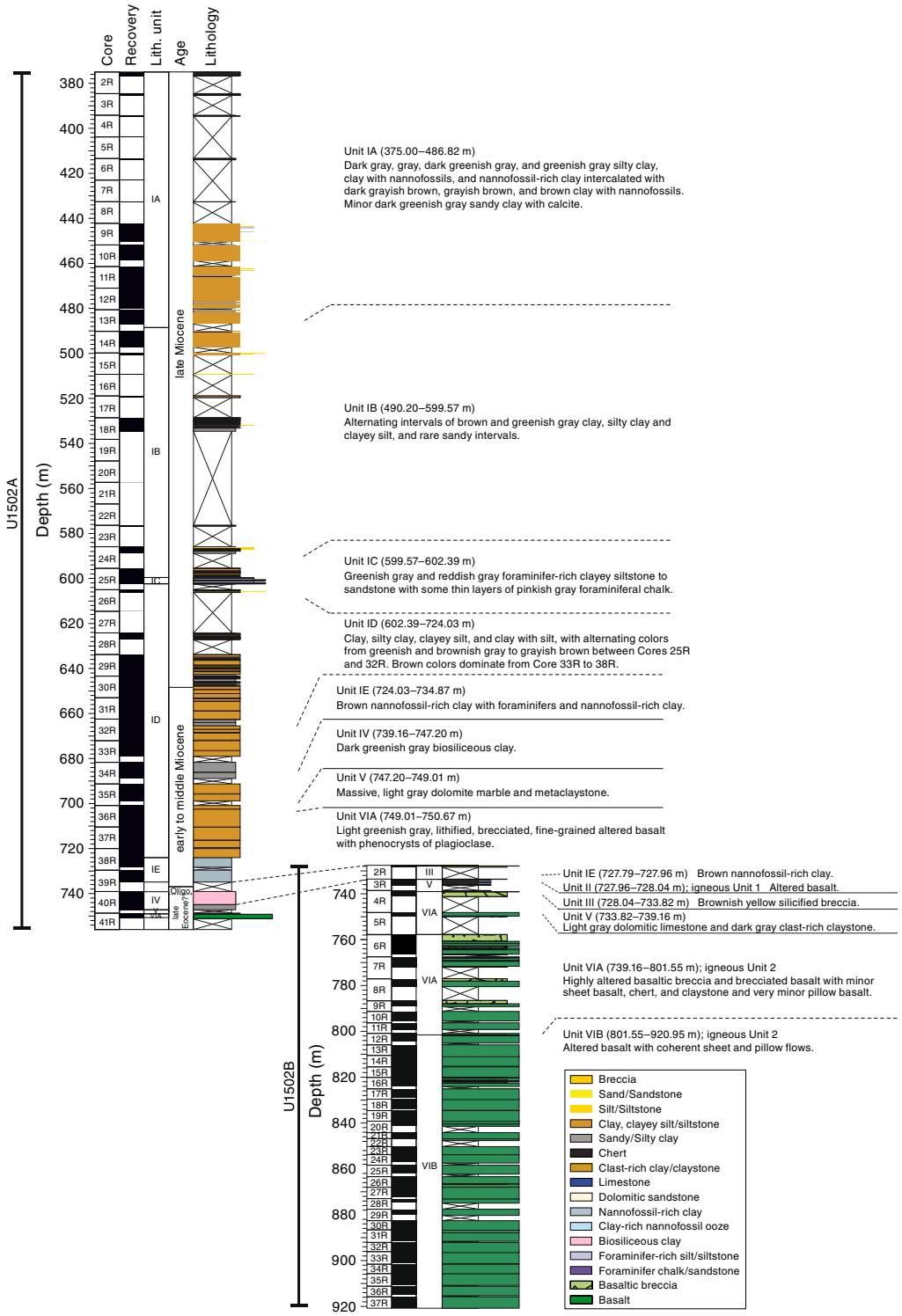

where the original composition and texture are difficult to determine, to replacement of mineral phases with little change to the texture. Glassy pillow rinds are completely replaced, and multiple phases of veining and halos are ubiquitous throughout the rocks. Three vein types were observed: (1) white to green to black silica-epidote veins, (2) apple green pyrite-epidote veins, and (3) white silica and/or calcite veins. Sulfide mineralization (disseminated and veined) is widespread throughout Unit 2 and is dominated by pyrite, with minor sphalerite, chalcopyrite, and covellite.

Handheld portable X-ray fluorescence (pXRF) analyses show no significant differences in contents of alteration-resistant elements such as Ti and Zr within Unit 2, but Subunit 2a has lower MgO, FeO, and MnO than Subunit 2b, which is consistent with the higher degree of alteration. Subunit 2b is also strongly affected by second-

Figure F5. Lithostratigraphic summary of Holes U1502A and U1502B with main igneous lithologies and deformation structures. A. Highly plagioclase-phyric basalt with up to 50% plagioclase phenocrysts. B. Highly altered, sparsely plagioclase phyric pillow basalt with a well-preserved pillow. C. Moderately altered aphyric basalt flow with sparse vesicles. Note the change to a bluish gray color. D. Slump folds. E. Microfaults showing striations/slickensides on exposed surfaces. F. Distributed shear geometries with shear bands and tilted bedding. G. Brecciated basalt. H. Basaltic breccia. I. Network of composite epidote-rich veins.

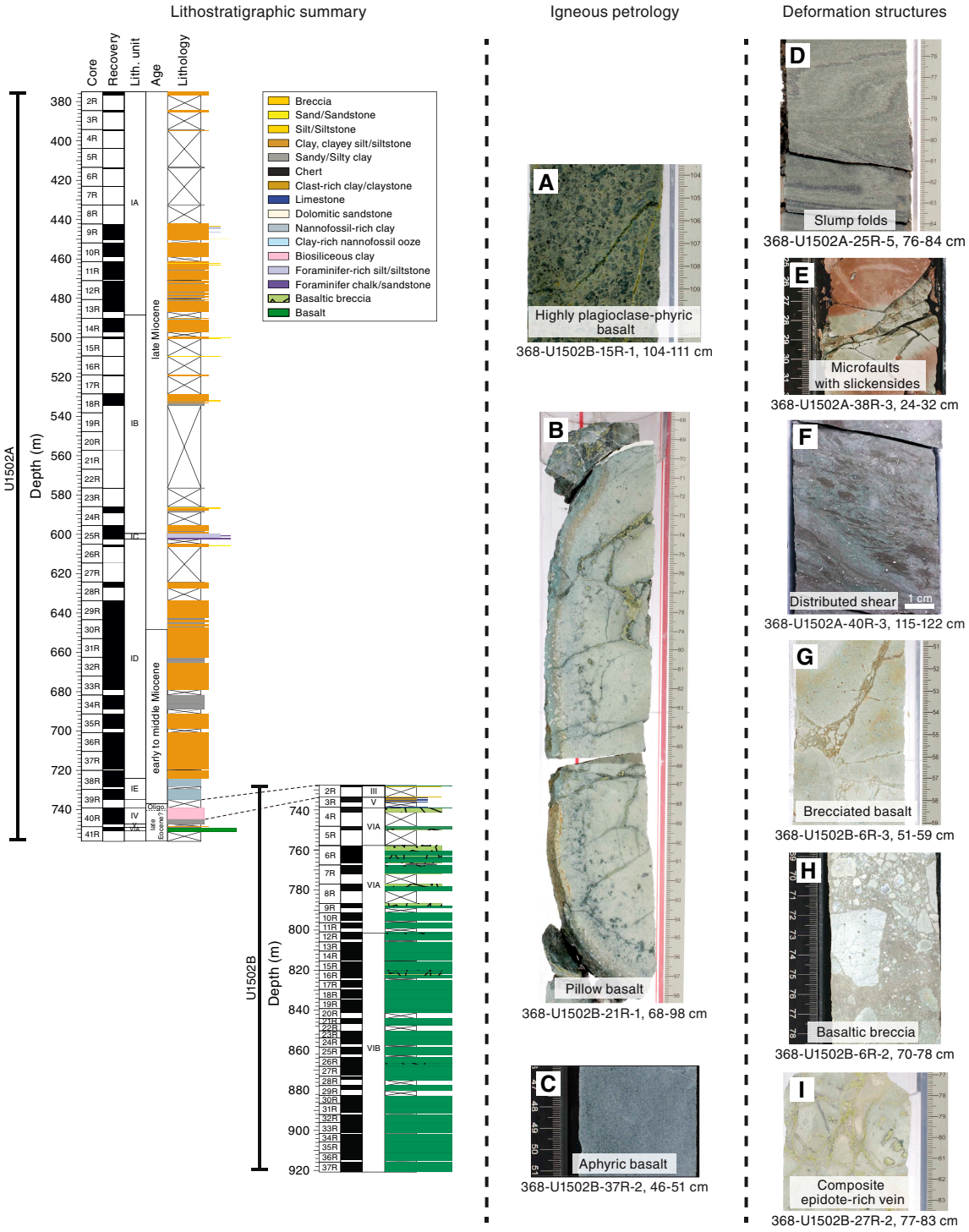

ary alteration, but areas of less intense alteration are indicated by higher magnetic susceptibility and high CaO and Fe_2O_3 contents. Unit 1 appears to be compositionally distinct from Unit 2 and has, for example, higher Ti/Zr ratios.

Structural geology

Deformation structures are scarce in Unit I above Core 368-U1502A-37R, with only a local, convolutely bedded sequence in Core 25R. Downhole from Core 37R at ~700 m, a gradual increase

in deformation structures was observed (Figure **F5**). Cores 37R through 39R are characterized by microfaults, as evidenced by downward-dip plunging striations and slickensides on exposed fracture surfaces, systematically associated with greenish halos. No deformation structures were encountered in Unit II. Unit III consists of extremely silicified breccia that was poorly recovered. The nature of this breccia, however, as sedimentary, tectonic, or hydrothermal remains unconstrained at the moment. In Unit IV, a small-scale transition from distributed to localized shear in unlithified sediments was documented. No deformation structures were encountered in Unit V.

Unit VI is essentially composed of basalts that were heterogeneously affected by brecciation and veining associated with the circulation of hydrothermal fluids. Subunit VIA is dominated by brecciated basalt/basaltic breccia, whereas Subunit VIB comprises a rather coherent series of lava flows crosscut by a multistage network of polymineralic veins. The uppermost part of Unit VI contains severely fractured and fragmented basalt locally filled by fine-grained unconsolidated greenish rock. Subunit VIA is characterized by diverse brecciation horizons associated with veins and microcracks. Depending on the intensity of fragmentation and the clast/matrix ratio, the rocks are referred to as brecciated basalt or basaltic breccia. A typically observed feature is the jigsaw-puzzle structure, suggesting possible in situ fragmentation. Macro- and microscopic observations show that the breccia-clasts consist mainly of sparsely to moderately plagioclase phyric basalts that were hydrothermally altered to variable degrees. Thus, formation of such breccias likely involved fluid-assisted fracturing of basalt. In contrast, Subunit VIB is characterized by a progressive decrease of breccia horizons and the development of different vein types, almost always polymineralic. Notably, vein composition and their orientation changes through Subunit VIB. Although numerous small-scale veins often related with major veins were observed, three first-order vein types were categorized: (1) composite silica-rich veins, (2) composite epidote-rich veins, and (3) composite carbonate- and/or silica-rich veins.

Biostratigraphy

All core catcher samples from Hole U1502A and selected samples from Hole U1502B were analyzed for calcareous nannofossils, foraminifers, diatoms, and ostracods. Additional samples were taken from the working-half core intervals when necessary to refine the ages. The preservation of calcareous microfossils is mostly good to moderate in the upper sections (Cores 368-U1502A-2R through 13R) and moderate to poor in the lower sections (Cores 14R through 41R). Planktonic foraminifers and calcareous nannofossils are abundant to common in Cores 2R through 10R, 25R, and 37R through 39R and rare to barren in all other sections. Diatoms were only observed in Sections 40R-1 through 40R-3. In Hole U1502B, foraminifers were observed only in Section 3R-1 and are represented by well-preserved agglutinated deepwater taxa. Ostracods are extremely rare; single occurrences were observed only in three samples in Hole U1502A (Samples 3R-CC, 4R-CC, and 5R-CC).

Fourteen planktonic foraminifer and calcareous nannofossil biostratigraphic events were used to provide an age-depth model for Site U1502 from the late Oligocene to the late Miocene. The Pliocene/Miocene boundary is placed tentatively within Core 368-U1502A-2R, but it may be shallower than the cored section. The Miocene/Oligocene boundary was determined to lie between Samples 39R-CC and 40R-1, 7 cm. Sedimentation rates vary from ~10 mm/ky in the early–middle Miocene to ~39 mm/ky in the late Miocene. No planktonic microfossils were found in Hole U1502B, but a sample from the sandy interval in Core 3R revealed abundant and diverse abyssal agglutinated benthic foraminifers. The composition of this agglutinated benthic foraminifer assemblage provides a possible age of late Eocene for this interval.

Paleomagnetism

The magnetic behavior of sediments at Site U1502 correlates with their color (greenish gray or reddish brown). Reddish brown sediment shows alternating field (AF) magnetization indicative of magnetite or titanomagnetite and hematite (responsible for the color). In contrast, greenish gray sediment hosts magnetite or titanomagnetite and pyrrhotite. The predominance of steep normal inclinations (~75°; Figure **F48**) across all late Oligocene to late Miocene units (375.00–750.67 m) affects the superconducting rock magnetometer (SRM) section measurements and prevents any reliable magnetostratigraphy to be established for Holes U1502A and U1502B.

The basalt has natural remanent magnetization (NRM) intensity one order of magnitude higher than sediment. The main magnetically remanent phase is titanomagnetite, but its alteration produces maghemite or hematite. Magnetic susceptibility (κ) has a bimodal distribution with a median at 327×10^{-6} SI. κ does not show any strong correlation with any chemical ($R^2 = 0.343$ for Fe_2O_3 wt%). Intervals of high κ might correspond to the bottoms of flows with a massive, less altered structure. Altered basalts have higher Koenigsberger ratios (Q_n = 1–10) than fresher basalts (Q_n = 0.001–1). The mean dip of magnetic foliation is 8°.

Cores 368-U1502B-9R and 10R show less-pervasive drilling overprint, and two discrete samples show both a normal (soft) component and a reverse (hard) component, suggesting a possible reversal.

Geochemistry

Site U1502 contains very low high-hydrocarbon gas abundances and total organic carbon (TOC), nitrogen, and sulfur contents, likely reflecting the poor preservation of organic matter. Instances of high carbonate content are associated with siderite, and on occasion this mineral comprises >50 wt% by mass of intervals in lithostratigraphic Subunit ID. The interstitial water at Site U1502 is enriched in Ca, Mg, and K and has notably high alkalinity but is depleted in Na, Cl, and Br. The linear increase of major anion and cation contents implies upward movement of fluid from deeper sediments. The hemipelagic sediments within Unit I have some similarities to the geochemical characteristics of the hemipelagic and pelagic units at Sites U1501 and U1505, but Site U1502 sediments are enriched in Fe, K, and clay concentrations, likely as a result of regions of increased alteration. All of the analyzed igneous rocks from Units II–VI are heavily altered, although samples from igneous lithologic Subunit 2b are altered to a lesser degree than those from Subunit 2a.

Physical properties

Physical property data acquired at Site U1502 include density, magnetic susceptibility, *P*-wave velocity, natural gamma radiation (NGR), color reflectance, and thermal conductivity (Figure **F63**). These data allow us to characterize four physical property (PP) units. PP Unit 1 (375–740 m) corresponds to the nannofossil-rich and biosiliceous-rich clay lithologies and exhibits small variations in NGR between 50 and 70 counts/s and uniformly increasing *P*-wave velocities with depth that average <2500 m/s. Unit 1 sediments have similar porosities to those recorded at nearby Sites U1499 and

U1500 in the same depth interval, suggesting the same compaction history. A significant increase in bulk density (up to 2.7 g/cm^3) in Core 368-U1502B-3R is associated with strongly lithified limestone beds. Variations of high and low magnetic susceptibility values correspond to sediment color changes in Unit 1 and may be controlled by the amount of pyrrhotite within the sediments.

PP Unit 2 (740–750 m) in Hole U1502A is characterized by lower *P*-wave velocities and bulk densities and higher NGR than the strata above. Low densities and *P*-wave velocities found in Unit 2 reflect the clast-rich claystone from lithostratigraphic Unit V.

PP Units 3 and 4 represent the basaltic basement and are characterized by relatively low NGR (<10 counts/s), high densities, and *P*-wave velocities that vary over a broad range (3000–6000 m/s). The boundary between Units 3 and 4 is marked by an abrupt increase in density, *P*-wave velocity, and thermal conductivity and coincides with the change from igneous lithologic Subunit 2a to 2b. Prominent magnetic susceptibility peaks (up to 4000 × 10^{-5} SI) in Units 3 and 4 correspond to relatively less altered basalt. Thermal conductivity in Units 3 and 4 is variable but generally increases in line with decreasing porosity with depth.

Downhole measurements

Wireline logging was conducted in Hole U1502B using a modified triple combination (triple combo) tool string and the VSI tool string. The modified triple combo tool string included the Hostile Environment Natural Gamma Ray Sonde (HNGS), Hostile Environment Litho-Density Sonde (HLDS), and Dipole Sonic Imager (DSI) for acoustic velocity. The triple combo run collected good data downhole from 875.3 m (~45 m above the bottom of Hole U1502B) and allowed us to define eight logging units, which correlate in great part to the lithostratigraphic units and core physical properties. Logging Units 1–5 are defined by data collected through the casing and drill pipe. Unit 6 data was collected outside the casing but inside the drill pipe, whereas data in Units 7 and 8 were collected in the open hole. For measurements inside the casing and/or drill pipe, only NGR and the associated K, Th, and U components provide meaningful data, although they are highly attenuated by the casing and/or drill pipe. Open borehole conditions from the bottom of the casing at 723 m to 875.3 m were generally good, with measured diameters from 12 to 14.5 inches. Log and core data generally show good agreement, and downhole measurements provide information in zones of poor core recovery in Hole U1502B. The log data exhibit increasing densities and *P*-wave velocities with depth. The amplitude of NGR increases gradually with depth throughout Units 1–3 (seafloor to ~630 m), with an interval of relatively constant values between 150 and 350 m. NGR values are lowest in Units 4–8 (~630–850 m).

The VSI tool string was run only inside the casing because the tool could not pass through an obstruction encountered at the end of the casing. Eight stations were attempted. The two deepest stations (at 715.1 and 695.2 m) are associated with large noise levels, which were possibly caused by poor mechanical coupling of the casing with the surrounding formation. The remaining upper six stations, located at 290.2, 350.3, 450.3, 550.1, 590.3, and 630.3 m, recorded good quality waveforms.

Background and objectives

Site U1502 within the SCS northern margin (Figures **F2**, **F6**) is located at a water depth of 3764 m on a prominent basement ridge

Figure F6. Two-way traveltime to (A) basement (Tg reflector) and (B) T60 unconformity. Proposed drilling transect (thick black line) is approximately at the center of a margin segment bounded to the southwest by a transform fault. Northeastern boundary of margin segment around Site U1435. At this location, OMH and Ridge A seem to coalesce, and Ridges B and C (COT) become indistinct toward the northeast within the next margin segment. Note that OMH is slightly oblique to more parallel Ridges A, B, and C.

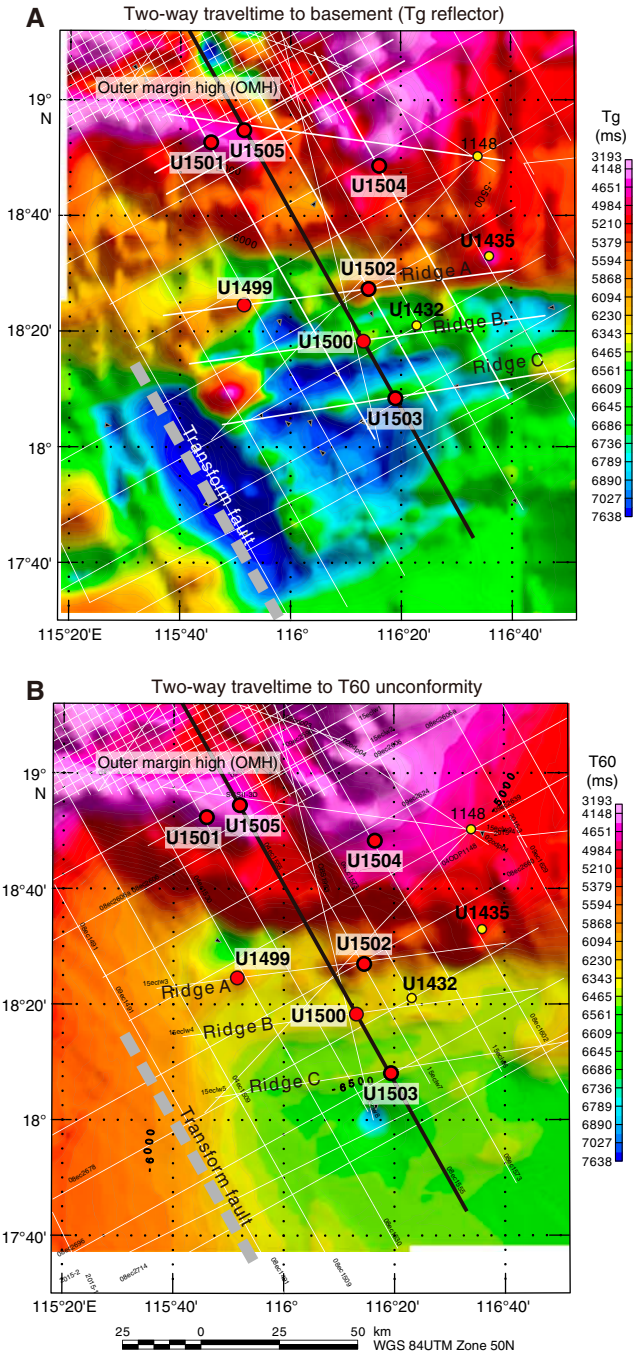

(Ridge A) within the seaward end of the COT. Ridge A is one of four distinct basement highs found across the COT (Figure **F3**). The OMH is the most landward of these highs (see the **Site U1501** chapter [Larsen et al., 2018]) within the COT and is followed seaward by the nearly parallel Ridges A, B, and C. The crustal thickness

below Ridge A is significantly smaller (~8 km) than below the OMH (~15 km) and close to the thickness found ~6 km further seaward within the COT. The oldest interpreted seafloor-spreading magnetic anomaly seaward of Site U1502 is Chron C11n (~30 Ma), which runs parallel to Ridge A (Figures **F1**, **F3**) ~20 km to the south of the ridge.

Site U1499 was also drilled on Ridge A ~70 km west of Site U1502 and recovered a Neogene sediment section on top of the basin-wide Tg reflector. Below the Tg reflector, Site U1499 recovered Oligocene sediments (see the **Site U1499** chapter [Sun et al., 2018b]). The pre-Miocene sediments comprise sandstone, claystone, matrix-supported breccia, and gravel. They are interpreted to have a proximal source and to possibly reflect a tectonically active environment. True crystalline basement was not recovered at Site U1499 due to the collapse of Hole U1499B.

Site U1502 on Ridge A is located near the crossing of seismic Lines 15eclLW7 and 15eclLW3 (Figure **F2**, site specific bathymetry). Ridge A can be followed along the margins for more than 100 km (Figure **F6**). Before drilling, it was interpreted to be fault bounded (Figure **F7**, main line). The structure is narrower and steeper in this location than elsewhere along the ridge. Along strike, it forms an elongated local high on Ridge A (Figure **F8**, cross-line).

Figure F7. Original and predrilling interpretation of seismic dip Line 15ecLW7 crossing (projected) with seismic Line 15ecLW3 (red tick mark) (CDP distance = 6.25 m). Seismic stratigraphic Unconformities T30 (5.3 Ma), T32 (10.0 Ma), T60 (23.0 Ma), and T70 (33.9 Ma) and acoustic basement Unconformity Tg are shown (see Seismic stratigraphic framework in the Expedition 367/368 methods chapter [Sun et al., 2018a]). In places, there are clear but not extensively coherent seismic reflectors below Tg.

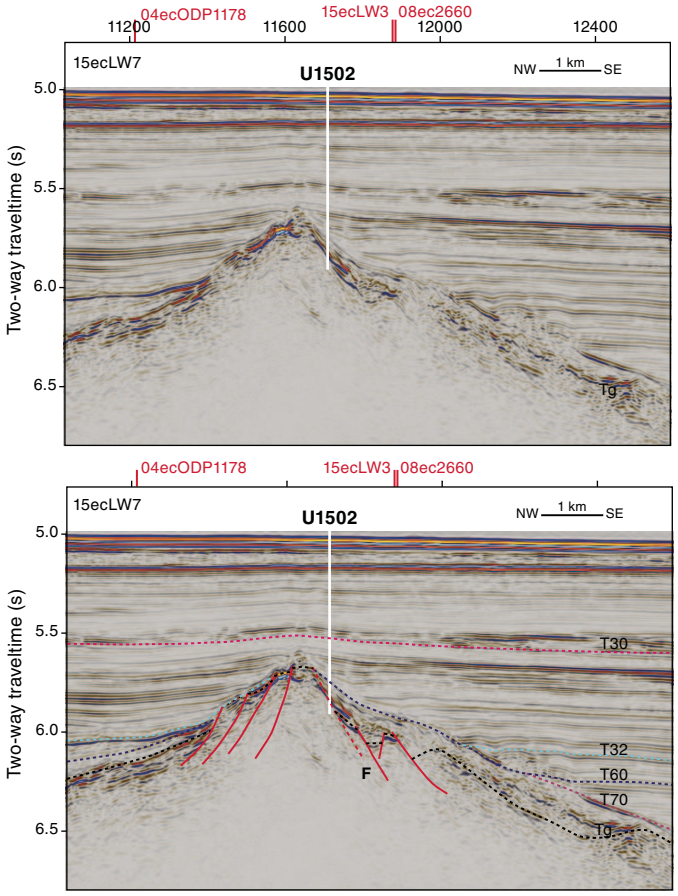

This seismic line along the ridge also shows evidence of normal faulting. In general, however, the seismic reflectors do not show significant dip that would be indicative of major fault-block rotation. The one exception is the set of strong reflectors overlying the interpreted fault on the seaward flank of the ridge (Figure **F7**, main line). No 3-D interpretation of faults was possible.

The predrilling interpretation of the seismic unconformities (T30 to T70 and Tg reflector; see **Correlation to seismic data** in the Expedition 367/368 methods chapter [Sun et al., 2018a]) around Site U1502 is shown in Figure **F7** (main line). This shows the regional T60 unconformity rising from the basin seaward of Ridge A, possibly present almost to the top of the structure, and reappearing on the landward side of the ridge. It is also possible, however, that the T32 unconformity has completely removed (eroded) the T60 unconformity across the ridge, in which case sediments of lower and middle Miocene age should be missing at this site. The high-amplitude, dipping reflectors at Site U1502 just below this unconformity were interpreted predrilling as synrift deposits of pre-T60 (~23 Ma) age, possibly sediments of the same age and nature as those recovered at Site U1499, and related to rifting. However, as detailed in this chapter, the high-amplitude reflector (Tg) represents the top of a sequence of seaward-dipping, submarine basaltic lava flows, implying that the structure is a seaward rotated fault block bounded entirely by landward-dipping normal faults.

A key objective of Expeditions 367 and 368 was to examine the nature of the crust within Ridge A. This ridge is considered a key element in the transition from continental to oceanic crust. Specific questions to be answered by drilling:

Figure F8. Original and predrilling interpretation of seismic strike Line 15ecLW3 crossing with seismic Line 15ecLW7 (red tick mark) (CDP distance = 6.25 m). See Figure F7 for description of seismic interpretations. Dashed lines = unconformities, red solid lines = faults.

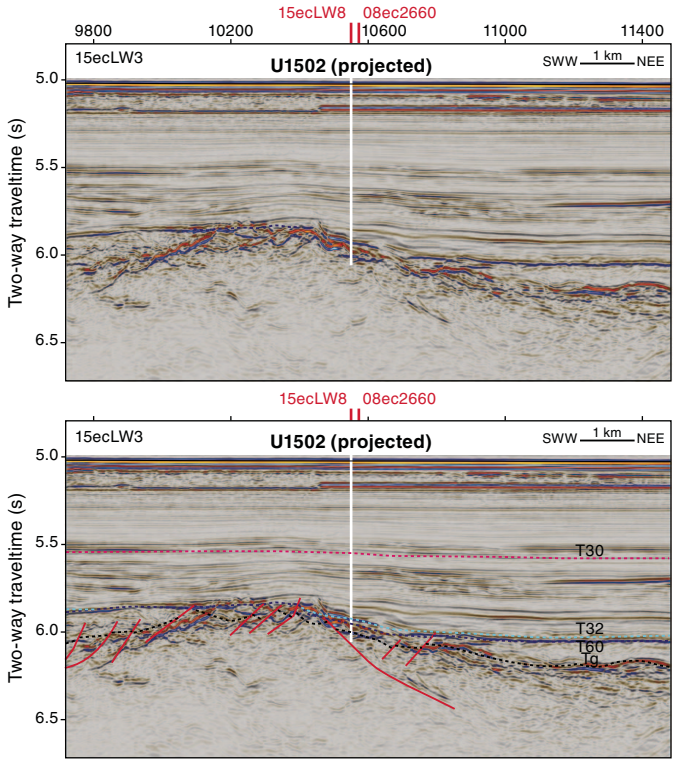

- Does it represent continental crust, and if so, does it represent upper or lower crust?
- Did tectonic exhumation reach into the lithospheric mantle, and did serpentinization take place?
- Or is the structure possibly partly or wholly of igneous origin (see the **Expedition 367/368 methods** chapter [Sun et al., 2018a])?

Because Site U1499 failed to provide conclusive evidence of the nature of the crystalline basement of Ridge A, the key objective of Site U1502 was to drill through the interpreted fault zone and into the crystalline basement at this location on Ridge A. Information on the nature and age of interpreted synrift deposits overlying the fault forms a secondary objective, along with the nature and age of the overlying unconformities, their depositional environment, and the constraints they can offer on basin subsidence.

In this deep water, post-Miocene sediments were deposited below the carbonate compensation depth (CCD) and were therefore not a coring objective. Site operations were planned to drill without coring through the sediments postdating the T30 unconformity, core from there to basement in Hole A, drill in Hole B with casing almost to the T60 unconformity, and then core from there until conclusive results regarding basement were obtained (see **Operations**).

Operations

We conducted operations in two holes at Site U1502 with the objective of sampling the lowermost sediment and underlying basalt. We successfully penetrated from the seafloor to the sediment/basalt contact at 728 m and 180 m into the underlying basalt. The sedimentary section was not continuously cored, and recovery in the cored intervals was highly variable and relatively low (46%). In contrast, core recovery in the basalt was significantly better (70%). Downhole logging was conducted in Hole U1502B with the triple combo and VSI tool strings.

Hole U1502A is located at 18°27.8720′N, 116°13.8381′E, at a water depth of 3763.2 m. Operations in Hole U1502A were designed to provide information on the formation characteristics and drilling conditions so that we could decide the length of casing to drill into the seafloor at the second, deep-penetration Hole U1502B. Given this purpose and the amount of time needed to drill Hole U1502B, we did not core continuously in Hole U1502A. Instead, we drilled without coring from the seafloor to 375 m and RCB cored from 375 to 758.2 m, recovering 176.81 m (46%).

Hole U1502B is located at 18°27.8798′N, 116°13.8409′E, at a water depth of 3763.6 m. We conducted the following operations in Hole U1502B:

- Drilled a reentry funnel and 727.7 m of 10.75 inch casing into the seafloor,
- RCB cored the sediment sequence from 727.7 to 739.16 m (11.46 m cored; 3.55 m recovered; 31%),
- RCB cored 180 m into the underlying basalt (739.16–920.95 m; 128 m recovered [70%]), and
- Collected downhole log data with the triple combo and VSI tool strings.

Hole U1502A and U1502B coring summaries are presented in Table **T1**. A diagram of the reentry cone and casing in Hole U1502B is shown in Figure **F9**.

Hole U1502A

The R/V *JOIDES Resolution* made the 36.5 nmi transit from Site U1501 to Site U1502 in 3.6 h, averaging 10.1 kt. The vessel arrived over the site coordinates at 2142 h on 24 April 2017. At 2240 h, an acoustic beacon was deployed approximately 100 m west of the site coordinates. Upon arrival at Site U1502, a new C-4 RCB bit with a mechanical bit release (MBR) was assembled onto the bottom of the bottom-hole assembly (BHA). The core barrel space out was checked, and the BHA was lowered to 161 mbsl. The precision depth recorder measurement taken on arrival showed a calculated seafloor depth of 3768.4 m.

The bit was lowered to 3733 mbsl, stopping every 20 stands to fill the pipe with water. The upper guide horn (UGH) was pulled, and the underwater camera system was deployed to the seafloor to observe the end of the pipe tag the seafloor. While the camera was being lowered, 115 feet of drill line was slipped and cut. After the

Table T1. Site U1502 core summary. DRF = drilling depth below rig floor, DSF = drilling depth below seafloor. Core type: R = rotary core barrel, numeric core type = drilled interval. (Continued on next two pages.) **Download table in CSV format.**

Hole U1502A	
Latitude:	18°27.8720′N
Longitude:	116°13.8381′E
Seafloor (drill pipe measurement below rig floor, m DRF):	3763.72
Time on hole (days):	5.22
Total depth (drill pipe measurement from rig floor, m DRF):	3774.7
Distance between rig floor and sea level (m):	10.98
Total penetration (drilling depth below seafloor, m DSF):	758.2
Total length of cored section (m):	383.2
Total core recovered (m):	176.81
Core recovery (%):	46.14
Drilled interval (m):	375
Total cores (no.):	40

Hole U1502B	
Latitude:	18°27.8798′N
Longitude:	116°13.8409′E
Seafloor (drill pipe measurement below rig floor, m DRF):	3763.58
Time on hole (days):	14.06
Total depth (drill pipe measurement from rig floor, m DRF):	3774.7
Distance between rig floor and sea level (m):	11.12
Total penetration (drilling depth below seafloor, m DSF):	920.8
Total length of cored section (m):	193.1
Total core recovered (m):	131.57
Core recovery (%):	68.14
Drilled interval (m):	727.7
Total cores (no.):	36

Core	Type	Top of interval DSF (m)	Bottom of interval DSF (m)	Interval advanced (m)	Core recovered length (m)	Curated length (m)	Recovery (%)	Time on deck UTC (h)	Time to cut core (min)	Core barrel type	Mud pumped (bbl)	Driller's notes
368-U1502A-												
1	1	0	375.0	375.0	*****Drilled interval*****			4/25/2017 00:00	150		135	
2	R	375.0	384.6	9.6	1.81	1.81	19	4/26/2017 01:05		Nonmagnetic		
3	R	384.6	394.2	9.6	0.85	0.85	9	4/26/2017 02:30		Nonmagnetic	15	

Table T1 (continued). (Continued on next page.)

Core	Type	Top of interval DSF (m)	Bottom of interval DSF (m)	Interval advanced (m)	Core recovered length (m)	Curated length (m)	Recovery (%)	Time on deck UTC (h)	Time to cut core (min)	Core barrel type	Mud pumped (bbl)	Driller's notes
4	R	394.2	403.8	9.6	0.47	0.47	5	4/26/2017 03:35	15	Nonmagnetic		
5	R	403.8	413.4	9.6	0.05	0.05	1	4/26/2017 05:45		Nonmagnetic	15	
6	R	413.4	423.0	9.6	0.64	0.64	7	4/26/2017 06:50		Nonmagnetic		
7	R	423.0	432.6	9.6	0.05	0.05	1	4/26/2017 07:50	15	Nonmagnetic		
8	R	432.6	442.2	9.6	0.14	0.14	1	4/26/2017 09:15		Nonmagnetic	20	
9	R	442.2	451.8	9.6	8.02	8.02	84	4/26/2017 11:00		Nonmagnetic		
10	R	451.8	461.4	9.6	7.01	7.01	73	4/26/2017 13:00	15	Nonmagnetic		
11	R	461.4	471.0	9.6	9.15	9.15	95	4/26/2017 15:30		Nonmagnetic	20	
12	R	471.0	480.6	9.6	9.23	9.23	96	4/26/2017 17:55	20	Nonmagnetic		
13	R	480.6	490.2	9.6	6.27	6.27	65	4/26/2017 20:10		Nonmagnetic		
14	R	490.2	499.8	9.6	7.06	7.06	74	4/26/2017 22:35	20	Nonmagnetic	20	Drilling break at 497 m
15	R	499.8	509.3	9.5	0.90	0.90	9	4/27/2017 00:30		Nonmagnetic	20	
16	R	509.3	518.9	9.6	0.35	0.35	4	4/27/2017 02:20		Nonmagnetic		
17	R	518.9	528.6	9.7	0.75	0.75	8	4/27/2017 04:10	20	Nonmagnetic	20	
18	R	528.6	538.2	9.6	6.06	6.06	63	4/27/2017 06:00		Nonmagnetic		
19	R	538.2	547.8	9.6	0.00	0.00	0	4/27/2017 07:45		Nonmagnetic	20	
20	R	547.8	557.3	9.5	0.00	0.00	0	4/27/2017 09:25	20	Nonmagnetic		
21	R	557.3	566.9	9.6	0.01	0.01	0	4/27/2017 11:15		Nonmagnetic	20	
22	R	566.9	576.4	9.5	0.00	0.00	0	4/27/2017 01:05		Nonmagnetic		
23	R	576.4	585.9	9.5	0.42	0.42	4	4/27/2017 15:10		Nonmagnetic	20	
24	R	585.9	595.5	9.6	3.05	3.05	32	4/27/2017 17:05		Nonmagnetic		
25	R	595.5	605.0	9.5	7.00	7.00	74	4/27/2017 19:20		Nonmagnetic	20	
26	R	605.0	614.6	9.6	1.31	1.31	14	4/27/2017 21:05	20	Nonmagnetic		
27	R	614.6	624.2	9.6	0.01	0.01	0	4/27/2017 22:55	40	Nonmagnetic	20	
28	R	624.2	633.8	9.6	2.98	2.98	31	4/28/2017 00:55		Nonmagnetic		
29	R	633.8	643.4	9.6	9.66	9.66	101	4/28/2017 03:30		Nonmagnetic	20	
30	R	643.4	653.0	9.6	9.87	9.87	103	4/28/2017 05:50		Nonmagnetic		
31	R	653.0	662.5	9.5	9.75	9.75	103	4/28/2017 08:10		Nonmagnetic	20	
32	R	662.5	672.1	9.6	9.37	9.37	98	4/28/2017 10:15		Nonmagnetic		
33	R	672.1	681.7	9.6	6.98	6.98	73	4/28/2017 13:10		Nonmagnetic	20	
34	R	681.7	691.3	9.6	7.22	7.22	75	4/28/2017 15:20		Nonmagnetic		
35	R	691.3	700.9	9.6	7.55	7.55	79	4/28/2017 17:30		Nonmagnetic	20	
36	R	700.9	710.4	9.5	9.56	9.56	101	4/28/2017 19:35		Nonmagnetic		
37	R	710.4	720.0	9.6	9.22	9.22	96	4/28/2017 22:00		Nonmagnetic	20	
38	R	720.0	729.6	9.6	8.32	8.32	87	4/29/2017 01:00		Nonmagnetic		
39	R	729.6	739.1	9.5	5.27	5.27	55	4/29/2017 03:30		Nonmagnetic	20	
40	R	739.1	748.7	9.6	8.43	8.43	88	4/29/2017 05:40		Nonmagnetic		
41	R	748.7	758.2	9.5	2.02	2.02	21	4/29/2017 09:40		Nonmagnetic	30	
	Hole U1502A totals (excluding drilled interval):			383.2	176.81	176.81	46.14					
368-U1502B-												
1	1	0	727.7	727.7	*****Drilled interval*****			5/4/2017 03:00	1225		20	
2	R	727.7	733.7	6.0	0.84	0.85	14	5/4/2017 04:15	35	Nonmagnetic		
3	R	733.7	738.7	5.0	2.71	2.71	54	5/4/2017 07:40	110	Nonmagnetic	15	
4	R	738.7	748.3	9.6	2.60	2.60	27	5/4/2017 11:30	135	Nonmagnetic		
5	R	748.3	757.9	9.6	1.75	1.75	18	5/4/2017 17:40	240	Nonmagnetic	15	
6	R	757.9	767.5	9.6	8.80	8.80	92	5/4/2017 23:10	230	Nonmagnetic		
7	R	767.5	777.1	9.6	4.48	4.48	47	5/5/2017 03:25	170	Nonmagnetic	15	
8	R	777.1	786.7	9.6	3.41	3.41	36	5/5/2017 08:15	200	Nonmagnetic		
9	R	786.7	791.3	4.6	2.48	2.48	54	5/5/2017 12:05	135	Nonmagnetic	15	
10	R	791.3	796.3	5.0	4.19	4.19	84	5/5/2017 15:55	140	Nonmagnetic		
11	R	796.3	800.9	4.6	2.88	2.88	63	5/5/2017 19:30	120	Nonmagnetic		
12	R	800.9	805.9	5.0	3.55	4.205	71	5/5/2017 23:50	165	Nonmagnetic		
13	R	805.9	810.5	4.6	4.90	5.20	107	5/6/2017 04:25	175	Nonmagnetic	20	
14	R	810.5	815.5	5.0	4.72	4.72	94	5/6/2017 09:00	190	Nonmagnetic		
15	R	815.5	820.1	4.6	4.62	4.62	100	5/6/2017 12:40	125	Nonmagnetic	15	
16	R	820.1	825.1	5.0	3.96	3.96	79	5/6/2017 16:40	145	Nonmagnetic		
17	R	825.1	829.6	4.5	3.75	4.70	83	5/7/2017 00:20	135	Nonmagnetic		Deplugger run
18	R	829.6	834.6	5.0	4.48	4.86	90	5/7/2017 03:50	115	Nonmagnetic	15	
19	R	834.6	839.2	4.6	4.60	4.98	100	5/7/2017 07:30	125	Nonmagnetic		
20	R	839.2	844.2	5.0	2.03	2.22	41	5/7/2017 12:50	145	Nonmagnetic	40	
21	R	844.2	846.8	2.6	3.04	3.48	117	5/7/2017 16:50	80	Nonmagnetic	45	
22	R	846.8	850.3	3.5	0.19	0.25	5	5/9/2017 09:40	95	Nonmagnetic		
23	R	850.3	853.8	3.5	3.21	3.53	92	5/9/2017 13:00	95	Nonmagnetic	25	
24	R	853.8	858.4	4.6	3.10	3.65	67	5/9/2017 16:50	110	Nonmagnetic	25	
25	R	858.4	863.4	5.0	3.53	3.90	71	5/10/2017 12:05	105	Nonmagnetic	20	
26	R	863.4	868.0	4.6	4.34	4.57	94	5/10/2017 16:10	135	Nonmagnetic	20	
27	R	868.0	873.0	5.0	4.39	5.15	88	5/10/2017 20:20	95	Nonmagnetic		

Table T1 (continued).

Core	Type	Top of interval DSF (m)	Bottom of interval DSF (m)	Interval advanced (m)	Core recovered length (m)	Curated length (m)	Recovery (%)	Time on deck UTC (h)	Time to cut core (min)	Core barrel type	Mud pumped (bbl)	Driller's notes
28	R	873.0	877.6	4.6	1.50	1.94	33	5/10/2017 23:40	100	Nonmagnetic	20	
29	R	877.6	882.6	5.0	2.25	2.70	45	5/11/2017 02:50	80	Nonmagnetic		
30	R	882.6	886.6	4.0	3.85	4.39	96	5/11/2017 06:35	120	Nonmagnetic	20	
31	R	886.6	892.1	5.5	4.64	5.01	84	5/11/2017 10:50	140	Nonmagnetic	20	
32	R	892.1	896.1	4.0	4.05	4.41	101	5/11/2017 14:45	120	Nonmagnetic	20	
33	R	896.1	901.6	5.5	5.09	5.26	93	5/11/2017 19:15	140	Nonmagnetic	20	
34	R	901.6	905.7	4.1	3.75	4.13	91	5/11/2017 22:50	105	Nonmagnetic	20	
35	R	905.7	911.2	5.5	5.10	5.13	93	5/12/2017 02:00	105	Nonmagnetic		
36	R	911.2	915.8	4.6	3.75	4.16	82	5/12/2017 05:30	105	Nonmagnetic	20	
37	R	915.8	920.8	5.0	5.04	5.15	101	5/12/2017 09:45	135	Nonmagnetic		
	Hole U1502B totals (excluding drilled interval):			193.1	131.57	140.425	68.14					

Figure F9. Hole U1502B reentry system and casing.

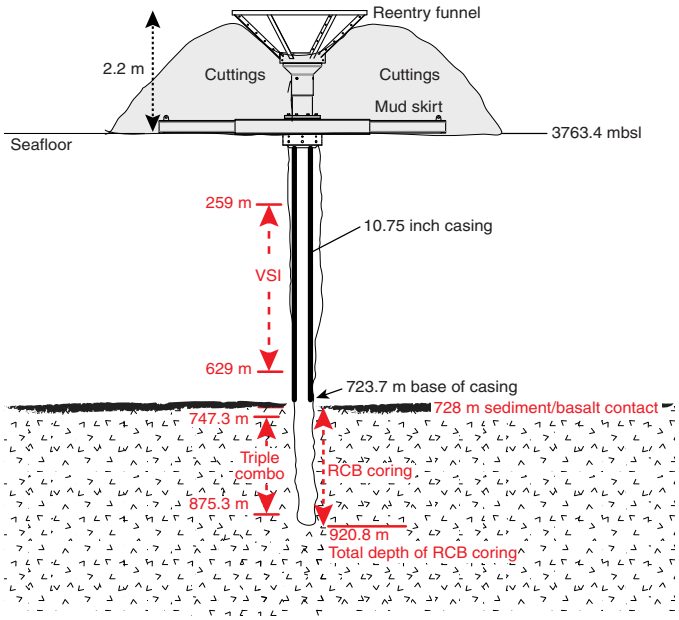

slip and cut operations were completed, the bit was spaced out to 3750.7 m and slowly lowered until it was observed that the bit had tagged the seafloor. Seafloor was determined to be at 3763.7 m. The bit was again spaced out to 3750.7 m, and the top drive was picked up. The UGH was raised, and the underwater camera was recovered at 1215 h. A center bit was dropped, and drilling in Hole U1502A started at 1300 h on 25 April. The hole was advanced without coring to 375 m in 18 h. The center bit was removed, and an RCB core barrel was dropped to begin coring operations. One of the main objectives in Hole U1502A was to RCB core to a depth in the formation that would provide a stable casing set point for the next hole.

Cores 2R through 7R were drilled very quickly and had little recovery. This low-recovery area was interpreted as an unconsolidated sand interval. Penetration rates slowed for Cores 8R through 14R, with the bit taking approximately 15,000 lb of weight during coring operations. Recovery improved through this mudstone interval but dropped off in what was interpreted as another unconsolidated sand interval from 499.5 to 585.9 m (Cores 15R through 23R). A second mudstone interval was sampled with very good recovery from Core 24R at 585.9 m to Core 39R at 739.1 m. The last 2 m of the following core, Core 40R, drilled very slowly, indicating a major change in formation. One more core was drilled to confirm the continuity of the formation change. At that point, coring in Hole U1502A was terminated in favor of continuing to core in a cased hole. The drill string was pulled to the surface, clearing the seafloor at 0330 h on 30 April and ending Hole U1502A and beginning Hole U1502B.

Total time spent on Hole U1502A was 125.25 h (5.2 days). A total of 40 RCB cores were taken over a 383.2 m interval with 176.81 m of recovery (46%). One interval was drilled without coring from the mudline to 375.0 m.

Hole U1502B

We secured the RCB components of the BHA and prepared the rig floor for reentry and casing operations. The vessel was offset to the coordinates provided from the science office, and the UGH was removed and laid out to the drill collar racks.

The hydraulic release tool (HRT) was made up to a landing stand and racked back in the derrick. The prepared mud skirt was moved onto the moonpool doors and centered underneath the rotary table. After rigging up to run 10¾ inch casing, 62 joints of 10¾ inch casing (723.7 m) were run through the mud skirt. The landing stand was picked up, and the casing was lowered to the moonpool and latched into the mud skirt. The adapter flange was unbolted, and the landing stand was pulled back to the rig floor and racked back in the derrick.

The bit, bit sub, underreamer, and mud motor were assembled, and a pump-in sub was connected to the top of the mud motor. The mud motor and underreamer were function tested in the moonpool with good results. The remainder of this drilling stinger was assembled. The landing joint was again picked up, and the mock hanger and HRT were attached to the top of the casing and mud skirt. The adapter flange was bolted up and tightened with a torque wrench to the recommended torque. The reentry funnel was picked up in the moonpool and securely welded to the mock hanger.

The drilling and casing assemblies were lowered to the seafloor, stopping every 20 stands to secure the drill string and fill it with water to prevent collapse from differential pressure. After running in to 3744 m, the subsea camera was lowered to the bottom of the pipe to observe the drilling activity. While the camera descended, the top drive was picked up and the rig was serviced. The drill string was spaced out, and slow circulating rates were recorded. Drilling the casing into Hole U1502B started at 3763.7 mbsl at 1255 h on 1 May 2017. Drilling continued until the 723.7 m long casing string had

been fully drilled into the seafloor and the mud skirt landed on the seafloor. The go-devil was inserted into the drill pipe and pumped down to release the casing at 2220 h on 2 May. The drill string was released from the casing assembly, and the bit and underreamer were pulled back through the casing and back to the rig floor. The bit cleared the seafloor at 0115 h on 3 May. The remainder of the drill string was pulled back to the rig floor, and the bit cleared the rotary table at 1130 h on 3 May.

After the tricone bit was removed, the mud motor and underreamer were flushed with freshwater and laid out. The UGH was reinstalled, and the drill floor was reassembled. The RCB outer core barrel was set up in the rotary table, and the core barrels were spaced out to the outer core barrel. The remainder of the RCB BHA was made up, and the bit was lowered to 3732 m. The subsea camera system was deployed and run to near bottom in preparation for reentering Hole U1502B to begin coring operations. While the subsea camera was lowered to the seafloor, 115 feet of drill line was slipped and cut. After a 3.5 h search, we found the Hole U1502B reentry cone and reentered the hole at 0400 h on 4 May. The camera was then pulled back to the surface and secured.

The bit was lowered through the casing until it encountered fill at 715.3 m, 12.4 m above the total depth of the hole. The top drive was picked up, a core barrel was dropped, and the hole was washed and reamed to bottom. A 20 bbl mud sweep was circulated to help clean cuttings from the hole. Once the hole was clean, RCB coring began from 727.7 m and continued through Core 21R at 846.8 m. While cutting Core 21R, the driller noticed some excessive torque while on bottom. With 48.8 h on the bit, it was decided to pull out of the hole for a bit change. The bit was found to be in relatively good condition.

The drill string was pulled inside the casing before setting back the top drive. Overpull of 60,000 lb was noted between 740.3 m and the casing shoe. The bit was then raised to the mouth of the reentry cone, and the vibration isolated television (VIT) camera was run to the seafloor to verify the condition of the base and cone. The cone was visible but was below the sediment surface. Seawater was circulated in a successful attempt to clear the funnel of cuttings, and the VIT camera was retrieved to the moonpool. The bit was then retrieved to the surface, clearing seafloor at 0600 h and the rotary table at 1345 h on 8 May 2017.

A new 9⅞ inch C-7 RCB bit and an MBR were installed in the BHA, and the bit was run back to seafloor, followed by the subsea camera, for reentry. The cone was clearly visible, and Hole U1502B was reentered at 0240 h on 9 May. The camera was recovered, and the bit was lowered to 728.3 m, ~1.5 m below the casing shoe. The top drive was picked up, and a center bit was dropped. The hole was then washed to total depth, with the fill holding 10,000 lb weight on bit from 733.3 to 770.3 m.

A mud sweep was circulated, and the center bit was retrieved prior to resuming coring operations. Coring continued to 858.4 m, at which depth the low clutch diaphragm failed for the second time during the expedition at 0115 h on 10 May. The bit was pulled inside the casing and up to 715.3 m, and the drill pipe was hung off the elevators. The clutch diaphragm was replaced, and the drill string was lowered again by 0945 h on 10 May. While running in the hole, the driller noticed a spike in pressure, and a deplugger was dropped to clear any obstruction in the bit. The deplugger was retrieved, and a center bit was deployed so that the bit could be worked to the bottom of the hole. Before reaching the total depth of the hole, 3 m of fill was cleared. The center bit was then recovered, and coring resumed from 858.4 m (Core 25R) to a final depth of 920.8 m (Core 37R). Recovery was generally high over this interval (82%–101%), except for Cores 28R and 29R, which recovered only 33% and 45% and had higher rates of penetration of 2.76 and 3.75 m/h, respectively. The hole was then prepared for logging operations by circulating a high-viscosity mud sweep and performing a wiper trip. The bit was then released in the bottom of the hole. The end of pipe was raised to a logging depth of 747.3 m to ensure that the logging tools could bypass obstructions encountered by the bit when reentering the hole below casing.

Downhole logging

Two logging tool strings were deployed in Hole U1502B: a modified triple combo and the VSI. The triple combo tool string was then rigged up, zeroed, presurvey calibrated, and deployed in the hole with the following tools:

- DSI,
- HLDS with source,
- HNGS,
- Enhanced Digital Telemetry Cartridge (EDTC), and
- Logging Equipment Head (model QT) (LEH-QT).

The string made it into the open hole without any issue, but it stopped at a maximum depth of 4639 m wireline depth below rig floor (WRF), roughly 45.5 m higher than the driller's total depth. Based on an unexpected drop in gamma ray readings through casing, this obstacle was believed to be fill from above that had slumped and fallen to the bottom of the hole.

The repeat pass was taken from that depth up to the point where the logging head was just outside the pipe. The tool was then returned to maximum depth, which remained firmly at 4639 m WRF. The main log started there and continued up past the seafloor to provide a continuous gamma ray log of the entire interval. The caliper was closed at 4549 m to facilitate pipe entry, which was accomplished without any problems. The tools were pulled to surface with ease until the final joint of pipe at the top.

With the EDTC already sticking out of the top of the pump-in sub during the process of pulling the tool up to remove the density source, a large overpull was observed, causing the tension alarms to trip and disable winch function. Several attempts were made to free the tool, but they only resulted in it becoming too stuck to move up or down significantly. An alternate plan to disconnect the first joint of drill pipe to permit access to the tool inside and then disassemble whichever portion was free to move was successful, and the radioactive source was rigged down along with the majority of the string. The portion remaining stuck in the top single consisted only of the LEH-QT and EDTC, which were extracted relatively quickly and easily from the bottom of that single using an air tugger.

There was no sign of damage to the tool string itself, nor was there any sign of a problem in the affected joint of pipe. The cause of the problem could have been a fragment of shear pin from coring or some other small debris such as a pebble or shear pin, but these items were never located. The string was safely rigged down with only ~30 min of additional time required. The wireline was extracted from the traveling blocks to facilitate pulling the pipe up to approximately 69 mbsl for the seismic run, and wireline operations were paused for that action.

The VSI string was rigged up, zeroed, presurvey calibrated, and lowered in Hole U1502B with the VSI, EDTC, and LEH-QT. While pulling up the pipe, the drill crew observed that the hole was beginning to flow and made an unplanned break in the tripping operation

to pump down some seawater and stop the flow. Once the flow was halted, the seismic string was rigged up and lowered inside the hole without finishing the pull-out because the pipe was already at 4023 mbsl (259 m) and sufficiently high to avoid any major complication with the seismic experiment and because it was getting too late to raise the pipe any higher and still have sufficient time to finish the survey before dark.

The tool was rigged up as quickly as was safe and was run in the hole at a somewhat accelerated rate to make as much use as possible of the remaining daylight. The depth was correlated and adjusted to be on-depth in real time using a distinct gamma ray peak at 4413 meters below rig floor (mbrf) (corrected depth based on field pick of sea bed; raw depth of 4411.3 mbrf on main pass of first run). With the seismic tool on-depth, several attempts were made to get out of the casing and down to the bottom of the hole so that the deepest requested stations for the survey could be recorded, but the tool appeared to be hanging up on a ledge and was unable to pass into the open-hole section.

With very little daylight remaining, the open-hole stations were canceled in order to concentrate on getting as many of the cased-hole stations as time would permit. In all, eight stations were attempted, all in casing. Of those, the deepest two did not produce any useful signal, but the upper six all resulted in good seismic arrivals. The seismic survey was concluded roughly at sunset, and the tool was pulled out of the hole and rigged down in the usual manner. The heave compensator was not required for any portion of the logging because the total heave was just ±2 inches throughout the entire operating time.

The logging equipment was then rigged down, and the crew began recovering the drill string. The bit cleared the seafloor at 2235 h on 13 May. The beacon was recovered at 0015 h on 14 May, and the vessel began moving toward Site U1503 in dynamic positioning mode. The bit cleared the rotary table at 0445 h on 14 May, ending Hole U1502B and Site U1502.

Total time spent on Hole U1502B was 337.25 h (14.1 days). A total of 36 RCB cores were taken over a 193.1 m interval in Hole U1502B with 126.94 m of recovery (66%). There was one drilled interval from the mudline to 727.7 m, with 10¾ inch casing installed to 723.7 m. The triple combo string collected data in the open hole between 747.3 and 875.3 m, and the VSI logging experiment was conducted only inside casing between 259 and 629 m.

Lithostratigraphy

We examined the lithostratigraphy of Holes U1502A (Figure **F10**) and U1502B (Figure **F11**) and defined six lithostratigraphic units and seven subunits based on visual core description, smear slide and thin section inspection, and X-ray diffraction (XRD) analysis (see **Lithostratigraphy** in the Expedition 367/368 methods chapter [Sun et al., 2018a]). Four units (I, III, IV, and V) are sedimentary, and two units (II and VI) are igneous. Units II and III were only recovered in Hole U1502B, and Unit IV was only recovered in Hole U1502A. Several of the subunits exhibit gradual changes, complicating a clear definition of their boundaries. The precise depth of boundaries between certain lithostratigraphic subunits within the intervals of poor core recovery is difficult to determine. The boundaries were refined using physical property measurements (e.g., changes in magnetic susceptibility, color reflectance spectroscopy, and seismic velocity) (see **Physical properties**; also see **Physical properties** in the Expedition 367/368 methods chapter [Sun et al., 2018a]) and carbonate measurements (Figure **F56**).

The sedimentary succession recovered at Site U1502 extends from the early Oligocene to the late Miocene (see **Biostratigraphy**), includes four units (I, III, IV, and V), and comprises mainly clay, nannofossil-rich clay, biosiliceous-rich clay, limestone, and clast-rich clay. The two igneous units (II and VI) are composed of highly to moderately altered basalt, basaltic breccia, and brecciated basalt. The base of the sedimentary succession is a sequence of clay and metasedimentary rocks (dolomite marble and dolomitic limestone) that form the contact above a unit of altered basalt (Unit VI). Unit I is dominated by clay and silty clay with varying amounts of nannofossils and foraminifers. The base of Unit I is defined at the base of the clay interval that has millimeter-sized pale green nodules. The contacts between Units II, III, and IV were not recovered. Unit II is a basalt clast. Unit III is silicified breccia. Unit IV consists of biosiliceous-rich silty clay transitioning downhole into silty clay barren of siliceous microfossils. Unit V is an interval of alternating metasedimentary rocks, including epidote-rich metaclaystone and dolomite marble. Unit VI consists of highly to moderately altered basaltic breccia, brecciated basalt, pillow basalt, and sheet basalt. Unit I is divided into five subunits, and Unit VI is divided into two subunits, described below.

Unit description

Unit I

Intervals: 368-U1502A-2R-1, 0 cm, to 39R-CC, 19 cm; 368-U1502B-2R-1, 0–26 cm
Depths: Hole U1502A = 375.00–734.87 m; Hole U1502B = 727.79–727.96 m
Age: Miocene

Lithology and sedimentary structures

Unit I is dominated by clay, silty clay with varying proportions of nannofossils, clay-rich nannofossil ooze, minor sandy clay with calcite, nannofossil-rich clay with foraminifers, and sandy silt. The unit is divided into five subunits, IA–IE, based on slight lithologic variation. Recovery within the upper part of Unit I is very poor.

Bulk mineralogy

The bulk mineralogy results of XRD analyses are listed in Table **T2**. Unit I sediments in Hole U1502A are composed mainly of quartz, plagioclase, K-feldspar, siderite, clay minerals (smectite, illite, kaolinite and chlorite), and halite, as well as minor amounts of calcite and dolomite. The relative content of minerals changes significantly downhole (Figure **F12**). Siderite is a major component of the sediments and has a relatively high content (average ~39%) throughout Subunits IA–IC and the upper part of Subunit ID (410–680 m) but is almost absent in the lower part of Subunit ID between 680 and 750 m, except for an interval with an abnormally high content (~15%) at about 734.8 m. In Subunits IA and IB, the abundance of siderite corresponds well to the alternation of greenish gray (lower siderite) and brownish gray (higher siderite) layers. Other minerals, including quartz, plagioclase, smectite, and halite, show the reverse trend to siderite, possibly because of a dilution effect. K-feldspar and chlorite decrease downhole, whereas illite and kaolinite increase. Calcite and dolomite are rare, except for exceptionally high abundances in Subunits IC and IE.

Figure F10. Lithostratigraphic summary, Hole U1502A.

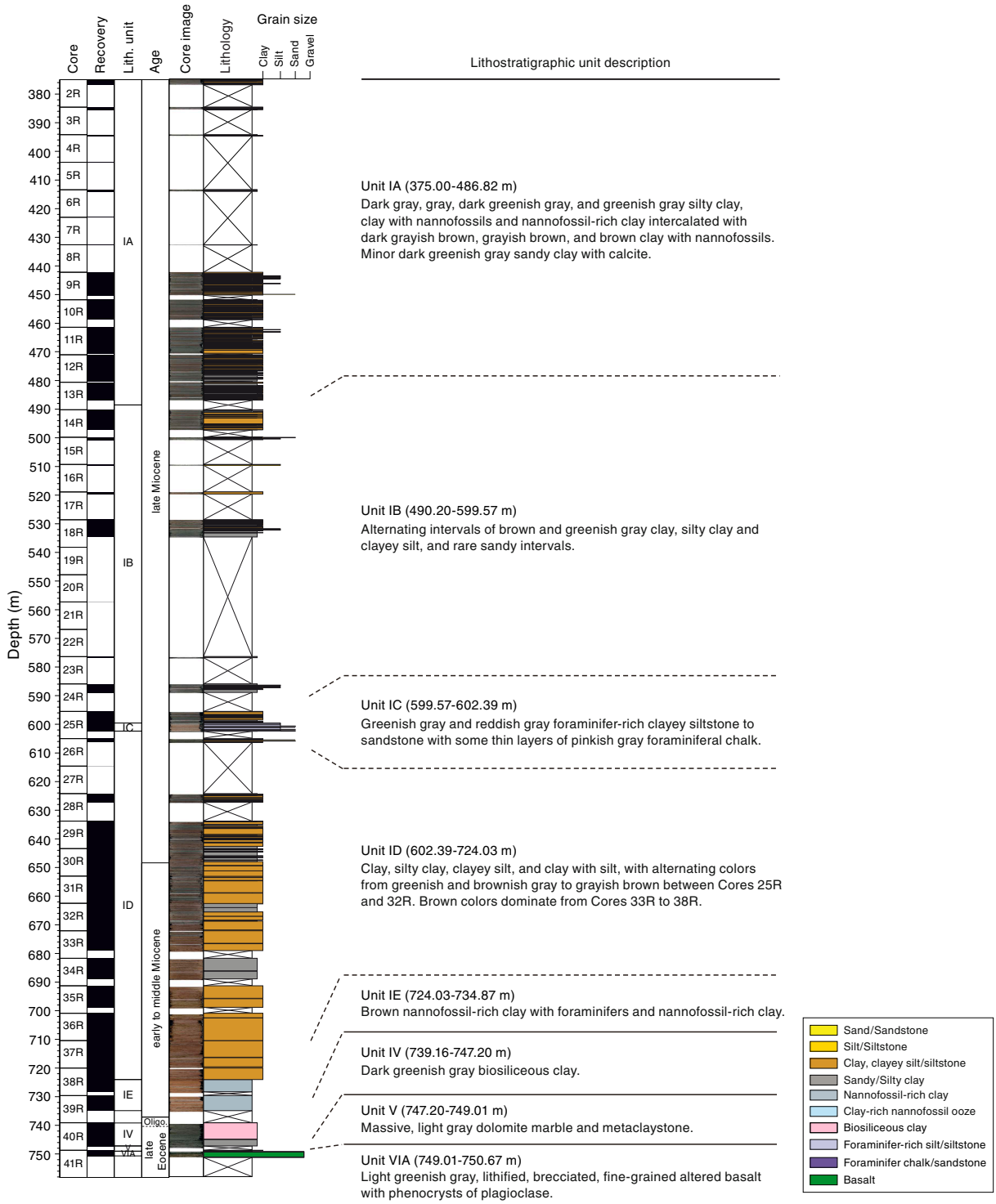

Subunit IA

Interval: 368-U1502A-2R-1, 0 cm, to 13R-5, 79 cm
Depth: 375.00–486.82 m
Age: late Miocene

Subunit IA spans the uppermost 111.82 m of Unit I and comprises dark gray, gray, dark greenish gray, and greenish gray silty clay; clay with nannofossils; and nannofossil-rich clay intercalated with dark grayish brown, grayish brown, and brown clay with nannofossils. There is also minor dark greenish gray sandy clay with calcite. The lithologies are dominantly dark gray and dark greenish gray in the upper cores (375.15–432.67 m). Intervals that fine upward are common (Figure **F13**). The lithology changes downhole (442.2–486.82 m) to more greenish gray, dark grayish brown, and rarely brown lithologies. Lithologic variations are not directly tied to color boundaries, and some burrows extend across areas of con-

Figure F11. Lithostratigraphic summary, Hole U1502B.

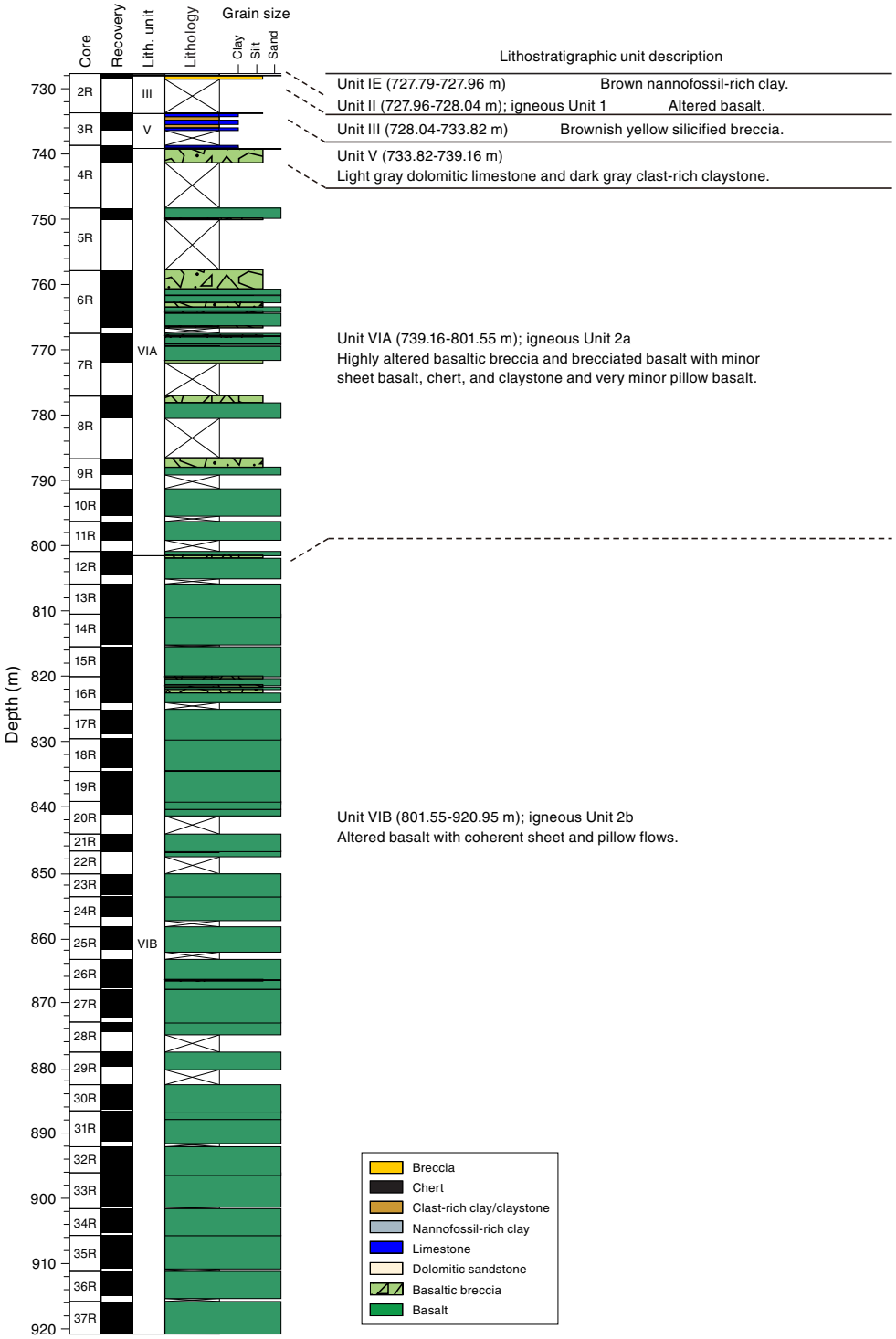

trasting color. The clay contains varying amounts of nannofossils, as well as foraminifers in some intervals. The terrigenous component is mainly quartz and clay, with lesser feldspar and rare singular volcanic glass shards. Most lithologies have calcite or dolomite crystals, as well as accessory glauconite, pyrite, and iron oxide grains in the more brownish lithologies.

Bioturbation is heavy throughout most of Subunit IA, with *Planolites* and *Chondrites* as the main ichnospecies (Figure **F13**). Recovery between 375 and 445 m was very poor, possibly because sand layers were washed out.

The boundary between Subunits IA and IB is defined by the absence of nannofossils in Subunit IB.

Table T2. Mineral percentages, Hole U1502A. **View table in PDF format. Download table in CSV format.**

Figure F12. Bulk mineralogy data from shipboard XRD analysis, Holes U1502A and U1502B. Units IV and V are plotted based on depth and not stratigraphic order. The incorrect stratigraphic order of these units is due to overlap of Holes U1502A and U1502B.

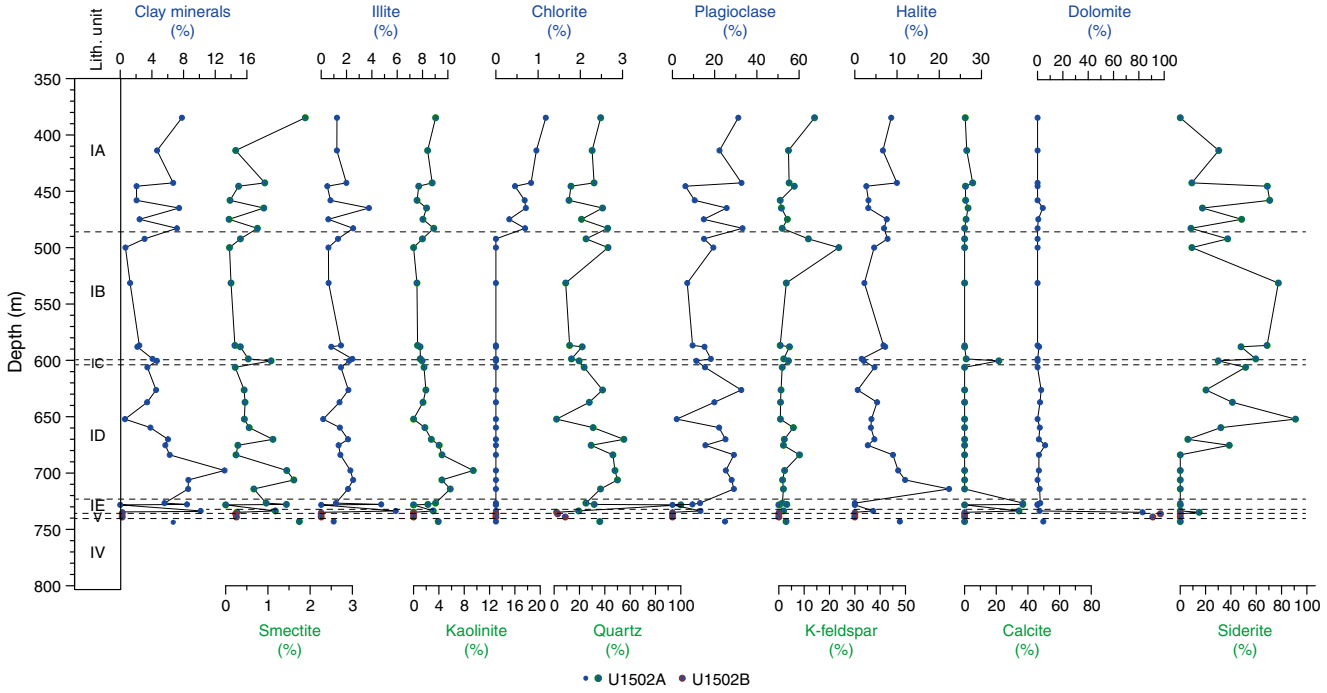

Subunit IB

Interval: 368-U1502A-14R-1, 0 cm, to 25R-3, 109 cm
Depth: 490.20–599.57 m
Age: late Miocene

Subunit IB is 109.37 m thick and composed of alternating intervals of brown and greenish gray clay, silty clay, and clayey silt. Sandy intervals are rare. Two intervals of (light) greenish gray calcareous ooze occur in intervals 14R-1, 23–57 cm, and 15R-1, 63–69 cm (Figure **F14**). In general, the lithology (clay dominated) does not change across color boundaries, and some burrows extend across areas of contrasting color. Intervals that fine upward are common in the greenish gray layers. The sediment is dominated by clay minerals, quartz, feldspar, and authigenic siderite, as well as traces of pyrite.

Bioturbation is heavy in Subunit IB. Recovery was poor, which might be due to the presence of unconsolidated sand beds between the clay intervals.

The boundary between Subunits IB and IC is marked by a distinct change in lithology and in the consolidation and bedding structure of the sediments. Subunit IB is overall massive and well consolidated, whereas Subunit IC is laminated and lithified.

Subunit IC

Interval: 368-U1502A-25R-3, 109 cm, to 25R-5, 91 cm
Depths: 599.57–602.39 m
Age: late Miocene

Subunit IC is 2.82 m thick and coarser grained than the other subunits of Unit I. The dominant lithology is greenish gray and reddish gray foraminifer-rich clayey siltstone to sandstone with some thin layers of pinkish gray foraminiferal chalk (Figure **F15**). Foraminifers make up 25%–30% of Subunit IC, and foraminifer tests are

Figure F13. Bioturbation and burrows, Subunit IA. A. Dark grayish brown clay with nannofossils and greenish gray clayey silt that fines upward. B. Intercalated dark gray silty clay with nannofossils and grayish brown clay with silt. C. Dark grayish brown clay with nannofossils and greenish gray silty layer (368-U1502A-12R-1A, 64–73 cm).

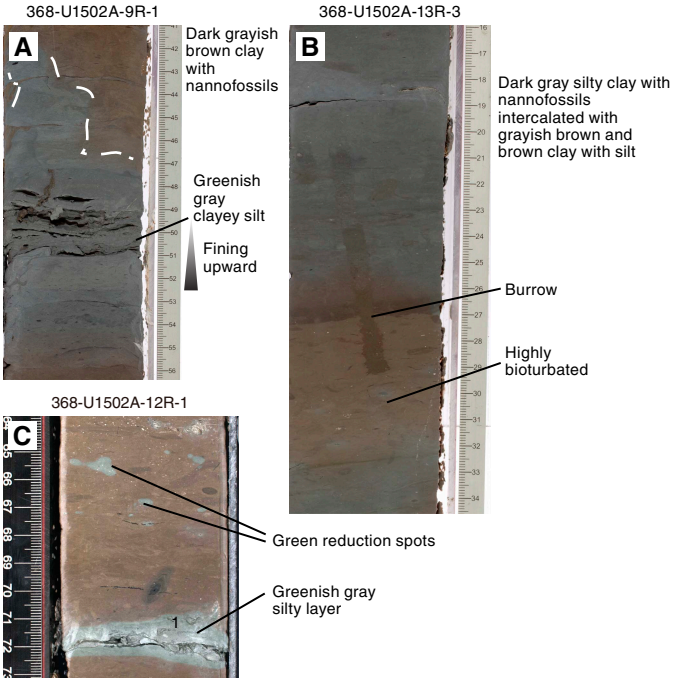

embedded within a matrix of nannofossil-rich micritic calcite. The subunit consists of several layers that are characterized by erosive

and inclined bottom contacts and upward fining. Within these intervals, the sediments show parallel laminations and convolute bedding.

In contrast to the subunits above and below, Subunit IC is only slightly bioturbated. The contact with Subunit ID was not recovered but was interpreted on the basis of a change in the lithology from lithified foraminifer-rich siltstone to greenish gray clay.

Subunit ID

Interval: 368-U1502A-25R-CC, 91 cm, to 38R-3, 131 cm
Depth: 602.39–724.03 m
Age: late to early Miocene

Subunit ID is 121.64 m thick and mainly composed of clay, silty clay, clayey silt, and clay with silt. The sediment has alternating colors from greenish and brownish gray to grayish brown between Cores 25R and 32R. Brown colors dominate in Cores 33R through 38R, and greenish gray colors only occur along fractures and burrows (Figure **F16**). The sediments are well consolidated and slightly laminated. Clay minerals are abundant, and quartz is common. Glauconite, pyrite, and siderite are rare to common.

Subunit ID is heavily bioturbated, and some thin yellowish layers contain abundant diagenetic siderite (e.g., Core 33R; Figure **F16**).

The boundary between Subunits ID and IE is characterized by the appearance of abundant nannofossils and foraminifers in Subunit IE, accompanied by a slight change in color from darker to lighter brown.

Subunit IE

Intervals: 368-U1502A-38R-3, 131 cm, to 39R-CC, 19 cm; 368-U1502B-2R-1, 0–26 cm
Depths: Hole U1502A = 724.03–734.87 m; Hole U1502B = 727.79–727.96 m
Age: early Miocene

Subunit IE is 10.84 m thick and composed of brown nannofossil-rich clay with foraminifers and nannofossil-rich clay. Pale green colors are restricted to halos around fractures (Figure **F17**) and are not related to a change in lithology. The sediment contains abundant clay minerals and, commonly, quartz and calcite. Pyrite was found in patches throughout the subunit. At the base of Unit I, within Core 368-U1502A-39R, are single, green, up to centimeter-size concretions (various green alteration minerals, including epidote) with black rims. The number of concretions increases downhole.

Unit II (igneous rock) was not recovered in Hole U1502A, and only a clast (fall-in) of Unit III was recovered in the uppermost few centimeters of Core 40R at the top of Unit IV. The boundary between Units I and IV is marked by a change in color from brown to dark greenish gray, a change in lithology from nannofossil-rich clay to biosiliceous clay, and an increase in NGR. However, there is a ~5 m gap in recovery between Cores 39R and 40R (see **Operations**). The contact between Units I and II was not recovered in Hole U1502B, but the lithology changes from sediment to igneous rock (Figure **F18**).

Unit II

Interval: 368-U1502B-2R-1, 26–34 cm
Depth: 727.96–728.04 m
Age: early Miocene or older

Figure F14. A. Color change from greenish gray to brown in Subunit IB. B. Close-up image (red square in A) of calcareous ooze and silty clay to clay. C. Smear slide image showing siderite-rich clay of Subunit IB.

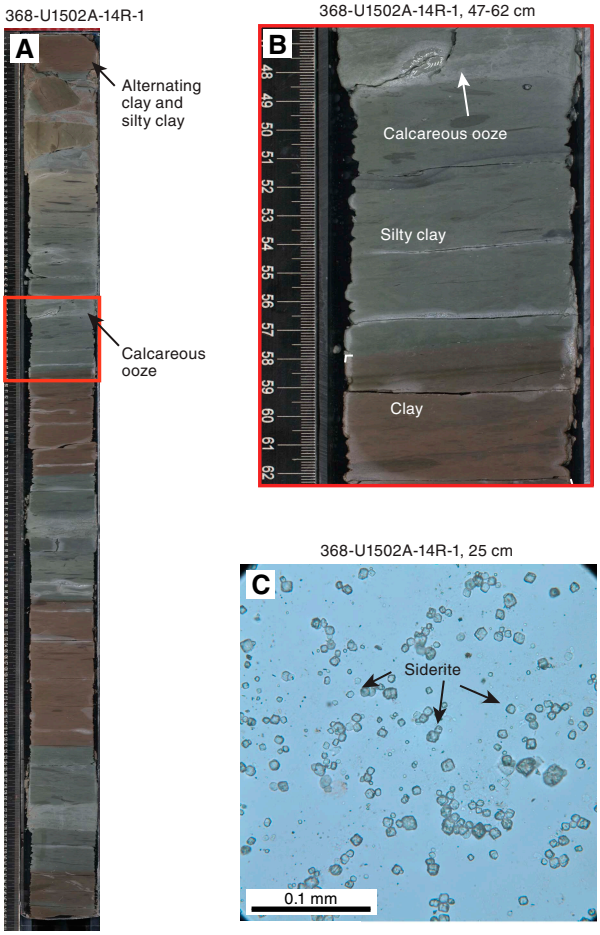

Unit II is a ~10 cm clast of greenish gray basalt with an equigranular texture (Figure **F18**). The basalt is highly altered, and most of the primary mineral phases are replaced by an alteration assemblage. Plagioclase laths as large as 3 mm make up approximately 1% of Unit I. The groundmass is intersertal with possible altered olivine, clinopyroxene, and/or altered glass between a felt of plagioclase crystals. The plagioclase has swallow-tail and bow-tie textures, indicating quenching.

The contact with Unit III was not recovered but is marked by a change in lithology (Figure **F18**).

Unit III

Intervals: 368-U1502A-40R-1, 0–6 cm (fall-in); 368-U1502B-2R-1, 34 cm, to 3R-1, 12 cm
Depths: Hole U1502A = 739.10–739.16 m; Hole U1502B = 728.04–733.82 m
Age: Miocene/Oligocene boundary

Unit III is composed of a brownish yellow, silicified, very hard, poorly sorted breccia (Figures **F18**, **F19**). The average grain size is granule, and maximum clasts are pebble sized. The clasts consist of alteration minerals (Fe hydroxides) cemented by a matrix of annealed quartz in various grain sizes (see **Structural geology** for interpretation of textures).

Figure F15. Dominant lithology of Subunit IC is greenish gray and reddish gray foraminifer-rich clayey siltstone to sandstone with some thin layers of pinkish gray foraminiferal chalk. A. Greenish and reddish clayey siltstone and pinkish gray foraminiferal chalk. Red square = parallel laminations and convolute bedding, green square = color change is interpreted as fluid interaction. B. Clayey siltstone with abundant foraminifers. C. More clay-rich upper part of Subunit IC.

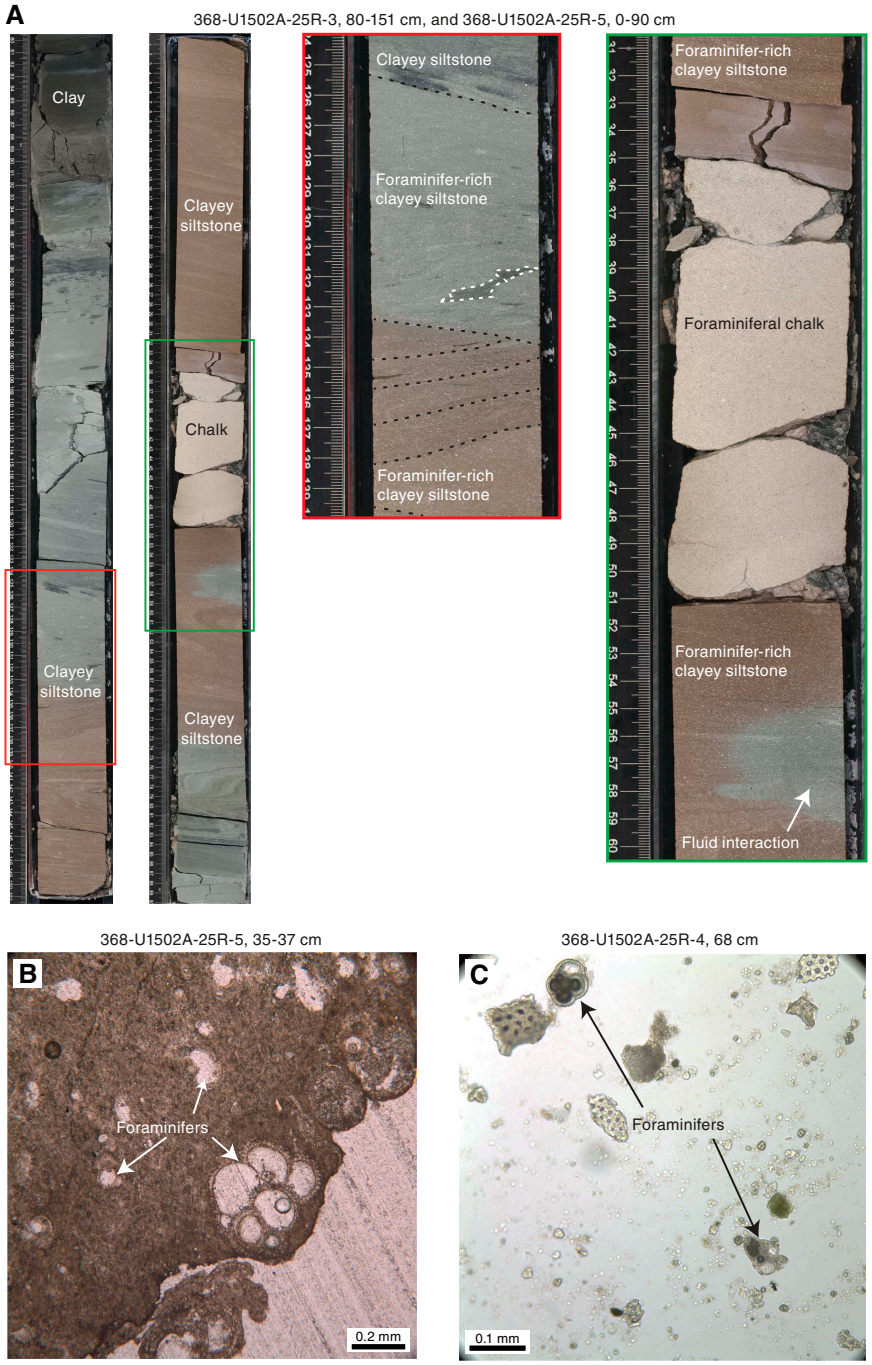

In Hole U1502A, Unit III is represented by a single clast (fall-in) in the uppermost centimeters of Core 40R (Figure **F20**), whereas in Hole U1502B, an interval of 0.63 m (interval 2R-1, 34 cm, to 3R-1, 12 cm) was recovered (Figure **F19**). The contact with the underlying Unit IV was not recovered in Hole U1502A but is indicated by a change in lithology from poorly sorted silicified breccia to dark greenish gray biosiliceous clay. Unit IV was not recovered in Hole U1502B.

Unit IV

Interval: 368-U1502A-40R-1, 6 cm, to 40R-6, 83 cm
Depth: 739.16–747.20 m
Age: late Oligocene

Lithology and sedimentary structures

Unit IV is 8.1 m thick and was recovered only in Hole U1502A. The unit is dominated by dark greenish gray biosiliceous clay (Fig-

Figure F16. Subunit ID is dominated by sediment with greenish and brownish gray and grayish brown colors from Cores 368-U1502A-25R through 32R and brown colors from Cores 33R through 38R. A. Brownish clay with greenish halos along fractures. Red square = 38R-1, 91–106 cm. Subunit ID is heavily bioturbated. B. Yellowish layers contain abundant diagenetic siderite. C. Siderite-rich clay.

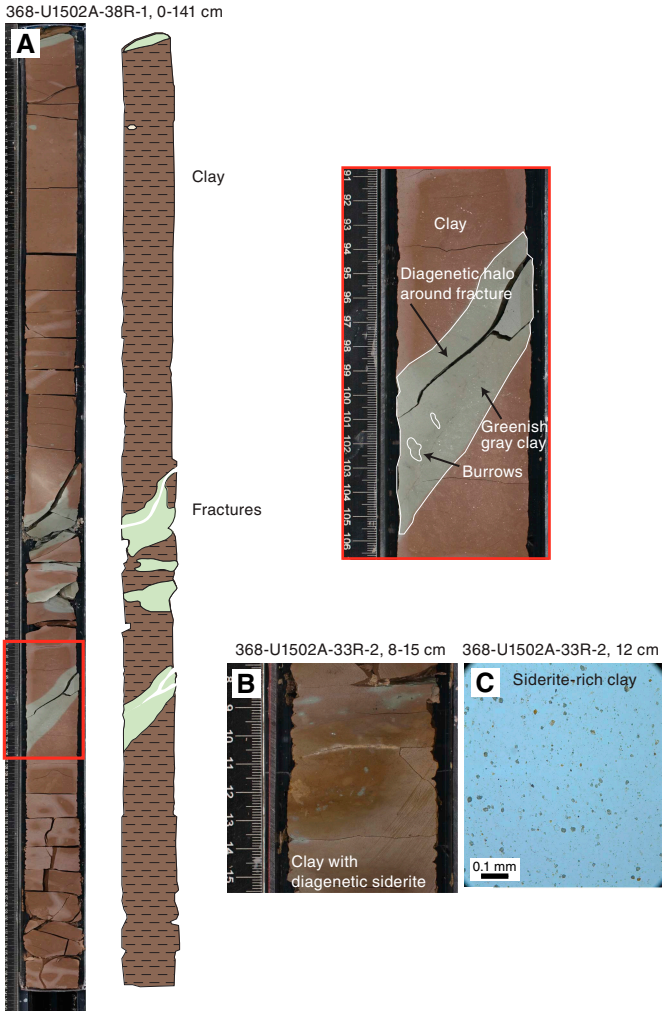

Figure F17. A. Subunit IE sediments are brown nannofossil-rich clay with foraminifers and clay with nannofossils. Pale green colors are restricted to fractures and are not related to a change in lithology. B. Nannofossil-rich clay with foraminifers (cross-polarized light [XPL]). C. Greenish clasts/concretions in the lower part of Subunit IE. The material is soft and easily scratched with a fingernail. D. Green concretions in brown clay. Green minerals are probably alteration sheet silicates. Thin section was made from a fall-in clast.

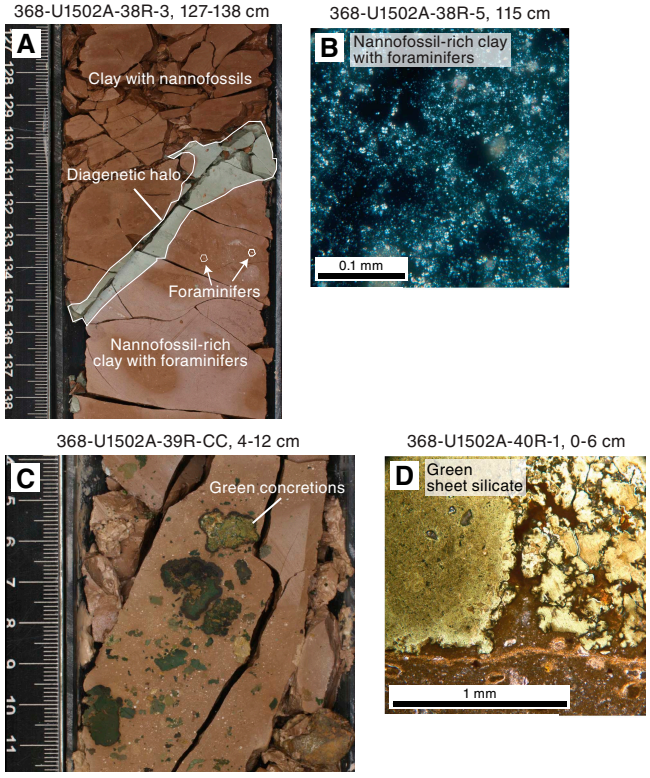

ure F20). The amount of nannofossils decreases rapidly within Section 40R-1, and diatoms, sponge spicules, and radiolarians are abundant. Diatom abundance decreases significantly from Section 40R-1 to Section 40R-3. The calcareous nannofossil abundance is rare to barren in Unit IV. Pyrite occurs in centimeter-sized patches and along cracks (Figure F20).

Unit IV is heavily bioturbated and, in the upper section, contains the same green concretions found in the lower part of Subunit IE. The layering in Unit IV is inclined (~20°) and slightly deformed (see **Structural geology**).

The bottom contact of Unit IV is irregular and subhorizontal, and the boundary is characterized by a lithology change from dark greenish gray, well-consolidated, biosiliceous clay to light gray, lithified marble. The boundary between Units IV and V is associated with a distinct increase in magnetic susceptibility in Unit V (see **Physical properties**).

Bulk mineralogy

One XRD sample from Unit IV (Table T2) indicates that the bulk mineralogy of the sediments is quartz, plagioclase, K-feldspar, and clay minerals (smectite, illite, and kaolinite), as well as minor amounts of halite and dolomite. No siderite, calcite, or chlorite were detected in the XRD sample. Apart from the absence of these minerals, Unit IV has a very similar mineral assemblage to Unit I but with slightly more abundant smectite (Figure F12).

Unit V

Intervals: 368-U1502A-40R-6, 83 cm, to 41R-1, 31 cm; 368-U1502B-3R-1, 12 cm, to 4R-1, 46 cm
Depths: Hole U1502A = 747.20–749.02 m; Hole U1502B: 733.82–739.16 m
Age: unknown (at least pre-late Oligocene, possibly late Eocene)

Unit V is 1.82 m thick in Hole U1502A when calculated using the curated section lengths; however, only 43 cm of rock was recovered. In Hole U1502B, 3.05 m was recovered. The unit is composed of massive, light gray dolomite marble and meta claystone in Hole U1502A and dolomitic limestone intercalated with clast-rich clay and sandstone in Hole U1502B (Figures F21, F22).

The dolomite marble in Hole U1502A is very fine grained, equigranular with an annealing texture, and crossed by fine dark gray bands. The marble is dominated by dolomite (~95%), with minor amounts of magnetite (~3%) and calcite (~2%) (Figure F22). The calcite occurs in enclaves, whereas magnetite forms dark gray bands or occurs as singular grains within the dolomite marble and limestone. The presence of magnetite explains the high magnetic susceptibility of this unit.

Figure F18. A. Subunit IE and Units II and III. The brown clay with green concretions of Subunit IE is not in contact with Unit II (altered basalt); contact between Units II and III was not recovered. Unit III is brownish yellow silicified breccia. Overall recovery of Core 368-U1502B-2R was only 14%. B. Unit II basalt with plagioclase and alteration minerals (e.g., epidote). C, D. Silicified breccia. Texture is interpreted as cataclastic, and matrix is rich in recrystallized annealed quartz.

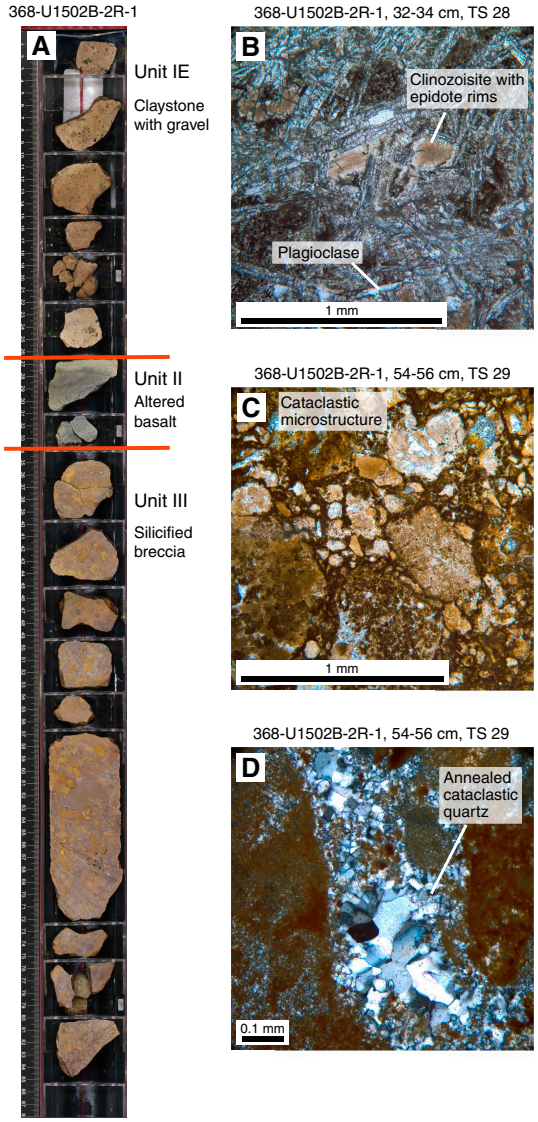

The gray, fine-grained dolomitic limestone in Hole U1502B is intercalated with a well-consolidated, very dark greenish gray clay with 10%–15% igneous clasts (Figure **F21**). The clay is composed of clay minerals, calcite, feldspar, quartz, and pyrite in decreasing order of abundance. Abundant benthic agglutinated foraminifer tests occur in Section 3R-1 (see **Biostratigraphy**). Gray, coarse-grained dolomitic sandstone occurs at the base of Unit V and is lithified and well sorted.

The boundary between Units V and VI is characterized by a change in lithology from (meta)sedimentary dolomite marble, dolomitic limestone, clay, and sandstone to igneous Unit VI (Figure **F22**).

Figure F19. A, B. Brownish yellow silicified breccia, Unit III. C. Silicified breccia with possible foraminifer tests filled by Fe hydroxides and quartz. D. Matrix of Unit III dominated by secondary quartz.

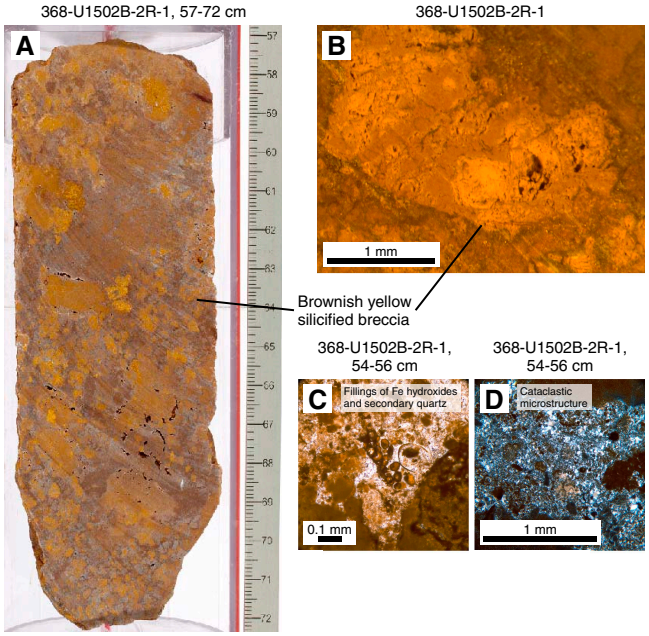

Unit VI

Intervals: 368-U1502A-41R-1, 31 cm, to 41R-CC, 18 cm; 368-U1502B-4R-1, 46 cm, to 37R-4, 141 cm
Depths: Hole U1502A = 749.01–750.67 m; Hole U1502B = 739.16–920.95 m
Age: Unknown (at least pre-late Oligocene, possibly Eocene)

Unit VI consists of highly to locally moderately altered basalt. The unit is divided into two subunits, VIA and VIB. The upper part of Hole U1502A (interval 41R-1, 30–62 cm) is greenish gray, highly altered, and heavily fractured, possibly due to drilling disturbance (Figure **F23**). Interval 41R-1, 62–90 cm, is light greenish gray, lithified, brecciated, fine-grained rock with phenocrysts of plagioclase. From Section 41R-1, 90 cm, downhole, the rock is still heavily but less altered. The rock is light gray and coarser grained with subrounded amygdules as large as 0.5 cm in diameter. Reddish iron oxides are common and occur as single crystals and along fractures, together with rare sulfides. Fragments show yellowish concentric alteration horizons. All basalt in Hole U1502A is within Subunit VIA.

Unit VI was recovered in Hole U1502B from Section 4R-1, 46 cm, downhole to 920.95 m. Unit VI is divided into two subunits, VIA (Section 4R-1, 46 cm, to 12R-1, 105 cm) and VIB (Section 12R-1, 105 cm, to 37R-4, 141 cm). The basalt is heavily altered and fractured, and veins with quartz, carbonates, epidote, and sulfides are common. Highly fractured, matrix-supported intervals and intervals with a mixture of basaltic and sediment clasts are described as basaltic breccia (Figure **F23**). Intervals that are fractured but clast supported are described as brecciated basalt. Fractured basalt without any matrix between the basaltic fragments is described as basalt (with optional prefixes for phyric basalts).

Subunit VIA is composed of highly altered basaltic breccia and brecciated basalt with infrequent sheet basalt, chert, and claystone

Figure F20. Unit IV is dominated by dark greenish gray biosiliceous clay. A. Dark greenish gray biosiliceous silty clay. Red square = location of B. B. Pyrite occurs as centimeter-sized patches and along cracks. C, D. Biosiliceous silty clay with sponge spicules. Diatom abundance decreases significantly in Sections 368-U1502A-40R-1 through 40R-3, whereas sponge spicules and radiolarians are present throughout Unit IV.

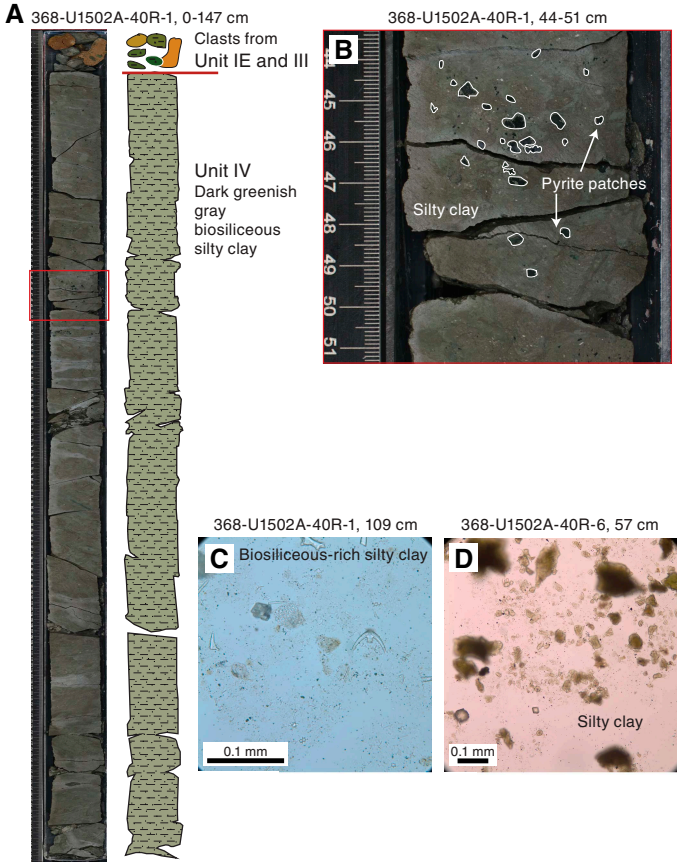

Figure F21. Unit V is composed of dolomite marble, dolomitic limestone, and clay. A. Dolomitic limestone intercalated with clast-rich clay. B. Fine-grained dolomite limestone with magnetite enclaves. C. Epidote veins. D. Close-up image (red square in A) of clast-rich clay that contains igneous clasts (368-U1502B-3R-2, 64–74 cm). E. Clay (XPL).

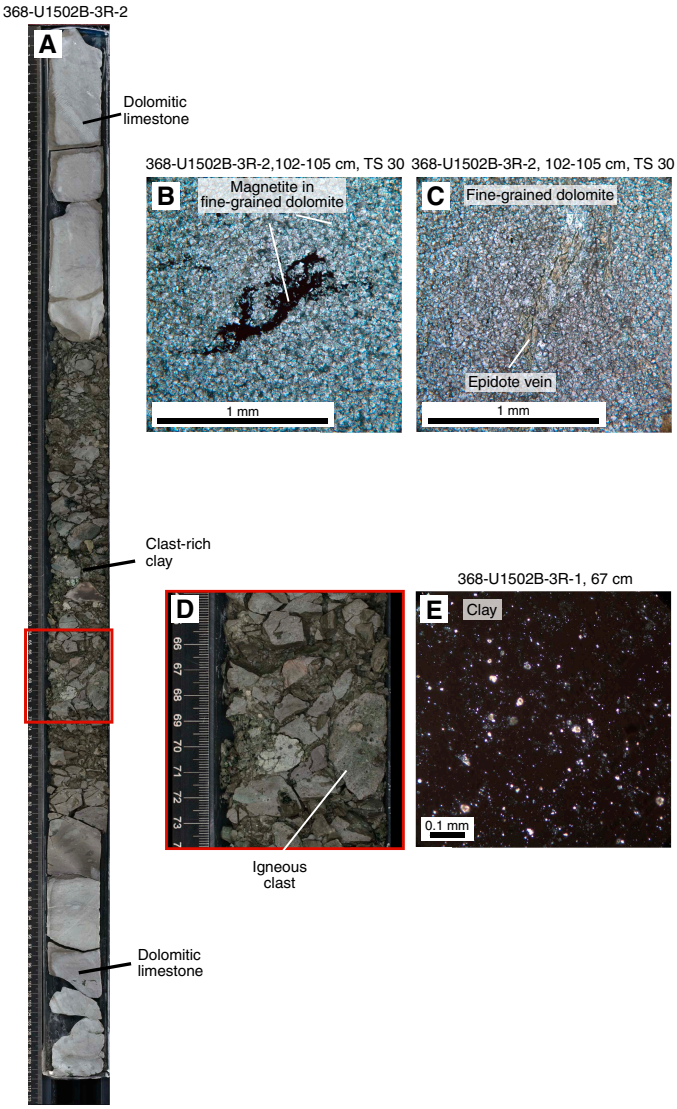

and very minor pillow basalt. The basaltic breccia in Sections 4R-1 through 6R-2 is a mixture of light gray and greenish gray claystone and basaltic clasts in an altered matrix (e.g., Section 6R-1; Figure **F23**). Chert and claystone layers and clasts were recovered between the brecciated basalt and basaltic breccia in Sections 6R-3 through 7R-2. No sedimentary clasts were recovered from Section 7R-2 downhole. From Core 11R downhole, pillow lavas were recovered in between the sheet lava flows and the basalt is locally less altered (moderately highly altered) and less brecciated.

The boundary between Subunits VIA and VIB is placed at the base of a fine-grained interval (12R-1, 105 cm), which might be a tectonic or hydrothermal breccia (see **Structural geology**). This interval also marks the boundary between the basaltic breccia and brecciated basalt of Subunit VIA and the more coherent sheet and pillow flows in Subunit VIB. Veins are more localized and larger in Subunit VIB, crosscutting the complete length of core sections (e.g., Sections 13R-3 and 14R-1).

The lithology of Unit VI basalt is described in more detail in **Igneous and metamorphic petrology**, and its structures are described in more detail in **Structural geology**.

Discussion

Depositional environment of Unit V

Unit V is composed of dolomite marble and limestone intercalated with clast-rich clay. Although the sediment is overprinted by secondary high-temperature processes (likely hydrothermal fluid sediment interaction or possibly contact metamorphism), it still retains primary sedimentary bedding and bioturbation features. The clay lithology and presence of deep-water benthic agglutinated foraminifers (see **Biostratigraphy**) indicate the unit was deposited in a deep abyssal environment.

Depositional environment of Unit IV

Unit IV is composed of dark greenish gray biosiliceous clay (Figure **F20**), and calcareous nannofossils are rare. The lower part of the unit (Section 368-U1502A-40R-6) is barren of diatoms, but their abundance increases with time, and diatoms are abundant at the top of the unit (Section 40R-1). Sponge spicules occur throughout the unit. The lower part of Unit IV is slightly deformed and interpreted as being postdepositional (see **Structural geology**).

Comparing the dominantly calcareous microfossil assemblage in the early to late Miocene Unit I with the dominantly biosiliceous microfossil assemblage in Unit IV may either indicate deposition of

Figure F22. Contact between Unit V and Subunit VIA, Hole U1502A. A. Contact of light gray dolomite marble (Unit V) and greenish gray altered basalt (Unit VI). B. Fine-grained dolomite marble with calcite patches. The marble is dominated by dolomite (~95%) with minor amounts of magnetite (~3%) and calcite (~2%). C. Altered basalt showing plagioclase and alteration minerals.

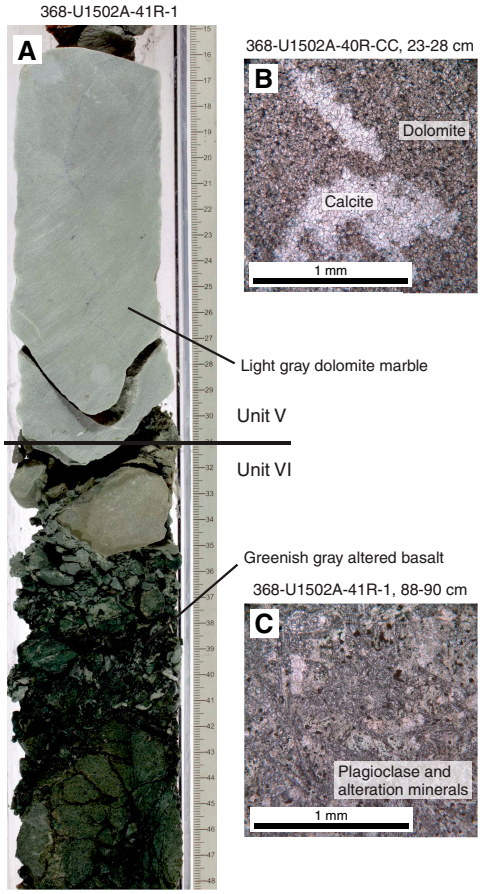

Figure F23. Basaltic breccia, brecciated basalt, and sedimentary rocks, Subunit VIA. A. Basaltic breccia with sediment clasts. B. Claystone and chert intervals within the brecciated basalt. C. Brecciated basalt with dolomitic matrix and basaltic clasts. Location of D is marked on the image. D. Thin section (TS) 34 showing (left) dolomitic matrix around basalt clasts and (right) euhedral dolomite and epidote with high interference colors.

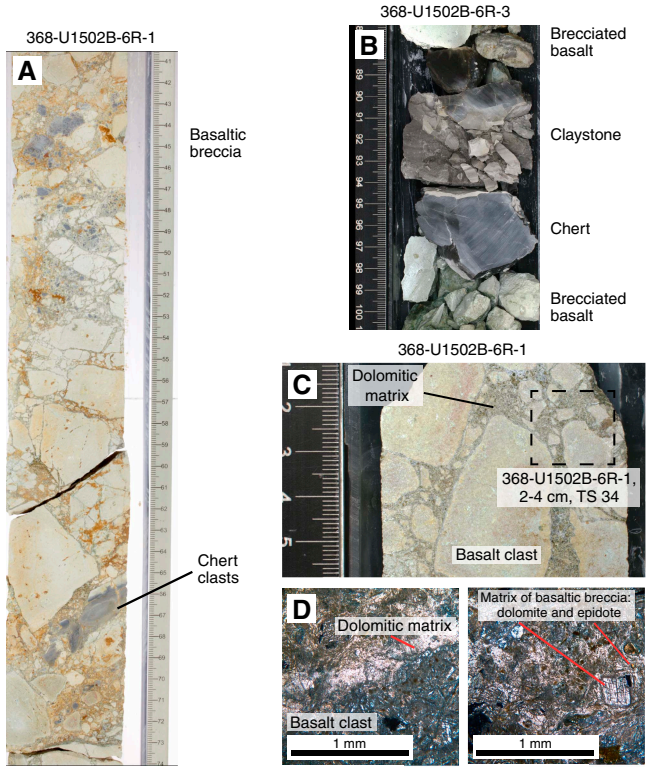

Unit IV in deeper water or the existence of a shallower CCD during its time of deposition (see **Biostratigraphy**).

Depositional environment of Unit I

Lithostratigraphic Unit I (late Miocene–late Oligocene) at Site U1502 was deposited in a deep-marine environment. The dominant lithologies in Unit I are clay and silty clay with nannofossils and nannofossil-rich clay, which are interbedded with centimeter-scale silt layers and rarely foraminifer-rich siltstone. There are variable amounts of foraminifers in all lithologies.

Some thin silty beds and thick silty laminae in Unit I (Sections 368-U1502A-9R through 33R; ~440–680 m) have upward fining and erosive bottom contacts that are interpreted as fine-grained (mostly Bouma sequence) turbidite deposits. Similar beds were observed at Site U1499.

Subunit IC comprises an approximately 3 m thick foraminifer-rich siltstone interbedded with foraminiferal sand. The subunit has parallel lamination and convolute bedding, which we interpret as evidence of downslope slumping of slightly to moderately consolidated sediments on the continental slope.

Site U1502 is located at the boundary between the lower continental slope and the deep-sea basin, and a similar depositional environment probably existed during the deposition of Unit I. This environment is very prone to redeposition of sediment by sediment-gravity processes, including slides, slumps, debris flow, and turbidity currents. Sea level change and tectonic uplift are two important mechanisms that may trigger sediment gravity flows.

According to the preliminary age model of Site U1502 (see **Biostratigraphy**), the variation in sedimentation rate correlates well with the lithologic change from Subunit IE to Subunit IA. Between the early Oligocene and middle Miocene (~30–15 Ma), the sedimentation rate was very low (~1 cm/ky). Sediment from this interval has a low siderite abundance and a monotonous reddish-brown color, likely indicating an oxidizing environment (Subunits ID and IE; 670–740 m). The sedimentation rate increases to ~3.9 cm/ky between the middle and late Miocene (~15–6 Ma), consistent with the many thin turbidite beds (Subunits IA–ID; 440–670 m). Here, the sediment is also siderite rich.

Unit I has likely been affected by diagenetic processes. For example, the decrease in the abundance of nannofossils within Subunit ID correlates with an increase in the abundance of single calcite crystals in the sediment. This correlation may indicate that the nannofossils have been dissolved and redeposited as crystalline calcite during diagenesis. Alternately, the decrease may simply indicate a decrease in the overall nannofossil abundance.

A striking feature of Unit I is the alternation of brownish gray to greenish gray intervals along the core. This alternation is most pronounced in Subunits IA–ID (e.g., Cores 368-U1502A-9R through 31R; Figure **F14**), where the alternations occur as thick, approximately bedding-parallel bands, typically 10–50 cm long, with some crosscutting relations between the color change and the bedding.

The number of greenish gray intervals decreases downhole, and Cores 34R through 39R are dominantly brownish in color. In these lower sections, greenish gray intervals usually crosscut the bedding (Figures **F16**, **F17**).

The color change from brownish gray to greenish gray sediment within Subunit IE and the lower part of Subunit ID (Cores 34R through 39R) is evidently related to secondary processes because it occurs along faults, fractures, and silty beds and in burrows (Figure **F16**). Halos of greenish sediment around these features do not extend more than a few centimeters, and the color change is most likely the result of interaction of the oxidized sediment with reducing fluids. Boundaries between the color bands from Subunit IA through the upper part of Subunit ID (Cores 9R through 31R) crosscut biogenic features such as burrows and are sometimes discordant to bedding. However, the boundaries are most often approximately parallel to the bedding. An association of greenish gray sediment with thin silt beds was interpreted as turbidites. Therefore, the cause of the color change in the upper part of the core may be related to (secondary) diagenetic fluids, differences in the input of detrital matter associated with turbidites (e.g., Wilson et al., 1986), changes in bottom water conditions (e.g., Dean et al., 1989), or allocyclic change such as climate (e.g., Gardner et al., 1982).

Interpretation of Units II–VI

The interpretation of Units II and VI is given in **Igneous and metamorphic petrology**, and the interpretation of Unit III is given in **Structural geology**.

Igneous and metamorphic petrology

At Site U1502, we recovered two igneous lithologic units (Figures **F10**, **F11**). Three small, altered basalt fragments were recovered in interval 368-U1502B-2R-1, 26–34 cm (727.96–728.04 m), and they represent igneous Unit 1, which corresponds to lithostratigraphic Unit II (see **Lithostratigraphy**). Hole U1502A terminated in highly altered basalt that comprises the upper part of igneous lithologic Unit 2 (corresponding to lithostratigraphic Unit VI; see **Lithostratigraphy**). This unit was drilled from 749.0 to 750.7 m with a total recovered core length of 1.7 m. A more complete section of igneous lithologic Unit 2 was drilled in Hole U1502B below 739.16 m. This sequence of strongly (hydrothermally) altered aphyric to highly plagioclase phyric basalts has a total drilled thickness of 181.79 m. These basalts are divided into two igneous lithologic subunits, 2a and 2b, based on flow morphology and alteration style (Figure **F24**). Subunit 2a contains an upper sequence of brecciated and fractured massive lava flows (739.16–801.95 m), and Subunit 2b contains a lower sequence of interbedded pillows with lobate and sheet lava flows (801.95–920.95 m).

The igneous lithologic units were described macroscopically and microscopically from thin sections (see **Igneous and metamorphic petrology** in the Expedition 367/368 methods chapter [Sun et al., 2018a]). Chemical analyses were carried out by inductively coupled plasma–atomic emission spectroscopy (ICP-AES) and the handheld pXRF to check for any major compositional changes, both primary and from the alteration process. Alteration assemblages were recognized through a combination of hand specimen examination, thin section examination, and XRF and XRD data.

Igneous lithologic Unit 1 (lithostratigraphic Unit II)

Interval: 368-U1502B-2R-1, 26–34 cm
Depth: 727.96–728.04 m
Thickness: 0.08 m
Lithology: altered basalt
Age: early Miocene–late Oligocene or older

The greenish gray basalt of igneous lithologic Unit 1 is altered, and an assemblage of alteration minerals has replaced most of the primary mineral phases (Figure **F18B**). The aphanitic, fine-grained basalt is nonvesicular to moderately vesicular and contains rare (as large as 6 mm) plagioclase phenocrysts. Alteration of the unit is intense, with less than 50% of the primary crystals remaining, which makes it difficult to determine the primary phases that were originally present. Thin section observations indicate a primary mineralogy of plagioclase with a potential assemblage of pyroxene and Fe-Ti oxides ± mesostasis. The texture is equigranular, and plagioclase laths as large as 1 mm make up approximately 40% of the unit. The groundmass is intersertal with possible altered pyroxene, olivine, and altered glass between a felt of tightly woven, quench-textured plagioclase crystals (Figure **F18B**). The groundmass is replaced by green clay minerals, clinozoisite, zeolites, and Fe (hydr)oxides. Zeolites radially fill pore space, which may represent original vesicularity.

The contacts with lithostratigraphic Units I and III were not recovered due to low overall recovery in this core (2R; Figure **F18A**).

Igneous lithologic Unit 2 (lithostratigraphic Unit VI)

Intervals: 368-U1502A-41R-1, 31 cm, to 41R-CC, 18 cm; 368-U1502B-4R-1, 46 cm, to 37R-4, 141 cm
Depths: Hole U1502A = 749.01–750.67 m; Hole U1502B = 739.16–920.95 m
Thickness: Hole U1502A = 1.71 m; Hole U1502B = 181.79 m
Lithology: highly altered, aphyric to highly plagioclase phyric pillow and sheet basalt, brecciated basalt, and basaltic breccia
Recovery: 75%
Age: late Oligocene–late Eocene or older

Igneous lithologic Unit 2 (lithostratigraphic Unit VI) encompasses a sequence of basaltic breccia, brecciated basalt, pillow basalt, and sheet-flow basalts that range from aphyric to highly plagioclase phyric volcanics and minor chert (Figure **F25**). The entire section of igneous rock recovered in Hole U1502B has undergone some degree of hydrothermal alteration within the temperature range representative for zeolite to greenschist facies conditions (200°–500°C). This alteration varies from complete replacement of the rock, where the original composition and texture are difficult to determine, to replacement of mineral phases with little change to the texture. Glassy pillow rinds are completely replaced, and multiple phases of veining and halos are ubiquitous throughout the rocks.

Igneous lithologic Unit 2 is divided into two subunits based on morphological character and alteration style (Figure **F24**). Subunit 2a, in Cores 368-U1502B-4R through 12R, is dominantly basaltic breccia and brecciated basalt (e.g., interval 5R-CC, 19–29 cm) with strong carbonate alteration forming a matrix between the basalt clasts (Figures **F25**, **F26**). Subunit 2b is moderately to highly altered and less brecciated than Subunit 2a. It comprises pillow lavas alternating with sheet flows. The change between both subunits is gradual, but the boundary was placed at the base of interval 12R-1, 64–105 cm, which was interpreted as hydrothermal breccia and possibly represents a fault gouge (see **Structural geology**).

Figure F24. Lithostratigraphic summary of igneous lithologic Unit 2 showing lithology, lava flow type, and igneous Subunits 2a (basaltic breccia and brecciated basalt) and 2b (interbedded pillow lava and massive/sheet lava flows), Hole U1502B. Intervals of highly (>10% plagioclase phenocrysts) and very highly (>20% plagioclase phenocrysts) phyric basalts, pillow or chilled margins, and intervals sampled for bulk rock ICP-AES analysis are also shown.

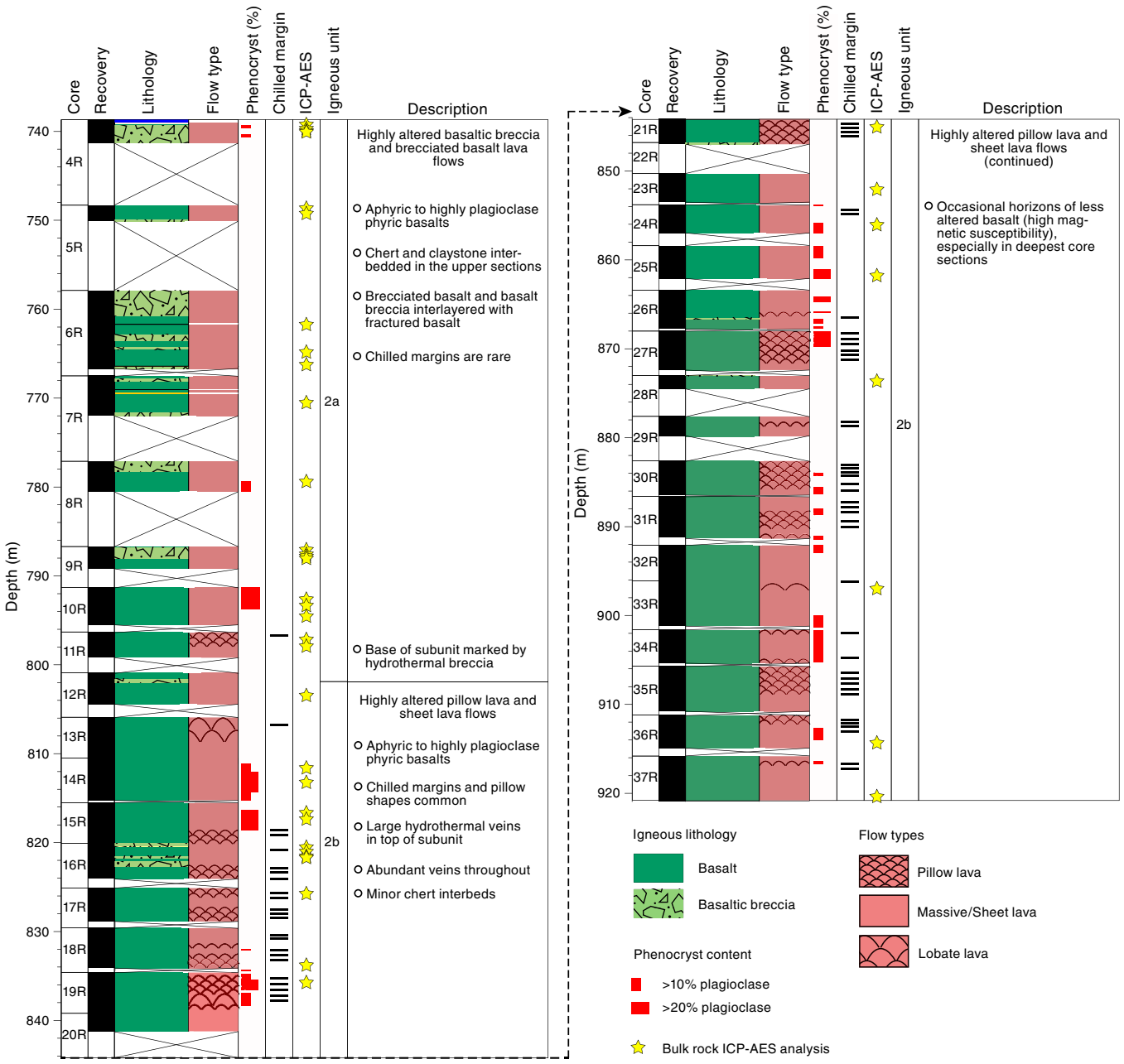

Igneous lithologic Subunit 2a (lithostratigraphic Subunit VIA)

Intervals: 368-U1502A-41R-1, 31 cm, to 41R-CC, 18 cm; 368-U1502B-4R-1, 46 cm, to 12R-1, 105 cm
Depths: Hole U1502A = 749.01–750.67 m; Hole U1502B = 739.16–801.95 m
Lithology: highly altered, brecciated basalt, and basaltic breccia
Age: late Oligocene–late Eocene or older

Igneous Subunit 2a is composed of pale green, yellowish, light gray, light greenish gray, and greenish gray highly altered basaltic breccia and brecciated basalt, with minor sheet basalt, chert, and claystone and very minor pillow basalt (Core 368-U1502B-11R) (Figure F25). The color change along the core in Hole U1502B is mostly subtle, from pale green or yellowish at the contact with lithostratigraphic Unit V (Figure F22) to light greenish gray to greenish gray without an apparent relationship to flow structure. The basaltic breccia in Sections 4R-1 through 6R-3 is a mixture of predominantly basaltic clasts and subordinate light gray and greenish gray claystone and chert in an altered matrix (e.g., Section 6R-1; Figure F23).

The basaltic breccia and brecciated basalt differ in the proportion of matrix and arrangement of clasts (Figure F25). The clasts are either sparsely to moderately porphyritic basalt with altered plagioclase phenocrysts (2%–15%) in an altered groundmass of plagioclase and alteration minerals or aphyric with a groundmass of

Figure F25. Lithologies, Hole U1502B. A. Fractured and highly altered basalt with reddish, yellowish, and light green alteration colors and spots of iron (hydr)oxide, igneous Subunit 2a. B. Highly altered brecciated basalt with jigsaw arrangement of clasts and a matrix of carbonate and clay minerals, Subunit 2a. C. Highly altered basaltic breccia. Clasts are angular and have random, sometimes matrix-supported texture. Matrix is largely made up of dolomite with calcite, albite, clay minerals, quartz, and minor epidote. Rare clasts of fine-grained sedimentary rock occur in some sections. D. Highly plagioclase phyric basalt with up to 50% phenocrysts. Veins of calcite, epidote, and green sheet silicate minerals are also visible. E. Highly altered, moderately plagioclase phyric basalt lobate flow with sparse amygdules filled with green sheet silicate. Pillow margins visible in 19R-3, 70–114 cm (shown in D). F. Highly altered, sparsely plagioclase phyric pillow basalt with a well-preserved pillow that has a very fine grained dark greenish margin and alteration zones that parallel the pillow margin. Pipe vesicles and fractures are perpendicular to the pillow margin. Veins filled with epidote, chlorite, silica, and minor carbonate and pyrite cut the pillow. G. Moderately altered, aphyric basalt flow with sparse vesicles. Note the change to a bluish gray color.

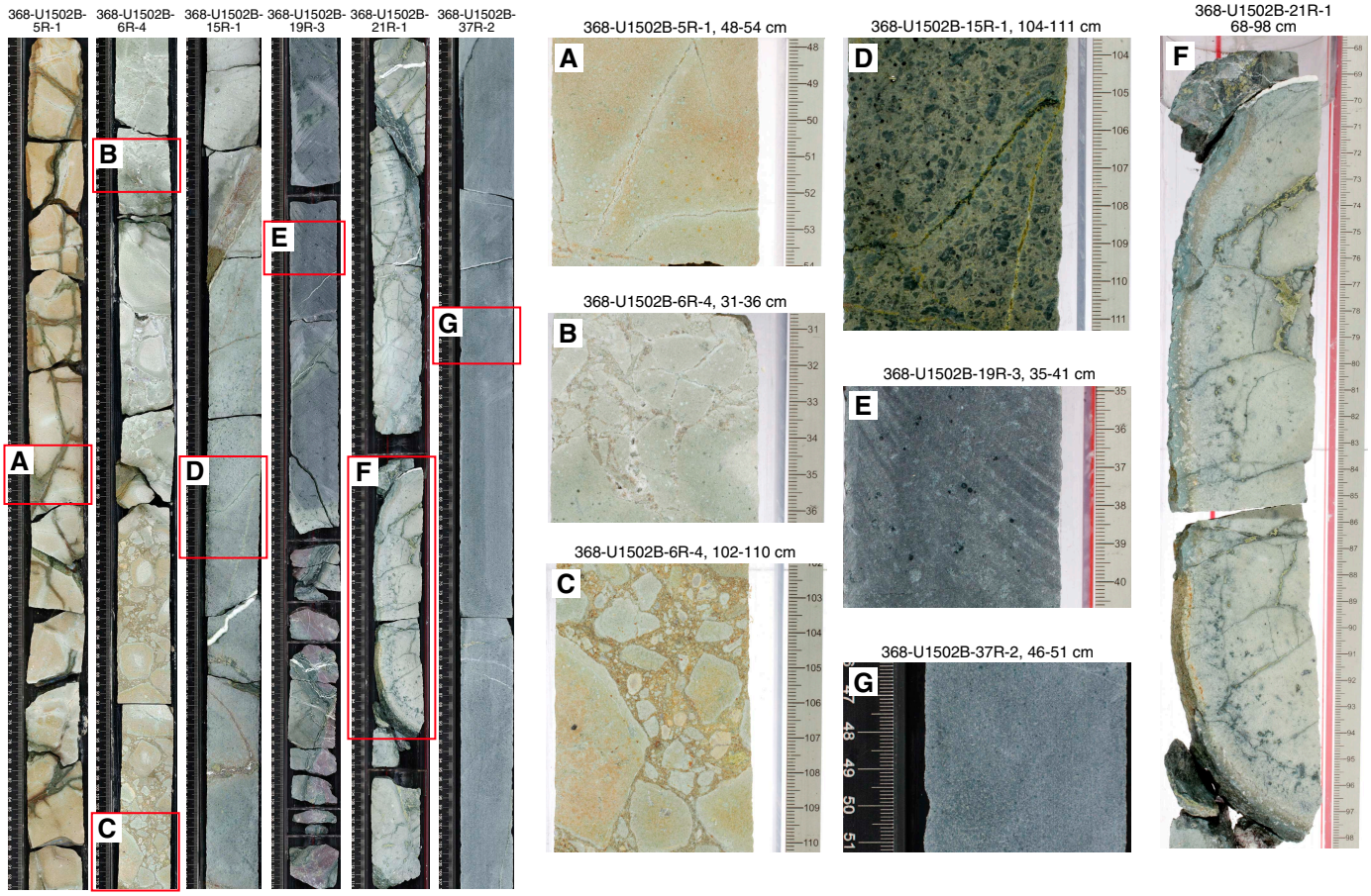

plagioclase and alteration minerals. The groundmass comprises variably altered plagioclase partially replaced by a combination of albite, sericite, calcite or dolomite, clinozoisite, zeolite minerals, Fe hydroxides, and clay minerals, with a felty, intersertal, often tightly interwoven texture (Figure F27B). Plagioclase phenocrysts have a similar alteration assemblage. Potential former interstitial pyroxene may contain some relict fresh areas but is largely replaced by chlorite, zeolite minerals, epidote-group minerals, and clay minerals, with accessory pyrite. The basalt clasts vary from nonvesicular to having approximately 10% amygdules. The amygdules are dark to light green and filled with carbonate, epidote, zeolite minerals, and pyrite (Figure F28B). The matrix of the breccia and veins that cut the brecciated basalt are dominantly pale green-gray to yellowish and reddish brown and consist largely of carbonate (likely dolomite or siderite) crystals with lesser calcite, epidote, chlorite, Fe (hydr)oxides, quartz, zeolite minerals, and clay minerals (Figure F28).

Igneous lithologic Subunit 2b (lithostratigraphic Subunit VIB)

Interval: 368-U1502B-12R-1, 105 cm, to 37R-4, 141 cm
Depth: 801.95–920.95 m
Lithology: highly to moderately altered pillow basalt, lobate basalt, and sheet basalt
Age: late Oligocene–late Eocene or older

Igneous Subunit 2b is composed of (light) greenish gray and bluish gray, highly to moderately altered pillow basalt and sheet basalt, with minor lobate basalts and brecciated basalt (Figure F25). Pillow basalt is recognized by pillow rims and chilled margins in the cores (e.g., interval 19R-1, 117–128 cm; Figures F29, F30). Some pillows show pipe vesicles that are perpendicular to the pillow rim. No glass is preserved in the basalt. The altered pillow rims, which may originally have been glass, are dark greenish gray and completely altered to chlorite, calcite, epidote, zeolite minerals, Fe hydroxides, and clay minerals (Figure F29). Pillow rims are interpreted as having been glassy prior to alteration due to their extremely fine grain size, variolitic texture (variolites are millimeter sized), and different alteration style compared to the pillow cores. Some pillow rims are plagioclase phyric, with often better-preserved plagioclase than in the adjacent basalt. One thin section of a pillow rim has quench-texture plagioclase laths in an altered groundmass with relict perlitic cracking (Figure F29). Alteration minerals highlight the perlitic cracks. The perlitic cracking and quench textures also indicate that

Figure F26. Representative minerals and textures in veins and areas of alteration, igneous Subunit 2b. A. Calcite (Cal)-rich vein crosscutting altered basalt with plagioclase (Pl) and clay minerals (XPL). B, C. Composite epidote (Ep)-rich vein with chlorite (Chl) crosscut by calcite vein, both crosscutting altered basalt with plagioclase, chlorite, and clay minerals (B: plane-polarized light [PPL]; C: XPL). D–F. Highly altered basalt crosscut by vein with an assemblage of epidote, quartz (Qtz), pyrite (Py), plagioclase, clay minerals, and zeolite minerals (D: PPL; E: XPL; F: reflected light). G, H. Highly altered basalt with an assemblage of plagioclase, chlorite, pyrite, clay minerals, and zeolite minerals (G: PPL; H: XPL). I. Altered plagioclase phenocryst, partially replaced with veins of calcite, chlorite, and epidote in an altered groundmass of plagioclase, chlorite, epidote, clay minerals, and zeolite minerals (XPL).

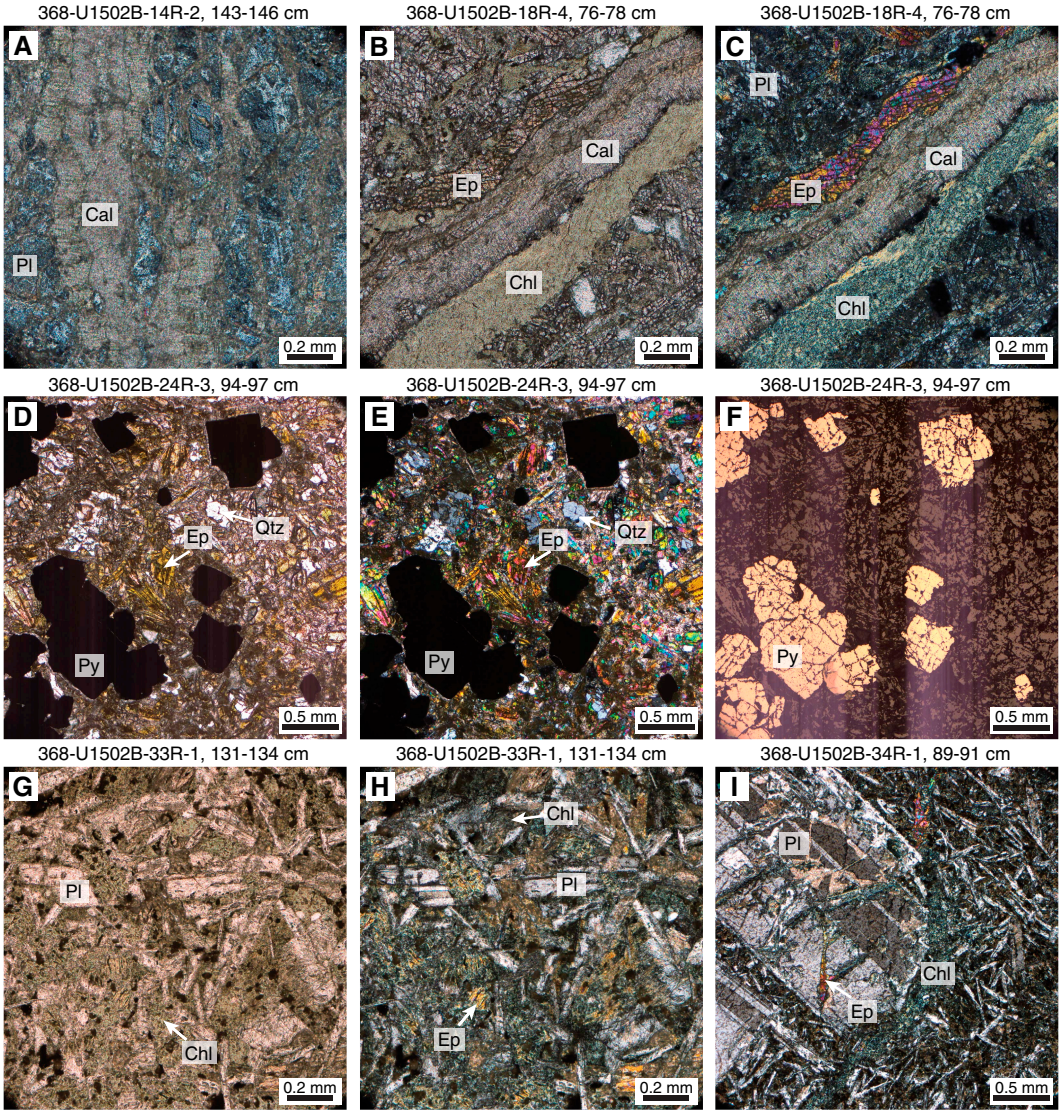

the pillow rims were glassy prior to alteration. Very thin (<1 mm) carbonate veins occur mostly parallel to the pillow margin within the altered glass (e.g., interval 17R-1, 33–43 cm).

Sheet flows were recognized by the absence of pillow or intrusive margins. Rare flow boundaries are defined by chilled margins and areas of brecciation and drilling-induced fragmentation that may be brecciated flow tops. Depending on the degree of alteration, the basalt is greenish gray (high alteration) to bluish gray in some intervals and patches (e.g., interval 35R-3, 103–120 cm) that we interpret as less altered (consistent with thin section observations).

Subunit 2b basalt varies from sparsely to highly plagioclase phyric (e.g., interval 19R-3, 35–41 cm), partially reflecting glomeroporphyritic assemblages, with only minor intervals of equigranular and aphyric texture (Figure **F25**). The texture and petrography (Figure **F27C–F27J**) of Subunit 2b is similar to the clasts in the Subunit 2a breccia and brecciated basalt. Subunit 2b includes intervals with as much as 50% tabular to equant plagioclase phenocrysts (e.g., interval 15R-1, 104–111 cm; Figure **F25D**). Chlorite and sulfides are more abundant in thin sections of Subunit 2b, and several of the samples are also high in epidote (Figure **F26G–F26I**). Pseudomorphs, replaced by a brown mineral with first-order interference colors, probably a clay mineral such as saponite, may represent either olivine or filled vesicles (Figure **F27E**). Interstitial areas that may have been glass now show an amorphous gray, isotropic mineral and opaque minerals (Figure **F27I, F27J**). Carbonate and zeolite minerals occur in the groundmass, but they are not as abundant as in Subunit 2a. Veins are filled with dark and apple green minerals (chlorite and epidote), carbonates (dolomite, calcite, and siderite), zeolite minerals, pyrite, quartz, and secondary feldspar (Figures **F28**, **F31**).

The coarse-grained basalt flow in Sections 37R-2 and 37R-3 contains several thin (0.5–1.5 cm wide), fine-grained gray basaltic

Figure F27. Representative minerals and textures, igneous lithologic Units 1 and 2. A. Altered basalt with an intersertal, tightly interwoven texture, Unit 1 (PPL). Plagioclase laths (Pl) are partly altered and display quench textures (e.g., swallow-tail). Interstitial material consists of secondary minerals (clay and zeolite minerals and Fe [hydr]oxides). B. Very fine grained altered basalt with intersertal texture, Subunit 2a (XPL). Plagioclase laths are partly altered and display quench textures (e.g., swallow-tail and sheath). Interstitial material consists of secondary minerals (clay and zeolite minerals and Fe [hydr]oxides). C, D. Highly to moderately altered, highly plagioclase phyric basalt with intersertal texture, Subunit 2b (C: PPL; D: XPL). Plagioclase phenocrysts (Pl) are relatively fresh. Interstitial material between altered plagioclase grains in the groundmass is an assemblage of epidote, sericite, chlorite, carbonate, clay minerals, and opaques (Op). E, F. Sparsely plagioclase phyric (Pl) basalt with intersertal groundmass of altered plagioclase and an alteration assemblage that includes chlorite, epidote (Ep), sericite, quartz, zeolite minerals, and minor pyrite and chalcopyrite, Subunit 2b (E: PPL; F: XPL). Regular areas of chlorite and zeolite minerals may be pseudomorphs after a ferromagnesian mineral or amygdules (former olivine [Ol]/vesicle). G, H. Highly altered, highly plagioclase phyric basalt with intersertal texture, Subunit 2b (G: PPL; H: XPL). Interstitial material between altered plagioclase grains is an assemblage of epidote, sericite, chlorite (Chl), carbonate, clay minerals, and pyrite. Note the thin rims on the twinned plagioclase phenocrysts (Pl). I, J. Fine and even-grained, moderately altered, sparsely plagioclase phyric (Pl) basalt, Subunit 2b (I: PPL; J: XPL). Quench-textured plagioclase and an interstitial assemblage of chlorite (Chl), epidote (Ep), clay minerals, and minor pyrite.

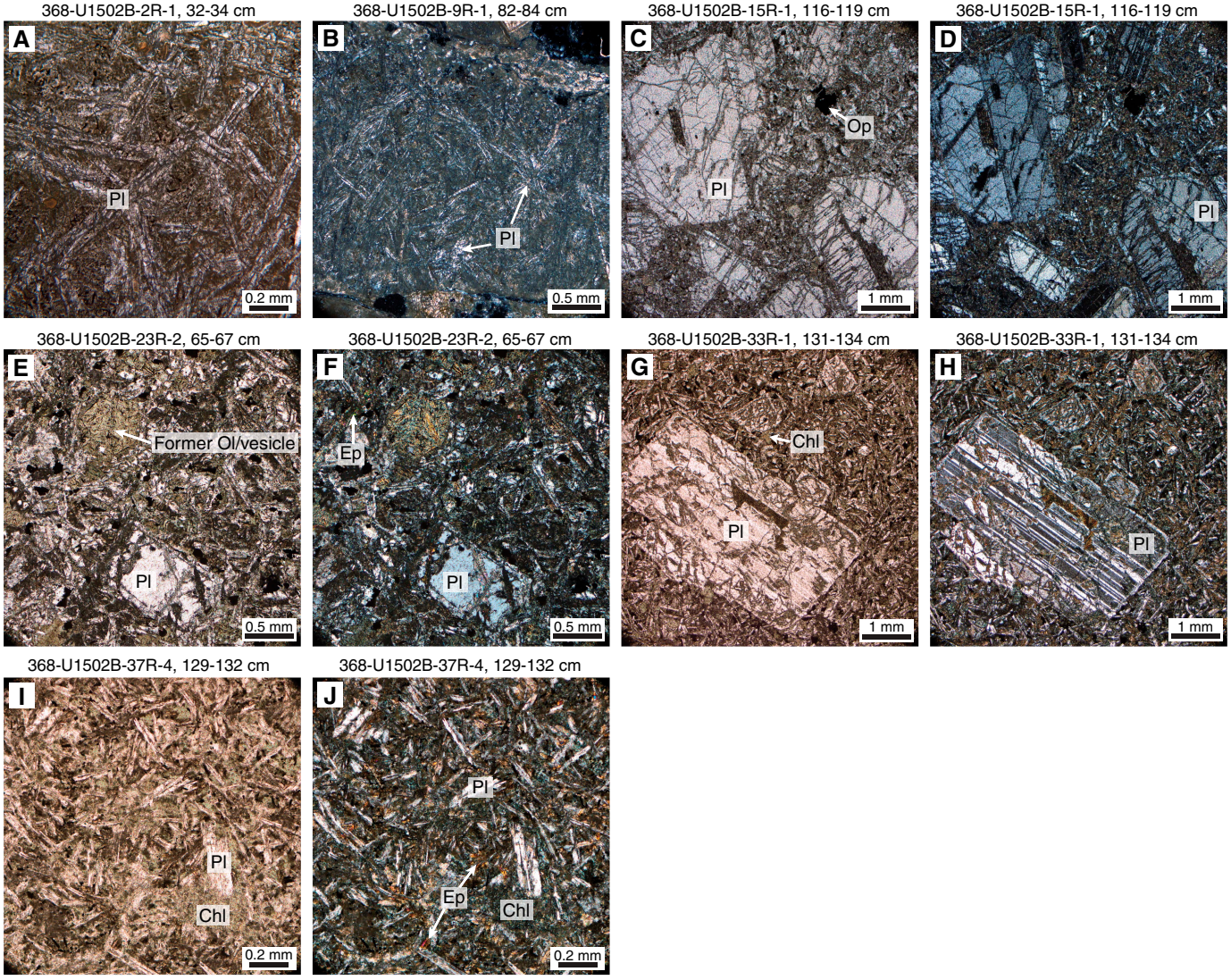

veins with irregular margins (intervals 37R-2, 134–137 cm; 37R-3, 0–2 cm; and 37R-3, 3–10 cm). Analyses using the pXRF show that, relative to the coarse-grained host lava, these veins have lower TiO_2 (1.1 wt% versus 1.7 wt%) and Ni (20 ppm versus 40 ppm), as well as higher Zr (400 ppm versus 170 ppm). These data indicate that the veins have more evolved compositions than the host lava and therefore may represent segregation veins that formed just prior to final solidification of the flow.

Veins and alteration

The pervasive greenish gray color of the samples indicates that the basalt is altered from its original mineralogy (e.g., Figure **F29**). Plagioclase, as phenocrysts and in the groundmass, appears only partially altered in some thin sections (Figures **F27**, **F26**), and XRD indicates that it is labradorite (Figure **F32**). XRD data also indicates abundant albite, and therefore in some sections the plagioclase may now be albitized. The plagioclase is sericitized or altered to clay minerals in other thin sections. Some relict areas of pyroxene may

Figure F28. Representative minerals and textures in veins and areas of alteration, igneous Subunit 2a. A. Dolomite (Dol), chlorite (Chl), quartz, and clay minerals in a vein crosscutting altered plagioclase phyric basalt (PPL). B. Amygdule filled with a brown zeolite mineral in altered basalt; amygdule has a rim rich in Fe hydroxide minerals (PPL). C. Matrix in a basaltic breccia with dolomite rhombs and Fe hydroxide minerals and minor clay minerals, calcite, epidote, and zeolite minerals (PPL). D. Nodules of radiating calcite (Cal) crystals with minor dolomite, clay minerals, quartz, and epidote (PPL). E. Vein (Type 1) with calcite, quartz (Qtz), and pyrite (Py) in altered basalt with chlorite (XPL). F. Matrix in a breccia at the base of subunit (XPL); dolomite and/or siderite (Dol/Sd) with quartz, pyrite, and clay minerals are predominant in the breccia matrix.

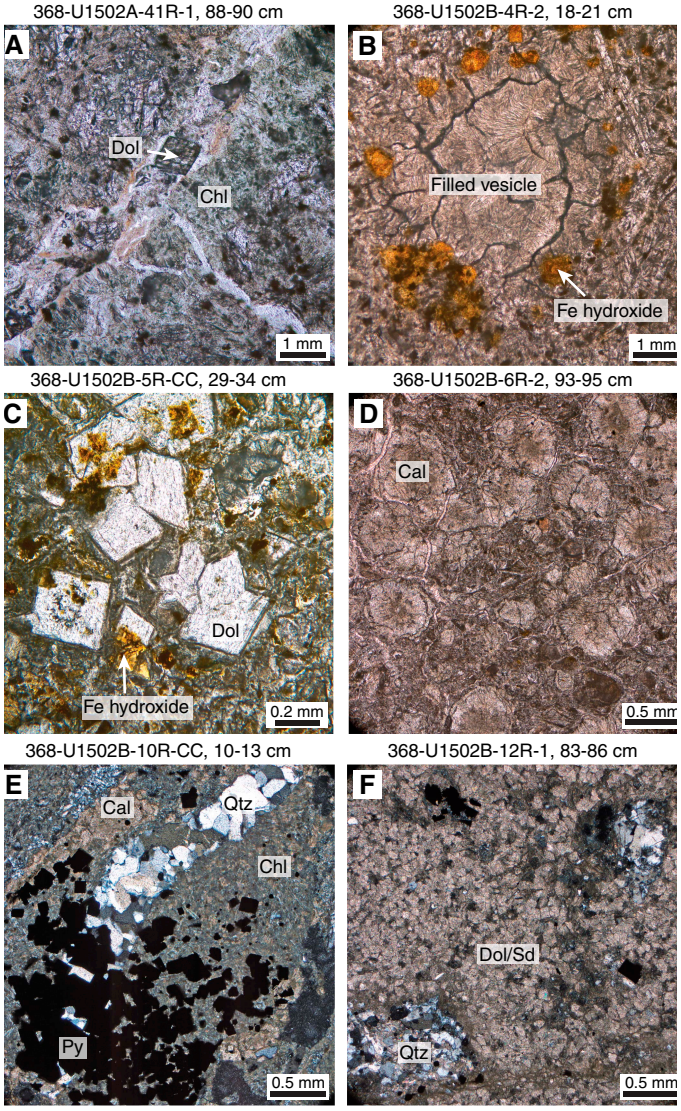

be visible in thin section, as well as some Fe-Ti oxides, but no other primary magmatic minerals are present. The green color of the basalt is most likely due to the presence of epidote, green zeolite minerals, and green clay minerals in the upper sections and chlorite in the lower sections (Figures **F26**, **F28**, **F31**). Other common alteration minerals are calcite, dolomite, quartz, chalcedony, and Fe (hydr)oxide (Figures **F26**, **F28**). Pyrite is pervasive and is found in the fractured basalt, in the matrix and clasts of the basalt breccia, in pillows, as vesicle filling, and in veins (Figures **F26**, **F31**). In addition, minor amounts of chalcopyrite, sphalerite, and covellite are found in the groundmass and veins in Cores 23R through 32R.

There are at least three vein types. Type 1 is white to green to black in color, with cryptocrystalline silica, epidote, Fe (hydr)oxide, carbonates (dolomite/siderite), and traces of pyrite (e.g., intervals 10R-1, 68–85 cm, and 13R-4, 90–100 cm; Figures **F26B, F26C**, **F28E**). Some veins have less abundant quartz and are green to grayish green, whereas others have red jasper. Type 2 is pyrite rich with pistachio green and dark green minerals, probably epidote and zeolite minerals and quartz (e.g., interval 13R-3, 110–120 cm; Figure **F26D–F26F**). Type 3 veins are rich in calcite with minor epidote and pyrite (e.g., interval 19R-2, 50–68 cm) (Figures **F26A–F26C**, **F31**).

Bulk mineralogy

The bulk mineralogy results of XRD analyses on igneous samples from Site U1502 are listed in Table **T3** and shown in Figures **F31** and **F32**. Igneous Unit 2 basalts are composed mainly of plagioclase (mean = 78%), with minor amounts of augite (mean = 11%), quartz (mean = 6%), and clay minerals (smectite; mean = ~1%) (Figure **F32**; Table **T3**). Pyrite is found both in veins and as a disseminated phase in numerous basalt intervals within igneous Unit 2, and it is a common accessory phase in many of the basalt XRD analyses. Differences in additional mineral phases are found between Subunits 2a and 2b. Chlorite is not common in Subunit 2a basalts, and when detected, it is <1%. In contrast, most basalts in Subunit 2b contain chlorite, and its abundance increases with depth, reaching 5% in Section 368-U1502B-37R-4. Many basalt samples in Subunit 2a contain as much as 3% calcite and/or dolomite, and two samples (intervals 7R-1, 23–25 cm, and 7R-2, 122–124 cm) are notable for having 9%–12% siderite. Kaolinite is found in the lowermost 7 m of Subunit 2a and throughout Subunit 2b, where its abundance increases downhole from ~1% to 8%. XRD samples taken from highly fragmented (drilling-disturbed) intervals (e.g., 10R-2, 125–127 cm; 10R-3, 16–18 cm; and 11R-2, 4–6 cm) generally have lower amounts of plagioclase and higher amounts of quartz, pyrite, and siderite ± dolomite.

XRD analyses were made to confirm the identity of epidote (olive green) and chlorite (dark green) in veins from intervals 16R-2, 15–19 cm, and 16R-1, 93–96 cm, respectively (see Figure **F31**). Samples from interval 16R-2, 15–19 cm, contain 21% epidote (with 8% chlorite because it was difficult to hand pick a clean sample of the epidote), and samples from interval 16R-2, 15–19 cm, contain 13% chlorite plus feldspar and clay minerals.

Chemical composition (pXRF and XRF core scanning)

Compositional analyses of the igneous lithologic Unit 2 basalts, as well as veins and clasts, were made directly on the archive half of the core using the handheld pXRF (see **Igneous and metamorphic petrology** in the Expedition 367/368 methods chapter [Sun et al., 2018a]). The average pXRF sample spacing was about every 1 m. Additional representative samples were also taken for major and trace element analysis by ICP-AES (see **Geochemistry**). The pXRF data are shown in Figure **F33** and Table **T4**. Subunit 2a has lower MgO (<4 wt%) and MnO (<0.1 wt%) contents than Subunit 2b (MgO = >4 wt%; MnO = >0.1 wt%), and on average it also has lower Fe_2O_3 (4.8 ± 3.1 wt% versus 8.5 ± 2.6 wt%). This difference is interpreted as a secondary feature related to the pervasive alteration of Subunit 2a because there are no significant differences in abun-

Figure F29. Pillow lavas, igneous Subunit 2b. A. Partial pillow showing altered rim. Formerly glassy areas in the rim are altered to an assemblage of dominantly chlorite, kaolinite, and smectite (see Figure F31 for XRD pattern of this material). Altered rim is plagioclase phyric, and pipe vesicles in whitish altered basalt close to the rim run perpendicular to it. Detail of rim is shown in C. B. Two partial pillows. Rims are altered to green minerals, including chlorite, clay, and zeolite minerals cut by veins of calcite and epidote. Pipe vesicles are perpendicular to pillow rims. Light green alteration minerals occur in a zone parallel to the pillow rim and as a halo to an epidote-rich vein. C. Pillow rim displayed in A with highly altered plagioclase phenocrysts (now albite, sericite, epidote, and calcite) in an altered groundmass of quenched plagioclase, calcite, clay minerals, epidote, pyrite, and zeolite minerals (PPL). D. Pillow rim with highly altered plagioclase phenocrysts (now albite, sericite, and calcite) in a formerly glassy groundmass now altered to clay minerals, zeolite minerals, epidote, pyrite, and calcite and plagioclase microlites (PPL). E. Pillow rim with highly altered plagioclase microlites in a formerly glassy groundmass now altered to epidote, clay minerals, zeolite minerals, pyrite, and calcite (PPL). Relict perlitic cracking is highlighted by the texture of the alteration minerals. F. Pillow rim with highly altered plagioclase phenocrysts and microlites (quench textured) in a formerly glassy groundmass now altered to epidote, clay minerals, zeolite minerals, pyrite, and calcite (XPL). Relict perlitic cracking is highlighted by the texture of the alteration minerals.

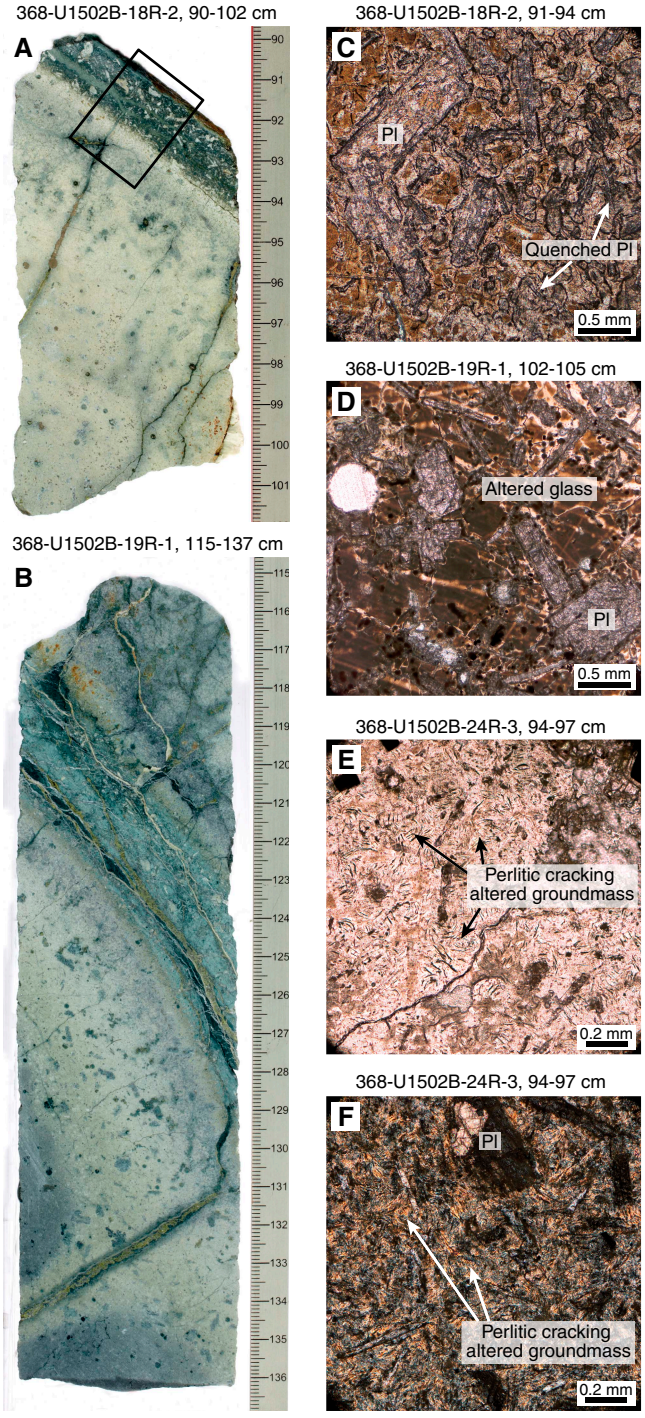

Figure F30. Core composites of igneous lithologic Unit 2 basalts, highlighting all observed chilled contacts and (glassy) margins, as well as flow margins (ends of flow reflected by the presence of breccias or chert [for example] without a chilled contact), Hole U1502B. (Continued on next five pages.)

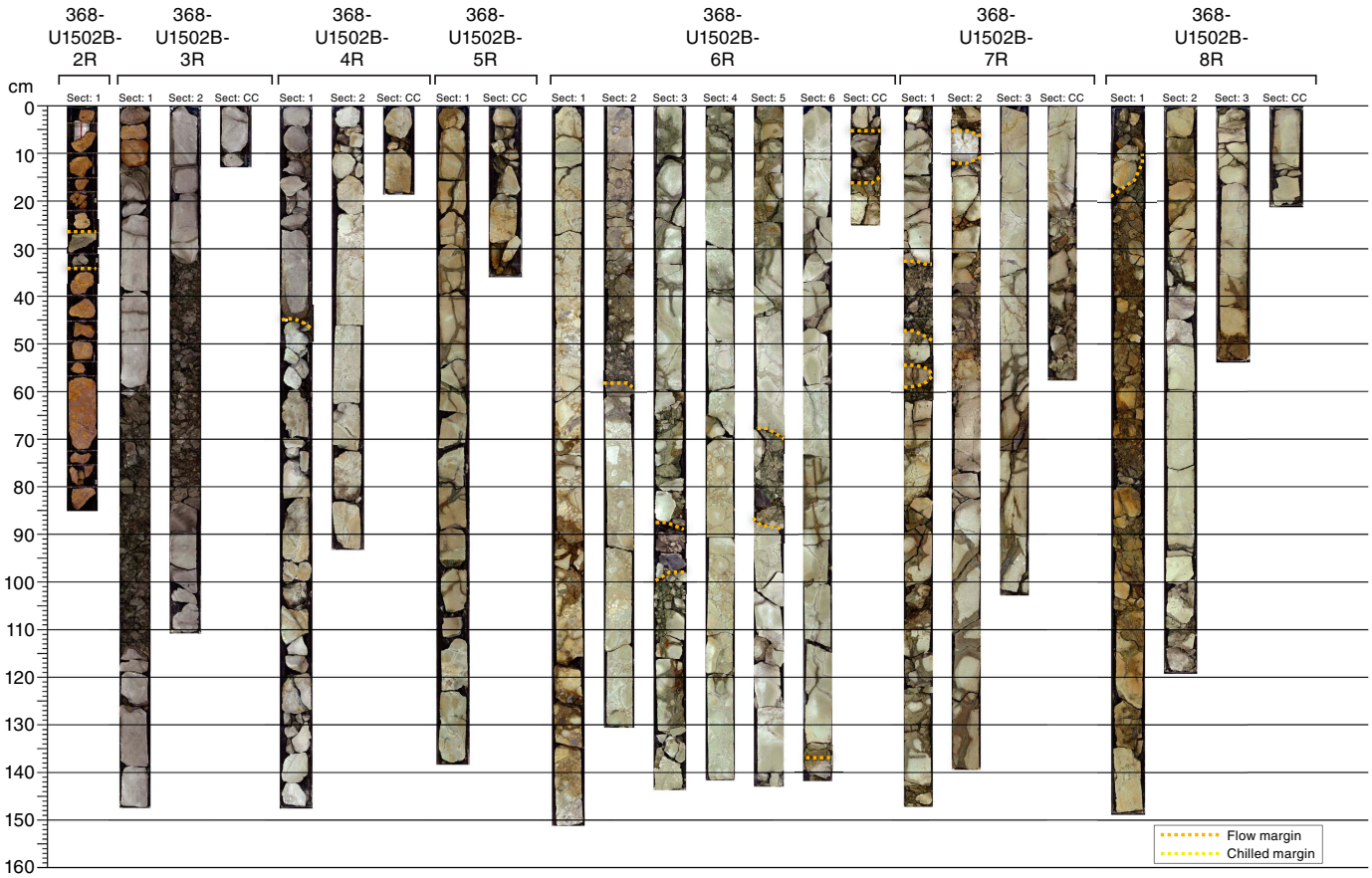

dances of alteration-resistant elements such as Ti and Zr between these two units. Subunit 2a has TiO_2 contents of 2.2 ± 0.5 wt% and Zr concentrations of 161 ± 44 ppm, whereas Subunit 2b has TiO_2 contents of 1.8 ± 0.4 wt% and Zr concentrations of 131 ± 32 ppm. Although Subunit 2b has MgO contents more typical of basalts, other elements show that these basalts are still strongly affected by secondary alteration. CaO and Fe_2O_3 have wide ranges (CaO = 1–10 wt%; Fe_2O_3 = 3–14 wt%), and the highest values tend to be found in zones of significantly higher magnetic susceptibility (Figure **F33**) (see also **Physical properties**) that might indicate areas of less intense alteration.

Elevated S values (as high as 6.4 wt%) in many analyses are consistent with the widespread sulfide mineralization seen throughout igneous lithologic Unit 2. Visual inspection of the core shows that the sulfide mineralization is dominated by pyrite, but other sulfide minerals were also found: sphalerite ([Zn,Fe]S) in interval 368-U1502B-23R-3, 0-86 cm, chalcopyrite ($CuFeS_2$) in Sections 24R and 25R; and covellite (CuS) in interval 14R-2, 143–146 cm. The pXRF results can be used to determine the extent of Zn and Cu mobilization within the hydrothermal system at Site U1502. Cores 33R through 37R have high magnetic susceptibility and low Zn concentrations (average = 112 ± 22 ppm) that are typical of oceanic basalts (e.g., White and Klein, 2014). In the overlying cores (32R through 30R), there is a sudden jump to values as high as 800 ppm, and Zn remains at variably elevated levels until the upper part of Subunit 2a (Cores 4R–8R) (Figure **F33**), confirming significant pervasive mobilization of Zn. In contrast, there is little evidence for significant Cu mobilization. Cu concentrations average ~80 ppm with values mostly below 300 ppm, and only one analysis gave high Cu (interval 17R-1, 57 cm = 2035 ppm).

Variations in ratios of immobile incompatible elements, such as Ti and Zr, can be used to assess whether there were any changes in parental magma compositions. The Ti/Zr ratio is the same in Subunit 2a (85 ± 14) and Subunit 2b (83 ± 13), implying that there were no significant changes in the melt generation process during the period of eruption of the basalts recovered at Site U1502. However, within Subunit 2b a jump in Ti/Zr ratios at 865 m (91 ± 12 above and 77 ± 10 below this depth) might indicate a small change in magma chemistry. Small-scale flow-by-flow differences in Zr and TiO_2 abundances are most likely due to variations in the extent of magmatic differentiation. The few measurements made on igneous lithologic Unit 1 show compositions quite distinct from those of igneous lithologic Unit 2, with a higher average Ti/Zr ratio of 218 ± 8 and Nb concentration of 19.4 ± 0.7 ppm (compared to 10.8 ± 2.6 ppm for Unit 2), as well as higher P_2O_5 and Cr but lower Zr and V abundances.

A high-resolution XRF core scanning data set for the Site U1502 volcanic rock section was produced onshore (see **Igneous and metamorphic petrology** in the Expedition 367/368 methods chapter [Sun et al., 2018a]) and can be retrieved as shipboard data from the IODP database (**http://web.iodp.tamu.edu/LORE**). At the time of this publication, assessment and discussion of this data set have not been concluded yet.

Figure F30 (continued). (Continued on next page.)

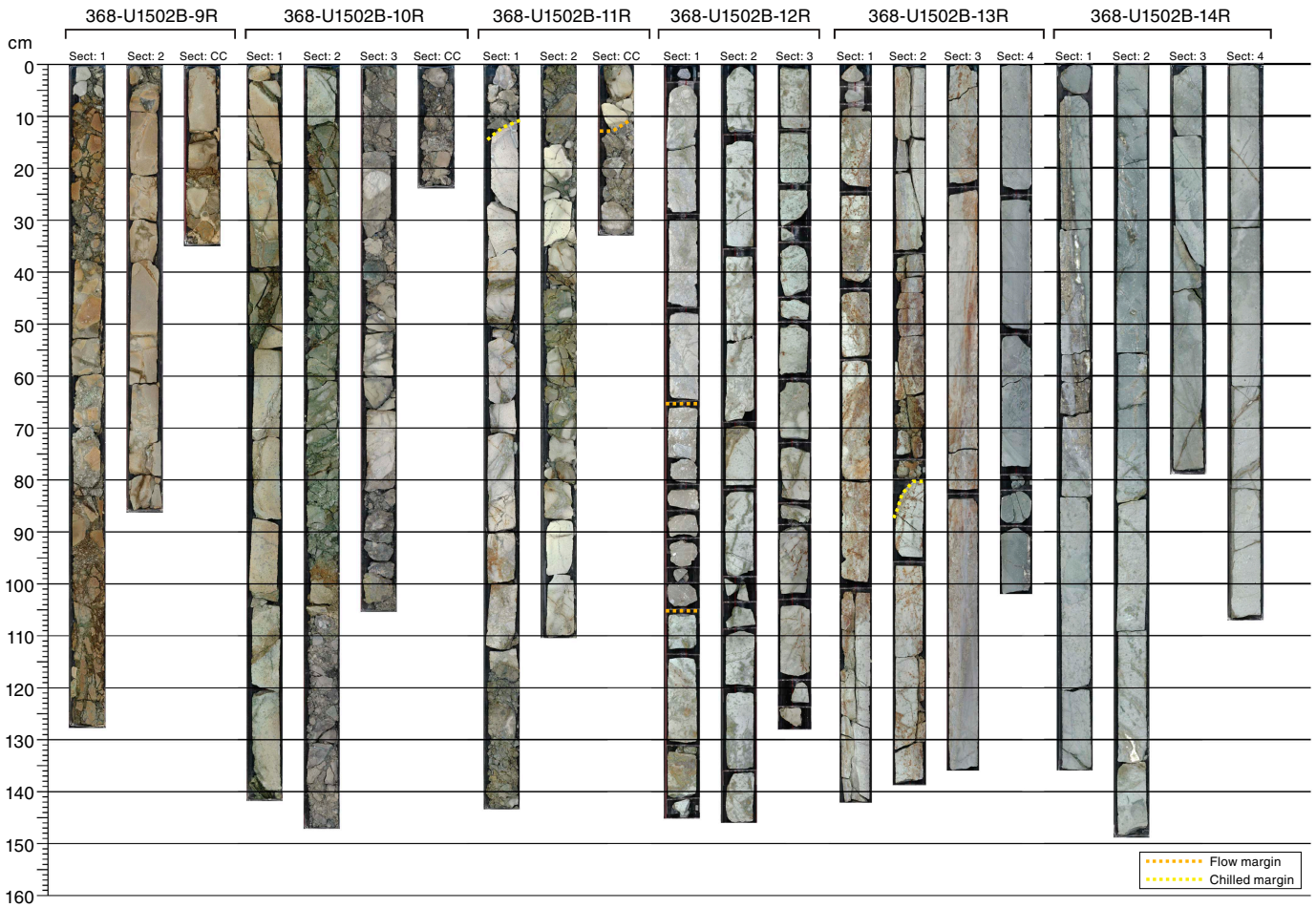

Interpretation

Igneous lithologic Unit 2 shows typical mid-ocean ridge basalt (MORB) flow morphologies with pillow basalts with quenched rims and sheet lavas, as well as a typical MORB mineralogy. The presence of agglutinated benthic foraminifers in the overlying Unit V and pillow basalts indicate that Unit 2 was emplaced in a marine environment. The agglutinated foraminifers indicate abyssal water depths (see **Biostratigraphy**). A combination of pillow basalts and sheet flows is common in submarine volcanic settings, with the change from sheet to pillow flows probably controlled by the magma discharge rate (Gregg and Fink, 1995; Fink, 2017) and the slope of the ridge axis (Kennish and Lutz, 1998). Some eruption sequences start with high flow rates and sheet morphologies and change to pillow flows as the rate declines (McClinton et al., 2014). For example, the 2005–2006 eruption on the East Pacific Rise (Soule et al., 2007) produced a flow that changed from inflated lobate and sheet morphologies in the flow interiors to pillow lavas at terminal flow fronts. This change was probably controlled by a reduction in the flow rate and a gentler slope away from the ridge axis (e.g., Kennish and Lutz, 1998). The chemistry of the freshest basalts (in areas with high magnetic susceptibility) also overlaps with typical MORB lava compositions (e.g., White and Klein, 2014). Compared to Site U1500 lavas (see **Igneous and metamorphic petrology** in the Site U1500 chapter [Stock et al., 2018]), igneous lithologic Unit 2 samples have slightly higher TiO_2 content (1.72 wt% versus 1.51 wt%), which may indicate a slightly more enriched source or a more differentiated magma. Subunit 2b has multiple intervals where the plagioclase phenocryst content is more than 10% and in places as high as 50% (Figure **F24**). Basalts with >10% plagioclase phenocrysts are known as plagioclase ultraphyric basalts (PUBs) (Cullen et al., 1989) and are typically found at mid-ocean ridges with ultraslow to intermediate spreading rates and in off-axis seamounts (Flower, 1980; Lange et al., 2013), consistent with the spreading rates of 35–50 mm/y inferred for the SCS (Briais et al., 1993). Recent models (Lange et al., 2013) argue that PUBs form through magma interaction with preexisting lower crustal plagioclase-rich cumulates, and they are erupted only when ascent rates are sufficiently high (>0.5 cm/s) and where the conduit system lacks or bypasses an axial magma chamber.

The combination of intense alteration, multiple veins, and brecciation in the basalt sequence, particularly in Subunit 2a (e.g., interval 368-U1502B-4R-2, 84–93 cm), suggests alteration due to hydrothermal fluids. The abundant pyrite indicates that the fluids were rich in sulfur. Hydrothermal fluids can lead to hydraulic fracturing, which may have caused some of the brecciation in the unit (e.g., Jébrak, 1997). The alteration mineral assemblage belongs to the albite-epidote to lower greenschist facies and suggests high-temperature water-rock interaction. The presence of epidote and quartz shows that this interaction took place at temperatures higher than ~200°C (Reyes, 1990). This style of alteration is referred to as propylitic. The intensity of both alteration and brecciation de-

Figure F30 (continued). (Continued on next page.)

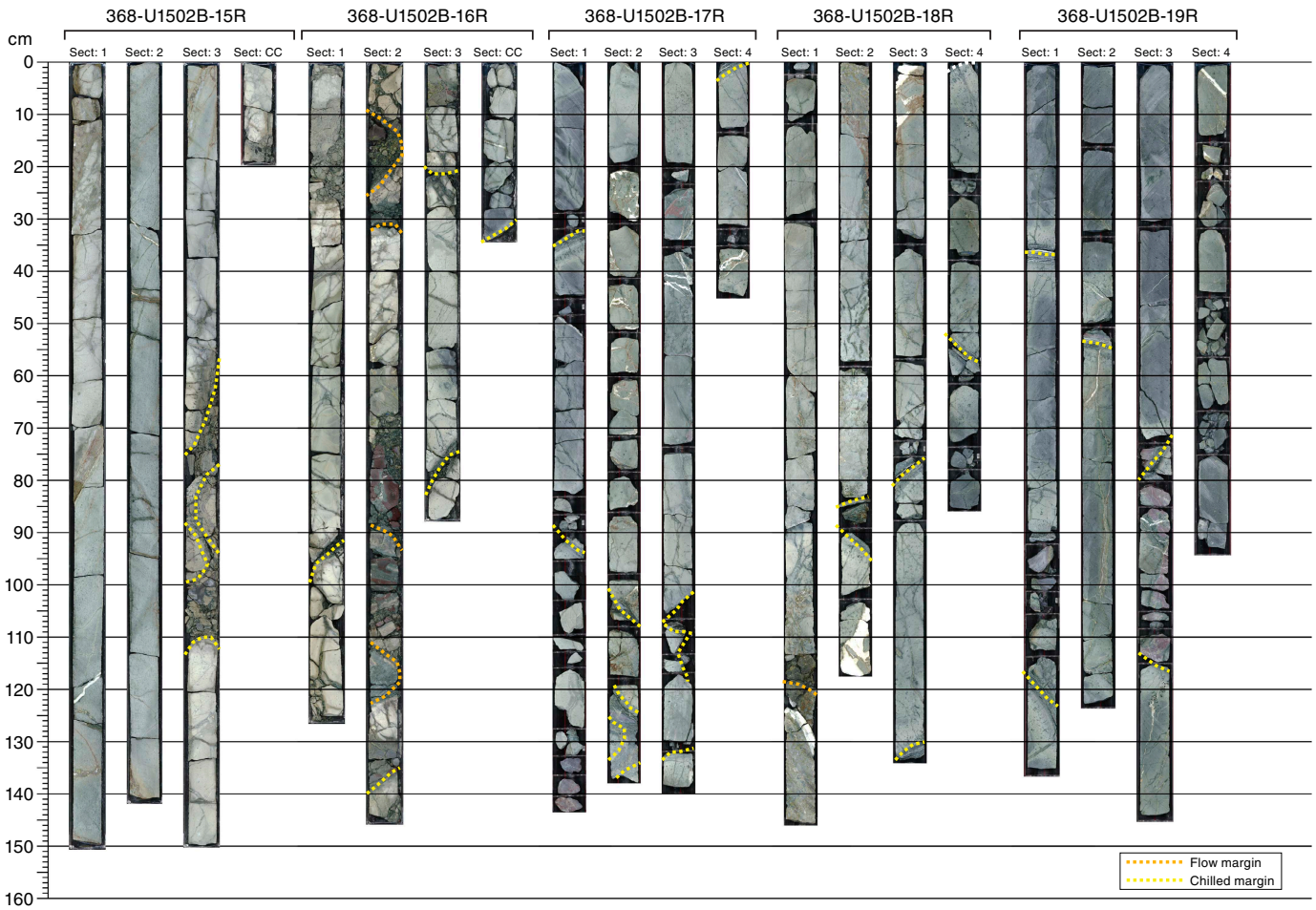

creases with depth in the volcanic pile. Alteration in Subunit 2b is dominated by epidote, sulfides, and chlorite, whereas Subunit 2a shows more carbonate and clay alteration, which may indicate lower temperature alteration for the upper section of Unit 2.

The age of igneous lithologic Unit 2 can only be inferred from the biostratigraphy of the overlying sedimentary units because the sparse sedimentary material found between the basalts in the upper part of Unit 2 is barren of microfossils. Lithostratigraphic Unit IV (Core 368-U1502A-40R) is late Oligocene in age based on nannofossils and diatoms, and Unit V (Core 368-U1520B-3R) is inferred to be late Eocene or older in age based on agglutinated benthic foraminifers (see **Biostratigraphy**).

Igneous lithologic Unit 1 is only represented by a few basaltic fragments found between the early Miocene–late Oligocene lithostratigraphic Unit II and the late Oligocene lithostratigraphic Unit IV and could represent a unit with a younger age than igneous lithologic Unit 2. It is possible that igneous lithologic Unit 1 might be older than the late Oligocene if these fragments represent reworked material derived from nearby exposures of the underlying Unit 2 basalts. Nevertheless, there seem to be petrographic differences between igneous lithologic Units 1 and 2, although they are difficult to determine due to the high degree of alteration in both units. Unit 1 may have contained more olivine as phenocrysts, now completely altered, than Unit 2. In addition, preliminary shipboard analyses using ICP-AES and the pXRF indicate some distinct compositional differences between Units 1 and 2. Igneous lithologic Unit 1 has higher TiO_2, P_2O_5, Cr, and Nb contents and lower Zr and V contents than Unit 2. Another possible reworked source for the Unit 1 basalt fragments are late Oligocene–early Miocene basalts recovered from oil exploration wells (BY2 and BY7-1) in Baiyun Sag, about 200 km north-northwest of Site U1502 (Zhao et al., 2016). The relationship between igneous lithologic Units I and 2 and other basalts in the surrounding area will be evaluated further with postexpedition geochemical analysis.

Figure F30 (continued). (Continued on next page.)

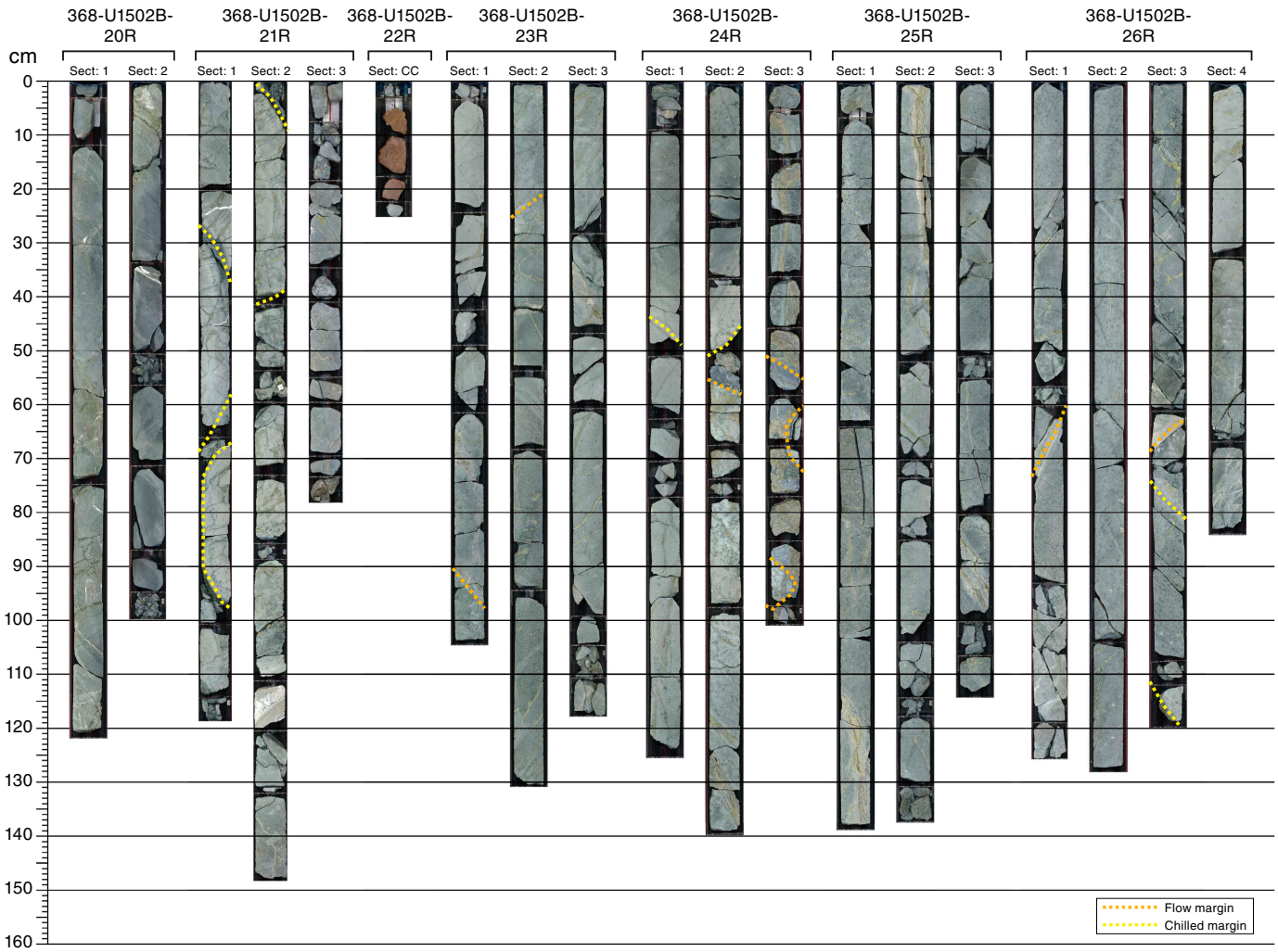

Figure F30 (continued). (Continued on next page.)

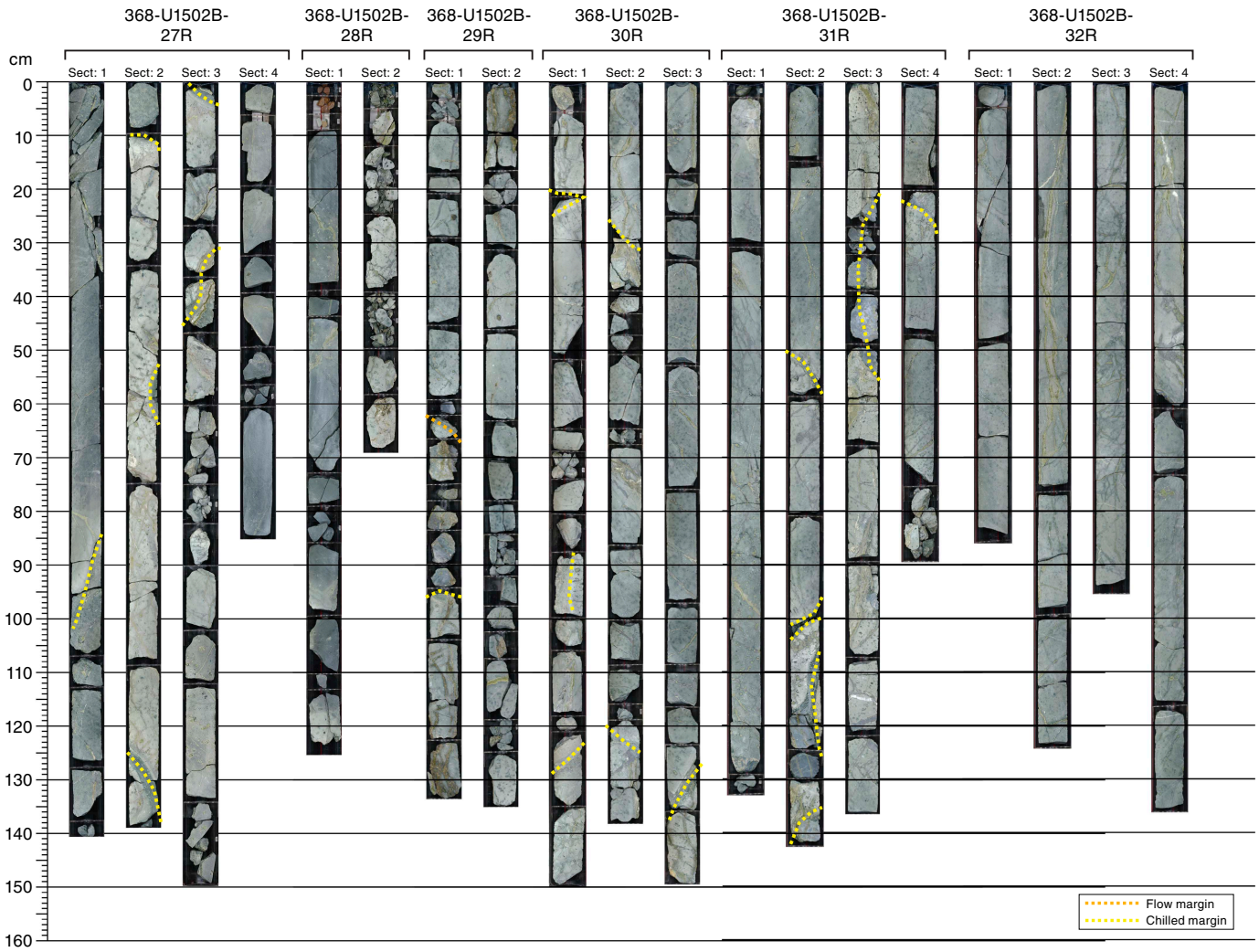

Figure F30 (continued).

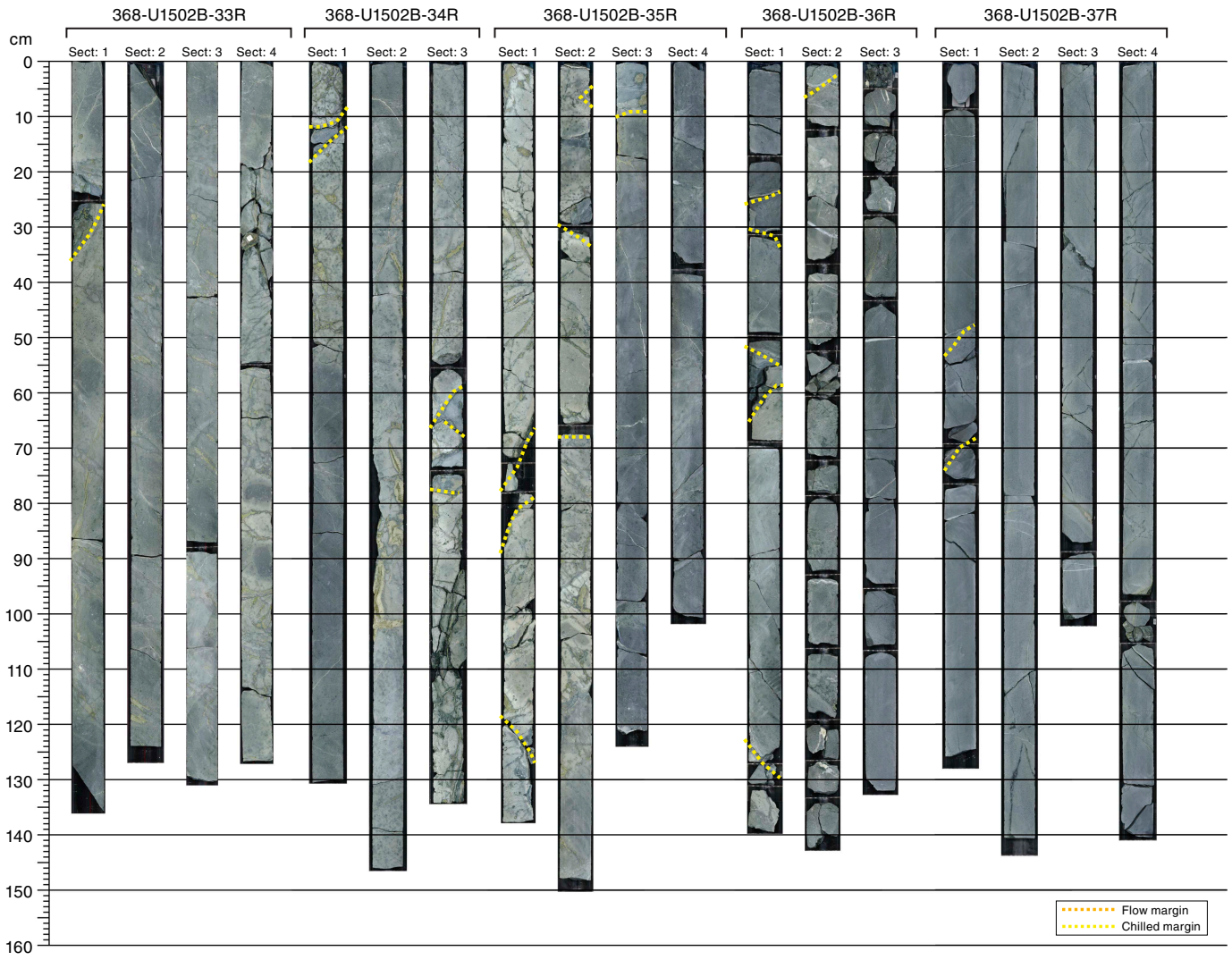

Figure F31. XRD pattern and close-up core image of (A) an epidote-rich light green vein and (B) a chlorite-rich dark green vein.

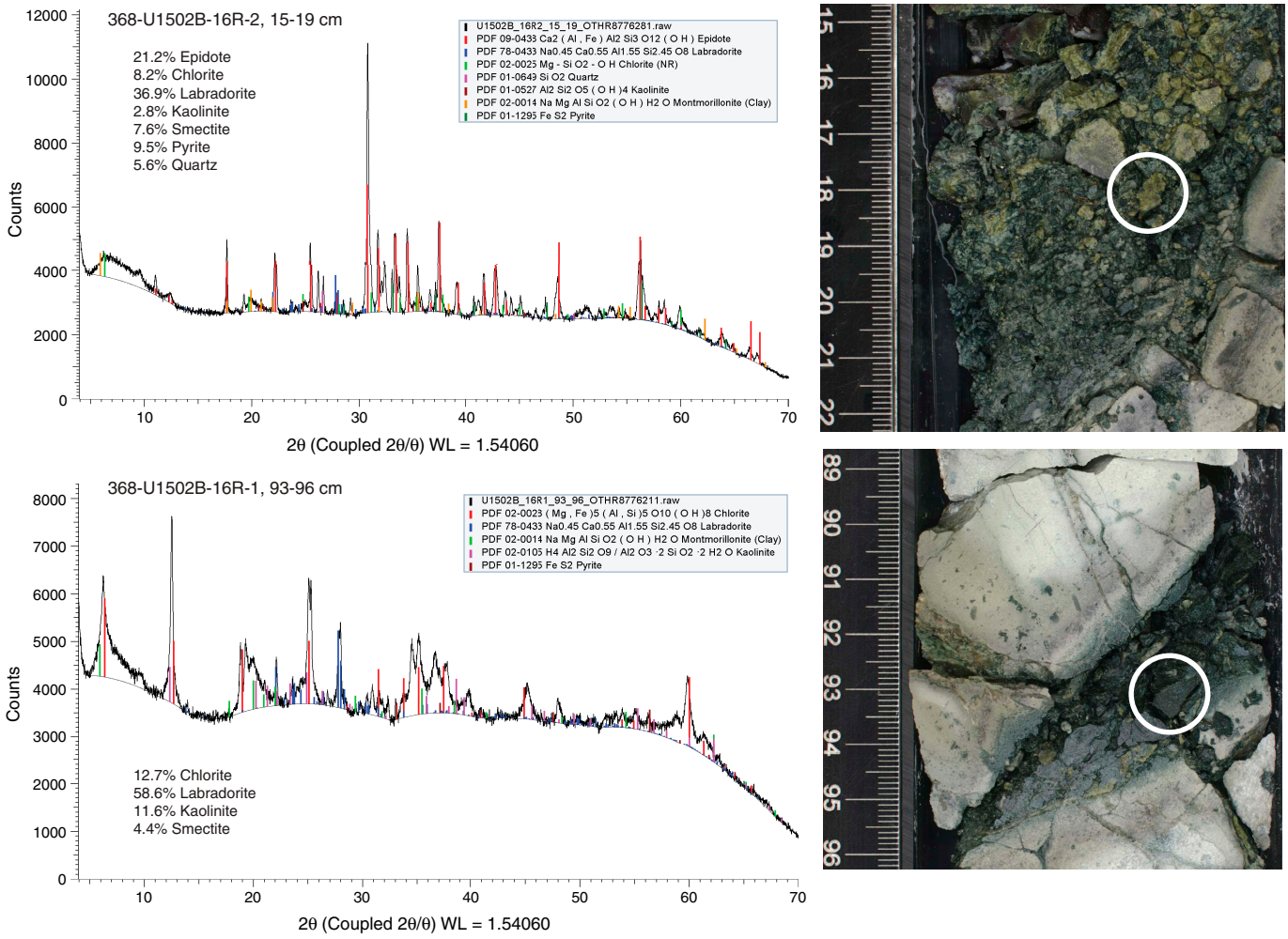

Figure F32. XRD bulk mineralogy, Hole U1502B.

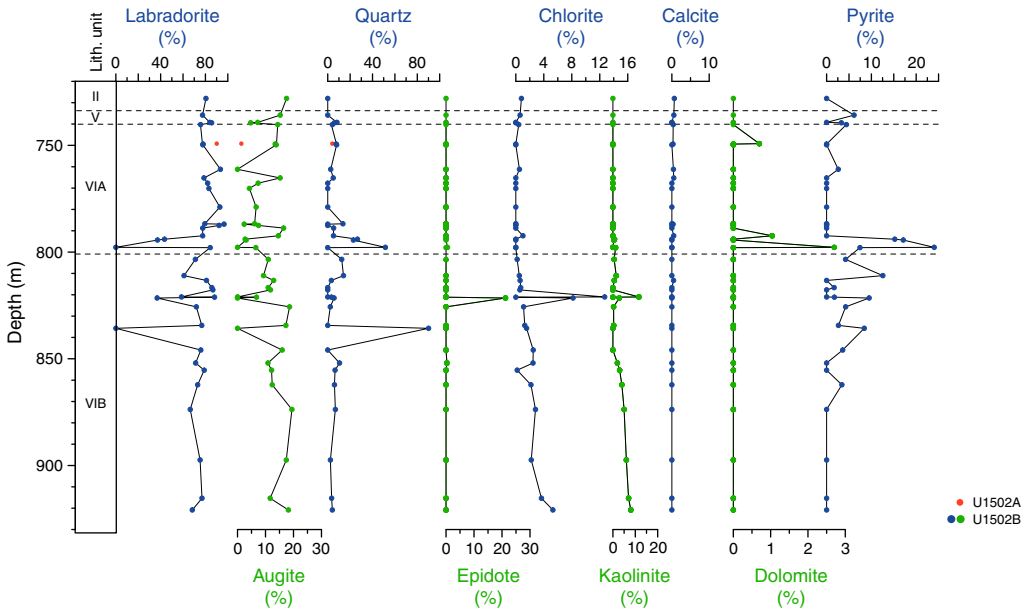

Table T3. Mineral percentages, Hole U1502B. **View table in PDF format. Download table in CSV format.**

Figure F33. pXRF compositional data for selected major element oxides and trace elements: Fe_2O_3, TiO_2/Zr, MgO, CaO, and Zn. Gray (in background) = magnetic susceptibility data measured on whole-round sections, vertical dashed lines = composition of average MORB, stars = thin section sample locations.

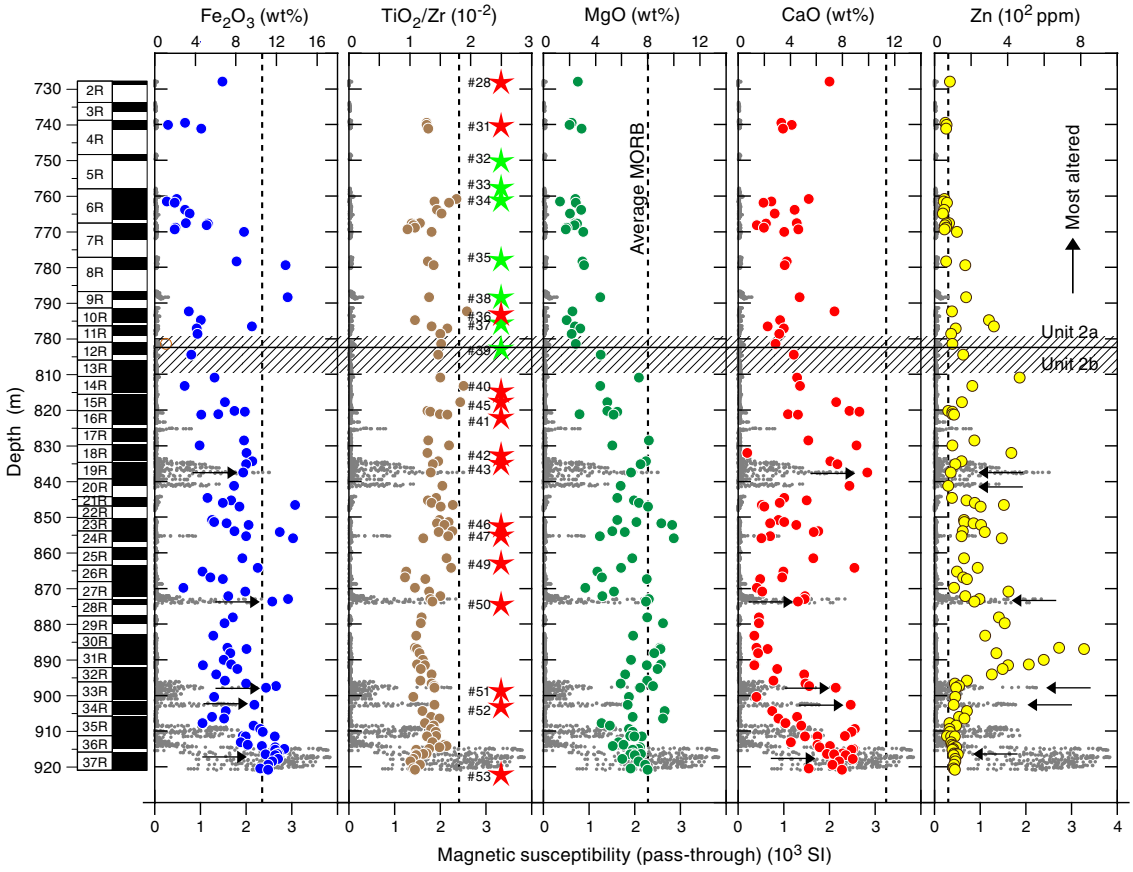

Table T4. Major element oxides and minor elements in rocks, Site U1502. **View table in PDF format. Download table in CSV format.**

Structural geology

Site U1502 is located on Ridge A, which represents a northeast-southwest–trending basement high within the COT zone, about 40 km east of Site U1499 and 15 km north of Site U1500 (Figure **F1**).

Lithostratigraphic Unit I structures

Deformation structures are scarce in lithostratigraphic Unit I downhole to Core 368-U1502A-37R. This upper interval is weakly deformed to undeformed and characterized by horizontal to slightly dipping bedding (Figure **F34**). However, Sections 25R-3 through 25R-5 contain a convolutely bedded sequence (Figure **F35**), indicating soft-sediment deformation during mass movements (i.e., slump folding) before lithification of the sediments. Below Core 25R, a slight but consistent tilt with apparent dips on split core surfaces up to ~10° is recorded (Figure **F34**).

Starting from Core 37R at ~700 mbsf, a gradual increase in deformation structures was observed. Cores 37R, 38R, and 39R are characterized by microfaults evidenced by down-dip plunging striations and slickensides on exposed fracture surfaces at an average frequency of about two per meter (Figure **F36**). These fractures are systematically associated with greenish halos from 3 to 40 mm wide within the well-consolidated brownish clay.

Lithostratigraphic Unit II structures

No deformation structures were encountered in Unit II.

Lithostratigraphic Unit III structures

Lithostratigraphic Unit III consists of an extremely silicified breccia that was poorly recovered with only a few decimeters in Sections 368-U1502B-2R-1 and 3R-1 and a single fall-in clast in the uppermost centimeters of Core 368-U1502A-40R (**Lithostratigraphy**). This breccia is essentially composed of quartz showing a fractal grain-size distribution evident in both macroscopic and microscopic observations, with a maximum clast size of ~2 cm and minimum clast size in the submillimeter scale (Figure **F19**). Quartz microstructures in the silicified matrix of this breccia show some domains governed by partially annealed fractal grain-size distribution. Other domains in the breccia may preserve evidence for initial sedimentary structures or microfossil shapes that were silicified, suggesting important fluid circulation. However, the nature of this breccia as either sedimentary, tectonic, or hydrothermal remains unconstrained.

Figure F34. Locations of apparent dip measurements of bedding, convolute bedding, fractures and microfaults, Hole U1502A.

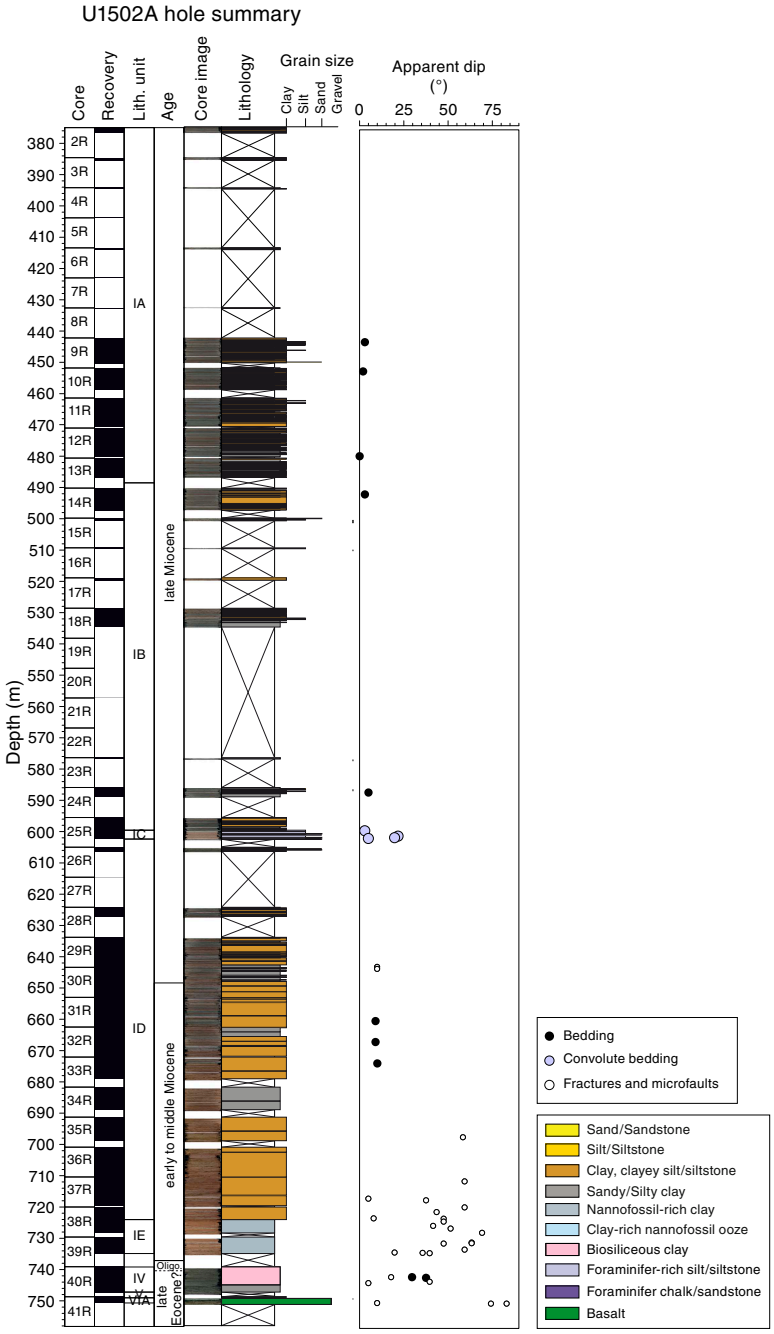

Lithostratigraphic Unit IV structures

In Core 368-U1502A-40R, a small-scale transition from distributed to localized shear in unlithified sediments of Unit IV (biosiliceous-rich clay; see **Lithostratigraphy**) was encountered. Tilted bedding (~20°) with diffuse shear bands and a sigma clast in Section 40R-3 (Figures **F34**, **F37B, F37C**) indicate passive creep. From Section 40R-1 to Section 40R-5, an increasing occurrence of microfaults with striations and slickensides grades into a microfault network strongly affected by drilling disturbance (Figure **F37D, F37E**).

Lithostratigraphic Unit V structures

No deformation structures were encountered in Unit V.

Lithostratigraphic Unit VI structures

Unit VI is composed of basalts that were heterogeneously affected by brecciation and veining associated with the circulation of hydrothermal fluids. Subunit VIA is dominated by brecciated basalts/basaltic breccias, whereas Subunit VIB comprises a rather coherent series of lava flows crosscut by a multistage network of polymineralic veins.

Figure F35. A. Core composite image comprising two lithostratigraphic subunit boundaries (IB/IC and IC/ID), Hole U1502A. Subunit IC consists of a convolutely bedded sequence indicative for mass transport deposition. B. Detail of centimeter-scale slump folds.

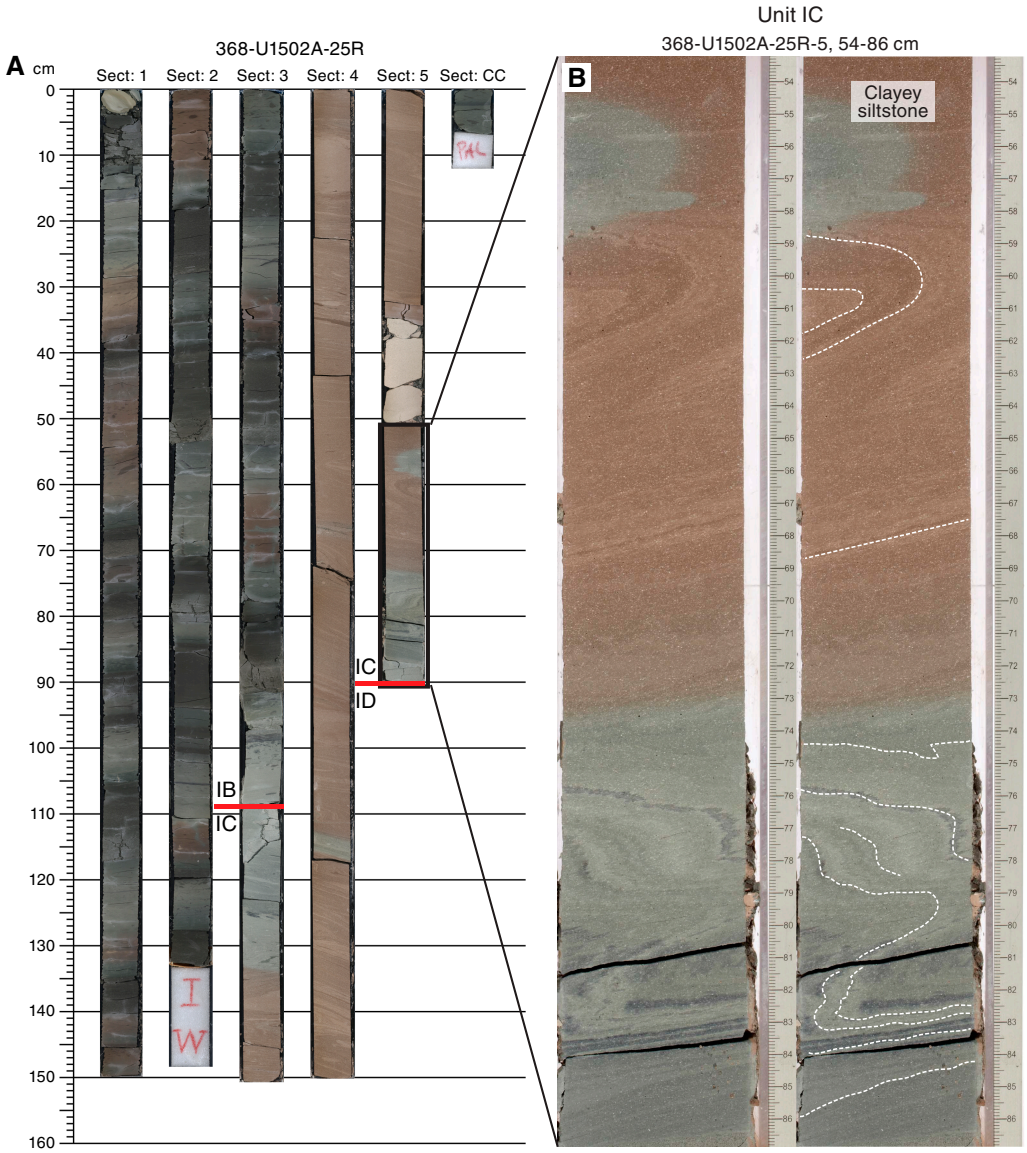

Subunit VIA

Core 368-U1502A-41R, representing the very top of Unit VI, contains severely fractured and fragmented basalt (Figure **F38**). The fractures are locally filled by fine-grained unconsolidated greenish rocks. In Cores 368-U1502B-4R through 12R, Subunit VIA is characterized by diverse brecciated horizons associated with veins and microcracks (Figures **F39**, **F40**). Depending on the intensity of fragmentation and the clast/matrix ratio, the rocks are referred to as brecciated basalt or basaltic breccia (for more information about lithology definitions, see **Igneous and metamorphic petrology** in the Expedition 367/368 methods chapter [Sun et al., 2018a]). Such breccias contain angular clasts of variable size up to ~8 cm and are generally clast supported. A commonly observed feature is the jigsaw-puzzle structure, suggesting possible in situ fragmentation (Figure **F39A, F39B**).

Macro- and microscopic observations show that the breccia clasts consist mainly of sparsely to moderately plagioclase phyric basalts that were hydrothermally altered to variable degrees. However, some breccia varieties also contain sedimentary components (e.g., chert) as clasts and/or matrix constituents. In places, a possible initial veining episode predating the eventual brecciation is preserved in breccia clasts that are fragmented by silica, epidote, and carbonate veins (Figure **F40A, F40B**). The matrix between individual clasts is made of euhedral Ca-, Mg-, and/or Fe-carbonate crystals in a fine-grained groundmass of zeolite, clay minerals, and various Fe oxides (e.g., Section 368-U1502B-5R-CC; thin section [TS] 32; Figure **F40C, F40D**). The contact between the basalt clasts and the matrix is generally sharp with clearly defined edges. The matrix itself provides no evidence for a shear-induced brittle fabric (e.g., a Riedel-type fracture pattern). Locally, however, carbonate crystals are anhedral and exhibit undulose extinction at clast/matrix contacts, indicating a strained crystal lattice (Figure **F40E, F40F**). Thus, formation of such breccias likely involved fluid-assisted fracturing of basalt with limited displacement.

Section 368-U1502B-12R-1 displays a gradual transition from a clast-supported brecciated basalt to a matrix-supported basaltic

Figure F36. Microfaults in Subunit ID, Hole U1502A. A. Core composite image highlighting consistent steep orientation and high occurrence frequency (~2/m) of observed microfaults. B, C. Details of microfaults outlined in A showing striations/slickensides on exposed surfaces. Microfaults are consistently associated with greenish alteration zones of up to 4 cm width.

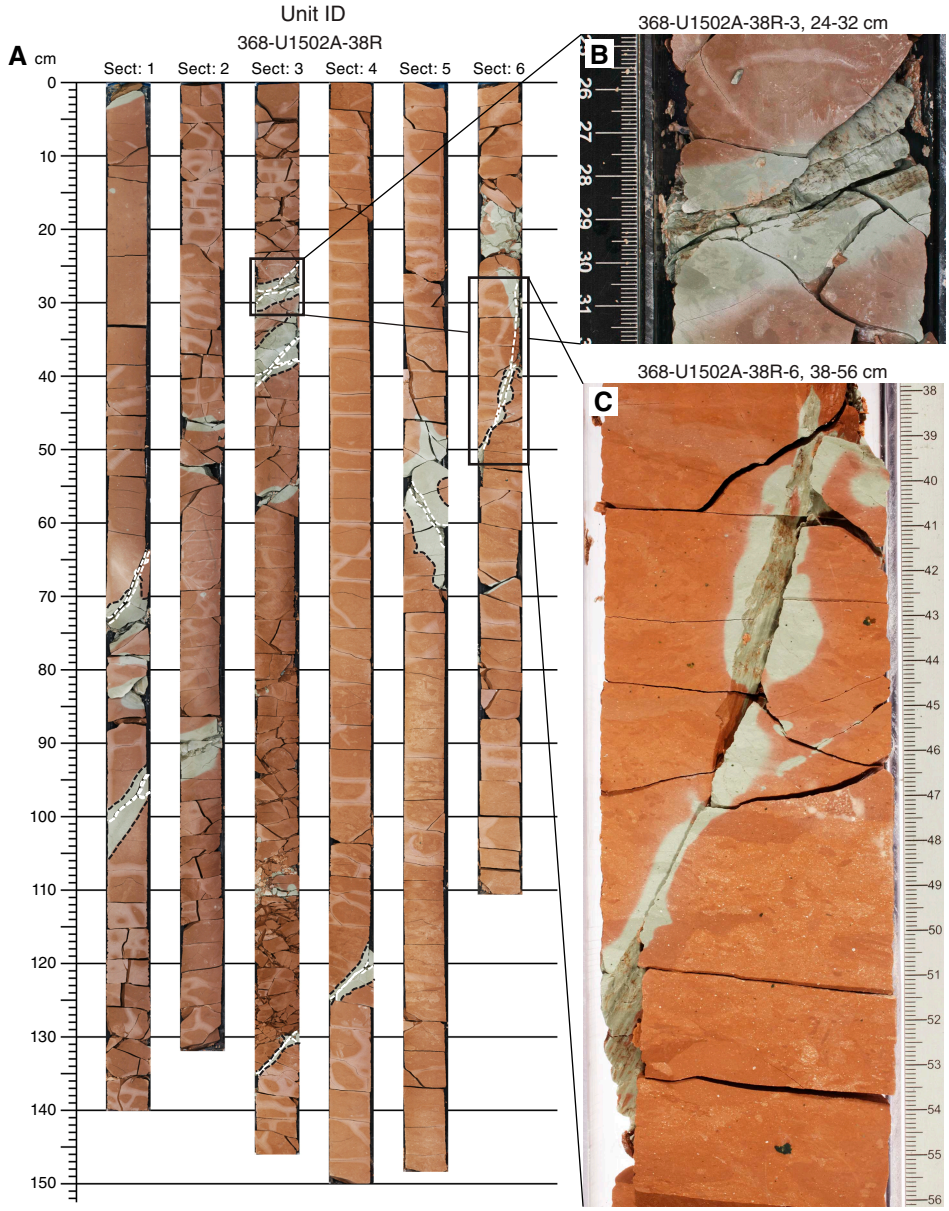

breccia (Figure F39). This transition is accompanied by progressive rounding of clasts and severe grain-size reduction within the breccia matrix. Macroscopically, the structure of this rock therefore falls into our first-order definition of a fault gouge. However, thin section observations cannot provide support for a deformation process involving significant shear movements because the original matrix geometry is erased by static overgrowth of euhedral carbonate crystals, most likely as precipitates from a circulating fluid postdating the brecciation process (Figure F40G, F40H). Locally, the healed matrix is cut by a second generation of veins, indicating that multiple pulses of fluid-assisted fracturing were involved in the formation of this breccia.

Subunit VIB

Subunit VIA is characterized by small-scale veins and microcracks only a few millimeters wide, showing a complex network generally in direct relation with the brecciation. In contrast, Subunit VIB is characterized by a progressive decrease of breccia horizons and the development of different vein types, almost always polymineralic. Notably, the composition and orientation of the veins change throughout Subunit VIB (Figure F41). Although numerous small-scale veins often related with major ones can be observed, only the main veins are represented in this figure, therefore providing only a first-order trend. In Cores 368-U1502B-12R through 37R, three vein types were identified: (1) composite silica-rich vein, (2) composite epidote-rich vein, and (3) composite carbonate and/or silica-rich vein. For more information about their mineralogy, see **Igneous and metamorphic petrology**.

The first category includes silica-rich veins that are not particularly abundant. They are characterized by irregular shapes and single to branched connectivity (Figures F42, F43) and often appear

Figure F37. Deformation structures in Unit IV, Hole U1502A. A. Core composite image with locations of detailed images in B–E. B, C. Distributed shear geometries with shear bands, sigma clast, and tilted bedding. D. Striations/slickensides on exposed microfault surface. E. Dense network of shear bands and fractures enhanced by drilling disturbance.

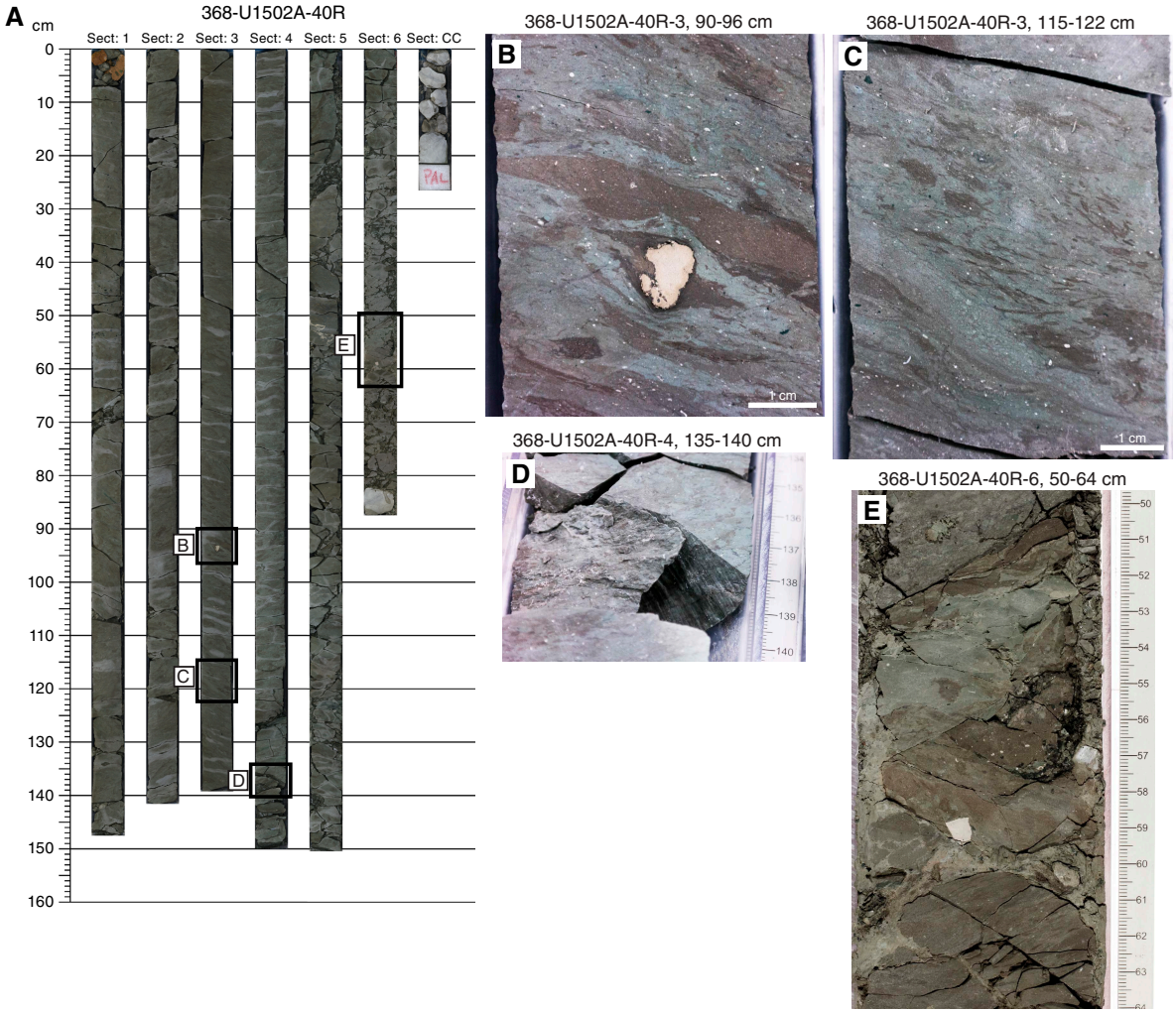

crosscut by composite epidote-rich veins (Figure **F42A**), whereas locally the opposite relations are also inferred. These epidote-rich veins, observed from Core 10R downhole, are associated with sulfides, silica, chlorite, various clay minerals, and zeolites. These veins are generally vertical to subvertical, from 1 to 25 mm wide, and typically irregular in shape. Individual veins are continuous for only short distances (less than a few tens of centimeters) and commonly terminate on other veins, forming an interconnected network (Figure **F43D**), although branched geometries are also common (Figure **F43B**, **F43C**, **F43F**). Locally, the epidote vein displays a radial geometry in relation to a pillow margin (Figure **F43E**). From Core 35R downhole, this vein type becomes gradually less abundant. Eventually, these composite epidote-rich veins are overprinted by a third type composed of composite carbonates and/or silica-rich veins (Figure **F42B, F42C**). These veins show various sizes ranging from 1 to 10 mm with various orientations. In Cores 35R–37R, these veins are more abundant and are associated with shallow to moderate dips (<50°) with a straight shape (Figure **F43**). They record a texture from massive to slip fiber showing single to branched to network connectivity.

Interpretation

The upper part of the sedimentary record encountered at Site U1502 is essentially devoid of deformation structures apart from Core 368-U1502A-25R, which contains a convolutely bedded sequence in Sections 25R-3 through 25R-5 (Subunit IC). The formation of this soft-sediment deformation structure most probably involved mass movements related to gravitational instabilities on a slope in close vicinity of a basement high (i.e., Ridge A).

A gradual downhole increase of predominantly brittle deformation is recorded within the sediments directly overlying the volcanic basement (Cores 368-U1502A-37R through 40R), whereas severe brecciation was observed within the uppermost ~50 m of the basement top (Cores 368-U1502B-4R through 12R). The observed deformation structures are interpreted to be related to the emplacement history of the basalt and the subsequent development of a hydrothermal system. Assuming such a setting, local strain accumulations resulting from possible thermal reequilibration and triggered by the circulation of fluids in both magmatic rocks and sedimentary cover may well be expected.

Figure F38. Strongly fractured and fragmented basalt filled by fine-grained unconsolidated greenish rock, top of Unit VI.

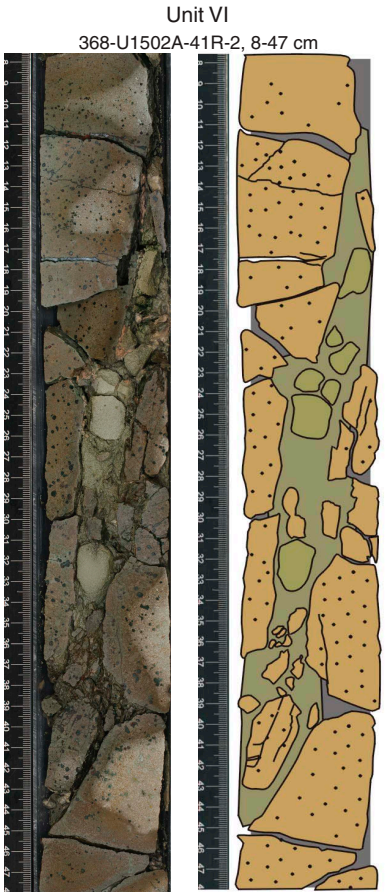

The numerous brecciated horizons observed in Subunit VIA are most probably related to fluid-assisted fracturing associated with hydraulic (and) in situ fragmentation of basalts. In that context and from a mechanical perspective, rock failure may have occurred in the tensile regime associated with low differential stress and high fluid pressure. Such rocks are commonly described in hydrothermal systems (e.g., Jébrak, 1997; Clark and James, 2003) and are identified as hydrothermal breccias. In some cases, however, a clear distinction between hydrothermal and tectonic breccias remains unconstrained, as it does in Section 368-U1502B-12R-1, which marks the boundary between Subunits VIA and VIB. Indeed, macroscopic observations from this section are compatible with a fault breccia, showing a gradual increase of the brittle deformation passing from a clast-supported cataclasite to a matrix-supported fault gouge. However, the identification of characteristic microstructures resulting from shear deformation are precluded by a pervasive fluid circulation associated with replacement, destabilization, and recrystallization of the initial texture. Therefore, at its present stage, two possible scenarios are considered regarding the formation mechanism of this breccia: (1) the breccia results essentially from hydrothermal fluid-assisted brecciation associated with the replacement and destabilization of the initial basalts, or (2) the breccia represents a fault zone with cataclastic deformation processes and was subsequently overprinted by pervasive hydrothermal fluid circulation.

Figure F39. Breccias in Unit VI, Hole U1502B. A, B. Brecciated basalt with jigsaw-puzzle structure. C. Core composite image showing spatial relationships between brecciated basalts and basaltic breccias. D. Basaltic breccia with fractal grain size distribution and high clast to matrix ratio. E. Initial stage of breccia matrix development, note how amount of angular clasts in each crack increases with crack width. F. Gradual transition from clast-supported brecciated basalt to matrix-supported basaltic breccia, macroscopically resembling a transition from cataclastic fabric to fault gouge.

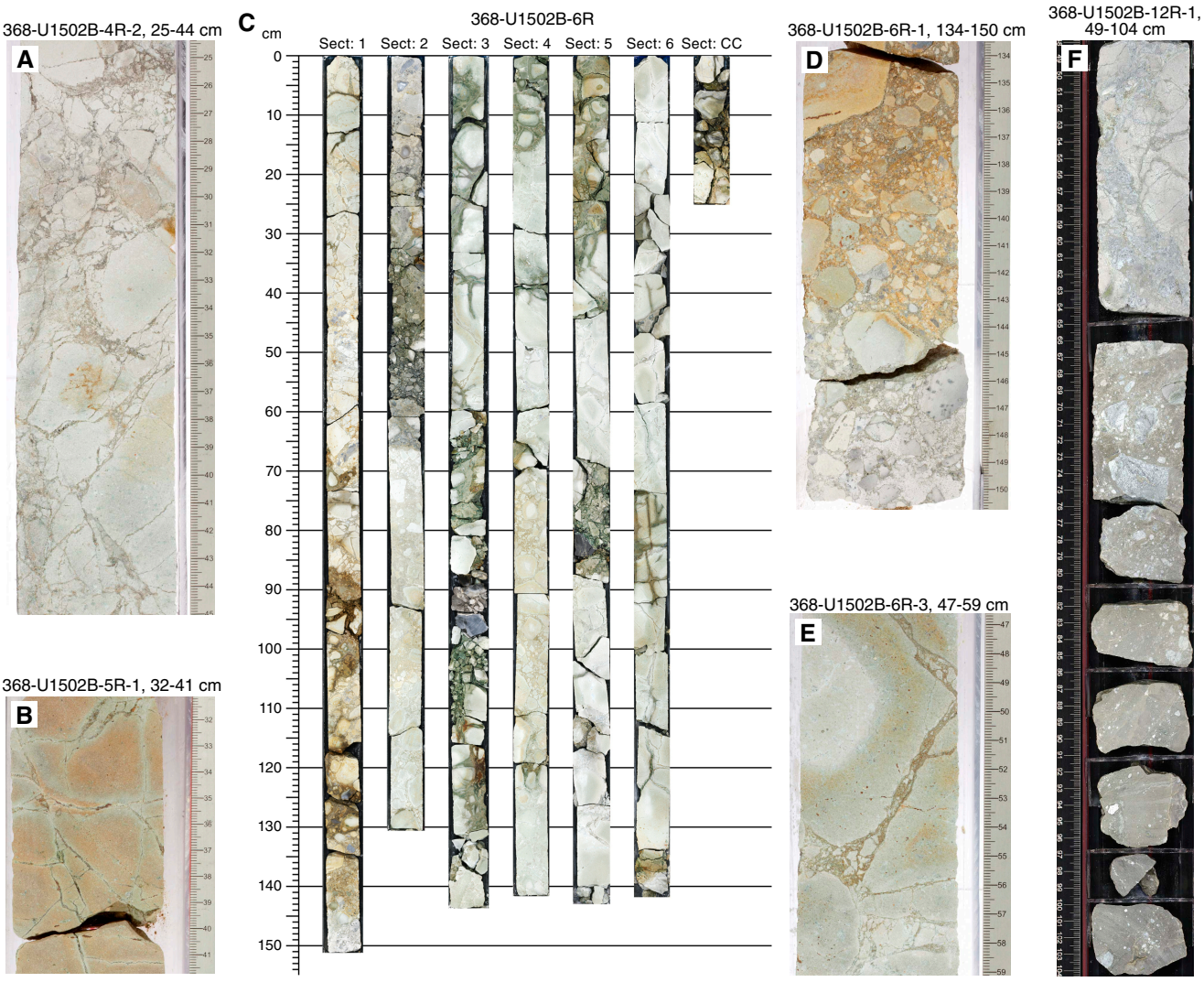

Figure F40. Progressing stages of brecciation process in macro- and microscopic view. A, B. Initial carbonate veining in basalt. C, D. Altered basalt clasts forming a jigsaw-puzzle texture within healed matrix. E, F. Altered basalt clasts surrounded by matrix carbonates with undulose extinction (i.e., strained matrix). G, H. Statically overgrown matrix by euhedral carbonate crystals, whereas altered basalt clast is crosscut by vein composed of fine-grained minerals consisting mainly of carbonate, zeolite, clay minerals and various Fe oxides.

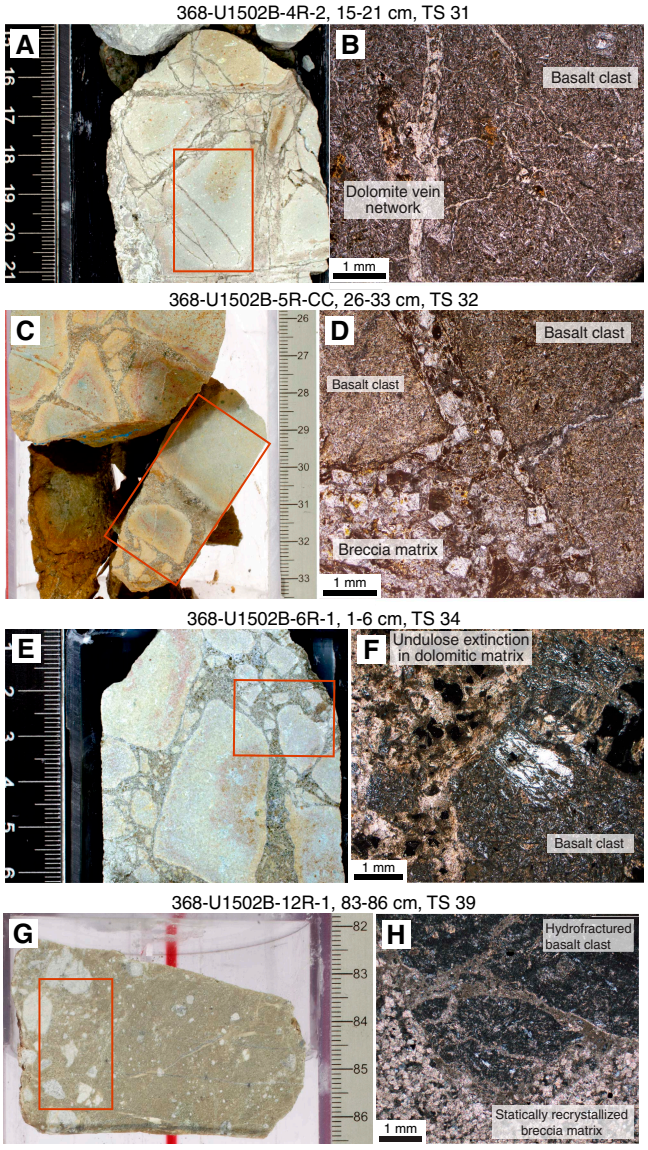

Figure F41. Calculated true dip angles of composite veins crosscutting brecciated basalts, basaltic breccias, and lava flows showing broad overall trends, as only principal veins were measured, Unit VI. For example, Subunit VIA contains numerous small-scale (millimeter) veins and microcracks associated with brecciation that generally show highly variable orientations. Furthermore, their mineralogy usually consists of fine-grained minerals that cannot be unambiguously identified, so only major veins are represented. Note the predominantly steep orientations of epidote-rich veins, and in contrast, the rather shallowly dipping silica- and carbonate-rich veins in lowermost part of Hole U1502B starting from Core 30R. CRF = core reference frame.

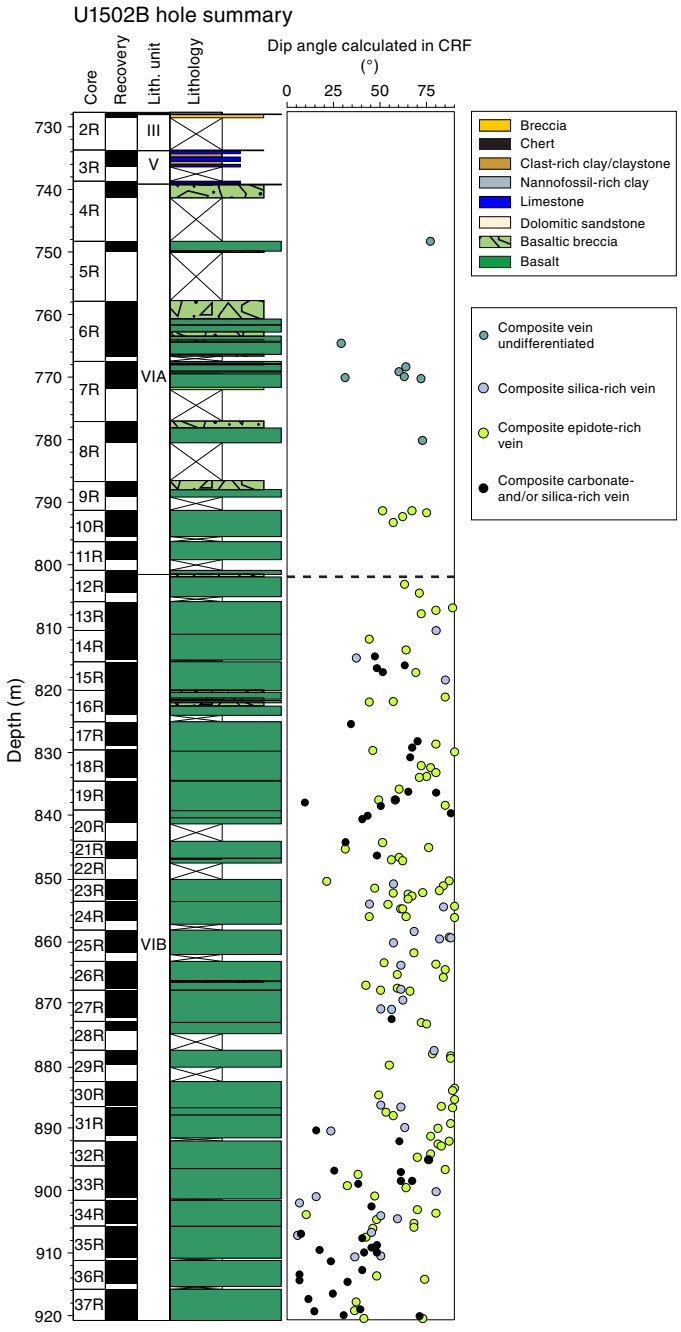

Figure F42. Principal generations of veins observed in Subunit VIB according to crosscutting relationships. A. Composite silica-rich vein crosscut by composite epidote-rich vein. B. Composite carbonate and/or silica-rich vein crosscutting branched composite epidote-rich veins with pyrite. C. Vertical composite epidote-rich vein crosscut by subhorizontal straight composite carbonate vein.

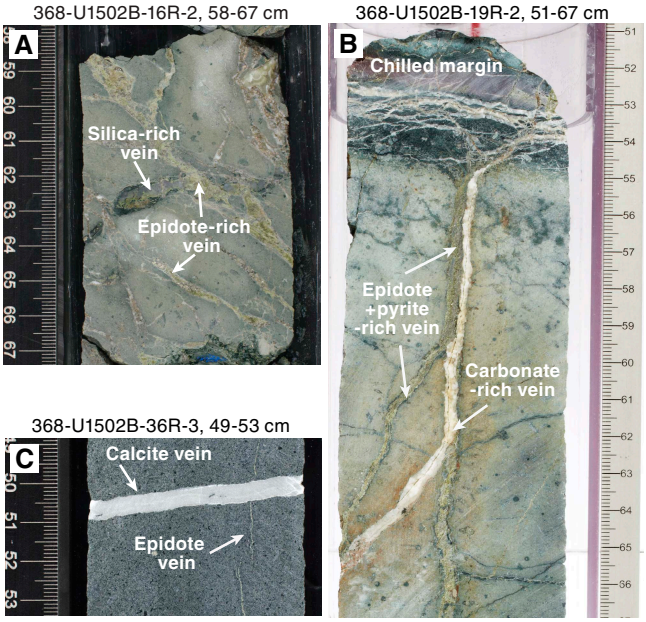

Figure F43. Distinct vein shapes, connectivity, and mineral compositions observed, Subunit VIB. A. Straight, single carbonate vein (white) and silica vein (gray). B. Branched thick composite epidote-rich vein on whole round. C. Composite of epidote and pyrite-rich veins in whole round. D. Network of composite epidote-rich veins. E. Composite epidote-rich veins showing radial geometry near chilled margin. F. Branched subvertical composite veins (epidote, sulfide, silica, and carbonate).

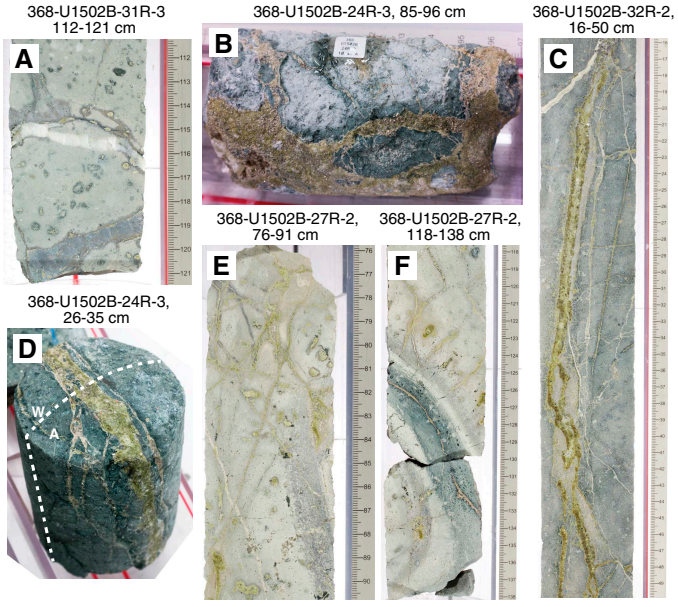

Biostratigraphy

All core catcher samples from Hole U1502A and selected samples from Hole U1502B were analyzed for calcareous nannofossils, foraminifers, diatoms, and ostracods. Additional samples were taken from intervals within the working-half cores when necessary to refine the ages. The preservation of calcareous microfossils is mostly good to moderate in the upper sections (Cores 368-U1502A-2R through 13R) and moderate to poor in the lower sections (Cores 14R through 41R). Planktonic foraminifers and calcareous nannofossils are abundant to common in Cores 2R through 10R, 25R, and 37R through 39R and rare to barren in all the other sections. Diatoms were only observed in Sections 40R-1 through 40R-3. In Hole U1502B, foraminifers were observed only in Section 3R-1 and are represented by well-preserved agglutinated deepwater taxa. Ostracods are extremely rare and were observed only in Samples 368-U1502A-3R-CC to 5R-CC.

Fourteen biostratigraphic events from the planktonic foraminifers and calcareous nannofossils were used to provide an age-depth model for Site U1502 from the late Miocene to late Oligocene (Tables **T5**, **T6**; Figure **F44**). The Pliocene/Miocene boundary is placed tentatively within Core 368-U1502A-2R, but it may be above the cored section, and the Miocene/Oligocene boundary was determined to lie between Samples 39R-CC and 40R-1, 7 cm. Sedimentation rates varied from ~39 mm/ky in the late Miocene to ~10 mm/ky in the middle and early Miocene.

No planktonic microfossils were found in Hole U1502B, but Sample 3R-1, 94–99 cm, from a sandy interval) revealed abundant and diverse abyssal agglutinated benthic foraminifers. The taxonomic composition of this agglutinated benthic foraminifer assemblage suggests a late Eocene age for this interval.

Calcareous nannofossils

The calcareous nannofossil biostratigraphy for Hole U1502A is based mainly on the analysis of core catcher samples, with occasional toothpick samples from the working-half cores to better constrain the biostratigraphic events (Table **T7**). Calcareous nannofossils are abundant and well preserved in Cores 2R through 6R, deteriorating to moderate preservation with abundant to common occurrences in Cores 7R through 12R. Calcareous nannofossils are absent in Cores 13R through 36R with the exception of a few samples where they are present but the assemblages are affected by strong dissolution. In contrast, nannofossils are abundant in Cores 37R through 40R. Reworking, overgrowth, and fragmentation were observed in most samples from Hole U1502A, whereas heavy dissolution occurred in discoasterid-dominated assemblages, if present, in the middle part of the sequence. Nine nannofossil biostratigraphic datums were recognized from the late Oligocene through late Miocene sediment sequence in Hole U1502A (Table **T5**). The oldest nannofossil event identified in Hole U1502A is the last appearance datum (LAD) of *Sphenolithus predistentus* (26.93 Ma) observed in Sample 40R-1, 69 cm (739.79 m), whereas the first appearance datum (FAD) of *Sphenolithus distentus* (30.0 Ma) cannot be determined due to the nannofossil-barren interval from the immediately underlying sample to the bottom of Hole U1502A, indicating an age older than 26.93 Ma but possibly younger than 30.0 Ma. All core catchers and toothpick samples from within the work-

Table T5. Calcareous nannofossil biostratigraphic events, Site U1502. O = occurrence, T = top/last appearance datum, B = bottom/first appearance datum. **Download table in CSV format.**

Epoch		Biozone (Martini, 1971)	Calcareous nannofossil event	Top		Bottom		Age model	
				Core, section, interval (cm)	Depth CSF-A (m)	Core, section, interval (cm)	Depth CSF-A (m)	Depth (m)	Age (Ma)
				368-U1502A-		368-U1502A-			
			O *Discoaster quinqueramus*			2R-CC	376.81	376.81	>5.59
	late	NN11	T *Nicklithus amplificus*	4R-CC	394.67	5R-CC	403.85	408.95	5.94
			B *Amaurolithus* spp.	9R-CC	450.22	10R-CC	458.81	454.52	7.42
Miocene			B *Discoaster berggrenii*	13R-2, 89–90	483.01	13R-CC	486.87	484.94	8.29
	middle	NN6	T *Cyclicargolithus floridanus*	29R-CC	643.46	30R-CC	653.27	648.37	11.85
	early	NN2	T *Triquetrorhabdulus carinatus*	36R-CC	710.46	37R-CC	719.62	715.04	18.28
			B *Sphenolithus belemnos*	38R-CC	728.32	39R-CC	734.87	731.60	19.03
			B *Sphenolithus disbelemnos*	39R-CC	734.87	40R-1, 7	739.17	737.02	22.76
Oligocene		NP24	T *Sphenolithus predistentus*	39R-CC	734.87	40R-1, 7	739.17	737.02	26.93

Table T6. Planktonic foraminifer biostratigraphic events, Site U1502. O = occurrence, T = top/last appearance datum, B = bottom/first appearance datum. **Download table in CSV format.**

Epoch	Biozone (Blow, 1969)	Planktonic foraminifer event	Top		Bottom		Age model	
			Core, section	Depth CSF-A (m)	Core, section	Depth CSF-A (m)	Depth (m)	Age (Ma)
			368-U1502A-		368-U1502A-			
early Pliocene	N19	O *Globoturborotalita nepenthes*			2R-CC	376.81	376.81	>4.37
Miocene	N17	B *Globorotalia margaritae*	8R-CC	432.74	9R-CC	450.22	441.48	6.08
	N8	B *Globoturborotalita nepenthes*	30R-CC	653.27	31R-CC	662.75	658.01	11.63
	N6	T *Catapsydrax dissimilis*	36R-CC	710.46	37R-CC	719.62	715.04	17.54
	N4	T *Paragloborotalia kugleri*	37R-CC	719.62	38R-CC	728.32	723.97	21.12

ing-half cores of Hole U1502B are barren of calcareous nannofossils.

Miocene

Four events occur in the late Miocene strata of Hole U1502A. The top of Zone NN11 is defined by the LAD of *Discoaster quinqueramus* (5.59 Ma), which was observed in the uppermost Sample 2R-CC (376.81 m), indicating an age older than 5.59 Ma. The LAD of *Nicklithus amplificus* (5.94 Ma) was found in Sample 5R-CC (403.85 m). The FAD of *Amaurolithus* spp. (7.42 Ma) was found in Sample 10R-CC (458.81 m). The bottom of Zone NN11 is placed in Sample 13R-2, 89–90 cm (483.01 m), where the apparent FAD of *Discoaster berggrenii* (8.29 Ma) was found right above a nannofossil-barren interval. The LAD of *Cyclicargolithus floridanus* (11.85 Ma) within Zone NN6 is placed in Sample 30R-CC (653.27 m), and this sole event in the middle Miocene strata of Hole U1502A approximates the top of Zone NN6 (11.90 Ma) and the late/middle Miocene boundary. Three bioevents were found in the early Miocene strata of Hole U1502A. The top of Zone NN2 is marked by the LAD of *Triquetrorhabdulus carinatus* (18.28 Ma), which was observed in Sample 37R-CC (719.62 m) immediately below a nannofossil-barren interval; the FAD of *Sphenolithus belemnos* (19.03 Ma; Zone NN2) was also found in this same sample. The base of Zone NN2 and the Miocene/Oligocene boundary are inferred by the FAD of *Sphenolithus disbelemnos* (22.76 Ma), which was observed in Sample 39R-CC (734.87 m). Notably, the co-occurrence of *Sphenolithus delphix* (23.11–23.21 Ma) in this same sample and the LAD of *Reticulofenestra bisecta* >10 µm (23.13 Ma) in the immediately underlying Sample 40R-1, 7 cm (739.17 m), may be the result of the sample size (5 cm thick) and/or the presence of a hiatus.

Oligocene

One Oligocene bioevent was identified in Hole U1502A. The LAD of *S. predistentus* (26.93 Ma) within Zone NP24 was observed in Sample 40R-1, 7 cm (739.17 m). The occurrence of *S. distentus* (first occurrence dated to 30.0 Ma) immediately overlies a barren interval, indicating a possible deeper position of its FAD and therefore an age younger than 30 Ma at 739.79 m (Sample 40R-1, 7 cm).

Planktonic foraminifers

All core catcher sediment samples from Holes U1502A and U1502B were processed for foraminiferal analyses. Additional samples were taken and analyzed from the split cores to supplement the biostratigraphic work (Table **T8**). Planktonic foraminifers are moderately to well preserved and abundant to common in samples from Cores 368-U1502A-2R through 10R and moderately to poorly preserved or even recrystallized and less abundant in Cores 11R through 13R, 25R, and 29R through 31R. Samples from Cores 14R through 24R, 26R through 28R, 32R through 36R, and 40R through 41R and all samples from Hole U1502B are barren of planktonic foraminifers, whereas planktonic foraminifers in samples from Cores 368-U1502A-37R through 39R are poorly preserved with relatively high abundance.

Five planktonic foraminiferal datums spanning from the late Pliocene to the early Miocene were recognized in Hole U1502A (Table **T6**). The planktonic foraminiferal biostratigraphy for Hole U1502A was established by these events and the planktonic foraminiferal assemblages at successive depth intervals. No planktonic foraminiferal biostratigraphy events are recognized for Hole U1502B.

The middle–late Miocene planktonic foraminiferal assemblage in samples from Cores 368-U1502A-3R through 29R is dominated

Figure F44. Age-depth model, Site U1502. Plotted event data are in Tables T5 and T6.

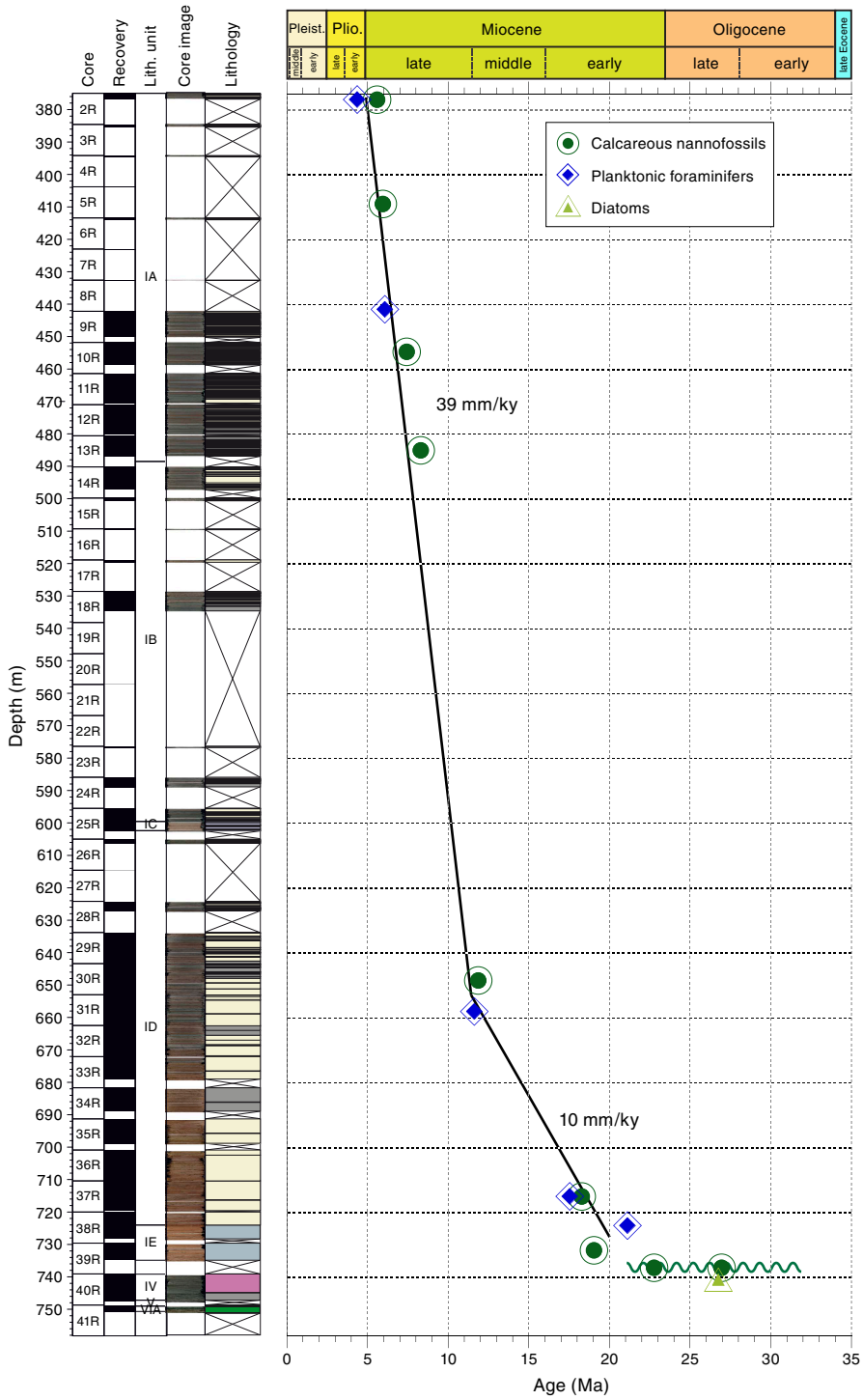

Table T7. Distribution of calcareous nannofossils, Site U1502. **View table in PDF format. Download table in CSV format.**

Table T8. Distribution of planktonic foraminifers, Site U1502. **View table in PDF format. Download table in CSV format.**

by *Sphaeroidinellopsis seminulina, Globoturborotalita nepenthes,* and *Sphaeroidinellopsis kochi* (Plate **P1**), whereas *Dentoglobigerina altispira* is also a common species in Samples 3R to 9R. The early Miocene–Oligocene planktonic foraminiferal assemblage in Samples 37R to 40R is dominated by *Catapsydrax dissimilis* and *Globoquadrina venezuelana*.

The presence of *S. seminulina* and *G. nepenthes* in Sample 2R-CC (376.81 m) indicates the top age of this hole should be older than 4.37 Ma. Four other events occur in the Miocene strata of Hole U1502A. The FAD of *Globorotalia margaritae* (6.08 Ma) was found in Sample 8R-CC (432.74 m), the FAD of *G. nepenthes* (11.63 Ma) was found in Sample 30R-CC (653.27 m), the LAD of *C. dissimilis*

Plate P1. Principal planktonic foraminifers (Hole U1502A), benthic foraminifers (Hole U1502B), and ostracods (Hole U1502A) used in biostratigraphy and paleoecology analyses, Site U1502. 1–10, 18: scanning electron microscope (SEM) (scale bar = 100 µm); 11–17: optical (scale bar = 1 mm). 1. *Sphaeroidinellopsis seminulina* (U1502A-5R-CC). 2, 3. *Globorotalia margaritae* (4R-CC). 4. *Globoturborotalita nepenthes* (5R-CC). 5. *Sphaeroidinellopsis kochi* (3R-CC). 6. *Globoquadrina venezuelana* (39R-CC). 7. *Catapsydrax dissimilis* (38R-CC). 8. *Paragloborotalia kugleri* (39R-CC). 9–17. U1502B-3R-1, 94–99 cm; (9) *Psammosiphonella cylindrica*; (10) *Cribrostomoides* sp.; (11) *Ammodiscus* cf. *Ammodiscus cretaceus* sp. with *Ammolagena clavata* attached; (12) *Ammobaculites* sp. aff. *Ammobaculites agglutinans*; (13, 14) *Reticulophragmium amplectens*; (15, 16) *Reticulophragmium gerochi*; (17) *Psamminopelta gradsteini*. 18. *Rugocythereis horrida* (U1502A-3R-CC).

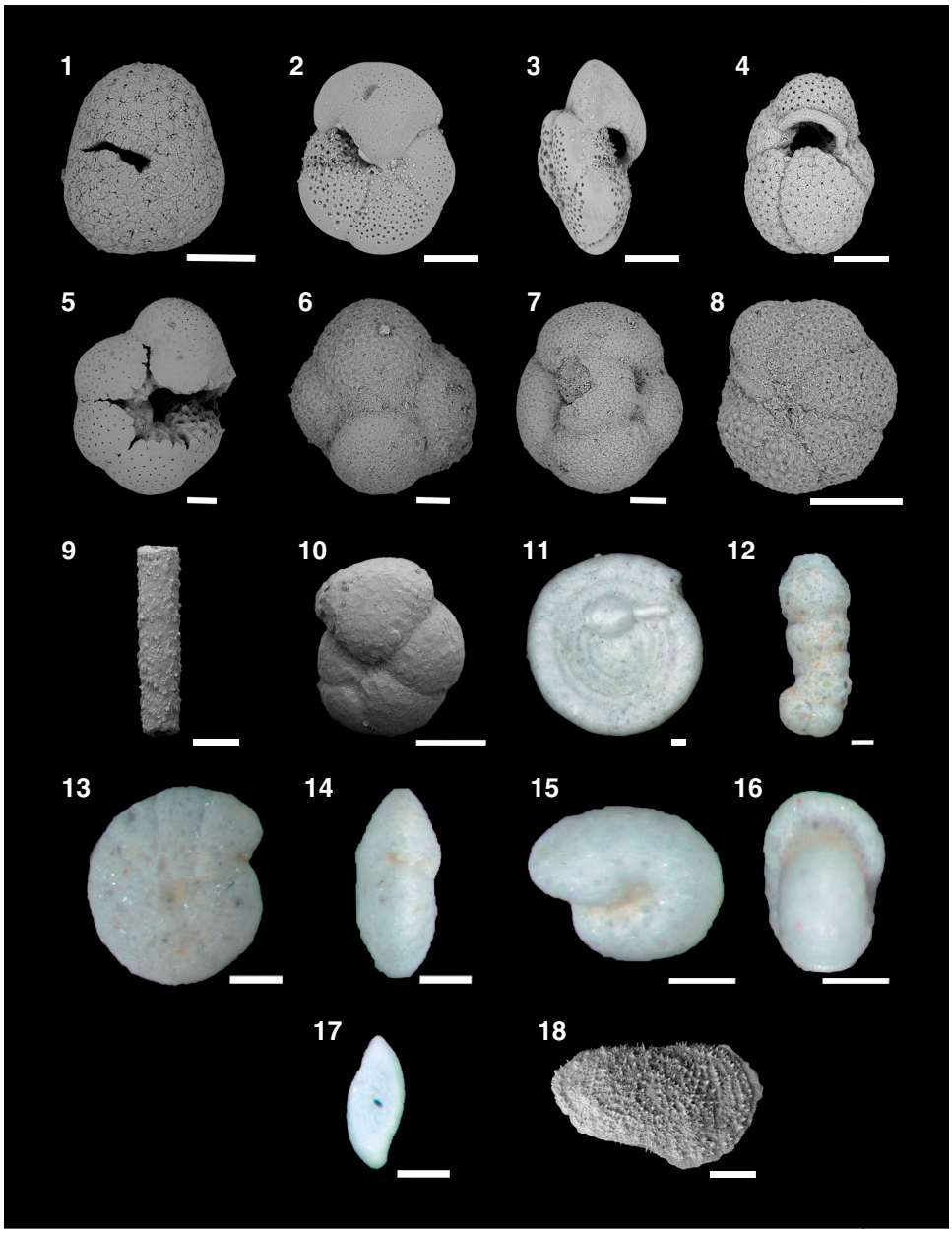

(17.54 Ma) was found in Sample 37R-CC (719.62 m), and the LAD of *Paragloborotalia kugleri* (21.12 Ma) within Zone N4 occurs in Sample 38R-CC (728.32 m).

Benthic foraminifers

In Hole U1502B, only one studied sample (interval 3R-1, 94–99 cm) yielded agglutinated benthic foraminifers. In this sample, the agglutinated foraminifers are abundant and the assemblage is dominated by typical abyssal species (e.g., *Psammosiphonella cylindrica, Cribrostomoides* sp., *Ammodiscus* cf. *Ammodiscus cretaceous, Ammolagena clavata, Ammobaculites* sp., *Reticulophragmium amplectens, Reticulophragmium gerochi, Psamminopelta gradsteini*, and *Rugocythereis horrida*). Compared to the calcareous microfossil assemblage found in Hole U1502A, the agglutinated assemblage indicates that either a very deepwater paleodepth or a shallower CCD existed during this time. The taxonomic composition of the benthic assemblage, in particular the association between *A. clavata, Ammodiscus* sp., *P. gradsteini, R. amplectens*, and *R. gerochi*, indicates an age of late Eocene (M. Kaminski, pers. comm., 2017) for this layer. Moreover, the on-growth of *A. clavata* on *Ammodiscus* sp.

Table T9. Distribution of diatoms, Site U1502. **View table in PDF format. Download table in CSV format.**

Table T10. Diatom biostratigraphic event, Site U1502. O = occurrence. **Download table in CSV format.**

Epoch	Diatom zonation (Barron, 1985)	Diatom event	Top		Bottom		Age model	
			Core, section, interval (cm)	Depth CSF-A (m)	Core, section, interval (cm)	Depth CSF-A (m)	Depth (m)	Age range (Ma)
Oligocene	*Rocella vigilans–Rocella gelida*	O *Rocella vigilans*	40R-1, 32	739.42	40R-2, 136	741.93	741.93	23.9–29.6

(Plate **P1**, figure 11) was previously reported from Eocene coarse pyroclastic sediments overlying basement at Ocean Drilling Program (ODP) Site 643 (plate 21.3 in Kaminski and Gradstein, 2005).

Ostracods

The deepwater species *R. horrida* was found as single valves, one each in Samples 368-U1502A-3R-CC, 4R-CC, and 5R-CC.

Diatoms

The core catchers of Hole U1502A were processed into smear and strewn slides for diatom analysis with 57 additional toothpick samples taken from selected intervals of the working-half cores for further resolution. All core catcher samples and most additional samples were found to be barren of diatoms (Table **T9**). Toothpick samples from the top of Section 40R-1 contain abundant but poorly preserved diatoms, decreasing in abundance to barren in Section 40R-4. *Chaetoceros* spp. are few to common in these sections, with few *Cyclotella* spp., *Distephanosira architecturalis, Paralia sulcata*, and *Thalassiothrix* spp. Sections 40R-1 through 40R-3 have an early Oligocene diatom assemblage; the presence of *Rocella vigilans* indicates the sections are between 30 to 24 Ma in age (Table **T10**).

Paleomagnetism

Shipboard measurements

Shipboard paleomagnetic investigations combined three complementary approaches (see **Paleomagnetism** in the Expedition 367/368 methods chapter [Sun et al., 2018a]): (1) measurement and in-line AF demagnetization of archive-half sections on the pass-through 2G Enterprises SRM at 2.5 and 2 cm spacing for sediments and basalts, respectively; (2) measurement and thermal demagnetization of oriented discrete samples on the SRM; and (3) measurement and AF demagnetization of oriented discrete samples on the spinner magnetometer (AGICO JR-6A). For sedimentary units, 40 representative discrete samples were collected for thermal demagnetization and 15 for AF demagnetization from sections where recovery was higher than ≈20%. For igneous basement units, 8 discrete samples were collected for thermal demagnetization and 41 for AF demagnetization.

First, we used scalar data from discrete samples that were thermally demagnetized up to 700°C or AF demagnetized up to 120 mT to assess the nature of the magnetic assemblage. Second, we used the directional and intensity data of archive-half sections measured after in-line AF demagnetization of 25 mT to determine magnetic polarity along the core. The thermal instability of the sedimentary rocks combined with the lack of laboratory shielding prevented the use of thermal demagnetization to confirm magnetic polarities. Thermal demagnetization of samples from the igneous basement was successful due to intrinsically higher NRM in basaltic rocks. Directional data were analyzed using Zijderveld diagrams (Zijderveld, 1967), and the characteristic remanent magnetization (ChRM) direction(s) were calculated by principal component analysis (PCA) (Kirschvink, 1980) using PuffinPlot (version 1.03, 23 April 2015) (Lurcock and Wilson, 2012).

Demagnetization behavior of sedimentary rocks and implications for magnetic assemblages

Units: IA to V

Depths: Hole U1502A= 375.00–750.67 m core depth below seafloor, Method A (CSF-A); Hole U1502B = 727.79–739.16 m CSF-A.

Cores 368-U1502A-2R through 41R; 368-U1502B-2R through 3R

The data from thermal demagnetization at the 95°, 120°, and 200°C heating steps were irreparably lost because of an error in drift-and-background corrections on the SRM. Subsequent measurements at higher temperature steps were successfully performed on 30 representative samples using the JR-6A spinner magnetometer. However, stepwise thermal demagnetization of the NRM above 200°C failed because instead of losing magnetization the samples gained magnetization (Figure **F45A**). However, these failed experiments show that the behavior of the sedimentary material is strongly associated with its color (red or green), which primarily reflects distinct mineral assemblages.

Red beds (e.g., discrete Sample 368-U1502A-37R-5, 122–124 cm) initially display normal behavior marked by a decrease in magnetization up to 350°C, followed by an anomalous increase in magnetization from 350° to 600°C and finally a normal decrease above 600°C (Figure **F45**). The increase in magnetization results from at least one thermally induced reaction that forms, upon heating, one (or several) magnetically remanent phases. Although such reactions are common in sedimentary materials, the acquisition of magnetization in the magnetically shielded TD-48 SC oven is anomalous. The gain in magnetization does not increase with the duration of time before measurement (outside the oven), which suggests that the samples are remagnetized at high temperature in the ≈60 nT residual field (measured with Applied Physics System APS 550 fluxgate probe at room temperature) present in the oven. The magnetic phase formed by the heating-induced reaction must be able to acquire a high chemical remanent magnetization (CRM) to contribute so significantly to bulk magnetization. Because magnetization generally decreases above 600°C, this phase is likely to consist primarily of magnetite (Fe_3O_4; saturation magnetization: $\sigma \approx 92$ Am^2/kg) and hematite (αFe_2O_3; $\sigma \approx 0.4$ Am^2/kg). Potential precursors to thermally induced magnetite and hematite in sedimentary rocks include siderite (paramagnetic), greigite (Fe_3S_4; $\sigma \approx 25$ Am^2/kg), and pyrite (paramagnetic). Although siderite ($FeCO_3$) has been reported in red bed interval 368-U1502A-33R-2, 8–15 cm, and detected by XRD in Sample 33R-3, 25–27 cm (see **Lithostratigraphy**), it does not constitute a major or ubiquitous phase in the sedimentary units of Holes U1502A or U1502B, and therefore its breakdown into magne-

Figure F45. Thermal demagnetization showing relative magnetization with respect to NRM, Hole U1502A. A. Behavior of sedimentary material strongly reflects distinct mineral assemblages. B. Greenish beds with decrease of magnetization up to 350°C followed by increase in magnetization. C. Reddish bed with anomalous increase in magnetization from 350°C. D. Reddish beds with anomalous increase in magnetization from 350° to 600°C.

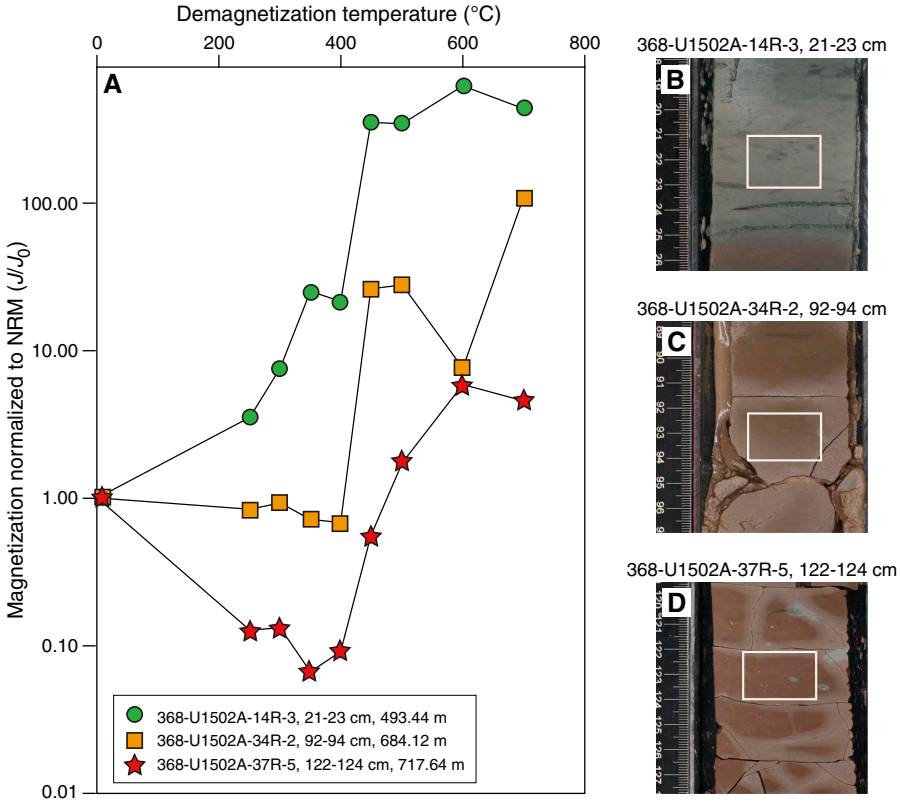

tite around 350°C (Ellwood et al., 1986; Hirt and Gehring, 1991; Pan et al., 2000) is unlikely to cause the observed large gain in magnetization. The breakdown of greigite into magnetite around 330°C (Roberts et al., 2011) would cause an insufficient increase in magnetization (≈ 3.68). Finally, the breakdown of pyrite (FeS_2), a common paramagnetic phase in sedimentary units of Holes U1502A or U1502B, into magnetite and hematite (αFe_2O_3) around 350°C (Tarling and Hrouda, 1993) best accounts for the substantial increase in magnetization between 350° and 600°C:

$$3\ FeS_2 + 8\ O_2 = Fe_3O_4 + 6\ SO_2$$

for pyrite + oxygen = magnetite + sulfur dioxide, and

$$2\ FeS_2 + 5.5\ O_2 = \alpha Fe_2O_3 + 4\ SO_2$$

for pyrite + oxygen = hematite + sulfur dioxide.

The green beds (e.g., discrete Sample 368-U1502A-14R-3, 21–23 cm) display significantly higher reactivity to heating (Figure **F45A**). These samples consistently display a very large magnetization enhancement, up to 600 times the NRM, above 200°C.

Stepwise AF demagnetization was performed up to 120 mT. Most samples display a demagnetization behavior corresponding to the color of sedimentary material (red or green), although some sediments of intermediate color show mixed behaviors. Red sediments show an initial 50% loss of magnetization by 25 mT (Figure **F46**), a soft behavior indicative of magnetite or titanomagnetite in the multidomain to pseudosingle-domain size range. This behavior changes drastically above 30 mT and up to 120 mT. The reddish color of the sediment combined with this magnetically harder behavior supports the presence of hematite in these sediments. In contrast, green sediments exhibit a very soft AF behavior characterized by rapid demagnetization below 15 mT, which is typical of multidomain–pseudosingle domain magnetite or titanomagnetite. Many samples gain magnetization above 70 mT, a phenomenon attributed to gyroremanent magnetization (GRM) or rotational remanent magnetization (e.g., Thompson, 1990; Snowball, 1991; Hu et al., 2002) that is common in pyrrhotite and greigite. The low saturation isothermal remanent magnetization to magnetic susceptibility (χ) ratios of these green sediments (Table **T11**) does not support the presence of greigite. Generally, AF treatments on discrete samples removed the steep overprint component more successfully with respect to the SRM in-line treatment on the archive sections (Figures **F47**, **F48**, **F49**).

Demagnetization behavior, rock magnetism data, and implications for magnetic assemblages of igneous rocks

Unit: igneous lithologic Unit 2
Depth: 739.16–920.95 m CSF-A
Cores 368-U1502B-4R through 37R

The igneous rocks of Hole U1502B consist of various types of altered basalt (see **Igneous and metamorphic petrology**). The basalt cores have an average initial intensity (NRM) of magnetization one order of magnitude higher than sediments (Figure **F48**). This leads to successful AF and thermal demagnetization for both archive halves and discrete samples. Typical examples of demagneti-

Figure F46. AF demagnetization of red and green samples, Hole U1502A. Reddish and greenish sediments are represented with red and green symbols, respectively. Reddish sediments show magnetically harder behavior that supports the presence of hematite (9R-1, 133–135 cm; 39R-1, 65–67 cm). Green sediments show very soft behavior typical of magnetite or titanomagnetite. Some sediments of intermediate color show mixed behaviors (25R-3, 135–137 cm; 36R-5, 41–43 cm). The gain in magnetization above 70 mT is attributed to GRM common in pyrrhotite and greigite (12R-5, 139–141 cm; 13R-1, 44–46 cm; 14R-3, 18–20 cm).

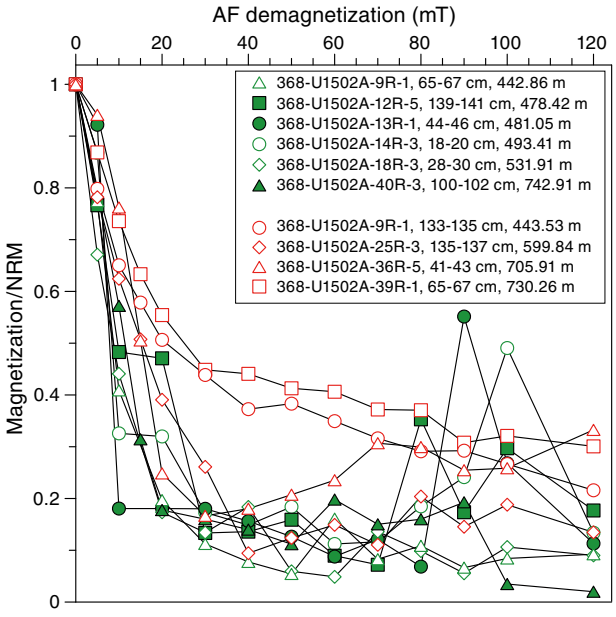

zation behavior and polarity interpretation are shown in Figure **F50**. AF and thermal demagnetization of twin samples collected at the same depth interval lead to comparable results. AF demagnetization shows two types of behaviors, with 90% magnetization loss either before 45 mT (soft) or 100 mT (hard).

Magnetic susceptibilities obtained by point measurement on section halves range widely from $\kappa \approx 18 \times 10^{-6}$ SI to $33{,}000 \times 10^{-6}$ SI, with median values around 327×10^{-6} SI (Figure **F51**). The distribution of magnetic susceptibility from 728 to 920.8 m CSF-A shows a bimodal distribution with two asymmetric maxima, negatively skewed toward lower κ values (histogram in Figure **F51**). Progressive increasing alteration of magmatic magnetite into maghemite and hematite, both phases with lower intrinsic magnetic susceptibilities, best explains the skewness of the κ distribution.

The bimodal nature of the κ distribution and the variations of κ with depth have a different origin. Although magnetic susceptibility κ decreases with increasing alteration, such a process should produce a continuum of κ values from fresh to altered rocks instead of a bimodal distribution. The Fe_2O_3 versus κ diagram (Figure **F52**) indeed shows a gap in magnetic susceptibility, which further questions a chemical alteration origin for the κ bimodality. Several 4 to 13 m thick discrete intervals of consistently high magnetic susceptibility occur throughout these volcanic rocks (gray intervals in Figure **F51**). These intervals show abrupt variations of κ with depth. These high-κ intervals could be interpreted as gravitational accumulation of magnetite toward flow bottoms, as has been observed in basalt flows elsewhere (e.g., Caballero-Miranda et al., 2016). Alternatively, since basaltic flows often develop a tabular structure with more massive lower parts (e.g., Boiron et al., 2013), the lack of

Table T11. Rock magnetic properties of representative samples, Hole U1502A. **Download table in CSV format.**

Core, section, interval (cm)	$SIRM_{2.3\,T}$ (A/m)	χ (10^{-6}), at 300 A/m	SIRM/χ (kA/m)
368-U1502A-			
Red sediment			
39R-1, 65–67	1.287	176	7.313
9R-1, 133–135	1.158	175	6.616
25R-3, 135–137	0.571	181	3.156
36R-5, 41–43	5.519	292	18.900
Green sediment			
9R-1, 65–67	0.132	150	0.878
12R-5, 139–141	0.109	218	0.501
13R-1, 44–46	0.094	131	0.718
14R-3, 18–20	0.098	335	0.292
18R-3, 28–30	0.156	90	1.728
40R-3, 100–102	0.084	137	0.612

fractures in basalts of the lowermost part of Hole U1502B could significantly prevent pervasive alteration, which in turn would result in higher κ values. In many other magnetic studies of basaltic flows, flow boundaries are marked by jumps in magnetic susceptibility (e.g., Cañón-Tapia, 2004; Boiron et al., 2013; Caballero-Miranda et al., 2016). Regardless of the origin of high-κ intervals, these intervals most likely mark boundaries between effusive units with unit thickness ranging between ≈14 and 28 m and an average thickness of ≈19 ± 5 m (Figure **F51**). The variation of magnetic susceptibility (point measurement on section halves) versus chemical composition from pXRF (see **Igneous and metamorphic petrology**) shows no distinct correlation ($R^2 = 0.343$ for Fe_2O_3; Figure **F52**), suggesting that alteration may not be the primary control on κ.

NRM at room temperature and magnetic susceptibility from archive halves were used to compute the Koenigsberger ratio, which indicates the capacity of a rock to carry magnetic anomalies. The Koenigsberger ratio (Q_n) is defined as the ratio between the remanent magnetization and magnetization induced by the geomagnetic field (43,103.1 nT = 34.3 A/m at Site U1502 according to World Magnetic Model 2015; Chulliat et al., 2015):

$$Q_n = \text{NRM (A/m)}/[\kappa\,\text{(SI)} \times H\,\text{(A/m)}].$$

The distribution of the Koenigsberger ratio (Figure **F53**) indicates that altered basalts may contribute more to magnetic anomalies (Q_n = 1–10) than fresher basalts (Q_n = 0.001–1).

The mean dip angle of magnetic foliation calculated for Hole U1502B basalts (43 discrete samples, most of which are anisotropic samples is 8° (at the 95% confidence level) and thus lower than expected considering the apparent dip of seismic reflectors at this site (see **Background and objectives**), but it is characterized by a large ellipse of confidence. It is not possible to determine if this dip angle is primary or was acquired during subsequent tilting. However, the degree of magnetic anisotropy (P') of these basalts is overall very small: $P' < 1.02$ (Figure **F54**). Such low degrees of anisotropy are common in basaltic flows that rapidly cooled on gentle slopes with <10° of dip (e.g., Boiron et al., 2013).

The magnetic shape parameter (T) shows a general ellipsoid symmetry close to 0, as would be expected from a magnetostatic fabric carrier such as magnetite or titanomagnetite (Figure **F54**). The low magnetite content in the altered basalts combined with the contribution of mafic silicates results in weak anisotropy of mag-

Figure F47. Demagnetization plots of (A, B) discrete samples and (C, D) archive-half sections, Hole U1502A sedimentary rocks. Zijderveld plots: solid squares = declination, open squares = inclination. Stereographic plots: solid squares = positive (down) inclination, open squares = negative (up) inclination. Calculated ChRM (blue line; red squares = measurements used in calculation) using PCA is also shown. A. Reversal polarity, Subunit IB B. Normal polarity, Subunit IE. C. Normal polarity, Subunit IA. D. Normal polarity, Subunit IA. MAD = maximum angular deviation.

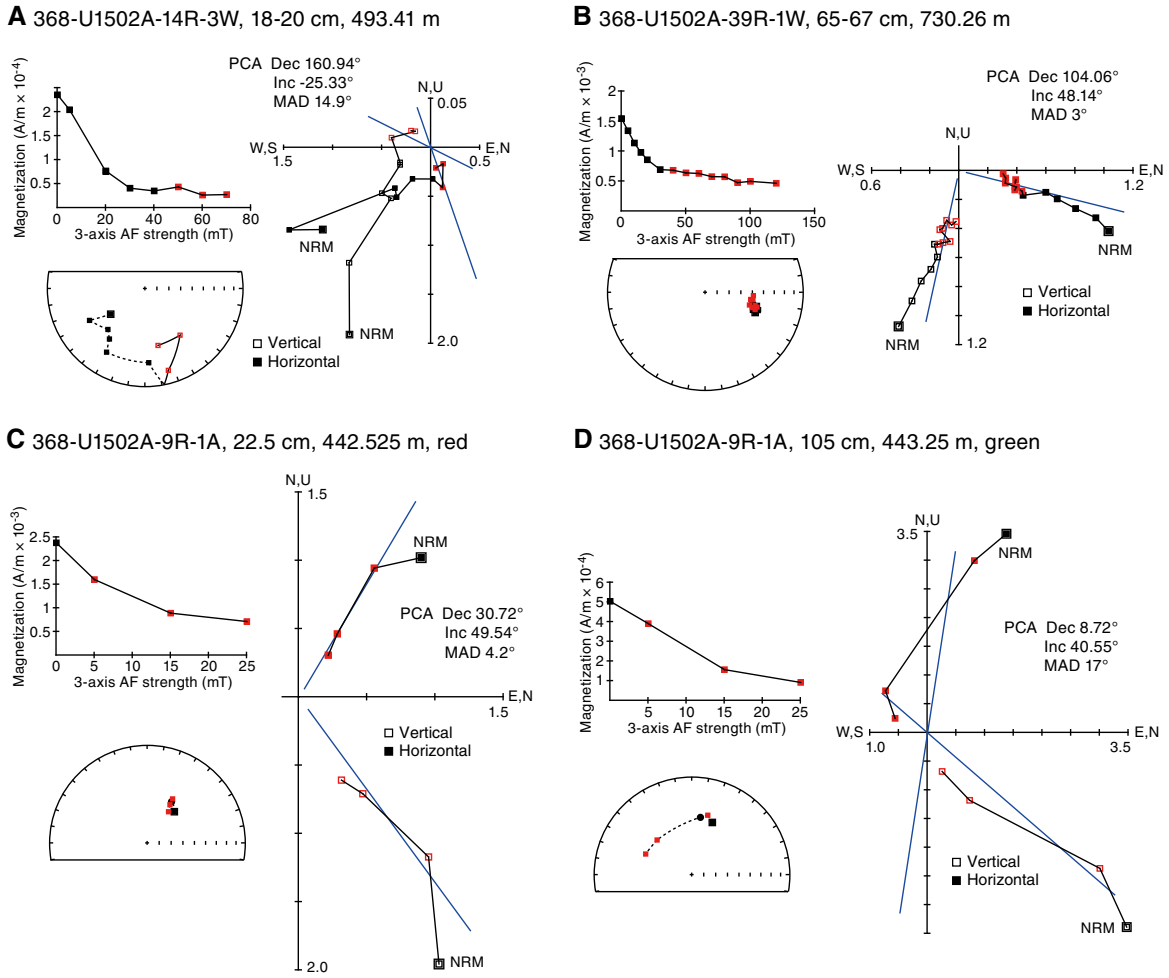

netic susceptibility (AMS). Hence, this type of volcanic material is unlikely to yield valuable AMS data for subsequent magma flow studies.

Magnetostratigraphy

The general AF demagnetization behavior of sedimentary rocks shows that 80% of the NRM is removed with a field of 25 mT. However, the predominance of steep normal inclinations (≈75°) across all late Oligocene to late Miocene units (375.00–750.67 m CSF-A) indicates that this remanence is caused by a large magnetic drilling overprint (Figure **F49**). Notwithstanding their higher NRM, the drilling overprint is partially removed but still present in most of the archive sections (Figure **F55**). This steep overprint is so strong that we are unable to remove it with in-line AF on the SRM, making paleoinclination data suspicious and preventing any reliable magnetostratigraphy to be established for both Holes U1502A and U1502B. This situation arises from (1) the use of the RCB coring system, which is known to impart a strong overprint (e.g., Richter et al., 2007), (2) the naturally weak NRM of sediments, and (3) the magnetically soft nature of the magnetic assemblage present in these sediments.

The drilling overprint also considerably affects basalt. In several intervals between 728 and 920.8 m CSF-A, magnetic inclination displays negative values (Figure **F55**). However, the only data validating this magnetic reversal hypothesis occurs in Cores 368-U1502B-9R and 10R in two discrete samples (9R-2, 79–81 cm, and 10R-3, 16–18 cm). In this interval (gray shaded zone in Figure **F55**), the drilling overprint is less pervasive and the two discrete samples document both a normal (soft) component and a reversed (hard) component. Should this reversal be confirmed, it would imply that magmatic activity at Site U1502 lasted long enough to record a magnetic polarity reversal.

Figure F48. Magnetization intensity vs. inclination showing effect of steep drilling overprint, Site U1502. Basalts have higher magnetization intensity than sediments. Green lines = expected normal and reversal inclination at present latitudes.

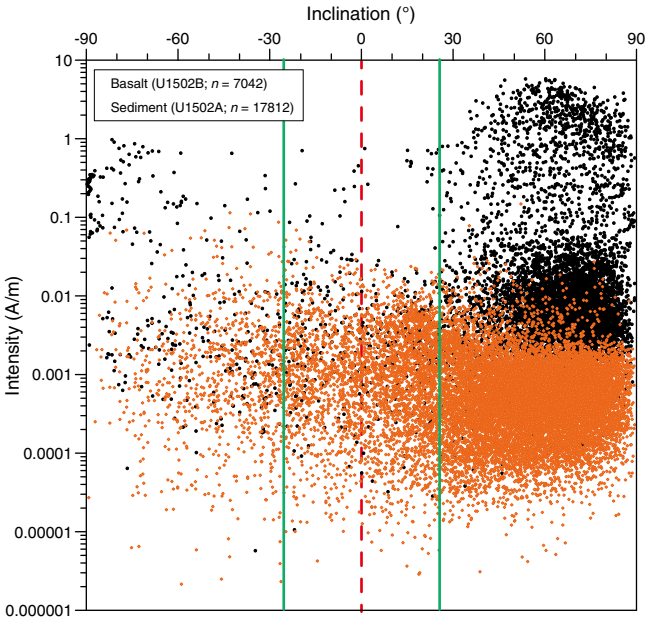

Figure F49. Paleomagnetic measurements, Hole U1502A. AFD = AF demagnetization. Green lines = expected normal and reversal inclination at present latitudes.

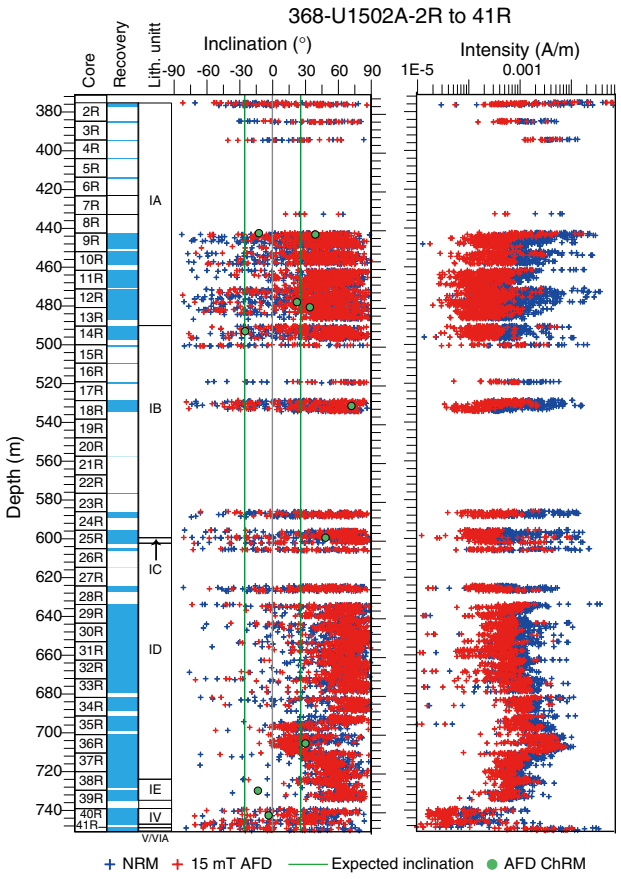

Figure F50. AF and thermal demagnetization plots of (A, C, D) discrete samples and (B) archive-half section, Hole U1502B basalts. Zijderveld plots: solid squares = declination, open squares = inclination. Stereographic plots: solid squares = positive (down) inclination, open squares = negative (up) inclination. Calculated ChRM (blue line; red squares = measurements used in calculation) using PCA is also shown. A, B. Normal polarity. C. Normal polarity, thermally demagnetized. D. Normal polarity, AF demagnetized. MAD = maximum angular deviation.

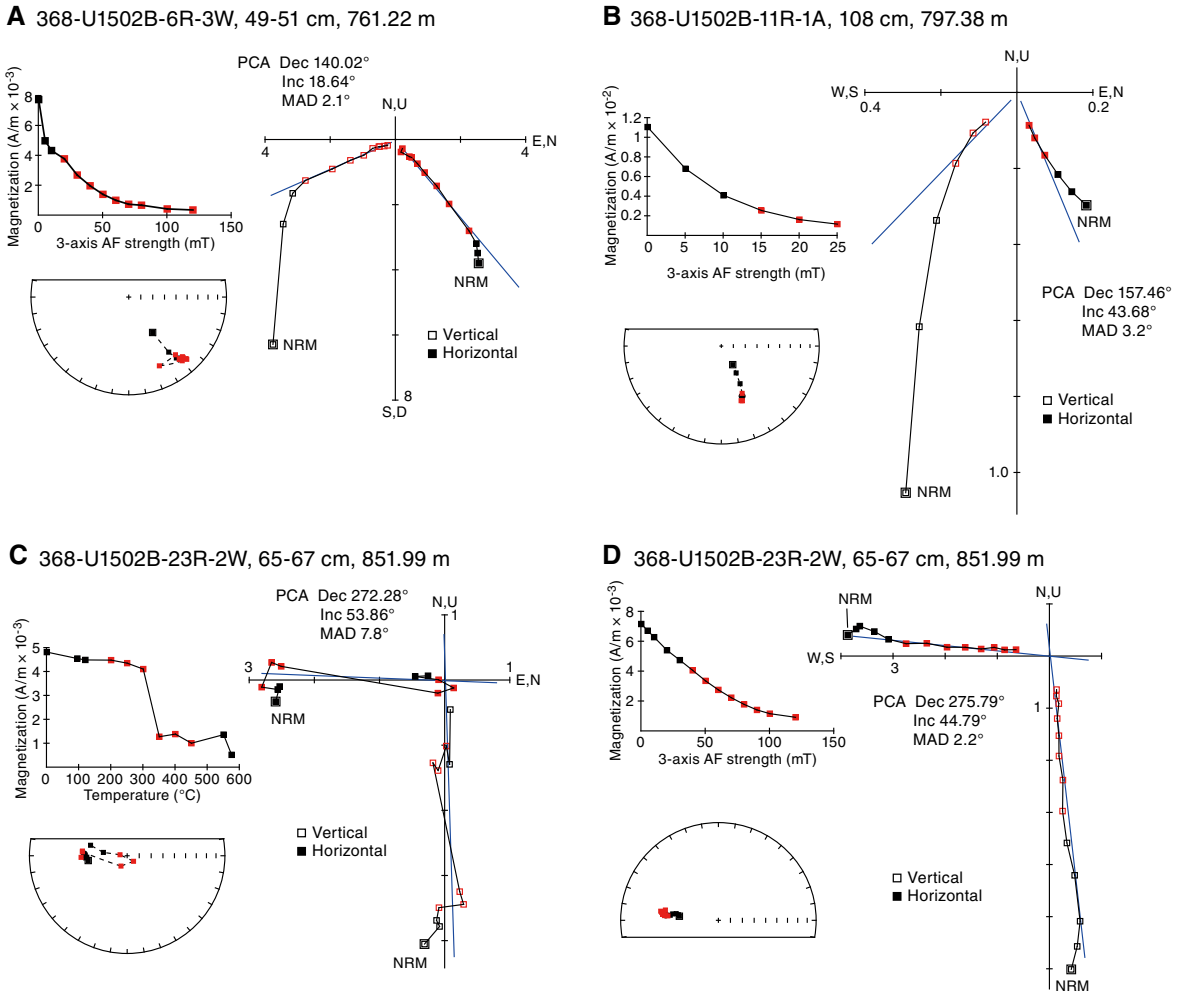

Figure F51. Magnetic susceptibility of basalts, Hole U1502B. Gray bands correspond to abrupt variations of magnetic susceptibility. These boundaries have different origins: in some cases they are very close to flow margins (e.g., 6R-2W, 65–66 cm; Figure F30A), whereas in other cases they correspond to more massive/isotropic, and therefore less altered, intervals of flows. Gravitational accumulation of magnetite toward flow bottoms could cause an increase in magnetic susceptibility as shown elsewhere in basalt flows (Caballero-Miranda et al., 2016). If correct, this provides an independent tool to interpret basaltic flow boundaries. Green dashed line = boundary between more altered basalts above and less altered basalts below. Inset: bimodal distribution of magnetic susceptibility.

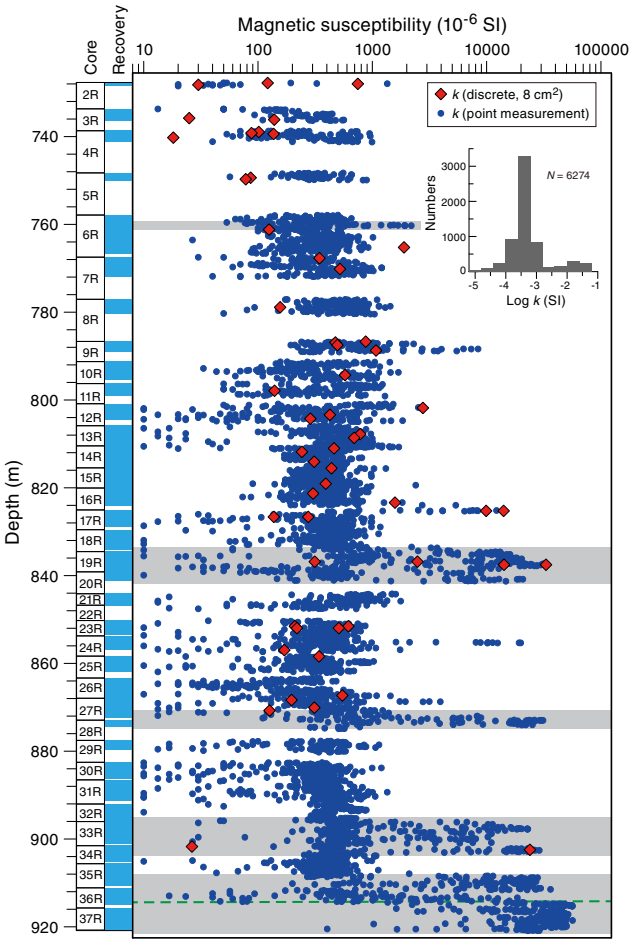

Figure F52. Fe_2O_3 vs. κ showing a gap in magnetic susceptibility between stratigraphic units, Hole U1502B. Green = 368-U1502B-2R-1 to 35R-1, black = 35R-2 to 37R-4.

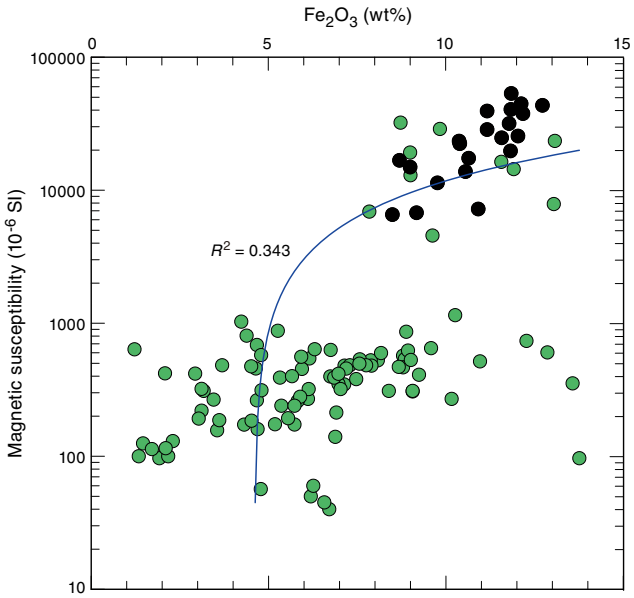

Figure F53. Koenigsberger ratio showing relatively modest potential contributions (Q_n < 10), Hole U1502B basalts.

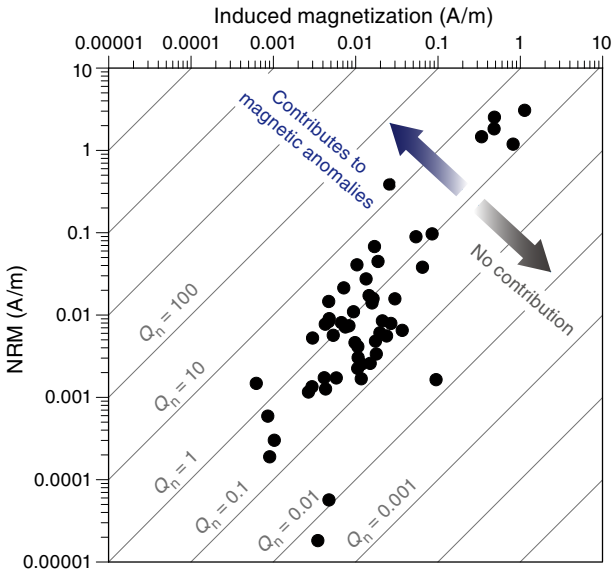

Figure F54. AMS data, Hole U1502B igneous rocks. A. Stereonet of AMS directions (lower hemisphere, equal-area projection). K_1 = maximum principal axis, K_2 = intermediate principal axis; K_3 = minimum principal axis. Confidence ellipses at 95% level are shown in corresponding color. Tensorial means are shown with larger symbols of same color. B. Degree of magnetic anisotropy (P') vs. magnetic susceptibility (K_m). C. Magnetic shape parameter (T) vs. P'.

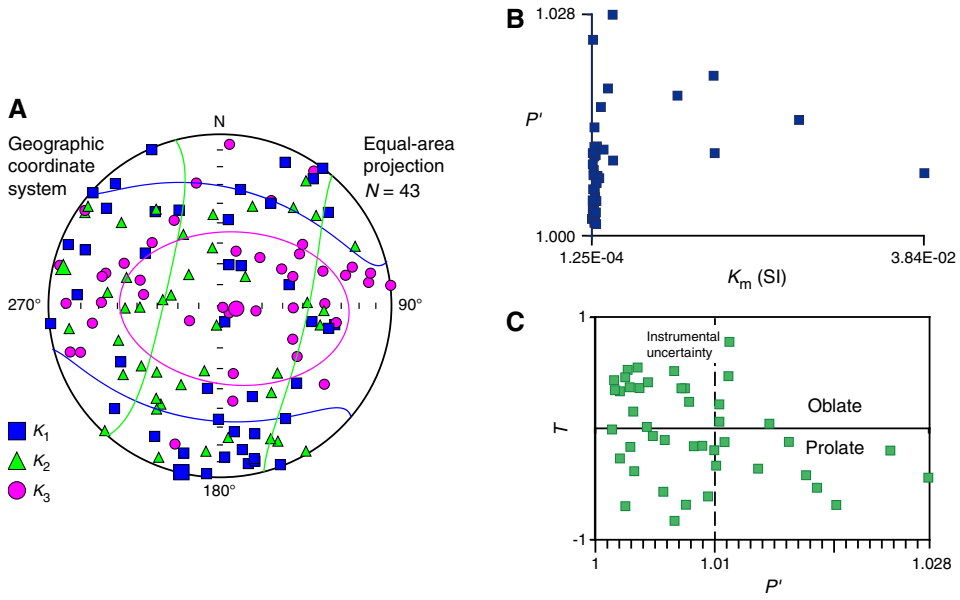

Figure F55. Paleomagnetic measurements, Hole U1502B. Gray shaded area = interval of possible negative inclination. TD = thermal demagnetization, AFD = AF demagnetization.

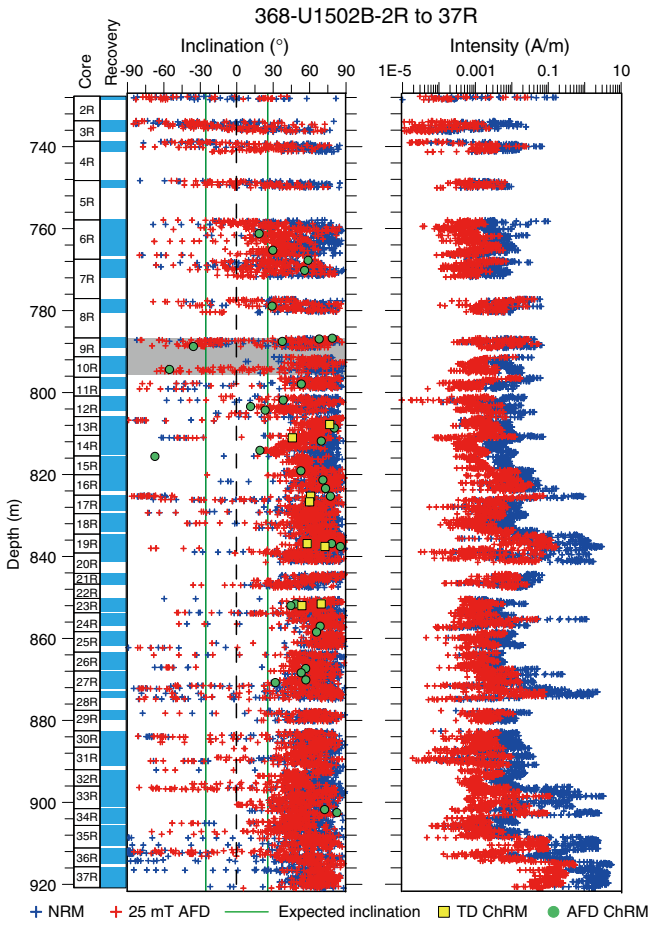

Geochemistry

Hydrocarbon gases were not abundant at Site U1502, and TOC, nitrogen, and sulfur contents were low, likely reflecting the poor preservation of organic matter. Instances of high carbonate content were associated with siderite and hydrothermal alteration, with siderite comprising greater than 50% of rock mass in parts of lithostratigraphic Subunit ID. The interstitial water at Site U1502 is enriched in Ca, Mg, K, and alkalinity and depleted in Na, Cl, and Br. The linear decrease and increase of major anion and cation contents, respectively, imply the upward diffusion of fluid from the deep sediment. Sediments within lithostratigraphic Unit I have some geochemical similarity to hemipelagic and pelagic units from Site U1501, but Site U1502 sediments have distinctively higher iron, potassium, and clay contents, likely due to patches of alteration resulting from different processes acting over various different timescales. Thus, the mechanisms and timing of iron enrichment do not need to be the same. Analyzed igneous rocks from lithostratigraphic Units II and VI (i.e., igneous lithologic Units 1 and 2) are all altered, and in general, samples from igneous Subunit 2b are altered to a lesser degree than those from igneous Subunit 2a.

Headspace gas

Headspace gas samples were taken at a frequency of one sample per core or per 10 m of drilling advance for routine safety monitoring to Core 368-U1502B-16R. Because of the absence of methane in previous samples and the nature of the igneous lithologies encountered, an operational decision was made to no longer collect headspace samples after this point. A small cluster of high methane values was encountered deeper than 650 m in an interval corresponding to a zone of intense siderite formation in lithostratigraphic Subunit ID, but at no point did hydrocarbon gas levels exceed the 5 ppmv detection limit. Traces of propene and butene were observed on chromatograms, but their occurrence was sporadic and not quantified.

Table T12. Carbon, nitrogen, and sulfur, Site U1502. **View table in PDF format. Download table in CSV format.**

Bulk sediment organic geochemistry

Lithostratigraphic Unit I

TOC, nitrogen, and sulfur levels were low in all samples collected from lithostratigraphic Unit I (TOC < 1 wt%, nitrogen < 0.1 wt%, and sulfur frequently less than detection limit) (Table **T12**; Figure **F56**). These levels likely represent the consequence of a bioturbated environment that was unfavorable for the preservation of high quantities of organic matter (Morris and Calvert, 1977). The low C/N ratios (C/N < 10) are consistent with organic carbon being derived from marine sources (Hedges et al., 1988) or with a very high level of thermal alteration.

Higher carbonate contents are found where greater quantities of siderite occur within sediments, such as in lithostratigraphic Subunits IB and ID. Siderite can affect the acid digestion–based assay used by IODP to estimate carbonate contents. In Figure **F56**, siderite-corrected values are shown as red circles (assuming 100% siderite) alongside calcite values (blue, assuming 100% calcite). Because TOC is determined by the difference between total carbon and carbonate carbon, the anomalously high value for TOC in Table **T12**

Figure F56. Methane, TOC and total sulfur, carbon/nitrogen ratio, and carbonate (blue = assays assuming 100% calcite, red = assays assuming 100% siderite), Site U1502. OB = overburden. TN = total nitrogen.

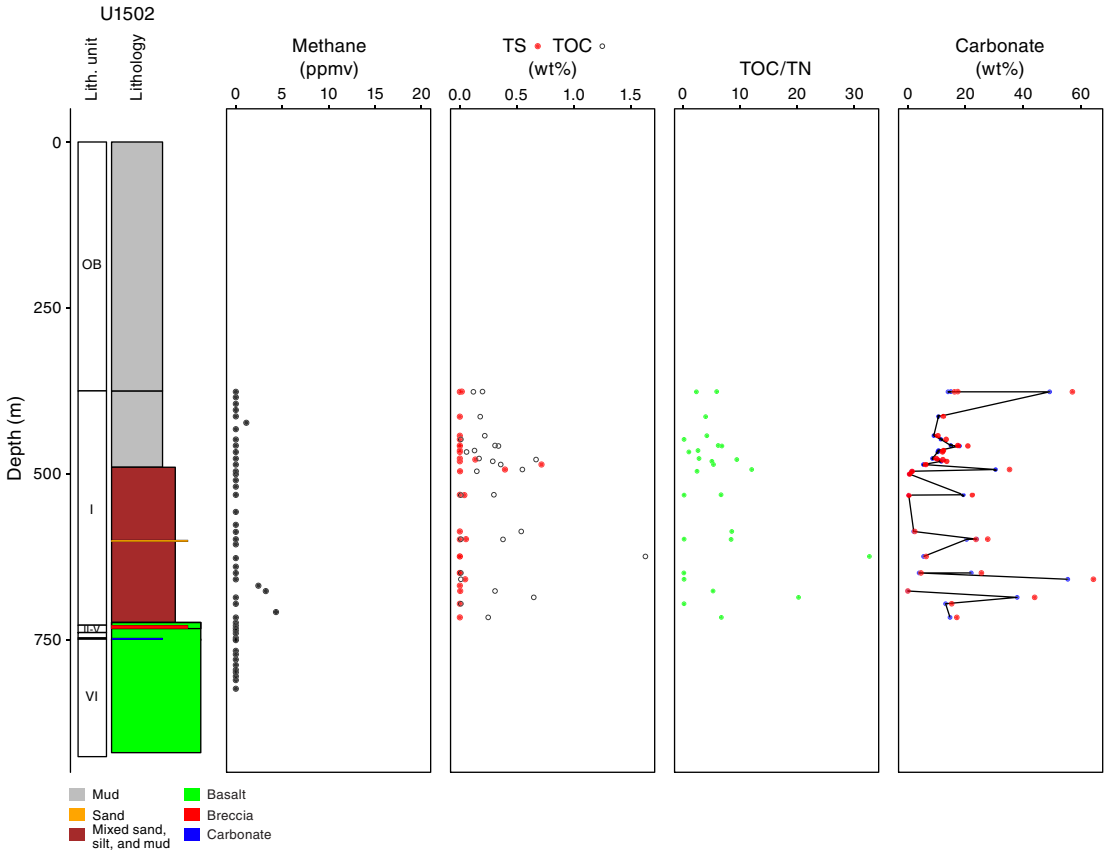

Figure F57. Crossplot of organic geochemical parameters: carbonate vs. carbon/nitrogen ratio and total sulfur vs. TOC, Site U1502. Solid circles = Subunit IA, open triangles = Subunit IB, open circles = Subunit ID.

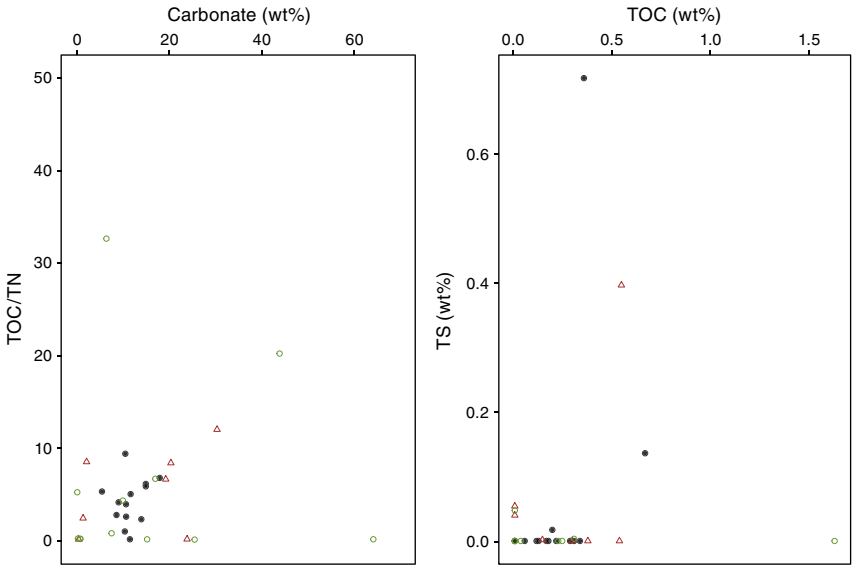

Table T13. Interstitial water analyses, Hole U1502A. **View table in PDF format. Download table in CSV format.**

likely reflects underestimation of the amount of inorganic carbon present.

Crossplots (Figure **F57**) do not help discriminate different organic geochemical units on the basis of lithostratigraphic units. In most cases there is a cluster of values with one or two outliers, which could be a consequence of comparing similar depositional environments (e.g., the units are all the same from a geochemical perspective) or indicate that hydrothermal alteration has overprinted any variation by reducing organic carbon and nitrogen content to levels beneath which it can be accurately measured.

Lithostratigraphic Units II–VI

Only sporadic samples were collected from lithostratigraphic Units II–VI. These units are not organic carbon rich, and carbonate content is mostly low. The few instances of high TOC often correspond to carbonate-rich intervals, many of which are Fe, Mn, and Mg rich and could represent types of carbonate that are underestimated by the carbonate assay employed. The low sulfur content for some of these intervals may be unexpected given the prominence of pyrite within many cores. However, the metal content of most sulfides is high; thus, pyrite has a relatively low sulfur content in comparison to the mass of iron.

Raman and surface-enhanced Raman spectroscopy

Because of time and resource constraints, Raman measurements were not performed at this site.

Interstitial water chemistry

We collected 19 whole-round samples (15–20 cm long) for interstitial water measurements in Hole U1502A. For Cores 2R through 33R, 15 cm long samples were squeezed for interstitial water and yielded ~15 mL per sample. For Cores 34R and 35R (15 cm long) and 37R (20 cm long), whole-round samples yielded <8 mL of interstitial water per sample and even then only after squeezing for durations longer than 8 h. Interstitial water geochemical parameters are listed in Table **T13** and presented by depth in Figure **F58**.

No samples were obtained from depths shallower than 376.39 m (Section 2R-1) because this section was not cored (see **Operations**); therefore, in the following discussion comparisons are made to geochemical data from Holes U1499A and U1501C to set the data in context. In Hole U1502A, alkalinity increases linearly with depth from 7.6 to 45.9 mM. The maximum alkalinity was measured at 625 m, and the remaining measurements are constant at ~45 mM. In Hole U1501C, the alkalinity is at least 10 times greater than that found at the equivalent depth in Hole U1502A. At the same time, pH in Hole U1502A is lower than in Holes U1501C and U1499A, ranging from 7.2 to 7.9. The pH value decreases sharply from 376 to 531 m and is 7.3 at the bottom of the hole. Sulfate concentrations range from 4.0 to 9.9 mM with an increase from Core 2R to Core 37R. The bottom water in Hole U1502A is thus enriched in alkalinity and sulfate and has a higher pH than both modern seawater and most other interstitial water obtained in the region.

The chlorinity, bromide, and sodium depth profiles are similar; there is a 10% decrease from Core 2R to Core 37R (Figure **F58**). The uppermost sample from Core 2R is similar to modern seawater (Cl = 569 mM; Br = 0.89 mM; Na = 478 mM), whereas the bottom sample from Core 37R has low values of Cl (509 mM), Br (0.79 mM), and Na (421 mM). The decreased chlorinity, bromide, and sodium are similar to the "freshwater" in interstitial water Zone 3 in Hole U1501C.

Contrary to the halide anions, Ca, Mg, and K concentrations increase with depth (Figure **F58**). The calcium concentration ranges from 11 to 32.7 mM; the maximum is about three times that of modern seawater (10.5 mM). K concentrations vary between 3.2 and 5.3 mM; the maximum concentration is twice that found at similar depth samples in Holes U1501C and U1499A.

Dissolved strontium concentrations range from 61.9 to 144 μM and decrease with increasing depth, in contrast to the chemically similar Ca and Mg (Ca, Mg, and Sr covary in Hole U1499A). Interstitial water Sr concentration is often controlled by the dissolution

Figure F58. Interstitial water alkalinity, major cations, and anions, Site U1502.

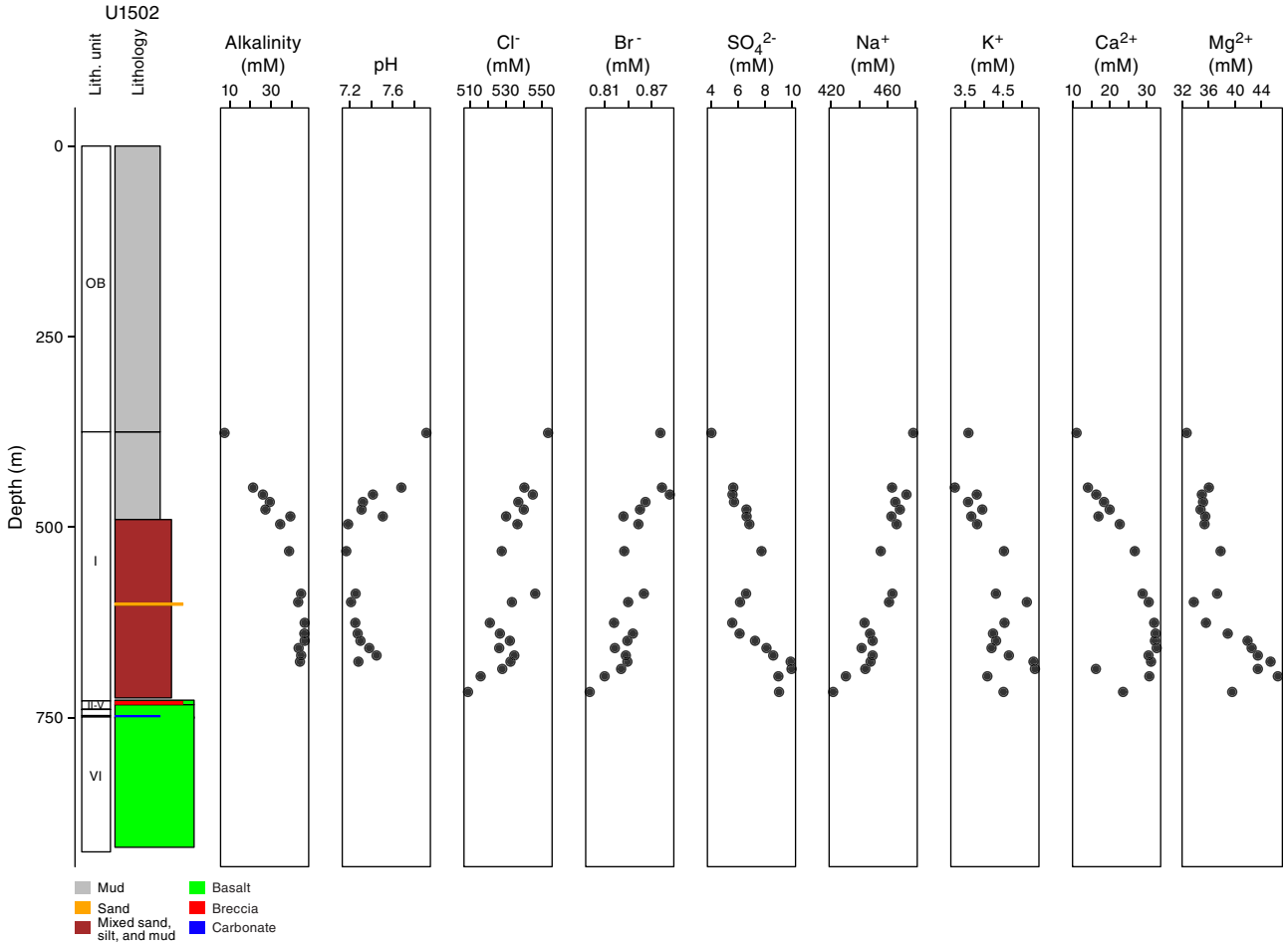

of biogenic calcite. The minimum Sr concentration (61.9 µM) at 676 m is lower than modern seawater and corresponds to elevated Ca and Mg.

Concentrations of Fe, Si, and Li vary in a similar way and generally increase with depth. Dissolved Fe concentrations range from 1.68 to 102.3 µM in the 477–716 m interval. The maximum Fe (102.3 µM) at 676 m corresponds to maximum values of Si, Mg, and Ca. The abnormally high Fe is likely related to the dissolution of mafic minerals within the basalt. Silica concentrations increase from 250 to 1182 µM in Hole U1502A and are much higher than both modern seawater (0–180 µM) and Hole U1499A (280–822 µM) contents. The dissolved Si profile reflects lithology and silicate mineral diagenesis. Lithium concentrations increase linearly from 91 µM at 376 m to the maximum of 855 µM at 695 m, which is higher than the Li concentration at Site U1499 (13.7–31.2 µM).

Dissolved Mn concentrations increase from 1.14 to 47.73 µM to the bottom of the hole.

Bulk sediment and rock geochemistry

The following sections describe sediments and igneous rock geochemistry based on ICP-AES analysis. Compositions are reported in Table **T14**.

Lithostratigraphic Unit I

Site U1502 sediments have high and variable Fe_2O_3 contents (2.81–38.59 wt%) that are significantly higher than those at Site U1501 (Figure **F59**). Manganese is also enhanced (MnO = 0.01–1.49 wt%), with the highest contents found in carbonate-rich intervals, likely a result of the presence of Mn within siderite-rich intervals. PCA was used to compare sediments at Sites U1501 and U1502 (Figure **F60**) and shows some overlap with the oozes and hemipelagic mudstones (lithostratigraphic Units I and II at Site U1501), indicating unaltered samples. However, the greatest difference between the sediment samples is the proportion of K, Na, and Al (PC1) and the proportion of Si (PC2) (see Table **T15**). Some of the samples from Site U1502 contain notably more K, Al, and Ti (as well as Fe, although this was not included in the PCA), although by no means all of them. Given the hydrothermal alteration observed at this site, the enrichment of these elements in some of the sediment samples could reflect a clay or carbonate zone within an epithermal hydrothermal system (a low-temperature zone of phyllosilicate and carbonate formation; Sillitoe and Hedenquist, 2003), an increased proportion of clays in a depositional environment far from siliciclastic sources (Heezen and Hollister, 1972), poor preservation of siliceous fossils, or a combination of these processes. Lesser Ca contents within carbonate intervals may be the result of hydrothermal alteration and replacement by Fe, Mn, and Mg.

Table T14. Major element oxide and trace element contents of sediment and whole-rock samples, Site U1502. **View table in PDF format. Download table in CSV format.**

Figure F59. Major oxide composition in sediments and select geochemical parameters, Site U1502.

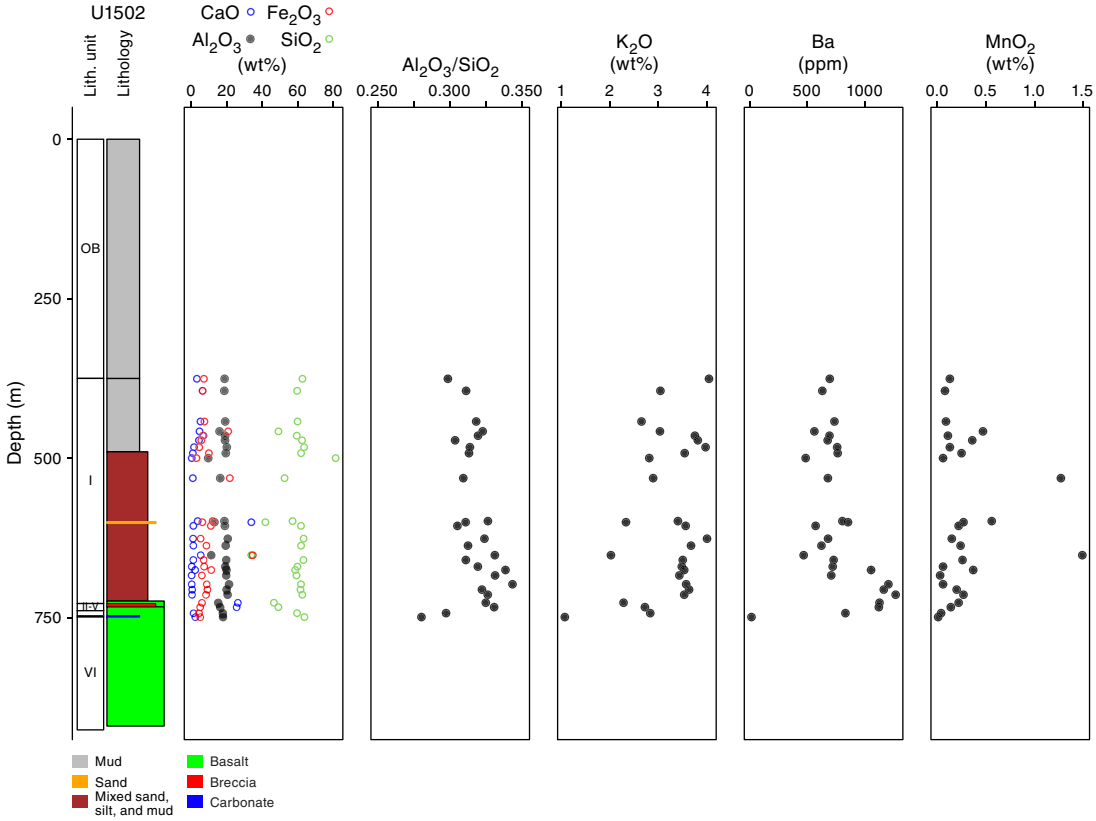

Figure F60. PCA crossplot for the two components that explain the greatest variation within data (PC1 = proportion of potassium, sodium, and aluminum; PC2 = proportion of silica), Site U1502. Circles and ellipses = 95% confidence intervals.

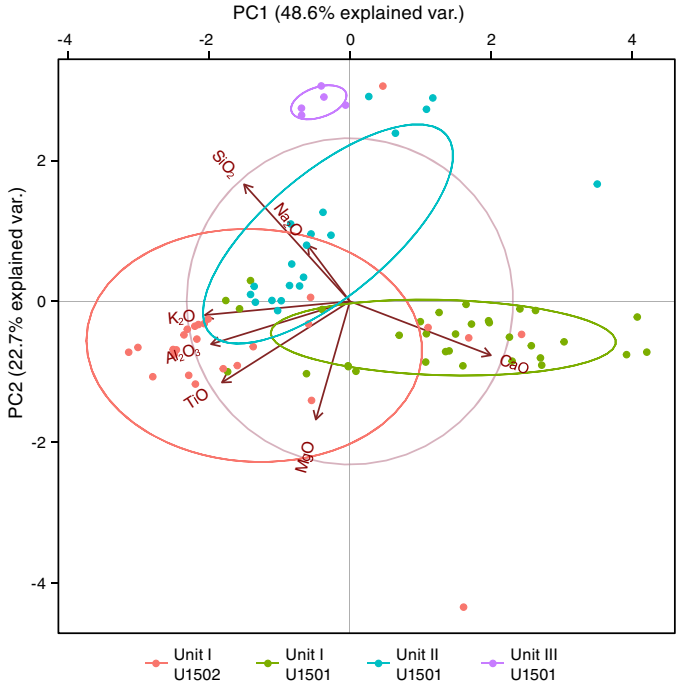

Table T15. Major element oxide variance, Site U1502. **Download table in CSV format.**

Major element oxide	PC1 43% variance explained	PC1 29% variance explained
Al_2O_3	–0.461184109	–0.208145574
CaO	0.468018816	–0.262202401
SiO_2	–0.351496063	0.568850519
Na_2O	–0.139784587	0.271894389
K_2O	–0.481527489	–0.066640626
TiO	–0.424884295	–0.394468828
MgO	–0.113061955	–0.57477058

Lithostratigraphic Units II and VI (igneous lithologic Units 1 and 2)

Major element oxides and minor element concentrations were normalized to TiO_2, which is thought to be constant during aqueous alteration processes (Staudigel, 2014). To provide a frame of reference, the resulting element ratios are plotted next to samples from IODP Expedition 349 Sites U1431, U1433, and U1434 in Figure F61.

When considered as a depth profile, a significant boundary appears to separate the samples into two groups of basalts at around 797.9 m (interval 368-U1502B-11R-2, 18–20 cm). This interval roughly corresponds with the boundary between igneous Subunits 2a and 2b (~801.55 m). Samples from shallower than 797.9 m are depleted in Fe, Mg, and Mn compared to those from deeper than 797.9 m (797.9–920.8 m). Also, these elements reveal lower contents than those of samples from fresh/less altered basalts from Ex-

Figure F61. Ti-normalized major element oxide and minor element concentration profiles, Site U1502. Green circles = whole rock samples from igneous lithologic Unit 1, black solid circles = samples from igneous lithologic Unit 2, red dots = fresh/less altered basalt samples from Expedition 349 (Li et al., 2015).

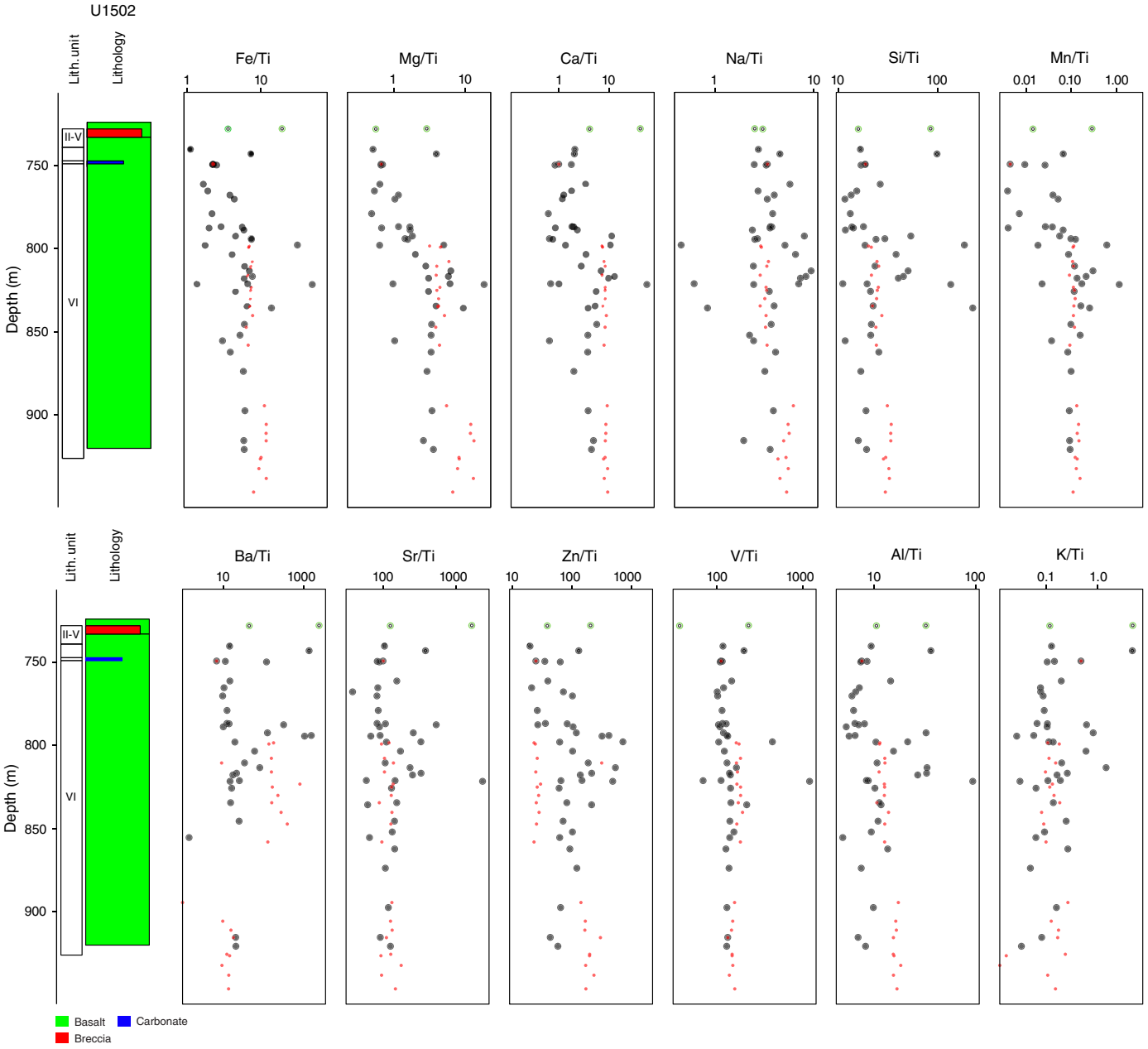

pedition 349 (Figure **F61**). This depletion is less pronounced with depth. The Site U1502 basalts recovered from shallower than 797.9 m are also slightly less enriched in Ca, Si, Al, and subordinate V.

Na and K vary mostly within the ranges observed for fresher basalts from the study area, except for the 727.9–821.5 m interval (Figure **F61**). Ba, Sr, and Z are generally enriched relative to the samples of fresh/less altered basalts from the study area, which reflects the presence of veins rather than demonstrating a primary geochemical feature. Overall, when normalized to TiO_2, there are differences in the degree of alteration between igneous Subunits 2a and 2b; rock samples from igneous Subunit 2b suffered less alteration than those from igneous Subunit 2a.

Acidic interstitial water was encountered in overlying sediments, and if taken as representative of water from deeper sections could indicate the potential for metasomatic alteration. Fe, Mg, Mn, and Al could all be mobilized by the dissolution of Fe-, Mg- or Al-bearing silicates such as olivine, pyroxene, and plagioclase (Pirajno, 2009). The likely products of such alteration are chlorite, phyllosilicates, and zeolites.

Discussion

To gain insight into the nature of authigenic mineralization in Hole U1502A, a 1-D material balance was performed (e.g., results are returned as grams Fe_2O_3 per square centimeter). The net gain or loss in Fe_2O_3 was calculated by making a comparison to Site U1501 in terms of sediment, to Site U1500 with respect to the basalts, and to shallower samples from Site U1501 in the case of interstitial water. For a given unit, the 1-D concentration was calculated as

Figure F62. Ti-normalized major element oxide and minor element concentration profiles, Site U1502. References are from fresh/less altered basalt samples from Expedition 349 (Li et al., 2015). mst = mudstone.

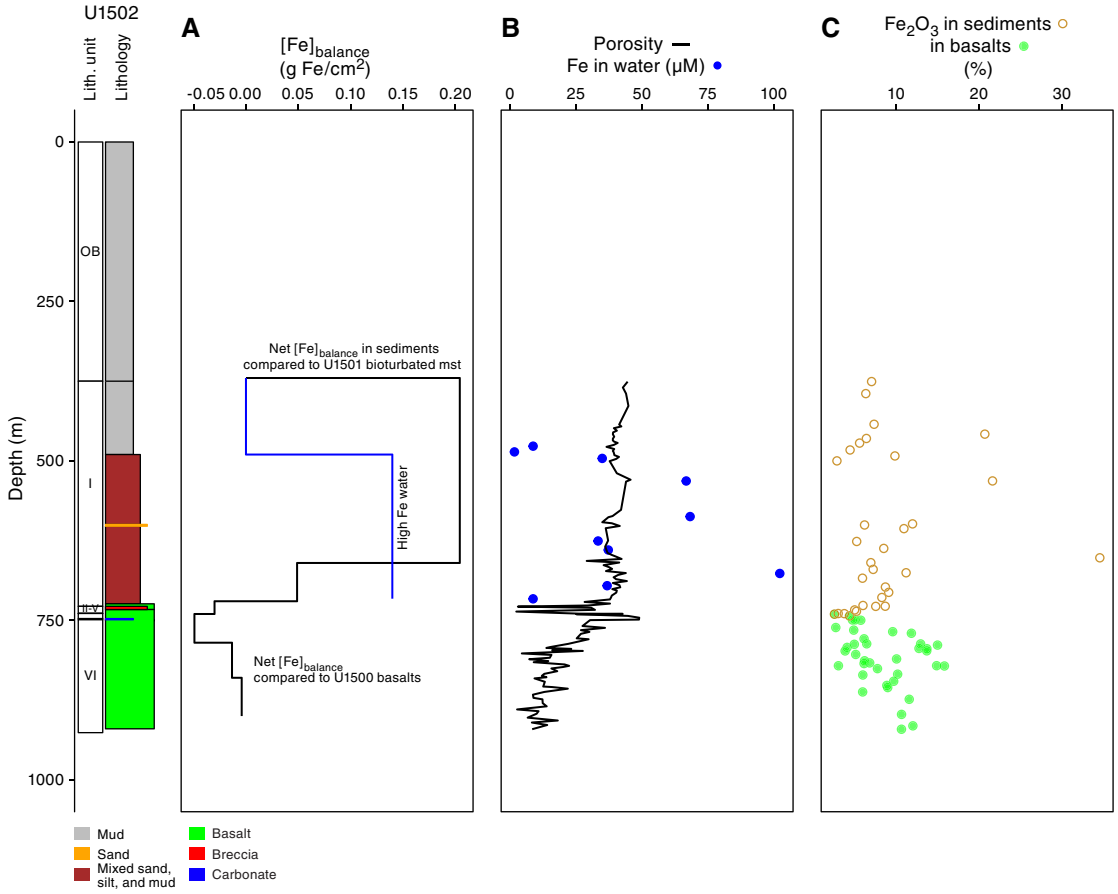

$$[Fe]_{balance} = [Fe]_{U1502} - [Fe]_{ref},$$

where $[Fe]_{balance}$ is the net gain or loss in grams Fe per square centimeter for a given unit, $[Fe]_{U1502}$ is the measured iron content of a unit (grams Fe per square centimeter) at Site U1502, and $[Fe]_{ref}$ is the expected Fe content based on the lithologic points of reference listed above.

Fe contents per unit area were obtained using

$$[Fe] = h \times \%Fe_2O_3 \times \rho,$$

where ρ is the average moisture and density (MAD) density within a given interval (in grams per cubic centimeter), h is the length of a given interval (in centimeters), and $\%Fe_2O_3$ is the Fe content of a given interval expressed as a fractional content from 0 to 1. The results are displayed in Figure **F62**.

Interstitial water present in lithostratigraphic Subunits IA–IC and in intervals with a high siderite content is greatly enriched in Fe. The base of the interval spanning lithostratigraphic Subunits IA–IC coincides with Fe-enriched interstitial water that is consistent with instances of very low porosity that likely indicate hydraulic barriers that bound the interstitial water body. On a 1-D basis, it would be difficult to account for the high Fe content within the interstitial water by dissolution of the basalts at the top of lithostratigraphic Unit VI because of the magnitude of Fe involved.

The basalts at the top of lithostratigraphic Unit VI (igneous lithologic Unit 2) are depleted in Fe but are not significantly depleted in Fe at the bottom of the recovered volcanic section, implying not that these basalts are not altered or depleted relative to Ti or in terms of their mineralogy, but that relative to the area of the rock the net depletion in Fe is slight. The slightness of the depletion may reflect the presence of Fe within the basalts in the form of sulfides or veins that precipitated from water not enriched in dissolved Ti (Staudigel, 2014). The level of Fe enrichment in sediment immediately above the basement (lithostratigraphic Subunit ID) is of a similar magnitude to the loss of Fe from the shallower basalt units. Compared to the upper part of lithostratigraphic Unit I, it is more reasonable that Fe mineralization within the lower part is genetically linked to the Fe depletion in parts of lithostratigraphic Unit VI.

These considerations represent a 1-D approximation and thus do not enable implications for structure, sedimentary architecture, or the geological history of the site. Therefore, they would not apply if the Fe was released from basalts significantly before the deposition of lithostratigraphic Unit I or if the precipitation of Fe occurred only within a small area yet leached from a greater area.

Physical properties

Physical properties were measured on cores from Holes U1502A (375–758.2 m) and U1502B (727.7–920.8 m). Magnetic susceptibility, gamma ray attenuation (GRA) bulk density, and *P*-wave velocity were measured on the whole-round cores using the Whole-Round Multisensor Logger (WRMSL) at a 2 cm interval. NGR was then measured on whole-round cores with the Natural

Gamma Radiation Logger (NGRL). Color reflectance and point magnetic susceptibility were measured on all archive-half sections. *P*-wave velocity was also measured along the *x*-axis with the *P*-wave caliper (PWC) system on working-half sections with liner and on discrete samples without liner. MAD measurements were performed on discrete samples taken at a sampling resolution of one every other section per core. Thermal conductivity measurements were performed on the third section of every core. Based on the variations of physical properties, four petrophysical (PP) units were distinguished at Site U1502 (Figure **F63**):

- PP Unit 1 (375–740 m in Hole U1502A),
- PP Unit 2 (740–750 m in Hole U1502A and 727.7–740 m in Hole U1502B),
- PP Unit 3 (740–808 m in Hole U1502B), and
- PP Unit 4 (808–920 m in Hole U1502B).

PP Unit 1 is characterized by slight increases with depth in bulk density (average = 2.1 g/cm^3) and *P*-wave velocity (average = 1950 m/s) and NGR values of 50–70 counts/s. PP Unit 2 lies immediately above the basaltic basement and is defined in both holes by a variety of different lithostratigraphic units. PP Unit 2 in Hole U1502A is marked by lower *P*-wave velocity and bulk density and higher NGR values than overlying PP Unit 1. The base of PP Unit 2 is marked by a sharp decrease in NGR in both holes (Figures **F63**, **F64**). PP Units 3 and 4 represent the basaltic basement and are characterized by relatively low NGR (<10 counts/s) and a wider range of *P*-wave velocities (3000–5000 m/s). The interface between PP Units 3 and 4 is marked by an abrupt increase in density, *P*-wave velocity, and thermal conductivity and corresponds to the boundary between igneous Subunits 2a and 2b (see **Igneous and metamorphic petrology**).

Natural gamma radiation

In PP Unit 1, NGR counts generally range between 50 and 70 counts/s with two exceptions (Figure **F63**). The first is a decrease in NGR at ~600 m to ~30 counts/s. The second interval starts at ~710 m, where NGR begins to decrease with depth, reaching ~35 counts/s at ~730 m, close to the top of PP Unit 2. PP Unit 2 is characterized by high NGR (70 counts/s) that decreases sharply near the base of this unit.

PP Unit 3 is characterized by relatively low NGR (3–10 counts/s) that decreases slightly with depth (Figures **F63**, **F64**). At 735 m, close to the top of PP Unit 3, a spike in NGR to ~50 counts/s cor-

Figure F63. Physical properties for Holes U1502A and U1502B with petrophysical units. Logarithmic scale is used for magnetic susceptibility. Descriptions of variations in *P*-wave velocity and bulk density in text are based on discrete measurements of *P*-wave velocity (PWC) and bulk density (MAD). cps = counts per second.

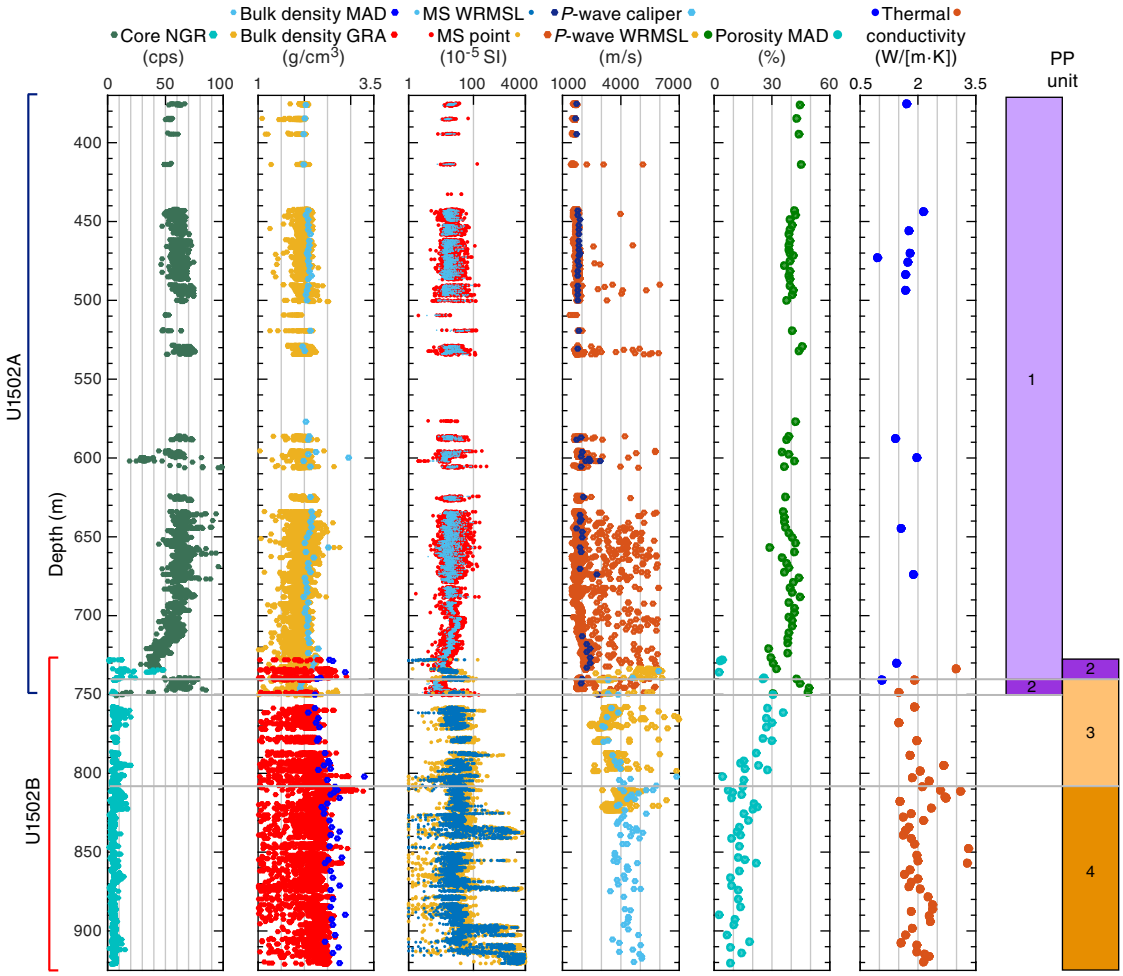

Figure F64. Physical properties measured, Hole U1502B. Logarithmic scale is used for magnetic susceptibility. Descriptions of variations in *P*-wave velocity and bulk density in text are based on discrete measurements of *P*-wave velocity (PWC) and bulk density (MAD). cps = counts per second.

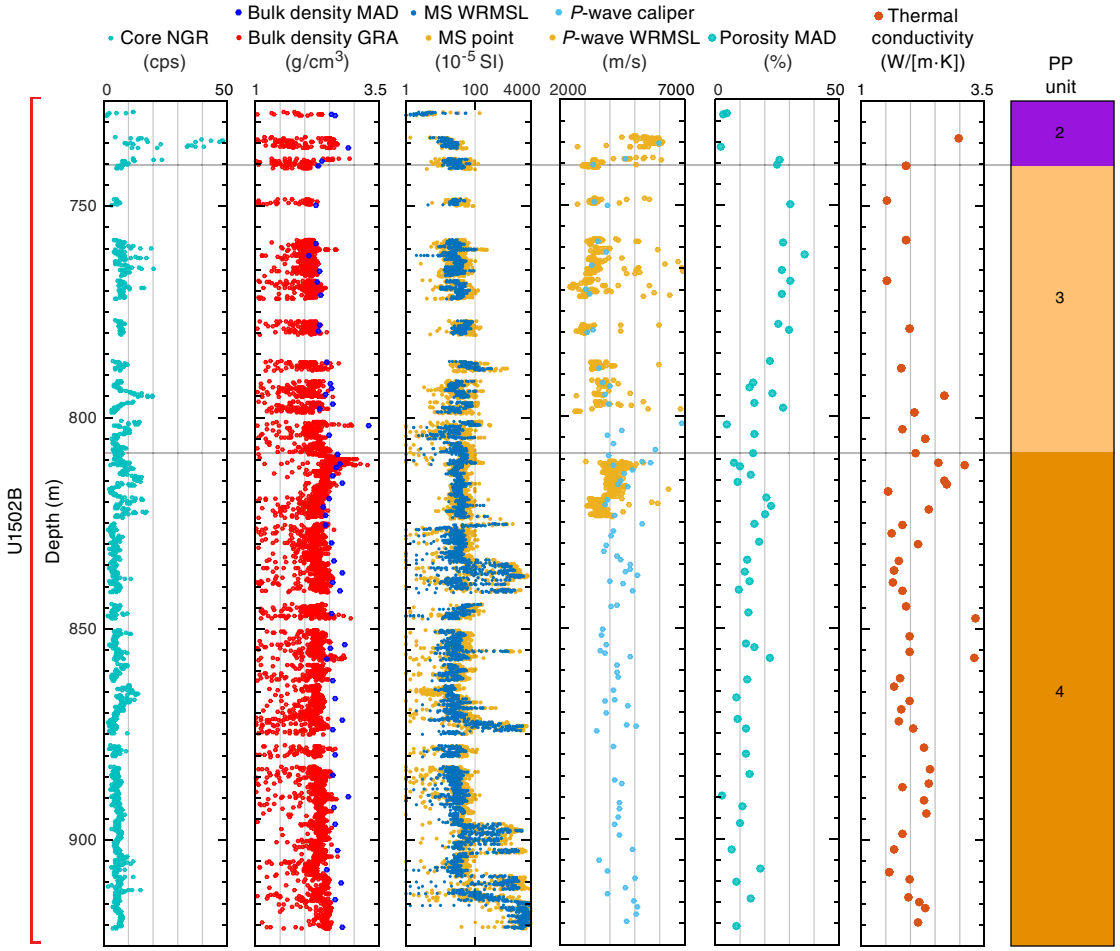

relates with high *P*-wave velocity. Numerous smaller excursions in NGR values are present between 760 and 825 m. In contrast, deeper than 825 m (PP Unit 4), NGR values show only small-scale variations and remain less than ~5 counts/s.

Concentrations of K, U, and Th were estimated using the NGR counts and bulk density measurements for Hole U1502A according to the methods by De Vleeschouwer et al. (2017). Overall, element concentrations have trends similar to the total NGR counts per second values (Figure **F65**).

P-wave velocity

Descriptions of variations in *P*-wave velocity are based on measurements made with the PWC system because measurements on the whole-round cores are more scattered due to the space between the core and core liner. In PP Unit 1, *P*-wave velocities increase gradually from 1735 m/s at ~375 m to ~2000 m/s at 715 m (Figure **F63**). This trend is interrupted by a spike in velocity at ~600 m to ~2910 m/s. Another spike in velocity occurs in the lowermost section of Hole U1502A, where velocity increases to ~2500 m/s over a narrow depth range (715–725 m). Below this interval, velocity rapidly decreases to ~1995 m/s at 740 m, marking the top of PP Unit 2. At the base of PP Unit 2 (~750 m), *P*-wave velocity increases abruptly to 2810 m/s.

In contrast to Hole U1502A (375–750 m), where *P*-wave velocity is consistently <3000 m/s, velocities in Hole U1502B (727.7–920.8 m) all exceed 3000 m/s (Figure **F64**). Two main intervals were observed in Hole U1502B: a shallower interval at 740–795 m in basaltic basement (PP Unit 3; see **Lithostratigraphy**) with velocities in the 3000–4000 m/s range, and a deeper interval (PP Unit 4) starting at ~800 m with velocities that generally exceed 4000 m/s.

Thermal conductivity

Thermal conductivity within PP Unit 1 varies between ~0.98 and ~1.90 W/(m·K) (Figure **F63**). A slight decrease in values from 1.5 to 1.1 W/(m·K) was observed at the bottom of PP Unit 1. A gradual increase in PP Unit 3 (740–808 m) from 1.9 to 2.3 W/(m·K) is followed by a sharp increase to 2.7 W/(m·K) at the boundary with PP Unit 4. Thermal conductivity decreases to 1.6 W/(m·K) in the upper portion of PP Unit 4 (843 m) (Figure **F64**) and averages ~2.2 W/(m·K) to the bottom of the unit. Two elevated thermal conductivity measurements (~3.2 W/[m·K]) were observed at 848 and 857 m.

Density and porosity

In general, bulk density determined from discrete samples agrees well with those obtained from GRA on the whole-round cores (Figure **F66**). However, GRA bulk density displays large variations throughout Holes U1502A and U1502B because of space between the core and core liner. Thus, the following descriptions of variations in bulk density are based on measurements from discrete samples. Bulk density increases slightly with depth in PP Unit 1,

Figure F65. NGR measurements, Hole U1502A. K, U, and Th concentrations are derived from NGR and GRA density measurements using method of De Vleeschouwer et al. (2017).

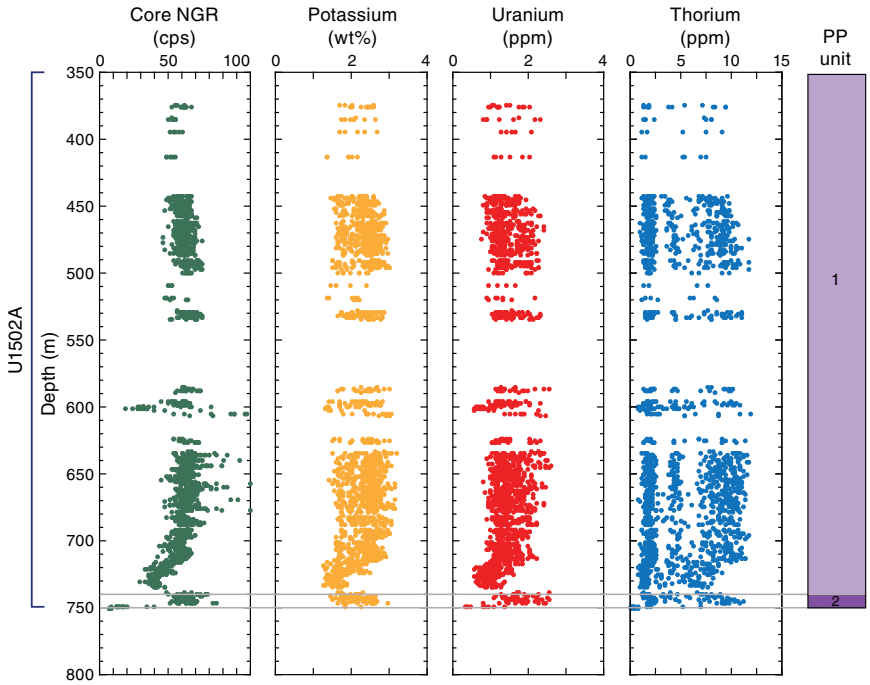

varying from 1.9 to 2.3 g/cm³. Porosity decreases from 45% to 35% with depth and shows a good negative correlation with bulk density. Grain density remains relatively constant at 2.8 g/cm³. At 725 m, bulk density increases from 2.1 to 2.3 g/cm³ and dry density increases from 1.7 to 1.9 g/cm³. A sharp shift toward lower values at the bottom of this interval (740 m) marks the boundary with PP Unit 2. Densities then decrease slightly with depth to the bottom of PP Unit 2.

Bulk density in PP Unit 3 varies between 2.1 and 2.6 g/cm but generally increases with depth (Figure **F66**). Porosity fluctuates between 5% and 35% but decreases overall downhole.

The boundary between PP Units 3 and 4 is marked by a sharp increase followed by a drop in bulk, dry, and grain densities from 2.5 to 2.7 g/cm³, 2.3 to 2.5 g/cm³, and 2.8 to 3.0 g/cm³, respectively. Grain, bulk, and dry densities in PP Unit 4 are slightly more variable, ranging from 2.7 to 3.0 g/cm³, 2.4 to 2.8 g/cm³, and 2.1 to 2.7 g/cm³, respectively. Bulk and dry densities increase slightly with depth throughout PP Unit 4.

Color reflectance spectrophotometry

L* values in PP Unit 1 remain relatively constant with an average of 40 and abruptly increase to 60 at the onset of PP Unit 2 (Figure **F67**). Throughout PP Units 2–4, L* values fluctuate between 20 and 70 without any general trend. From 375 to 675 m, reflectance parameters a* and b* show relatively narrow ranges of ~0–5 and approximately −4 to 2, respectively. Toward the lower portion of PP Unit 1 (~675–740 m), a* and b* display high values of ~5–10 and ~0–10, respectively, corresponding to the interbedded brownish and reddish clay (see **Lithostratigraphy**). The beginning of PP Unit 2 is marked by a rapid decrease in a* and b* followed by an overall decreasing trend through PP Units 2–4.

Magnetic susceptibility

Magnetic susceptibility varies between ~10 × 10⁻⁵ and 100 × 10⁻⁵ SI in the upper portion of PP Unit 1 without any general trend, and the fluctuations are relatively muted and narrow to 5 × 10⁻⁵ to 40 × 10⁻⁵ SI between ~700 and 740 m (Figure **F63**). Throughout PP Units 3 and 4, magnetic susceptibility generally has a narrow range between ~10 × 10⁻⁵ and 80 × 10⁻⁵ SI (Figure **F64**), except for the intervals where it peaks to ~2000 × 10⁻⁵ to 4000 × 10⁻⁵ SI (~835–842, 855–855.4, 872–875, 896–903, 908–912, and 914–921 m).

RGB color values

Red, green, blue (RGB) values are generally constant with depth in PP Unit 1 (Figure **F68**). A marked increase in RGB from 100 to 150 occurs in the lower portion of PP Unit 1 (~725 m) and is related to the presence of brownish nannofossil-rich clay in the sediment cores (see **Lithostratigraphy**). RGB decreases in PP Unit 2 (740 m), marking a transition to dark gray biosiliceous clay over this interval (see **Lithostratigraphy**). RGB increases in PP Units 3 and 4 to between 100 and 200.

Discussion and summary

The trends of physical properties allow us to characterize four petrophysical units at Site U1502. PP Unit 1 (375–740 m) reflects nannofossil- and biosiliceous-rich clay lithologies (see **Lithostratigraphy**) and exhibits small-scale changes in NGR values between 50 and 70 counts/s and uniformly increasing *P*-wave velocities with depth that are <2500 m/s. PP Unit 1 sediments have porosities similar to those recorded at nearby Sites U1499 and U1500 in the same depth interval, suggesting the same compaction history. A significant increase in bulk density (up to 2.7 g/cm³) was observed in Core 368-U1502B-3R and is associated with strongly lithified limestone beds (Figure **F69A**). Variations of high and low magnetic susceptibility values correspond to sediment color changes in PP Unit 1 (Figure **F69B**) and may be controlled by the amount of pyrrhotite within the sediment (Tauxe, 2010; see **Paleomagnetism**).

PP Unit 2 (740–750 m) in Hole U1502A is characterized by lower *P*-wave velocities and bulk densities and higher gamma ray readings than the strata above. Low densities and *P*-wave velocities

Figure F66. GRA bulk density; MAD bulk density, dry density, and grain density; and porosity, Holes U1502A–U1502B. Note that descriptions of variations in bulk density in text are based on discrete measurements of bulk density (MAD). MAD porosity from Sites U1499 and U1500 are also plotted for comparison.

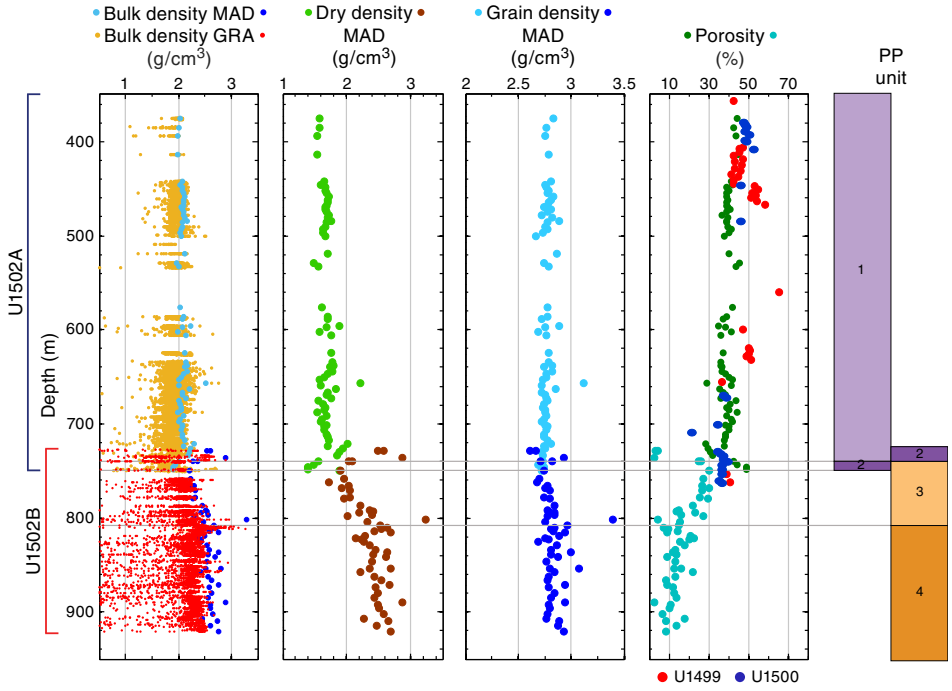

Figure F67. Sediment color reflectance parameters L*, a*, and b*, Holes U1502A and U1502B.

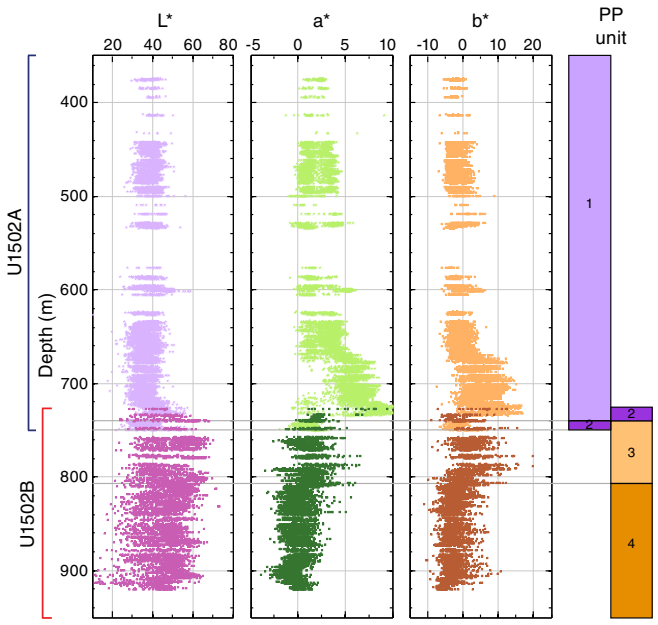

Figure F68. RGB values, Holes U1502A and U1502B.

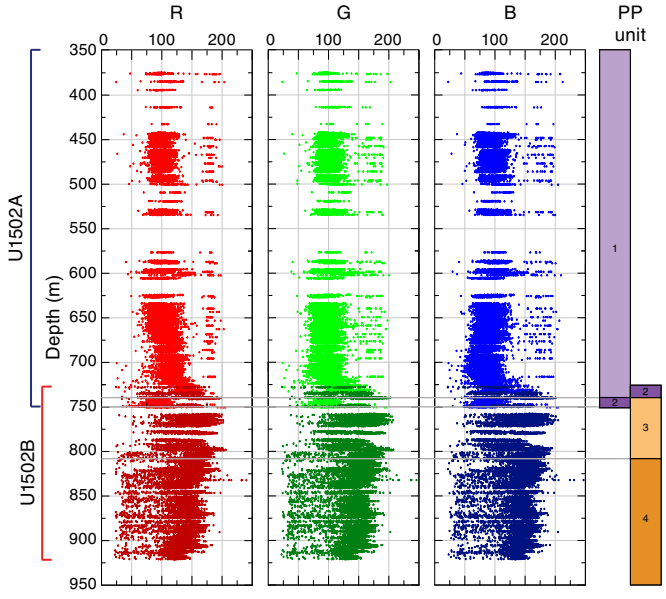

suggest that PP Unit 2 is less compacted and highly saturated with pore water.

PP Units 3 and 4 represent the basaltic basement and are characterized by relatively low NGR values (<10 counts/s), high densities, and *P*-wave velocities that vary over a broad range (3000–6000 m/s) (Figure **F64**). The boundary between PP Units 3 and 4 is marked by an abrupt increase in physical properties (i.e., density, *P*-wave velocity, and thermal conductivity) and coincides with the change from igneous Subunit 2a to 2b (Figures **F64**, **F65**, **F66**; see **Igneous and metamorphic petrology**). Prominent peaks of magnetic susceptibility (up to 4000 × 10^{-5} SI) in PP Units 3 and 4 correspond to relatively less altered basalt. Reflectance L* from these basalt layers records the lowest values in PP Unit 4, reflecting the dark nature of the less altered basalts. Thermal conductivities in PP Units 3 and 4 are variable but with an overall increasing trend, in line with the decreasing porosities with depth (Figure **F64**).

Figure F69. Comparison of sediment physical properties with lithology. A. Bulk density and NGR (368-U1502B-3R). B. magnetic susceptibility (MS) (368-U1502A-12R).

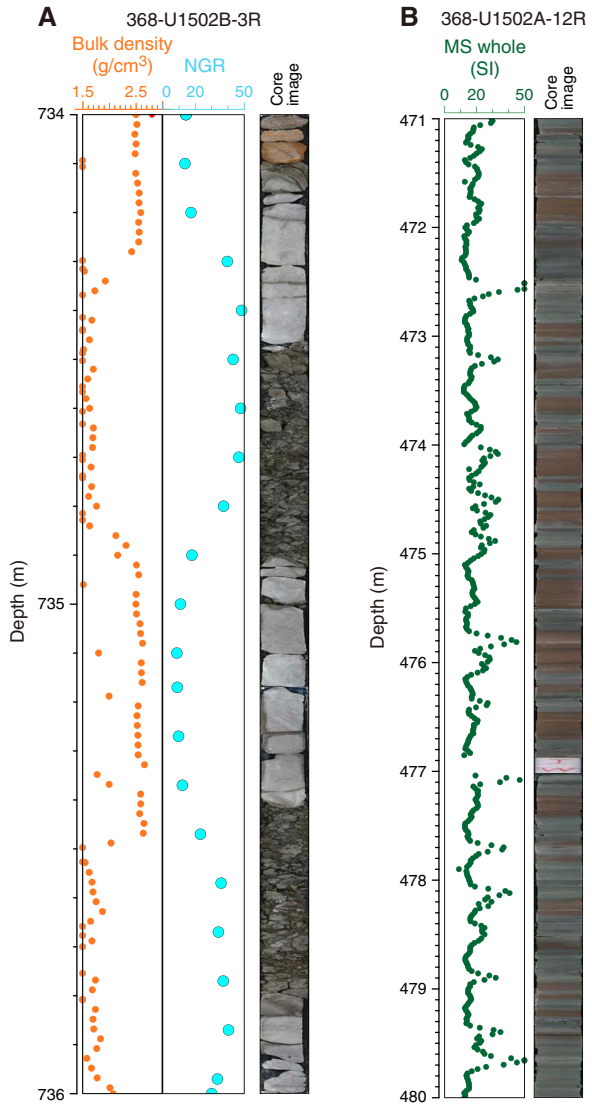

Downhole measurements

Logging operations

Two downhole logging strings were run in Hole U1502B. The first string was the triple combo tool string with DSI, and the second was the VSI tool string (Figures **F70**, **F71**). The end of the 10¾ inch casing was at 723 m, and the end of the drill pipe was initially set at 747.3 m. The modified triple combo tool string was able to reach 875 m in the open hole (~46 m above the total depth of RCB coring), and data were collected from that depth. The VSI tool string could not pass into the open hole, and check shots were conducted inside the casing. A summary of the log data compared to lithostratigraphy is shown in Figure **F72**.

Logging Run 1: triple combo with sonic tool

After coring to 920.8 m in Hole U1502B, a wiper trip was made to verify the condition of the hole, and the RCB drill bit was released at the bottom of the hole. The drillers noted a ledge that might have developed a few meters below the casing; thus, the end of the drill pipe was raised to 747.3 m (~24 m below the end of casing), which became the top of open-hole logging in Run 1 (Figure **F70**).

Figure F70. Logging operations summary, Hole U1502B. Left: Run 1; triple combo with DSI. Right: Run 2; VSI. mbsl = meters below sea level.

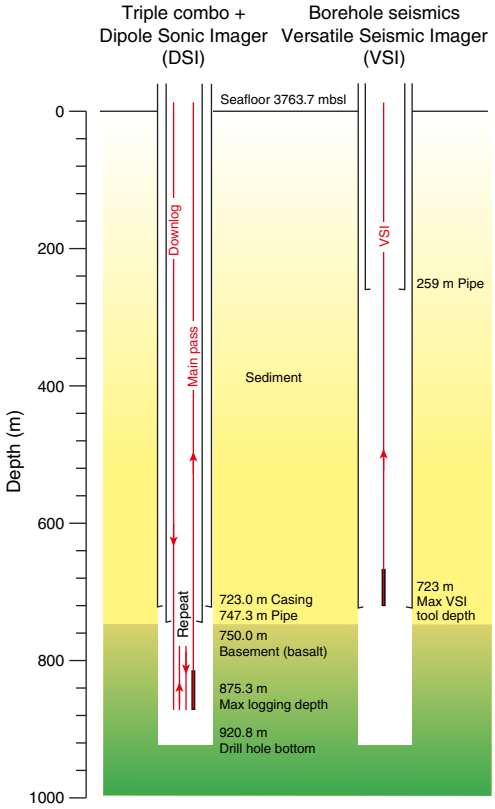

Rig-up for the first downhole logging run started at 0000 h (local time; UTC + 8 h) on 13 May 2017. A modified triple combo with a sonic tool string was lowered into the hole at 0320 h and reached a maximum depth of 875.3 m at 0655 h, ~45 m above the total cored depth of Hole U1502B. The first upward pass began at 0655 h and ended at 0710 h, reaching 785.3 m in the open hole. The second upward pass started at 0720 h and ended at 0835 h, reaching close to the seafloor. Heave conditions were excellent for the entire logging operation, so the active heave compensator was not used.

In the modified triple combo run, the tool string included the HNGS, HLDS, and DSI for acoustic velocity (Figure **F71**). The centralized tools were run in the lower part of the tool string so that it would be easier to lower the tool string past ledges than it would be with an eccentralized tool (see **Downhole measurements** in the Expedition 367/368 methods chapter [Sun et al., 2018a]). The triple combo tool string did not encounter obvious obstructions in the open hole below the end of the drill pipe.

Logging Run 2: VSI tool

Rig-up for the second downhole logging run using a VSI tool string started at 1230 h on 13 May 2017. By 1430 h, the drill pipe was pulled up to ~259 m, which was still deeper than the original planned depth of 80 m for the end of the drill pipe. However, it was determined that this would not affect the overall check shot stations, and thus the drill pipe was not pulled up any further. The VSI tool string was deployed at 1520 h and reached the end of casing (723.0 m) at 1730 h. Several attempts were made to get the VSI tool string to pass into the open hole below the casing, but it appeared to

Figure F71. Tools used in downhole logging operations, Hole U1502B. A. Run 1: triple combo with DSI. B. Run 2: VSI. LEH-MT = logging equipment head-mud temperature, EDTC = Enhanced Digital Telemetry Cartridge.

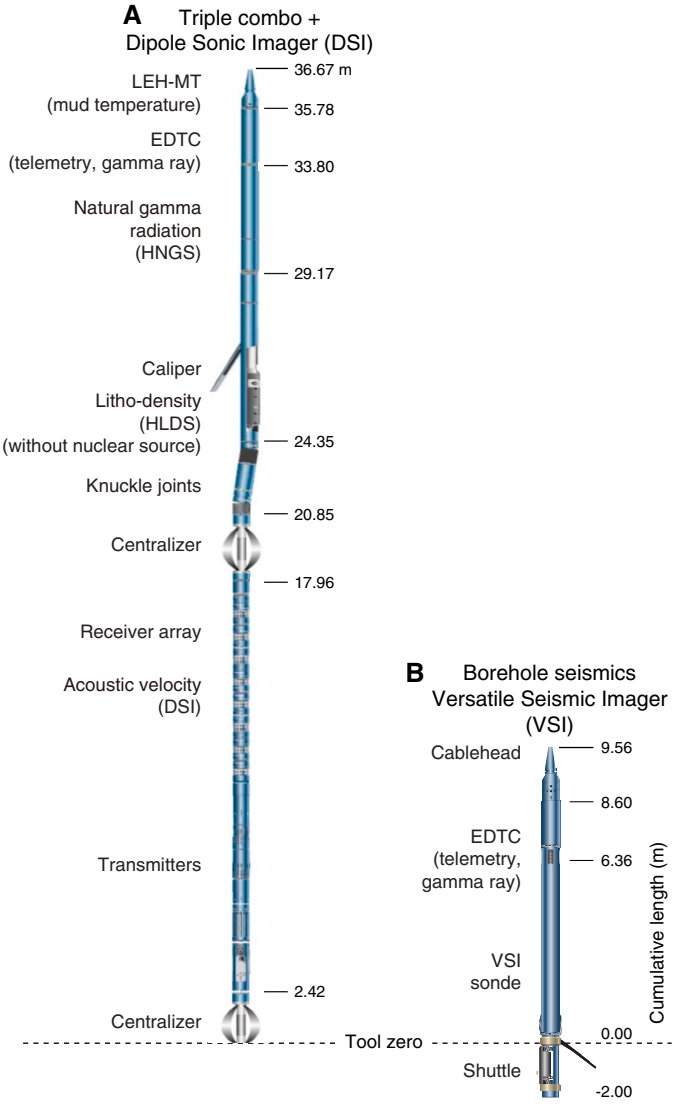

be hanging up on a ledge and was unable to pass into the open hole section. With very little daylight remaining, we decided to concentrate on getting as many check shots inside the cased hole as time permitted.

In all, eight stations were attempted, all in casing. The two deepest stations (at 715.17 and 695.20 m) are associated with large noise, suggesting possible poor mechanical coupling of the casing with the surrounding rock formation. During the first run with the triple combo tool string, we noted that the amplitude of the natural gamma dropped significantly at the depth interval of ~640–747 m. Therefore, we suspected that the rock formation behind the casing might have collapsed and the debris fallen to the bottom of the hole, resulting in poor casing/hole contact. The remaining upper six stations, located at 290.23, 350.28, 450.31, 550.09, 590.27, and 630.34 m, recorded good quality waveforms (Figure **F73**; Table **T16**).

During the VSI operation, the IODP protected species procedures were implemented. A soft ramp-up of the seismic source was performed to a maximum pressure of 2000 psi. No protected species were observed. The seismic source was deployed by the aft port crane at 38 m from the moonpool and 7 m below the sea surface (Figure **F74**). The seismic source has a cluster of two generator-injectors, each with a volume of 250 inch^3. A MP-24 hydrophone was deployed at 9 m below the sea surface. The sea condition was calm. The VSI tool string was combined with telemetry and gamma ray tools (Figure **F71**). The VSI tool string has a downhole sampling rate and recording length of 1.0 and 3000 ms, respectively. A total of 47 seismic source shots were made during the experiment, from which 29 downhole seismic traces were used and processed to identify waveforms and first arrivals. After the VSI experiment, the tool was brought back to the surface and rigged down at 2200 h on 13 May.

Logging units

The triple combo tool string run in Hole U1502B allowed us to define eight logging units (Table **T17**), many of which are correlated with changes in lithostratigraphic units, lithology, and physical properties (Figure **F72**). Logging Units 1–5 are inside both the casing and drill pipe, Unit 6 is outside the casing but inside the drill pipe, and Units 7 and 8 are in the open hole. When the logging tool is inside the casing and/or drill pipe, only measurements of NGR and the associated K, Th, and U components are meaningful, together with the understanding that the measured values were highly attenuated by the casing and/or drill pipe.

Logging Units 1–6: seafloor to 747.3 m

Logging Units 1–5 were defined primarily based on the characteristics of the measured NGR within the casing (Figure **F72**). In Logging Unit 1 (seafloor–435.0 m), the amplitude of NGR increases gradually with depth from ~150 to 350 m to a relatively constant value; the amplitude of NGR then decreases toward the bottom of logging Unit 1 at 435 m. The bottom part of this logging unit (~380–435 m) corresponds to a zone of relatively poor recovery in Hole U1502A.

In logging Unit 2 (435.0–510.0 m), NGR is greater than it is in the adjacent logging units. Logging Unit 2 coincides with the interval of good core recovery in Hole U1502A and corresponds to the lower portion of lithostratigraphic Subunit 1A (Figure **F72**; see **Lithostratigraphy**). Logging Unit 3 (510.0–640.0 m) has NGR values similar to the bottom part of logging Unit 1. This unit coincides with the poor core recovery interval and is interpreted to represent sandy layers.

Logging Unit 4 (640.0–685.0 m) is associated with a major reduction (>50%) in the amplitude of NGR compared to logging Unit 3. Logging Unit 5 (685.0–723.0 m) has even greater reduction in the amplitude of NGR compared to logging Unit 4. We hypothesize that the rock formation throughout logging Units 4 and 5 might have become unstable and collapsed behind the casing. Such failure could cause poor acoustic contact between the casing and the adjacent formation, as reflected in the significant noise in the waveforms of the two check shot stations (at 715.17 and 695.20 m).

Logging Unit 6 (723.0–747.3 m) is outside of the casing but still inside the drill pipe. This logging unit corresponds to lithostratigraphic Subunit IE (Figure **F72**; see **Lithostratigraphy**).

Logging Units 7 and 8: 747.3–853.0 m

Logging Units 7 and 8 are both in the open hole, outside of the casing and drill pipe. Logging Unit 7 (747.3–806.0 m) has relatively large hole diameters of 12–14.5 inches, logging bulk densities of 1.7–2.7 g/cm^3, and V_P values of 2.8–4.0 km/s. Logging bulk density is more scattered than the core sample density from MAD labora-

Figure F72. Downhole logs, lithostratigraphic units, and logging units, Holes U1502A and U1502B. HSGR = total spectral gamma ray, HCGR = computed (U-free) gamma ray, MAD = moisture and density (discrete samples), VSP = vertical seismic profile, PWC = *P*-wave caliper. Downhole logs were taken in Hole U1502B, whereas MAD, PWC, lithology, and core recovery data are from both Holes U1502A and U1502B.

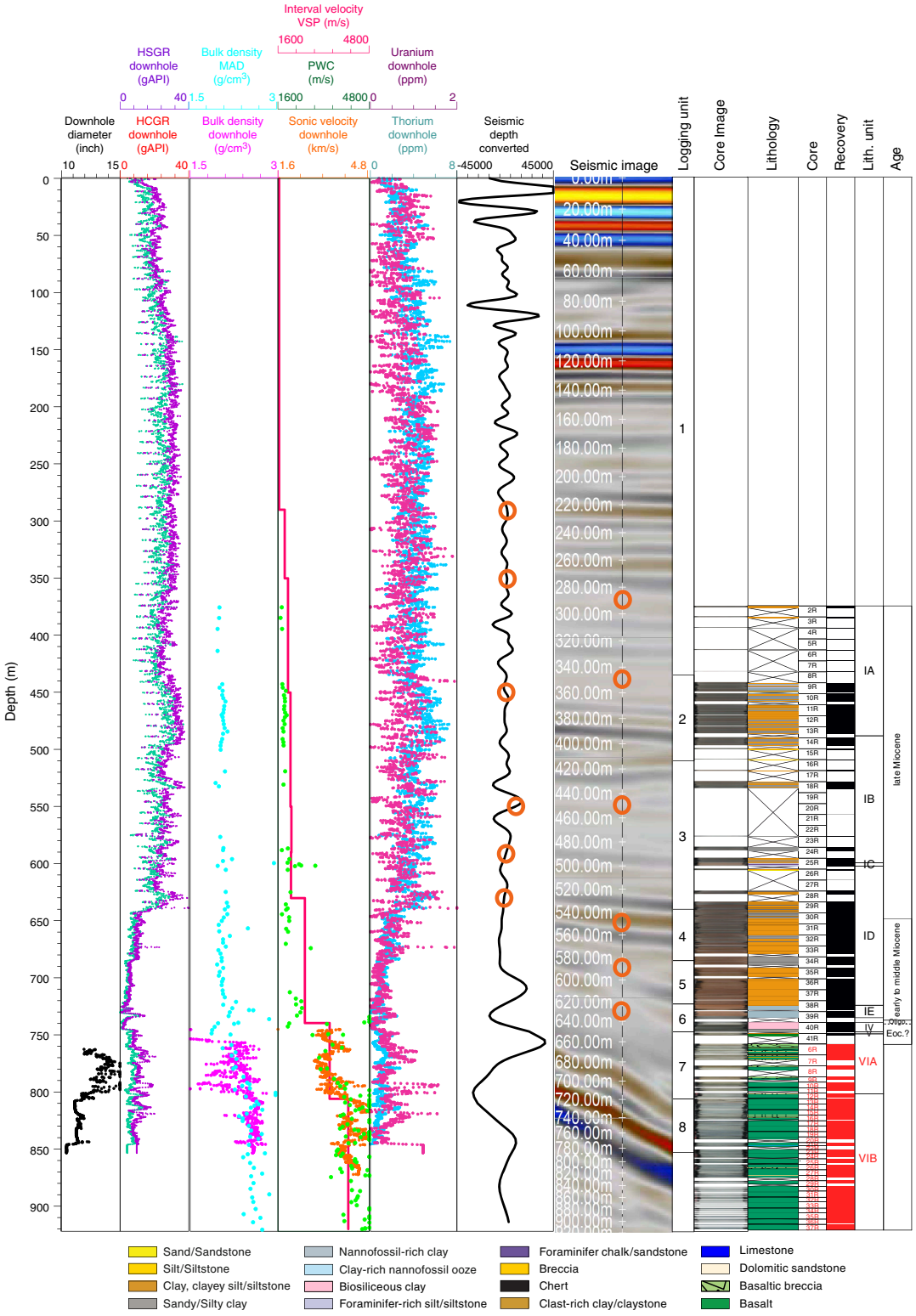

tory measurements. The logging velocity values are consistent with the *P*-wave velocity of core samples. The top of logging Unit 7 corresponds to a major change in lithology from sediment to altered basalt. Logging Unit 7 corresponds to lithostratigraphic Subunit VIA (Figure **F72**; see **Lithostratigraphy**).

Figure F73. Waveforms and first arrivals of six check shot stations of good data quality, Site U1502. Red arrows = first arrivals picked using Schlumberger software.

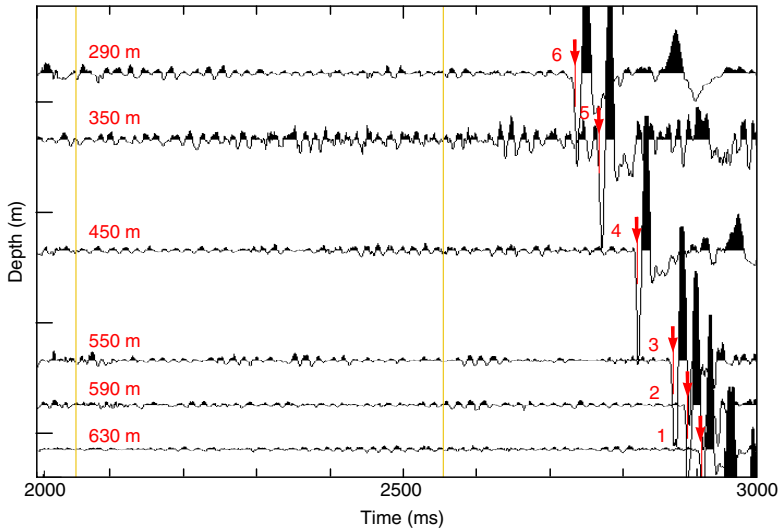

Table T16. Versatile Seismic Imager check shot stack summary, Hole U1502B. Two-way traveltime corrections were made by logging specialists at the Lamont-Doherty Earth Observatory and sent back to the ship. **Download table in CSV format.**

Depth (m)	One-way traveltime (s)	Two-way traveltime after correction (s)
290.225	2.67962599	5.17452002
350.278	2.71228576	5.21342325
450.306	2.76361561	5.27017117
550.092	2.81246138	5.32176971
590.265	2.83186769	5.3419137
630.339	2.85131097	5.36195803

Figure F74. Deployment scheme of seismic source used during VSI tool string logging run, Site U1502.

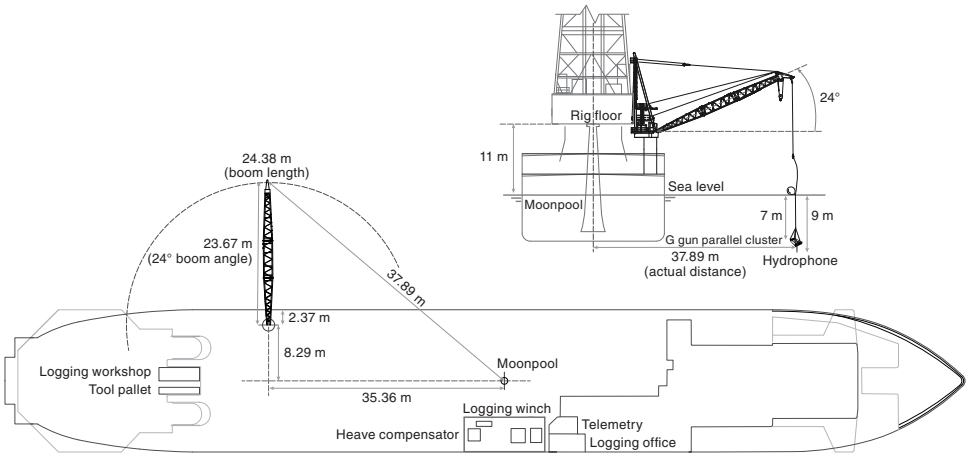

Logging Unit 8 (806.0–853.0 m) has a relatively stable hole diameter of ~11–12 inches. Logging density and V_P of Unit 8 are consistent with those measured from core samples. Density and V_P in logging Unit 8 are greater than in logging Unit 7. Logging Unit 8 corresponds to the top part of lithostratigraphic Subunit VIB (Figure F72; see **Lithostratigraphy**).

Table T17. Logging units, Hole U1502B. **Download table in CSV format.**

Logging unit	Depth (m)	
	Top	Bottom
1	0	435
2	435	510
3	510	640
4	640	685
5	685	723
6	723	750
7	750	800
8	800	853

Correlation to seismic data

We conducted two sets of analyses to correlate the core measurements (in meters below seafloor) to the time-based seismic data at Site U1502. First, we analyzed core data and investigated correlation to the seismic reflection profile. Second, we constructed synthetic seismograms using Site U1502 core data and compared the results with the traces in seismic profiles. Preliminary calculations were done during the expedition using a combination of Matlab scripts and Petrel software.

Velocity and density data and comparison with seismic reflectors

Whole-round core measurements, including *P*-wave velocity logger (PWL) and GRA density measurements, were conducted from 375.0 to 750.7 m in Hole U1502A and from 727.7 to 920.8 m in Hole U1502B (Figure **F75**). *P*-wave velocity was also measured along the *x*-axis with the PWC on working-half sections. MAD measurements were performed on discrete samples, one every other section. Sonic velocity and HLDS density measurements were obtained from downhole logging in Hole U1502B at 747.3–853.0 m (see **Physical properties** and **Downhole measurements**).

With the outliers filtered out, the whole-round PWL velocity and GRA density data are in good agreement with the PWC velocity and MAD density of core samples, respectively (Figure **F75**). Sonic velocities from downhole logging agree well with the PWC data, and the HLDS density from logging is also in good agreement with the MAD core density for intervals away from borehole enlargements (Figure **F72**; see **Physical properties** and **Downhole measurements**).

The VSI logging run yielded one-way traveltime (OWT) values at six depths: 290.23, 350.28, 450.31, 550.09, 590.27, and 630.34 m (Figure **F75**; see **Downhole measurements**). The corresponding interval velocities were calculated for six depth intervals, respectively: 0–290.23, 290.23–350.28, 350.28–450.31, 450.31–550.09, 550.09–590.27, and 590.27–630.34 m. V_P and density noticeably increase at ~740 m, coinciding with the lithologic change from sediment to altered basalt (see **Lithostratigraphy**). We hypothesize that the strongest amplitude in the seismic traces in Hole U1502A might correspond to the major changes in lithology and physical properties at 740 m and define a first reference point (RP1). To correlate the maximum amplitude in the seismic trace expressed in time (milliseconds) with the depth of 740 m, the calculated interval velocity for the 630.34–740.0 m interval should be 2.5 km/s. Another depth of noticeable changes in V_P and density is at ~800.0–806.0 m, which we chose as a second reference point (RP2). For the 740.0–806.0 m interval, an interval velocity of 3.3 km/s was chosen, which corresponds to the average PWC and PWL velocity. Similarly, for the 806.0–920.0 m interval, an interval velocity of 4.0 km/s was calculated based on the average PWC and PWL V_P values (Figure **F75**).

Time-depth relationship

The check shot data from Hole U1502B and the PWC data from Holes U1502A and U1502B were used to calculate the time-depth relationship (TDR) model of seismic waves. OWT values were directly observed at the six check shot depths from 290.23 to 630.34 m, from which a TDR model was readily calculated (Figure **F76**). The TDR for the deeper sections was based on the interval velocity at intervals of 630.34–740.0, 740.0–806.0, and 806.0–920.8 m. The calculated TDR model was similar to that of Site U1500 for depths shallower than 740 m. For depths greater than 740 m, however, the Site U1502 TDR model corresponds to the relatively high velocities of altered basalts, whereas the Site U1500 model corresponds to the relatively low velocities of sediment layers.

Using the best-fitting TDR model for Site U1502 (Figure **F76**), we were able to convert "depth scale" to "timescale" for all core measurements. This conversion enabled us to display the core measurements directly on top of the time-based seismic sections, facilitating identification of correlated features, as illustrated in the example of Figure **F77**.

Synthetic seismograms

To further illustrate the relationship between the core measurements at Site U1502 and the seismic reflection profile, the Seismic interpretation module in Petrel was used to compute synthetic seismograms based on the relevant core measurements (Figure **F78**). Synthetic traces were generated by convolving the reflectivity from the density of core samples after smoothing by a 20-point running window, by a smoothed-interval velocity model, and with the source wavelet that best fits the seismic data (Ricker 2; Figure **F78**).

Seismic impedance (SI) of a rock layer is the product of its average seismic velocity (V_P) and density (ρ) (i.e., SI = V_P × ρ). The seismic reflection coefficient (RC), in turn, equals the change in the seismic impedance between two adjacent rock layers. Thus, we can expect greater amplitudes in the modeled seismogram for rock interfaces with larger values of RC. The resulting synthetic seismogram shows strong reflectors at 730 and 810 m, consistent with the observed range of seismic reflectors (Figure **F78**).

Figure F75. Comparison of a subset of physical properties (MS, velocity, and density) with seismic waveform (converted to depth scale using best-fitting TDR model) and seismic image (in timescale). Red circles = check shot points (top six) and reference points (bottom two). Vint = velocity for TDR.

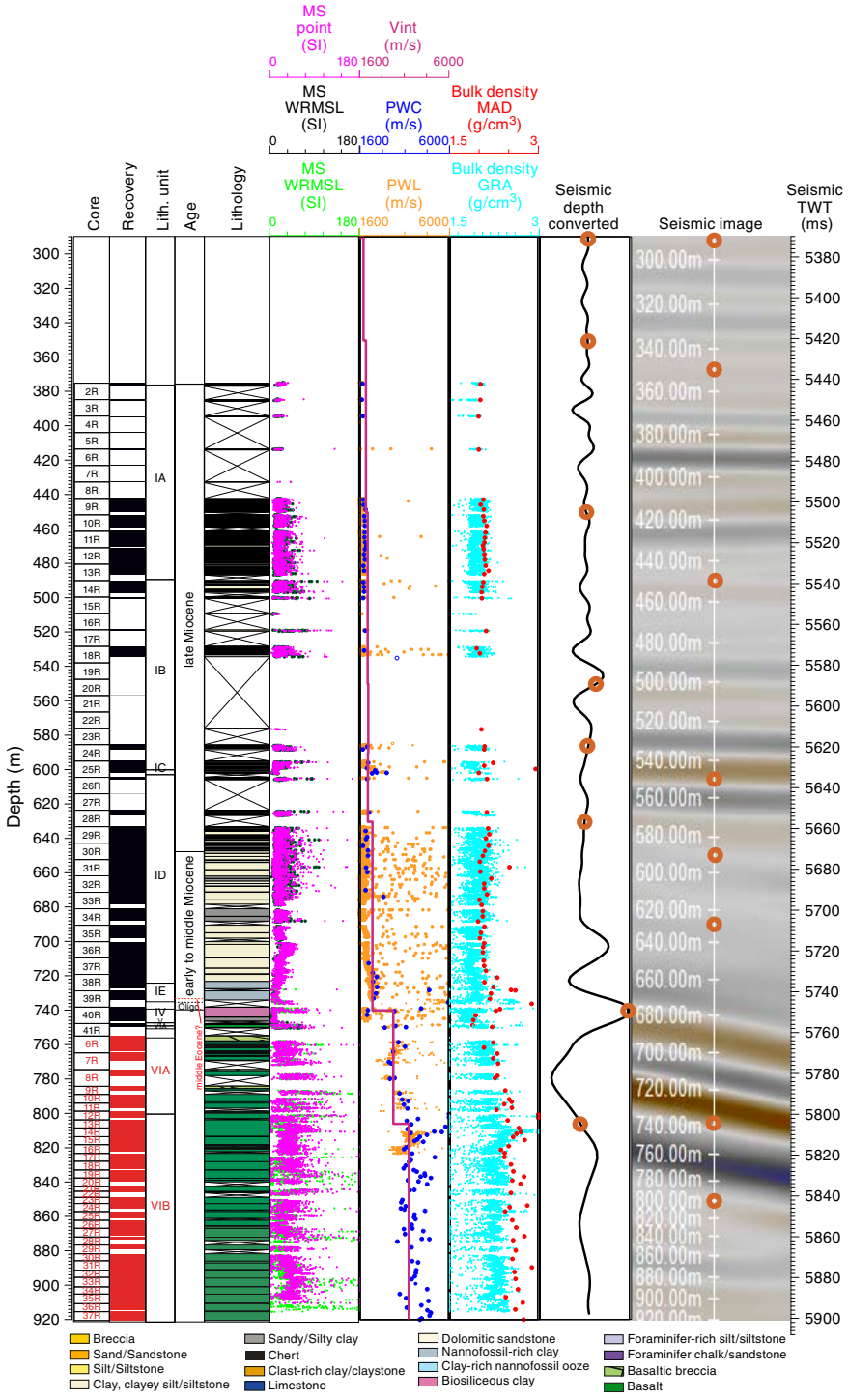

Figure F76. A. Site U1502 time-depth relation curve compared to Site U1500. TDR model for Site U1502 was constrained by check shot data at six depths (CS1–CS6; red circles). Red squares = reference points at 750.0 and 806.0 m (RP1 and RP2), coinciding with noticeable changes in density and velocity. B. Hole U1502A and U1502B PWC data and Hole U1502B logging V_P. Interval velocity model was derived using both check shot data (above 630.34 m) and average PWC and logging velocities (below 630.34 m).

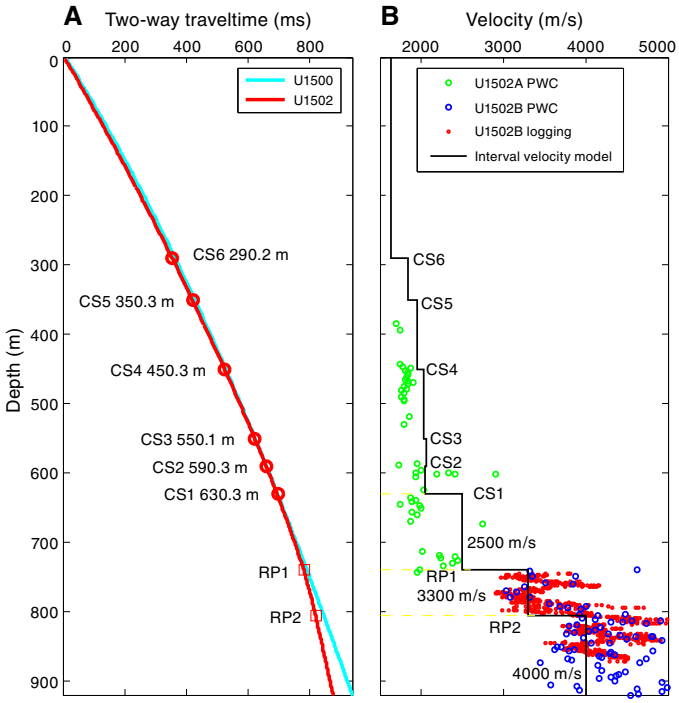

Figure F77. Seismic section at Site U1502 with lithostratigraphic units overlain at drill hole location. Also shown are selected core measurements converted to depth scale using best-fitting TDR model (density, MS, PWL and PWC, porosity, and NGR).

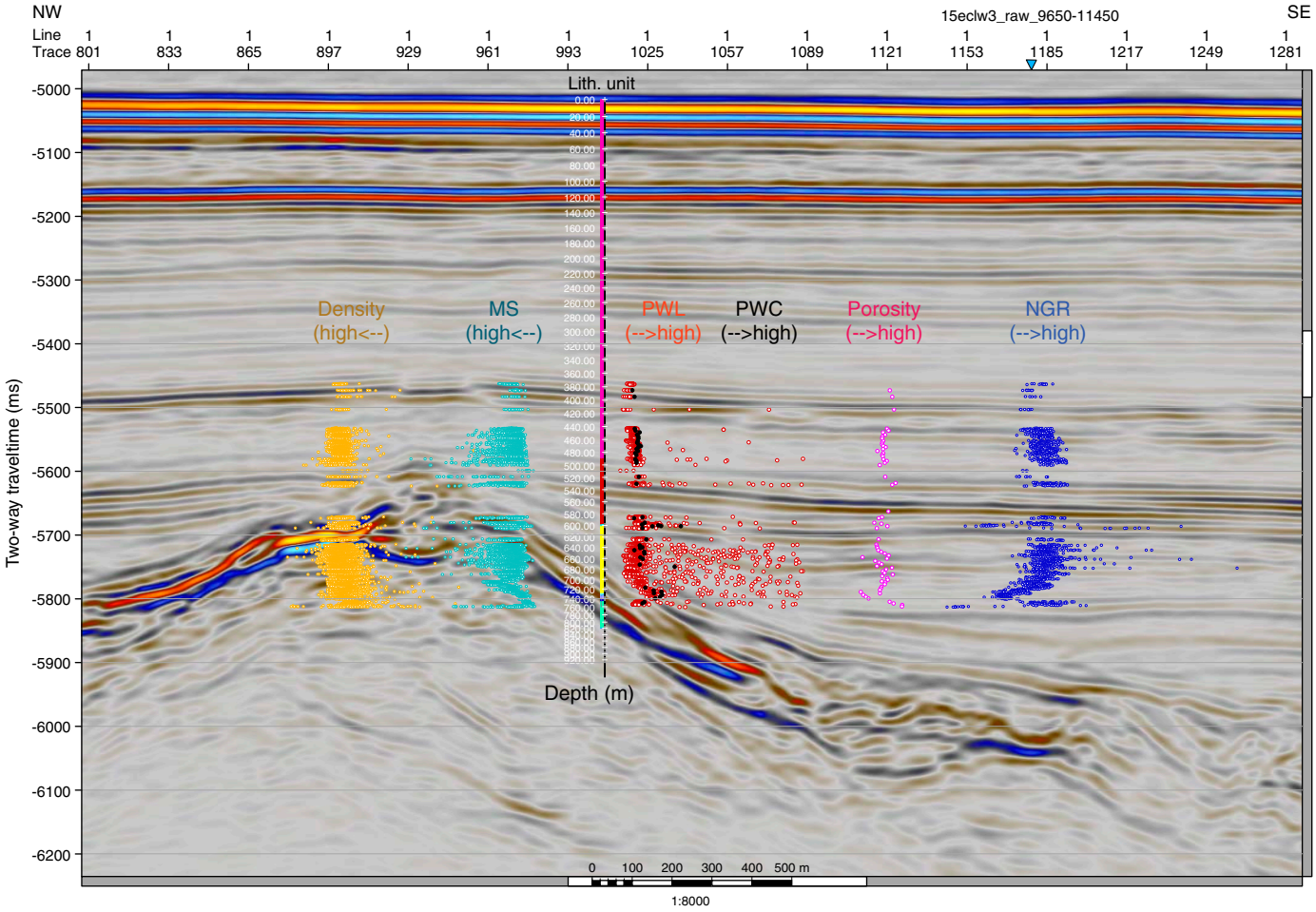

Figure F78. Synthetic seismogram, Site U1502. Panels from left to right: smoothed velocity and MAD density used in the calculation, resultant reflection coefficient (RC), real seismic traces with synthetic seismogram inserted in the center, and seismic source function "Ricker 2" used in modeling. TVD = true vertical depth calculated by Petrel software.

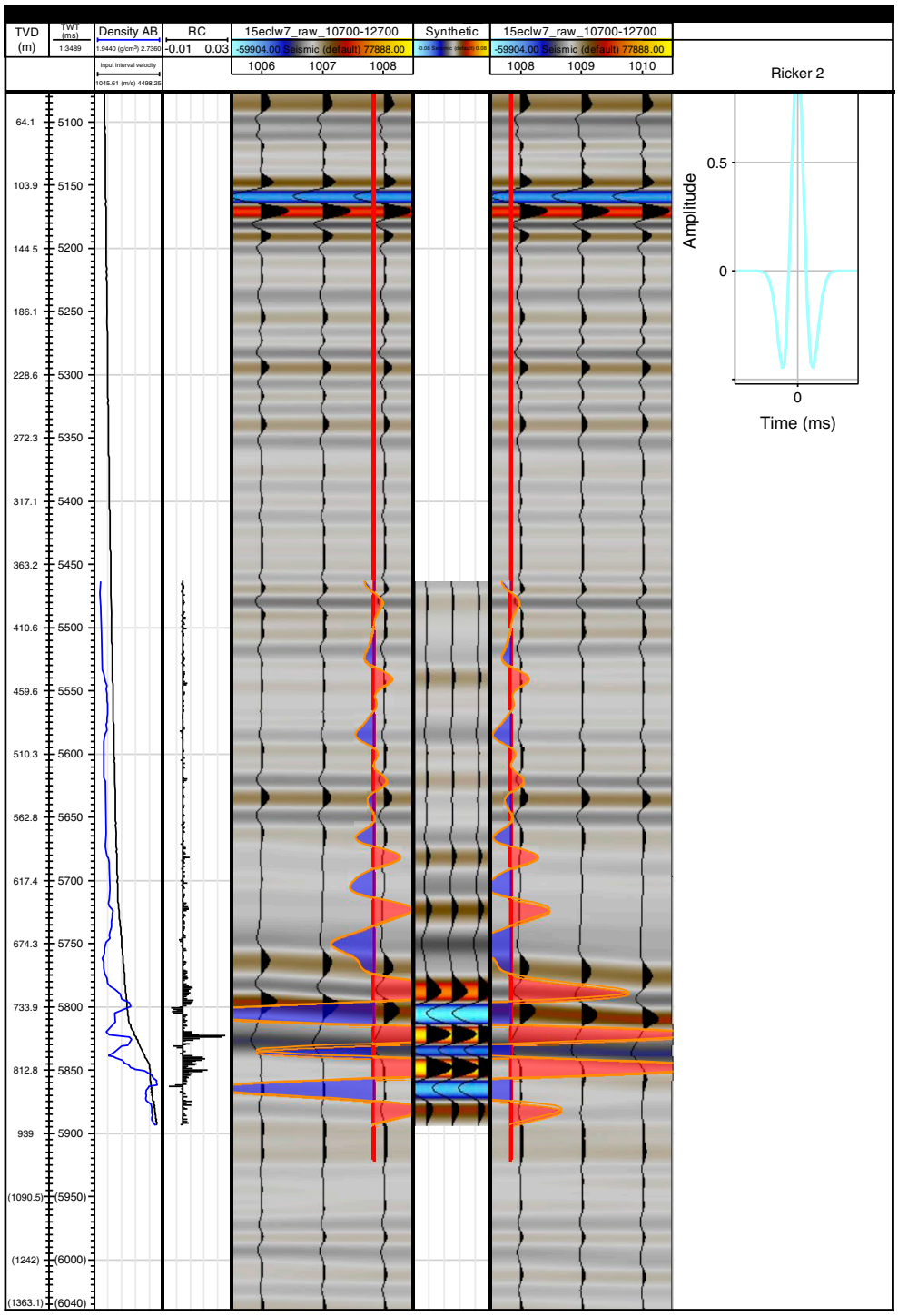

References

Barron, J.A., 1985. Miocene to Holocene planktic diatoms. *In* Bolli, H.M., Saunders, J.B., and Perch-Nielsen, K. (Eds.), *Plankton Stratigraphy:* Cambridge, United Kingdom (Cambridge University Press), 763–809.

Briais, A., Patriat, P., and Tapponnier, P., 1993. Updated interpretation of magnetic anomalies and seafloor spreading stages in the South China Sea: implications for the Tertiary tectonics of Southeast Asia. *Journal of Geophysical Research: Solid Earth*, 98(B4):6299–6328. **https://doi.org/10.1029/92JB02280**

Boiron, T., Bascou, J., Camps, P., Ferré, E.C., Maurice, C., Guy, B., Gerbe, M.-C., and Launeau, P., 2013. Internal structure of basalt flows: insights from magnetic and crystallographic fabrics of the La Palisse volcanics, French

massif central. *Geophysical Journal International,* 193(2):585–602. **https://doi.org/10.1093/gji/ggs115**

Caballero-Miranda, C.I., Alva-Valdivia, L.M., González-Rangel, J.A., Gogitchaishvili, A., Urrutia-Fucugauchi, J., and Kontny, A., 2016. Vertical AMS variation within basalt flow profiles from the Xitle volcano (Mexico) as indicator of heterogeneous strain in lava flows. *Journal of Volcanology and Geothermal Research,* 311:9–28. **https://doi.org/10.1016/j.jvolgeores.2016.01.003**

Cañón-Tapia, E., 1994. Anisotropy of magnetic susceptibility parameters: guidelines for their rational selection. *Pure and Applied Geophysics,* 142(2):365–382. **https://doi.org/10.1007/BF00879310**

Chulliat, A., Macmillan, S., Alken, P., Beggan, C., Nair, M., Hamilton, B., Woods, A., Ridley, V., Maus, S., and Thomson, A., 2015. *The US/UK World Magnetic Model for 2015–2020: Technical Report.* Boulder, CO (NOAA National Geophysical Data Center). **https://doi.org/10.7289/V5TB14V7**

Clark, C., and James, P., 2003. Hydrothermal brecciation due to fluid pressure fluctuations: examples from the Olary Domain, South Australia. *Tectonophysics,* 366(3–4):187–206. **https://doi.org/10.1016/S0040-1951(03)00095-7**

Cullen, A., Vicenzi, E., and McBirney, A.R., 1989. Plagioclase-ultraphyric basalts of the Galapagos Archipelago. *Journal of Volcanology and Geothermal Research,* 37(3–4):325–337. **https://doi.org/10.1016/0377-0273(89)90087-5**

Dean, W.E., Gardner, J.V., and Hemphill-Haley, E., 1989. Changes in redox conditions in deep-sea sediments of the subarctic North Pacific Ocean: possible evidence for the presence of North Pacific Deep Water. *Paleoceanography,* 4(6):639–653. **https://doi.org/10.1029/PA004i006p00639**

De Vleeschouwer, D., Dunlea, A.G., Auer, G., Anderson, C.H., Brumsack, H., de Loach, A., Gurnis, M., et al., 2017. Quantifying K, U, and Th contents of marine sediments using shipboard natural gamma radiation spectra measured on DV *JOIDES Resolution*. *Geochemistry, Geophysics, Geosystems,* 18(3):1053–1064. **https://doi.org/10.1002/2016GC006715**

Ellwood, B.B., Balsam, W., Burkart, B., Long, G.J., and Buhl, M.L., 1986. Anomalous magnetic properties in rocks containing the mineral siderite: paleomagnetic implications. *Journal of Geophysical Research: Solid Earth,* 91(B12):12779–12790. **https://doi.org/10.1029/JB091iB12p12779**

Fink, J., 2017. Laboratory Simulations of Submarine Lava Flow Morphology: A Quarter Century of Progress [presented at the American Geophysical Union 2017 Chapman Conference, Hobart, Tasmania, Australia, 29 January–3 February 2017].

Flower, M.F.J., 1980. Accumulation of calcic plagioclase in ocean-ridge tholeiite: an indication of spreading rate? *Nature,* 287(5782):530–532. **https://doi.org/10.1038/287530a0**

Gardner, J.V., Dean, W.E., Klise, D.K., and Baldauf, J.G., 1982. A climate-related oxidizing event in deep-sea sediment from the Bering Sea. *Quaternary Research,* 18(1): 91–107. **https://doi.org/10.1016/0033-5894(82)90023-0**

Gregg, T.K.P., and Fink, J.H., 1995. Quantification of submarine lava-flow morphology through analog experiments. *Geology,* 23(1):73–76. **https://doi.org/10.1130/0091-7613(1995)023<0073:QOSLFM>2.3.CO;2**

Hedges, J.I., Clark, W.A., and Come, G.L., 1988. Organic matter sources to the water column and surficial sediments of a marine bay. *Limnology and Oceanography,* 33(5):1116–1136. **https://doi.org/10.4319/lo.1988.33.5.1116**

Heezen, B.C., and Hollister, C.D., 1971. *The Face of the Deep:* New York (Oxford University Press USA).

Hirt, A., and Gehring, A.U., 1991. Thermal alteration of the magnetic mineralogy in ferruginous rocks. *Journal of Geophysical Research: Solid Earth,* 96(B6):9947–9953. **https://doi.org/10.1029/91JB00573**

Hu, S., Stephenson, A., and Appel, E., 2002. A study of gyroremanent magnetisation (GRM) and rotational remanent magnetisation (RRM) carried by greigite from lake sediments. *Geophysical Journal International,* 151(2):469–474. **https://doi.org/10.1046/j.1365-246X.2002.01793.x**

Jébrak, M., 1997. Hydrothermal breccias in vein-type ore deposits: a review of mechanisms, morphology and size distribution. *Ore Geology Reviews,* 12(3):111–134. **https://doi.org/10.1016/S0169-1368(97)00009-7**

Kaminski, M.A., and Gradstein, F.M., 2005. Atlas of Paleogene cosmopolitan deep-water agglutinated foraminifera. *Grzybowski Foundation Special Publication,* 10. **http://www.foraminifera.eu/atlas.html**

Kennish, M.J., and Lutz, R.A., 1998. Morphology and distribution of lava flows on mid-ocean ridges: a review. *Earth-Science Reviews,* 43(3–4):63–90. **https://doi.org/10.1016/S0012-8252(98)00006-3**

Kirschvink, J.L., 1980. The least-squares line and plane and the analysis of palaeomagnetic data. *Geophysical Journal of the Royal Astronomical Society,* 62(3):699–718. **https://doi.org/10.1111/j.1365-246X.1980.tb02601.x**

Lange, A.E., Nielsen, R.L., Tepley, F.J., III, and Kent, A.J.R., 2013. The petrogenesis of plagioclase-phyric basalts at mid-ocean ridges. *Geochemistry, Geophysics, Geosystems,* 14(8):3282–3296. **https://doi.org/10.1002/ggge.20207**

Larsen, H.C., Jian, Z., Alvarez Zarikian, C.A., Sun, Z., Stock, J.M., Klaus, A., Boaga, J., Bowden, S.A., Briais, A., Chen, Y., Cukur, D., Dadd, K.A., Ding, W., Dorais, M.J., Ferré, E.C., Ferreira, F., Furusawa, A., Gewecke, A.J., Hinojosa, J.L., Höfig, T.W., Hsiung, K.-H., Huang, B., Huang, E., Huang, X.-L., Jiang, S., Jin, H., Johnson, B.G., Kurzawski, R.M., Lei, C., Li, B., Li, L., Li, Y., Lin, J., Liu, C., Liu, C., Liu, Z., Luna, A., Lupi, C., McCarthy, A.J., Mohn, G., Ningthoujam, L.S., Nirrengarten, M., Osono, N., Peate, D.W., Persaud, P., Qui, N., Robinson, C.M., Satolli, S., Sauermilch, I., Schindlbeck, J.C., Skinner, S.M., Straub, S.M., Su, X., Tian, L., van der Zwan, F.M., Wan, S., Wu, H., Xiang, R., Yadav, R., Yi, L., Zhang, C., Zhang, J., Zhang, Y., Zhao, N., Zhong, G., and Zhong, L., 2018. Site U1501. *In* Sun, Z., Jian, Z., Stock, J.M., Larsen, H.C., Klaus, A., Alvarez Zarikian, C.A., and the Expedition 367/368 Scientists, *South China Sea Rifted Margin*. Proceedings of the International Ocean Discovery Program, 367/368: College Station, TX (International Ocean Discovery Program). **https://doi.org/10.14379/iodp.proc.367368.105.2018**

Li, C.-F., Lin, J., Kulhanek, D.K., Williams, T., Bao, R., Briais, A., Brown, E.A., Chen, Y., Clift, P.D., Colwell, F.S., Dadd, K.A., Ding, W., Hernández-Almeida, I., Huang, X.-L., Hyun, S., Jiang, T., Koppers, A.A.P., Li, Q., Liu, C., Liu, Q., Liu, Z., Nagai, R.H., Peleo-Alampay, A., Su, X., Sun, Z., Tejada, M.L.G., Trinh, H.S., Yeh, Y.-C., Zhang, C., Zhang, F., Zhang, G.-L., and Zhao, X., 2015. Expedition 349 summary. *In* Li, C.-F., Lin, J., Kulhanek, D.K., and the Expedition 349 Scientists, *South China Sea Tectonics.* Proceedings of the International Ocean Discovery Program, 349: College Station, TX (International Ocean Discovery Program). **https://doi.org/10.14379/iodp.proc.349.101.2015**

Lurcock, P.C., and Wilson, G.S., 2012. PuffinPlot: a versatile, user-friendly program for paleomagnetic analysis. *Geochemistry, Geophysics, Geosystems,* 13(6):Q06Z45. **https://doi.org/10.1029/2012GC004098**

McClinton, J.T., White, S.M., Colman, A., Rubin, K.H., and Sinton, J.M., 2014. The role of crystallinity and viscosity in the formation of submarine lava flow morphology. *Bulletin of Volcanology,* 76:854. **https://doi.org/10.1007/s00445-014-0854-2**

Morris, R.J., and Calvert, S.E., 1977. Geochemical studies of organic-rich sediments from the Namibian shelf: 1. The organic fractions. *In* Angel, M. (Ed.), *Voyage of Discovery:* Oxford, United Kingdom (Pergamon Press), 647–665.

Pan, Y., Zhu, R., Banerjee, S.K., Gill, J., and Williams, Q., 2000. Rock magnetic properties related to thermal treatment of siderite: behavior and interpretation. *Journal of Geophysical Research: Solid Earth,* 105(B1):783–794. **https://doi.org/10.1029/1999JB900358**

Pirajno, F., 2009. *Hydrothermal Processes and Mineral Systems:* Dordrecht, Netherlands (Springer). **https://doi.org/10.1007/978-1-4020-8613-7**

Reyes, A.G., 1990. Petrology of Philippine geothermal systems and the application of alteration mineralogy to their assessment. *Journal of Volcanology and Geothermal Research,* 43(1–4):279–309. **https://doi.org/10.1016/0377-0273(90)90057-M**

Richter, C., Acton, G., Endris, C., and Radsted, M., 2007. *Technical Note 34: Handbook for Shipboard Paleomagnetists.* Ocean Drilling Program. **https://doi.org/10.2973/odp.tn.34.2007**

Roberts, A.P., Chang, L., Rowan, C.J., Horng, C.-S., and Florindo, F., 2011. Magnetic properties of sedimentary greigite (Fe_3S_4): an update. *Reviews of Geophysics,* 49(1):RG1002. **https://doi.org/10.1029/2010RG000336**

Sillitoe, R.H., and Hedenquist, J.W., 2003. Linkages between volcanotectonic settings, ore-fluid compositions, and epithermal precious metal deposits. *In* Simmons, S.F., and Graham, I. (Eds.), *Volcanic, Geothermal, and Ore-Forming Fluids: Rulers and Witnesses of Processes within the Earth.* Society of Economic Geologists Special Publication, 10:315–343.

Snowball, I.F., 1991. Magnetic hysteresis properties of greigite (Fe_3S_4) and a new occurrence in Holocene sediments from Swedish Lappland. *Physics of the Earth and Planetary Interiors,* 68(1–2):32–40. **https://doi.org/10.1016/0031-9201(91)90004-2**

Soule, S.A., Fornari, D.J., Perfit, M.R., and Rubin, K.H., 2007. New insights into mid-ocean ridge volcanic processes from the 2005–2006 eruption of the East Pacific Rise, 9°46′N–9°56′N. *Geology,* 35(12):1079–1082. **https://doi.org/10.1130/G23924A.1**

Staudigel, H., 2014. Chemical fluxes from hydrothermal alteration of the oceanic crust. *In* Rudnick, R.L. (Ed.), *Treatise on Geochemistry* (2nd edition) (Volume 4): *The Crust.* Holland, H.D., and Turekian, K.K. (Series Eds.): New York (Elsevier), 583–606. **https://doi.org/10.1016/B978-0-08-095975-7.00318-1**

Stock, J.M., Sun, Z., Klaus, A., Larsen, H.C., Jian, Z., Alvarez Zarikian, C.A., Boaga, J., Bowden, S.A., Briais, A., Chen, Y., Cukur, D., Dadd, K.A., Ding, W., Dorais, M.J., Ferré, E.C., Ferreira, F., Furusawa, A., Gewecke, A.J., Hinojosa, J.L., Höfig, T.W., Hsiung, K.-H., Huang, B., Huang, E., Huang, X.-L., Jiang, S., Jin, H., Johnson, B.G., Kurzawski, R.M., Lei, C., Li, B., Li, L., Li, Y., Lin, J., Liu, C., Liu, C., Liu, Z., Luna, A., Lupi, C., McCarthy, A.J., Mohn, G., Ningthoujam, L.S., Nirrengarten, M., Osono, N., Peate, D.W., Persaud, P., Qui, N., Robinson, C.M., Satolli, S., Sauermilch, I., Schindlbeck, J.C., Skinner, S.M., Straub, S.M., Su, X., Tian, L., van der Zwan, F.M., Wan, S., Wu, H., Xiang, R., Yadav, R., Yi, L., Zhang, C., Zhang, J., Zhang, Y., Zhao, N., Zhong, G., and Zhong, L., 2018. Site U1500. *In* Sun, Z., Jian, Z., Stock, J.M., Larsen, H.C., Klaus, A., Alvarez Zarikian, C.A., and the Expedition 367/368 Scientists, *South China Sea Rifted Margin*. Proceedings of the International Ocean Discovery Program, 367/368: College Station, TX (International Ocean Discovery Program). **https://doi.org/10.14379/iodp.proc.367368.104.2018**

Sun, Z., Jian, Z., Stock, J.M., Larsen, H.C., Klaus, A., Alvarez Zarikian, C.A., Boaga, J., Bowden, S.A., Briais, A., Chen, Y., Cukur, D., Dadd, K.A., Ding, W., Dorais, M.J., Ferré, E.C., Ferreira, F., Furusawa, A., Gewecke, A.J., Hinojosa, J.L., Höfig, T.W., Hsiung, K.-H., Huang, B., Huang, E., Huang, X.-L., Jiang, S., Jin, H., Johnson, B.G., Kurzawski, R.M., Lei, C., Li, B., Li, L., Li, Y., Lin, J., Liu, C., Liu, C., Liu, Z., Luna, A., Lupi, C., McCarthy, A.J., Mohn, G., Ningthoujam, L.S., Nirrengarten, M., Osono, N., Peate, D.W., Persaud, P., Qui, N., Robinson, C.M., Satolli, S., Sauermilch, I., Schindlbeck, J.C., Skinner, S.M., Straub, S.M., Su, X., Tian, L., van der Zwan, F.M., Wan, S., Wu, H., Xiang, R., Yadav, R., Yi, L., Zhang, C., Zhang, J., Zhang, Y., Zhao, N., Zhong, G., and Zhong, L., 2018a. Expedition 367/368 methods. *In* Sun, Z., Jian, Z., Stock, J.M., Larsen, H.C., Klaus, A., Alvarez Zarikian, C.A., and the Expedition 367/368 Scientists, *South China Sea Rifted Margin*. Proceedings of the International Ocean Discovery Program, 367/368: College Station, TX (International Ocean Discovery Program). **https://doi.org/10.14379/iodp.proc.367368.102.2018**

Sun, Z., Stock, J., Jian, Z., McIntosh, K., Alvarez Zarikian, C.A., and Klaus, A., 2016. *Expedition 367/368 Scientific Prospectus: South China Sea Rifted Margin.* International Ocean Discovery Program. **https://doi.org/10.14379/iodp.sp.367368.2016**

Sun, Z., Stock, J.M., Klaus, A., Larsen, H.C., Jian, Z., Alvarez Zarikian, C.A., Boaga, J., Bowden, S.A., Briais, A., Chen, Y., Cukur, D., Dadd, K.A., Ding, W., Dorais, M.J., Ferré, E.C., Ferreira, F., Furusawa, A., Gewecke, A.J., Hinojosa, J.L., Höfig, T.W., Hsiung, K.-H., Huang, B., Huang, E., Huang, X.-L., Jiang, S., Jin, H., Johnson, B.G., Kurzawski, R.M., Lei, C., Li, B., Li, L., Li, Y., Lin, J., Liu, C., Liu, C., Liu, Z., Luna, A., Lupi, C., McCarthy, A.J., Mohn, G., Ningthoujam, L.S., Nirrengarten, M., Osono, N., Peate, D.W., Persaud, P., Qui, N., Robinson, C.M., Satolli, S., Sauermilch, I., Schindlbeck, J.C., Skinner, S.M., Straub, S.M., Su, X., Tian, L., van der Zwan, F.M., Wan, S., Wu, H., Xiang, R., Yadav, R., Yi, L., Zhang, C., Zhang, J., Zhang, Y., Zhao, N., Zhong, G., and Zhong, L., 2018b. Site U1499. *In* Sun, Z., Jian, Z., Stock, J.M., Larsen, H.C., Klaus, A., Alvarez Zarikian, C.A., and the Expedition 367/368 Scientists, *South China Sea Rifted Margin*. Proceedings of the International Ocean Discovery Program, 367/368: College Station, TX (International Ocean Discovery Program). **https://doi.org/10.14379/iodp.proc.367368.103.2018**

Tarling, D.H., and Hrouda, F., 1993. *The Magnetic Anisotropy of Rocks:* London (Chapman and Hall).

Tauxe, L., 2010. *Essentials of Paleomagnetism:* Berkeley, California (University of California Press).

Thompson, G.F., 1990. The anomalous demagnetization of pyrrhotite. *Geophysical Journal International,* 103:425–430.

White, W.M., and Klein, E.M., 2014. Composition of the oceanic crust. *In* Rudnick, R.L. (Ed.), *Treatise on Geochemistry* (2nd edition) (Volume 4): *The Crust.* Holland, H.D., and Turekian, K.K. (Series Eds.): New York (Elsevier), 457–496. **https://doi.org/10.1016/B978-0-08-095975-7.00315-6**

Wilson, T.R.S., Thomson, J., Hydes, D.J., Colley, S., Culkin, F., and Sørensen, J., 1986. Oxidation fronts in pelagic sediments: diagenetic formation of metal-rich layers. *Science,* 232(4753):972–975. **https://doi.org/10.1126/science.232.4753.972**

Yan, P., Zhou, D., and Liu, Z., 2001. A crustal structure profile across the northern continental margin of the South China Sea. *Tectonophysics,* 338(1):1–21. **https://doi.org/10.1016/S0040-1951(01)00062-2**

Zhao, F., Alves, T.M., Wu, S., Li, W., Huuse, M., Mi, L., Sun, Q., and Ma, B., 2016. Prolonged postrift magmatism on highly extended crust of divergent continental margins (Baiyun Sag, South China Sea). *Earth and Planetary Science Letters,* 445:79–91. **https://doi.org/10.1016/j.epsl.2016.04.001**

Zijderveld, J.D.A., 1967. AC demagnetization of rocks: analysis of results. *In* Collinson, D.W., Creer, K.M., and Runcorn, S.K. (Eds.), *Developments in Solid Earth Geophysics* (Volume 3): *Methods in Palaeomagnetism:* Amsterdam (Elsevier), 254–286. **https://doi.org/10.1016/B978-1-4832-2894-5.50049-5**

Sun, Z., Jian, Z., Stock, J.M., Larsen, H.C., Klaus, A., Alvarez Zarikian, C.A., and the Expedition 367/368 Scientists
Proceedings of the International Ocean Discovery Program Volume 367/368
publications.iodp.org

https://doi.org/10.14379/iodp.proc.367368.107.2018

Site U1503[1]

Check for updates

Hans Christian Larsen, Zhimin Jian, Carlos A. Alvarez Zarikian, Zhen Sun, Joann M. Stock, Adam Klaus, Jacopo Boaga, Stephen A. Bowden, Anne Briais, Yifeng Chen, Deniz Cukur, Kelsie A. Dadd, Weiwei Ding, Michael J. Dorais, Eric C. Ferré, Fabricio Ferreira, Akira Furusawa, Aaron J. Gewecke, Jessica L. Hinojosa, Tobias W. Höfig, Kan-Hsi Hsiung, Baoqi Huang, Enqing Huang, Xiao-Long Huang, Shijun Jiang, Haiyan Jin, Benjamin G. Johnson, Robert M. Kurzawski, Chao Lei, Baohua Li, Li Li, Yanping Li, Jian Lin, Chang Liu, Chuanlian Liu, Zhifei Liu, Antonio Luna, Claudia Lupi, Anders J. McCarthy, Geoffroy Mohn, Lachit Singh Ningthoujam, Michael Nirrengarten, Nobuaki Osono, David W. Peate, Patricia Persaud, Ning Qiu, Caroline M. Robinson, Sara Satolli, Isabel Sauermilch, Julie C. Schindlbeck, Steven M. Skinner, Susanne M. Straub, Xiang Su, Liyan Tian, Froukje M. van der Zwan, Shiming Wan, Huaichun Wu, Rong Xiang, Rajeev Yadav, Liang Yi, Cuimei Zhang, Jinchang Zhang, Yang Zhang, Ning Zhao, Guangfa Zhong, and Lifeng Zhong[2]

Keywords: International Ocean Discovery Program, IODP, *JOIDES Resolution*, Expedition 367, Expedition 368, Site U1503, northern South China Sea, continent–ocean transition zone, Ridge C, hyperextension, continental breakup, thinning, rifting, Cenozoic

Contents

1 Site summary
2 Background and objectives
3 Operations
6 References

Site summary

Background and objectives

International Ocean Discovery Program (IODP) Site U1503 (proposed Site SCSII-9B; Sun at al., 2016) is located at 3868 meters below sea level (mbsl) near the top of the structural high named Ridge C (Figures **F1**, **F2**). Ridge C is the most seaward ridge of the three margin-parallel Ridges A, B, and C that characterize the lower continental slope underlain by thin (5–7 km) crust. Ridge C is believed to represent at least partly, if not fully, igneous crust and hence the completion of continental breakup along this margin segment of the northern South China Sea (SCS).

A key operational objective of Site U1503 was to sample the lowermost ~300 m of sediments on top of basement to constrain the age and subsidence history of the crust at this location, the timing of normal faulting, and the environment of the early half-graben fill. The most important goal was to sample the igneous stratigraphy to at least 100 m below the basement. Because of a rig floor equipment failure (drawworks), we abandoned the site after installing casing in Hole U1503A to 991.5 m.

Deep, representative sampling of the basaltic material at this site would have provided an important reference frame for breakup modeling. With an estimated 1640 m sediment thickness overlying basement, obtaining basement samples and log data at this site represented a challenging operation.

Operations

To reach our objectives, we conducted operations in one hole (U1503A; 18°08.6300′N, 116°18.8456′E; 3868 mbsl). We successfully installed a reentry system and 991.5 m of 10¾ inch casing in Hole U1503A. However, we were unable to deepen the hole below the casing because of repeated breakdowns of the low clutch diaphragm in the drawworks and concerns that we did not have enough spares to last the remainder of the expedition. Without the drawworks' low

[1] Larsen, H.C., Jian, Z., Alvarez Zarikian, C.A., Sun, Z., Stock, J.M., Klaus, A., Boaga, J., Bowden, S.A., Briais, A., Chen, Y., Cukur, D., Dadd, K.A., Ding, W., Dorais, M.J., Ferré, E.C., Ferreira, F., Furusawa, A., Gewecke, A.J., Hinojosa, J.L., Höfig, T.W., Hsiung, K.-H., Huang, B., Huang, E., Huang, X.-L., Jiang, S., Jin, H., Johnson, B.G., Kurzawski, R.M., Lei, C., Li, B., Li, L., Li, Y., Lin, J., Liu, C., Liu, C., Liu, Z., Luna, A., Lupi, C., McCarthy, A.J., Mohn, G., Ningthoujam, L.S., Nirrengarten, M., Osono, N., Peate, D.W., Persaud, P., Qui, N., Robinson, C.M., Satolli, S., Sauermilch, I., Schindlbeck, J.C., Skinner, S.M., Straub, S.M., Su, X., Tian, L., van der Zwan, F.M., Wan, S., Wu, H., Xiang, R., Yadav, R., Yi, L., Zhang, C., Zhang, J., Zhang, Y., Zhao, N., Zhong, G., and Zhong, L., 2018. Site U1503. *In* Sun, Z., Jian, Z., Stock, J.M., Larsen, H.C., Klaus, A., Alvarez Zarikian, C.A., and the Expedition 367/368 Scientists, *South China Sea Rifted Margin*. Proceedings of the International Ocean Discovery Program, 367/368: College Station, TX (International Ocean Discovery Program). https://doi.org/10.14379/iodp.proc.367368.107.2018

[2] **Expedition 367/368 Scientists' addresses.**

MS 367368-107: Published 28 September 2018

This work is distributed under the **Creative Commons Attribution 4.0 International** (CC BY 4.0) license.

Figure F1. Bathymetry and seismic lines, Site U1503.

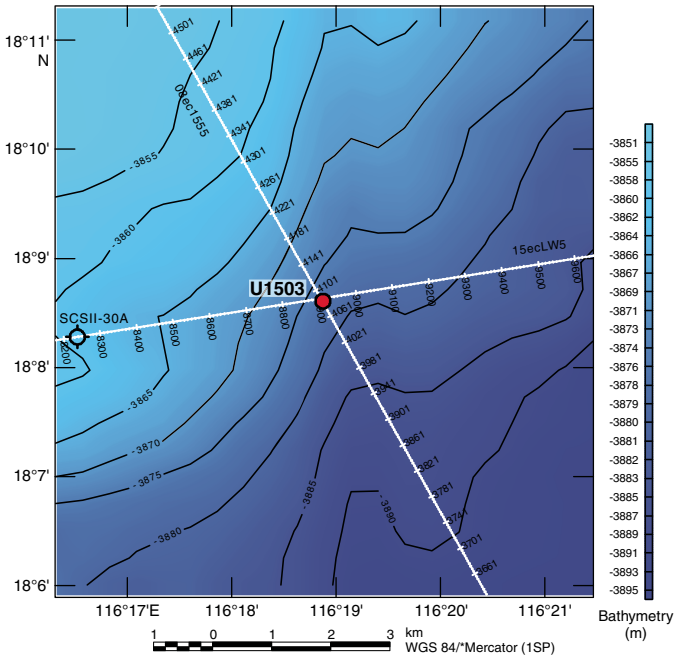

clutch, we could not conduct drilling operations deeper than 3400 m (water depth plus penetration depth). Because Site U1503 had a planned depth of 5695 m (water depth plus penetration depth), we abandoned Hole U1503A without addressing any scientific objectives. Hole U1503A remains cased and open for possible future occupation.

Background and objectives

Site U1503 is located at 3867.7 mbsl (Figures **F1**, **F2**) near the top of the structural high named Ridge C. Ridge C is the most seaward ridge of the three margin-parallel Ridges A, B, and C that characterize the lower continental slope underlain by thin (5–7 km) crust (Figures **F3**, **F4**). Ridge C is believed to represent at least partly, if not fully, igneous crust and hence the completion of continental breakup along this margin segment of the northern SCS.

Ridge C is a remarkably continuous basement ridge consisting of two ridges separated by seaward-dipping normal faults (Figures **F4**, **F5**, **F6**). The offset of the normal faults is as high as ~400 ms two-way traveltime (TWT; ~400 m), and faulting apparently was active shortly after the formation of the igneous crust. Only the oldest of the overlying sediments filling the half-graben basins seems to be offset by the faults, whereas the younger sediments filling in the majority of the accommodation space generated by normal faulting shows a draping (and compaction) structure over the tectonically generated basement relief. Ridge C is very linear and parallel to Ridge B (see the **Site U1500** chapter [Stock et al., 2018]) and seafloor spreading anomalies south of the ridge (Figure **F2**). The top of the ridge is also remarkably flat along strike.

One important objective of Site U1503 was to sample the lowermost ~300 m of sediments on top of the basement to constrain the age and subsidence history of the crust in this location, the timing of normal faulting, and the environment of the early half-graben fill. The most important goal was to sample the igneous stratigraphy to at least 100 m below top of basement.

Figure F2. Bathymetric maps showing Expedition 367/368 sites (stars), and (A) regional and (B) local coverage of multichannel seismic reflection data and OBS data. Thick blue and red lines are key seismic lines used for planning of the drilling transect. A. Magnetic isochrons (orange lines) from Briais et al. (1993). B. Magnetic picks (orange squares) from the same reference, extracted from the Seton et al. (2014) compilation. Chron labels for the picks correspond to the old edge of the normal polarity intervals (see Ogg et al. [2016] timescale for ages). Orange square = Leg 184 Site 1148, yellow squares = Expedition 349 Sites U1432 and U1435.

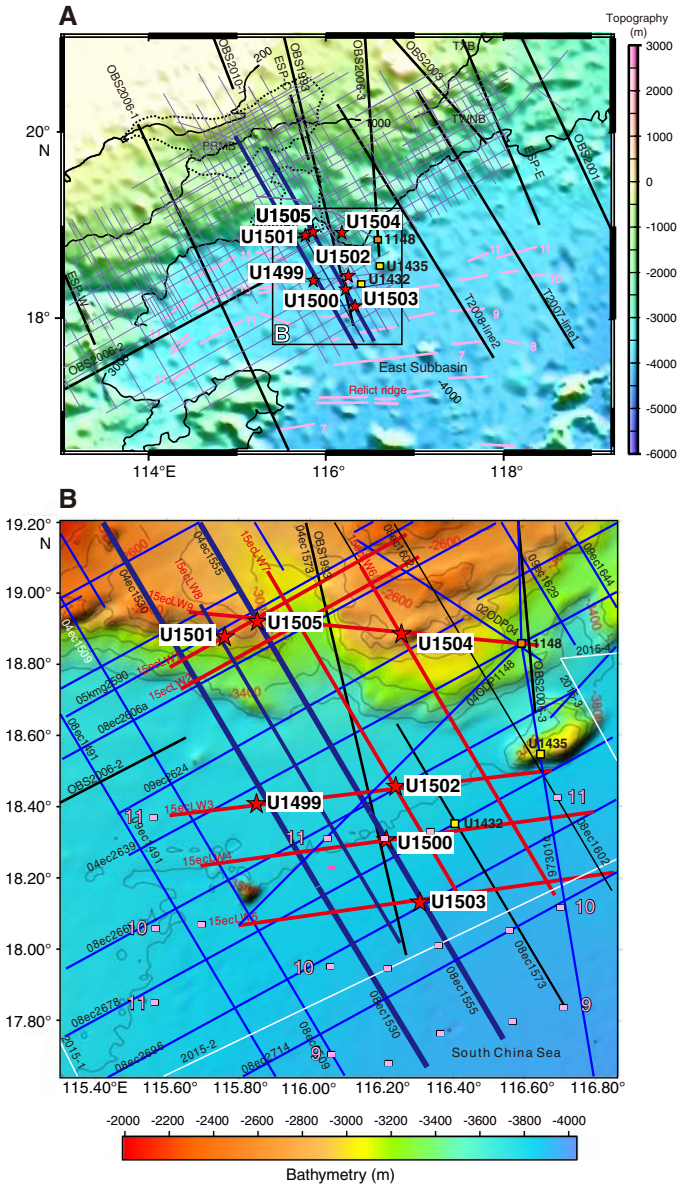

Based on the breakup-related basaltic magmatism found at both Sites U1502 (Ridge A) and U1500 (Ridge B), we believe that this rifted margin, unlike magma-starved Iberia-type margins, experienced massive igneous activity during breakup and that highly extended subcontinental lithosphere within the continent–ocean transition (COT), if present at all, now is likely to be more or less covered by igneous rocks. By implication, the reading of the terminal stages of lithospheric thinning prior to final breakup needs to be gleaned from the detailed composition of the igneous products, such as continental crustal contamination of the magmas, depth of

Figure F3. Two-way traveltime to (A) basement (Tg reflector) and (B) T60 unconformity. Proposed drilling transect (thick black line) is approximately at the center of a margin segment bounded to the southwest by a transform fault. Northeastern boundary of margin segment is around Expedition 349 Site U1435. At this location, outer margin high (OMH) and Ridge A seem to coalesce, and Ridges B and C of the COT become indistinct toward the northeast within the next margin segment. Note that the OMH is slightly oblique to the more parallel Ridges A, B, and C.

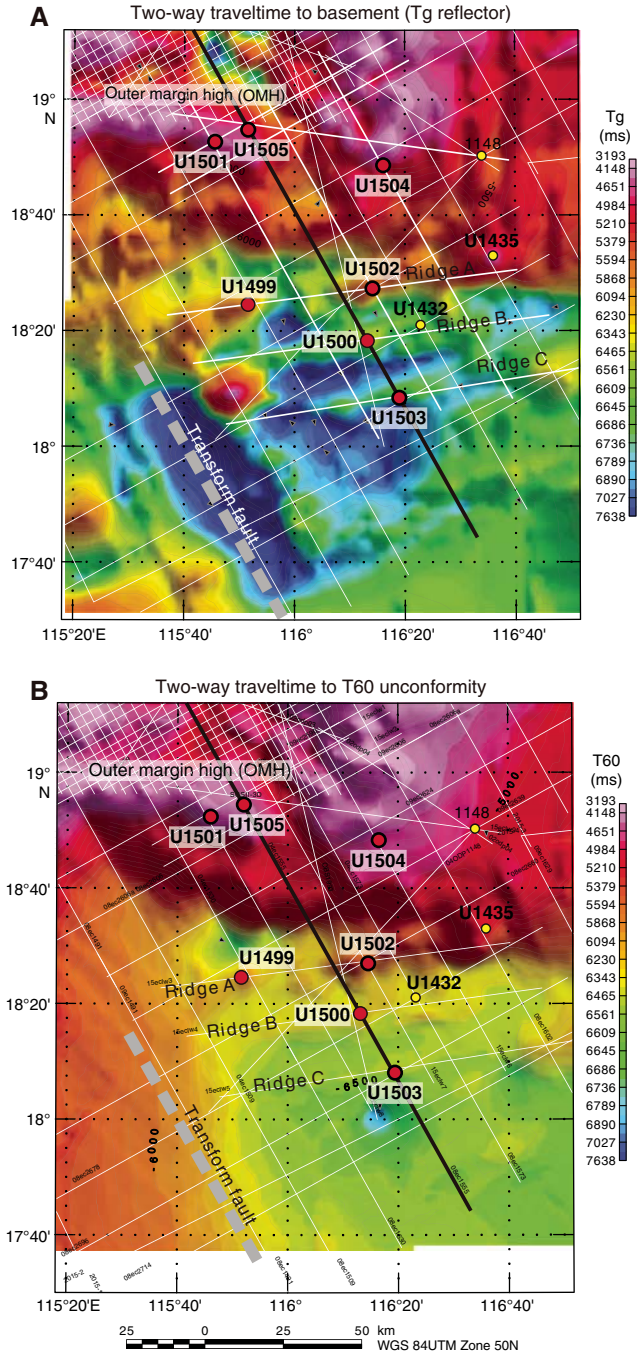

and shallowing of mantle melting with time, and mantle composition, including wetness and possible temperature anomalies. The crust at Ridge C is interpreted to represent the end-member of the transition from breakup igneous activity initially modified by an overlying lid of continental lithosphere to accretion of igneous crust unmodified by a preexisting lithosphere. Deep representative sampling of the basaltic material at this site therefore forms an important reference frame for the modeling of breakup, and basement penetration must be sufficient to provide a representative sampling of igneous units. With an estimated 1640 m of sediment to basement, Site U1503 was a challenging operation. Unfortunately, following installation of 990 m of steel casing within the upper sediments, repeated breakdown of the drawworks' low clutch diaphragm (see **Operations**) prevented Expedition 368 from deploying a drill string longer than 3400 m (water depth plus penetration), and Site U1503 was left for possible occupation during a future expedition.

The 3400 m depth limit imposed by the flawed drawworks left very few drilling options for continuation of Expedition 368 operations. Almost all proposed sites are in water depths greater than 3400 m and/or had deep targets. One exception was Site U1504, which is located in 2823 mbsl and has a shallow coring target (see **Background and objectives** in the Site U1504 chapter [Larsen et al., 2018]).

Operations

We conducted operations in one hole at Site U1503 (Table **T1**) with the objective of sampling the lowermost sediments and 150 m into the underlying basalt. Hole U1503A is located at 18°08.6300′N, 116°18.8456′E, at a water depth of 3867.7 m. We installed a reentry system and 991.5 m of casing (10¾ inch) in this hole. However, we were unable to continue deepening the hole because of mechanical problems with the drawworks, including a fourth clutch diaphragm failure and a breakdown of the aft shaft bearing on one of the Elmagco brakes. The continuing failures of the low clutch diaphragm and the lack of available spares to last until the end of the expedition limited the operation of the ship's drilling equipment to depths shallower than 3400 m. Therefore, Site U1503 was abandoned without achieving any scientific objectives. Despite this major setback to the expedition and the South China Sea Rifted Margin program, Hole U1503A remains as a legacy hole for future occupation.

Hole U1503A

The R/V *JOIDES Resolution* began the transit from Site U1502 to Site U1503 in dynamic positioning mode while tripping pipe. The mud skirt and reentry cone intended for Site U1503 were moved to the center of the moonpool and stationed on the moonpool doors. With the mud skirt and reentry cone secured, the thrusters were pulled, and the vessel was underway at full speed at 0806 h on 14 May 2017.

The vessel arrived on site at 0930 h on 14 May but was unable to occupy the site until 1130 h because the Chinese R/V *Shiyan 2*, operated by the South China Sea Institute of Oceanology, was conducting a seismic survey in the area. The *JOIDES Resolution* completed the 19.8 nmi voyage from Site U1502 in 8.6 h (7.2 h in dynamic positioning mode and 1.4 h at cruise speed).

Once on site, a seafloor positioning beacon was deployed and the crew made up the bottom-hole assembly (BHA) with a 14¾ inch bit to drill a hole without coring to 1000 m for installation of 10¾ inch casing. The bit was lowered through the reentry cone and base that was assembled and placed in the moonpool. The precision depth recorder (PDR) measurement taken upon arrival placed the seafloor at 3873.1 mbsl. The bit was lowered to 3846 mbsl, the top drive was picked up, and drilling in Hole U1503A started at 2010 h on 14 May. Drilling of the 14¾ inch diameter hole penetrated to a total depth of 902.8 m at 0100 h on 16 May. At this time, the rig

Figure F4. Deep crustal time-migrated seismic reflection data without and with interpretation. Note the rather thin lower crust (two layers) above a strong Mohorovičić seismic discontinuity (Moho) reflector that can be followed oceanward. Moho reflection is weak to absent seaward from around the interpreted COT. Wide-angle seismic data (Yan et al., 2001) confirm ~6 km thick ocean crust (OC) seaward of the COT. A large detachment fault ~150 km inland of the COT separates more stable crust landward from that of highly extended crust seaward. An OMH is a fairly consistent feature along this margin segment. Key seismic unconformities are shown in purple (T70; ~32 Ma breakup unconformity?) and blue (T60; ~23 Ma regional basin event). These ages are inferred from long-distance (>100 km) correlation of seismic unconformities with industry holes and ODP Leg 184 Site 1148 (T60); ages need confirmation by coring and are only tentative. Tg (black) is basement. Arrows = approximate positions of seafloor magnetic anomalies with chron numbers. Seismic data are from Line 04ec1555-08ec1555 (courtesy of Chinese National Offshore Oil Corporation [CNOOC]). Location of line is shown in Figure F1. CDP = common depth point. C11n, C10n, and C9n = approximate location of normal polarity magnetic isochrons. MSB = midslope basin.

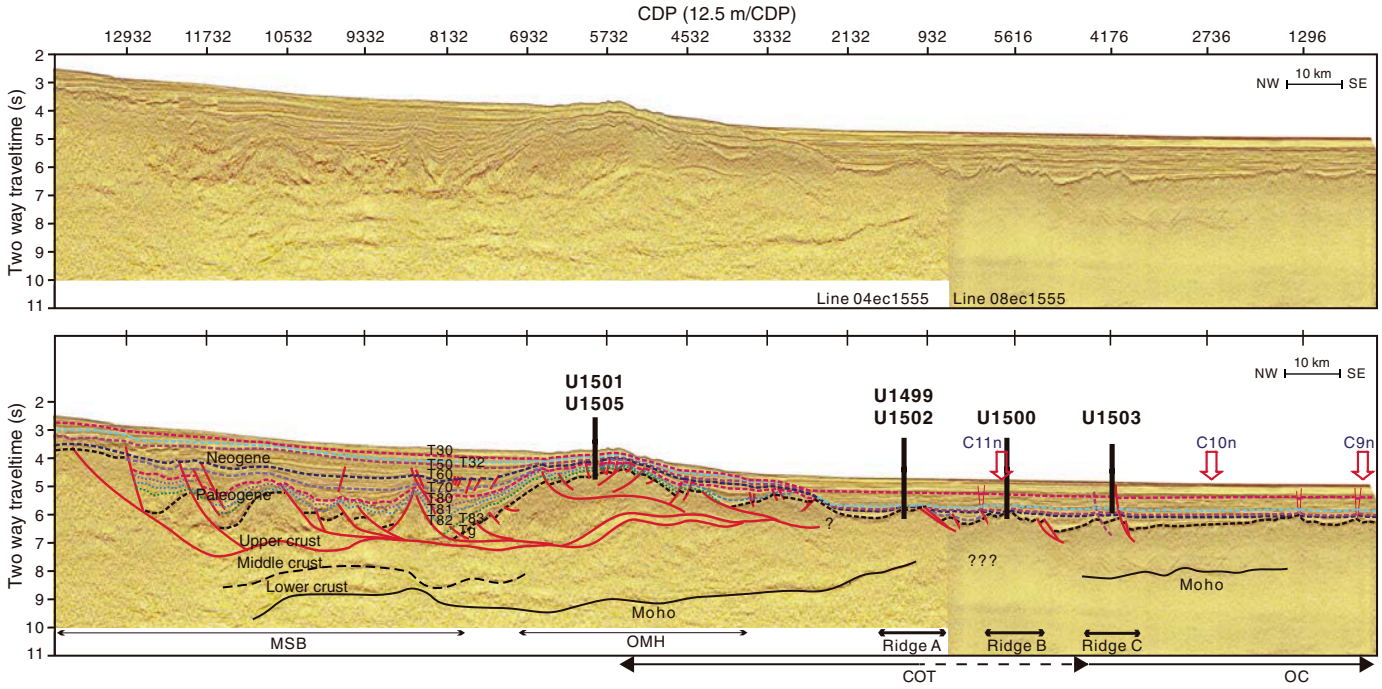

mechanic noticed a leak in the low clutch diaphragm, which had already been replaced once during Expedition 367 and twice during Expedition 368. It was decided to pull the bit to the surface before the diaphragm failed completely. The bit was raised to 97.6 m below the seafloor, and a reentry cone was deployed. The subsea camera was lowered to observe the landing orientation of the cone (Figure **F7A**). Once the camera was near the seafloor, the bit was pulled out of the hole, clearing the seafloor at 0750 h on 16 May. The bit tagged the internal aperture of the cone to verify a seafloor depth of 3867.7 m, 5.4 m higher than previously thought. The seafloor depth for this hole was adjusted to 908.2 m.

The bit was then pulled to 3846 m, and 215 ft of drill line was slipped and cut. The bit was pulled to the surface, clearing the rotary table at 1655 h. With no spare clutch diaphragms aboard and no possible delivery of spare diaphragms until ~20 May, it was decided to proceed with all operations that would not require use of the low drive of the drawworks.

The drill crew assembled 85 joints (989.3 m) of 10¾ inch casing and crossed over to a 16 inch casing hanger. During an attempt to engage the DrilQuip running tools, it was noted that the seal diameter on the casing hanger was too small. The crew modified the hanger to enlarge the seal diameter and engaged the running tool. The casing was then lowered into the moonpool and hung off the moonpool doors.

The crew then picked up the mud motor and underreamer, lowered the drilling assembly into the moonpool, and tested them. The rest of the drilling assembly was made up and lowered through the casing. The running tool was then reengaged into the casing hanger, and the entire casing string and drilling assembly were lowered as far as possible (2379 m) without using the drawworks low clutch and then hung off the traveling blocks. The last operation was to make up three stands of knobbies and pump a pig through each stand to clean any rust. The stands were then racked back in the derrick for use when drilling in the casing.

The rig then went on downtime on Thursday, 18 May, at 0915 h until the replacement parts (low clutch diaphragms) were delivered to the ship at 2310 h on 20 May. The seagoing tug *Taikoo* arrived on site with three spare low clutch diaphragms. The tug stationed itself on the port aft side of the *JOIDES Resolution*. Supplies were offloaded, the tug departed by 2320 h on 20 May, and the crew began replacing the low clutch diaphragm.

Repairs were completed by 0415 h on 21 May. The driller continued lowering the casing string from 2379 mbsl to the seafloor, filling the pipe with seawater every 25 stands. The subsea camera was deployed, and Hole U1503A was reentered at 1005 h on 21 May with the 10¾ inch casing string. The casing began taking weight at 342 m, so it was pulled back, the top drive was installed, and the mud motor, bit, and underreamer were used to drill in the casing to the bottom of the predrilled hole at 908.2 m. We continued drilling in the last 86.9 m of casing until we reached 991.5 m. The casing was released at 0915 h on 22 May, and the camera and drilling assembly were recovered. The mud motor and underreamer were flushed with freshwater and laid out. The casing running tool was detorqued and laid out.

The upper guide horn (UGH) was installed, and the drill crew began making up and deploying a rotary core barrel (RCB) BHA.

Figure F5. Seismic Line 08ec1555, primary seismic line for Site U1503 and crossing seismic line for proposed Site SCSII-30A. Dashed lines = unconformities, red solid lines = faults.

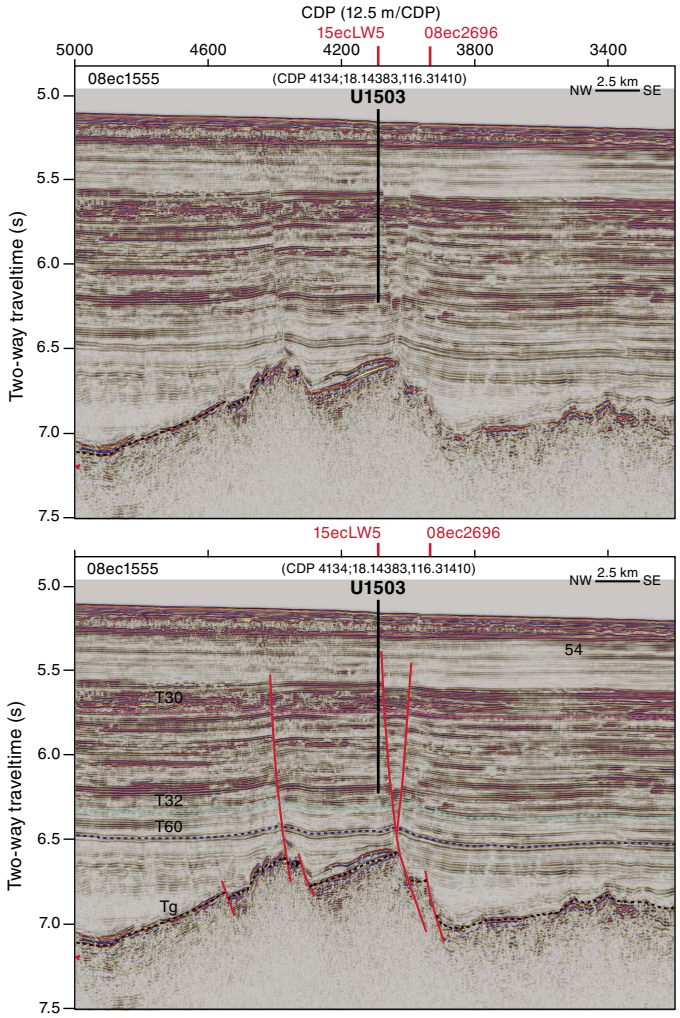

The bit was lowered to 1232 mbsl, at which depth the drill crew noticed a loud noise coming from the forward Elmagco brake of the drawworks. The aft bearing on the forward Elmagco brake had failed. The crew began working to replace the brake with a reconditioned unit that was loaded aboard in Hong Kong. This job was scheduled for the maintenance period following Expedition 368. We were lucky that the seas were calm because this typically can't be done at sea.

Repairs began at ~0530 h on 23 May. Because of the calm seas, the crew was able to make the required heavy crane lifts. The forward brake was disconnected and moved to the rig floor where the hub could be removed for use on the replacement. The 28,000 lb (12.7 MT) nonfunctioning brake was then transferred to the main deck, and the replacement brake was moved to the rig floor to have the hub fitted and to be installed on the forward end of the drawworks. The brake was moved into place, the electrical and water connections were made, and the shaft was aligned by 0600 h on 25 May.

Operations resumed with lowering the bit to 3819 mbsl at 1100 h on 25 May, at which time it was noticed that the low clutch diaphragm was leaking again. The diaphragm was replaced for the

Figure F6. Crossing seismic line (15ecLW5) for Site U1503. Dashed lines = unconformities.

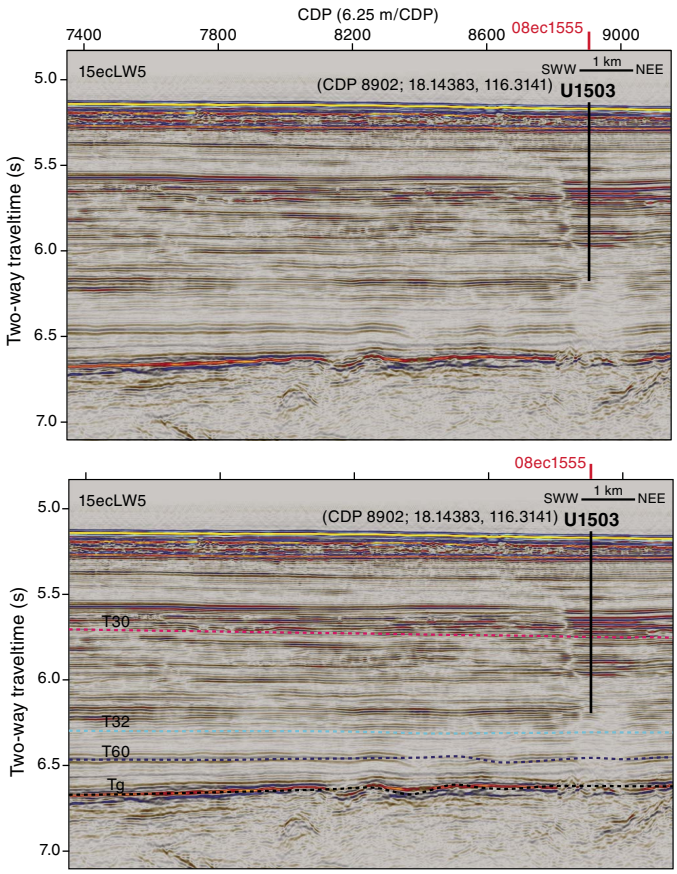

fourth time during this expedition (completed at 2100 h on 25 May). Because of the great water depth at the site's location combined with the planned deep penetration at Site U1503, extensive use of the low clutch would have been required to continue operations. Considering this fact, along with the number of diaphragm failures so far and a single remaining spare left on board the ship, it was determined that the safest action would be to terminate operations in Hole U1503A without reentering the cased hole. An optimistic delivery date for additional clutch diaphragm spares, if available, was estimated for 2 June. If Hole U1503A was reentered and an additional clutch diaphragm failed while coring below the casing, the remaining spare would be enough only to get the drill string out of the hole, and any failed operations in the open hole could have prevented a future reentry operation. With two more weeks left of the expedition, the very difficult decision was made to switch to operations at sites with shallower water depths and penetration that did not require the use of the low clutch while drilling or coring. Therefore, we decided to transit to Site U1504 (2816 mbsl) and continue operations there.

Before departing from Site U1503, the subsea camera was deployed to the seafloor to inspect the Hole U1503A reentry. The cone appeared to be 1–2 m below the seafloor but was clearly visible and expected to be available for reentry at a later date (Figures **F7B**, **F8**). Consequently, the site can be considered a legacy site for future expeditions. The camera was retrieved, the bit was recovered, and the rig was secured for transit. The thrusters were up at 0930 h on 26 May, and the vessel began the 42.5 nmi transit to Site U1504.

Table T1. Site U1503 core summary. DRF = drilling depth below rig floor, DSF = drilling depth below seafloor. Numerical core type = drilled interval. **Download table in CSV format**.

Hole U1503A

Latitude:	18°8.6300′N
Longitude:	116°18.8456′E
Seafloor (drill pipe measurement below rig floor, m DRF):	3867.71
Time on hole (days):	11.88
Total depth (drill pipe measurement from rig floor, m DRF):	3879
Distance between rig floor and sea level (m):	11.88
Total penetration (drilling depth below seafloor, m DSF):	995.1
Total length of cored section (m):	0
Total core recovered (m):	0
Core recovery (%):	0
Drilled interval (m):	995.1
Total cores (no.):	0

Core	Type	Top of interval DSF (m)	Bottom of interval DSF (m)	Interval advanced (m)	Core recovered length (m)	Curated length (m)	Recovery (%)	Time on deck UTC (h)	Time to cut core (min)	Core barrel	Mud pumped (bbl)	Driller's notes
368-U1503A-												
1	1	0.0	908.2	908.2	*****Drilled interval *****			5/16/2017 08:55				
2	1	908.2	995.1	86.9	*****Drilled interval *****			5/22/2017 14:00				

Figure F7. Reentry system on seafloor after free fall, Hole U1503A. The hole remains as a legacy hole for future occupation. A. Free-fall funnel after landing. B. Inspection of reentry cone after casing installation.

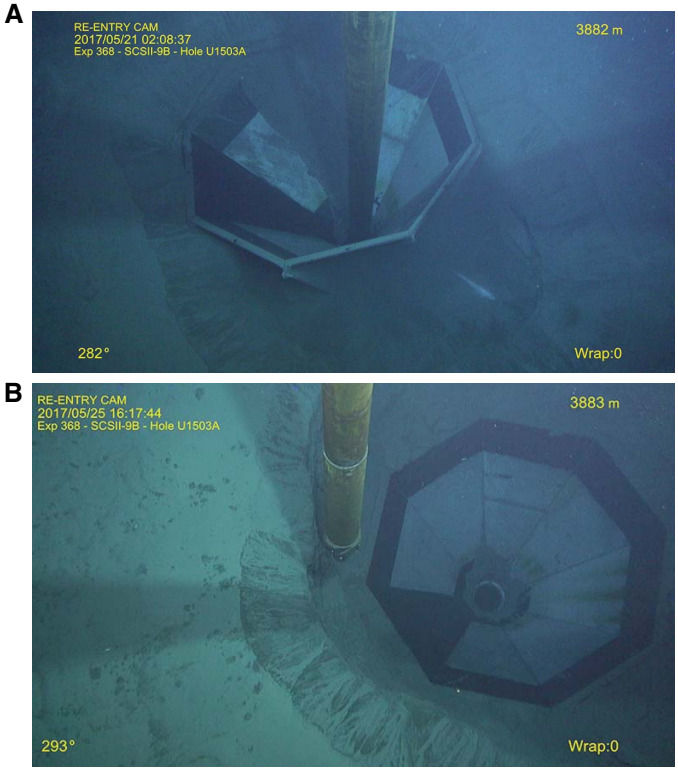

Figure F8. Reentry system and casing, Hole U1503A.

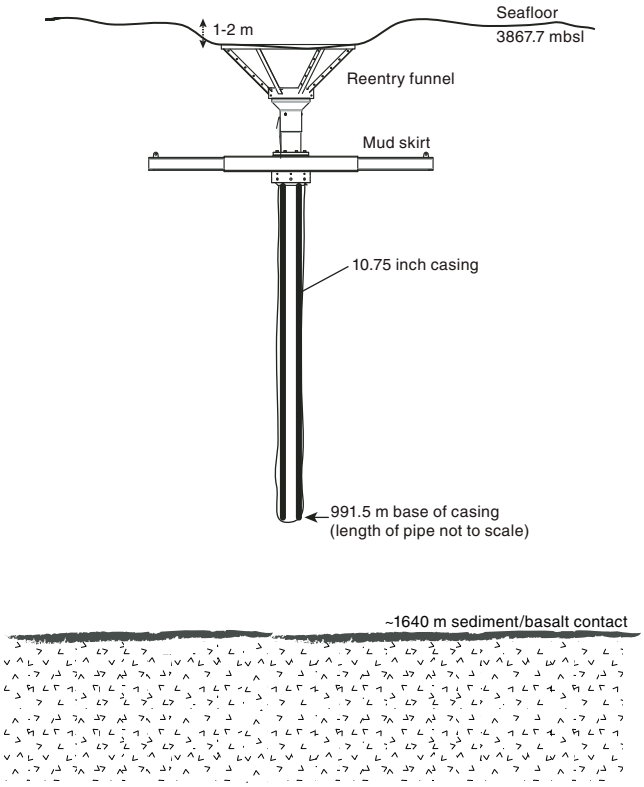

References

Briais, A., Patriat, P., and Tapponnier, P., 1993. Updated interpretation of magnetic anomalies and seafloor spreading stages in the South China Sea: implications for the Tertiary tectonics of Southeast Asia. *Journal of Geophysical Research: Solid Earth,* 98(B4):6299–6328. **https://doi.org/10.1029/92JB02280**

Larsen, H.C., Jian, Z., Alvarez Zarikian, C.A., Sun, Z., Stock, J.M., Klaus, A., Boaga, J., Bowden, S.A., Briais, A., Chen, Y., Cukur, D., Dadd, K.A., Ding, W., Dorais, M.J., Ferré, E.C., Ferreira, F., Furusawa, A., Gewecke, A.J., Hinojosa, J.L., Höfig, T.W., Hsiung, K.-H., Huang, B., Huang, E., Huang, X.-L., Jiang, S., Jin, H., Johnson, B.G., Kurzawski, R.M., Lei, C., Li, B., Li, L., Li, Y., Lin, J., Liu, C., Liu, C., Liu, Z., Luna, A., Lupi, C., McCarthy, A.J., Mohn, G., Ningthoujam, L.S., Nirrengarten, M., Osono, N., Peate, D.W., Persaud, P., Qui, N., Robinson, C.M., Satolli, S., Sauermilch, I., Schindlbeck, J.C., Skinner, S.M., Straub, S.M., Su, X., Tian, L., van der Zwan, F.M., Wan, S., Wu, H., Xiang, R., Yadav, R., Yi, L., Zhang, C., Zhang, J., Zhang, Y., Zhao, N., Zhong, G., and Zhong, L., 2018. Site U1504. *In* Sun, Z., Jian, Z., Stock, J.M., Larsen, H.C., Klaus, A., Alvarez Zarikian, C.A., and the Expedition 367/368 Scientists, *South China Sea Rifted Margin.* Proceedings of the International Ocean Discovery Program, 367/368: College Sta-

tion, TX (International Ocean Discovery Program). **https://doi.org/10.14379/iodp.proc.367368.108.2018**

Stock, J.M., Sun, Z., Klaus, A., Larsen, H.C., Jian, Z., Alvarez Zarikian, C.A., Boaga, J., Bowden, S.A., Briais, A., Chen, Y., Cukur, D., Dadd, K.A., Ding, W., Dorais, M.J., Ferré, E.C., Ferreira, F., Furusawa, A., Gewecke, A.J., Hinojosa, J.L., Höfig, T.W., Hsiung, K.-H., Huang, B., Huang, E., Huang, X.-L., Jiang, S., Jin, H., Johnson, B.G., Kurzawski, R.M., Lei, C., Li, B., Li, L., Li, Y., Lin, J., Liu, C., Liu, C., Liu, Z., Luna, A., Lupi, C., McCarthy, A.J., Mohn, G., Ningthoujam, L.S., Nirrengarten, M., Osono, N., Peate, D.W., Persaud, P., Qui, N., Robinson, C.M., Satolli, S., Sauermilch, I., Schindlbeck, J.C., Skinner, S.M., Straub, S.M., Su, X., Tian, L., van der Zwan, F.M., Wan, S., Wu, H., Xiang, R., Yadav, R., Yi, L., Zhang, C., Zhang, J., Zhang, Y., Zhao, N., Zhong, G., and Zhong, L., 2018. Site U1500. *In* Sun, Z., Jian, Z., Stock, J.M., Larsen, H.C., Klaus, A., Alvarez Zarikian, C.A., and the Expedition 367/368 Scientists, *South China Sea Rifted Margin*. Proceedings of the International Ocean Discovery Program, 367/368: College Station, TX (International Ocean Discovery Program). **https://doi.org/10.14379/iodp.proc.367368.104.2018**

Sun, Z., Stock, J., Jian, Z., McIntosh, K., Alvarez Zarikian, C.A., and Klaus, A., 2016. *Expedition 367/368 Scientific Prospectus: South China Sea Rifted Margin.* International Ocean Discovery Program. **https://doi.org/10.14379/iodp.sp.367368.2016**

Yan, P., Zhou, D., and Liu, Z., 2001. A crustal structure profile across the northern continental margin of the South China Sea. *Tectonophysics,* 338(1):1–21. **https://doi.org/10.1016/S0040-1951(01)00062-2**

Sun, Z., Jian, Z., Stock, J.M., Larsen, H.C., Klaus, A., Alvarez Zarikian, C.A., and the Expedition 367/368 Scientists
Proceedings of the International Ocean Discovery Program Volume 367/368
publications.iodp.org

https://doi.org/10.14379/iodp.proc.367368.108.2018

Site U1504[1]

Check for updates

Hans Christian Larsen, Zhimin Jian, Carlos A. Alvarez Zarikian, Zhen Sun, Joann M. Stock, Adam Klaus, Jacopo Boaga, Stephen A. Bowden, Anne Briais, Yifeng Chen, Deniz Cukur, Kelsie A. Dadd, Weiwei Ding, Michael J. Dorais, Eric C. Ferré, Fabricio Ferreira, Akira Furusawa, Aaron J. Gewecke, Jessica L. Hinojosa, Tobias W. Höfig, Kan-Hsi Hsiung, Baoqi Huang, Enqing Huang, Xiao-Long Huang, Shijun Jiang, Haiyan Jin, Benjamin G. Johnson, Robert M. Kurzawski, Chao Lei, Baohua Li, Li Li, Yanping Li, Jian Lin, Chang Liu, Chuanlian Liu, Zhifei Liu, Antonio Luna, Claudia Lupi, Anders J. McCarthy, Geoffroy Mohn, Lachit Singh Ningthoujam, Michael Nirrengarten, Nobuaki Osono, David W. Peate, Patricia Persaud, Ning Qiu, Caroline M. Robinson, Sara Satolli, Isabel Sauermilch, Julie C. Schindlbeck, Steven M. Skinner, Susanne M. Straub, Xiang Su, Liyan Tian, Froukje M. van der Zwan, Shiming Wan, Huaichun Wu, Rong Xiang, Rajeev Yadav, Liang Yi, Cuimei Zhang, Jinchang Zhang, Yang Zhang, Ning Zhao, Guangfa Zhong, and Lifeng Zhong[2]

Keywords: International Ocean Discovery Program, IODP, *JOIDES Resolution*, Expedition 367, Expedition 368, Site U1504, northern South China Sea, continent–ocean transition zone, hyperextension, continental breakup, thinning, rifting, greenschist, rifting, Eocene, larger benthic foraminifers, coral reef, rapid subsidence

Contents

1 Site summary
5 Background and objectives
6 Operations
8 Lithostratigraphy
15 Igneous and metamorphic petrology
20 Structural geology
24 Biostratigraphy
27 Paleomagnetism
31 Geochemistry
33 Physical properties
36 Correlation to seismic data
40 References

Site summary

Background and objectives

Site U1504 (alternate Site SCSII-27A) was proposed during International Ocean Discovery Program (IODP) Expedition 367 and approved by the Environmental Protection and Safety Panel during Expedition 368 as an alternate site should there be time left following completion of the high-priority sites included in the *Scientific Prospectus* (Sun et al., 2016). Expedition 368 occupied Site U1504 because of the inability to continue drilling below the 990 m deep, cased Hole U1503A. Most of our remaining approved sites were in water deeper than 3400 m and/or required deep penetration. One exception was Site U1504, which is located at 2823 m below sea level (mbsl) ~45 km east of Site U1501 on the outer margin high (OMH) and has a shallow coring target (Figures **F1**, **F2**).

Operations

Two holes were drilled at Site U1504. In Hole U1504A (18°50.9199′N, 116°14.5397′E; 2816.6 mbsl), we cored with the rotary core barrel (RCB) system from the seafloor to metamorphic basement at 134.8 m and then into basement to 165.5 m, recovering 52.77 m (32%). In Hole U1504B (~200 m southeast of Hole U1504A; 18°50.8213′N, 116°14.5978′E; 2843.0 mbsl), we drilled without recovery to 88.2 m, cored with the RCB system to metamorphic basement at 107.9 m, and then cored into basement to 200 m, recovering 21.48 m (19%).

Lithostratigraphy

The succession recovered at Site U1504 includes two sedimentary units (I and II) underlain by a metamorphic unit (III). Litho-

[1] Larsen, H.C., Jian, Z., Alvarez Zarikian, C.A., Sun, Z., Stock, J.M., Klaus, A., Boaga, J., Bowden, S.A., Briais, A., Chen, Y., Cukur, D., Dadd, K.A., Ding, W., Dorais, M.J., Ferré, E.C., Ferreira, F., Furusawa, A., Gewecke, A.J., Hinojosa, J.L., Höfig, T.W., Hsiung, K.-H., Huang, B., Huang, E., Huang, X.-L., Jiang, S., Jin, H., Johnson, B.G., Kurzawski, R.M., Lei, C., Li, B., Li, L., Li, Y., Lin, J., Liu, C., Liu, C., Liu, Z., Luna, A., Lupi, C., McCarthy, A.J., Mohn, G., Ningthoujam, L.S., Nirrengarten, M., Osono, N., Peate, D.W., Persaud, P., Qui, N., Robinson, C.M., Satolli, S., Sauermilch, I., Schindlbeck, J.C., Skinner, S.M., Straub, S.M., Su, X., Tian, L., van der Zwan, F.M., Wan, S., Wu, H., Xiang, R., Yadav, R., Yi, L., Zhang, C., Zhang, J., Zhang, Y., Zhao, N., Zhong, G., and Zhong, L., 2018. Site U1504. *In* Sun, Z., Jian, Z., Stock, J.M., Larsen, H.C., Klaus, A., Alvarez Zarikian, C.A., and the Expedition 367/368 Scientists, *South China Sea Rifted Margin*. Proceedings of the International Ocean Discovery Program, 367/368: College Station, TX (International Ocean Discovery Program). https://doi.org/10.14379/iodp.proc.367368.108.2018

[2] **Expedition 367/368 Scientists' addresses.**

MS 367368-108: Published 28 September 2018

This work is distributed under the **Creative Commons Attribution 4.0 International** (CC BY 4.0) license.

Figure F1. Bathymetry at Site U1504 and location of the site in relation to seismic lines. Note that the clear offset in bathymetry along the margin may indicate some transform offset within the deeper margin structure. Seismic Line 15ecLW6 crossing the structural high is shown in Figure F4.

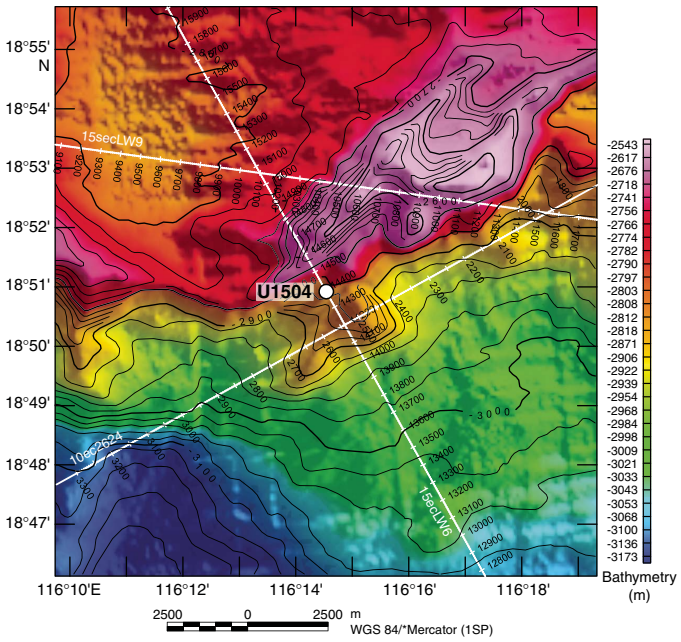

Figure F2. Bathymetric maps showing Expedition 367/368 sites (stars), and (A) regional and (B) local coverage of multichannel seismic reflection data and OBS data. Thick blue and red lines are key seismic lines used for planning of the drilling transect. A. Magnetic isochrons (orange lines) from Briais et al. (1993). B. Magnetic picks (orange squares) from the same reference, extracted from the Seton et al. (2014) compilation. Chron labels for the picks correspond to the old edge of the normal polarity intervals (see Ogg et al. [2016] timescale for ages). Orange square = Leg 184 Site 1148, yellow squares = Expedition 349 Sites U1432 and U1435.

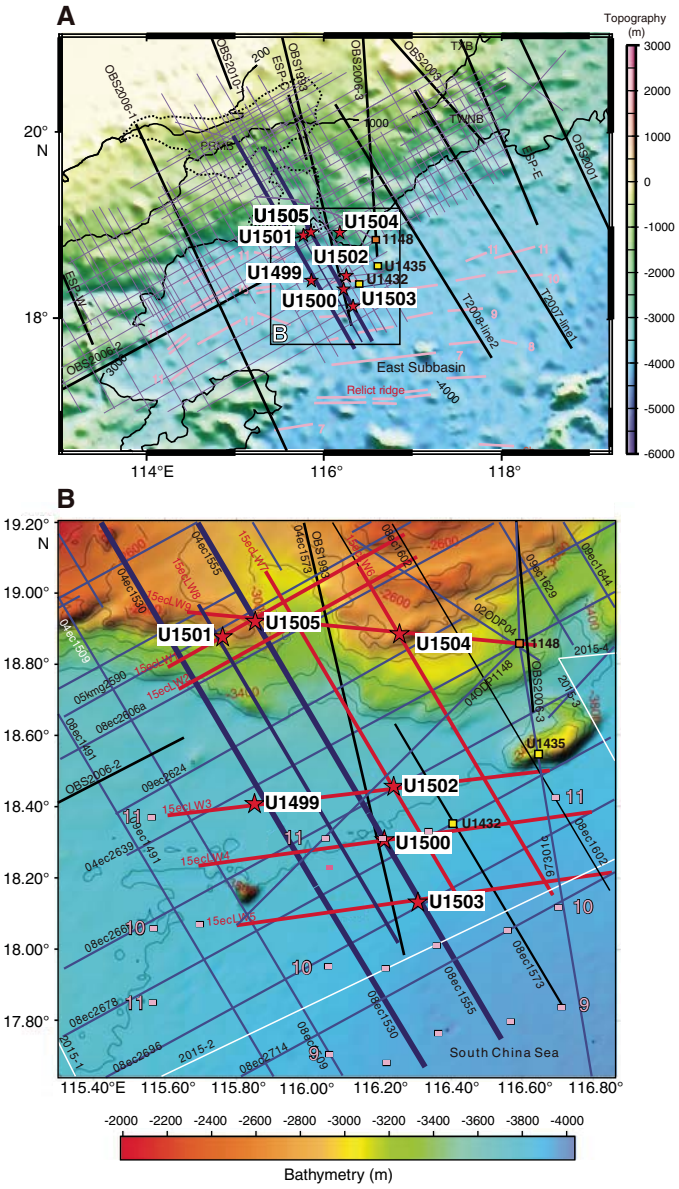

stratigraphic Unit I (early Miocene–Pleistocene) is dominated by nannofossil and foraminiferal ooze and minor nannofossil-rich clay and is divided into four subunits (IA–ID). Subunit IA (Hole U1504A = 17.50–46.59 m) is composed of nannofossil-rich clay, nannofossil ooze, nannofossil ooze with biogenic silica, and clay-rich nannofossil ooze. The color of the ooze gradually changes downhole from dark greenish gray to greenish gray and gray. Distinct intervals contain more silt. Thin silt laminations are often disrupted by bioturbation. Layering is contorted at the base of the subunit. Subunit IB (Hole U1504A = 46.59–59.73 m) is composed of light brown foraminifer-rich nannofossil ooze and pale brown nannofossil ooze with foraminifers. Subunit IC (Hole U1504A = 65.80–104.99 m) is composed of light greenish gray, greenish gray, light brownish gray, pale brown, and light gray nannofossil ooze with clay and greenish gray clay-rich nannofossil ooze intercalated with light gray nannofossil-rich foraminiferal ooze with clay, light brownish gray foraminifer-rich nannofossil ooze, and foraminifer-rich nannofossil ooze with clay. Subunit ID (Hole U1504A = 104.99–112.66 m; Hole U1504B =88.20–92.31 m) is composed of light brown to yellowish brown nannofossil ooze with foraminifers intercalated with pink or brownish yellow foraminifer-rich nannofossil ooze. Unit II (Hole U1504A = 114.72–134.80 m; Hole U1504B = 97.90–107.91 m) is clast-supported, bioclast-rich limestone with larger benthic foraminifers (as large as 15 mm). Unit III (Hole U1504A = 136.40–163.70 m; Hole U1504B = 117.40–196.28 m) is composed of fine- to coarse-grained epidote-chlorite schist (Subunit IIIA) and calc-silicate schist (Subunit IIIB) with granofels clasts.

Metamorphic petrology

We recovered 27 m (Hole U1504A) and 79 m (Hole U1504B) of a variety of mylonitic epidote-chlorite to calc-silicate schists containing granofels clasts. Recovery was <20% in metamorphic lithologic Unit 1. Lithologic changes with depth and between the two holes were observed, and Unit 1 is divided based on a change in the predominant metamorphic lithology (Figure **F3**). Metamorphic lithologic Subunit 1a was recovered in both Holes U1504A and U1504B and consists of greenish gray, microcrystalline to coarse-grained epidote-chlorite schist with dark greenish gray granofels clasts (<10 cm) and epidote-chlorite breccia. The schists show a strong mylonitic foliation, whereas the clasts have generally isotropic textures showing local weakly developed foliation. Both the schist and the granofels clasts show, in general, a comparable mineral assemblage consisting of epidote, chlorite, feldspar, and quartz

Figure F3. Lithostratigraphic, petrographic/petrological, and structural observations at Site U1504 with strong focus on the metamorphic basement. A, B. Clast-supported limestone with large benthic foraminifers and coral fragments. C. Severely quartz-veined, angular clast of chlorite-epidote granofels enclosed in mylonitic foliation of a typical epidote-chlorite schist. D. Steep (~75°) widely anastomosing foliation in a quartz + feldspar-rich variety of the rock. Arrow = extensively stretched veined clast of chlorite-epidote granofels oriented parallel to the foliation. E. Epidote-chlorite schist with granofels clasts split parallel to the *xy*-plane of finite strain. Large granofels clast is crosscut by a shear band within the epidote-chlorite schist. Several sigma clasts are observed right above the shear band. Both deformation structures indicate normal sense of shear. A late, postkinematic vein crosscuts both the mylonitic foliation and the granofels clast. F. Tight foliation affected by crenulation cleavage in quartz-poor (i.e., more melanocratic) variety of the rock. G. Local occurrence of foliated impure calcite marble. H. Veined and altered aphyric mafic granofels clast (left side) and granofels clast interpreted as protolithic epidote vein (right side). Both clasts are internally undeformed but show synkinematic deformation together with the mylonitic fabric at their rims. I. Rigid (left) and strongly deformed (upper end) granofels clasts embedded in calc-silicate schist. Note the deflection of the mylonitic foliation at the clast boundaries. J. Long piece of core showing the characteristic morphology of the mylonitic foliation in calc-silicate schist of Subunit IIIB. Note the steep inclination and anastomosing geometry enclosing heterolithic clasts that are strongly elongated, folded, and oriented parallel to the foliation.

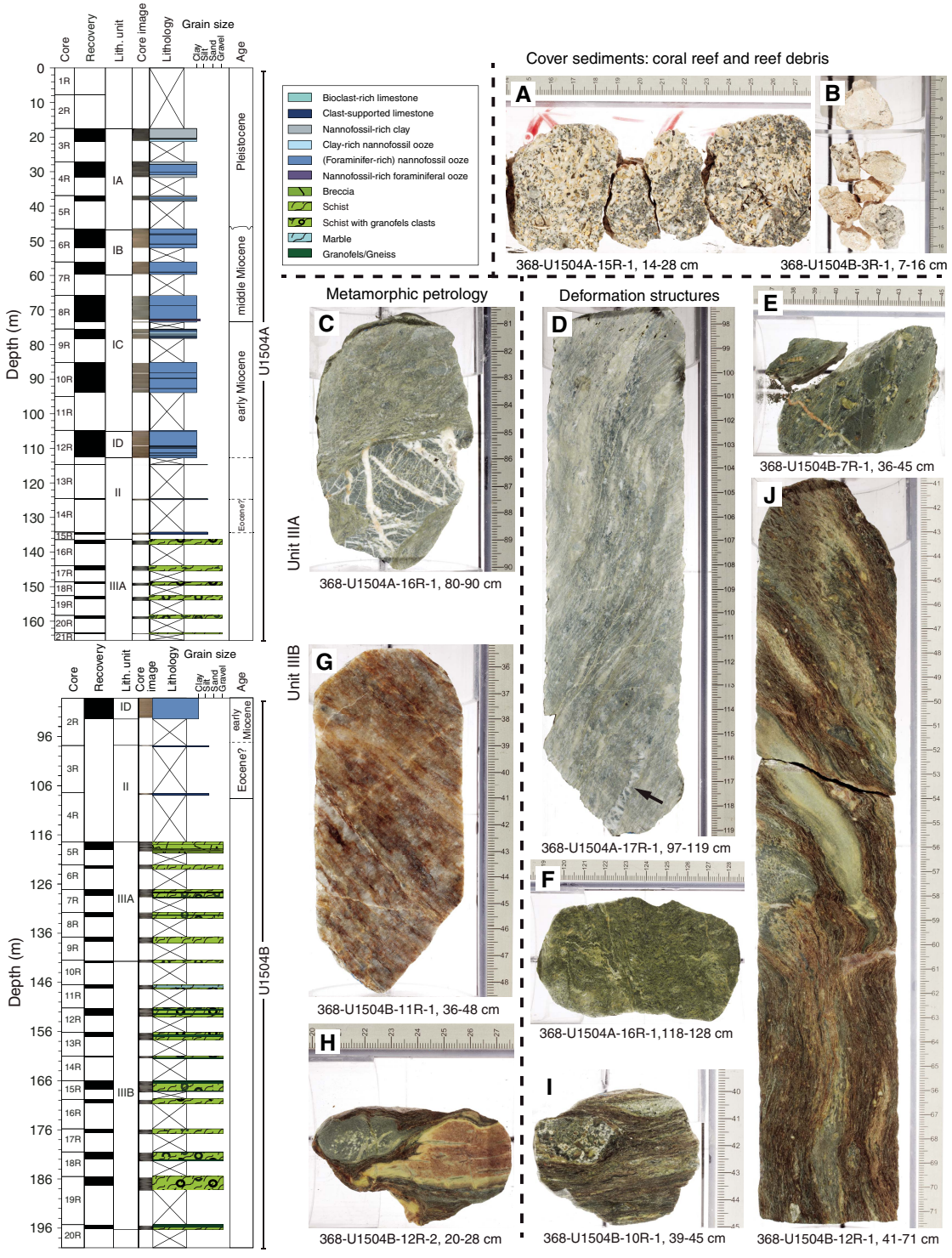

± other phyllosilicates and accessory minerals and locally isolated subhedral dark minerals (pyroxene?). The granofels clasts are often crosscut by a network of quartz veins. Subunit 1b contains an alternation of calc-silicate schist and epidote-chlorite schist with granofels clasts, epidote and/or chlorite granofels, chlorite schist with epidote, epidote-chlorite gneiss, and minor marble. The lithologies are fine grained to coarse grained with mostly an inequigranular texture and some bimodal or equigranular textures, and the schistose sections show a strong mylonitic foliation. Several of the schists show reddish brown alteration, and late calcite veins crosscut the foliation of the deepest schists recovered (e.g., in Core 368-U1504A-20R). Minerals observed are epidote, quartz, chlorite, calcite, and feldspar. Subunit 1b contains numerous clasts with variable lithologies: cryptocrystalline granofels either with or without quartz and/or calcite veins, porphyritic rocks with tabular phenocrysts (possibly altered plagioclase), brecciated (epidote, calcite, and/or quartz) veins, and foliated granofels.

Handheld portable X-ray fluorescence (pXRF) analyses show an average mafic igneous composition for both the schist and the clasts but with a spread toward ultramafic (in Hole U1504B Subunit 1a) and more felsic compositions (in Subunit 1b). A clear change in sulfur contents occurs between Subunits 1a and 1b, the latter of which is below the detection limit. High Nb contents compared to mid-ocean-ridge basalt (MORB) indicate a potentially enriched source for the protolith.

Lithostratigraphic Unit III (metamorphic lithologic Unit 1) consists of mylonitic greenschist facies metamorphic rocks, as indicated by the presence of epidote and chlorite. We infer that the protolith most likely was breccia based on the different clast sizes and types and styles of deformation. The protolith likely had a mafic igneous composition. It is, however, unclear if this breccia with mafic clasts has a sedimentary origin (e.g., volcaniclastic) or represents a potentially hydrothermally altered form of basalt, gabbro, or ultramafic protolith. At present, the metamorphic evolution of this unit and its possible connection with the opening of the South China Sea (SCS) is unknown.

Structural geology

Lithostratigraphic Unit I shows subhorizontal bedding and locally some minor possible slump folds, as observed in Section 368-U1504A-5R-1. Unit II is devoid of any deformation structures. The metamorphic basement at Site U1504 is formed by greenschist facies mylonitic epidote-chlorite schists and calc-silicate schists (Unit III). The rocks preserve distinct deformation structures resulting from changes in the mode of deformation (brittle/ductile); the modal amount of quartz + feldspar governing the (local) rheological behavior; the amount of accumulated strain; the occurrence of variably sized (up to decimeter scale), prekinematic, heterolithic clasts that mostly form rigid (i.e., internally undeformed) bodies within the ductile foliation; and/or superimposed multiple deformation phases. The steeply dipping (up to 75°) mylonitic foliation is characterized by distinct morphologies: (1) a widely spaced anastomosing foliation associated with leucocratic bands; (2) a tight, closely spaced, and often crenulated foliation associated with more melanocratic schist variations; and (3) a tight anastomosing foliation associated with calc-silicate schists enclosing angular to rounded heterolithic granofels clasts. Locally, the sense of shear is indicated by shear bands and sigma clasts. In metamorphic lithologic Subunit 1a (Figure **F3**), granofels clasts are consistently microcrystalline (chlorite + epidote) and dismembered by a network of mostly parallel and perpendicular quartz veins cutting each other. They often form apparently stretched, elongated bodies oriented parallel to the foliation. Subunit 1b shows a wide range of prekinematic (mostly mafic) clasts enclosed by the foliation. Encountered varieties encompass highly phyric to aphyric rocks, as well as fragmented former (epidote/calcite/quartz) vein fillings. In some cases, such clasts show ductile internal deformation. Clast boundaries can be either distinctly sharp or diffuse, the latter indicating mechanical and/or chemical interactions with the surrounding foliation. Deformation in Subunit 1b is presumably strongly controlled by an inherited (protolithic) brecciated structure.

Biostratigraphy

All core catcher samples at Site U1504 were analyzed for calcareous nannofossils, foraminifers, and diatoms. Additional samples were taken from intervals within the working-half core sections when necessary to refine the ages. Preservation of calcareous microfossils is good to very good in Cores 368-U1504A-2R through 12R, and 368-U1504B-2R and is poorly preserved (recrystallization) in the reefal limestone below Core 368-U1504A-12R. Planktonic foraminifers and calcareous nannofossils are abundant in Cores 368-U1504A-2R through 12R and 368-U1504B-2R and barren in Cores 368-U1504A-13R through 15R. Diatoms are present but poorly preserved in Cores 368-U1504A-2R through 5R and absent in rest of the samples. Twenty biostratigraphic datums were identified in a succession from the late Pleistocene to the early Miocene.

A possible hiatus between the early Pleistocene and late Miocene was determined within Core 368-U1504A-6R by abrupt planktonic foraminifer and nannofossil assemblage changes. Sedimentation rates at this site varied from ~6 mm/ky in the early middle Miocene to ~22 mm/ky during the Pleistocene.

Cores 368-U1504A-13R through 15R are mainly composed of reefal and larger benthic foraminiferal limestone. Thin section examination of these carbonate rocks indicates the presence of abundant *Nummulites*, suggesting an Eocene age. The abundant larger benthic foraminifers indicate deposition in a warm shallow-marine environment. In contrast, the abundant planktonic foraminifers and calcareous nannofossils in the carbonate ooze in the overlying sedimentary section (Cores 2R through 12R) indicate a deepwater environment since the early Miocene.

Paleomagnetism

Most of the discrete sediment samples analyzed show an initial soft magnetic behavior attributed to titanomagnetite followed by a gyroremanent magnetization (GRM) greater than 70 mT attributed to greigite, a mineral already identified in Hole U1501C. Consistently steep normal inclinations (~60°) across all sedimentary units indicate a significant drilling overprint that is removed by alternating field (AF) demagnetization up to 15 mT. A succession of nine normal and eight reversed polarities are defined, particularly in the upper part of the cores (Figure **F29**).

Discrete samples show low κ values, a moderate degree of magnetic anisotropy, and strongly oblate symmetry, probably of depositional origin. This subhorizontal planar fabric indicates deposition in a calm, pelagic environment with moderate traction.

Natural remanent magnetization (NRM) intensities of metamorphic rocks, measured on the superconducting rock magnetometer (SRM) and on four discrete cubes, are relatively weak and indicate a complex magnetic assemblage composed of magnetite and hematite. The anisotropy of magnetic susceptibility (AMS) fabrics consistently dip steeply and show a moderate to high degree of magnetic anisotropy, oblate symmetries, and oblique magnetic lineations, possibly indicating an oblique motion within this high-strain shear zone.

Geochemistry

Hydrocarbon gases were not detected above background levels at Site U1504, and total organic carbon (TOC), total nitrogen (TN), and total sulfur (TS) contents were low (<0.5 wt%). Instances of high carbonate content were associated with bioclast-rich and clast-supported limestone. The upper part of the sediment was not cored. Interstitial water data from the cored sediments are broadly comparable to other sites.

Physical properties

Four petrophysical (PP) units are identified at Site U1504 according to variations in the core physical properties. Core material in PP Units 1 and 2 consists of soft sediments. In general, with respect to Unit 2, Unit 1 has a higher average natural gamma radiation (NGR) count (~30 versus 20 counts/s), a weaker color reflectance (mean L* of ~40 versus 50), and a lower average RGB value (100 versus 150). These changes in physical properties between Units 1 and 2 correspond to a switch in sediment composition from nannofossil-rich clay to nannofossil ooze. A general increase in bulk (from ~1.4 to 1.8 g/cm^3) and dry (from ~0.7 to 1.2 g/cm^3) densities and a downhole decrease in porosity (from 75% to 56%) in Units 1 and 2 mainly indicate sediment compaction with time. The boundary between Units 1 and 2 is marked by a relatively rapid increase in *P*-wave velocity and bulk density and a rapid decrease in porosity compared with the general trends mentioned above. This physical property boundary corresponds to an unconformity in the seismic profile and to a hiatus confirmed by the biostratigraphic data.

P-wave velocity and bulk density increase from ~3800 to 5000 m/s and from ~2.4 to 2.9 g/cm^3, respectively, within Unit 3, which corresponds to a transition in lithology from coral-rich limestone to clast-supported limestone. Coral-rich limestone in the upper portion of Unit 3 is also associated with a moderately high porosity of ~23%. Unit 4 is characterized by uniformly high velocity of ~5500 m/s, high bulk density of ~2.9 g/cm^3, and low porosity of ~3%, which correspond to the epidote-chlorite schist. A large increase in both velocity and density at the Unit 2/3 and Unit 3/4 boundaries corresponds to strong reflectors in the seismic data. The gradual downhole increase in thermal conductivity values at shallow depths is likely due to progressive compaction of the sediments.

Background and objectives

Site U1504 was proposed together with other relatively shallow penetration sites during Expedition 367. These sites were approved by the Environmental Protection and Safety Panel and IODP as alternate sites for Expedition 368 should there be time left following completion of the high-priority sites included in the *Scientific Prospectus*. Expedition 368 occupied Site U1504 because of the inability to continue drilling below the 990 m deep, cased Hole U1503A (see **Operations** in the Site U1503 chapter [Larsen et al., 2018b]). The depth limit of 3400 m (water depth plus penetration) imposed by the flawed drawworks left very few drilling options for continuation of Expedition 368 operations because almost all proposed sites are in water depths greater than 3400 m and/or require deep penetration. One exception was Site U1504, which is located in ~2830 m water depth and has a shallow coring target (Figure **F2**).

Figure F4. Seismic Profile 15ecLW6 with location of Holes U1504A and U1504B. Fault structures and basement location are complex to interpret. Drill holes were placed in the most simple, well-defined locations with a high probability to reach crystalline basement. Drill site choice was constrained by seabed communications cables in the area (to the north). Basement at drill site is interpreted to be at the strong (second) reflector at ~3940 ms TWT. Distance between Holes U1504A and U1504B is ~200 m. CDP = common depth point. Dashed lines = unconformities, red solid line = fault.

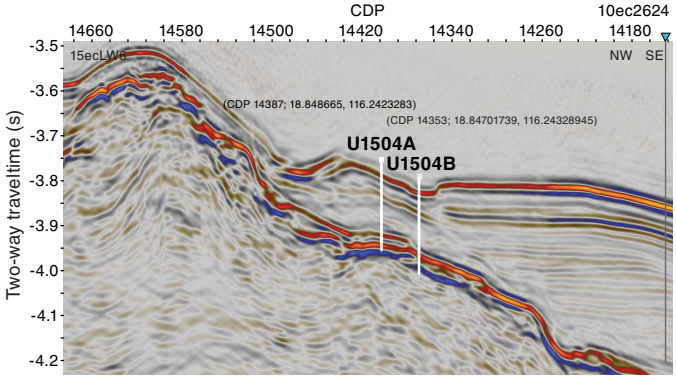

Site U1504 is located near the top of a structural high (Figures **F1**, **F2**, **F4**) that can be interpreted as an easterly extension of the OMH. The OMH was drilled at Sites U1501 and U1505 (Figure **F5**). At Site U1501, acoustic basement at ~600 m consists of highly lithified sandstones and conglomerate likely of pre-Cenozoic age (see the **Site U1501** chapter [Larsen et al., 2018a]). Site U1504 is ~50 km east of Site U1501 (Figure **F2**), and the OMH at Site U1504 is much narrower and bounded to the north (landward) by a major normal fault. The OMH appears faulted (complex) to the south (seaward) and lacks the small rift basins that formed an important coring target at Sites U1501 and U1505 (Figure **F5**). These basins may, however, be present south (seaward) of Site U1504, where the top of the basement rapidly deepens in parallel with basinward crustal thinning. Site U1504 may be located within a transition zone into another (eastern) margin segment with a different rifting structure (Figure **F1**).

Site U1504 was designed to sample the basement below the thin (~120 m) layers of sediments covering this basement high (Figure **F4**). The specific goal was to find out how deeply tectonic exhumation during breakup might have reached into the lithosphere, or alternatively, whether the basement would be of igneous origin and related to breakup, similar to Site U1502. There was no predrilling interpretation of the seismic stratigraphy. The site is located in a place with a strong basement reflector with a reasonable horizontal extension. Basement appears to be heavily faulted both north and south of the drill site.

Figure F5. TWT to (A) basement (Tg reflector) and (B) T60 unconformity. Proposed drilling transect (thick black line) is approximately at the center of a margin segment bounded to the southwest by a transform fault. Northeastern boundary of margin segment around Expedition 349 Site U1435. At this location, OMH and Ridge A seem to coalesce, and Ridges B and C of the continent–ocean transition (COT) become indistinct toward the northeast within the next margin segment. Note that the OMH is slightly oblique to the more parallel Ridges A, B, and C.

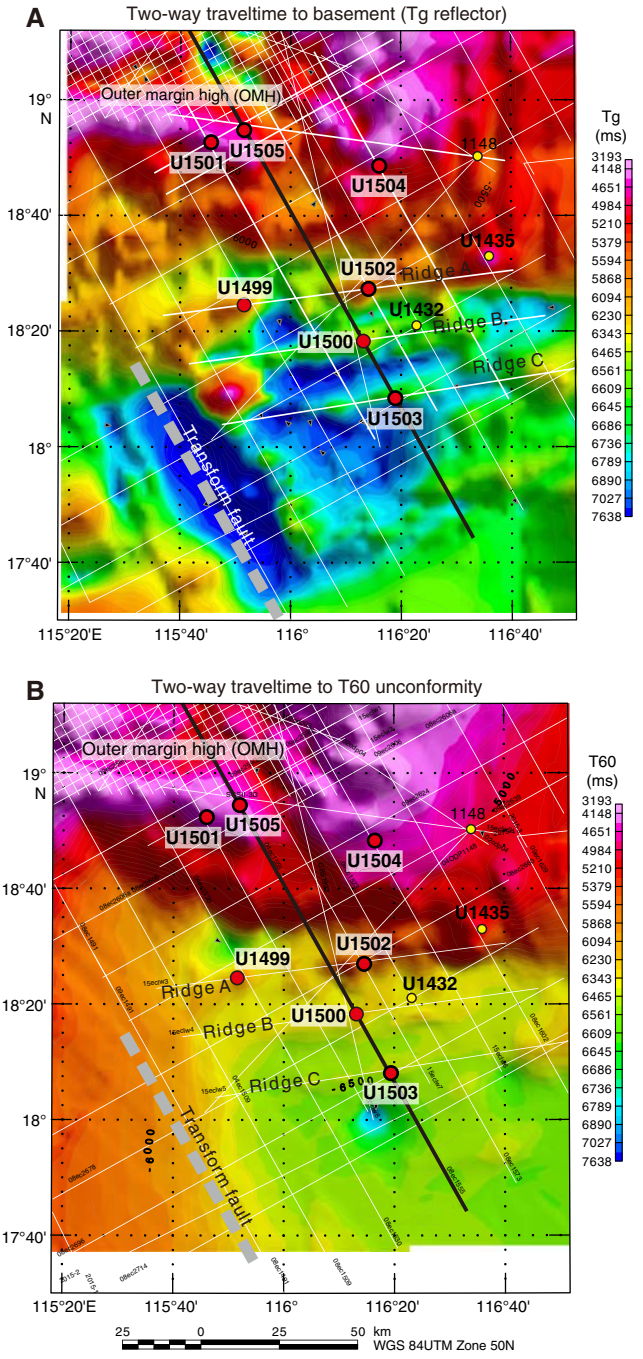

Operations

We drilled two holes at Site U1504 (Table T1). Hole U1504A is located at 18°50.9199′N, 116°14.5397′E, in a water depth of 2816.6 m. In this hole, we cored with the RCB system from the seafloor to 165.5 m, recovering 52.77 m (32%) of sedimentary and metamorphic rocks. Hole U1504B is located ~200 southeast of Hole U1504A at 18°50.8213′N, 116°14.5978′E, in a water depth of 2843.0 m. In this hole, we drilled without recovery to 88.2 m and then cored with the RCB system over a 111.8 m interval, recovering 21.48 m (19%) of mostly metamorphic rock.

Transit to Site U1504

The R/V *JOIDES Resolution* began the transit from Site U1503 to Site U1504 at 0948 h on 26 May 2017 and arrived on site at 1400 h the same day. The thrusters were lowered, and the vessel was switched to dynamic positioning mode at 1432 h, beginning operations at Site U1504. An RCB bottom-hole assembly (BHA) was made up and deployed to 1720 mbsl before failure of the pipe spinner on the iron roughneck. The spinner was replaced, and the crew continued to lower the pipe to 2776 mbsl. The subsea camera was deployed, and the bit was placed at 2813 mbsl for a short seafloor survey to verify that no seafloor cables were in the area. The seafloor was tagged after the survey, determining a water depth of 2816.6 m. The camera was retrieved, and the top drive was picked up in preparation for starting Hole U1504A.

Hole U1504A

Coring in Hole U1504A started at 0215 h, and the bit reached the sediment/basement contact at 136.4 m (at 1455 h on 27 May 2017). Coring continued to 165.5 m, at which depth erratic torque and overpull caused termination of coring operations at 1100 h on 28 May. The bit was recovered to the surface, clearing the seafloor at 1220 h and the rotary table at 1740 h. The rig floor was secured for the 22 nmi transit to Site U1505 by 1825 h on 28 May, temporarily ending operations at Site U1504.

Total time spent in Hole U1504A was 50.5 h (2.1 days). A total of 21 RCB cores were taken over a 165.5 m interval of loosely to well-consolidated sedimentary rock and metamorphic rocks with 52.77 m of recovery (32%).

Return to Site U1504

We returned to Site U1504 after completing operations at Site U1505. The 22.2 nmi transit from Site U1505 to Site U1504 was completed at 0048 h on 03 June 2017. The thrusters were lowered, and the heading was controlled at 0357 h, beginning operations at Site U1504.

Hole U1504B

An RCB BHA was made up, and core barrels were spaced out. A center bit was installed, and the drill string was lowered to 2776 m. The subsea camera was deployed to the bit, and the drill string was hung off the elevator stool. The low clutch was then dismantled, and the diaphragm was replaced for the fifth time. The diaphragm failed during operations at Site U1505 but was not replaced there because it was not necessary for operations at that site and the rig crew recommended installing the new diaphragm at the seafloor in Hole U1504B in case it was necessary during operations there. The replacement took 7.75 h. Once completed, the top drive was picked up and the bit was lowered to the seafloor.

Seafloor was tagged at 2843.0 mbsl. The subsea camera was recovered to the moonpool, and Hole U1504B was spudded at 2250 h on 4 June 2017. The hole was advanced without coring to 88.2 m.

Table T1. Site U1504 core summary. DRF = drilling depth below rig floor, DSF = drilling depth below seafloor. NA = not applicable. Core type: R = rotary core barrel, numeric core type = drilled interval. **Download table in CSV format.**

Hole U1504A		**Hole U1504B**	
Latitude:	18°50.9199′N	Latitude:	18°50.8213′N
Longitude:	116°14.5397′E	Longitude:	116°14.5978′E
Seafloor (drill pipe measurement below rig floor, m DRF):	2816.57	Seafloor (drill pipe measurement below rig floor, m DRF):	2842.97
Time on hole (days):	2.17	Time on hole (days):	3.33
Total depth (drill pipe measurement from rig floor, m DRF):	2828	Total depth (drill pipe measurement from rig floor, m DRF):	2854.5
Distance between rig floor and sea level (m):	11.43	Distance between rig floor and sea level (m):	11.53
Total penetration (drilling depth below seafloor, m DSF):	165.5	Total penetration (drilling depth below seafloor, m DSF):	200
Total length of cored section (m):	165.5	Total length of cored section (m):	111.8
Total core recovered (m):	52.93	Total core recovered (m):	21.48
Core recovery (%):	31.98	Core recovery (%):	19.21
Drilled interval (m):	NA	Drilled interval (m):	88.2
Total cores (no.):	21	Total cores (no.):	19

Core	Type	Top of interval DSF (m)	Bottom of interval DSF (m)	Interval advanced (m)	Core recovered length (m)	Core curated (m)	Recovery (%)	Time on deck UTC (h)	Time to cut core (min)	Core barrel	Mud pumped (bbl)
368-U1504A-											
1	R	0.0	7.8	7.8	0.00		0	5/26/2017 19:50	5	Nonmagnetic	
2	R	7.8	17.5	9.7	0.05	0.05	1	5/26/2017 20:35	5	Nonmagnetic	
3	R	17.5	27.2	9.7	3.85	3.85	40	5/26/2017 21:10	5	Nonmagnetic	
4	R	27.2	36.9	9.7	4.55	4.55	47	5/26/2017 22:10	5	Nonmagnetic	
5	R	36.9	46.5	9.6	1.63	1.63	17	5/26/2017 22:45	5	Nonmagnetic	
6	R	46.5	56.1	9.6	5.63	5.63	59	5/26/2017 23:30	5	Nonmagnetic	
7	R	56.1	65.8	9.7	3.68	3.68	38	5/27/2017 00:15	10	Nonmagnetic	
8	R	65.8	75.5	9.7	7.76	7.76	80	5/27/2017 01:10	5	Nonmagnetic	
9	R	75.5	85.2	9.7	2.81	2.81	29	5/27/2017 01:45	5	Nonmagnetic	
10	R	85.2	95.0	9.8	8.76	8.76	89	5/27/2017 02:40	10	Nonmagnetic	
11	R	95.0	104.8	9.8				5/27/2017 03:35	10	Nonmagnetic	
12	R	104.8	114.7	9.9	7.86	7.86	79	5/27/2017 04:20	10	Nonmagnetic	
13	R	114.7	124.5	9.8	0.07	0.10	1	5/27/2017 05:10	15	Nonmagnetic	
14	R	124.5	134.2	9.7	0.35	0.38	4	5/27/2017 05:55	10	Nonmagnetic	
15	R	134.2	136.4	2.2	0.66	0.66	30	5/27/2017 06:55	20	Nonmagnetic	
16	R	136.4	143.9	7.5	1.15	1.34	15	5/27/2017 09:25	100	Nonmagnetic	
17	R	143.9	148.6	4.7	1.30	1.59	28	5/27/2017 12:30	45	Nonmagnetic	
18	R	148.6	152.6	4.0	0.59	0.90	15	5/27/2017 15:50	30	Nonmagnetic	30
19	R	152.6	158.3	5.7	0.88	1.28	15	5/27/2017 20:00	65	Nonmagnetic	15
20	R	158.3	163.3	5.0	0.90	0.80	18	5/27/2017 22:55	65	Nonmagnetic	15
21	R	163.3	165.5	2.2	0.45	0.40	20	5/28/2017 03:00	120	Nonmagnetic	30
		Hole U1504A totals:		165.5	52.93	54.03	32				
368-U1504B-											
1	1	0.0	88.2	88.2		*****Drilled interval*****		6/4/2017 16:50	65		
2	R	88.2	97.9	9.7	4.17	4.17	43	6/4/2017 18:35	10	Nonmagnetic	
3	R	97.9	107.6	9.7	0.10	0.16	1	6/4/2017 19:35	15	Nonmagnetic	
4	R	107.6	117.4	9.8	0.18	0.31	2	6/4/2017 21:15	50	Nonmagnetic	
5	R	117.4	122.1	4.7	1.65	2.13	35	6/4/2017 23:40	85	Nonmagnetic	
6	R	122.1	127.1	5.0	0.69	0.89	14	6/5/2017 02:20	85	Nonmagnetic	
7	R	127.1	131.8	4.7	1.30	1.72	28	6/5/2017 05:00	80	Nonmagnetic	15
8	R	131.8	136.8	5.0	0.90	1.23	18	6/5/2017 07:15	60	Nonmagnetic	
9	R	136.8	141.5	4.7	1.00	1.23	21	6/5/2017 09:05	20	Nonmagnetic	15
10	R	141.5	146.5	5.0	0.45	0.55	9	6/5/2017 11:25	45	Nonmagnetic	
11	R	146.5	151.2	4.7	0.75	0.85	16	6/5/2017 14:15	50	Nonmagnetic	30
12	R	151.2	156.2	5.0	1.55	1.86	31	6/5/2017 18:00	125	Nonmagnetic	
13	R	156.2	161.0	4.8	0.95	1.45	20	6/5/2017 20:40	65	Nonmagnetic	15
14	R	161.0	166.0	5.0	0.30	0.43	6	6/5/2017 23:20	70	Nonmagnetic	
15	R	166.0	169.8	3.8	1.85	2.25	49	6/6/2017 03:00	70	Nonmagnetic	15
16	R	169.8	175.8	6.0	0.75	0.84	13	6/6/2017 05:20	45	Nonmagnetic	30
17	R	175.8	180.5	4.7	0.75	0.92	16	6/6/2017 08:15	45	Nonmagnetic	30
18	R	180.5	185.5	5.0	1.50	1.84	30	6/6/2017 11:05	80	Nonmagnetic	30
19	R	185.5	195.3	9.8	1.85	2.65	19	6/6/2017 15:30	120	Nonmagnetic	55
20	R	195.3	200.0	4.7	0.79	0.98	17	6/6/2017 18:25	70	Nonmagnetic	
		Hole U1504B totals:		111.8	21.48	26.46	19				
		Site U1504 totals:		311.8	42.96	52.92	17				

The center bit was recovered, and an RCB core barrel was dropped to begin coring. Sediments were recovered in Core 2R. The following two cores, 3R and 4R, contained limestone fragments. Basement rubble was recovered from Core 4R downhole. RCB coring continued through Core 20R at 200 m. Torque was erratic throughout coring operations in basement, and half cores were cut for all basement cores except Core 19R.

Coring was terminated due to time limitations after Core 20R, and the bit was recovered to the surface, clearing the seafloor at 0455 h and the rotary table at 1040 h on 7 June. Total time spent in Hole U1504B was 80 h (3.3 days). A total of 19 RCB cores were taken over a 111.8 m interval with 21.48 m of recovery (19%).

The rig floor was secured and made ready for the 946 nmi transit to Shanghai, China, by 1130 h on 7 June. The vessel was underway at 1200 h, ending Hole U1504B and Site U1504. After a 4 day transit, the *JOIDES Resolution* arrived in Shanghai, China, and Expedition 368 concluded with the first line ashore at Lingang Terminal at 1212 h on 11 June.

Lithostratigraphy

We examined the lithostratigraphy of Holes U1504A and U1504B (Figure **F6**), which are approximately 200 m apart. Three lithostratigraphic units are defined; two sedimentary and one metamorphic. Lithostratigraphic Unit I is further divided into four subunits based on visual core description, smear slide and thin section inspection, and X-ray diffraction (XRD) analysis (see **Lithostratigraphy** in the Expedition 367/368 methods chapter [Sun et al., 2018]).

The recovered sediment succession extends from 17.50 to 134.80 m in Hole U1504A (Sections 3R-1 through 15R-1) and from 88.20 to 107.91 m in Hole U1504B (Sections 2R through 4R) and overlies greenish gray metamorphic rocks. The uppermost cores in Hole U1504A (Cores 1R and 2R) had no recovery.

Unit I is dominated by nannofossil and foraminiferal ooze with minor nannofossil-rich clay. Unit II is defined by a change from clay and ooze to bioclast-rich and clast-supported limestone with large benthic foraminifers. The contact between Units I and II was not recovered. Unit III is composed of fine- to medium-grained epidote-chlorite schist, calc-silicate schist, epidote-chlorite breccia, and marble.

Unit description

Unit I

Intervals: 368-U1504A-3R-1, 0 cm, to 12R-CC, 18 cm;
368-U1504B-2R-1, 0 cm, to 2R-CC, 17 cm
Depths: Hole U1504A = 17.50–112.66 m; Hole U1504B = 88.20–92.31 m
Age: Pleistocene to early Miocene

Lithology and sedimentary structures

Unit I is dominated by nannofossil and foraminifer ooze with minor nannofossil-rich clay intervals at the top of the unit. The unit is divided into four subunits, IA–ID, based on changes in the biogenic component of the sediment and on color changes that coincide with subtle changes in the sediment components (Figure **F7**).

The boundary between Units I and II is marked by a change in lithology from ooze-dominated sediments to bioclast-rich and clast-supported limestone.

Bulk mineralogy

The bulk mineralogy results of XRD analyses are listed in Table **T2** and shown in Figure **F8**. Unit I sediments are mainly composed of calcite, quartz, plagioclase, K-feldspar, halite, pyrite, and clay minerals (including smectite, illite, kaolinite, and chlorite). Calcite is present throughout Unit I (mostly in the form of nannofossils and foraminifers) and becomes more abundant in Subunits IB–ID. Pyrite has a downhole trend similar to that of calcite. In contrast, the percentages of terrigenous minerals (quartz, plagioclase, and chlorite) and authigenic halite have much lower contents in Subunits IB–ID than in Subunit IA. These general characteristics are consistent with the observed lithologic change from nannofossil-rich clay to foraminifer-rich nannofossil ooze.

Subunit IA

Interval: 368-U1504A-3R-1, 0 cm, to 6R-1, 9 cm
Depth: 17.50–46.59 m
Age: Pleistocene

Subunit IA spans the recovered uppermost 20.09 m of Unit I and is dominated by nannofossil-rich clay, nannofossil ooze, nannofossil ooze with biogenic silica, and clay-rich nannofossil ooze (Figures **F7**, **F9**). The color of the ooze gradually changes from dark greenish gray to greenish gray and gray. The ooze comprises calcareous nannofossils and foraminifers; siliceous diatoms; sponge spicules; radiolarians; and terrigenous grains, including clay minerals, rare quartz, and feldspar (Figure **F9**). The sediment is well sorted and unlithified. The average grain size is clay, and silt is the maximum grain size.

Bioturbation is moderate to heavy. Individual burrows are difficult to distinguish but are mostly horizontal with recognizable *Planolites, Thalassinoides*, and *Cylindrichnus concentricus*. Distinct intervals (368-U1504A-3H-3, 0–34 cm, and 3H-4, 107–122 cm) contain more silt, and thin silt laminations are often disrupted by bioturbation (interval 3H-3, 69–56 cm). Layering is contorted at the base of the subunit.

The base of Subunit IA is marked by both a color change from greenish gray to pale brown and light brown sediment in Subunit IB and by a lithologic change that reflects an increase in the percentage of foraminifers. This increase is also seen in the progressive increase in measured carbonate content from an average of ~20 wt% in Subunit IA to an average of ~50 wt% in Subunit IB (Figure **F32**). Starting from approximately 1 m above this boundary, there is an uphole increase in biogenic silica, including diatoms, sponge spicules, and radiolarians. Below this boundary, Subunit IA is barren of siliceous microfossils.

Subunit IB

Interval: 368-U1504A-6R-1, 9 cm, to 7R-3, 62 cm
Depth: 46.59–59.73 m
Age: middle Miocene

Subunit IB is 13.14 m thick and composed of light brown foraminifer-rich nannofossil ooze and pale brown nannofossil ooze with foraminifers (Figures **F7**, **F9**). The sediment is well sorted and unlithified. The average grain size is clay, and silt is the maximum grain size. Boundaries are horizontal or irregular. A contorted layer was observed in Section 368-U1504A-6R-4, 65–105 cm, possibly indicating intraformational slumping. Bioturbation is moderate to heavy.

The boundary between Subunits IB and IC is defined by a change from brownish foraminifer-rich nannofossil ooze (Subunit IB) to greenish nannofossil ooze with clay (Subunit IC).

Subunit IC

Interval: 368-U1504A-8R-1, 0 cm, to 12R-1, 19 cm
Depth: 65.80–104.99 m
Age: middle–early Miocene

Figure F6. A. Lithostratigraphic summary of Hole U1504A with simplified lithology and unit descriptions. B. Lithostratigraphic summary of Hole U1504B with simplified lithology and unit descriptions. (Continued on next page.)

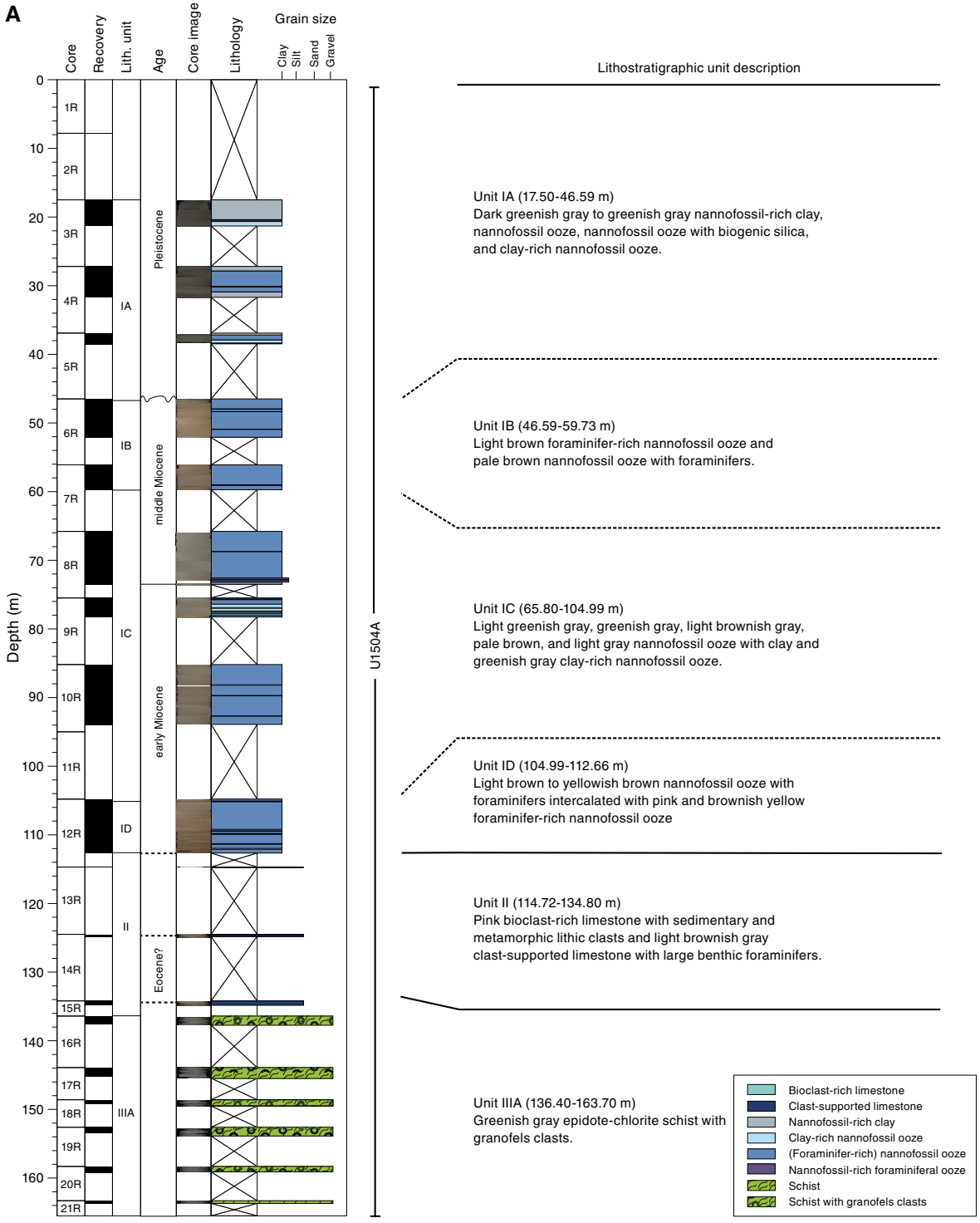

Subunit IC is 39.19 m thick and composed of light greenish gray, greenish gray, light brownish gray, pale brown, and light gray nannofossil ooze with clay and greenish gray clay-rich nannofossil ooze (Figures **F7**, **F9**). These lithologies are intercalated with light gray nannofossil-rich foraminiferal ooze with clay, light brownish gray foraminifer-rich nannofossil ooze, and foraminifer-rich nannofossil ooze with clay. The sediment color is more brownish downhole in the subunit. The sediment is well sorted and slightly consolidated. The average grain size is clay, and very fine sand is the maximum grain size.

Figure F6 (continued).

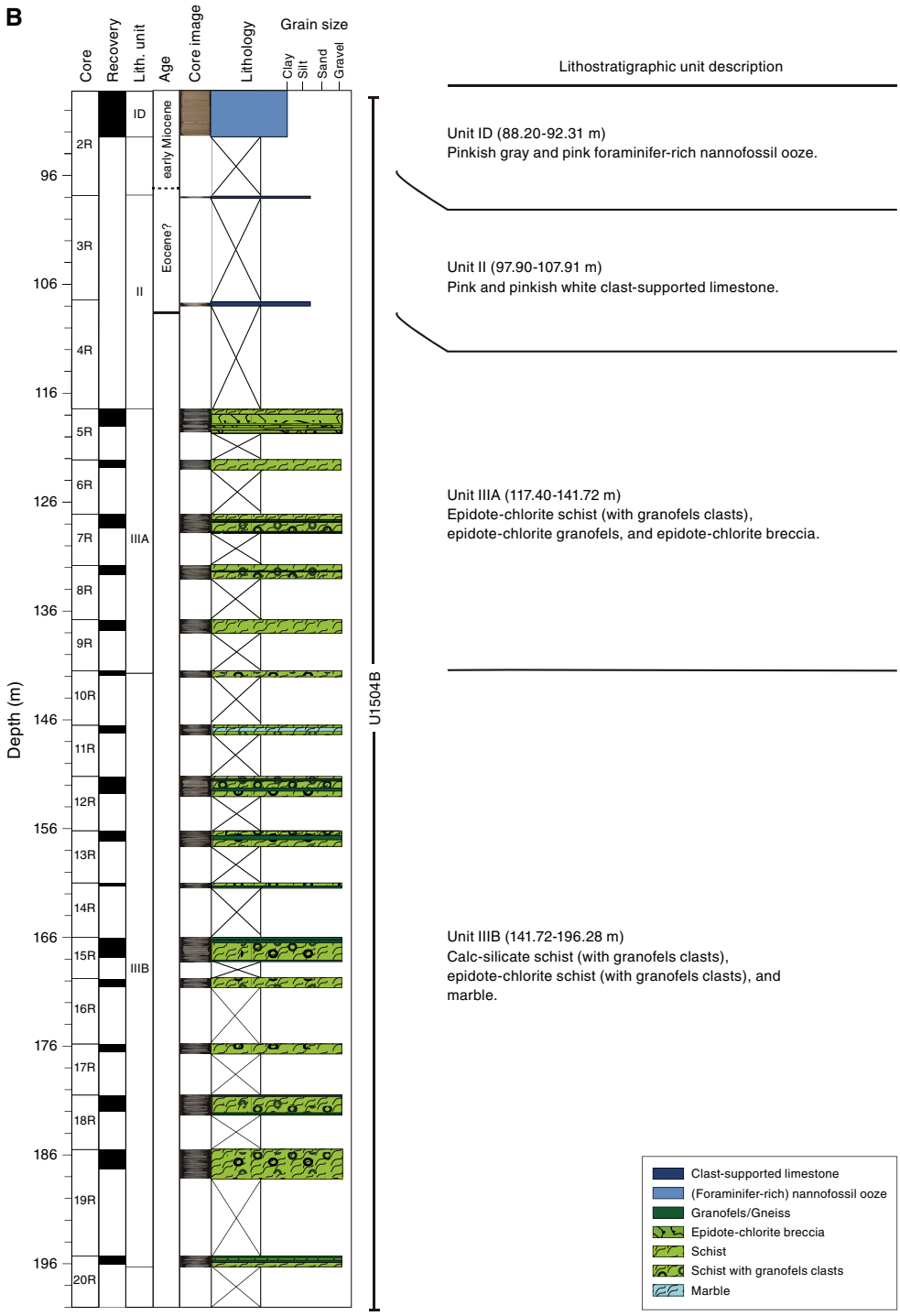

Contacts between layers are normally planar and subhorizontal. The bioturbation in Subunit IC sediment is heavy. There are foraminifer-filled burrows, especially in the middle to upper portion of the subunit.

The boundary between Subunits IC and ID is characterized by a change in color from grayish to more brownish in Subunit ID (Figure F7).

Subunit ID

Intervals: 368-U1504A-12R-1, 19 cm, to 12R-CC, 18 cm; 368-U1504B-2R-1, 0 cm, to 2R-CC, 17 cm
Depths: Hole U1504A = 104.99–112.66 m; Hole U1504B = 88.20–92.31 m
Age: early Miocene

Figure F7. Representative images of core sections from Unit I. Subunit IA (4R-3) includes dark greenish gray nannofossil-rich ooze with biogenic silica (0–70 cm) and nannofossil-rich clay (70–139 cm). Subunit IB (6R-2) consists of pale and light brown nannofossil ooze with varying amounts of foraminifers. Subunit IC (8R-3 and 10R-3) is composed of greenish gray and pale brown nannofossil ooze with clay. Subunit ID (12R-3) contains light brown nannofossil ooze with foraminifers.

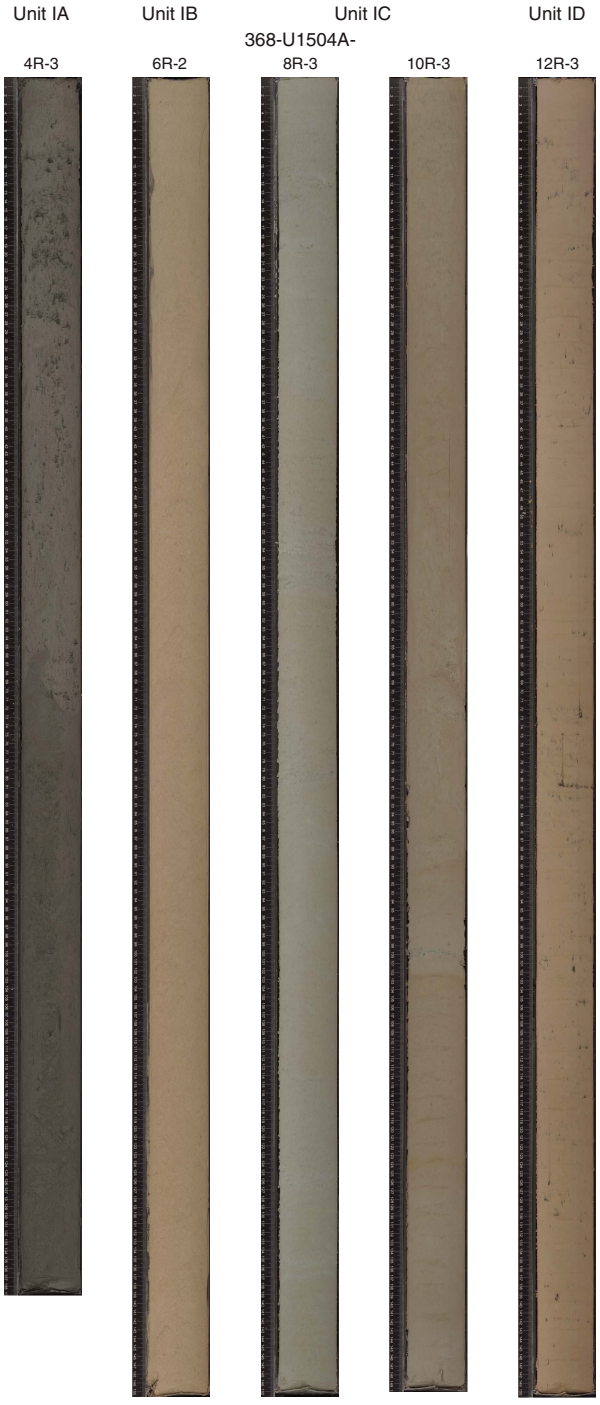

Table T2. Mineral percentages, Site U1504. **View table in PDF format. Download table in CSV format.**

Subunit ID is composed of light brown to yellowish brown nannofossil ooze with foraminifers intercalated with pink, pinkish gray, or brownish yellow foraminifer-rich nannofossil ooze (Figures **F7**, **F9**, **F10**). The nannofossil ooze is moderately consolidated and well sorted, with silt as the maximum grain size. Contacts are horizontal and planar. Millimeter-sized pyrite patches (burrows?) are developed on the core surface (Figure **F10**). There are two large (1–4 cm) pyrite nodules in Section 368-U1504A-12R-5. Pyritized burrows are found in Section 368-U1504B-2R-1.

Bioturbation is high throughout the subunit. The large circular to oval patches 1–4 cm in diameter in the lower portion of Subunit ID are identified as burrows.

The Subunit ID lithology is different from the that of the underlying Unit II. The contact with Unit II was not cored due to low core recovery across this boundary.

Unit II

Intervals: 368-U1504A-13R-CC, 0 cm, to 15R-1, 64 cm; 368-U1504B-3R-1, 0 cm, to 4R-1, 31 cm
Depths: Hole U1504A = 114.72–134.80 m; Hole U1504B = 97.90–107.91 m
Age: Eocene?

Lithology and sedimentary structures

In Hole U1504A, Unit II is 20.08 m thick, but only 1.04 m of sediment was recovered. The upper part of Unit II in Hole U1504A is composed of pink bioclast-rich limestone with clasts of sedimentary and metamorphic origin (interval 368-U1504A-13R-CC, 0 cm, to 14R-1, 12 cm). The lower part is light brownish gray clast-supported limestone with large benthic foraminifers and common epidote grains (Figures **F11**, **F12**). The clast-supported limestone is overall poorly sorted and dominated by coarse sand but also contains pebble-sized sedimentary and metamorphic clasts. Shell fragments (bivalves) and large benthic foraminifers (as large as 15 mm) are the main biogenic components. The benthic foraminifers were identified as predominantly *Nummulites* and *Assilina* species that give a possible Eocene or slightly younger age for this unit. Some clasts have Fe-Mn coatings (Figure **F11**).

In Hole U1504B, only 47 cm of white and pink limestone was recovered. The limestone is mainly composed of coral fragments, shell fragments, and coated grains. The rock has high porosity and little matrix.

The contact between Units II and III was not recovered.

Bulk mineralogy and chemistry

Compositional analyses of Unit II carbonates were made directly on the archive half of the core using the handheld pXRF (see **Igneous and metamorphic petrology** in the Expedition 367/368 methods chapter [Sun et al., 2018]) (Table **T3**). Four representative samples from Unit II and one black-coated clast were analyzed. The limestone has high CaO contents (38–48 wt%), SiO_2 contents of 6–19 wt%, and minor Fe_2O_3 (up to 7 wt%) and MgO (up to 4 wt%) abundances. Sr abundance varies between 183 and 402 ppm, and S abundance varies broadly from 148 to 11632 ppm. The analyses of the black-coated clast support the interpretation of an Fe-Mn coating with high Fe_2O_3 (~15 wt%) and MnO (~18 wt%) contents. The coating is enriched in trace elements like Ni (1604 ppm), V (1009 ppm), Cu (757 ppm), Sr (1111 ppm), Mo (491 ppm), and Pb (1103 ppm).

Figure F8. Bulk XRD mineralogy analysis data, Site U1504.

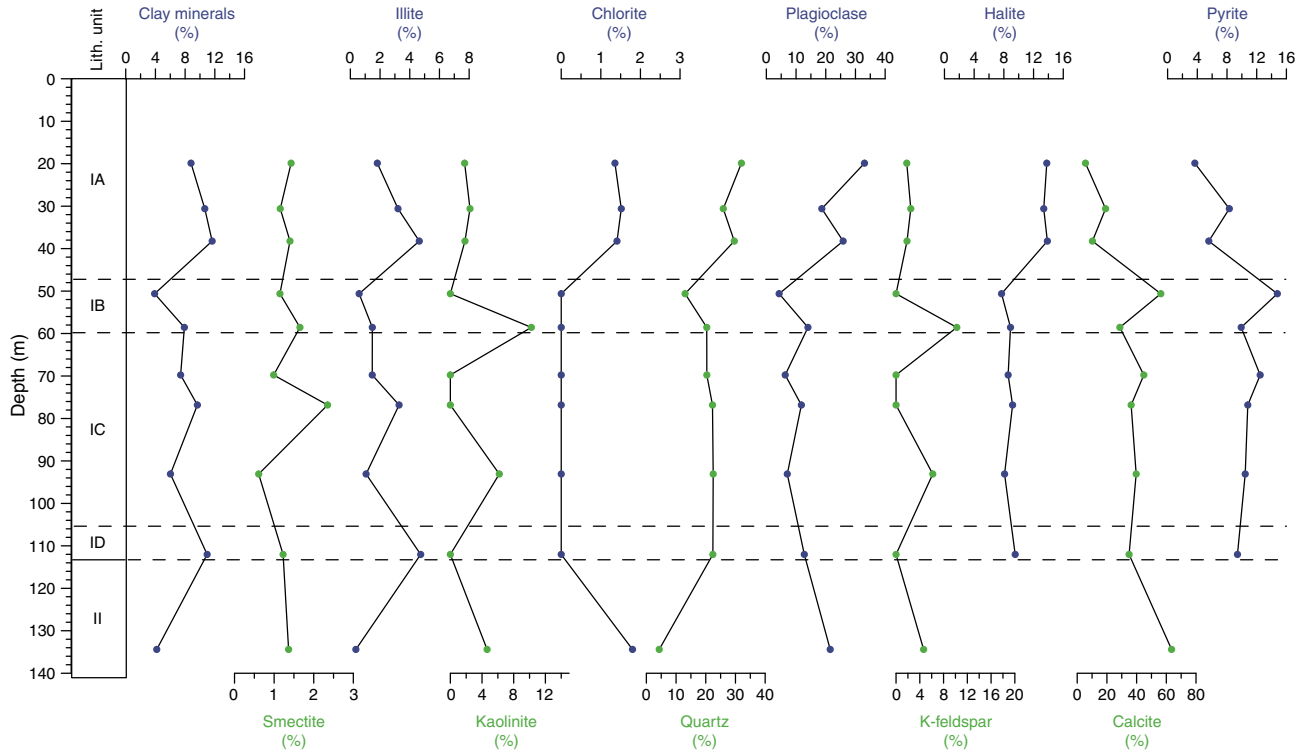

The bulk mineralogy results of XRD analyses are listed in Table T2. One XRD sample from Unit II indicates that the bulk mineralogy of the limestone is calcite (64%) and plagioclase (22%), with minor amounts of quartz, K-feldspar, and chlorite (Figure F8).

Unit III

Intervals: 368-U1504A-16R-1, 0 cm, to 21R-1, 40 cm; 368-U1504B-5R-1, 0 cm, to 20R-1, 98 cm
Depths: Hole U1504A = 136.40–163.70 m; Hole U1504B = 117.40–196.28 m
Age: unknown (older than Eocene?)

Unit III is 27.30 m thick in Hole U1504A and 78.69 m thick in Hole U1504B. The unit is divided into two subunits, IIIA and IIIB. Subunit IIIA is composed of greenish gray epidote-chlorite schist (with granofels clasts) and epidote-chlorite breccia, and Subunit IIIB is composed of calc-silicate schist (with granofels clasts), epidote-chlorite schist (with granofels clasts), and marble (see **Igneous and metamorphic petrology**). The schist contains angular, heavily veined granofels clasts. Brittle and ductile deformation structures were observed.

The fine- to coarse-grained rocks are fragmented due to drilling disturbance.

A more detailed macroscopic and microscopic description and interpretation of this unit is provided in **Igneous and metamorphic petrology**.

Discussion

Depositional environment of Unit I

Lithostratigraphic Unit I at Site U1504 was deposited in a deep-marine environment. The dominant lithology is nannofossil ooze with variable amounts of clay and foraminifers and minor foraminiferal ooze. The top subunit, IA, contains siliceous microfossils, including diatoms, radiolarians, and sponge spicules, except in the lowermost meter below a prominent, steeply inclined silty interval (368-U1504A-5R-1, 100 cm). Lithologic changes between subunits likely reflect variations in the amount of terrigenous input into a relatively open ocean setting, as well as changes in climate and oceanographic conditions. The terrigenous input may be delivered as buoyant plumes from shallower shelf environments. There is little change in the composition of the terrigenous grains, suggesting a common source area throughout Unit I. Thin laminae of silt are found rarely throughout Subunit IA. Some are graded, and all have sharp bases; however, many are disrupted by bioturbation and interpreted as distal turbidites.

Soft-sediment deformation in Subunits IA and IB, including inclined bedding and irregular sediment color boundaries, indicates slumping downslope of parts of the sequence. Bedding below this interval is consistently horizontal, indicating the deformation was synsedimentary.

Depositional environment of Unit II

The dominant lithologies in Unit II are bioclast-rich limestone and clast-supported limestone with large benthic foraminifers. The major skeletal clasts include coarse sand- to pebble-sized corals, large benthic foraminifers (e.g., *Nummulites* and *Assilina*), bivalves, and epidote (Figure F11). *Nummulites* are tropical, shallow-water foraminifers (Beavington-Penney and Racey, 2004). The combination of poorly sorted, subangular, sand- to pebble-sized bioclasts, metamorphic and sedimentary rocks, coral fragments, and large benthic foraminifers suggests deposition in a shallow marine environment. The lithic clasts were most likely derived from adjacent

Figure F9. A. Dark greenish gray nannofossil-rich ooze, Subunit IA. B. Greenish gray nannofossil ooze with foraminifers (red) (Subunit IA; 0–9 cm) and pale brown nannofossil ooze with foraminifers (green) (Subunit IB; 9–145 cm). C. Light brownish gray nannofossil ooze with clay (Subunit IC). D. Light brown nannofossil ooze with foraminifers (Subunit ID).

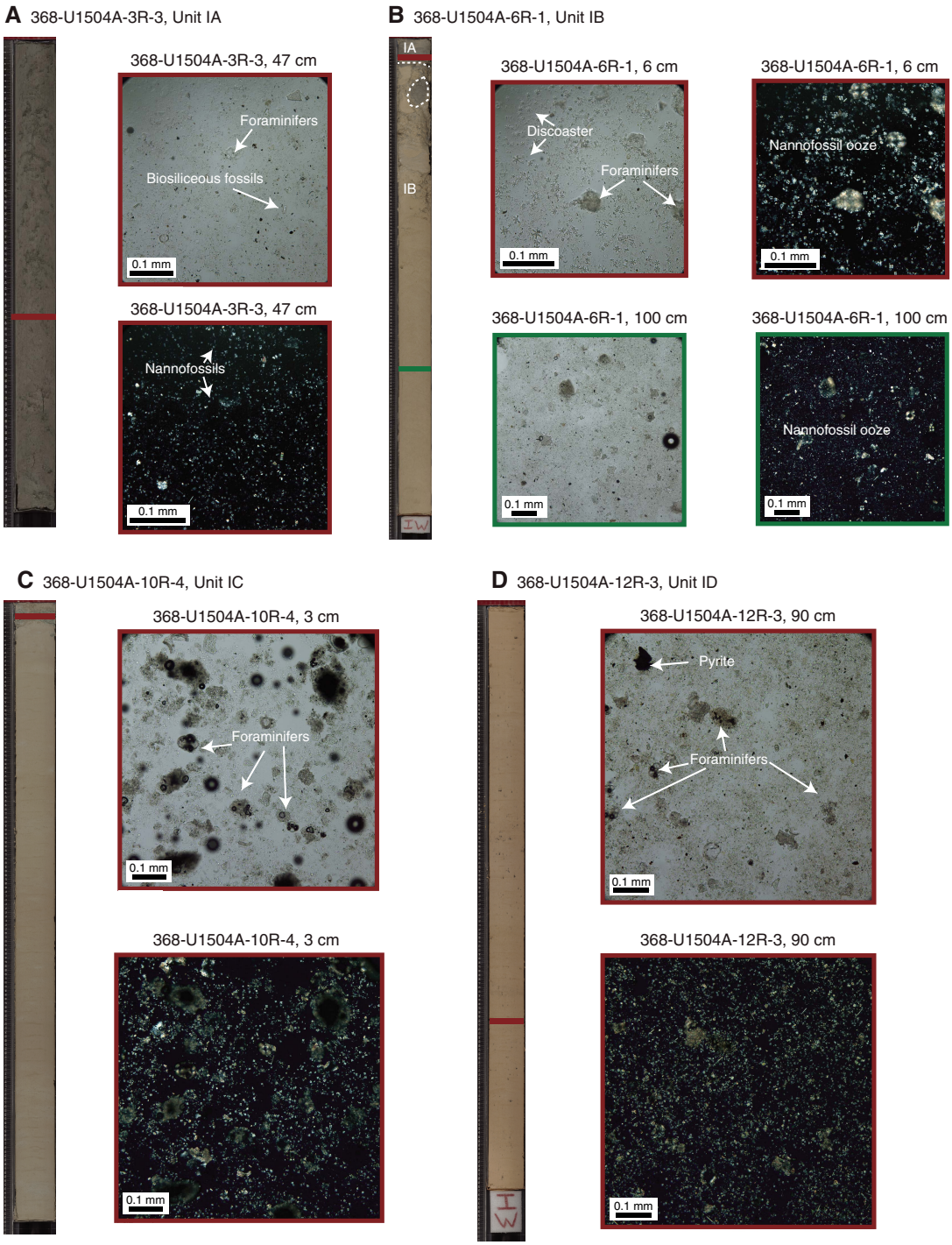

parts of the basement high. The Fe-Mn coating on some of the metamorphic and sedimentary clasts suggests there was a hiatus or reduction in the depositional rate following accumulation of the Unit II sediment. Manganese nodules were also recovered in the Miocene sequence of nearby IODP Site U1435 (Li et al., 2015). Manganese deposits form in sediment-starved settings (Cronan, 1980), which is consistent with the very low sedimentation rates (~0.5 cm/ky) at both Sites U1504 (see **Biostratigraphy**) and U1435.

Figure F10. Subunit ID. A. Brownish yellow layer with foraminifer-rich nannofossil ooze. B, C. Smear slide images of brownish yellow layer showing foraminifers and discoasters. D. Black pyrite nodule in yellowish brown foraminifer-rich nannofossil ooze. E. Smear slide image of pyrite nodule.

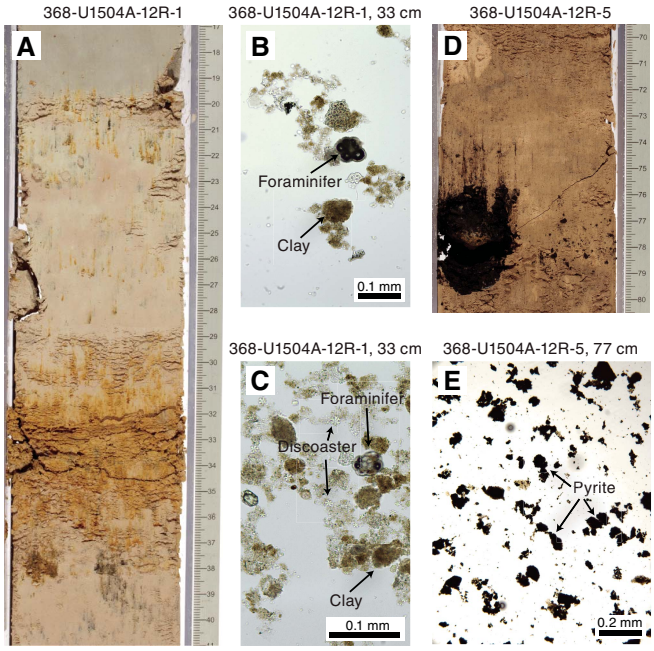

Figure F11. Unit II. A. Bioclast-rich and clast-supported limestone. Lithic clasts of metamorphic schist (13–24 cm). B. Lithic clasts with iron manganese coatings. C. Clast-supported limestone. D. Large benthic foraminifer in clast-supported limestone.

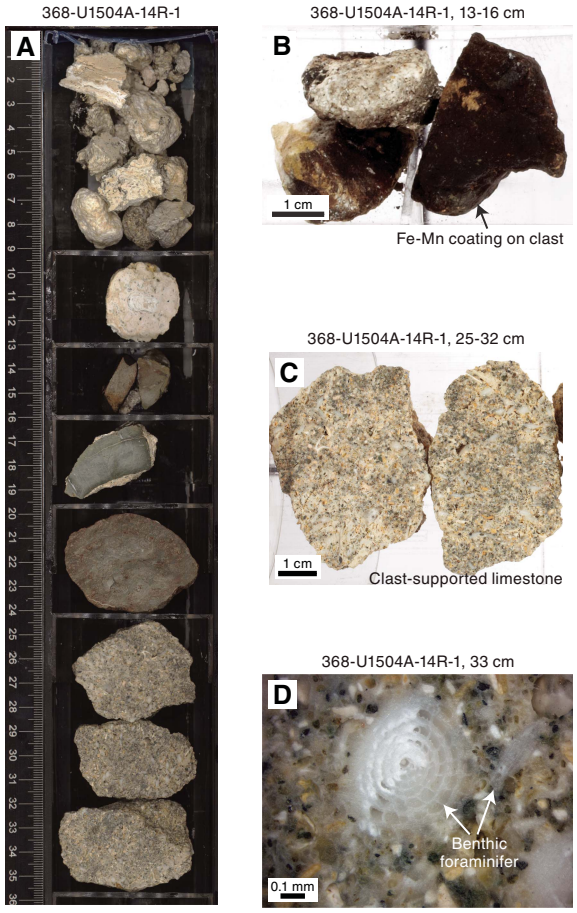

Preliminary correlation between Unit I subunits, Sites U1501 and U1504

Sites U1501 and U1504 are located 50.28 km apart on the OMH. Today's water depths are very similar at Sites U1501 and U1504 (2857 and 2816 m, respectively). The recovered Pleistocene to early Miocene/Oligocene sediment successions can be correlated based on their major lithologies and the age of deposition. We suggest a correlation between Pleistocene Subunit IA (Site U1504) and Pleistocene to Pliocene Subunits IA and IB (Site U1501), which are both dominated by dark greenish gray nannofossil-rich clay and clay-rich nannofossil ooze with siliceous microfossils. At Site U1504, a hiatus is apparent below Subunit IA (see **Biostratigraphy**). Middle Miocene Subunit IB (Site U1504) correlates well with late to middle Miocene Subunit IC (Site U1501). These subunits are both composed of greenish gray and light brownish gray nannofossil ooze with clay-rich and foraminifer-rich intervals. Middle Miocene Subunit IC (Site U1504) can be correlated to middle Miocene to Oligocene Subunits ID and IE (Site U1501). These subunits are characterized by greenish gray and gray nannofossil ooze with clay.

Figure F12. Limestone in Unit II (U1504A-15R-1, 21–23 cm [TS 55]). A, C, D. Large benthic foraminifers *Nummulites* (Num) and *Assilina* (Assi) and epidote (Ep) grains. B. Overview image. A: cross-polarized light (XPL); C, D: plane-polarized light (PPL).

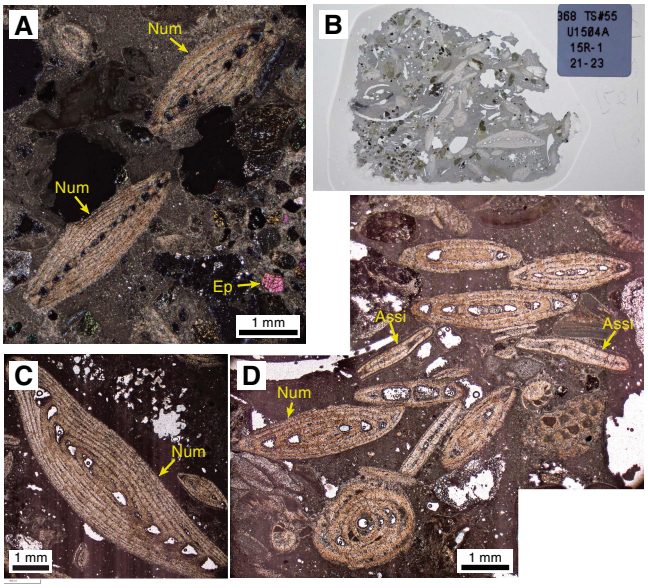

Table T3. Major element oxides and minor elements in rocks, Site U1504.
View table in PDF format. Download table in CSV format.

Igneous and metamorphic petrology

Metamorphic lithologic Unit 1

Intervals: 368-U1504A-16R-1, 0 cm, to 21R-1, 45 cm; 368-U1504B-5R-1, 0 cm, to 20R-1, 98 cm
Depths: Hole U1504A = 136.40–163.75 m; Hole U1504B = 117.40–196.28 m
Thickness: Hole U1504A = 27.35 m; Hole U1504B = 78.88 m
Lithology: epidote-chlorite schist with granofels clasts, epidote-chlorite breccia, calc-silicate schist with granofels clasts, chlorite granofels, epidote granofels, epidote-chlorite granofels, chlorite schist with epidote, epidote-chlorite gneiss clasts, and marble
Recovery: Hole U1504A = 19%; Hole U1504B = 21%
Age: unknown, older than late Eocene

Metamorphic lithologic Unit 1 (lithostratigraphic Unit III) (Figure **F13**) consists of a variety of metamorphic schistose rocks and granofels clasts. The clasts have variable lithologies but are generally termed granofels due to the lack of foliation. Weak foliation was observed locally in some clasts, but for the sake of simplicity and to mark the contrast with the schist, they were grouped with the unfoliated rocks and we applied the term granofels to those rocks as well. Lithologic changes were encountered with depth and also between the two holes (U1504A and U1504B). Recovery of Unit 1 was poor in both holes (averaging 18.5% and 21%, respectively), with only a limited number of coherent cores. Many of the recovered pieces are small and rounded and do not preserve their original orientation. Metamorphic lithologic Unit 1 is divided into two subunits based on a change in the metamorphic lithology. Subunit 1a was recovered in both Holes U1504A and U1504B and consists of epidote-chlorite schist with granofels clasts and epidote-chlorite breccia. Subunit 1b is defined from interval 368-U1504B-10R-1, 22 cm, through Core 20R and consists of an alternation of calc-silicate schist and epidote-chlorite schist with granofels clasts, epidote and/or chlorite granofels, chlorite schist with epidote, epidote-chlorite gneiss, and minor marble.

Metamorphic lithologic Subunit 1a

Intervals: 368-U1504A-16R-1, 0 cm, to 21R-1, 45 cm; 368-U1504B-5R-1, 0 cm, to 10R-1, 22 cm
Depths: Hole U1504A = 136.40–163.75 m; Hole U1504B = 117.40–141.72 m
Lithology: epidote-chlorite schist with granofels clasts and epidote-chlorite breccia

Hole U1504A

Subunit 1a in Hole U1504A is composed of strongly deformed greenish gray, fine- to medium-grained epidote-chlorite schist with granofels clasts (Figure **F14A**). This unit is generally characterized by a mylonitic foliation with a wide geometrical and textural spectrum that is further described in **Structural geology**. Throughout Cores 16R–21R, the macroscopic mineral assemblage is made up of quartz, epidote, chlorite, and microcrystalline plagioclase (albite?).

The schist contains about 10% angular to rounded granofels clasts as large as 6 cm. These clasts are composed of dark greenish gray fine-grained minerals crosscut by abundant quartz veins that show reddish alteration in a few cases (Figure **F14B**). Minor horizons possibly representing clasts and/or veins have a coarse-grained (0.5–1 cm), patchy texture of epidote, quartz, and most likely chlorite (Figure **F14C**). Several intervals in Core 17R have small cavities likely resulting from dissolution (Figure **F14D**).

Hole U1504B

Subunit 1a lithologies in Hole U1504B are generally similar to those in Hole U1504A and characterized by a greenish gray, microcrystalline to coarse-grained epidote-chlorite schist that contains dark greenish gray microcrystalline granofels clasts. The schist and granofels clasts have a comparable mineral assemblage that consists of epidote, chlorite, quartz, and potentially plagioclase ± other phyllosilicates and accessory minerals. Quartz does not usually form part of the original metamorphic assemblage of the granofels clasts but cuts them as veins. The steep (>50°) mylonitic foliation recorded in Hole U1504A was also observed in Hole U1504B, and the intensity of the deformation varies from moderate to strong (see **Structural geology**). However, Hole U1504B differs from Hole U1504A in several aspects. Isolated subhedral dark minerals can be observed locally within the epidote-chlorite schist (e.g., interval 5R-1, 117–124 cm; Figure **F15B**). Core 5R recovered epidote-chlorite breccia (Figure **F15A**) that is clast- to matrix-supported with angular, decimeter-sized clasts made of mainly quartz-veined granofels, although other lithologic varieties were also observed. The granofels clasts in the epidote-chlorite schist seem heterolithic. Notably, granofels clasts are more abundant in Hole U1504B; this finding is emphasized by the recovery of pieces (usually <10 cm) completely made up of such epidote-chlorite granofels clasts. These clasts have generally isotropic textures with only a weakly developed foliation and are either strongly veined as in Hole U1504A or devoid of macroscopic veining. Downhole, some clasts reveal more quartz or calcite veins and/or reddish alteration features (Cores 7R–9R).

Figure F13. Lithostratigraphic summary of metamorphic lithologic Unit 1 rocks showing recovered lithologies and their metamorphic division into Subunits 1a and 1b, Holes U1504A and U1504B.

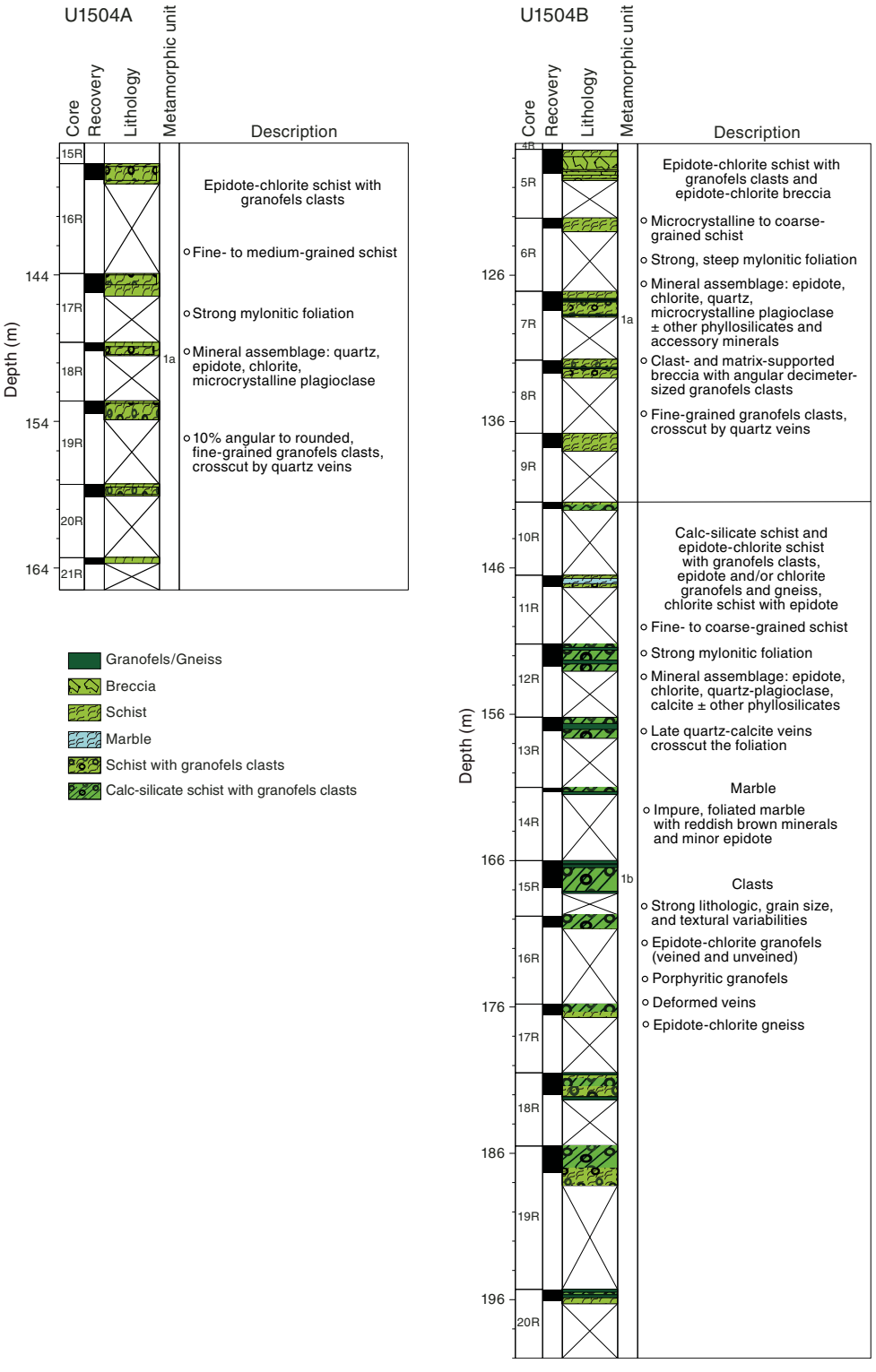

Microscopic observations

In thin sections, discontinuous, elongated, fine-grained (<100 μm), leucocratic aggregates and bands alternate with very fine grained assemblages of chlorite, epidote, phyllosilicates, and other finer grained minerals, together defining the foliation (Figure **F16A, F16B**). In detail, the leucocratic bands contain feldspar (plagioclase) and quartz with sparse, very fine grained epidote and other fine-grained minerals such as chlorite. The thickness of the leucocratic and chlorite bands is highly variable in individual samples, resulting in either a more felsic or a mafic overall appearance. Within these

Figure F14. Textural diversity in epidote-chlorite schists in Subunit 1a, Hole U1504A. A. Typical medium-grained epidote-chlorite schist. B. Severely quartz-veined angular clast of chlorite-epidote granofels within the schist matrix. C. Domain (clast or vein) formed by patchy epidote and quartz in a chlorite-rich matrix. D. Strongly foliated variety of the schist with abundant small cavities, likely resulting from dissolution.

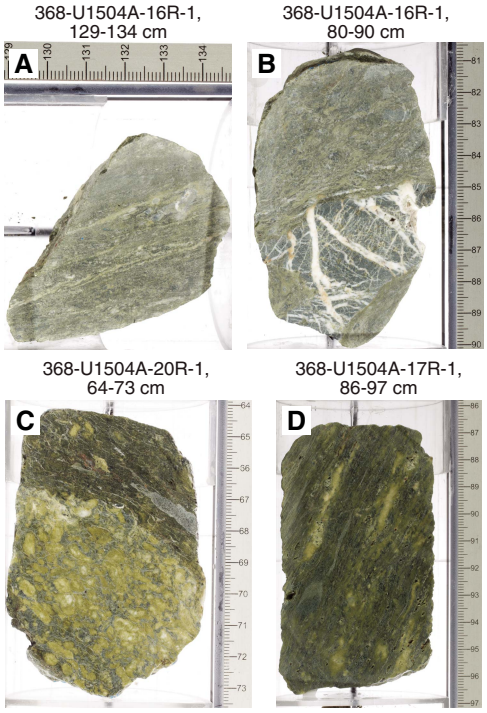

Figure F15. Lithologies in Subunits 1a and 1b, Hole U1504B. (A) Coarse-grained and (B) fine-grained variety of mafic granofels breccias. C. Foliated impure calcite marble. D. Typical calc-silicate schist with granofels clasts. Granofels clasts are mafic in nature, being highly phyric, possibly vesicular, and strongly altered. E. Deformed chlorite schist interpreted as a large "granofels" clast.

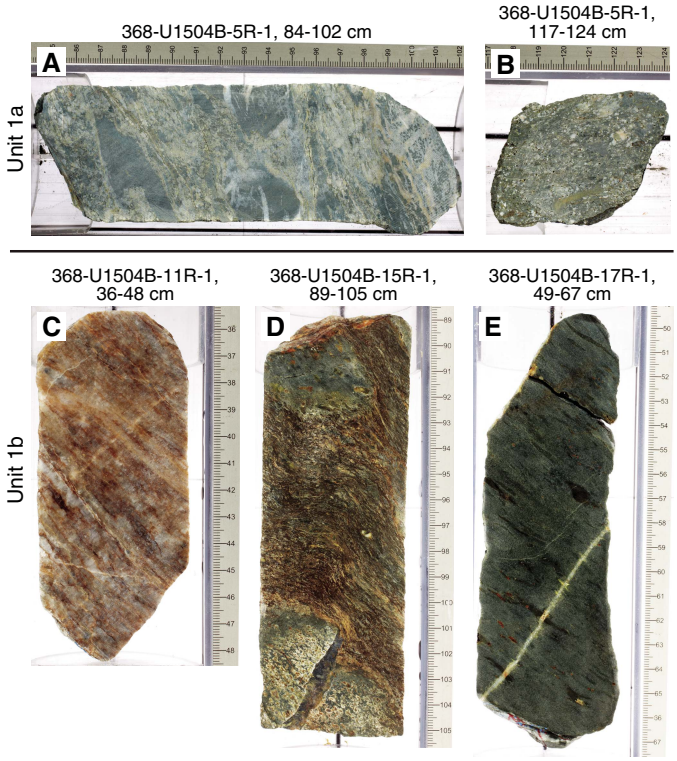

bands, coarser grained euhedral epidote as large as 0.3 mm is also abundant, recrystallizing locally into fine-grained mineral aggregates (Figure **F16B**).

The fine-grained veined clasts within the schist consist of microcrystalline chlorite and epidote with no relics or indicators of a protolithic mineral assemblage and are accordingly termed chlorite-epidote granofels (Figure **F16C**). Dynamically recrystallized quartz veins crosscut the granofels clasts (see **Structural geology** for detailed microstructural observations).

In Sections 368-U1504B-5R-1 and 5R-2, dark euhedral–subhedral minerals have characteristics that are consistent with clino- and possibly orthopyroxenes (Figure **F17**). Clinopyroxenes may be replaced by chlorite (possibly mixed with serpentine) or crosscut by calcite veins.

Metamorphic Subunit 1b

Interval: 368-U1504B-10R-1, 22 cm, to 20R-1, 98 cm
Depth: 141.72–196.28 m
Lithology: calc-silicate schist and epidote-chlorite schist with granofels clasts, epidote and/or chlorite granofels, epidote-chlorite gneiss, chlorite schist with epidote, marble

Subunit 1b is only found in Hole U1504B and is marked at interval 10R-1, 22 cm, by the appearance of calc-silicate schists with granofels clasts (Figure **F15D**) that alternate with the lithologies found in Subunit 1a. Two distinctive intervals were observed: (1) in interval 11R-1, 22–58 cm, an impure foliated marble with reddish brown minerals and minor epidote was identified within the schists (Figure **F15C**), and (2) in interval 17R-1, 38–92 cm, a locally foliated chlorite schist with epidote was recovered, but it is unclear whether this interval represents a clast (Figure **F15E**).

The calc-silicate and epidote-chlorite schists are fine to coarse grained with a mostly inequigranular texture. The schistose sections reveal strong mylonitic foliation (see **Structural geology**). The calc-silicate schists are characterized by the assemblage of epidote, quartz, chlorite, carbonate (e.g., calcite), and plagioclase (possibly albite). Several of the schists show reddish-brown alteration. Late quartz-calcite veins crosscut the foliation of some schists (e.g., in Core 20R).

Subunit 1b is characterized by strong lithologic, grain size, and textural diversity of the clasts embedded in the schist. The clasts are (1) microcrystalline to medium-grained epidote-chlorite granofels like those found in Subunit 1a, either with or without quartz and/or calcite veins (e.g., Figures **F14B**, **F18**); (2) porphyritic "granofels" with unknown tabular euhedral to subhedral phenocrysts (possibly altered plagioclase) and in some cases probable vesicles; (3) deformed (epidote, calcite and/or quartz) veins; and (4) epidote-chlorite gneiss. Most of these clasts are locally deformed and foliated according to the mylonitic deformation observed in the surrounding schist and show diffuse boundaries between the clasts and the surrounding schists.

Microscopic observations

Subunit 1b thin sections reveal the same metamorphic mineralogy as those of Subunit 1a and are dominated by feldspar-quartz, epidote, chlorite, calcite and phyllosilicate, and minor zeolites, ox-

Figure F16. Greenschist facies mineral assemblage and structural relationships of different minerals in epidote-chlorite schist, Subunit 1a. A. Alternating bands dominated by quartz and fine-grained chlorite + epidote, defining the foliation. B. Band dominated by chlorite and coarse-grained subhedral epidote. C. Clast of chlorite-epidote granofels with quartz veins.

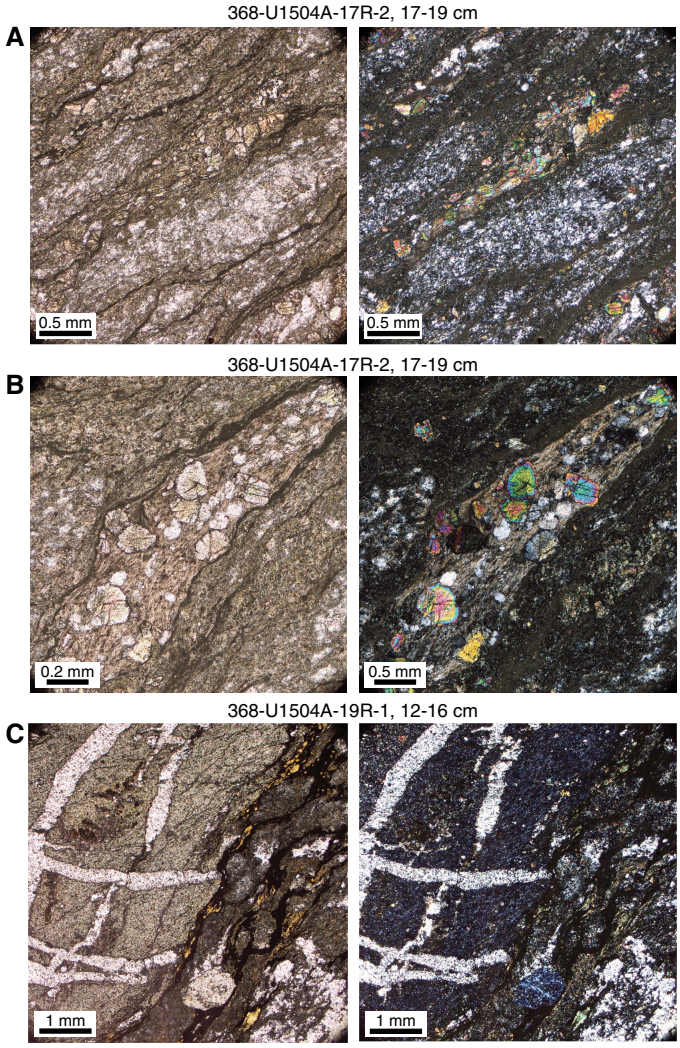

Figure F17. Greenschist facies mineral assemblage and textural variety in epidote-chlorite and calc-silicate schist in Subunits 1a and 1b, Hole U1504B. A. Epidote-chlorite schist with clinopyroxene crystal dissected by chlorite veins embedded in a matrix of quartz, albite, chlorite, and disseminated epidote. B. Calc-silicate schist with angular (upper half) and sigmoidally deformed (lower half) granofels clasts embedded in a poorly foliated matrix of quartz/albite, phyllosilicates, and epidote. Upper clast is cut by calcite-quartz vein. C. Microcrystalline chlorite schist with weaker foliation and rare large epidote grains.

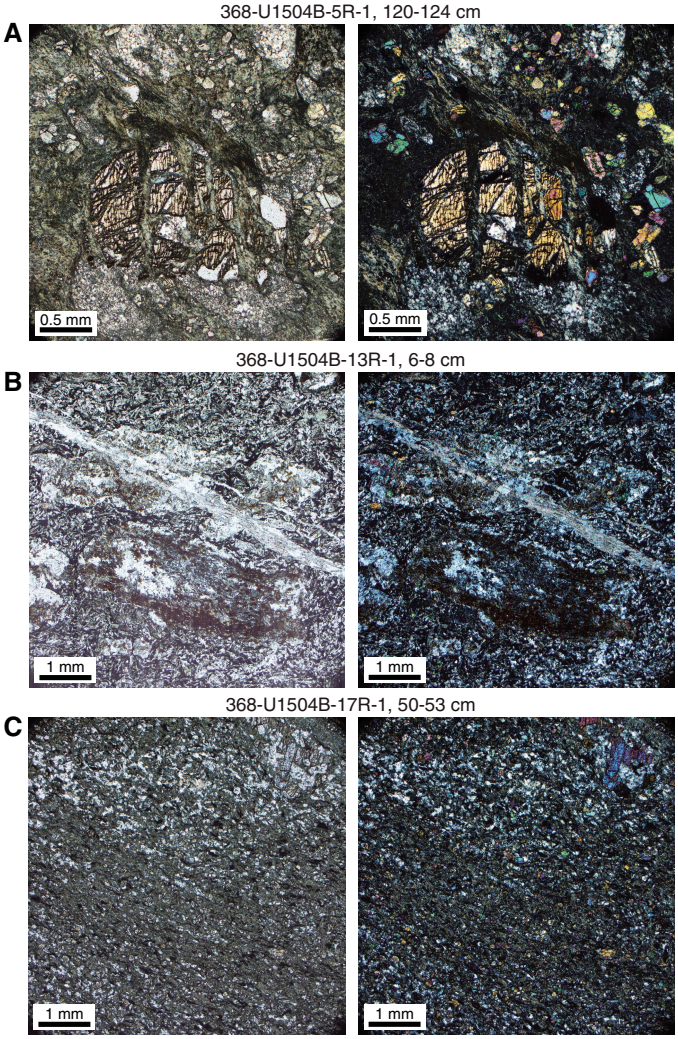

ides, and hydroxides (Figure F17). Based on three thin sections from Cores 368-U1504B-13R, 17R, and 19R, the amount of calcite is variable and may decrease downhole. Bands of phyllosilicate that alternate with commonly elongated and occasionally deformed lens-like aggregates and quartz-rich bands principally define the foliation. The aggregates can also consist of chlorite and some epidote ("epidosite"). Chlorite also occurs in bands and can have an intense brownish-yellow color. In some instances, chlorite (together with zeolite) has completely replaced mafic minerals. The origin of the aggregates or clasts is uncertain, although they seem to be heterolithic and may include various types of mafic igneous rock fragments (phyric or aphyric basalts? dike fragments?) and individual phenocrysts (potentially plagioclase). Epidote is disseminated throughout the matrix and often concentrated in veins, including those that dissect and disaggregate the leucocratic accumulations. The fine-grained chlorite schist with epidote in Core 19R has the same mineralogy and differs principally by its microcrystalline, largely homogeneous texture and the weaker foliation due to the sparseness of phyllosilicate bands, lending a leucocratic appearance.

Bulk mineralogy

XRD analyses of four metamorphic samples from different lithologies within metamorphic lithologic Unit 1 indicate that the bulk mineralogy is predominantly characterized by plagioclase (albite?) ± epidote ± chlorite ± quartz (Table T4). A Subunit 1a chlorite-epidote schist sample (368-U1504A-17R-2, 17–19 cm) contains plagioclase and chlorite. A Subunit 1b brown calc-silicate schist sample (368-U1504B-12R-2, 50–51 cm) contains plagioclase + calcite + epidote with trace amounts of chlorite and a clay mineral (illite-montmorillonite, smectite?). A gray granofels clast sample (368-U1504A-20R-1, 8–11 cm) contains plagioclase + epidote + dolomite

Figure F18. Granofels clasts enclosed in calc-silicate schists and epidote-chlorite schists in Subunit 1b, Hole U1504B. A. Veined and altered aphyric mafic granofels clast (left) and granofels clast interpreted as protolithic epidote vein (right). Both clasts are internally undeformed but show synkinematic deformation together with a mylonitic fabric at their rims. B. Highly phyric granofels clast, most likely of igneous origin, showing euhedral, probably replaced crystals and deformed epidote-calcite vein. C. Strongly deformed epidote chlorite gneiss interpreted as deformed "granofels" clast. D. Highly phyric igneous granofels clast with subhedral, probably replaced crystals. E. Slightly deformed phyric igneous granofels clast. F. Protolithic predominantly epidote vein forming a granofels clast.

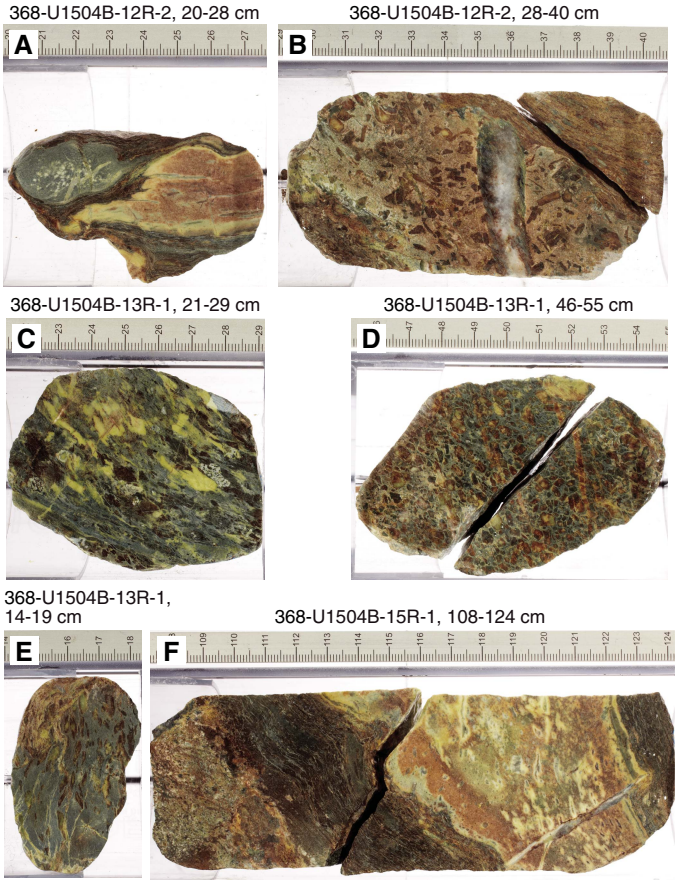

with trace amounts of chlorite. A crystal-rich granofels clast sample (368-U1504B-13R-1, 6–7 cm) contains plagioclase + chlorite with trace amounts of epidote, a clay mineral (illite-montmorillonite?), and mica.

Chemical composition

The handheld pXRF was used to determine the compositional characteristics of the diverse clast and schist lithologies seen in the metamorphic rocks of Unit 1 in Holes U1504A and U1504B. Analyses were made directly on the archive half of the core (see **Igneous and metamorphic petrology** in the Expedition 367/368 methods chapter [Sun et al., 2018]). A total of 149 representative samples from metamorphic lithologic Unit 1 and two metamorphic clasts from lithostratigraphic Unit II were analyzed (Figure **F19**; Table **T5**). The average pXRF sample spacing was ~20 cm within the recovered core material. Unit 1 rocks have a broadly mafic composition with the following contents: SiO_2 = 50 ± 3 wt%, MgO = 7 ± 3 wt%, Fe_2O_3 = 11 ± 4 wt%, Al_2O_3 = 16 ± 3 wt%, TiO_2 = 1.9 ± 0.7 wt%, and CaO = 9 ± 3 wt%. In detail, the Subunit 1a rocks in Hole U1504B tend to have lower Al_2O_3 and higher MgO, MnO, and Fe_2O_3 contents compared to those in Hole U1504A (Figure **F19A**). Furthermore, the schist matrix of Subunit 1a rocks in Hole U1504B, in general, has high S contents (mean = 0.6 wt%; range from below detection limit to almost 3 wt%) compared to the Subunit 1a schists in Hole U1504A (S = <0.25 wt%). In contrast, S is at or below the detection limit (<0.02 wt%) in all Subunit 1b samples.

Table T4. Mineral percentages, Site U1504. **View table in PDF format. Download table in CSV format.**

Within Hole U1504B, the schist matrix of the Subunit 1b rocks has lower MgO (5.5 ± 1.1 wt%) and Ni (20 ± 6 ppm) compared to the schist matrix of the overlying Subunit 1a rocks (MgO = 9.7 ± 2.1 wt%; Ni = 78 ± 40 ppm) (Figure **F19C**). In detail, Subunit 1b schists show a negative correlation between MgO and CaO (Figure **F19B**), with the brown foliated calc-silicate schists generally having higher CaO and lower MgO. Subunit 1b rocks are also typically more enriched in Zr relative to Ti (Figure **F19D**), which is seen in their lower Ti/Zr ratios (56 ± 22) compared to Subunit 1a rocks (85 ± 10).

The textural and mineralogical diversity of clasts within the schist is reflected in their chemical compositions (Figure **F19**). One lithologically distinctive group of clasts is the coarse-grained brown, dark-green, and yellow green clasts seen, for example, in intervals 368-U1504B-12R-2, 24–28 cm, and 15R-1, 116–122 cm (Figure **F18A, F18F**). These clasts are also compositionally distinct and have high Zr (390–1000 ppm), low TiO_2 (0.4–0.8 wt%), and low MgO (2–3 wt%) (Figure **F19**). Fine-grained gray granofels clasts ± white veins are common throughout Unit 1 (Figures **F14B**, **F15A, F15D**) and in general have compositional features similar to the surrounding schist material (Figure **F19**). In detail, there are some compositional differences between the granofels clasts in the different subunits and holes. The granofels clasts in Subunit 1a rocks in Hole U1504B have higher MgO and lower Al_2O_3 contents compared to those in Subunit 1a and 1b rocks in Holes U1504A and U1504B (Figure **F19A**). The Subunit 1b clasts in Hole U1504B have similar MgO concentrations to the Subunit 1a clasts in Hole U1504A, but they typically show higher MnO contents. A few of the Subunit 1a veined clasts in Hole U1504A have elevated Zr concentrations (as high as 500 ppm) relative to TiO_2 (Figure **F19D**).

Interpretation

Metamorphic lithologic Unit 1 consists of mylonitic, greenschist facies metamorphic rocks, as indicated by the presence of epidote and chlorite. The present mineral assemblage consists of epidote + chlorite + feldspar (plagioclase) ± quartz ± carbonate. The exact protolith of these rocks cannot be determined from the macroscopic and microscopic observations because of the strong and pervasive metamorphic overprint of the samples. We can infer that the protolith most likely was a breccia based on the different clast sizes and observed deformation styles. The pXRF and XRD data indicate a mafic igneous composition for both clasts and schists but reveal a spread from ultramafic (Subunit 1a in Hole U1504B) to more felsic (in Subunit 1b) compositions that are variable within sections and between holes at this site. However, it is unclear if this breccia with mafic clasts has a sedimentary origin (e.g., volcaniclastic) or represents an altered (potentially hydrothermally) form of a basalt, gabbro, or ultramafic protolith. Determination of the exact nature and origin of the clasts will require more detailed postexpedition research. The presence of marble layers is often used as an argument for a metasedimentary origin of a metamorphic sequence. However,

Figure F19. pXRF data showing compositional variations in metamorphic rocks of metamorphic lithologic Unit 1. A. MgO vs. Al_2O_3. B. MgO vs. CaO. C. MgO vs. Ni. D. TiO_2 vs. Zr.

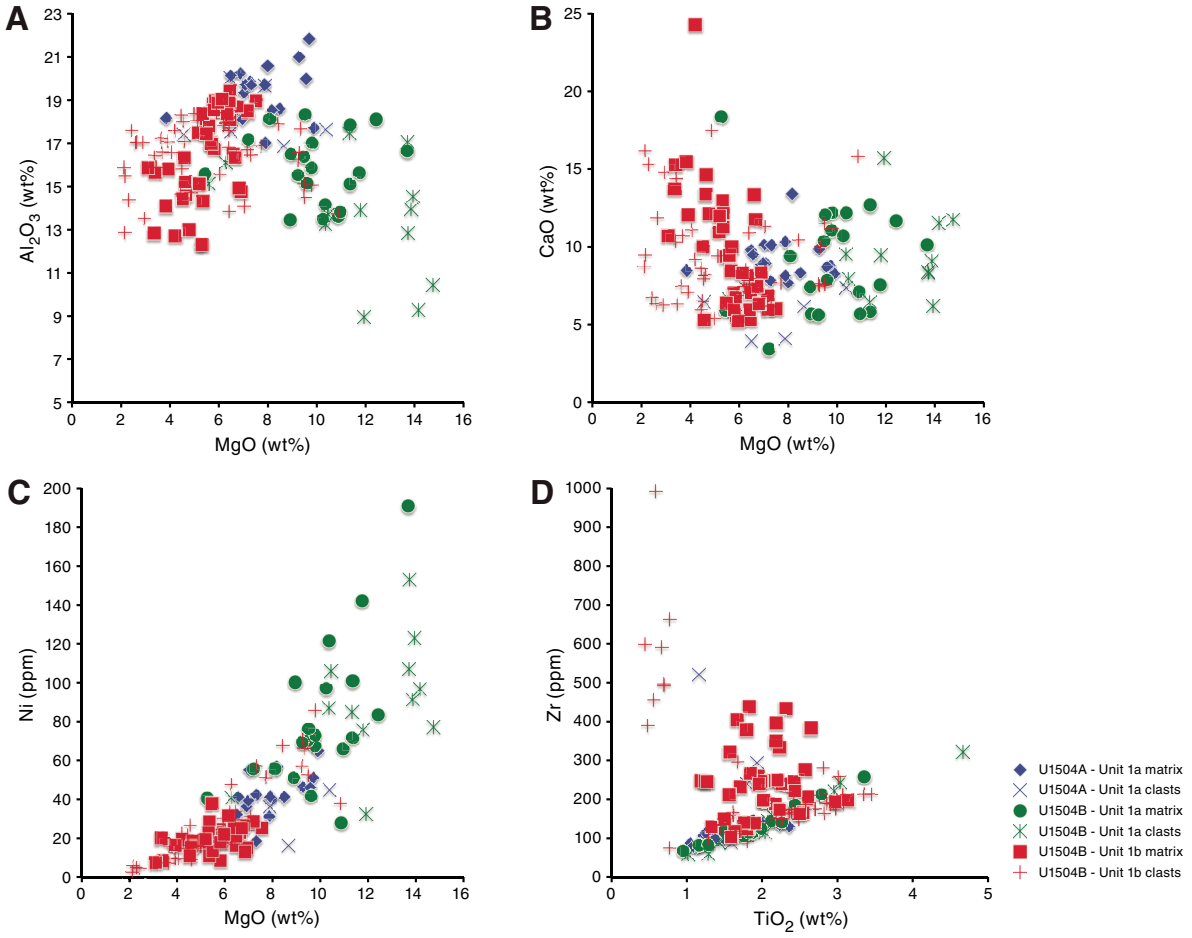

Table T5. Major element oxides and minor elements in rocks, Site U1504. **View table in PDF format. Download table in CSV format.**

the very localized occurrence of marble observed here, as well as its impure character, could also be explained by hydrothermal modification of the protolith. In this context, the calc-silicate schists, which have variable amounts of calcite, could also be consistent with a preexisting hydrothermal breccia matrix cemented by interaction with CO_2-rich fluids.

The timing of the metamorphism and its relation to the rifting of the SCS is uncertain. A key observation is that the observed mylonitic foliation is overlain by undeformed Eocene sediments from lithostratigraphic Unit II, which implies that the metamorphism is Eocene or older. Unit 1 could therefore represent an earlier metamorphosed part of the OMH and be a part of the prerift (continental) crust. Metamorphic basement rocks (schists and quartzites) have been recovered in industry wells in the western part of the offshore Pearl River Mouth Basin (Zhou and Yao, 2009) about 200 km west-northwest of Site U1504, where they are inferred to represent the offshore continuation of the early Paleozoic Caledonian fold belt in South China (Li et al., 1989). Metamorphic rocks are also found on the conjugate margin in the northern part of Palawan Island in the Philippines (e.g., Suggate et al., 2014). The Northern Palawan Continental Terrane contains upper Paleozoic to lower Mesozoic metasedimentary rocks (including schists; Sales et al., 1997) that experienced medium-grade regional metamorphism (Suzuki et al., 2000). Alternatively, the metamorphic event might have been related to the SCS rifting. Therefore, metamorphic lithologic Unit 1 might represent either metamorphosed continental crust (sedimentary) or metamorphosed basalts (see **Structural geology**). Detailed petrological and geochemical examination and accurate dating of the samples will be needed to address the metamorphic history of these rocks.

Structural geology

Site U1504 is located on a basement high ~45 km north of Site U1502 and 50 km east of Site U1501 in a water depth of 2827 m. This basement high may be interpreted as a continuation of the OMH cored at Sites U1501 and U1505.

Lithostratigraphic Unit I structures

Lithostratigraphic Unit I shows evidence for variable bedding dips, locally dipping steeply, associated with possible folds such as those observed in Section 368-U1504A-5R-1 (Figure **F20**). Such patterns are related to mass movements of unlithified sediments (i.e., slump folding).

Figure F20. Convolutely bedded sequence indicative of mass transport deposition in Subunit IA, Hole U1504A.



Lithostratigraphic Unit II structures

No deformation structures were observed within lithostratigraphic Unit II.

Lithostratigraphic Unit III structures

Macroscopic description

The mylonitic epidote-chlorite schists and calc-silicate schists that form the metamorphic basement at Site U1504 (see **Igneous and metamorphic petrology**) consist of epidote + chlorite + quartz + microcrystalline (plagioclase) feldspar ± calcite ± accessory minerals. The rocks preserve distinct deformation structures resulting from changes in the mode of deformation (brittle/ductile); the modal amount of quartz + feldspar governing the (local) rheological behavior; the amount of accumulated strain; the occurrence of variably sized (up to decimeter scale), prekinematic, heterolithic clasts that mostly form rigid (i.e., internally weakly to undeformed) bodies within the ductile foliation; and/or superimposed multiple deformation phases.

In Hole U1504A, measurements of the epidote-chlorite schist mylonitic foliation were often hampered by strong drilling disturbance and poor recovery. Therefore, measurements were only possible in the few continuous pieces recovered in Cores 368-U1504A-16R through 21R. These pieces show evidence for a steeply dipping foliation (as steep as 75°) (Figure **F21**). This mylonitic foliation is characterized by distinct morphologies: (1) a widely spaced anastomosing foliation associated with leucocratic bands (Figure **F22A**) and (2) a tight, closely spaced foliation associated with more melanocratic variations. Locally, a crenulation cleavage was observed (i.e., interval 368-U1504A-16R-1, 118–129 cm) (Figure **F22B**). Because of the combined effects of drilling disturbance and steeply inclined foliation, stretching or intersection lineations were only observed in a few rare cases.

Along this unit, angular to rounded chlorite-epidote granofels clasts (see **Igneous and metamorphic petrology**) are recognized and form rigid bodies within the ductile foliation (Figures **F20**, **F22**). Such clasts are consistently dismembered by a network of mostly parallel and perpendicular quartz veins cutting each other. They often form apparently stretched, elongated bodies oriented parallel to the foliation (Figure **F22A**). This veining is limited to the clasts and is absent from the epidote-chlorite schist. A folded epidote vein was observed within the epidote-chlorite schist in Section 368-U1504A-16R-1 (Figure **F22C**).

In Hole U1504B, more coherent pieces were recovered, allowing for a more representative record of foliation dips (Figure **F21**). Throughout Cores 5R through 16R, the mylonitic foliation shows predominantly steep dips >50°, and it tends to be shallower in Cores 17R through 20R, with dips clustering around ~30°–40°. In places, subvertical inclinations were encountered.

Deformation structures in Cores 5R through 9R, which represent lithostratigraphic Subunit IIIA (see **Igneous and metamorphic petrology**), are generally comparable to those encountered in Hole U1504A, which represent the same subunit. The prominent crenulation cleavage, especially, is a reoccurring feature (Figure **F23B**). Locally, epidote-chlorite schist split parallel to the *xy*-plane of finite strain shows sigma clasts and a shear band cutting across a granofels clast, both indicating a normal sense of shear synkinematic with the mylonitic foliation (Figure **F23A**).

Deformation in Subunit IIIB (Cores 368-U1504A-10R through 20R; see **Igneous and metamorphic petrology**) is presumably strongly controlled by an inherited (protolithic) brecciated structure. The characteristic feature of these mylonites is a tight microcrystalline to medium-grained foliation, locally folded, enclosing heterolithic clasts of various sizes up to the decimeter scale. The clasts most often form rigid, internally weakly to undeformed bodies showing isotropic textures with sharp boundaries with the enclosing foliation (Figure **F23D, F23E**). However, in some cases and especially at greater depths, the clasts tend to be ductily deformed and elongated within the mylonitic foliation (Figure **F23C**). These clasts often show diffuse clast boundaries, indicating mechanical and/or chemical clast-matrix interactions.

Another characteristic feature of Subunit IIIB is a general increase of various quartz, calcite, ± epidote veins that can be clearly distinguished between prekinematic (mostly epidote/quartz) veins that are ductily deformed together with the foliation (Figure **F23C,**

Figure F21. Corrected true dip angles of mylonitic foliation measured in metamorphic lithologic Unit 1/lithostratigraphic Unit III, Holes U1504A and U1504B. CRF = core reference frame.

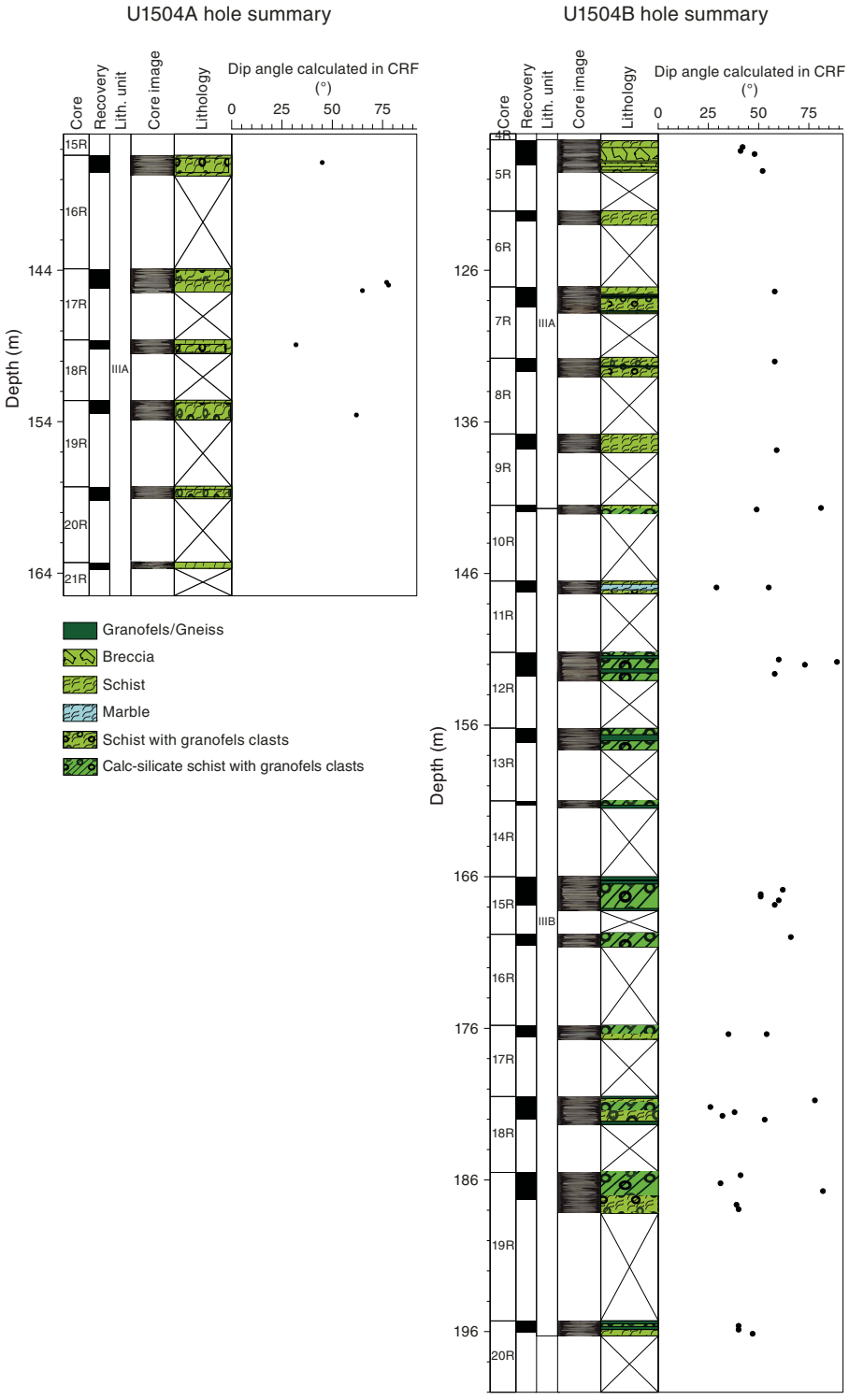

F23F) and late to postkinematic slightly deformed to undeformed (calcite) veins cutting the mylonitic foliation (Figure F23G).

Microscopic observations

In thin sections, the mylonitic fabric is defined by alternating bands dominated by fine-grained leucocratic (quartz ± cryptoplagioclase) and mostly chloritic aggregates. The leucocratic bands/aggregates form locally stretched sigma clasts and ductile boudins, whereas fine-grained quartz shows evidence for dynamic recrystallization through both bulging and subgrain rotation recrystallization (Figure F24B). In quartz- to feldspar-rich levels, an

Figure F22. Ductile deformation structures in epidote-chlorite schists in Subunit IIIA, Hole U1504A. A. Steep (~75°) widely anastomosing foliation in a quartz-rich variety of the rock. Arrow = extensively stretched veined clast of chlorite-epidote granofels, oriented parallel to the foliation. B. Tight foliation affected by crenulation cleavage in quartz-poor variety of the rock (top: core photo; bottom: interpretation). C. Folded epidote vein.

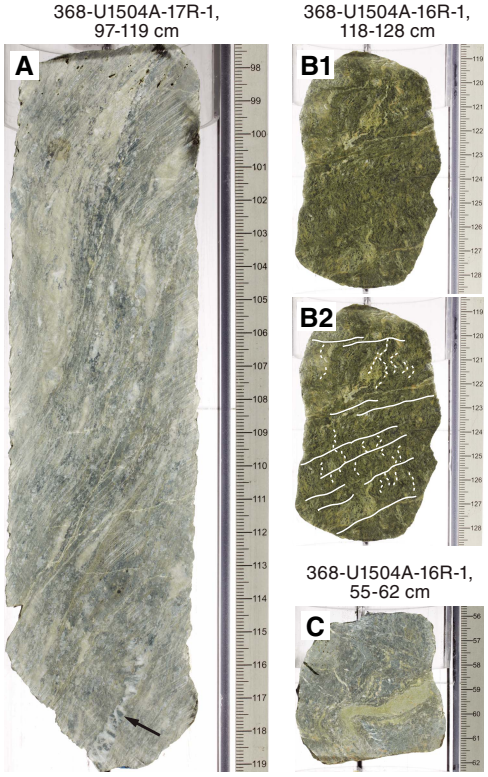

anastomosing foliation was locally observed. Some bands are recognized as highly deformed and extensively stretched former chlorite-epidote granofels clasts that partially preserve the original veining (Figure **F24A**). Chlorite is very fine grained and most probably accommodates a large amount of strain. Within the fine-grained chlorite-dominated bands, coarse-grained subhedral epidote with grain sizes as large as ~0.3 mm is commonly wrapped by the foliation and affected by brittle boudinage and brittle deformation, suggesting a prekinematic to early synkinematic crystallization with respect to the mylonitic foliation (Figure **F24C**). These boudinaged grains show a prismatic habitus and are aligned within the foliation, whereas other grains are strongly fractured. Locally, the coarse-grained subhedral epidote seems to partially recrystallize into fine-grained minerals and possibly into a second generation of epidote parallel to the foliation (Figure **F24D**). In more phyllosilicate rich levels, a seemingly pervasive crenulation cleavage is recognized (Figure **F24A**) that was also macroscopically visible in interval 368-U1504A-16R-1, 118–128 cm (Figure **F22B**).

Interpretation

The Cenozoic sediments encountered at Site U1504 are essentially devoid of deformation structures apart from Cores 368-U1504A-4R and 5R, which are characterized by a convoluted bedding sequence. The formation of this soft-sediment deformation structure most probably involved mass movements related to gravitational instabilities on a slope in close vicinity of the top of this basement-high.

Figure F23. Deformation structures, Hole U1504B. A. Epidote-chlorite schist with granofels clasts split parallel to the *xy*-plane of finite strain. Large granofels clast is crosscut by shear band within the epidote-chlorite schist. Several sigma clasts are observed right above the shear band. Both deformation structures indicate normal sense of shear. A late, postkinematic vein crosscuts both mylonitic foliation and granofels clast. B. Epidote-chlorite schist with crenulation cleavage. C. Long piece of core showing characteristic morphology of mylonitic foliation in calc-silicate schist, Subunit IIIB. Note steep inclination and anastomosing geometry enclosing heterolithic clasts that are strongly elongated, folded, and oriented parallel to the foliation. D, E. Rigid granofels clasts embedded in calc-silicate schist. Note deflection of the mylonitic foliation at the clast boundaries. F. Segmented and deformed composite epidote + quartz vein within the almost gneissose foliation of more leucocratic schist variation. G. Late kinematic (left) to postkinematic (i.e., undeformed; right) calcite veins crosscutting tight mylonitic foliation.

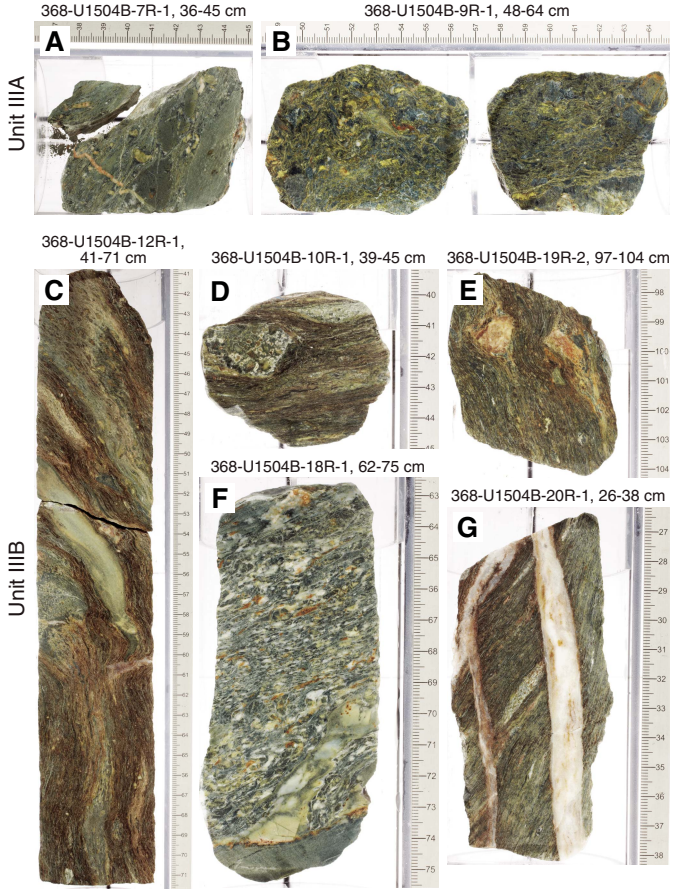

The metamorphic basement recovered at Site U1504 (lithostratigraphic Unit III) underwent a complex history of polyphase metamorphism and deformation. Formation of these rocks may have involved significant fluid-rock interactions that influenced both their chemical composition and rheological behavior.

The observed mylonitic fabric formed at greenschist facies conditions. The occurrence of a seemingly pervasive crenulation cleavage in macro- and microscopic observations on chlorite-rich samples may indicate either a reorientation of the local paleostress field during ongoing deformation or, alternatively, a polyphase structural evolution. A first brittle deformation phase is docu-

Figure F24. Metamorphic basement with focus on microstructural observations in metamorphic lithologic Unit 1/lithostratigraphic Unit III, Site U1504. Thin section domains are shown (left = PPL; right = XPL). A. Epidote-chlorite schist with minor modal quartz forming thin, discontinuous bands within foliation (black lines). Crenulation cleavage indicates a second deformation phase (white lines). Some quartz-rich aggregates are recognized as deformed chlorite-epidote granofels clasts preserving original veining. B. Sigma clast consisting of mainly quartz with minor chlorite and epidote probably representing deformed chlorite-epidote granofels clast preserving original veining. Sigma clast is synkinematic with respect to main mylonitic foliation and also affected by late crenulation cleavage. Tails of the sigma clast show clear evidence for subgrain rotation recrystallization. C. Prismatic, coarse, prekinematic epidote grain passively rotated into the foliation and underwent subsequent axial stretching and brittle boudinage. D. Coarse-grained epidotes showing irregular shapes, locally some crystals are observed to break down to fine-grained minerals.

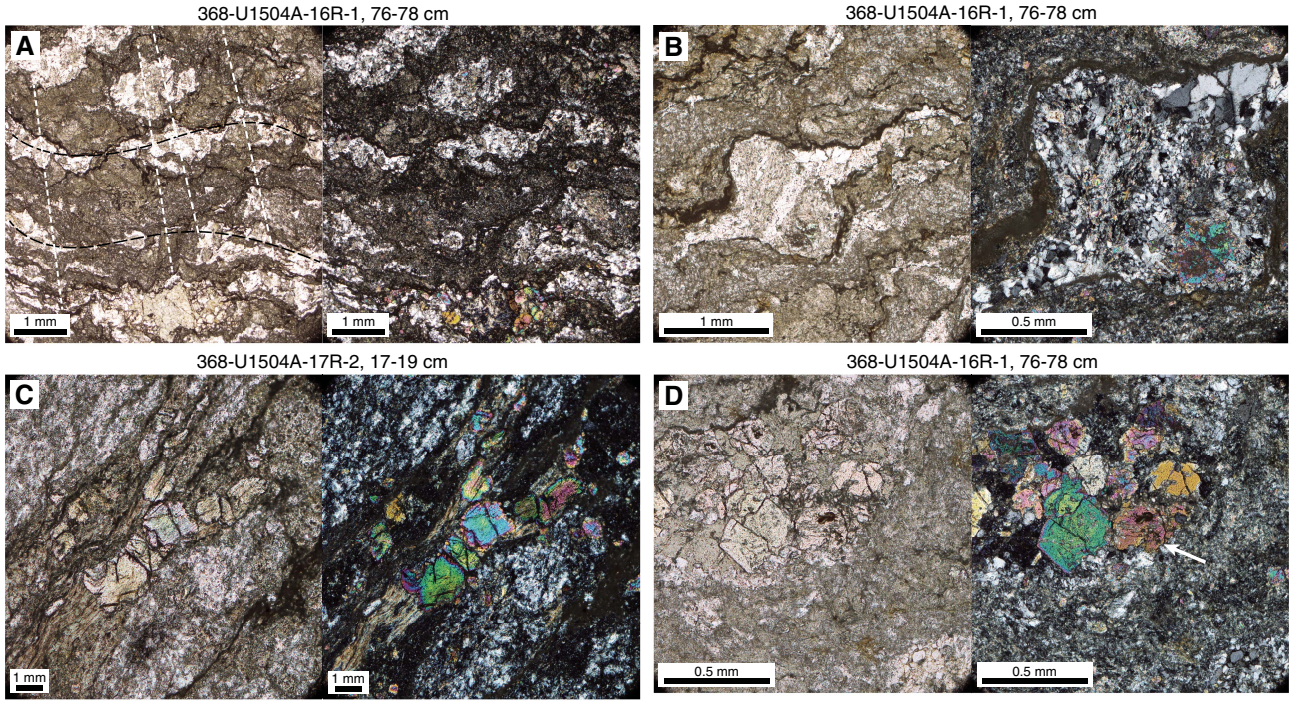

mented by the presence of strongly veined clasts, indicating possibly an early cataclastic and/or hydrothermal deformation episode, although the clasts themselves might also form part of a coarse (meta-) sedimentary protolith (e.g., a metamorphosed, volcaniclastic conglomerate/breccia). The veining episode apparently postdates a first metamorphic event because associated quartz veins clearly cut the chlorite-epidote granofels without any visible chemical interaction.

The origin of the encountered greenschist facies mylonites and their attribution to either SCS rifting or to Mesozoic or older tectonic events such as the Yenshanian orogeny (Hsieh, 1936) remains unknown at the moment, posing a challenging scientific question for postexpedition research (see **Igneous and metamorphic petrology**). Solving this question requires a determination of (1) the protolith of the rock, (2) its pressure-temperature (P-T) deformation history, and (3) accurate geochronological constraints. The present-day orientation of the mylonites with foliation dips as steep as 75°, however, seems too steep to represent a synrift, top-basement, low-angle detachment fault that may have exhumed deep crustal levels.

Biostratigraphy

All core catcher samples from Site U1504 were analyzed for calcareous nannofossils, foraminifers, and diatoms. Additional samples were taken from intervals within the working-half core sections when necessary to refine the ages. Preservation of calcareous microfossils is good to very good in Cores 368-U1504A-2R through 12R and Core 368-U1504B-2R and poorly preserved (recrystallization) deeper than Core 368-U1504A-12R, where reefal limestone was sampled. Diatoms were present but poorly preserved in Cores 368-U1504A-2R through 5R and absent from the rest of the samples (Table **T6**).

Table T6. Distribution of diatoms, Site U1504. **View table in PDF format. Download table in CSV format.**

Planktonic foraminifers and calcareous nannofossils are abundant in Cores 368-U1504A-2R through 12R and Core 368-U1504B-2R and barren in Cores 368-U1504A-13R through 15R. Twenty biostratigraphic datums were identified in a succession from the late Pleistocene to the early Miocene (Tables **T7**, **T8**; Figure **F25**).

A possible hiatus between the early Pleistocene and late Miocene was determined within Core 368-U1504A-6R by abrupt changes in the planktonic foraminiferal and nannofossil assemblages. Based on the site's biostratigraphy, sedimentation rates are estimated to vary from ~6 mm/ky in the early middle Miocene to ~22 mm/ky during the Pleistocene.

Cores 368-U1504A-13R through 15R are mainly composed of reefal and larger benthic foraminiferal limestone that indicates a warm shallow-marine environment. In contrast, the abundant planktonic foraminifers and calcareous nannofossils in Cores 2R through 12R suggest a deep-sea environment overlying the reefal rocks since the early Miocene.

Table T7. Calcareous nannofossil biostratigraphic events, Site U1504. O = occurrence, T = top/last appearance datum, B = bottom/first appearance datum. **Download table in CSV format.**

Epoch	Biozone (Martini, 1971)	Calcareous nannofossil event	Top		Bottom		Age model	
			Core, section, interval (cm)	Depth CSF-A (m)	Core, section, interval (cm)	Depth CSF-A (m)	Depth (m)	Age (Ma)
Pleistocene	NN21		368-U1504A-		368-U1504A-			
		B *Emiliania huxleyi*	3R-CC	21.35	4R-CC	31.75	26.55	0.29
	NN19	T *Pseudoemiliania lacunosa*	3R-CC	21.35	4R-CC	31.75	26.55	0.44
		B *Gephyrocapsa* spp. >4 µm	5R-CC	38.53	6R-1, 60–61	47.10	42.82	1.73
middle Miocene	NN6	T *Cyclicargolithus floridanus*	5R-CC	38.53	6R-1, 60–61	47.10	42.82	11.85
	NN5	T *Sphenolithus heteromorphus*	6R-CC	52.13	7R-CC	59.78	55.96	13.53
	NN4	T *Helicosphaera ampliaperta*	7R-CC	59.78	8R-CC	73.56	66.67	14.91
early Miocene	NN4	B *Sphenolithus heteromorphus*	9R-CC	78.31	10R-CC	93.96	86.14	17.71
	NN2	T *Triquetrorhabdulus carinatus*	9R-CC	78.31	10R-CC	93.96	86.14	18.28
		B *Sphenolithus belemnos*	12R-1, 3–5	104.85	12R-1, 40–42	105.22	105.04	19.03
		B *Helicosphaera ampliaperta*	12R-1, 3–5	104.85	12R-1, 40–42	105.22	105.04	20.43
		O *Sphenolithus disbelemnos*	12R-CC	112.66			112.66	<22.76

Table T8. Planktonic foraminifer events, Site U1504. T = top/last appearance datum, B = bottom/first appearance datum. **Download table in CSV format.**

Epoch	Biozone (Blow, 1969)	Calcareous nannofossil event	Top		Bottom		Age model	
			Core, section, interval (cm)	Depth CSF-A (m)	Core, section, interval (cm)	Depth CSF-A (m)	Depth (m)	Age (Ma)
			368-U1504A-		368-U1504A-			
	N22	T *Globigerinoides ruber* (pink)			2R-CC	7.85	3.93	0.12
Pleistocene	N22	B *Globigerinoides ruber* (pink)	4R-CC	31.75	5R-CC	38.53	35.14	1.16
	N20–N21	B *Globorotalia truncatulinoides*	5R-CC	38.53	6R-CC	52.13	45.33	1.93
	N12	T *Fohsella fohsi*	5R-CC	39.53	6R-CC	52.13	45.83	11.79
	N8	T *Praeorbulina circularis*	6R-CC	52.13	7R-CC	59.78	55.96	14.89
Miocene	N8	B *Praeorbulina glomerosa*	9R-CC	78.31	10R-CC	93.96	86.14	16.27
	N6	T *Catapsydrax dissimilis*	9R-CC	78.31	10R-CC	93.96	86.14	17.54
	N5	T *Globoquadrina binaiensis*	12R-1, 3–5	93.96	12R-1, 40–42	105.22	99.59	19.09
	N4	T *Paragloborotalia kugleri*	12R-1, 40–42	105.22	12R-CC	112.61	108.92	21.12

Calcareous nannofossils

The calcareous nannofossil biostratigraphy for Site U1504 is based mainly on the analysis of all core catcher samples from Hole U1504A (Table **T9**). To better constrain biostratigraphic events, a number of samples from intervals within cores were analyzed.

Calcareous nannofossils are very abundant and well preserved in the upper part of the succession (Cores 2R through 12R; 7.85–112.66 m) and become barren from Sample 13R-CC (114.8 m) to the bottom of Hole U1504A. Reworking is common in samples from the Pleistocene, and overgrowth is common in those from early Miocene.

Eleven nannofossil biostratigraphic datums were recognized in the early Miocene through Pleistocene sediment sequence at Site U1504 (Table **T7**). The Pliocene and late Miocene nannofossil Zones NN18 through NN7 are missing in Hole U1504A, but some specimens of those periods, such as *Discoaster brouweri, Discoaster pentaradiatus, Discoaster quinqueramus, Discoaster berggrenii, Reticulofenestra pseudoumbilicus*, and *Sphenolithus* spp., were observed in the Pleistocene samples. The oldest nannofossil event identified at Site U1504 is the occurrence of *Sphenolithus disbelemnos* (its first occurrence datum [FAD] dates to 22.76 Ma), which was observed in the lowermost nannofossil-bearing sample at 112.66 m, indicating an early Miocene age of <22.76 Ma.

Pleistocene

The top of Hole U1504A (Samples 2R-CC to 5R-CC; 7.85–38.53 m) is dated as late Pleistocene based on the presence of *Emiliania huxleyi* (marker species for Zone NN21). The last occurrence datum (LAD) of *Pseudoemiliania lacunosa* in Sample 4R-CC (31.75 m) defines the top of Zone NN19. Zone NN19 is further divided by the FAD of medium *Gephyrocapsa* spp. (>4 µm) in Sample 5R-CC (38.53 m).

Middle to early Miocene

Three events were observed in the middle Miocene strata of Hole U1504A. The top of Zone NN6 is marked by the LAD of *Cyclicargolithus floridanus* (11.85 Ma) in Sample 6R-1, 60–61 cm (47.1 m). The top of Zone NN5 is defined by the LAD of *Sphenolithus heteromorphus* (13.53 Ma) in Sample 7R-CC (59.78 m). The top of Zone NN4 is defined by the LAD of *Helicosphaera ampliaperta* (14.91 Ma) in Sample 8R-CC (73.56 m). The middle/early Miocene boundary is assigned between Samples 8R-CC (73.56 m) and 9R-CC (78.31 m).

Three events were observed in the early Miocene strata of Hole U1504A. The top of Zone NN2 is marked by the LAD of *Triquetrorhabdulus carinatus* (18.28 Ma) in Sample 10R-CC (93.96 m). The FADs of *Sphenolithus belemnos* (19.03 Ma) and *H. ampliaperta* (20.43 Ma) apparently co-occur in Sample 12R-1, 3–5 cm (104.85 m). The occurrence of *S. disbelemnos* (its FAD dated to 22.76 Ma) was observed in Sample 12R-CC (112.66 m), which lies immediately above the nannofossil-barren interval that extends down to the bottom of this hole, indicating an age younger than 22.76 Ma at this depth.

The sole sediment core catcher sample above a coral reef limestone in Hole U1504B (2R-CC; 92.37 m) yielded a nannofossil as-

Figure F25. Age-depth model, Site U1504. Plotted event data are in Tables T7 and T8.

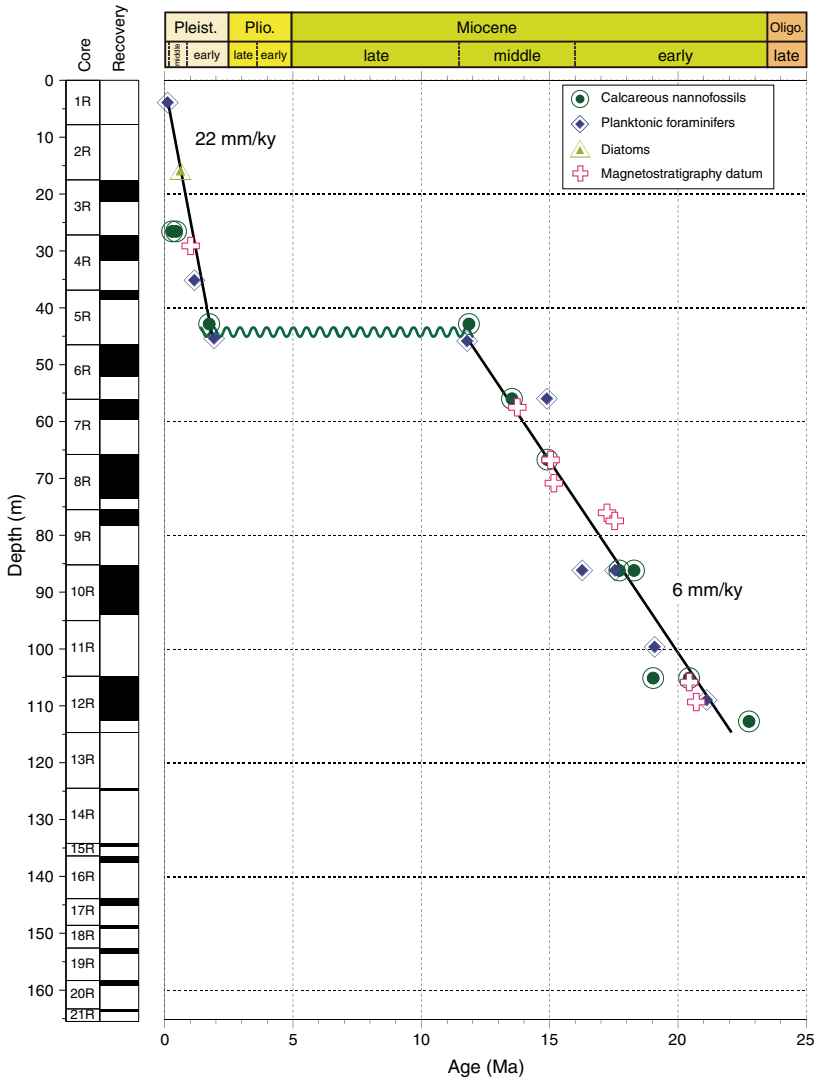

Table T9. Distribution of calcareous nannofossils, Site U1504. **View table in PDF format. Download table in CSV format.**

Table T10. Distribution of planktonic foraminifers, Site U1504. **View table in PDF format. Download table in CSV format.**

semblage similar to that of Sample 368-U1504A-12R-CC. An age of 20.43–22.76 Ma was assigned to this depth based on the occurrence of *S. disbelemnos* and the absence of *H. ampliaperta*.

Planktonic foraminifers

All core catcher samples and two additional samples from the working-half cores from Holes U1504A and U1504B were processed for planktonic foraminiferal analyses (Table **T10**). Planktonic foraminifers are well preserved and abundant in samples from Cores 368-U1504A-2R through 12R and Core 368-U1504B-2R and barren in Cores 368-U1504A-13R through 15R.

Nine planktonic foraminiferal datums were recognized in Hole U1504A, spanning from the early Miocene (>21.12 Ma) to the late Pleistocene (Table **T8**). The planktonic foraminiferal biostratigraphy for Hole U1504A was established based on these events and the planktonic foraminiferal assemblages at successive depth intervals.

The Pleistocene planktonic foraminifers are composed of *Globigerinoides ruber, Globigerinoides sacculifer, Globigerinoides conglobatus, Globorotalia menardii, Pulleniatina obliquiloculata, Neogloboquadrina dutertrei*, and *Orbulina universa*. The LAD of pink *G. ruber* (0.12 Ma) and the FAD of pink *G. ruber* (1.16 Ma) are placed within Sample 2R-CC and between Samples 4R-CC and 5R-CC, respectively. The FAD of *Globigerinoides truncatulinoides* (1.93 Ma) is located between Samples 5R-CC and 6R-CC. However, no Pliocene or late Miocene planktonic foraminiferal datum was recognized due to the distinct faunal changes between Samples 5R-CC and 6R-CC from the middle Miocene assemblage to the Pleistocene assemblage. The middle Miocene foraminiferal assemblages are dominated by *Dentoglobigerina altispira, Globoquadrina dehiscens, Globoquadrina venezuelana, Globoquadrina baroemoenensis,* and *Praeorbulina circularis*/*glomerosa*. The LAD of *Fohsella fohsi* (11.79 Ma) is located between Samples 5R-CC and 6R-CC. The LAD of *P. circularis* (14.89 Ma) is located between Samples 6R-CC and 7R-CC and marks the boundary of Zones N8 and N7. Both the FAD of *P. glomerosa* (16.27 Ma) and the LAD of *Catapsydrax dissimilis* occur

Figure F26. Larger benthic foraminiferal fragments (*Nummulites* sp.; 368-U1504A-14R-CC).



Figure F27. Abundant larger benthic foraminifers (*Nummulites* sp. and *Assilina* sp.; 368-U1504A-15R-CC).

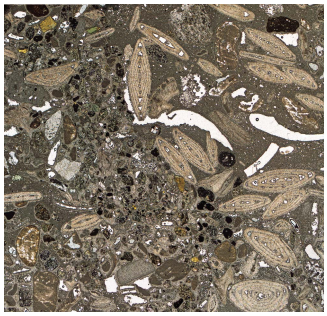

Table T11. Diatom event, Site U1504. T = top/last appearance datum. **Download table in CSV format.**

Epoch	Biozone (Scherer et al., 2007)	Calcareous nannofossil event	Bottom		Age model	
			Core, section	Depth CSF-A (m)	Depth (m)	Age (Ma)
Pleistocene	*Fragilariopsis doliolus*	T *Fragilariopsis reinholdii*	368-U1504A-4R-CC	31.75	31.75	<0.62

between Samples 9R-CC and 10R-CC, suggesting the middle/early Miocene boundary within Core 10R.

The early Miocene planktonic foraminifers are characterized by *G. dehiscens, G. venezuelana,* and *Paragloborotalia mayeri*. The LAD of *C. dissimilis* (17.54 Ma) is located between Samples 9R-CC and 10R-CC and indicates the boundary of Zones N7 and N6. The LAD of *Globoquadrina binaiensis* (19.09 Ma) is located between Samples 12R-1, 3–5 cm, and 12R-1, 40–42 cm. The LAD of *Paragloborotalia kugleri* (21.12 Ma) is located between Samples 12R-1, 40–42 cm, and 12R-CC and indicates the boundary of Zones N5 and N4.

In Hole U1504B, only one soft-sediment core was obtained above the coral reef limestone. The occurrence of *P. kugleri* and *G. dehiscens* in Sample 368-U1504B-2R-CC constrains the age between 21.12 and 22.44 Ma, which corresponds to the age of Sample 368-U1504A-12R-CC (Table **T8**).

Benthic foraminifers

Larger benthic foraminifers were observed in samples from Core 368-U1504A-14R (Figure **F26**) and Sample 15R-1, 21–23 cm (Figures **F12**, **F27**; see **Lithostratigraphy**), including *Nummulites* and other genera that indicate an Eocene or slightly younger age and a warm, shallow-marine environment.

Diatoms

All of the core catcher samples from Hole U1504A and one from U1504B were processed into smear and strewn slides for diatom analysis. Three additional toothpick samples were taken from selected intervals of the working-half cores for better resolution. Samples 368-U1504A-2R-CC, 3R-CC, and 4R-CC are composed of between 10% and 90% diatoms with poor preservation. The rest of the core catcher samples from Cores 5R through 12R were barren of diatoms (Table **T6**). Samples 2R-CC, 3R-CC, and 4R-CC contain a typical late Pleistocene (Table **T11**) tropical-subtropical diatom assemblage such as *Fragilariopsis doliolus* and *Nitzschia interruptestriata*. *Fragilariopsis reinholdii* (LAD = 0.62 Ma) was not observed in Sample 4R-CC, suggesting an age younger than 0.62 Ma.

Paleomagnetism

Shipboard measurements

Shipboard paleomagnetic investigations combined two complementary approaches (see **Paleomagnetism** in the Expedition 367/368 methods chapter [Sun et al., 2018]): (1) measurement and in-line AF demagnetization of archive-half sections on the pass-through 2G Enterprises SRM at 2.5 cm spacing and (2) measurement and AF demagnetization of oriented discrete samples on the spinner magnetometer (AGICO JR-6A). Thirteen representative discrete samples from sedimentary units and four from basement were collected for AF demagnetization.

We used scalar data from discrete samples from AF demagnetization up to 120 mT to assess the nature of the magnetic assemblage. We used the directional and intensity data of archive-half sections, measured after in-line AF demagnetization (up to 15 mT), to determine magnetic polarity along the core. Directional data were analyzed using Zijderveld diagrams (Zijderveld, 1967), and characteristic remanent magnetization (ChRM) direction(s) were calculated by principal component analysis (PCA) (Kirschvink, 1980) using PuffinPlot (version 1.03, April 23, 2015) (Lurcock and Wilson, 2012).

Demagnetization behavior and implications for magnetic assemblages

Sediment

Units: I and II
Depths: Hole U1504A = 17.50–134.80 m; Hole U1504B = 88.20–107.91 m
Sections 368-U1504A-3R-1 through 15R-1 and Cores 368-U1504B-2R through 4R

Most of the 13 discrete samples investigated show soft magnetic behavior characterized by loss of >50% of NRM below 20 mT (Figure **F28**). This low coercivity (soft behavior) justifies the steps chosen for in-line stepwise demagnetization (0, 5, 10, and 15 mT) on the SRM. Most discrete samples also display a gain in magnetization above 70 mT, up to 30% of the NRM, which is interpreted as resulting from GRM. Both greigite and pyrrhotite are known to display this behavior in marine sediments (e.g., Thompson, 1990; Roberts

Figure F28. AF demagnetization plots of (A) discrete samples and (B, C) archive-half sections of sedimentary rocks, Hole U1504A. Zijderveld plots: solid squares = declination, open squares = inclination. Stereographic plots: solid squares = positive (down) inclination, open squares = negative (up) inclination. Calculated ChRM (blue line; red squares = measurements used in calculation) using PCA is also shown. A. Soft demagnetization behavior up to 10 mT associated with removal of drilling overprint, followed by gradual demagnetization from 10 to 60 mT, characteristic of single-domain or pseudosingle-domain magnetite, and finally magnetization gain above 70 mT indicative of GRM, most likely due to greigite. B. Removal of drilling overprint in first step (5 mT). C. Soft demagnetization behavior and negative inclination of sample. MAD = maximum angular deviation.

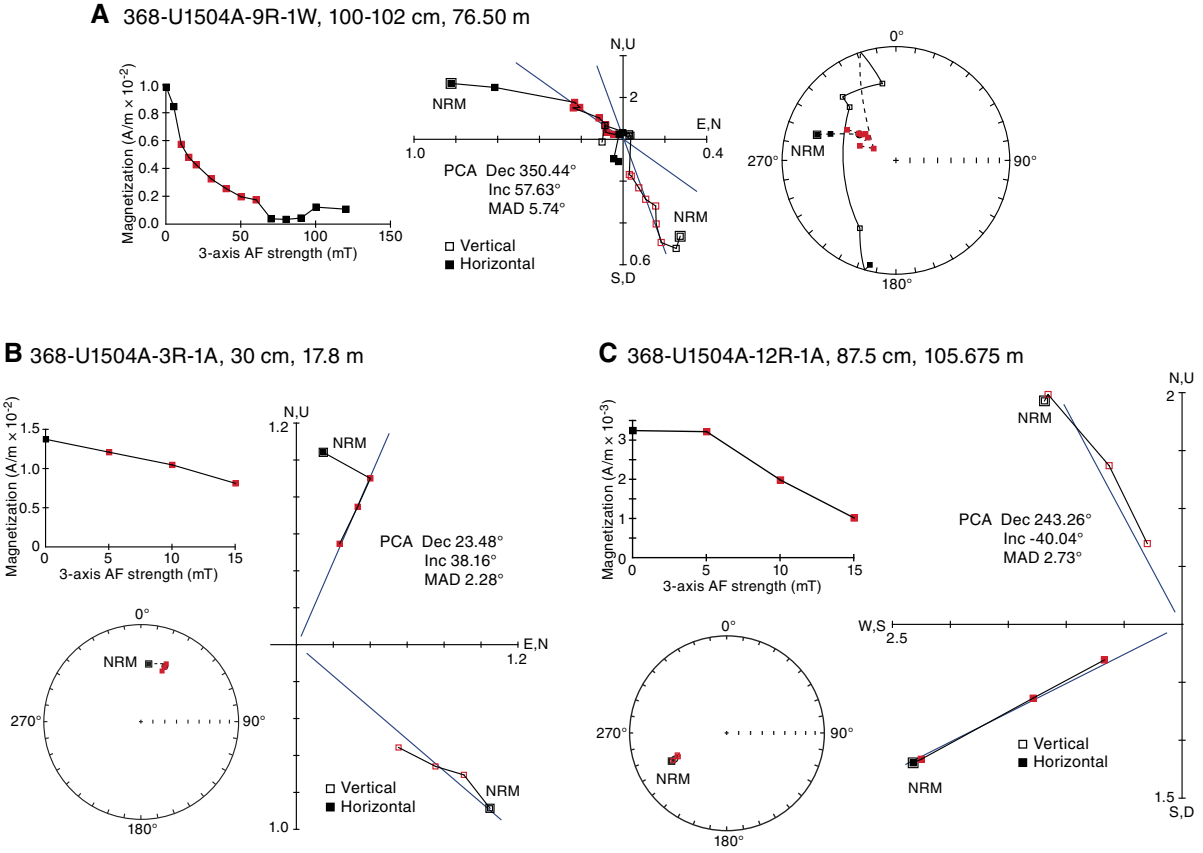

et al., 2011); however, greigite is more likely in shallow-marine sediments and has already been identified in lithostratigraphic Unit I in nearby Hole U1501C (see **Paleomagnetism** in the Site U1501 chapter [Larsen et al., 2018a]). Steep normal inclinations (≈60°) across all units suggest magnetic drilling overprint (Figure **F29**) that is easily removed by demagnetization to 10 mT (Figure **F28**). This behavior is consistent with the presence of a low-coercivity phase, such as relatively coarse grained titanomagnetite, in the sediments.

The core sections measured by in-line AF demagnetization on the SRM confirm the relatively soft demagnetization behavior observed on the discrete samples. Stepwise demagnetization up to 15 mT effectively removed the drilling overprint and allowed delineation of several reversals (Figure **F29**).

Basement rocks

Unit: III
Depths: Hole U1504A = 136.40–163.70 m; Hole U1504B = 117.40–196.28 m
Cores 368-U1504A-16R through 21R and 368-U1504B-5R through 20R

NRM intensities of basement rocks were measured on the SRM (archive-half Cores 368-U1504A-16R through 21R) and on the JR-6A spinner magnetometer (four discrete cubes, 8 cm^3 each). The intensities of magnetization are low (average = 78 × 10^{-6} A/m). Some of the discrete samples were not demagnetized because of their low NRM intensity (Figure **F29**), which requires measurements in a shielded laboratory.

Magnetostratigraphy

Inclination, declination, and intensity in Hole U1504A are reported in Figure **F29**. We constructed the magnetostratigraphy based on the polarity assigned to the archive-half cores, which was corroborated by directions obtained from oriented discrete samples. A succession of nine normal and eight reversed intervals was recognized. We tentatively correlated the magnetostratigraphic data in Hole U1504A to the standard timescale (Ogg et al., 2016) according to initial biostratigraphy age constraints reported in Table **T12** and Figure **F25**.

Anisotropy of magnetic susceptibility

Sediment

Units: I and II
Depth: Hole U1504A = 17.50–134.80 m
Cores 368-U1504A-3R-1 through 15R-1

Figure F29. Magnetic measurements, Hole U1504A. Inclination used to determine polarity. AFD = AF demagnetization. Magnetostratigraphic features are referred to as n1, etc., in a sequential manner for convenience and have no bearing on chrons. GPTS2016 = geomagnetic polarity timescale of Ogg et al. (2016).

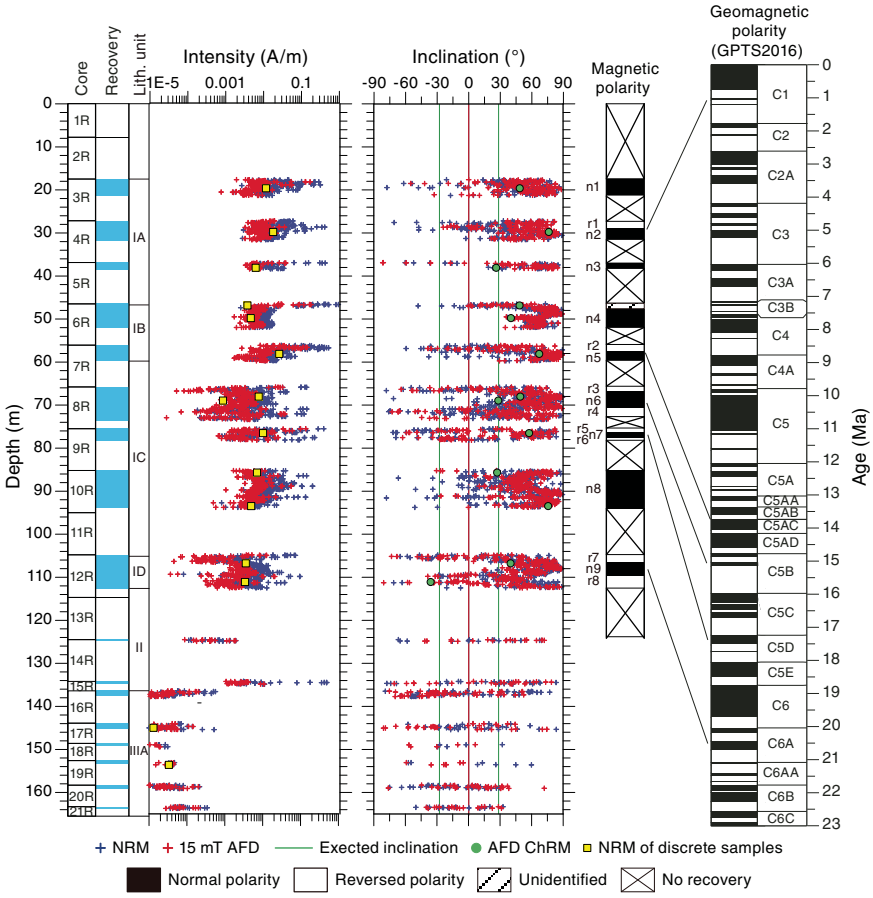

Table T12. Paleomagnetic age datums, Hole U1504A. r = reversed, n = normal. **Download table in CSV format.**

Magnetic polarity	Depth CSF-A at base of interpreted magnetic polarity (m)	Polarity chron	Base of chron (Ma)
r1	29.11	C1r.1r	1.008
r2	57.48	C5ABr	13.739
r3	66.73	C5Bn.1r	15.032
n6	70.81	C5Bn.2n	15.160
r5	76.02	C5Cr	17.235
n7	77.45	C5Dn	17.533
r7	105.77	C6An.1r	20.439
n9	109.28	C6An.2n	20.709

The 13 discrete samples have magnetic susceptibilities (κ) ranging from ≈60 × 10^{-6} to 405 × 10^{-6} SI. These low κ values combined with the low NRM suggest that the magnetic susceptibility is controlled by both paramagnetic silicates (e.g., clays and chlorite) and ferromagnetic phases (e.g., greigite and magnetite). The degree of magnetic anisotropy (P') is moderate (~1.025), whereas the AMS fabric is strongly oblate as shown by shape parameter (T), most likely of depositional origin. The Fisher distribution of AMS principal axes also suggests an oblate fabric (Figure **F30**) with a nearly horizontal planar fabric. These sedimentary fabrics are consistent with deposition in a calm, pelagic environment with very limited traction on sedimentary particles.

Basement rocks

Unit: III
Depths: Hole U1504A = 136.40–163.70 m; Hole U1504B = 117.40–196.28 m
Cores 368-U1504A-16R through 21R and 368-U1504B-5R through 20R

The four discrete basement samples show consistent AMS fabrics even though the core is azimuthally unoriented (Figure **F31**). These cubes show moderate to high degrees of magnetic anisotropy (P' ≈ 1.05–1.09), oblate (i.e., flattened) fabric symmetries (T ≈ 0.2–0.6), magnetic foliations with moderate to steep dip angles (44°–

81°), and variably plunging magnetic lineations. Based on these four samples, the direction of slip along the shear zone is most likely an oblique slip motion (with a normal or reversed component to be determined).

Figure F30. AMS data, Hole U1504A sediments. A. Stereonet of AMS principal directions for 13 discrete samples (lower hemisphere, equal-area projection). K_1 = maximum axis, K_2 = intermediate axis, K_3 = minimum axis. Confidence ellipses at 95% level (same color convention) show dominantly planar and subhorizontal fabric (oblate), consistent with sedimentary fabric acquired in a calm pelagic environment. Tensorial means are shown with larger symbols of same color. B. Degree of magnetic anisotropy (P') vs. magnetic susceptibility (K_m) showing a slight increase in P' with K_m; increase typically occurs in materials in which AMS is controlled, at least in part, by ferromagnetic phases. C. Shape parameter (T) vs. P' showing dominantly oblate symmetry of sedimentary fabric in Unit I and II.

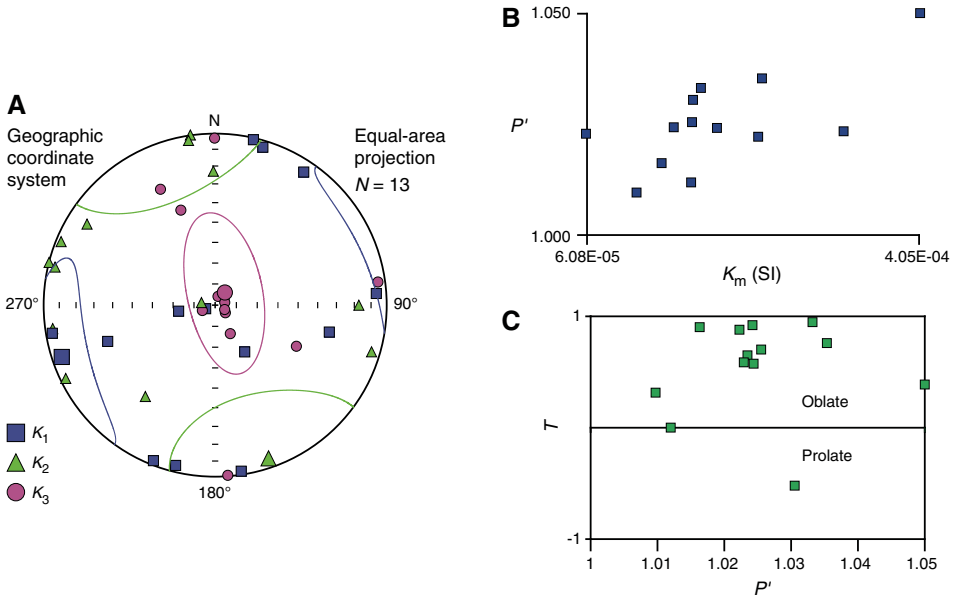

Figure F31. AMS data, Hole U1504A and U1504B basement. A. Stereonet of AMS principal directions for four discrete samples (lower hemisphere, equal-area projection). K_1 = maximum axis, K_2 = intermediate axis, K_3 = minimum axis. Confidence ellipses cannot be calculated due to low sample number. B. Degree of magnetic anisotropy (P') vs. magnetic susceptibility (K_m). C. Shape parameter (T) vs. P' showing oblate symmetry of basement rock fabric in Unit III. D. Stereonet of AMS foliations, defined by K_1–K_2 axes and plotted as a great circle with AMS lineations (K_1 axis) plotted as a square. Because RCB core is not azimuthally oriented, AMS fabrics of these samples can be rotated to any position about the vertical core axis. Because AMS foliation matches macroscopic foliation observed on core, both AMS fabrics can be arbitrarily reoriented to a common north–south foliation strike. After this vertical axis rotation, AMS lineations show variable plunges.

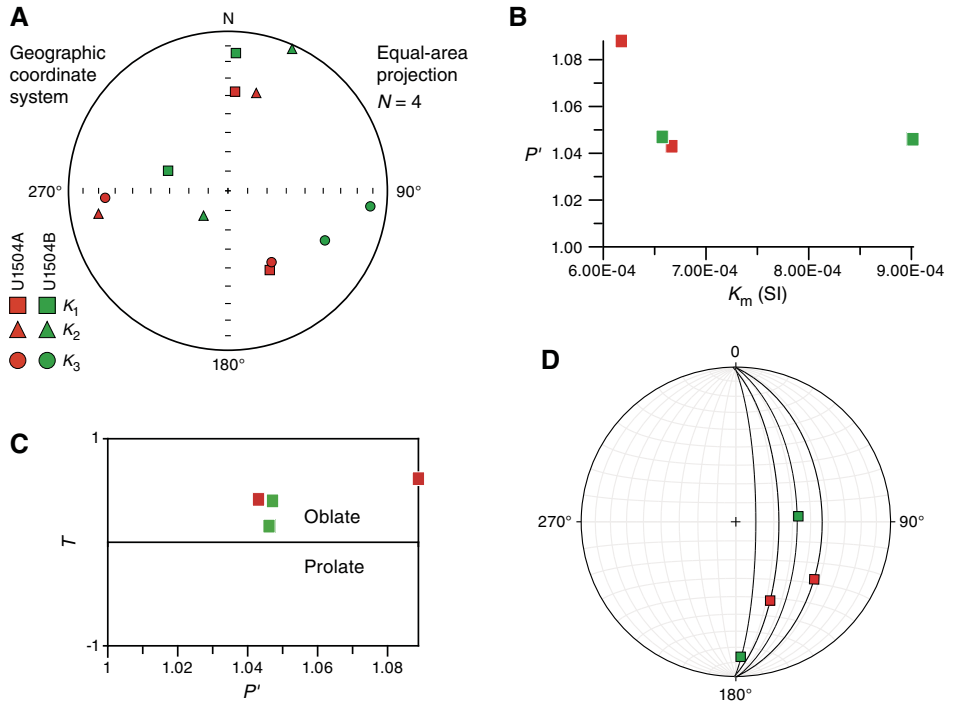

Geochemistry

Hydrocarbon gases were not detected above background levels at Site U1504, and TOC, TN, and TS contents were low, likely reflecting poor preservation of organic matter. Instances of high carbonate content were associated with carbonate lithology. The upper part of the sediment was not cored. Interstitial water major cations and anions from the cored sediments are broadly comparable to other sites. Inductively coupled plasma–atomic emission spectroscopy analysis was not performed on samples collected at Site U1504.

Headspace gas

Headspace gas samples were taken at a frequency of one sample per core or per 10 m of drilling advance for routine safety monitoring to Section 368-U1504A-18R-1 (149.18 m). After this depth, because of the absence of methane in previous samples and the nature of the metamorphic lithologies encountered (low porosity and organic carbon content), an operational decision was made to no longer make headspace gas measurements.

Bulk sediment organic geochemistry

Lithostratigraphic Unit I

TOC, TN, and TS levels are low in all samples collected from Unit I (TOC < 1 wt%, TN < 0.1 wt%, and TS is frequently below detection limit) (Table T13; Figure F32). Subunit IA has TOC values >0.5 wt%, notable sulfur contents, and low carbonate contents. Other lithostratigraphic subunits within Unit I had higher carbonate contents and lower sulfur contents.

Table T13. Carbon, nitrogen, and sulfur, Hole U1504A. **View table in PDF format. Download table in CSV format.**

Lithostratigraphic Unit II

Lithostratigraphic Unit II has a high carbonate content, and based on the results of the standard testing procedure used by IODP to determine TOC content by difference between total and inorganic carbon, it also has a TOC content as high as 1 wt%. Therefore, the higher TOC content could result from a carbon phase unamenable to acid digestion using a weak acid (in such a situation the proportion of inorganic carbon is underestimated and the proportion of organic carbon is overestimated). The TOC/TN ratio for the interval is high, indicating a nitrogen-poor material, which generally is interpreted as representing a terrestrial-derived source of organic matter (Hedges et al., 1988). It could, however, also result from organic matter being exposed and reworked in shallow water (e.g., a lagoon) or caused by overestimation of TOC.

Summary

Overall, the organic matter at Site U1504 falls into two categories (Figure F33). Subunit IA has relatively high TOC and TS, indicating reducing conditions during early diagenesis (Berner and Raiswell, 1984), and, based on its low TOC/TN ratio (high nitrogen content), it is likely derived from aquatic organic matter (Hedges et al., 1988). The rest of the samples have higher carbonate content and higher TOC/TN ratios due to biological inputs of calcite and reworked or land/plant-derived organic matter.

Figure F32. TOC, TOC/TN ratio and carbonate, and TS in bulk sediments. OB = overburden.

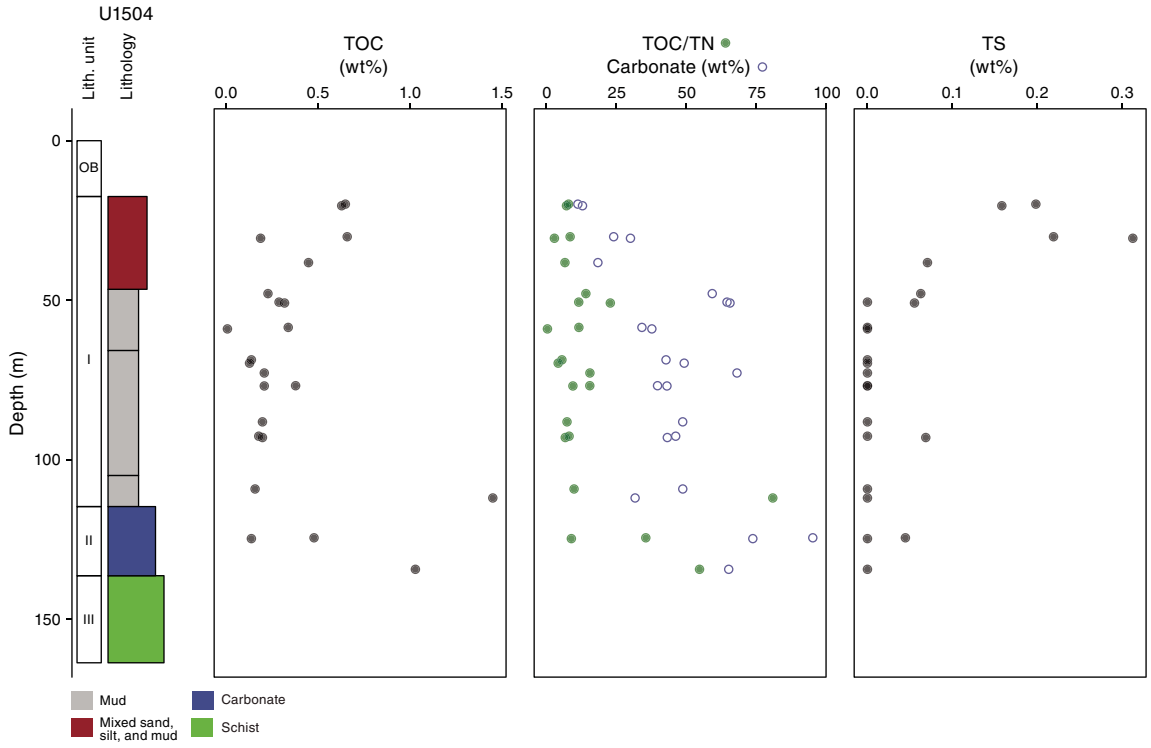

Figure F33. Geochemical parameters of bulk sediments: carbonate vs. TOC/TN ratio and TS vs. TOC. Solid circles = lithostratigraphic Subunit IA, open triangles = Subunits IB–ID, crosses = Unit II.

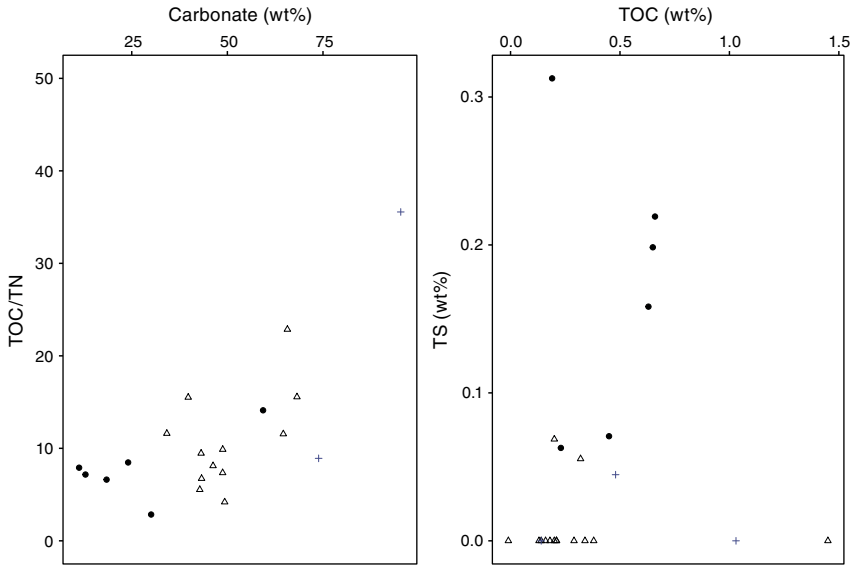

Table T14. Interstitial water analyses, Hole U1504A. **View table in PDF format. Download table in CSV format.**

Raman and surface enhanced Raman spectroscopy

Because of resource constraints, Raman measurements were not performed at this site.

Interstitial water chemistry

Shipboard analyses were performed on interstitial waters squeezed from 5–10 cm long whole-round sediment samples from Hole U1504A. About 30 mL of interstitial water was squeezed per sample. Interstitial water geochemical parameters are listed in Table **T14** and presented in Figure **F34**.

A maxima for alkalinity is observed in the uppermost sample (Section 368-U1504A-3R-2), and thereafter alkalinity decreases with increasing depth to the bottom of the hole. The phosphate and ammonium profiles are similar: both decease with depth, likely due to degradation of organic matter. Typically, these changes occur rapidly at shallow depths (uppermost few meters), and it is notable that both substrates still appear to be actively consumed. Sulfate concentrations vary from 22.5 to 24.7 mM throughout the cored sediment; these are low values compared to the seawater value (28.9 mM), indicating sulfate reduction likely linked to organic matter degradation. The range of pH values observed is from 7.7 to ~7.9, slightly lower than modern seawater; the variations of pH values show a similar trend to those of alkalinity.

Calcium concentrations increase with depth to a maximum at the bottom of the hole, whereas magnesium concentrations decrease with depth, likely because of carbonate dissolution and recrystallization of new carbonate phases. Potassium concentrations decrease linearly with depth from 12.2 to 9.6 mM, which could be interpreted as the consequence of vertical diffusion. Sodium concentrations range between 480 and 487 mM throughout the core. Only small variations in Cl and Br content were observed, and their concentrations are similar to those of modern seawater: 559–567 mM for chloride and 0.86–0.88 mM for bromide.

Discussion

Surface samples were not collected, which prevented evaluation of early stage diagenetic processes related to the breakdown of organic carbon. Hence, it cannot easily be verified if the site currently possess a sulfate–methane transition. However, it is notable that shallow sediments have high TS contents (solid-phase sulfur) that correspond to pyrite within the samples. This topmost-cored interval has low sulfate; thus, it is reasonable to assume that sulfate is converting to sulfide at some point and that this sulfide is now likely preserved in the sediments as pyrite. Methane may have been lost via oxidation to carbonate formation, diffusion, or other mass transfer processes. Relative to other Expedition 368 sites, the site has low organic carbon preservation with far more carbon sequestered as carbonate.

Figure F34. Interstitial water alkalinity, major cations, and anions.

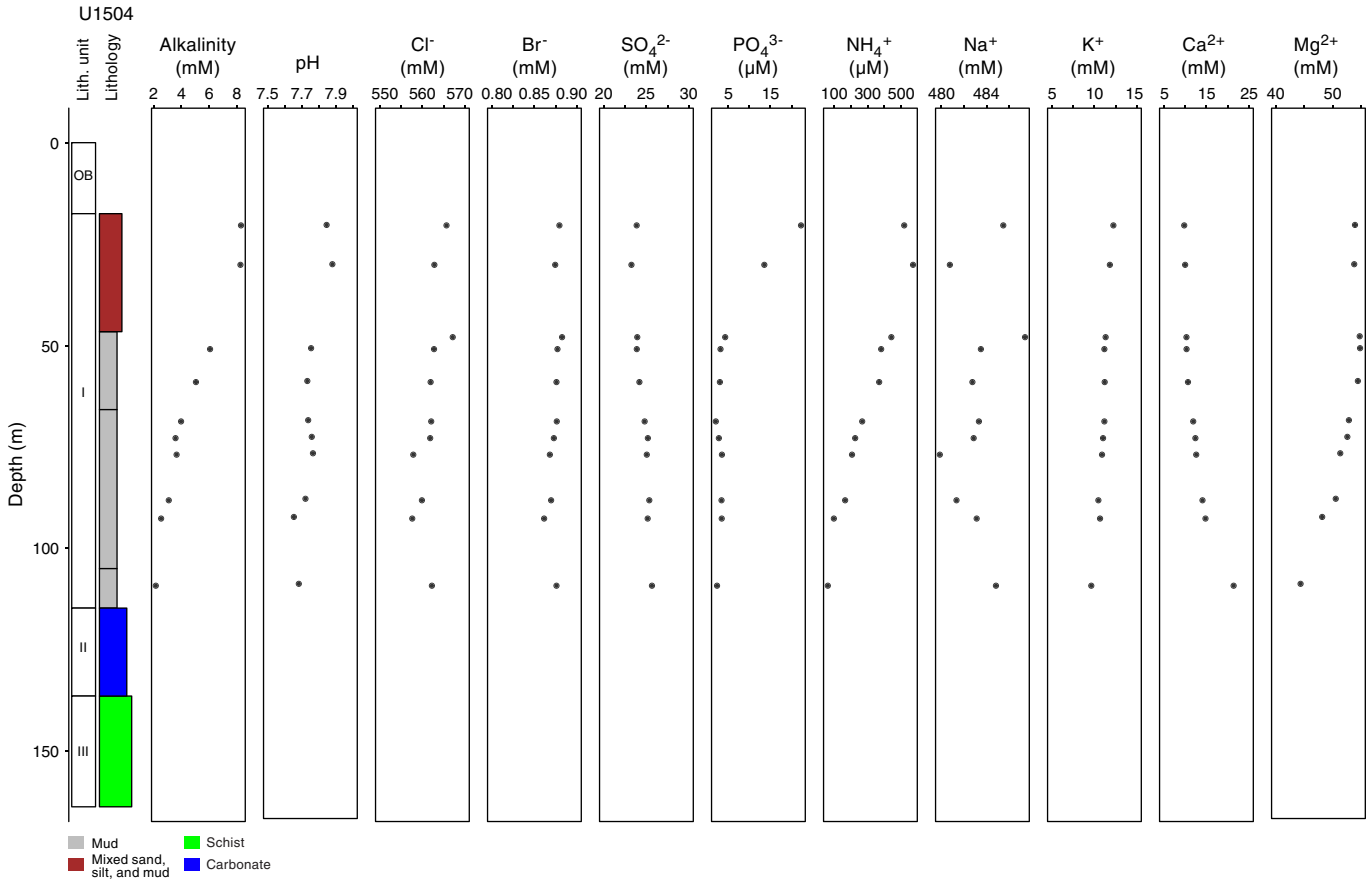

Physical properties

Physical property measurements were performed on cores from Hole U1504A (17.50–165.5 m) and Hole U1504B (88.2–195.2 m). NGR, magnetic susceptibility, gamma ray attenuation (GRA) bulk density, and *P*-wave velocity were measured on the whole-round cores. Point magnetic susceptibility, red green blue (RGB), and color reflectance were measured on archive-half sections. All analyses were conducted at a sampling resolution of 2 cm. *P*-wave velocity was also measured using the *P*-wave caliper (PWC) system on split cores in liner and on individual pieces from working-half sections without liner. Thermal conductivity measurements were performed on Section 3 of each core. Moisture and density (MAD) measurements in Hole U1504A were performed on discrete samples, generally taken at a resolution of 1 sample every other section. MAD samples were not taken from Hole U1504B to preserve material for postcruise research.

Physical property measurements from Holes U1504A and U1504B are consistent between the two holes and compare well to the lithostratigraphic units (see also **Lithostratigraphy**). At Site U1504, four PP units were distinguished according to variations in physical properties: PP Unit 1 (17.50–45 m in Hole U1504A) is characterized by very low density (average of ~1.5 g/cm^3), porosity (~75%), and *P*-wave velocity (~1500 m/s). PP Unit 2 (45–114 m in Hole U1504A and 88.2–93 m in Hole U1504B) has higher density (~1.7 g/cm^3) and *P*-wave velocity (average = 1590 m/s) values than the overlying PP Unit 1. PP Unit 3 (114–135 m in Hole U1504A and 93–110 m in Hole U1504B) is marked by significant increases in *P*-wave velocity and bulk density. However, very few physical property results were obtained from this unit because of poor core recovery. PP Unit 4 (135–165.5 m in Hole U1504A and 110–195.2 m in Hole U1504B) has the highest *P*-wave velocity and bulk density and the lowest NGR values compared with the three overlying units. A more detailed description of physical properties of different units is given below.

Natural gamma radiation

NGR counts range between ~25 and 35 counts/s in PP Unit 1 and exhibit no noticeable trend with depth (Figure **F35**), which may be due to limited core recovery. PP Unit 2 is generally characterized by greater amplitude in NGR values (15–35 counts/s) than Unit 1. In PP Units 3 and 4, NGR values show a slightly increasing trend from ~5 to 20 counts/s with depth. NGR values are relatively high (~50 counts/s) at ~152 and ~168 m in Hole U1504B.

P-wave velocity

In Holes U1504A and U1504B, *P*-wave velocity measurements are consistent between whole-round and split core sections (Figure **F35**). In PP Unit 1, *P*-wave velocity shows little variation with an average of 1500 m/s. PP Unit 2 is distinguished by a slight increase in velocity in the upper section to 1560 m/s and velocities that increase slowly with depth to ~1700 m/s. In contrast, PP Unit 3 is marked by an abrupt change to high *P*-wave velocities (~3000–5000 m/s). Similarly, the *P*-wave velocities of PP Unit 4 are high (~5000–6100 m/s) and represent the metamorphic rocks in lithostratigraphic Unit III (see **Lithostratigraphy**).

Figure F35. Physical properties for Holes U1504A and U1504B with petrophysical (PP) units. Note that in PP Units 3 and 4, the scattered GRA density measurements are less reliable due to void between core material and core liner. Descriptions and discussions in text are based on discrete samples of bulk density (MAD). cps = counts per second.

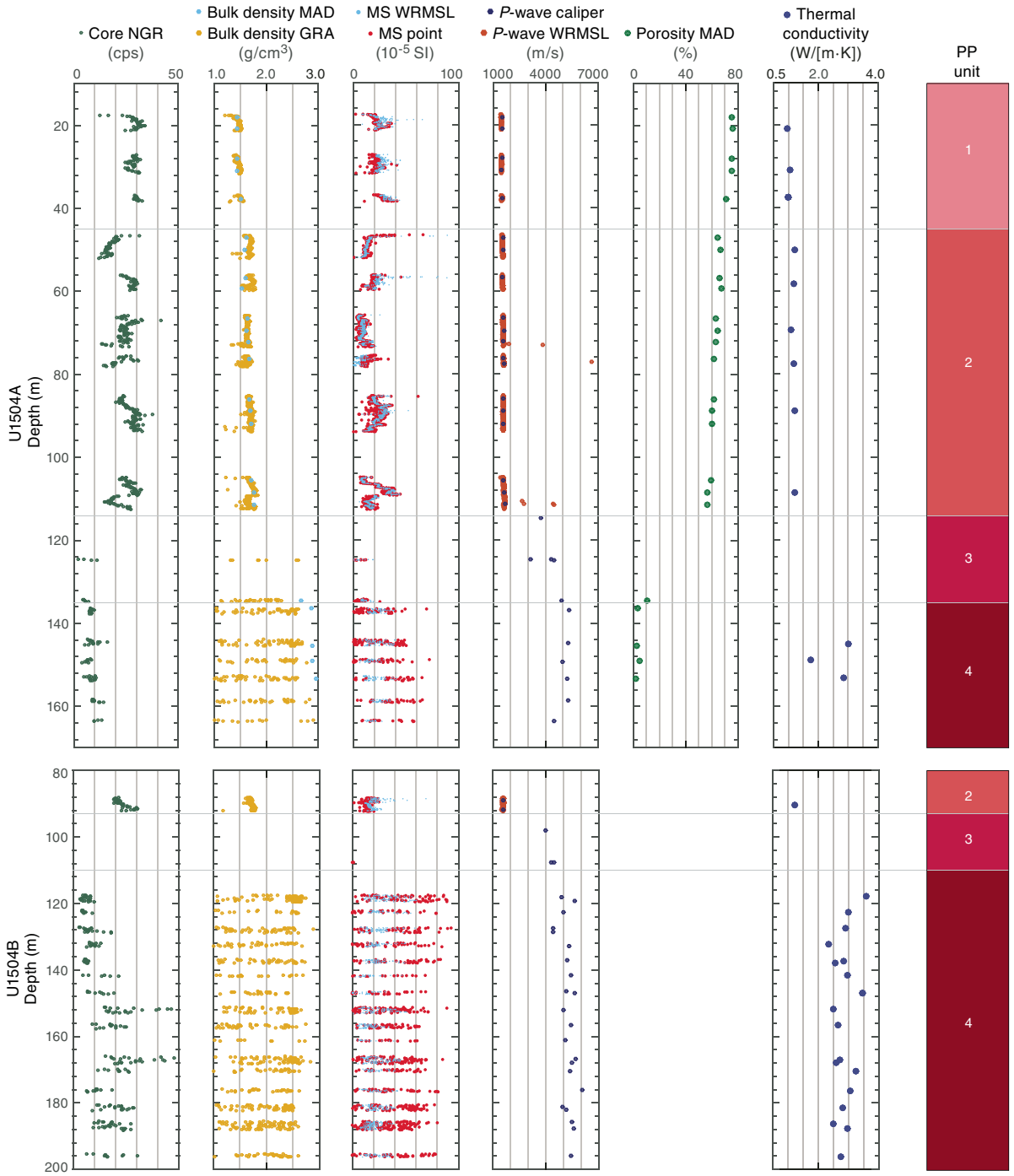

Thermal conductivity

Thermal conductivity measurements are well defined in the designated physical property units. In Hole U1504A, PP Unit 1 has lower thermal conductivity ranging from 0.970 to 1.047 W/(m·K) (Figure F35) followed by a higher thermal conductivity regime ranging from 1.089 to 1.204 W/(m·K) that corresponds to PP Unit 2. Because of the small size of core pieces recovered from PP Unit 3, no thermal conductivity measurements could be taken from this unit. Finally, PP Unit 4 shows values from 1.752 to 3.004 W/(m·K) that include the highest thermal conductivity measurements from the cores recovered at Site U1504.

Similarly, in Hole U1504B, PP Unit 2 has lower thermal conductivity values and no measurements could be taken in PP Unit 3. PP

Figure F36. Bulk density (GRA and MAD), dry density, grain density, and porosity, Hole U1504A. Note that in PP Units 3 and 4, the scattered GRA density measurements are less reliable due to void between core material and core liner. Descriptions and discussions in text are based on discrete samples of bulk density (MAD).

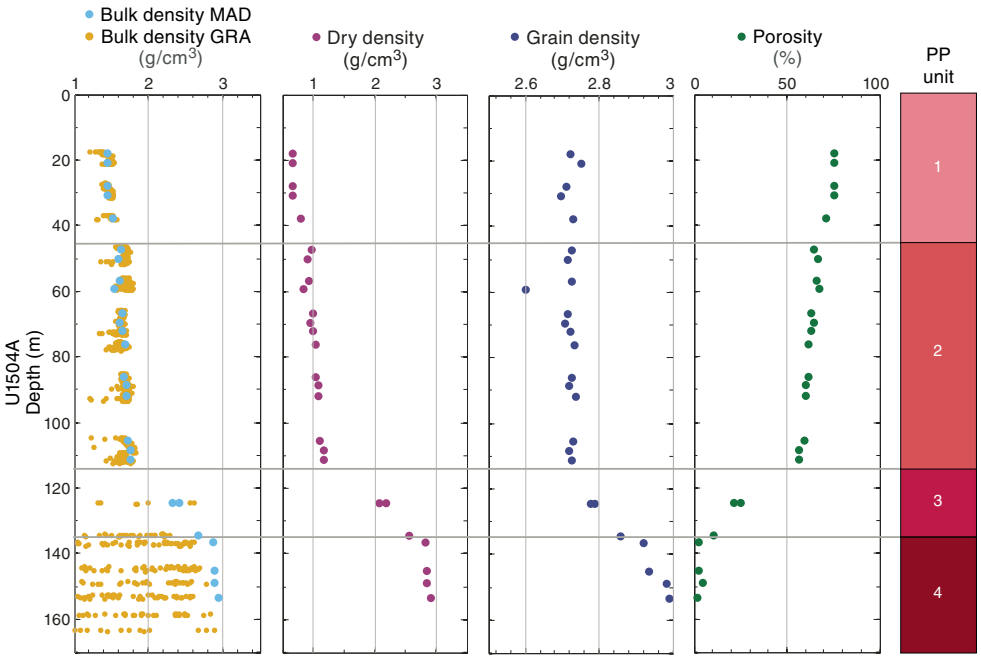

Unit 4 is characterized by a regime of higher thermal conductivity with values ranging from 2.353 to 3.475 W/(m·K).

Density and porosity

GRA densities generally match the trend of discrete bulk density values in PP Units 1 and 2 (Figure **F35**); however, the GRA density values are more scattered than the discrete measurements in PP Units 3 and 4 because whole-round measurements are affected by space between the core and the core liner. Hence, descriptions of variations in density are only based on discrete measurements of Hole U1504A (Figure **F36**).

In PP Unit 1, bulk density increases slightly with depth and ranges from ~1.4 to 1.5 g/cm^3. Dry densities in the upper portion of Unit 1 (18–30 m) remain relatively constant with an average of ~0.7 g/cm^3 followed by an increase to ~0.8 g/cm^3 at ~38 m. Porosity ranges from 70% to 75% and displays a negative correlation with bulk density, as expected. Grain density values are relatively uniform, averaging ~2.7 g/cm^3.

In PP Unit 2, bulk density gradually increases with depth from ~1.6 g/cm^3 at 47 m to ~1.8 g/cm^3 at 110 m. Dry density similarly increases with depth, whereas porosity decreases downcore from 67% to 57%. Grain density is relatively constant at ~2.7 g/cm^3.

Bulk density values in PP Unit 3 are higher than in the overlying Unit 2, ranging from ~2.3 to 2.7 g/cm^3 followed by a sharp shift toward higher values (>2.8 g/cm^3) at the boundary with PP Unit 4 (Figure **F36**). PP Unit 4 (135–165.5 m) represents the metamorphic basement and is characterized by very high bulk density (>2.9 g/cm^3). PP Unit 4 grain density increases downcore from ~2.9 to 3.0 g/cm^3, whereas porosity ranges from 2% to 5%.

Color reflectance spectrophotometry

In PP Unit 1, reflectance parameters L*, a*, and b* remain relatively constant with mean values of 42, 2, and –1, respectively (Figure **F37**). At the uppermost portion of PP Unit 2 in Hole U1504A, all parameters display a large increase to 63, 9, and 17, respectively. Over the rest of Unit 2 (48–114 m in Hole U1504A), L* values slightly decrease from ~60 to 50, whereas a* and b* show comparable larger variations between 65 and 114 m. In PP Units 3 and 4 in both holes, L*, a*, and b* values are relatively scattered. Unit 3 has a mean L* value of ~45 similar to Unit 4 but higher mean a* and b* values of ~5 compared with that of approximately –1 in Unit 4.

Magnetic susceptibility

Magnetic susceptibility shows very limited changes between ~5 × 10^{-5} and 80 × 10^{-5} SI throughout all four petrophysical units (Figure **F35**). Nevertheless, magnetic susceptibility differences between different units are still recognizable. PP Unit 1 has a relatively high mean magnetic susceptibility of ~30 × 10^{-5} SI compared with that of ~20 × 10^{-5} SI for PP Unit 2. Unit 2 also contains two depth intervals (~46.5–47.0 and 56.5–57.0 m in Hole U1504A) showing magnetic susceptibility as high as 80 × 10^{-5} SI. The distribution of magnetic susceptibility within PP Units 3 and 4 is scattered, possibly due to the fragmented core materials and voids within the rock core samples. The mean magnetic susceptibility is as low as ~10 × 10^{-5} SI in Unit 3 but increases to ~35 × 10^{-5} SI in Unit 4.

RGB

In Hole U1504A, RGB values are generally constant with depth in PP Units 1, 3, and 4 with small variations (Figure **F38**), but Units 3 and 4 have higher values than Unit 1 because Unit 1 consists of dark gray nannofossil ooze (see **Lithostratigraphy**). PP Unit 2 is marked by strong RGB intensity that corresponds to carbonate-rich lithology. All the units in Hole U1504B have value ranges similar to those of the corresponding units in Hole U1504A.

Discussion and summary

Core materials in PP Units 1 and 2 consist of soft sediments. In general, compared with Unit 2, Unit 1 has higher average NGR (~30

Figure F37. Core color reflectance parameters L*, a*, and b*, Holes U1504A and U1504B.

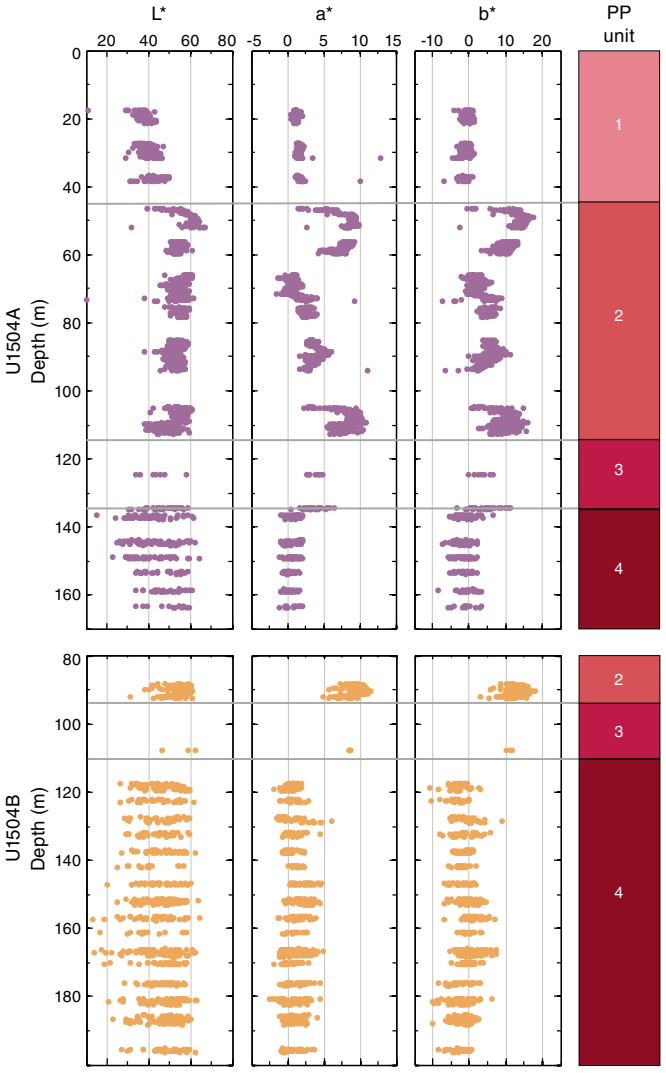

Figure F38. Core RGB values, Holes U1504A and U1504B.

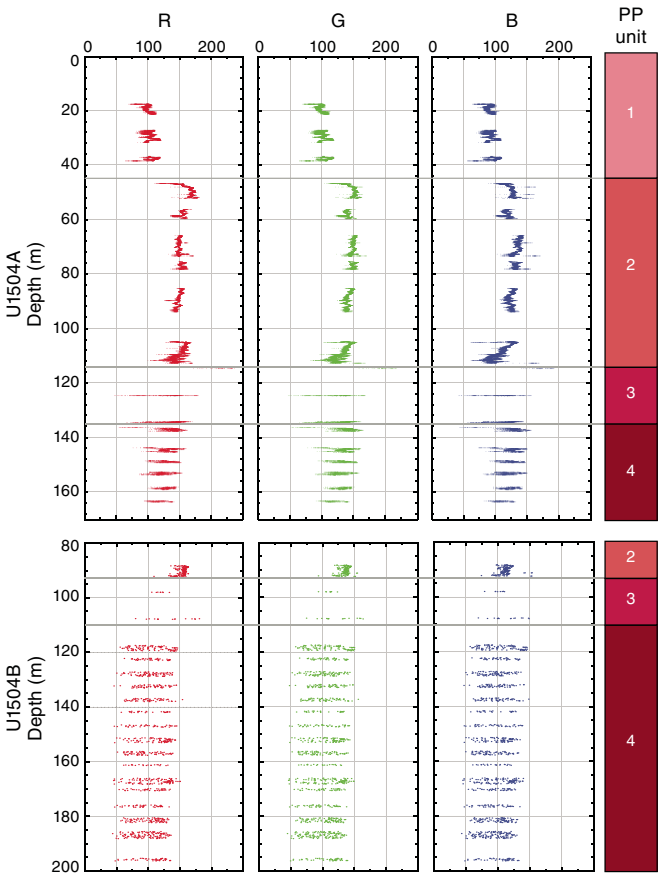

versus 20 counts/s), weaker color reflectance (mean L* of ~40 versus 50), and lower average RGB values (100 versus 150) (Figures **F35**, **F37**, **F38**). These changes in physical properties between Units 1 and 2 correspond to a change in sediment compositions from nannofossil-rich clay to nannofossil ooze (see **Lithostratigraphy**). General increases in bulk (from ~1.4 to 1.8 g/cm^3) and dry (from ~0.7 to 1.2 g/cm^3) densities and a downhole decrease in porosity (from 75% to 56%) in Units 1 and 2 mainly indicate sediment compaction with time. The boundary between Units 1 and 2 is marked by a relatively rapid increase in *P*-wave velocity and bulk density and a rapid decrease in porosity compared with the general trends mentioned above (Figures **F35**, **F36**). This physical property boundary corresponds to a clear unconformity in the seismic profile along this drilling site and to a large hiatus (see **Biostratigraphy**).

P-wave velocity and bulk density increase from ~3800 to 5000 m/s and from ~2.4 to 2.9 g/cm^3, respectively, within PP Unit 3, corresponding to a transition in lithology from coral-rich limestone to clast-supported limestone (see **Lithostratigraphy**). Coral-enriched limestone in the upper portion of Unit 3 is also associated with a moderately high porosity of ~23% (Figures **F35**, **F36**). PP Unit 4 is characterized by a uniformly high velocity of ~5500 m/s, high bulk density of ~2.9 g/cm^3, and low porosity of ~3%, all of which correspond to epidote-chlorite schist (see **Lithostratigraphy**). A large increase in both velocity and density at the boundaries between Units 2 and 3 and between Units 3 and 4 is also recorded by two strong positive seismic reflectors (Figure **F36**). The gradual downhole increase in thermal conductivity values at shallow depths is likely due to progressive compaction of the sediments. The higher RGB intensity in Unit 2 reflects the higher carbonate content.

Correlation to seismic data

We conducted two sets of analyses to correlate the core measurements (in meters below seafloor) to the time-based seismic data from Hole U1504A. First, we analyzed core data and investigated correlation to the seismic reflection profile. Second, we constructed synthetic seismograms using the core data of Site U1504 and compared the results with the traces in seismic profiles. Preliminary calculations were done during the expedition using a combination of Matlab scripts and Petrel software.

Velocity and density data and comparison with seismic reflectors

Whole-round core measurements were conducted in Hole U1504A from 17.5 to 163.5 m for GRA density and from 17.5 to 112.7 m for *P*-wave logger (PWL) measurements (Figure **F39**). *P*-wave velocity was also measured along the *x*-axis with the PWC system on working-half sections. MAD measurements were performed on discrete samples, one every other section. Wireline

Figure F39. Comparison of a subset of physical properties (magnetic susceptibility [MS], velocity, density, and NGR) with seismic waveform (converted to depth scale using best-fitting TDR model) and seismic image (in timescale) in Hole U1504A. Red circles = reference points (discussed in text).

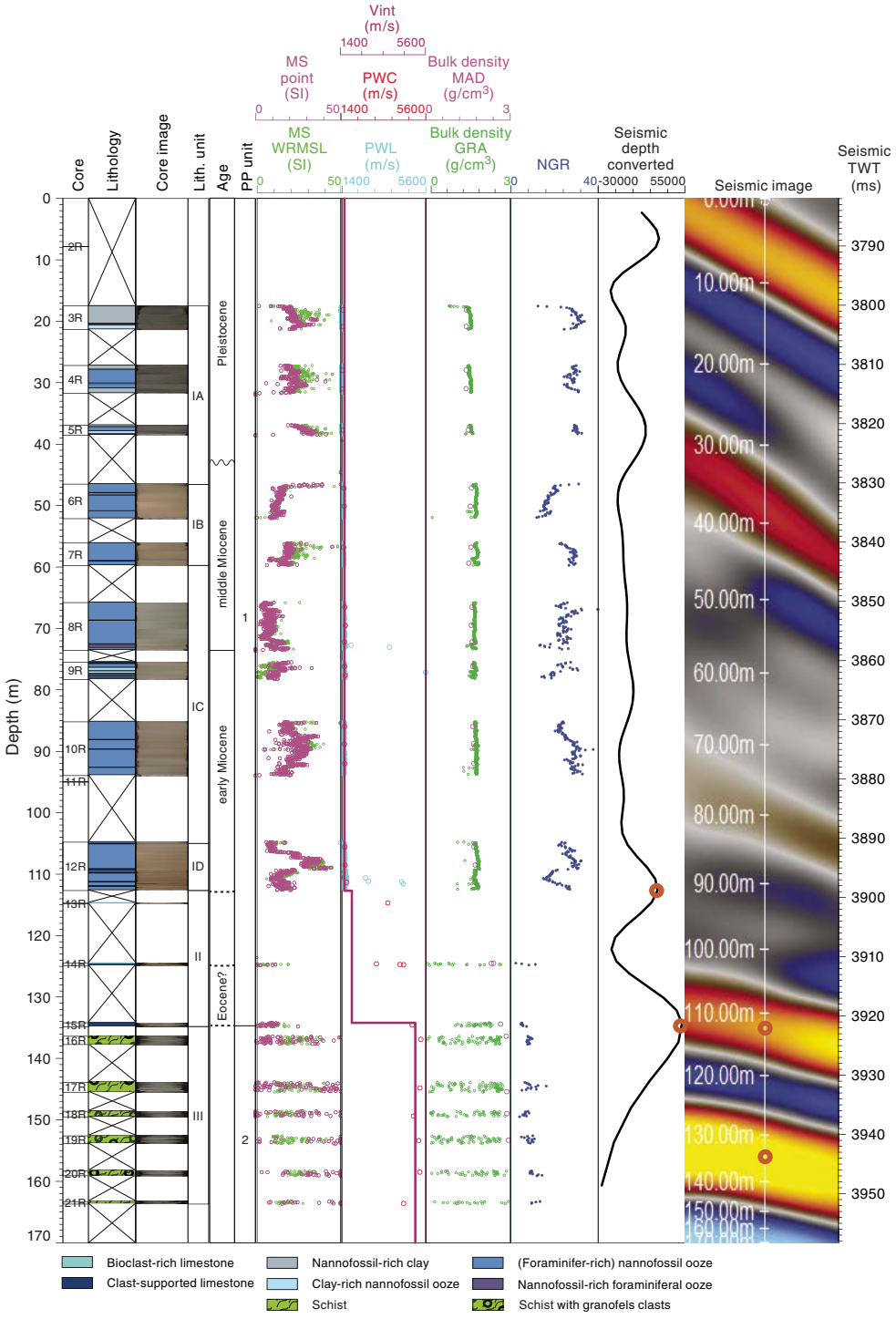

logging was not conducted at Site U1504. With the outliers filtered out, the whole-round PWL velocity and GRA density data show a good match with the PWC velocity and MAD density of core samples, respectively.

Although no downhole logging was conducted at Site U1504, two distinct changes in the physical property data from the cores helped in building a velocity model for the time-depth correlation on the seismic profiles from Hole U1504A. The first major change in V_P and density was identified at ~112.7 m, coinciding with the lithologic change from sediment to limestone (Figure **F39**; see **Lithostratigraphy**). We hypothesized that a relatively strong reflector in the seismic traces at Site U1504 (two-way traveltime [TWT] = 3922 ms) might correspond to the noticeable changes in lithology and physical properties at 112.7 m we refer to as reference Point RP1. A second major change in V_P and density, at ~134.2 m, is associated with a strong peak in the seismogram (TWT = 3944 ms) des-

ignated as reference Point RP2. Once the corresponding depths of the two reference points were assigned, the interval velocity at the 112.7–134.2 m depth range was calculated to be ~2 km/s. For the 134.2–163.5 m interval, an interval velocity of 5094 m/s was chosen, which corresponds to the average PWC values.

Time-depth relationship

Hole U1504A PWC data were used to calculate the time-depth relationship (TDR) model of seismic waves. We assigned the first strong reflector (TWT = 3922 ms; reference Point RP1) to be associated with the major changes in V_P and density at ~112.7 m. Similarly, we assigned the second strong reflector (TWT = 3944 ms; reference Point RP2) to be associated with the major changes in V_P and density at ~134.2 m. For the 134.2–163.5 interval, the TDR was calculated assuming an interval velocity of 5094 m/s, which is the average PWC for this interval (Figure **F40**).

Synthetic seismograms

To further illustrate the relationship between the core measurements in Hole U1504A and the seismic reflection profile, the "Seismic interpretation" module in Petrel was used to compute synthetic seismograms based on the relevant core measurements (Figure **F41**). Synthetic traces were generated by convolving the reflectivity from the density of core samples, an interval velocity model, and with the source wavelet that best fit the seismic data ("Ricker 2;" Figure **F41**).

Seismic impedance (SI) of a rock layer is the product of its average seismic velocity (V_P) and density (ρ) (i.e., SI = V_P × ρ). The seismic reflection coefficient, in turn, equals the change in the seismic impedance between two adjacent rock layers. Thus, we can expect greater amplitudes in the modeled seismogram for rock interfaces with larger values of reflection coefficient. The resulting synthetic seismogram shows two strong reflectors at ~110–142 m (Figure **F41**), consistent with the observed depth range of the two strong seismic reflectors.

Using the best-fitting TDR model for Hole U1504A (Figure **F40**), we were able to convert the depth scale to a timescale for all

Figure F40. A. Site U1504 time-depth relation curve in Hole U1504A compared to Site U1501. Red circles = reference points at 112.7 and 134.2 m (RP1 and RP2), coinciding with noticeable changes in density and velocity. B. Hole U1504A PWC and interval velocity model. Interval velocity for 112.7–134.2 m was calculated using TWT and depth range values of RP1 and RP2; interval velocity for 134.2–163.5 m corresponds to average PWC for that interval.

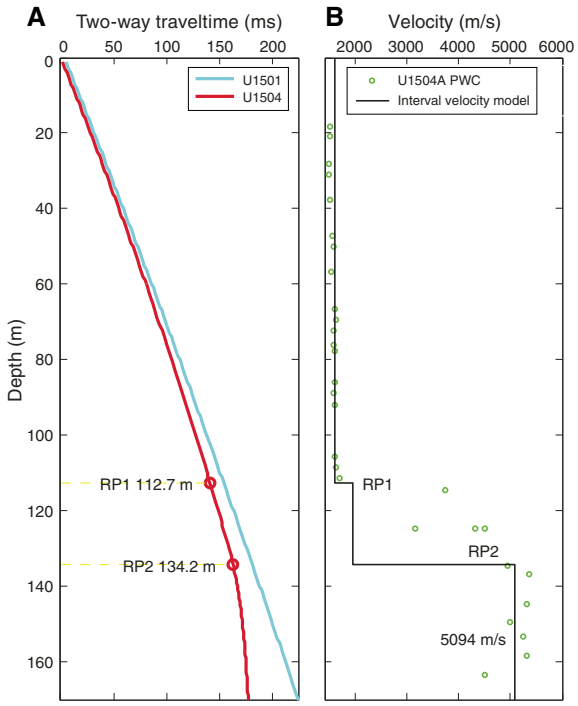

core measurements. This conversion enabled us to display the core measurements directly on top of the time-based seismic sections, facilitating identification of correlated features as illustrated in the example of Figure **F42**.

Figure F41. Synthetic seismogram, Hole U1504A. Panels from left to right: interval velocity and MAD density used in the calculation, resultant reflection coefficient (RC), real seismic traces with synthetic seismogram inserted in the center, and seismic source function "Ricker 2" used in modeling.

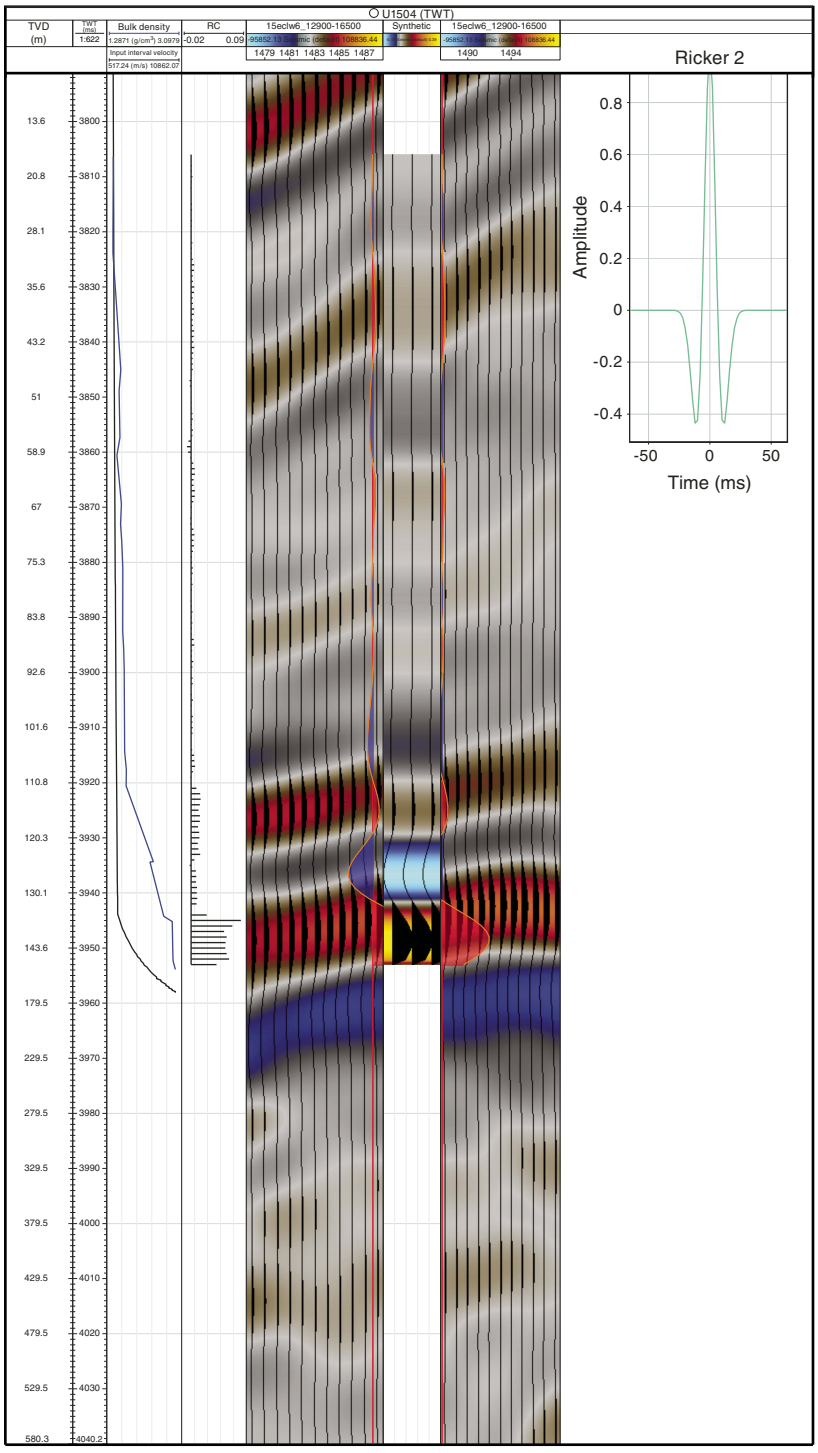

Figure F42. Seismic section at Site U1504 with lithostratigraphic units overlain at Hole U1504A location. Also shown are selected core measurements converted to depth scale using best-fitting TDR model, including Hole U1504A PWC and PWL, MAD density, GRA density, porosity, MS, and NGR.

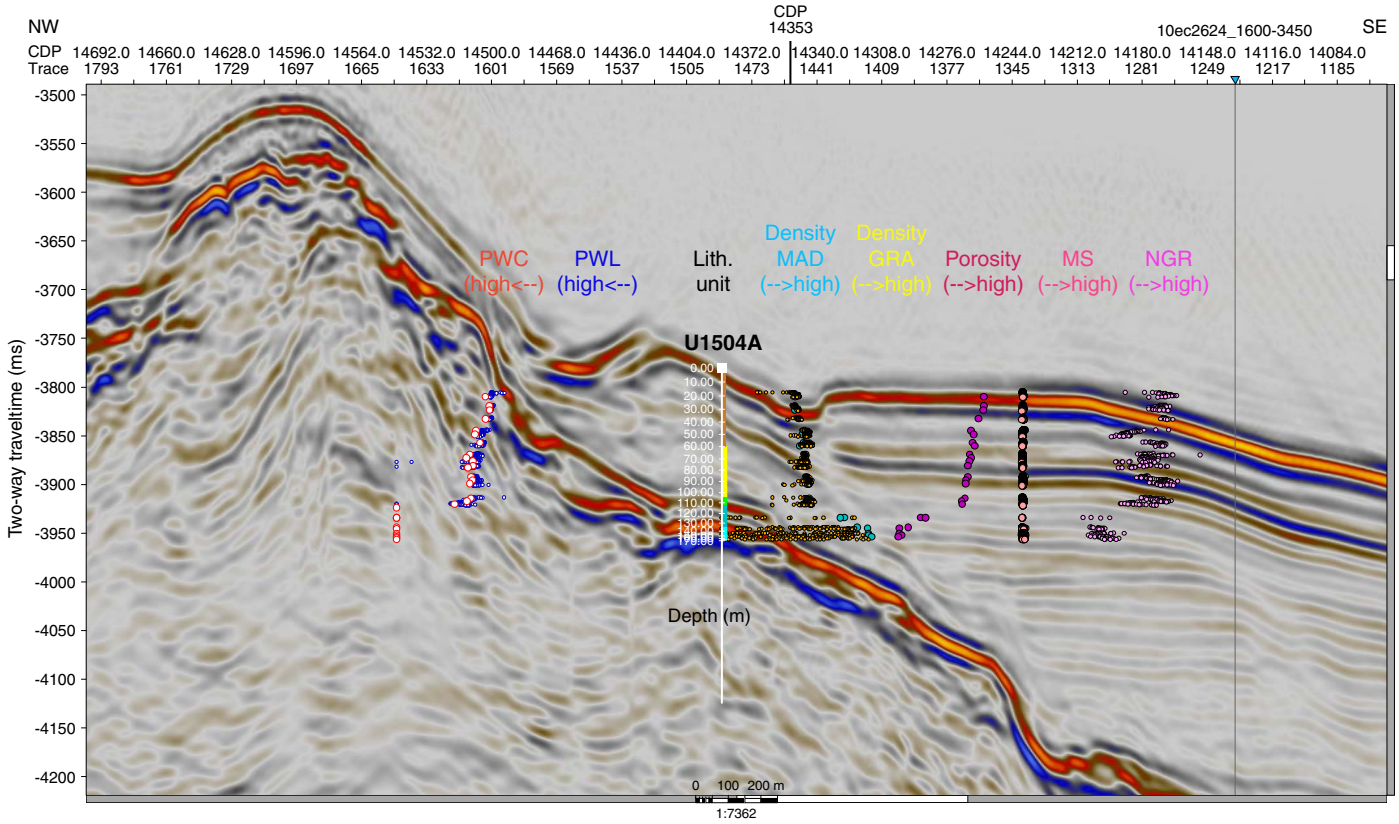

References

Beavington-Penney, S.J. and Racey, A., 2004. Ecology of extant nummilitids and other larger benthic foraminifera: applications in paleoenvironmental analysis. *Earth-Science Reviews,* 67, 219-265. **https://doi.org/10.1016/j.earscirev.2004.02.005**

Berner, R.A., and Raiswell, R., 1984. C/S method for distinguishing freshwater from marine sedimentary rocks. *Geology,* 12(6):365–368. **https://doi.org/10.1130/0091-7613(1984)12<365:CMFDFF>2.0.CO;2**

Blow, W.H., 1969. Late middle Eocene to recent planktonic foraminiferal biostratigraphy. *Proceedings of the International Conference on Planktonic Microfossils,* 1:199–422.

Briais, A., Patriat, P., and Tapponnier, P., 1993. Updated interpretation of magnetic anomalies and seafloor spreading stages in the South China Sea: implications for the Tertiary tectonics of Southeast Asia. *Journal of Geophysical Research: Solid Earth,* 98(B4):6299–6328. **https://doi.org/10.1029/92JB02280**

Cronan, D.S., 1980. *Underwater Minerals:* London (Academic Press).

Hedges, J.I., Clark, W.A., and Come, G.L., 1988. Organic matter sources to the water column and surficial sediments of a marine bay. *Limnology and Oceanography,* 33(5):1116–1136. **https://doi.org/10.4319/lo.1988.33.5.1116**

Hsieh, C.Y., 1936. On the late Mesozoic-early Tertiary Orogenesis and vulkanism, and their relation to the formation of metallic deposits in China. *Acta Geologica Sinica,* 15(1):61–74. **https://doi.org/10.1111/j.1755-6724.1936.mp15001005.x**

Kirschvink, J.L., 1980. The least-squares line and plane and the analysis of palaeomagnetic data. *Geophysical Journal of the Royal Astronomical Society,* 62(3):699–718. **https://doi.org/10.1111/j.1365-246X.1980.tb02601.x**

Larsen, H.C., Jian, Z., Alvarez Zarikian, C.A., Sun, Z., Stock, J.M., Klaus, A., Boaga, J., Bowden, S.A., Briais, A., Chen, Y., Cukur, D., Dadd, K.A., Ding, W., Dorais, M.J., Ferré, E.C., Ferreira, F., Furusawa, A., Gewecke, A.J., Hinojosa, J.L., Höfig, T.W., Hsiung, K.-H., Huang, B., Huang, E., Huang, X.-L., Jiang, S., Jin, H., Johnson, B.G., Kurzawski, R.M., Lei, C., Li, B., Li, L., Li, Y., Lin, J., Liu, C., Liu, C., Liu, Z., Luna, A., Lupi, C., McCarthy, A.J., Mohn, G., Ningthoujam, L.S., Nirrengarten, M., Osono, N., Peate, D.W., Persaud, P., Qui, N., Robinson, C.M., Satolli, S., Sauermilch, I., Schindlbeck, J.C., Skinner, S.M., Straub, S.M., Su, X., Tian, L., van der Zwan, F.M., Wan, S., Wu, H., Xiang, R., Yadav, R., Yi, L., Zhang, C., Zhang, J., Zhang, Y., Zhao, N., Zhong, G., and Zhong, L., 2018a. Site U1501. *In* Sun, Z., Jian, Z., Stock, J.M., Larsen, H.C., Klaus, A., Alvarez Zarikian, C.A., and the Expedition 367/368 Scientists, *South China Sea Rifted Margin*. Proceedings of the International Ocean Discovery Program, 367/368: College Station, TX (International Ocean Discovery Program). **https://doi.org/10.14379/iodp.proc.367368.105.2018**

Larsen, H.C., Jian, Z., Alvarez Zarikian, C.A., Sun, Z., Stock, J.M., Klaus, A., Boaga, J., Bowden, S.A., Briais, A., Chen, Y., Cukur, D., Dadd, K.A., Ding, W., Dorais, M.J., Ferré, E.C., Ferreira, F., Furusawa, A., Gewecke, A.J., Hinojosa, J.L., Höfig, T.W., Hsiung, K.-H., Huang, B., Huang, E., Huang, X.-L., Jiang, S., Jin, H., Johnson, B.G., Kurzawski, R.M., Lei, C., Li, B., Li, L., Li, Y., Lin, J., Liu, C., Liu, C., Liu, Z., Luna, A., Lupi, C., McCarthy, A.J., Mohn, G., Ningthoujam, L.S., Nirrengarten, M., Osono, N., Peate, D.W., Persaud, P., Qui, N., Robinson, C.M., Satolli, S., Sauermilch, I., Schindlbeck, J.C., Skinner, S.M., Straub, S.M., Su, X., Tian, L., van der Zwan, F.M., Wan, S., Wu, H., Xiang, R., Yadav, R., Yi, L., Zhang, C., Zhang, J., Zhang, Y., Zhao, N., Zhong, G., and Zhong, L., 2018b. Site U1503. *In* Sun, Z., Jian, Z., Stock, J.M., Larsen, H.C., Klaus, A., Alvarez Zarikian, C.A., and the Expedition 367/368 Scientists, *South China Sea Rifted Margin*. Proceedings of the International Ocean Discovery Program, 367/368: College Station, TX (International Ocean Discovery Program). **https://doi.org/10.14379/iodp.proc.367368.107.2018**

Li, C.-F., Lin, J., Kulhanek, D.K., Williams, T., Bao, R., Briais, A., Brown, E.A., Chen, Y., Clift, P.D., Colwell, F.S., Dadd, K.A., Ding, W., Hernández-

Almeida, I., Huang, X.-L., Hyun, S., Jiang, T., Koppers, A.A.P., Li, Q., Liu, C., Liu, Q., Liu, Z., Nagai, R.H., Peleo-Alampay, A., Su, X., Sun, Z., Tejada, M.L.G., Trinh, H.S., Yeh, Y.-C., Zhang, C., Zhang, F., Zhang, G.-L., and Zhao, X., 2015. Expedition 349 summary. *In* Li, C.-F., Lin, J., Kulhanek, D.K., and the Expedition 349 Scientists, *South China Sea Tectonics.* Proceedings of the International Ocean Discovery Program, 349: College Station, TX (International Ocean Discovery Program). **https://doi.org/10.14379/iodp.proc.349.101.2015**

Li, P.L., Wang, W.P., He, Y.C., et al., 1989. Tectonic structures and evolution of the Pearl River Mouth Basin. *China Offshore Oil and Gas (Geology),* 3(1): 11–18 (in Chinese with English abstract).

Lurcock, P.C., and Wilson, G.S., 2012. PuffinPlot: a versatile, user-friendly program for paleomagnetic analysis. *Geochemistry, Geophysics, Geosystems,* 13(6):Q06Z45. **https://doi.org/10.1029/2012GC004098**

Martini, E., 1971. Standard Tertiary and Quaternary calcareous nannoplankton zonation. *In* Farinacci, A. (Ed.), *Proceedings of the Second Planktonic Conference, Roma 1970:* Rome (Edizioni Tecnoscienza), 2:739–785.

Ogg, J.G., Ogg, G., and Gradstein, F.M., 2016. *A Concise Geologic Time Scale 2016:* Boston (Elsevier).

Roberts, A.P., Chang, L., Rowan, C.J., Horng, C.-S., and Florindo, F., 2011. Magnetic properties of sedimentary greigite (Fe_3S_4): an update. *Reviews of Geophysics,* 49(1):RG1002. **https://doi.org/10.1029/2010RG000336**

Sales, A.O., Jacobsen, E.C., Morado, A.A., Jr., Benavidez, J.J., Navarro, F.A., and Lim, A.E., 1997. The petroleum potential of deep-water northwest Palawan Block GSEC 66. *Journal of Asian Earth Sciences,* 15(2–3): 217–240. **https://doi.org/10.1016/S0743-9547(97)00009-3**

Scherer, R.P., Gladenkov, A.Y., and Barron, J.A., 2007. Methods and applications of Cenozoic marine diatom biostratigraphy. *In* Starratt, S.W. (Ed.), *Pond Scum to Carbon Sink: Geological and Environmental Applications of the Diatoms.* Paleontological Society Papers, 13:61–83.

Suggate, S.M., Cottam, M.A., Hall, R., Sevastjanova, I., Forster, M.A., White, L.T., Armstrong, R.A., Carter, A., and Mojares, E., 2014. South China continental margin signature for sandstones and granites from Palawan, Philippines. *Gondwana Research,* 26(2):699–718. **https://doi.org/10.1016/j.gr.2013.07.006**

Sun, Z., Jian, Z., Stock, J.M., Larsen, H.C., Klaus, A., Alvarez Zarikian, C.A., Boaga, J., Bowden, S.A., Briais, A., Chen, Y., Cukur, D., Dadd, K.A., Ding, W., Dorais, M.J., Ferré, E.C., Ferreira, F., Furusawa, A., Gewecke, A.J., Hinojosa, J.L., Höfig, T.W., Hsiung, K.-H., Huang, B., Huang, E., Huang, X.-L., Jiang, S., Jin, H., Johnson, B.G., Kurzawski, R.M., Lei, C., Li, B., Li, L., Li, Y., Lin, J., Liu, C., Liu, C., Liu, Z., Luna, A., Lupi, C., McCarthy, A.J., Mohn, G., Ningthoujam, L.S., Nirrengarten, M., Osono, N., Peate, D.W., Persaud, P., Qui, N., Robinson, C.M., Satolli, S., Sauermilch, I., Schindlbeck, J.C., Skinner, S.M., Straub, S.M., Su, X., Tian, L., van der Zwan, F.M., Wan, S., Wu, H., Xiang, R., Yadav, R., Yi, L., Zhang, C., Zhang, J., Zhang, Y., Zhao, N., Zhong, G., and Zhong, L., 2018. Expedition 367/368 methods. *In* Sun, Z., Jian, Z., Stock, J.M., Larsen, H.C., Klaus, A., Alvarez Zarikian, C.A., and the Expedition 367/368 Scientists, *South China Sea Rifted Margin.* Proceedings of the International Ocean Discovery Program, 367/368: College Station, TX (International Ocean Discovery Program). **https://doi.org/10.14379/iodp.proc.367368.102.2018**

Sun, Z., Stock, J., Jian, Z., McIntosh, K., Alvarez Zarikian, C.A., and Klaus, A., 2016. *Expedition 367/368 Scientific Prospectus: South China Sea Rifted Margin.* International Ocean Discovery Program. **https://doi.org/10.14379/iodp.sp.367368.2016**

Suzuki, S., Takemura, S., Yumul, G.P., Jr., David, S.D., Jr., and Asiedu, D.K., 2000. Composition and provenance of the Upper Cretaceous to Eocene sandstones in Central Palawan, Philippines: constraints on the tectonic development of Palawan. *Island Arc,* 9(4):611–626. **https://doi.org/10.1111/j.1440-1738.2000.00306.x**

Thompson, G.F., 1990. The anomalous demagnetization of pyrrhotite. *Geophysical Journal International,* 103(2):425–430. **https://doi.org/10.1111/j.1365-246X.1990.tb01781.x**

Zhou, D., and Yao, B., 2009. Tectonics and sedimentary basins of the South China Sea: challenges and progresses. *Journal of Earth Science,* 20(1):1–12. **https://doi.org/10.1007/s12583-009-0001-8**

Zijderveld, J.D.A., 1967. AC demagnetization of rocks: analysis of results. *In* Collinson, D.W., Creer, K.M., and Runcorn, S.K. (Eds.), *Developments in Solid Earth Geophysics* (Volume 3): *Methods in Palaeomagnetism:* Amsterdam (Elsevier), 254–286. **https://doi.org/10.1016/B978-1-4832-2894-5.50049-5**

Sun, Z., Jian, Z., Stock, J.M., Larsen, H.C., Klaus, A., Alvarez Zarikian, C.A., and the Expedition 367/368 Scientists
Proceedings of the International Ocean Discovery Program Volume 367/368
publications.iodp.org

https://doi.org/10.14379/iodp.proc.367368.109.2018

Site U1505[1]

Zhimin Jian, Hans Christian Larsen, Carlos A. Alvarez Zarikian, Zhen Sun, Joann M. Stock, Adam Klaus, Jacopo Boaga, Stephen A. Bowden, Anne Briais, Yifeng Chen, Deniz Cukur, Kelsie A. Dadd, Weiwei Ding, Michael J. Dorais, Eric C. Ferré, Fabricio Ferreira, Akira Furusawa, Aaron J. Gewecke, Jessica L. Hinojosa, Tobias W. Höfig, Kan-Hsi Hsiung, Baoqi Huang, Enqing Huang, Xiao-Long Huang, Shijun Jiang, Haiyan Jin, Benjamin G. Johnson, Robert M. Kurzawski, Chao Lei, Baohua Li, Li Li, Yanping Li, Jian Lin, Chang Liu, Chuanlian Liu, Zhifei Liu, Antonio Luna, Claudia Lupi, Anders J. McCarthy, Geoffroy Mohn, Lachit Singh Ningthoujam, Michael Nirrengarten, Nobuaki Osono, David W. Peate, Patricia Persaud, Ning Qiu, Caroline M. Robinson, Sara Satolli, Isabel Sauermilch, Julie C. Schindlbeck, Steven M. Skinner, Susanne M. Straub, Xiang Su, Liyan Tian, Froukje M. van der Zwan, Shiming Wan, Huaichun Wu, Rong Xiang, Rajeev Yadav, Liang Yi, Cuimei Zhang, Jinchang Zhang, Yang Zhang, Ning Zhao, Guangfa Zhong, and Lifeng Zhong[2]

Keywords: International Ocean Discovery Program, IODP, *JOIDES Resolution*, Expedition 367, Expedition 368, Site U1505, northern South China Sea, continent–ocean transition zone, outer margin high, hyperextension, continental breakup, thinning, rifting, T60 unconformity, Oligocene, high sedimentation rate, greigite

Contents

1 Site summary
5 Background and objectives
6 Operations
9 Lithostratigraphy
14 Structural geology
14 Biostratigraphy
19 Paleomagnetism
22 Geochemistry
27 Physical properties
31 Downhole measurements
34 Correlation to seismic data
38 References

Site summary

Background and objectives

Site U1505 (proposed Site SCSII-3D; Sun et al., 2016) is located at 2916.6 m water depth on a broad regional basement high (Figure F1). This site was an alternate to Site U1501, should time be left for drilling following completion of the high-priority sites included in the *Scientific Prospectus* (Sun et al., 2016). Site U1505 was included in Expedition 368 because it might complement findings at Site U1501 and it was within the operational limits of 3400 m drill string imposed by the failure of the drawworks.

Both Sites U1505 and U1501 are located on the same structural high at similar water depths and are 10.5 km apart (Figure F2). The seismic section at Site U1505 generally shows a more horizontal orientation of the seismic reflectors and concordant relationship of the strata than the one at Site U1501, indicating the sediment sequence at Site U1505 should be more complete. The key objective at Site U1505 was to sample the stratigraphic record above seismic unconformity T80 (inferred before drilling to be ~38 Ma in age), and specific goals were to constrain both (1) the sediment responses to the tectonic events and basin evolution since the Eocene and (2) Neogene paleoceanographic and paleoclimatological changes along the northern South China Sea (SCS) margin.

The relatively shallow 2916.6 m water depth at Site U1505 makes it one of the few Ocean Drilling Program (ODP)/Integrated Ocean Drilling Program/International Ocean Discovery Program (IODP) sites above the modern carbonate compensation depth (CCD) of the SCS. The site's hemipelagic deposits, rich in calcareous microfossils, enable the application of stable isotopes, faunal analyses, and other multidisciplinary methods. Key objectives were to reconstruct the east Asian monsoonal climate record in the SCS and upper- and deep-water variations in the western Pacific. Site U1505 will, for the first time, provide an almost continuous sequence of paleoceanographic studies at orbital and millennial timescales since the late Eocene in the SCS. We cored two holes at this site with the advanced piston corer (APC) system to obtain a continuous record of the Pliocene–Pleistocene interval for high-resolution paleoceanographic studies.

[1] Jian, Z., Larsen, H.C., Alvarez Zarikian, C.A., Sun, Z., Stock, J.M., Klaus, A., Boaga, J., Bowden, S.A., Briais, A., Chen, Y., Cukur, D., Dadd, K.A., Ding, W., Dorais, M.J., Ferré, E.C., Ferreira, F., Furusawa, A., Gewecke, A.J., Hinojosa, J.L., Höfig, T.W., Hsiung, K.-H., Huang, B., Huang, E., Huang, X.-L., Jiang, S., Jin, H., Johnson, B.G., Kurzawski, R.M., Lei, C., Li, B., Li, L., Li, Y., Lin, J., Liu, C., Liu, C., Liu, Z., Luna, A., Lupi, C., McCarthy, A.J., Mohn, G., Ningthoujam, L.S., Nirrengarten, M., Osono, N., Peate, D.W., Persaud, P., Qui, N., Robinson, C.M., Satolli, S., Sauermilch, I., Schindlbeck, J.C., Skinner, S.M., Straub, S.M., Su, X., Tian, L., van der Zwan, F.M., Wan, S., Wu, H., Xiang, R., Yadav, R., Yi, L., Zhang, C., Zhang, J., Zhang, Y., Zhao, N., Zhong, G., and Zhong, L., 2018. Site U1505. *In* Sun, Z., Jian, Z., Stock, J.M., Larsen, H.C., Klaus, A., Alvarez Zarikian, C.A., and the Expedition 367/368 Scientists. *South China Sea Rifted Margin.* Proceedings of the International Ocean Discovery Program, 367/368: College Station, TX (International Ocean Discovery Program). https://doi.org/10.14379/iodp.proc.367368.109.2018

[2] **Expedition 367/368 Scientists' addresses.**

MS 367368-109: Published 28 September 2018

This work is distributed under the **Creative Commons Attribution 4.0 International** (CC BY 4.0) license.

Figure F1. Bathymetry with seismic lines, Site U1505. Note that the site is not at the exact crossing of seismic Lines 04ec1555 and 15ecLW1. Seismic profiles across Site U1505 are shown in Figures F5 and F6. Common depth point (CDP) numbers are shown along seismic lines.

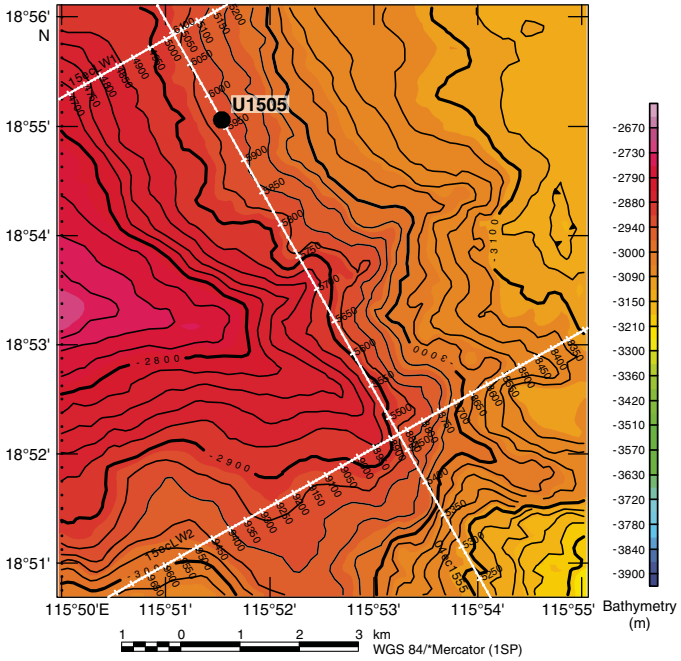

Operations

Four holes were cored with the APC and extended core barrel (XCB) systems at Site U1505. In Hole U1505A (18°55.0560′N, 115°51.5369′E; 2916.6 m water depth), Core 1H misfired and recovered only 0.3 m. In Hole U1505B (18°55.0562′N, 115°51.5370′E; 2918.6 m water depth), a 3.23 m long mudline core was recovered for future education and outreach activities. Hole U1505C (18°55.0570′N, 115°51.5370′E; 2917.4 m water depth) was cored with the APC system to 317 m and then cored with the XCB system to 480.2 m, recovering 480.15 m (100%). Hole U1505D (18°55.0485′N, 115°51.5501′E; 2917.5 m water depth) was cored with the APC system to 184.5 m and recovered 191.43 m (104%). Downhole logging with a modified triple combination (triple combo) tool string was conducted in Hole U1505C from 341.2 m uphole. The maximum drilling depth of 480.2 m was determined by the possible maximum total length (3400 m) of drill string deployment.

Lithostratigraphy

The sediment succession recovered at Site U1505 extends from the Oligocene to the Pleistocene. Two sedimentary units (I and II) were observed (Figure **F3**). Lithostratigraphic Unit I is dominated by nannofossil ooze with varying amounts of foraminifers and clay, as well as biogenic silica in the upper interval of the hole. Unit I is divided into three subunits (IA–IC). Subunit IA (Hole U1505C = 0.00–27.76 m) is composed of dark greenish gray and greenish gray biosiliceous-rich clay with nannofossils, nannofossil-rich clay with biogenic silica, and nannofossil-rich biosiliceous ooze with clay. The abundance of biogenic silica decreases downhole. A pinkish gray, ~6 cm thick, slightly fining upward ash layer occurs at 20.8 m (Hole U1505C), and ash pods were observed at 20.3 m in Hole U1505D. Subunit IB (Hole U1505C = 27.76–273.39 m) is composed of gray to brown nannofossil ooze with minor silty intervals. The color change

Figure F2. Bathymetric maps showing Expedition 367/368 sites (stars), and (A) regional and (B) local coverage of multichannel seismic reflection data and OBS data. Thick blue and red lines are key seismic lines used for planning of the drilling transect. A. Magnetic isochrons (orange lines) from Briais et al. (1993). B. Magnetic picks (orange squares) from the same reference, extracted from the Seton et al. (2014) compilation. Chron labels for the picks correspond to the old edge of the normal polarity intervals (see Ogg et al. [2016] timescale for ages). Orange square = Leg 184 Site 1148, yellow squares = Expedition 349 Sites U1432 and U1435.

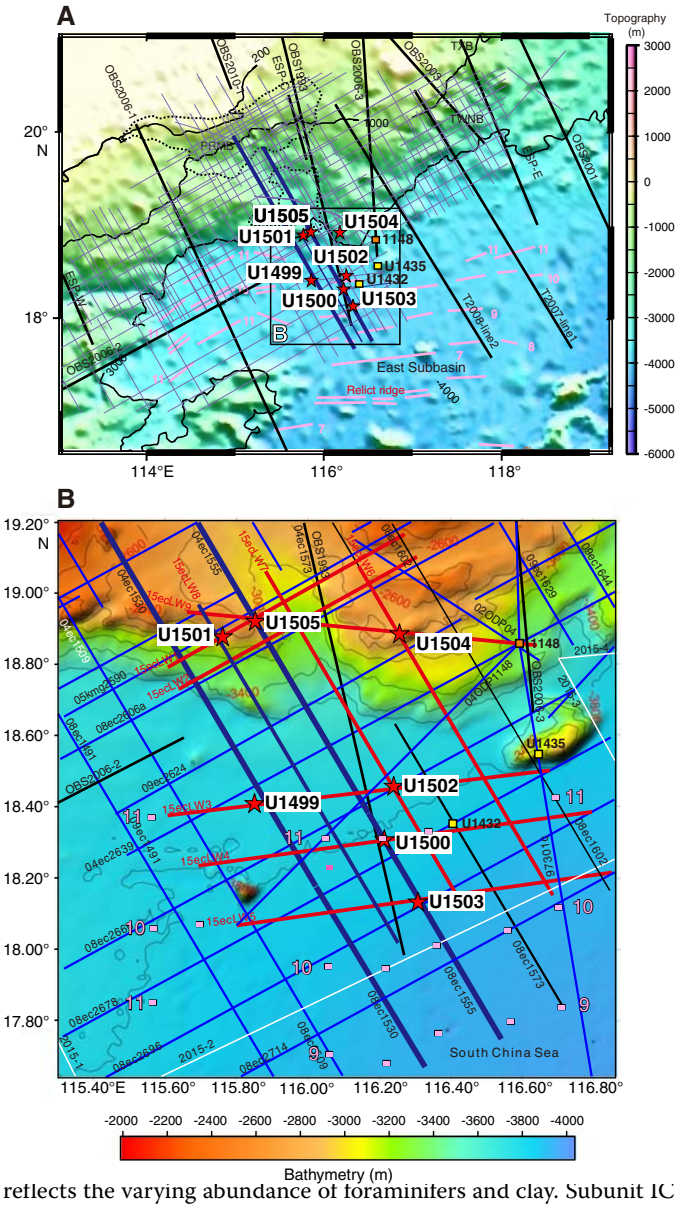

reflects the varying abundance of foraminifers and clay. Subunit IC (Hole U1505C = 273.39–403.79 m) is composed of gray, greenish gray, and light brownish gray clay-rich nannofossil ooze (with foraminifers) and foraminifer-rich nannofossil ooze with clay and minor amounts of nannofossil-rich clay. Unit II (Hole U1505C = 403.50–480.54 m) is dominated by dark greenish gray, well-consolidated silty clay and clayey silt (with nannofossils).

Biostratigraphy

All core catcher samples from Holes U1505A–U1505C were analyzed for calcareous nannofossils, planktonic foraminifers, and diatoms. Additional samples were taken from intervals within the

Figure F3. Lithostratigraphic and biostratigraphic summary, Site U1505.

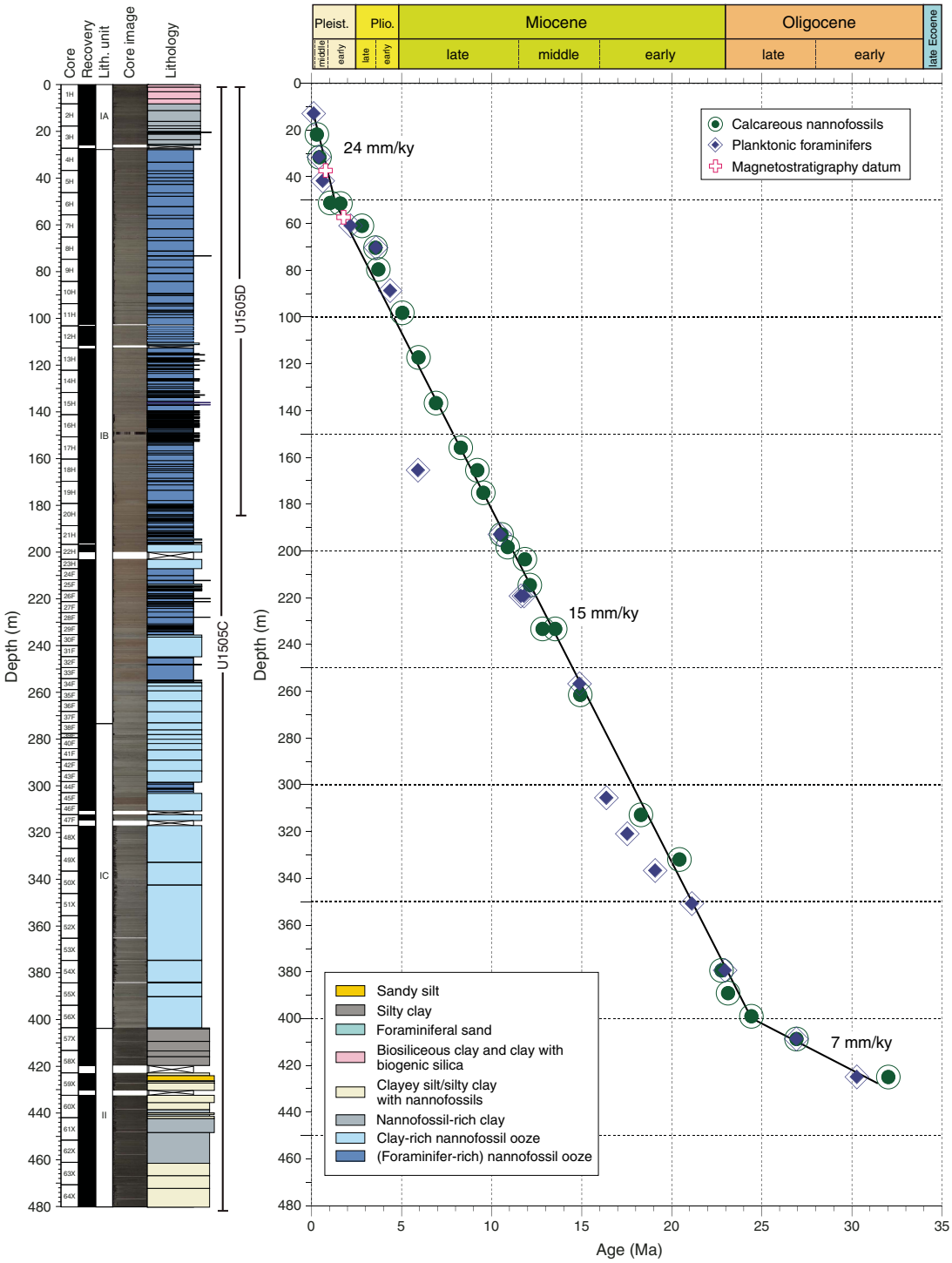

working-half sections when necessary to refine the ages. Hole U1505D was not sampled continuously for biostratigraphic analyses because of time constraints at the end of the expedition, but the sequence recovered spans from the late Miocene to the present (Figure **F3**). Preservation of calcareous microfossils is good in Cores 368-U1505C-1H through 48X and moderate to poor in Cores 49X through 64X. Planktonic foraminifers are abundant or common in Cores 1H through 56X and 59X through 62X and rare in Cores 57X, 58X, 63X, and 64X. Calcareous nannofossils are generally abundant to common in most samples from Hole U1505C, except for those from the upper part of Core 57X.

Forty-five biostratigraphic datums identified in Hole U1505C suggest a continuous succession from the early Oligocene to the Holocene (Figure **F3**). The Pleistocene/Pliocene boundary is placed within Core 7H, the Pliocene/Miocene boundary is placed between Cores 11H and 13H, and the Miocene/Oligocene boundary is

Figure F4. Data characterizing chemical anomalies associated with the T60 regional seismic marker, Site U1505.

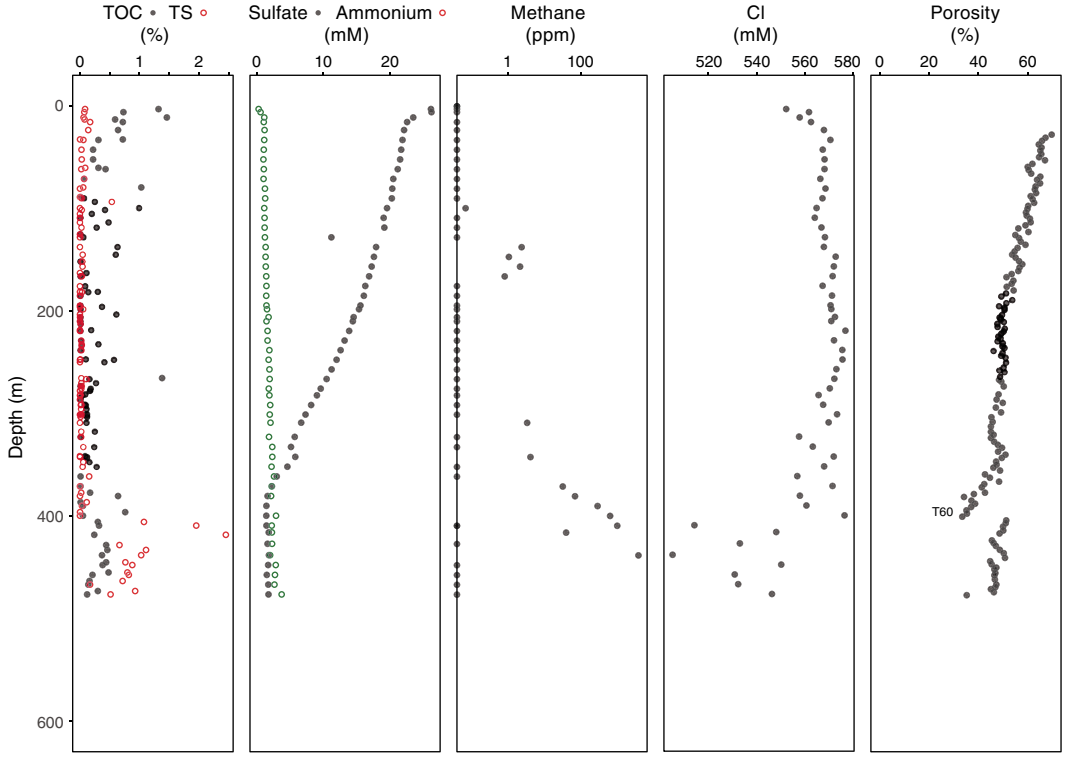

placed between Cores 54X and 55X. Sedimentation rates are ~7 mm/ky in the Oligocene, ~15 mm/ky during the Miocene–Pliocene, and ~24 mm/ky during the Pleistocene.

Relatively low abundances of planktonic foraminifers deeper than Core 57X indicate bathyal depths during the early Oligocene, whereas much higher abundances of planktonic foraminifers shallower than Core 56X suggest a deeper water environment since the late Oligocene.

Paleomagnetism

Only natural remanent magnetization (NRM) was measured with the superconducting rock magnetometer (SRM) in Hole U1505C, except for Sections 1H-1 through 3H-1, which were in-line alternating field (AF) demagnetized in three steps. Most of the 55 AF demagnetized discrete samples show very soft magnetic behavior responsible for the acquisition of a strong, vertical drilling overprint (average inclination = ~81°) that was removed by demagnetization to 10–15 mT. This soft behavior shows that magnetic remanence is dominated by multidomain to pseudosingle-domain titanomagnetite or magnetite. The drilling overprint appears to impact discrete samples far less than core sections (Figure **F19**). The lower part of the hole (Cores 48X through 64X) is characterized by severe drilling disturbance, which causes a large scatter of NRM directions and inclinations.

Magnetostratigraphic data are based on polarities assigned to the archive-half sections and corroborated by directions obtained from oriented discrete samples. The lower boundary of the Brunhes (C1n) normal chron is at 37.4 m (0.781 Ma). The lower boundary (57.4 m) of the reverse polarity r1 is the base of Subchron C1r.3r with an age of 1.778 Ma.

Geochemistry

Low but measurable hydrocarbon gases were detected only in Cores 368-U1505C-53X through 60X (371–438 m). The base of the hole has methane distributions similar to those at Site U1499, whereas the uppermost section is barren of methane, similar to Site U1501. Except for the shallowest 30 m of sediment, total organic carbon (TOC), total nitrogen (TN), and total sulfur (TS) contents are mostly low in lithostratigraphic Unit I, but TS and TOC are slightly higher in Unit II; however, in all cases they are typically <1 wt% (Figure **F4**). Interstitial water chemistry has two important features. The upper part of the hole exhibits patterns similar to those at Site U1501; inhibited sulfate reduction and low chlorine, bromine, and salinity suggest the presence of freshwater at depth. Freshwater at >400 m coincides with the presence of low quantities of methane and the T60 regional seismic unconformity.

Physical properties and downhole measurements

Physical property data were acquired from cores from Holes U1505C (0–480.5 m) and U1505D (0–184 m), including density, magnetic susceptibility, *P*-wave velocity, natural gamma radiation (NGR), color reflectance, and thermal conductivity. Physical property trends allow us to define two physical property units, PP Units 1 (0–403 m) and 2 (403–480 m). The boundary between Units 1 and 2 displays a distinct color change from greenish and light brownish gray to dark greenish gray. This boundary, which corresponds to the seismic stratigraphic T60 unconformity, is associated with a sharp change in physical properties. In Unit 1, sediments in the upper part are composed of foraminifer-rich nannofossil ooze with clay that gradually changes to clay-rich nannofossil ooze in the lower part.

This change is well reflected in the NGR, which increases with depth. The higher NGR values in Unit 2 are related to sediment that primarily consists of silty clay. Magnetic susceptibility values overall gradually decrease with depth. The boundary between Units 1 and 2 shows that density and *P*-wave velocity values drop sharply from ~2.2 to ~1.8 g/cm^3 and from ~2250 to 1750 m/s, respectively. Porosity values abruptly increase from ~35% to ~50%. Thermal conductivity also shows a sharp change at the boundary. Reflectance parameters L* and red, green, blue (RGB) data are well correlated with carbonate content.

Wireline logging was conducted in Hole U1505C using the triple combo tool string, which included the Hostile Environment Natural Gamma Ray Sonde (HNGS), Hostile Environment Litho-Density Sonde (HLDS), Dipole Sonic Imager (DSI), and magnetic susceptibility sonde (MSS). This logging string collected good data from 341.2 m (139.1 m above the bottom of Hole U1505C), which allows the definition of six logging units that mostly correlate with the lithostratigraphic units and core physical property data. Logging Unit 1 extends from the seafloor to the base of the drill pipe at 78 m. NGR is highly attenuated inside the drill pipe. Logging Unit 2 (base of the drill pipe to 96 m) exhibits NGR values that are ~50% lower than the underlying logging Unit 3. In Unit 3 (96–136 m), NGR increases with depth. Logging Unit 4 (136–220 m) exhibits relatively constant V_P and V_S. In logging Unit 5 (200–296 m), resistivity increases with depth, whereas most of the other physical properties are relatively constant. Logging Unit 6 (296–341.2 m) has higher magnetic susceptibility values than logging Unit 5.

Four downhole temperature measurements were conducted in Hole U1505C using the advanced piston corer temperature tool (APCT-3). The temperature values range from 4.7°C at 36.7 m to 11.7°C at 122.8 m, giving a geothermal gradient of 84.6°C/km. A heat flow of 94.0 mW/m^2 was obtained from the linear fit between temperature and thermal resistance. The geothermal gradient and heat flow at Site U1505 are comparable to the relatively high values observed in a number of ODP and IODP sites in this part of the SCS.

Background and objectives

Site U1505 is located at a water depth of 2917.4 m on a broad, regional basement high named the outer margin high (OMH) (Figure **F1**). This site was an alternate for Site U1501, should time be left for drilling following completion of the high-priority sites included in the *Scientific Prospectus*. Both Sites U1505 and U1501 are located on the same structural high at similar water depths and are only 10.46 km apart (Figure **F2**), so the two sites should have similar tectonic backgrounds and scientific objectives. The acoustic basement at Site U1501 consists of highly lithified sandstones and conglomerate, most likely of pre-Cenozoic age. However, the main target for Site U1505 was not the nature of the basement but the sediments within the small Cenozoic half-graben basins present on the OMH. According to the seismic profiles, the sediment sequences at the two sites should be similar to each other and the sedimentation rates should be suitable for high-resolution paleoceanographic and paleoenvironmental reconstructions. The seismic reflectors (Figures **F5**, **F6**) at Site U1505 are more distinctive and in general show a more horizontal orientation and concordant relationship of the strata, indicating the sediment sequence here would be more complete. Therefore, Site U1505 was selected for occupation following the failure to drill down below the cased hole at Site U1503 and the depth limit of 3400 m (water depth plus penetration) imposed by the mechanical failure of the drilling equipment (see **Operations** in the Site U1503 chapter [Larsen et al., 2018b]).

Figure F5. Site U1505 location and penetration depth on seismic dip Line 15ecLW1 (original predrilling interpretation). Seismic stratigraphic T30 (5.3 Ma), T32 (10.0 Ma), T50 (19.1 Ma), T60 (23.0 Ma), T80 (38.0 Ma), T82 (unknown age), and T83 (unknown age) unconformities and acoustic basement Tg reflector are shown (for inferred predrilling ages, see Seismic stratigraphic framework in the Expedition 367/368 methods chapter [Sun et al., 2018]).

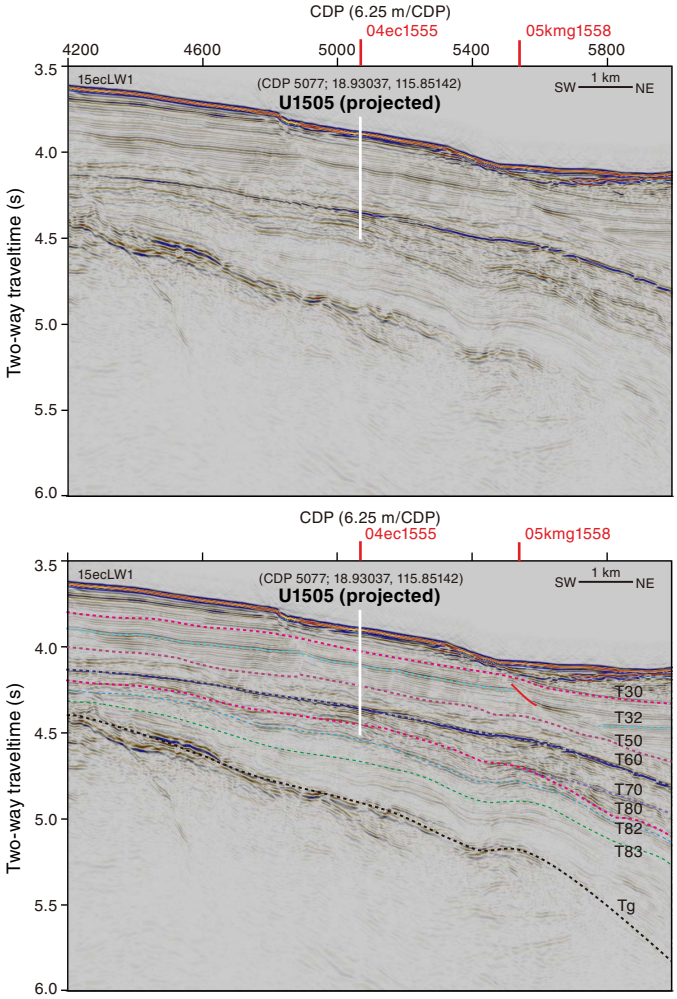

Site U1505 is located near the crossing of seismic Lines 04ec1555 and 15eclLW1 (Figure **F1**). The predrilling interpretation of the seismic unconformities (T30 to T83 and Tg reflector; see the **Expedition 367/368 methods** chapter [Sun et al., 2018]) around Site U1505 is shown in Figures **F5** and **F6**. Using the velocity model (see **Physical properties** and **Correlation to seismic data**), the sedimentary sequence overlying the acoustic basement is ~1220 m thick. Because of the 3400 m depth limit, the maximum targeted drill depth at Site U1505 was 480 mbsf. The key objective at Site U1505 was to sample the stratigraphic record representing all stages since the T80 unconformity (including prerift sediments through synrift to postrift fill). The specific goal was to constrain the sediment responses to the tectonic events and basin evolution since the Eocene, as well as the Neogene paleoceanographic and paleoclimatological changes at the SCS northern margin.

Sampling sediments from the T80 unconformity (38.0 Ma; inferred age before drilling) to the T60 unconformity (23.0 Ma; in-

Figure F6. Site U1505 seismic strike location and penetration depth on Line 04ec1555 (original and predrilling interpretation). See Figure F5 for description of seismic interpretations. Dashed lines = unconformities, red solid lines = faults.

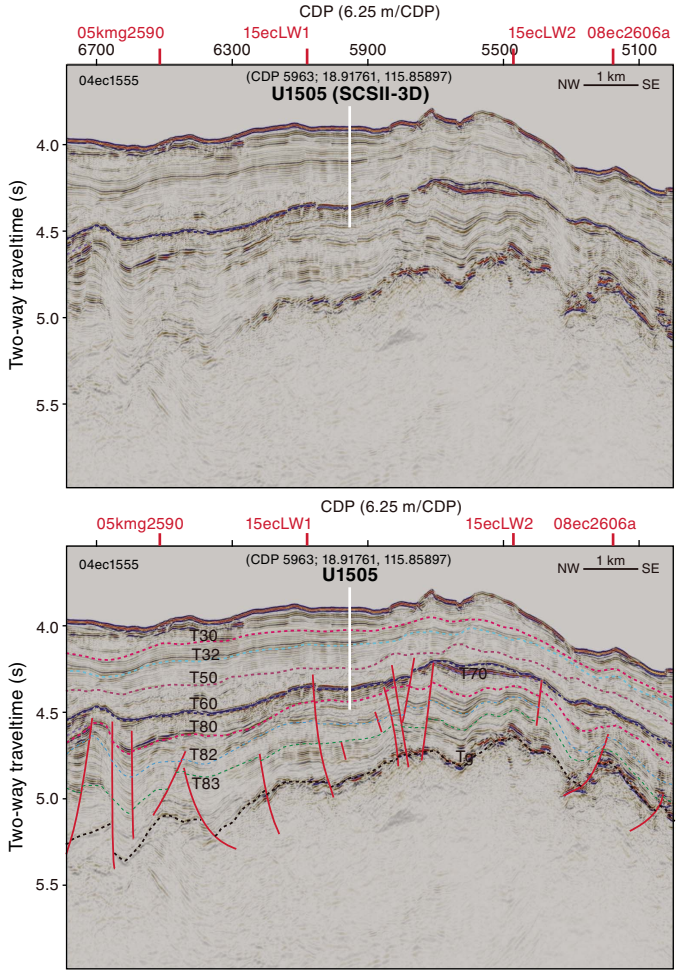

ferred age before drilling) will help us determine the environment before the SCS ocean basin formed, particularly the history of paleowater depth changes from shallow water to deep sea. The basin-wide T60 unconformity is a strong negative reflector showing conformable relationships below and above Site U1505. The nature of this profound reflector is an important objective together with the post-T60 stratigraphic interval, which is also expected to provide information to constrain the rate of thermal subsidence following initial tectonic subsidence recorded within the Eocene to early Oligocene sediments.

The younger stratigraphy above the T60 unconformity is the focus of the Neogene environmental development of the SCS and adjacent landmasses of Southeast Asia. The relatively shallow water depth of 2916.6 m at Site U1505 makes it one of the few ODP/IODP sites above the modern CCD of the SCS. Its hemipelagic deposits rich in calcareous microfossils enable the application of stable isotopes, faunal analyses, and other multidisciplinary methods. Key objectives of this interval sampled by a number of ODP/IODP sites are reconstruction of (1) the East Asian monsoonal climate changes of the SCS and surrounding land and (2) upper and deep-water variations in the western Pacific. For the first time, Site U1505 will underpin an almost continuous oxygen isotope sequence at the orbital and millennial timescales since the late Eocene in the SCS. To achieve this goal, relatively complete sediment sequences are required. Double APC holes were designed at this site to establish a continuous record of the Pliocene to Pleistocene interval for high-resolution paleoceanographic study.

Operations

Four holes were cored at Site U1505 (Table **T1**) using the APC and XCB systems with the objective of recovering a complete sedimentary succession from the early Miocene to Holocene that can supplement the interval sampled at Site U1501 for postexpedition paleoceanographic and paleoclimatological studies. In Hole U1505A (18°55.0560′N, 115°51.5369′E; 2916.6 m water depth), Core 1H misfired (shear pins) and recovered only 0.3 m. In Hole U1505B (18°55.0562′N, 115°51.5370′E; 2918.6 m water depth), Core 1H penetrated 3 m into the seafloor, recovering 3.23 m (107%). With a good mudline core, the hole was terminated. Hole U1505C (18°55.0570′N, 115°51.5370′E; 2917.4 m water depth) was cored to 480.2 m, recovering 480.15 m (100%). Hole U1505D (18°55.0485′N, 115°51.5501′E; 2917.5 m water depth) was cored to 184.5 m, recovering 191.43 m (104%). Downhole logging with a modified triple combo tool was conducted in Hole U1505C.

Transit to Site U1505

The R/V *JOIDES Resolution* began the transit from Site U1504 to Site U1505 at 1854 h on 28 May 2017 and arrived on site at 2112 h the same day. The thrusters were lowered, and the heading was controlled at 2148 h, beginning operations at Site U1505.

Holes U1505A and U1505B

An APC/XCB bottom-hole assembly (BHA) was made up, and a precision depth recorder (PDR) measurement was taken to help determine the seafloor depth. As the drill string was being lowered to the seafloor, we deployed the subsea camera system to observe the end of the pipe tag the seafloor. APC coring started in Hole U1505A at 0545 h on 29 May 2017 at a water depth of 2916.6 m. With the bit at 2911.2 m, the core barrel was recovered to the surface after an apparent misfire (failed shear pins) of the APC. The barrel had 0.38 m of core, far less than anticipated, and the hole was terminated at 1200 h to attempt a better mudline.

The bit was spaced out to 2912.1 m below sea level (mbsl), and coring in Hole U1505B started at 1235 h on 29 May. The core was recovered with 3.23 m of sediment. With a good mudline core, Hole U1505B was terminated at 1300 h.

Hole U1505C

The vessel was offset 20 m east, and the bit was spaced out to 2916.1 mbsl. Because of a leak in the newly replaced low clutch diaphragm, the decision was made to core with the APC system and then core with the XCB system to refusal or to the maximum drill string weight that could be lifted using the high clutch (whichever came first). Hole U1505C (18°55.0570′N, 115°51.5370′E) was started at 1340 h on 29 May 2017. Seafloor was calculated at 2917.4 mbsl based on recovery from Core 1H. The full-length APC system was used to refusal at 207.1 m with APCT-3 temperature measurements taken on Cores 4H, 7H, 10H, and 13H. All four deployments produced good temperature data. APC refusal was determined after partial strokes on five consecutive cores, beginning with Core 19H and continuing through Core 23H. The half-length APC (HLAPC) system was then deployed and used to recover Cores 24F through

Table T1. Site U1505 core summary. DRF = drilling depth below rig floor, DSF = drilling depth below seafloor. NA = not applicable. Core type: H = advanced piston corer (APC), F = half-length APC, XCB = extended core barrel. APCT-3 = advanced piston corer temperature tool. (Continued on next page.) **Download available in CSV format**.

Hole U1505A

Latitude:	18°55.0506′N
Longitude:	115° 51.5369′E
Seafloor (drill pipe measurement below rig floor, m DRF):	2916.57
Time on hole (days):	0.59
Total depth (drill pipe measurement from rig floor, m DRF):	2928
Distance between rig floor and sea level (m):	11.43
Total penetration (drilling depth below seafloor, m DSF):	0.3
Total length of cored section (m):	0.3
Total core recovered (m):	0.38
Core recovery (%):	126.67
Drilled interval (m):	NA
Total cores (no.):	1

Hole U1505B

Latitude:	18°55.0562′N
Longitude:	115°51.5370′E
Seafloor (drill pipe measurement below rig floor, m DRF):	2918.57
Time on hole (days):	0.04
Total depth (drill pipe measurement from rig floor, m DRF):	2930
Distance between rig floor and sea level (m):	11.43
Total penetration (drilling depth below seafloor, m DSF):	3
Total length of cored section (m):	3
Total core recovered (m):	3.23
Core recovery (%):	107.67
Drilled interval (m):	NA
Total cores (no.):	1

Hole U1505C

Latitude:	18°55.0570′N
Longitude:	115°51.5491′E
Seafloor (drill pipe measurement below rig floor, m DRF):	2917.37
Time on hole (days):	4.29
Total depth (drill pipe measurement from rig floor, m DRF):	2928.8
Distance between rig floor and sea level (m):	11.43
Total penetration (drilling depth below seafloor, m DSF):	480.2
Total length of cored section (m):	480.2
Total core recovered (m):	480.15
Core recovery (%):	99.99
Drilled interval (m):	NA
Total cores (no.):	64

Hole U1501D

Latitude:	18°55.0458′N
Longitude:	115°51.5501′E
Seafloor (drill pipe measurement below rig floor, m DRF):	2917
Time on hole (days):	1.2
Total depth (drill pipe measurement from rig floor, m DRF):	2928.5
Distance between rig floor and sea level (m):	11.5
Total penetration (drilling depth below seafloor, m DSF):	184.5
Total length of cored section (m):	184.5
Total core recovered (m):	191.43
Core recovery (%):	103.76
Drilled interval (m):	NA
Total cores (no.):	20

Core	Type	Top of interval DSF (m)	Bottom of interval DSF (m)	Interval advanced (m)	Core recovered length (m)	Curated length (m)	Recovery (%)	Time on deck UTC (h)	Time to cut core (min)	Core barrel	Mud pumped (bbl)	Driller's notes
368-U1505A-												
1	H	0	0.3	0.3	0.38	0.38	127	5/29/2017 03:40				
		Hole U1505A totals:		0.3	0.38	0.38	127					
368-U1505B-												
1	H	0	3	3	3.23	3.23	108	5/29/2017 04:55				
		Hole U1505B totals:		3	3.23	3.23	108					
368-U1505C-												
1	H	0	8.2	8.2	8.23	8.23	100	5/29/2017 06:05		Nonmagnetic		
2	H	8.2	17.7	9.5	9.54	9.54	100	5/29/2017 07:05		Nonmagnetic		
3	H	17.7	27.2	9.5	8.34	8.34	88	5/29/2017 08:05		Nonmagnetic		
4	H	27.2	36.7	9.5	9.97	9.97	105	5/29/2017 09:10		Nonmagnetic		APCT-3
5	H	36.7	46.2	9.5	9.81	9.81	103	5/29/2017 10:10		Nonmagnetic		
6	H	46.2	55.7	9.5	10.03	10.03	106	5/29/2017 11:10		Nonmagnetic		
7	H	55.7	65.2	9.5	10	10	105	5/29/2017 12:15		Nonmagnetic		APCT-3
8	H	65.2	74.7	9.5	9.75	9.75	103	5/29/2017 13:15		Nonmagnetic		
9	H	74.7	84.2	9.5	9.48	9.48	100	5/29/2017 14:10		Nonmagnetic		
10	H	84.2	93.7	9.5	9.45	9.45	99	5/29/2017 15:25		Nonmagnetic		APCT-3
11	H	93.7	103.2	9.5	9.08	9.08	96	5/29/2017 16:25		Nonmagnetic		
12	H	103.2	112.7	9.5	8.53	8.53	90	5/29/2017 17:20		Nonmagnetic		
13	H	112.7	122.2	9.5	10.01	10.01	105	5/29/2017 18:35		Nonmagnetic		APCT-3
14	H	122.2	131.7	9.5	10.03	10.03	106	5/29/2017 19:30		Nonmagnetic		
15	H	131.7	141.2	9.5	9.62	9.62	101	5/29/2017 20:35		Nonmagnetic		
16	H	141.2	150.7	9.5	9.7	9.7	102	5/29/2017 21:25		Nonmagnetic		
17	H	150.7	160.2	9.5	9.97	9.97	105	5/29/2017 22:25		Nonmagnetic		
18	H	160.2	169.7	9.5	10.08	10.08	106	5/29/2017 23:30		Nonmagnetic		
19	H	169.7	179.2	9.5	10.05	10.05	106	5/30/2017 00:25		Nonmagnetic		
20	H	179.2	188.7	9.5	10.06	10.06	106	5/30/2017 01:20		Nonmagnetic		
21	H	188.7	196.7	8	7.83	7.83	98	5/30/2017 02:10		Nonmagnetic		
22	H	196.7	203.1	6.4	3.36	3.36	53	5/30/2017 03:05		Nonmagnetic		
23	H	203.1	207.1	4	3.95	3.95	99	5/30/2017 03:55		Nonmagnetic		
24	F	207.1	211.8	4.7	5.08	5.08	108	5/30/2017 05:15		Nonmagnetic		
25	F	211.8	216.5	4.7	5.12	5.12	109	5/30/2017 06:10		Nonmagnetic		
26	F	216.5	221.2	4.7	5.04	5.04	107	5/30/2017 07:00		Nonmagnetic		
27	F	221.2	225.9	4.7	5.13	5.13	109	5/30/2017 08:05		Nonmagnetic		
28	F	225.9	230.6	4.7	5.03	5.03	107	5/30/2017 09:00		Nonmagnetic		
29	F	230.6	235.3	4.7	5.09	5.09	108	5/30/2017 09:45		Nonmagnetic		
30	F	235.3	240	4.7	5.02	5.02	107	5/30/2017 11:10		Nonmagnetic		

Table T1 (continued).

Core	Type	Top of interval DSF (m)	Bottom of interval DSF (m)	Interval advanced (m)	Core recovered length (m)	Curated length (m)	Recovery (%)	Time on deck UTC (h)	Time to cut core (min)	Core barrel	Mud pumped (bbl)	Driller's notes
31	F	240	244.7	4.7	5.02	5.02	107	5/30/2017 11:55		Nonmagnetic		
32	F	244.7	249.4	4.7	5.04	5.04	107	5/30/2017 12:50		Nonmagnetic		
33	F	249.4	254.1	4.7	5.06	5.06	108	5/30/2017 13:45		Nonmagnetic		
34	F	254.1	258.8	4.7	5.07	5.07	108	5/30/2017 14:40		Nonmagnetic		
35	F	258.8	263.5	4.7	5.03	5.03	107	5/30/2017 15:35		Nonmagnetic		
36	F	263.5	268.2	4.7	5.03	5.03	107	5/30/2017 16:30		Nonmagnetic		
37	F	268.2	272.9	4.7	4.81	4.81	102	5/30/2017 17:20		Nonmagnetic		
38	F	272.9	277.6	4.7	5.05	5.05	107	5/30/2017 18:10		Nonmagnetic		
39	F	277.6	279.4	1.8	1.8	1.8	100	5/30/2017 20:00		Nonmagnetic		
40	F	279.4	284.1	4.7	5.04	5.04	107	5/30/2017 21:30		Nonmagnetic		
41	F	284.1	288.8	4.7	4.91	4.91	104	5/30/2017 22:30		Nonmagnetic		
42	F	288.8	293.5	4.7	5.03	5.03	107	5/30/2017 23:15		Nonmagnetic		
43	F	293.5	298.2	4.7	4.72	4.72	100	5/30/2017 00:00		Nonmagnetic		
44	F	298.2	302.9	4.7	5.01	5.01	107	5/31/2017 00:50		Nonmagnetic		
45	F	302.9	307.6	4.7	5.02	5.02	107	5/31/2017 01:40		Nonmagnetic		
46	F	307.6	312.3	4.7	3.14	3.14	67	5/31/2017 02:40		Nonmagnetic		
47	F	312.3	317	4.7	2.6	2.6	55	5/31/2017 03:35		Nonmagnetic		
48	X	317	326.8	9.8	9.93	9.93	101	5/31/2017 05:55				
49	X	326.8	336.5	9.7	9.9	9.9	102	5/31/2017 08:15				
50	X	336.5	346.1	9.6	9.62	9.62	100	5/31/2017 10:25				
51	X	346.1	355.6	9.5	9.87	9.87	104	5/31/2017 13:20				
52	X	355.6	365.2	9.6	9.38	9.38	98	5/31/2017 16:10				
53	X	365.2	374.7	9.5	9.35	9.37	98	5/31/2017 18:15				
54	X	374.7	384.3	9.6	9.23	9.25	96	5/31/2017 20:40				
55	X	384.3	393.9	9.6	9.81	9.81	102	5/31/2017 23:10				
56	X	393.9	403.5	9.6	9.94	9.94	104	6/1/2017 01:45				
57	X	403.5	413.2	9.7	9.99	9.99	103	6/1/2017 03:40				
58	X	413.2	422.8	9.6	6.38	6.38	66	6/1/2017 06:15				
59	X	422.8	432.4	9.6	7.46	7.46	78	6/1/2017 09:40				
60	X	432.4	442	9.6	9.91	9.91	103	6/1/2017 12:45				
61	X	442	451.6	9.6	9.93	9.93	103	6/1/2017 15:20				
62	X	451.6	461.1	9.5	9.86	9.89	104	6/1/2017 17:40				
63	X	461.1	470.7	9.6	9.99	9.99	104	6/1/2017 20:00				
64	X	470.7	480.2	9.5	9.84	9.84	104	6/1/2017 22:30				
			Hole U1505C totals:	480.2	480.15	480.15	100					
368-U1505D-												
1	H	0	4	4	3.95	3.95	99	6/2/2017 14:20		Nonmagnetic		
2	H	4	13.5	9.5	9.62	9.62	101	6/2/2017 15:15		Nonmagnetic		
3	H	13.5	23	9.5	9.78	9.78	103	6/2/2017 16:20		Nonmagnetic		
4	H	23	32.5	9.5	9.8	9.8	103	6/2/2017 17:35		Nonmagnetic		
5	H	32.5	42	9.5	9.92	9.92	104	6/2/2017 18:25		Nonmagnetic		
6	H	42	51.5	9.5	9.91	9.91	104	6/2/2017 19:20		Nonmagnetic		
7	H	51.5	61	9.5	10.01	10.01	105	6/2/2017 20:15		Nonmagnetic		
8	H	61	70.5	9.5	9.98	9.98	105	6/2/2017 21:10		Nonmagnetic		
9	H	70.5	80	9.5	9.91	9.91	104	6/2/2017 22:10		Nonmagnetic		
10	H	80	89.5	9.5	9.84	9.84	104	6/2/2017 23:05		Nonmagnetic		
11	H	89.5	99	9.5	10.1	10.1	106	6/2/2017 23:55		Nonmagnetic		
12	H	99	108.5	9.5	9.94	9.94	105	6/3/2017 00:45		Nonmagnetic		
13	H	108.5	118	9.5	9.78	9.78	103	6/3/2017 01:35		Nonmagnetic		
14	H	118	127.5	9.5	9.82	9.82	103	6/3/2017 02:25		Nonmagnetic		
15	H	127.5	137	9.5	9.17	9.17	97	6/3/2017 03:20		Nonmagnetic		
16	H	137	146.5	9.5	10.1	10.1	106	6/3/2017 04:10		Nonmagnetic		
17	H	146.5	156	9.5	9.66	9.66	102	6/3/2017 05:10		Nonmagnetic		
18	H	156	165.5	9.5	10.14	10.14	107	6/3/2017 06:05		Nonmagnetic		
19	H	165.5	175	9.5	10.18	10.18	107	6/3/2017 07:00		Nonmagnetic		
20	H	175	184.5	9.5	9.82	9.82	103	6/3/2017 08:10		Nonmagnetic		
			Hole U1505D totals:	184.5	191.43	191.43	101					
			Site U1505 totals:	668.0	675.19	675.19	101					

47F. All HLAPC cores were considered partial strokes, with the standpipe retaining pressure after each core. The residual pressure in the standpipe was bled off using the Cameron Orbit valve. HLAPC refusal was determined with recovery of 3.14 m and 2.60 m on Cores 46F and 47F, respectively. While bleeding pressure on Core 47F, the diaphragm on the pneumatic actuation for the Orbit valve failed. The pressure was bled by manually opening the valve, and the valve was taken out of service and repaired.

The XCB system was then deployed and used to core to 480.2 m before reaching the maximum allowable drill string weight dictated the end of coring operations. The hole was displaced using heavy mud, and the bit was raised to 80.1 m in preparation for logging.

A modified triple combo tool string was rigged up and lowered into the hole. The tool string was exceptionally long, consisting of all tools typically run as part of the triple combo (MSS; High-Resolution Laterolog Array [HRLA]; HLDS, with source; HNGS; Enhanced Digital Telemetry Cartridge [EDTC]; and logging equipment head-q tension [LEH-QT]), with the addition of the DSI tool for acoustic velocity. The DSI was added to the first run in anticipation of potential hole problems that might prevent subsequent runs based on experience at nearby sites with similar lithology. The triple combo began collecting data a few meters above the seafloor and recorded continuously to the deepest point the tools could reach, a firm hole obstruction at 341.2 m. The tool string was unable to pass below that depth even after several attempts. Accordingly, the repeat pass was conducted from that depth for a length of ~110 m, and then the main pass was also conducted from that depth up to just above the seafloor. During the run, the triple combo collected NGR, density (with caliper), acoustic velocity, neutron porosity, and magnetic susceptibility data. The caliper indicated that the hole diameter was too large (>14 inches) for effectively collecting useful data with the Formation MicroScanner (FMS) and Versatile Seismic Imager tool strings. Therefore, the decision was made to end downhole logging operations in Hole U1505C. The tools were pulled to the surface after logging was completed and rigged down. The bit was then raised, clearing the seafloor at 1755 h on 2 June and ending Hole U1505C.

Total time spent on Hole U1505C was 103 h (4.3 days). The APC, HLAPC, and XCB systems were deployed in the hole, coring a 480.2 m interval and recovering 480.15 m (100%). The APC system was used to cut 23 cores over a 207.1 m interval with 100% recovery. The HLAPC system was used to cut 24 cores over a 109.9 m interval, recovering 112.9 m (103%). The XCB system recovered 160.4 m of sediment (98%) over a 163.2 m interval. Nonmagnetic core barrels were used on all cores from this hole. All full-length APC cores were oriented. APCT-3 temperature measurements were taken on Cores 4H, 7H, 10H, and 13H.

Hole U1505D

The vessel was offset 20 m south, and the bit was spaced out to 2911.6 m. APC coring in Hole U1505D started at 2200 h on 2 June 2017. Seafloor was calculated at 2917.5 mbsl based on recovery from Core 1H. The hole was cored to a total depth of 184.5 m using only the APC system. The bit was then recovered to the surface, clearing the seafloor at 1800 h and the rotary table at 2310 h on 2 June. The beacon was recovered while raising the pipe and was on deck at 1953 h. The thrusters were raised, and the rig floor was secured for transit. The vessel was underway to return to Site U1504 at 0048 h on 3 June, ending Hole U1505D and Site U1505. Our plan was to use the time remaining on the expedition to drill a second hole to basement at Site U1504.

Overall, 20 APC cores were taken in Hole U1505D over a 184.5 m interval, with 191.43 m recovered (104%). Nonmagnetic core barrels were used for all cores, and all cores were oriented using the Icefield MI-5 core orientation tool.

Lithostratigraphy

We examined the lithostratigraphy in Holes U1505A, U1505C, and U1505D (Figure **F7**) and defined two lithostratigraphic units. In Hole U1505A, the mudline core misfired (see **Operations**), and therefore only a 0.33 m interval of the sediment section was recovered. In Hole U1505B, only a mudline core was recovered for educational use, and the core was not described. Hole U1505C was cored to ~480 m using the APC and XCB systems and was used to define the lithostratigraphic unit boundaries. Hole U1505D only recovered the upper section of lithostratigraphic Unit I. Unit I is defined and divided into three subunits based on visual core description, smear slide and thin section inspection, and X-ray diffraction (XRD) analysis (see **Lithostratigraphy** in the Expedition 367/368 methods chapter [Sun et al., 2018]).

The sediment succession recovered at Site U1505 extends from 0.00 to 480.54 m (Cores 368-U1505A-1H, 368-U1505C-1H through 64X, and 368-U1505D-1H through 20H).

Unit I is dominated by nannofossil ooze with varying amounts of foraminifers and clay and, in the upper interval of the core, with biogenic silica. The change downhole to Unit II is marked by a sharp change from greenish gray nannofossil ooze (Unit I) to dark greenish gray silty clay and clayey silt with nannofossils (Unit II). The contact between Units I and II occurs between two full-recovery cores but may not have been fully recovered.

Unit description

Unit I

Intervals: 368-U1505A-1H-1, 0 cm, to 1H-1, 33 cm;
368-U1505C-1H-1, 0 cm, to 56X-CC, 37 cm;
368-U1505D-1H-1, 0 cm, to 20H-CC, 20 cm
Depths: Hole U1505A = 0–0.33 m; Hole U1505C = 0–403.79 m;
Hole U1505D = 0–184.82 m
Age: Pleistocene–late Oligocene

Lithology and sedimentary structures

Lithostratigraphic Unit I is dominated by nannofossil ooze with varying amounts of foraminifers and clay. The upper part is biosiliceous-rich clay (Figure **F8D**) with minor nannofossil-rich biosiliceous ooze with clay. The unit is divided into three subunits, IA–IC, based on changes in the biogenic component of the sediment and color changes that coincide with subtle changes in the sediment components.

The boundary between Units I and II is marked by a sharp change in lithology from nannofossil ooze–dominated sediments to silt and clay–dominated sediments.

Bulk mineralogy and chemistry

The bulk mineralogy results of XRD analyses are listed in Table **T2** and shown in Figure **F9**, which also shows the downcore variations in the relative abundance of minerals in bulk sediments at Site U1505. Unit I sediment is composed mainly of calcite, quartz, plagioclase, halite, and pyrite, as well as K-feldspar and clay minerals, including smectite, illite, kaolinite, and chlorite. In general, the percentages of halite and most terrigenous minerals in Unit I, including quartz, plagioclase, K-feldspar, and clay minerals (illite, kaolinite, and chlorite) decrease downhole, whereas calcite and pyrite increase.

Compositional analyses of the nannofossil ooze in Sections 368-U1505C-56X-7 and 56X-CC (Subunit IC) were made directly on the archive half of the core using the handheld portable X-ray fluorescence spectrometer (pXRF) (see **Igneous and metamorphic petrology** in the Expedition 367/368 methods chapter [Sun et al., 2018]) to examine in detail the transition between Units I and II (Table **T3**). The 16 intervals analyzed in Unit I show no variation in composition, with CaO contents of ~30 wt%, SiO_2 contents of ~20–

Figure F7. Lithostratigraphic summary, Site U1505.

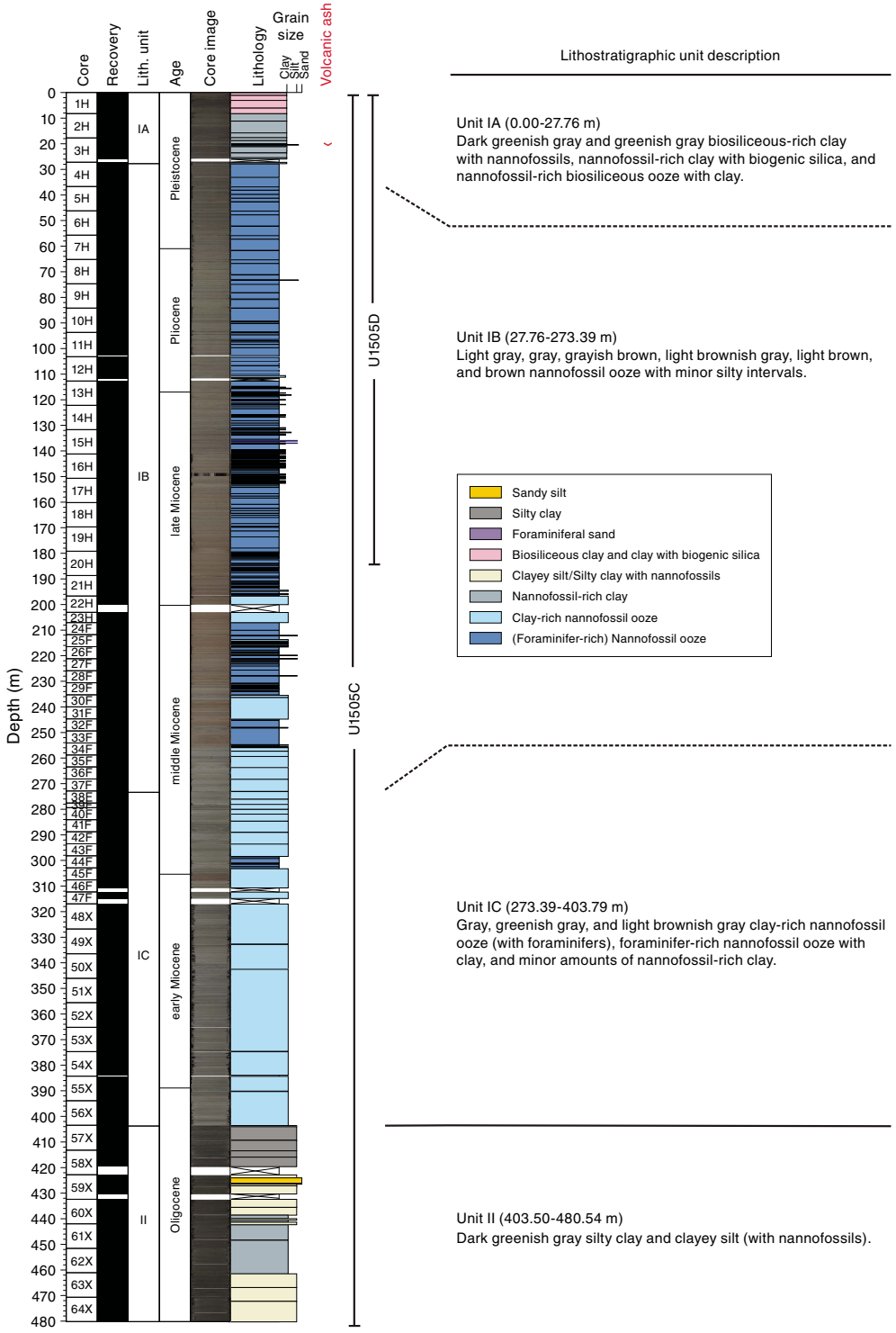

24 wt%, and lower Al_2O_3 (~5 wt%), Fe_2O_3 (<3 wt%), and MgO (<2 wt%) abundances. The ooze has Sr contents between 700 and 800 ppm and Zr contents between 50 and 60 ppm.

Subunit IA

Intervals: 368-U1505A-1H-1, 0–33 cm;
368-U1505C-1H-1, 0 cm, to 4H-1, 56 cm;
368-U1505D-1H-1, 0 cm, to 4H-3, 150 cm

Depths: Hole U1505A = 0–0.33 m; Hole U1505C = 0–27.76 m; Hole U1505D = 0–27.50 m

Age: Pleistocene

Subunit IA spans the recovered uppermost 27.76 m in Hole U1505C and 27.50 m in Hole U1505D and is dominated by dark greenish gray and greenish gray biosiliceous-rich clay with nannofossils, nannofossil-rich clay with biogenic silica, and nannofossil-rich biosiliceous ooze with clay (Figure **F8A**). The abundance of bio-

Figure F8. Representative images of core sections from three subunits in Unit I, Hole U1505C. A. Dark greenish gray biosiliceous-rich clay with nannofossils. A vague lamination is disrupted by bioturbation. B. Slight variation in texture and color related to changes in the percentage of clay and foraminifers. Upper part is more clay rich than the lower section. C. Light brownish gray clay-rich nannofossil ooze (with foraminifers). As for B, the variation in color and texture in Subunit IC corresponds to variations in the lithology. Mottled color variation is due to bioturbation. D. Nannofossil-rich clay with nannofossils, sponge spicules, radiolarians, and terrigenous grains in Subunit IA.

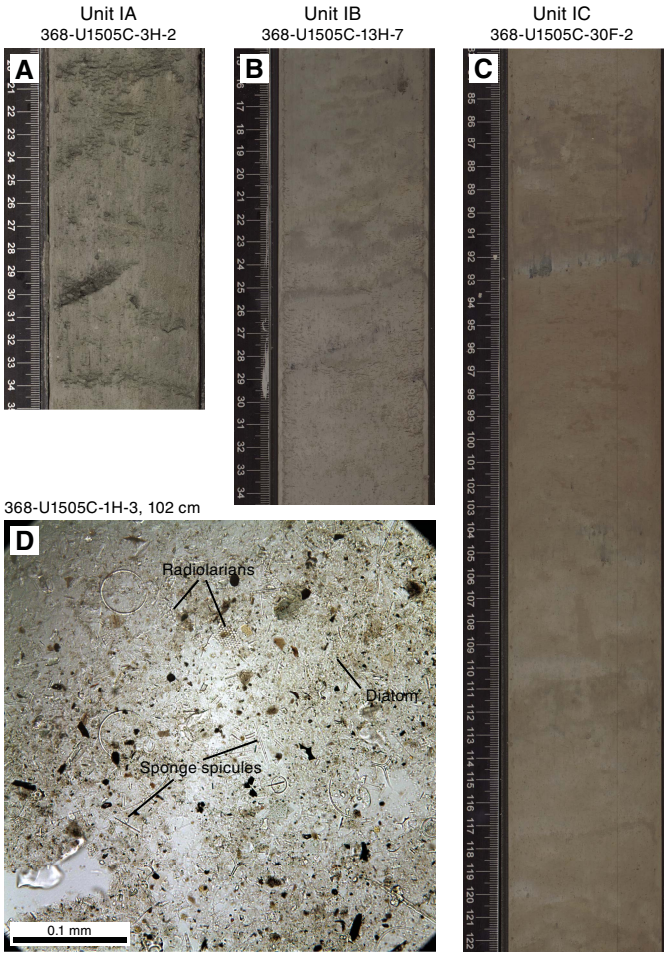

Table T2. Mineral percentages, Site U1505. **View table in PDF format. Download available in CSV format.**

genic silica decreases downhole. The fine-grained component comprises nannofossils, foraminifers, diatoms, sponge spicules, radiolarians, and terrigenous grains, including clay minerals, and rare quartz and feldspar (Figure **F8D**). The sediment is well sorted and unlithified. The average grain size is clay, and very fine sand is the maximum grain size. Bioturbation is heavy (Figure **F8A**).

A pinkish gray, ~6 cm thick, slightly normally graded ash layer was found in interval 368-U1505C-3H-3, 24–32 cm (Figure **F10A**), and ash pods were found at the corresponding depth in Hole U1505D in interval U1505D-3H-5, 83–86 cm (Figure **F10B**).

The base of Subunit IA is marked by both a color change from dark greenish gray to dark gray sediment in Subunit IB and by a lithologic change that reflects an increase in the percentage of foraminifers.

Subunit IB

Intervals: 368-U1505C-4H-1, 56 cm, to 38F-1, 49 cm; 368-U1505D-4H-4, 0 cm, to 20H-CC, 20 cm
Depths: Hole U1505C = 27.76–273.39 m; Hole U1505D = 27.50–184.82
Age: Pleistocene to middle Miocene

Subunit IB is 245.63 m thick and comprises light gray, gray, grayish brown, light brownish gray, light brown, and brown nannofossil ooze with minor silty intervals (Figure **F8B**). The color change reflects the varying abundance of foraminifers and clay. The sediment is well sorted and slightly consolidated. The sediment structure is massive. The average grain size is clay, and medium sand is the maximum grain size. Boundaries are subhorizontal, horizontal, or inclined. Bioturbation is moderate to heavy. Thin, silty, fining-upward intervals with erosive bottom contacts are common in Subunit IB (Figure **F11**). One ~5 cm thick very dark greenish gray ash layer with a dispersed top and a sharp basal contact is found in interval 368-U1505C-8H-6, 47–52 cm (Figure **F10C, F10D**). Pyrite patches are common.

From Core 19H downhole, basal flow-in destroys the sediment structures (Figure **F12**).

The boundary between Subunits IB and IC is defined by the first occurrence of burrows of *Zoophycos*.

Subunit IC

Interval: 368-U1505C-38F-1, 49 cm, to 56X-CC, 37 cm
Depth: 273.39–403.79 m
Age: middle Miocene to late Oligocene

Subunit IC is 130.40 m thick and composed of gray, greenish gray, and light brownish gray clay-rich nannofossil ooze (with foraminifers), foraminifer-rich nannofossil ooze with clay, and minor amounts of nannofossil-rich clay (Figure **F8C**). The sediment is well sorted and well consolidated. The average grain size is clay, and very fine sand is the maximum grain size.

Contacts between layers are often bioturbated or gradational, horizontal to subhorizontal, or inclined. The bioturbation in Subunit IC sediment is heavy to complete. Greenish reduction spots are common and are related to burrows. Burrows are often filled with foraminifers and are dark gray in color. The trace fossil assemblage includes *Chondrites, Thalassinoides, Planolites,* and *Zoophycos* (Figure **F13**).

Compositional analyses of the ooze in Subunit IC were made directly on the archive half of the core using the handheld pXRF instrument (see **Igneous and metamorphic petrology** in the Expedition 367/368 methods chapter [Sun et al., 2018]) (Table **T3**). The ooze (16 analyses) in Sections 368-U1505C-56X-7 and 56X-CC shows only minor variation in bulk composition. The major components are CaO (28–35 wt%), SiO_2 (18–25 wt%), and Al_2O_3 (4–6 wt%). The ooze has Sr contents of 730–840 ppm.

The boundary between Subunit IC and Unit II is characterized by a sharp change from greenish gray clay-rich nannofossil ooze to very dark greenish gray silty clay.

Unit II

Interval: 368-U1505C-57X-1, 0 cm, to 64X-CC, 36 cm
Depth: 403.50–480.54 m
Age: Oligocene

Figure F9. Bulk mineralogy data from shipboard XRD analysis, Hole U1505C.

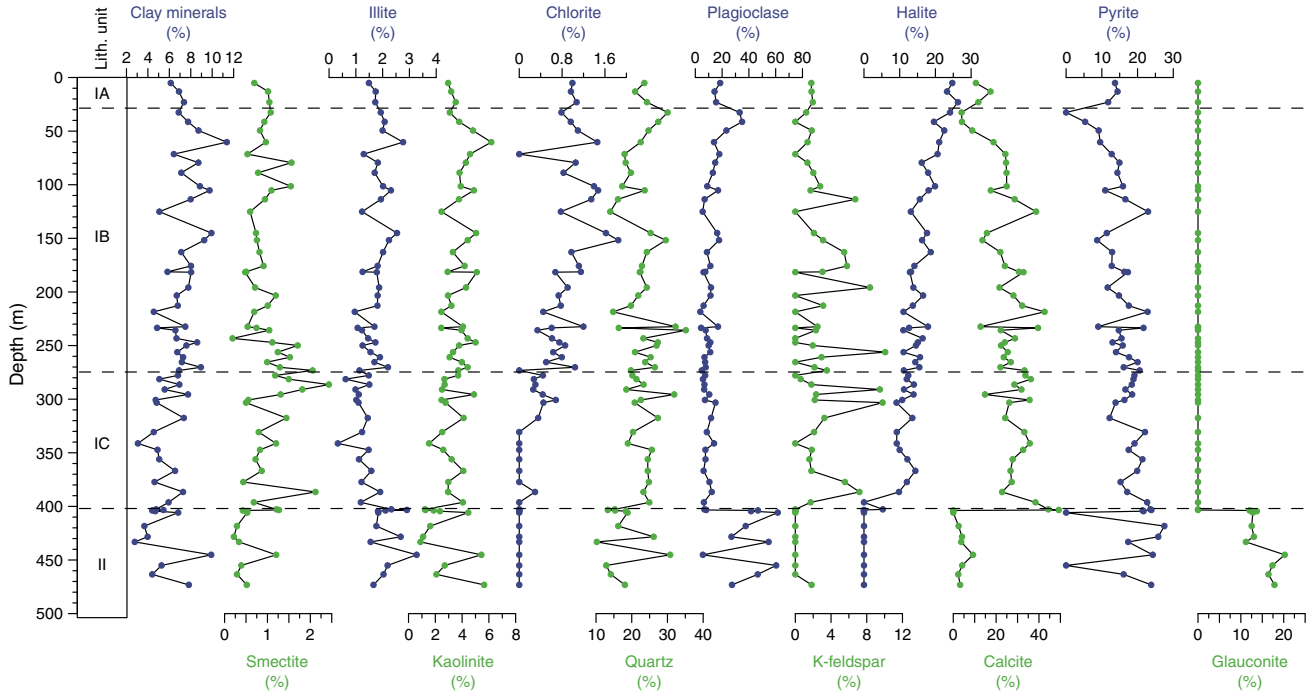

Table T3. Bulk chemistry data obtained from shipboard handheld portable X-ray fluorescence analysis, Site U1505. **View table in PDF format. Download available in CSV format.**

Lithology and sedimentary structures

Unit II is dominated by dark greenish gray, well-consolidated silty clay and clayey silt (with nannofossils). The amount of nannofossils increases downhole (nannofossil-rich silty clay and clayey silt with nannofossils) to Core 368-U1505C-62X and then decreases in Cores 63X and 64X. The average grain size is silt and clay, and fine to medium sand is the maximum grain size. The sediment is thinly laminated. Bioturbation is heavy, and foraminifers and shell fragments are common (Figure **F14E**). Pyrite forms up to centimeter-sized patches, and rare concentrations of organic matter were also observed (Figure **F14C, F14D**). Glauconite grains are especially abundant in Sections 58X-4 (Figure **F14A, F14B**) and 59X-2.

Bulk mineralogy and chemistry

The bulk mineralogy results of XRD analyses are listed in Table **T2**. Unit II sediments are composed mainly of glauconite, quartz, plagioclase, clay minerals (including smectite, illite, and kaolinite), and minor amounts of pyrite and calcite. Figure **F9** shows the downhole variations in the relative abundance of minerals identified by XRD in bulk sediments at Site U1505. Compared to Unit I, Unit II shows distinctly higher percentages of glauconite, plagioclase, kaolinite, and illite. In contrast, Unit II sediments have lower percentages of calcite, halite, K-feldspar, chlorite, and smectite.

Compositional analyses of Unit II clay were made directly on the archive half of the core using the handheld pXRF instrument (see **Igneous and metamorphic petrology** in the Expedition 367/368 methods chapter [Sun et al., 2018]) (Table **T2**). The clay (eight analyses) in Section 368-U1505C-57X-1 shows little variation in bulk composition. The major components are SiO_2 (~45 wt%), Al_2O_3 (12–16 wt%), and minor MgO (2–4 wt%) and K_2O (~2 wt%). The clay has Sr contents of ~150 ppm and Zr contents of ~80 ppm.

Discussion

Depositional environment of Unit II

Unit II was most likely deposited in a moderately deep water (upper slope) marine-depositional environment based on the high clay content, abundance of nannofossils, and presence of glauconite. In general, the sediment is fine grained (silty clay) and dominated by terrigenous materials (quartz, feldspar, and clay minerals), with lesser calcareous microfossils, including nannofossils and foraminifers, minor authigenic glauconite and calcite, and rare radiolarians. Small shelly fragments, microfossils, and organic fragments are visible on the core surface, along with occasional macrofossils, including bivalves.

Glauconite grains are present between Sections 368-U1505C-58X-4 and 62X-6. The presence of glauconite indicates that the sediment was most likely deposited at temperatures ranging from 7°C to 15°C (Margielewski et al., 2017) in low oxygen conditions and in shelf to lower slope environments from 20 to 700 m water depth (e.g., Drzewiecki and Simo, 2002; Margielewski et al., 2017).

Depositional environment of Unit I

Lithostratigraphic Unit I was deposited in a deep-marine environment. The dominant lithology is nannofossil ooze with variable amounts of clay and foraminifers. The top of Unit I is more clay rich and contains siliceous microfossils. Lithologic differences between subunits likely reflect changes in the amount of terrigenous input into a relatively open ocean setting, climate change, and changes in oceanographic conditions. The terrigenous input may be delivered as buoyant plumes from shallower shelf environments and rarely by weak (distal) turbidity currents. There is little change in the composition of the terrigenous grains through Unit I, so we envisage a similar source for these grains. Thin laminae of silt, often with pyrite, are found sparsely throughout Unit I. Some are graded, and all have sharp bases; however, many are disrupted by bioturbation and interpreted as distal turbidites.

Figure F10. A. Pinkish gray ash layer. B. Transparent glass shards dispersed in nannofossil-rich clay. C. Thin black ash layer and dispersed ash. D. Glass shards with clay minerals in the black ash shown in C.

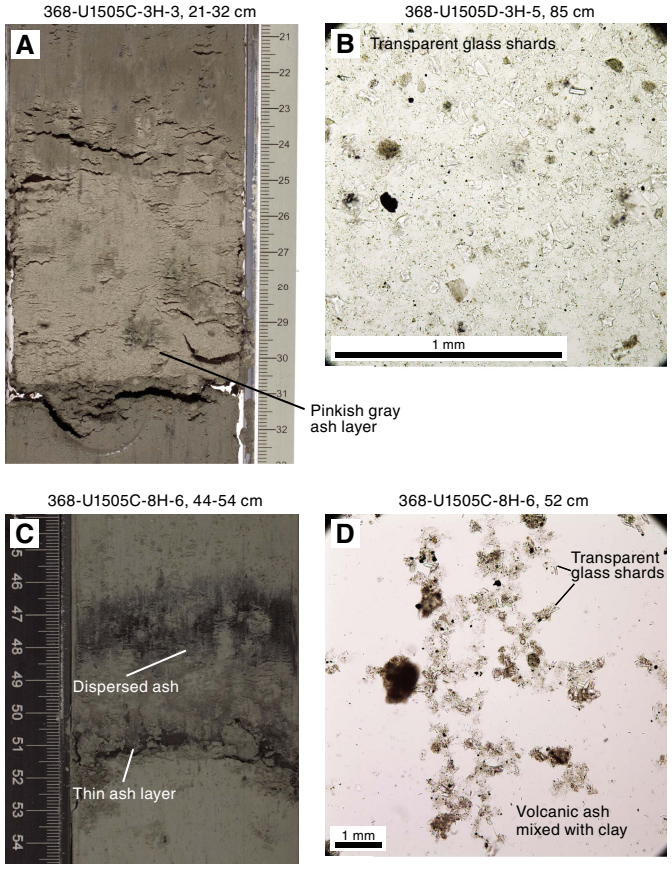

Figure F11. A. Fining-upward interval with foraminiferal silty sand grading upward to nannofossil-rich silty clay and then to nannofossil ooze with foraminifers. B. Two fining-upward intervals with nannofossil-rich silty clay grading upward into nannofossil ooze with clay. C. Fining-upward interval with pyrite-rich silty sand grading upward into clay-rich nannofossil ooze. The interval has been disrupted by bioturbation. Note the green reduced sediment in the silty sand interval and green reduction spots in the clay-rich nannofossil ooze. D. Detail of foraminiferal silty sand shown in A. E. Detail of silty sand shown in C.

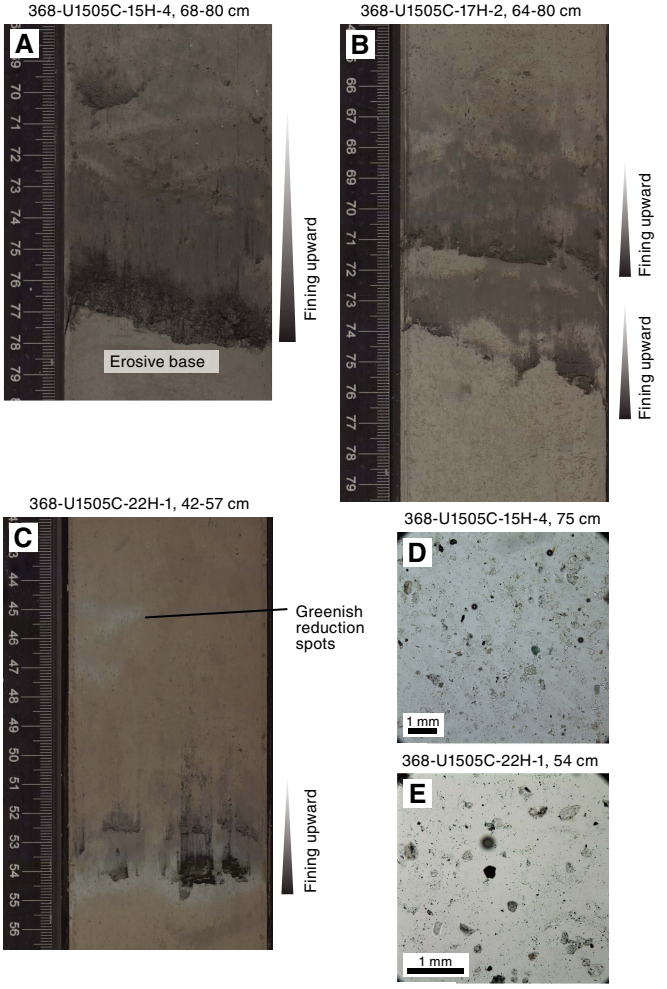

Preliminary correlation between Units I and II at Sites U1501, U1504, and U1505

Site U1501 is located 50.28 km west of Site U1504 on the OMH. Site U1505 is in the vicinity of Site U1501 (10.46 km east). Today's water depths are very similar at Sites U1501, U1504, and U1505 (2857, 2816, and 2917 mbsl, respectively). The recovered Pleistocene to early Miocene/Oligocene sediment successions can be correlated based on their major lithologies and the age of deposition. We suggest a correlation between Pleistocene Subunit IA (Site U1505), Pleistocene Subunit IA (Site U1504), and Pleistocene to Pliocene Subunits IA and IB (Site U1501) because all are dominated by dark greenish gray nannofossil-rich clay and clay-rich nannofossil-ooze with siliceous microfossils. At Site U1504, there seems to be a hiatus below Subunit IA (see **Biostratigraphy**). Between Sites U1504 and U1501, middle Miocene Subunit IB (Site U1504) correlates well with late to middle Miocene Subunit IC (Site U1501). These subunits are both composed of greenish gray and light brownish gray nannofossil ooze with clay- and foraminifer-rich intervals. Middle Miocene Subunit IC (Site U1504) can be correlated with middle Miocene to Oligocene Subunits ID and IE (Site U1501). These subunits are characterized by greenish gray and gray nannofossil ooze with clay.

Despite being close to Site U1501, the lack of distinct boundaries in the lithology at Site U1505 makes correlation between these sites difficult. Pleistocene to late Oligocene Subunits IB and IC (Site U1505) correlate in time to Subunits IC–IF at Site U1501 and Subunit IB and Unit II at Site U1504. In addition, although there is a change from brownish to grayish layers at Site U1505, as was observed at Sites U1501 and U1504, the color changes are more subtle and without clear boundaries, making correlation difficult. Therefore, a more detailed correlation of the post-Oligocene sediments between the three sites will require postexpedition research.

Unit II at Site U1505 correlates well with Unit II at Site U1501. There is an unconformity at the boundary between Unit I and Unit II at Site U1501 and a sharp lithologic boundary between the two units at Site U1505. The carbonate-to-clay ratio abruptly changes at this boundary at both sites, and Unit I has more abundant calcareous microfossils than Unit II. The sedimentation rate is very low below the Unit II/I boundary at both sites (see **Biostratigraphy**).

Figure F12. A, B. Destruction of sedimentary features caused by drilling disturbance (basal flow-in) that affected Cores 368-U1505C-19H through 47F.

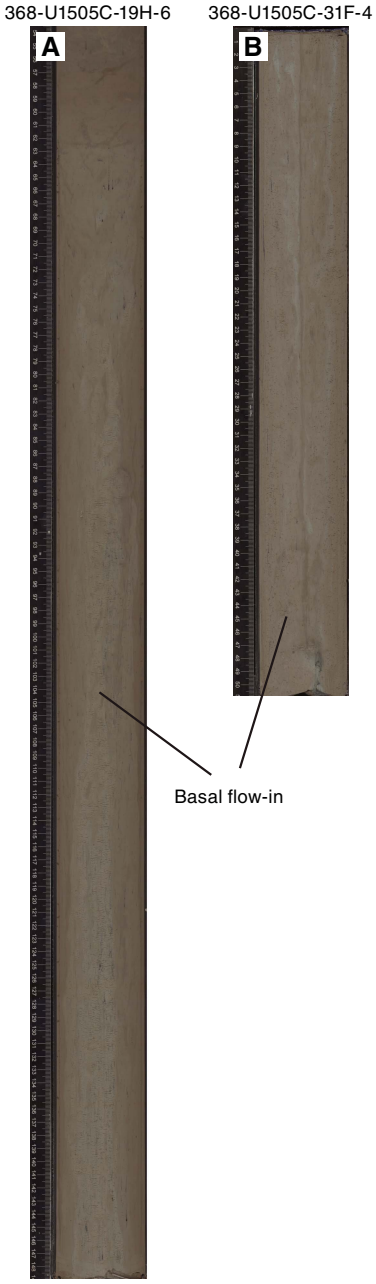

Structural geology

Site U1505 is located on the OMH at a water depth of 2917 m roughly 10 km from Site U1501. The sedimentary and structural record at these two sites is very similar.

Lithostratigraphic Unit I structures

Lithostratigraphic Unit I, which consists of nannofossil oozes, shows predominantly horizontal to subhorizontal bedding that in most cases is erased due to moderate to strong bioturbation and drilling disturbance. Unit I is devoid of any visible structures related to tectonic deformation.

Figure F13. Typical ichnospecies in Subunit IC. A. Large inclined burrow with uneven walls. B. *Chondrites* (Ch), *Planolites* (Pl), and *Zoophycos* (Zo). Note the foraminifers on the core surface. C. Combination of horizontal, vertical, and inclined burrows. D. Inclined *Zoophycos* burrow.

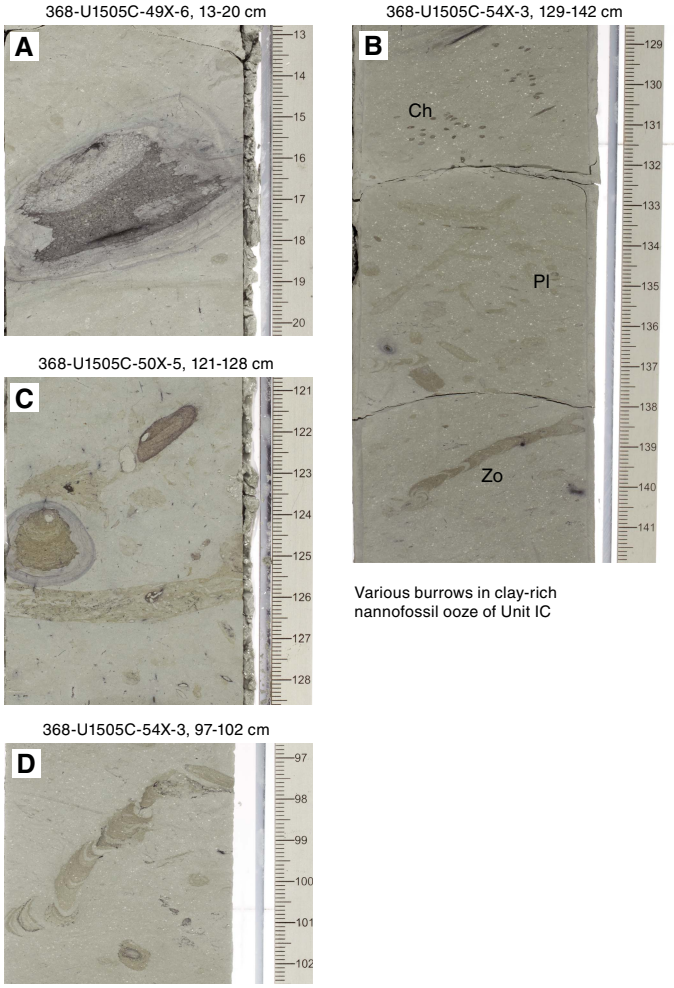

Lithostratigraphic Unit II structures

Lithostratigraphic Unit II is characterized by subhorizontal to gently dipping bedding as shallow as 10°. Similar to Site U1501, some minor deformation structures are heterogeneously distributed within Unit II. In Core 368-U1505C-60X (Figure **F15**), millimeter-scale normal faults and joints show comparable geometries to those described in **Structural geology** in the Site U1501 chapter (Larsen et al., 2018a). In most cases, these deformation structures are overprinted by drilling disturbance, making their recognition difficult.

Biostratigraphy

All core catcher samples from Holes U1505A, U1505B, and U1505C were analyzed for calcareous nannofossils, planktonic foraminifers, and diatoms. Additional samples were taken from intervals within the working-half cores when necessary to refine the ages. Preservation of calcareous microfossils is good in Cores 368-U1505C-1H through 48X and moderate to poor in Cores 49X

Figure F14. Special features in Unit II. A. Thick lamination rich in glauconite grains interbedded with dark greenish gray silty clay with disseminated glauconite. B. Glauconite grains in silty clay. C. Diagenetic pyrite grains possibly replacing a burrow fill and lamination in heavily bioturbated nannofossil-rich silty clay. D. Organic matter in nannofossil-rich silty clay. E. Bivalve macrofossil in nannofossil-rich silty clay. Note the small shelly fragments on the core surface.

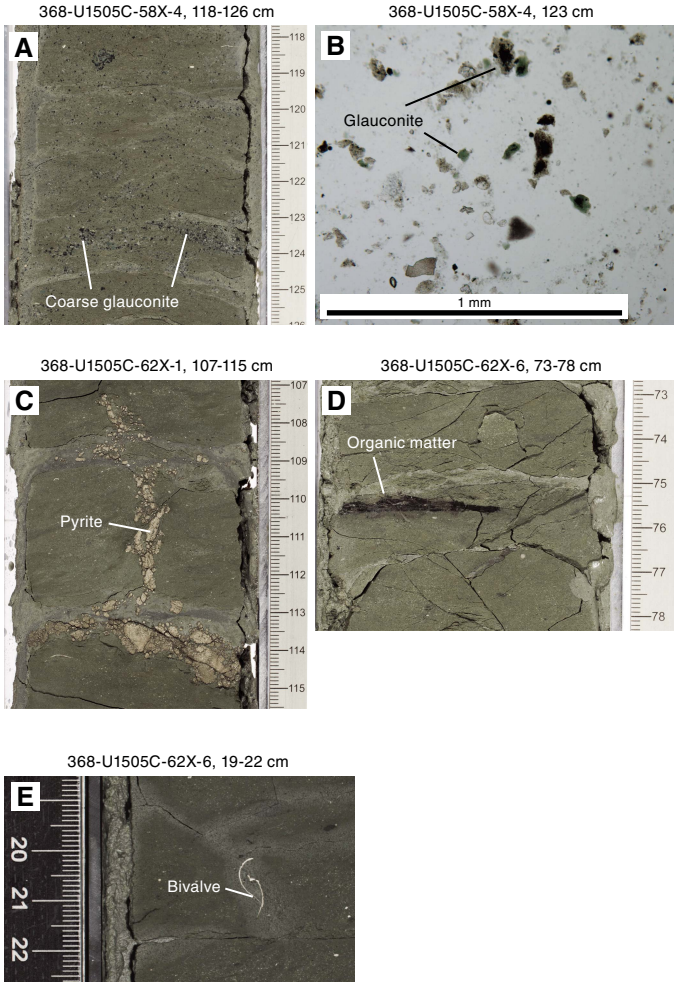

through 64X. Planktonic foraminifers are abundant or common in Cores 1H through 56X and 59X through 62X and few or rare in Cores 57X, 58X, 63X, and 64X. Calcareous nannofossils are generally abundant to common in most samples from Hole U1505C, except in the upper part of Core 57X, where they are rare to absent.

Forty-five biostratigraphic datums identified in Hole U1505C suggest a continuous succession of early Oligocene to Holocene age (Tables **T4**, **T5**; Figure **F16**). The Pleistocene/Pliocene boundary was placed within Core 7H, the Pliocene/Miocene boundary between Cores 11H and 13H, and the Miocene/Oligocene boundary between Cores 54X and 55X. Sedimentation rates vary from ~7 mm/ky in the Oligocene to ~15 mm/ky during the Miocene–Pliocene and ~24 mm/ky during the Pleistocene.

Relatively lower planktonic foraminifer content below Core 57X indicates a shoaling marine environment during the early Oligocene, whereas much higher abundances of planktonic foraminifers above Core 56X suggest a deep-water environment since the late Oligocene.

Figure F15. Deformation structures made of en echelon millimeter-scale normal faults and fractures, Unit II. Structures resemble those observed in Subunit IIA at Site U1501 (see Figure F27 in the Site U1501 chapter [Larsen et al., 2018a]).

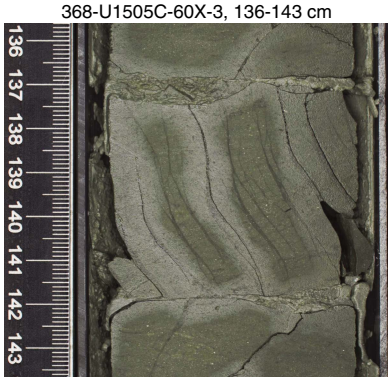

Calcareous nannofossils

Core catchers from Holes U1505A, U1505B, and U1505C were examined (Table **T6**). Calcareous nannofossil biostratigraphy for Site U1505 was based mainly on the analysis of all core catcher samples from Hole U1505C, and a number of samples from intervals within cores were analyzed to better constrain the biostratigraphic events.

Nannofossils are abundant to common in most samples from Hole U1505C with the exception of those from the upper part of Core 57X. They are barren in Samples 57X-1, 0–1 cm, and 57X-1, 24–25 cm, rare in Sample 57X-1, 144–145 cm, and resume common to abundant occurrences below Sample 57X-6, 1–2 cm. These occurrences indicate a significant change in nannofossil abundance between Samples 57X-1, 144–145 cm, and 57X-6, 1–2 cm.

Nannofossil preservation is good in most samples from Hole U1505C with the exception of Samples 52X-CC to 60X-CC. In this interval, discoasterids and *Sphenolithus* show slight to heavy overgrowth.

Twenty-seven nannofossil biostratigraphic datums were recognized in the Oligocene through Pleistocene sediment sequence (Table **T4**). The oldest nannofossil event identified at Site U1505 is the last appearance datum (LAD) of *Reticulofenestra umbilicus*, which occurs at 430.26 m in Hole U1505C and indicates an age older than 32.02 Ma.

Pleistocene

The top of Hole U1505C (Samples 1H-CC to 2H-CC; 17.74 m) is dated as late Pleistocene based on the presence of *Emiliania huxleyi* (marker species for Zone NN21). The LAD of *Pseudoemiliania lacunosa* in Sample 4H-CC (37.17 m) defines the top of Zone NN19. Zone NN19 is further divided by two nannofossil events, the first appearance datum (FAD) of *Gephyrocapsa* spp. >4 µm reentrance in Sample 5H-CC (46.51 m) and the LAD of *Calcidiscus macintyrei* in Sample 6H-CC (56.23 m).

Pliocene

Pliocene nannofossil Zones NN16, NN15, and NN12 were recognized in Hole U1505C. Two events occur in the lower part of Zone NN16: the LAD of *Discoaster tamalis* (2.8 Ma) in Sample 7H-CC (65.70 m) and the LAD of *Sphenolithus* spp. (3.54 Ma) in Sample 8H-CC (74.95 m). The LAD of *Reticulofenestra pseudoumbilicus* (3.70 Ma) in Sample 9H-CC (84.18 m) defines the top of Zone

Table T4. Calcareous nannofossil biostratigraphic events recognized at Site U1505. T = top/last appearance datum, B = bottom/first appearance datum. **Download available in CSV format.**

Epoch		Biozone (Martini, 1971)	Calcareous nannofossil event	Top		Bottom		Age model	
				Core, section	Depth CSF-A (m)	Core, section, interval (cm)	Depth CSF-A (m)	Depth (m)	Age (Ma)
				368-U1505C-		368-U1505C-			
Pleistocene		NN21	B *Emiliania huxleyi*	2H-CC	17.74	3H-CC	26.04	21.89	0.29
		NN19	T *Pseudoemiliania lacunosa*	3H-CC	26.04	4H-CC	37.17	31.61	0.44
			B *Gephyrocapsa* spp. >4 µm reentrance	5H-CC	46.51	6H-CC	56.23	51.37	1.04
			T *Calcidiscus macintyrei*	5H-CC	46.51	6H-CC	56.23	51.37	1.60
Pliocene		NN16	T *Discoaster tamalis*	6H-CC	56.23	7H-CC	65.70	60.97	2.80
			T *Sphenolithus* spp.	7H-CC	65.70	8H-CC	74.95	70.33	3.54
		NN15	T *Reticulofenestra pseudoumbilicus*	8H-CC	74.95	9H-CC	84.18	79.57	3.70
		NN12	T *Ceratolithus acutus*	10H-CC	93.65	11H-CC	102.78	98.22	5.04
Miocene	late	NN11	T *Nicklithus amplificus*	12H-CC	111.73	13H-CC	122.71	117.22	5.94
		NN11	B *Nicklithus amplificus*	14H-CC	132.23	15H-CC	141.32	136.78	6.91
		NN11	B *Discoaster berggrenii*	16H-CC	150.90	17H-CC	160.67	155.79	8.29
		NN10	T *Discoaster bollii*	17H-CC	160.67	18H-CC	170.28	165.48	9.21
		NN9	T *Discoaster hamatus*	18H-CC	170.28	19H-CC	179.75	175.02	9.53
		NN9	B *Discoaster hamatus*	20H-CC	189.26	21H-CC	196.53	192.90	10.55
		NN8	B *Catinaster coalithus*	21H-CC	196.53	22H-CC	200.06	198.30	10.89
	middle	NN6	T *Cyclicargolithus floridanus*	22H-CC	200.06	23H-CC	207.05	203.56	11.85
		NN6	T *Coronocyclus nitescens*	24F-CC	212.18	25F-CC	216.92	214.55	12.12
		NN6	B *Reticulofenestra pseudoumbilicus*	28F-CC	230.93	29F-CC	235.69	233.31	12.83
		NN5	T *Sphenolithus heteromorphus*	28F-CC	230.93	29F-CC	235.69	233.31	13.53
		NN4	T *Helicosphaera ampliaperta*	34F-CC	259.17	35F-CC	263.83	261.50	14.91
	early	NN2	T *Triquetrorhabdulus carinatus*	46F-CC	310.74	47F-CC	314.90	312.82	18.28
			B *Helicosphaera ampliaperta*	48X-CC	326.93	49X-CC	336.70	331.82	20.43
			B *Sphenolithus disbelemnos*	53X-CC	374.57	54X-CC	383.95	379.26	22.76
Oligocene		NP25	T *Reticulofenestra bisecta* >10 µm	54X-CC	383.95	55X-CC	394.11	389.03	23.13
			T *Sphenolithus ciperoensis*	55X-CC	394.11	56X-CC	403.84	398.98	24.43
		NP24	T *Sphenolithus predistentus*	56X-CC	403.84	57X-6, 1–2	411.07	407.46	26.93
		NP22	T *Reticulofenestra umbilicus*	58X-CC	419.58	59X-CC	430.26	424.92	32.02

Table T5. Planktonic foraminifer events, Site U1505. T = top/last appearance datum, B = bottom/first appearance datum, Bc = bottom/first common appear-ance datum (acme). **Download available in CSV format.**

Epoch	Biozone (Blow, 1969)	Calcareous nannofossil event	Top		Bottom		Age model	
			Core, section	Depth CSF-A (m)	Core, section	Depth CSF-A (m)	Depth (m)	Age (Ma)
			368-U1505C-		368-U1505C-			
Pleistocene	N22	T *Globigerinoides ruber* (pink)	1H-CC	8.23	2H-CC	17.74	12.99	0.12
	N22	Bc *Globigerinoides ruber* (pink)	3H-CC	26.04	4H-CC	37.17	31.61	0.40
	N23	T *Globorotalia tosaensis*	4H-CC	37.17	5H-CC	46.51	41.84	0.61
	N20–N21	T *Globorotalia multicamerata*	6H-CC	56.23	7H-CC	65.70	60.97	2.18
Pliocene	N20–N21	T *Sphaeroidinellopsis seminulina*	7H-CC	65.70	8H-CC	74.95	70.33	3.59
	N19	T *Globoturborotalita nepenthes*	9H-CC	84.18	10H-CC	93.21	88.70	4.37
Miocene	N17	T *Globoquadrina dehiscens*	17H-CC	160.67	18H-CC	170.28	165.48	5.92
	N14	T *Paragloborotalia mayeri*	20H-CC	189.26	21H-CC	196.53	192.90	10.46
	N13	B *Globoturborotalita nepenthes*	25H-CC	216.92	26H-CC	221.54	219.23	11.63
	N12	T *Fohsella fohsi*	25H-CC	216.92	26H-CC	221.54	219.23	11.79
	N8	T *Praeorbulina circularis*	33F-CC	254.46	34F-CC	259.17	256.82	14.89
	N8	B *Praeorbulina sicana*	44F-CC	303.21	45R-CC	307.92	305.57	16.38
	N6	T *Catapsydrax dissimilis*	47F-CC	314.90	48F-CC	326.93	320.92	17.54
	N5	T *Globoquadrina binaiensis*	49F-CC	336.70	49F-CC	336.70	336.70	19.09
	N4	T *Paragloborotalia kugleri*	50F-CC	346.12	51F-CC	355.58	350.85	21.12
Oligocene	N4	T *Globigerina ciperoensis*	53X-CC	374.57	54X-CC	383.95	379.26	22.90
	P21	T *Paragloborotalia opima*	56X-CC	403.84	57X-CC	413.49	408.67	26.93
	P19	T *Turborotalia ampliapertura*	58X-CC	419.58	59X-CC	430.26	424.92	30.28

NN15. The LAD of *Ceratolithus acutus* (5.04 Ma) in Sample 11H-CC (102.78 m) defines the top of Zone NN12. The Pliocene/Miocene boundary in Hole U1505C was placed between Samples 11H-CC (102.78 m) and 13H-CC (122.71 m) based on the LADs of *C. acutus* and *Nicklithus amplificus*, respectively.

Miocene

Seven events occur in the late Miocene strata of Hole U1505C. Zone NN11 includes three events: the LAD of *N. amplificus* (5.94 Ma) in Sample 13H-CC (122.71 m), the FAD of *N. amplificus* (6.91 Ma) in Sample 14H-CC (132.23 m), and the FAD of *Discoaster berg-*

Figure F16. Age-depth model, Site U1505. Plotted event data are in Tables T4 and T5 (see Paleomagnetism).

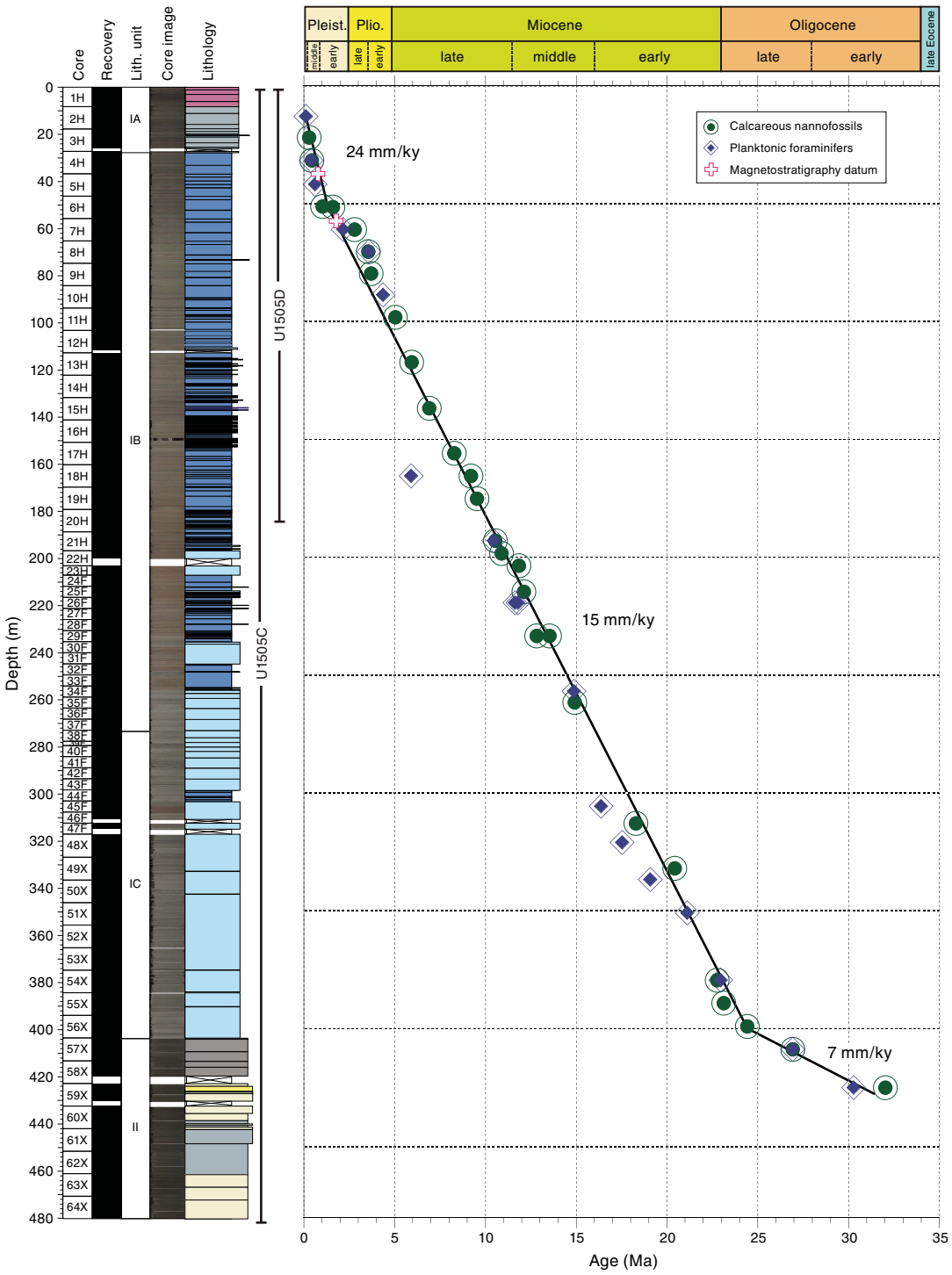

Table T6. Distribution of calcareous nannofossils, Site U1505. **View table in PDF format. Download available in CSV format.**

grenii (8.29 Ma) in Sample 16H-CC (150.90 m). The LAD of *Discoaster bollii* (9.21 Ma) in Sample 18H-CC (170.28 m) falls within Zone NN10. The LAD (9.53 Ma) and FAD (10.55 Ma) of *Discoaster hamatus*, which occur in Samples 19H-CC (179.75 m) and 20H-CC (189.26 m), respectively, define Zone NN9. The FAD of *Catinaster coalitus* (10.89 Ma) was used to mark the base of Zone NN8, which occurs in Sample 21H-CC (196.53 m). The late/middle Miocene boundary in Hole U1501C was assigned between Samples 21H-CC (196.53 m) and 23H-CC (207.05 m) based on the FAD of *C. coalitus* (10.89 Ma) and the LAD of *Cyclicargolithus floridanus* (11.85 Ma), respectively.

Five events are recorded in the middle Miocene strata of Hole U1505C. The top of Zone NN6 is marked by the LAD of *C. floridanus* (11.85 Ma) in Sample 23H-CC (207.05 m). Two additional events were found in Zone NN6: the LAD of *Coronocyclus nitescens* (12.12 Ma) in Sample 25F-CC (216.92 m) and the FAD of *R. pseudoumbilicus* (12.83 Ma) in Sample 28F-CC (230.93 m). The top of

Zone NN5 is marked by the LAD of *Sphenolithus heteromorphus* (13.53 Ma) in Sample 29F-CC (235.69 m). The top of Zone NN4 is defined by the LAD of *Helicosphaera ampliaperta* (14.91 Ma) in Sample 35F-CC (263.83 m). The middle/early Miocene boundary was assigned between Samples 35F-CC (263.83 m) and 47F-CC (314.90 m).

Three events were recognized in the early Miocene strata of Hole U1505C. The top of Zone NN2 is marked by the LAD of *Triquetrorhabdulus carinatus* (18.28 Ma) in Sample 47F-CC (314.90 m). The bottom of Zone NN2 is defined by the FAD of *Sphenolithus disbelemnos* (22.76 Ma), which occurs in Sample 53X-CC (374.57 m). One additional event, the FAD of *H. ampliaperta* (20.43 Ma) within Zone NN2, was found in Sample 48X-CC (326.93 m). The Miocene/Oligocene boundary was assigned between Samples 53X-CC (374.57 m) and 55X-CC (394.11 m) based on the FAD of *S. disbelemnos* (22.76 Ma) and the LAD of *Reticulofenestra bisecta* >10 µm (23.13 Ma), respectively.

Oligocene

Four events were identified in the Oligocene strata of Hole U1505C. The top of Zone NP25 is marked by the LAD of *R. bisecta* (>10 µm; 23.13 Ma) in Sample 55X-CC (394.11 m). The LAD of *Sphenolithus ciperoensis* (24.43 Ma) within Zone NP25 occurs in Sample 56X-CC (403.84 m). The top of Zone NP24 was recognized by the LAD of *Sphenolithus predistentus* (26.93 Ma) in Sample 57X-6, 1–2 cm (411.07 m). The top of Zone NP22 is marked by the LAD of *R. umbilicus* (32.02 Ma) in Sample 59X-CC (430.26 m).

Nannofossil assemblages in Samples 59X-CC through 64X-CC are characterized by relatively abundant *Braarudosphaera bigelowii, Helicosphaera bramlettei, Helicosphaera compacta,* and *Pontosphaera* spp. In particular, a significant portion of the nannofossil assemblage is composed of some late Eocene or older species such as *Pontosphaera exilis, Pontosphaera pectinata, Pontosphaera pulchripora, Reticulofenestra erbae, Reticulofenestra* cf. *reticulata, Reticulofenestra isabellae,* and *Reticulofenestra westerholdii*, suggesting that the age of the bottom of Hole U1505C is possibly the late Eocene. This evaluation warrants quantitative study during postcruise research because the definition of the late Eocene nannofossil zonation is based on their changes in abundance.

Planktonic foraminifers

All core catcher samples and several additional samples from the split cores from Holes U1505A, U1505B, and U1505C were processed for planktonic foraminiferal analyses (Tables **T7**). Planktonic foraminifers are well preserved and abundant in Cores 368-U1505C-1H through 48X and moderately preserved and few in Cores 49X through 64X, except for the poorly preserved and rare condition in Cores 57X to 58X.

Only mudline cores were recovered from Holes U1505A and U1505B. No pink *Globigerinoides ruber* specimens were found in Samples 368-U1505A-1H-CC and 368-U1505B-1H-CC. Compared to the planktonic foraminiferal occurrence in Hole U1505C, the bottom age of Holes U1505A and U1505B might be younger than 0.12 Ma.

Eighteen planktonic foraminiferal datums were recognized in Hole U1505C, spanning from the early Oligocene (>32.03 Ma) to the late Pleistocene (Table **T5**). The planktonic foraminiferal biostratigraphy for Hole U1505C was established by these events and the planktonic foraminiferal assemblages at successive depth intervals.

The Pleistocene planktonic foraminifers are composed of *G. ruber, Globigerinoides sacculifer, Globorotalia menardii, Pulleniatina obliquiloculata,* and *Neogloboquadrina dutertrei*. The LAD of pink *G. ruber* (0.12 Ma) and the FAD of pink *G. ruber* acme (0.40 Ma) occur between Samples 368-U1505C-1H-CC and 2H-CC and Samples 3H-CC and 4H-CC, respectively. The LAD of *Globorotalia tosaensis* (0.61 Ma) is located between Samples 4H-CC and 5H-CC. The LAD of *Globorotalia multicamerata* (2.18 Ma) is located between Samples 6H-CC and 7H-CC.

Table T7. Distribution of planktonic foraminifers, Site U1505. **View table in PDF format. Download available in CSV format.**

The Pliocene planktonic foraminiferal assemblage is characterized by the higher content of *Dentoglobigerina altispira* and *Sphaeroidinellopsis seminulina*. The LAD of *S. seminulina* (3.59 Ma) is located between Samples 7H-CC and 8H-CC. The LAD of *Globoturborotalita nepenthes* (4.37 Ma) is located between Samples 9H-CC and 10H-CC and defines the boundary of Zones N20 and N19.

The late Miocene foraminiferal assemblage is dominated by *D. altispira, S. seminulina, G. menardii, Globoquadrina venezuelana,* and *Globoquadrina dehiscens*. The LAD of *G. dehiscens* (5.92 Ma) is located between Samples 17H-CC and 18H-CC and defines the boundary of Zones N18 and N17. The FAD of *Paragloborotalia mayeri* (10.46 Ma) is located between Samples 20H-CC and 21H-CC and defines the boundary of Zones N15 and N14.

The middle Miocene foraminiferal assemblage is dominated by *D. altispira, S. seminulina, G. venezuelana, G. dehiscens,* and *Praeorbulina* spp. The FAD of *G. nepenthes* (11.63 Ma) and the LAD of *Fohsella fohsi* (11.79 Ma) are both located between Samples 25H-CC and 26H-CC and define the boundary of Zones N13 and N12 (i.e., boundary of the late/middle Miocene). The LAD of *Praeorbulina circularis* (14.89 Ma) is located between Samples 33F-CC and 34F-CC.

The late Oligocene–early Miocene planktonic foraminifers are characterized by *G. dehiscens, G. venezuelana, Catapsydrax dissimilis,* and *P. mayeri*. The FAD of *Praeorbulina sicana* (16.38 Ma) is located between Samples 44F-CC and 45F-CC and marks the boundary of Zones N8 and N7. The LAD of *C. dissimilis* (17.54 Ma) is located between Samples 47F-CC and 48F-CC and indicates the boundary of Zones N7 and N6. The LAD of *Globoquadrina binaiensis* (19.09 Ma) is located between Samples 48F-CC and 49F-CC. The LAD of *Paragloborotalia kugleri* (21.12 Ma) is located between Samples 50X-CC and 51X-CC as the boundary of Zones N5/N4. The LAD of *Globigerina ciperoensis* (22.90 Ma) is located between Samples 53X-CC and 54X-CC and represents the Miocene/Oligocene boundary.

The early Oligocene planktonic foraminifers are characterized by *Paragloborotalia nana/opima, Turborotalia ampliapertura,* and *G. ciperoensis*. The LAD of *P. opima* (26.93 Ma) is located between Samples 56X-CC and 57-CC as the boundary of Zones P22/P21. The LAD of *T. ampliapertura* (30.28 Ma) is located between Samples 58X-CC and 59X-CC as the boundary of Zones P20/P19.

The relative abundance of planktonic foraminifers decreases below Core 56X, clearly indicating a shallower water environment during the late to early Oligocene.

Diatoms

The core catcher samples from Hole U1505C were processed into smear and strewn slides for diatom analysis. A total of 28 additional toothpick samples were taken from selected intervals of the working-half cores for better resolution. Samples from the mudline to Sample 3H-CC are composed of between 1% and 50% diatoms

Table T8. Distribution of diatoms, Site U1505. **View table in PDF format. Download available in CSV format.**

Table T9. Diatom events, Site U1505. T = top/last appearance datum. **Download available in CSV format.**

Epoch	Biozone (Scherer et al., 2007)	Diatom event	Top		Bottom		Age model	
			Core, section, interval (cm)	Depth CSF-A (m)	Core, section, interval (cm)	Depth CSF-A (m)	Depth (m)	Age range (Ma)
Pleistocene	*Fragilariopsis doliolus*	T *Fragilariopsis reinholdii*			368-U1505C-3H-3, 31	20.84	20.84	<0.62

with poor preservation (Table **T8**). The rest of the samples, with the exception of Samples 63X-CC and 64X-CC, were barren of diatoms.

Samples 1H-CC, 2H-CC, and 3H-CC contain a typical late Pleistocene tropical–subtropical diatom assemblage such as *Fragilariopsis doliolus* and *Nitzschia interruptestriata* (Table **T9**). *Fragilariopsis reinholdii* (LAD = 0.62 Ma) was not observed in Sample 4R-CC, suggesting an age younger than 0.62 Ma.

Smear slides from Samples 63X-CC and 64X-CC are devoid of diatoms, but the washed residues for foraminiferal analysis contain a few specimens of large (~250 µm) heavily recrystallized diatoms that are similar to *Arachnoidiscus* in appearance.

Paleomagnetism

Shipboard measurements

Shipboard paleomagnetic investigations on Hole U1505C cores combined two complementary approaches (see **Paleomagnetism** in the Expedition 367/368 methods chapter [Sun et al., 2018]): (1) measurement of archive-half sections on the pass-through 2G Enterprises SRM at 2.5 cm spacing and (2) measurement and AF demagnetization of 55 oriented discrete samples on the spinner magnetometer (AGICO JR-6A). Additionally, the anisotropy of magnetic susceptibility (AMS) was measured on discrete samples with the KLY 4 Kappabridge.

Except for Sections 368-U1505C-1H-1 through 3H-1, which were in-line AF demagnetized in 3 steps (5, 10, and 15 mT), only NRM was measured with the SRM for Hole U1505C. This decision was made after a comparison of magnetization intensities between discrete samples and sections led us to suspect that the SRM was not properly calibrated (geometrically) for core sections. U-channel samples will be collected on shore to analyze and demagnetize this core.

Scalar data from discrete samples from AF demagnetization up to 120 mT were used to assess the nature of the magnetic assemblage and the directional and intensity data. Directional data were analyzed using Zijderveld diagrams (Zijderveld, 1967), and the characteristic remanent magnetization (ChRM) direction(s) were calculated by principal component analysis (PCA) (Kirschvink, 1980) using PuffinPlot (version 1.03, April 23, 2015) (Lurcock and Wilson, 2012).

Demagnetization behavior and implications for magnetic assemblages

Units: lithostratigraphic Units I and II
Depth: 0.00–480.54 m
Sections 368-U1505C-1H-1 through 64X-CC

Most of the 55 discrete samples investigated show very soft magnetic behavior characterized by loss of more than 60% of NRM below 15 mT. This very low coercivity (soft behavior) is the reason for the strong vertical drilling overprint (average inclination ≈ 81°) that is particularly visible in the APC cores. The drilling overprint is easily removed by demagnetization to 10–15 mT (Figure **F17**). The soft behavior shows that magnetic remanence is dominated by titanomagnetite or magnetite. The contribution of greigite to the magnetic assemblages is visible in a few discrete specimens between Cores 368-U1505C-11H and 17H through a minute increase in magnetization above 70 mT. The lower part of the hole (Cores 48X through 64X) is characterized by severe drilling disturbance, resulting in destruction of the NRM vector, which is visible in the scatter of inclinations (Figure **F18**). The drilling overprint affects discrete samples (yellow squares in Figure **F19**) far less than core sections (blue crosses).

Magnetostratigraphy

Inclination, intensity, and polarity for Hole U1505C are reported in Figure **F19**. We constructed the magnetostratigraphy based on the polarity assigned to the archive-half cores and corroborated by directions obtained from oriented discrete samples. A succession of two normal and three reversed polarities was recognized. We tentatively correlated the magnetostratigraphic data of Site U1505C with the standard timescale (Ogg et al., 2016) according to biostratigraphy age constraints as reported in Figure **F16**. The normal polarity Zone n1 is interpreted as the Brunhes Chron (C1n), with the lower boundary at 37.415 m with an age of 0.781 Ma. The lower boundary (57.365 m) of reversed Polarity r1 is the base of Subchron C1r.3r with an age of 1.778 Ma.

Anisotropy of magnetic susceptibility

The 55 discrete samples have magnetic susceptibility (κ) values ranging from ≈ 60×10^{-6} to 628×10^{-6} SI (Figure **F20**). These low κ values combined with the low NRM suggest that both paramagnetic silicates (e.g., clays and chlorite) and minor ferromagnetic phases (e.g., titanomagnetite or magnetite) control the magnetic susceptibility. The degree of magnetic anisotropy (P') is moderate (~1.025), whereas the AMS fabric has a strongly oblate fabric, as shown by shape parameter (T), most likely of depositional origin. The Fisher distribution of AMS principal axes also suggests an oblate fabric with a nearly horizontal planar fabric. These sedimentary fabrics are consistent with deposition in a calm, pelagic environment with very limited traction on sedimentary particles.

Figure F17. AF demagnetization plots of (A) archive-half section and (B–D) discrete samples, Hole U1505C sedimentary rocks. Zijderveld plots: solid squares = declination, open squares = inclination. Stereographic plots: solid squares = positive (down) inclination, open squares = negative (up) inclination. Calculated ChRM (blue line; red squares = measurements used in calculation) using PCA is also shown. A. Removal of drilling overprint in first step (5 mT). B. Soft demagnetization behavior up to 10 mT associated with removal of drilling overprint, followed by gradual demagnetization from 10 to 60 mT, characteristic of single-domain and pseudosingle-domain magnetite, and negative inclination of sample. C. Soft demagnetization behavior. D. Soft demagnetization behavior. MAD = maximum angular deviation.

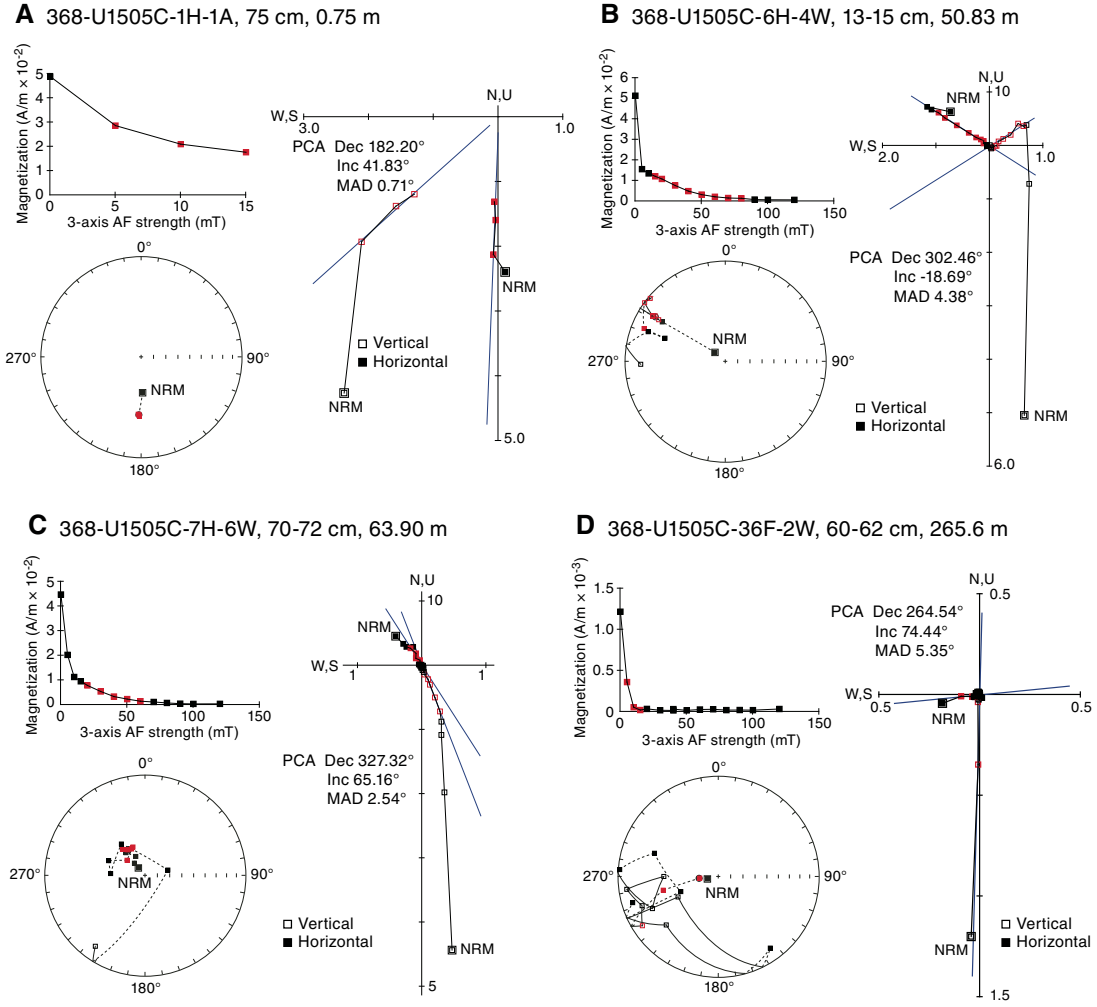

Figure F18. Magnetization intensity vs. inclination showing effect of steep drilling overprint and core disturbance in Cores 368-U1505C-48X through 64X. Red dashed line = mean inclination for Cores 48X through 64X, black dashed line = mean inclination for Cores 1H through 47F.

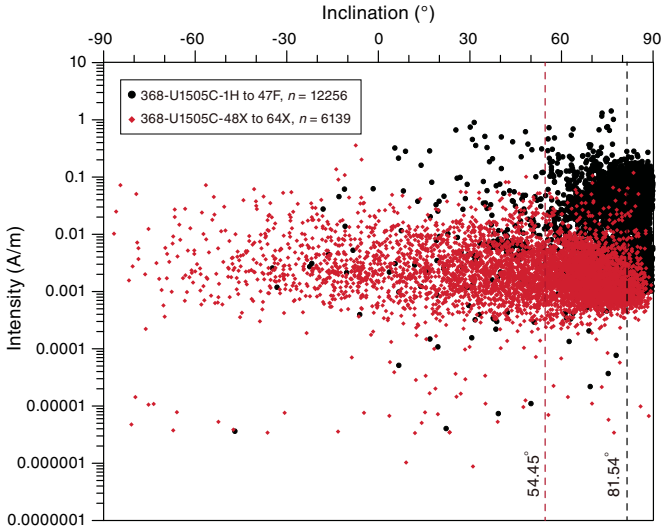

Figure F19. Magnetic measurements, Hole U1505C. Inclination was used to determine polarity. AFD = AF demagnetization. Magnetostratigraphic features are referred to as n1, etc., in a sequential manner for convenience and have no bearing on chrons. Discrete samples are yellow and green. GPTS2016 = geomagnetic polarity timescale of Ogg et al. (2016).

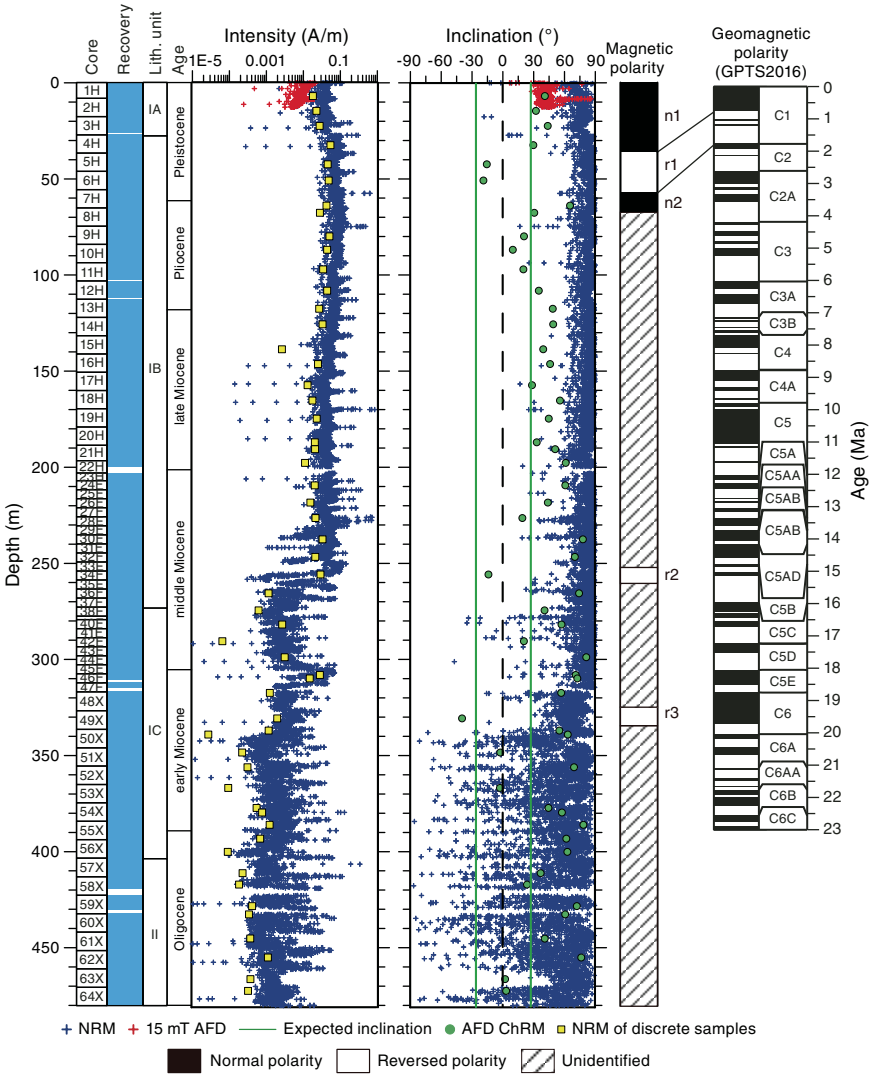

Figure F20. AMS data, Hole U1505C. A. Stereonet of AMS principal directions (lower hemisphere, equal-area projection). K_1 = maximum axis, K_2 = intermediate axis; K_3 = minimum axis. Confidence ellipses at 95% level (same color convention) show dominantly planar and subhorizontal fabric (oblate), consistent with sedimentary fabric acquired in a calm pelagic environment. Tensorial means are shown with larger symbols of same color. B. Degree of magnetic anisotropy (P') vs. magnetic susceptibility (K_m). C. Shape parameter (T) vs. P' showing dominantly oblate symmetry of sedimentary fabric.

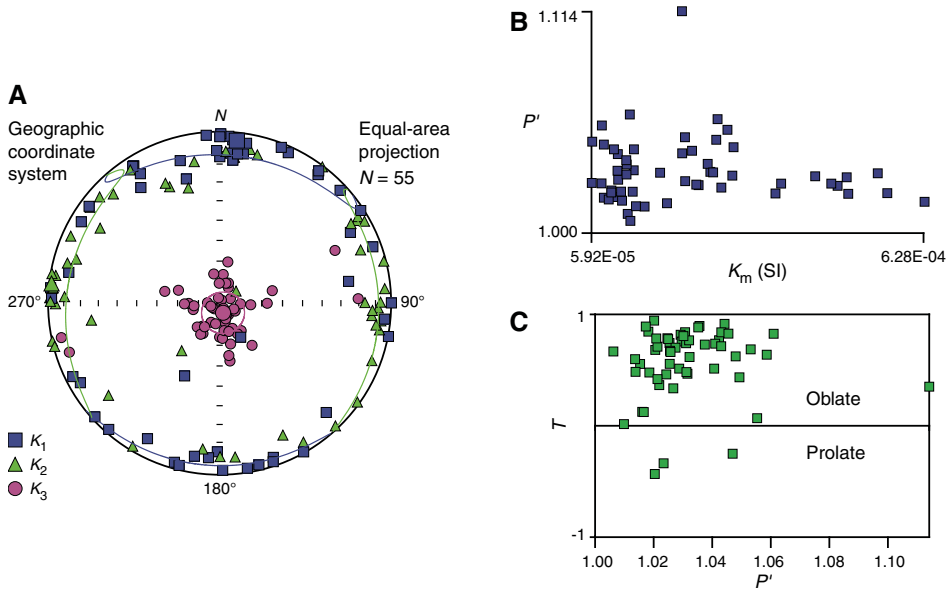

Geochemistry

Hydrocarbon gases were detected in deeper sediments only at Site U1505 and not at shallow depths. Thus, the base of the hole has methane distributions similar to those at Site U1499 (which has methane at depth), whereas the uppermost section is similar to Site U1501, which is barren of methane. Except for the shallowest 30 m of sediment, TOC, TN, and TS contents were mostly low in shallower lithostratigraphic Unit I, but TS and TOC were slightly higher in Unit II. Thus, in terms of solid organic geochemistry, Sites U1505 and U1501 are similar. Instances of high carbonate content are associated with bioclastic oozes. Interstitial water chemistry has two important features. The upper part exhibits patterns similar to those at Site U1501 in several respects (e.g., inhibited sulfate reduction), and there is evidence of freshwater input in deeper sediments (based on low chlorine, bromide, and salinity). Inductively coupled plasma–atomic emission spectroscopy analysis was not performed on samples collected at Site U1505.

Headspace gas

Headspace gas samples were taken at a frequency of one sample per core or per 10 m of drilling advance for routine safety monitoring. As at Site U1501, methane was not abundant in shallow sediments at Site U1505 (uppermost 50 m), although it was detected deeper in the hole at ~150 and ~ 400 m. Concentrations range from 70 to 3899 ppmv from 380 to 438 m, with a single instance of ethane found at this depth. A small concentration of methane was also detected at 150 m.

Bulk sediment geochemistry

Solid geochemistry parameters are listed in Table **T10**.

Lithostratigraphic Unit I

As seen at Site U1501, the uppermost black mud (lithostratigraphic Subunit IA) has relatively high TOC and TN contents relative to the units beneath. Sulfur content, although low in this unit, is higher than in the subunits immediately beneath it (Figure **F21**). Lithostratigraphic Subunits IB and IC have generally low TOC (<1 wt%) and low TS, which is also the case for Site U1501, where organic carbon is also least well preserved in these units.

Table T10. Carbon, nitrogen, and sulfur, Hole U1505C. **View table in PDF format. Download available in CSV format.**

Lithostratigraphic Unit II

Lithostratigraphic Unit II has high sulfur and low carbonate content, and relative to Subunits IB and IC, it has significant organic carbon content (typically 0.5 wt%). The TOC/TN ratio for the interval is low, indicating high-nitrogen material, which would classically be interpreted as well-preserved organic matter of aquatic origin (Hedges et al., 1988).

High carbonate contents were found in bioclast-rich Subunits IB and IC. On a crossplot, Subunit IA and Unit II both have distinctively low carbonate contents and low TOC/TN ratios (Figure **F22**), indicating a high proportion of aquatic organic matter, and Subunits IB and IC appear to have organic matter that has been more heavily degraded or is terrestrial in origin (Hedges et al., 1988). On a carbon-sulfur crossplot, the distinctively high sulfur content in Unit II is a little unusual because it does not have much organic matter. The unit appears to have a high abundance of reduced sulfur, whereas Subunit IA has low sulfide content, given that it is relatively organic carbon–rich marine mud (Berner and Raiswell, 1984).

Raman and surface-enhanced Raman spectroscopy

Surface-enhanced Raman measurements were performed on shallow core and mudline samples from Holes U1505A–U1505D. Concentrations are reported as nanograms asphaltene per gram of sediment in Figure **F23**.

Figure F21. Methane, TOC/TN ratio and carbonate, and TOC and TS, Site U1505.

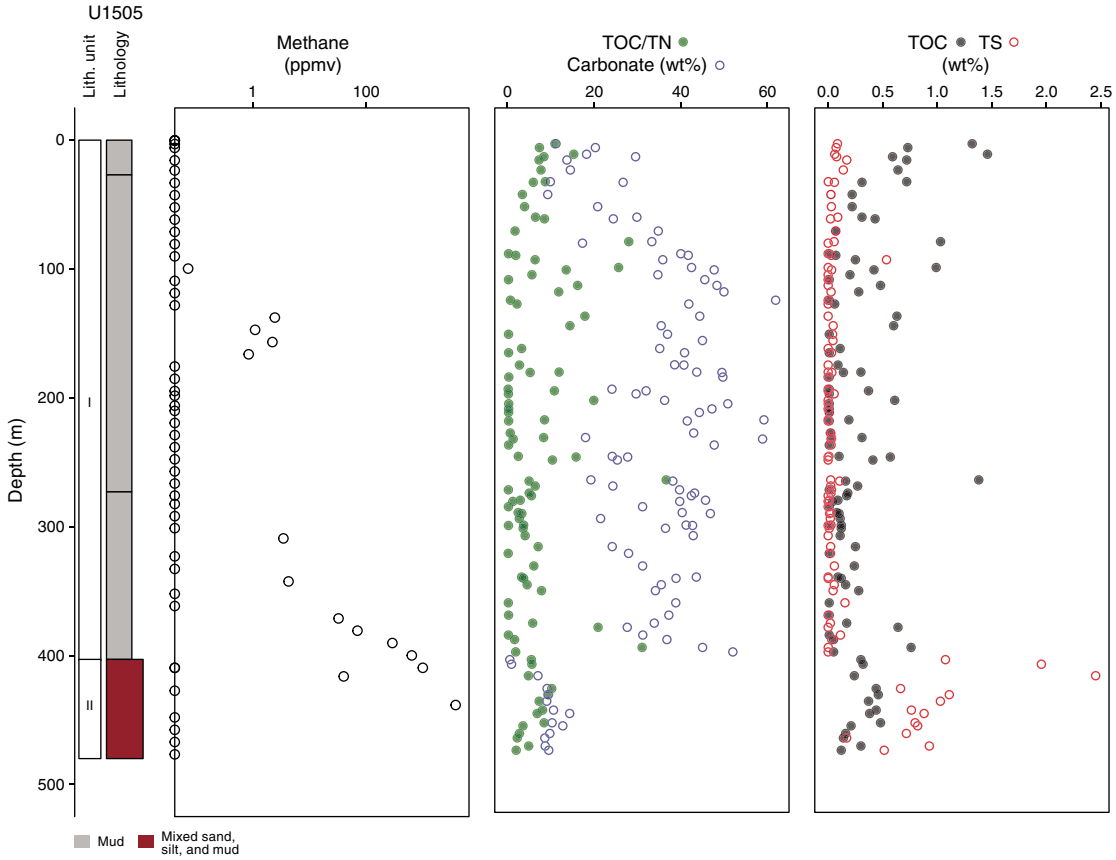

Figure F22. Crossplot of organic geochemical parameters, Site U1505. Solid circles = lithostratigraphic Subunit IA, open squares = Subunit IB, crosses = Subunit IC, open circles = Unit II.

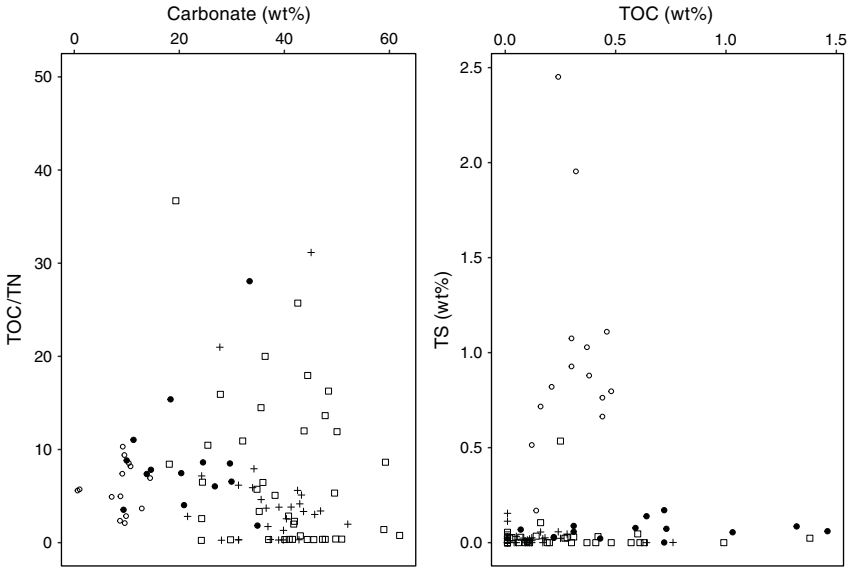

Interstitial water chemistry

Shipboard analyses were performed on interstitial water squeezed from 5–20 cm long whole-round sediment samples from Hole U1505C. From Cores 1H through 46F, 5–15 cm long intervals were squeezed for interstitial water and yielded >30 mL per sample. From Cores 46F through 64X, 20 cm long whole-round sediment cores were squeezed and yielded 5–20 mL of interstitial water. Interstitial water geochemical parameters are presented in Table **T11** and Figure **F24**.

In general, the geochemical parameters of interstitial water at Site U1505 are similar to those at Site U1501. We also defined three geochemical interstitial water zones at Site U1505 based on the variations of geochemical parameters (listed in Table **T11**). Interstitial water Zone 1 (interval 368-U1505C-1H-2, 0–5 cm, to 3H-4, 0–

Figure F23. Asphaltene concentrations per gram of sediment for mudline cores, Holes U1505A–U1505D.

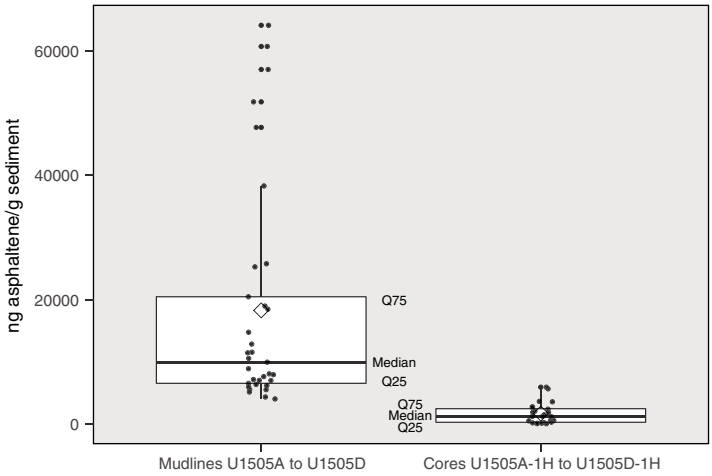

Table T11. Interstitial water analyses, Hole U1505C. **View table in PDF format. Download available in CSV format.**

Figure F24. Interstitial water alkalinity, major cations, and anions, Site U1505.

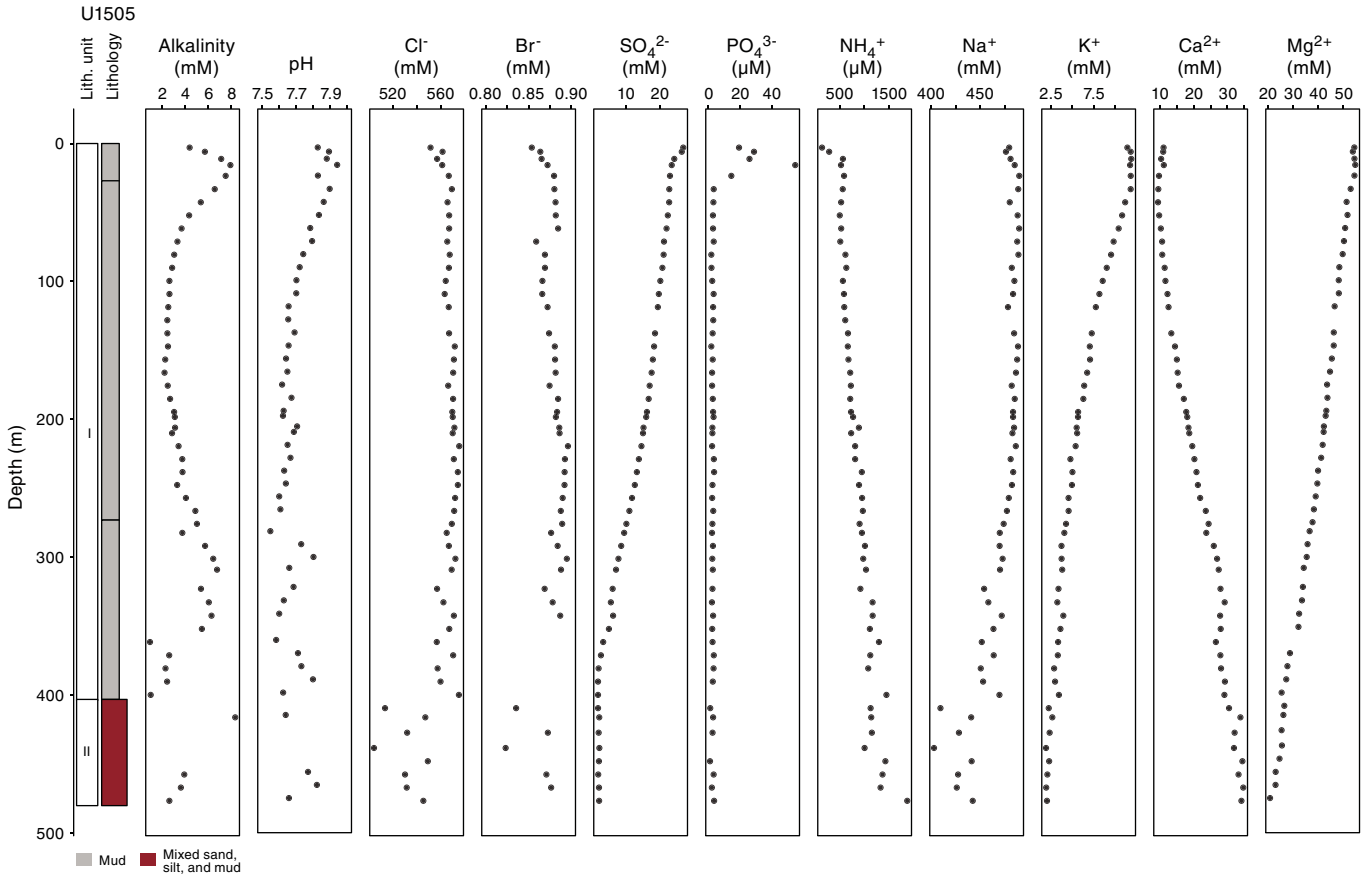

10 cm) comprises samples obtained close to the mudline (sediment/water interface). Within this interval, the maximum values of sulfate, alkalinity, and phosphate were observed and are likely related to degradation of organic matter. In interstitial water Zone 2 (interval 4H-4, 0–10 cm, to 56X-4, 0–20 cm), sulfate decreases and alkalinity is buffered by high carbonate concentrations within foraminifer-rich oozes. Atypically for this marine setting (Li et al., 2015), in which sulfate reduction is prevalent in marine sediments, diffusion processes dominate the sulfate profile. Decreasing K and Mg and increasing Ca reflect the typical diffusion-formed profile of interstitial water. In interstitial water Zone 3 (interval 57X-4, 0–20 cm, to 64X-4, 0–20 cm), sodium, chloride, and bromide concentrations are anomalously low.

Alkalinity varies within Hole U1505C, ranging from 1.0 to 8.3 mM (Figure **F24**). In interstitial water Zone 1, alkalinity increases to a peak concentration of 7.9 mM at 15.65 m (Sample 2H-5, 0–5 cm). The change in alkalinity is most likely caused by degradation of organic matter. In interstitial water Zone 2, alkalinity decreases to <3 mM at 90 m and remains constant until 185 m. Alkalinity increases again to a peak concentration of 6.8 mM at 308 m and then decreases downhole to the base of interstitial water Zone 2. The pH value decreases slowly from the seafloor to the bottom of interstitial water Zone 2 and then increases to a maximum (pH = 7.82) at the bottom of interstitial water Zone 3 (Sample 63X-4, 0–20 cm).

Profiles of Cl, Br, and Na are similar (Figure **F24**). In interstitial water Zone 1, Cl, Br, and Na concentrations increase slightly with depth. In interstitial water Zone 2, Cl, Br, and Na remain constant to 322 m (Sample 48X-4, 0–20 cm) with concentrations similar to seawater, and then between 322 and 400 m, Cl and Na concentrations vary. Interstitial water Zone 3 has low Cl, Br, and Na concentrations that decrease to a minimum in interstitial water Zone 3. A similar phenomenon was also observed in Hole U1501C, although the depth at which it occurs is different. In both cases, this minimum corresponds to the stratigraphic level of the T60 seismic unconformity. This correlation is discussed in detail later.

The dissolved sulfate profile decreases from 27.1 mM at the seafloor to <2 mM at the bottom of Hole U1505C (Figure **F24**). In interstitial water Zone 1, sulfate concentrations decrease sharply, most likely caused by bacterially mediated organic matter diagenesis in upper sediments. In interstitial water Zone 2, this decline is gradual until near-minimum concentrations are observed. In interstitial water Zone 3, sulfate concentrations are low.

Dissolved NH_4^+ concentrations increase from 143.6 µM at 2.96 m to a maximum of 1874 µM at the bottom of Hole U1505C. In interstitial water Zone 1, a sharp increase in NH_4^+ was observed that would typically be explained by degradation of organic matter releasing reduced nitrogen. In interstitial water Zones 2 to 3, continuous increases in NH_4^+ concentration suggest the existence of a source of NH_4^+ that diffuses upward from the bottom. A maximum dissolved phosphate concentration was observed in interstitial water Zone 1 (54.85 µM at 15.65 m). In interstitial water Zones 2–3, phosphate concentrations are generally low (several micromolar concentration).

The K^+ and Mg^{2+} profiles decrease in a similar way to each other from the surface to the bottom of the hole. The decreases of K and Mg are possibly due to diagenetic reactions occurring in sediment, such as clay ion exchange. Contrary to the K and Mg pore water profiles, the Ca^{2+} profile increases from the surface to a maximum concentration (33.5 mM) at the bottom of Hole U1505C. Changes in calcium concentration are mostly caused by carbonate diagenesis (i.e., dissolution of biogenic carbonate and recrystallization of authigenic carbonates).

Discussion

Sulfate–methane transition zones

Figure **F25** illustrates geochemical parameters that help explain the shallow biogeochemical processes occurring in SCS sediments. The sulfate–methane transition zone (SMTZ) occurs where organic matter degradation consumes dissolved substrates (foremost oxygen and then others such as phosphate, ammonium, etc.) and anaerobic conditions develop (Barnes and Goldberg, 1976). The SMTZ can be defined by the depletion of sulfate within pore water and the beginning of methanogenesis (elevated methane concentrations within sediments). Site U1499 has an SMTZ at ~70 m that likely reflects present-day processes. Site U1505 has a possible SMTZ at ~400 m, but it is not sharply defined (e.g., sulfate does not sharply inflect at this depth).

Both sedimentation rate and the presence of organic matter are important for the development of an SMTZ. TOC contents are essentially comparable between the three sites, with Site U1499 perhaps having a lower TOC because of a high input of sediment (sediment dilutes the organic carbon content). Despite the low absolute TOC, the net accumulation rate per unit time may still be comparable for all three sites. Thus, differing supply of organic carbon is not likely to be a key factor, with differences in sedimentation rate being the more likely differentiator between sites. High sedimentation rates promote anaerobic conditions by more rapidly burying organic matter to depths below which oxygen can diffuse (Demaison and Moore, 1980).

Evidence of past SMTZs can be preserved in a number of ways: high methane concentrations may remain in hydrostatic waters and reduced sulfur (sulfide) may mineralize in the form of sulfide minerals such as pyrite or greigite. Thus, a past SMTZ may be preserved beneath the T60 unconformity at Site U1505 where low pore water sulfate, high methane, and high TS are observed. Seepage from this zone at 400 m may also thus explain the methane present at shallower depths. The three sites together form an interesting study potentially demonstrating that the T60 unconformity surface is an important boundary affecting biogeochemical processes by controlling the flux of deeper fluids to shallower sediments.

Sub-T60 unconformity halide formation water anomaly

Important anions for understanding the formation water anomaly in chloride and bromide beneath the T60 unconformity are shown in Figure **F26**. Any such explanation must take account of the conservative nature of the halide ions—they are not generated from diagenetic reactions typical of marine sediments. Any explanation must also allow for the linear changes in depth (reflecting temperature) observed in the major cations such as magnesium, calcium, and potassium.

Two possible explanations for the sub-T60 unconformity halide anomaly are postdepositional recharge under a hydrodynamic regime or trapping of an original fresher water body depleted in these ions. The salinities and halide concentrations observed are low for marine water but toward the high end of brackish water. Such a water body might have been deposited with the sediment or potentially moved into the sediment very early in its history through subtidal pumping (Shum and Sundby, 1996), albeit only during storm events for deeper water sediments. The origin of the bromide, chloride, and sodium anomaly can best be explained by a trapped water body depleted in these anions and subsequent alteration of calcium, magnesium, and potassium in pore waters during diagenesis. Were the current water hydrodynamically emplaced after deposition, it would have to contain exactly the correct proportions of calcium, magnesium, and potassium to not disturb the depth-dependent trend.

Instead, it is more feasible that subsequent diagenetic processes such as smectite-illite transformation (Boles and Franks, 1979) or cation exchange involving carbonate minerals, which are temperature dependent (depth dependent), has released or taken up calcium, magnesium, and potassium from pore waters and thereby altered a trapped water body. A trapped water body would not be

Figure F25. Comparison of SMTZs and key biogeochemical elements at Sites U1499, U1501, and U1505. T60 unconformity is a basin-wide regional marker.

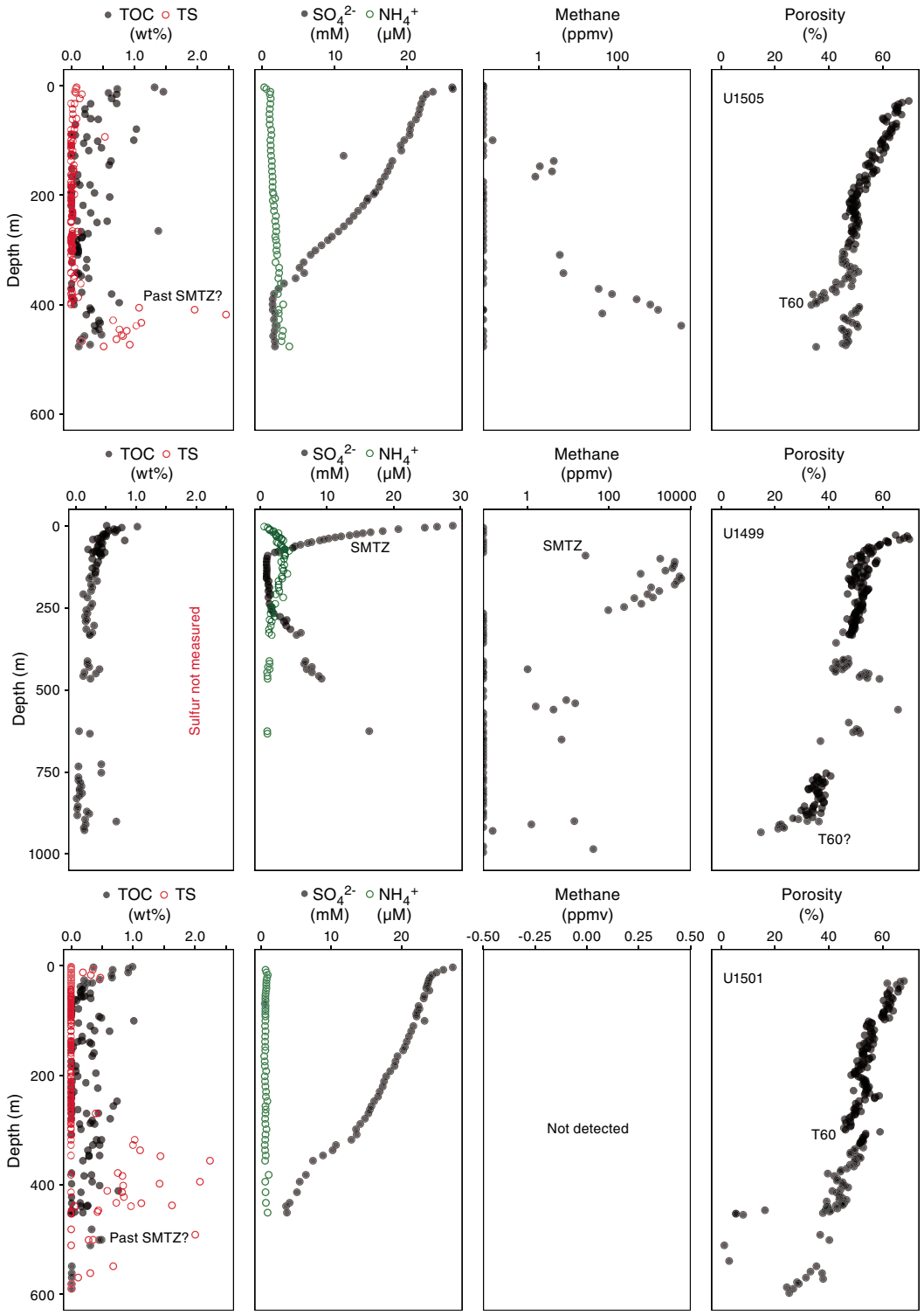

able to acquire a new halide-anion composition but would be able to equilibrate during diagenesis and produce the linear increase with depth seen here in calcium, magnesium, and potassium. Such a trapped water body might also cause a formation to be lithostatically pressured and hence undercompacted, leading to the higher porosities observed in the sub-T60 unconformity lithologies (Bethke, 1986).

Figure F26. Data illustrating sub-T60 unconformity halide interstitial water anomaly at Site U1505 and comparators at Sites U1499 and U1501.

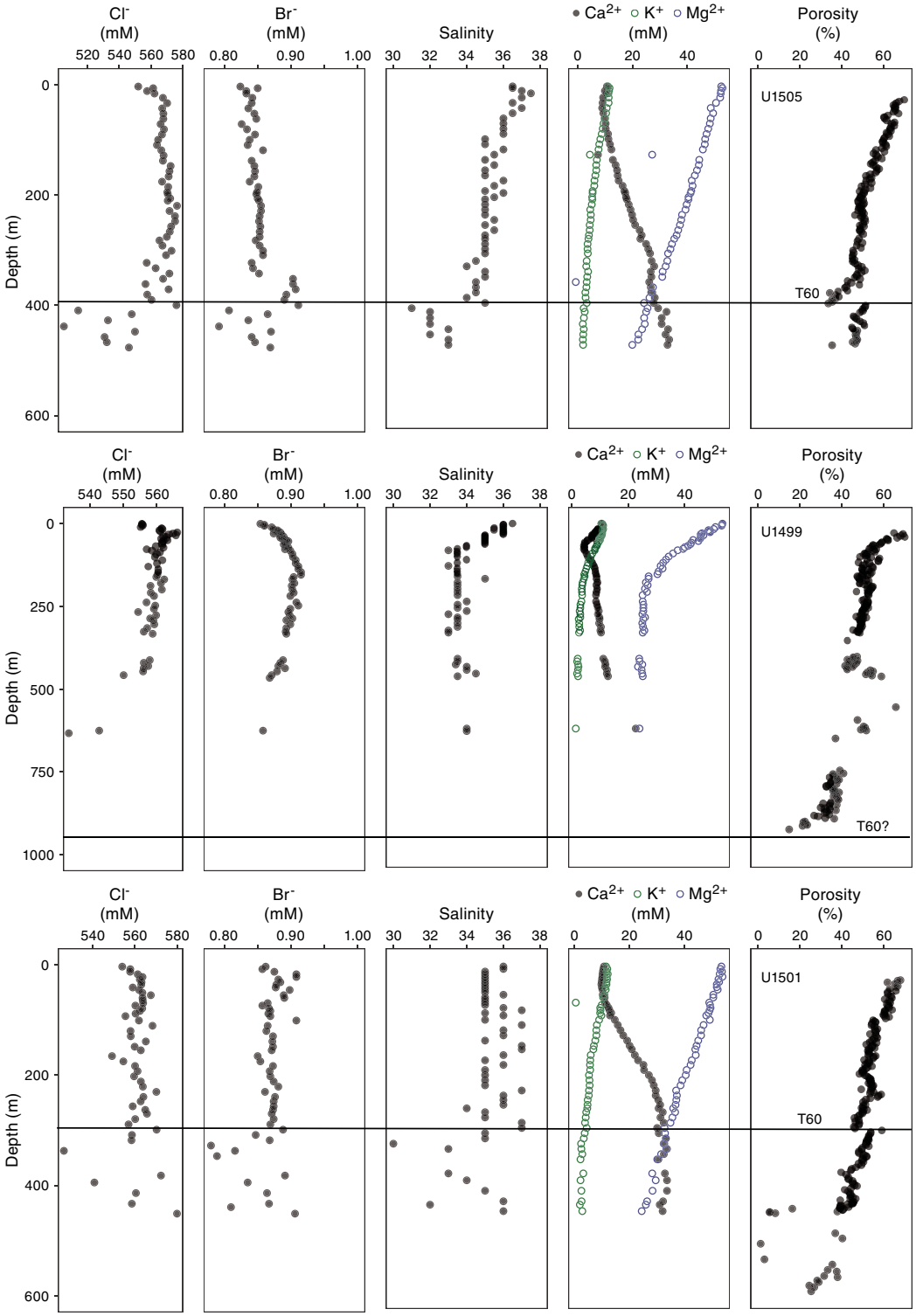

Physical properties

Whole-round measurements of magnetic susceptibility, gamma ray attenuation (GRA) bulk density, *P*-wave velocity (*P*-wave logger [PWL]), and NGR were made on each core recovered from Holes U1505C (0–480.2 m) and U1505D (0–184 m). Only nondestructive measurements were performed on the cores from Hole U1505D, which is a duplicate of Hole U1505C downcore to 184 m. *P*-wave velocity was also measured on working-half sections using the *P*-wave caliper (PWC) system. Thermal conductivity was measured on one section, typically Section 3, for each core. Additionally, discrete samples from Hole U1505C were analyzed for bulk density,

Figure F27. Physical properties, Hole U1505C. cps = counts per second.

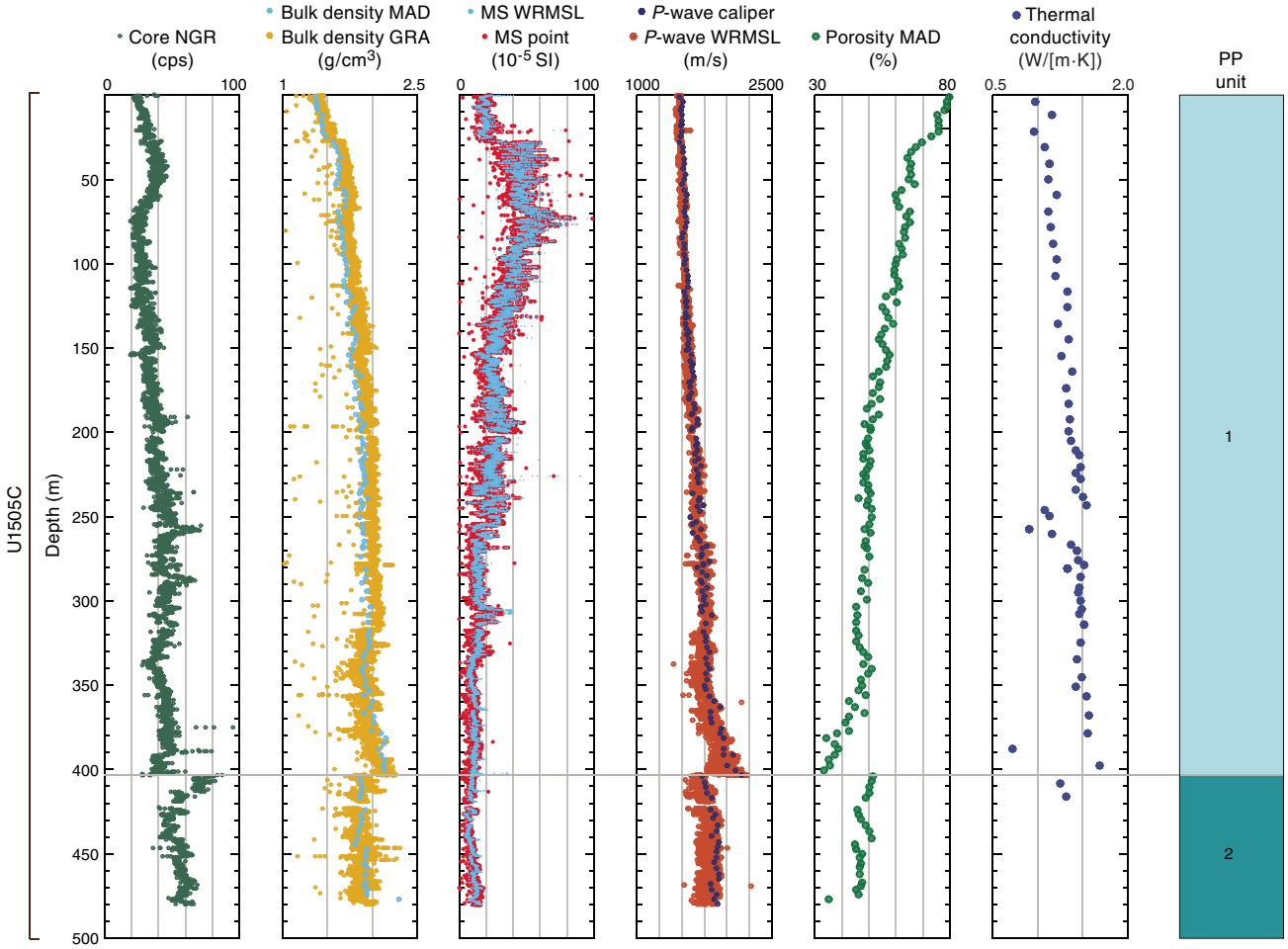

porosity, and dry and grain density. Color reflectance, RGB color spectra, and point magnetic susceptibility were measured on all archive-half sections from Holes U1505C and U1505D.

Because the cores recovered from Hole U1505D sampled the same lithologic section as in the uppermost ~180 m in Hole U1505C, the discussion here will focus on Hole U1505C. Based on the physical property characteristics, the lithologic sequence recovered from Hole U1505C was divided into two petrophysical (PP) units, PP Units 1 and 2, with a boundary at 403 m (Figure **F27**). This boundary corresponds to the boundary between lithostratigraphic Units I and II. The interface between these two units is marked by an abrupt shift in physical property measurements. The entire sequence recovered from Hole U1505D was assigned to PP Unit 1 (Figure **F28**). Hole U150C cores show some drilling disturbance deeper than ~250 m (see **Lithostratigraphy**).

Natural gamma radiation

NGR values in PP Unit 1 are represented by three major intervals (Figure **F27**). The upper interval from the seafloor to ~65 m ranges from ~20 to ~45 counts/s, and NGR values peak around the middle of this depth range. The second interval (~65–~335 m) is also marked by initially increasing NGR between ~20 and ~55 counts/s. NGR values then gradually decrease at the bottom of this interval to 35 counts/s at ~335 m. The lowermost interval of PP Unit 1 displays a general increase in NGR. This interval ends with an abrupt decrease in NGR to 35 counts/s close to 403 m, followed by a sharp increase to ~75 counts/s at ~403 m associated with the top of PP Unit 2. In PP Unit 2, NGR decreases to ~45 counts/s at 440 m and then increases.

P-wave velocity

In PP Unit 1, *P*-wave velocity values gradually increase with depth from ~1470 m/s at the seafloor to ~1765 m/s at ~335 m, followed by an increase that reaches ~2166 m/s at ~403 m (Figure **F27**). *P*-wave velocity values decrease sharply at the PP Unit 1/2 boundary to 1725 m/s and then remain relatively constant at ~2000 m/s from this point downhole to ~480 m.

Thermal conductivity

Thermal conductivity values show a well-defined trend in the designated petrophysical units. PP Unit 1 has a gradual increasing trend with depth. In this unit, thermal conductivity ranges from 0.906 to 1.684 W/(m·K) (Figure **F27**). The trend is interrupted with scattered values at ~250–270 m. This scatter could be due to drilling disturbance. PP Unit 2 shows a sudden drop in thermal conductivity with values ranging from 1.248 to 1.314 W/(m·K). In PP Unit 2, more measurements could not be done due to the high drilling disturbance in the cores.

Density and porosity

In PP Unit 1 (0–403 m), bulk density increases with depth from 1.4 g/cm^3 at the seafloor to ~2.1 g/cm^3 at the base of the unit (Fig-

Figure F28. Physical properties, Hole U1505D.

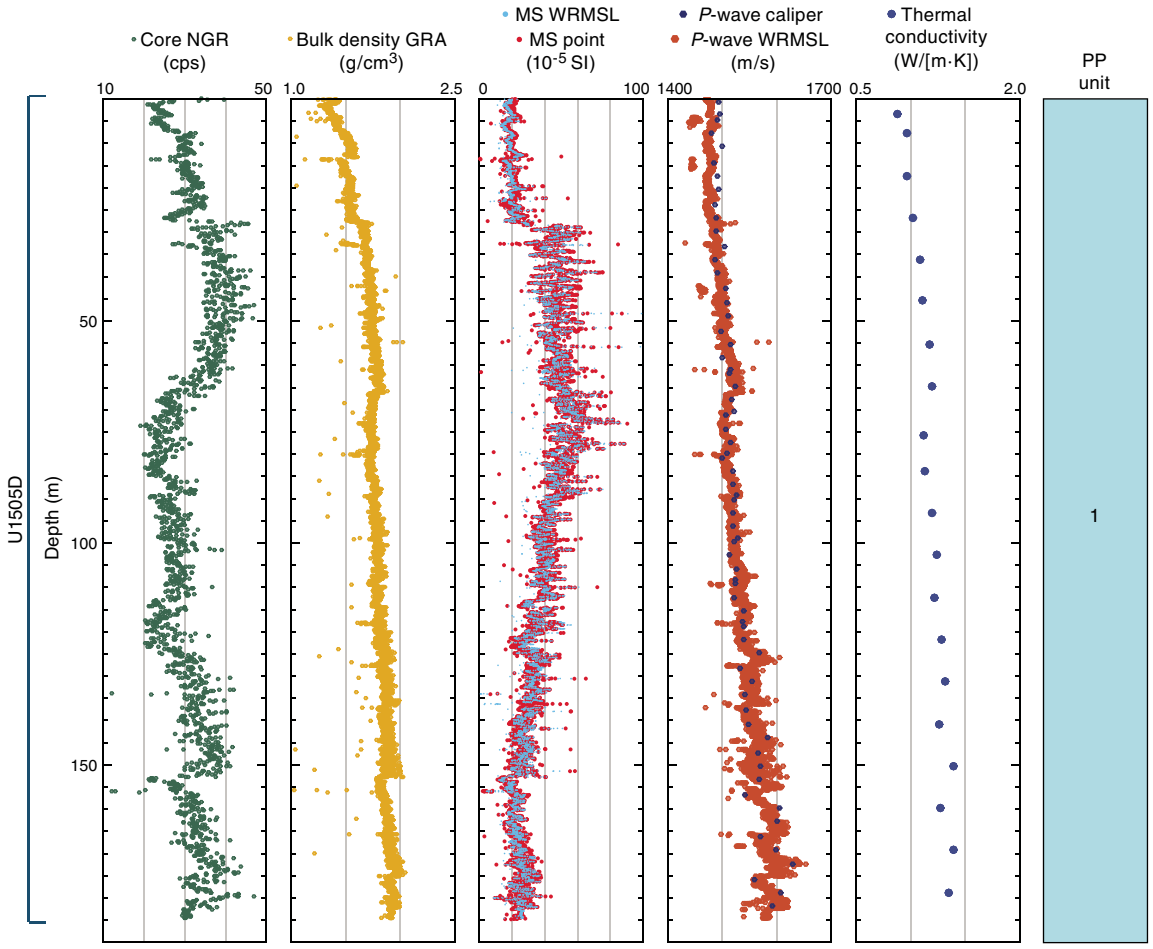

ures F27, F29). Porosity shows an inverse trend to density and decreases from ~80% to ~35%. Grain density varies between 2.7 and 2.8 g/cm^3 with no visible downcore trend (Figure F29). The interface between PP Units 1 and 2 (~403 m) is marked by an abrupt decrease in bulk density from 2.1 to 1.9 g/cm^3 and dry density from 1.8 to 1.3 g/cm^3. In contrast, porosity increases dramatically across this depth interval from ~34% to ~52%. This boundary coincides with the T60 seismic unconformity (see **Correlation to seismic data**) and can also be clearly recognized in other physical property data, including NGR, *P*-wave velocity, and color data (Figures F27, F29, F30, F31). In PP Unit 2 (403–480.2 m), bulk density increases slightly with depth from 1.86 to >1.96 g/cm^3 and dry density increases from ~1.3 to ~1.5 g/cm^3. Porosity decreases with depth from 51% to 35%.

Color reflectance spectrophotometry

Sediment color reflectance values are in very good agreement between Holes U1505C and U1505D, as expected (Figure F30). L* represents luminosity, or total reflected light, and is well correlated to $CaCO_3$ content in sediments (see **Geochemistry**). In PP Unit 1, L* overall increases with depth from the seafloor to ~75 m; thereafter, downhole L* values fluctuate between 50 and 60 but overall remain relatively constant to ~400 m, where they drop to <40 in PP Unit 2.

Reflectance a* and b* values indicate redness and yellowness of sediments, respectively, and show consistent variations with core depth (Figure F30). In PP Unit 1, both a* and b* gently increase in the upper portion (0 to ~180 m), followed by a section with high-amplitude variability between ~200 and 260 m, before they drop to minimum and relatively constant values to the base of the record. No significant shift in a* and b* was observed at the unit boundary.

Magnetic susceptibility

Whole-round magnetic susceptibility and point magnetic susceptibility values show a good, consistent trend throughout all core sections from Holes U1505C and U1505D (Figures F27, F28). In PP Unit 1, the magnetic susceptibility profile can be viewed as three windows of different trends: (1) low and constant magnetic susceptibility from 0 to 30 m with a mean value of ~20 × 10^{-5} SI, (2) high and constant magnetic susceptibility from 30 to 80 m with a mean value of ~45 × 10^{-5} SI, and (3) gradually decreasing magnetic susceptibility from 80 to 403 m. In PP Unit 1, the trend is frequently interrupted by spikes downcore. Finally, PP Unit 2 is associated with a persistently low and constant magnetic susceptibility of ~5.

RGB

RGB in PP Unit 1 steadily increases with depth from the seafloor to 70 m, reaching a maximum of 130 followed by constant values until the bottom of PP Unit 1 (Figure F31). At 403 m, corresponding to the boundary between PP Units 1 and 2, RGB values show a marked decrease (from 110 to 75). Below this depth, RGB remains relatively constant to the bottom of PP Unit 2.

Figure F29. MAD bulk density, dry density, grain density, and porosity, Hole U1505C.

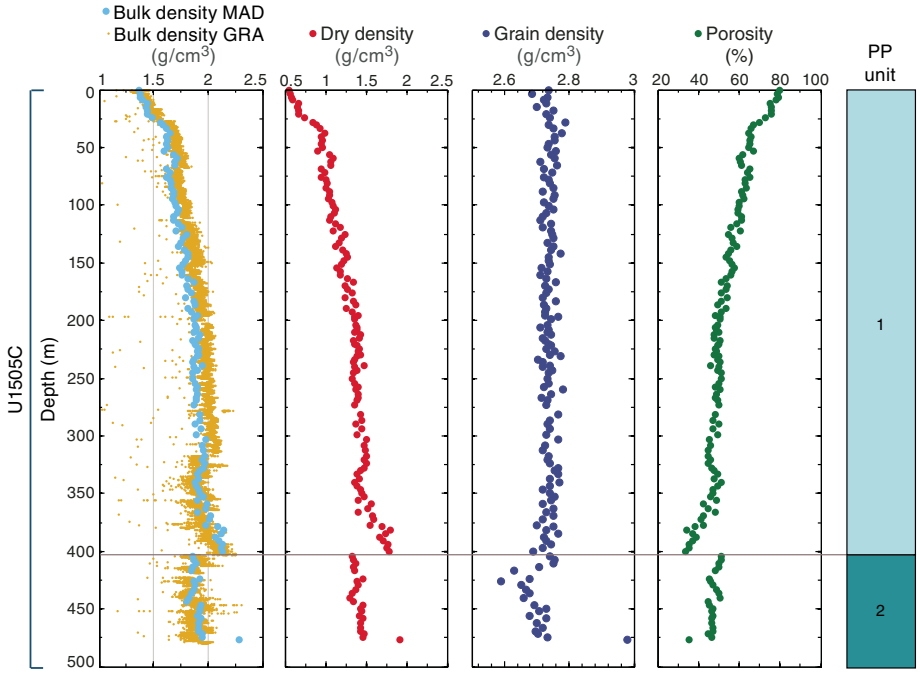

Figure F30. Sediment color reflectance parameters L*, a*, and b* for Holes U1505C and U1505D and $CaCO_3$ content for Hole U1505C (see Geochemistry).

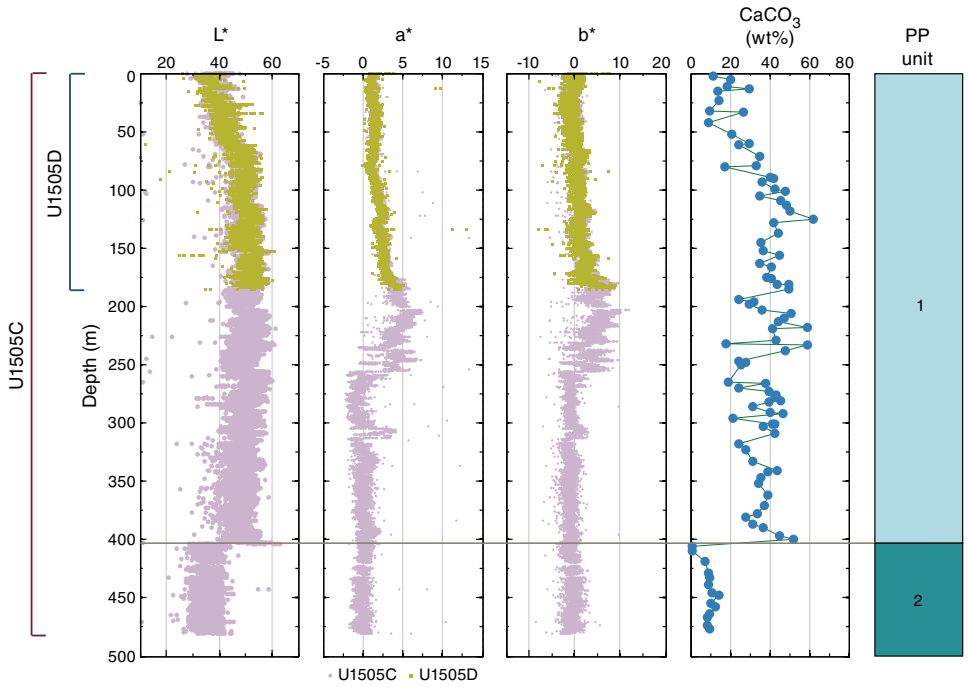

Discussion and summary

The observed physical properties allow us to characterize two major petrophysical units at Site U1505. The sediments recovered display a distinct color change from greenish and brownish light gray to greenish dark gray at 403 m (see **Lithostratigraphy**). This boundary, which represents the seismic stratigraphic T60 unconformity, is associated with a sharp change in physical properties.

PP Unit 1 shows overall gradually increasing NGR, bulk density, *P*-wave velocity, and thermal conductivity and decreasing magnetic susceptibility and porosity (Figures **F27**, **F28**). In contrast, PP Unit 2 (403–480 m) is characterized by a sharp change in physical properties at its upper boundary (403 m) but a relatively constant trend downhole within the unit.

In PP Unit 1 (0–403 m), sediments are composed of foraminifer-rich nannofossil ooze with clay in the upper part, which gradually changes to clay-rich nannofossil ooze in the lower portion of the unit. This transition is well reflected in NGR, which increases with depth. The higher NGR in PP Unit 2 is related to sediment that pri-

Figure F31. RGB values, Holes U1505C and U1505D.

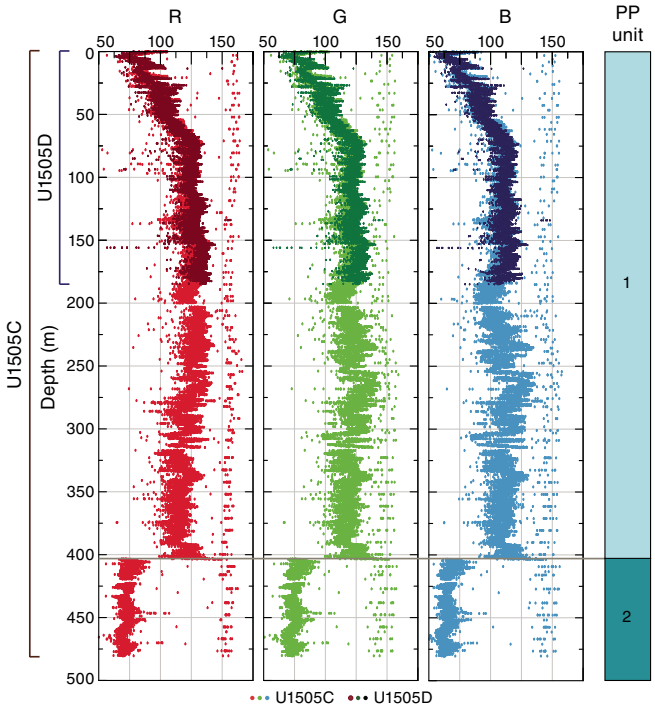

Figure F32. Logging operations summary, Hole U1505C.

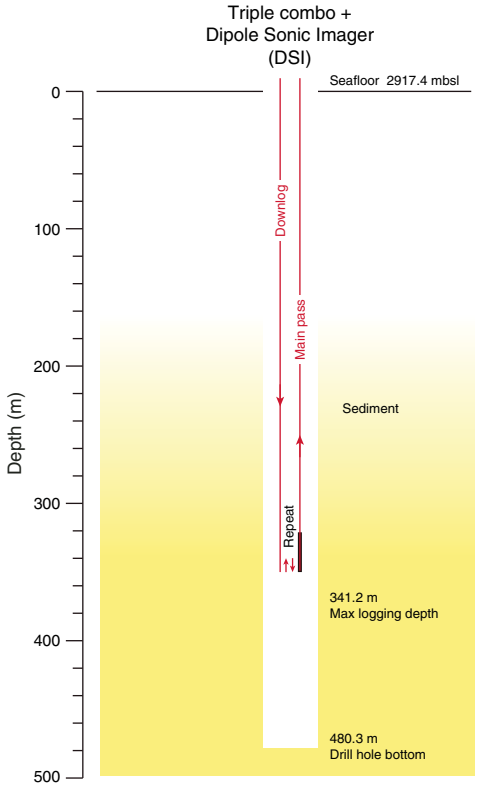

marily consists of silty clay (Figures **F27**, **F28**). The NGR and magnetic susceptibility trends have frequent spikes.

Density, porosity, and *P*-wave velocity suggest compaction is a major factor responsible for the observed downhole trend in PP Unit 1. Sediments in PP Unit 1 show porosity values similar to those recorded at nearby Site U1501 at a similar depth interval, suggesting the same compaction history. In PP Unit 2, density and *P*-wave velocity decrease abruptly at the boundary and then increase relatively constantly downhole, whereas porosity shows the opposite trend (Figures **F27**, **F29**). Thermal conductivity overall increases with depth. The higher magnetic susceptibility values in the upper portion of PP Unit 1 could be due to higher concentrations of magnetic materials like magnetite.

In the PP units, reflectance L* and RGB channels show similar trends that are well correlated with the percent carbonate trend. The higher L* and RGB values reflect higher carbonate contents. Lower values in L* and RGB correspond to the dark gray sediments in PP Unit 2 (Figures **F30**, **F31**).

Downhole measurements

Logging operations

After coring to 480.3 m in Hole U1505C, a wiper trip was made to verify hole conditions and allow debris collected around the drill collars to fall into the bottom of the hole. After the last core, the rotary core barrel (RCB) drill bit was released at the bottom of the hole. The drill pipe was raised to 78 m prior to logging (Figure **F32**). Rig-up for downhole logging started at 0930 h (local time; UTC + 8 h) on 2 June 2017. The modified triple combo tool string started downhole at 1130 h on 2 June. The uphole pass of the triple combo run began at 1350 h. After completing two down- and uphole passes, the tool string reached the seafloor at 1550 h, and the logging tools were rigged down at 1910 h. The wireline active heave compensator (AHC) was used throughout the logging operations.

Because the drill hole diameter for most of the logging depth was greater than 14–16 inches, it was decided not to run a second logging run with the FMS tool string.

The modified triple combo tool string included the HNGS, HLDS, HRLA, MSS, and DSI (Figure **F33**). The tool string encountered difficulty going down at approximately 341.2 m, where several attempts to pass that depth failed; thus, the logging depth was 341.2 m.

Logging units

The triple combo run in Hole U1505C allowed us to define six logging units that are correlated with hole conditions, lithostratigraphic units, lithology, and physical properties (Figure **F34**).

Logging Unit 1: seafloor to base of drill pipe

Logging Unit 1 extends from the seafloor to the base of the drill pipe at 78 m. The natural gamma ray (total spectral gamma ray [HSGR] and computed gamma ray [HCGR]) is highly attenuated inside the drill pipe. The potassium, thorium, and radium components of the natural gamma ray are also attenuated.

Logging Units 2 and 3: base of drill pipe to 136 m

Logging Unit 2 is from the base of the drill pipe to 96 m. The drill hole diameter is unknown for this unit. The natural gamma ray (HSGR and HCGR) of this unit is about 50% of the values of the formation below. The logging density (high-resolution corrected bulk density) is low at 90–96 m, which might reflect a relatively large hole diameter.

Logging Unit 3 is at 96–136 m. The drill hole diameter reached the maximum caliper width of 18 inches for most of this unit. The natural gamma ray increases with depth. The logging compressional

Figure F33. Tools used in triple combo tool string, Site U1505.

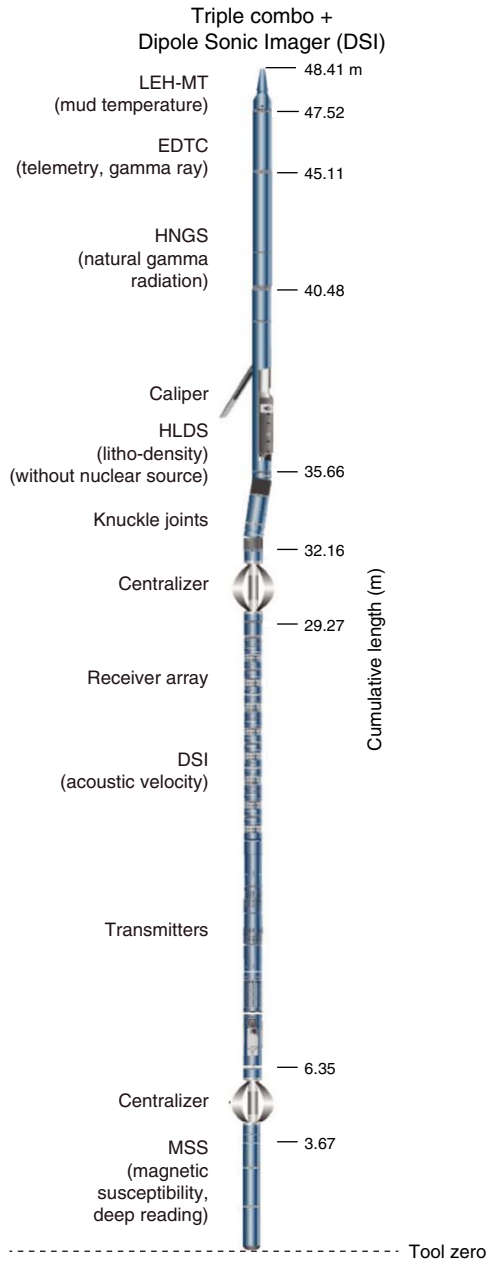

wave velocity (V_P) exhibits large fluctuations that could be due to the enlarged hole dimensions. The shear wave velocity (V_S) shows an anomalous value at 104–110 m for an unknown reason. Logging Units 2 and 3 both correspond to a section of lithostratigraphic Subunit IB (Figure **F34**; see **Lithostratigraphy**).

Logging Units 4–6: 136–341.2 m

Logging Unit 4 is at 136–220 m. The upper portion of this unit has a relatively large hole diameter. Both V_P and V_S are relatively constant. This logging unit corresponds to a section of lithostratigraphic Subunit IB (Figure **F34**; see **Lithostratigraphy**).

Logging Unit 5 is at 200–296 m. The drill hole diameter is close to 14–16 inches for this logging unit. Resistivity increases with depth, whereas most of the other physical properties remain relatively constant. This logging unit corresponds to the bottom of lithostratigraphic Subunit IB and the top of Subunit IC (Figure **F34**; see **Lithostratigraphy**).

Logging Unit 6 is at 296–341.2 m. The drill hole diameter is relatively smaller for this unit. Magnetic susceptibility for this unit is greater than that of logging Unit 5. Logging Unit 6 corresponds to the lower part of lithostratigraphic Subunit IC (Figure **F34**; see **Lithostratigraphy**). Where the logging velocity has relatively good quality (~141.5–333.0 m), the logging V_P is systematically greater than the *P*-wave velocity measured by caliper (PWC) on the working halves of the core sections.

Downhole temperature and heat flow

Four downhole temperature measurements were conducted at Hole U1505C using the APCT-3. The temperature values range from 4.7°C at 36.7 m to 11.7°C at 122.8 m, giving a geothermal gradient of 84.6°C/km (Figure **F35A**). These values, together with the seafloor temperature of 1.4°C, indicate that the temperature increases linearly with depth.

Thermal conductivity under in situ conditions was estimated from laboratory-determined thermal conductivity from Hole U1505C using the method of Hyndman et al. (1974) (see **Physical properties** in the Expedition 367/368 methods chapter [Sun et al., 2018]). Thermal resistance (Figure **F35C**) was then calculated by integrating the inverse of the in situ thermal conductivity over depth (Figure **F35B**). A heat flow of 94.0 mW/m^2 was obtained from the linear fit between temperature and thermal resistance (Figure **F35D**) (Pribnow et al., 2000). The geothermal gradient and heat flow at Site U1505 are comparable to the relatively high values observed at a number of ODP, Integrated Ocean Drilling Program, and IODP sites in this part of the SCS, including Sites U1432 (100.1 mW/m^2), U1499 (114 mW/m^2, this volume), and U1501 (100.2 mW/m^2, this volume).

Figure F34. Downhole logs, Hole U1505C. HSGR = total spectral gamma ray, HCGR = computed (U-free) gamma ray, HROM = high-resolution corrected bulk density, RT = "true" resistivity, MS = magnetic susceptibility, HTHO = HNGS thorium, HURA = HNGS uranium.

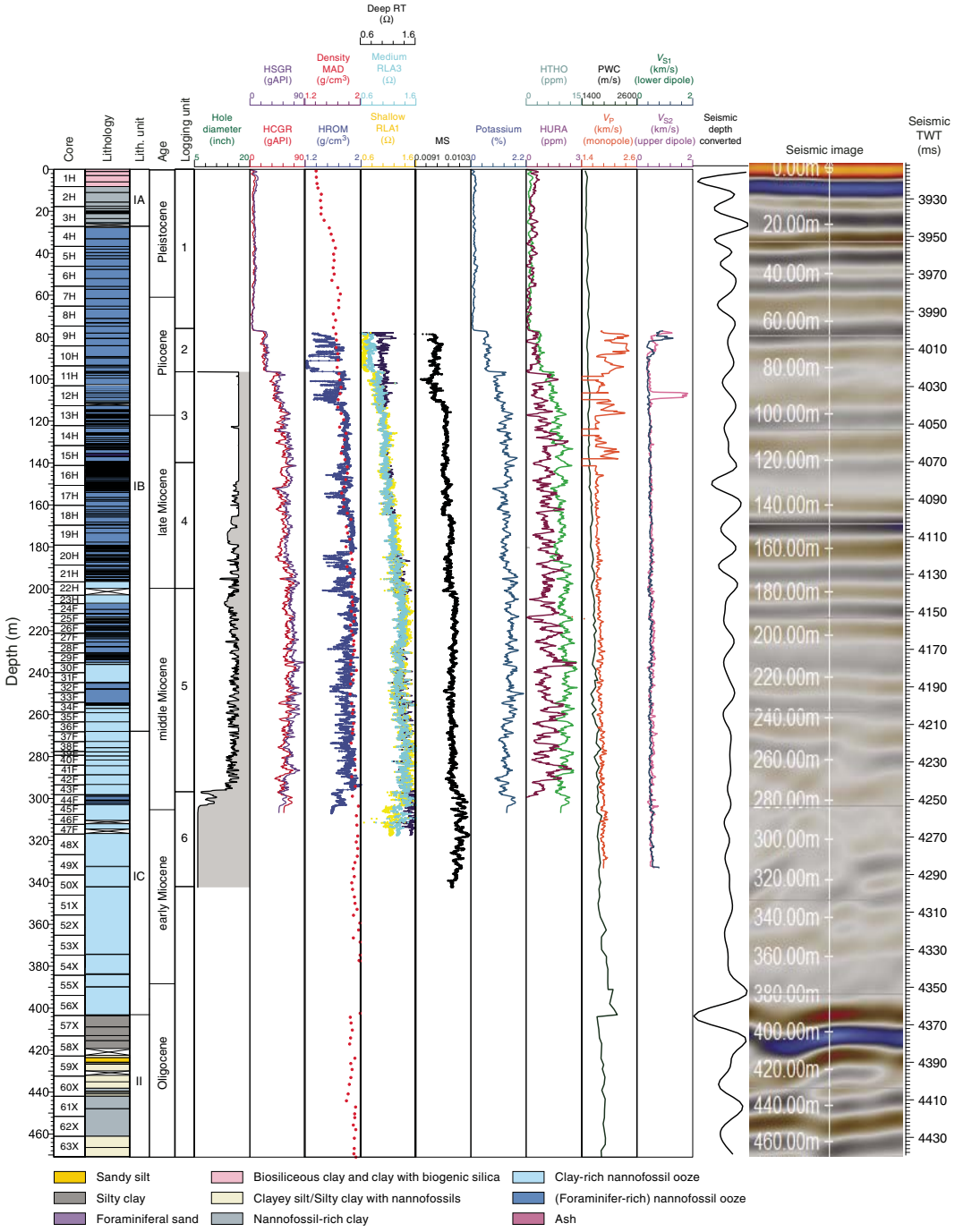

Figure F35. Heat flow calculations, Site U1505. A. Sediment temperatures. B. Thermal conductivity data, Hole U1505C. C. Calculated thermal resistance. D. Bullard plot of heat flow calculated from a linear fit of temperature data.

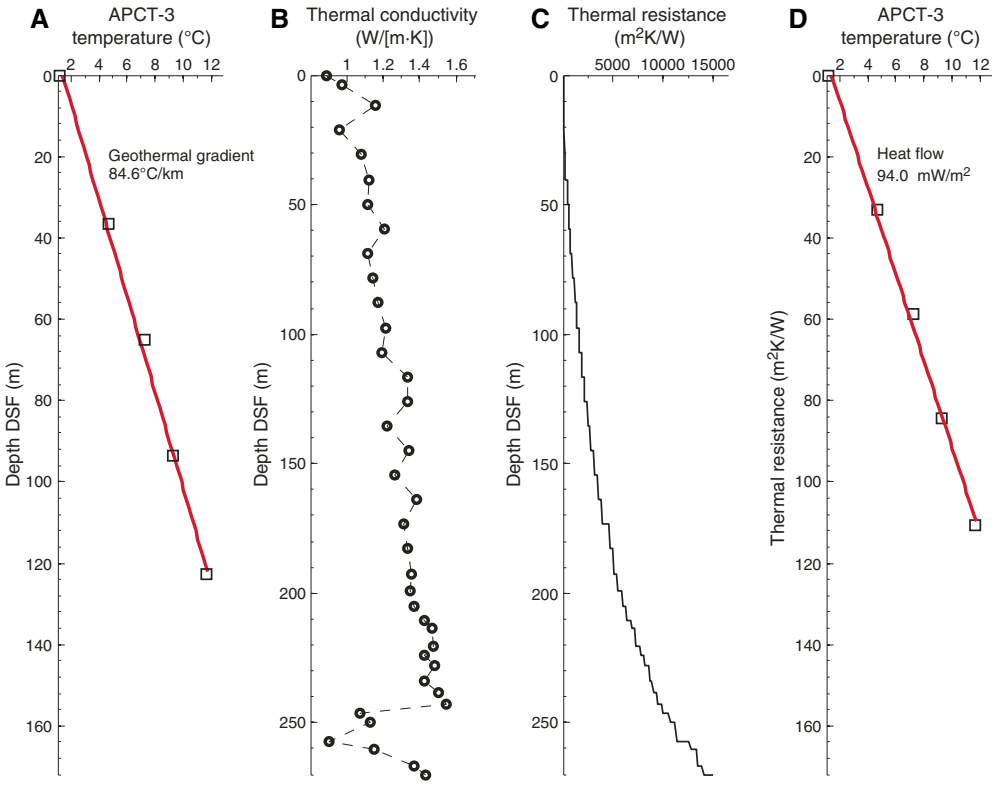

Correlation to seismic data

We conducted two sets of analyses to correlate the core measurements (in meters below seafloor) to the time-based seismic data at Site U1505. First, we analyzed core data and investigated correlation to the seismic reflection profile. Second, we constructed synthetic seismograms using Site U1505 core data and compared the results with the traces in the seismic profile. Preliminary calculations were done during the expedition using a combination of Matlab scripts and Petrel software.

Velocity and density data and comparison with seismic reflectors

Whole-round core measurements were conducted from the seafloor to 480.3 m in Hole U1505C (Figure **F36**) and from the seafloor to 185 m in Hole U1505D. *P*-wave velocity was also measured along the *x*-axis with the PWC system on working-half sections. MAD measurements were performed on discrete samples, one every other section. In addition, HLDS density, V_P, and V_S measurements were obtained from downhole logging in Hole U1505C at 78–341.2 m (see **Physical properties** and **Downhole measurements**). With the outliers filtered out, the whole-round PWL velocity and GRA density data show a good match with the PWC velocity and MAD density of core samples, respectively (Figure **F36**). However, the logging V_P is systematically greater than PWC for depth intervals of good logging velocity data quality (Figure **F37**; see **Downhole measurements**).

A major change in V_P and density was identified at ~403 m, coinciding with the lithologic change from nannofossil ooze–dominated sediments to silt and clay–dominated sediments (Figure **F36**; see **Lithostratigraphy**). We hypothesized that the strong negative reflection (4374 ms two-way traveltime [TWT]) at Site U1505 corresponds to the basin-wide T60 seismic unconformity (reference Point 1; Figures **F36**, **F38**).

Time-depth relationship

A time-depth relationship (TDR) model for Site U1505 was calculated using a polynomial function (Figure **F38A**):

$$d = 0.000285t^2 + 0.745t,$$

where d is depth in meters below seafloor and t is TWT in milliseconds.

We correlated a strong reflector (reference Point RP1; 4374 ms TWT) to a major change in V_P and density at ~403 m (Figure **F36**). This calculated TDR function yields an interval velocity that increases with depth (red line in Figure **F38B**). Where the logging velocity values (blue dots in figure) are relatively good quality (~141.5–333.0 m), they are systematically greater than the PWC core values (green dots) by as much as ~200 m/s. The calculated interval velocity from the TDR model (red line in figure) is much closer to the observed logging V_P than the PWC values.

Using the best-fitting TDR model for Site U1505 (red line in Figure **F38A**), we were able to convert "depth scale" to "timescale" for all core measurements. This conversion enabled us to display the core measurements directly on top of the time-based seismic sections, facilitating identification of correlated features, as illustrated in Figure **F39**.

Figure F36. Comparison of a subset of physical properties (MS, velocity, density, resistivity, and NGR) with seismic waveform (converted to depth scale using best-fitting TDR model) and seismic image (in timescale). Red circle = reference point (discussed in text).

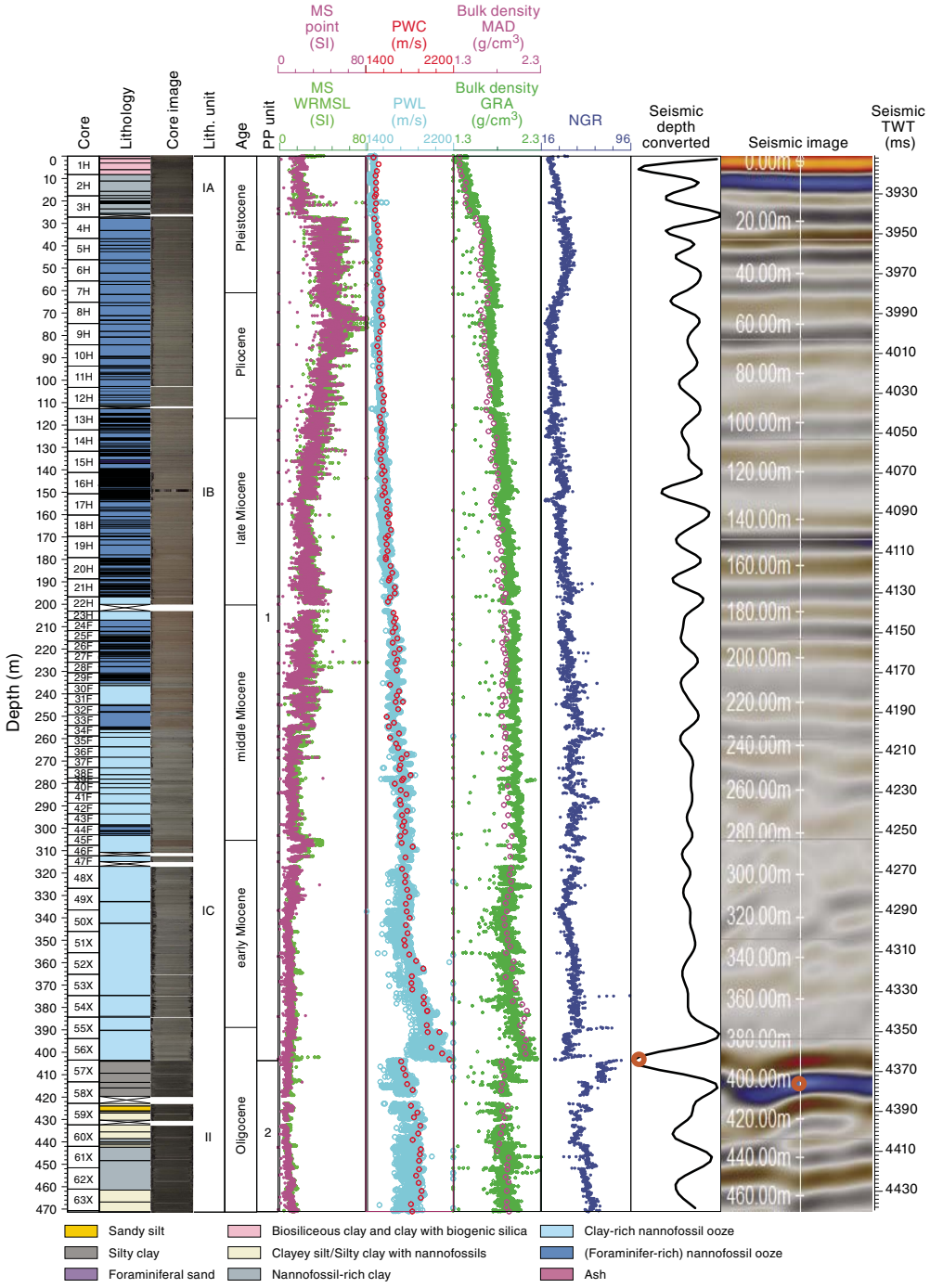

Synthetic seismograms

To further illustrate the relationship between the core measurements at Site U1505 and the seismic reflection profile, the "Seismic interpretation" module in Petrel was used to compute synthetic seismograms based on the relevant core measurements (Figure F37). Synthetic traces were generated by convolving the reflectivity from the density of core samples, an interval velocity model, and with the source wavelet that best fits the seismic data ("Ricker 2"; Figure F37).

Seismic impedance (SI) of a rock layer is the product of its average seismic velocity (V_P) and density (ρ) (i.e., SI = V_P × ρ). The seismic reflection coefficient, in turn, equals the change in seismic impedance between two adjacent rock layers. Thus, we can expect greater amplitudes in the modeled seismogram for rock interfaces with larger values of reflection coefficient. The resulting synthetic seismogram shows a strong "negative" phase reflector at ~400–405 m, consistent with the observed depth of a strong seismic reflector (Figure F37).

Figure F37. Synthetic seismogram, Site U1505. Panels from left to right: PWC seismic velocity used in the calculation, resultant reflection coefficient (RC), real seismic traces with synthetic seismogram inserted in the center, and seismic source function "Ricker 2_25 Hz" used in modeling. TVD = true vertical depth.

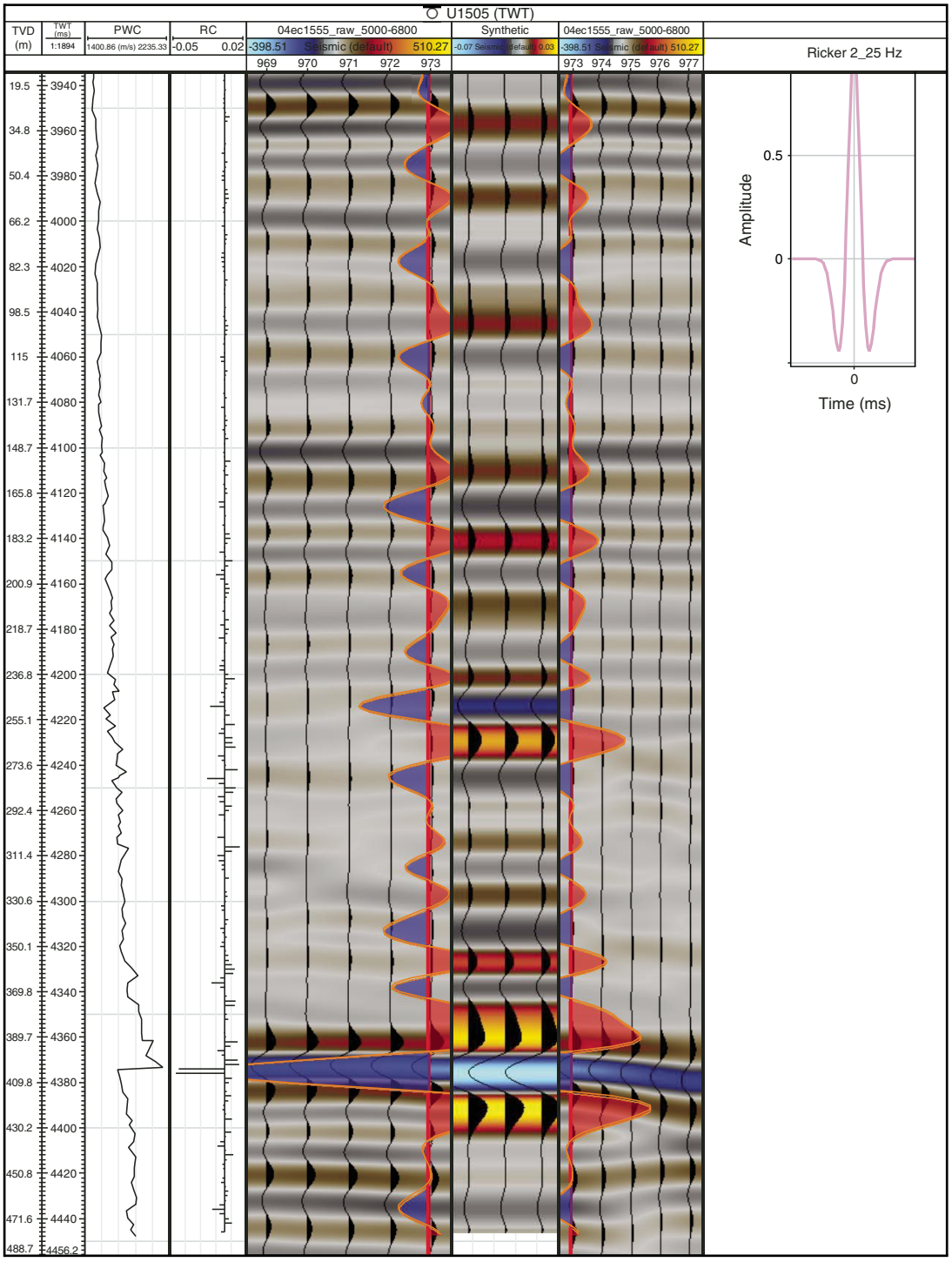

Figure F38. A. Site U1505 TDR curve compared to Site U1501 TDR curve. Red circle = reference Point RP1 at 403 m, which coincides with noticeable changes in density and velocity. B. Hole U1505C PWC, logging V_P, and calculated interval velocity model from TDR model.

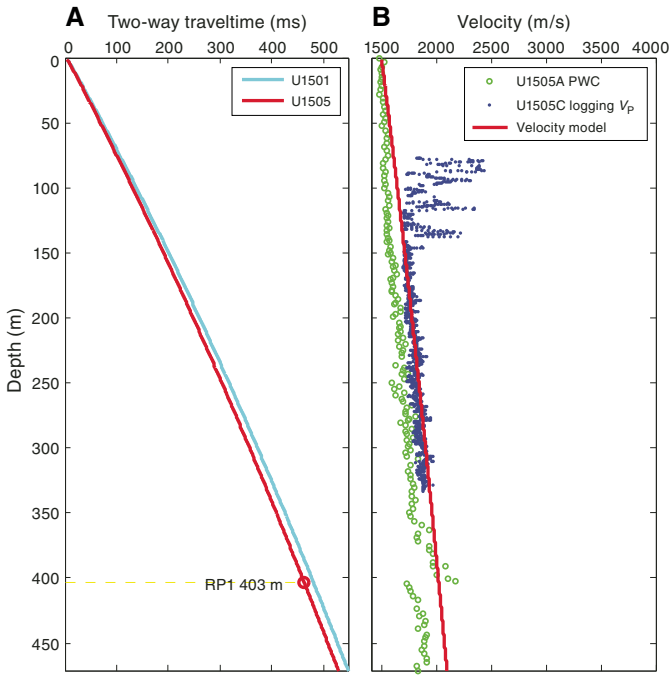

Figure F39. Seismic section (seismic Line 04ec1555) at Site U1505 with lithostratigraphic units overlain at drill hole location. Also shown are selected core measurements converted to depth scale using best-fitting TDR model.

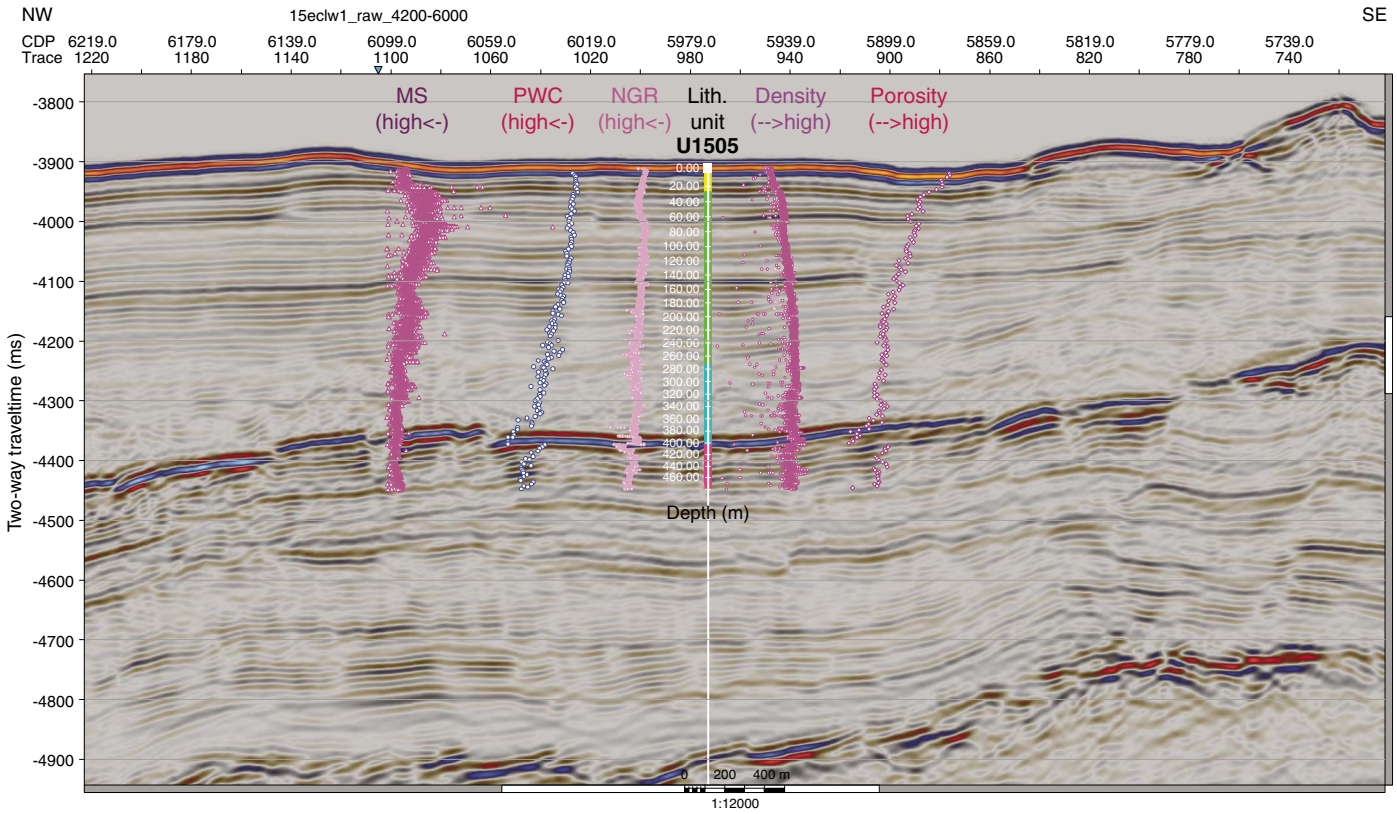

References

Barnes, R.O., and Goldberg, E.D., 1976. Methane production and consumption in anoxic marine sediments. *Geology,* 4(5):297–300. **https://doi.org/10.1130/0091-7613(1976)4<297:MPACIA>2.0.CO;2**

Berner, R.A., and Raiswell, R., 1984. C/S method for distinguishing freshwater from marine sedimentary rocks. *Geology,* 12(6):365–368. **https://doi.org/10.1130/0091-7613(1984)12<365:CMFDFF>2.0.CO;2**

Bethke, C.M., 1986. Inverse hydrologic analysis of the distribution and origin of Gulf Coast-type geopressured zones. *Journal of Geophysical Research: Solid Earth,* 91(B6):6535–6545. **https://doi.org/10.1029/JB091iB06p06535**

Blow, W.H., 1969. Late middle Eocene to recent planktonic foraminiferal biostratigraphy. *Proceedings of the International Conference on Planktonic Microfossils,* 1:199–422.

Boles, J.R., and Franks, S.G., 1979. Clay diagenesis in Wilcox sandstones of southwest Texas: implications of smectite diagenesis on sandstone cementation. *Journal of Sedimentary Petrology,* 49(1):55–70. **https://doi.org/10.1306/212F76BC-2B24-11D7-8648000102C1865D**

Briais, A., Patriat, P., and Tapponnier, P., 1993. Updated interpretation of magnetic anomalies and seafloor spreading stages in the South China Sea: implications for the Tertiary tectonics of Southeast Asia. *Journal of Geophysical Research: Solid Earth,* 98(B4):6299–6328. **https://doi.org/10.1029/92JB02280**

Demaison, G.J., and Moore, G.T., 1980. Anoxic environments and oil source bed genesis. *AAPG Bulletin,* 64:1179–1209.

Drzewiecki, P.A., and Simó, J.A., 2002. Depositional processes, triggering mechanisms and sediment composition of carbonate gravity flow deposits: examples from the Late Cretaceous of the south-central Pyrenees, Spain. *Sedimentary Geology,* 146(1–2):155–189. **https://doi.org/10.1016/S0037-0738(01)00171-3**

Hedges, J.I., Clark, W.A., and Come, G.L., 1988. Organic matter sources to the water column and surficial sediments of a marine bay. *Limnology and Oceanography,* 33(5):1116–1136. **https://doi.org/10.4319/lo.1988.33.5.1116**

Hyndman, R.D., Erickson, A.J., and Von Herzen, R.P., 1974. Geothermal measurements on DSDP Leg 26. *In* Davies, T.A., Luyendyk, B.P., et al., *Initial Reports of the Deep Sea Drilling Project,* 26: Washington, DC (U.S. Govt. Printing Office), 451–463. **https://doi.org/10.2973/dsdp.proc.26.113.1974**

Kirschvink, J.L., 1980. The least-squares line and plane and the analysis of palaeomagnetic data. *Geophysical Journal of the Royal Astronomical Society,* 62(3):699–718. **https://doi.org/10.1111/j.1365-246X.1980.tb02601.x**

Larsen, H.C., Jian, Z., Alvarez Zarikian, C.A., Sun, Z., Stock, J.M., Klaus, A., Boaga, J., Bowden, S.A., Briais, A., Chen, Y., Cukur, D., Dadd, K.A., Ding, W., Dorais, M.J., Ferré, E.C., Ferreira, F., Furusawa, A., Gewecke, A.J., Hinojosa, J.L., Höfig, T.W., Hsiung, K.-H., Huang, B., Huang, E., Huang, X.-L., Jiang, S., Jin, H., Johnson, B.G., Kurzawski, R.M., Lei, C., Li, B., Li, L., Li, Y., Lin, J., Liu, C., Liu, C., Liu, Z., Luna, A., Lupi, C., McCarthy, A.J., Mohn, G., Ningthoujam, L.S., Nirrengarten, M., Osono, N., Peate, D.W., Persaud, P., Qui, N., Robinson, C.M., Satolli, S., Sauermilch, I., Schindlbeck, J.C., Skinner, S.M., Straub, S.M., Su, X., Tian, L., van der Zwan, F.M., Wan, S., Wu, H., Xiang, R., Yadav, R., Yi, L., Zhang, C., Zhang, J., Zhang, Y., Zhao, N., Zhong, G., and Zhong, L., 2018a. Site U1501. *In* Sun, Z., Jian, Z., Stock, J.M., Larsen, H.C., Klaus, A., Alvarez Zarikian, C.A., and the Expedition 367/368 Scientists, *South China Sea Rifted Margin*. Proceedings of the International Ocean Discovery Program, 367/368: College Station, TX (International Ocean Discovery Program). **https://doi.org/10.14379/iodp.proc.367368.105.2018**

Larsen, H.C., Jian, Z., Alvarez Zarikian, C.A., Sun, Z., Stock, J.M., Klaus, A., Boaga, J., Bowden, S.A., Briais, A., Chen, Y., Cukur, D., Dadd, K.A., Ding, W., Dorais, M.J., Ferré, E.C., Ferreira, F., Furusawa, A., Gewecke, A.J., Hinojosa, J.L., Höfig, T.W., Hsiung, K.-H., Huang, B., Huang, E., Huang, X.-L., Jiang, S., Jin, H., Johnson, B.G., Kurzawski, R.M., Lei, C., Li, B., Li, L., Li, Y., Lin, J., Liu, C., Liu, C., Liu, Z., Luna, A., Lupi, C., McCarthy, A.J., Mohn, G., Ningthoujam, L.S., Nirrengarten, M., Osono, N., Peate, D.W., Persaud, P., Qui, N., Robinson, C.M., Satolli, S., Sauermilch, I., Schindlbeck, J.C., Skinner, S.M., Straub, S.M., Su, X., Tian, L., van der Zwan, F.M., Wan, S., Wu, H., Xiang, R., Yadav, R., Yi, L., Zhang, C., Zhang, J., Zhang, Y., Zhao, N., Zhong, G., and Zhong, L., 2018b. Site U1503. *In* Sun, Z., Jian, Z., Stock, J.M., Larsen, H.C., Klaus, A., Alvarez Zarikian, C.A., and the Expedition 367/368 Scientists, *South China Sea Rifted Margin*. Proceedings of the International Ocean Discovery Program, 367/368: College Station, TX (International Ocean Discovery Program). **https://doi.org/10.14379/iodp.proc.367368.107.2018**

Li, C.-F., Lin, J., Kulhanek, D.K., Williams, T., Bao, R., Briais, A., Brown, E.A., Chen, Y., Clift, P.D., Colwell, F.S., Dadd, K.A., Ding, W., Hernández-Almeida, I., Huang, X.-L., Hyun, S., Jiang, T., Koppers, A.A.P., Li, Q., Liu, C., Liu, Q., Liu, Z., Nagai, R.H., Peleo-Alampay, A., Su, X., Sun, Z., Tejada, M.L.G., Trinh, H.S., Yeh, Y.-C., Zhang, C., Zhang, F., Zhang, G.-L., and Zhao, X., 2015. Expedition 349 summary. *In* Li, C.-F., Lin, J., Kulhanek, D.K., and the Expedition 349 Scientists, *South China Sea Tectonics.* Proceedings of the International Ocean Discovery Program, 349: College Station, TX (International Ocean Discovery Program). **https://doi.org/10.14379/iodp.proc.349.101.2015**

Lurcock, P.C., and Wilson, G.S., 2012. PuffinPlot: a versatile, user-friendly program for paleomagnetic analysis. *Geochemistry, Geophysics, Geosystems,* 13(6):Q06Z45. **https://doi.org/10.1029/2012GC004098**

Margielewski, W., Jankowski, L., Krapiec, M., Garecka, M., Hałas, S., and Urban, J., 2017. Analysis of reworked sediments as a basis of the Palaeogene-Neogene palaeogeography reinterpretation: case study of the Roztocze region (SE Poland). *Sedimentary Geology,* 352:14–29. **https://doi.org/10.1016/j.sedgeo.2017.02.009**

Martini, E., 1971. Standard Tertiary and Quaternary calcareous nannoplankton zonation. *In* Farinacci, A. (Ed.), *Proceedings of the Second Planktonic Conference, Roma 1970:* Rome (Edizioni Tecnoscienza), 2:739–785.

Ogg, J.G., Ogg, G., and Gradstein, F.M., 2016. *A Concise Geologic Time Scale 2016:* Boston (Elsevier).

Pribnow, D., Kinoshita, M., and Stein, C., 2000. *Thermal Data Collection and Heat Flow Recalculations for Ocean Drilling Program Legs 101–180:* Hanover, Germany (Institute for Joint Geoscientific Research, Institut für Geowissenschaftliche Gemeinschaftsaufgaben [GGA]). **http://www-odp.tamu.edu/publications/heatflow/ODPReprt.pdf**

Scherer, R.P., Gladenkov, A.Y., and Barron, J.A., 2007. Methods and applications of Cenozoic marine diatom biostratigraphy. *In* Starratt, S.W. (Ed.), *Pond Scum to Carbon Sink: Geological and Environmental Applications of the Diatoms.* Paleontological Society Papers, 13:61–83.

Shum, K.T., and Sundby, B., 1996. Organic matter processing in continental shelf sediments—the subtidal pump revisited. *Marine Chemistry,* 53(1–2):81–87. **https://doi.org/10.1016/0304-4203(96)00014-X**

Sun, Z., Jian, Z., Stock, J.M., Larsen, H.C., Klaus, A., Alvarez Zarikian, C.A., Boaga, J., Bowden, S.A., Briais, A., Chen, Y., Cukur, D., Dadd, K.A., Ding, W., Dorais, M.J., Ferré, E.C., Ferreira, F., Furusawa, A., Gewecke, A.J., Hinojosa, J.L., Höfig, T.W., Hsiung, K.-H., Huang, B., Huang, E., Huang, X.-L., Jiang, S., Jin, H., Johnson, B.G., Kurzawski, R.M., Lei, C., Li, B., Li, L., Li, Y., Lin, J., Liu, C., Liu, C., Liu, Z., Luna, A., Lupi, C., McCarthy, A.J., Mohn, G., Ningthoujam, L.S., Nirrengarten, M., Osono, N., Peate, D.W., Persaud, P., Qui, N., Robinson, C.M., Satolli, S., Sauermilch, I., Schindlbeck, J.C., Skinner, S.M., Straub, S.M., Su, X., Tian, L., van der Zwan, F.M., Wan, S., Wu, H., Xiang, R., Yadav, R., Yi, L., Zhang, C., Zhang, J., Zhang, Y., Zhao, N., Zhong, G., and Zhong, L., 2018. Expedition 367/368 methods. *In* Sun, Z., Jian, Z., Stock, J.M., Larsen, H.C., Klaus, A., Alvarez Zarikian, C.A., and the Expedition 367/368 Scientists, *South China Sea Rifted Margin*. Proceedings of the International Ocean Discovery Program, 367/368: College Station, TX (International Ocean Discovery Program). **https://doi.org/10.14379/iodp.proc.367368.102.2018**

Sun, Z., Stock, J., Jian, Z., McIntosh, K., Alvarez Zarikian, C.A., and Klaus, A., 2016. *Expedition 367/368 Scientific Prospectus: South China Sea Rifted Margin.* International Ocean Discovery Program. **https://doi.org/10.14379/iodp.sp.367368.2016**

Zijderveld, J.D.A., 1967. AC demagnetization of rocks: analysis of results. *In* Collinson, D.W., Creer, K.M., and Runcorn, S.K. (Eds.), *Methods in Palaeomagnetism:* Amsterdam (Elsevier), 254–286.